

AD-A253 867



AGARD-CP-479

1

AGARD-CP-479

# AGARD

ADVISORY GROUP FOR AEROSPACE RESEARCH & DEVELOPMENT

7 RUE ANCELLE 92200 NEUILLY SUR SEINE FRANCE

AGARD CONFERENCE PROCEEDINGS No.479

## Hypersonic Combined Cycle Propulsion

(La Propulsion Hypersonique à Cycles Combinés)

DTIC  
ELECTE  
JUN 05 1992

NORTH ATLANTIC TREATY ORGANIZATION



DISTRIBUTION AND AVAILABILITY  
ON BACK COVER

# COMPONENT PART NOTICE

THIS PAPER IS A COMPONENT PART OF THE FOLLOWING COMPILATION REPORT:

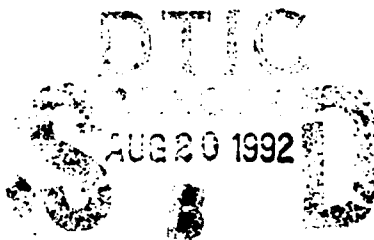
TITLE: Hypersonic Combined Cycle Propulsion Panel Symposium (75th) Held  
in Madrid, Spain on 28 May - 1 June 1990 (La Propulsion Hypersonique a  
Cycles Combines.

TO ORDER THE COMPLETE COMPILATION REPORT, USE AD-A253 867.

THE COMPONENT PART IS PROVIDED HERE TO ALLOW USERS ACCESS TO INDIVIDUALLY AUTHORED SECTIONS OF PROCEEDING, ANNALS, SYMPOSIA, ETC. HOWEVER, THE COMPONENT SHOULD BE CONSIDERED WITHIN THE CONTEXT OF THE OVERALL COMPILATION REPORT AND NOT AS A STAND-ALONE TECHNICAL REPORT.

THE FOLLOWING COMPONENT PART NUMBERS COMPRISE THE COMPILATION REPORT:

AD#: AD-P007 938 AD#: AD-P007 965  
AD#:                      AD#:                       
AD#:                      AD#:                     



**DISTRIBUTION STATEMENT A**  
Approved for public release;  
Distribution Unlimited

Accession For	
NTIS GRA&I	<input checked="checked" type="checkbox"/>
DTIC TAB	<input type="checkbox"/>
Unannounced	<input type="checkbox"/>
Justification	
By	
Distribution	
Availability Codes	
Dist	
A-1	20

NORTH ATLANTIC TREATY ORGANIZATION  
 ADVISORY GROUP FOR AEROSPACE RESEARCH AND DEVELOPMENT  
 (ORGANISATION DU TRAITE DE L'ATLANTIQUE NORD)

AGARD Conference Proceedings No.479

# Hypersonic Combined Cycle Propulsion

(La Propulsion Hypersonique à Cycles Combinés)



Accession For	
NTIS CRA&I	<input checked="" type="checkbox"/>
DTIC TAB	<input type="checkbox"/>
Unannounced	<input type="checkbox"/>
Justification	
By	
Distribution /	
Availability	
Dist	Availability for Special
A-1	

# The Mission of AGARD

According to its Charter, the mission of AGARD is to bring together the leading personalities of the NATO nations in the fields of science and technology relating to aerospace for the following purposes:

- Recommending effective ways for the member nations to use their research and development capabilities for the common benefit of the NATO community;
- Providing scientific and technical advice and assistance to the Military Committee in the field of aerospace research and development (with particular regard to its military application);
- Continuously stimulating advances in the aerospace sciences relevant to strengthening the common defence posture;
- Improving the co-operation among member nations in aerospace research and development;
- Exchange of scientific and technical information;
- Providing assistance to member nations for the purpose of increasing their scientific and technical potential;
- Rendering scientific and technical assistance, as requested, to other NATO bodies and to member nations in connection with research and development problems in the aerospace field.

The highest authority within AGARD is the National Delegates Board consisting of officially appointed senior representatives from each member nation. The mission of AGARD is carried out through the Panels which are composed of experts appointed by the National Delegates, the Consultant and Exchange Programme and the Aerospace Applications Studies Programme. The results of AGARD work are reported to the member nations and the NATO Authorities through the AGARD series of publications of which this is one.

Participation in AGARD activities is by invitation only and is normally limited to citizens of the NATO nations.

The content of this publication has been reproduced  
directly from material supplied by AGARD or the authors.

Published December 1990

Copyright © AGARD 1990  
All Rights Reserved

ISBN 92-835-0594-8



*Printed by Specialised Printing Services Limited  
40 Chigwell Lane, Loughton, Essex IG10 3TZ*



# Recent Publications of the Propulsion and Energetics Panel

## CONFERENCE PROCEEDINGS (CP)

### Engine Handling

AGARD CP 324, February 1983

### Viscous Effects in Turbomachines

AGARD CP 351, September 1983

### Auxiliary Power Systems

AGARD CP 352, September 1983

### Combustion Problems in Turbine Engines

AGARD CP 353, January 1984

### Hazard Studies for Solid Propellant Rocket Motors

AGARD CP 367, September 1984

### Engine Cyclic Durability by Analysis and Testing

AGARD CP 368, September 1984

### Gears and Power Transmission Systems for Helicopters and Turboprops

AGARD CP 369, January 1985

### Heat Transfer and Cooling in Gas Turbines

AGARD CP 390, September 1985

### Smokeless Propellants

AGARD CP 391, January 1986

### Interior Ballistics of Guns

AGARD CP 392, January 1986

### Advanced Instrumentation for Aero Engine Components

AGARD CP 399, November 1986

### Engine Response to Distorted Inflow Conditions

AGARD CP 400, March 1987

### Transonic and Supersonic Phenomena in Turbomachines

AGARD CP 401, March 1987

### Advanced Technology for Aero Engine Components

AGARD CP 421, September 1987

### Combustion and Fuels in Gas Turbine Engines

AGARD CP 422, June 1988

### Engine Condition Monitoring — Technology and Experience

AGARD CP 448, October 1988

### Application of Advanced Material for Turbomachinery and Rocket Propulsion

AGARD CP 449, March 1989

### Combustion Instabilities in Liquid-Fuelled Propulsion Systems

AGARD CP 450, April 1989

### Aircraft Fire Safety

AGARD CP 467, October 1989

### Unsteady Aerodynamic Phenomena in Turbomachines

AGARD CP 468, February 1990

### Secondary Flows in Turbomachines

AGARD CP 469, February 1990

### Hypersonic Combined Cycle Propulsion

AGARD CP 479, December 1990

92-14767  


## **ADVISORY REPORTS (AR)**

**Through Flow Calculations in Axial Turbomachines** (*Results of Working Group 12*)  
AGARD AR 175, October 1981

**Alternative Jet Engine Fuels** (*Results of Working Group 13*)  
AGARD AR 181, Vol.1 and Vol.2, July 1982

**Suitable Averaging Techniques in Non-Uniform Internal Flows** (*Results of Working Group 14*)  
AGARD AR 182 (in English and French), June/August 1983

**Producibility and Cost Studies of Aviation Kerosines** (*Results of Working Group 16*)  
AGARD AR 227, June 1985

**Performance of Rocket Motors with Metallized Propellants** (*Results of Working Group 17*)  
AGARD AR 230, September 1986

**Recommended Practices for Measurement of Gas Path Pressures and Temperatures for Performance Assessment of Aircraft Turbine Engines and Components** (*Results of Working Group 19*)  
AGARD AR 245, June 1990

**The Uniform Engine Test Programme** (*Results of Working Group 15*)  
AGARD AR 248, February 1990

**Test Cases for Computation of Internal Flows in Aero Engine Components** (*Results of Working Group 18*)  
AGARD AR 275, July 1990

## **LECTURE SERIES (LS)**

**Operation and Performance Measurement of Engines in Sea Level Test Facilities**  
AGARD LS 132, April 1984

**Ramjet and Ramrocket Propulsion Systems for Missiles**  
AGARD LS 136, September 1984

**3-D Computation Techniques Applied to Internal Flows in Propulsion Systems**  
AGARD LS 140, June 1985

**Engine Airframe Integration for Rotorcraft**  
AGARD LS 148, June 1986

**Design Methods Used in Solid Rocket Motors**  
AGARD LS 150, April 1987  
AGARD LS 150 (Revised), April 1988

**Blading Design for Axial Turbomachines**  
AGARD LS 167, June 1989

**Comparative Engine Performance Measurements**  
AGARD LS 169, May 1990

## **AGARDOGRAPHS (AG)**

**Manual for Aeroelasticity in Turbomachines**  
AGARD AG 298/1, March 1987  
AGARD AG 298/2, June 1988

**Measurement Uncertainty within the Uniform Engine Test Programme**  
AGARD AG 307, May 1989

**Hazard Studies for Solid Propellant Rocket Motors**  
AGARD AG 316, September 1990

## **REPORTS (R)**

**Application of Modified Loss and Deviation Correlations to Transonic Axial Compressors**  
AGARD R 745, November 1987

**Rotorcraft Drivetrain Life Safety and Reliability**  
AGARD R 775, June 1990

# Theme

Hypersonic vehicles for military and space transportation applications are receiving increased attention among the leading aerospace nations. Hypersonic vehicle technologies have been the subject of meetings of several AGARD Panels, each addressing the technical issues from their particular discipline perspectives. It is appropriate and timely for the Propulsion and Energetics Panel to sponsor a Symposium on hypersonic propulsion. The proposed Symposium will deal with the major propulsion aspects including high temperature materials, components, combustion and computational methods. The Symposium will also explore relevant propulsion and propulsion/vehicle concepts. The interest of the member countries is high, reflecting both the several hypersonic vehicle development efforts and the broad interest in key areas as propulsion and computational methods. Adequate basic research is going on in many countries, and a technical interchange will be of great value.

# Thème

Les véhicules hypersoniques destinés à des applications militaires et spatiales suscitent de plus en plus d'intérêt de la part des pays les plus avancés en matière de recherche et de réalisations aérospatiales.

La technologie des véhicules hypersoniques a déjà fait l'objet de différentes réunions organisées par les Panels de l'AGARD, chaque Panel abordant les aspects techniques de son propre point de vue. Nous considérons qu'il est opportun et approprié que le Panel de Propulsion et d'Energétique organise un symposium sur la propulsion hypersonique. Le symposium proposé traitera les principaux aspects de la question, y compris les matériaux à haute résistance thermique, les composants, la combustion et les méthodes de calcul. Des concepts de propulsion et d'intégration propulsion/véhicule applicables seront également examinés lors de la réunion.

Les pays membres de l'OTAN s'intéressent vivement à ce sujet, ce qui est le reflet à la fois des différents projets de développement de véhicules hypersoniques qui sont en cours, et de l'intérêt manifesté de façon générale pour les domaines clés tels que la propulsion et les méthodes de calcul.

Des travaux de recherche de base appropriés ont été entamés par de nombreux pays et un échange d'informations techniques serait d'une grande utilité.

# Propulsion and Energetics Panel

**Chairman** M. l'Ing. Princ. de l'Armement Ph. Ramette  
Société Européenne de Propulsion  
Attaché au Directeur Technique pour  
les Activités Spatiales  
Boîte Postale 303  
92156 Suresnes Cedex  
France

**Deputy Chairman** Prof. Dr A.Üçer  
Middle East Technical University  
ODTÜ  
Makina Muh. Bölümü  
Ankara  
Turkey

## PROGRAMME COMMITTEE

Prof. Dr-Ing. H.Weyer (Chairman)  
Direktor  
Institut für Antriebstechnik  
DLR  
Postfach 90 60 58  
5000 Köln 90  
Federal Republic of Germany

Ir W.B.de Wolf  
National Aerospace Laboratory  
P.O. Box 153  
8300 AD Emmeloord  
The Netherlands

Dr E.Fraga Fernandez Cuevas  
Instituto Nacional de Tecnica  
Aeroespacial (INTA)  
Motopropulsion y Energia  
Carretera de Ajalvir, km.5  
Torrejon de Ardoz (Madrid)  
Spain

Mr K.R.Garwood  
Rolls Royce Ltd.  
Whittle House, P.O. Box 3  
Filton, Bristol BS12 7QE  
United Kingdom

Prof. Ch.Hirsch  
Vrije Universiteit Brussel  
Dienst Stromingsmechanica  
Pleinlaan 2  
1050 Brussel  
Belgium

Dr-Ing. G.Maoli  
FIAT s.p.A. Direzione  
Via L.Bissolati 57  
00187 Roma  
Italy

M. l'Ing. Princ. de l'Armement Ph.Ramette  
Société Européenne de Propulsion  
Boîte Postale 303  
92156 Suresnes Cedex  
France

Mr G.M.Reck  
Director, Propulsion, Power and  
Energy Division  
OAST-Code RP  
NASA Headquarters  
Washington DC 20546  
United States

## HOST NATION COORDINATOR

Dr E.Fraga Fernandez Cuevas

## PANEL EXECUTIVE

Mr G.Gruber

**Mail from Europe**  
AGARD-OTAN  
Attn: PEP Executive  
7 rue Ancelle  
92200 Neuilly-sur-Seine  
France

**Mail from US and Canada**  
AGARD-NATO  
Attn: PEP Executive  
APO New York 09777

Telephone: 33 (1) 47 38 57 85  
Telex: 610 176 (France)  
Telefax: 33 (1) 47 38 57 99

## ACKNOWLEDGEMENT

The Propulsion and Energetics Panel wishes to express its thanks to the National Authorities from Spain for the invitation to hold this meeting in Madrid, and for the facilities and personnel which made the meeting possible.

# Contents

	Page
<b>Recent Publications of PEP</b>	iii
<b>Theme/Thème</b>	v
<b>Propulsion and Energetics Panel</b>	vi
<b>Technical Evaluation Report</b> by G.Winterfeld	x
	<b>Reference</b>
<b>Keynote Address</b> <b>The Potential and Practicality of High Speed Combined Cycle Engines</b> by E.T.Curran	K
 <b>SESSION I – TECHNOLOGY REVIEW OF HYPERSONIC PROPULSION/MISSION REQUIREMENTS</b>	
<b>Hypersonic Propulsion: Past and Present</b> by C.S.Tarifa	1
<b>L'Etude du Statoréacteur Supersonique et Hypersonique en France de 1950 à 1974</b> <i>Application aux Moteurs Combinés Aérobie</i> par R.Marguet, P.Berton et F.Hirsinger	2
<b>Navigation, Guidance and Trajectory Optimization for Hypersonic Vehicles</b> by R.L.Schultz, M.J.Hoffman, A.M.Case and S.I.Sheikh	3
<b>Trajectory Optimization Considerations for Ramjet Engines</b> by F.G.J.Kremer	4
 <b>SESSION II – PROPULSION CONCEPTS</b>	
<b>Etude Comparative de Différents Systèmes de Propulsion Combinée</b> par Ph.Ramette, D.Scherrer et M.Doublier	5
<b>Hypersonic Propulsion: Status and Challenge</b> by R.W.Guy	6
<b>Paper 7 withdrawn</b>	
<b>Airbreathing Propulsion for Space Transport: New Concepts, Special Problems and Attempts at Solutions</b> by H.Künkler	8
<b>Turbojet Potential for Hypersonic Flight</b> by J.M.Stricker and D.J.Essman	9
 <b>SESSION III – PROPULSION CONCEPTS</b>	
<b>Airbreathing Propulsion for Transatmospheric Flight</b> by G.Andrei, U.Borio and M.Maiurano	10

	<b>Reference</b>
<b>Echangeur Compact pour Moteur à Composants Inverses (M.C.I.)</b> par Y.Ribaud	<b>11</b>
<b>Design Considerations for Combined Air Breathing — Rocket Propulsion Systems</b> by D.L.Kors	<b>12</b>
<b>Paper 13 withdrawn</b>	
<b>Cryogenic Hydrogen-Induced Air-Liquefaction Technologies</b> by W.J.D.Escher	<b>14</b>

#### **SESSION IV — AIR INTAKE FLOW**

<b>Aerodynamics of High Speed Air Intakes — Status Report on AGARD FDP-WG 13 Results</b>	<b>15</b>
<b>Etudes de Prises d'Air pour Lanceurs Aérobies Hypersoniques</b> <i>Supersonic-Hypersonic Inlet Studies for Aerospaceplane</i> par C.Sans, P.Champigny, P.Duveau et C.Ginovart	<b>16</b>
<b>Some Aspects of Shock-Wave Boundary Layer Interaction Relevant to Intake Flows</b> by J.L.Stollery	<b>17</b>
<b>Computational Modeling and Validation for Hypersonic Inlets</b> by L.A.Povinelli	<b>18</b>

#### **SESSION V — TURBOMACHINERY**

<b>Design Considerations of a High Expansion Ratio Hydrogen Turbine</b> by A.T.Holmes and R.Varvill	<b>19</b>
<b>Etude d'une Turbine Multi-Etages à Hydrogène pour des Applications en Propulsion Combinée</b> par Y.Marion et J.Desclaux	<b>20</b>

#### **SESSION VI — COMBUSTION AND RAM/SCRAMJETS**

<b>Aerodynamics and Stabilization of Combustion of Hydrogen Jets Injected into Subsonic Airflow</b> by J.Koopman, M.Rachner, H.Wiegand and H.Eickhoff	<b>21</b>
<b>Experimental Investigations on the Transition from Stable to Unstable Combustion by Means of Active Instability Control</b> by S.Gleis, D.Vortmeyer and W.Rau	<b>22</b>
<b>Design Techniques for Dual Mode Ram-Scramjet Combustors</b> by F.S.Billig, S.Corda and P.P.Pandolfini	<b>23</b>
<b>Use of Secondary Flows for Rapid Mixing in Scramjet Combustors</b> by G.V.R.Rao and A.A.Heiba	<b>24</b>
<b>Performance Characteristics of Hypersonic Detonation Wave Ramjets</b> by T.M.Atamanchuck and J.P.Sislian	<b>25</b>

#### **SESSION VII — COMBUSTION AND RAM/SCRAMJETS**

<b>Analytical and Experimental Investigations of the Oblique Detonation Wave Engine Concept</b> by G.P.Menees, H.G.Adelman and J.L.Cambier	<b>26</b>
<b>Paper 27 withdrawn</b>	

**Reference**

**Etude Expérimentale de Statoréacteurs pour Missiles et Applications Potentielles pour les Statoréacteurs dans la Propulsion Combinée** 28  
par A.Chevalier, P.-G.Sava et J.-P.Minard

**Theoretical and Experimental Performance of a Solid Fuel Ramjet Combustion Cycle for Hypersonic Flight Conditions** 29  
by P.J.M.Elands, P.A.O.G. Korting, R.G.Veraar and F.Dijkstra

**Highly Integrated Ducted Rocket Propulsion Modules for Future Hypersonic Tactical Missiles** 30  
by H.L.Weinreich

**SESSION VIII – NOZZLE FLOW**

**Pitot Surveys of Two Moderately Under-Expanded Jets** 31  
by T.M.Cain and T.V.Jones

**The Effect of Combustor Flow Nonuniformity on the Performance of Hypersonic Nozzles** 32  
by P.Goel, S.L.Barson and S.D.Halloran

**Reacting Shock Waves in Hypersonic Propulsion Applications** 33  
by M.Onofri

**Viscous Three-Dimensional Analyses for Nozzles for Hypersonic Propulsion** 34  
by G.J.Harloff, D.R.Reddy and H.T.Lai

**2-D Supersonic Nozzle Design** 35  
by M.Going and J.Heyse

**SESSION IX – HIGH TEMPERATURE MATERIALS**

**Materials for Hypersonic Engines** 36  
by T.M.F.Ronald

**Paper 37 withdrawn**

**Matériaux et Systèmes de Matériaux pour la Propulsion Combinée** 38  
par D.Boury, A.Beaurain, A.Lasalmonie et Y.Honnorat

**Paper 39 withdrawn**

## TECHNICAL EVALUATION REPORT

by

G. Winterfeld  
Deutsche Forschungsanstalt für Luft- und Raumfahrt e.V.  
Institute for Propulsion Technology  
Linder Höhe, 5000 Köln 90, W.-Germany

### INTRODUCTION

Since the middle of the last decade the trends in aerospace research and development are characterized by renewed scientific and technical interest in problems of hypersonic flight. Technology programs have been set up in the alliance's countries, which in the long run aim at the realization of transatmospheric vehicles for space transportation. Work in progress, presently, is oriented towards concrete flight missions, as well as to basic technologies needed for hardware demonstration. The magnitude of this fascinating technological task demands for increased cooperation as well as for extended exchange of information and experience between the experts. Therefore, after a break of more than 20 years, AGARD's Propulsion and Energetics Panel has returned to this field of work and selected "Hypersonic Combined Cycle Propulsion" as the subject of its 75th. Meeting, held at Madrid, Spain, May 28, to June 1, 1990.

The meeting comprised a keynote lecture and 34 technical papers, arranged in nine sessions. Five originally scheduled papers had to be withdrawn due to restrictions imposed by national authorities. In order to bridge the gap to former activities historical aspects of the subject have been partly included. The technical content of these 35 papers will be evaluated under the following subject areas, which differ slightly from the published program of the meeting.

1. General overview and flight mechanics considerations
2. Propulsion systems for hypersonic vehicles and missiles
3. Component technology
4. Materials for hypersonic engines
5. Conclusions and recommendations.

### GENERAL OVERVIEW AND FLIGHT MECHANIC CONSIDERATIONS

In his keynote lecture, E.T. Curran reviewed the potential of hypersonic propulsion systems. Besides stressing the need for engine/vehicle integration he pointed to several important features which determine the practical application of combined cycle engines. Of paramount importance is to stretch the performance of the basic engine types over a larger range of operating parameters than hitherto usual. For turbo-based accelerators, application of new materials, all-supersonic throughflow as well as inlet and nozzle designs promise higher thrust-to-weight ratios, whereas extension of the Mach number range can be achieved by precooling. Improvements in specific impulse of rocket-based accelerators can be obtained by a variety of combinations of the main components, ranging from simple ejector rockets to complicated liquid-air collecting engines. A main challenge is posed for all engine cycles employing precooling or liquefaction by the need for compact and low-mass heat exchangers, which demand also for cryogenic or endothermic fuels as heat sinks. As far as hardware testing of combined cycle engines during their development is concerned new problems are posed by the requirement for demonstration of stable transition from one operational mode to the next. Also new processes for the true simulation of high-speed high-altitude conditions in a ground test facility, avoiding vitiation of the test air are required. Lastly, flight testing of propulsion systems will be a fundamental need in the development process.

One of the most important requirements of hypersonic flight missions is minimum fuel consumption, demanding for a continuous optimization of aerodynamic, trajectory and engine parameters along the whole flight path. This is brought to the attention of engine designers by paper 4 of F. Kremer, using the ramjet part of a hypersonic engine as an example. He shows that flight mechanic and aerodynamic parameters like acceleration, climb angle, angle of attack, wing loading, trajectory dynamic head and vehicle mass, and engine parameters like thrust vector angle and specific fuel consumption are all closely interrelated and have to be optimized jointly, if minimum fuel consumption is to be achieved. Thus, the right choice of the engine size needs the close cooperation of engine and vehicle designers, and still more important, vehicle design and trajectory optimization has to involve the engine designer.

The system of mathematical relationships between flight mechanics, aerodynamic, structural and engine operational parameters is also the basis for optimum guidance and control for a hypersonic vehicle. In paper 3, R.L. Schultz et al. reported on a computational system which is capable of on-board generation of energy-optimized flight trajectories for vehicle control, thereby improving vehicle autonomy. Minimum fuel usage, flight trajectory constraints, accommodation for uncertainties of the individual design models are basic inputs to the computation system, of which the above mentioned interrelationship between trajectory and aerodynamic parameters and engine parameters are substantial parts.

These three introductory papers have clearly shown that hypersonic vehicle design and operation is strongly coupled to the flight mission objectives and to the characteris-



tics of the propulsion systems. Thus, studies on the design optimization of hypersonic propulsion systems, which concentrate on the hardware aspects of the propulsion system only, are surely not sufficient, if optimum vehicle design and operation is to be achieved.

#### PROPULSION SYSTEMS FOR HYPERSONIC VEHICLES AND MISSILES

Presentations on this subject were introduced by 2 historical reviews of combined cycle and ramjet propulsion. The first report by Sanchez Tarifa described the evolution of ramjets since the beginning of this century. The second report by Marguet summarized the numerous and well-known French activities on the application of combined cycle propulsion systems in the range of low to medium flight Mach numbers. Projects like the turbo-ramjet powered "Griffon" or the Leduc 22 aircraft, the missiles ASMP, Stalalex, Scorpion or the dual-model ramjet ESOPE shows the wealth of theoretical and practical experience, by ground as well as by flight testing, which is available in France.

#### Studies on Combined Propulsion Systems for Space Transportation Vehicles

Propulsion systems for hypersonic vehicles, preferably space launchers, have been treated in several contributions. Emphasis was placed on the qualification of the individual basic engine types and their integration into a propulsion system for single-stage and two-stage space transportation vehicles. As these investigations were partly carried out from a general point of view and not always based on specific ascent trajectories, the results and conclusions from these papers differ to some extent. Nevertheless, there seems to be agreement, that for SSTO-vehicles propulsion systems based on combinations of ramjets/scramjets and rockets as boosters for the lower and higher speed level of the ascent trajectory are best suited. This, mainly because of their high thrust-to-mass ratio, and although in the lower speed range relatively low specific impulses have to be encountered (papers 5, 10, 12). On the other hand, for the propulsion systems of the first stage of TSTO-vehicles, priority is placed with high specific impulse; hence combinations of turbo engines for the lower speed range with ramjets for the higher Mach numbers are favoured (papers 5, 8, 10). The higher flexibility of turbo engines is viewed as an advantage despite their lower thrust-to-mass ratio. Whether precooling the air mass flow before it enters the turbo engine is a suitable means for shifting the transition to the ramjet mode to higher flight Mach numbers depends on the demonstration of extremely light-weight heat exchangers. For this purpose H. Kunkler proposes in paper 8 to use heat exchangers with rather low effectiveness. The subject of extending the operational range of turbo engines towards Mach 5 is treated in Paper 9 by J.M. Stricker et al.. The necessary prerequisites are improvements in nozzle gross thrust coefficient, component efficiencies and matching, as well as increased turbine inlet temperatures. The analysis shows that, based on components optimized for the enlarged operational range and on the application of advanced materials, an afterburning turbojet without precooling promises good performance, if compared to a turboramjet or a turboexpander-ramjet. Although none of the papers dug into the depth of the specific problem, a chance is given to the turbofan engine only, if the trajectory includes longer cruise phases at low speed. Design criteria for turbo engines and ramjets were discussed in paper 5. As to the results, it has to be remarked that, if the design strategy were based on the requirements of the specific mission objective (e.g. paper 4), different recommendations for the design of ramjets may be deduced.

A description of the progress achieved in the field of scramjets in recent years as well as a trade-off study for the development and application of scramjets are given in papers 6 and 12. The latter shows the high Mach number limits of scramjet application if in performance calculations the efficiencies of inlet, combustor and nozzle are varied with realistic component efficiencies. The useful range of application of scramjets is predicted to end between Mach 12 and 14, if compared to liquid rockets. As is well known, the decisive parameters are inlet and nozzle efficiency. However, the total pressure loss of the supersonic combustion process, which is not specifically mentioned, may worsen the quantitative results still more.

In view of a possible development of hypersonic propulsion systems several general conclusions and requirements can be formulated from what has been discussed in the above mentioned papers. The selection of a propulsion system for a hypersonic vehicle depends strongly on the mission objective, as well as on the development risk, one is prepared to take. The latter concerns mainly the technology base for combined cycle hypersonic engines which is not yet firmly established. Therefore, particularly the estimate achievable thrust-to-mass ratios contain major uncertainties, at present. Here, improvements can be expected from progress in the development of new light-weight high-temperature materials. Both, the complexity of the space flight missions and of the propulsion systems determine a number of problem areas in which progress is urgently needed. First, the proper integration of the propulsion system and the vehicle has to be mastered, this the more, as the complete undersurface of the vehicle is used for propulsion purposes and different power settings influence the force and momentum book-keeping and thus vehicle control. Moreover, for SSTO-vehicles solutions for the integration of the rocket engines without additional external drag are needed. The smooth transition from one engine mode to the next places very difficult requirements with the control system, since not only much more control variables have to be handled, but also control of the engine transients as well as the thermal management (e.g. active cooling) of the vehicle has to be included.

The proof of concept of hypersonic propulsion systems including mode transition requires ground test facilities as well as flight-testing. Larger facilities which can handle continuous testing at high Mach numbers of engine modules of larger size than

hitherto would be urgently needed, in order to establish a data base for upscaling. However, they are very expensive to build and operate. For Mach numbers beyond about 8, pulse type facilities are hoped to be an alternative. They promise, at least partly, less vitiation of the test air, however they allow only short test times of 0.5 - 1 msec. Therefore, doubts are raising as to whether these facilities are actually suitable for scramjet engine testing. This seems to indicate that in the future more emphasis might be placed with flight testing of hypersonic engines.

A positive development must be registered in the field of CFD application in hypersonic engine development and testing. Progress made in this field in recent years allows to use theoretical calculations as a reliable tool not only for engine component design but also for the support of propulsion module testing in wind tunnels. However, further progress is needed in the field of turbulence modeling particularly for supersonic flows with mixing and chemical reaction. Nevertheless, CFD will be increasingly used in hypersonic engine design and investigations, not the least, because of the limited availability of suitable test facilities.

#### Specific Problems of Hypersonic Propulsion Systems and Modules

Air liquefaction techniques for the use in hypersonic propulsion systems as developed in the US during the last decades are described in a very comprehensive report by W. Escher (paper 14). Starting from the basic LACE-proposal of the fifties, it is elaborated how by several innovative steps some of the basic cycle limitations have been removed in the following years, e.g. by the air collection and enrichment system ACES. Component technology is discussed, as well as improvements of the cycle by new possibilities, e.g. use of para/ortho-H<sub>2</sub>-shift conversion catalysts. A brief overview of combined propulsion systems employing liquid-air collection terminates this elucidating report. However, it still remains to show whether such improved concepts will be actually competitive in terms of thrust-to-mass ratio.

Problems of oblique detonation wave engines (ODWE) are the subjects of papers 25, 33 and 26. The first paper by T.M. Atamanchuck et al. analyzes theoretically the performance of this engine type at Mach numbers above 10. It shows that due to the special thrust/drag relationship of the relevant vehicles the design Mach number must be chosen at the lower end of the operating range of the ODWE. Off-design performance seems to depend on vehicle geometry. Paper 26 by G. Menees et al. reports on recent analytical and experimental work in the field of ODWE at NASA-Ames. Firstly, performance calculations show that the ODWE is only slightly superior to the normal scramjets above Mach 14. Secondly, the main problem of the ODWE, fuel-air mixture formation, is addressed experimentally showing the difficulties to be expected in practice. It is obvious that the use of injectors fuelling the whole flow field of the ODWE cannot be circumvented. Thus, the ensuing disturbances of the flow field together with premature burning induced by the hot air boundary layers of the injectors might easily spoil the shock pattern required for good performance. Together with the reduced performance flexibility this might lead to increased inferiority of the ODWE compared to "conventional" scramjet engines. Lastly, computational problems of the modelling of a shock wave plus chemical reaction as to be found in an ODWE engine, are addressed in paper 33 by M. Onofri. A technique of decoupling the system of differential equation by using separate gas dynamic and chemical operators is proposed and applied.

Missile propulsion up to Mach numbers in the lower hypersonic range is discussed in paper 30, where the specific problems of the optimization of solid fuel ramjets (or ducted rockets) for this speed range are treated. Observing the constraints set by military application, H.L. Weinreich shows that by clever design of optimized inlet, propellant and gas generator, and the nozzle it should be possible to adapt this type of propulsion systems to low-level missions with flight speeds up to about Mach 5. A similar extension of the Mach number range of solid-fuel ramjets is investigated for high-altitude missions in paper 29 by P.J.M. Eland et al.. They conclude that by experimental and theoretical optimization of the solid-fuel gas generator/combustor the performance of the propulsion system can be improved such that sustained flight with Mach numbers of about 4 should be possible at altitudes of 13 km.

#### HYPERSONIC ENGINE COMPONENT TECHNOLOGY

Inlet diffusers are critical components of hypersonic airbreathing propulsion systems, largely determining their performance. Their design will profit strongly by the application of advanced CFD-methods if the codes describe the flow phenomena within the inlet adequately. This presumes adequate and sufficient knowledge about the physical processes in hypersonic inlets. As, in this respect, deficiencies are existing presently, validation against experimental test cases is mandatory. W. Schmidt reported on relevant activities of Working Group 13 of AGARD's Fluid Mechanics Panel, which are directed towards the collection of suitable experimental test cases. However, only one test case for a hypersonic inlet (Mach number 7) has been offered, up to now. Furthermore, inlet test data including real gas effects are practically non-existent, and even with the available lower Mach number test cases code validation is difficult because of the scarcity of data. Therefore, an important research task for the future is to set up generic test cases for hypersonic inlets, producing all data, that are needed for code validation. This requires close cooperation between CFD-experts and experimentalists.

One way to improve the insight into flow phenomena in hypersonic inlets is presently pursued at NASA-Lewis (paper 18 by L. Povinelli), where computer simulations using advanced 3D-Navier-Stokes codes are compared with experimental results of flow fields in

hypersonic inlets for Mach numbers 5, 12 and 18. Although, partly good agreement had been achieved, more and improved experimental information is needed, for example, on the state of the wall boundary layers including corner flows, as well as on hypersonic inlet flows with real gas effects. This poses new challenges for measuring and testing techniques; on the theoretical side, new mathematical models for flow effects are required, particularly for the adequate description of turbulence and of glancing shock/boundary layer interaction. Similarly, paper 17 by J. Stollery demonstrated by means of experimental results some of the deficiencies in understanding important inlet flow phenomena, like shock/boundary layer, shock/shock and viscous interaction, which can lead to flow separation, extremely high heat transfer, and unsteadiness. Clearly, more information is needed on how the whole inlet flow field including interaction phenomena is influenced by boundary layer transition and real gas effects before proper mathematical modeling is achieved.

Unconventional inlet designs are mentioned in two of the papers, namely sidewall contraction (paper 18) and an all-internal compression inlet (paper 16), using symmetrical variable geometry, similar to a proposal of Busemann many years ago. This latter paper addresses also design problems of hypersonic inlets using semi-empirical engineering as well as numerical methods. An important conclusion is that numerical methods are not yet advanced far enough as to be used for inlet performance estimations. Thus, wind tunnel testing of inlets is still necessary for that purpose.

Subsonic and supersonic combustor technology problems were treated by two papers each. Paper 21 by H. Koopman et al. investigated transverse injection of gaseous hydrogen into a subsonic ramjet combustor model by means of experimental and numerical studies. CFD-calculations showed reasonable agreement for jet penetration except for burning jets, where improvement of turbulence and flame models are needed. Concerning flame stabilization by such jets in subsonic cross-flow, a new correlation based on the main variables determining the ratio of characteristic times is derived from experiments, which can be used for the selection of flame stabilizing jet parameters. This interesting work needs extension into the range of parameters pertaining to actual ramjet combustor conditions, particularly higher flow temperatures. In paper 22, S. Gleis et al. reported on a technique for the investigation of combustion instabilities, the "Active Instability Control" (AIC). Applied to an enclosed jet burner it is shown how sound radiation can be used to control oscillating combustion, thus permitting conclusions on the mechanisms driving the combustion instability. This new experimental technique could be a powerful tool for the investigation of such processes during the development of highly loaded ramjet combustors provided that the necessary sound energy input can be realized with AIC; therefore, the method should be extended towards more complex engine combustor flow fields, exhibiting also tangential and radial instability modes.

One of the processes governing the design of scramjet combustors is fuel-air mixing in supersonic flow. Paper 24 by G.V.R. Rao describes a numerical attempt to improve hydrogen-air mixing by generation of axial vorticity using conical ramp injectors. The computations using an Euler code show the existence of axial vorticity if a "skewed" hydrogen nozzle is incorporated in the conical ramp, however, no experimental results are available, as yet. Although, there is presently much interest in ramp injectors for improved mixing, there are several reservations as to the specific method and the results presented here. They concern the numerical code used, the influence of glancing shock/boundary layer interaction on the resulting flow field, as well as the effectiveness of a conical ramp injector as compared to the usual swept or unswept ramps with rectangular cross-sections.

The design of scramjet combustors is described in detail by F. Billig et al. in paper 23, using his well-known method of flow analysis. The design procedure consists of a 2-step iterative computation, where in the first step the 1D-conservation equations for supersonic flow with heat addition are solved using estimations for three of the unknown flow quantities at the combustor outlet. In the second step the estimated flow quantities are improved using a finite difference method, and the iteration is repeated until convergence is obtained. The procedure employs empirical or semi-empirical models for important phenomena, such as the pressure rise in the shock train at combustor inlet, wall shear and heat transfer, transverse fuel injection by wall jets, as well as mixing and combustion. These models are outlined in detail (with the exception of mixing and combustion), placing emphasis with the pressure field in the combustor, particularly with the shock train in the isolator/combustor inlet region. The paper shows the wealth of experimental and theoretical experience and results resting with the author and his co-workers. However, due to the high complexity of supersonic flows with heat addition, shocks and viscous effects, a thorough understanding of the solutions of the design process can be obtained only by penetrating deeply into the related physical problems. In addition to the calculated curves a more detailed explanation of the physical meaning of individual results would be very helpful.

Two papers on rotating components (papers 19 and 20) are devoted to multistage hydrogen turbines, as they are proposed for turboexpander engines, mainly for SSTO propulsion systems. The well-known equations for the design of turbines are applied for hydrogen as the turbine fluid in order to derive the aerodynamic design parameters leading to optimum conditions. A comparison between corotating and counterrotating wheels, included in paper 20, showed advantages in turbine efficiency in favour of the counterrotating case. In general, the design exercises did not reveal unusual problems, except for the higher number of stages compared to air or combustion gases. Problems of hydrogen interaction with the turbine materials as well as solutions for adequate mechanical design

are discussed in paper 19; however, durability of turbine hardware and sufficient operational life has yet to be demonstrated.

Heat exchangers will be found in future hypersonic propulsion systems performing several important duties; however, this system component was only marginally represented at the Meeting. Paper 11 by Ribaud et al. discusses the design of heat exchangers as components of inverse cycle engines, based on current technology and using the well-established equations for the heat exchange process. The results of this exercise give rise to doubts with respect to a hardware application, particularly, as far as the high ratio of heat exchanger weight to total engine mass, estimated in the paper to be about 10, is concerned. Moreover, if the losses in the heat exchanger inlet and outlet area, which are neglected in the paper, are taken into account, one recognizes easily that a tremendous amount of research and development work has to be done before light-weight high-performance heat exchangers are available as main components for hypersonic engines.

Nozzles of hypersonic propulsion systems are critical components, too, for which a very careful design is needed. Although there is accelerated flow in a nozzle, flow phenomena associated with shocks and boundary layer separation can be encountered, which can lead to a deterioration of thrust, and this the more, since nozzle geometry will mostly be 2D and asymmetric, and geometric constraints from the integration of the nozzle into the vehicle have to be observed. Therefore, one of the most important areas of work on future hypersonic propulsion technology should be to generate a sound basis for nozzle design and to understand and to avoid detrimental flow effects.

Three relevant problem areas have been treated in papers 32, 34, and 35. Paper 35 by M. Göing and J. Heyse dealt with the very first step in nozzle design, namely the generation of an idealized optimum nozzle geometry. By means of the methods of characteristics, and employing simplifying assumptions, e.g. inviscid flow, a family of length-optimized 2D-nozzles is derived, which is bounded by the symmetric nozzle, the single expansion ramp nozzle and the Prandtl-Meyer-type nozzle. By combining different elements of these three basic types, adaptation to different requirements is feasible. However, the integration of those optimized nozzle geometries into a hypersonic vehicle is very difficult, mainly because of their length. Hence, the described design procedure represents only the very first step, from which nozzle geometries with shorter lengths, allowing for variable geometry and meeting the integration constraints must be derived.

Analysis of nozzle flow properties and problems requires versatile and complicated CFD-codes, which are now available or in the process of development. An example of their capabilities is given in paper 34 by G.J. Harloff et al., using a 3D-Navier-Stokes code, PARC3D. After validation of the code by means of two known specific test cases, the code is applied to analyze several nozzle flows in the Mach number range between 3 and 20, including 2D and 3D, laminar and turbulent flow cases, in order to gain confidence in the calculated results. Although these calculations have been carried out with some simplifying assumptions, like perfect gas and frozen flow, the results are encouraging, particularly for the case of the single expansion ramp nozzle. Realistic flow phenomena have been predicted, like flow separation characteristics, divergence of flow vectors in the nozzle outlet plane or change in flow direction of shear layers by shocks leaving the nozzle. Where pressure measurements were available a fairly good agreement with computed results is registered. It appears, that for future realistic calculations on nozzle performance, e.g. nozzle coefficients and thrust vectors, the use of such codes is absolutely mandatory. However, what still remains to be done is to include in these codes real gas effects and also finite rate chemistry, where necessary. Likewise, non-uniformity effects of the flow at the nozzle inlets will have to be taken into account, although the latter problems might yet be beyond our present computer capabilities.

This latter aspect of non-uniformity with respect to flow variables, gas composition and recombination processes is very important for hypersonic nozzle performance. An example, which is still rather simple, namely the effect of a non-uniform static pressure distribution at the entrance to the supersonic portion of a single ramp nozzle, is demonstrated in paper 32, by P. Goel et al.. A CFD-analysis using a 3D-Euler code is carried out assuming several pressure profiles with high or low pressure at the upper and the lower nozzle wall and keeping constant the other flow parameters. In cases with high pressure at the lower wall, an improved thrust and nozzle coefficient was calculated, whereas in the opposite case a deterioration of the nozzle performance was found. This exercise shows that, at least in the case of highly asymmetric 2D-nozzles, non-uniformity effects at the entrance are amplified in the complicated nozzle flow field. Therefore, it is important, that in future work on hypersonic nozzles, both experimental and theoretical, much emphasis has to be placed with studies on these effects.

#### MATERIALS FOR HYPERSONIC ENGINES

New structural materials, which combine low density, high-load bearing capabilities with highest possible temperature performance represent one of the most important key technologies, which can permit or prevent flying at hypersonic speeds for extended time. Particularly, the low-density requirements point to new classes of materials for use in hypersonic engines and airframes than hitherto employed. Recognising their importance the meeting closed with two papers devoted to the development of suitable materials and their application to structural parts within engines and airframe. Unfortunately, for two additionally scheduled papers on related subjects permission for their presentation could not be obtained. This is to be regretted the more, as engine design has to rely highly on suitable high-duty materials and their performance data.

Paper 36 by T. Ronald presented a brief survey on the structural materials which are under development within the US NASP-program. It concentrates on Ti-Aluminides, Ti-based metal matrix composites, c/c-composites and ceramic-matrix composites, as well as on copper-matrix composites and beryllium alloys, the latter two particularly because of a possible use in cooled engine parts. Advantages and disadvantages as well as manufacturing problems are discussed, thus representing a comprehensive introduction into the problem area. Paper 38 by D. Boury et al. deals with the same problem area, as viewed from the French activities and experiences (SEP/SNECMA). In particular, properties and problems of glass-ceramic composites, C/C composites (type SEPCARB, SEPCARBINOX) and SiC/SiC composites (type CERASEP) are discussed, together with considerations on their application to specific engine types and components. The presentation is illustrated with figures for materials properties; and estimations for possible life time and numbers of thermal cycles under high-load high-temperature situations are given. In both papers the progress which has been made with respect to the manufacture of large and complicated structural parts from the new materials was demonstrated by impressive examples.

#### CONCLUSIONS AND RECOMMENDATIONS

This 75th. PEP-meeting on hypersonic combined cycle propulsion attracted a large number of participants, in the order of 180 authors and observers. On the average, the technical papers were of considerable interest and of high technical standard. The presentations enclosed a rather wide range of technical subjects related to hypersonic propulsion, which, for a first AGARD-meeting on that theme after a long time, is surely justified. On the other hand, there was only little discussion immediately after many of the presentations. This phenomenon is known from other Panel meetings on similarly wide-spread areas; it could be avoided in the future by keeping to sufficiently narrow meeting subjects. Another comment to be made is that the withdrawal of 12% of the papers on important topics and recent work, due to restrictions from outside the Panel, represented a heavy loss for the meeting.

Taking all facts into account, the meeting was surely successful, although not all hopes for technical exchange connected with the meeting have been fulfilled. The Panel is definitely encouraged to continue with further activities in that field. There are enough well-defined subject areas in hypersonic propulsion technology which warrant further Panel meetings. Preferably, Specialists' Meetings should be organized on subjects the scope of which is chosen narrow enough to provide both detailed presentations as well as lively discussion and exchange of information and experience. Based on the technical evaluation in the preceding paragraphs, tentative subjects for Specialists' Meetings could be

- hypersonic inlets and nozzles, possibly as a joint effort with FDP,
- combustion problems in hydrogen-fuelled ram-/scramjets
- heat transfer and cooling problems in hypersonic propulsion systems;

after sometime from now another Specialists' Meeting could be interesting on:

- systems aspects of hypersonic engines, including for example variable geometry aspects, integration and testing techniques.

In addition to the subjects mentioned above there are other problems of hypersonic propulsion technology which need presentation and discussion at technical meetings, too, but where the number of expected contributions might not warrant a dedicated meeting. It should be considered whether it is appropriate to include them into those running Panel activities which deal with related physical aspects of propulsion technology. This could concern subjects like, for example, instrumentation, measuring and testing techniques (a topic which - in view of future research still in preparation - would also be suited for a lecture series), boundary layer problems in hypersonic ram/scramjets, CFD-methods for hypersonic propulsion components, multi-variable control of combined cycle engines, high-temperature lubrication, fuel systems, or secondary energy generation on board of hypersonic vehicles, etc..

In view of the high degree of integration of hypersonic vehicles it might be recommendable to undertake some of the efforts jointly with other Panels.

THE POTENTIAL AND PRACTICALITY OF HIGH SPEED  
COMBINED CYCLE ENGINES

by

AD-P007 938

EDWARD T. CURRAN  
AERO PROPULSION AND POWER LABORATORY  
WRIGHT RESEARCH AND DEVELOPMENT CENTER  
UNITED STATES AIR FORCE  
WRIGHT-PATTERSON AFB OHIO 45433-6563

## SUMMARY

The current renewal of interest in hypersonic flight, and in low-cost access to space has emphasized the accelerative aspects of aircraft performance in contrast to the traditional emphasis on cruising flight. The consequent trade-off between specific fuel consumption and engine thrust-to-weight ratio has generated renewed interest in a wide variety of existing and new engine cycles. Furthermore, the requirement to fly efficiently over a wide Mach number range demands that multi-mode propulsion systems be integrated into the vehicle.

In this paper the emergence of combined cycle engines from their rocket and airbreathing progenitors is reviewed and the task of bringing such engine cycles to practical reality is examined. Particular emphasis is laid on the requirements for airframe-engine integration, and on the ground testing of such engine systems.

## INTRODUCTION

The early decades of aviation were characterized by the pursuit of speed, of range, and of extended range at high flight speeds. Further advances in speed will require the development of combined-cycle engine technologies. Some exploratory flight experience has been gained in the past with both airbreathing and rocket elements. A major push for higher speed was characterized by the X-series of aircraft which explored the supersonic regime in the 1950's and 1960's. The X-series culminated in the rocket powered X-15-A2 which propelled man to his highest speed in an airplane, namely Mach 6.7. In a similar time period several other interesting projects were pursued, for example, the rocket-airbreathing powered fighters such as the Republic XF-91 (1949) and Saunders Roe SR53 (1957). The turbo-ramjet engine also appeared as the powerplant of the outstanding Nord Aviation Griffon 02 aircraft in France and as the power plant of choice for the ill-fated Republic XF-103 fighter. The work of Rene Leduc in pioneering ramjet and turboramjet propulsion must also be noted: The flight programs involving the ramjet powered Leduc 0.10, Leduc 0.21 (with Turbomeca turbojet) and Leduc 0.22 (with Atar turbojet) were significant steps in aviation progress. In this time frame it is also important to note the contribution to U.S. ramjet engine technology of the unmanned Lockheed X-7 ramjet-powered test-vehicle program which has not received wide publicity.

At the time of writing, maximum speeds of commercial aircraft and military aircraft appear to have reached a plateau with Concorde in the Mach 2 region and the SR71 in the Mach 3 region, but currently there is a renewal of interest in the utilization of airbreathing combined cycle engines for vehicles cruising at high flight speeds and for vehicles dedicated to acceleration to hypersonic speeds.

In regard to cruising flight the potential of high speed commercial vehicles has been evaluated in the USA under NASA's High Speed Civil Transport (HSCT) program. Also, in recent years, there has been a proliferation of studies of aircraft-like vehicles as first-stage space launchers or indeed as single-stage-to-orbit (SSTO) vehicles. Such studies, at various levels of investment, include efforts by the USA, the United Kingdom, Germany, France, Japan, and the USSR. Although these various studies can arbitrarily be divided into cruising vehicles and accelerator vehicles this is not a hard and fast distinction. Thus the acceleration phase of a predominately cruising hypersonic vehicle is a significant segment of the total flight-path, and similarly a dedicated accelerator vehicle may require substantial cruise capability, for example, to obtain access to desired orbit planes, or for subsonic-ferry capability.

A general discussion of the probable evolution of high speed commercial transports is difficult, because the foundational technologies such as; aerodynamic configuration, power plant, structure, and fuel type, change markedly with increasing flight speed. In the last major U.S. effort to build an SST the need to accommodate both low speed and high speed flight requirements led to the evolution of a significant new engine technology, namely that of variable-cycle engines. With even higher maximum flight speeds it is to be expected that advanced variable-cycle engines, combined cycle or mixed engine types, and also novel engine cycles will emerge to bridge the wide speed range. The right choice of terminology and classification of such engines is not a trivial problem<sup>2</sup>.

The ultimate aeronautical challenge however, is the achievement of orbital conditions with a single-stage vehicle using primarily airbreathing propulsion. This elegant but elusive approach to space transportation is a classical aeronautical concept. For this vehicle the flight spectrum from horizontal take-off to orbital speed is encompassed and a combined cycle system is required for efficient operation over this wide speed range. The propulsion installation will probably require significant variable geometry features. However the vehicle aerodynamic configuration will presumably not incorporate variable geometry in the interest of low structural weight.

It is important to note that with increasing flight speed, the fuel type typically changes from conventional JP fuels at the lower speeds to cryogenic fuels such as methane or liquid hydrogen at hypersonic speeds, with endothermic fuels currently emerging for possible use at intermediate speeds. The introduction of liquid hydrogen fuel with its high cooling capacity and its high work capability, has introduced major new opportunities for the synthesis of efficient aero-propulsion systems. Hydrogen may be used to cool both internal (engine) and external flow surfaces, or to cool the working fluid (air) and thus impact the engine thermodynamic cycle. Also, hydrogen may be used as a working fluid in its own right providing opportunities for additional energy interactions as an intrinsic part of the aero-propulsive system.

From this point forward the discussion will primarily apply to the accelerator class of vehicle. There is, of course, much which is also applicable to hypersonic cruising vehicles.

#### OVERALL PROPULSION CONSIDERATIONS

The potential performance of conventional engine cycles, using hydrogen fuel, is shown in Figure 1. It is apparent that as flight speed increases the turboaccelerator class of engine is supplanted first by the subsonic combustion ramjet and second by the supersonic combustion ramjet: rocket propulsion may also be needed at the higher flight speeds. Consequently, for a hypersonic flight vehicle operating at a maximum speed above about Mach 5.0, a multi-mode propulsion system will be required. Bearing in mind the limitations of materials, such an engine system might operate as a turboaccelerator to speeds of the order of Mach 4.0, then transition to subsonic ramjet operation up to speeds of about Mach 6.0, and then be operating totally as a supersonic combustion engine for speeds above about Mach 7.0. Now Figure 1 affords a simple comparison of various engine cycles based on fuel specific impulse (Isp) and therefore generally appropriate to cruise flight performance, where the Breguet equation is used to compare ranges. However, for acceleration missions, the engine weight becomes an even more important variable and the performance of the engine may be evaluated initially on the basis of both its specific impulse and its corresponding thrust-to-weight ratio.

It is clear that for maximum flight speeds of about Mach 6 the use of a conventional ramjet cycle is imperative and for higher maximum flight speeds the scramjet is the appropriate high speed engine. The lower speed engine cycle must be integrated with the appropriate ramjet element(s) to form a truly combined cycle engine. In the following discussion the term low speed engine applies typically to turbo-accelerator or rocket-based systems used to accelerate the vehicle up to speeds of roughly Mach 4.0.

For purposes of discussion, let us consider a hypersonic vehicle with maximum speed in excess of say Mach 7, and consequently using a supersonic combustion ramjet as its dominant propulsion system. A plausible overall propulsion installation for such a vehicle is one which uses a low speed engine of the turbo-accelerator class for take-off (and landing), and for acceleration to speeds of about Mach 4.0, followed by an initial transition to ramjet operation. A subsequent transition to scramjet operation takes place at about Mach 6.0. The vehicle then accelerates to a terminal Mach number on scramjet power.

It is appropriate to point out that because of the complexities of mode transition, there is a substantial payoff to eliminating such transitions. For example, the turbo-accelerator speed capability may be "stretched" to permit direct transition to a scramjet mode. Alternatively, for say a Mach 7 system, the ramjet performance may be "stretched" to avoid transition to a true scramjet mode. Simultaneously the scramjet take-over Mach number may be reduced or "stretched" down to eliminate the ramjet mode. Similarly in relation to fuels it is desirable where possible to stretch the performance of hydrocarbon class fuels to higher Mach numbers to defer the logistical problems of operating with cryogenic fuels. Consequently the propulsion engineer must place emphasis on "stretched" capability wherever appropriate, and where mission requirements will not be compromised.

#### LOW SPEED PROPULSION TRADE-OFFS

For maximum payload capability it is desirable for a candidate engine to possess high specific impulse, a high installed thrust-to-weight ratio and the capability to function over a broad Mach number range. For an acceleration mission a typical trade-off curve between specific impulse and thrust-to-weight ratio for a given payload is of the form shown in Figure 2.



Note that for each class of engine the thrust loading of the vehicle must be chosen to optimize the appropriate payload fraction. Different aircraft thrust-loadings are required for each engine class and consequently the corresponding initial vehicle accelerations are different. Thus the rocket class of engine requires a higher initial acceleration for optimum payload fraction than the turbo-accelerator class. (Of course a pinch point in excess thrust may exist, requiring additional thrust loading.) In regard to Figure 2 it is unfortunately true that for propulsion systems there is no class of engine which simultaneously possesses high specific impulse and high installed thrust-to-weight ratio. Typically, high specific impulse engines such as turbojets are mechanically complex, and therefore heavy, whereas lightweight engines such as liquid fuel rockets generate relatively low specific impulses. Barrere<sup>3</sup> has recently drawn attention to the relationship between engine thrust-to-weight ratio and basic specific impulse: a similar functional relationship was also noted by Bialder and Cuadra<sup>4</sup> in evaluating candidate transonic acceleration engines.

In order to improve the payload potential of engines three simplistic approaches can be outlined: for the turboaccelerator class of engine the appropriate approach is to increase the engine thrust-to-weight ratio; for the rocket class of engine, attention should be focused on improving the specific impulse; it would be expected that an engine type intermediate between the turboaccelerator and the rocket engine, for example the air turborocket, may offer a performance superior to its progenitors. This expectation, of course, accounts for the current renewal of interest in combined cycle engines.

#### CANDIDATE LOW SPEED ENGINES

One stream of development is, as noted above, to improve the thrust-to-weight ratio of turbo-accelerators. The specific thrust of the engine can be increased by a modest but useful amount by increasing the turbine inlet temperature, and also by increasing the efficiency of the internal flow processes. However, there are potentially larger benefits available by significantly reducing engine weight by use of new materials allied with innovative structural concepts. In this regard a major initiative is underway in the USA to double the thrust-to-weight ratio of advanced turbine engines by the year 2000. This initiative is known by the acronym IHPTET - Integrated High Performance Turbine Engine Technology. Similar efforts are being pursued internationally.

The rotating machinery of a turbo-accelerator is a major contributor to the engine weight; it also dictates the basic air swallowing characteristics of the propulsion device, and imposes mechanical limitations on the Mach number capabilities of such engines. Also, with increasing Mach number, the size and complexity of the inlet-nacelle-nozzle in which the core engine is housed, becomes increasingly heavy and results in a significantly reduced installed thrust-to-weight ratio. Additionally, the internal pressure and temperature loads imposed on such inlet ducts become a limiting factor. In this regard, there is a driving need to devise compact inlet and exhaust nozzle configurations. Another approach to reducing the inlet weight is to reduce the amount of flow diffusion by maintaining supersonic flow either throughout the engine or through a fan stage: this latter concept has been worked on intermittently over the years. Recent studies<sup>5</sup> of the potential performance of Air Turboramjets (ATRs) using a variable geometry Supersonic Through-Flow Fan (STFF) have shown significant gains in performance compared to a conventional over-under turboramjet arrangement. Furthermore the installation of the STFF-ATR is much simpler leading to a lighter-weight, reduced drag power plant. Much more work needs to be done to develop high efficiency, rugged supersonic fans and this work is currently in progress.

It is also well known that the overall engine total pressure ratio of the turbojet (turbine exit to compressor face) decreases rapidly with Mach number, for a given turbine temperature. Typically, the performance capability of the basic turbojet is increased either by use of afterburning or by use of an integrated ramjet system. Such turboramjets may be of tandem or of parallel design, or the basic turbojet and ramjet may be installed as discrete units. Such a mechanical integration of turbojet core and ramjet engine may result in a relatively heavy and complex installation.

An alternative approach to the turbomachine-based compression process is the use of non-mechanical pumps and/or crypto-steady compressors. However such devices frequently produce very low overall pressure ratios and are therefore very sensitive to losses in the flow process. The combination of a ramjet (or scramjet) with a rocket (liquid or solid) driven ejector-pump has received major attention in the literature. Examples of such engines are the Ejector Ramjet (ERJ), the Supercharged Ejector Ramjet (SERJ) and the Ejector Scramjet (ESCRJ). The evolution of these engine systems is described in Reference 6. It is also interesting to note that an early mixed mode engine, named the "Hyperjet" was flight tested by the Marquardt Corporation, under USAF sponsorship, in 1959/1960. This engine was basically a ramjet engine with a valved intake, and was capable of operation as a rocket (inlet valve closed), yielding thrust at either static or high altitude conditions, or as a ramjet (valve open). In many ways the Hyperjet was the precursor of the integral-rocket ramjet which has found application in several missile systems.



We have previously noted that whereas the acceleration capability of turbo-accelerator engines is best improved by seeking increased thrust-to-weight ratio, the capability of the rocket class of engine is best improved by increasing specific impulse. It is interesting to note that, historically, improvements in rocket efficiency have been sought by extracting work from the thrust chamber to drive propellers or fans. As early as 1932, Dr R.H. Goddard was reported as working on a "turbine rocket plane" in which a rocket-driven turbine was used to drive two propellers. A related concept is the engine described by Sloop<sup>1</sup> for the REX-1 Aircraft System (1954). This engine used a series of three gas-generator powered turbine units to drive a propeller system. This concept evolved to the REX II engine - a form of turbo-rocket, and subsequently to the REX III engine - a form of hydrogen expander. The hydrogen-expander class of engine was extensively studied in the USA in the mid-1950s time frame, as discussed also by Sloop. These initial designs involved complex, and therefore heavy, heat exchangers. The overall performance was also constrained by the inability to reach a high hydrogen temperature due to materials limitations. The fan-turbine work balance also imposes limitations on the cycle performance which is achievable without added mechanical complexity.

A more familiar engine, which also largely decouples the turbine mass flow from that of the compressor, is the so-called Air-Turbo-Rocket (more recently, and perhaps more appropriately, called the Air-Turbo-Ramjet). In this case, the gas generator can be fed by mono or bi-propellant combinations with a significant increase in gas generator temperature compared to the expander cycle: the ATR cycle is, however, also dominated by fan-turbine matching constraints. Obviously, cycle elements from both the basic expander engine and Air Turbo-ramjet can be combined to yield new engine cycles. Another variation on the turbo-rocket theme is the rocket fan<sup>2</sup> in which a fan is driven directly by small rocket nozzles at the blade tips. The hydrogen that is exhausted through these nozzles is then burned with the fan discharge air in an afterburner.

An interesting approach to the problem of improving the specific impulse of rocket type engines during atmospheric flight is to replace, either completely or partially, the conventional liquid oxidizer by atmospheric air: the immediate problem is the compression of such air from free stream to combustion chamber pressure levels (see Figure 3). One approach to this, which avoids heavy turbomachinery, is to pump the air in the liquid phase; obviously a direct approach to condensing the engine airflow is to use the on-board cooling capacity of cryogenic fuels and oxidizers, or cryogenic diluents, such as liquid nitrogen. An intermediate approach is strong pre-cooling of the inlet flow without actual liquification: this effect permits substantial reduction in turbomachinery mass but of course introduces the mass of a heat exchanger.

Precooling has also received attention in regard to conventional turboaccelerator designs, initially from the point of view of extending the flight Mach number capability of such engines. In cases where the maximum Mach number of the engine is limited by the compressor exit temperature then precooling of the air can permit significant increases in flight speed. However, it was soon realized that additional potential performance advantages exist and that the pre-cooled turboaccelerator can be a significant contender for high speed flight. The precooling concept has also been extended to include both air-hydrogen and air-air heat exchangers in the air cooling system. In an overall sense the introduction of precooling can potentially improve engine thrust performance, and reduce engine size: nevertheless, inlet flow matching with minimal variable geometry is a challenge. Also, because of the increased flight Mach number capability it may be possible to defer transition to other engine modes to higher speeds. Furthermore the ground test problem is simplified in that the core engine, which experiences temperatures less severe than those corresponding to the flight Mach number, can be developed in available test facilities. The potential performance advantages are however tempered by the practical difficulties of fabricating lightweight, reliable heat exchangers and avoiding the fouling problems of flight operations. The thermodynamic spectrum of some candidate pre-cooled engines is illustrated in Figure 4. The potential performance advantages of air precooling have led to a re-emphasis on the role of heat exchanger processes and components in jet engine technology. Of course, heat exchangers have been previously considered for conventionally fueled engines but are now receiving renewed emphasis with cryogenically fueled systems.

The above discussion does not exhaust the innovative uses of cryogenic fuels in new engine cycles. One such novel cycle is the inverted turbojet cycle intended for operation in the range Mach zero to six; this cycle received its first wide attention in 1961<sup>10</sup>. In this engine the sequence of the core-engine components was arranged in the order turbine - heat exchanger - compressor - combustor. Although this engine did not give acceptable cycle performance at low speeds it did lead directly to a variant cycle which became known as the pre-cooled turbojet discussed earlier.

An improved version of the inverted cycle engine (ICE) has recently been proposed<sup>11</sup> in France which incorporates an additional burner installed between the inlet and the turbine. At low speeds the additional burner allows a heat input upstream of the initial turbine to augment thrust: the fuel-rich mode of operation is particularly beneficial; as speed increases the burner equivalence ratio can be reduced and eventually reduced to zero. A bypass duct can also be incorporated in this engine. In regard to internal engine flows the potential (and necessity) to

radically improve hot-section and exhaust nozzle cooling may permit significant increases in maximum combustion temperature. Similarly the use of hydrogen as an engine/airframe coolant produces a source of hot hydrogen which can be used to do work in the overall propulsion system. The fuel turbopump subsystem, for the hydrogen cooled systems, introduce a further set of choices for the turbine-drive cycle which parallel the traditional cycle choices for liquid fueled rockets, for example<sup>12</sup>: gas generator cycle, combustion or coolant bleed cycles; staged combustion or expander cycle, or other variants.

Although it is not always possible to separate rigorously the airflow associated with a hypersonic vehicle into external and internal airflows, it is still conventional to treat such flows as separate aerothermodynamic systems. Such an approach cannot continue since the efficient production of the overall aero-propulsion forces on an actively cooled vehicle is inextricably linked through the cryogenic fuel circuits and many other coupling mechanisms, see for example Figure 5. The overall energy bookkeeping of the total aerothermodynamic system which constitutes the vehicle can be rationally addressed by the explicit use of Available Energy methods which have been successfully applied to many complex thermodynamic systems<sup>13</sup> in recent years.

#### HIGH SPEED PROPULSION

For speeds in excess of Mach 4 it is generally necessary to transition from the turboaccelerator to the conventional ramjet mode. However, as outlined in the previous section, it may be possible in the future to extend the capability of the turboaccelerator class to speeds in excess of Mach 4.0. In this case direct transition to a scramjet mode may become possible.<sup>14</sup> The characteristics of the conventional subsonic-combustion hydrogen-burning ramjet are well understood and have been verified in ground tests to speeds in excess of Mach 6. As is well known the performance of the subsonic-combustion ramjet deteriorates at hypersonic speeds due to real gas effects and internal losses; and the structural design of the engine becomes very difficult due to the high internal temperatures and pressures.

Thus for really high speeds it is necessary to utilize the supersonic combustion engine (scramjet). The scramjet engine potentially offers outstanding specific impulse performance to high hypersonic Mach numbers as pointed out by several authors. Such performance estimates are, of course, theoretical and the practical upper speed limits of such engines have not generally been established on an engineering basis.

The speed range between the conventional ramjet and the scramjet can be bridged by the dual mode ramjet engine. The dual mode engine is one in which, initially, subsonic combustion is employed at lower speeds (typically Mach 3-6) with transition to the supersonic combustion mode at speeds in excess of about Mach 6. This class of engine has undergone extensive analysis and ground test in the USA, in France, and the USSR. It is probable that the dual mode engine will be the next workhorse engine for future hypersonic vehicles.

As shown in Figure 1 the supersonic combustion ramjet engine offers higher performance than the conventional ramjet engine at speeds in excess of about Mach 6. It is difficult to be precise about the point of transition to supersonic combustion because mixed flow conditions can exist in the combustor until substantially higher flight Mach numbers are attained; and in any event, one-dimensional flow concepts and criteria are difficult to apply. The phenomenon of supersonic flow through the engine introduces totally new technology challenges compared to the conventional ramjet: these challenges are principally associated with the wave interaction phenomena generated by the basic mixing, combustion, and expansion processes.

Up to this point, heat addition to only the internal flow has been considered. Heat addition to the external flow is of considerable relevance primarily to relieve base drag in the transonic speed range. It is also possible to modify the basic lifting and propulsive forces associated with a high speed vehicle by selective external heat addition. Thus the approach used in internal flows, namely to synthesize a multi-dimensional flow where the basic wave structures constructively interact with regions of heat addition may also be applied to external flow fields.

#### INTEGRATION

For optimum flight performance the aerodynamic, structural, and propulsion elements of the vehicle have to be integrated into a cohesive whole taking every opportunity to synergistically enhance performance. For a single stage vehicle where vehicle integration is critical, some technological relief could be obtained by refueling or by air collection. In the acceleration case it should be noted that the overall propulsive parameter is the "effective" specific impulse, which couples the basic impulse of the flight engine to the overall vehicle thrust/drag characteristics. For an airbreathing engine such characteristics are of course dependent of the flight trajectory. There are conflicting flight path requirements: to maintain high engine thrust, a high dynamic pressure trajectory is desirable; however, the converse is true in regard to heating and pressure loads. Thus trajectory optimization is also an integration issue. In regimes of minimum thrust margin a sharp loss in effective impulse can occur. This can be relieved by thrust augmentation typically by simple mass addition. Thus the use of water injection to augment turbojet and ramjet thrust is well documented. Similarly, augmentation by simple fuel and/or oxidant injection

can also be an effective way to increase thrust and enhance overall performance. The overall spectrum of such airbreathing elements utilizing thrust augmentation or rocket-augmentation is well covered in an early foundational paper by Lindley<sup>15</sup>. Such techniques may be an attractive alternative to over-sizing an acceleration engine simply to overcome regimes of minimum thrust margin.

As flight speed increases the engine size also grows and soon dominates the vehicle configuration. The only efficient way to accommodate this reality is by total integration of the vehicle and propulsion systems. Essentially, the entire undersurfaces of the forebody and aftbody provide propulsion functions, and their contributions to the thrust, drag, and control of the vehicle are of paramount importance. Considerable ingenuity is required to tailor the vehicle configuration and its associated flow fields, to the engine installation and its mass flow characteristics. Typically, matching of the engine flow characteristics and the available airflow over a wide speed range requires variable geometry. Some complexities may be alleviated by the judicious use of precooling in cryogenic engine systems.

In addition to the basic engine installation, the thermodynamics of both the overall active cooling circuits and the engine fuel system must be such as to avoid unnecessary losses of available energy. The energy of the basic hydrogen-air system is marginal for the single-stage-to-orbit (SSTO) mission. Thus energy must be conserved, and utilized in the most effective manner. Once again, an Exergy based approach can be used to address total vehicle thermodynamics.

Regarding minimization of the structural weight fraction, the design problems are severe. The vehicle will be subject externally to both high dynamic pressures and high temperature levels during ascent, while internally, low temperature cryogenic storage must be maintained. The engine structure is also subject to even higher internal pressures and temperatures, possibly in box-like actively cooled structures. Integration of the basic engine and airframe structures is desirable to avoid duplicative weight elements. Fortunately new high-temperature materials are emerging to alleviate the design problems; nevertheless the achievement of a reusable high temperature structure of minimum structural fraction is a major challenge. As in the case of the engine, ground test validation of candidate structural approaches and assemblies is a demanding requirement.

A similar challenge is the development of a comprehensive vehicle control system. This is a significant architectural and engineering problem.

#### TEST FACILITIES

In previous years the testing of high speed flight engines has evolved to a disciplined sequential ground test process leading to flight qualification and flight demonstration. Full simulation of supersonic flight conditions has involved large scale plant, handling substantial mass flows at high enthalpy and high pressure conditions. The process of producing a large high quality supersonic stream tube at the correct simulated flight Mach number is not trivial. Correctly designed axisymmetric nozzles can be used for discrete Mach number simulation. Such conventional facilities can currently simulate conditions which approximately correspond to typical Mach 7/8 flight speeds. Traditional criteria for both tunnel starting, with various blockages, and the avoidance of excessive transient loads can be applied. One new requirement for multi-mode engines will be the convincing demonstration of stable mode transitions. Such transitions will generally occur at Mach numbers below about eight and thus such tests can be undertaken in suitably modified conventional facilities.

For significantly higher speeds, ultra-high enthalpies (and of course correspondingly high pressures) are required, and although many schemes have been postulated to achieve such enthalpies, the currently available test facilities are limited to relatively short duration systems: the use of such short-duration facilities to test scramjet engine components has been well established over the last twenty five years in the USA, the USSR and other locations.

Such facilities, supported by increasingly sophisticated instrumentation and diagnostics have been invaluable in estimating the potential aerothermodynamic performance of inlets, combustors, and nozzles through tests lasting only a few milliseconds. The application of the supercomputer to the analysis of both aerothermodynamic flows and structural design, can make maximum use of such short-duration test data. However the process of validating the performance and durability of a full scale flight engine is somewhat removed from the elemental tests performed in short-duration facilities, although these latter tests are essential. Currently an incremental flight test procedure appears to be the only logical course to proceed safely with engine certification.

In the future, extended duration ground tests for high speed will require novel facilities. Such facilities must avoid generating the simulated stagnation (or reservoir) conditions in the facility both because of engineering limitations and because the test gas may often be in a dissociated state. Consequently one must look to generating the required test enthalpy by progressive acceleration of the test gas by MHD or other energy transfer processes.

In any event a fundamental need exists for the incremental flight testing of hypersonic engine systems.

## CONCLUSIONS

Currently we stand at a crucial point in aeronautical progress. Aeronautics has advanced along the traditional flight corridor to achieve relatively conventional flight to speeds approaching Mach 4.0. Such cruising flight may be regarded as an established stable boundary condition at the lower speed end of the flight corridor. At higher speeds another established steady condition exists namely orbital "flight." Between these established stable states a wide range of transatmospheric flight paths exist. Currently, passage through the transatmospheric region is of a transient nature involving insertion to, and re-entry from, orbital conditions, or transient "zoom" operations. However, in the longer term, ability to operate in the transatmospheric region may be of considerable interest as the fields of aeronautics and space continue to merge: once again combined-cycle propulsion will be key.

It is clear that entry into the hypersonic flight regime means that long term commitments must be made to embark on new areas of technology in engines, fuels, aerothermodynamics, materials and structures. Similarly the whole infrastructure supporting operation of hypersonic cryogenically-fueled vehicles must be addressed. Such changes will tend to be more revolutionary than evolutionary and should be recognized as a major shift in traditional aeronautical development. As previously noted we stand at an exciting point in aeronautical, or rather aerospace, history: new vehicle configurations and engine concepts are emerging, and these opportunities need to be addressed in a cohesive, imaginative fashion. Fortunately, the supercomputer is now available to address both engineering and management problems. However, the overall strategy for evolving such efficient high-speed vehicles is a complex and major challenge - a point first stressed by Kuchemann<sup>10</sup>. Although such major changes in aeronautical development have been latent for some decades, the current emphasis in hypersonics now requires dedicated attention so that the required engineering disciplines and methodologies can be brought together in appropriate management structures.

## REFERENCES

1. Harris, Roy V., "On the Threshold - The Outlook for Supersonic and Hypersonic Aircraft," Paper No. AIAA-89-2071, AIAA/AHS/ASME Aircraft Design, Systems and Operations Conference, Seattle WA, Jul 31-Aug 2, 1989.
2. Fishbein, B.D., "On the Development of a Flight Vehicle Engine Classification," *Izvestiya vuz Aviatсионnaya Tekhnika (Soviet Aeronautics)*, Vol 32, No. 1, 1989, pp 70-74.
3. Barrere, M., "Quelques Remarques Sur Les Systems De Propulsion Multifonctions Ou 'Combines'," *Acta Astronautica*, Vol 15, No. 11, 1987, pp 931-935.
4. Builder, C.H., and Caudra, E., "An Elemental Approach to Propulsion Selection for the Supersonic Transport," IAS Paper No. 62-72, Presented at the IAS 30th Annual Meeting, New York NY, 22-24 Jan 1962.
5. Kepler, C., Champagne, G., "Performance Potential of Air Turboramjet Employing Supersonic Through-Flow Fan, AIAA 89-0010, 27th Aerospace Sciences Meeting, Reno NV, Jan 9-12, 1989.
6. Bendot, J.G., "Composite Propulsion Systems for an Advanced Reusable Launch Vehicle Application," Proceedings of the Second International Symposium on Air Breathing Engines, Royal Aeronautical Society, 1974.
7. Sloop, J.L., Liquid Hydrogen as a Propulsion Fuel, 1945-1959, NASA SP 4404, NASA, Washington DC, 1978.
8. Kerr, W.B., Marra, J., "Rocket Fan - A Hybrid Air-Breathing Hydrogen-Fueled Engine," AIAA-87-2000, AIAA/SAE/ASME/ASME 23rd Joint Propulsion Conference, San Diego CA, Jun 29-Jul 2, 1987.
9. Hewitt, F.A., "Air Breathing Propulsion for Advanced Orbital Launch Vehicles," Paper No. IAF-87-266, Presented at the 38th Congress of the International Astronautical Federation, Brighton, UK, Oct 1987.
10. D.L. Mordell, F.W. Eyre and A.V. Sreenath, "The Inverted Turbojet," Proceedings of the Eighth Anglo-American Aeronautical Conference, London, Sep 11-14, 1961.
11. Y. Ribaud, "Inverse Cycle Engine for Hypersonic Air-Breathing Propulsion," ISABE-89-7111, Proceedings of the Ninth International Symposium on Air Breathing Engines, AIAA 1989.
12. T. Kanda, et al., "A Comparison of Scramjet Engine Performances Among Various Cycles," AIAA-89-2676, AIAA/ASME/SAE/ASME 25th Joint Propulsion Conference, Monterey CA, Jul 10-12, 1989.

13. Murthy, S.N.B., and Czysz, P., "Energy Analysis of High Speed Vehicle Systems," AIAA-90-0089, AIAA Aerospace Sciences Meeting, Reno NV, Jan 8-11, 1990.
14. Stricker, T.M., and Essman, D.J., "Turbojet Potential for Hypersonic Flight," Preprint submitted for Agard 75th Symposium of the Propulsion and Energetics Panel, May 1990.
15. Lindley, C.A., "Performance of Air-Breathing and Rocket Engines for Hypervelocity Aircraft," ICAS Paper 64-557, Presented at the ICAS Fourth Congress, Paris, 1964.
16. Kuchemann, D., The Aerodynamic Design of Aircraft, Pergamon Press, 1978.

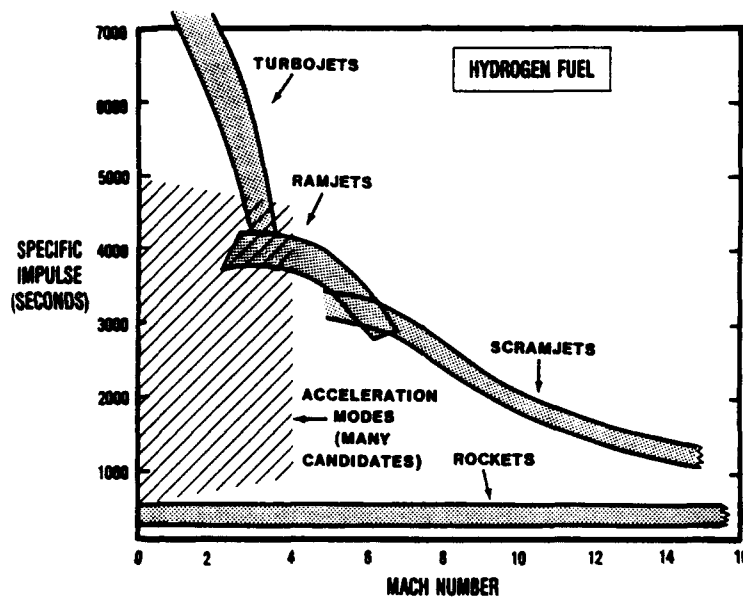


FIGURE 1 APPROXIMATE PERFORMANCE OF HYDROGEN FUELED ENGINES

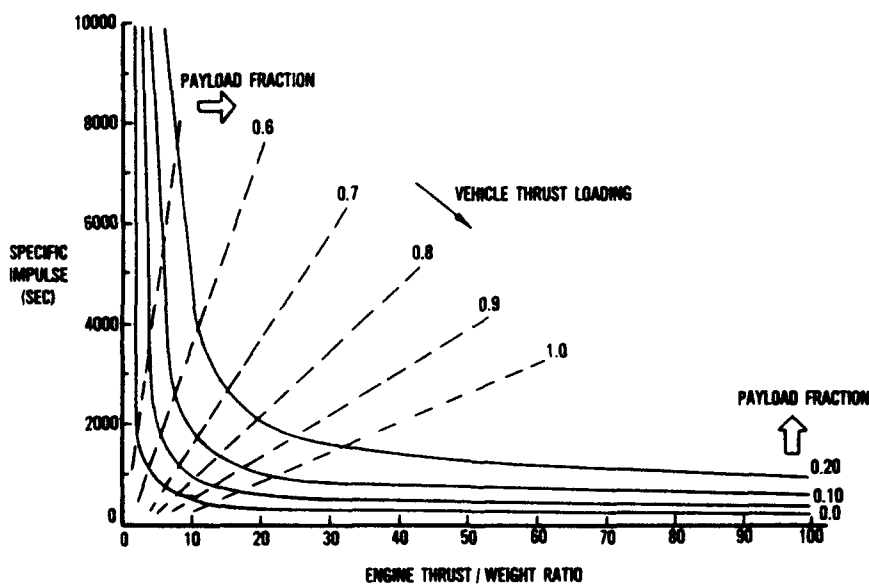


FIGURE 2 TYPICAL TRADE-OFF: SPECIFIC IMPULSE AND ENGINE THRUST-TO-WEIGHT RATIO

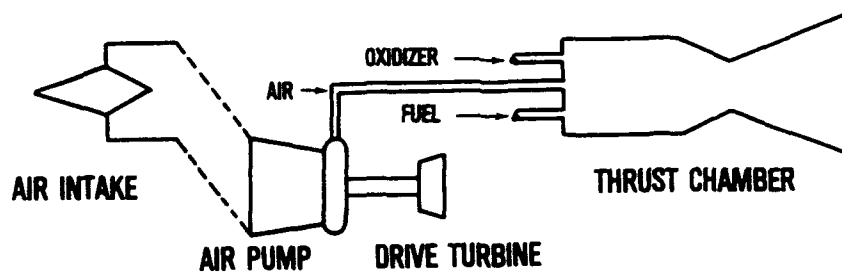


FIGURE 3 CHALLENGE OF PUMPING TO HIGH PRESSURE WITH MINIMUM WEIGHT

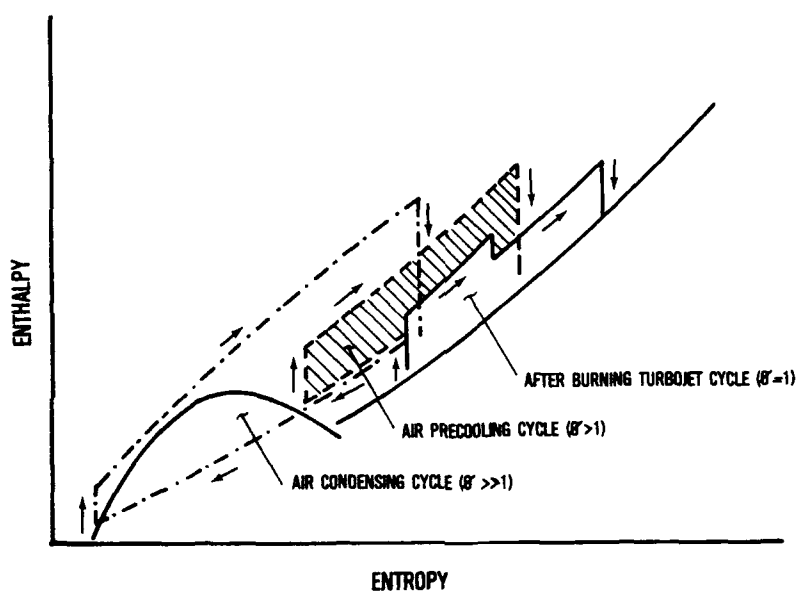


FIGURE 4 THERMODYNAMIC CYCLE SPECTRUM

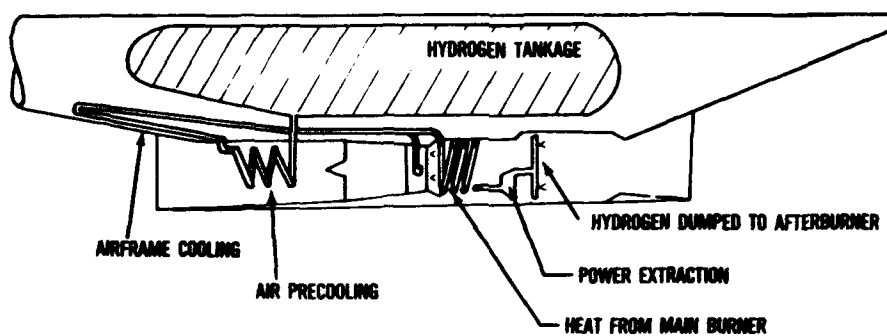


FIGURE 5 POTENTIAL USES OF HYDROGEN

## HYPERSONIC PROPULSION: PAST AND PRESENT

92-16977

by

C. Sánchez Tarifa  
SENER  
Edificio Windsor  
r. Fdez Villaverde, 65-20º  
Madrid 3  
Spain

AD-P007 939

SUMMARY

The change of the concept of hypersonic speed with time is in the first place briefly discussed.

The evolution of the hypersonic propulsion is restricted to the history of the ramjets. Considering the abundance of excellent literature on the subject only the most remarkable achievements are commented. Less divulged historical events, such as the propulsion of helicopters by ramjets are discussed with more detail, and special attention is given to the contributions of Spain to supersonic combustion.

The present state of the hypersonic propulsion is commented, reviewing from the literature on the subject some of the most demanding problems facing the propulsion systems of the Aerospace Plane and of the Hypersonic Cruise Aircraft.

1. INTRODUCTION. HYPERSONIC SPEEDS

The history of the hypersonic propulsion systems should begin with the definition of hypersonic speed, because it has changed with time.

Up to the middle 1950's the hypersonic regimen was considered as the flow region at which the linearized theories to study supersonic flows developed by Ackeret<sup>1</sup> and other aerodynamicists, such as Von Kármán and Busemann in the 1920's and 1930's did not longer apply<sup>2</sup>.

The approximated theories developed for the study of the hypersonic regime by Hayes, Goldsworthy and others<sup>3</sup>, depended not only on the Mach number, but on a geometrical parameter which in turn was a function of the thickness and camber

of the profile and of the angle of attack. Therefore, the hypersonic flow region might begin at different Mach numbers.

The same thing happens nowadays, but for very different physical concepts. In the supersonic region when the Mach number increases, several well known phenomena become gradually important; such as curved strong shocks and thin shock layers, entropy layers in blunt bodies, thick and hot boundary layers and the existence of high temperature regions in which the flow is no longer at constant chemical composition, but a reacting flow. When all or some of these phenomena have to be taken into account the flow is considered hypersonic<sup>4</sup>.

Therefore, there is not a Mach number defining the change from supersonic to hypersonic, but a transition region. However, for simplicity, it is generally agreed that at Mach number 5 the flow may be considered hypersonic.

The first man-made craft to achieve a hypersonic speed according to the above mentioned definition was a WAC Corporal rocket as a second stage of a German V-2, in White Sands, USA, on 24th February 1949. From that date hypersonic speeds have been reached by the ballistic missiles developed in the 1950's; followed by unmanned and manned spacecrafts reaching orbital speeds and reentry Mach number in the region of 25-27; deep space sondes and even hypersonic piloted aircraft. All these hypersonic vehicles have been powered by rocket motors, due to its relative simplicity, and above all because their performances are practically independent of the outside conditions and they can be fully tested on the ground.

## 2. AIRBREATHING HYPERSONIC PROPULSION DEVELOPMENT

### 2.1. INTRODUCTION

The huge potential advantages of the airbreathing engines in terms of fuel consumption in comparison with rocket engines for hypersonic high altitude flights was very early recognized, when jet propulsion was still in its infancy. It is also well known that its development is much more complex, among other things because the performances of the airbreathing engines are fully dependant on the external air flow conditions and because testing at high Mach numbers is extremely difficult. These complicated development problems coupled with the



lack of adequated funds for many years\* have resulted in that up to date no operational hypersonic airbreathing engines have been developed.

The history of the development of the airbreathing hypersonic propulsion systems, is essentially, the history of the ramjet. In all hypersonic propulsion systems, ramjets are coupled with jet engines and/or rocket motors in a large variety of combinations. However, the ramjet is the essential component of the propulsion systems and it is the only airbreathing engine with the capability of reaching hypersonic speeds. Accordingly, and in order to keep this work within reasonable limits, it will be fundamentally restricted to the evolution of those engines. Special emphasis will be placed on supersonic combustion, the applied technology that gives the ramjet its hypersonic capability.

Many publications have been written on the history of the ramjets. From the early development up to 1955 and excellent history of the ramjet development was published by Avery<sup>5</sup>.

In a recent AGARD Conference, Waltrup<sup>6</sup> has published an extensive study on the evolution of ramjets, with special dedication to scramjets, as part of a more extense work on the evolution of hypersonic airbreathing propulsion systems.

Taking into account the excellent and abundant literature on the subject, the part of this work dedicated to the history of the ramjets will be restricted to comment the most important achievements or landmarks, and to detail some less well known contributions, with special emphasis on those of Spain to the supersonic combustion problems.

## 2.2. EARLY DEVELOPMENTS

Among the many names of early inventors, patents and studies, which are cited in many publications, due credit has to be given to the french R. Lorin<sup>7</sup>, who was the first to carry out a study on the potential utilization of ramjets for subsonic applications, recognizing its low efficiency. What makes this work so remarkable it is its pioneering nature and that it was written in 1913, when flight was in a very primitive stage. As a consequence, no practical investigations were carried out.

---

\* Air breathing engines were left with little money available for research, when most of the resources for propulsion in the United States were devoted for many years to the development of the ICBM and other missiles as well as on space vehicles powered by rocket motors.

Another remarkable achievement for its anticipation was the Fono<sup>5,8</sup> patent of a supersonic ramjet. This patent was granted in Germany in 1928, and in these 1920's it was then when thanks to the works of distinguished aerodynamicists, such as Ackeret, Mach and Prandtl the possibility of supersonic flight was given a real consideration.

Extensive description of these early developments are given in ref. 5 and 9.

### 2.3. WAR DEVELOPMENTS

The development of the ramjets during the Second World War was carried out mainly in Germany<sup>5,10</sup>. Sänger, of the Air Research Institute at Brunswick, was a leader in the field, and in 1943 he had developed a full scale ramjet which was tested in flight in a D017Z. His works and the contributions of distinguished scientists and engineers, such as Oswatitsch and Busemann (aerodynamics); Damköhler, Lippisch, Schwalb and Pabst (combustion) and the involvement of some important engine and aircraft companies of Germany (Walter, Focke-Wulf, Heinkel and Messerschmitt), produced the design and test of large units including designs of fighter with full ramjet propulsion<sup>11</sup>.

Design and tests were also carried out on artillery projectiles accelerated by ramjets, propulsion of missiles and propulsion of helicopters with tip placed ramjets. It may be pointed out that the design and studies conducted on ramjets in Germany during the War established the foundation of the modern technologies of this propulsion system.

However, due credit must be given to the research and development efforts carried out in the United States. The special relevance were the works of Kantrowitz and Donaldson on supersonic diffusers<sup>12</sup>, and the combustion research programme carried out at the Massachusetts Institute of Technology (MIT)<sup>5</sup>. Special mention should be made of R. Marquardt, who founded the Marquardt Company in 1945, which has been since that time one of the leaders in the field.

It is interesting to mention the Bumblebee programme<sup>5</sup>, initiated near the end of the war to develop missiles against the Kamikaze attacks of the Japanese fighters. A large number of institutions and companies were involved and the ramjet development programme received a very large impulse.

## 2.4. POST-WAR DEVELOPMENTS. AIRCRAFTS AND MISSILES

Ramjets development after the war followed several courses. The main ones were the propulsion of aircrafts and missiles; and there existed a limited and not much divulged programme on ramjet propulsion of helicopters and an isolated military laboratory programme on nuclear powered ramjets.

Propulsion of aircrafts by ramjets was a short lived effort, although some remarkable achievements may be mentioned, mainly the Leduc<sup>13</sup> developments and flights in France and the development of flight models of subsonic ramjets by the Marquardt Company in the United States, where a Lockheed F-80 Shooting Star was the first piloted aircraft to fly powered only by ramjets<sup>10</sup>.

The development of missiles powered by ramjets were mainly carried out in the United States and in the United Kingdom (not counting the Soviet Union), where surface to air missiles reached operational state.

In the United States the research and development efforts carried out by the John Hopkins University Applied Physics Laboratory, NASA Langley Research Center, NASA Lewis, MIT, the Marquardt Company and others, lead to the development and manufacture of operational ramjets for the missiles Boeing Bomarc (US Army) and Bendix Talos (US Navy) in 1955. This last missile resulted from the Bumblebee programme and was followed some years later by the advance version Typhone.

There are several facts about the research and development efforts carried out in the United Kingdom, mainly by the Rolls Royce company (on that time Bristol Aeroengines) which should be specially pointed out.

This company developed the Thor ramjet for the Bloodhound missile for the RAF, and the Odin ramjet for the Sea Dart missile for the Navy; and the remarkable fact is that the lasts versions of these missiles are still in service. This has provided Rolls Royce with an unique experience on operational reliability of ramjets<sup>14</sup>.

Another remarkable fact is the wide range of applications studied by the company in early days, including aircraft propulsion and hypersonic vehicles.

Aside of the abovementioned ramjets developments in the United States and in the United Kingdom, no other operational missiles with ramjet propulsion followed these early efforts; until recent years when the development of integrated

rocket-ramjet propulsion systems took place, which gave a very important impulse to the ramjet powered missiles, as it will be later described.

## 2.5. RAMJETS FOR HELICOPTER PROPULSION

The idea of using air conducted through the blades of the rotor of a helicopter, with or without combustion at the tips, as a propulsion system, is an old one and it is still alive. With these jet powered helicopters the mechanical transmission is eliminated as well as the reaction torque.

Pulse-jets and rockets have been utilized placed on the tips of the rotor blades, with the same purpose, but they were very short lived experiments.

On the other hand, a considerable effort has been carried out to utilize ramjet powered helicopter rotors. Actually, this is the only subsonic applications of ramjets.

The thermal efficiency of a subsonic ramjet is very low, and therefore, the specific fuel consumption of the helicopter is very high. However, a subsonic ramjet is a low cost and low weight machine, which added to the aforementioned advantages made the idea attractive for some special applications.

The original idea is of the german origin. There were some studies and test programmes conducted in Germany during the War, specially in the Focke Wulf Company, although no flying models were developed.

After the War some developments took place in the United States<sup>\*</sup>.

The austrian engineer Doblhoff<sup>\*\*</sup>, developed the first ramjet powered helicopter: the "Little Henry" for the Douglas Aircraft in 1949. The ramjets had a thrust of 50 N at full tip speed (26 HP total). After a long test programme the Air Force cancelled the project.

The Hiller Company, after rejecting pulse-jets, developed in 1955 the Hornet helicopter, utilizing ramjets. The prototype was initially a great success, and

---

<sup>\*</sup>The data on the developments of ramjet powered helicopters in the United States and in the Netherlands have been taken from refs. 15 and 16.

<sup>\*\*</sup>He was heavily involved during the War developing jet powered helicopters for the Wiener Neustaedter Flugzeugwerke.

a contract was placed on the company to manufacture 15 helicopters for the armed services. The 200 N ramjets were certified by the FAA, but not the helicopter, and therefore, no further orders were received.

The most important achievement on this technology of ramjet powered helicopters was the "Hummingbird" or "Kolibrie", developed by J. Drees for the Nederlandse Helicopter Industrie.

After a research program some prototype helicopters were developed in 1955 powered by two light weight ramjets (9 Kg each). Certification was granted in the Netherlands in 1958 (not in the United States) and a small series of 25 helicopters was manufactured. They were utilized in several countries, mainly for agricultural tasks. Until recent years, some of them were still flying.

In Spain a contribution to the development of ramjet powered helicopters was carried out in the early 1950's.

The german engineer O. Roeder conducted for the Aeronautica Industrial S.A. (AISA) a ground test programme of a rotor powered by ramjets (Fig. 1). The theoretical calculations were carried out at the Instituto Nacional de Técnica Aeroespacial (INTA) by the aeronautical engineer J. de la Cierva, eldest son of the spanish inventor of the autogiro.

A second model (Fig. 2) was developed with foldable ramjets, which constituted a new development to improve autorotation. The programme ended because no funds were allocated to develop a flying model, coinciding with the untimely death of J. de la Cierva.

Ramjets powered helicopters did not succeed for a variety of reasons; mainly the very high fuel consumptions, noise and some autorotation problems.

Modern technologies in the fields of high strength low density materials and on the aerodynamics of supersonic rotors might improve the problem of fuel consumption by increasing rotor tip speeds. However, the problem of noise would have to be alleviated in commercial applications, and there would be the problem of high infrared emission for military applications.

## 2.6. NUCLEAR POWERED RAMJETS

At the height of the Cold War some research programmes were carried out in the United States directed to the utilization of nuclear energy to power both jet and ramjet engines.

The purpose of the programmes was the development of aircrafts and weapons with the capability of flying for practically unlimited time thus avoiding in this way the possibility of being destroyed by pre-emptive attack on the ground by hostile missiles.

Three experimental programmes were carried out; two on jet engines<sup>\*</sup> and one on ramjets, the Pluto programme.

In the Pluto programme an air cooled nuclear reactor was utilized instead of a combustion chamber. Inlet diffuser and nozzles were of the conventional type.

The idea was to keep ramjets flying at low altitudes over unpopulated areas around the arctic regions.

Of the three programmes, the nuclear powered ramjet was the one with less technical problems. After many studies and laboratory tests, the three programmes were cancelled due to their huge political implications.

## 2.7 SUPERSONIC COMBUSTION. SCRAMJETS DEVELOPMENTS.

From the early development of the ramjets their limitations regarding maximum speed were well known, mainly originated by the compressed air reaching temperatures near the equilibrium values of the hydrogen-air mixtures, at which the only available thrust would be obtained via recombination reactions in the nozzle.

It is generally agreed that the practical limit is around Mach 7. The introduction of supersonic combustion in the ramjets, from there on denominated scramjets, represented a tremendous break in performances, since it gave them

---

<sup>\*</sup>One of the programmes (General Electric) was of the open cycle type with a nuclear reactor replacing the combustion chamber. The other programme (Pratt & Whitney) was of the double cycle type, with a sodium loop.

the unique theoretical potential of being able to function up to orbital speeds.

As it has already been pointed out in paragraph 2.1, there is abundant literature on the evolution of supersonic combustion and on other all aspects of scramjets. A review of supersonic combustion has been recently published by Barrere<sup>17</sup>. Early developments were reviewed by Ferri<sup>18</sup>, and a modern review of the scramjet evolution has been carried out by Waltroup<sup>6</sup>, who also published a review on liquid fueled scramjets<sup>19</sup>.

Supersonic combustion was initially studied in external flows, directed either to increase lift or to reduce drag. The first practical laboratory demonstration was carried out by Smith and Davies<sup>20</sup> in 1952.

Supersonic combustion was initially achieved in scramjets by means of a shock wave. Diffusive combustion type was introduced by Ferri<sup>21</sup>, and it proved to be superior, specially at high Mach numbers.

After these early studies and model tests, in the late 1950's and early 1960's, very important and extensive research programmes on supersonic combustion and on all other aspects of scramjets were conducted. The brunt of the research effort was carried out in the United States; but with relevant contribution in the United Kingdom, France, Germany and Spain (not counting the Soviet Union). In Spain the contributions were of the theoretical type.

One of the main reasons behind that great impulse on the research efforts was the possibility of developing aircrafts with the capability of taking off from normal airports and reaching low orbits, powered only by airbreathing engines: the aerospace plane concept.

The obvious strategic interest of this aerospace plane was the reason why many researchs programmes were sponsored by the armed services.

The first important programme on the aerospace plane concept was conducted by Ferri<sup>21</sup> at the Applied Sciences Laboratory with the collaboration of the Republic company. Subsequently, the USAF launched a major programme: the Aerospace Plane in which collaborated the companies Douglas and Republic. The USAF also sponsored three important programmes on scramjets developments<sup>22</sup>, carried out by the Applied Sciences Laboratory, the Marquardt company and the United Aircraft Research Laboratory.

Another major programme was carried out in NASA Langley : The Hypersonic Research Engine, directed to the propulsion of manned vehicles<sup>22</sup>. The US Navy sponsored the programme: the Supersonic Combustion Ramjet Airbreathing Missile, under the direction of the John Hopkins University, Applied Physics Laboratory.

During the same period of time lesser research efforts, but with relevant contributions, were carried out in Western Europe. They are described in detail in refs. 6 and 13, including those carried out in the Soviet Union.

All these important research programmes carried out in the United States and in Europe did not conclude with the development of any operational hypersonic aircraft or missile powered by air breathing engines, and in the 1970's the research efforts decreased considerably and many programmes were cancelled.

It is generally agreed that the reason is that the technological level on that time was not sufficiently advanced to accomplish the formidable task of developing aerospace planes or atmospheric hypersonic vehicles.

## 2.8 CONTRIBUTIONS IN SPAIN TO SUPERSONIC COMBUSTION

In 1954 a combustion group was constituted at the Instituto Nacional de Técnica Aeroespacial (INTA) of Spain. This group was promoted by the World known aerodynamicist, the late Prof. Von Kármán, and directed for several years by his collaborator on combustion, Prof. and Academician G. Millán\*.

The combustion group worked continuously for over 20 years under research contracts sponsored by the Air Force Office of Scientific Research\*\*, of the United States.

The combustion group also worked for other US organizations: The Forest Fire Research Service (6 years), the European Office of the Army and the Arnold Engineering Development Center.

When in the late 1950's the US Air Force became highly interested on supersonic combustion, the Spanish combustion group carried out a number of research

---

\* Von Kármán and Millán gave a course on combustion at La Sorbonne in Paris in 1953. The lecture notes considerably enlarged were published by Millán for the Air Research and Development Command of the USAF in 1954 under the title: Aerothermochemistry.

\*\* Formerly, Office of Aerospace Research of the Air Research and Development Command, of the United States Air Force.



programmes for the aforementioned organization, on several aspects of supersonic combustion and on hydrogen-air flames.

These activities were conducted mainly in the period 1962-1970.

An early work was a study carried out by Pérez del Notario and this author<sup>23</sup> in 1962. Premixed and diffusion laminar hydrogen-air flames were studied with a spherico-symmetrical model, and chemical kinetics was approximated by parametric overall reaction rates, since no overall reactions rates for the hydrogen-air reactions were known. Solution of the problem was obtained by means of approximated integral methods.

The experimental work was carried out by injecting hydrogen in air through porous spheres. With the same experimental equipment the diffusion hydrogen-oxygen flame was studied by injecting oxygen through the same spheres in hydrogen (Fig. 3). There are little or no free convection effects when burning oxidizers in hydrogen and the flame is nearly spherical<sup>24</sup>. (Fig. 4).

On the other hand, when hydrogen is injected in air, free convection exists but the flame is located very close to the sphere surface (Fig. 3) and the spherico-symmetrical model holds.

Several conclusions were obtained\* and it was shown the advantages of this spherical model in order to obtain from the experimental results information on the main parameters that characterize the flame.

A comprehensive analysis of a supersonic combustion process of the diffusive type was carried out by Da. Riva, Liñán and Fraga<sup>25</sup> in 1964. The model included the study of turbulent mixing. Chemical kinetics non-equilibrium effects were treated with special emphasis on flame extinction for the laminar case, with a tentative extension to the turbulent case. A discussion on the application of the model to the hydrogen-air flame was also included.

Da. Riva<sup>26</sup>, carried out in 1966 a study on the internal structure of hydrogen-air diffusion flames by means of singular perturbation methods, utilizing the fact that for large reaction rates the flame is close to chemical equilibrium. The main contribution of the work was the introduction of a very

---

\*The mathematical possibility of obtaining three stationay solutions with spherical models was analized.

completed chemical kinetics scheme. The study had a direct application to supersonic combustion.

Liñán, Urrutia and Fraga<sup>27</sup>, studied chemical kinetics effects in hydrogen-air supersonic combustion of the diffusive type, showing the existence of three regions: the first region close to the injector exit where the flow may be considered frozen for the main reacting species, which is the ignition delay region; a second transition region and a third region far from the injector in which the flow is close to chemical equilibrium.

An ignition delay model was investigated by Da Riva and Urrutia<sup>28</sup> in 1968 in diffusive supersonic combustion under conditions of two-dimensional mixing. It was shown that the temperature of the injector outer wall and to a lesser extent, pressure, injector length and the conditions outside the boundary layer, control the ignition process.

Liñán and Urrutia<sup>29</sup>, studied the hydrogen-air flame utilizing singular perturbation methods at temperatures typical of supersonic combustion. A model of eight chemical reactions was utilized.

It was shown the existence of several reaction stages clearly differentiated, which were studied for particular cases obtaining characteristics times and simplified kinetics schemes for each region.

The formation of nitrogen oxides in the hydrogen-air reaction was studied by Sanmartín, Fraga and this author<sup>30\*</sup>.

A complex chemical kinetics model of 34 reactions was utilized and overall reaction rates were obtained for different temperatures, including those of interest for supersonic combustion.

Fraga, Crespo and this author carried out a review of the principal problems involved in hydrogen combustion, including supersonic combustion<sup>31</sup>.

---

\*This work was part of a programme sponsored by the Fundación Juan March of Spain on emission of contaminants in hydrocarbons and hydrogen combustion processes, directed by this author.

Another contribution of the Spanish group to supersonic hydrogen-air combustion problems was the work by Liñán and Crespo<sup>32</sup>. They carried out an asymptotic analysis of unsteady diffusion flames for large activation energy\*.

The works uncovered the existence of three regimes, an ignition regime a deflagration regime and a diffusion flame regime. It was pointed out the existence of experimental evidence supporting this complex picture.

This work was continued in 1987 by Jackson and Hussaini<sup>33</sup>. They utilized the same model but including the effect of free shear and Mach number on the ignition regime, on the deflagration regime and on the diffusion flame regimen.

### 3. PRESENT SITUATION.

#### 3.1 RAMJET POWERED MISSILES.

The development of integrated ramjet-rocket propulsion systems, coupled with advances in technologies, such as on board microcomputers to facilitate control, has given a strong impulse to the design and manufacture of low consumption ramrocket powered tactical missiles for medium and long range missions.

No operational ramjet powered missiles had been developed for many years. Now, the Soviet Union has in operation the well known SA-N family of surface to air missiles, and France<sup>13</sup> has developed the ASME, air to ground missile with nuclear warhead, powered by a liquid fueled ramjet, and the Rustic, with a solid fuel ramjet. In addition, France and Germany are developing in cooperation an antiship missile, the ANS.

All these ramjet powered missiles are only of the supersonic type.

A study to apply scramjets hypersonic propulsion to missiles was carried out by Billig<sup>34</sup>.

---

\*This work was sponsored by the ARO company of the Arnold Engineering Development Center. USA.

### 3.2 HYPERSONIC AIRBREATHING PROPULSION. CURRENT MANNED PROGRAMMES.

Research and development on hypersonic airbreathing propulsion for manned system is again in a high level of activity and it is the object of political and public interest.

In the United States, the National Aerospace Plane (NASP) is in progress with the goal of developing stage to orbit capability (SSTO) vehicles, based on airbreathing propulsion. Two X-30 manned SSTO high test vehicles are planned to be developed and another one for ground tests.

The programme is now in the phase of developing technologies, with the main effort on propulsion, and conducting conceptual and preliminary designs.

The programme is being funded by NASA, the Air Force Defense Advanced Research Project Agency (DARPA), the Strategic Defense Initiative and the Navy. 50 organisations and companies are involved and about 6000 people.

Decision to develop the X-30 has been postponed until 1994. A total of \$ 3.3 billions will be spent up to that date.

A derivative of the NASP programme would be a hypersonic cruise atmospheric aircraft, the "Orient Express", of which many studies are also in progress.

In Germany there is the Sänger space plane programme and in the UK the Horizontal Take-off and Landing (HOTOL) programme, both vehicles with SSTO capabilities.

In Sänger, airbreathing propulsion will be utilized up to Mach numbers of the order of 7; and from there on rocket propulsion will take over. This programme is significantly funded by the German government and the prime contractor is the company MBB.

HOTOL is, for the present moment, with little or no funds allocated. It is been announced that it will utilize airbreathing propulsion up to altitudes of 25-26 km and up to Mach numbers of the order of 6 or 7.

There are also hypersonic propulsion activities in France and in Japan, and it has been reported that the Soviet Union is heavily engaged in evaluating aerospace plane concepts and developing the required scramjet technologies.

The reasons behind this renewal of the high level of interest in hypersonic airbreathing powered aircrafts, in addition to commercial reasons, it is that the technology has reached a level at which the development appear as feasible in a near future.

Three technologies are specially significant: Computational Fluid Dynamics (CFD) and the high capability supercomputers; the development of new composite low weight heat resistance materials, and new diagnosis methods to carry out tests, specially the non-intrusive optical methods.

CFD and the new generation of supercomputers are making possible approximated calculations of the complex flow problems in intakes and nozzles, and above all in the combustor. An evaluation of the CFD analysis applied to scramjets is reviewed in ref. 22.

The introduction of the new light weight heat resistance materials in the structure of the aerospace plane, would permit higher Mach numbers at every altitude, making wider and more efficient the so called flight corridor up to orbit<sup>35</sup> (Fig. 5).

These light weight materials would reduce the empty weight of the vehicle and of the power plant, which would decrease the sensitivity factor\* to acceptable levels<sup>36</sup>.

Finally, non intrusive measurement methods would give more accurate information from tests and better validation of theoretical models<sup>37 38</sup>.

### 3.3 HYPERSONIC PROPULSION SYSTEMS. PRESENT SITUATION.

The propulsion system of the NASP is partially classified. It is known that the main engines will be hydrogen fueled scramjets. No data have been released on the propulsion system from take off up to Mach numbers of the order of 3 or 4.

In addition to the NASP scramjets the US Navy is sponsoring the development of liquid fueled dual combustor scramjets, designed for applications in the range of Mach number 3-7.

---

\* An error in the empty weight is considerably amplified in the total weight and the same thing occurs with the errors in the estimation of the hydrogen consumption for the mission.

No scramjets developments are reported to being carried out in Western Europe. Airbreathing propulsion in the Sänger will be a combination of jet engines and ramjets. Several possible combinations are being studied by MTU and MBB<sup>39-40</sup>.

On the other hand, the propulsion system of the HOTOL has been classified by the UK government, and no information has been released.

Some comments will be included on the extremely difficult problems facing the development of scramjets operating up to or near to orbital speeds.

A review of these and other hypersonic propulsion problems has been carried out by Cheng<sup>41</sup>. In this analysis it is pointed out that the boundary control in the diffuser, and the nozzles problems although difficult will be solved and that the main difficulties lie in the combustor.

In a flight corridor that a space plane will have to follow such as that shown on Fig. 5, the spacecraft will follow a trajectory of maximum admissible dynamic pressure in order to optimize combustion. This maximum pressure, dictated by the airframe, is estimated in ref. 35 to be of the order of six times the value admitted in actual commercial subsonic transports.

At a certain Mach number, (12-13) the aircraft will have to climb faster, in order to avoid excessive heating of the heat shield of the structure (Fig. 5). Then, the very rapid exponential decrease of the atmospheric density could not be compensated with dynamic pressure, and combustion might not be possible. Cheng<sup>41</sup>, believes that with present scramjets combustion systems, they will not be able to operate at altitudes higher than 60 km. Hydrogen reaction rates are of second order, and then proportional to the square of density, which originates that thrust falls rapidly with height. He proposes to utilize at high altitude a catalytic first order reaction in which oxygen will react on a molecular layer of hydrogen absorbed on platinum or other metals. The reaction rate will only be proportional to the density and the thrust of the scramjet will decrease much slower with height and it would be much easier to produce a positive thrust margin over drag at very high altitudes.

On the other hand, Waltrup<sup>6</sup>, proposes a scramjet utilizing different types of injector systems, and the injection of hot combustion products and fuel, which might be produced by the exhaust of a hydrogen rich rocket exhaust for high altitude operation.

A simple solution would be to utilize rocket propulsion in the last part of the flight path, which would be needed in all cases in orbit for manoeuvres and during re-entry. We would like to remark that an important feature of the space plane would be its capability to reach high Mach numbers at relatively low altitudes, because the difference in potential energy between orbit level (~ 150 km.) and a height of 60 km is less than two orders of magnitude in comparison with the kinetic energy of orbital speeds.

Finally, we would like to comment on the hypersonic propulsion systems of the "Orient Express".

They are very different proposals for that propulsion system, which depend, to some extent, on the cruise conditions selected.

It has been mentioned that scramjets would be an ideal power plant for cruise Mach numbers of the order of 5-6 with cruise altitudes of about 40 km<sup>41</sup>. On the other hand, Schwab and Hewit<sup>42</sup>, estimated that a hypersonic aircraft would require to have a subsonic speed capability over long distances in the event of engine malfunction. In consequence, they propose a dual mode turbojet-ramjet power plant, carrying out several optimization studies for Mach numbers ranging between 4 and 6.

There are doubts about if this type of aircraft will ever be constructed, in addition or substituting a Mach 2-3 supersonic transport. There is the old known problem of the maximum admissible acceleration for ordinary passengers, estimated to be of the order of 0.2g<sup>42-43</sup>, which coupled with the time lost on the ground makes imperative long ranges (Fig. 6). Hydrogen must be utilized, and in addition to all technical problems of this type of aircraft, it would have to be included the logistic problem of having storage and fueling facilities of liquid hydrogen in most major airports throughout the World.

On the other hand, utilization of hydrogen would not be a major problem in selected aerodromes for the aerospace plane operation.

#### REFERENCES

1. Ackeret, J.: LüftKräfte auf Flügel, die mit grösserer als Schallgeschwindigkeit bewegt werden. Z. Flugtech. u. Motorluftschiffahrt 16, 72-74 (1925)

2. Von Kármán, Th.: On the Foundation of High Speed Aerodynamics. High Speed Aerodynamics and Jet Propulsion Vol. VI Princeton University Press. 1954.
3. Heaslet, M.A. and Lomax, H.: Small Perturbation Theories of Transonic and Hypersonic Flows. High Speed Aerodynamics and Jet Propulsion Vol. VI Princeton University Press. 1954.
4. Anderson Jr., J.D.: Hypersonic and High Temperature Gas Dynamics. McGraw-Hill Book, 1989.
5. Avery, W.H.: Twenty Five Years of Ramjet Development. Jet Propulsion, November, 1955.
6. Waltrup, P.J.: Hypersonic Airbreathing Propulsion: Evolution and Opportunities. The John Hopkins University, U.S.A. AGARD Conference on Aerodynamics of Hypersonic Lifting Vehicles. Proceedings, 1987.
7. Lorin, R.: L'Aerophile 21, 229, 1913.
8. Zucrow, M.J.: Aircraft and Missile Propulsion. John Wiley and Sons, 1958.
9. Smith, G.G.: Gas Turbines and Jet Propulsion for Aircraft. Fifth edition. Published by "Flight", Iliffe and Sons, London 1950.
10. Baxter, A.D.: Historical Development of Jet Propulsion. High Speed Aerodynamics and Jet Propulsion. Vol. XII, Chapter 3. Princeton University Press, 1959.
11. Sänger, E.: The Place of Lorin Propulsion Unit in Jet Fighters. Zent. Wissensch. Berichtsw. über Luftfahrtforsch. Berlin. Rept. UM 3509, 1943. NRCC Rept. Tech. Transl. TT-30, 1947.
12. Kantrowitz, A. and Donaldson, C.: Preliminary Investigation of Supersonic Diffusers. NACA. Wartime Rep. 1-713 May 1945.
13. Marguet, R.: Ramjet Research and Applications in France. 9th ISABE, September 1989. Proceedings.
14. Lane, R.J. 1959-1989, 30 Years of Service Experience with Ramjets. Rolls Royce 687 MIS Communication. March 1989.



15. Boulet, J.: L'Histoire de L'Helicoptère.  
France-Empire, 1982.
16. Prouty, R.W.: Tip Driven Rotors: Potential and Pitfalls. Rotor and Wing International. March 1990.
17. Barrère, M.: La Combustion Supersonique. Problèmes Posés pour son Développement.  
L'Aeronautique et l'Astronautique, N° 128, 1988.
18. Ferri, A.: Review of Problems in Application of Supersonic Combustion. Journal of the Royal Aeronautical Society, 1964.
19. Waltrup, P.J.: Liquid Fueled Supersonic Combustion Ramjets: A Research Perspective of the Past, Present and Future.  
AIAA 24th Aerospace Sciences Meeting, 1986.
20. Smith, E.H. and Davis, T.: The Creation of Thrust and Lift by Combustion on External Surfaces of Airfoils.  
Smith and Davis, Physicists (Bu Ord Contract NOrd 12141) 1952.
21. Ferri, A.: Possible Directions of Future Research in Air Breathing Engines. AGARD Combustion and Propulsion Colloquium. Milan, Italy 1960.
22. White, M.E., Drummond, J.P. and Kumar, A: Evolution and Application of CFD Techniques for Scramjet Engine Analysis. AIAA 24th Aerospace Sciences Meeting. Reno. USA. 1986
23. Pérez del Notario, P. and Sánchez Tarifa, C: On the Structure of Premixed and Diffusion Laminar Spherico-Symmetrical Flames. Ninth International Symposium on Combustion , Cornell University, USA, 1962. Also: Sánchez Tarifa, C., Pérez del Notario, P. and García Moreno, F.: Combustion of Liquids Monopropellant and Bipropellant in Droplets. 8th Internacional Symposium on Combustion, 1960.
24. Sánchez Tarifa, C.: and Muñoz Torralbo, M.: Some Fundamentals Problems on the Combustion of Liquids Oxidizers in Hydrogen. XVII International Astronautical Federation Congress, Madrid, 1968.
25. Da Riva, I., Liñán, A. and Fraga, E.: Some Results in Supersonic Combustion. 4th ICAS Congress. París 1964.

26. Da Riva, I.: The Internal Structure of Hydrogen - Air Diffusion Flames. *Astronautical Acta*. Vol. 12. No. 4, 1966.
27. Liñán, A., Urrutia, J.L. and Fraga E.: On Diffusive Supersonic Combustion. 5th ICAS Congress. Proceedings, 1967.
28. Da Riva, I. and Urrutia, J.L.: Ignition Delay in Diffusive Supersonic Combustion. *AIAA Journal*. November 1968.
29. Liñán, A. and Urrutia, J.L.: Análisis de la Reacción Hidrógeno-Aire Mediante Métodos de Perturbaciones Singulares. (AFOSR Contract AF-EOAR 67-4). *Revista de Ingeniería Aeronáutica*, July-August 1969, Madrid.
30. Sánchez Tarifa, C., Sanmartín, J.R. and Fraga, E.: On the Formation of Nitrogen Oxides in the Combustion Processes of Hydrogen in Air. Ninth World Energy Conference. Detroit USA, Proceedings, 1975.
31. Sánchez Tarifa, C.: Fraga, E. and Crespo, A.: Hydrogen as a Fuel. Some Aspects of its Combustion Processes. Tenth World Energy Conference. Istanbul. Turkey, Proceedings 1977.
32. Liñán, A, and Crespo, A.: An Asymptotic Analysis of Unsteady Diffusion Flames for Large Activation Energies. *Combustion Science and Technology*. Vol. 00 1976.
33. Jackson, T.L. and Hussaini, M.: An Asymptotic Analysis of Supersonic Reacting Mixing Layers. *Combustion Science and Technology*. Vol. 87. 1987.
34. Billig, F.S.: Ramjet and Ramrocket Propulsion Systems for Missiles, AGARD PEP lectures Series 136, 1984.
35. Johnston, P.J, Whitehead, A.H. and Chapman, G.T.: Fitting Aerodynamics and Propulsion into the Puzzle. *Aerospace America*. Sept. 1987.
36. Gregory, T.J.: Credibility of NASP. *Aerospace America*. Sept. 1989.
37. Timnat, Y.M.: Diagnosis Techniques for Propulsion Systems. *Prog. Aerospace Sciences*. Vol. 26 1989.
38. Antclift, R.R.: Application of CARS (Coherent Anti-Stokes Raman Spectroscopic) to Scramjet Combustion. NASA-CR-178245, 1987.

39. Hertrich, H.A.: The German Hypersonic Technology Programme. 2nd European Aerospace Conference in Progress in Space Transportation. Proceedings. 1989.
40. Albers, M., Eckardt, D., Kramer, P.A. and Voss, N.H.: Technology Preparation for Hypersonic Air-Breathing Combined Cycle Engines. IX ISABE International Symposium on Air-Breathing Engines. Athens Greece. Sept. 1989.
41. Cheng, S.I.: Hypersonic Propulsion. Prog. Energy Combust. Sci. Vol. 15, 1989.
42. Schwab, R.R. and Hewitt, F.A.: Optimisation of Hybrid Propulsion Systems. European Symposium on Future Supersonic/Hypersonic Transportation Systems. Strasbourg, France, Nov. 1989.
43. Weber, R.J.: Propulsion for Hypersonic Aircraft. 4th ICAS Congress, Proceedings, 1964.

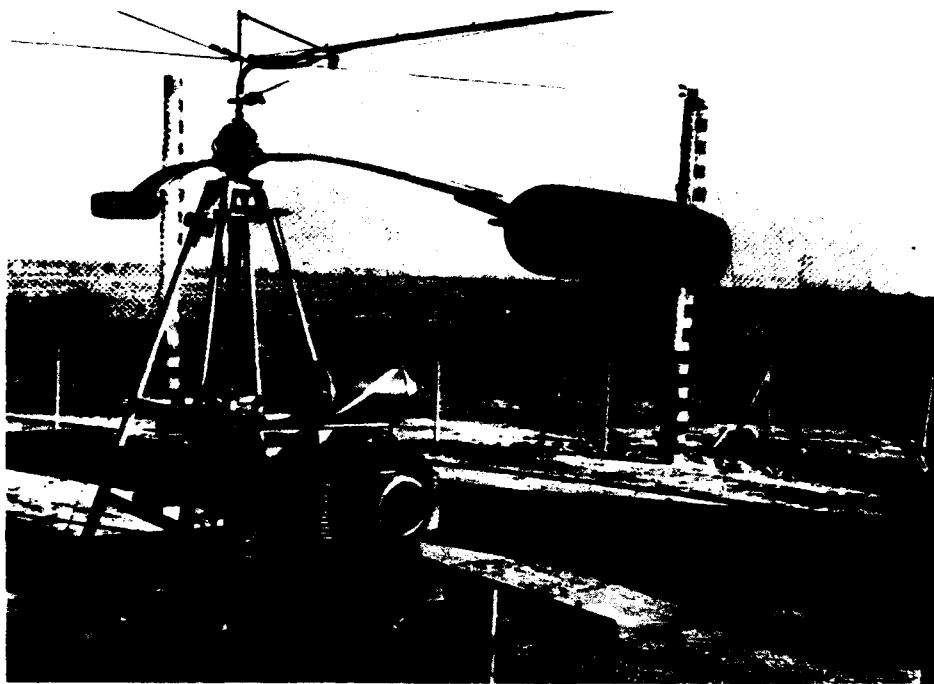


FIG. 1 GROUND TEST OF THE AISA RAMJET POWERED HELICOPTER ROTOR.

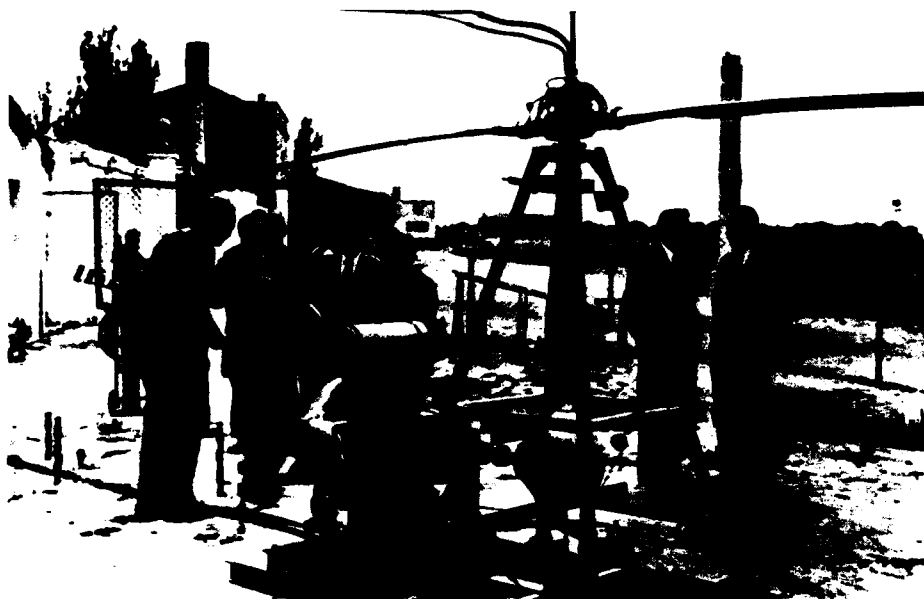
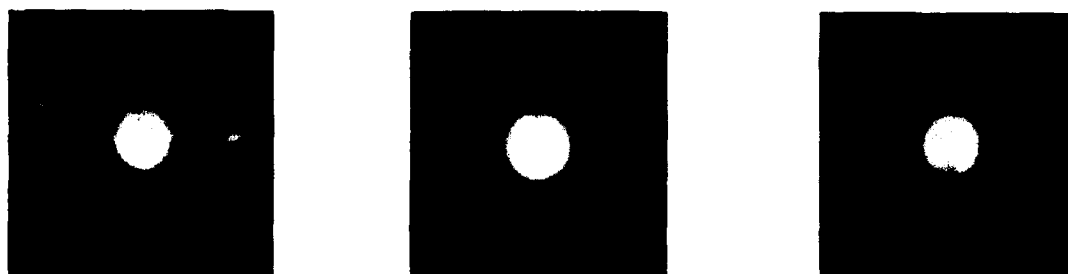


FIG. 2 AISA HELICOPTER ROTOR WITH FOLDABLE RAMJETS.



FIG. 3 OXYGEN BURNING IN HYDROGEN (LEFT) AND HYDROGEN BURNING IN AIR (RIGHT).



$T = 0 \text{ SEC.}$

$T = \frac{1}{12} \text{ SEC.}$

$T = \frac{2}{12} \text{ SEC.}$

FIG. 4 NITRIC ACID DROPLETS BURNING IN HYDROGEN.

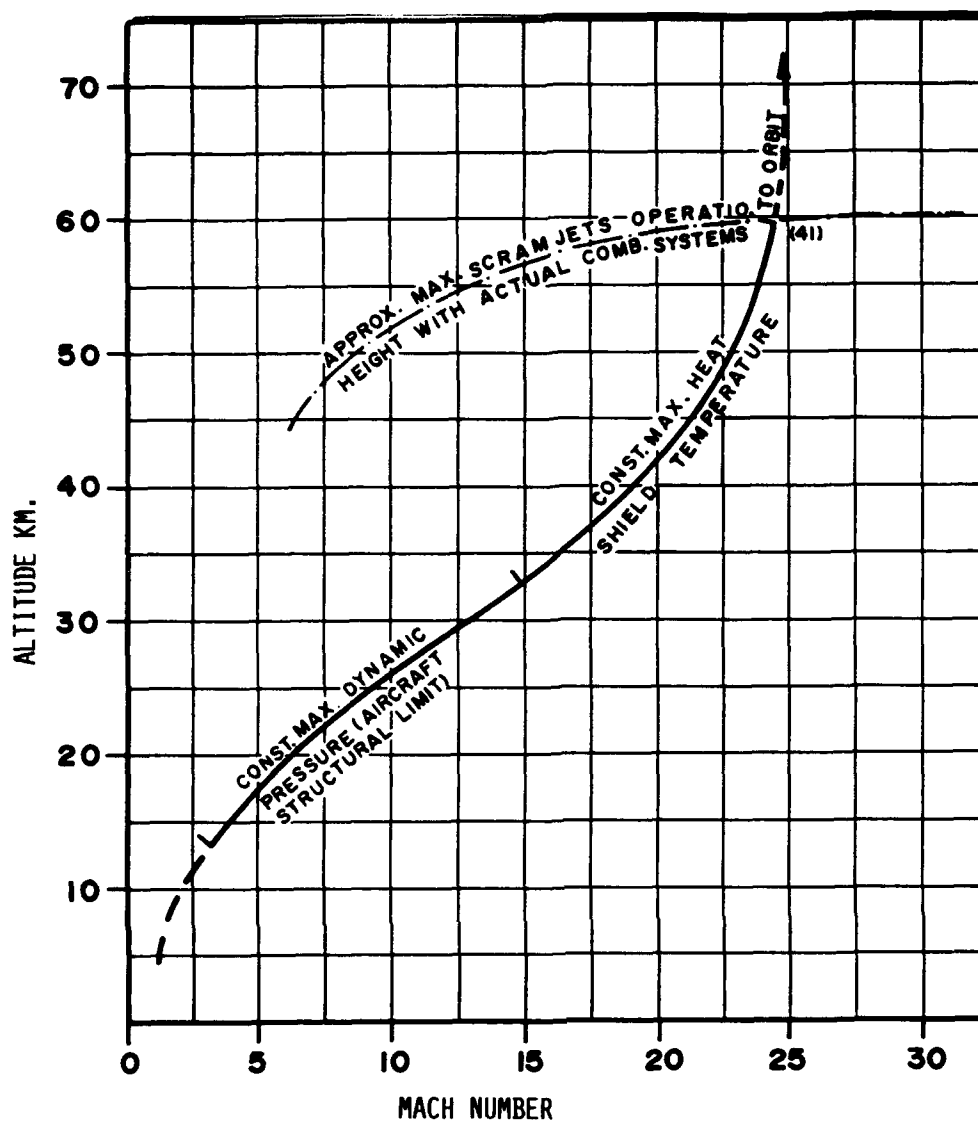


FIG. 5 APPROXIMATED FLIGHT PATH OF AN AIRBREATHING SINGLE STAGE TO ORBIT VEHICLE.

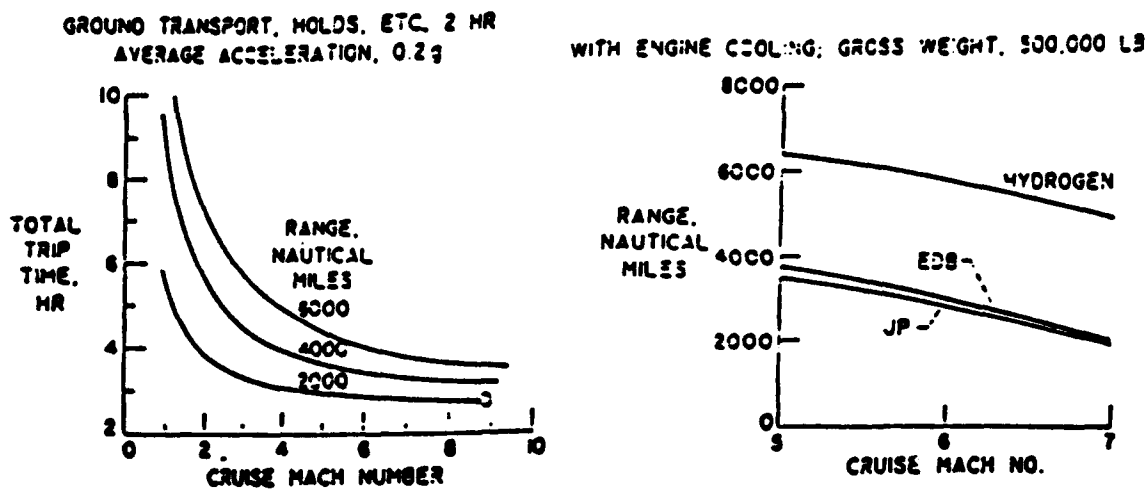


FIG. 6 INFLUENCE OF RANGE (LEFT) AND TYPE OF FUEL IN A HYPERSONIC CRUISE AIRCRAFT (REPRODUCED FROM REF. 43.)

**L'ETUDE DU STATOREACTEUR SUPERSONIQUE ET HYPERSONIQUE  
EN FRANCE de 1950 à 1974  
( APPLICATION AUX MOTEURS COMBINES AEROBIES )  
par  
Roger MARGUET, Pierre BERTON et Francis HIRSINGER  
ONERA  
92322 CHATILLON-Cedex ( France )**

Résumé

La France dispose aujourd'hui d'un potentiel de recherches et d'études théoriques et expérimentales sur le statoréacteur qui lui a permis de réaliser des programmes opérationnels tels que l'ASMP (Air-Sol Moyenne Portée à charge nucléaire), d'orienter les investigations et de dégager des tendances pour le futur, en particulier dans le domaine des très hautes vitesses, avec l'utilisation des moteurs combinés.

Cette situation est due pour une large part aux importantes activités nationales sur le statoréacteur, pendant la période 1951-1972, au cours de laquelle de nombreux essais en vol ou au sol ont été réalisés sur les concepts de statoréacteurs conventionnels, de combinés turbo-stato, ainsi que sur celui de statoréacteur hypersonique à double mode, ce dernier faisant intervenir une combustion subsonique puis supersonique. Des essais au point fixe, à échelle significative, ont été réalisés dans les souffleries de l'ONERA à Modane.

A la demande des organisateurs du 75ème Symposium du Panel Propulsion de l'AGARD, cet exposé rappelle les étapes, les principaux travaux et résultats conduits et obtenus en France pendant cette période. Une analyse sera tentée pour évaluer l'acquis de cette expérience et son apport au niveau des actions menées actuellement pour une éventuelle utilisation du statoréacteur en propulsion hypersonique.

1. Introduction

Pour répondre à la demande des organisateurs de ce symposium de l'AGARD, le but de cette présentation est de rappeler la contribution française au développement de la propulsion par statoréacteur (conventionnel ou combiné avec d'autres réacteurs), au cours de la période de 1950 à 1974, marquée par une intense activité dans ce domaine.

Des avions et des missiles expérimentaux, propulsés par statoréacteur, combiné ou non, furent étudiés, réalisés et essayés en vol en grand nombre : plusieurs centaines de vols d'avions et de tirs d'engins furent effectués dans le domaine du supersonique à Mach inférieur ou égal à 5, souvent avec un remarquable succès, tandis que des essais probatoires au point fixe permettaient les premières incursions dans le domaine de l'hypersonique à Mach 6.

C'est grâce à ce foisonnement fécond de travaux, menés avec ténacité et enthousiasme, que la France dispose depuis quelques années du prestigieux missile aéroporté supersonique, ASMP, à charge thermonucléaire, et propulsé par un statoréacteur à kérosène, combiné avec un accélérateur intégré ; il est capable de trajectoires diversifiées, en volant à basse et haute altitude sur plusieurs centaines de kilomètres et possède une très haute manoeuvrabilité (Figure 1).



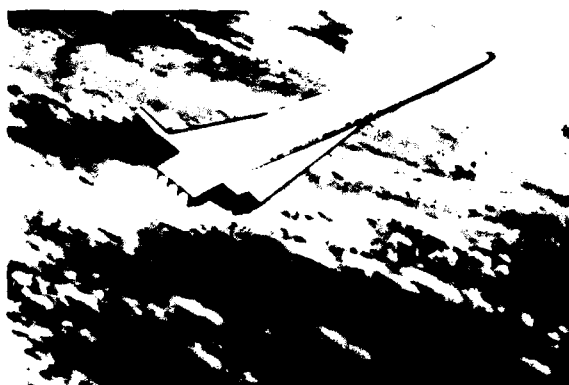
**Fig. 1 - ASMP missile with MIRAGE 2000 N launcher**

Ce missile opérationnel, déployé par les avions MIRAGE 2000 N de l'Armée de l'Air et SUPER-ETENDARD de la Marine Nationale, ouvre la voie à une famille d'engins à domaine de vol augmenté en vitesse et altitude, étudiée en ce moment, et permettant une portée accrue.

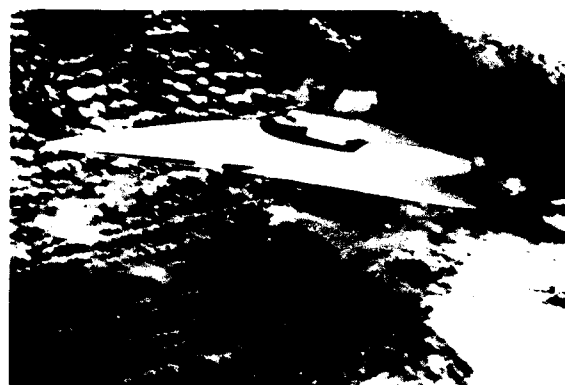
Une autre retombée de l'active période 1950/1974 peut être également espérée dans le domaine de l'hypersonique, où la France consacre maintenant une petite partie de son potentiel de recherches à établir la possibilité et l'intérêt du vol à très grande vitesse, au profit de missions civiles ou militaires, telles que celles de transporteur ou de lanceur, réutilisable, de satellites, à décollage horizontal (Figure 2), ou encore de missiles à très grande vitesse.

Enfin, si toutes ces activités sont à l'honneur du français LORIN, à qui la paternité du concept est fréquemment attribuée, grâce au brevet qu'il déposa en 1913, on ne peut évoquer le statoréacteur sans rendre hommage à l'action de pionnier, jouée par le grand ingénieur français René LEDUC qui, à

partir de 1930, redécouvrant le principe de la "tuyère thermopropulsive", en prévit d'emblée l'application à des véhicules supersoniques allant jusqu'à Mach 5, à haute altitude, tandis qu'il se lançait dans l'aventure industrielle de "l'avion thermopropulsé".



Single-stage STS 2000 (Aérospatiale)



Two-stage STAR-H (Dassault)

Fig. 2 - Conceptual orbital aircraft

En rappelant les principaux travaux effectués et les résultats acquis, nous tenterons de montrer l'évolution du statoréacteur, en France, pendant cette période de 1950 à 1974, que l'on peut diviser en deux époques :

- jusqu'en 1966 : priorité aux recherches sur le statoréacteur conventionnel jusqu'à Mach 5 et sur les applications avec moteur combiné supersonique,

- de 1966 à 1974 : priorité aux très grandes vitesses, avec des études sur le statoréacteur conventionnel jusqu'à Mach 6, et des recherches sur le statoréacteur hypersonique, à combustion supersonique, pour applications civiles ou militaires (Figure 3).

PERIOD	NATIONAL ACTIVITY	MISSION
SUPERSONIC PERIOD 1950 / 1966	<b>AIRPLANES</b>	
	LEDUC 022	} Experimental Flight tested at $M \leq 2.2$
	GRIFFON 02	
	<b>MISSILES</b>	
	Separated booster { STATALTEX VEGA, CT41, X422 ...	} Experimental Flight tested at $M \leq 5$
	Integral booster { INTEGRAL RAMROCKET	
HYPERSONIC PERIOD 1966 / 1974	<b>MISSILES</b>	
	SCORPION (Subsonic combustion)	} Experimental Ground tested at $M \leq 6$
	ESOPE (Subsonic & supersonic combustion)	

Fig. 3 - Ramjet in France between 1950 & 1974

## 2. Travaux sur le statoréacteur et le moteur combiné, à vitesse supersonique (1950-1974)

Les années qui suivirent la fin de la Seconde Guerre Mondiale virent se développer en France une très grande activité dans le domaine aéronautique, afin de tenter de combler les retards dus à la guerre.

Pour le statoréacteur, ses caractères attractifs d'apparente simplicité et de forte potentialité en supersonique conduisirent à de nombreuses études aboutissant à des réalisations intéressantes de missiles et d'avions, mais qui, paradoxalement, ne donnèrent jamais lieu à des développements opérationnels, ni pour les programmes militaires, ni pour ceux civils.

C'est, qu'en France, comme dans d'autres pays, les programmes militaires furent orientés vers les missiles stratégiques à trajectoire balistique en dehors de l'atmosphère, pour les engins, et vers l'avion de combat à turboréacteur (pour les Mach inférieurs à 2,5) en raison des rapides progrès de ce moteur (réchauffe, puis double-flux), surclassant alors le statoréacteur à bas Mach, tandis que les programmes civils allaient vers les lanceurs propulsés par fusée. Quant aux missiles tactiques, il n'était pas apparu de missions exigeant la spécificité du statoréacteur.

### 2.1 Missiles supersoniques propulsés par statoréacteur conventionnel

De 1950 à 1966, NORD-AVIATION, SUD-AVIATION, SNCASE (regroupés aujourd'hui dans l'AEROSPATIALE),



MATRA et l'ONERA vont étudier de multiples projets, réaliser beaucoup de statoréacteurs expérimentaux et procéder à des essais au sol et en vol.

On peut citer quelques-unes des plus remarquables études de cette époque, successivement :

- l'engin VEGA, de NORD-AVIATION (Figure 4), préfigurant un missile sol-air de calibre 645 mm ; en vol en 1960,

- l'engin-cible CT41, de NORD-AVIATION (Figure 5) propulsé par 2 statoréacteurs SIRIUS de calibre 650 mm ;  $M = 2,5$  à  $z = 22$  km ; en vol en 1962,

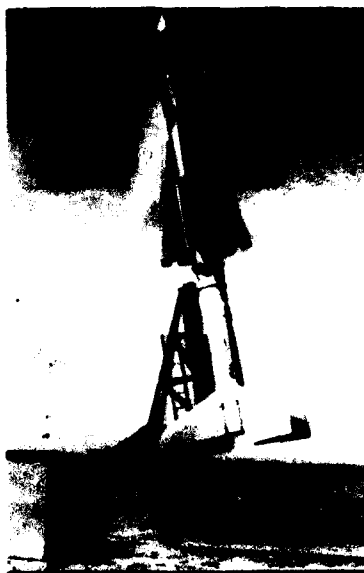


**Fig. 4 - Nord-Aviation ground-to-air VEGA missile**



**Fig. 5 - Nord-Aviation supersonic target CT 41 missile**

- l'engin X422, de la SNCASE, de calibre 800 mm, à entrée d'air en écope, préfigurant une arme stratégique, voisine du cruise missile, mais non retenue au bénéfice des missiles balistiques (Figure 6),

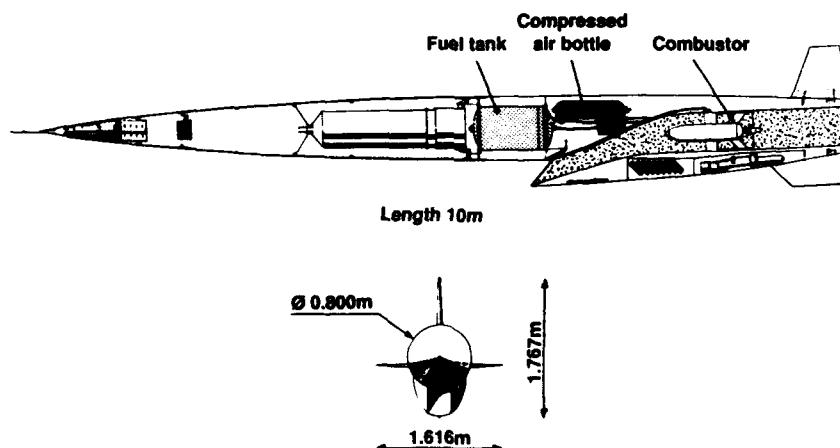


**Fig. 6 - SNCASE experimental ramjet X422 missile**

- le missile expérimental STATATLEX de l'ONERA (Figure 7), statoréacteur à hautes performances, de calibre 372 mm ;  $M = 5$  à 30 km d'altitude, tiré en vol de 1960 à 64.

Ces divers engins, utilisant le kérosène comme carburant du stato, étaient mis en vitesse initiale par un accélérateur à poudre, séparé et largable.

Toutes ces réalisations avaient été rendues possible grâce à de vastes programmes de recherches, balayant l'ensemble des disciplines, telles que :

- les calculs généraux de performance, de trajectoire et de dynamique du vol, ainsi que d'aérodynamique, de thermodynamique et de propulsion (ceci avec les moyens informatiques limités de l'époque),



**Fig. 7 - ONERA Mach 5 STATALTEX  
experimental missile**

- les études de configurations des missiles et les essais correspondants,
- les études théoriques et expérimentales des constituants, tels que :
  - . l'entrée d'air, à pointe émergente conique, ou évolutive, à compression interne ou externe, et du type Pitot pour les basses vitesses,
  - . la chambre de combustion, à vitesse subsonique, réglée par le col de l'éjecteur, et présentant la plus faible longueur compatible avec le domaine de vol, caractérisée par la température d'entrée de l'air, la pression et la richesse, la stabilité de la combustion étant obtenue par des accroche-flammes mécaniques,
  - . les systèmes de mise en oeuvre du carburant liquide tels que : réservoirs, chasse (gaz comprimé ou turbopompe), régulateurs, injecteurs,
- les nouveaux matériaux, tels que les alliages au cobalt pour la tenue des parties chaudes, ou les stratifiés composites et résines diverses pour les protections thermiques internes (combustion) ou externes (échauffement cinétique),
- les essais au sol, qui, utilisant non seulement les souffleries supersoniques existantes pour la mise au point de l'aérodynamique interne et externe, avaient nécessité la création de puissants moyens en bancs d'essai pour l'étude de la combustion dans la totalité du domaine envisagé (restitution du débit d'air avec pression et température réelles) et ceci à l'échelle grandeur. Des bancs spéciaux furent créés à l'ONERA (Palaiseau et Modane), à NORD-AVIATION (Centre des Gâtines) et à Saclay (Centre d'Etudes des Propulseurs),
- les moyens de mesure, avec création d'instruments adaptés pour les essais au sol, tels que balances d'efforts, capteurs de pression, débitmètres à liquide, etc., permettant d'évaluer le bilan poussée-trainée avec une précision meilleure que 5 %, et enfin les télémesures appropriées.

En résumé, toute cette activité se traduit par l'exécution de plus de 300 essais en vol, représentant une somme supérieure à six millions d'heures de travail.

Arrêtons-nous maintenant quelques instants sur le missile expérimental STATALTEX, qui fut longtemps l'engin à statoréacteur le plus rapide au monde, atteignant  $M = 5$  et propulsé jusqu'à 39 km d'altitude, en délivrant des accélérations allant jusqu'à  $30 \text{ m.s.}^{-2}$  (Figure 8).

Cet exceptionnel succès provenait de la simplicité et de l'efficacité de la machine, réalisant entre le largage de l'accélérateur et l'épuisement du combustible, une accélération de Mach 3,2 à 5 sur une importante dénivellée, avec un moteur à géométrie fixe (entrée d'air frontale à pointe de compression isentropique, adaptée à Mach 3,5, et éjecteur à col fixe) avec régulation simplifiée du débit de kérosène assurant une richesse compatible avec le foyer pendant la totalité du vol.

La Figure 9 montre le domaine de vol exploré par les différents missiles expérimentés et les performances d'impulsion spécifique correspondantes.

Si cette première période d'activité avait bien mis en évidence l'intérêt énergétique du statoréacteur pour le vol supersonique, elle avait aussi révélé des points faibles comme la compacité insuffisante du propulseur, due à la configuration bi-étage, la sensibilité de la combustion au déclenchement d'instabilités, incompatibles avec les structures, dans certaines conditions de fonctionnement, et, surtout la nécessité d'intégrer profondément le moteur à l'ensemble de la cellule pour obtenir la traînée minimale du véhicule (l'accélération fournie par un statoréacteur est très inférieure à celle d'un moteur-fusée) : d'autre part, cette dernière sujétion avait conduit à concevoir la plupart des engins expérimentaux avec un corps principal à passage d'air annulaire, peu propice à une utilisation opérationnelle.

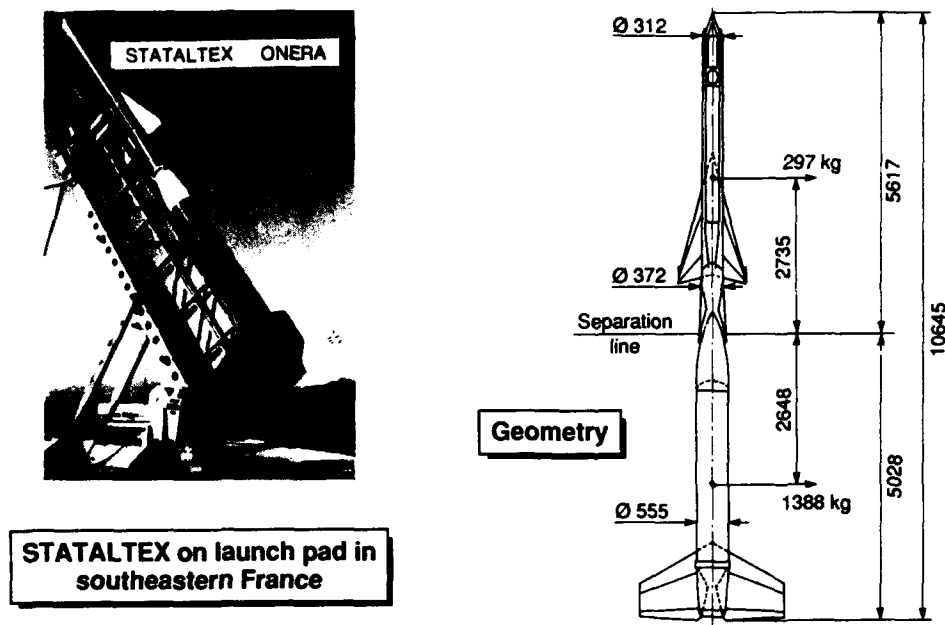


Fig. 8 - Experimental Mach 5 STATALTEX missile

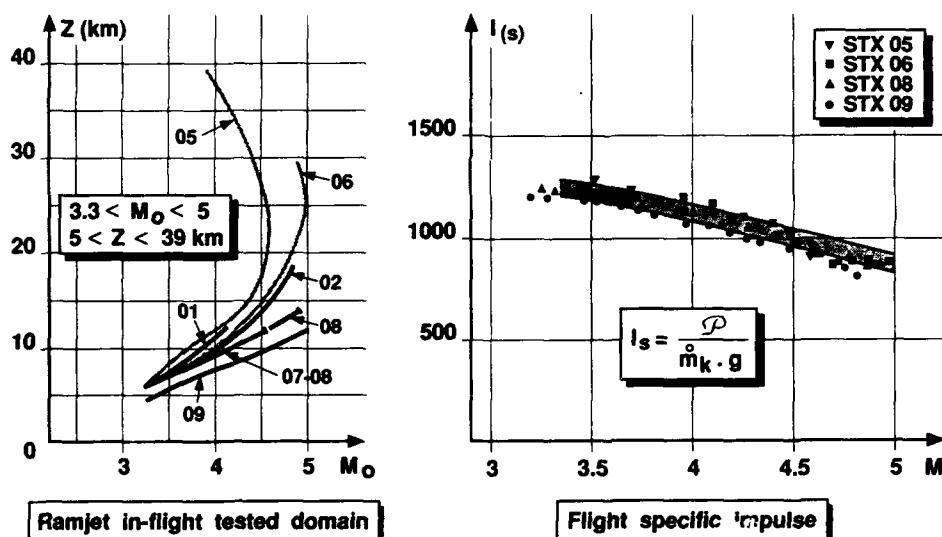


Fig. 9 - STATALTEX missile performances

Le moment d'une seconde génération de statoréacteurs supersoniques était venu : l'accélérateur et le statoréacteur devaient être combinés et la configuration du missile profondément remaniée.

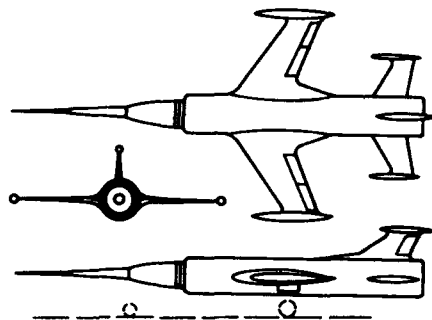
## 2.2 Avions à moteurs combinés turbo-stato

L'intérêt d'un tel couplage est d'autant plus évident qu'il s'adresse à un avion hautement supersonique, puisque le turboréacteur assurera toujours aisément les fonctions de décollage, d'accélération initiale, puis d'atterrissage, tandis que le statoréacteur verra son efficacité d'autant plus confirmée que la vitesse recherchée sera élevée.

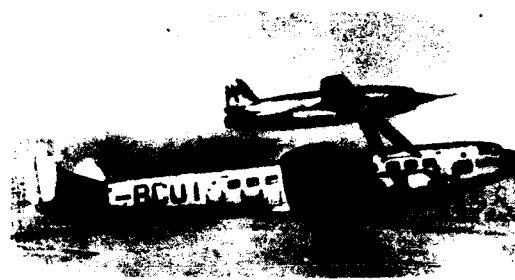
### 2.2.1 Avions LEDUC 022

Ce fut le premier avion combiné turbo-stato, prévu pour le supersonique à Mach 2, il était équipé d'un réacteur ATAR 101 F, installé coaxialement au statoréacteur, avec entrée d'air et éjecteur communs ; il vola en 1956 en faisant la preuve de sa souplesse au cours de nombreux essais, mais l'objectif final du vol supersonique ne put malheureusement pas être atteint.

La Figure 10 montre la configuration de l'avion et rappelle aussi son prédécesseur, subsonique, le LEDUC 010, qui de 1949 à 1956 vola parfaitement, en atteignant Mach 0,9 à 12 km d'altitude.



**LEDUC 022 turbo-ramjet aircraft  
(ATAR 101 engine)**



**LEDUC 010 subsonic ramjet aircraft on top of  
LANGUEDOC launch-plane**

**Fig. 10 - French early ramjet aircraft**

#### 2.2.2 Avion NORD 1500 GRIFFON 2

C'est en 1953, que les Services Officiels commandèrent à NORD-AVIATION l'étude d'un avion expérimental, préfigurant un intercepteur supersonique propulsé par un moteur combiné turboréacteur-statoréacteur (Figure 11) ; c'était un avion de 6 800 kg, dont 1 700 kg de propulseur (turboréacteur ATAR 101 E3 et statoréacteur de diamètre 1 500 mm) profondément intégré à la cellule, avec les deux moteurs, coaxiaux, utilisant la même entrée d'air et le même éjecteur, caractéristique majeure de ce système (Figure 12a).



**Fig. 11 - Nord-Aviation turboramjet**

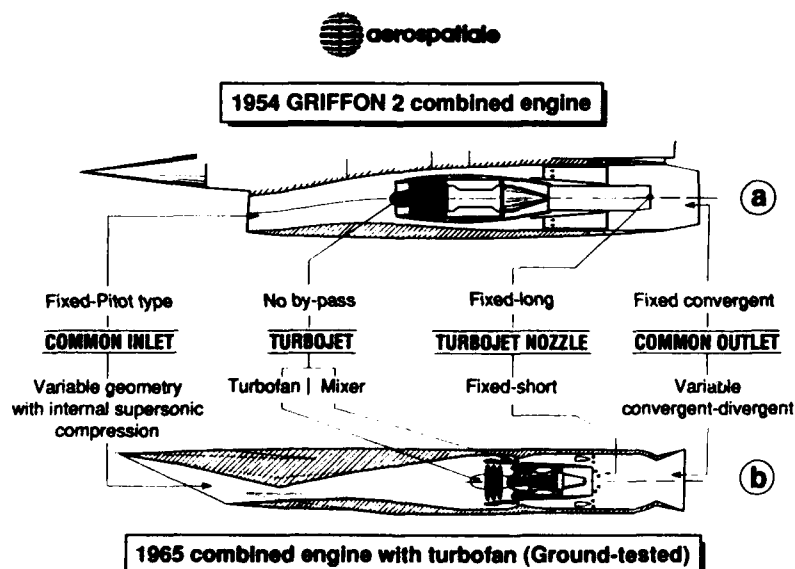


**Fig. 12 - Evolution of the Nord-Aviation combined engine for aircraft**

De cette disposition, NORD-AVIATION espérait bénéficier d'une traînée minimale et des qualités propres aux deux moteurs en fonction du domaine de vol, c'est-à-dire :

- du turboréacteur pour les faibles vitesses jusqu'au supersonique modéré,
- du statoréacteur pour les vitesses en supersonique moyennement élevé.

Un autre avantage était que la nécessité d'un turboréacteur efficace à fort Mach n'existait plus ; au contraire, il était plus indiqué de l'adapter au vol à basse vitesse, et de le réduire, voir de le stopper, à Mach élevé.

C'est bien ce qui fut réalisé avec le GRIFFON 2 qui atteignit  $M = 2,19$  à 18 500 mètres en montée accélérée (record mondial de vitesse ascensionnelle), avec une poussée excédentaire qui lui aurait permis d'atteindre Mach 2,5, si la cellule n'avait pas été thermiquement limitée à Mach 2,2, tandis que le réacteur ATAR 101 E3 était, lui, prévu pour un Mach maximal de 1,8.

Remarquons aussi que la réduction de régime du turboréacteur à vitesse élevée permettait de diminuer la fatigue thermique des parties chaudes.

La Figure 13 montre des caractéristiques de fonctionnement du combiné : d'une part, le rapport des débits d'air avalé par le turbo et le stato en fonction du Mach (13a) et d'autre part le pourcentage de poussée du stato qui atteignait 80 % à Mach 2 (13b).

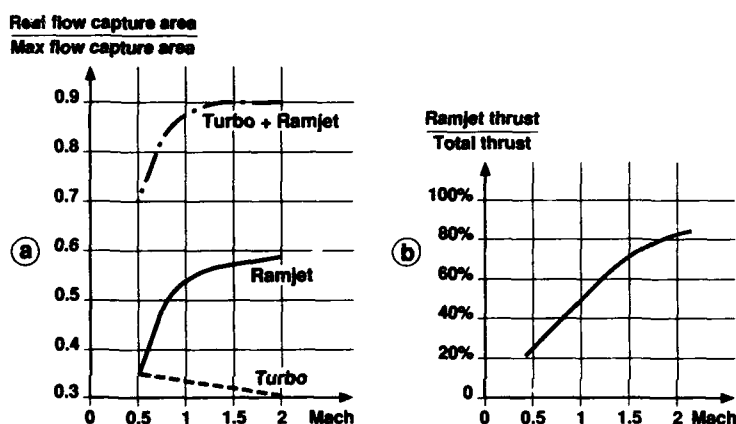


Fig. 13 - Performances of Nord-Aviation 1500 "GRIFFON 2" aircraft

L'opération fut très réussie et le GRIFFON 2 effectua 330 vols entre 1957 et 1961, s'attribuant aussi un record mondial de vitesse en circuit fermé sur 100 km, prouvant ainsi sa haute manoeuvrabilité.

Par la suite, riche de cette expérience, NORD AVIATION prépara le lancement d'un nouveau prototype, en utilisant cette fois un turboréacteur à double flux, l'entrée d'air et l'éjecteur devenant à géométrie variable (Figure 12b).

Cette étude fut proposée aux Services Officiels Américains qui envisageaient de l'appliquer à un transporteur commercial supersonique, ou à un intercepteur pour l'USAF, pour Mach 3.

Le programme, entre 1960 et 1965, fit l'objet d'études théoriques et expérimentales, au sol, sur les entrées d'air et la tuyère variables, la chambre de combustion et les interactions entre flux primaire et secondaire. Un domaine de fonctionnement allant jusqu'à Mach 4 à 30 km d'altitude, fut validé avec de très bonnes performances par des essais au sol, mais le projet ne reçut pas d'application et les travaux s'arrêtèrent là.

### 2.3 Combiné statoréacteur et fusée, monoétage, pour missile supersonique (principe du statofusée)

En 1972, l'ONERA examinait une solution simple de moteur combiné pour missile, associant une fusée et un statoréacteur dans la même structure ; l'étude visait une application en supersonique moyen (Mach 3), répondant ainsi à l'évolution des souhaits des militaires pour disposer d'un propulseur plus compact et plus performant que la fusée, tout en présentant une simplicité équivalente.

La configuration proposée (Figure 14b) comportait une fusée accélératrice à poudre et un statoréacteur, en tandem, qui débouchaient dans une tuyère annulaire bi-fonction : le conduit interne correspondait à la fusée et celui annulaire au statoréacteur.

Cette solution présentait des avantages de compacité évidents par rapport au statoréacteur bi-étage à accélérateur largable.

De plus, la nouvelle disposition avec les quatre entrées d'air latérales représentait un avancement majeur dans l'utilisation opérationnelle du statoréacteur, en offrant une accessibilité et une possibilité de conception modulaire incomparablement supérieures à celles du missile à entrée frontale.

En associant à ce moteur, un générateur de gaz combustible pour le stato, on obtenait aussi une meilleure compacité que celle du statoréacteur à kérosène, et on franchissait une nouvelle étape vers l'extrême simplicité (absence de systèmes de pressurisation, chasse, régulation et injection d'un liquide).

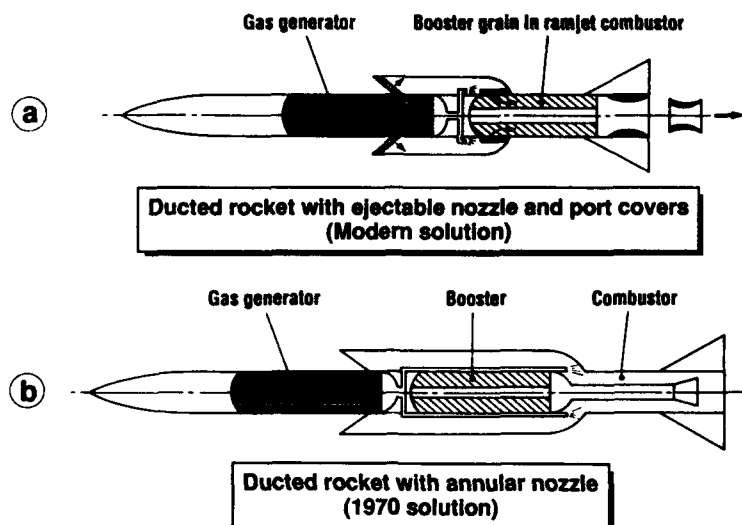


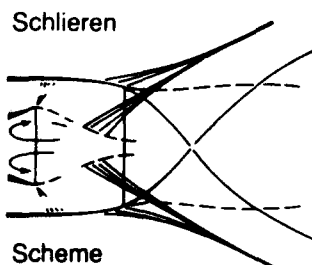
**Fig. 14 - Integral boost ducted rocket  
(rocket-ramjet combined engine)**

En résumé, la solution proposée constituait un statoréacteur à accélérateur intégré que l'on peut comparer à la formule actuelle (Figure 14a) où la chambre stato devient bivalente en recevant le bloc de l'accélérateur, disposition plus compacte mais nécessitant généralement des pièces éjectables ou mobiles comme : des volets d'obturation des entrées d'air pendant la phase accélérée, des opercules éjectables obstruant temporairement les orifices d'entrée d'air dans la chambre, et une tuyère d'accélérateur largable.

Les avantages suivants étaient revendiqués du statofusée en tandem :

- pas de pièces éjectables
- pas de traînée supplémentaire due aux entrées d'air, puisque celles-ci restaient ouvertes pendant l'accélération ; pas de risque de pompage non plus
- possibilité de fonctionnement simultané des deux propulseurs
- grande sécurité à l'allumage du générateur, les gaz débouchant dans une chambre ouverte
- gain de longueur avec la tuyère annulaire qui ne demandait qu'une longueur d'un tiers de calibre.

Des essais de principe sur une maquette complète de diamètre 200 mm, montée en jet libre dans la soufflerie S3 de Modane, pour des conditions simulées  $M = 2$ ,  $Z = 1$  km, furent entrepris (Figure 15).



**Nozzle streamlines  
study in wind-tunnel**



**Rocket ramjet model in S3 wind tunnel  
at  $M = 2$   $Z = 1$  km**

Time (sec)	Events
0	Wind tunnel start
8	Gas generator ignition
8	Supply of 45-bar air (booster simulation)
12	Ramjet ignition
16.5	End of compressed air supply (simulation of transition)
75	End of ramjet operation
100	Wind tunnel stop

**Results** - No interaction between rocket  
& ramjet, during acceleration.  
- Acquired specific impulse  $\approx 1200$ s.

**Fig. 15 - Annular nozzle ducted rocket**

Ils avaient pour but :

- de vérifier le principe d'intégration de l'accélérateur, en particulier pendant la phase de transition où les deux propulseurs fonctionnaient ensemble
- de déterminer les performances du statoréacteur avec la tuyère annulaire.

Les essais, réussis, révélèrent une impulsion volumique supérieure à celle du kérosène, tandis que la tuyère annulaire montrait une efficacité comparable à celle du convergent-divergent classique.

Ces résultats validaient le principe du combiné statofusée à tuyère annulaire.

En résumé de cette première période, les bases du vol supersonique avec le stato avaient été établies, grâce aux nombreuses études théoriques et expérimentales ; les concepts proposés étaient validés, avec des résultats très étendus, comme le montre la figure 16, domaine exploré en Mach/altitude ; d'un autre côté, certaines difficultés étaient réhaussées, ou révélées, comme, par exemple, le réglage pointu du statoréacteur entraîné par sa faible accélération, son manque de compacité, et, pour les missiles surtout, l'inaptitude d'une cellule à passage d'air annulaire à satisfaire les exigences opérationnelles ; également, le réglage de la combustion se révélait difficile en l'absence de modèles de référence, et exigeait des moyens d'essais importants et très spécialisés ; mais des progrès notables étaient en cours, avec l'apparition de la configuration à entrées d'air et manches latérales et celle de l'accéléromètre intégré. Quant aux avions à combiné turbo-stato de la classe Mach 2/2,5, leur intérêt, malgré les brillants résultats obtenus, était insuffisant face au développement rapide du turboréacteur.

Cependant, la maîtrise démontrée dans tous ces domaines, ouvrait la voie vers l'hyper-sonique, qui paraissait à l'époque être l'évidente et naturelle continuité.

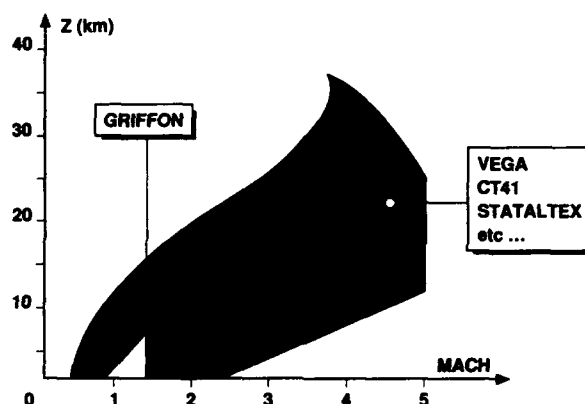


Fig. 16 - Ramjet in-flight tested area from 1950 to 1974

### 3. Travaux sur le statoréacteur hypersonique (1966-1974)

Dès le début des années 1960, en France, et à l'ONERA en particulier, avait été mis en évidence l'intérêt énergétique du statoréacteur pour les grandes vitesses.

Sur la Figure 17, on voit que l'hyper-sonique modéré (Mach 6) peut être atteint avec le stato-réacteur à combustion subsonique ou supersonique ; c'est le domaine de transition entre les deux types de combustion que l'ONERA a évalué à cette époque, en proposant le statoréacteur à combustion subsonique pour un missile de Mach 3/6 (opération SCORPION), puis le statoréacteur à combustion évolutive du subsonique au supersonique, pour un domaine voisin de Mach 3,5/7 (opération ESOPÉ).

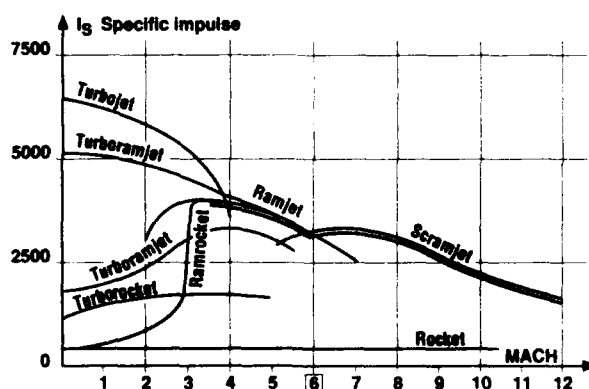


Fig. 17 - Specific impulse with combined engines

### 3.1 Statoréacteur Mach 3/6 à combustion subsonique (SCORPION)

Vers 1970, l'ONERA, à la demande des Services Officiels, a évalué la faisabilité d'un missile sol-air longue portée, propulsé par un statoréacteur à combustion subsonique, accélérant de Mach 3 à 6, puis volant à altitude de 30 km avant l'interception finale, réclamant une manoeuvrabilité tous azimuts.

L'étude théorique et expérimentale qui s'ensuivit a porté sur un modèle propulsé par un statoréacteur à kérosène, comportant un accélérateur à poudre en tandem, largué à Mach 3.

Si l'engin biétage était encore conservé (Figure 18a), par contre apparaissait là pour la première fois la configuration à entrées d'air et manches latérales, déjà citée sur le statofusée monoétage, de réalisation postérieure, et assurant captation d'air et portance du missile, en dégageant l'avant, constitué par le radôme, la charge militaire et le réservoir de combustible (Figure 18b).

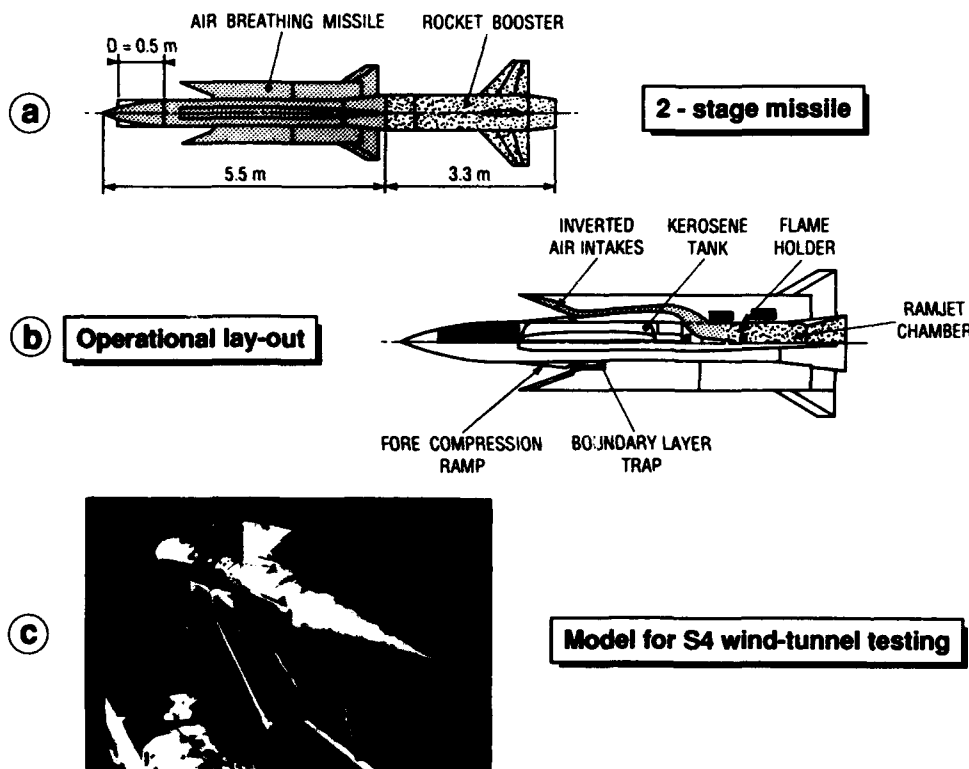


Fig. 18 - Mach 6 SCORPION ramjet

Le statoréacteur moderne était né, comme allaient le démontrer les réalisations futures.

Les travaux portèrent sur :

- la détermination des entrées d'air pour fonctionner dans le domaine Mach 3/6 avec une géométrie fixe, compatible avec les distorsions rencontrées en phase finale manoeuvrante,
- l'étude de la chambre de combustion, à tuyère fixe, dans un large domaine de richesse, et en présence des distorsions de vitesse.

De la maquette expérimentale, réalisée en calibre 200 mm, on tirait deux études séparées :

- l'une pour la mise au point des entrées d'air, en soufflerie classique à Mach 3, puis dans la soufflerie S4 de Modane, à haute enthalpie, qui aboutissait à la définition d'entrées d'air bidimensionnelles inversées, très performantes (Figure 19a),
- l'autre pour la mise au point de la combustion, en conduite forcée sur une installation de Palaiseau, également à haute enthalpie, mais en air vicié, qui se traduisait par le choix d'un système d'accroche-flamme mécanique, compatible avec le domaine de vol simulé et les distorsions importantes de l'écoulement (Figure 19b).

Les travaux se terminaient ensuite par une synthèse, où, réunissant aérodynamique et combustion sur une maquette pour jet libre, essayée à S4 (Figure 18c), les résultats montraient que les spécifications étaient bien tenues et que le projet constituait une avancée importante dans le domaine du statoréacteur hypersonique.

### 3.2 Combiné stato à double mode, Mach 3,5/7+ (ESOPE)

En 1962, les Services Officiels avaient demandé à NORD-AVIATION d'étudier la faisabilité d'un planeur hypersonique, capable de vols sustentés sur de longue durée à haute altitude, pour un Mach supérieur à 7, projet baptisé VERAS pour lequel une structure expérimentale avait été qualifiée par des essais au sol.



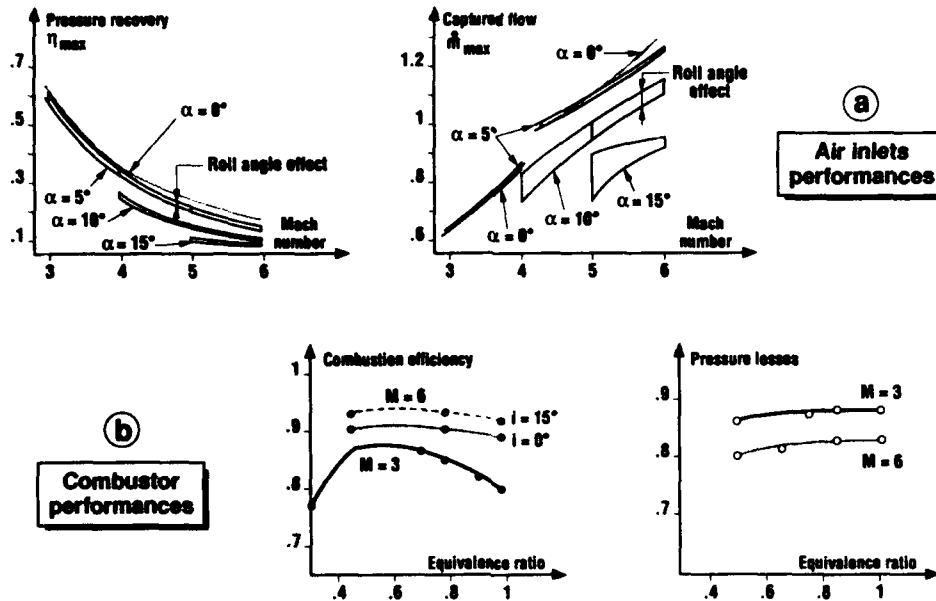


Fig. 19 - SCORPION ramjet internal performances

Quelques années plus tard, l'ONERA proposa, à titre de recherche prospective, d'associer à ce projet un statoréacteur à double mode, combustion subsonique, puis supersonique dans la même chambre, pour constituer un véhicule capable d'effectuer des missions de Mach 3,5 à 7 et plus (Figure 20a), soit qu'il s'agisse d'un éventuel avion hypersonique ou d'un lanceur aérobie réutilisable : ce fut le projet ESOPE.

L'intérêt de la configuration résidait dans la possibilité de disposer le propulseur en nacelle, comme le montre la Figure 20b, sous l'intrados de l'aile, afin de profiter de la recompression engendrée par le choc de bord d'attaque, la prise d'air bénéficiant, en plus, d'une alimentation peu sensible au champ aérodynamique.

Une première étude avait montré que de bonnes performances pouvaient être atteintes avec un statoréacteur à géométrie fixe (la géométrie variable aurait entraîné des difficultés technologiques rédhibitoires), fonctionnant successivement en combustion subsonique, puis supersonique, pourvu que le Mach d'adaptation de la prise d'air soit choisi pour assurer un compromis optimal sur l'ensemble de la mission (Figure 21a) ; les deux modes de fonctionnement étaient obtenus par déplacement des points d'injection (Figure 20a).

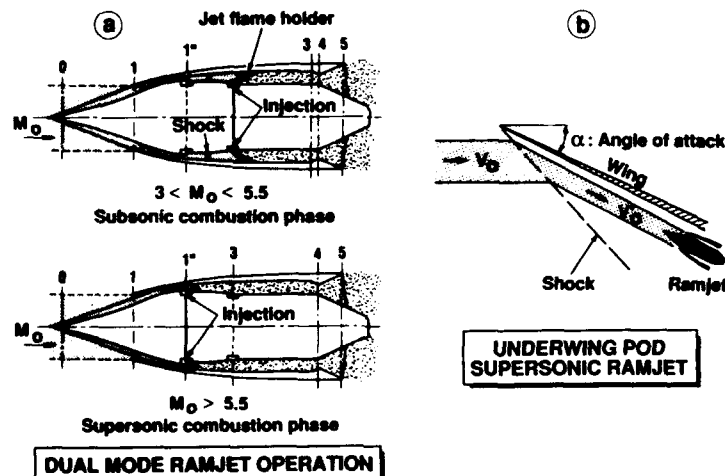


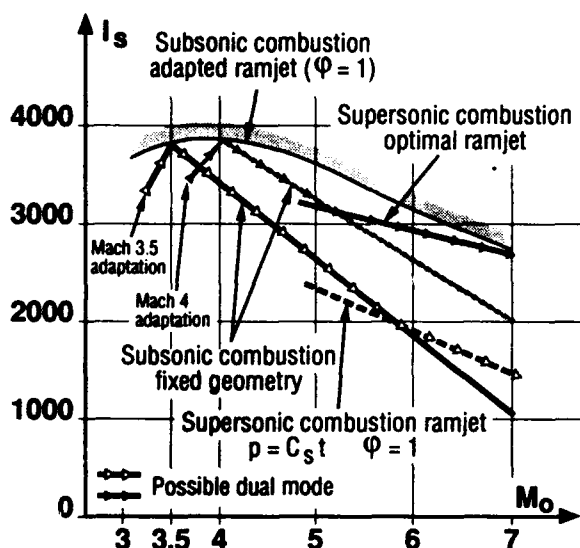
Fig. 20 - ESOPE concept

Mais, cette étude révélait aussi des incertitudes de fonctionnement de ce statoréacteur telles que l'auto-allumage du mélange air/hydrogène non assuré pour Mach 5,5 et aussi des pertes de performances vers Mach 6 où la supériorité de la combustion supersonique n'est pas encore établie, de sorte que le concept évolua vers celui dit de la combustion à transition, où pour cette vitesse de Mach 6, la zone amont est le siège d'un écoulement, très stratifié (mélange subsonique élevé et supersonique), tandis que la vitesse sonique est atteinte plus loin, par un col thermique et que la combustion se poursuit au-delà en supersonique ; aux vitesses supérieures à Mach 7, la combustion est entièrement supersonique.

Le projet fut donc réorienté suivant ce processus de combustion, comportant trois phases :

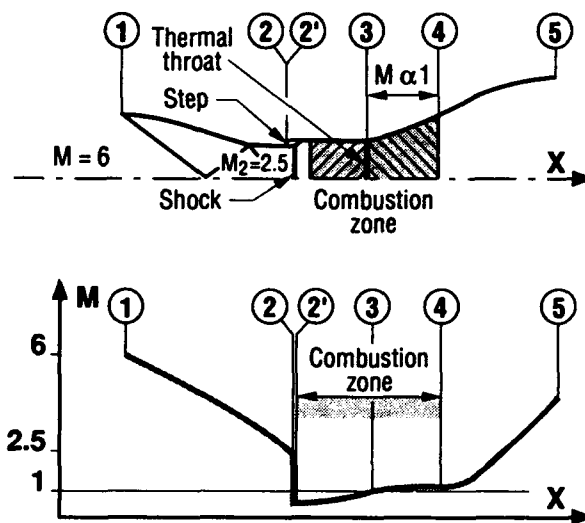
- combustion subsonique de Mach 3,5 à 5 environ,

- combustion de transition entre Mach 5 et 7,
- combustion supersonique pour les Mach supérieurs à 7.



Fixed geometry performances

(a)



Optimal transition combustion

(b)

Fig. 21 - ESOPE principes

Des techniques d'optimisation sous contraintes, utilisant des principes variationnels appliqués à la dynamique de sortie et à la loi de combustion ont été mises en oeuvre par F. HIRSINGER [8] ; elles ont montré l'intérêt de réaliser la partie subsonique de la combustion dans une zone cylindrique à l'amont du foyer, le col thermique s'accrochant à la cassure entre cette zone et le début du divergent, configuration également favorable pour la combustion supersonique ; de plus, la présence d'une marche à l'entrée de la partie cylindrique, augmentant brutalement la section de passage à la sortie du diffuseur, permettait d'accroître notablement l'apport de chaleur dans la zone subsonique (Figure 21b).

De ce vaste projet, seule une partie fut réalisée : d'une part, l'étude et les essais en soufflerie de la prise d'air, et, d'autre part, des essais de combustion, en conduite forcée, du moteur en régime de transition.

- Pour l'entrée d'air, les essais furent effectués en soufflerie, entre Mach 3,5 et 7, avec un Mach d'adaptation de 3,5 et de 4, cette dernière valeur étant finalement retenue.

A Mach 6, le Mach interne de fin de recompression était alors d'environ 2,4.

- Pour le moteur, des essais partiels avaient d'abord été menés sur les bancs d'essai de Palaiseau, afin de mettre en évidence la combustion de transition ; ensuite, l'expérimentation s'est portée vers la soufflerie à haute enthalpie S4 de Modane, capable de simuler, en pression et en température, un écoulement de Mach 6 avec de l'air non vicié.

Cependant, l'essai en conduite forcée étant limité à la chambre de combustion, le montage fut effectué avec une tuyère supersonique annulaire directement reliée à la chambre et assurant les conditions de fin de recompression, soit, un Mach de 2,4, une température génératrice voisine de 1 600 K, une pression totale d'environ 15 bar, avec un débit d'air de 5 kg/s (Figure 22).

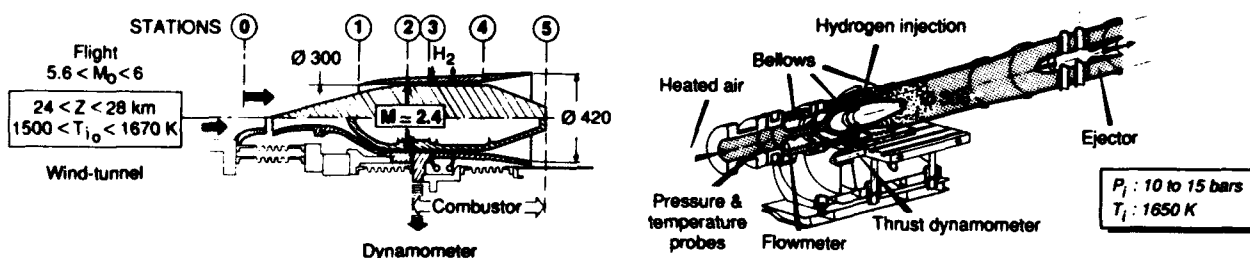


Fig. 22 - S4 wind-tunnel hypersonic combustion testing

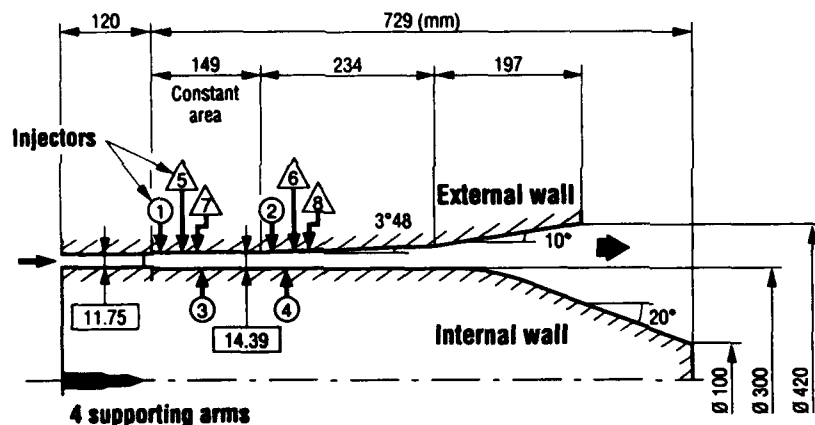
Au raccordement entre tuyère et chambre, un découplage mécanique de la structure autorisait la mesure de la force axiale s'exerçant sur le foyer, à l'aide d'un dynamomètre, permettant ainsi, après les corrections convenables, le calcul de la poussée du moteur.

Avec l'hydrogène gazeux, retenu pour ses bonnes propriétés énergétiques, la stabilisation de la flamme était recherchée par décollement de la couche limite avec les jets pariétaux de combustible ainsi que par l'effet de sillage de ces jets ; l'injection était composée de deux rampes, l'une avec des orifices resserrés et de faible diamètre et l'autre avec des orifices plus écartés et de diamètre plus important, solution de compromis mélangeant jets à forte et à faible pénétration répartis sur les faces interne et externe du canal annulaire (Figure 23a).

La maquette avait un diamètre de 420 mm (Figure 23b) et les conditions simulées furent les suivantes :

- altitude : 25 à 29 km
- nombre de Mach de vol : 5,5 à 6
- température génératrice : de 1 550 à 1 670 K

des mesures portaient principalement sur les pressions statiques de paroi et les résultats obtenus sont représentés sur la Figure 24.



△ A injection (high penetration) ○ E injection (low penetration)

Injection pattern

(a)



Rear part of the model for thrust measurement

(b)

Fig. 23 - Transition combustion test model

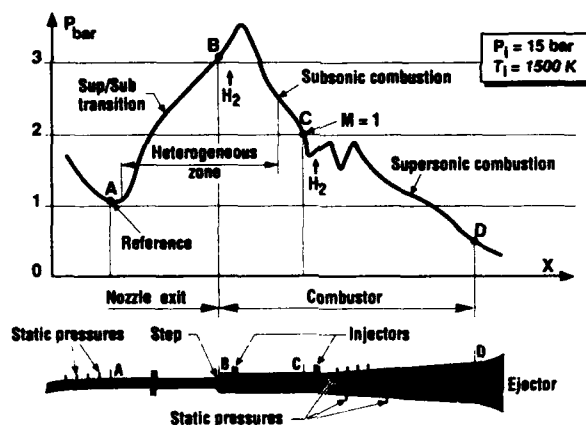


Fig. 24 - Pressure profile along combustor

Le profil de pression montre un désamorçage partiel de l'écoulement amont, par ailleurs fortement stratifié. En aval de la marche, une zone de combustion subsonique à Mach élevé est mise en évidence et le col thermique est franchi très exactement en début de divergent.

Le code de dépouillement a permis d'accéder aux différents paramètres de l'écoulement, et de calculer le débit de combustible brûlé dans les sections successives (Figure 25a) ; cependant, à cause de l'hétérogénéité de l'écoulement, le calcul ne devient réaliste que vers la fin de la zone de transition.

La Figure 25b, qui montre l'évolution de ce débit de combustible brûlé en fonction du nombre de Mach dans le foyer, fait apparaître le partage entre les deux types de combustion.

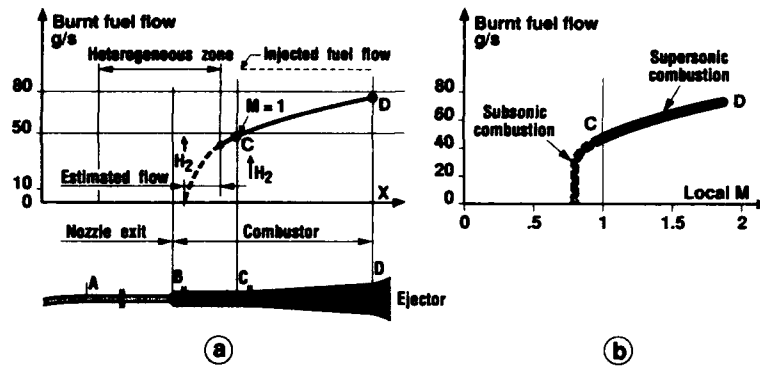


Fig. 25 - Transition combustion process

Quant à la poussée issue de la mesure dynamométrique, elle put être calculée avec une précision de l'ordre de 2 %.

En résumé, cette étude a montré la faisabilité du statoréacteur à combustion de transition, avec une injection gazeuse d'hydrogène ; à Mach 6, l'impulsion spécifique était de l'ordre de 2 500 secondes et le rendement de combustion de 0,80 en régime stœchiométrique (Figure 26).

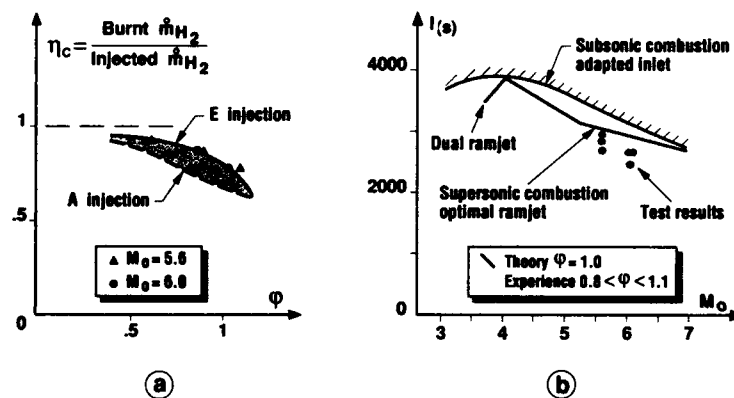


Fig. 26 - Combustion performance results

Ces performances, acquises avec une géométrie fixe, approchaient celles du statoréacteur à combustion subsonique avec géométrie variable ; des études et essais complémentaires auraient été nécessaires pour améliorer le rendement de combustion, par exemple en programmant la répartition de l'injection en fonction de la vitesse de vol.

La poursuite vers des Mach supérieurs, au-delà de la combustion de transition ( $M \gg 7$ ), aurait nécessité des températures génératrices plus élevées, toujours avec de l'air pur, qui ne pouvaient pas être envisagées à l'époque, ni à S4, ni ailleurs.

Il en résulta que les travaux s'arrêtèrent là, avec l'acquis essentiel d'une maîtrise certaine de la combustion évolutive entre le subsonique et le supersonique.

#### 4. Conclusion

Si la multiplicité des études de statoréacteur et de moteurs combinés, en France, de 1950 à 1974, n'engendra au cours de la décennie suivante que le seul programme opérationnel ASMP, malgré le consensus général sur l'intérêt énergétique, nul doute que le succès de cette opération n'ait été largement préparé par les travaux antérieurs.

Pour l'hypersonique, les moteurs aérobies seront certainement utilisés dans l'avenir ; cette perspective rend utile le rappel des résultats acquis il y a 20 ans, sans omettre les difficultés, intrinsèques aux principes, dont la plupart subsistent toujours.

En quelques lignes, évoquons donc le bilan des activités passées. En premier lieu, le domaine d'emploi des systèmes (stato à combustion subsonique, turboréacteur, turbostato, statoréacteur à combustion supersonique) fut étudié et défini avec précision.

- Pour le statoréacteur à combustion subsonique, la méthodologie fut établie : calculs théoriques, choix des configurations, intérêt des combustibles solide et liquide, choix des entrées d'air, organisation de la chambre de combustion, moyens d'essais en conduite forcée, éventuellement en jet libre, essais en vol : tous ces travaux aboutirent à rendre parfaitement cohérente la confrontation théorie-expérience.

De tout cela, on put dégager une réflexion pour l'avenir et établir les règles de conception du

statoréacteur moderne pour missile, compact et adapté aux exigences opérationnelles.

- Dans le domaine des moteurs combinés pour avions, ou lanceurs, le concept du turbostato fut étudié et sa faisabilité obtenue, en vol, jusqu'à Mach 2.2 ; pour les Mach plus élevés, les études montrèrent qu'une géométrie profondément variable de l'entrée d'air et de l'éjecteur était nécessaire, engendrant ainsi une complexité technologique du véhicule considérable, tandis que la mission restait à élaborer et l'intérêt à démontrer.

- Pour le statoréacteur hypersonique, une première approche fut faite avec l'étude d'un moteur à géométrie fixe, capable d'évoluer de Mach 3,5 à 7, en combustion successivement subsonique puis supersonique.

Des calculs généraux furent effectués sur les systèmes aérobies utilisant l'hydrogène dont l'intérêt énergétique était à mettre en balance avec la faible compacité, les températures de combustion élevées, les matériaux pour les hautes températures, etc ...

En plus, l'importance rapidement prohibitive des moyens d'essais nécessaires, lorsque le calibre et le domaine de Mach augmentent, était mise en lumière.

Cependant, le projet ESOPE démontra bien la faisabilité de la combustion supersonique avec l'hydrogène et l'intérêt du passage par la combustion de transition, avec des performances intéressantes.

Ces résultats et les méthodes développées pour les obtenir devraient constituer un apport appréciable dans l'étude des propulseurs hypersoniques de l'avenir.

La Figure 27a montre une synthèse du domaine de Mach expérimentalement balayé à l'époque, en fonction de l'altitude de vol et du concept propulsif utilisé.

Enfin, la Figure 27b exprime, à titre d'exemple, l'une des difficultés de l'hypersonique, avec la rapide croissance de la sensibilité des performances des aérobies lorsque le Mach augmente, rappelant aux concepteurs d'aujourd'hui les considérables difficultés auxquelles ils se heurteront, en hypersonique, pour l'évaluation précise du bilan poussée-trainée. De nombreuses recherches au sol, à l'aide de moyens d'essais réalistes, actuellement quasi-inexistants, devront être associées à des expériences fondamentales en vol pour vérifier la validité des modèles, avant de pouvoir établir la crédibilité des éventuels futurs concepts opérationnels hypersoniques.

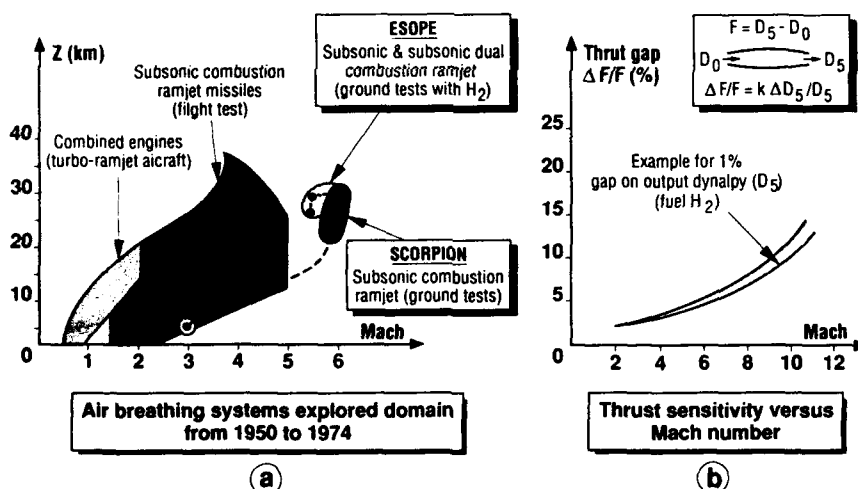


Fig. 27 - Resumed ramjet activity

#### REFERENCES

- [1] R. MARGUET, C. HUET, G. LARUELLE,  
"Définition et performances d'un statofusée monoétage",  
3è Congrès ISABE, Munich, 8 Novembre 1976.
- [2] R. MARGUET  
"Etude et essais en vol d'un statoréacteur expérimental à Mach 5",  
Note Technique ONERA n° 94, 1966.
- [3] R. MARGUET, C. HUET  
"Recherche d'une solution optimale de statoréacteur à géométrie fixe, de Mach 3 à Mach 7 avec combustion subsonique puis supersonique",  
AFITAE, 5è Colloque d'Aérodynamique Appliquée, CEAT Poitiers, 6-8 Novembre 1968.
- [4] F.S. BILLIG  
"Design of supersonic combustors based on pressure-area fields",  
Eleventh Symposium International on Combustion, University of California, August 14-20, 1966.

- [5] P. CONTENSO, R. MARGUET, C. HUET  
"Etude théorique et expérimentale d'un statoréacteur à combustion mixte (domaine de vol Mach 3,5/7)",  
La Recherche Aérospatiale n° 1973-5, p. 259-274.
- [6] J. LEYNAERT  
"Prises d'air pour le vol à Mach 7",  
AFITAE, 5è Colloque d'Aérodynamique Appliquée, CEAT Poitiers, 6-8 Novembre 1966.
- [7] A. MESTRE, L. VIAUD  
"Combustion supersonique dans un canal cylindrique",  
"Chemical Processus and radiative transfer",  
D.B. HOLSE, N.V. ZAKAY, AGARD Pergamon Press, 1964.
- [8] F. HIRSINGER  
"Optimisation des performances d'un statoréacteur supersonique - Etude théorique et expérimentale",  
1st International Symposium on Air Breathing Engines,  
Marseille, June 19-23, 1972.
- [9] R. MARGUET  
"Ramjet research and applications in France",  
9è Congrès ISABE, Athènes, 4 septembre 1989.

# Navigation, Guidance, and Trajectory Optimization for Hypersonic Vehicles

R.L. Schultz, M.J. Hoffman, A.M. Case, and S.I. Sheikh  
Honeywell Systems and Research Center  
3660 Technology Drive  
Minneapolis, Minnesota USA 55416

## 1.0 Summary

A computationally efficient, real-time trajectory optimization and guidance approach for hypersonic aircraft is described. The optimization algorithms compute, in flight, minimum fuel trajectories within constraints from the current aircraft position to its final destination. In flight trajectory computation can provide a high degree of vehicle autonomy which could greatly reduce aircraft ground support costs.

The optimization approach is based on Euler-Lagrange theory and energy-state approximations. A three-dimensional, spherical earth, aircraft motion model, with constraints on temperature, dynamic pressure and stall, is employed. An exact optimal iterative solution method and an approximate closed-form feedback solution method are developed. In the exact approach, solutions are computed by iteration on adjoint constants. Each iteration requires a complete forward trajectory integration. In the approximate closed-form feedback approach, the adjoint constants are expressed in terms of the states. No forward trajectory calculations are required, thus, the computations are minimal. Minimum-fuel climb to orbit, powered abort, and unpowered abort trajectories are computed with both methods. The approximate closed-form feedback solution closely matches the optimal iterative solution.

A computationally efficient method for generating unpowered descent footprints is also described. Footprints are used to identify candidate landing sites under an engine failure or other emergency conditions, and to initiate final descent. A hypersonic vehicle guidance, navigation and control configuration employing the optimal closed-form feedback guidance and the footprint generator is described.

This research was sponsored by the Air Force Wright Research and Development Center (WRDC).

## 2.0 Nomenclature

$a$	= Speed of sound	$w_f$	= Weight of fuel
$A_c$	= Cowl area	$x$	= State vector
$a_n$	= Normal acceleration	$z$	= Roll control variable ( $z = \tan \sigma$ )
$C_a$	= Capture area	$\theta$	= Longitude
$cd_0$	= Parasite drag coefficient	$\phi$	= Crossrange position
$c_{l_\alpha}$	= Lift curve slope	$\alpha$	= Angle of attack
$D$	= Drag	$\delta_e$	= Elevator deflection
$E$	= Specific energy	$\sigma$	= Roll angle
$F_z$	= Normal forces	$\gamma$	= Flight path angle
$F_x$	= Horizontal forces	$\lambda_E$	= Energy adjoint
$g$	= Gravity	$\lambda_\theta$	= Longitude adjoint
$h$	= Altitude	$\lambda_\psi$	= Heading adjoint
$I_{sp}$	= Specific impulse	$\lambda_\phi$	= Latitude adjoint
$k$	= Induced drag coefficient	$\lambda_w$	= Fuel adjoint
$L$	= Lift	$\rho$	= Density
$m$	= Mass	$\pi$	= Engine throttle
$M$	= Mach number	$\psi_e$	= Heading angle error
$Q$	= Dynamic pressure		
$R_{tg}$	= Range to go		
$R_e$	= Equilibrium glide descent range		
$R_c$	= Range to center of footprint		
$S$	= Wing area		
$S_{tg}$	= Arc length to go		
$T$	= Engine thrust		
$T_{max}$	= Maximum temperature		
$t$	= Time		
$u$	= Control vector		
$V$	= Velocity		

92-16979

### 3.0 Introduction

A key requirement of optimizing performance and operability of hypersonic aircraft is the ability to generate onboard flight trajectories that optimize energy management in response to mission phase demands and contingencies. The goal is to compute these trajectories on board as a step toward providing the autonomous capability required for hypersonic vehicle operations. Past space vehicle programs lacked this autonomy and consequently required complex ground support services. A truly autonomous aerospace vehicle would greatly reduce this associated cost by providing the capability to accommodate takeoff delays, changing mission conditions, low fuel conditions, engine failures, and other emergencies.

The flight profile for a flight to orbit and the return mission are shown in Figure 1. The goal is to fly to orbit employing a single stage. Minimization of fuel usage and avoidance of high temperature, high dynamic pressure, engine flame-out, and stall regions are required. The guidance system must accommodate deviations from the design model, such as aerodynamic model errors, thrust model errors, and atmospheric model errors, and external disturbances such as winds.

Also, the guidance system must accommodate emergency conditions such as aborts before reaching orbit. The abort could be due to a power loss or other failure. The vehicle must be returned to Edwards Air Force Base or to an alternate landing site if a return to Edwards is not possible.

Automatic guidance may be required because, as is known, unpowered hypersonic vehicles, for example, the Space Shuttle, are difficult for the pilot to fly in the high-speed regime. Also, it is expected that it will be difficult for the pilot to fly a powered aircraft in regions where there are a number of active constraints.

Based on these requirements, a potential configuration for the guidance system is shown in Figure 2.

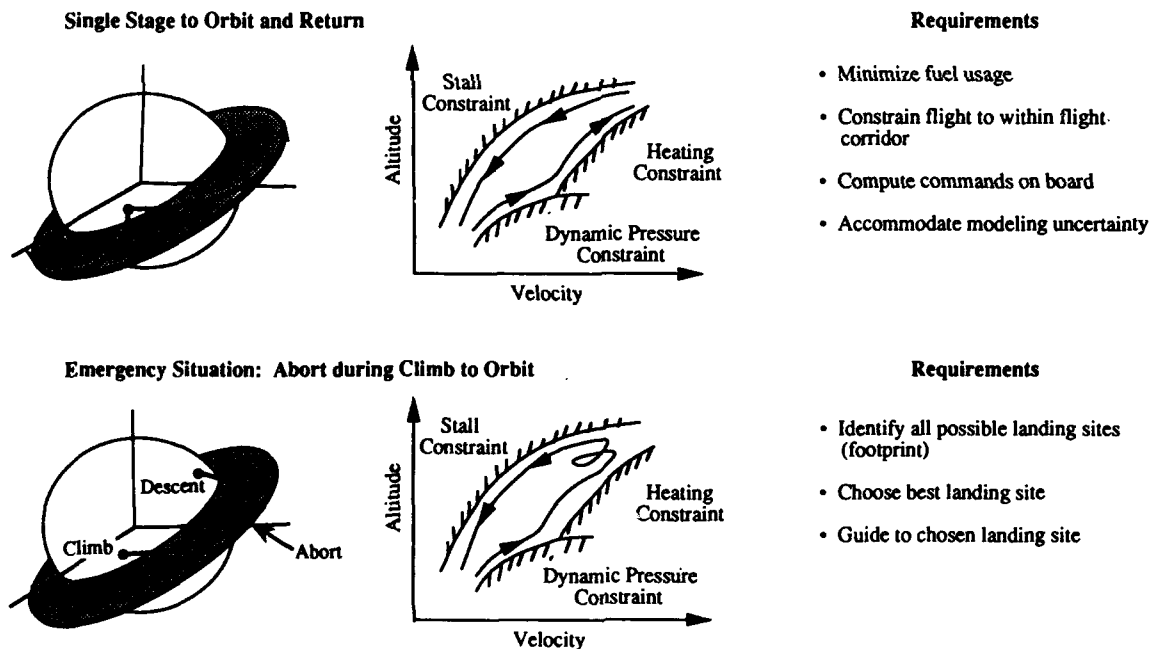


Figure 1. Single Stage to Orbit and Return Mission Requirements

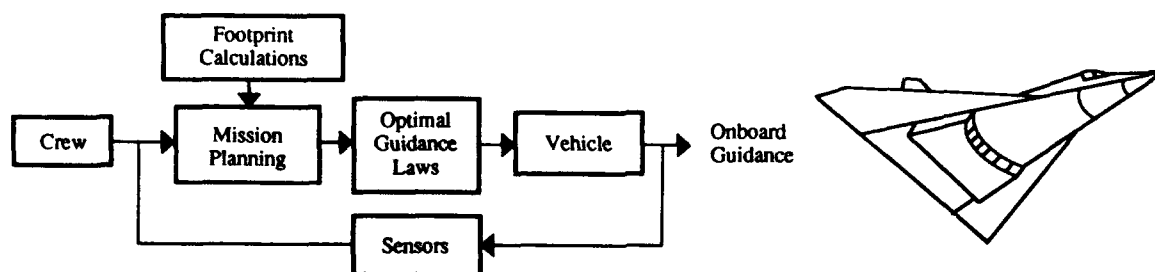


Figure 2. Guidance System Configuration



#### 4.0 Optimization Problem and Solution Approach

The objectives of this problem are to fly from a given latitude, longitude, altitude, and velocity to a specified longitude, latitude, altitude, and velocity using the minimum amount of fuel, and to continuously compute in flight the optimal trajectories between the changing current vehicle state conditions and the specified final state. The flight regime includes Mach numbers from 0.5 to 25. The optimization problem, then, is one of managing kinetic, potential, thermal, and chemical energy.

The solution approach, which is based on the Euler-Lagrange theory, is summarized in this section. The topics covered are:

- Mathematical statement of the optimization criterion
- Mathematical models for engines and aerodynamics
- Euler-Lagrange optimization theory
- Energy-state approximations
- Equation simplification
- Iterative and closed-form solutions
- Final descent reformulation

**4.1 Optimization Criterion**—The minimum-fuel performance objective is expressed as

$$J = \int_0^{t_f} \dot{w}_f dt$$

where  $w_f$  is the weight of fuel. Within the general problem, some specific problems having different end conditions are addressed:

- Minimum fuel to orbit
- Minimum-fuel climb/descent to final downrange position
- Minimum fuel to a specified downrange and crossrange position

**4.2 Vehicle Models**—The vehicle configuration and coordinate systems are defined in Figure 3.

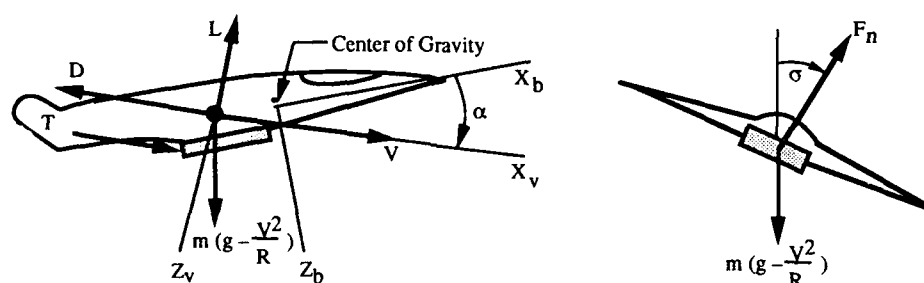


Figure 3. Vehicle Models

The equations of motion for a spherical, nonrotating earth are

$$\begin{aligned} \dot{V} &= \frac{T_x - D}{m} - g \sin \gamma \\ \dot{\gamma} &= \frac{(-T_z + L) \cos \sigma}{mV} - \left(g - \frac{V^2}{R}\right) \frac{\cos \gamma}{V} \\ \dot{\psi} &= \frac{(-T_z + L) \sin \sigma}{mV \cos \gamma} - \frac{V}{R} \cos \gamma \cos \psi \tan \phi \\ \dot{h} &= V \sin \gamma \\ \dot{\theta} &= \frac{V \cos \gamma \cos \psi}{R \cos \phi} \\ \dot{\phi} &= \frac{V \cos \gamma \sin \psi}{R} \quad ; \quad R = R_0 + h \\ \dot{w}_f &= \frac{T}{I_{sp}} \end{aligned}$$

The states are

$V$  = Velocity  
 $\gamma$  = Flight path angle  
 $\psi$  = Heading  
 $\theta$  = Longitude  
 $\phi$  = Latitude  
 $w_f$  = Weight of fuel

The control variables are

$\alpha$  = Angle of attack  
 $\sigma$  = Roll angle  
 $\pi$  = Engine throttle

The aerodynamic model and airbreathing engine model are based on the generic hypersonic aerodynamic model example (GHAME) (Reference 1). The GHAME engine model is of this form:

$$T = I_{sp} K_t \pi g \rho M a C_a A_c$$

For this study, the GHAME engine was modified. The  $I_{sp}$  curve was inverted with respect to throttle and increased in magnitude.

The GHAME aerodynamic drag ( $D$ ) and lift ( $L$ ) are expressed as

$$D = QS [C_{d0} + KC_1^2]$$

$$L = QSC_l(M, \alpha)$$

The constraints on the trajectory variables may be of the equality or inequality type. The system must operate in such a way that the resulting trajectory does not violate the constraints. Some typical hypersonic vehicle constraints are shown in Figure 4. The plot on the left shows some of the constraints on an altitude-velocity grid. The plot on the right shows the throttle constraints. The flame-holding constraint prevents the fuel-to-air ratio from becoming so small that the engine ceases operating. It is currently assumed that the engine cannot be restarted in flight. The other throttle constraint is an active-cooling constraint. Fuel flow must be retained if active cooling is employed.

The constraints can be put in this form:

$$C(x, u, t) \leq 0$$

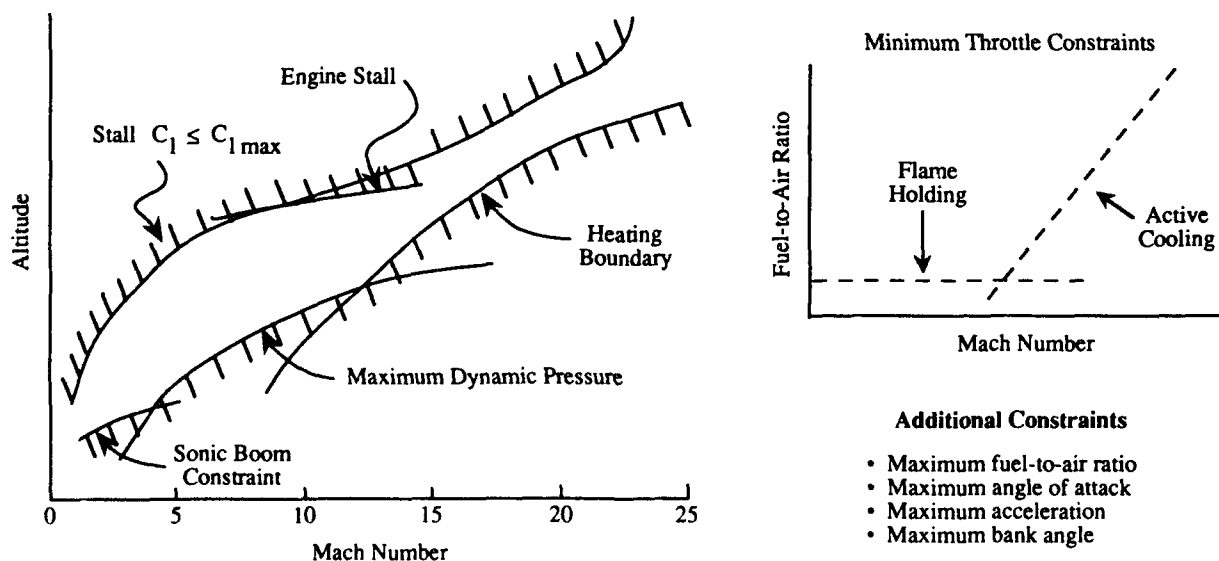


Figure 4. Typical Form of Constraints

**4.3 Euler-Lagrange Solution Equations**—The solution approach used is the Euler-Lagrange method. The general statement of the optimization problem and its solution via calculus of variations are stated below.

Minimize the performance criterion  $J$ ,

$$J = \int_0^t G(x, u, t) dt$$

subject to these constraints:

$$\begin{aligned} \dot{x} &= f(x, u, t) & ; & \quad x(t_0) = x_0 \\ C(x, u, t) &\leq 0 \end{aligned}$$

The solution to this optimization problem is the following set of Euler-Lagrange equations.

The controls are found by minimizing the Hamiltonian:

$$\min_u (H)_x$$

The Hamiltonian is given by

$$H = G + \lambda^T f$$

The adjoint variables  $\lambda$  are given by

$$\dot{\lambda} = - \frac{\partial H}{\partial x}$$

The boundary conditions on  $\lambda$  and  $x$  are given by the transversality conditions

$$\left[ H dt - \lambda^T dx \right]_{t_0}^t = 0$$

When  $H$  is independent of time, it must also satisfy  $H = 0$ .

Although these equations specify a solution in principle, the actual solution is still quite difficult to obtain because a two-point boundary value problem results. In a two-point boundary value problem, the initial conditions on the state variables  $x(t_0)$  are specified but the initial conditions on the adjoint variables  $\lambda(t_0)$  are not specified while some final condition may be specified. The set of equations cannot be directly integrated on a computer because an initial value for all variables is required to start the integration. Additional iterative data processing techniques, which correct errors in initial guesses, are required to solve the problem. Even with elaborate iteration methods, the solution may not converge because of the extreme sensitivity to the adjoint variables.

**4.4 Energy-State Approximations**—To avoid the difficulties mentioned above, an approach based on simplifying approximations is considered. In this approach, assumptions and simplifications are made to reduce the number and complexity of the adjoint variables. The goal is to eliminate or significantly reduce the difficulty of the two-point boundary value problem.

In the energy-state approximations illustrated in Figure 5, it is assumed that vertical motion has higher frequency dynamics than horizontal motion. This assumption is similar to the assumption that the attitude dynamics are at a higher frequency than the positional dynamics. Ultimately, both assumptions imply that an attitude controller and a vertical motion controller are supplied where the control frequencies of the successively higher dynamics are separated by a factor of 10. The  $\gamma$  and  $h$  differential equations are eliminated and replaced by their equilibrium conditions. The energy-state equations are

$$\begin{aligned}
 E &= (T - D) \frac{V}{m} & ; \quad E &= \frac{V^2}{2} + gh \\
 \dot{\psi} &= \frac{\bar{g}}{V} \tan \sigma - \frac{V}{R_0} \cos \psi \tan \phi & ; \quad \bar{g} &= g - \frac{V^2}{R_0} \\
 \dot{\theta} &= \frac{V \cos \psi}{R_0 \cos \phi} \\
 \dot{\phi} &= \frac{V \sin \psi}{R_0} & ; \quad R &= R_0 + h \\
 \dot{w}_t &= \frac{T}{I_{sp}}
 \end{aligned}$$

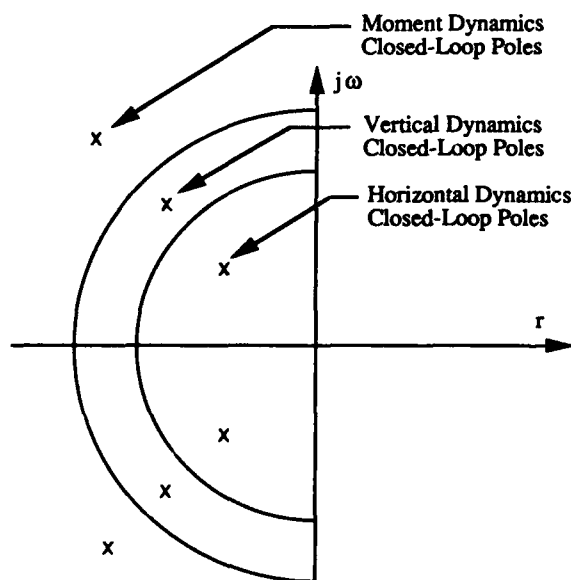
The energy-state assumptions result in a vertical force equality constraint:

$$F_z = L - T_z - m\bar{g} = 0$$

This equation is solved for  $h$  for given values of  $\alpha$  and  $\pi$ .

Using vertical equilibrium, the maximum acceleration and stall inequality constraints become

$$\frac{\frac{m\bar{g}}{\cos \sigma} + T_z}{.5\rho V^2 S} \leq C_{lmax} \quad ; \quad \frac{m\bar{g}}{\cos \sigma} \leq a_{nmax}$$



#### Energy-State Approximations

- Neglect higher frequency dynamics, both vertical and moment
- Replace with equilibrium condition  $F_z = 0$

Figure 5. Energy-State Approximations

**4.5 Equation Simplification**—The Euler-Lagrange equations can be simplified as follows.

**Analytical Solution to Adjoint Equation**—Following Vinh (Reference 2), an analytical solution to the adjoint equation is determined by

$$\begin{aligned}
 \lambda_\theta &= C_1 \\
 \lambda_\psi &= C_2 \sin \theta - C_3 \cos \theta \\
 \lambda_\psi &= C_1 \sin \phi + (C_2 \cos \theta + C_3 \sin \theta) \cos \phi
 \end{aligned}$$

**Reformulation of Adjoint Constants of Integration**—The adjoint constants are expressed in terms of three other constants that have physical meaning. One constant is eliminated using the transversality condition on final heading. The reformulation approach is illustrated in Figure 6. From Vinh, the adjoint constants form a vector that is perpendicular to the final position and velocity vector. The final condition on  $\lambda_\psi$  ( $\lambda_\psi = 0$ ) has been used to eliminate one parameter. The constants in terms of the new parameters are

$$C_1 = \cos\phi_f \cos\psi_f C_0$$

$$C_2 = (\sin\theta_f \sin\psi_f - \cos\theta_f \sin\phi_f \cos\psi_f) C_0$$

$$C_3 = (-\cos\theta_f \sin\psi_f - \sin\theta_f \sin\phi_f \cos\psi_f) C_0$$

$\psi_f$  is the final heading angle and  $C_0$  is related to the cruise minimum-fuel flow rate.

**Elimination of the Adjoint Constant  $\lambda_E$** —The adjoint constant  $\lambda_E$  is eliminated using the minimum principle and the first integral, i.e.,

$$H(u^*) \leq H(u^* + \Delta u) ; H = 0$$

where  $u^*$  is the optimal control and  $u^* + \Delta u$  is the nonoptimal control. The derivation, which is presented in Reference 3, results in two possible operations on a new Hamiltonian  $H_a$ :

$$\min_u [H_a(u)] ; \text{ if } \dot{E} > 0$$

$$\max_u [H_a(u)] ; \text{ if } \dot{E} < 0$$

The new Hamiltonian is

$$H_a = \left[ \frac{\frac{T}{I_{sp}} + \lambda_\theta \frac{V \cos\psi}{R_0 \cos\phi} + \lambda_\phi \frac{V \sin\psi}{R_0} + \lambda_\psi \left( \frac{\bar{g}}{V} \tan\sigma - \frac{V}{R_0} \cos\psi \tan\phi \right) + \lambda_w \frac{T}{I_{sp}}}{(T_x - D) \frac{V}{m}} \right]$$

**Selection of Extremum Operation**—The elimination of the adjoint variable  $\lambda_E$  results in two possible extremum operations. The condition for switching between extremum operations can be determined by using the continuity of  $\lambda_E$  and  $\lambda_E = -\min(H_a)$  or  $\lambda_E = -\max(H_a)$ . The switching condition, which is derived in Reference 3, is

$$\max_{\dot{E} < 0} (H_a) = \min_{\dot{E} > 0} (H_a)$$

Typical switching conditions are shown in Figure 7. The starting operation is still unknown at this point.

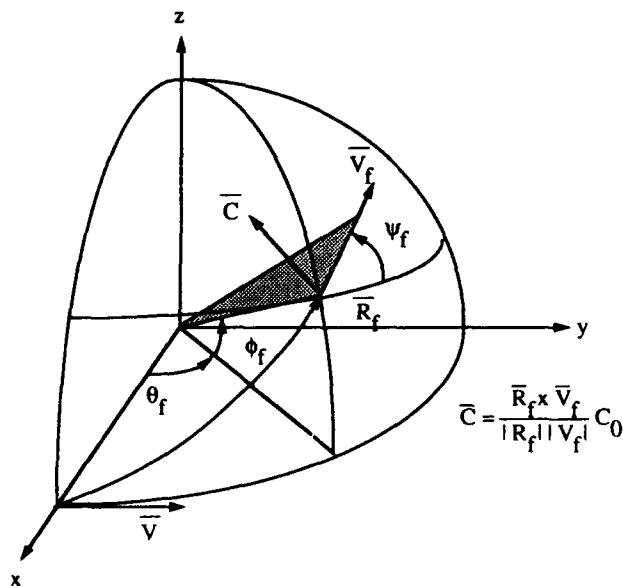


Figure 6. Reformulation of Adjoint Constants

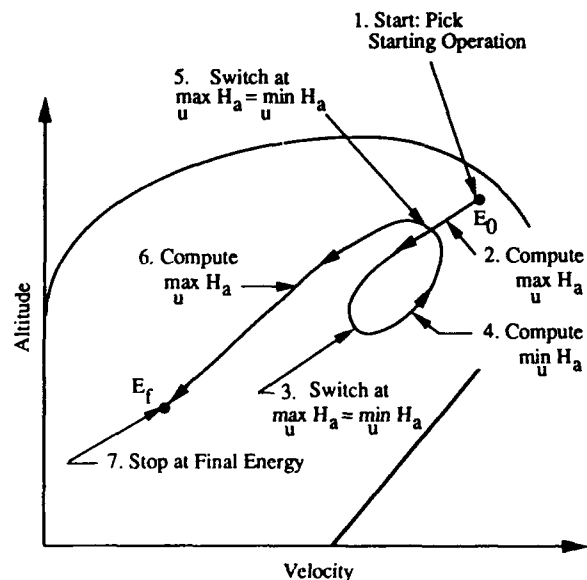


Figure 7. Switching Conditions between Maximum and Minimum Operations

**General Methods to Find Extrema of the Hamiltonian**—The optimal controls are found by determining the extrema of the Hamiltonian with respect to the controls:

$$\text{Extremum } (H_u)_{t_f=0} ; \text{Extremum} = \begin{cases} \max; E < 0 \\ \min; E \geq 0 \end{cases}$$

Some general methods to find the extrema are shown in Figure 8.

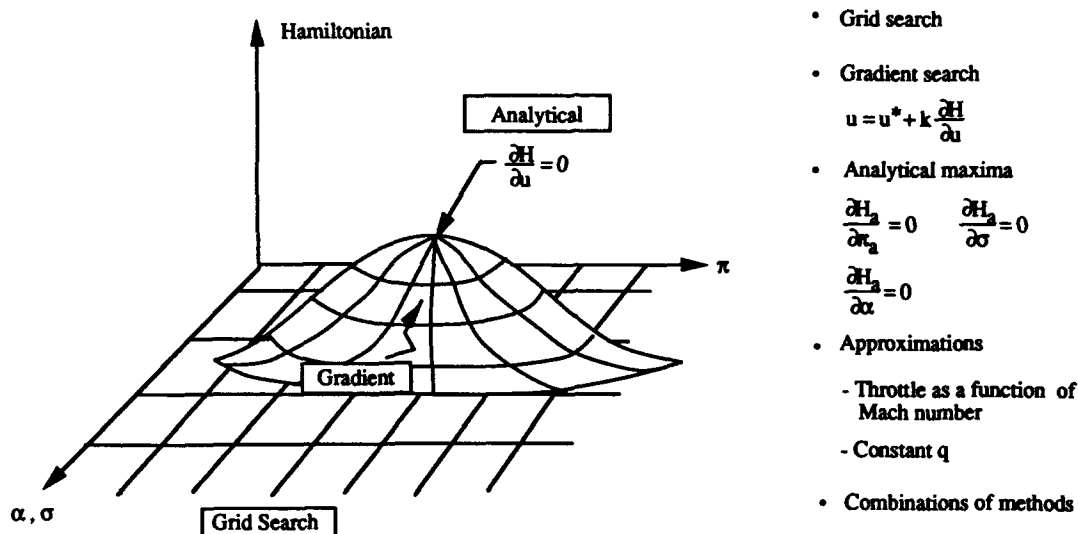


Figure 8. Methods to Determine the Extrema of the Hamiltonian

**4.6 Optimal Solution Methods**—The determination of the adjoint constants  $C_0$  and  $\lambda_\psi$  and the starting extremum operation are still required. Table 1 compares two solution methods.

Table 1. Solution Method Comparison

Optimal Iterative Solution	Optimal Closed-Form Solution
<ul style="list-style-type: none"> <li>• Adjoint constants selected at start</li> <li>• Extremum operation selected at start</li> <li>• Controls found by full search for extremum of Hamiltonian</li> <li>• Requires trajectory integrations</li> <li>• Adjoint constants updated with terminal misses</li> <li>• Most exact solution</li> </ul>	<ul style="list-style-type: none"> <li>• Adjoint constants expressed in terms of states</li> <li>• Extremum type selected using endpoint location</li> <li>• Controls found by analytical and simple search for extrema of Hamiltonian</li> <li>• No trajectory integrations required</li> <li>• Approximate solution</li> </ul>

**Iterative Solution**—The optimal iterative solution procedure is illustrated in Figure 9. In the iterative solution,  $\psi_f$  and  $C_0$  are selected at the start. The trajectory is then integrated to the end. The solution, however, is sensitive to  $\psi_f$ . If  $\psi_f$  is not correctly chosen, the trajectory diverges near the end. A method employed to reduce this sensitivity is

$$\text{if } |\lambda_\psi(t)| \geq |\lambda_\psi(t-\tau)|; \sigma = 0$$

**Closed-Form Solution**—Closed-form feedback solutions can be obtained by expressing the adjoint constants in terms of the state variables. The method to generate closed-form feedback solutions is

illustrated in Figure 10. The closed-form solution eliminates the need to iteratively update the adjoint constants and to forward integrate the equations of motion. Computations are performed only at the current energy level. The optimal controls are used to directly control the real vehicle.

Exact closed-form solutions can be determined for linear equations with quadratic performance measures. However, for nonlinear problems, closed-form solutions, in general, are difficult to find. The hypersonic aircraft performance problem is a nonlinear problem.

**Adjoint Constant Solution**—The solution approach for adjoint constants is to express  $C_0$  and  $\psi_f$  in terms of the states. In Reference 4, the adjoint constant  $C_0$  is shown to be related to the negative of the cruise minimum-fuel flow rate:

$$C_0 = -\min_{\pi, \alpha} \left( \frac{T}{L_p} \right) \left( \frac{R_0}{V} \right)_{\substack{F_x=0 \\ F_z=0}} ; F_x = T_x - D; F_z = L - T_z - m\bar{g}$$

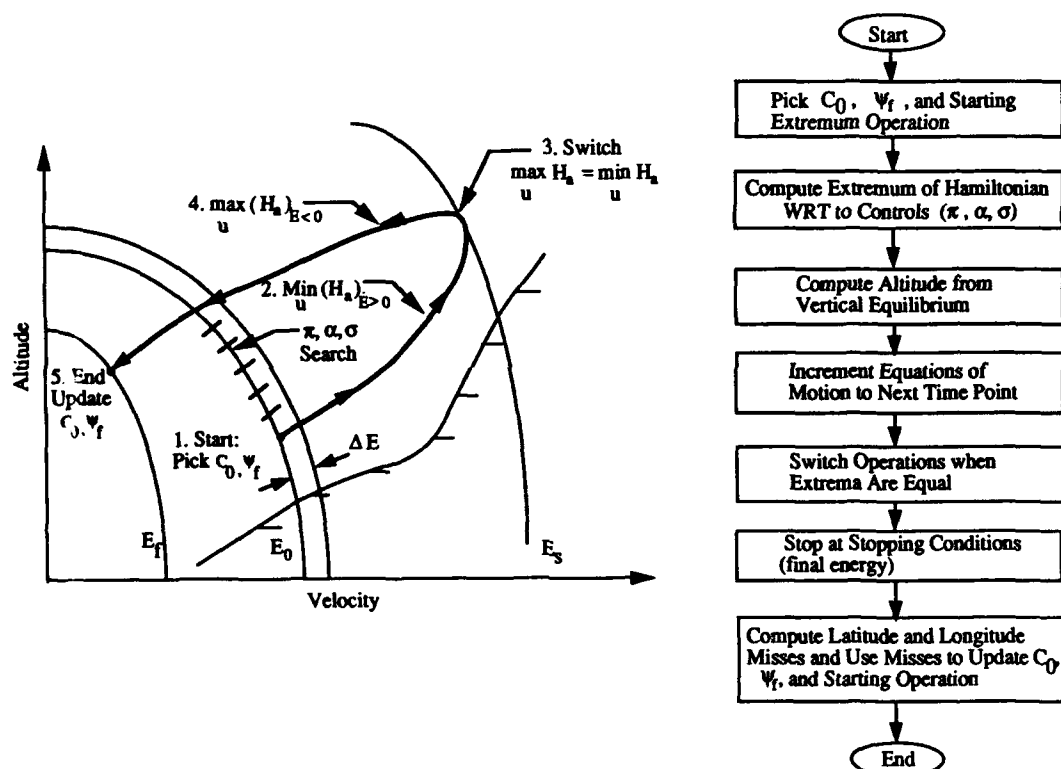


Figure 9. Optimal Iterative Solution Procedure

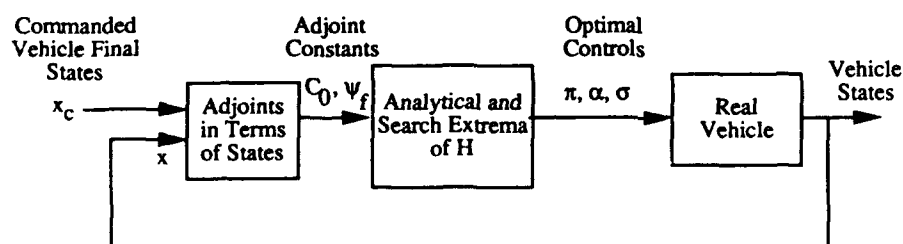


Figure 10. Optimal Closed-Form Feedback Approach

A typical plot showing the line of best cruise points and the values of  $C_0$  at different energy levels is shown in Figure 11. For a vehicle that has the fuel flow rate decreasing with increasing energy, the range is increased for smaller values of  $C_0$ ; thus the value of  $C_0$  is dependent on the remaining range. The method for approximating  $C_0$  from the current states is

$$C_0 = C_{0_c} + (C_{0_c} - C_{0_f}) \left( \frac{R_{des}}{R_{tg}} \right)^n ; n = \frac{1}{2}$$

where

$C_{0_c}$  = Current  $C_0$

$C_{0_f}$  = Final  $C_0$

$R_{des}$  = Computed range traveled during unpowered descent ( $R_{des} = R_c + \Delta R_c$ )

$R_{tg}$  = Range to go

The closed-form solution approach for determining  $\psi_f$  is to express it in terms of the current heading errors ( $\Delta\psi$ ) and the angle to the relative position vector at the final point ( $\psi_{tf}$ ).  $\psi_f$  is made equal to the sum of the angle to the relative position vector at the final point ( $\psi_{tf}$ ) and a gain multiplied by the heading angle error:

$$\psi_f = \psi_{tf} + k_a \Delta\psi$$

The current heading error is the angle between the current velocity vector and the relative position vector ( $\Delta R$ ), both defined in Figure 12.

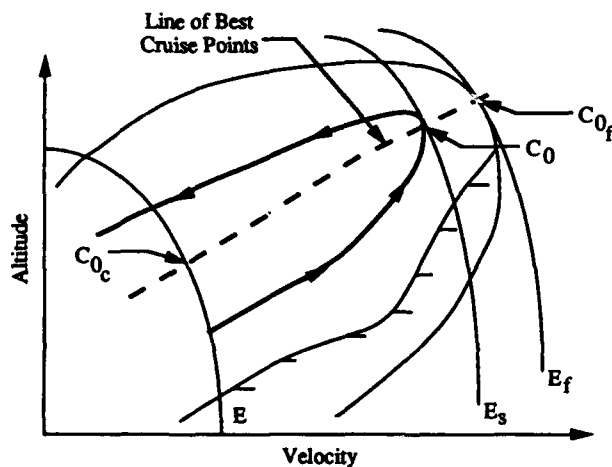


Figure 11. Closed-Form Feedback Solution for Adjoint Constant  $C_0$

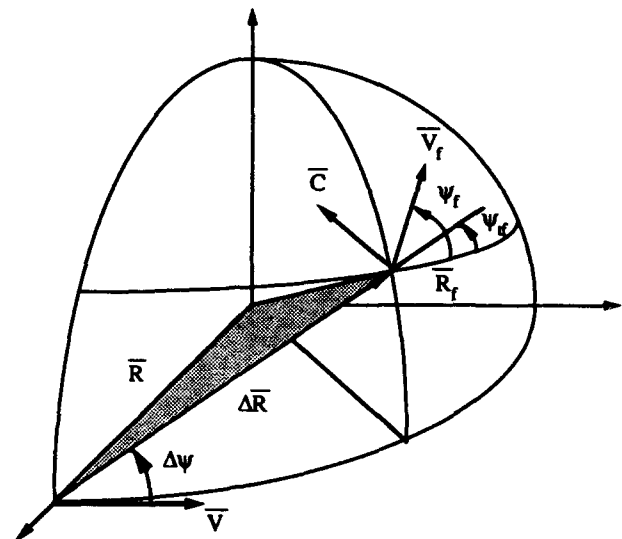


Figure 12. Closed-Form Solution for Adjoint Constant  $y_f$

**Logic for Selecting the Hamiltonian Extremum Operation**—For a closed-form feedback solution, logic to select the type of starting extremum operation, i.e., the maximum of  $H_a$  (energy descent) or the minimum of  $H_a$  (energy climb), is required. The form of the selection logic depends on the location of the endpoint with respect to the current point and the current energy. Logic for selecting the energy climb or energy descent is shown in Figure 13.

Three flight regimes are possible. First, if the endpoint is inside the no-power descent footprint (a method to calculate the zero-power footprint is described later), then the maximization operation (energy descent) is chosen. Second, if the endpoint is outside the zero-power descent footprint but inside a heading angle limit, then the minimizing solution (energy climb) is chosen first. A switch to the no-power descent is made when the endpoint moves into the zero-power descent footprint. Third, if the endpoint is outside the heading angle boundary, the initial segment is a maximizing operation (descent solution). After the heading angle error is inside the heading angle limit, the climbing solution (min  $H_a$ ) is used. Again, if the endpoint moves inside the zero-power footprint, the final descent solution (max  $H_a$ ) is used.



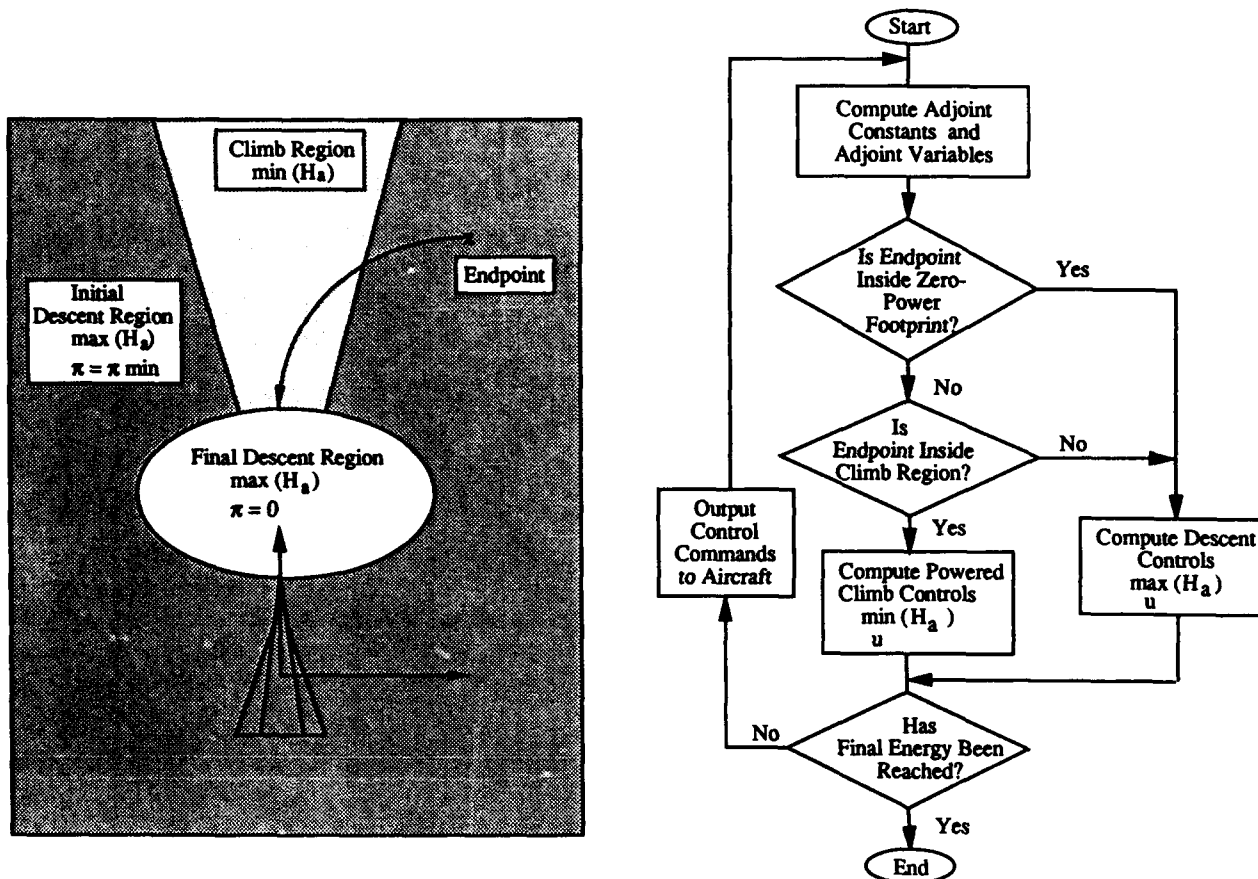


Figure 13. Climb Descent Switch Logic

The heading angle boundary was determined from simulation analysis comparing the fuel used for a three-segment flight and a two-segment flight. An approximate analytical expression for the heading angle boundary is

$$\Delta\psi_e = 40 \deg \left( 1 - \frac{V_{opt}}{26000 \text{ ft/sec}} \right)$$

*Simplified Extrema of Hamiltonian*—To simplify the solution, approximate analytical expressions for the extrema of the Hamiltonian are obtained. Analytical solutions for the minimum and maximum of the Hamiltonian are examined separately.

*Analytical Solutions for the Minimum of  $H_a$  (energy climb)*—The analytical minimum of  $H$  with respect to roll angle can be found by taking the partial derivative with respect to  $z$  ( $z = \tan\sigma$ ) and setting it equal to zero. This shows that  $z$  is proportional to  $\lambda_\psi$ .  $\lambda_\psi$  can be expressed as the projection of the adjoint constant vector on the current position vector; thus  $\lambda_\psi$  and  $z$  are proportional to the heading error. The specific form of the proportionality constant is unknown, but it can be adjusted to match the profile from the optimal iterative solution. That the gain should be inversely proportional to range is intuitive. Based on this assumption, a  $z$  controller of this form is chosen:

$$z = \frac{24V^2}{g R_{tg}} \sin \Delta\psi$$

The minimum of  $H_a$  with respect to  $\pi$  can be found by taking the partial derivative of  $H_a$ . Simulation studies using a full search on the throttle show that another good approximation to  $\pi$  is

$$\pi = a_0 + a_1 M + a_2 M^2$$

The minimum of  $H_a$  with respect to  $\alpha$  for the energy gain case is difficult to obtain analytically; thus a search method is used. The optimum  $\alpha$  ( $\alpha^*$ ) is given by

$$\alpha^* = \arg \left\{ \min_{\alpha} [H_a]_{E>0} \right\}$$

$$F_z = 0 ; C(x,u) \leq 0$$

The analytical solutions for  $\pi$  and  $z$  are used in computing the minimum with respect to  $\alpha$ .

**Analytical Solution for the Maximization of  $H_a$  (energy loss)**—The roll angle solution for maximizing the Hamiltonian is assumed to be the same as that for minimizing the Hamiltonian. The optimal throttle determined from the iterative solution shows that the throttle for the energy loss case is small or approximately zero. Thus, the descent throttle is

$$\pi = \begin{cases} \pi_{\min} & \text{for flame-holding initial descent} \\ 0 & \text{for final descent} \end{cases}$$

This throttle is for engine control. Additional fuel flow may be required for cooling.

The optimum density for energy descent can be determined by examining the the Hamiltonian  $H_a$  with zero throttle. The numerator does not contain the angle of attack for  $\pi = 0$ ; thus the optimal angle of attack maximizes or minimizes the drag depending on the sign of the numerator. For the initial descent, the drag will be a minimum. For the final descent, the drag will be a maximum or minimum depending on the location of the endpoint on the footprint boundary. For the initial descent, the optimum angle of attack ( $\alpha^*$ ) is computed from

$$\alpha^* = \arg \left\{ \max_{\alpha} [H_a]_{E<0} \right\} ; \pi = 0$$

$$F_z = 0 ; C(x,u) \leq 0$$

The angle of attack for the final descent is described in the next subsection.

**4.7 Final Descent Reformulation**—The optimal minimum-fuel trajectories have powered climbs at high dynamic pressures followed by low-throttle or zero-throttle turning descents at maximum or minimum drag. For a perfect system, after the descent is started, the decent trajectory characteristics stay the same: the throttle stays at zero and the path stays at minimum drag or maximum drag until the terminal point is hit. However, for an imperfect system (e.g., modeling errors), a predicted terminal miss error could occur and the new optimal path then would contain a short powered climb segment followed by a minimum or maximum drag descent. The entire descent trajectory could consist of short pulses of thrust. For a practical system, this is undesirable. Thus the descent guidance approach is reformulated.

The approach for descent trajectory determination is to: 1) start the descent when the the terminal point is well inside the footprint and 2) change the performance criterion after the descent is started. The area to begin descent can be either an area smaller than the footprint or a circular area around the center point on the footprint, as shown in Figure 14. The performance criterion after the descent is started is chosen to be

$$J = \int_0^t \left[ w_t V + w_d \left( \frac{D}{m} \right)^2 + k_z z^2 \right] dt ; \quad w_d = \begin{cases} V \left( \frac{E}{E_s} \right)^3 & ; E > E_s \\ 1 & ; E < E_s \end{cases}$$

The first term is the distance traveled, the second is the average drag over energy, and the third is the integral of the roll angle squared. For short distances traveled, a large drag is required; thus the criterion trades drag for distance traveled. The weight  $w_d$ , which is a function of energy, can be chosen to shape drag to a temperature profile.

A closed-form solution for the controls can be determined for the zero-power descent with this performance criterion. The full nonlinear equations of motion are difficult to integrate in closed form, but if flat Earth and small crossrange assumptions are made, the equations can be integrated in closed form. The approximate solution can be extended to the nonlinear problem. The solution reduces to the form of the Space Shuttle analytic drag controller (Reference 5). The closed-form feedback solution for the criterion is

Throttle:

$$\pi = 0$$

Roll Angle:

$$z = \frac{3V^2 \sin \Delta \psi}{\bar{g} R_{tg}}$$

Angle of Attack:

$$S_{tg} = R_{tg} (1 + 0.3 |\sin \Delta \psi|)$$

$$\left(\frac{D}{m}\right) = \begin{cases} \left(\frac{E_s}{E}\right) \left[ E_s - E_f + \frac{1}{2E_s} (E^2 - E_s^2) \right] \frac{1}{S_{tg}} ; E > E_s \\ \frac{E_f - E}{S_{tg}} ; E < E_s \end{cases}$$

$$\rho = \left(\frac{D}{m}\right) + \sqrt{\left(\frac{D}{m}\right)^2 - 4a_4 a_5 (1 + z^2)}$$

$$\alpha = \frac{2m\bar{g} (1 + z^2)}{\rho V^2 SC_{l\alpha}}$$

If the density exceeds the constraints, it is replaced by its constraint value.

If the circular region is chosen to begin descent after a powered segment, the center of this region is computed from

$$R_c = \begin{cases} \left(\frac{E_s}{E}\right) \left[ E_s - E_f + \frac{1}{2E_s} (E^2 - E_s^2) \right] \left(\frac{D}{m}\right)_c ; E > E_s \\ \frac{E_f - E}{\left(\frac{D}{m}\right)_c} ; E < E_s \end{cases}$$

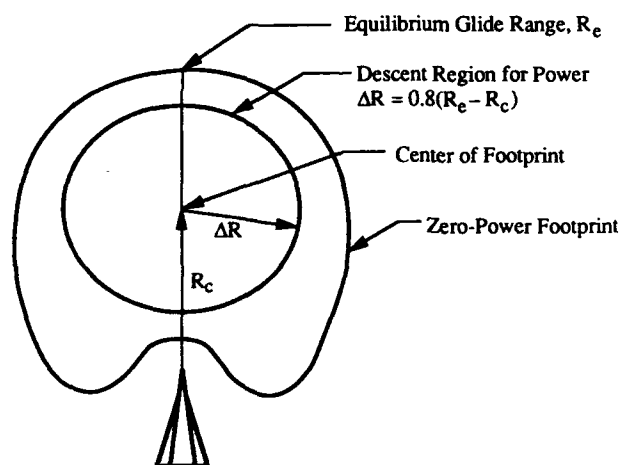


Figure 14. Area to Begin Descent with Power

The drag parameter  $(D/m)_c$  is chosen to be between the minimum drag and the drag at maximum  $q$ . The radius of the circle is chosen to be some factor multiplied by the difference between the equilibrium glide range and the footprint center range:

$$\Delta R_c = 0.8 (R_e - R_c)$$

where the equilibrium glide range  $R_e$  is approximately

$$R_e = \frac{R_0}{4S_f \sqrt{C_{d_0} k}} \ln \left[ \frac{1 - \frac{2E_f}{gR_0}}{1 - \frac{2E}{gR_0}} \right]$$

The center of the footprint and the equilibrium glide range can also be taken from the footprint calculation. The footprint calculation is described in the next section.

## 5.0 No-Power Footprint Generator

The footprint generator finds the area of attainable final points for unpowered flight. The footprint is calculated using closed-form control equations. The closed-form iterative footprint calculator is accurate for spherical earth and includes earth's rotation effect and complex constraints. The method for calculating and continuously updating a footprint is shown in Figure 15.

The footprint is calculated starting with the vehicle's initial altitude, velocity, heading, fuel mass, and position. The energy state equations of motion are integrated along a commanded heading angle until a minimum energy is reached. A variable time step depending on the magnitude of the bank angle turn rate is used. At the minimum energy point, the final latitude and longitude define the footprint boundary. A 540-deg sweep of heading angles is conducted employing minimum and maximum drag flight conditions. The trajectory termination points create a closed boundary. A total of 69 position coordinates define the footprint boundary. The central processing unit (CPU) time to create a footprint is approximately 5 sec.

An interpolation routine is used to create a smooth transition between successive footprints computed a fixed amount of time apart. Using the current five states, a footprint is generated and stored in memory. Then, using the current state rates, the states are projected along the current flight path for a fixed elapsed time. A future footprint is then generated using the new projected states. A linear interpolation between the current footprint and the future footprint is used to create footprints along the flight between the current state and the future state.

The footprint for unpowered flight is shown superimposed over a United States map in Figure 16. If Edwards Air Force Base is in the footprint, it is chosen as the landing site; otherwise another site near the center of the footprint is chosen. After the landing site is selected, a trajectory to the landing site is computed. The vehicle is guided to this point.

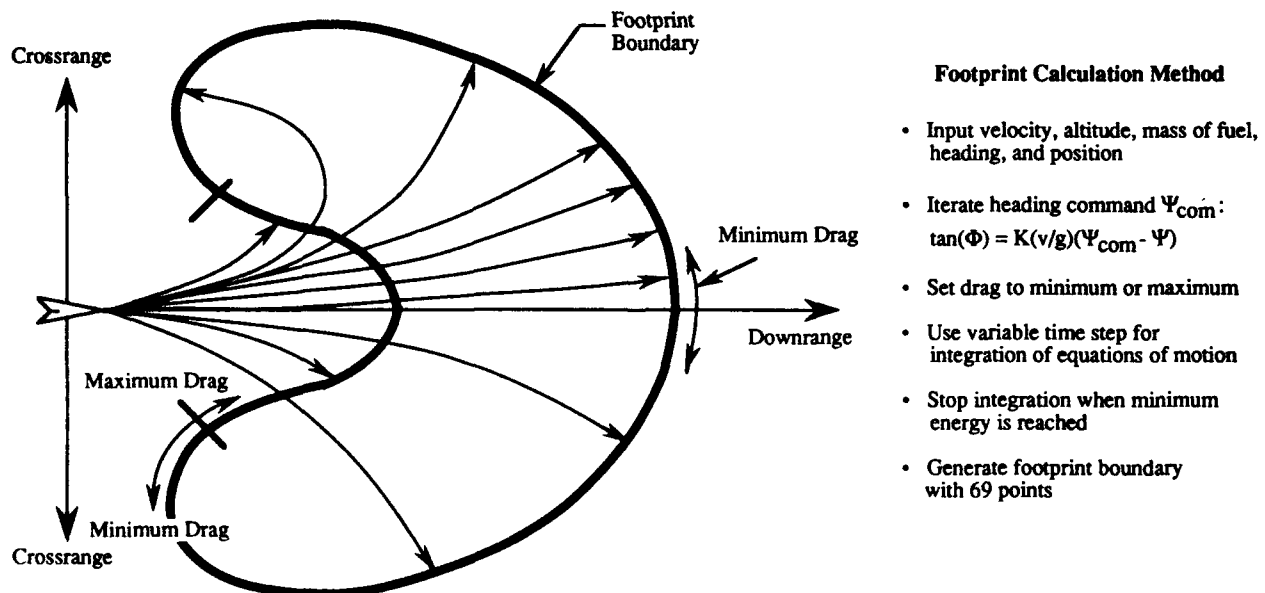


Figure 15. Footprint Generation Approach

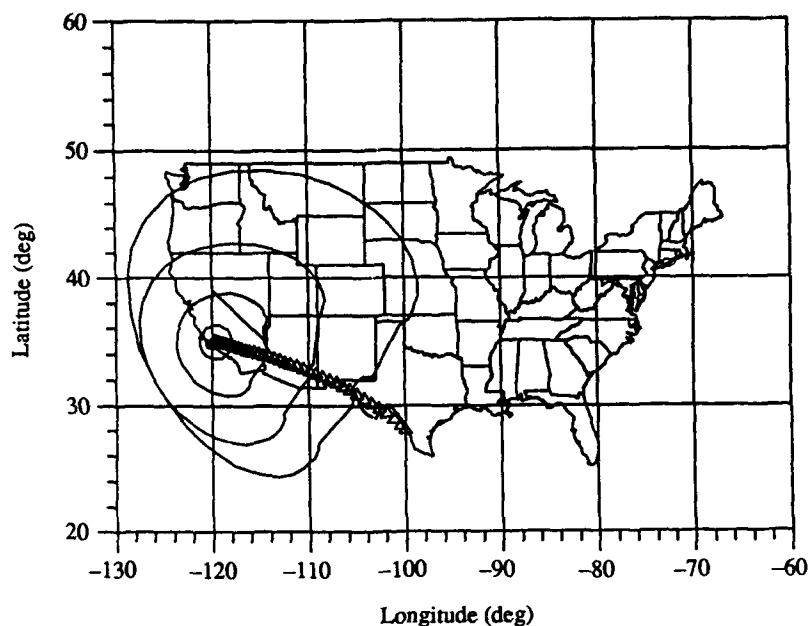


Figure 16. Hypersonic Vehicle Footprint

## 6.0 Trajectory Coupler

The vertical dynamics that were neglected in the energy-state solutions are now reintroduced. A controller that stabilizes these dynamics is incorporated. The commands to the controller are the optimal controls and the equilibrium values of the vertical dynamics determined from the energy-state solution. The trajectory coupler controls the vehicle to the computed optimal altitude. The trajectory coupler is

$$\frac{L}{m} = \frac{1}{\cos \sigma} \left[ g - \frac{V^2}{R_0} + k_h (h - h_{opt}) + k_{\dot{h}} (\dot{h} - \dot{h}_{opt}) \right]$$

## 7.0 Guidance, Control, and Navigation Control System Configuration

A guidance, navigation, and control structure is shown in Figure 17. The aircraft guidance configuration consists of a trajectory generator, a trajectory coupler, and a footprint calculator.

The guidance system is the set of optimal closed-form feedback solution equations. No forward prediction is required; thus updates of the guidance commands can be made very rapidly. Forward trajectory computation, however, still may be required for pilot information. One forward trajectory computation takes approximately 2 sec of CPU time for a 2000-sec trajectory.

The trajectory coupler is an altitude feedback controller that controls the vehicle altitude to an optimal altitude computed from the energy-state optimization. The optimal roll angles and throttle are direct commands to the engine controller and the attitude controller.

The footprint generator finds the area of attainable final points for unpowered flight. If Edwards Air Force Base is in the footprint, it is chosen as the landing site; otherwise another site near the center of the footprint is chosen. After the landing site is selected, a trajectory to the landing site is computed and the vehicle is guided to this point.

## 8.0 Optimal Solutions for Different Cases

Optimal trajectory solutions for different cases are discussed below.

**Minimum-Fuel Climb to Orbit**—The aircraft takes off from Edwards Air Force Base on an ascent to orbit. For this case,  $C_0$  and  $\psi_f$  are zero. The time histories of several variables are shown in Figure 18. The plot in the upper left is an altitude vs. velocity profile. The two lower curves are the temperature constraint and the dynamic pressure constraint. The upper curve is the stall constraint. The other plots show the throttle, thrust, fuel used, and angle of attack vs. time.

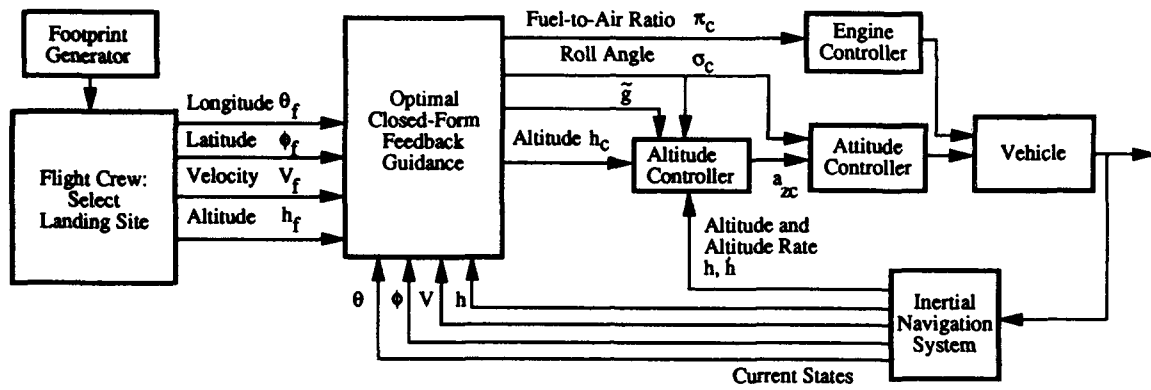


Figure 17. Guidance, Navigation, and Control Configuration

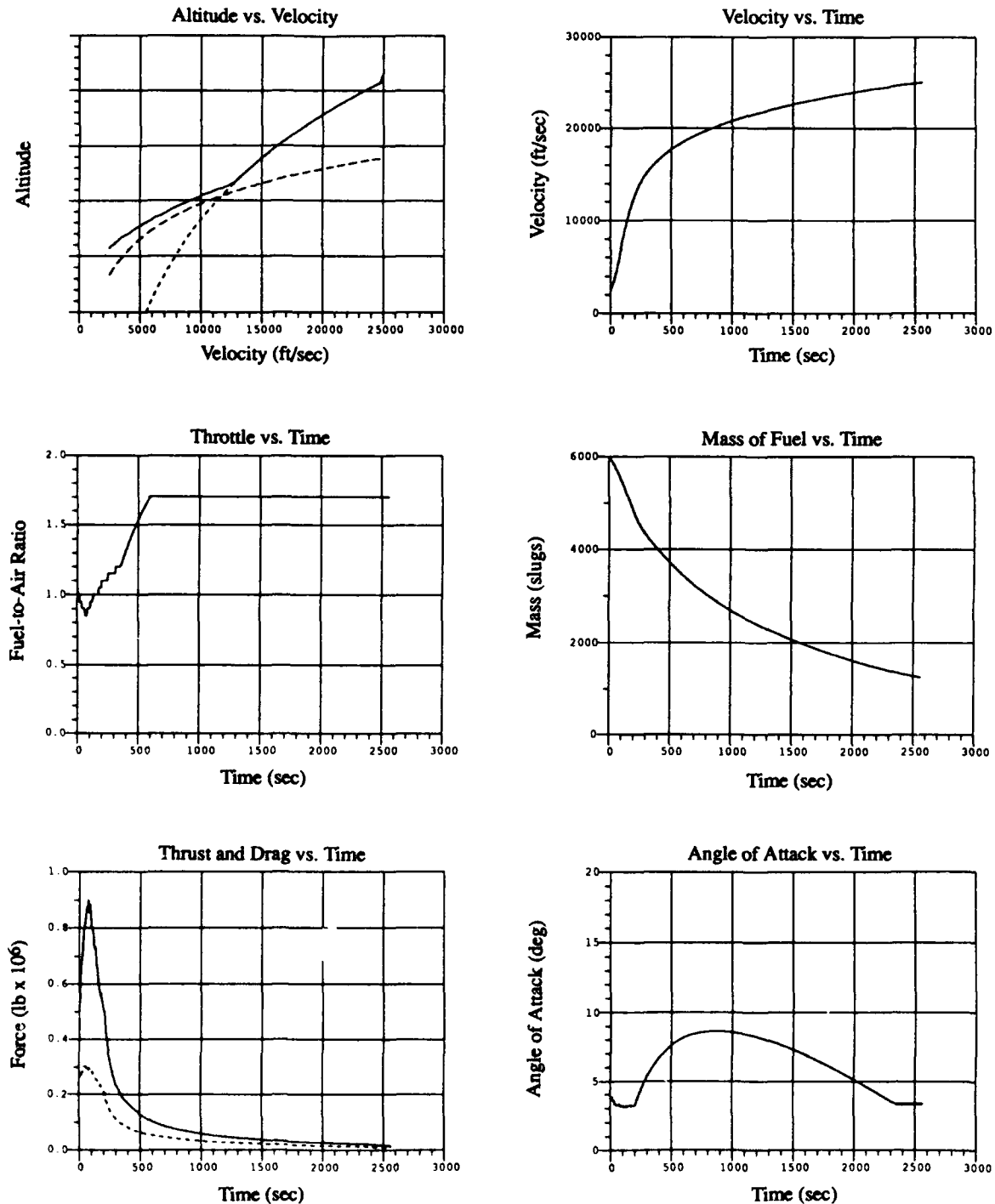


Figure 18. Time Histories for a Minimum-Fuel Climb to Orbit

**Abort with No Power and Land at Langley Air Force Base**—The aircraft takes off from Edwards Air Force Base with the intent of ascending to orbit. The vehicle encounters an emergency situation at Mach 15. In this scenario, the vehicle has lost use of its engines and is unable to return to Edwards. The trajectory of the vehicle is shown in Figure 19. In the no-power abort procedure, a footprint is first calculated from the point of abort. Then a landing site in the footprint is chosen. From the plot, we see that the vehicle is just able to make it back to the United States. Langley Air Force Base in Virginia is inside the footprint and is chosen as the landing site. If the abort had occurred later in the ascent, the aircraft would have had to land outside the United States at a landing site inside the footprint. The time histories of several variables are shown in Figure 20. The plots show the throttle, thrust, angle of attack, and roll angle vs. time. After the abort, the scenario shows first a hard turn. This turn occurs under high drag, high roll, and high angle of attack.

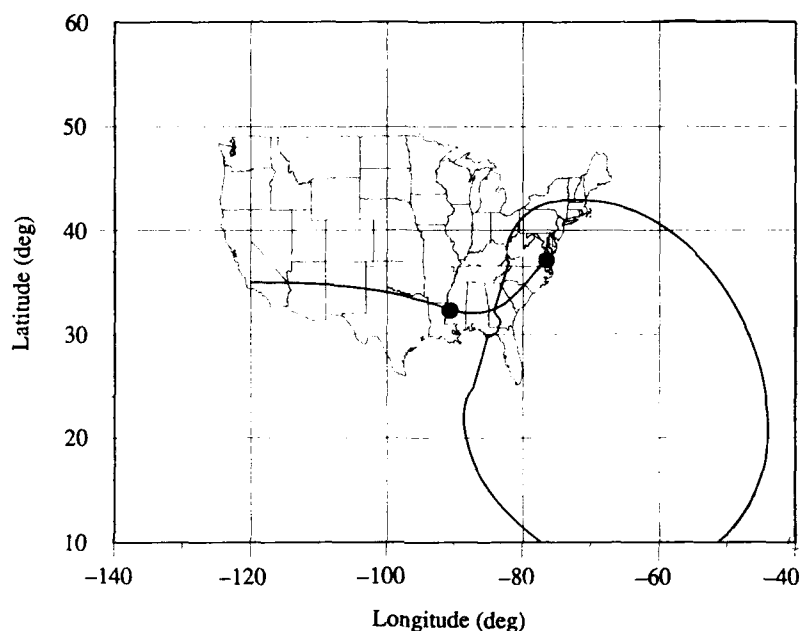


Figure 19. Trajectory Plot for an Abort with No Power

**Abort with Power and Return to Edwards Air Force Base**—The aircraft takes off from Edwards Air Force Base with the intent of ascending to orbit. The vehicle encounters an emergency situation at Mach 15. The engine remains operating and the vehicle is able to return to Edwards Air Force Base. The trajectory of the vehicle is shown in Figure 21. The time histories of several variables are shown in Figure 22. After the abort, first a hard turn occurs with the throttle set to zero. The aircraft descends to make a smaller radius turn. This turn occurs under high drag, high roll, and high angle of attack. After the vehicle is headed toward Edwards, the power is turned on again and the aircraft gains energy. When the vehicle is within gliding range of Edwards, the power is shut off and the vehicle glides back to Edwards.

**Comparison of Feedback Solutions for the Energy-State Model and the Full-State Model**—A comparison of the energy-state iterative solution, the energy-state closed-form feedback solution, and the full-state closed-form feedback solution is shown in Figure 23. In the full-state model, the vertical equations of motion are included. The vehicle is controlled with closed-form guidance and the trajectory coupler (altitude controller). For the energy-state model, the feedback solution gives similar results to the more exact optimal iterative solution. The full-state model results are similar to the energy-state model results.

## 9.0 Conclusions

The closed-form approach gives trajectories very close to full optimal solution trajectories for minimum fuel. The computing time for the closed-form feedback solution is much less than that for the full optimal iterative solution because no forward trajectory computation is required; computations are performed only at the current time. Thus, the closed-form feedback method is chosen for the hypersonic vehicle guidance, navigation, and control system. The solution equations developed above are general in nature and can be applied in different problems.

The significant contributions made by this study are listed below.

- The Euler-Lagrange energy-state optimization solutions are extended to powered-vehicle, three-dimensional, spherical earth motion models.
- Exact solutions are obtained by iteration on the adjoint constants.
- An approximate closed-form optimal feedback solution that closely approximates the iterative optimal solution is determined.
- A computationally efficient method for generating footprints for use in identifying alternate landing sites under an engine abort or other emergency condition is developed.

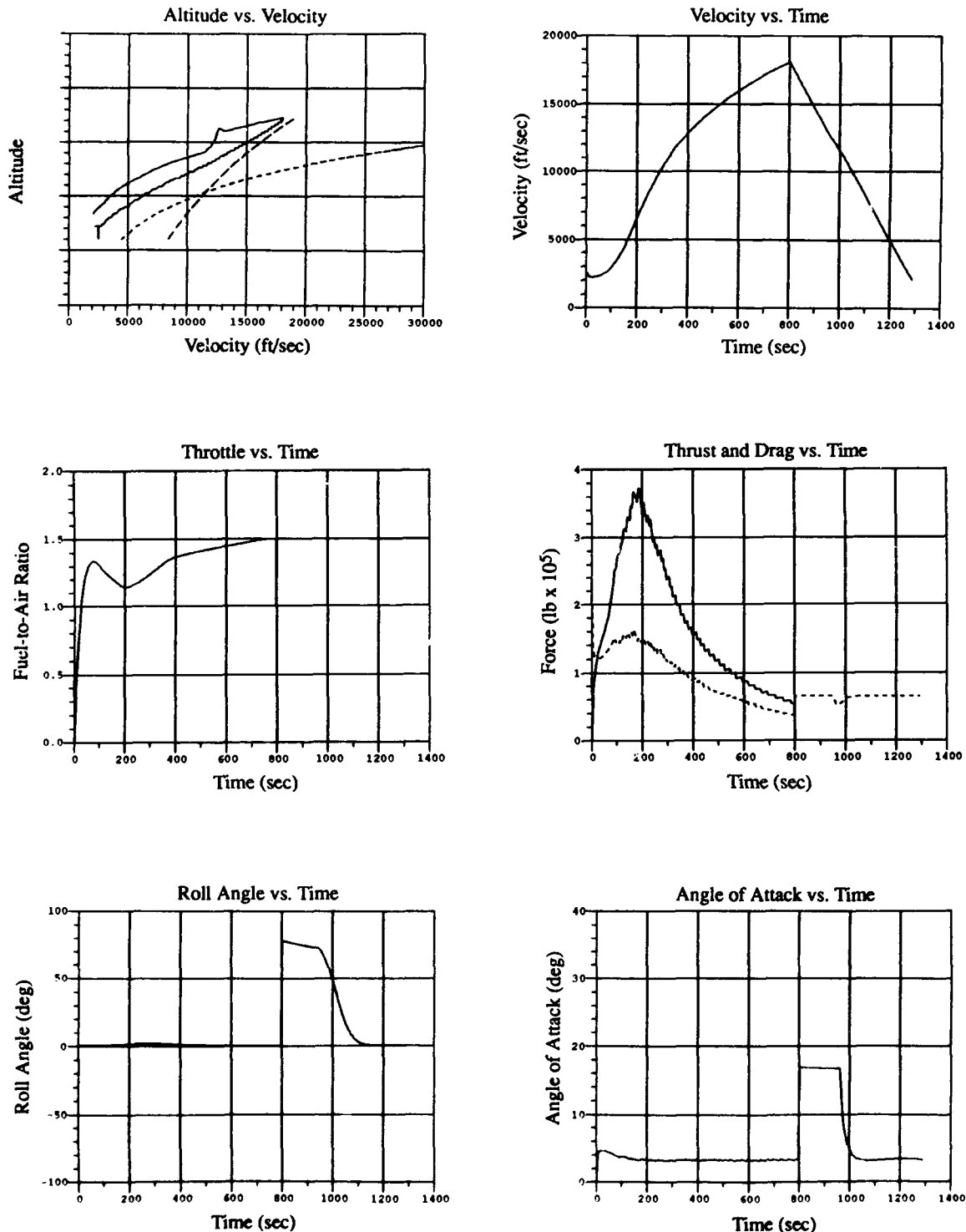


Figure 20. Time Histories for an Abort with No Power



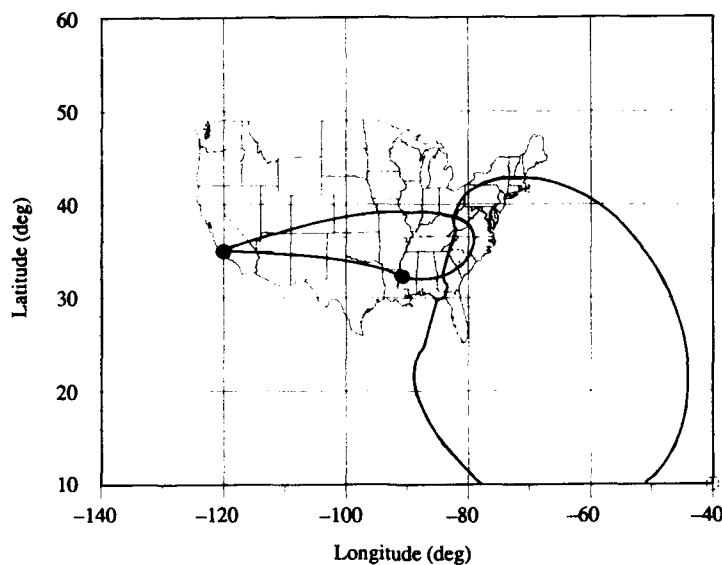


Figure 21. Trajectory Plot for an Abort with Power

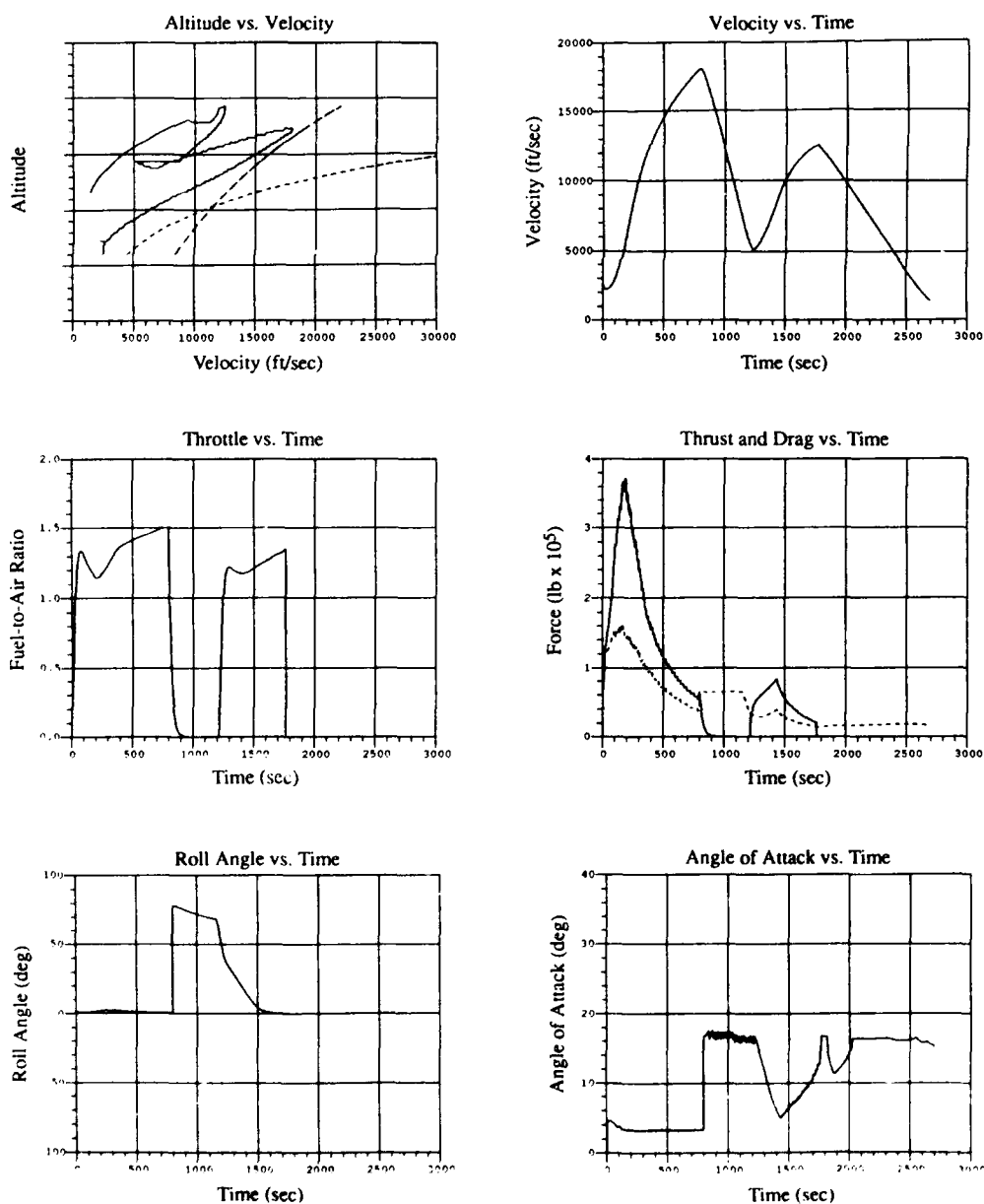


Figure 22. Time Histories for an Abort with Power

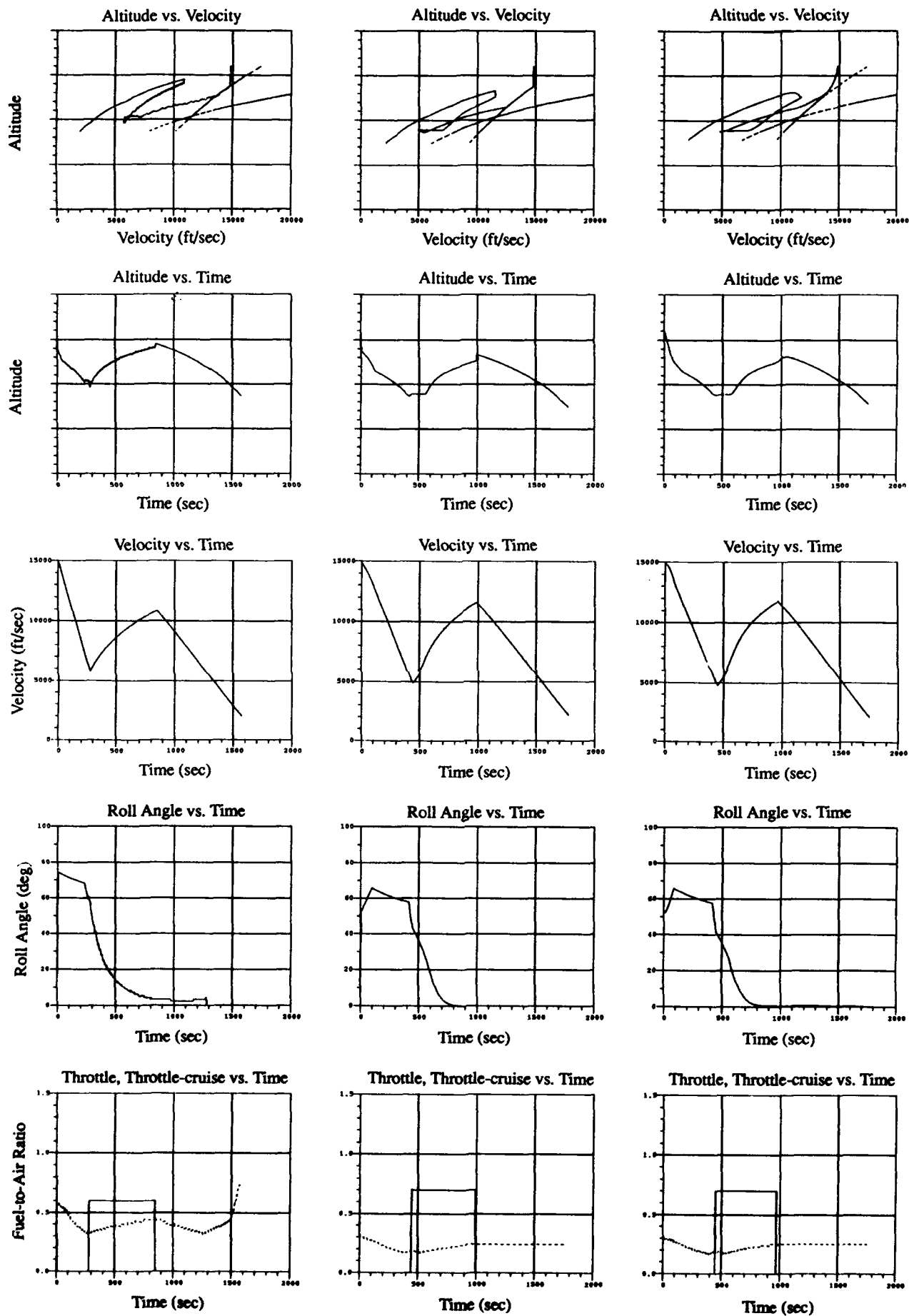
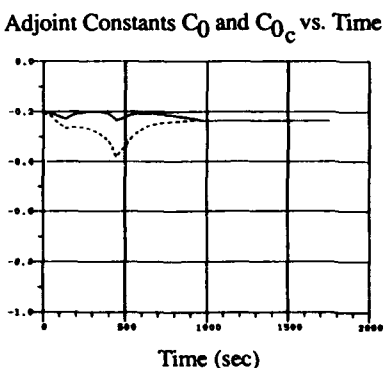
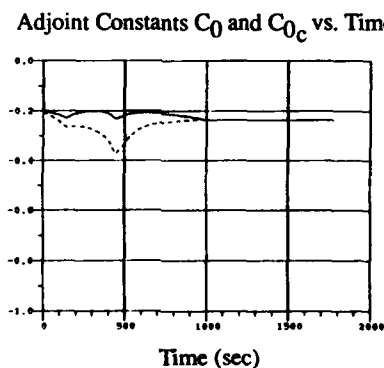
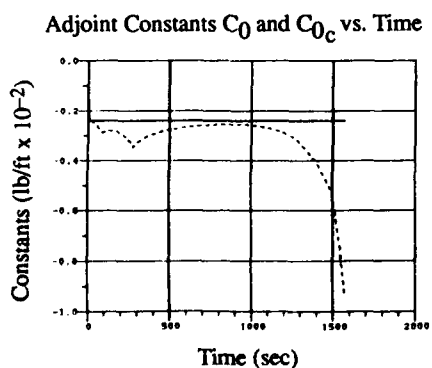
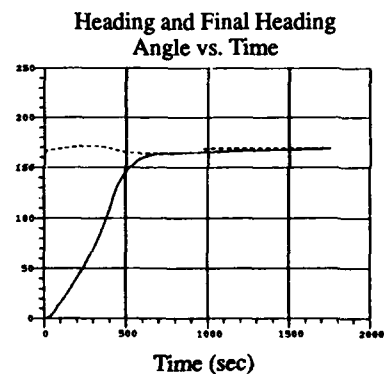
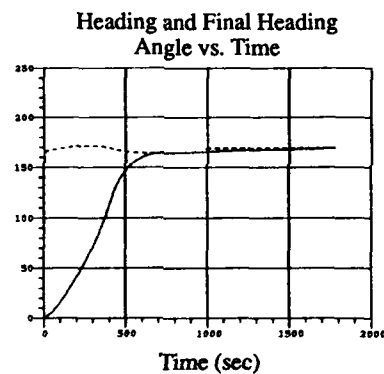
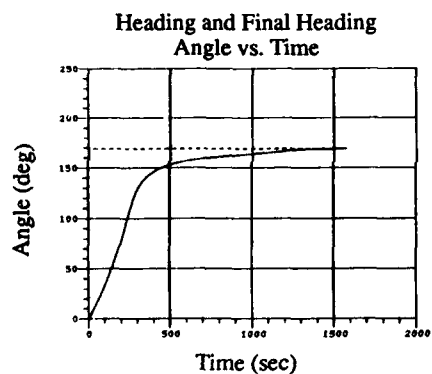
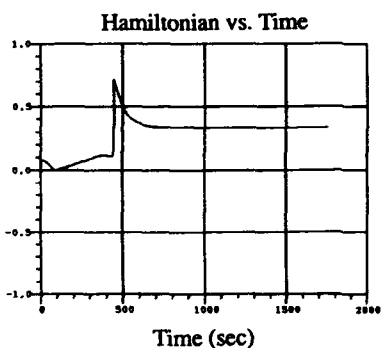
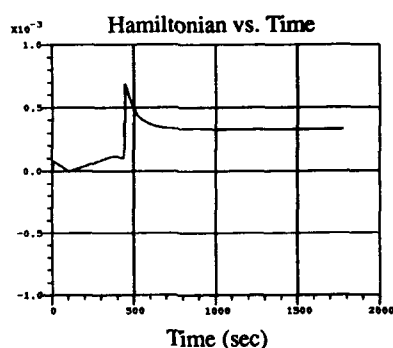
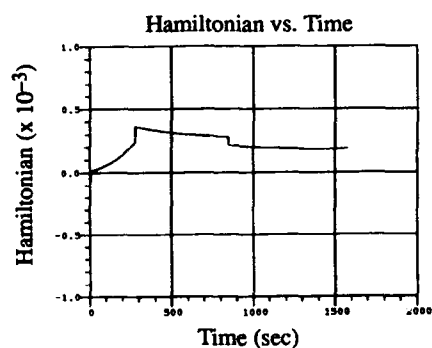
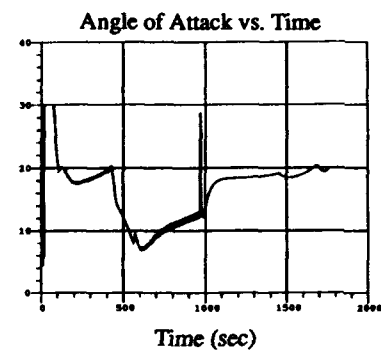
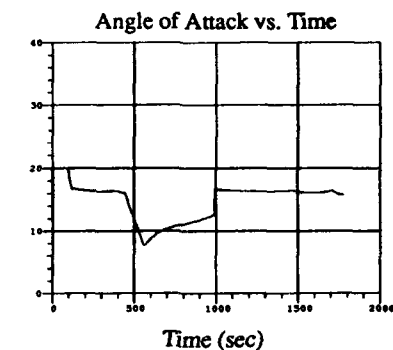
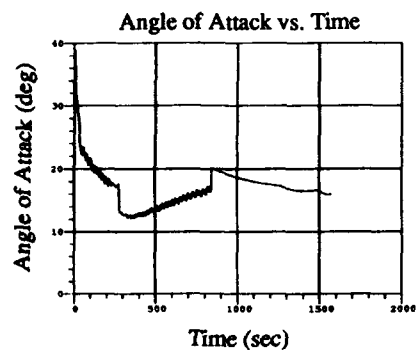


Figure 23. Comparison of Feedback Solutions for the Energy-State Model and the Full-State Model ( $V_0 = 15000$  ft/sec,  $\theta_f = 60$  deg,  $\phi_f = 60$  deg)



Energy-State Iterative  
Solution

Fuel used = 850 slugs

Energy-State Feedback  
Solution

Fuel used = 980 slugs

Full-State Feedback  
Solution

Fuel used = 1010 slugs

## References

1. Bowers, A.H., and Iliff, K.W., *A Generic Hypersonic Aerodynamic Model Example (GHAME) for Computer Simulation*, NASA Ames-Dryden Flight Research Facility, August 3, 1987.
2. Vinh, N.X., *Optimal Trajectories in Atmospheric Flight*, (Amsterdam: Elsevier, 1981).
3. Schultz, R.L., "Three-Dimensional Trajectory Optimization for Aircraft," *Journal of Guidance, Control and Dynamics*, to be published.
4. Schultz, R.L., and Zagalsky, N.R., "Aircraft Performance Optimization for Aircraft," *Journal of Aircraft*, Vol. 9, No. 2, February 1972, pp. 108-114.
5. Graves, C.A. Jr., and Harpold, J.C., *Shuttle Entry Guidance American Astronautical Society 25th Anniversary Conference Proceedings*, Paper AAS78-147, Houston, October 30 to November 2, 1978.

## Discussion

TARIFA.

How is the final orbit insertion accomplished?

AUTHOR'S REPLY.

The final orbital insertion may be accomplished by: 1) use of a rocket engine or 2) flying faster than the orbital velocity then converting this kinetic energy to potential energy.

WEYER.

You discussed emergencies at Ma 15 with powerless descend flight. What about cooling of engine and airframe structures? Is your model taking into account cooling requirements and cooling capacity which depends on fuel flow?

AUTHOR'S REPLY

Yes, at the present time simple generic models for cooling are incorporated in the computer simulation. For minimum power (flame holding) descents dumping of fuel used for cooling may be required.



# Trajectory optimization considerations for ramjet engines.

**Dipl.-Ing. Frans G.J. Kremer**

DLR; Institut für Antriebstechnik

Linder Höhe, Postfach 90 60 58

5000 Köln 90, Germany

TEL: 02203/601-3266, FAX: 02203/601-2353

## 1 Abstract

For supersonic and hypersonic flight conditions with ramjets, trajectory calculations have necessarily to be coupled with the engine performances. In space transportation systems ramjets will be employed in a relatively wide range of Machnumbers, and therefore not always near the optimum design point.

Optimization of several physical parameters along the trajectory will be inevitable. This paper discusses some of these parameters and their importance for an ascent trajectory, having a minimum fuel requirement.

## 2 Nomenclature

### Symbols

$A$	Area	$p$	Pressure
$B_S$	Specific fuel consumption	$q$	Dynamic pressure
$C_L$	Lift coefficient	$T$	Thrust
$C_{L_0}$	Lift coefficient for zero angle of attack	$t$	Flight time
$C_{L_\alpha}$	$dC_L/d\alpha$	$v$	Velocity
$g$	Gravity	$\dot{v}$	Acceleration
$G$	Weight	$x$	Flight distance
$G_V$	Fuel consumption term	$\alpha$	Angle of attack
$G/A_w$	Wing loading	$\delta$	Nozzle exit area angle against roll axis
$h$	Altitude	$\theta$	Flow vector direction against roll axis
$H_b$	Constant in atmospheric model	$\lambda$	Oxidation ratio
$L/D$	Lift over drag	$\sigma$	Thrust angle against velocity vector
$m$	Vehicle total mass	$\sigma_T$	Thrust vector angle against roll axis
$M$	Machnumber		
$\dot{m}_f$	Fuel rate		

### Subscripts

$\infty: -1$	Undisturbed flow	2	Combustion chamber inlet
0	After front shock	3	Combustion chamber outlet
0'	Diffusor inlet	4, *	Nozzle critical point
1	Diffusor outlet	5	Nozzle exit

92-16980

### 3 Introduction

In worldwide hypersonic technology programmes various concepts of airborne space transportation vehicles are under consideration. In Europe a.o. TSTO-systems are analysed with the first stage to carry the orbiter close to the equator, where separation is scheduled at a medium hypersonic Machnumber. Whereas the first stage returns to its base, the upper stage ascends into orbit, using conventional rocket engines. The first stage will most likely be propelled by hydrogen fueled turbo-ramjet engines. The turbo engines are used for taking off and accelerating the vehicle to about Mach 3. Beyond this speed ramjets will supply the required thrust.

Unlike conventional designing of turbo engines, for supersonic flight vehicles with fully integrated engines, it is necessary to consider the whole system of flight vehicle and engine. Flight mechanic and engine specific parameters are closely connected and interacting. Therefore trajectory optimization is not possible without considering both systems simultaneously.

### 4 Force balance for winged vehicle

In order to find the relevant physical parameters relating to the fuel requirement it is necessary to look at the distribution of forces on the vehicle, with mass  $m$ . Fig. 1 shows the forces acting on the considered configuration. Not regarded are mass forces (for instance Coriolis force) because these are required for discription of the flightpath relatively to the observer standing on the rotating earth. For our purposes the effects, due to the rotation of the earth, will be neglected. Curvilinear flight is not considered. The vehicle is climbing, which is indicated by the angle of incidence  $\gamma$  between the horizon and the velocity vector. The angle of attack  $\alpha$  is also indicated, being the angle between the velocity vector and the roll axis of the vehicle. Since the engine will not be symmetrical also thrust vector components perpendicular to the roll axis can be expected. This is indicated with thrust vector angle  $\sigma_T$ . The sum of the angle of attack  $\alpha$  and thrust vector angle  $\sigma_T$  are defined as thrust angle  $\sigma$ . Also the aerodynamic forces are drawn in Fig. 1: drag opposite to the velocity vector and lift perpendicular upward. Finally the vehicle is speeding up in velocity direction, indicated with acceleration  $\dot{v}$ . Accelerations perpendicular to the velocity vector are neglected. Applying the law of equilibrium of forces in speed direction and perpendicular, the following set of equations can be obtained:

$$\begin{cases} m\dot{v} = T \cos \sigma - G \sin \gamma - D \\ 0 = T \sin \sigma - G \cos \gamma + L \end{cases} \quad (1)$$

For an accelerated flight point, angle of incidence  $\gamma$  and acceleration  $\dot{v}$  are related [1]:

$$\dot{v} = v \sin \gamma \cdot \frac{dv}{dh} \quad (2)$$

Introducing a usual atmospheric model and furthermore assuming flight with a constant dynamic pressure the following expression between the angle of incidence  $\gamma$  and acceleration  $\dot{v}$  can be derived [1]:

$$\sin \gamma = \frac{2H_b \dot{v}}{v^2}, \quad (3)$$

with the parameter  $H_b = 6.338 \text{ km}$ , coming from the atmospheric model. Only small angles of incidence will be considered, allowing the approximation  $\cos \gamma \approx 1$ . Eq. (1) now becomes:

$$\begin{cases} m\dot{v} = T \cos \sigma - \frac{2H_b G \dot{v}}{v^2} - D \\ 0 = T \sin \sigma - G + L \end{cases} \quad (4)$$

This set of equations can be combined introducing  $L/D$  as one parameter:

$$\frac{T}{G} = \frac{\frac{\dot{v}}{g} \left(1 + \frac{2H_b g}{v^2}\right) + \frac{1}{L/D}}{\cos \sigma + \frac{\sin \sigma}{L/D}} \quad (5)$$

This equation already shows some of the important parameters to be discussed furtherdown.

Instead of the thrust requirement above deduced, we are interested in the fuel requirement. First a pure accelerated flight mission is considered, so accumulating speed is of only interest. A small time interval  $\Delta t = \frac{\Delta v}{\dot{v}}$  is being considered, in which acceleration  $\dot{v}$  and fuel mass flow  $\dot{m}_f = \frac{\Delta m}{\Delta t}$  are of constant value. Furthermore the change of mass  $\Delta m$  is being neglected compared to the total vehicle mass  $m$ . With these assumptions and using the definition for the specific fuel consumption,  $B_S = \frac{\dot{m}_f}{T}$ , Eq. (5) can be rewritten:

$$\frac{\Delta m_f}{m} = \frac{1 + \frac{2gH_A}{v^2} + \frac{g}{\dot{v} \cdot L/D}}{\cos \sigma + \frac{\sin \sigma}{L/D}} \cdot B_S \cdot \Delta v. \quad (6)$$

Eq. (6) shows, that the fuel requirement  $\Delta m_f$  for speeding up  $\Delta v$  depends on five parameters: velocity  $v$ , acceleration  $\dot{v}$ , lift over drag value  $L/D$ , thrust angle  $\sigma$  and the specific fuel consumption  $B_S$ . It is recognized, that typical flight mechanic and typical engine parameters have impact on the fuel requirement. Also the vehicle mass  $m$  is important. Here it always will be assumed that this mass is the same at the highest Machnumber. Minimizing the fuel consumption then leads to defining the minimum starting mass at the lowest considered Machnumber. To minimize fuel requirement it is necessary to optimize all above parameters. Therefore all parameters first are considered separately.

## 5 Flight parameters

At first the term  $G_V = 1 + \frac{2gH_A}{v^2} + \frac{g}{\dot{v} \cdot L/D}$  is considered, being a function of velocity  $v$  (Fig. 2). It is evident, that higher speeds are beneficial for fuel consumption. Acceleration  $\dot{v}$  has been varied too in this figure, showing an even stronger impact of this parameter on fuel requirement. It is advantageous to realize high acceleration, although the positive effect diminishes with increasing acceleration.

For the data (Fig. 2) the lift over drag value  $L/D$  has been kept constant at  $L/D = 4$ . However it should be recognized, that this parameter is as important as the above considered acceleration, since both quantities appear in the denominator of term  $G_V$ . Maximum values of  $L/D$  are the matter of fact of the aerodynamics of the hypersonic vehicle. The behavior of a specific configuration usually is described by aerodynamic parameters, as for instance lift coefficient  $C_L = \frac{2L}{\rho v^2 A_w}$ , which depends on Machnumber, angle of attack and Reynoldsnumber. An appropriate aerodynamic model for hypersonic vehicles as developed in [2] is used. Fig. 3 shows the lift over drag value  $L/D$  as a function of angle of attack  $\alpha$  for several Machnumbers. It is mentioned, that this aerodynamic model does not include an explicit function between the considered parameters and the Reynoldsnumber. For each Machnumber just one angle of attack can be found with lift over drag  $L/D$  being a maximum. These optimum angles of attack are plotted versus Machnumber in Fig. 4 also indicating the angle of attack variation, if lift over drag  $L/D$  differs five and ten per cent respectively. For each Machnumber, the angle of attack should be set near the plotted optimum value, to provide a high value of lift over drag  $L/D$ . The parameters determining the angle of attack are considered in the next subsection.

Eq. (6) points also to the thrust angle  $\sigma$  having an influence on the fuel requirement  $\Delta m_f$ . The term  $\cos \sigma + \frac{\sin \sigma}{L/D}$ , which has to be maximized in this context, is shown in Fig. 5 as a function of thrust angle  $\sigma$  and several values of  $L/D$ . Depending on lift over drag  $L/D$ , thrust angles  $\sigma$  up to  $20^\circ$  are of positive effect on fuel consumption. It should not be concluded from this figure, that small values of lift over drag  $L/D$  are beneficial, since this parameter also is of great but opposite importance in the term  $G_V$ .

It is reminded, that thrust angle  $\sigma$  is the sum of angle of attack  $\alpha$  and thrust vector angle  $\sigma_T$ . The last parameter is determined by the engine and will be considered in more detail in the next section. Since the angle of attack has revealed to be important for fuel requirement it will be examined more closely in the next subsection.

### 5.1 Angle of attack

In order to define the parameters influencing the angle of attack  $\alpha$ , Eq. (4) is used again, now differentiating between angle of attack  $\alpha$  and thrust vector angle  $\sigma_T$ . Fig. 6 illustrates that, for any Machnumber, the lift coefficient  $C_L$  is linearly increasing with the angle of attack  $\alpha$ :

$$C_L = C_{L_0} + C_{L_\alpha} \cdot \alpha. \quad (7)$$

Eliminating thrust  $T$  in Eq. (4) and using Eq. (7) leads to a quadratic equation:

$$\begin{aligned} & \left[ C_{L_0} \cdot \left( \frac{\cos \sigma_T}{L/D} - \sin \sigma_T \right) \right] \cdot \alpha^2 \\ & + \left[ \frac{G}{A_w} \frac{1}{q} \left( \frac{\dot{v}}{g} \cos \sigma_T \cdot \left( 1 + \frac{2gH_A}{v^2} \right) + \sin \sigma_T \right) + C_{L_0} \cdot \left( \frac{\cos \sigma_T}{L/D} - \sin \sigma_T \right) + C_{L_0} \cdot \left( \cos \sigma_T + \frac{\sin \sigma_T}{L/D} \right) \right] \cdot \alpha \\ & + \left[ \frac{G}{A_w} \frac{1}{q} \left( \frac{\dot{v}}{g} \sin \sigma_T \cdot \left( 1 + \frac{2gH_A}{v^2} \right) - \cos \sigma_T \right) + C_{L_0} \cdot \left( \cos \sigma_T + \frac{\sin \sigma_T}{L/D} \right) \right] = 0. \end{aligned} \quad (8)$$

An analysis of this equation for a fixed value of wing loading  $G/A_w$  is plotted in Fig. 7, demonstrating that the dynamic pressure has particular influence on the angle of attack. For a certain Machnumber the dynamic pressure decreases by increasing altitude. Furthermore it is obvious, that an increasing thrust vector angle  $\sigma_T$  decreases the angle of attack, verifying the influence of an engine parameter on the flight mechanics. An increasing thrust vector angle  $\sigma_T$  signifies that the thrust component perpendicular to the roll axis of the vehicle increases and therefore lift can decrease, which is again achieved by decreasing of the angle of attack (See Eq. (7)).

Higher acceleration  $\dot{v}$  leads to a smaller angle of attack as evident from Fig. 7. Increasing acceleration  $\dot{v}$  requires more thrust parallel to the velocity vector. Given a certain thrust vector angle  $\sigma_T$ , this signifies an increase of the thrust perpendicular to the velocity vector, reducing the angle of attack. This effect diminishes with decreasing thrust vector angle  $\sigma_T$ , as shown in Fig. 7. If the thrust vector angle  $\sigma_T$  gets negative and equals the angle of attack  $\alpha$ , the thrust angle  $\sigma$  will be zero and acceleration will have no effect on the angle of attack. For even smaller thrust vector angles  $\sigma_T$  the above effect becomes opposite, i.e. the angle of attack increases with increasing acceleration (not evident in Fig. 7).

It is shown, which influence on the flight mechanics can be expected from the engine specific value  $\sigma_T$ . This parameter and the specific fuel consumption  $B_S$ , having also an impact on the fuel requirement (Eq. (6)), are dealt with in the next section.

## 6 Engine specific parameters

As mentioned in the introduction the ramjet part of the mission is considered in this paper. In order to determine thrust, thrust vector angle and fuel consumption, a calculation model of a ramjet has been established (Fig. 8), which allows to calculate all thermodynamic data in characteristic cross sections.

The undisturbed flow is deflected and compressed by the front shock of the vehicle ( $\infty \rightarrow 0$ ). Ahead of the engine a boundary layer builds up, causing a displacement and a momentum loss. Total pressure loss within the diffuser ( $0 \rightarrow 1$ ) is accounted for by using a kinetic efficiency. Further pressure loss is caused by the drag of the flow around the turbo engine tube, which holds the turbo engine, and by fuel-airflow mixing ( $1 \rightarrow 2$ ). In the combustion chamber ( $2 \rightarrow 3$ ) the fuel is burnt; because of the high temperatures (up to 3000 K) dissociation occurs, which results in a loss of total enthalpy. Part of the dissociation enthalpy is regained within the convergent part of the nozzle ( $3 \rightarrow 4$ ). The critical area of the nozzle is variable and adjusted to pass the incoming massflow. Finally the flow is expanded in the divergent part of the nozzle ( $4 \rightarrow 5$ ). An asymmetrical nozzle is chosen, since it is fair to assume that the tail base of the vehicle will be used for additional expansion. In order to obtain the flow angle  $\theta_5$ , it's assumed, that a Mach line is located at the oblique nozzle exit area, which is not variable.

### 6.1 Thrust vector angle $\sigma_T$

Fig. 9 shows the thrust vector angle  $\sigma_T$  for various flight conditions, revealing that the angle first increases towards a maximum around Mach 4.5. Higher dynamic pressures only causes the level to be slightly lower and the maximum to be shifted to somewhat lower Machnumbers. For this effect it is necessary to look at the thrust components, which form the thrust vector angle:

$$\sigma_T = \arctan \frac{T_y}{T_x}, \quad (9)$$

with the  $x$ -axis being parallel and the  $y$ -axis being perpendicular to the roll axis. The thrust components again are built up by the diffuser inlet and nozzle outlet forces, which are plotted in



Fig. 10: in  $x$ -direction the nozzle force  $T_4$  increases with Machnumber, but the diffussor drag  $T_3$  increases even more. The difference is the net thrust  $T_x$  parallel to the roll axis of the vehicle. The diffussor also causes a lift  $T_1$  because of the outer compression shocks. In Fig. 10, 11 and 13  $T_1$  is arbitrarily set negative to illustrate the difference of the  $y$ -forces at engine in- and outlet. This lift gradually decreases with increasing Machnumber but constant dynamic pressure. The shown behavior of thrust vector angle  $\sigma_T$  is mainly determined by the nozzle outlet force perpendicular to the roll axis  $T_2$ . The particular behavior of the curve is due to the two parts of this force: first the momentum  $\dot{m} \cdot v_5 \cdot \sin \theta_5$ , in which nozzle exit flow angle  $\theta_5$  increases with increasing Machnumber; secondly the pressure force  $(p_5 - p_\infty) \cdot A_5 \cdot \cos \delta$ . The pressure force is about zero at Mach 3, but produces a lift at higher speeds, which is increasingly counteracted by the impuls force. This explains the decrease for higher Machnumbers of thrust vector angle  $\sigma_T$  in Fig. 9. For Machnumbers below 3 the nozzle is over expanded. This results in a negative lift with the thrust vector angle  $\sigma_T$  getting negative. It is added, that above effect would diminish, if the effective nozzle exit area is reduced for Machnumbers below 3.

Thrust vector angle  $\sigma_T$  is furthermore affected by the angle of attack (Figs. 11 and 12). The angle of attack is varied for a fixed flight condition: an increasing angle of attack causes a stronger compression at the front shock of the vehicle, resulting in an increasing mass flow into the engine and therefore increasing thrust. Also lift  $T_1$  is increased at the diffussor, because of the increased massflow. Because of the increased massflow the critical area of the nozzle has to be enlarged reducing the expansion ratio. Nozzle exit speed  $v_5$  and flow angle  $\theta_5$  decrease, but nozzle pressure  $p_5$  increases; the overall effects are plotted in Figs. 11 and 12: an increase of the angle of attack results in an increase of the thrust vector angle.

Another parameter influencing the thrust vector angle is the fuel equivalence ratio or the reciprocal oxidation ratio  $\lambda$ . The relevant results are plotted in Figs. 13 and 14, again for a fixed flight condition. The oxidation ratio has no impact on the incoming forces, identified as horizontal lines (1,3) in Fig. 13. Decreasing the fuel flow results of course in a decreasing thrust and the lift at the nozzle also decreases, but thrust vector angle  $\sigma_T$  is not much affected, although velocity  $v_5$  decreases. The reason is that, the critical area of the nozzle has to be reduced leading to an increased expansion and resulting in a lower nozzle pressure  $p_5$ , which predominantly causes the drop in nozzle lift  $T_2$ .

## 6.2 Specific fuel consumption

The specific fuel consumption is always particularly emphasized, because it directly affects fuel requirement (Eq. (6)). The effect of leading parameters on specific fuel consumption is examined in the following.

Fig. 15 shows the specific fuel consumption as a function of Machnumber for various dynamic pressures and oxidation ratios. The specific fuel consumption rapidly increases with speed and oxidation ratio, but is about independent of the dynamic pressure and altitude, especially for smaller Machnumbers. Fig. 16 illustrates, that the specific fuel consumption decreases little with increasing angle of attack and confirms its independence of altitude. A useful approach for trajectory optimization is drawn sofar from the figure, that the specific fuel consumption of the ramjet considered changes little with changing altitude or angle of attack, both parameters being important for maximizing the lift over drag value  $L/D$ .

Fig. 15 already revealed the strong influence of the oxidation ratio  $\lambda$  on the specific fuel consumption. For several fixed flight conditions this has been plotted in Fig. 17, showing, that for Machnumbers above 3 an optimum oxidation ratio  $\lambda$  exists, for which the specific fuel consumption has a minimum value. This optimum oxidation ratio, which is independent of the dynamic pressure, increases with Machnumber and is indicated in Fig. 18. It also identifies the allowable range for the oxidation ratio, if a ten per cent deviation from the minimum specific fuel consumption is acceptable (Fig. 17). This range decreases for speeds below Mach 4, as does the optimum oxidation ratio, which is in contradiction with Fig. 17. It is reminded, that for these Machnumbers negative thrust vector angles  $\sigma_T$  occur if the fuel flow decreases. The reasons for the combined effect on thrust vector angle  $\sigma_T$  of low Machnumber (Fig. 9) and high oxidation ratio (Fig. 14) have both seperately been explained above. Since a negative thrust vector angle is undesired from the point of view of fuel requirement optimization (Eq. (6)) only the thrust component parallel to the roll axis was considered, when drawing Fig. 18.

## 7 Optimal acceleration trajectories

Eq. (6) is used for finding optimum acceleration trajectories. To optimize the engine specific parameters it's sufficient to choose the oxidation ratio  $\lambda$  according to Fig. 18. Prescribing the oxidation ratio determines the engine size required for a fixed flight Machnumber. The combustion chamber inlet area (index '2' in Fig. 8) is chosen as the reference area of the engine. Varying the flight Machnumbers reveals a curve of required engine sizes, which can be used to design the final engine size. Selecting, for instance, the largest required engine size for design, means that the oxidation ratio must be increased for all off-design flight points (less fuel is needed to obtain the required thrust). In order to be sure to improve specific fuel consumption for the flight conditions under consideration the lower curve of prescribed oxidation ratios in Fig. 18 has been chosen for the calculation.

The specific fuel consumption can roughly be treated as being independent of the altitude and the angle of attack. The angle of attack however is quite important for a maximum lift over drag ratio  $L/D$  and should be set near its optimum value, which might be done by choosing the adequate altitude, taking in account all governing parameters, as acceleration, thrust vector angle and wing loading.

Fig. 19 shows the resulting acceleration fuel consumption  $\Delta m_f / \Delta v$  for two different accelerations, which have been kept constant for all flight points. As could be expected an increased acceleration is advantageous for the fuel requirement. (Compare Tab. 1, listing the total fuel consumption for the whole trajectory). The wing loading  $G/A_w$  was varied, having little effect on the accelerating fuel consumption, but having strong effect on the flight altitude as shown in Fig. 20. Obtaining optimum angle of attack with lower wing loadings necessarily leads to lower dynamic pressures (term  $\frac{G}{A_w} \frac{1}{q}$ , in Eq. (8)), which means high flight altitude. This also affects the required engine size, as evident in Fig. 21. Doupling the wing loading causes smaller engine sizes, even with acceleration  $\dot{v}$  doubled, demonstrating the tremendous impact of a typical structure parameter of the flight vehicle on the ramjet design size.

## 8 Accelerated flight with included cruise flight

The vehicle under consideration in this section is to start from Europe, because separation of the upper stage will occur near the equator a cruise flight has to be included into the mission. If a certain distance is to be flown, the acceleration determines the cruise flight distance (see Fig. 22), which already implies another point of view of the fuel requirement being the distance fuel requirement  $\Delta m / \Delta x$ , instead of the acceleration fuel requirement  $\Delta m / \Delta v$ . The latter becomes infinite in cruise flight ( $1/\dot{v}$  in Eq. (6)). The relevant modification of Eq. (6) results in:

$$\frac{\Delta m_f}{m} = \frac{\dot{v} \cdot \left(1 + \frac{2gH_h}{v^2} - \frac{qH_h}{qv} \frac{dq}{dv}\right) + \frac{q}{L/D}}{\cos \sigma + \frac{\sin \sigma}{L/D}} \cdot \frac{B_s}{v} \cdot \Delta x. \quad (10)$$

This equation shows, that a low value for acceleration  $\dot{v}$  is beneficial for fuel requirement, if cruise is included, since acceleration  $\dot{v}$  now appears in the numerator. All other parameters must be optimized as discussed before.

Except during cruise flight the acceleration is kept constant for all flight points. The flight distance needed for vehicle acceleration increases with decreasing acceleration  $\dot{v}$  (Fig. 22). The overall flight distance determines the minimum value for acceleration  $\dot{v}$ . Any higher value requires cruise operation. The cruise distance increases with increasing acceleration (Fig. 22).

Eq. (10) can be used for finding the optimum cruise flight point (minimum distance fuel requirement  $\Delta m / \Delta x$ ) by setting acceleration  $\dot{v}$  equal zero and varying flight speed and altitude. For each altitude, an optimum cruise flight point can be found at Mach 4.25 [1], which is chosen for the here considered acceleration mission with included cruise flight. Fig. 23 illustrates the reduced total fuel consumption for decreased acceleration  $\dot{v}$ . Also the total flight time will be shortened, if a smaller acceleration is chosen. It can be concluded, that for missions starting at Europe a small acceleration will be preferable, if minimized fuel consumption is required. Furthermore it is reminded, that speeding up with a smaller acceleration leads to smaller required engine sizes (Fig. 21). Reducing the engine size reduces the structural weight and therefore increases the payload.

## 9 Summary

The parameters, having impact on fuel requirement of vehicles using a ramjet, have been deduced and discussed. It has been shown, that lift over drag  $L/D$  always should be maximized. To achieve this, a discrete angle of attack has to be flown at particular flight Machnumber. This can be done by choosing the appropriate altitude, which depends mainly on the wing loading. Also the acceleration and the thrust vector angle have an influence on the angle of attack, which have to be taken in account. For each flight Machnumber an optimum oxidation ratio can be pointed out, for which the specific fuel consumption is minimal. When designing a ramjet, the engine size should be chosen such, that the needed oxidation ratio is near the optimum oxidation ratio during the most time of the mission.

The angle of attack and the thrust vector angle have an impact on fuel requirement. Positive thrust angles up to  $20^\circ$  are beneficial. For speeds above Mach 3 such angles can be realised.

The best choice for the acceleration for speeding up depends on the kind of mission. A purely accelerated flight mission requires large values for acceleration. In case of an included cruise flight, it's better to speed up with low acceleration, which also leads to smaller required engine sizes. Also the size of the ramjet engine is closely related to the wing loading.

## References

- [1] Kremer F.G.J.: *Einfache Bahnoptimierungsbetrachtungen für Reise- und beschleunigte Flugpunkte mit Staustrahltriebwerke.*  
Internal paper IB 325-03-90, DLR Cologne, February 1990.
- [2] Kremer F.G.J.: *Flugleistungsrechnungen für Staustrahlantriebe von Raumtransporter vom Typ "Sänger".*  
Diplomarbeit, RWTH Aachen, July 1988.
- [3] Dusa D.J.: *Exhaust nozzle system design considerations for turboramjet propulsion systems.*  
9th ISABE, Athens, september 1989.
- [4] Lehrach R.P.C.: *Thrust/Drag accounting for aerospace plane vehicles.*  
AIAA-87-1966, San Diego, June 1987.
- [5] Schöttle, Grallert, Hewitt: *Advanced air-breathing propulsion concepts for winged launch vehicles.*  
IAF-88-248, Bangalore, October 1988.

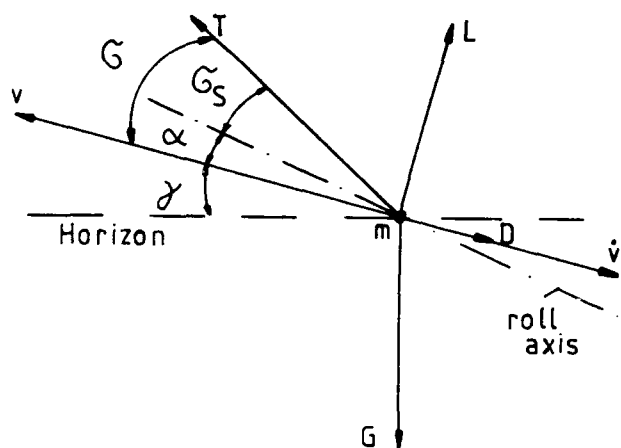


Figure 1: Force distribution for accelerated flight point.

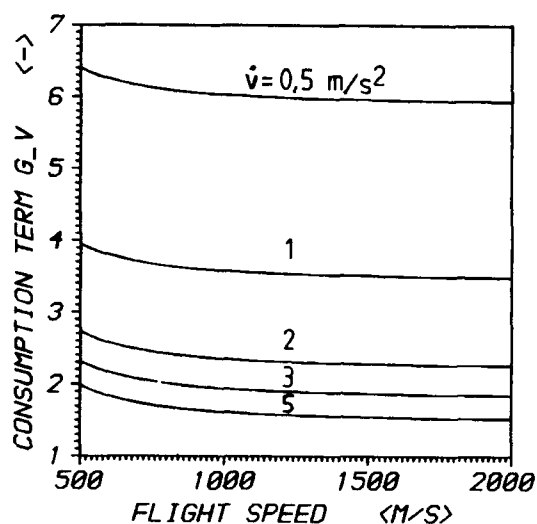


Figure 2: Influence of velocity  $v$  and acceleration  $\dot{v}$  on term  $G_v$ , for  $L/D = 4.0$ .

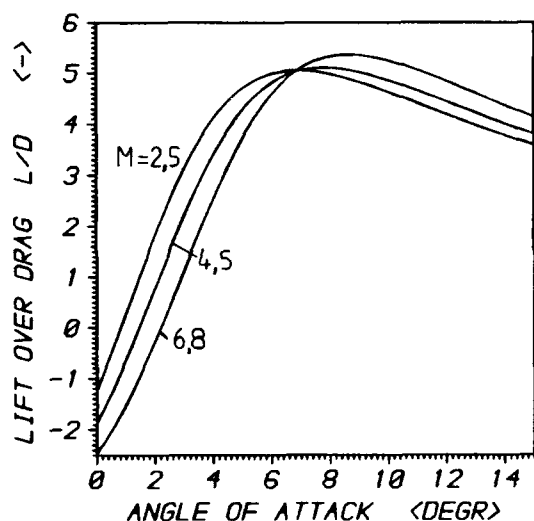


Figure 3: Lift over drag  $L/D$  as a function of angle of attack  $\alpha$  and variation of Mach-number.

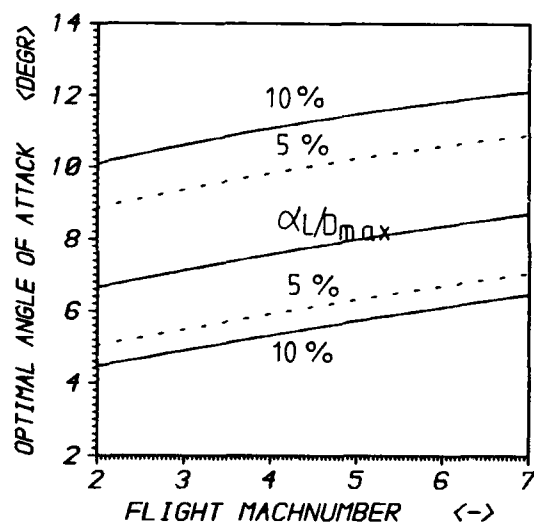


Figure 4: Optimum angle of attack and angle of attack for 5 % and 10 % deviation of maximum  $L/D$  as a function the Machnumber.

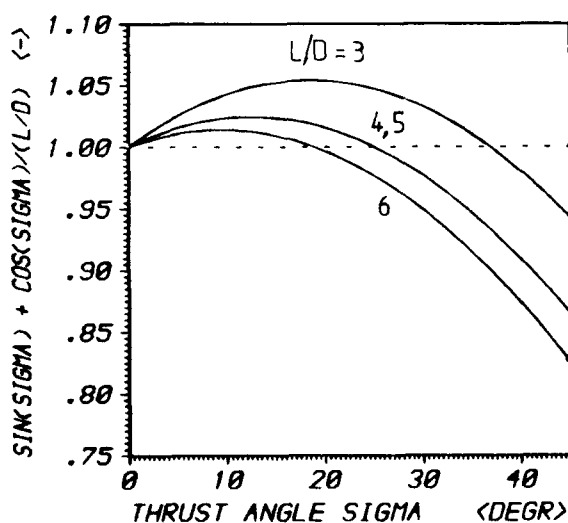


Figure 5:  $\cos \sigma + \frac{\sin \sigma}{L/D}$  as a function of thrust angle  $\sigma$  and various values of lift over drag.

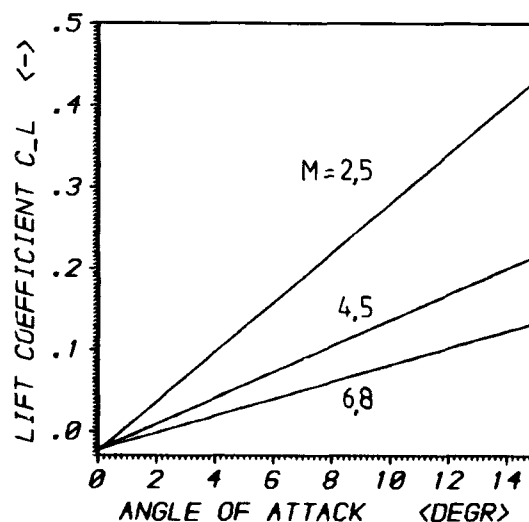


Figure 6: Lift coefficient as a function of angle of attack and variation of Machnumber.

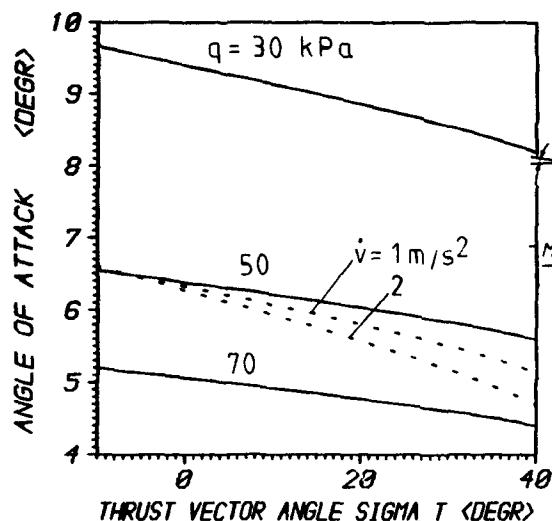


Figure 7: Angle of attack as a function of thrust vector angle  $\sigma_T$  and variation of dynamic pressure and acceleration.

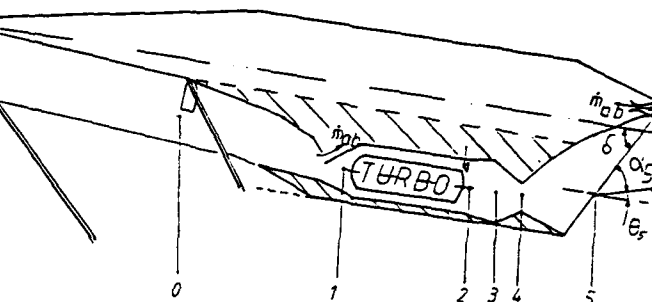


Figure 8: Model used for ramjet.

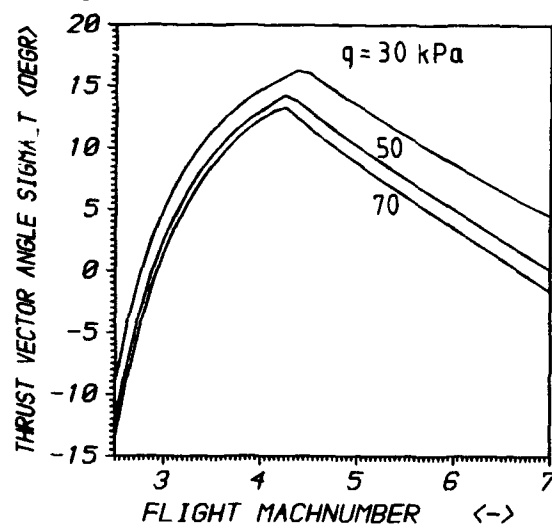


Figure 9: Thrust vector angle  $\sigma_T$  for various dynamic pressures ( $\lambda = 1$ ).

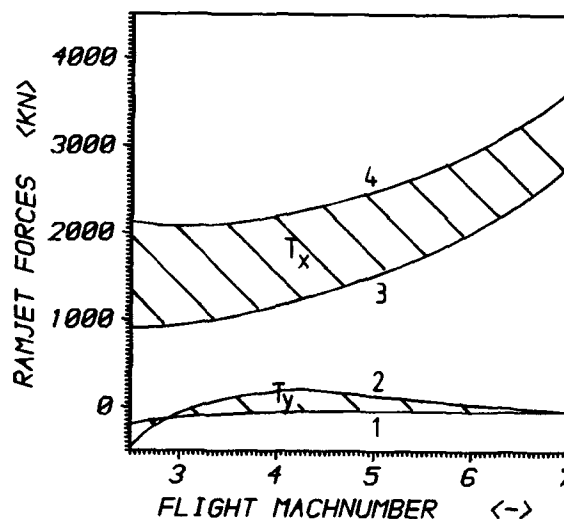


Figure 10: Forces at diffuser inlet (1,3) and nozzle outlet (2,4) of the ramjet for  $q = 50$  kPa and  $\lambda = 1$ .

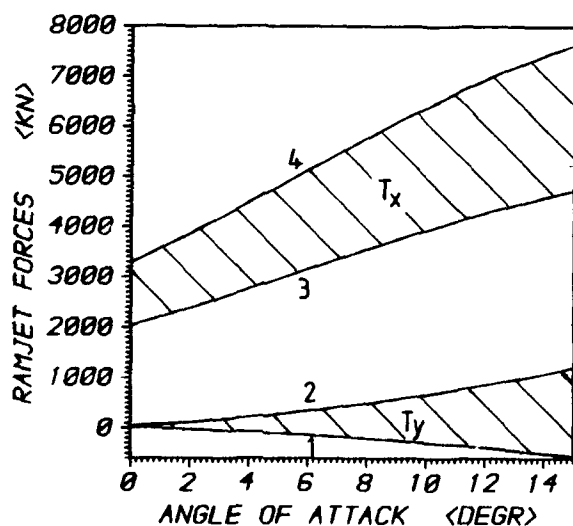


Figure 11: Forces at diffuser inlet (1,3) and nozzle outlet (2,4) of the ramjet as a function of angle of attack for  $M = 5$ ,  $q = 50$  kPa and  $\lambda = 1$ .

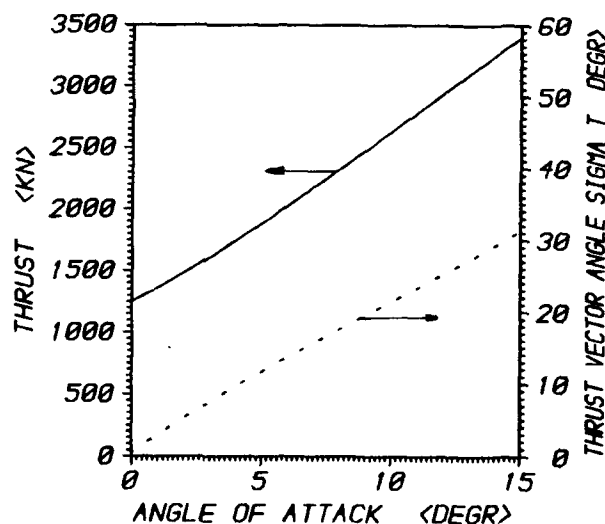
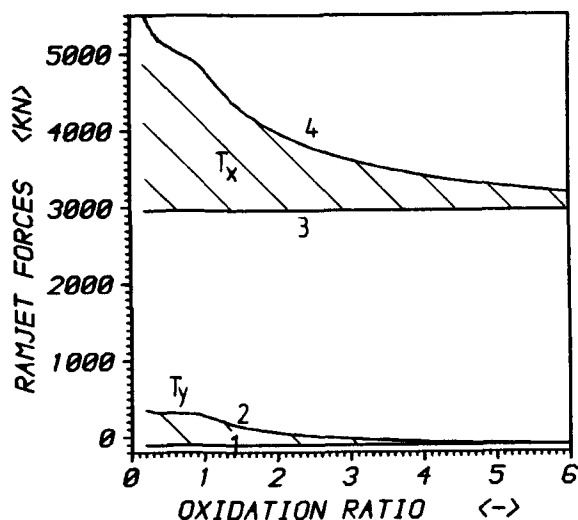
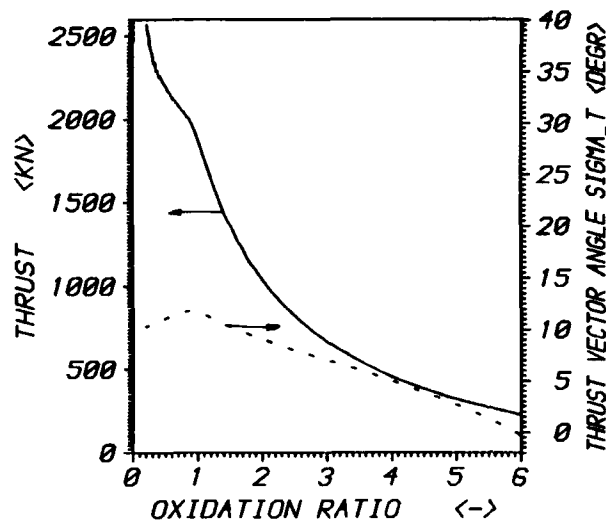


Figure 12: Thrust  $T$  and thrust vector angle  $\sigma_T$  of the ramjet as a function of angle of attack  $\alpha$  for  $M = 5$ ,  $q = 50$  kPa and  $\lambda = 1$ .



**Figure 13:** Forces at diffuser inlet (1,3) and nozzle outlet (2,4) of the ramjet as a function of oxidation ratio for  $M = 5$ ,  $q = 50$  kPa and  $\alpha = 5^\circ$ .



**Figure 14:** Thrust  $T$  and thrust vector angle  $\sigma_T$  of the ramjet as a function of oxidation ratio  $\lambda$  for  $M = 5$ ,  $q = 50$  kPa and  $\alpha = 5^\circ$ .

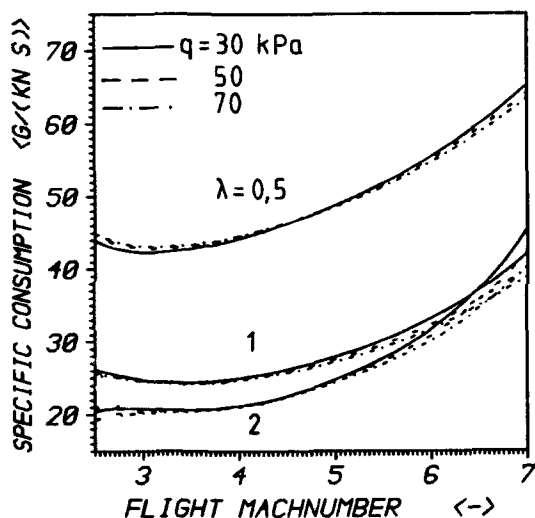


**Figure 15:** Specific fuel consumption  $B_s$  for various dynamic pressures and oxidation ratios.

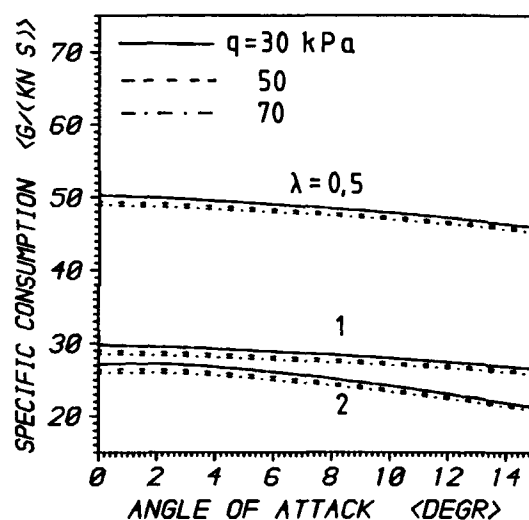


**Figure 16:** Specific fuel consumption  $B_s$  as a function of angle of attack  $\alpha$  for  $M = 5$ ,  $q = 50$  kPa and  $\lambda = 1$ .

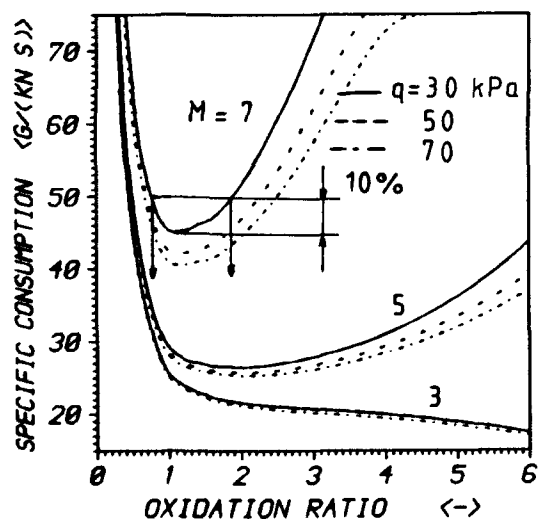


**Figure 17:** Specific fuel consumption  $B_s$  as a function of oxidation ratio  $\lambda$  for  $\alpha = 5^\circ$  and various Machnumbers and various dynamic pressures.

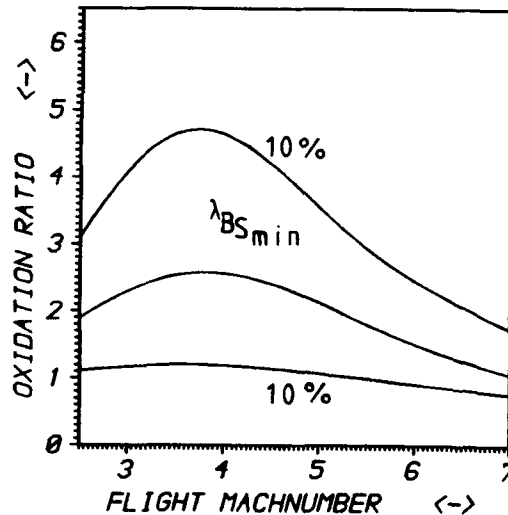


**Figure 18:** Optimum oxidation ratio  $\lambda_{BSmin}$  as a function of Machnumber and the range for 10% deviation of minimum specific fuel consumption  $B_s$ .

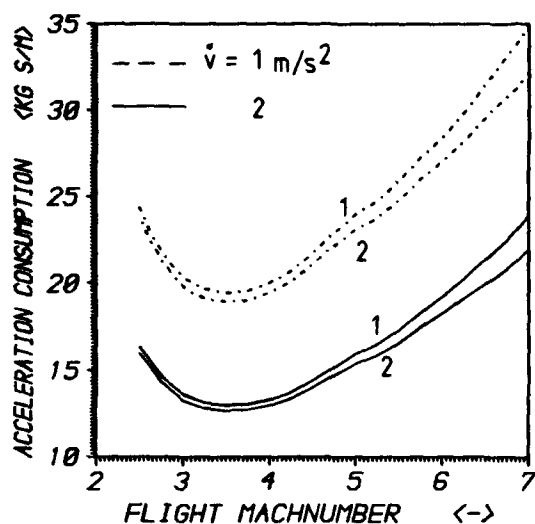


**Figure 19:** Fuel requirement  $\Delta m_f$  for speeding up  $\Delta v$  for optimum acceleration trajectories for wing loading  $\frac{G}{A_w} = 2$  (1) and  $4 \text{ kN/m}^2$  (2) and various accelerations.

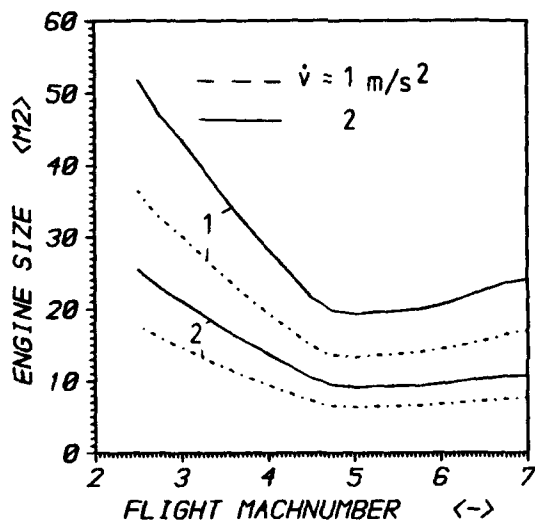


**Figure 21:** Required engine size as function of Machnumber for optimum acceleration trajectories for wing loading  $\frac{G}{A_w} = 2$  (1) and  $4 \text{ kN/m}^2$  (2) and various accelerations.

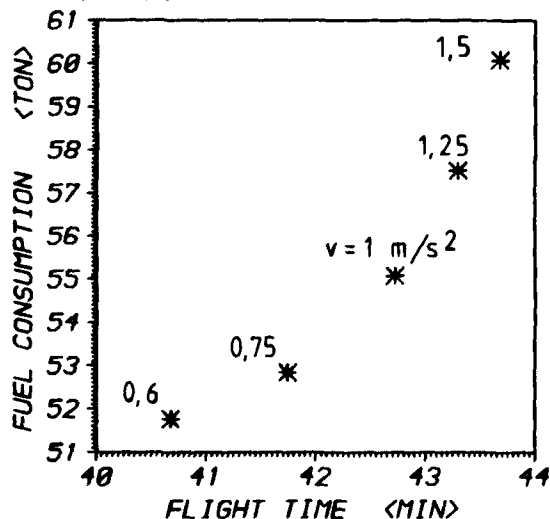


**Figure 23:** Fuel consumption as a function of overall flight time for different accelerations and for wing loading  $G/A_w = 2 \text{ kN/m}^2$ .

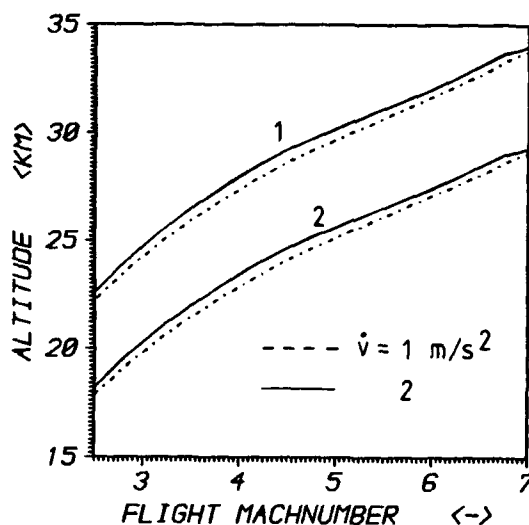


**Figure 20:** Flight altitude profiles for optimum acceleration trajectories for wing loading  $\frac{G}{A_w} = 2$  (1) and  $4 \text{ kN/m}^2$  (2) and various accelerations.

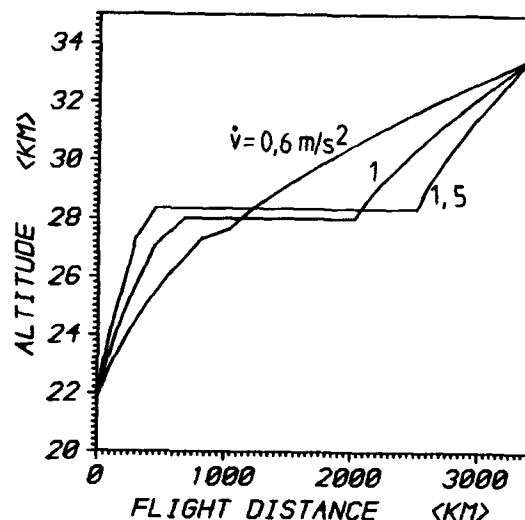


**Figure 22:** Flight paths with same starting and ending point, but different accelerations during climbing phase.

$\frac{G}{A_w}$	$\dot{v}$	distance	fuel
$\text{kN/m}^2$	$\text{m/s}^2$	km	consumption
2	1	2025	34.5
2	2	1015	23.2
4	1	1950	32.2
4	2	976	21.6

**Table 1:** Flight distance and fuel consumption for purely accelerated flight from Machnumber 2.5 till 7.

## Discussion

TOWNEND L. H.

Your paper is largely concerned with Mach numbers above 2.5 . Have you applied optimisation to lower flightspeeds, in particular to the problem of transonic acceleration? (Which strongly influences the size of the propulsion installation, and is strongly influenced by transonic base drag).

### AUTHOR'S REPLY

This paper only deals with that part of the trajectory, where the ramjet is in use. However the deducted equation (Eq.6) also can be used for lower flight speeds. Here a turbo engine will be in use.

To be able to say something about the optimal flight trajectory in this speed range a closer examination of the turbo engine is required, simular as has been done for the ramjet.

Furthermore an aerodynamic model of the vehicle has to be defined for the low and transonic speeds.

The aerodynamic model used in this paper is only valid for high speeds.

### WINTERFELD

COMMENT : We made a thesis last year in which we adressed the optimisation of the size of the low Mach number turbojet. One of the results is that there is a coupling between the size of the turbojet engine and its afterburner and the ramjet's size. The two optimisation processes should be coupled.



# ETUDE COMPARATIVE DE DIFFERENTS SYSTEMES DE PROPULSION COMBINEE

Philippe RAMETTE, HYPERSPACE (France)  
Dominique SCHERRER, ONERA (France)  
Michel DOUBLIER, SNECMA (France)

SEP  
24, rue Salomon de Rothschild  
92150 SURESNES  
FRANCE

## RESUME

Depuis 1986, le CNES soutient des études comparatives de différents concepts de moteurs combinés effectuées conjointement par la SNECMA, la SEP et l'ONERA. La SNECMA et la SEP viennent de rassembler leurs efforts en propulsion combinée en créant un Groupement d'Intérêt Economique commun appelé HYPERSPACE. L'avancement des études de comparaison des différents cycles de moteurs combinés est présenté en se concentrant sur les concepts suivants :

- la famille des turbofusées comprenant le turbofusée-stato et le turboexpander-stato ;
- la famille des turboréacteurs avec la turbosoufflante-stato et le turbo-stato ;
- le fusée-stato ;
- la fusée à air liquéfié ;
- la fusée à air refroidi (étude en cours) ;
- et le statoréacteur à combustion supersonique qui est également en cours d'examen.

La comparaison de ces concepts inclut leurs performances théoriques, des considérations de dimensionnement et une évaluation approximative des problèmes technologiques associés à chaque concept.

# COMPARATIVE STUDY OF DIFFERENT SYSTEMS OF COMBINED CYCLE PROPULSION

## ABSTRACT

Since 1986 the French Space Agency CNES is sponsoring some comparative studies of different concepts of combine cycle engines made jointly by SNECMA, SEP and ONERA. SNECMA and SEP recently joined their efforts in combined cycle propulsion by creating a common Joint Venture ("Groupement d'Intérêt Economique") named HYPERSPACE. The recent progress of comparative studies of different combined cycle engine systems is presented focusing on the following concepts :

- the turborocket family including the turbo rocket-ramjet and the turbo expander-ramjet ;
- the turbojet family with the turbofan-ramjet and the turbo-ramjet ;
- the rocket-ramjet ;
- the liquefied air rocket ;
- the cooled air rocket (study in progress) ;
- and the scramjet (supersonic combustion ramjet) which is also presently in progress.

The comparison of these concepts includes their theoretical performances, some design considerations and an approximate evaluation of the technological difficulties associated with each concept.

## **I. INTRODUCTION**

Au début du 21ème siècle, une nouvelle famille de lanceurs à décollage et atterrissage horizontal avec une propulsion combinée commencera à devenir opérationnelle.

De tels lanceurs devraient conduire à une réduction des coûts de lancement et à des améliorations importantes en souplesse et en flexibilité d'emploi par rapport aux lanceurs classiques à décollage vertical et à propulsion fusée.

L'optimisation de ces lanceurs du futur dépend en grande partie du concept de propulsion combinée sélectionné aussi bien pour un lanceur monoétage que pour un lanceur biétage. La sélection des concepts de propulsion combinée est donc fondamentale pour le succès de ces nouveaux lanceurs futurs.

L'objectif de l'étude présentée est de comparer certains des concepts de propulsion combinée qui peuvent être envisagés pour de tels lanceurs.

## **2. ANALYSE DE DIFFERENTS CONCEPTS DE PROPULSION COMBINEE**

### **2.1. Turbofusée-Stato**

Le principe schématique de fonctionnement de ce concept est représenté sur la Fig.1 ; la combustion d'un mélange hydrogène-oxygène dans une chambre de type fusée produit des gaz d'échappement qui entraînent la turbine entraînant le compresseur ; l'écoulement qui traverse la turbine est riche en hydrogène, ce qui permet une combustion complémentaire dans la chambre principale du moteur suivant un mode de type statoréacteur.

A partir d'un nombre de Mach de vol de l'ordre de 3, le compresseur ne présente qu'un faible taux de compression et est pratiquement en autorotation. Le fonctionnement du Turbofusée-Stato est limité, comme tous les concepts de type Turbofusée, à un nombre de Mach de vol de l'ordre de 6 à cause des températures élevées au niveau des aubes du compresseur tout en supposant l'utilisation de matériaux composites thermostrostructuraux comme le carbone-carbure de silicium pour les aubes.

Les paramètres suivants ont été choisis, dans les conditions sol :

rapport de pression : 3.75  
 rapport de mélange : 0.75  
 (oxygène/hydrogène)

La détermination des performances théoriques du Turbofusée-Stato conduit à des impulsions spécifiques qui sont représentées sur la Figure 2. Les performances du Turbo-Fusée-Stato présentent l'avantage d'une impulsion spécifique assez élevée (entre 2000s et 2500s) sur une plage importante en nombre de Mach de vol (jusqu'à  $M = 6$ ) ; cette impulsion spécifique est néanmoins plus faible que pour d'autres concepts de moteurs combinés qui sont présentés plus loin.

Un dimensionnement de ce type de concept a été effectué et conduit à l'architecture qui est présentée en Figure 3. Les hypothèses prises au niveau des matériaux supposent que les matériaux composites thermostrostructuraux et en particulier les composites à matrice céramique soient largement utilisés.

La figure 4 montre à titre indicatif l'ensemble des pièces d'un Turbofusée-Stato qui pourraient être réalisées en matériau composite à matrice céramique.

De tels matériaux permettront une augmentation sensible des températures de fonctionnement à l'intérieur du moteur et une réduction de masse importante par rapport à des matériaux métalliques.

## 2.2. Turboexpander-Stato

Le schéma de fonctionnement du Turboexpander-Stato est présenté sur la Figure 5. L'hydrogène est d'abord utilisé pour refroidir les parois de la chambre suivant un mode régénératif, ce qui le réchauffe suffisamment pour que sa détente ultérieure permette d'entraîner la turbine entraînant le compresseur sans introduction d'oxygène.

De même que dans le cas du Turbofusée-Stato, le fonctionnement aérobie du Turboexpander-Stato est possible jusqu'à un nombre de Mach de vol de l'ordre de 6 à condition que des matériaux composites thermostrostructuraux soient utilisés pour les aubes de compresseur.

Un rapport de pression du compresseur de 3 a été choisi (dans les conditions sol). Les impulsions spécifiques calculées sont présentées sur la Figure 6. Ces impulsions spécifiques sont très élevées (entre 3500s et 4500s) sur une large plage en nombre de Mach de vol (jusqu'à Mach 6). Par rapport au Turbofusée-Stato, les impulsions spécifiques du Turboexpander-Stato sont largement supérieures de 1500s à 2000s. L'inconvénient du Turboexpander-Stato porte sur la masse et la complexité technologique du système de refroidissement régénératif par l'hydrogène. Un dimensionnement du Turboexpander-Stato a été effectué et conduit à une architecture qui est représentée sur la Figure 7 en supposant un emploi très fréquent des matériaux composites thermostrostructuraux.

Ses performances très élevées en impulsion spécifique font du Turboexpander-Stato un bon candidat parmi les différents concepts de propulsion combinée envisageables pour des lanceurs spatiaux, en particulier pour un premier étage d'un lanceur bi-étage.

Les difficultés technologiques associées au Turboexpander-Stato portent en particulier sur l'échangeur qui permet à l'hydrogène de refroidir la veine stato (masse, fiabilité, etc) et sur l'introduction large des matériaux composites à matrice céramique pour les différentes pièces du moteur en contact avec le flux d'air chaud (aubes de compresseur, chambre, tuyère, etc).

## 2.3. Turbosoufflante-Stato

La Turbosoufflante-Stato est un turboréacteur double flux avec réchauffe pour lequel le turboréacteur est en autorotation aux grands nombres de Mach de vol, ce qui correspond alors à un mode de propulsion du type statoréacteur.

En mode turbo, le nombre de Mach de vol maximum est d'environ 4,5 et est limité par la température au niveau de la turbine qui est alors voisine de 2000K.

En mode stato, le nombre de Mach de vol maximum est d'environ 6 et cette limitation provient de la température perçue par les aubes du compresseur, de manière similaire aux concepts du type turbofusée-stato présentés ci-dessus.

Les niveaux de performance en impulsion spécifique calculés pour la turbosoufflante-stato sont présentés sur la Figure 8. L'impulsion spécifique est très élevée (entre 4000s et 4500s) en mode turbo jusqu'à Mach 4,5 environ ; elle est moins forte en mode stato pour un Mach compris entre 4,5 et 6 (de l'ordre de 3000s).

Une architecture schématique de turbosoufflante-stato est présentée sur la Figure 9. Un inconvénient de la turbosoufflante-stato est son poids qui est assez important. Le poids d'un tel moteur pourrait être de l'ordre de 3,4 tonnes pour une poussée au sol de 400 kN, en supposant qu'une partie des composants du moteur soit réalisée en matériaux composites à matrice céramique (les aubes de compresseur en particulier).

La turbosoufflante-stato est un candidat intéressant pour la propulsion d'un premier étage de lanceur bi-étage à cause de son impulsion spécifique élevée, mais ne conviendrait pas a priori à la propulsion d'un lanceur mono-étage à cause des problèmes de masse qui sont dûs en grande partie au turboréacteur.

## 2.4. Turbo-stato

Contrairement à la turbosoufflante-stato pour lequel le turbo est double flux, le concept turbo-stato suppose que le turboréacteur est monoflux. Suivant que le statoréacteur est disposé derrière le turboréacteur, autour ou en veine parallèle, le turbo-stato est alors intégré, coaxial ou parallèle.

L'étude des différentes variantes du turbo-stato est actuellement en cours ; elle devrait conduire à des performances comparables à celles de la turbosoufflante stato et faire l'objet d'une présentation ultérieure.

## 2.5. Fusée-Stato

Dans un fusée-stato, la fusée est disposée à l'entrée du foyer du statoréacteur et fonctionne en mélange riche, permettant ainsi une combustion avec l'air sans injection supplémentaire de combustible dans la veine stato. Afin de réduire les longueurs de mélange et de combustion, l'ensemble fusée est souvent constitué de plusieurs mini-moteurs fusées appelés éjecteurs (d'où l'appellation de stato à éjecteurs). En sortie du foyer stato, le mélange est subsonique et est ensuite accéléré dans une tuyère convergente-divergente. La Figure 10 présente un schéma de fonctionnement du fusée-stato. L'entrée d'air est à géométrie variable pour les rampes de compression et le diffuseur, ce qui permet une meilleure adaptation aux nombres de Mach de vol. La tuyère est bidimensionnelle (dans la 1ère version étudiée), à détente/déflexion (autoadaptable) et elle comporte un col variable.

Au décollage, l'essentiel de la poussée est assuré par les éjecteur. Un faible complément de poussée est apporté par l'effet d'aspiration provoqué par le mélange de l'air et des jets des éjecteurs (effet trompe). A partir de Mach 0,4 environ, l'effet trompe est remplacé par un classique effet stato qui assure un complément de poussée et donc un gain d'impulsion spécifique par rapport aux éjecteurs seuls. Quand la poussée du statoréacteur seul devient suffisante pour assurer la propulsion du véhicule (vers Mach 2,5 environ), les éjecteurs sont éteints et le moteur passe en mode stato, l'injection de combustible (l'hydrogène pour un lanceur spatial) étant alors effectuée soit par l'intermédiaire des éjecteurs, soit par des injecteurs indépendants.

Une configuration bidimensionnelle du fusée-stato a été étudiée avec une poussée au sol de 600 kN et une poussée minimum du stato de 400 kN. La chambre stato est dimensionnée avec une section de 3 m<sup>2</sup> (rectangulaire) avec 15 éjecteurs à l'intérieur (3 couches de 5 éjecteurs).

L'architecture de ce moteur conduit à une masse (hors prise d'air) de 3,65 tonnes.

La Figure 11 présente les performances en impulsion spécifique qui ont été calculées pour la configuration de fusée-stato étudiée. Les performances sont données jusqu'à Mach 4 en "mode éjecteur" (éjecteurs allumés) et à partir de Mach 2 en mode stato (éjecteurs éteints). Le Mach d'extinction des éjecteurs est à optimiser en fonction du véhicule, typiquement autour de 2,5.

Les calculs de trajectoire actuellement en cours montrent qu'il y a intérêt à diminuer les sections d'entrée d'air et de chambre stato afin de réduire la masse du moteur et la traînée induite sur le véhicule (au détriment de la poussée). Par ailleurs une architecture axysymétrique permettrait également de réduire la masse. Un nouveau dimensionnement dans une configuration axysymétrique est actuellement à l'étude.

Si la combustion du statoréacteur d'une fusée-stato reste subsonique, l'impulsion spécifique du moteur baisse très rapidement entre Mach 6 et Mach 8 ; Mach 8 semble être une limite au nombre de Mach de vol admissible dans le cas d'un statoréacteur à combustion subsonique. Au delà, les éjecteurs peuvent être à nouveau allumés pour permettre à un lanceur monoétage de quitter l'atmosphère pour se mettre en orbite (configuration du type fusée-stato-fusée).

Si le statoréacteur est conçu pour fonctionner à la fois en combustion subsonique et supersonique grâce à des géométries variables appropriées, le fonctionnement aérobie du fusée-stato peut alors être considérablement étendu jusqu'à des nombres de Mach de vol de l'ordre de 15 à 18.

Un avantage important du concept fusée-stato concerne son aptitude à transiter vers une combustion supersonique pour le stato qui améliore alors considérablement les performances potentielles au delà de Mach 6 et élargit donc la nature des missions envisageables avec des concepts de propulsion combinée du type fusée-stato.

## **2.6. Fusée à air liquéfié**

Le schéma de fonctionnement de la fusée à air liquéfié est représenté sur la Figure 12. L'air traverse un refroidisseur puis un liquéfacteur pour lequel le fluide réfrigérant est de l'hydrogène qui est ainsi réchauffé avant d'être introduit dans la chambre qui est du type fusée.

Un mélange d'hydrogène, d'oxygène et d'air liquéfié brûle dans la chambre de combustion. Par rapport à un moteur fusée, une partie de l'oxygène est ainsi remplacée par de l'air liquéfié, ce qui améliore sensiblement l'impulsion spécifique.

L'impulsion spécifique calculée pour une fusée à air liquéfié correspond à la Figure 13 dans le cas du cycle de base décrit ci-dessus. Les différentes courbes correspondent à la taille des échangeurs de chaleur par rapport à un cas de référence avec des échangeurs dimensionnés pour un nombre de Mach de vol de 4,5. Les courbes d'impulsion spécifique montrent qu'entre Mach 1 et Mach 4,5 l'impulsion spécifique est supérieure d'environ 50 % par rapport à celle d'un moteur fusée (600s au lieu de 450s) et qu'à un nombre de Mach plus élevé le gain en impulsion spécifique diminue jusqu'à s'annuler pour un nombre de Mach de vol d'environ 10.

Des améliorations du cycle de base pour la fusée à air liquéfié sont possibles par exemple en injectant de l'oxygène liquide dans l'écoulement d'air pour le refroidir ou en utilisant de l'hydrogène sous forme de boues (mélange liquide-solide ou "slush") dans des réservoirs (à une température de 14K).

Ces deux exemples devraient améliorer l'impulsion spécifique d'environ 80s et 50s respectivement. D'autres variantes du cycle du type fusée à air liquéfié sont possibles, en particulier avec une recirculation de l'hydrogène ou de l'oxygène vers les réservoirs (avec la possibilité d'utiliser des carburants "slush") ou en introduisant un compresseur d'air intermédiaire entre le refroidisseur et le liquéfacteur.

La principale difficulté technologique de la fusée à air liquéfié réside dans les échangeurs (refroidisseur et liquéfacteur) pour lesquels les spécifications sont très sévères : faible poids, faible perte de charge, très grande résistance et fiabilité, température d'entrée du refroidisseur élevée, conditions d'utilisation extrêmement variables et absence de givrage à basse altitude.

Le poids des échangeurs de chaleur risque de constituer un inconvénient majeur pour des cycles de moteurs combinés du type fusée à air liquéfié. Ce problème de poids associé au fait que l'impulsion spécifique de la fusée à air liquéfié est assez nettement plus faible que pour les autres cycles de moteurs combinés conduit à éliminer a priori les concepts de fusée à air liquéfié, sauf si une technologie nouvelle conduisant à des échangeurs de chaleur Air-Hydrogène légers et fiables est mise au point.

## **2.7. Fusée à air refroidi**

Le principe de la fusée à air refroidi (voir Figure 14) est très semblable à celui de la fusée à air liquéfié présenté ci-dessus, le refroidissement de l'air n'allant par contre pas jusqu'à la liquéfaction. En aval du refroidisseur, l'air est comprimé dans un compresseur avant d'être injecté dans la chambre. La puissance du compresseur est fournie soit par une turbine alimentée par un générateur de gaz, soit par un cycle expander.

L'impulsion spécifique d'une fusée à air refroidi est de l'ordre de 2500s à 3000s au sol et 1900s à Mach 7. Elle est nettement supérieure à celle d'une fusée, mais elle reste légèrement inférieure à celle des autres moteurs combinés (à l'exception de la fusée à air liquéfié) du fait du débit important d'hydrogène nécessaire au refroidissement de l'air et à sa compression. L'obtention des niveaux d'impulsion spécifiques indiqués suppose par ailleurs des échangeurs très importants et une optimisation de la performance pour une mission donnée conduira peut-être à choisir des échangeurs plus petits et plus légers au détriment de l'impulsion spécifique. Le nombre de Mach de vol maximum se situe autour de 7, à cause des problèmes de tenue en température au niveau de l'entrée d'air et du refroidisseur.

## 2.8. Statoréacteur à combustion supersonique

Dans un statoréacteur à combustion supersonique (ou "scramjet"), l'écoulement reste supersonique à l'intérieur de la chambre de combustion. La Figure 15 présente les niveaux d'impulsion spécifique qui pourraient être atteints pour le "scramjet" par rapport au statoréacteur et au turboréacteur. Ces courbes montrent que le "scramjet" est potentiellement intéressant au delà de Mach 6 environ. L'impulsion spécifique reste théoriquement supérieure à celle d'une fusée jusqu'à des nombres de Mach de vol de l'ordre de 15 à 18, à condition de savoir réaliser le mélange et la combustion de l'air et du combustible (hydrogène a priori) dans le délai très court imposé par le temps de séjour des molécules dans le foyer. Le nombre de Mach de vol maximum pour un véhicule hypersonique propulsé avec un "scramjet" est actuellement incertain du fait de l'imprécision sur la poussée du moteur et sur le bilan propulsif du véhicule et du besoin en refroidissement de la cellule et du moteur qui risque de limiter le nombre de Mach de vol maximum.

Le "scramjet" est le seul concept de propulsion combinée qui permette des impulsions spécifiques relativement élevées (entre 1000s et 3000s) sur une plage de nombres de Mach comprise entre 6 et 15 environ. Il est donc potentiellement très intéressant pour les missions utilisant largement cette plage en nombres de Mach, à savoir les lanceurs spatiaux monoétage ou deuxième étage de biétage (avec séparation vers Mach 6).

La modélisation des écoulements dans un "scramjet", en particulier la combustion supersonique dans la chambre, est nécessaire pour déterminer les performances qui peuvent être espérées dans un "scramjet". Les phénomènes physiques mis en jeu, particulièrement complexes, comportent le mélange turbulent du combustible dans un écoulement supersonique, la combustion turbulente associée, les effets catalytiques de paroi, les interactions entre ondes de choc de l'écoulement et entre ondes de choc et la paroi qui induisent des surchauffes en paroi qui peuvent être très importantes. D'autre part, dans le cas du "scramjet", l'intégration entre la cellule et le système propulsif (au niveau de l'entrée d'air et de la tuyère) est entièrement critique pour la détermination du bilan propulsif global du véhicule hypersonique et devra donc être modélisée avec précision (positionnement des ondes de choc, interactions entre ondes de choc d'une part, entre ondes de choc et paroi d'autre part, etc).

Aux difficultés de modélisation de phénomènes physiques associés au "scramjet" s'ajoutent de nombreux problèmes technologiques spécifiques : refroidissement des parois, système d'injection, entrée d'air à géométrie fortement variable.

Le "scramjet" a besoin d'un accélérateur pour le porter à Mach 6 environ. Un accélérateur de "scramjet" peut être soit intégré dans la veine du "scramjet" (concept fusée-stato pour lequel le stato est capable de transiter en combustion supersonique), soit positionné dans une veine parallèle suivant un concept du type turbo-stato ou turbofusée-stato. Une comparaison entre les différents concepts d'accélérateur doit prendre en compte les performances des moteurs correspondants (impulsion spécifique en particulier) et leur bilan de masse. Du point de vue masse, le concept fusée-stato transitant en combustion supersonique présente un avantage sensible, mais l'impulsion spécifique de la fusée sur le premier tronçon de la trajectoire (jusqu'à Mach 2 environ) est particulièrement faible. Seul le calcul complet des performances associées à une trajectoire permettra de sélectionner l'accélérateur le mieux adapté au "scramjet".

Le "scramjet" est un concept de propulsion combinée qui devrait permettre un "step" technologique important pour des applications lanceurs spatiaux ; c'est aussi un concept très complexe de part la nature des phénomènes physiques correspondants (combustion supersonique en particulier) et dont l'étude approfondie nécessite d'importants travaux de recherche.

### **3. COMPARAISON ENTRE LES DIFFERENTS CONCEPTS DE PROPULSION COMBINEE**

Pour une application lanceur spatial, deux types de véhicules doivent être considérés ; le monoétage et le biétage.

Pour un lanceur monoétage, des calculs sur trajectoires semblent montrer qu'a priori seule une propulsion combinée intégrant un "scramjet" conduit à une charge utile sensiblement positive, la fusée à air refroidi pouvant dans certains cas présenter de l'intérêt. Dans ce cas, un accélérateur du type fusée-stato ou plutôt fusée à air refroidi-stato conduirait à une intégration complète de l'accélérateur et du "scramjet". Un accélérateur à base de turboréacteur en veine parallèle (turbo-stato ou turbofusée-stato) améliorerait l'impulsion spécifique pendant la phase initiale de la trajectoire (Jusqu'à Mach 2 environ) mais présenterait une masse sensiblement plus importante que pour la fusée-stato.

Pour le premier étage d'un lanceur biétage, le critère d'impulsion spécifique devient prioritaire. Dans ce cas, seuls des concepts de propulsion combinée correspondant à une très forte impulsion spécifique (de l'ordre de 4000s) peuvent être retenus : le turbo-stato, le turboexpander-stato, la turbosoufflante-stato et le turbofusée-stato.

On recherchera une transition du turbo au stato pour un nombre de Mach de vol élevé, vers Mach 4 environ. Le fonctionnement en mode stato correspond à une combustion subsonique et sera étendu à un nombre de Mach maximum (entre 6 et 7).

Pour un deuxième étage d'un lanceur biétage, une fusée peut être envisagée mais d'autres concepts sont également possibles, en particulier le statoréacteur à combustion supersonique-fusée.

### **4. CONCLUSION**

Une analyse de différents concepts de propulsion combinée a été présentée pour une application à des lanceurs spatiaux (véhicule monoétage ou biétage). La comparaison de ces concepts montre que seul un petit nombre d'entre eux sont susceptibles d'être retenus pour un véhicule hypersonique futur à propulsion combinée.

Pour pouvoir affiner une analyse comparative de concepts de propulsion combinée de ce type, d'importants progrès doivent être réalisés dans le domaine de la modélisation des écoulements ("CFD" ou "Computational Fluid Dynamics") afin de prendre en compte les phénomènes physiques de turbulence, de mélange, de combustion (éventuellement supersonique), d'interaction d'ondes de choc, etc. Ce besoin en modélisation des écoulements est particulièrement critique dans le cas du statoréacteur à combustion supersonique ("scramjet") qui nécessite le développement de modèles spécifiques, en particulier pour prendre correctement en compte la combustion supersonique.

Un certain nombre d'hypothèses ont été faites concernant les solutions technologiques les plus appropriées. La validité de ces hypothèses reste à démontrer, par exemple pour l'introduction de matériaux composites thermostucturaux qui devraient permettre une augmentation des températures de fonctionnement et une réduction de la masse ; ces démonstrations conduiront à effectuer plusieurs expérimentations de validation.

L'activité de propulsion combinée qui a été présentée conjointement par la SNECMA, la SEP et l'ONERA. De tels travaux sur la propulsion combinée des véhicules hypersoniques futurs devront sans doute à terme être intégrés dans un large programme en coopération internationale.

### **Références**

1. IAF-89-312/MALAGA

Progress in Combined Cycle Propulsion  
Ph RAMETTE, M. DOUBLIER, D. SCHERRER

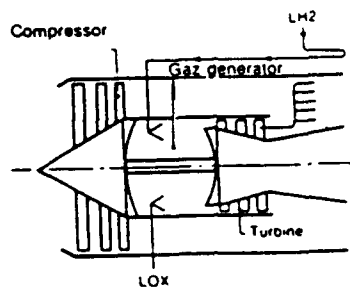
2. AIAA-89-2291/MONTEREY

Combined Engines for Space Transportation Systems  
E. HERMANT, A. LARDELLIER, D. SCHERRER

3. EAC-89/BONN

Progress in Airbreathing Combined Engines for  
Future European Launchers  
M. DOUBLIER, Ph RAMETTE, D. SCHERRER

## FIGURES



Figures 1 - Schéma de fonctionnement du Turbofusée-Stato

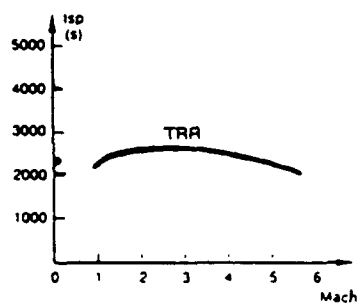


Figure 2 - Impulsion spécifique du Turbofusée-Stato

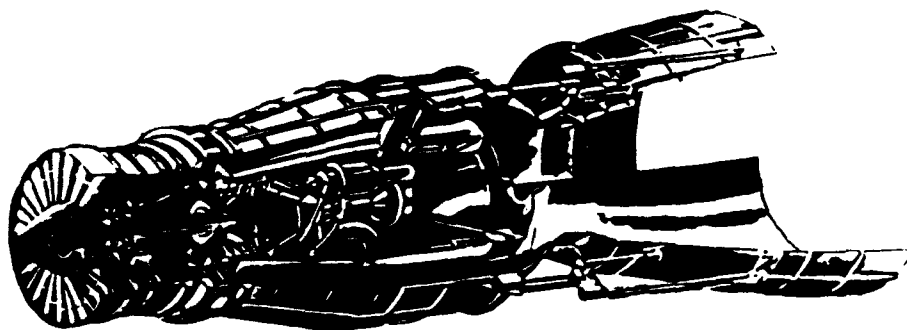


Figure 3 - Architecture du Turbofusée-Stato



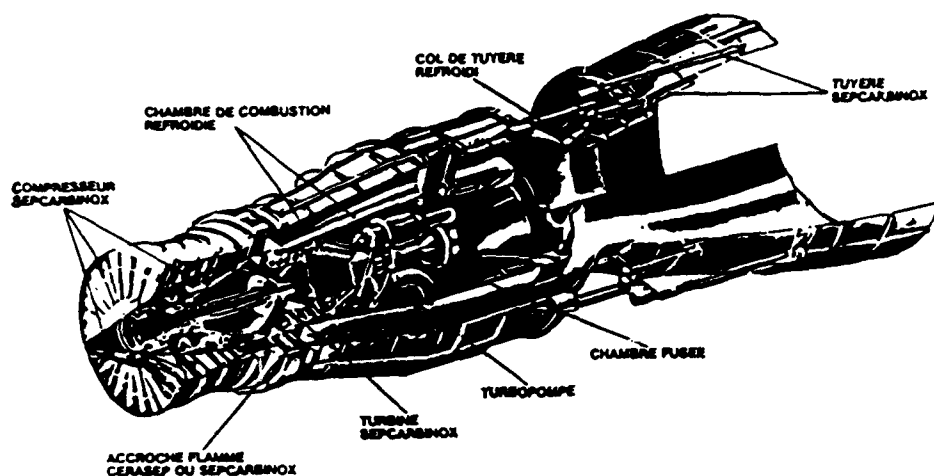


Figure 4 - Application des matériaux composites thermostrostructuraux au Turbofusée-Stato

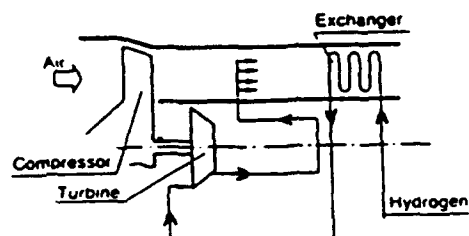


Figure 5 - Schéma de fonctionnement du Turboexpander-Stato

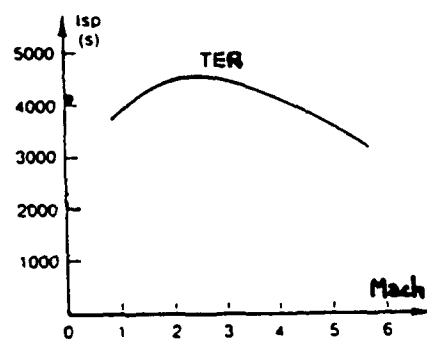


Figure 6 - Impulsion spécifique du Turbo expander-Stato

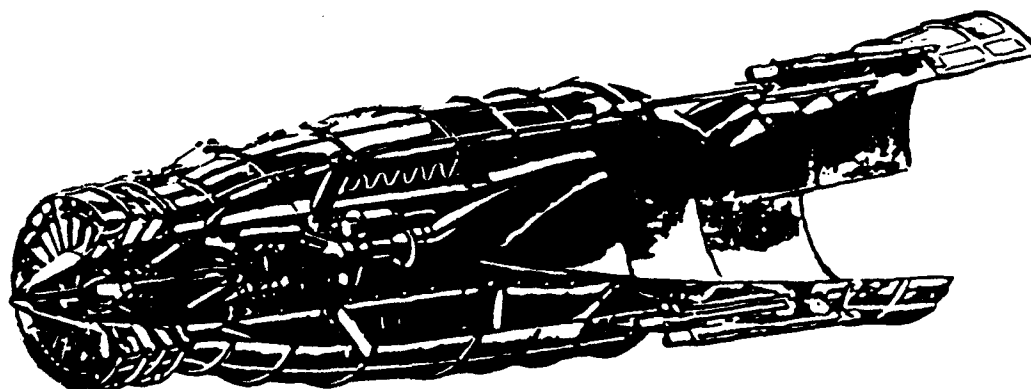


Figure 7 - Architecture du Turboexpander-Stato

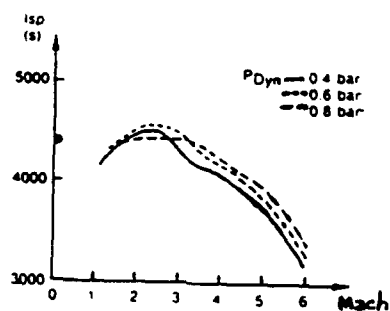


Figure 8 - Impulsion spécifique de la Turbosoufflante-stato

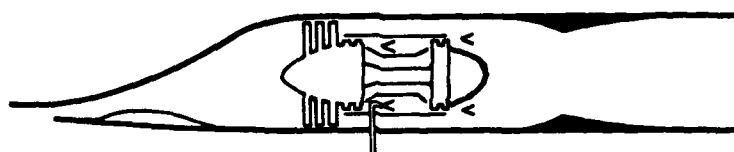


Figure 9 - Architecture de la turbosoufflante-Stato

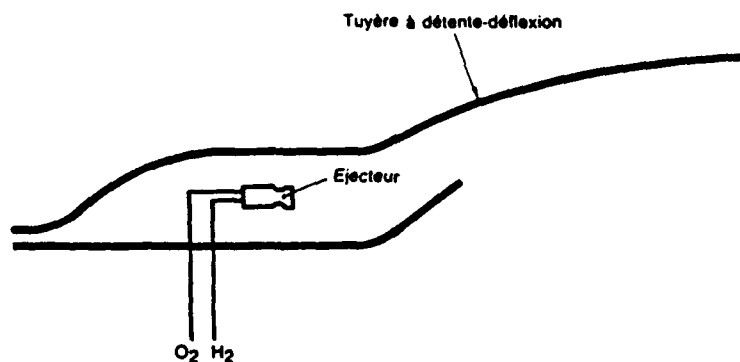


Figure 10 - Schéma de fonctionnement du Fusée-Stato

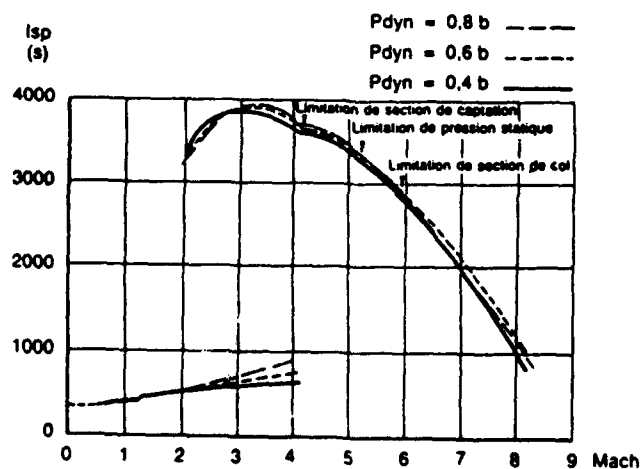


Figure 11 - Impulsion spécifique du Fusée-Stato

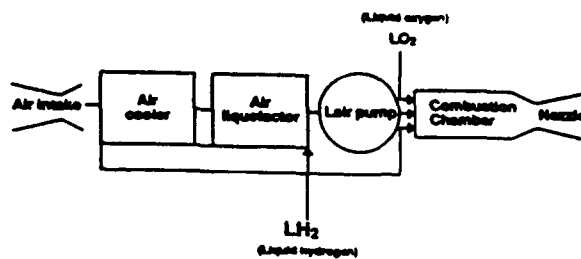


Figure 12 - Schéma de fonctionnement de la Fusée à air liquéfié

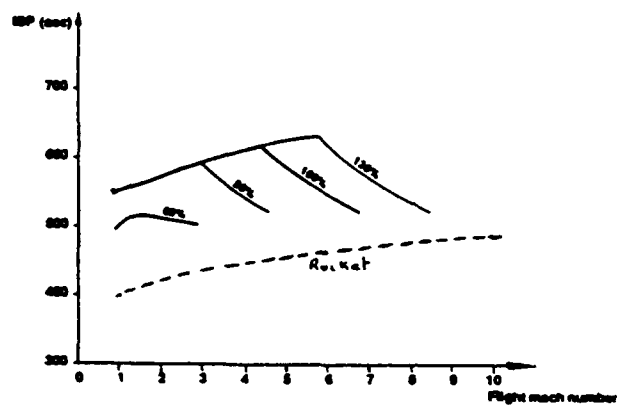


Figure 13 - Impulsion spécifique de la Fusée à air liquéfié

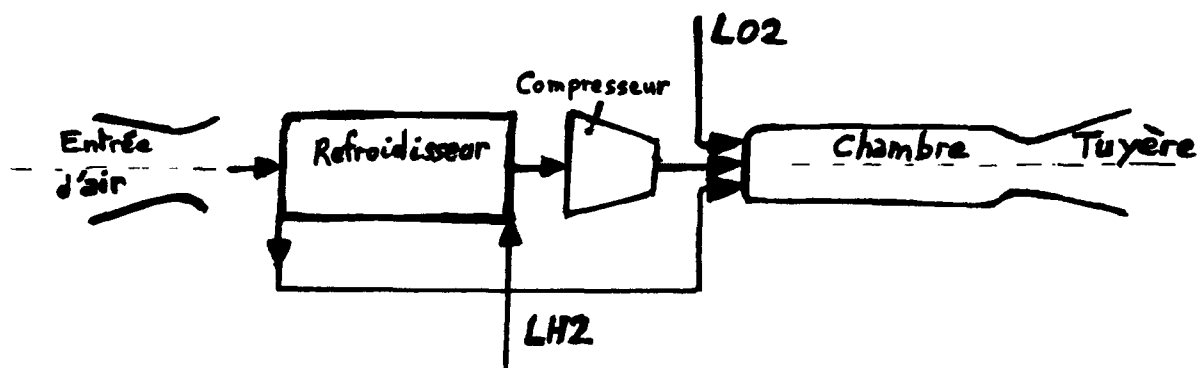


Figure 14 - Schéma de fonctionnement de la Fusée à air refroidi

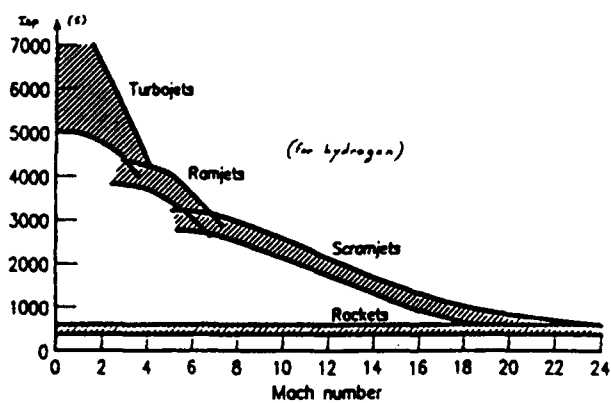


Figure 15 - Impulsion spécifique du "scramjet" par rapport au statoréacteur et au turboréacteur



## HYPERSONIC PROPULSION: STATUS AND CHALLENGE

R. Wayne Guy  
NASA Langley Research Center  
Hampton, VA 23665

92-16952



## ABSTRACT

Scientists in the United States are again focusing on the challenge of hypersonic flight with the proposed National Aero-Space Plane (NASP). This renewed interest has led to an expansion of research related to high-speed airbreathing propulsion, in particular, the supersonic combustion ramjet, or scramjet. This paper briefly traces the history of scramjet research in the United States, with emphasis on NASA-sponsored efforts, from the Hypersonic Research Engine (HRE) to the current status of today's airframe-integrated scramjets. The challenges of scramjet technology development from takeover to orbital speeds are outlined. Existing scramjet test facilities such as NASA Langley's Scramjet Test Complex as well as new high Mach number pulse facilities are discussed. The important partnership role of experimental methods and computational fluid dynamics is emphasized for the successful design of single-stage-to-orbit vehicles.

## INTRODUCTION

A concerted effort is underway in the United States to develop the technology for the proposed horizontal-takeoff, single-stage-to-orbit (SSTO) National Aero-Space Plane (NASP) shown in artist's concept in figure 1. To break the "thermal barrier" and achieve its mission, the best of propulsion, aerodynamics, structures, materials, subsystems, and controls will be required in this vehicle which must be the most carefully integrated functionally of any airplane ever designed (ref. 1). Several requirements for an SSTO vehicle are indicated in figure 2 where fuel fraction is plotted as a function of velocity achieved (ref. 2). This figure shows that an SSTO vehicle must have airbreathing engines, use hydrogen fuel, and have very high vehicle volume-to-weight ratios (compared to previous research aircraft such as the X-15). In addition, for the portion of the flight above Mach 6, supersonic combustion ramjets (scramjets) are essential to achieve the necessary fuel specific impulse (ref. 3). Furthermore, thrust requirements at high speeds (ref. 2) demand that engines be integrated with the aircraft to capture a large percentage of the airflow compressed by the forebody shock and to use the aircraft aft end as a nozzle for engine flow expansion. Therefore, it becomes clear that a hydrogen-fueled, airframe-integrated scramjet must be the propulsion workhorse for an SSTO mission.

Although scramjet research in the United States has been cyclic in nature since the early 1960's, a rich history is available for present-day researchers to use. The collective work by several government agencies and private industry from the early 1960's to the mid-1970's, including NASA's Hypersonic Research Engine (HRE), resulted in extensive proof of the scramjet cycle, a significant start on hydrogen-fueled, regeneratively-cooled hardware, and a keen realization of the need for engine-airframe integration (ref. 4). Although the decade from 1975 to 1985 was a period of relative inactivity in the hypersonic, airbreathing propulsion arena, small scramjet research efforts were maintained at The Johns Hopkins University/Applied Physics Laboratory (JHU/APL) and at the NASA's Langley Research Center. Scientists at Langley pursued research related to the hydrogen-fueled, modular, airframe-integrated scramjet (ref. 5) and tested three complete subscale engines up to Mach 8 during the time period. Projections of these data to engine performance installed on a vehicle suggested that the airframe-integrated scramjet was capable of propelling an aircraft up to the Mach 8 limit of the data. The success of these subscale scramjet tests together with significant advances in computational fluid dynamics (CFD), structures, and materials helped to promote renewed interest in SSTO vehicles.

Because of the emergence of the NASP, scramjet research in the United States is once again a national effort and the commitment has been made to explore scramjet performance over the speed range to orbital conditions. This commitment involves both experiment and computational fluid dynamics. New and modified ground test facilities, both blowdown and pulse, will be used to explore scale and speed. CFD and computer growth provide a tool which was not available during the 1960's in the first dedicated venture into hypersonic airbreathing propulsion. CFD is being applied in a partnership role with experiment to provide detailed understanding of the experimental scramjet data and to assist in projecting the ground facility data to flight.

This paper will trace in more detail the history of scramjet technology development in the United States leading to a statement of the present status of that technology. The challenges of scramjet propulsion from takeover Mach number to near-orbital speeds will be noted and the solution approaches will be discussed.

## THE STATUS

An understanding of the current status of scramjet technology in the United States demands a brief review of its history. Serious considerations of scramjet applications began around 1960. Since then, three distinct periods can be noted. The first was a period of relatively intense activity dating from the early 1960's to about 1975. The second was a period of an apparent, but perhaps deceptive, lull in scramjet research which occurred from about 1975 to 1985. The third, and current period, began around 1985 and is highlighted by renewed national interest in scramjets.

**Initial Interest: 1960-1975** - A good description of scramjet research activity during this period is contained in reference 4. This reference and discussions of scramjet chronology with Ernest A. Mackley of the Hypersonic Propulsion Branch at the NASA's Langley Research Center were most helpful in obtaining much of the information detailed here.

In the late 1950's and early 1960's, the United States Air Force was considering an "Aero-Space Plane." Various contractors and the NASA were also involved in this study and Dr. Antonio Ferri was suggesting the use of scramjets to Mach 20. The Aero-Space Plane was, in concept, a single-stage-to-orbit vehicle utilizing airbreathing propulsion and a small rocket. The study indicated that the optimum staging was greater than one stage (about 1.5) and that the state of the technology could not compete with rocket technology in terms of risk for an orbiting mission because of scramjet vehicle development costs. Other organizations involved in scramjet research during this period included The Johns Hopkins University/Applied Physics Laboratory under contract to the Navy, Marquardt, General Applied Science Laboratory (GASL), General Electric, and United Aircraft Research Laboratories (UARL).

In May 1965, the NASA awarded Phase I contracts to Marquardt, General Electric, and Garrett/AiResearch for competition to build a hydrogen-fueled, dual-mode scramjet called the Hypersonic Research Engine (HRE). The ultimate goal of the HRE program was to test a complete, hydrogen-fueled, regeneratively-cooled engine on the X-15 research airplane. In July 1966, Garrett/AiResearch was selected as the HRE Phase II contractor to work towards that goal.

As the NASA HRE effort was gaining momentum in the late 1960's, scramjet research was also being aggressively pursued by others (ref. 4). The Air Force funded tests of hydrogen-fueled scramjets developed by UARL, General Electric, GASL, and Marquardt. JHU/APL continued scramjet research for the Navy and began testing complete scramjet engines in free-jet tests in 1968. Also, in 1968, the Hypersonic Propulsion Branch at NASA Langley was beginning to work the problem of an airframe-integrated scramjet which would produce high installed thrust.

The X-15 research aircraft program was cancelled in January 1968, thwarting flight tests of the HRE. Only a mock-up of the external shape of the HRE (no through flow) had been flown at that time: one flight at Mach 4 and another at Mach 6.7 (figure 3). The HRE program was converted to a ground test program to test a Structural Assembly Model (SAM) and an Aerothermodynamic Integration Model (AIM). The SAM (figure 4) was a cryogenic hydrogen-cooled model which was used to verify heat transfer and cooling design. Tests of SAM were successfully conducted, but without engine combustion, in NASA Langley's 2.44-m High Temperature Structures Tunnel (HTST) at Mach 7 from September 1970 through May 1971 (ref. 6). The AIM was a water-cooled, hydrogen-fueled, boilerplate model which was used to verify propulsion performance. It was tested at Mach 5, 6, and 7 in the Hypersonic Tunnel Facility at the NASA Lewis Plum Brook Station from October 1972 through March 1974 (see refs. 7 and 8).

The airframe-integrated scramjet (figure 5) had evolved to a firm design at Langley in the early 1970's and was proceeding towards a research-scale engine for inhouse tests (ref. 5). A Langley inhouse thermal/structural design study of this lightweight airframe-integrated scramjet was started in 1972 (ref. 9). This study was followed by a competition resulting in a contract to Garrett/AiResearch to further this design study (ref. 10). Both studies initiated with and built upon HRE technology. Significant improvements in engine flight time and cycle life were projected.

The status of scramjet technology in the United States in 1975 at the end of this initial period of high interest can be summarized as follows. Efficient scramjet internal thrust performance (including dual-mode combustion) had been demonstrated in a variety of configurations with a variety of fuels (ref. 4). However, the issue of high installed thrust called for continued and increased study of the airframe-integrated scramjet designs. In addition to its contribution relative to thrust performance, the HRE program had initiated hydrogen-cooled structures technology. An excellent start had been made in the areas of design and fabrication of lightweight structures, cooling systems, and support hardware and software (fuel control valves, fuel pumps, a digital engine control system, etc.). The analytical thermal/structural studies of the airframe-integrated scramjet promised significant improvements over HRE technology.

**The Apparent Lull: 1975-1985** - This decade was a period of relative inactivity in the hypersonic airbreathing propulsion arena. This could partially be charged to the tremendous success of rockets in placing man on the moon and in propelling the U.S. Space Shuttle into orbit. Amidst this national lull, however, small scramjet research efforts were maintained at JHU/APL and at NASA Langley. JHU/APL continued to pursue its scramjet work for the Navy and Langley's Hypersonic Propulsion Branch continued to pursue the challenges associated with hydrogen-fueled scramjets. Langley's attention had shifted from the pod-mounted, axisymmetric HRE type of engine to the work which had begun in 1968 involving an engine with greater suitability for hypersonic flight in terms of installed thrust performance. This engine, called the airframe-integrated scramjet (figure 5), had rectangular cross sections perpendicular to the flow direction and, hence, grouped modules were very efficient in capturing airflow which had been precompressed by the aircraft forebody. In addition to the forebody acting as an external compression inlet, the aircraft aftbody was used to continue the engine nozzle expansion. This made the aircraft, in essence, a flying engine. The airframe-integrated aspect of this scramjet not only reduced the compression required by the module inlet but also reduced the

physical size of the engine module needed to produce the required thrust (compared to an engine located outside the shock layer). Smaller engine modules translated into lower drag, weight, and cooling requirements. The airframe integration also required, for performance at higher Mach numbers, the ingestion of the aircraft forebody boundary layer by the engine module.

At Langley, researchers were concentrating their efforts on a fixed-geometry version of the airframe-integrated scramjet for application up to the Mach 10 to 12 range (ref. 5). The design (figure 5b) featured inlet sidewall sweep and a cutback cowl which allowed the inlet bottom to be open for flow spillage and, hence, easier starting at the low flight Mach numbers. Three swept instream struts served to complete the inlet compression process and to provide multi-plane fuel injection points both perpendicular and parallel to the airflow. Airflow capture percentage automatically increased as Mach number increased because of the decrease in flow downturning caused by the sidewall and strut sweep.

To test engine components of airframe-integrated scramjets as well as complete scramjet modules, a Scramjet Test Complex had evolved at NASA Langley by the mid- to late-1970's. This complex consisted of existing aerodynamic facilities for inlet tests, a hydrogen-combustion-heated direct-connect combustor test facility capable of flight total enthalpy duplication to Mach 8, and two free-jet engine test facilities capable of testing complete, hydrogen-burning, subscale scramjet engine modules (approximately 18 cm by 15 cm frontal area) at duplicated flight total enthalpies from Mach 3.5 to Mach 8. (refs. 11-12). The Combustion-Heated Scramjet Test Facility (CHSTF), employing hydrogen/air combustion to heat the test gas, provided Mach 3.5 to 5.5 test capability. The Arc-Heated Scramjet Test Facility (AHSTF), employing an electric arc to heat the test gas, provided Mach 4.7 to 8 test capability. A summary of many of the research efforts in the Scramjet Test Complex from 1970 to 1986 as well as an extensive bibliography are presented in reference 13.

In December 1976, the first test of three Langley subscale airframe-integrated scramjet designs (figure 6) was conducted at Mach 7 in Langley's AHSTF. Two models of the initial scramjet design (figure 6a), which incorporated three swept instream fuel injection struts, were tested at Mach 4 and Mach 7 at both Langley and GASL from 1976 to 1979 (ref. 14). This particular engine had also been the focus of the earlier propulsion, aerodynamic, and thermal/structural studies (refs. 9 and 10).

Tests of a second Langley airframe-integrated scramjet design, the strutless parametric scramjet, were conducted in various entries into Langley's CHSTF and AHSTF from June 1982 to April 1988. This engine (figures 6b and 6d) was a versatile research model which could easily be changed into numerous configurations without removal from the test facility. Parametrics studied included inlet sweep, inlet compression angle, contraction ratio, cowl position, fuel injection location, flameholder design, combustor-inlet isolator length, and degree of boundary layer ingestion. Extensive research with this engine covered a simulated flight Mach number range from Mach 3.5 to 8.

The third Langley airframe-integrated scramjet design, the step-strut model (figure 6c), was actually a variation of the parametric scramjet engine. The variations consisted of different (unswept) inlet sidewalls, a single instream fuel injection strut featuring a stepped leading edge, and the addition of inlet top surface compression and combustor/nozzle top surface expansion. This engine was tested in Langley's CHSTF at simulated flight Mach numbers ranging from 3.5 to 5.5 from July 1983 to December 1984 and it awaits tests in the AHSTF from Mach 4.7 to 8.

Results from the Langley subscale scramjet tests were projected to a flight situation using cycle theory. This projection included consideration of multiple modules, forebody boundary layer ingestion, heat losses, and increased scramjet nozzle expansion. Comparison of engine thrust with calculated aircraft drag indicated sufficient acceleration thrust margin.

The conclusion from the above discussion is that the apparent national lull in scramjet research in the U.S. from 1975 to 1985 was somewhat deceptive. Although the number of researchers involved during this period was small, significant progress had been made in airframe-integrated scramjet research. More than 1500 tests associated with airframe-integrated scramjet modules had been conducted from Mach 3.5 to 8 and numerous factors affecting engine performance had been investigated including degree of forebody boundary layer ingestion, flow profiles, combustor-inlet isolation requirements, fuel/air mixing, piloting and flameholding, and scramjet geometry. The status of the technology demonstrated a positive outlook for scramjet propulsion with flight projections indicating thrust margin.

**Renewed National Interest: 1985-1990** - The success of the subscale scramjet tests together with significant advances in computational fluid dynamics, structures, and materials helped to create interest in the National Aero-Space Plane. Because of the NASP, scramjet research in the United States has become a national effort. The NASP program is a three-pronged effort involving three airframers, two propulsion contractors, and a Technology Maturation Program involving government laboratories, universities, and private industry. Both NASP prime propulsion contractors, Rocketdyne and Pratt and Whitney, have tested their scramjet concepts in Langley's subscale engine test facilities. In addition, an airframe-integrated scramjet designed by JHU/APL has been tested in Langley's CHSTF as a part of the NASP program (figure 7). Parameters studied with the JHU/APL engine included inlet bleed, boundary layer energization, combustor-inlet

isolator length, fuel injection location, heated hydrogen, and film cooling. Tests of the Rocketdyne, Pratt and Whitney, and JHU/APL engines have added to and extended significantly the existing Langley data base on airframe-integrated scramjets.

The number and capabilities of the available and planned engine test facilities have also continued to grow. Engine Test Facilities (ETF's) have been constructed at Aerojet and Marquardt for use in the NASP program. These facilities, with free-jet nozzles about 1 meter square, permit larger scramjet modules (relative to the Langley subscale modules) to be tested up to Mach 8. The planned reactivation of the Hypersonic Tunnel Facility at NASA Lewis' Plum Brook Station will offer scale similar to the ETF's with duplicated flight Mach numbers of 5, 6, and 7. In addition, the capabilities of the Langley Scramjet Test Complex will increase as the 2.44-m High-Temperature Tunnel (2.44-m HTT) comes back into service in 1991. This facility (ref. 15), with its new oxygen replenishment system and two new facility nozzles, will allow tests at Mach 4, 5, and 7 of multiple subscale scramjets complete with fore and aft body simulation. Also, much larger single module tests will be possible including hydrogen-fueled and regeneratively-cooled, lightweight structures. Preflight testing of actual flight engine modules would be possible (with limits on scale) to provide for reliability and flight safety at least up to Mach 7. Flight envelope expansion techniques would be required beyond Mach 7.

The proposed use of scramjets to near-orbital speeds on the NASP has focused attention on techniques to determine scramjet performance at these more extreme conditions. Certainly, CFD must play a key role in this high Mach number regime just as it must over the whole speed range. However, experimental methods are required for testing scramjets and/or scramjet components at conditions simulating flight to orbit. This requirement exists not only to determine scramjet performance experimentally, but also to provide CFD code validation to instill confidence for more extended use of CFD where experimentation may not be feasible.

The huge power requirements, high pressures, and high heating rates associated with near-orbital, true-temperature flight simulation has forced reliance upon pulse facilities as key facilities for scramjet research. Scramjet combustor tests have been underway for some time in the Calspan reflected shock tunnels and in the reflected shock tunnels with free piston drivers at the University of Queensland in Australia. The existing NASA Ames reflected shock tunnel as well as new reflected shock tunnels with free piston drivers currently under construction at Rocketdyne (RHYFL) and at the California Institute of Technology (ref. 16) will provide the U.S. with Mach number capability for propulsion testing up to orbital speeds. The RHYFL facility will be the largest facility of its type and will permit tests of full-scale engine components (ref. 17).

Shock tunnels, in heating an essentially stagnated gas, are plagued by large amounts of nonequilibrium dissociated oxygen and, hence, do not offer real air as a test gas. To diminish this problem, a unique pulse facility called the shock expansion tube (refs. 16, 18, and 19), has been reactivated at the General Applied Science Laboratory and scramjet combustion tests are in progress. This facility, now called HYPULSE, was originally constructed in the 1960's at NASA Langley and was operated there until 1983. Its distinguishing feature is enthalpy levels above Mach 20 flight simulation without significant oxygen dissociation.

The current status of scramjet technology in the U.S. can be summarized as follows. Research is more intense and more national in scope than it has been at any previous time. Progress in subscale scramjet tests, CFD, materials, and structures has encouraged this renewed interest. Projection of the subscale engine data to flight has resulted in sufficient confidence in the scramjet cycle up to Mach 8 that a commitment has been made to pursue this technology to larger scale and much higher speeds.

#### THE CHALLENGES

The primary challenge to the use of scramjet propulsion for single-stage-to-orbit vehicles is to prove the cycle over the speed range (from takeover Mach number to orbital) in ground facilities and to reliably project the results to flight with demonstration of adequate thrust margin. To meet this challenge, more extensive ground tests are required to explore scramjet performance which emphasize larger scale and increased speed and a close partnership between experiment and CFD will be essential.

**The Challenge of Scale** - Subscale tests of airframe-integrated scramjets at Mach 8 and below have been in progress since 1976. These tests have generally consisted of a single subscale module (18 cm high by 15 cm wide by 1.8 m long) either centered in the facility nozzle free jet or mounted to ingest a portion of the facility nozzle boundary layer. Larger test facilities are required to experimentally investigate both multiple module installations of the subscale engines (three or more modules) and larger single engine modules. These challenges of scale can be faced at Mach 4, 5, and 7 in NASA Langley's 2.44-m HTT. This facility (ref. 15), which uses methane/air combustion to heat the test gas, represents the commitment to study scramjet scale effects with the addition of the oxygen replenishment system and new Mach 4 and 5 nozzles. Shakedown tests of the facility are currently in progress. The 7.9-m-diameter test pod of this propulsion facility is shown in figure 8.

Three of the initial scramjet tests planned in the 2.44-m HTT are shown schematically in figure 9. The first is a subscale engine, the strutless parametric scramjet which was tested previously in the CHSTF and the AHSTF, mounted on a sled which

simulates an aircraft forebody (figure 9a). The 18-cm high engine also has an (optional) larger nozzle exit area to more nearly simulate the expansion achievable on the aircraft aft end. Both the engine module and the module/sled combination can be mounted on three-component force balances to measure axial and normal forces and pitching moments. The purpose of the test is twofold. The first is to assess the 2.44-m HTT as a scramjet test facility by comparing engine results directly with those from the smaller facilities (CHSTF AND AHSTF). The second is to assess the effects of various nozzle exit areas on engine performance. Testing of this configuration will commence in late 1991.

The second scramjet test in the 2.44-m HTT will consist of three subscale modules mounted side by side on the same aircraft sled used for the first test (figure 9b). The purpose of this test series is to investigate the realities of a more flight-like scramjet installation. The effects associated with outboard modules encountering different flow fields than inboard modules will be noted. Interactions between modules caused by combustor-inlet interaction or unstart of one module will also be investigated. Again, the module group and the module-group/sled combination will be mounted on three-component balances while side forces will be measured with extensive pressure instrumentation.

The third scramjet test in the 2.44-m HTT will be a single larger scale engine module (figure 9c). This model will be at least two times the scale of the previously tested single subscale modules (36-cm high with four times the captured air flow). Much larger scale modules are also under consideration, perhaps as large as 0.75-m high by 0.6-m wide by 7.50-m long. Modules of other shapes could also be tested with widths or heights up to 1.2 meters. Model length is more restricted unless further tunnel modifications are made. These larger modules will deliver information on the effects of engine scale when compared with results from the smaller engine modules. In addition, at least some parts of these larger engines will be lightweight hardware complete with hydrogen regenerative cooling and these configurations would hopefully evolve to a full flightweight engine module.

**The Challenge of Speed** - We have experienced a Mach 8 barrier to date in testing scramjets. Not only do facility flow vitiation and nonequilibrium effects grow in importance above Mach 8, but total enthalpy requirements increase dramatically. Total power requirements also increase significantly if modules are sizable and test times are similar to those of lower Mach number (less than Mach 8) facilities. For instance, as shown in figure 10, with a fixed dynamic pressure simulation, the total enthalpy requirements at Mach 16 are roughly four times the requirements at Mach 8 and power requirements are doubled for a given flow area. Both total enthalpy and power requirements dictate shorter test times for reasons of thermal survivability and economy.

A partial answer to this challenge of speed appears to be pulse facilities, i.e., devices such as shock tunnels and expansion tunnels which operate at total enthalpies representative of high flight Mach numbers (up to orbital), but with very short test times (1 ms typical for shock tunnels, 0.5 ms typical for expansion tunnels). The altitude/Mach number location of pulse facilities relative to an airbreathing SSTO flight corridor is shown in figure 11 (private communication with Dr. John I. Erdos, CASL). The requirements for pulse facilities cover the upper two-thirds of the Mach number range. The operating principles of these facilities are illustrated in the wave diagrams shown in figure 12. By providing an acceleration tube in place of the reflected shock, the expansion tube produces high total temperature gas with far less dissociation than is the case in the reflected shock tube. The addition of the free piston driver to both types of facilities produces higher total enthalpy, higher total pressure test flows.

As mentioned in THE STATUS section of this paper, scramjet efforts are underway in some pulse facilities, including reflected shock tunnels in Australia (ref. 20) and in CASL's expansion tube. Reflected shock tunnels at Cal Tech, NASA Ames, and Rocketdyne will be available in the future for scramjet testing. The Rocketdyne facility, figure 13, will offer full-scale testing of engine components.

While providing valuable scramjet test data, these facilities are not the sole answer to the challenge of speed and each has serious drawbacks. For instance, in most cases, only some components of a scramjet will be tested, usually a combustor section in direct connect. Oxygen dissociation in the test gas is a severe problem in the reflected shock tubes as shown in figure 14 (private communication with Dr. John I. Erdos, CASL). This problem is certainly alleviated considerably in the expansion tube. However, very short test times are a concern in all of the pulse facilities. This is illustrated in figure 15 where representative test times are shown for the RHYFL facility as a function of simulated flight velocity (private communication with Dr. Patrick Hurdle, Rockwell International/Rocketdyne Division). Test times in this facility will be greater than other pulse facilities discussed in this paper. Test time translates into test flow length and ultimately to the size model which may be tested. The rule generally used for the aerodynamics of external flows is that the model size can be only about one-third of the length of the test gas slug. The required test times for propulsion experiments are less certain and the question is raised of the suitability of some pulse facilities for exploring certain flow phenomena, i.e., some techniques for increasing fuel/air mixing might not be appropriate for investigation, time for boundary layer separations to form may be questionable, etc. Hence, data from these facilities must be scrutinized carefully to avoid misinterpretation and CFD can help in this assessment. CFD is already beginning to play a role in the pulse facility arena by attempting to duplicate the small amount of scramjet data available to learn flow field details as illustrated in figure 16. Here, Rogers and Weidner (ref. 21) compared CFD estimates of pressure distributions



in a supersonic combustor with experimental results obtained by Stalker (ref. 20) at simulated Mach 9 and Mach 16 flight conditions.

**The Challenge of Design for Performance** - The key challenge for engine design is to invent an integrated engine flow path with practical features to obtain near-optimum hypervelocity performance with adequate thrust across the speed range. Several aspects of this challenge have been addressed up to Mach 8 in the Langley subscale scramjet tests as illustrated in figure 17 by the representations of scramjet data obtained experimentally (not actual data). Precompression effects, or angle-of attack effects, are important for the airframe-integrated scramjet as demonstrated by the scramjet internal pressure distributions and thrust performance curves shown in figure 17a. Data of this type were obtained by varying the total enthalpy of the test flow (to simulate variation of flight Mach number) with the facility nozzle Mach number constant. For a fixed value and location of fuel injection, the expected increased pressure level and upstream influence is noted as incoming total enthalpy is reduced. The resulting increase in thrust performance (at constant stagnation pressure) is also shown. In figure 17b, the use of an ignitor gas (20 percent  $\text{SiH}_4$ , 80 percent  $\text{H}_2$ , by volume) and physical flameholders are illustrated. Note that flameholding and thrust performance are achieved when hydrogen is injected both from the ignitor gas orifices and the primary fuel injection orifices. The flame is extinguished and thrust is lost when the upstream hydrogen is eliminated. Means for appropriate inlet-combustor isolation must also be included in the engine design for use at the lower flight Mach numbers as demonstrated in figure 17c. Large combustion-induced pressure rises occurred on inlet forward-facing surfaces as fuel flow rates were increased. The isolator eliminated this combustion-induced inlet drag with resulting increases in thrust performance. The relative effect of facility nozzle boundary layer ingestion on thrust performance (in partial simulation of forebody boundary layer ingestion in flight) is illustrated in figure 17d. Contributors to the performance differences may be captured air mass flow rate, total pressure, and effectiveness of fueling the incoming air profile. Inlet compression must also provide the proper throat height and flow conditions for adequate fuel/air mixing, ignition, and flameholding. The effects of inlet contraction ratio on thrust performance are shown in figure 17e to illustrate this point. As contraction ratio is increased, engine width is decreased allowing increased fuel/air mixing, and the higher static pressures and temperatures with lower flow velocities promote ignition and combustion. Note that combustion does not occur at the lower contraction ratios except at higher fuel equivalence ratios.

At higher flight speeds (greater than Mach 8), inlet, combustor, and nozzle problems take on new proportions. Viscous effects become considerably more important at the higher Mach numbers because the thicker boundary layer can change the effective inlet shape near the inlet entrance and increase local pressures significantly. Fuel/air mixing and efficient combustion are extremely important at the higher Mach numbers, and the fuel must be injected in the airflow direction to preserve the momentum of the injected fuel. Here, shear layer mixing may not be sufficient and other induced-mixing methods may be required. In all cases, care must be taken that total pressure losses caused by these mixing enhancement techniques do not diminish performance. Finally, it is extremely important that the nozzle expansion process be accomplished very efficiently in a reasonable length, but not so rapidly that thrust is lost due to lack of recombination of dissociated combustion products.

All of the problems discussed above are being attacked experimentally and progress is apparent. However, a complete understanding of the various problems is difficult experimentally because of the sparsity of appropriate instrumentation, especially in the internal scramjet flows. To complicate the issue, incoming flow to the scramjet from the facility nozzle may contain flow peculiarities which affect the scramjet internal flow and, hence, thrust performance (i.e., flow nonuniformity, boundary layer characteristics, turbulence levels, different gas species due to the test gas heating process or to nozzle flow nonequilibrium, etc.). To help sort out the effects of incoming flow irregularities and to understand scramjet internal phenomena, CFD must be used in concert with the experimental data. Once agreement is obtained between CFD and experiment on key measured parameters, details of the flow field can be ascertained from the CFD results.

The CFD/experimental partnership is being pursued ever more vigorously in scramjet research programs. Figure 18 illustrates the application of CFD to a scramjet test conducted in NASA Langley's AHSTF (ref. 22). The CFD simulation was applied to the entire experimental configuration including the facility nozzle and the scramjet inlet, combustor, and nozzle (figure 6d). For simplicity, a zonal method of solution was used where the problem was computed in distinct axial sections. Therefore, flow conditions where scramjet component interactions were likely were avoided to insure validity of the numerical predictions. The types of CFD programs used for each flow zone are noted in figure 18a. Full elliptic techniques were applied where flow separation was likely.

Pressure distributions calculated along the scramjet sidewall with and without fuel injection are shown in figure 18b. Comparison of this type of CFD data with experiment would be used as a qualifier of the CFD adequacy. An example of the insight to flowfield details provided by CFD is shown in figure 18c at several combustor axial stations. Hydrogen mass fractions are shown for one-half of the combustor width beginning with the fuel injection station. The seven discrete orifice fuel injection locations can be clearly seen. Integrations at each station quantify bulk mixing efficiencies. In the high pressure region near the cowl, initial penetration of the fuel is reduced. In addition, because of this high pressure region, the hydrogen is deflected upwards resulting in a fuel deficit near the cowl which persists throughout the engine. This

effect is noticed even more in the hydrogen mass fraction profiles on the sidewall shown in figure 18d. Very little combustion occurred in the hydrogen-deficit region near the cowl; combustion was also decreased in the lower pressure regions near the top of the combustor (figure 18e). These types of flowfield details, especially the lack of fuel near the cowl and the reasons for this deficit, illustrate the importance of the CFD/experimental partnership. As CFD capability grows in accuracy and confidence, techniques to improve scramjet design to overcome problems such as fuel/air mixing and combustion at all speeds can be screened by CFD prior to pursuing experimental verification.

**The Challenge of Projection to Flight** - The ultimate goal of ground-based tests of scramjets is to prove that the engines will provide adequate performance in flight. Hence, reliable techniques for projecting the ground data to flight must be developed. Recall that projection of the Langley subscale scramjet data to flight using cycle analysis techniques was partially responsible for the current interest in NASP. However, these analytical and empirical techniques may not be completely sufficient for development of the scramjet as a flightworthy propulsion system.

To understand the problems associated with projecting ground data to flight, one must understand the deficiencies of some of the ground data. As noted in the previous section, the flow approaching the scramjet from the facility nozzle is usually not totally representative of that approaching a flight engine. Techniques to heat the test gas (combustion, electric arcs, etc.) to the appropriate total enthalpy for flight Mach number simulation normally leave undesirable species such as water vapor and carbon dioxide in the flow. In addition, the very high stagnation temperatures required result in dissociation of molecular species, especially oxygen, in the plenum chamber. If flow conditions are such that recombination does not occur during the facility nozzle expansion, atomic oxygen and nitric oxide (in addition to polyatomic molecules in vibrational nonequilibrium) will enter the scramjet model. Therefore, the test gas approaching the engine is not real air.

Test gas composition irregularities in the test flow of typical hydrogen-combustion-heated and electric arc-heated scramjet test facilities such as Langley's CHSTF and AHSTF are illustrated in figure 19a and 19b. Water mass fractions of more than 30 percent result if hydrogen combustion facilities are used to produce Mach 8 total temperature levels. In figure 19b, calculated nitric oxide (NO) mass fractions up to 9 percent are in the flow exiting the AHSTF arc heater. After dilution with ambient temperature air to achieve the desired total temperature for flight Mach number duplication, calculated NO levels are lower and vary with Mach number. Nitric oxide concentrations measured spectroscopically are slightly lower than the calculated values on the average. The effects of the water vapor and the nitric oxide on scramjet performance must be duplicated analytically or numerically and understood before the scramjet test data can be reliably projected to flight.

Forebody boundary layers which are ingested into the engines during ground tests are almost certainly not proper simulations. Turbulence levels vary widely between facilities, usually are not quantified, and are probably not representative of flight. Also, flow irregularities due to facility nozzle design may be present, as shown in figure 20 in both two-dimensional (2-D) contoured nozzles (ref. 23) and in square-cross-section nozzles contoured on all four surfaces (ref. 24). These particular irregularities involve counter rotating vortices near the center lines of all walls of the square-cross-section nozzles (note Mach number contours in figure 20b) and the flat sidewalls of the 2-D contoured nozzle (figure 20a). In reference 23, CFD analyses were performed (using a zonal approach similar to that of reference 22) of the 2-D Mach 6 nozzle flow and of the flow through a scramjet inlet (figure 6d) situated in various positions at the nozzle exit (figure 20c). Vertical centerline unit mass flow rate ( $\rho u$ ) profiles at the inlet throat are shown in figure 20d for three different inlet orientations. In the first case, the inlet ingests the vortical flow from the flat sidewall; in the second case, the inlet ingests a more normal boundary layer from the top contoured nozzle surface; and, in the third case, uniform flow enters the inlet (a similar case to the inlet centered in the nozzle exit). Note the significant differences in the  $\rho u$  profiles from the top surface to the cowl at the inlet throat. This emphasizes the necessity of complete CFD simulation of experimental cases if the most accurate use is to be made of the experimental data in understanding the flow field and in projecting the data to flight.

The issue of model scale must also be considered. Fuel/air mixing is viewed as a scalable quantity in the absence of combustion. However, scaling of fuel/air mixing to different size engines is not so straight-forward in the real case with combustion and the situation is worse if kinetics are a factor. Testing at increased pressures in an attempt to apply pressure/dimension product scaling may not be possible due to facility limitations and may be suspect anyway in the complex scramjet flowfield.

At present, CFD codes have limitations in modeling internal flows and these limitations increase as Mach number increases. However, as CFD grows in validated capability and as computers provide more storage and faster computations, the CFD codes will provide us with tools which were not available in the 1960's during our first venture into airbreathing hypersonic propulsion. Using CFD, one can envision the following path to flight which can be accomplished with increased confidence relative to empirical and analytical techniques.

The first step in projecting ground facility data to flight is to predict, using CFD, the results from the ground facility scramjet tests. This means that all known flow

conditions must be calculated beginning with the flow through the facility nozzle and proceeding completely through the engine. This process must include flow contaminants and nonequilibrium effects in the nozzle, actual nozzle and model wall temperatures for proper boundary layer simulation, proper fuel injection and mixing modeling, and, of course, the inclusion of actual chemical and vibrational kinetics (as opposed to the assumption of either equilibrium or frozen flow). Early attempts are already underway to apply this predictive approach as discussed in the previous section of this paper. However, this approach is in its infancy and will require computations in the scramjet where component interactions can be observed as opposed to the zonal method used to date. Success in this predictive capability for the ground-based results should be more challenging than the actual flight situation and, hence, should lend confidence for the second, and final, step to flight projection.

The second step is simply to calculate the scramjet performance in flight using CFD. Certainly, quantities such as turbulence levels will be different from the ground tests (where this parameter may even have been a variable used to achieve agreement between CFD and experiment) and will not be well-known over the entire flight regime of the NASP. However, this partnership between CFD and experiment for projection of ground-based data to flight should be the most accurate technique to instill confidence in flight success in terms of scramjet performance.

#### SUMMARY

Scientists in the United States are focusing once again on the challenge of hypersonic flight with the proposed National Aero-Space Plane. The extensive research of the 1960's has been revisited in the light of new airframe-integrated scramjet engines. Small, but persistent, scramjet research efforts during the national lull in hypersonic airbreathing propulsion research demonstrated the high probability of satisfactory thrust margin in flight up to Mach 8. With this knowledge, as well as advances in CFD, structures, and materials, a commitment has been made to pursue challenges associated with scale and speed to assess scramjet performance to orbital conditions. This national commitment involves airframers, engine companies, government laboratories, universities, and other parts of private industry. New facilities to explore both scale and speed are evolving and research is proceeding at a more rapid pace than ever before. The current effort in hypersonic airbreathing propulsion has a tool which was not available to the similar effort of the 1960's, i.e., computational fluid dynamics. The success of the NASP single-stage-to-orbit mission is highly dependent on a close partnership roll between experimental methods and computational fluid dynamics.

#### REFERENCES

1. Anderson, Griffin Y.: An Outlook on Hypersonic Flight. AIAA Paper 87-2074, July 1987.
2. Jones, Robert A.; and Donaldson, Coleman duP.: From Earth to Orbit in a Single Stage. Aerospace America, Aug. 1987, pp. 32-34.
3. Dugger, G. L.: Comparison of Hypersonic Ramjet Engines with Subsonic and Supersonic Combustion. Combustion and Propulsion, Fourth AGARD Colloquium, High Mach Number Airbreathing Engines, H. L. Jaumotte, A. H. Lefebvre, A. M. Rothrock, eds., Pergamon Press, New York, 1961, pp. 84-110.
4. Waltrup, Paul J.; Anderson, Griffin Y.; and Stull, Frank D.: Supersonic Combustion Ramjet (Scramjet) Engine Development in the United States. Proceedings, 3rd International Symposium on Air Breathing Engines, Dietmar K. Hennecke and Gert Winterfeld, eds., DGLR-Fachbuchreihe Bd. 6, 1976, pp. 835-861.
5. Henry, John R.; and Anderson, Griffin Y.: Design Considerations for the Airframe-Integrated Scramjet. NASA TM X-2895, Dec. 1973.
6. Staff, AiResearch: Hypersonic Research Engine Project - Phase II, Structures and Cooling Development - Final Technical Data Report (AP-72-8237, AiResearch Manufacturing Company of California, NAS1-6666), NASA CR-112087, May 1972.
7. Staff, AiResearch: Hypersonic Research Engine Project - Phase II, Aerothermodynamic Integration Model Development - Final Technical Data Report (AP-75-11133, AiResearch Manufacturing Company of California, NAS1-6666), NASA CR 132654, May 1975.
8. Andersen, W. L.; and Kado, L.: Hypersonic Research Engine Project - Phase II, Aerothermodynamic Integration Model (AIM) Test Report. (AP-74-10784, AiResearch Manufacturing Company of California, NAS1-6666), NASA CR-132655, May 1975.
9. Wieting, Allan R.; and Guy, Robert W.: Preliminary Thermal-Structural Design and Analysis of an Airframe-Integrated Hydrogen-Cooled Scramjet. AIAA Paper No. 75-137, Jan. 1975.
10. Killackey, J. J.; Katinszky, E. A.; Tepper, S.; Uigner, A. A.; Wright, C. C.; and Stockwell, G. G.: Thermal-Structural Design Study of an Airframe-Integrated Scramjet: Final Report. NASA CR-159039, May 1980.
11. Andrews, Earl H., Jr.; Torrence, Marvin G.; Anderson, Griffin Y.; Northam, G. Burton, and Mackley, Ernest A.: Langley Mach 4 Scramjet Test Facility. NASA TM-86277, 1985.

12. Thomas, Scott R.; and Guy, Robert W.: Expanded Operational Capabilities of the Langley Mach 7 Scramjet Test Facility. NASA TP 2186, June 1983.
13. Northam, G. Burton; and Anderson, G. Y.: Supersonic Combustion Ramjet Research at Langley. AIAA Paper 86-0159, Jan. 1986.
14. Guy, Robert W.; and Mackley, Ernest A.: Initial Wind Tunnel Tests at Mach 4 and 7 of a Hydrogen-Burning, Airframe-Integrated Scramjet. Paper 79-8045, presented at the 4th International Symposium on Air Breathing Engines, Lake Buena Vista, Florida, April 1979.
15. Puster, R. L.; Rebush, D. E.; and Kelly, H. N.: Modification to the Langley 8' High Temperature Tunnel for Hypersonic Propulsion Testing. AIAA Paper 87-1887, July 1987.
16. Morrison, W. R. B.; Stalker, R. J.; and Duffin, J.: New Generation of Free-Piston Shock Tunnels. Presented at the 17th International Conference on Shock Waves and Shock Tunnels, Lehigh University, Pennsylvania, July 1989.
17. Scott, William B.: Rocketdyne Developing Facility for Hypersonic Propulsion Tests. Aviation Week and Space Technology, January 30, 1989, p. 65.
18. Rizkalla, Oussama; Bakos, Robert J.; Chinitz, Wallace; Pulsonetti, Maria V.; and Erdos, John I.: Use of an Expansion Tube to Examine Scramjet Combustion at Hypersonic Velocities. AIAA Paper 89-2536, July 1989.
19. Paull, A.; Stalker, R.; and Stringer, I.: Experiments on an Expansion Tube with a Free Piston Driver. AIAA Paper 88-2018, May 1988.
20. Stalker, R. J.; and Morgan, R. G.: Supersonic Combustion with a Short Thrust Nozzle. Journal of Combustion and Flame, vol. 57, no. 1, July 1984, pp. 55-70.
21. Rogers, R. Clayton; and Weidner, Elizabeth H.: Analysis of Hydrogen Combustion in High Enthalpy Supersonic Air Flows from a Shock Tunnel. Presented at the 23rd JANNAF Combustion Meeting, Hampton, Virginia, October 20-24, 1986.
22. Srinivasan, S.; McClinton, C. R.; and Kamath, P. S.: Numerical Simulation of flow Through the Langley Parametric Scramjet Engine. SAE Technical Paper 892314, September 1989.
23. Sekar, B.; Thomas, S.; and Srinivasan, S.: A Numerical Study of a Scramjet Inlet in a Mach 6 Arc-Heated Test Facility. AIAA Paper 90-0531, Jan. 1990.
24. Ostrander, Mark J.; Thomas, Scott R.; Volland, Randall T.; Guy, Robert W.; and Srinivasan, Shivakumar: CFD Simulation of Square Cross-Section, Contoured Nozzle Flows: Comparison with Data. AIAA Paper 89-0045, Jan. 1989.



Figure 1.- The National Aero-Space Plane.

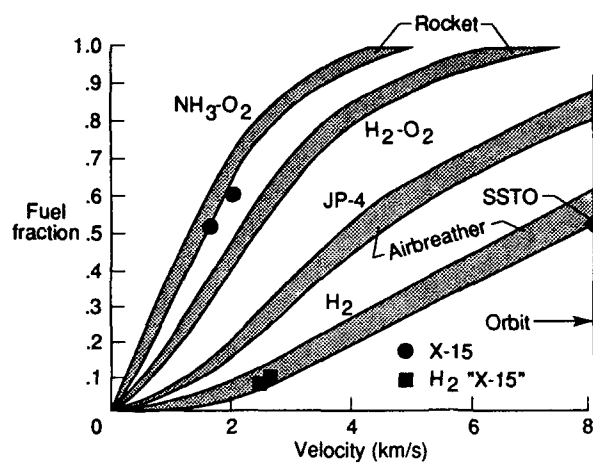


Figure 2.- Fuel fraction required to accelerate to velocity.



Figure 3.- The HRE on the X-15.

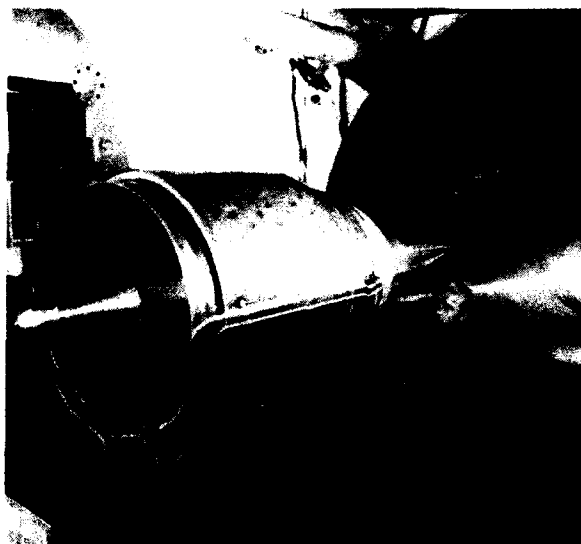
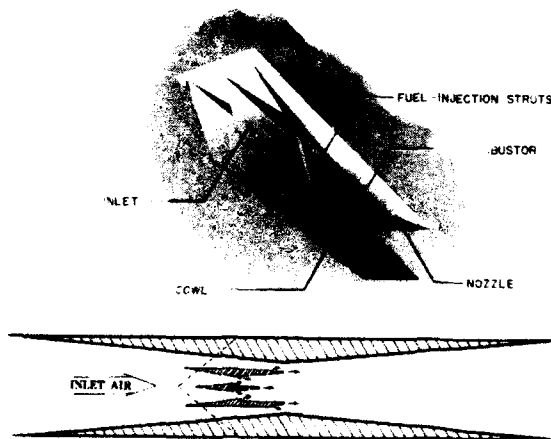


Figure 4.- HRE SAM in Langley's 2.44-m HTST.



(a) Aircraft with integrated scramjet.



(b) Scramjet modules.

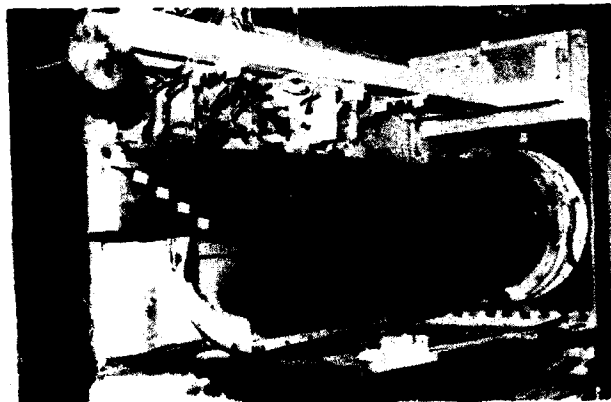
Figure 5.- The airframe-integrated scramjet.



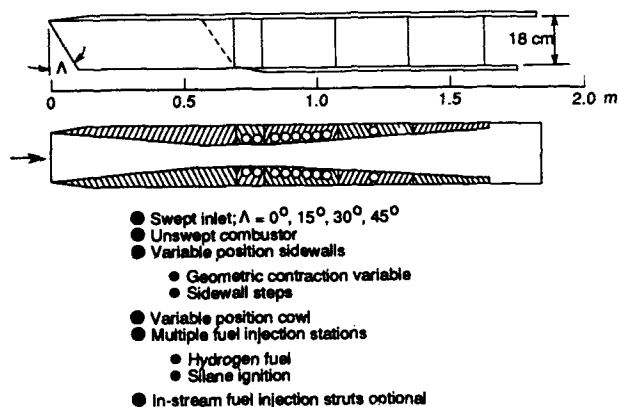
(a) Three-strut engine model.



(b) Strutless parametric engine model.



(c) Step-strut engine model.

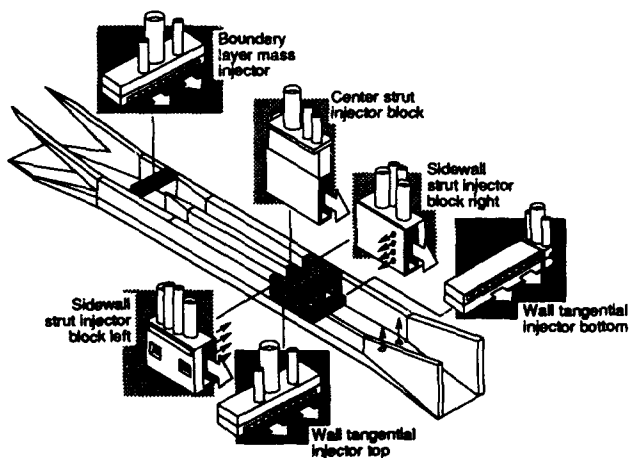


(d) Strutless parametric engine model details.

Figure 6.- Langley subscale airframe-integrated scramjet models.



(a) Engine photograph.

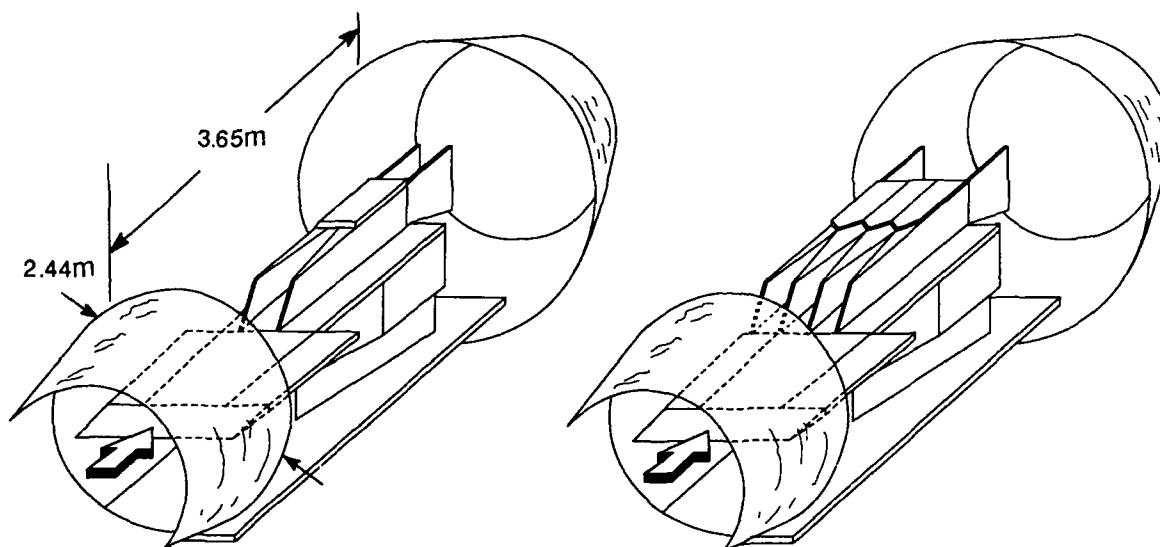


(b) Engine details.

Figure 7.- The JHU/APL scramjet rigged for tests in Langley's CHSTF.

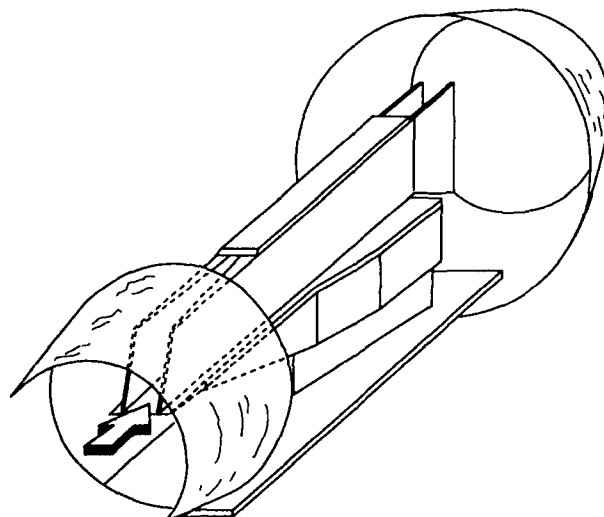


Figure 8.- The test section of the 2.44-meter High Temperature Tunnel.



(a) Subscale scramjet mounted on forebody.

(b) Multiple subscale modules mounted on forebody.



(c) Larger-scale scramjet.

Figure 9.- Scramjet tests planned for the 2.44-meter HTT.

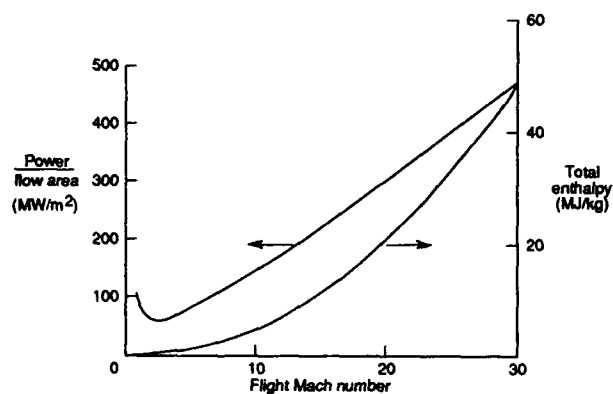


Figure 10.- Total enthalpy and power requirements as a function of flight Mach number. Dynamic pressure =  $47.9kP_a$

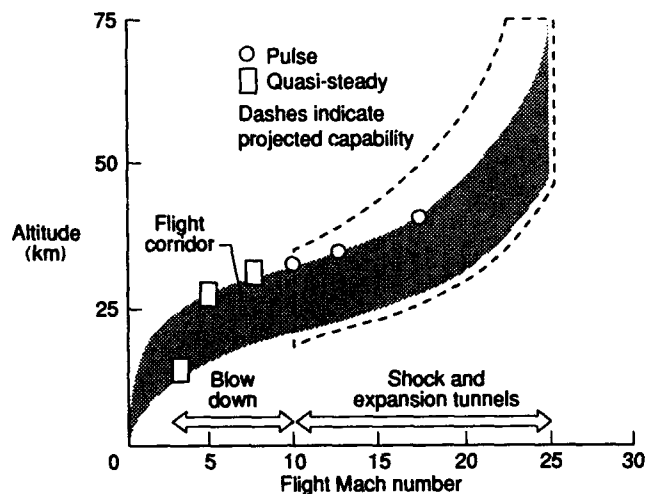
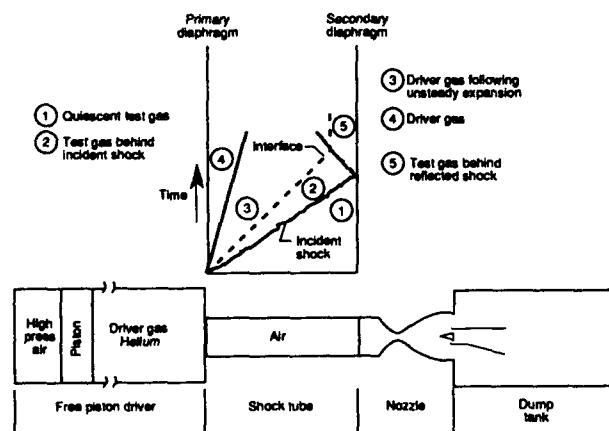
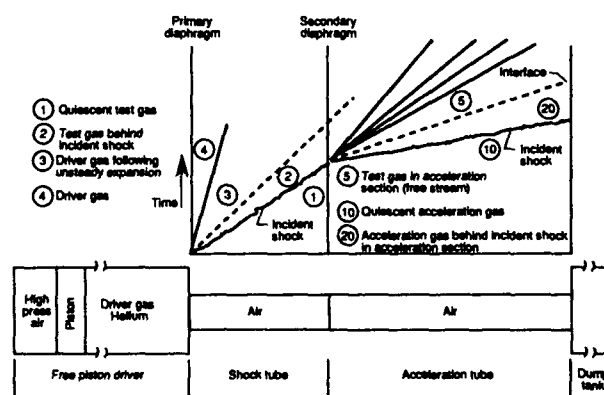


Figure 11.- Propulsion test facilities.



(a) Shock tunnel.



(b) Shock expansion tunnel.

Figure 12.- Schematics and wave diagrams for the reflected shock tunnel and the shock expansion tunnel (both with free piston drivers).



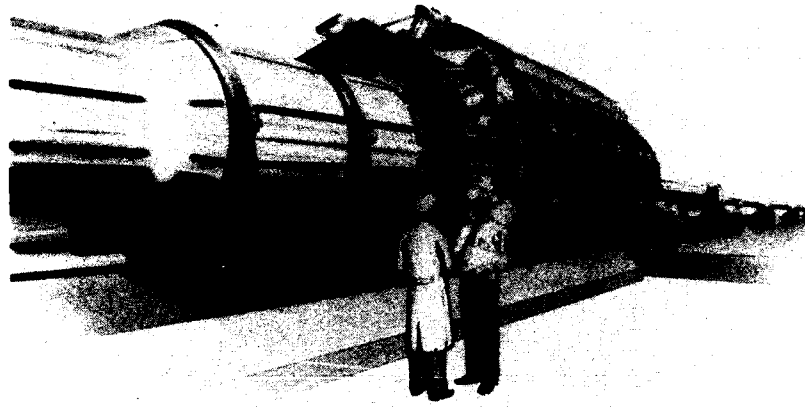


Figure 13.- Rocketdyne Hypersonic Flow Laboratory (RHYFL).

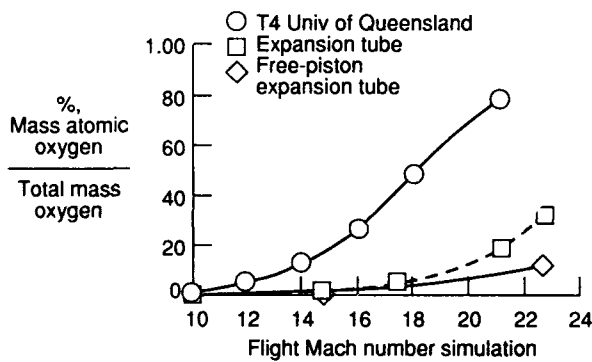


Figure 14.- Oxygen dissociation in HYPULSE and T4.

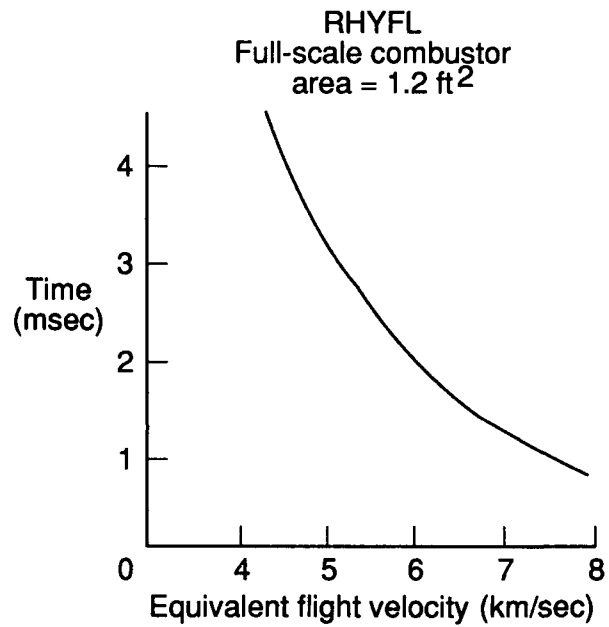


Figure 15.- Representative test flow time in RHYFL.

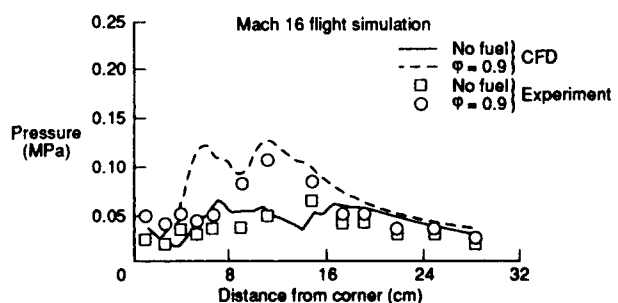
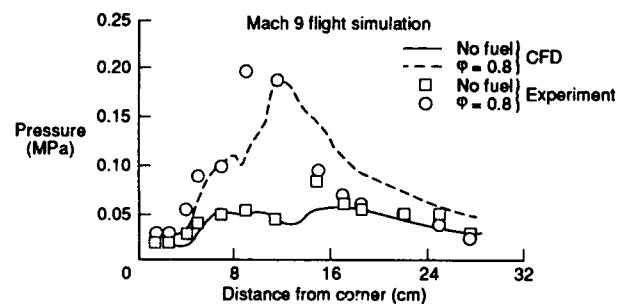
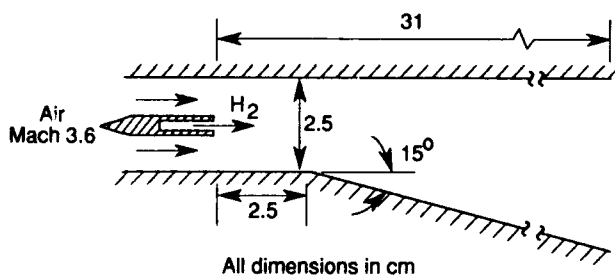
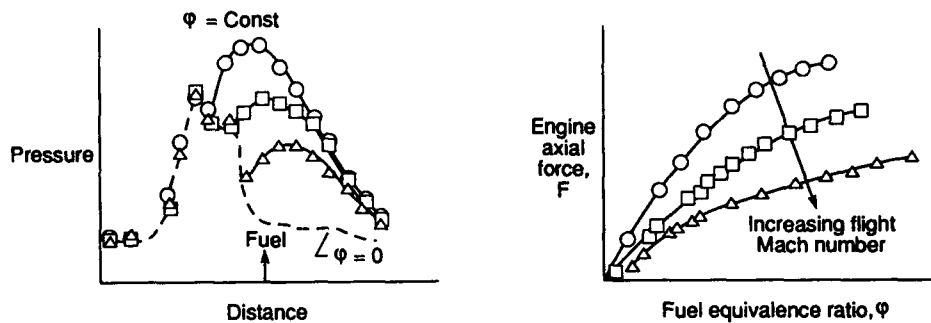
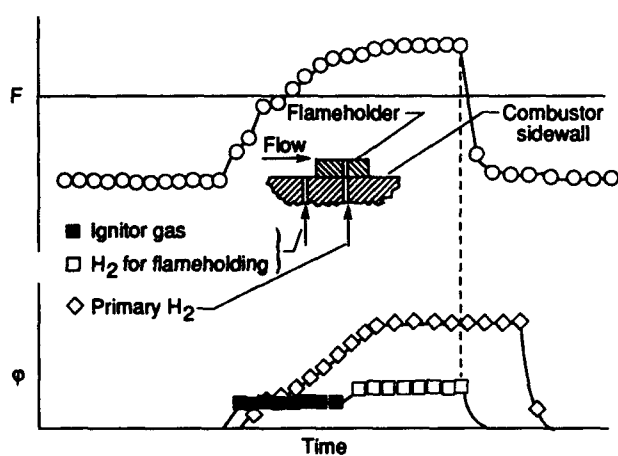


Figure 16.- University of Queensland shock tunnel data on supersonic combustion.

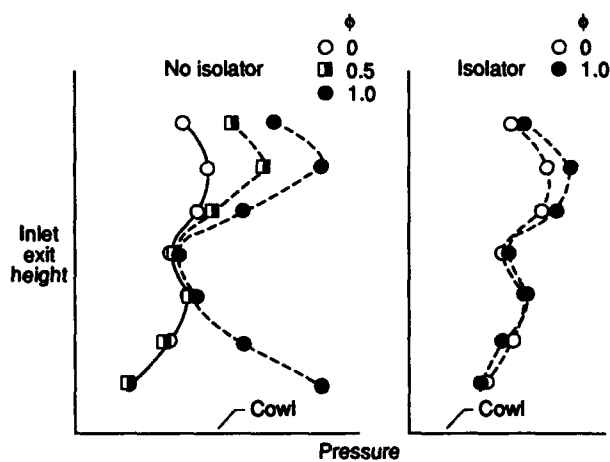
Constant total pressure  
Constant inlet Mach number



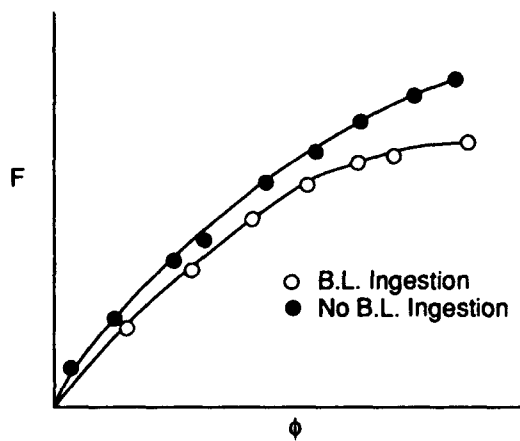
(a) Precompression effects.



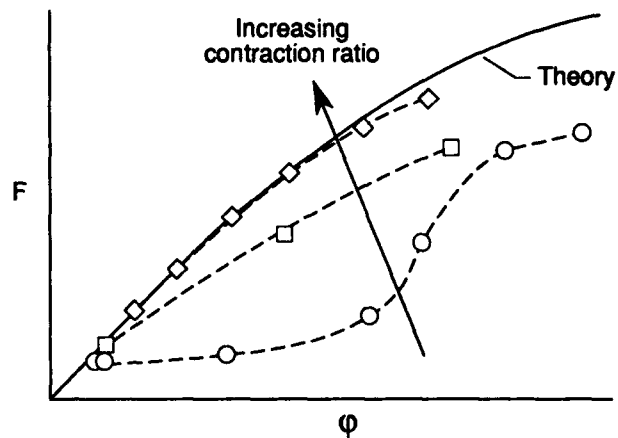
(b) Flameholding techniques.



(c) Combustor-inlet interaction.

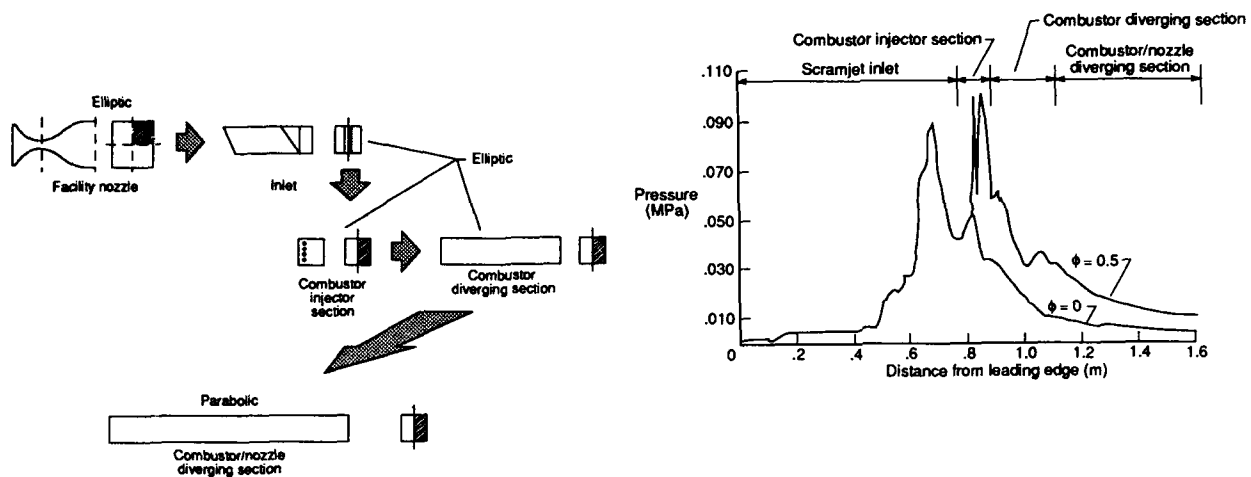


(d) Boundary layer ingestion effects.



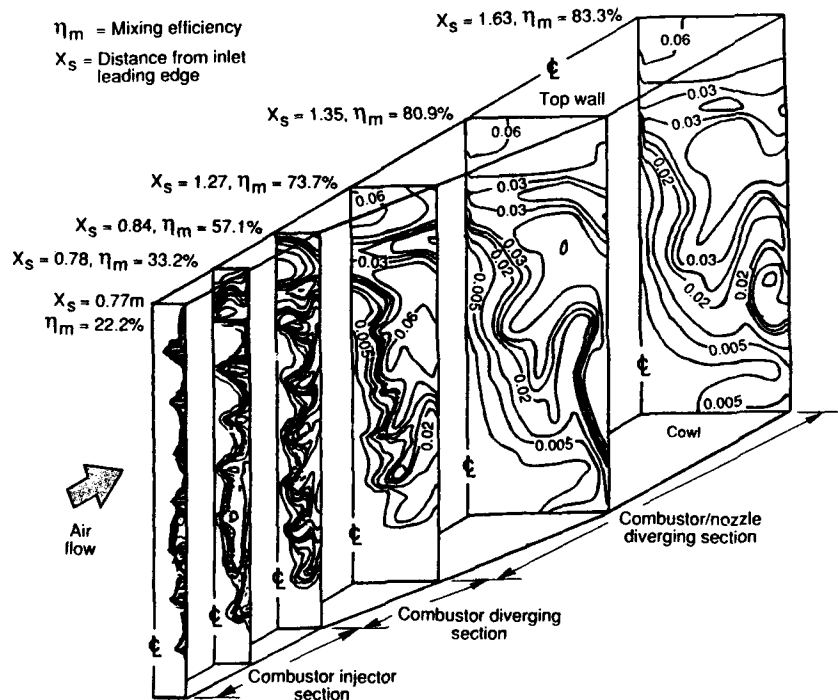
(e) Mixing/kinetics effects

Figure 17.- Representations of typical subscale scramjet experimental data.

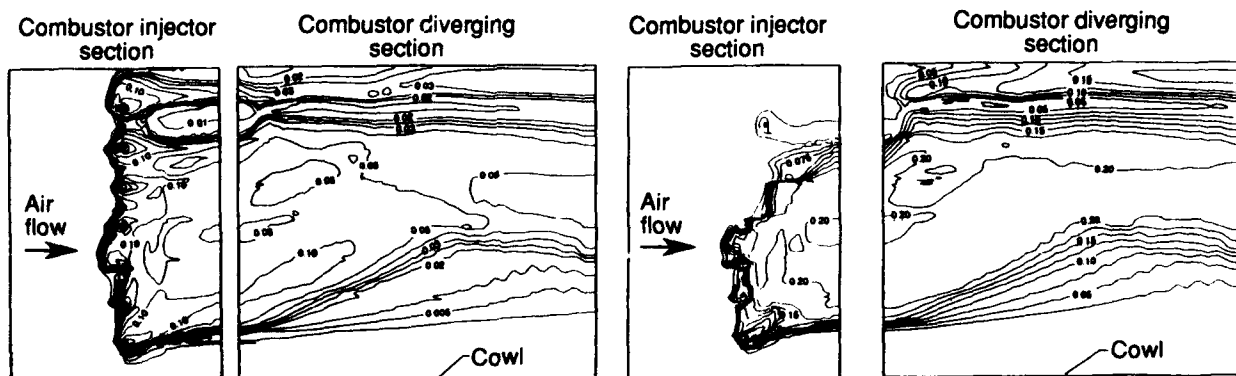


(a) CFD zonal solution methodology.

(b) Calculated scramjet sidewall pressure distributions.

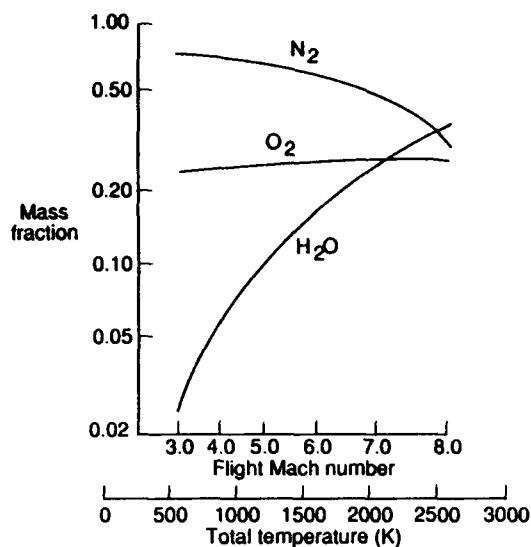


(c) Hydrogen mass fraction throughout the scramjet combustor.

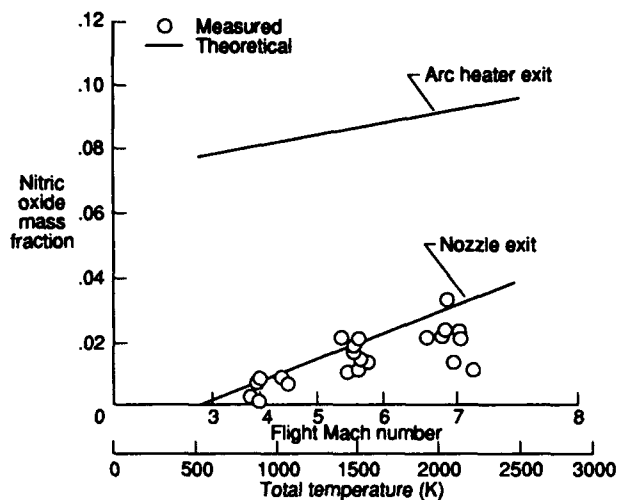


(d) Hydrogen mass fraction on the sidewall. (e) Water mass fraction on the sidewall.

Figure 18.- Simulation on an AHSTF scramjet test using computational fluid dynamics.

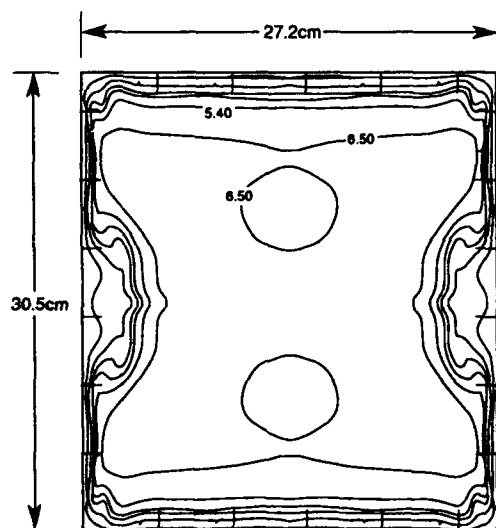


(a)  $H_2$  combustion-heated test flow composition.

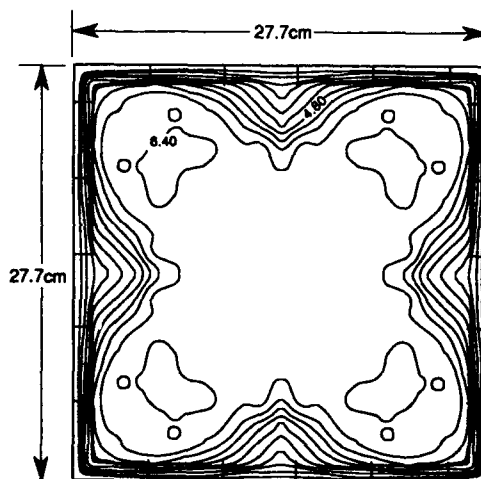


(b) Nitric oxide concentrations in the AHSTF test flow.

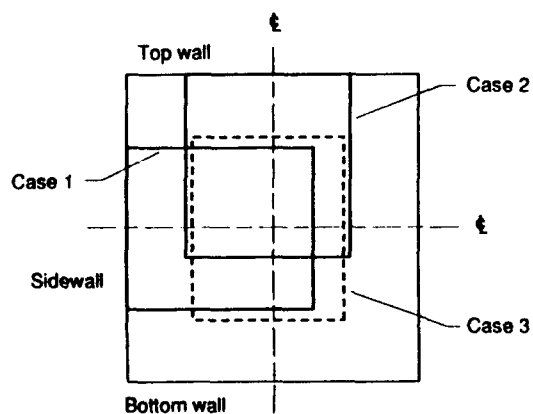
Figure 19.- Flow vitiates in  $H_2$  combustion-heated and electric arc-heated scramjet test facilities.



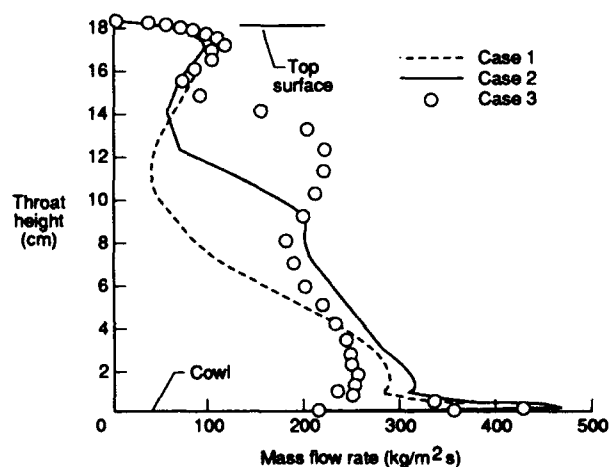
(a) Mach number contours at the exit of the 2-D contoured nozzle.



(b) Mach number contours at the exit of the square-cross-section contoured nozzle.



(c) Scramjet inlet orientations at the exit of the 2-D contoured nozzle.



(d) Unit mass flow rate profiles on the centerline of the inlet throat.

Figure 20.- Flow irregularities caused by nozzle design.

## Discussion

### RAMETTE

About subscale scramjet, it seems that there is a minimum length limitation due to the kinetics of the supersonic combustion at high Mach number. Could you comment about this minimum length order?

### AUTHOR'S REPLY

First considerations of minimum length will depend on the scale of the scramjet and the corresponding length required for the fuel/air mixing to occur with the particular mixing techniques employed. As you suggest, however, the actual "minimum length" for the mixed fuel to burn may be greater than that required for fuel/air mixing due to the flow kinetics. A positive factor in reducing the kinetics problem could be higher combustion entrance pressure at the higher Mach numbers created either by higher inlet contraction ratios or by higher test facility total pressure (pressure-scale relationship). In the final analysis, however the available subscale data will have to be predicted using CFD and CFD will be used to aid in the assessment of the performance of larger scramjets, particularly at higher Mach number.

### MARGUET

In view of the existing state of research on supersonic combustion, how accurately can you predict the performances at Mach 8, 12 and 20? Is it of the order of a few percent points at Mach 8 and 100% at Mach 20?

### AUTHOR'S REPLY

I understand that your question is in reference to the figure which you presented this morning which showed much less tolerance for uncertainty in scramjet performance at high Mach numbers than at the lower Mach numbers. As I noted in my presentation, a significant quantity of scramjet performance is in existence at Mach numbers below 8, but there is much less data at higher Mach numbers. I believe we feel comfortable with performance prediction capabilities below Mach 8. As scramjet-related pulse facility data become more abundant, we can assess our quantitative prediction capability in the high Mach number range more accurately than is possible at the present time.

### NINA

How to enhance fuel/air mixing in supersonic combustion? Should we look for a combination of mechanisms (shock waves, jet penetration, ...)?

### AUTHOR'S REPLY

At Langley, we use criteria developed by Anderson several years ago which relates fuel/air mixing for a given fuel equivalence ratio to orifice size and spacing and to the air gap which is to be fueled. These criteria exist for both normal (to the airflow) and parallel fuel injection. Enhancements to exceed this degree of fuel/air mixing would no doubt employ combinations of the mechanisms you mention, as has been discussed in the literature.

### CAZIN

Pour un "Program Manager" responsable d'essai en vol avec un nouveau moteur, pensez-vous qu'il soit possible de faire des essais en vol, sans avoir auparavant des essais au sol dans des conditions réalistes? Il ne suffit pas de vérifier les performances pendant quelques millisecondes, il faut aussi vérifier le comportement du moteur en ambiance thermique, l'injection, la

régulation ....

AUTHOR'S REPLY

I believe the 2.44-m HTT at Langley can be used to conduct such flight-qualifying tests of very large scale scramjets (flightweight hardware) up to Mach 7. I don't see the use of pulse facilities for such large scale testing of scramjets at the higher Mach number except possibly the testing of scramjet combustors in a facility such as RHYFL. And, as you mention, this would only be for a few milliseconds. Hence, flight-qualifying of a scramjet to very high Mach numbers will probably consist of an extremely close partnership role between all forms of experimental data and computational methods coupled with a very gradual flight expansion program which will be re-coupled with computational methods.

WINTERFELD

Is there any information on the problem of reaching the steady-state situation in the pulse facilities for supersonic combustion? The temperature of the wall plays a key role for the ignition. The testing times are low.

AUTHOR'S REPLY:

This is a big issue. There is a computational paper to be presented at ORLANDO to determine the flow time necessary to reach a steady state situation.



# AIRBREATHING PROPULSION FOR SPACE TRANSPORT

## New Concepts, Special Problems and Attempts at Solutions

H. KÜNKLER

IABG

Einsteinstraße 20, 8012 Ottobrunn  
Federal Republic of Germany

92-16953

### SUMMARY

The design requirements of airbreathing propulsion for space transport application strongly depend on the particular mission demands and differ markedly from those of conventional airbreathing propulsion systems. Especially the low thrust densities and high thermal loads at high Mach numbers demand a systematic approach to design and selection of possible propulsion concepts.

This paper intends to discuss main problems of propulsion system concepts and of their development/realization as well as to present attempts for possible solutions.

### 1. INTRODUCTION

A hypersonic technology programme following an aerodynamic space transportation concept using airbreathing propulsion and/or constituting a hypersonic aircraft could become a technology vehicle for Europe in the next decades. Since this technology vehicle requires innovative solutions throughout it would justify longterm engagement, creating a series of subsequent high technology developments in important existing fields of endeavour.

Apart from development of technologies for a hypersonic vehicle the development of appropriate propulsion systems is of prime importance.

### 2. ADVANCED HYPERSONIC PROPULSION

Two main areas of hypersonic flight are "Hypersonic Transport" and "Space Transportation Systems".

Besides next generation of supersonic civil aircraft (SST) the global air traffic demand for much faster going aircraft could possibly lead to the development of a HST in the medium/far future. The more relevant use of a hypersonic aircraft/propulsion technology will be in space transportation systems.

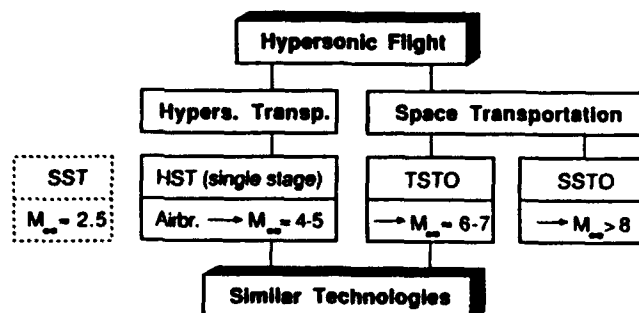


FIG. 1: Areas of Hypersonic Flight

Airbreathing propulsion should be applicable up to flight Mach numbers shown in FIG. 1 for the HST resp. the twin stage to orbit (TSTO) or the single stage to orbit system (SSTO).

Technologies needed for realization of a HST-vehicle for global distances and of the TSTO booster stage are similar within a lot of aspects. Therefore this paper will discuss the process of design optimization for the propulsion system of a TSTO-system with a long-range-cruise option.

The aerodynamic first stage of a TSTO with its airbreathing propulsion system and the rocket propelled second stage combine the advantages of both, aircraft and rocket without forcing to much of a compromise.

Airbreathing propulsion of a SSTO should perform up to very high flight Mach numbers. The supersonic combustion ramjet (SCRamjet) theoretically could manage this but even last 40 years of development are not promising that it will do it with a positive overall system pay-off in the near future.

### 3. MISSION TASK

The twofold mission task of the first stage of a TSTO-system like Sanger is shown in FIG. 2. Besides performing the ambitious accelerated climb to stage separation at high Machnumber also an ambitious cruise phase could be required to avoid dependence on an extra-European take-off site or to enlarge the launch window.

Based on well known experience, development phase should be planned taking into account that component shortfalls will occur (drag, weight, thrust, SFC). Minor or larger parts of the cruise phase are to be abandoned if the small payload ratio which is very sensitive to component shortfalls, is not allowed to diminish.

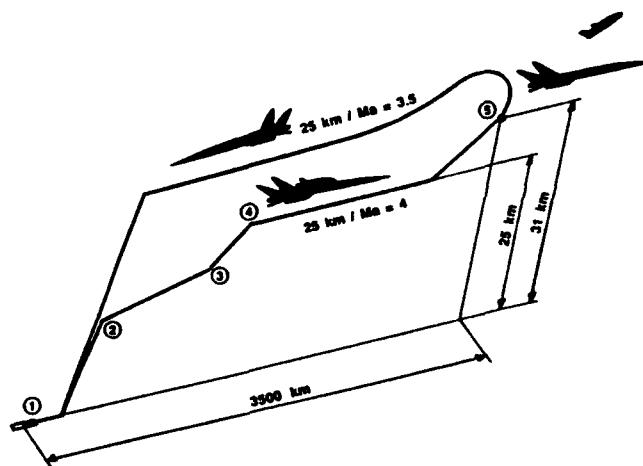


FIG. 2: Twofold Mission Task of a TSTO

Therefore the following priority of design compromise must be given for both the vehicle and the propulsion system:

1. Absolute design priority given to accelerated climb phase.
2. Cruise capability added by dimensioning fuel capacity.

Taking into account the influence of staging Mach number on engine and vehicle design (heat protection, aerodynamic compromise, engine size, etc.) the optimum Mach number of stage separation respectively switch-over to rocket mode will be limited to:

TSTO: airbreathing up to  $M_{\infty} \approx 6 - 7$

SSTO: airbreathing up to  $M_{\infty} \approx 8$ .



#### 4. SPECIFIC REQUIREMENTS TO PROPULSION SYSTEM

The mission induced requirements differ markedly from those of conventional airbreathing propulsion systems. The three most demanding requirements are defined in FIG. 3.

Especially low thrust density and high thermal load of airbreathing propulsion at high Machnumbers demand a systematic approach to design and selection of possible propulsion concepts with lower priorities given to other design aims of the system.

##### MOST DEMANDING REQUIREMENTS

- o Sufficient Thrust at Take-Off and for Transonic Acceleration
- o Applicability up to  $M_\infty > 6$
- o High Thrust Density at High Mach Operation

FIG. 3: Requirements to Propulsion System

During accelerated high-Mach flight in the dense atmosphere an aerodynamic space transport will obviously be driven by a ramjet. For take-off, subsonic climb and acceleration to a suited switch-over point the ramjet is to be combined with any kind of a turbojet or with a rocketmotor.

FIG 4 shows the airflow specific thrust of a ramjet vs. flight Mach number. The slopes have been calculated for poor as well as for fuel-rich combustion with the given maximum heating temperatures. To get high thrust density even at the upper Mach numbers combustion should operate at nearly stoichiometric fuel/air ratio. To avoid extreme thermal loads at combustor and nozzle ( $> 3000$  K at  $M_\infty = 7$ ) gas temperature could be limited to a reasonable  $T_{tmax} = 2600$  K by fuel-rich combustion offering a further increase in thrust density.

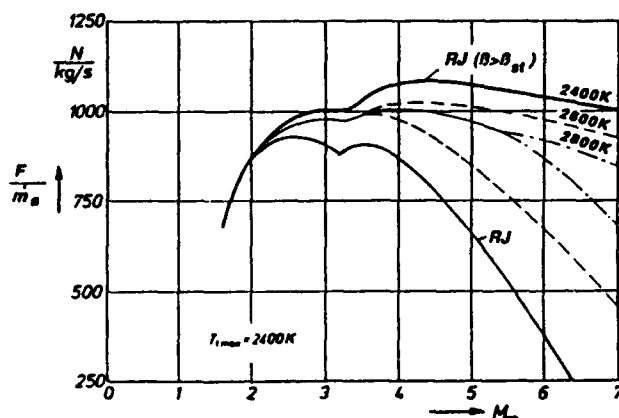


FIG 4: Airflow-Specific Thrust of Ramjet

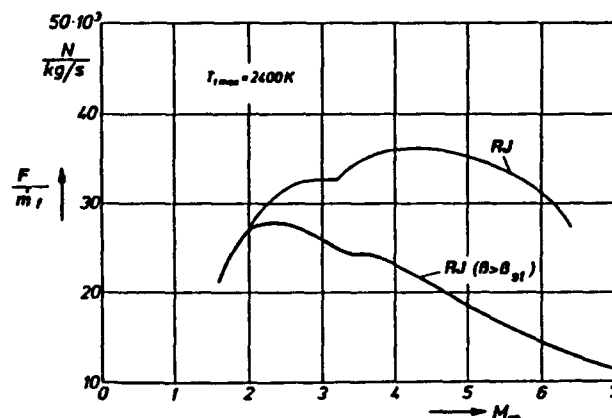


FIG. 5: Fuel-Specific Thrust of Ramjet

Fuel-specific thrust, "specific impulse", gets markedly worse if combustion is fuel-rich (FIG. 5). Therefore this mode will not be allowed during cruise. During accelerated climb however the increased fuel flow will more or less be compensated by higher thrust density, especially at those peak Mach numbers where thrust demand is dimensioning the engine size. Drag losses and gravity losses will decrease.

Larger hydrogen fuel flow furthermore offers a larger heat sink to match increasing cooling problems at high Mach numbers.

## 5. PROPULSION SYSTEM CONCEPTS, PROBLEMS AND IDEAS

### 5.1 Parallel vs. Integral Arrangement

In FIG. 6 schematics are shown as examples only of two different arrangements combining a ramjet with a turbojet.

The upper figure shows a parallel arrangement. Both engines the turbojet and the ramjet use the same air inlet but different nozzles. At high Mach operation the turbo engine bay is hermetically sealed against hot through flow (ram air temperature  $> 2000$  K at Mach 7) and ventilated with air which is precooled by heat exchange with the ramjet fuelflow.

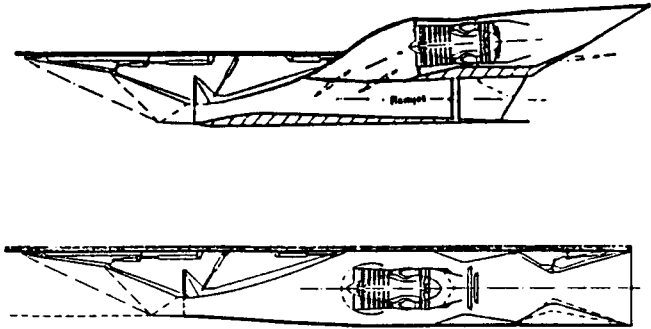


FIG. 6: Turbo-Ramjet Configurations /Lit. 3/

The bottom figure shows an integrale combination offering a nearly continuous transition of a mixed turbo/ramjet mode to a pure ramjet mode at high Mach operation. Throughflow of the ramjet burner will be realized even at take-off and low flight Mach numbers by the turbo engine working as ejector. Nozzle pressure ratio is slightly supercritical at take-off and will increase rapidly with flight Mach number.

When using it as an ejector the turbo engine of the integral arrangement (bottom) for same thrust at take-off and at transonic speed can be dimensioned about 25 % to 30 % smaller/lighter as almost double the airflow is reheated compared to the parallel arrangement (upper figure). A slightly increased SFC at low-Mach operation will easily be compensated.

On the other hand ramjet burner and surfaces of ramjet air duct, that are to be actively cooled at high Mach operation, could be dimensioned smaller of the parallel arrangement compared to the integral one.

In an only coaxial arrangement, with the turbojet and the ramjet not operating in an integral mode during take off and at transonic speed, the turbojet of course has to be sized to about the same dimensions of the parallel arrangement.

To make provisions for sealing the turbo engine and to ventilate it with precooled air always is necessary at high Mach operation. This is independent of arrangement and of the type of turbo engine used.

### 5.2 Fully Integral Turbo-Ramjet

In the fully integral turbofan-ramjet combination the rammed hot airflow passes the windmilling fan of the turbo engine even during pure ramjet mode operation. To be run up to flight Mach numbers near to  $M_\infty = 7$  the high temperature fan now has to resist air temperatures of more than 2000 K. Cooling technology well known of turbine blades is not easily to be transferred to blades of a fan.

The fan will be powered by an air-breathing turbo engine or by a turbine driven with rocket exhaust gases (turbo rocket, TR) or with heated hydrogen (turbo expander cycle engine, ATE).

Fig. 7 shows the MTU's Hyper Crisp with its air-breathing core engine driving the counterrotating variable-pitch fan.

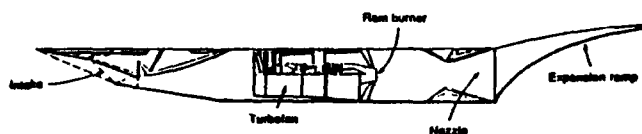


FIG. 7: Turbofan-Ramjet Hyper Crisp /Lit. 4/

At high Mach operation the core engine is to be sealed and ventilated with cold air.

If an air/fuel heat exchanger is integrated in front of the core engine, the fan could be run with a fan pressure ratio  $FPR > 1$  at flight Mach numbers up to  $M_\infty = 4.5$  instead of producing pressure losses only after the core has been run down and sealed at about  $M_\infty \approx 3$ . This could offer good advantage for fuel consumption of the Hyper Crisp if used in a hypersonic transport.

Limiting the peak flight Mach number to a value well below  $M_\infty = 6$  a turbo rocket or a turbo expander cycle engine could be run without air/fuel heat exchange if the high temperature fan and all cases are made out of carbon materials. Same as the Hyper Crisp with air intercooling they could be used with advantage as propulsion systems of a HST.

### 5.3 Heat-Exchanger Key Technology

Need of an air/fuel-cooler is evident with every type of turbo engine of a hypersonic propulsion system for flight Mach numbers beyond  $M_\infty = 5$  to 6. Size and arrangement depends on the airflow to be cooled, the effectiveness asked for and on integration conditions.

A heat exchanger should absolutely have an axisymmetric arrangement (FIG. 8) if installed upstream of a turbo engine or integrated into its flow path. This arrangement is of advantage even of an intercooler cooling down air for the turbine or for ventilation, as a lot of problems during development of a heat exchanger for high temperature gradients are based on the absence of rotational symmetry otherwise.

Elliptical tubes under development at MTU could predominantly be suited as matrix of such a heat exchanger. Its development is to be accounted for key technologies independent of a special engine concept as air inlet and material work are.

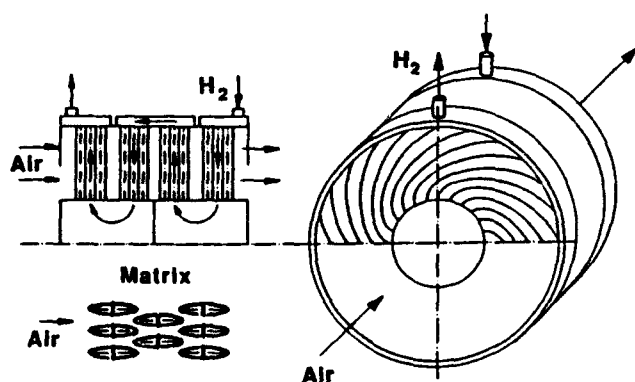


FIG. 8: Axisymmetric Heat Exchanger

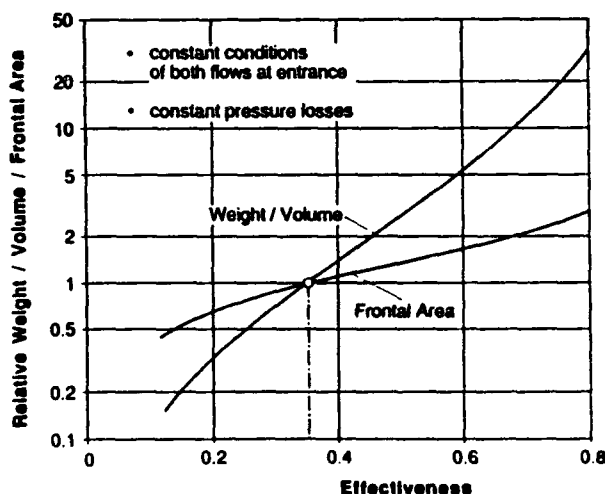


FIG. 9: Influence of Heat Exchanger Effectiveness on Weight, Volume and Frontal Area

The influence of heat exchanger effectiveness on weight, volume and frontal area is shown in FIG. 9 for constant conditions of both flows at heat exchanger entrance and for constant pressure losses.

Concerning weight and size of the heat exchanger as well as pressure losses and wall temperatures of the tubes, high heat exchange effectiveness intentionally is to be abandoned. This especially is important for the first rows of tubes where the wall temperature could eventually be homonized by a ceramic coating in the stagnation point area.

#### 5.4 Effects of Air Precooling on Turbojet Size

Thermal problems of turbo engines at high flight Mach numbers can markedly be reduced by integrating a  $H_2$ /air heat exchanger upstream the low pressure compressor. Engines then always feel a lower "apparent" flight Mach number.

The main effects of air precooling are listed in FIG. 10.

FIG. 11 shows in the first and in the second configuration integral combinations of a turbo-ramjet. While the upper one is the same as shown in FIG. 5 the turbojet of the second configuration is installed downstream of a  $H_2$ /air heat exchanger.

#### EFFECT OF AIR PRECOOLING

- o Increased flow density at compressor inlet  
→ Increased engine air flow
- o Lower power demand for compression
- o Lower temperature at compressor exit  
→ Increased Mach capability

FIG. 10: Main Effects of Air Precooling

As the large fuel flow for heating the total air flow within the ramjet combustor is available as heat sink for precooling, the heat exchanger can be designed for an unusual low effectiveness of less than 40 % in the design point. This will save weight, volume and pressure drop (see FIG. 8).

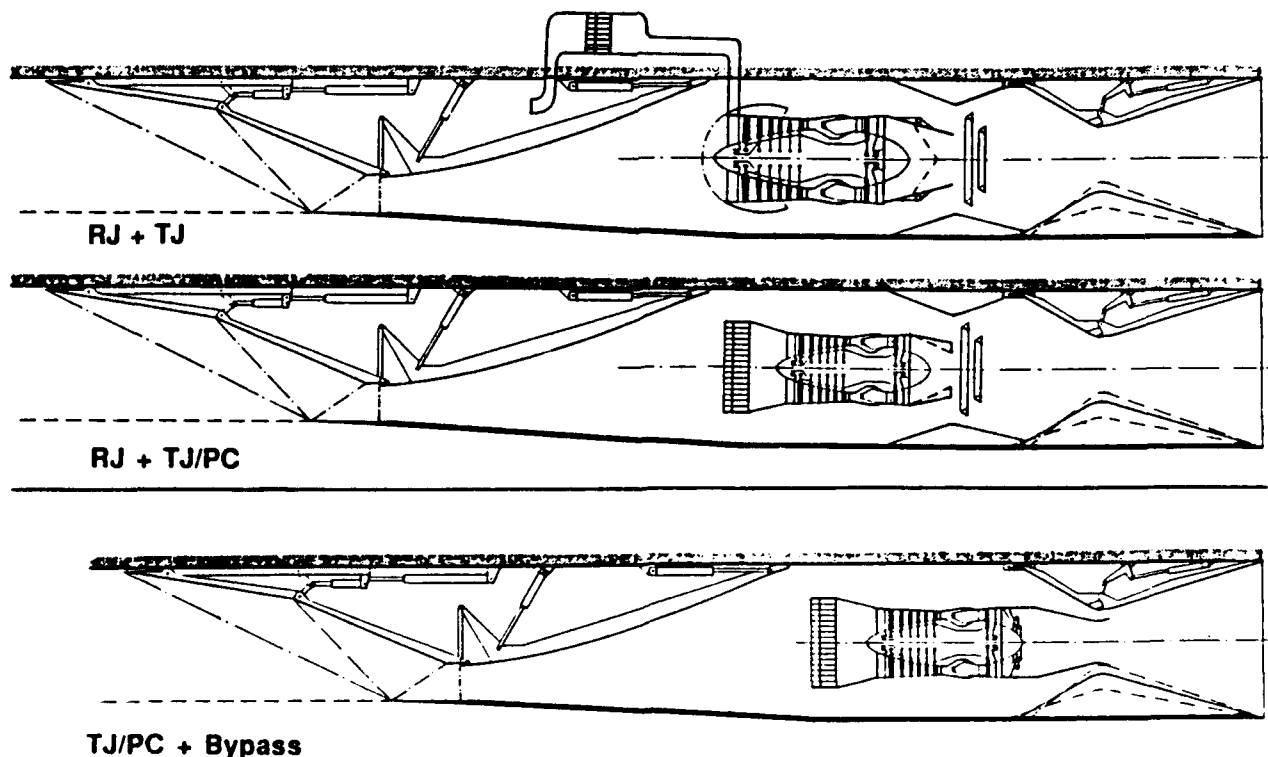


FIG. 11: Turbo-Ramjet and Precooled Turbojet

The following advantages of this configuration can be summarized:

1. For same total airflow and same thrust at transonic flight the turbo engine now can be dimensioned smaller by some 30 % depending on the effectiveness of the heat exchanger and when compared to the turbojet of the upper figure. That means about half the size of the turbojet when not being used as an ejector for the bypass/ramjet air (parallel arrangement shown in FIG. 5 or coaxial arrangement not operating in an integral TJ/RJ mode).
2. The turbojet can now be operated at full power up to a flight Mach number of about  $M_\infty = 4.5$  and improve thrust and SFC of the ramjet.
3. Beyond this flight Mach number the turbojet should continuously be throttled back limiting the temperature at compressor exit to a constant value of conventional engine technology and offering power supply to the secondary power system of the vehicle.
4. No hermetical sealing provisions at entrance and exit of the turbojet. The  $H_2$ /air heat exchanger needed for intercooling the air ventilating the sealed turbo engine of upper configuration during ramjet operation now is replaced by the same larger axisymmetric precooler.
5. If boundary layer of the fuselage forebody is sucked in by air intake and will not be spilled through the bypass channel then the heat exchanger will smoothen down the flow distortion in front of the turbojet. A boundary layer bleed channel therefore will not necessarily be used.

The influence of jet mixing and precooling on the propulsion system weight is shown in FIG. 12. It can be seen that the turbojet related weight by this measures could remarkably be reduced. In the case of the precooled turbo-ramjet the additional heat exchanger weight will mainly be overcompensated by the smaller turbo engine and by the omission of sealing provisions and of the boundary layer bleed channel. Weight saving by a simplified secondary power system is not included.

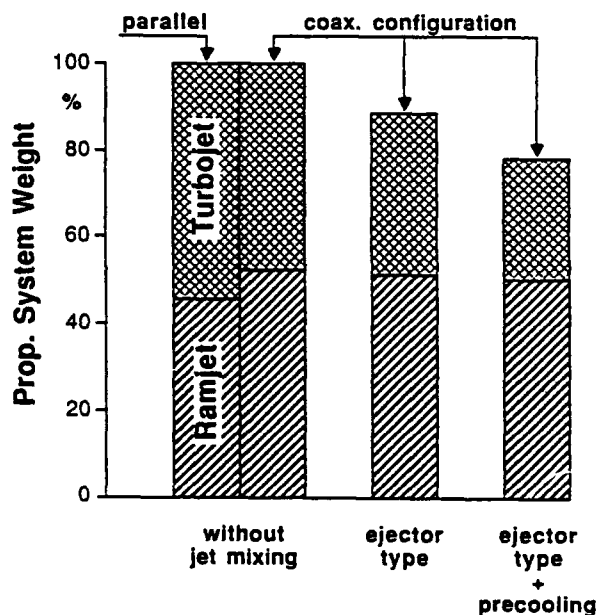


FIG. 12: Influence of Jet Mixing and Precooling on Turbo-Ramjet Weight (w/o fuel)

### 5.5 Precooled Turbojet with Unheated Bypass

The bottom FIG. 11 shows a precooled turbojet with reheat and with an unheated bypass passing surplus air to the outer nozzle throat at transonic flight conditions and up to about  $M_\infty = 4$ .

The use of this engine type in an aerodynamic space vehicle launcher up to a staging Mach number of about  $M_\infty = 6.5$  has been discussed in detail in /1/, also showing the savings in mission fuel compared to other turbo-ramjet configurations.

## 5.6 Air-Breathing Rocket

In a single stage to orbit vehicle (SSTO) the air-breathing rocket (FIG. 13) could accelerate the vehicle up to  $M_\infty > 8$  operating in air-breathing mode, if air inlet and heat exchanger are designed to be submitted corresponding high air temperatures.

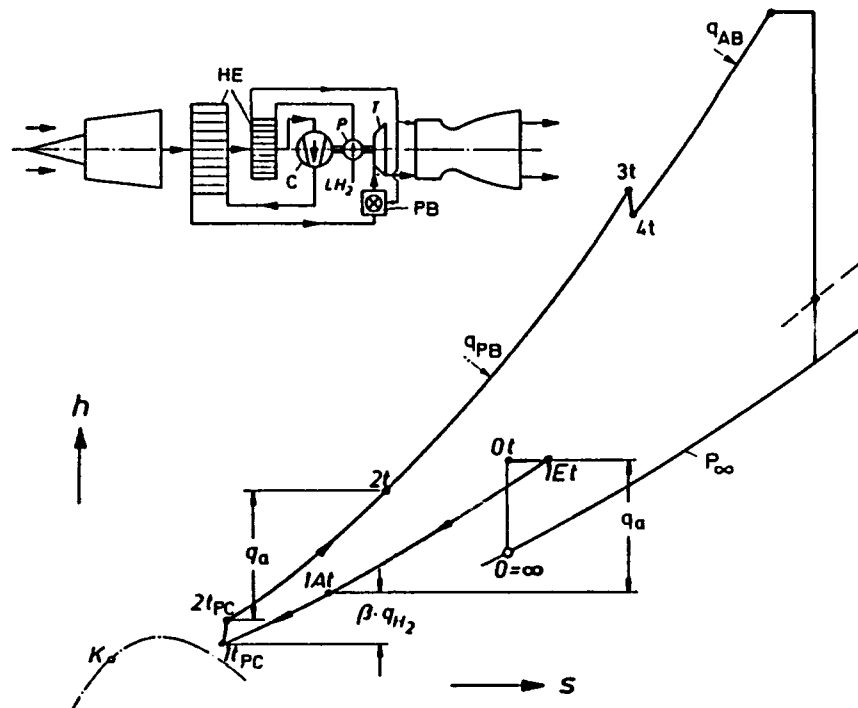


FIG. 13: Air-Breathing Rocket /Lit. 5/

In this engine type rammed air at first is cooled down by heat exchange with the cold air after leaving the compressor. Compression close to the boundary phase curve results in a considerable reduction in compression effort. Early calculations for cycle optimization have shown (Lit. /1/) that liquefaction of the air and compression in liquid phase will not pay off. Combustion in the high-pressure chamber preferably is somewhat fuel-rich.

While being very effective at medium and high flight Mach numbers this engine type will offer an unsufficient thrust at take-off and initial climb. The following procedure could be of advantage:

1. Sled assisted acceleration to about 250 m/s.
2. During take off and subsonic climb through the humid lower atmosphere, due to the icing danger, both precoolers are not to be through flown by liquid hydrogen and compressed air acting as heat sinks.

Dimensioned to less than half the flow capacity of the precooled turbojet shown in FIG. 11, the turbomachinery during this phase will operate as a conventional turbojet engine at partload conditions ( $\approx 70\%$  reduced rotor speed). To fulfil the initial-climb thrust demand a small LOX-flow is to enrich the somewhat fuel-rich combustion in the high-pressure afterburner.

3. After climb out to an altitude of about 8 km at first the  $H_2$ /air precooler and then the air/air heat exchanger will be switched on. Air flow and nozzle pressure ratio now will increase to more than three times the initial value.
4. With increasing flight Mach number preburner heating has continuously to be throttled back.

The nozzle throat downstream the high-pressure afterburner even at full-power operation needs to be controlled within the same extension as we are used of conventional ramjets. The reason is the overall pressure ratio of the total turbopart ( $p_{t4}/p_{t1E}$ ) being nearly independant of the flight Mach number and supercharging the pressure ratio of the conventional ramjet cycle by a factor of about 10.

While this engine type could offer high thrust density and a good fuel consumption especially at high Mach operation, the major problem will be that it needs a more efficient air/air heat exchanger of much larger size/weight than the engine types shown above.

## 6. INTERACTION OF VEHICLE, PROPULSION AND MISSION TAYLORING

When tailoring the design of vehicle, of propulsion system and of optimum flight trajectory to the mission requirements of a HST or of a TSTO booster stage we have to recognize that these three are stronger interconnected with each other than the design of subsystems of conventional aircraft we are used to be. Therefore any isolated optimization will lead to a nonharmonized overall solution.

### 6.1 Flight Trajectory

FIG. 14 shows a simplified but typical flight trajectory of a TSTO booster stage. It has been calculated for a constant ratio of total pressure/total temperature at exit of air intake. To limit induced drag during transonic flight where aircraft drag and engine installation losses are large, subsonic climb should not lead to dynamic pressure below 20 kPa.

For a TSTO system which will perform only a few launches/year, noise requirements to conventional airliners should not necessarily be design driving. Even with respect to European autonomy TSTO launches could perform in the south of Spain and go out over the Mediterranean Sea.

Flight trajectory/aircraft should climb quickly through the dense ozone layer. If a cruise phase requirement is superposed on a TSTO-launch (see design priorities given in chapter 3) then cruise out and cruise back could be flown in a flight altitude of about 25 km, the minimum altitude for a long range HST-cruise.

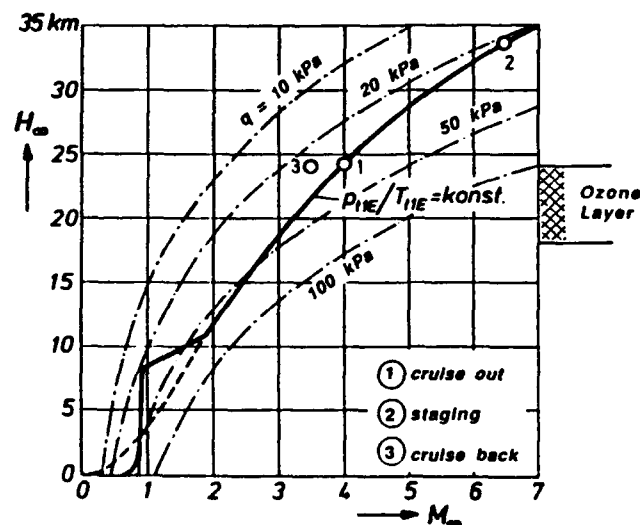


FIG. 14: Flight Trajectory

With increasing flight Mach number the trajectory should climb to lower dynamic pressure. This will cause the angle of attack growing up to values beyond the L/D-maximum important for a long range cruise phase (HST).

But for an accelerated climb of the TSTO booster stage maximum L/D is not permitted to be a main goal for overall vehicle design. In this case the influence of wing loading and of flight trajectory on the design of air intake and nozzle (dimensions and operational conditions) and on transonic drag will be of more importance.

## 6.2 Inlet Capture Area Augmentation

FIG. 15 shows increasing angle of attack vs. flight Mach number for the a.m. flight trajectory and for a design wing loading of about  $m_0/A_{tot} \approx 650 \text{ kg/m}^2$ . This has two main effects:

1. Growing up precompression by fuselage/wing will limit flow Mach number  $M_0$  at air inlet to lower values. The intake system is to be designed for little above  $M_0 \approx 4$  only even if the maximum flight Mach number will exceed  $M_\infty = 6.5$ . This will lead to a better pressure recovery, ease construction and save weight of intake and nozzle system.
2. Augmentation of free stream capture area rapidly increases with angle of attack and flight Mach number (FIG. 16). This will lead to smaller dimensions/lower weight of intake and nozzle system as thrust demand at high Mach operation is dimensioning for these ramjet components. Furthermore a lot of installation drag of the propulsion system will be saved during transonic flight.

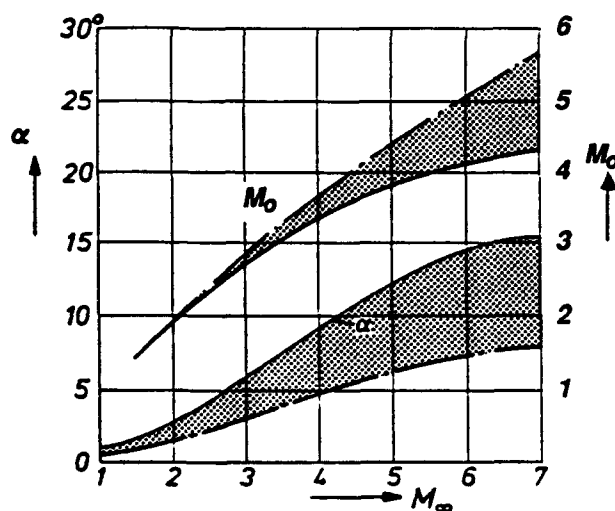


FIG. 15: Angle of Attack  $\alpha$  and Inlet Mach Number  $M_0$

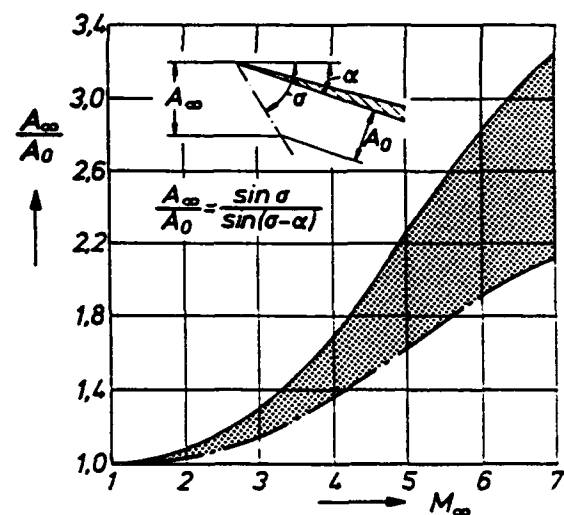


FIG. 16: Augmentation of Free Stream Capture Area

The dash-dotted slopes show minor positive effects if angle of attack would be decreased to half the value by selection of wing loading and flight trajectory.

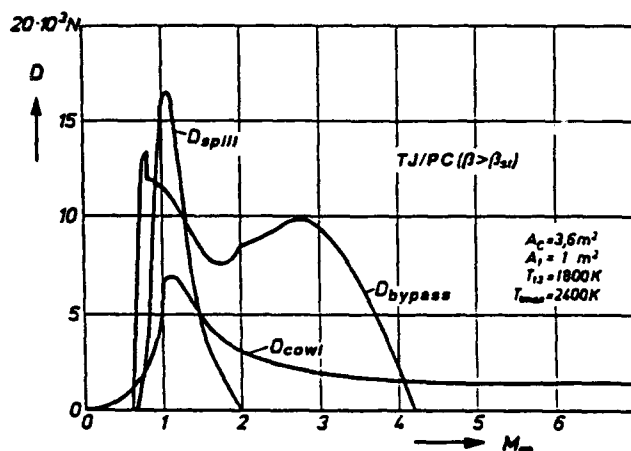


### 6.3 Installation Drag

Installation drag of the propulsion system mainly consists of three parts:

- drag of splitting the forebody boundary layer,
- inlet drag (spillage drag, bypass drag, cowl drag, bleed drag),
- propulsion related afterbody drag.

1. Significant drag of splitting the forebody boundary layer upstream the air intake could be avoided, if configuration of intake system and arrangement of the turbo engine in the propulsion system permit the boundary layer to be sucked in (e.g. all configurations of FIG. 11).
2. The three a.m. parts of inlet drag are plotted in FIG. 17 vs. flight Mach number of the engine configuration at bottom of FIG. 11. The corresponding geometrical/aerodynamical areas are also shown.



The extremely sensitive spillage drag can not be avoided at transonic flight due to geometrical reasons of construction.

The less sensitive bypass drag disappears at  $M_{\infty} \approx 4$ , when the turbojet takes the whole inlet airflow. If bypass air flow would be kept out of the intake, then spillage drag would be increased especially at transonic flight by values of about three times the bypass drag. Therefore the integration of a bypass channel along the turbo engine is not to be abandoned in most of hypersonic propulsion systems.

Ramp bleed drag has been neglected in FIG. 17 since it was supposed that shock system could be stabilized by the bleed of only a small part of the boundary layer at ramp edges.

Cowl drag is not critical especially as it offers additional lift.

3. Propulsion related afterbody drag mainly depends on nozzle design. It will be reduced markedly by the expansion of bypass air flow at transonic flight.

If no bypass would be integrated about one third of uninstalled thrust could be eaten up by inlet spillage drag and afterbody drag at this flight condition.

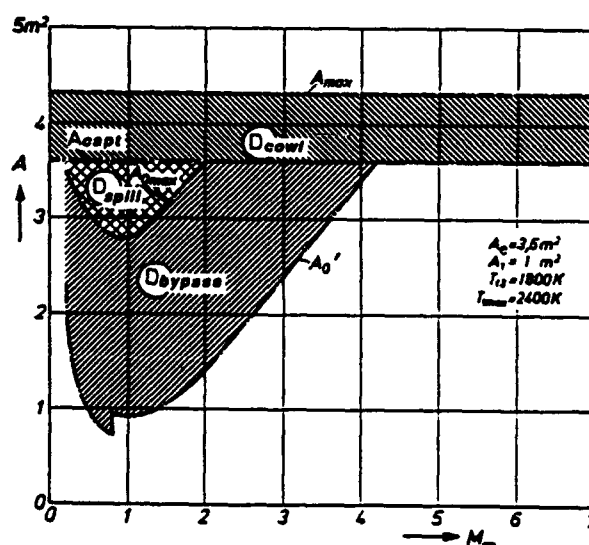


FIG. 17: Inlet Drag of TJ/PC and Corresponding Areas

## 6.4 Thrust Dimensioning Procedure

In FIG. 18 the vehicle drag divided by the number of engines is plotted vs. flight Mach number along flight trajectory  $p_{tE}/T_{tE} = \text{const}$ . Thrust slopes of the turbo ramjet and of the precooled turbojet (FIG. 11 upper resp. bottom configuration) show that transition to fuel-rich combustion could be necessary at high Mach operation if oversizing of the ramjet (weight, transonic drag) shall be avoided and though the effects of high angle of attack were taken into account.

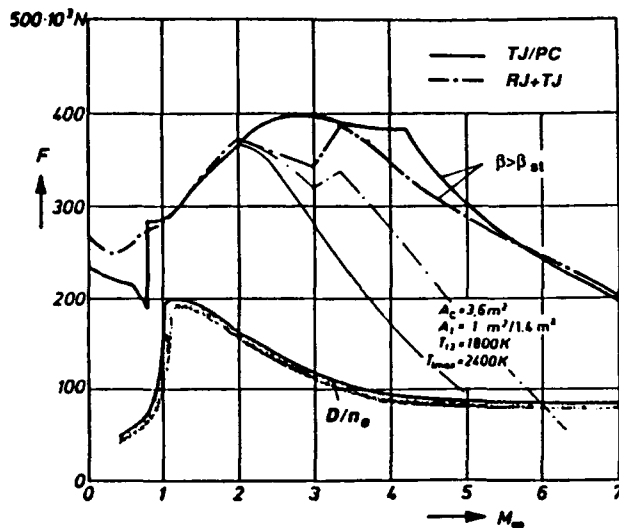


FIG. 18: Vehicle Drag and Fully Installed Thrust of RJ + TJ and TJ/PC

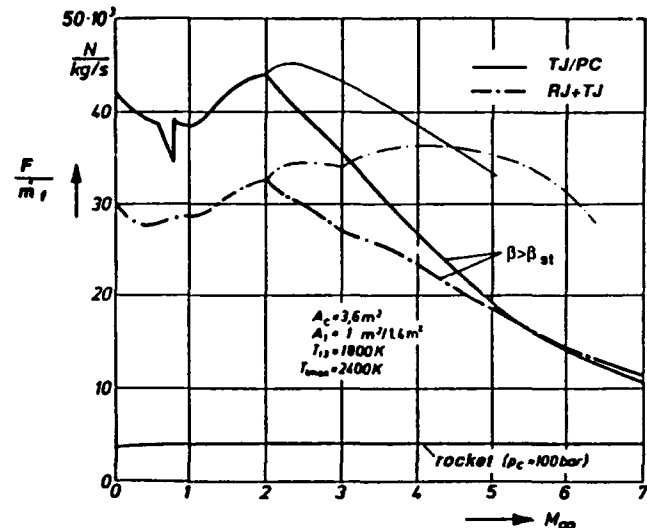


FIG. 19: Fuel-Specific Thrust (fully installed)

Due to icing danger the precooled turbojet has to perform take-off and subsonic climb without switching on the precooler.

Corresponding slopes of fuel-specific thrust are shown in FIG. 19. Concerning a comparable low maximum reheat temperature limit  $T_{tmax} = 2400 \text{ K}$  the optimum switch-over point to fuel-rich combustion was calculated for  $M_{\infty} = 3.2$  resp.  $M_{\infty} = 5.4$  in an overall optimization attempt including thrust dimensioning (engine size) and vehicle design (wing loading).

Pushing forward the temperature limit will shift the switch-over Mach number to some higher values.

An arbitrary oversizing of the installed thrust not oriented to the specific character of an aerodynamic booster stage with air-breathing propulsion could launch the vehicle out of the dense atmosphere in an unfavourable way. This would lead to wrong assessing the thrust/weight ratio and specific impulses of the propulsion system and the aerodynamic vehicle design.

To show the correlation between optimum installed thrust and ascent trajectory as an example the SÄNGER-mission was calculated with a predesigned system approach along two different ascent trajectories.

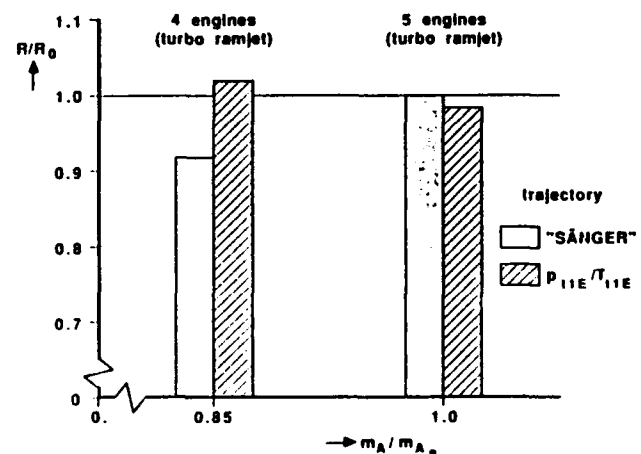


FIG. 20: Correlation of Installed Thrust, Flight Trajectory, Range, Launch Mass

A small disadvantage has been found with the a.m. flight trajectory compared to the original one. In FIG. 20 the range is plotted for both trajectories and the original overall vehicle design. With the flight trajectory of FIG. 14 leading to higher altitudes than the preliminary SÄNGER trajectory at high Mach operation ( $\rightarrow \infty$  and  $A_{\infty}/A_0$  increased) thrust will be oversized.

Left columns have been calculated with 20 % lower installed thrust. With the a.m. flight trajectory the vehicle design could be scaled down by 15 % fulfilling all range requirement while the scaled down design could not get the required range on the original ascent trajectory as acceleration at high Mach operation was too slow now with the 20 % lower thrust.

## 7. RESUMEE

To give an first idea of the complexity resp. development risk of the different propulsion system concepts discussed in this paper when compared to their performance, FIG. 21 shows an authors attempt to assess this problem. The assessment was based on the application in a TSTO system.

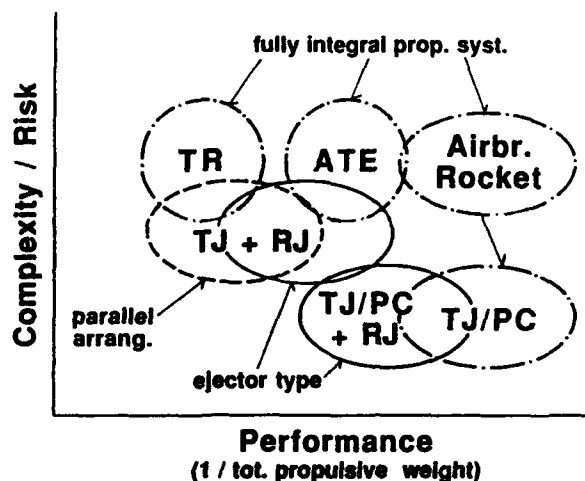


FIG. 21: Propulsion System Concepts  
(TakeOff to  $M > 6.5$ )

Main Problems and ideas are to be summarized:

### 1 TSTO SYSTEM:

Combines advantages of air-breather/rocket and aircraft/reentry vehicle without forcing to much of compromise.

### 2 TWOFOLD MISSION TASK OF TSTO BOOSTER STAGE:

Design priority to be given to accelerated climb phase.

### 3 EXTREME INTERACTION OF VEHICLE, PROPULSION, FLIGHT TRAJECTORY:

Optimization of isolated subsystem misleading.

### 4 MOST DEMANDING UNCONVENTIONAL REQUIREMENTS:

Applicability up to  $M_{\infty} > 6$ .  
High thrust density at high Mach operation.

### 5 HIGH TEMPERATURE LOAD AT HIGH MACH OPERATION:

Active cooling of combustor, nozzle and partially of inlet duct with  $H_2$ -fuel.  
Ventilating of turbo eng. with intercooled air.

### 6 THRUST DENSITY AT HIGH MACH OPERATION:

Increased by fuel-rich combustion.

**7 AIR LIQUEFACTION**

Not relevant for optimized cycle

**8 SCRAMJET**

Positive overall system pay-off not to be seen in the near future even if integrated into a dual-mode combustor.

**9 RAMJET SIZE/WEIGHT SAVING:**

Augmentation of inlet capture area by enlarged precompression (high  $\alpha$  by appropriate wing loading and flight trajectory).

Fuel-rich combustion.

**10 TURBO ENGINE SIZE/WEIGHT SAVING:**

About 25 % at same transonic thrust by integral arrangement.

About one third additional by air precooling.

**11 INLET DESIGN:**

Design Mach number depending on  $\alpha$  (wing loading, flight trajectory).

Abandoning boundary layer splitter and bypassing the turbo engine will reduce inlet drag.

**12 HEAT EXCHANGER:**

Axisymmetric arrangement keeps down lot of development problems.

High effectiveness intentionally must be abandoned.

**13 KEY TECHNOLOGIES:**

- air intake
- H<sub>2</sub>-technology (fuel-rich comb.)
- heat exchanger
- high temperature materials

**14 SPIN-OFF FOR FUTURE AERO SPACE ENGINEERING:**

Much larger benefit from development of aerodyn./air-breath. launch system compared to not recoverable rocket system.

**REFERENCES**

/1/ H. Künkler:

The Effect of Air Precooling Prior of Compression in Air-Breathing Engines for a Space Vehicle Carrier

Thesis 1973 (German)

NASA TT F-16, 093, 1975 (Englisch)

/2/ H. Künkler/H. Kuczera:

Turbo-Ramjet Propulsion System Concepts for Future European Space Transport (SÄNGER)

Paper IAF-87-265, 38th IAF- Congress, Brighton/UK, Okt. 1987

/3/ D.E. Koelle/H. Kuczera:

SÄNGER, An Advanced Launcher System for Europe

Paper IAF-87-207, 38th IAF-Congress, Brighton/UK, Oct 1987

/4/ Flight International  
8. Oct. 1988

/5/ H. Künkler:

Luftatmende Strahlantriebe für Raumfahrzeugträger  
Technische Rundschau, Bern  
TR Nr. 49, 25. Nov. 1975

## TURBOJET POTENTIAL FOR HYPERSONIC FLIGHT

by  
 Jeffrey M. Stricker & Douglas J. Essman  
 Turbine Engine Division  
 Wright Research & Development Center (WRDC/POTA)  
 Wright-Patterson Air Force Base, Ohio USA 45433

INTRODUCTION

Over the past few years, interest in manned hypersonic flight has increased significantly. System studies historically have utilized ramjet power for high supersonic/low hypersonic speeds and supersonic combustion ramjets (scramjets) at higher speeds. The drawback of these types of propulsion devices is their inability to perform at takeoff and relatively low speeds. Therefore, for relatively low speed operation (Mach 0-3), a third form of propulsion is required. The turbine engine has typically been chosen for this role.

The disadvantages of a three mode propulsion system (turbojet-ramjet-scramjet) are the complexity, weight and costs which accompany it. Inlet and exhaust geometry variations required for proper integration play a major role. Propulsion weight is a key factor to maximize vehicle capability. When a propulsion device is not being utilized, it is dead weight to the aircraft system. Therefore, for reasons of simplicity, reduced system weight, and cost, it seems prudent to minimize the number of propulsion mode transitions required.

This paper will explore the utilization of the turbine engine for aircraft propulsion up to the scramjet transition. Examination of the uninstalled cycle performance is presented as well as an assessment of installed engine operation in a hydrogen fueled aircraft. Both non-afterburning and afterburning (A/B) turbine engines are compared to turboramjet and air-turboramjet (ATR) engines for a Mach 5 long duration cruise mission along with a pure acceleration mission, i.e., the turbomachinery is used to accelerate the vehicle to a Mach number where the scramjet can take over. From this assessment, a baseline engine configuration/cycle is defined for feasibility studies and critical technology identification. A discussion of the feasibility of the preferred concept from an engine component by component standpoint is provided as well as a discussion of technology risk compared to the state-of-the-art.

UNINSTALLED PERFORMANCE

To determine the desirability of turbomachinery at hypersonic velocities, it is useful to ascertain whether the turbine engine provides competitive uninstalled performance compared to devices more commonly considered for hypersonic flight. Four types of turbopropulsion devices were studied; a cooled non-afterburning (dry) turbojet, an uncooled afterburning (A/B) turbojet, a turboramjet, and an uncooled recuperated air-turboramjet (ATR) (Figure 1). In all cases, hydrogen was used for fuel. For turbomachinery operating above Mach 4, a fuel-air heat exchanger was used for cooling compressor bleed air. Fuel inlet temperature to the heat exchanger was assumed to be 800°F, simulating fuel usage for vehicle cooling. The turbine inlet temperature of the ATR was limited to 2050°F due to heat exchanger, fuel delivery and uncooled expander turbine material limitations. Maximum burner temperature was limited to stoichiometric combustion. Table 1 shows a comparison of the various cycles.

Figure 2 illustrates the performance of the cooled non-A/B turbojet, uncooled A/B turbojet, turboramjet, and ATR operating between Mach 5 and 6. Even with extremely high turbine temperature capability, the dry turbojet exhibits poor specific thrust performance relative to the other forms of propulsion. The afterburning turbine engine utilizing a more conservative turbine rotor inlet temperature (TRIT = 2800°F) is very competitive with the turboramjet and ATR in thrust performance and advantageous from a fuel consumption standpoint. The competitive performance of the ATR is primarily due to the higher nozzle pressure ratio which may not be useful in an actual application due to nozzle size limitations (Figure 2 assumes full expansion of exhaust gasses). In all cases, performance degrades rapidly as Mach number is increased.

It is envisioned that the weapon system transitions to the scramjet propulsion mode at a Mach number between 5 and 5.5. This is primarily because of performance degradation and material constraints for the turbomachinery as well as minimum Mach number capability for the scramjet. Component design sensitivities to performance for the dry turbojet were evaluated to determine the criticality of the design parameters (Figure 3). The most vital parameters to performance were burner efficiency and exhaust nozzle performance (CFG). The latter was found to be the most critical with a 3.8 percent reduction in net specific thrust for each percent loss in thrust coefficient. Rotating component efficiencies were found to be less critical. The baseline leakage was .5%. This small level of leakage tends to make percentage changes in leakage appear

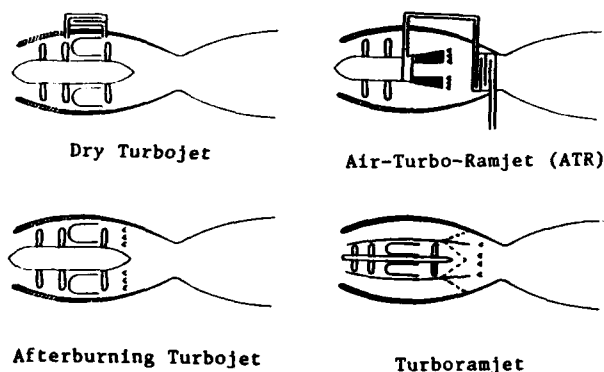


Figure 1 - Cycles Examined

92-16955

	A/B TJ	DRY TJ	TURBORAMJET	ATR
Pressure Ratio	10	10	10	5
Throttle Ratio ( $T_{4max}/T_4$ )	1.114	1.114	1.114	---
Main Burner Temp.	2800°F	4000°F	4000°F	---
Afterburner/Ramburner Temp.	Stoich	---	Stoich	Stoich
Efficiencies:				
Compressor	85%	85%	85%	85%
Main Burner	99%	99%	99%	99%
Turbine	85%	85%	85%	70%
Afterburner/Ramburner	95%	---	90%	---
Cooling:				
Turbine Stator	0.0%	5.5% <sup>1</sup>	5.5% <sup>1</sup>	0.0%
Turbine Rotor	0.0%	6.0% <sup>2</sup>	6.0% <sup>2</sup>	0.0%
Exhaust Nozzle	15% <sup>3</sup>	10% <sup>3</sup>	10% <sup>3</sup>	5%
Transition Mach Number	---	---	4-5	---
Pressure Losses:				
Main Burner	9%	9%	9%	9%
Rear Duct	1% (cold) <sup>4</sup>	4%	4% (cold) <sup>4</sup>	4% (cold) <sup>4</sup>
Gross Thrust Coefficient	.985	.985	.985	.985
Engine Thrust/Weight	10	10	10	10

- 1 - Varied to give 2800°F  $T_{metal}$   
 2 - Varied to give 2700°F  $T_{metal}$   
 3 - Compressor interstage bleed  
 4 - Hot loss is a function of exhaust temperature

Table 1 - Baseline Cycle Comparison (Sea Level Static)

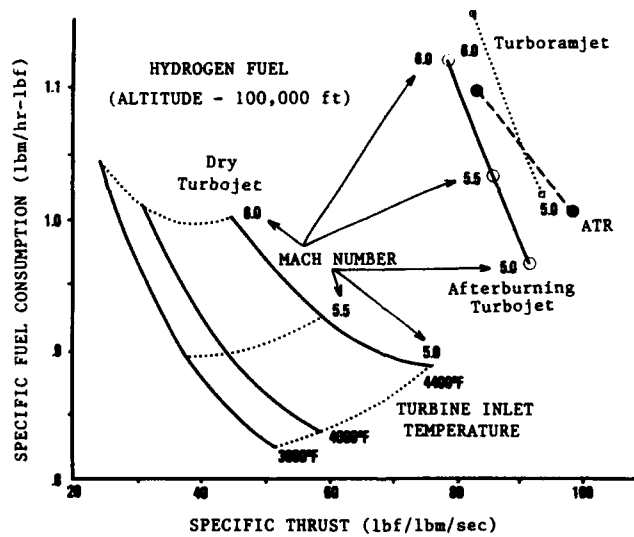


Figure 2 - Performance Comparison (Uninstalled)

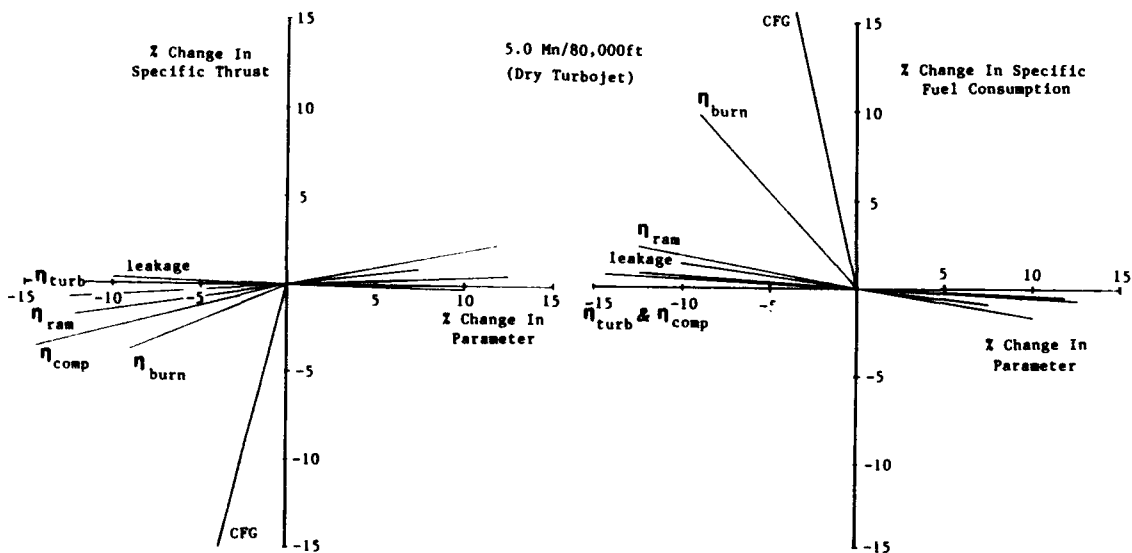


Figure 3 - Performance Sensitivity

to have a small impact on performance. In reality, leakage could increase dramatically which will have a profound impact on performance. Hence, leakage is also an important parameter to achieve good performance.

With the aid of an engine simulation model, part power performance of the various cycles was determined. Advanced compressor maps were generated and utilized for each engine. Both turbine engines were operated with a throttle ratio just over 1.1. Throttle ratio is defined as maximum combustor exit temperature over sea level static combustor exit temperature. Throttle ratio is a method to hold corrected airflow constant up to a given inlet temperature resulting in increased thrust at elevated inlet temperatures. As flight speed increases, turbine inlet temperature increases to maintain constant corrected flow. This can continue until maximum turbine inlet temperature is reached. An installed analysis to determine optimum throttle ratio was performed and will be discussed in a later section. Figure 4 illustrates that, at a given thrust level, the turbojet cycles have more favorable specific fuel consumption which potentially translates to increased range. The dry turbojet nearly equals the afterburning turbojet cruise fuel consumption, but pays a penalty in terms of reduced maximum specific thrust.

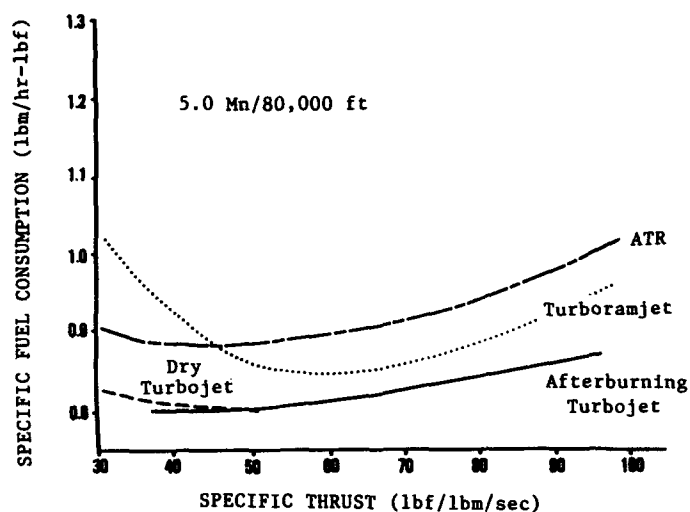


Figure 4 - Engine Cycle Power Hooks

Another key flight point occurs during acceleration through the transonic drag rise. A comparison of the various turbopropulsion system's performance is shown in Figure 5. For the turbojet cycles, increasing pressure ratio increases specific thrust and reduces specific fuel consumption. Diminishing improvements in performance for pressure ratios above 10 imply limited benefits for pressure ratios above this level. For the dry turbojet, increasing turbine inlet temperature increases specific thrust along with specific fuel consumption. For the afterburning engine, increasing turbine inlet temperature decreases specific fuel consumption accompanied by a smaller increase in specific thrust. The ATR nearly parallels the 5 pressure ratio afterburning engine in specific fuel consumption yet presents a much higher specific thrust. This is due to a much higher nozzle pressure ratio (NPR). Concluded are that both dry and afterburning turbojets should be designed for moderate SLS pressure ratios and that maximum turbine inlet temperature is critical to the dry turbojet. An installed analysis was performed to further examine desirable cycle characteristics.

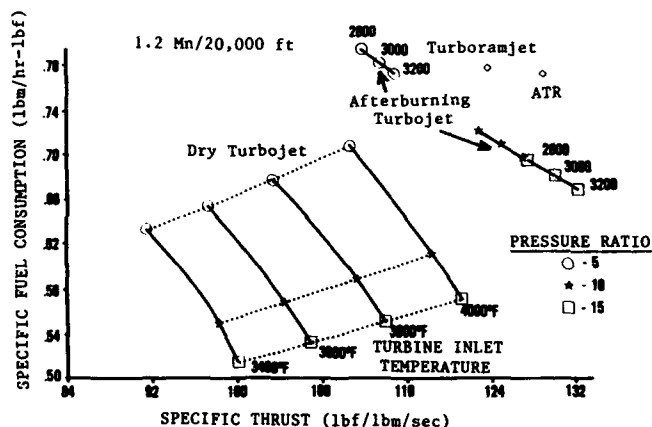
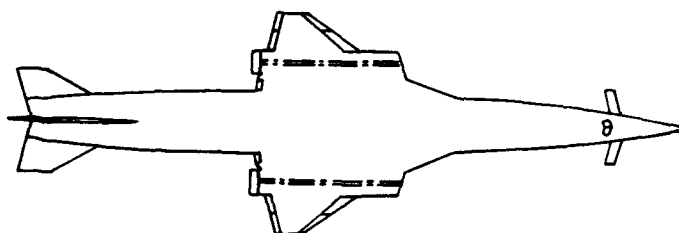


Figure 5 - Transonic Performance Comparison



From the uninstalled performance assessment, the afterburning and dry turbojet cycles are competitive with other forms of high speed propulsion devices. The afterburning turbojet offers desirable specific fuel consumption with competitive specific thrust compared to the ATR and turbooramjet. The dry turbojet offers favorable specific fuel consumption characteristics, but delivers low specific thrust relative to the other cycles.

#### INSTALLED PERFORMANCE - LONG DURATION CRUISE VEHICLE (LDCV)

The aircraft described in Table 2 was used for turbomachinery propulsion system evaluation for a Mach 5 cruise flight mission. Figure 6 illustrates the drag polars for the vehicle. The reference area used is 1764.3 square feet.

The inlet design was derived from the NASA HYCAT-1A (Ref. 2). This vehicle was designed for Mach 6 operation. Modifications were

Fuel	Hydrogen
Take Off Gross Weight	140,000 Lbs
Payload	5000 Lbs
Engine Plus Fuel Fraction	45.8%
Wing Span	54.8 Ft
Wing Loading	79.3 lbs/Sq Ft
Wing Aspect Ratio	1.7
Wing Planform	Cranked Arrow
Propulsion	4 Close Coupled, Pod Mounted Engines, (2 per Nacelle)
Inlet	Mixed Compression
Nozzle	Fully Expanded C-D Axisymmetric (Referee)

TABLE 2 - AIRCRAFT CHARACTERISTICS

necessary to utilize this inlet in a Mach 5 vehicle. A delta drag coefficient, as a function of flight Mach number, was applied to the HYCAT inlet to account for the variation of critical spillage drag. The delta spillage drag coefficient was subtracted from the total inlet drag coefficient across the flight envelope in order to redesign the inlet for Mach 5 operation.

The mission assumes that the aircraft takes off and climbs at a constant flight dynamic pressure ( $q$ ) of 1000 pounds per square foot (PSF) until it reaches Mach 5. It then begins a Brequet cruise radius mission with a 180 degree,  $1\frac{1}{2}g$  turn to return to base. Aircraft takeoff gross weight was held constant with radius being the figure of merit (FOM). For the installed performance assessment, all data is referenced to the baseline dry turbojet.

Evaluation of turbojet thrust sizing requirements revealed variations as a function of engine cycle. The dry turbojet is sized at the cruise condition due to its lack of hypersonic thrust performance while the afterburning engine, because of its stoichiometric augmentor, has its thrust sizing point in the transonic drag rise region.

Figure 7 shows how the turbine engines at various pressure ratios compare to the turboramjet and ATR. Inlet sizing was not optimized for the turboramjet, thereby allowing a qualitative assessment only. Maximum range for the dry turbojet occurs at higher pressure ratio designs than in the afterburning case due to balancing variations in thrust sizing and its effects on the amount of power throttling required at cruise. Both the dry and afterburning engines appear competitive to the ATR and turboramjet.

Figures 8 and 9 illustrate mission performance variations to key engine operating characteristics. High throttle ratio designs are attractive to the dry engine configuration since this increases the flow size of the engine transonically for better inlet matching and provides higher thrust for high Mach flight conditions. The afterburning engine with its inherently higher specific thrust optimizes at a lower throttle ratio for enhanced fuel management. Increasing the turbine temperature of the dry turbojet shifts the optimum pressure

### MACH 5 INTERCEPTOR DRAG POLARS

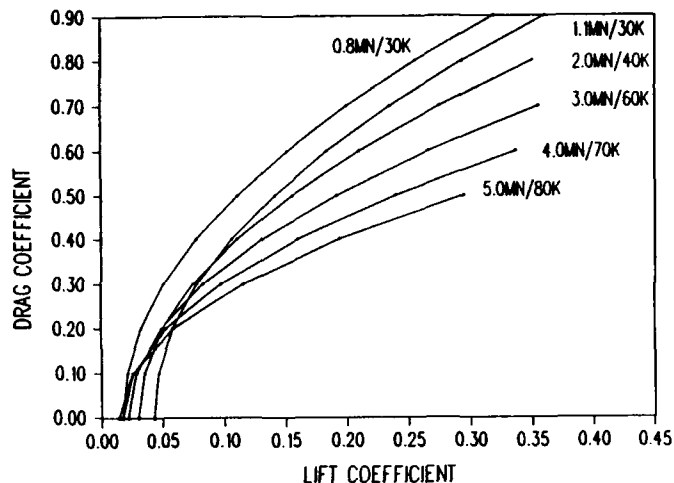


Figure 6 - Mach 5 Interceptor Drag Polar

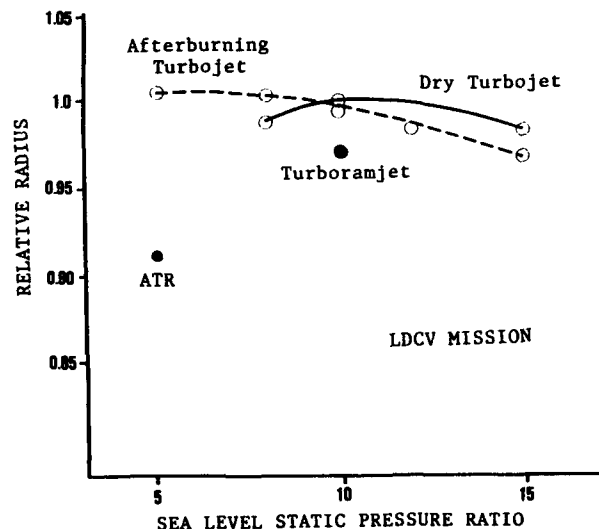


Figure 7 - Mission Performance Comparison

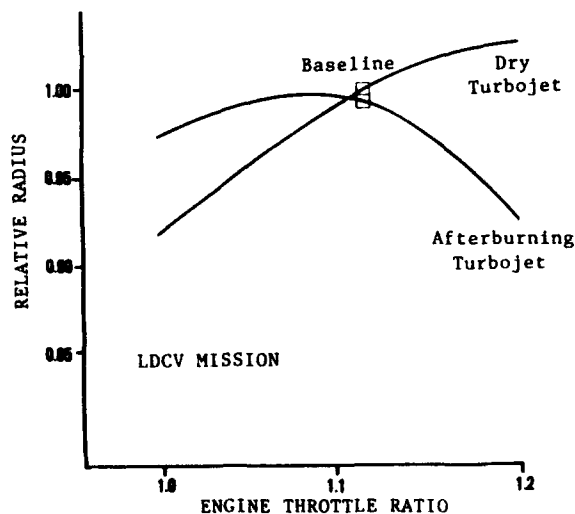


Figure 8 - Vehicle Sensitivity To Throttle Ratio

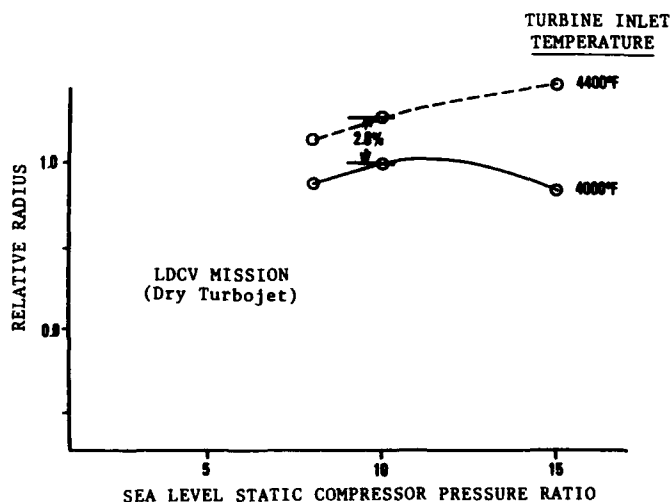


Figure 9 - Vehicle Sensitivity To Turbine Temperature



ratio to a higher value where the increased energy available can be better utilized. Assessments of SLS thrust-to-weight levels for both dry and afterburning turbojets indicated values of about 10 appear attractive. Radius benefits diminish rapidly at higher values.

As mentioned previously, future exhaust systems may not be able to fully expand the exhaust gases at all flight speeds. One suggestion is to utilize the airframe aftbody as an expansion surface at maximum flight speeds. At transonic flight, additional base drag may result because of overexpansion on that aerodynamic surface. A sensitivity analysis was conducted to determine vehicle performance impact due to increased transonic drag. Installed transonic thrust was reduced 15%. Figure 10 illustrates how optimum compressor pressure ratio increases due to reduced transonic thrust. Also illustrated is the substantial influence of transonic engine performance on vehicle radius.

An effort was undertaken to assess the sensitivity of the mission radius to the engine/inlet matching. Airflow at Mach 5 for the dry and A/B turbojets was decreased by 15%. This led to a reduced inlet capture area and lower inlet bypass drag at transonic/low supersonic flight. Figure 11 reveals how the flow change improved mission performance for all but the high pressure ratio dry turbojets and shifted the optimum pressure ratio for both the dry and augmented designs to a lower value.

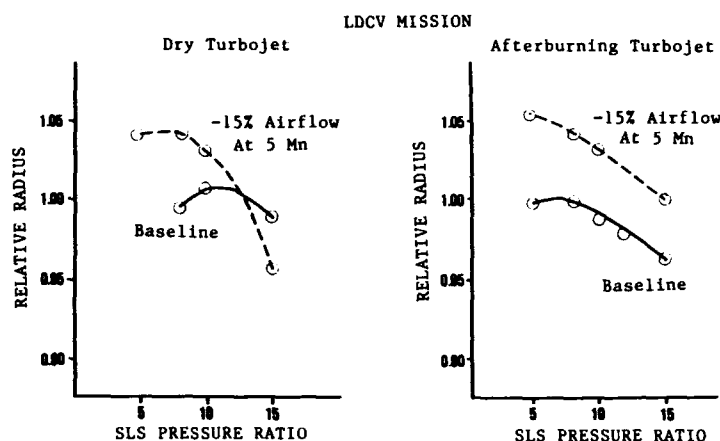


Figure 10 - Vehicle Sensitivity To Engine/Inlet Matching

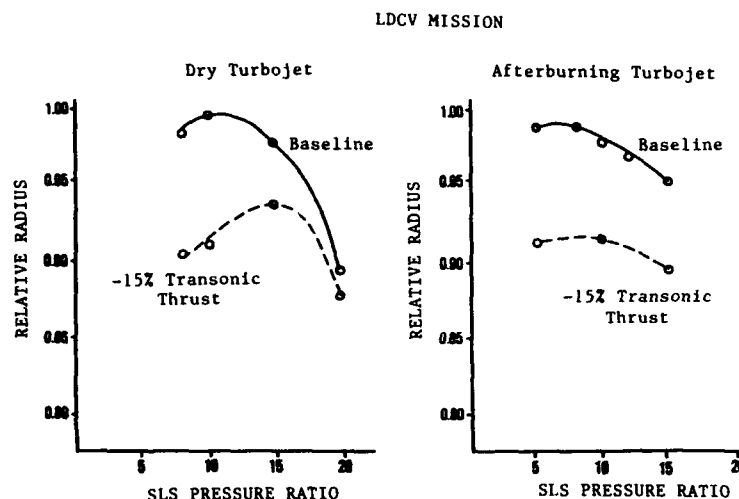


Figure 11 - Vehicle Sensitivity To Transonic Thrust

#### Short Duration High Acceleration Vehicle (SDHAV)

An alternate mission was examined which will be referred to in this paper as the Short Duration High Acceleration Vehicle (SDHAV). This mission utilized the same aircraft as described in Table 2. Conceived as a first stage accelerator, a maximum dynamic pressure ( $q$ ) climb profile of 1000 pounds/square foot was assumed from sea level static until Mach 5 transition speed was obtained. Engine size is set by a requirement for time to accel/climb of 13.3 minutes (based upon related study efforts). Engine plus accel fuel weight became the figure of merit. Minimizing this weight combination allows more payload by reducing overall propulsion "dead weight".

Since the mission is essentially a max power run to speed, Mach 5 cruise fuel efficiency is not as critical as in the LDCV mission. This amplifies the effect of transonic thrust sizing. Figure 12 illustrates how the various engines compare along with the effect of pressure ratio. Again, turbine engine propulsion appears competitive. Optimum pressure ratios for the dry turbojet now occur at a lower value than for the afterburning configuration. This reversal from the LDCV mission is due to the lack of balance needed between cruise specific fuel consumption and thrust sizing requirements. Optimum pressure ratio for the dry turbojet occurs when minimum excess thrust is provided at both the transonic and Mach 5 operating condition. This results in lower propulsion weight due to engine size reductions which more than offset the increased acceleration fuel required. The afterburning engines optimize at a higher pressure ratio as compared to the previous mission because of the desire for high transonic specific thrust.

Mission performance variations due to engine characteristics exhibited the same

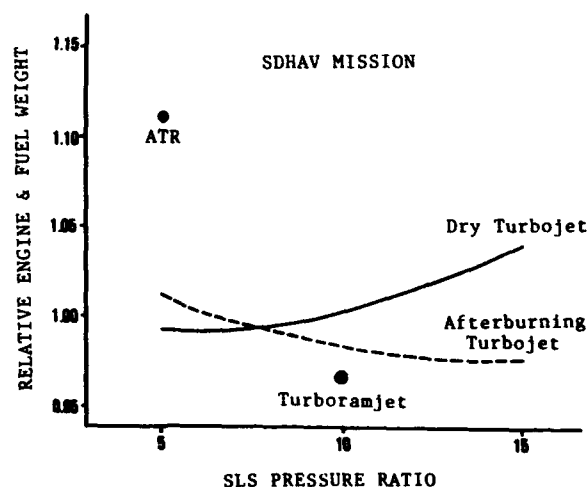


Figure 12 - Alternate Mission Performance Comparison

trends as described for the LDCV mission. Analysis of overexpansion at transonic flight speeds showed a moderate increase of optimum pressure ratio due to increased criticality of transonic thrust margin. For afterburning turbojets, reduced airflow at the inlet sizing point had a small effect on pressure ratio selection and tended to flatten out the performance curve. This is attributed to its thrust sizing point remaining at the transonic drag rise while reducing bypass and spillage drag. Conversely, a higher pressure ratio dry turbojet is thrust sized at maximum flight speeds which greatly increases the size and weight of the engines. Decreasing the flow size at this flight point amplified this condition.

Because of the special problems associated with turbine engines exposed to high speed flight, a conceptual study of various components including the compressor, turbine, combustor, heat exchanger, and nozzle was performed. The cycle selected for further analysis is described in Table 3. The conceptual design study encompassed a matrix of design variables and materials. The flight points used in the analysis are commensurate with a flight dynamic pressure of 1000 psf. For simplicity, only axial rotating stage configurations were considered.

#### Compressor

At Mach 5 flight, the compressor exit temperature presented in Figure 13 allows for three potential materials: Columbium, ceramic composite, and carbon-carbon. It is the opinion of the authors that carbon-carbon (c/c) represents the highest risk and columbium the lowest. To simplify the design matrix, each compressor was assumed to be monolithic (made of one material). Columbium blading was assumed to be uncoated. With this assumption, design constraints for columbium were considered to be equivalent to current metallic blading technology development. Ceramic composites and carbon-carbon were set at lower levels due to their structural limitations and coating requirements. Columbium first stage aerodynamic loading was limited to a level commensurate with advanced nickel alloy compressors. In this paper, aerodynamic loading is defined as:

$$\text{Aerodynamic loading} = \frac{g(J)(\Delta H)}{U_h^2}$$

Where:

- $g = 32.2 \text{ ft/sec}$
- $J = 778 \text{ ft-lbs/BTU}$
- $\Delta H = \text{Delta enthalpy (BTU/lbm)}$
- $U_h = \text{Hub speed (ft/sec)}$

Structural and mechanical limitations for the non-metallic materials are anticipated to restrict the blade camber and twist. Therefore, the aerodynamic loading for carbon-carbon was reduced 50% relative to columbium while the ceramic composite was fixed near the median between the two. For all compressor designs, a constant tip diameter design was chosen for simplicity and enhanced aerodynamic loading. To maximize the potential performance, each compressor configuration was assumed to be designed at its maximum loading. Figure 14 shows the tip relative Mach numbers for each material. Ceramic composites and carbon-carbon, because of structural and coating considerations, need large leading edge radii resulting in excessive shock losses at higher inlet relative Mach numbers. Hence, these materials cannot run at the inlet relative Mach number levels of the uncoated columbium.

With compressor size and speed determined by the inlet design, compressor exit size was found. Sea level static, maximum power was used as the design point based on an assessment of the variation of compressor exit axial Mach number along the flight path. Compressor exit axial Mach

#### AFTERBURNING TURBOJET (Sea Level Static, Standard Day)

Compressor Pressure Ratio	10
Max. Turbine Inlet Temp. (TIT)	2800°F
Afterburner Temperature	Stoichiometric
Throttle Ratio (TITmax/TITsls)	1.114
Component Adiabatic Efficiencies:	
Compressor	85%
Combustor	99%
Turbine	85%
Afterburner	95%
Pressure Losses:	
Combustor	9%
Exhaust Duct (dry)	1%
Cooling:	
Turbine Stator	0.0%
Turbine Rotor	0.0%
Exhaust Nozzle	15%
(Interstage Compressor Bleed)	
Fuel	Hydrogen
Nozzle Thrust Coefficient	.985

Table 3 - Baseline Engine Cycle Stack

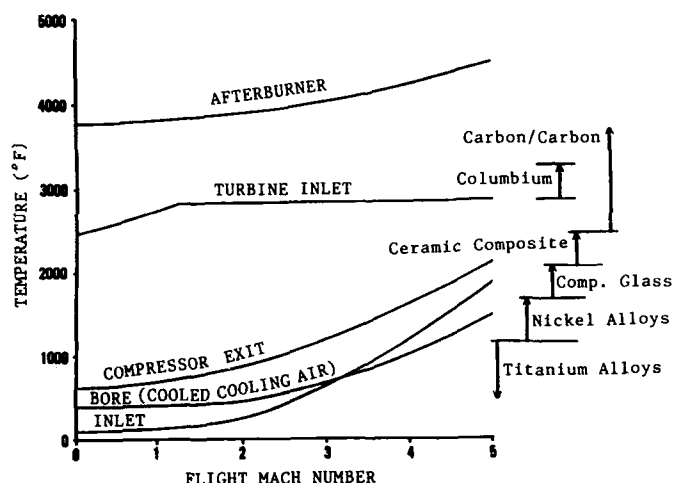


Figure 13 - Mach No. Impact On Component Gas Temperatures

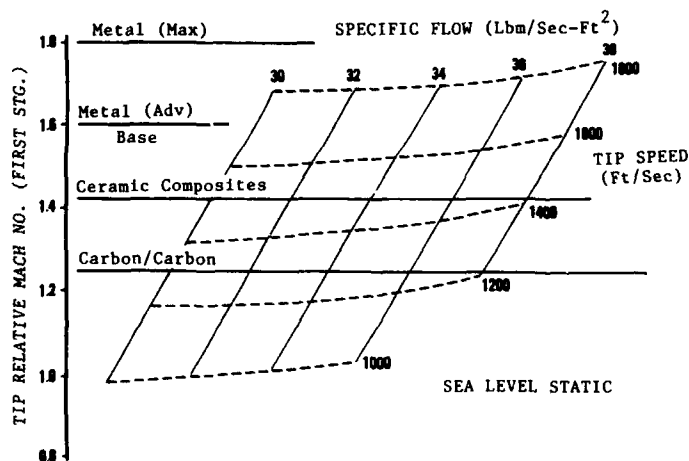


Figure 14 - Compressor Tip Relative Mach No. Comparison

number was set at 0.35 at design to satisfy diffuser and combustor requirements. Several variations of design pressure ratio and stage count were assessed. For this paper, only the baseline cycle will be presented.

Figure 15 shows compressor frontal area as a function of radius ratio. The inlet radius ratio of each material design is set by a desire for minimum compressor frontal area. Decreasing the stage count leads to increased stage work which requires increased blade speed and radius ratio to stay within design limits. For both carbon-carbon and ceramic composite compressors, increasing the number of stages beyond six appears to have diminishing returns when qualitatively evaluated against the added weight of extra stages as well as the structural implications of the low radius ratio design. For the columbium compressor, it was determined that the minimum number of compressor stages is three, in order to meet design requirements.

Figure 16 shows the baseline compressor designs for all three materials. Additional benefits of higher loading capability are exhibited by the significant frontal area reduction for the columbium and ceramic composite compressors relative to carbon-carbon. Figure 17 illustrates how the exit rim speeds of the three compressors compare to current man-rated designs as a function of compressor exit temperature. Shown is that all three designs require revolutionary advancements. Some reduction in engine life requirements would help to reduce this significant technology jump.

#### TURBINE

Figure 13 shows that for the uncooled turbine inlet temperature selected, only columbium and carbon-carbon are viable material candidates for an uncooled turbine. Figure 18 compares the baseline afterburning turbojet with and without turbine cooling at two flight conditions. The cooled turbine assumes 5% of the engine airflow is used for turbine cooling. Shown is that turbine cooling has little effect on overall engine performance. Therefore, a material with marginal temperature capability could be used with some degree of turbine cooling. Ceramic composite turbines were evaluated with the assumption that the turbine would be high risk in an uncooled configuration and moderate risk in a cooled configuration.

Evaluating the turbine design at its flow sizing condition, Figure 19 shows how the rim radius varies as a function of stage number and aerodynamic loading. Aerodynamic loading is defined in the same manner as specified for the compressor. The turbine was assumed to be a constant rim radius to enhance its energy extraction potential. As the stage aerodynamic load increases, the rim radius decreases yielding a more streamlined flowpath design, reducing frontal area and weight as well as turbine rim speed. Assuming a choked turbine inlet, a nominal flowpath divergence, and a representative exit Mach number, Figure 20 shows how the turbine flowpath varies relative to the three baseline compressors for one, two and three stage turbines at these aerodynamic loadings. The desire to minimize both frontal area and number of stages is most easily achieved with the columbium turbine which requires only a single stage turbine. For the non-metals, two stage designs appear most attractive at these loading levels. Higher loading levels

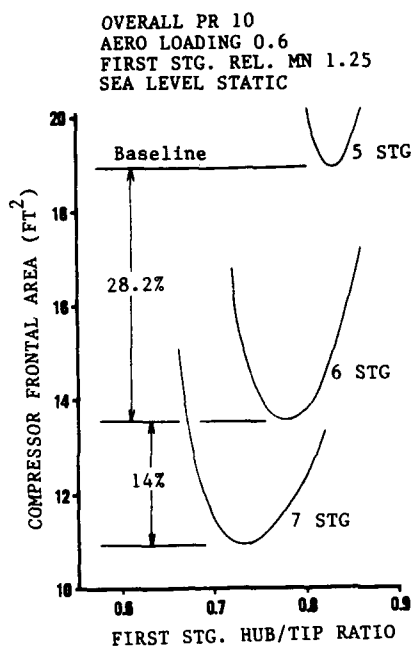


Figure 15 - Compressor Stage No.  
Impact On Frontal Area

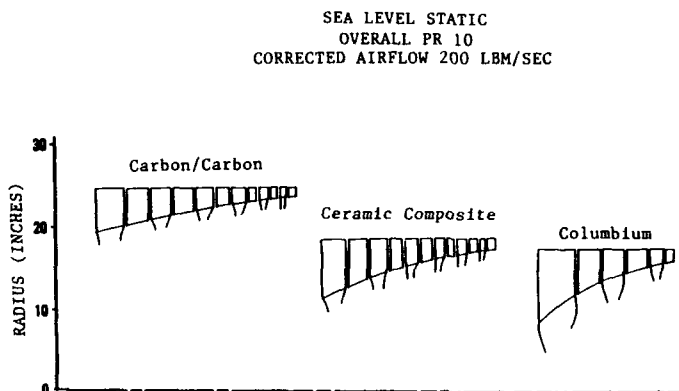


Figure 16 - Compressor Layout Options

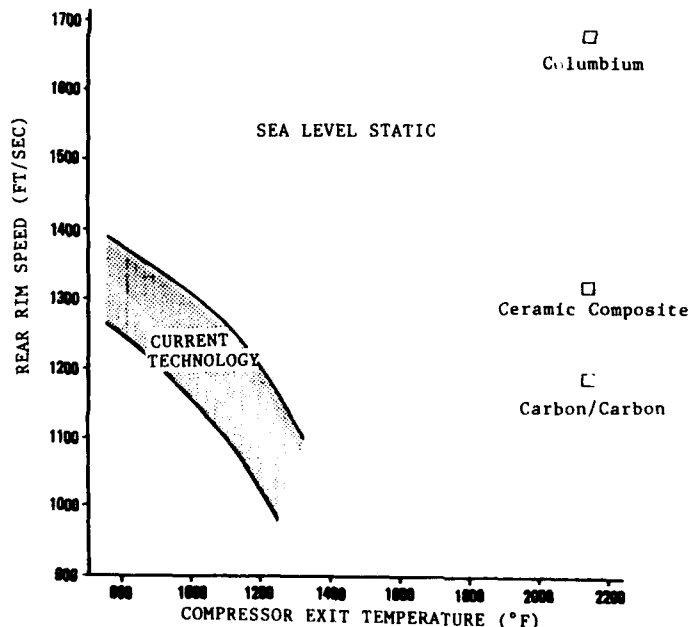


Figure 17 - High Mach Compressor Material Requirements

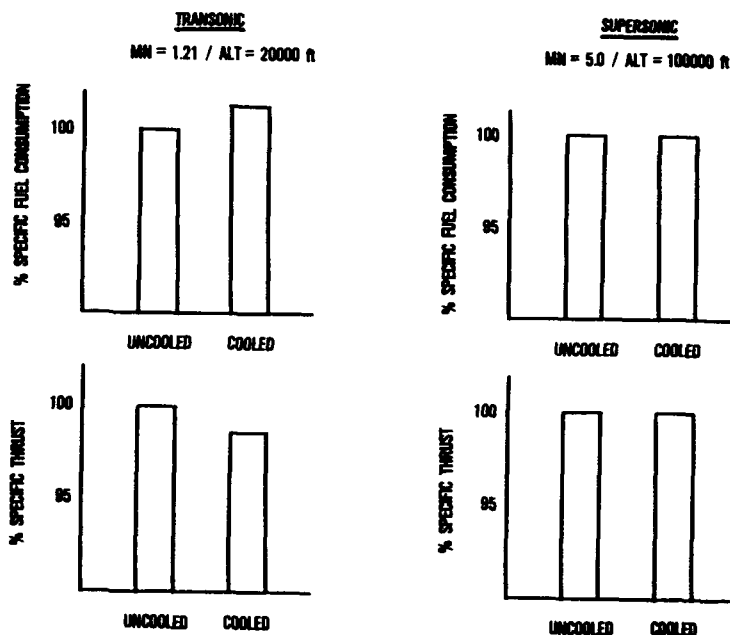


Figure 18 - Turbine Cooling Impact On Performance

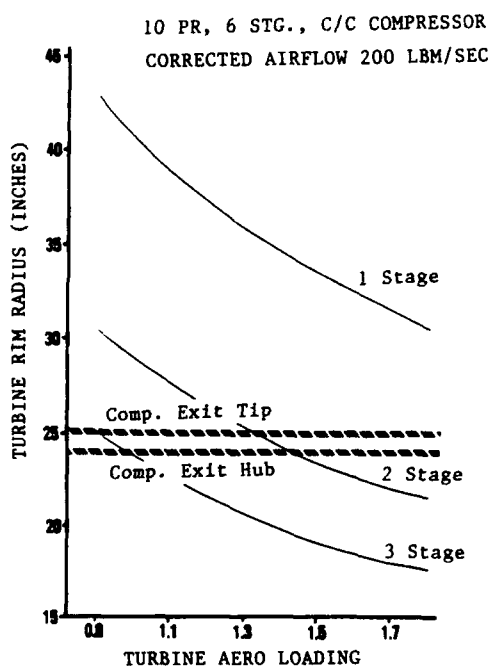


Figure 19 - Turbine Design Tradeoffs

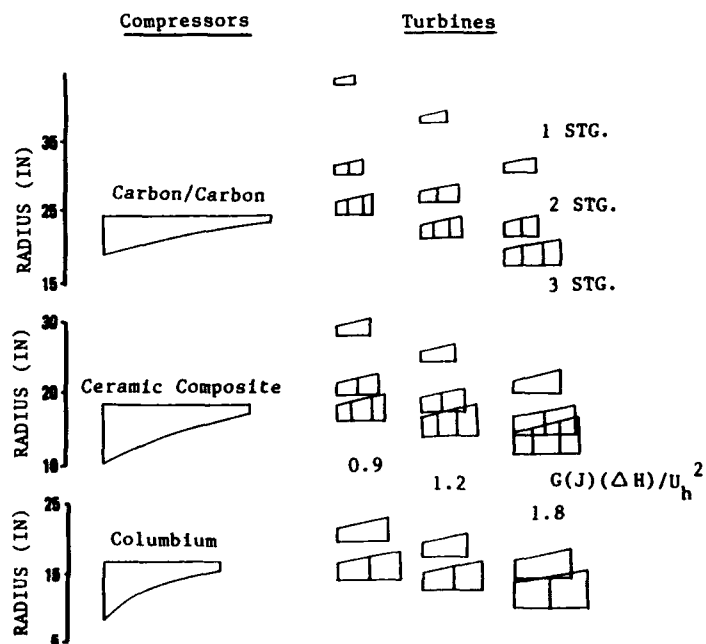


Figure 20 - Turbine Design Matrix

may be possible which result in a single stage turbine design. A single stage, non-metallic design presents higher structural and manufacturing risks.

Figure 21 shows the corrected work required as a function of flight Mach number. Corrected work is defined as:

$$W_{corr} = \frac{\Delta H}{\theta}$$

Where:

$\Delta H$  = Delta enthalpy  
 $\theta$  = Turbine Inlet Temperature  
 (deg R)/519.

Compared to current metallic turbines, work levels are well within the state-of-the-art for single stage designs. For non-metallics, the risk is considered moderate for the two stage designs. Two stage turbines were chosen for the non-metallic baseline designs while the metallic turbine utilized one stage.

### COMBUSTOR

The combustor geometry was defined by centering the inner and outer radii about the turbine inlet. Using the results of the engine cycle analysis and assumed values of combustor length to height, the combustor volume, space heat rate and burner residence time were calculated. Combustor sizing and heat release loadings were evaluated across the flight path.

Figure 22 shows the interrelationship between various combustor design parameters. Space heat rate increases rapidly with increasing combustor reference velocity. It was assumed that using hydrogen fuel would allow higher than typical space heat rates currently used for JP type fuels. A maximum space heat rate value of 20 million btu/hr-ft-atm was chosen resulting in a burner residence time of 4.6 milliseconds.

Indications are that with some development risk, the hydrogen combustor is feasible. The greatest challenge to the combustor design is projected to be in the fuel delivery system because of the high fuel inlet temperatures.

### HEAT EXCHANGERS

One of the more critical technologies for hypersonic flight will be the distribution and control of thermal loads. Figure 13 shows that even inlet air temperatures at Mach 5 are too high for cooling the nozzle and bore components. Using the heat sink capability of the hydrogen fuel, a fuel/air heat exchanger was used to cool engine air for critical system components at all flight speeds above Mach 4. The hydrogen fuel temperature entering the heat exchanger was elevated from its tank temperature to simulate aircraft cooling requirements.

Figure 23 shows the variation in combustor inlet fuel and cooling air temperature as a function of compressor exit bleed air and aircraft fuel delivery temperature. The shaded areas indicated regions of interest for various flight speeds. At Mach 5, the cooling air temperature is reduced 15% from compressor discharge temperature. Heat exchanger fuel inlet temperature was fixed at 800°F based upon estimated aircraft heat load requirements.

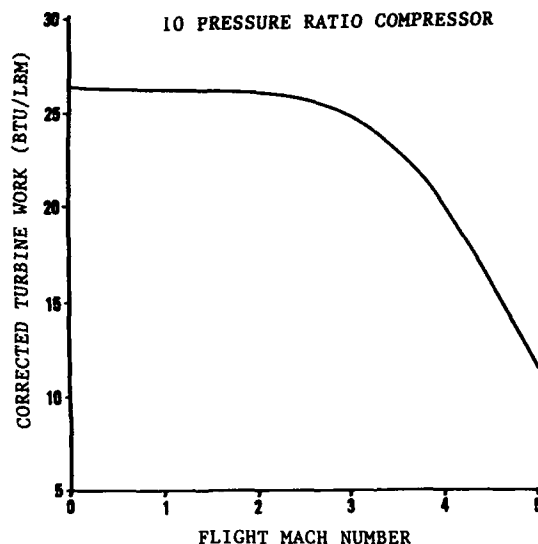


Figure 21 - Turbine Work Requirements

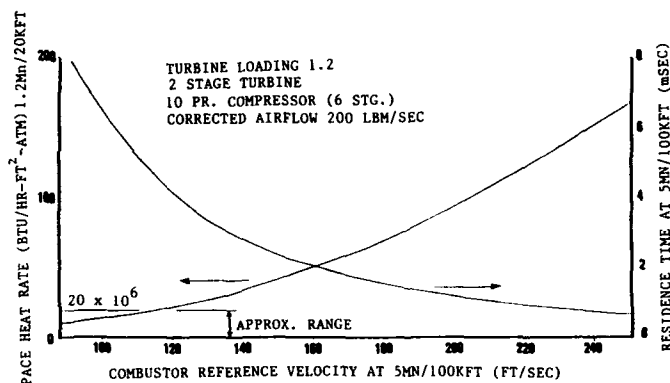


Figure 22 - Combustor Design Tradeoffs

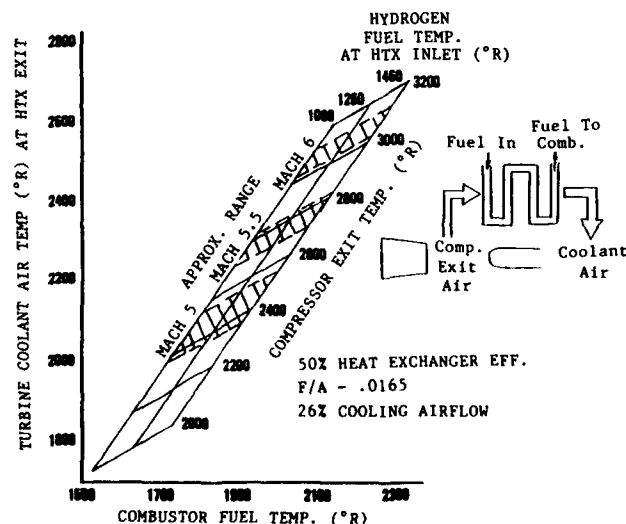


Figure 23 - Heat Exchanger (HTX) Temperature Tradeoffs

The engine bore will require further cooling than previously described. Suggested is that a portion of fuel be tapped prior to full aircraft routing and used to cool a small portion of compressor bleed air. Due to the small amount of flow required, this heat exchanger could conceivably be integrated into the bore area. With this approach, it is believed that the bore components may be cooled sufficiently for reasonable life retention. The high risk associated with this technology can be reduced by the introduction of advanced high temperature bore components (i.e. bearings, seals, etc.) and innovative structural/mechanical designs.

### EXHAUST NOZZLE

The exhaust nozzle represents the most critical technology for superior aircraft performance. Nozzle internal thrust performance must be balanced across the flight envelope with installation effects such as boat tail and wave drag. For this conceptual design, a simplistic approach was used with only internal performance considered using the loss stack-up shown in Figure 24. This figure illustrates the trade between expansion and angularity losses as a function of area ratio. A nozzle length to diameter ratio of 7 was assumed. Peak performance occurs between 15 and 16 area ratio. However, because of diminishing returns, an area ratio of 10 was considered in addition to a fully expanded design.

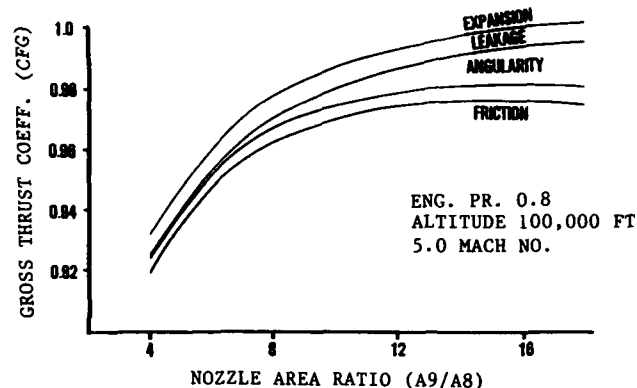
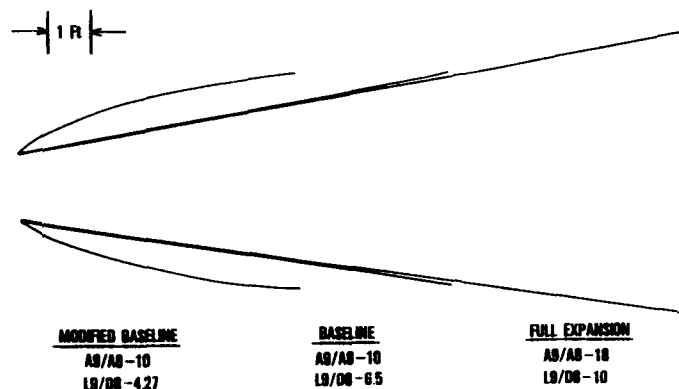


Figure 24 - Nozzle Loss Buildup

Figure 25 compares the full expansion nozzle, the 10 area ratio nozzle using straight flaps, and the 10 area ratio design using a bell curvature design for the diverging flap. The full expansion nozzle thrust coefficient is approximately 98.3% and is over 5.5 feet longer than the baseline area ratio nozzle which incorporated a thrust coefficient of 96.9%. The bell shaped nozzle is projected to have equivalent performance as the straight flapped version but with a reduced length of almost 4 feet. For reasons of reduced weight, the 10 area ratio, bell shaped nozzle was chosen.



Assuming End to End Straight Line Analysis

Figure 25 - Nozzle Design Options

### CONCLUSIONS/RECOMMENDATIONS

The performance analysis presented indicates that the turbine engine provides competitive performance up to low hypersonic flight velocities. Described have been the desirable operating characteristics, both uninstalled and installed. Sensitivity analyses at Mach 5 indicate that nozzle gross thrust coefficient is of prime importance, with component efficiencies having a secondary impact on performance. The dry turbojet requires very high levels of turbine inlet temperature to have competitive specific thrust. For all cycles, proper engine/inlet flow matching can substantially enhance vehicle performance. From a technology risk standpoint, the afterburning turbojet is more desirable. It does not require the very high levels of turbine inlet temperature as dictated for the dry turbojet cycle and provides competitive performance to the turboramjet with substantially reduced complexity.

Key components needed for an afterburning turbojet for Mach 5 operation have been assessed to determine their feasibility. From a conceptual design standpoint, there appears to be no technology barriers which preclude the development of this system. There are however, various levels of risk associated with the different components which can only be overcome by exploratory and advanced development efforts. It is recommended that research programs be formulated to address these technology challenges. It is further recommended that the turbomachinery concept be considered in future activities relating to hypersonic propulsion devices because of the tremendous potential payoffs in terms of simplicity and performance.

### ACKNOWLEDGMENT

The authors wish to thank Mr. Errol G. Blevins for his computer support and Messrs. Christopher M. Norden and Walter D. Hoy for their substantial assistance in generating data in all phases of this study. It is through their support that this study could be successfully completed.

### REFERENCES

1. APL TDR 64-61, "Inlet Efficiency Parameters for Supersonic Combustion Ramjet Engines," E. T. Curran, Sqn Ldr, RAF, M. B. Bergsten, June, 1964.
2. NASA-CR-158926-Vol 2, "Hypersonic Cruise Aircraft Propulsion Integration Study," 1979 (Lockheed-California Co., Burbank).

## Discussion

RAMETTE

For the carbon/carbon compressor, did you take into account the oxydation problem, the protective coating which is needed and the correlative impact on the air flow.

AUTHOR'S REPLY

Yes; the carbon/carbon and ceramic composite compressors were assumed to be coated. The result is a reduced aerodynamic loading and increased leading edge radius for these materials. This is why the carbon/carbon and ceramic composite compressor are larger in radius and require more stages to produce the pressure ratio of 10 at sea level static.

BOURY

Do you think that such an advanced turbojet could be a good accelerator for the NASP?

AUTHOR'S REPLY

Yes, I do. This in no way implies that this configuration is or is not currently under consideration. This study was performed totally outside the realm of NASP.

RODI

What kind of materials do you envisage for bearings and what kind of fluids for cooling and lubrication systems?

AUTHOR'S REPLY

I cannot comment on this question.

TARIFA

1. Would you explain the cooling system of your nozzles and the fig of 15% cooling flow.

2. Have you considered the possibility of the use of other nozzles as plug nozzles with advanced materials?

AUTHOR'S REPLY

1. We feel that 15% would be adequate to cool the various components.

2. No, we did not.



## AIRBREATHING PROPULSION FOR TRANSATMOSPHERIC FLIGHT

by

G. Andrei, U. Borio, M. Maiurano  
FiatAvio, Direzione Progettazione  
Corso Ferrucci 112, Torino, Italia

92-16954

## SUMMARY

This paper examines the application of Airbreathing Propulsion Systems to Winged Launchers.

The characteristics of Ramjet based, LH2 fuelled, powerplants are analysed.

In the first part the main Ramjet design parameters are highlighted.

In the second part options (Rocket, Turboengine) for the boost phase from take-off to Ramjet mode transition are described, and their potential applicability to Single Stage-to-Orbit (SSTO) and Two Stage-to-Orbit (TSTO) launchers is discussed.

## 1. INTRODUCTION

Winged Launchers with Airbreathing Propulsion are mainly aimed at a decrease of recurring costs of Space Transportation Systems and at an increase of their flexibility and reliability.

The launcher operating envelope, consisting of subsonic, supersonic and hypersonic flight regimes, requires combined cycle engines, which may be conceived starting from the basic concepts of Turbojet, Ramjet and Rocket.

Mission requirements in terms of cross range and launch window, as well as launcher configuration, determine the powerplant selection. A high Thrust-to-Weight ratio powerplant is mandatory for a satisfactory SSTO payload, while in the TSTO configuration the staging allows powerplant performance optimization to a higher extent.

From take-off up to low supersonic speed, adequate thrust may be obtained either in Turbomode or in Rocket mode.

From supersonic up to hypersonic flight regimes, the high stagnation pressure allows the Ramjet mode operation with high Specific Impulse. Alternatively a Turboengine may be selected, provided that the incoming air is precooled. This option leads to high Thrust-to-Weight ratio engines, with Specific Impulse penalties at high speed because of the required overfuelling. Precooled engines are suited for SSTO launchers conceived for a direct ascent mission. When flexibility in terms of cross range and launch window is required a Ramjet based powerplant is envisaged both for SSTO and TSTO launchers.

## 2. RAMJET DESIGN FEATURES

## 2.1 VEHICLE PRECOMPRESSION AND POWERPLANT SIZE

The maximum intake mass flow is increased by the precompression caused on the incoming air either by the wing or the fuselage depending on the engine installation. This effect is enhanced by the precompression surface incidence and by the flight Mach number (Figure 1).

At high speed (Mach 4-6), the increased mass flow is swallowed by opening the nozzle throat area, with a Net Installed Thrust improvement (Figure 2). The consequent reduction in the nozzle area ratio tends to decrease the Specific Impulse, while the improvement in the recovered pressure tends to increase it. The two counteracting effects lead to the trend in Figure 3.

At low speed (Mach 2-3), the increased mass flow leads to augmented intake spillage. The low total pressure limits in fact the maximum mass flow which the engine can swallow maintaining stoichiometric combustion. Net Installed Thrust and Specific Impulse penalties are consequent.

In order to assess the influence of the forebody precompression on the powerplant size, the interaction between flight incidence and dynamic pressure has to be investigated throughout the ascent trajectory. For a given wing loading, a higher flight incidence requires a lower dynamic pressure. While the former effect improves thrust, the latter tends to reduce it at the same extent. A trade-off is therefore necessary, which has to be closely related to the optimization of the ascent trajectory and to the vehicle aerodynamic design.



## 2.2 INTAKE

The simplest shock structure to compress the incoming air mass flow is the normal shock wave (Pitot intake). At high speed, this solution leads to a low pressure recovery factor. An improvement is allowed slowing the supersonic flow upstream the normal shock by a number of oblique shocks, which increase with the flight speed. The optimum pressure recovery factor is reported in Figure 4 for solutions at different number of shocks.

At constant flight dynamic pressure the intake configuration is determined by the thrust decay at high speed. The recovered pressure too has to be taken in account in the intake selection since the powerplant mass depends on the internal pressure. Figure 5 provides the guidelines for the selection of the shock structure. At Mach 6 the 4 shocks intake provides 85% of the isentropic intake Net Thrust. An additional oblique shock would in fact allow a thrust increase about 6% only; on the other hand, the recovered pressure increase would be  $\approx 50\%$ . The associated mass penalty for a Ramjet cylindrical configuration is about 30-40%, 1/1. The 4 shocks intake represents therefore a good compromise between powerplant performance and mass.

The incoming air may be compressed either outside the intake or inside, thereby determining the intake configuration. The increased flow turning caused by the external compression leads to a cowl drag penalty at low speed. The internal compression overcomes this, but starting problems and the risk of subcritical operating mode arise.

A design compromise is the mixed compression intake of Figure 6, with 2 external oblique shocks and 1 internal oblique shock. External oblique shocks are obtained by flat ramps, whose angle is controlled by jacks, in order to maximize the mass flow throughout the ascent trajectory.

## 2.3 COMBUSTOR

The design burner area at each flight speed is established by the recovered pressure and the intake mass flow. The burner area in Figure 7 has been evaluated assuming a combustor entry Mach number of 0.2, which is consistent with the aerothermodynamic design of a reheat type burner. The continuous line indicates stoichiometric combustion, while on the dashed line a lean combustion has been assumed to avoid thermal choking. In fact at low speed, the combustor is not able to swallow the maximum intake mass flow with stoichiometric combustion. The burner may then operate either lean with intake full capture or stoichiometric with intake spillage: in both cases a thrust penalty has to be paid. The Ramjet thrust at low speed is therefore fixed by the burner area, while at high speed the thrust is fixed by the intake lip area. The selection of the relative scale between burner and intake is hence established by the minimum flight speed required in the Ramjet mode, which on the other hand depends on the operating mode in the subsonic-transonic boost phase.

Another important aspect worth to be mentioned in this section is the fuelling schedule selection throughout the ascent trajectory.

Net Thrust increases with equivalence ratio (Figure 8): the reduced slope for rich mixtures is due to the combustion temperature decrease.

Specific Impulse (Figure 9) shows an optimum for lean mixtures, which shifts towards stoichiometric combustion at high speed.

Minimum propellant consumption for a direct ascent mission is achieved by minimizing the Effective Specific Impulse, which is defined by combining the Net Thrust and the Specific Impulse as the Net Thrust minus the Vehicle Drag divided by the Propellant Mass Flow. For a given powerplant size, stoichiometric combustion allows optimum acceleration up to supersonic speeds. The thrust decay at high speed requires overfuelling for an adequate acceleration (Figure 10). The optimum fuelling schedule is the dashed line through the maxima of the Effective Specific Impulse curves. As the powerplant size is enlarged (Figure 11), the degree of overfuelling at high speed decreases, and a better Effective Specific Impulse all over the ascent trajectory is obtained, thereby reducing the propellant consumption.

A trade-off is therefore necessary between mass and propellant consumption, in order to define powerplant size and fuelling schedule. Of course this procedure has to be integrated with the ascent trajectory optimization in terms of dynamic pressure and incidence.

## 2.4 NOZZLE

The area range required in the throat depends on the burner area and consequently on the minimum flight Mach number in the Ramjet mode (Figure 12). The throat area at high speed reduces because of the increase in the engine recovered pressure and the decrease in the intake mass flow. The resulting nozzle throat area range is about 10:1 for the Ramjet operation from Mach 2-3 to Mach 6-7.

Concerning exit area definition, for the operation at high speed (Mach 4-6), adequate flow expansion is provided by an exit area equal to the intake lip area. For the operation at low speed ( $\approx$  Mach 3), an area ratio of 2-2.5 is needed (Figure 13). The final selection depends again on the operating mode for the boost phase.

A 2-D nozzle with flat ramps in a configuration similar to the intake would represent the optimum geometric solution to meet the required throat area range. Unfortunately when a large nozzle exit area is needed for the operation at low speed the flat plates lead to high mass penalties. Mass savings in the 2-D nozzle configuration may be obtained by limiting the length of the nozzle ramps and expanding the gases in the rear of the fuselage (Single Expansion Ramp Nozzle, SERN).

Alternative solution to save mass is the axi-symmetric configuration. The area range in the throat may be achieved by a petalled system similar to the one used in conventional jet engines, and by arranging a central plug to meet the minimum throat area requirement (Figure 14).

The SERN nozzle requires a square configuration for the engine installation, while the plug nozzle requires a cylindrical one.

Installation mass and engine performance have to be carefully taken into account for the configuration selection in view of the high sensitivity of the Net Installed Thrust to the nozzle performance, particularly at high speed, as highlighted in Figure 15. A 1% reduction in nozzle efficiency causes a 2% reduction in the Net Installed Thrust at Mach 2, while the sensitivity increases up to 6-7% at Mach 7. In addition nozzle losses increase too, due both to kinetic effects, caused by dissociation in the combustion process, and to cold flow effects, i.e. form and friction losses, due to the increase in the nozzle area ratio.

### 3. LOW SPEED PROPULSION

Turboengine or Rocket may be utilized to accelerate the vehicle from take-off up to supersonic speed.

The Rocket option involves propellant consumption penalties because of the low Specific Impulse. On the other hand the powerplant mass is kept low because of the high Rocket Thrust-to-Weight ratio. The Ramjet-Rocket concept is particularly suited for the SSTO application on the basis of the light weight and of the vacuum operation capability.

#### 3.1 TURBOMODE

Either Turbojet or Turbofan may be selected among conventional Turboengines. Turbofan has to be preferred for its better dry Specific Impulse when long cruise phases at low speed are needed. On the contrary Turbojet Specific Impulse is superior in the reheated mode during acceleration phases.

Turborocket is an alternative option whose peculiar feature is the decoupling of compressor and turbine flows. The turbine is powered by the fuel which has been either preburned with onboard oxidizer or regeneratively pre-heated (Turboexpander).

In the Turborocket a compressor pressure ratio lower than in conventional Turboengines allows equal nozzle pressure. The reduced mass of the turboengine leads then to an increased Thrust-to-Weight ratio. In addition, if the same limit of Turbojet for compressor delivery temperature is considered, a higher maximum flight speed is allowed. For applications in which flexibility in terms of low acceleration levels or cruise phases is required conventional Turboengines are still to be preferred because of their better Specific Impulse.

In the present section the selection of the main Turbojet design parameters are discussed.

Turbine Entry Temperature (TET) has to be increased to its technological limits (1800 - 1900 K) throughout the ascent trajectory in order to optimize reheated Specific Impulse and Thrust-to-Weight ratio. Turbine Entry Temperature is therefore the engine main control parameter during acceleration phases.

The rotational speed is set at the allowable maximum value to run the engine with optimized performance throughout the trajectory.

As flight speed increases, the work required to compress the air increases, leading to compressor pressure ratio reduction and consequently to reduced thrust (Figure 16). Meanwhile compressor exit temperature progressively increases (Figure 18) approaching its technological limit, that is about 900 K for Nickel based alloys. Once this condition has been reached, Turbine Entry Temperature has to be reduced, thereby leading to the steep performance decay represented by the dashed lines in Figure 16 for Net Installed Thrust and in Figure 17 for Specific Impulse.

Considering these technological constraints leads to limit Turbojet operating mode up to about Mach 2-3, depending on the compressor design pressure ratio; Turbojet design is then defined by selecting compressor pressure ratio and size.

For the pressure ratio selection a trade-off is necessary among take-off, transonic and supersonic performance. The increase in the design pressure ratio improves take-off and transonic performance, but the limit on compressor exit temperature is rapidly reached as flight Mach number increases. A large reheat burning area is therefore required for transition to Ramjet, with consequent mass penalties and Specific Impulse reductions in the Mach 2-3 range. A good compromise is a design pressure ratio of 8-11 in the transonic flight regime, with a reheat burning area of about 1.25-1.5 times the intake lip area. The corresponding transition to the Ramjet mode takes place in the flight Mach number range of 2.7-3.0.

The Turbojet scale relative to the intake lip area is determined to provide an adequate acceleration at transition to the Ramjet mode. A large excess Thrust is in fact available at take-off and in the transonic flight regime. In addition, if a cylindrical powerplant configuration with the Ramjet bypass duct wrapped around the Turbojet is chosen, the compressor face area determines the nozzle exit area. These aspects lead to a nozzle exit area 2-2.5 times larger than the intake lip area.

As previously mentioned an alternative solution to the Turbojet could be the Turbofan to take advantage of its better Specific Impulse during cruise. Of course the final selection involves a fine definition of mission requirements.

### 3.2 ROCKET MODE

As already pointed out, the high Thrust-to-Weight ratio and the vacuum operation suggest the Ramjet-Rocket powerplant for the application to the SSTO launcher.

On the basis of the high sensitivity of this launcher with respect to the powerplant mass and performance, the definition of the engine main design parameters requires a close integration between propulsion system and launcher in the optimization process.

Payload sensitivity to a 1% change in Rocket vacuum Specific Impulse is 10-20%, /1/. The highest sensitivity comes out from the cross range requirement during the ascent trajectory, which may be necessary in order to meet latitude change requirements.

Figure 19 shows Ramjet and Rocket modules separately installed in the launcher rear fuselage. This configuration allows to decouple Rocket and Ramjet performance optimization and to avoid performance and mass penalties associated with the integration.

Both Rocket and Ramjet area ratios have to be defined on the basis of their influence on the launcher configuration and on its payload.

The Rocket nozzle exit area has to be traded-off by taking into account the influence on the vacuum Specific Impulse, on the installation drag in the airbreathing phase and overexpansion losses at low speed. Another parameter to be considered is the overall base area, which determines the fuselage finess ratio, thereby influencing structural efficiency and wave drag in opposite directions.

A trade-off for Ramjet area ratio, that is the nozzle exit area divided by the intake lip area, is also necessary. The increase of this parameter allows an enlarged combustor area, which improves performance at low speed but penalizes the powerplant mass.

For the trade-off analysis, a high pressure (25 MPa), LOX/LH<sub>2</sub>, staged combustion cycle rocket engine has been assumed.

The results in terms of payload injected in Low Earth Orbit (LEO) by a SSTO designed for a direct ascent mission are in Figure 19. An optimum Ramjet nozzle area ratio of 2.0-2.5 is needed, with a Rocket nozzle area ratio of 180:1. The resulting payload fraction is about 2.5%. Ramjet engine is operated from the transonic regime. The transition to the Ramjet mode takes place in the 2.0-2.5 Mach range by a progressive switch off of the Rockets. The maximum Mach number in the airbreathing phase is 5.5.

The eventual cross range requirement is met by reducing the acceleration in the airbreathing phase. This is obtained with a reduced size of the Ramjet, thus leading to a consequent propellant penalty. The requirement of european basing for the launcher, which corresponds to a cross range of about 2000 km, involves a 50% reduction in the payload fractions of Figure 19, at constant Gross Lift-off Mass (GLOM).

The Ramjet modules configuration of a SSTO with a Gross Lift-off Mass of 570 Mg, designed for a payload of 7 Mg in LEO (460 KM, 28.5°), launched from Istres, is depicted in Figure 20. Four Ramjet engines, 2.42 sqm intake lip area each, are packaged in a square configuration below wing and fuselage. Relevant performance of the Ramjet engine is shown in Figures 21 and 22 respectively in terms of Net Installed Thrust and Specific Impulse.

#### 4. CONCLUDING REMARKS

A Ramjet based powerplant has been envisaged for Winged Launchers.

The powerplant size, the fuelling schedule, as well as the intake configuration have to be defined on the basis of Ramjet thrust requirement at high speed, taking into account ascent trajectory and vehicle aerodynamic design.

The minimum Ramjet flight speed is determined by the burner area.

Exhaust nozzle selection determines powerplant installation configuration and performance.

In a Turboramjet configuration a conventional Turbojet allows acceleration from take-off up to Mach 2.7-3.0 with a minimum propellant consumption. Despite the low Thrust-to-Weight ratio of the Turboengine, this powerplant is envisaged for the application to TSTO.

In the Ramjet-Rocket configuration a high chamber pressure Rocket allows powerplant mass reductions with performance penalties in the boost phase. This configuration is suited for the application to SSTO launchers.

#### 5. REFERENCES

/1/: MBB with British Aerospace, Rolls-Royce, MTU, FiatAvio, VDK and Dornier, Winged Launchers Configuration Study: Final Presentation, ESTEC, May 1989, ESA Contract No. 7379/87

#### 6. ACKNOWLEDGEMENTS

The authors wish to acknowledge the assistance of colleagues in their own company and in the associated companies in the development of the ideas and methods which have been described in this paper.

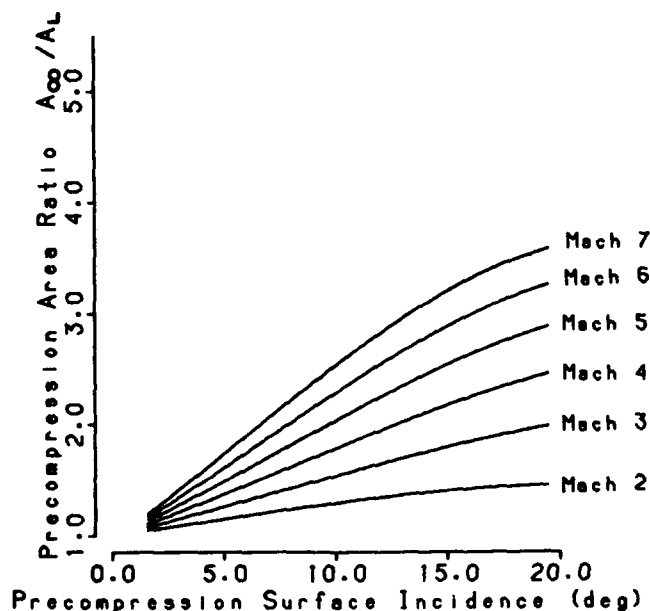


Figure 1: Sensitivity of Capture Area to Precompression and Flight Mach Number

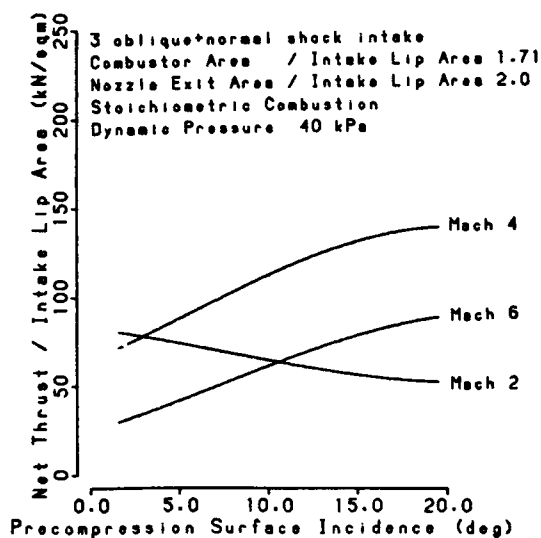


Figure 2: Sensitivity of Ramjet Net Installed Thrust to Precompression Surface Incidence

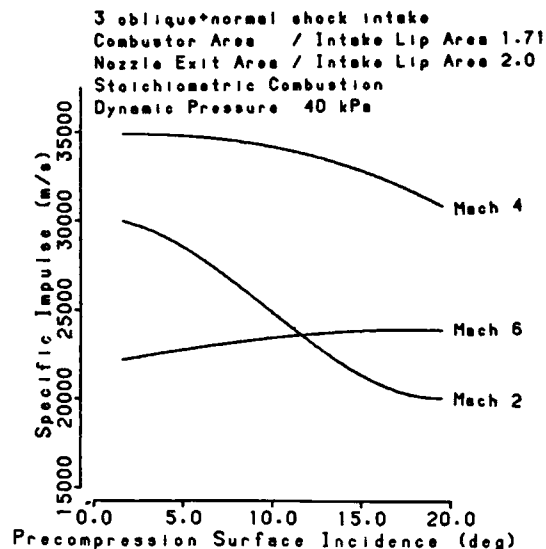


Figure 3: Sensitivity of Ramjet Specific Impulse to Precompression Surface Incidence

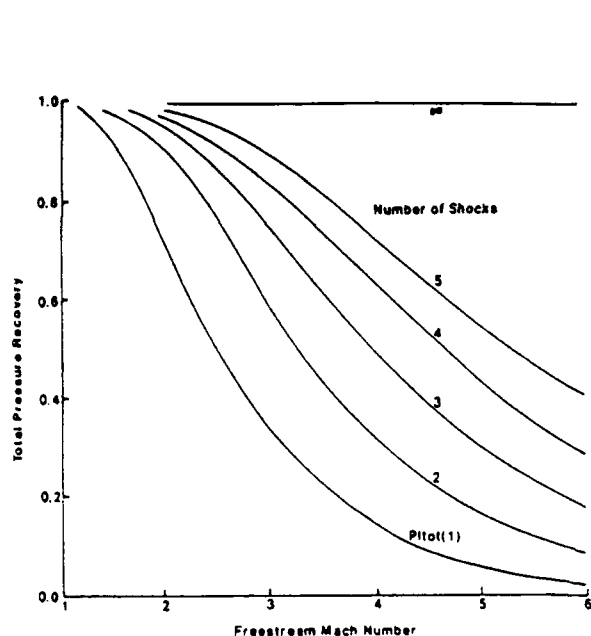


Figure 4: Influence of Shock Structure on Total Pressure Recovery

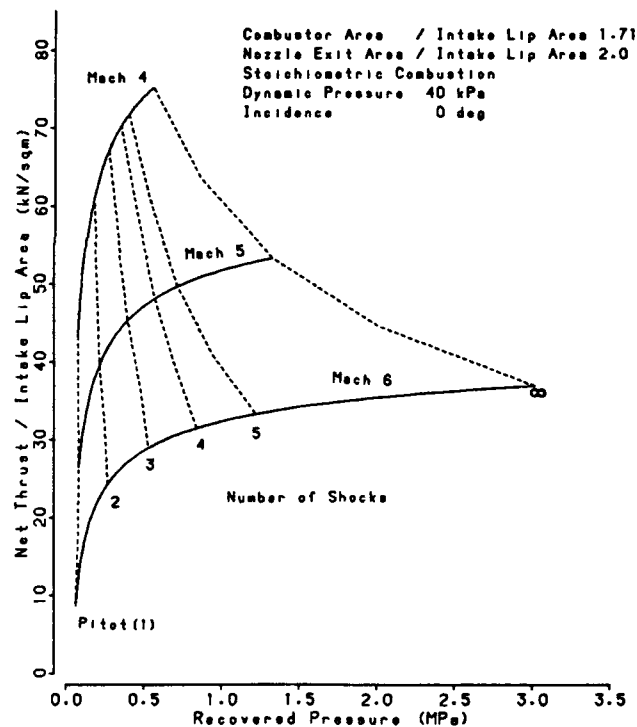


Figure 5: Sensitivity of Ramjet Net Installed Thrust to Recovered Pressure and Intake Shock Structure

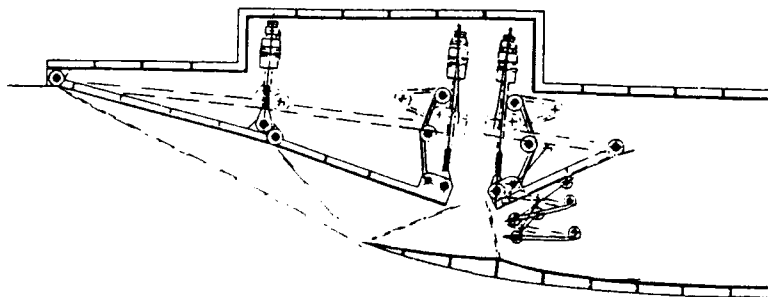


Figure 6: 2-D 3 oblique+normal shock intake, //

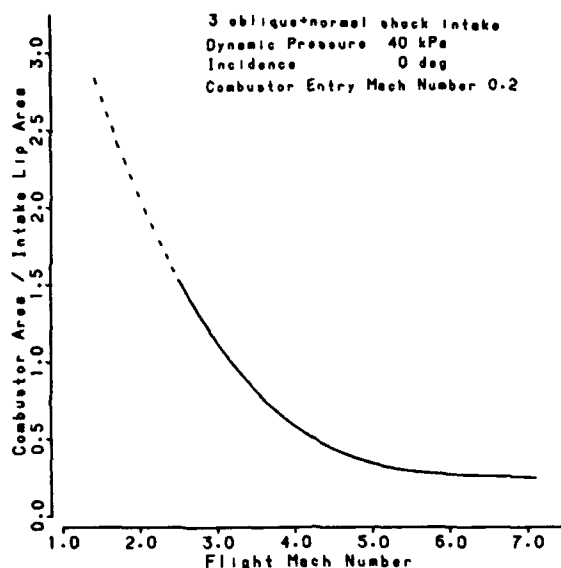


Figure 7: Ramjet Combustor Area vs. Flight Mach Number

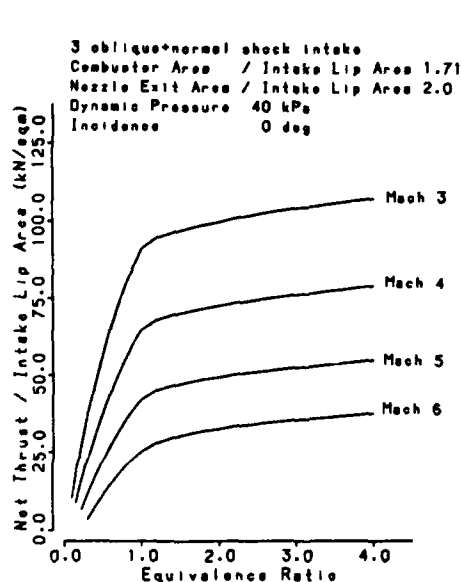


Figure 8: Sensitivity of Ramjet Net Installed Thrust to Equivalence Ratio

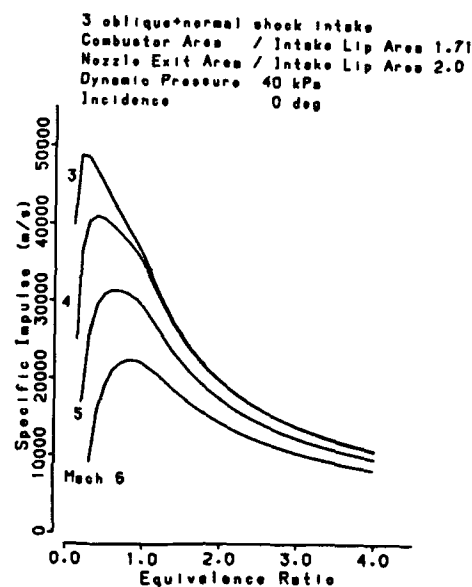


Figure 9: Sensitivity of Ramjet Specific Impulse to Equivalence Ratio

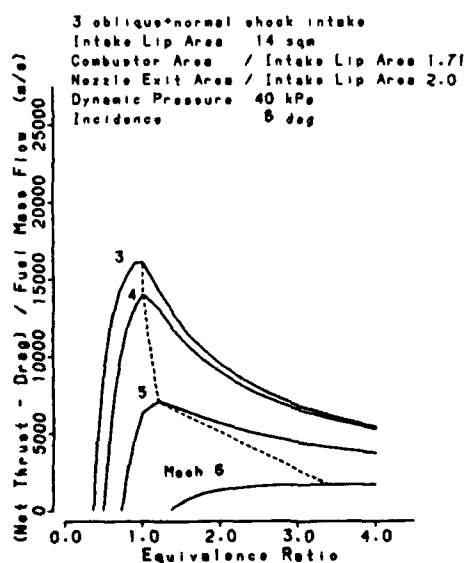


Figure 10: Sensitivity of Ramjet Effective Specific Impulse to Equivalence Ratio

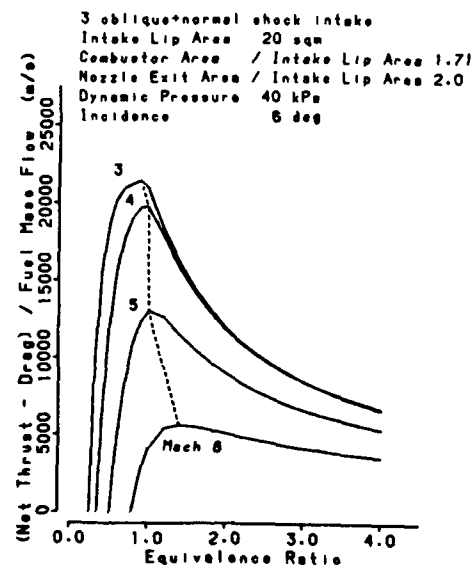


Figure 11: Reduction of Overfueling Requirement with Enlarged Engine Size

Figure 12: Ramjet Nozzle Throat Area Range Requirement vs. Combustor Area

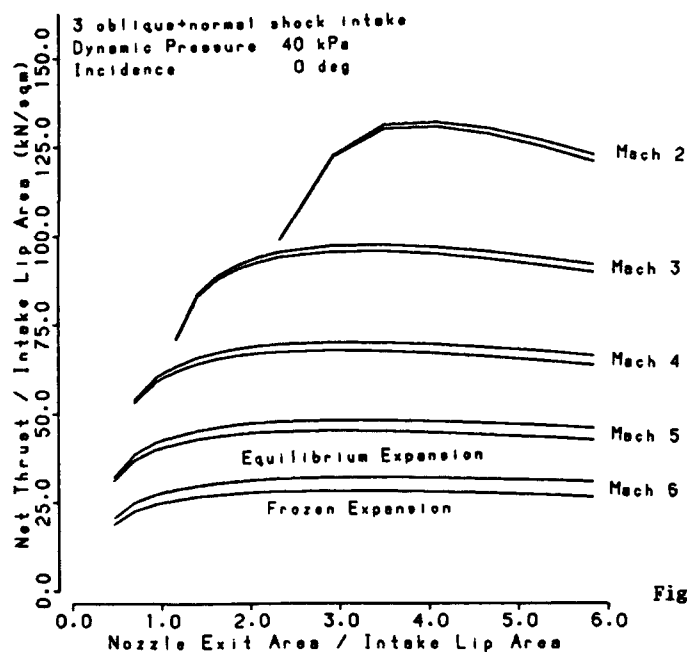
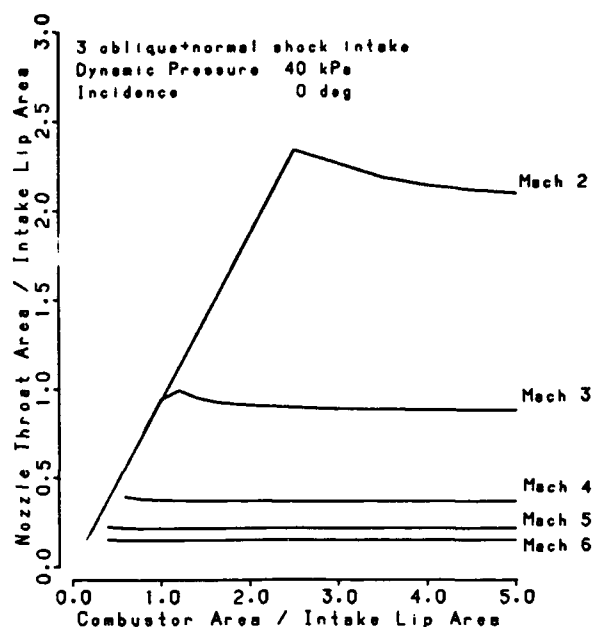


Figure 13: Sensitivity of Ramjet Net Installed Thrust to Nozzle Exit Area

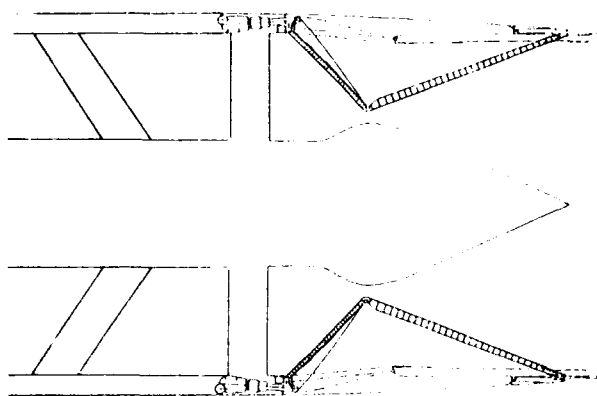


Figure 14: Ramjet Plug Nozzle Configuration, /1/

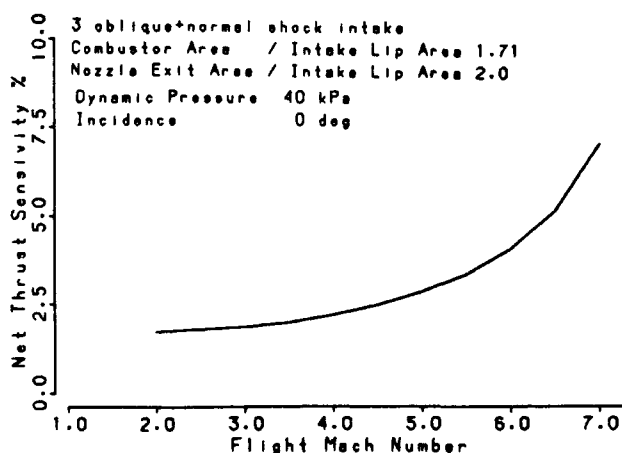


Figure 15: Sensitivity of Ramjet Net Installed Thrust to 1% Change in Nozzle Thrust Coefficient

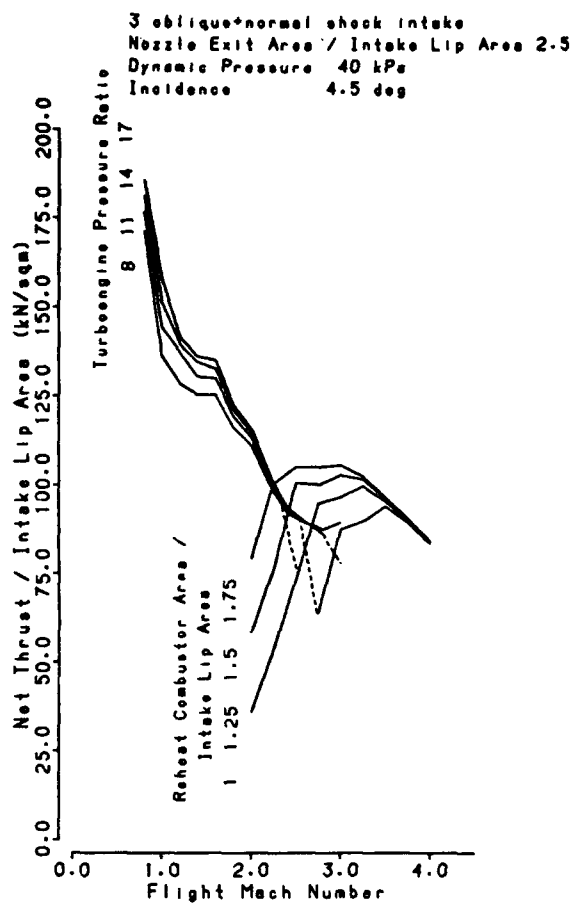


Figure 16: Turboramjet Net Installed Thrust vs. Flight Mach Number

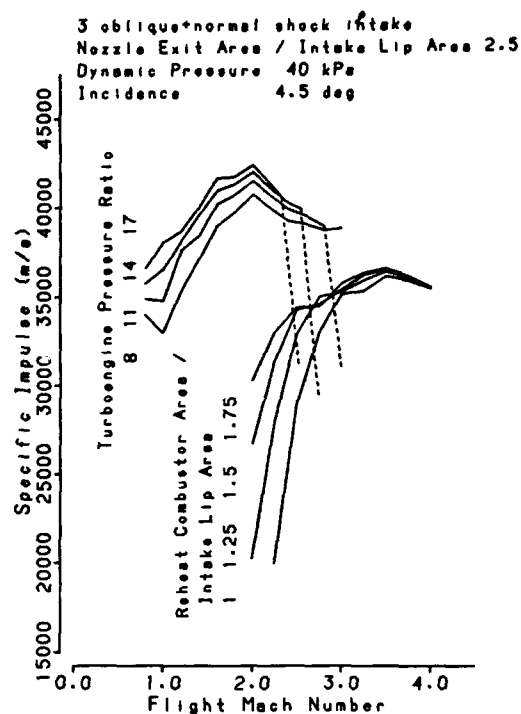


Figure 17: Turboramjet Specific Impulse vs. Flight Mach Number

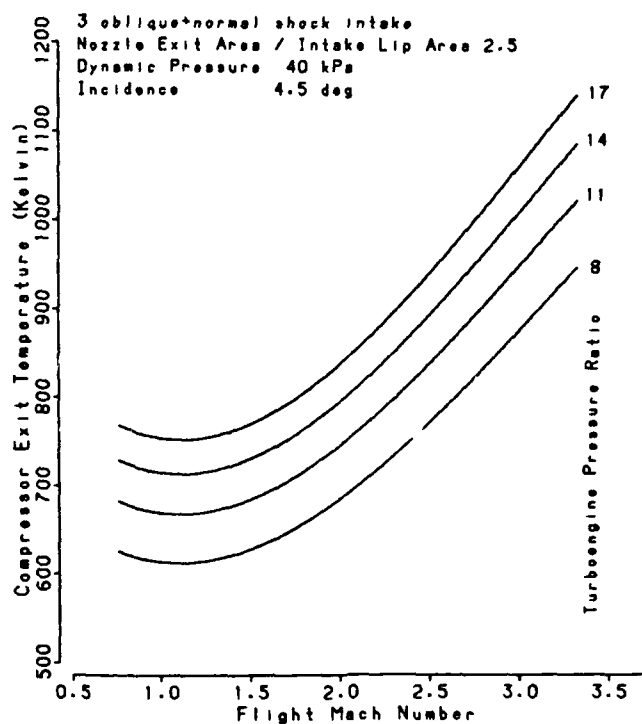


Figure 18: Turbojet Compressor Delivery Temperature vs. Flight Mach Number



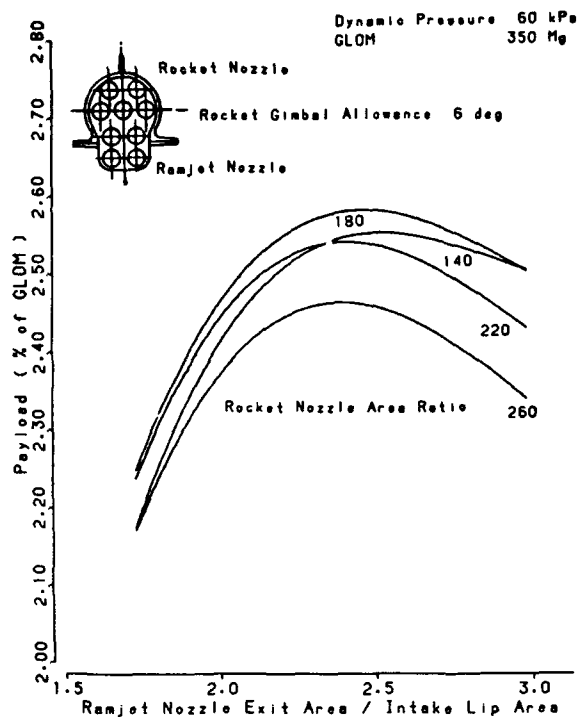


Figure 19: Sensitivity of SSTO Payload to Ramjet-Rocket Combustor Area

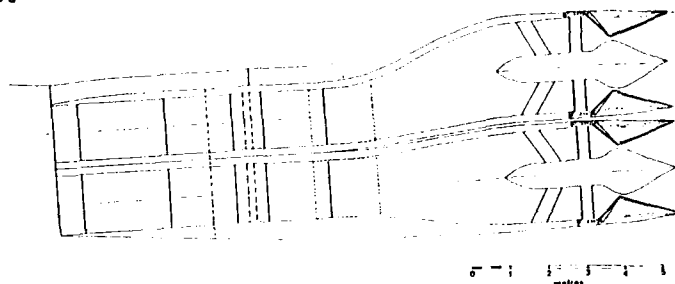


Figure 20: SSTO Ramjet Installation, /1/

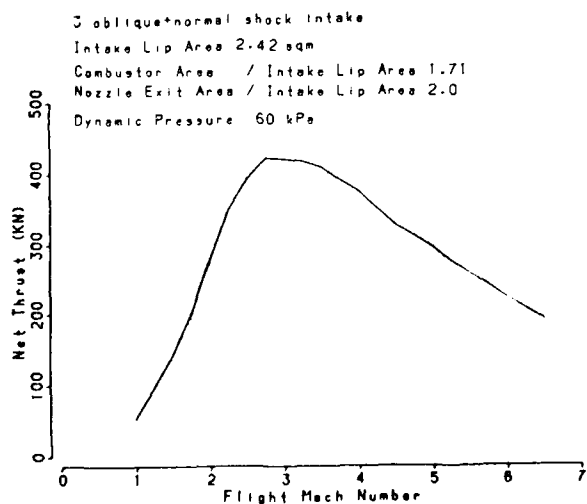


Figure 21: SSTO Ramjet Net Thrust vs. Flight Mach Number, /1/

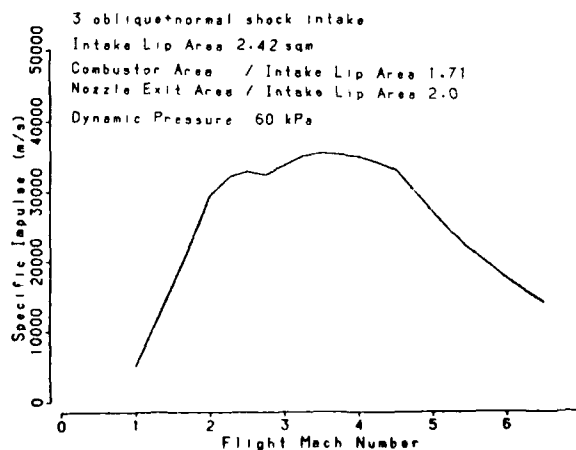


Figure 22: SSTO Ramjet Specific Impulse vs. Flight Mach Number, /1/

## Discussion

GARNERO

It seems to me that in your last results, you are not taking into account the effect of the forebody. Don't you think that some of your conclusions as for payload and thrust may be modified if you take into account the real local flow under the plane (local incidence, local Mach number, local total pressure recovery ...) in function of the forebody chosen and the position of the inlets under the plane?

AUTHOR'S REPLY

Results of figure 19 of my paper have been obtained by a complete optimisation procedure, in which engine performance has been determined on the basis of actual flight conditions (altitude, speed, incidence). Of course a relatively simple approximation has been chosen for forebody precompression, but this assumption is justified by the powerplant installation under the wing.

(If you need more information please do not hesitate to contact me).

# ECHANGEUR COMPACT POUR MOTEUR A COMPOSANTS INVERSES (M.C.I.)

par

Yves Ribaud  
ONERA  
B.P. 72  
F-92322 Châtillon — Cedex  
France

## Sommaire

Une préétude de dimensionnement d'un échangeur cryogénique à contre-courant pour moteur à composants inversés est effectuée en utilisant une formulation analytique puis un code de calcul. Au vu des premiers résultats l'intégration de l'échangeur dans l'axe moteur semble possible sans trop de pénalisation de poids et de longueur. Le principal axe de recherche dans le futur sera orienté vers une diminution du maître couple à l'échappement de la turbine.

## Summary

A pre-sizing study on a counter current heat exchanger fitted for the inverse components engine (I.C.E.) was performed first using analytical calculations and then with a calculation code. The first calculation results show that the heat exchanger integration on the engine axis seems to be possible without a too great penalty on weight and length. The future main research purpose will be directed towards the reduction of the turbine exhaust section.

## Notations

$C_p$	chaleur spécifique à pression constante
$d_h$	diamètre hydraulique
$dQ$	puissance calorifique
$dx$	élément de longueur de l'échangeur
$dy$	épaisseur du tube
$E$	efficacité thermique de l'échangeur
$h$	coefficient d'échange
$L$	longueur de l'échangeur
$M$	nombre de Mach
$m$	débit masse
$Nu$	nombre de Nusselt
$n$	nombre de tubes
$p$	périmètre mouillé
$p_i$	pression d'arrêt
$Pr$	nombre de Prandtl
$r$	richesse
$Re$	Reynolds
$s$	section de passage globale des gaz chauds
$T_i$	température d'arrêt
$U$	vitesse de l'écoulement
$\gamma$	constante isentropique
$\rho$	masse spécifique
$\mu$	viscosité dynamique
$\lambda$	conductivité thermique

## Indices

$c$	fluide chaud
$f$	fluide froid
$-$	pour perte de charge
$+$	pour effet thermique
$E$	entrée échangeur
$S$	sortie échangeur

## 1 - INTRODUCTION

Les études récentes effectuées à l'ONERA sur le moteur à composants inversés, utilisant l'hydrogène comme combustible, ont mis en évidence les qualités de ce concept destiné à la propulsion aérobie à grande vitesse. En particulier il faut souligner que le compresseur est protégé thermiquement, que le nombre de degrés de liberté pour ajuster le point de fonctionnement du moteur est important et qu'enfin les performances thermopropulsives sont excellentes [1] [2]. Cependant le maître-couple, la longueur et le poids de ce type de moteur sont les aspects critiques de cette architecture, au moins dans la mesure où l'on ne considère que le moteur et non pas l'avion spatial et sa mission. C'est pourquoi l'objectif de cette présentation est d'apporter un premier éclairage aux problèmes posés par les échangeurs cryogéniques à contre-courant qui pourraient être utilisés dans ce concept, des réponses même approchées devant être données en terme d'architecture, de performances, de dimensions, de poids et de matériaux.

## 2 - PRÉSENTATION SUCCINCTE DU M.C.I.

Le moteur à composants inversés, monoflux et de type ONERA comporte de l'amont vers l'aval (figure.1) une entrée d'air, un foyer avant, une turbine, un échangeur cryogénique à contre-courant entre

gaz principaux et hydrogène, un compresseur, un foyer aval ou rechauffe, une tuyère de sortie.

Le cycle thermopropulsif est présenté pour trois nombres de Mach : au décollage, à Mach intermédiaire ( $M \approx 3$ ) et à grand nombre de Mach (fig.2). Une compression efficace au décollage est réalisée par le cœur thermodynamique froid (turbine - échangeur - compresseur) sous réserve d'utiliser un débit d'hydrogène suffisant dans l'échangeur.

Pour le fonctionnement à richesse  $r = 2,4^*$  le compresseur est bien protégé thermiquement quel que soit le nombre de Mach de vol puisque la température à l'entrée de cet organe peut être maintenue au voisinage de  $T_1 = 300^\circ \text{K}$ .

La fig.3 montre que les performances thermopropulsives du moteur à composants inverses sont intéressantes et que le choix du mode riche  $r = 2,4$ , régime donnant la poussée maximale, est impératif au décollage.

### 3 - HYPOTHESES DE TRAVAIL ET CADRE DE L'ETUDE

- Le fonctionnement de l'échangeur est analysé en premier au décollage, c'est là que la fonction de refroidissement est essentielle d'un point de vue thermopropulsif.
- L'échangeur sera surtout étudié pour une richesse  $r = 2,4$ . Dans ces conditions la différence de température entre gaz chaud et gaz froid est constante tout le long de l'échangeur et la poussée du moteur est alors maximale (fig.3a).
- L'efficacité thermique de l'échangeur sera prise à  $E = 0,75$  environ. Pour  $E > 0,8$  les performances du moteur sont excellentes mais le poids de l'échangeur est trop important. Par contre pour  $E < 0,7$  le poids de l'échangeur est plus acceptable mais les performances du moteur sont trop faibles.
- Les calculs montrent (fig.4) que lorsque la pression d'arrêt dans la tuyère est grande par rapport à la pression extérieure alors on peut consentir une perte de charge non négligeable dans l'échangeur sans trop altérer la poussée. D'où l'idée d'utiliser un "échangeur rapide" et donc compact et dont le nombre de Mach de l'ordre de 0,3 à 0,5 soit le même que celui utilisé à l'échappement de la turbine.
- L'hypothèse d'un écoulement à grand nombre de Mach conduit à tenir compte dans l'échangeur de la variation de pression d'arrêt, d'origine thermique, dans les gaz principaux :

$$\frac{d p_i}{p_i} = - \frac{\gamma M^2}{2} \frac{d T_i}{T_i} \quad (1)$$

Les applications numériques montrent que cet effet est loin d'être négligeable et notamment lorsqu'on le compare aux pertes de charge.

- Les pertes de charge à l'entrée et à la sortie de l'échangeur sont négligées. Des architectures adéquates seront recherchées afin de minimiser ces pertes aérodynamiques.

### 4 - ETUDE DES CARACTERISTIQUES DE L'ECHANGEUR ET DE LA PERTE DE CHARGE DES GAZ PRINCIPAUX EN REGIME TURBULENT - ( $Re > 10^4$ )

#### Nombre de Reynolds

On suppose que les gaz principaux (indice c) passent dans l'échangeur à l'intérieur de  $n$  tubes de diamètre individuel  $d_h$  et de section de passage globale  $s = \pi \frac{d_h^2}{4} \times n$

Le nombre de Reynolds peut être exprimé en fonction du débit masse  $\dot{m}$ , du nombre de tubes et du diamètre de chaque tube ou de la section de passage globale des gaz chauds :

$$Re = \frac{\rho U d_h}{\mu} = \frac{4 \dot{m}}{\pi \mu d_h} = \frac{\dot{m}}{\mu} \left( \frac{4}{\pi s n} \right)^{0.5} \quad (2)$$

#### Coefficient d'échange thermique

Le coefficient d'échange entre la paroi et les gaz principaux est donné par le nombre de Nusselt dont le comportement en régime turbulent est décrit par la loi :

$$Nu = h_c d_h = 0,023 Re^{0.8} Pr^{1/3} \quad (3)$$

En tenant compte de (2) on obtient :

$$h_c = 0,022 \left( \frac{\dot{m}}{\mu} \right)^{0.8} Pr^{1/3} n^{0.1} s^{-0.9} \quad (4)$$

Cette formule est intéressante à manipuler. Elle permet notamment de vérifier que l'évolution du coefficient d'échange entre le décollage et les grands nombres de Mach de vol ne dépend que de l'évolution du débit-masse.

Remarque : le calcul analytique de la surface d'échange présenté dans les paragraphes suivants sera effectué en supposant que  $h_c$  (gaz froid) est grand devant  $h_c$  (gaz chaud). Pour des calculs plus exacts on utilisera les formules rappelées dans l'Annexe 1.

\*  $r$  : rapport de mélange hydrogène/air ramené au rapport de mélange stochiométrique.

### Surface et longueur d'échange

La surface d'échange, compte tenu de (3) (voir également l'Annexe 1) prend la forme :

$$pL = \frac{1}{0.022} \frac{E}{1-E} Pr^{2/3} \left( \frac{\dot{m}}{\mu} \right)^{0.2} n^{-0.1} s^{0.9} \quad (5)$$

- Cette formule montre que pour réduire le poids de l'échangeur il faut une petite section de passage offerte au fluide principal donc un grand nombre de Mach.
- Il est également intéressant mais à un degré moindre de multiplier le nombre de tubes, dans la mesure où l'on reste turbulent. Ainsi lorsque le nombre de tubes est multiplié par 1000 alors la surface d'échange est divisée par 2.

La longueur de l'échangeur peut s'écrire :

$$L = \frac{(4\pi)^{-1/2}}{0.022} \frac{E}{1-E} Pr^{2/3} \left( \frac{\dot{m}}{\mu} \right)^{0.2} n^{-0.6} s^{0.4} \quad (6)$$

Il apparaît que la longueur est fonction de la section de passage globale du fluide principal mais qu'elle dépend plus encore du nombre de tubes. Sa dépendance avec l'efficacité thermique  $E$  est par ailleurs bien connue.

### Pertes de charge

La perte de pression d'arrêt liée aux effets visqueux s'écrit en mouvement turbulent (hypothèse de tubes lisses et formule de Blasius).

$$\Delta P_1 = \frac{1.742}{\rho} \frac{E}{1-E} Pr^{2/3} \mu^{0.05} \dot{m}^{1.95} n^{0.025} s^{-1.975} \quad (7) \quad \text{après avoir tenu}$$

compte de (2) et de (6).

On constate que la perte de pression d'arrêt dépend très peu du nombre de tubes, d'où l'intérêt du choix d'un grand nombre de tubes pour diminuer le poids et la longueur. La perte de charge varie rapidement avec la section de passage. La perte de pression d'arrêt en valeur relative pour un débit masse donné et une géométrie donnée variera suivant la relation :

$$\Delta \frac{P_1}{P_1} \approx \left( 1 + \frac{\gamma - 1}{2} M^2 \right)^{\frac{1}{\gamma - 1}} \cdot \frac{T_1}{P_1^2} \quad (8)$$

On voit donc que le rendement aérodynamique de l'échangeur va s'améliorer sensiblement entre le fonctionnement au sol et celui à un nombre de Mach de vol de l'ordre de 6,5 dans la mesure où la pression d'arrêt va augmenter sensiblement.

### 5 - CARACTERISTIQUES DE L'ECHANGEUR EN REGIME LAMINAIRE ( $Re < 210^3$ ) (gaz principaux)

En écoulement laminaire et dans le cas d'un flux thermique constant à la paroi le Nusselt est défini par  $Nu = \frac{h_c d_h}{\lambda} = 4.36$  (9)

#### Coefficient d'échange

En suivant le même cheminement que pour les écoulements turbulents on trouve le coefficient d'échange qui est donné par la relation :

$$h_c = 4.36 \left( \frac{\pi}{4} \right)^{0.5} \left( \frac{\dot{m}}{s} \right)^{0.5} \lambda \quad (10)$$

Le coefficient d'échange dépend alors beaucoup plus du nombre de tubes qu'en écoulement turbulent et par contre le débit masse n'intervient plus.

#### Longueur et surface d'échange

La surface d'échange dépend essentiellement de l'efficacité thermique, du débit masse, de la section de passage globale offerte au fluide et du nombre de tubes :

$$pL = \frac{1}{4.36} \left( \frac{4}{\pi} \right)^{0.5} Pr \frac{E}{1-E} \frac{\dot{m}}{\mu} \left( \frac{s}{n} \right)^{0.5} \quad (11)$$

La longueur de l'échangeur est cette fois ci indépendante de la section de passage globale et inversement proportionnelle au nombre de tubes :

$$L = \frac{1}{4.36} \frac{1}{\pi} \cdot Pr \frac{E}{1-E} \frac{\dot{m}}{\mu} \cdot \frac{1}{n} \quad (12)$$

### Pertes de charge

La perte de pression d'arrêt par effets visqueux est cette fois-ci totalement indépendante du nombre de tubes :

$$\Delta P_1 = 1,835 \text{ Pr } \frac{E}{1-E} \frac{\dot{m}^2}{\rho s^2} \quad (13)$$

Néanmoins les formules (7) et (13) en laminaire et en turbulent prennent des formes assez voisines.

### 6 - FONCTIONNEMENT HORS ADAPTATION

Pour une géométrie donnée il apparaît (Annexe 2) que l'efficacité thermique dépend essentiellement du débit masse. La figure 10 montre que l'efficacité thermique de l'échangeur varie peu en écoulement turbulent. Ainsi lorsque le débit masse est égal à trois fois le débit masse à l'adaptation alors l'efficacité thermique passe de  $E = 0,75$  à  $0,71$ .

Au contraire en écoulement laminaire la diminution de l'efficacité thermique lorsque le débit masse augmente est beaucoup plus rapide. Ainsi quand le débit masse passe de l'adaptation à trois fois cette valeur alors  $E$  passe de  $0,75$  à  $0,5$ . Cette chute rapide de l'efficacité se traduit par une baisse brutale de la compression fournie par le moteur à composants inversés.

### 7 - APPLICATIONS

Un programme de calculs numériques de dimensionnement a été réalisé afin d'étudier des cas plus généraux que ceux décrits à l'aide des formules analytiques. Il est aussi possible d'étudier les cas où la richesse est différente de 2,4 ou encore les situations où le coefficient d'échange de l'hydrogène est comparable à celui des gaz principaux. Il est également possible de prévoir le maître-couple global de l'échangeur. Les calculs présentés ont été effectués pour une efficacité thermique  $E = 0,75$  et pour un nombre de Mach du circuit d'hydrogène  $M_H = 0,01$ . Les résultats sont fournis en supposant que les gaz principaux passent à l'intérieur des tubes d'épaisseur  $0,2 \text{ mm}$  et de densité 3. Notons que cette densité est envisageable car la majeure partie de l'échangeur peut être fabriquée en utilisant des alliages d'aluminium tandis que la partie chaude qui est sensiblement à la température de l'hydrogène sortant ( $t = 780^\circ\text{C}$ ) peut être constituée par des alliages de titane.

Les résultats sont présentés pour les régimes d'écoulement laminaire ( $Re < 210^3$ ) puis turbulent ( $Re > 10^4$ ) des gaz principaux. Dans les deux cas les courbes sont tracées à nombre de Nusselt constant. Dans le cas turbulent si le Nusselt est constant alors le Reynolds est constant. La fig. 5 donne l'évolution du poids de l'échangeur rapporté à la poussée, en fonction du nombre de Mach des gaz principaux. On vérifie qu'en écoulement laminaire le poids de l'échangeur dépend essentiellement du diamètre des tubes. Au contraire en écoulement turbulent le poids dépend à la fois du diamètre des tubes et du nombre de Reynolds. Le domaine d'étude est limité à  $M = 0,4$  en laminaire et à  $M = 0,45$  en turbulent car au delà (fig.6) la perte de pression d'arrêt dépasse  $50 \%$  et un blocage sonique s'installe alors rapidement à l'intérieur de l'échangeur. La fig.7 montre que la longueur de l'échangeur est très faible en écoulement laminaire et par contre qu'elle atteint plusieurs mètres en écoulement turbulent.

La fig.8 permet de préciser le nombre de tubes, qui bien sûr est très important en écoulement laminaire alors que des nombres beaucoup plus modérés sont obtenus en écoulement turbulent.

La fig.9 donne l'évolution de la section de passage des gaz chauds et du maître couple de l'échangeur avec le nombre de Mach. La section de passage de l'hydrogène altère peu le maître-couple ( $M_H=0,01$ ) par contre en écoulement laminaire le maître-couple est accru de  $3 \text{ m}_2$  environ du fait du grand nombre de tubes. L'examen de l'ensemble des résultats présentés sur les fig.5 à 9 montre que le meilleur compromis semble être obtenu pour un nombre de Mach des gaz chauds égal à  $0,45$  et un nombre de Reynolds égal à  $10^4$ . Le cas où l'écoulement est laminaire et où le diamètre hydraulique des tubes est égal à  $3 \text{ mm}$  semble attrayant mais il demande  $10^6$  tubes, ceux-ci étant distants l'un de l'autre de quelques dixièmes de millimètre. Cette configuration semble donc difficilement réalisable.

La solution optimale est présentée dans le tableau 1 ci-après. On vérifie que le coefficient d'échange pour l'hydrogène est à peu près dix fois plus grand que celui pour les gaz principaux.

### CONCLUSION

- Des formules analytiques ont été établies dans le cas d'hypothèses simplifiées pour permettre de dimensionner rapidement un échangeur cryogénique à contre-courant pour M.C.I. et notamment d'étudier les évolutions du poids, de la longueur de celui-ci en fonction du nombre de tubes et de la section de passage des gaz principaux.
- Un programme de calcul a été établi pour traiter des cas plus généraux et permettre d'accéder également au maître-couple de l'échangeur.
- Les applications numériques de ce programme de calcul ont permis d'explorer les domaines où le nombre de Reynolds des gaz principaux est laminaire puis turbulent. Les évolutions des grandeurs caractérisant la géométrie de l'échangeur en fonction du nombre de Mach des gaz principaux et du diamètre des tubes dans le cas laminaire ou du Reynolds dans le cas turbulent sont conformes à celle données par les formules analytiques. Le meilleur compromis sur les caractéristiques géométriques de l'échangeur est obtenu en régime thermique faiblement turbulent, le poids obtenu est environ  $10 \%$  de la poussée et la longueur de celui-ci est de  $2,50 \text{ mètre}$ .

- Le régime d'écoulement situé dans la transition laminaire-turbulent peut s'avérer intéressant pour parfaire l'optimisation de l'échangeur. Il reste cependant à vérifier que le déclenchement artificiel de la turbulence accroît autant le coefficient d'échange que la perte de charge. L'intérêt de tubes munis d'ailettes doit aussi être démontré.
- Les résultats de cette préétude montrent que le principal handicap du M.C.I. concerne l'importance du maître couple à l'échappement de la turbine. Cette difficulté doit pouvoir être minimisée d'une part en jouant sur les paramètres de fixation du cycle thermodynamique et d'autre part en adaptant l'architecture du moteur à composants inversés.

TABLEAU 1

CARACTERISTIQUES DE L'ECHANGEUR OPTIMISE A TUBES DE GAZ PRINCIPAUX
---

Géométrie, côté gaz chauds et perte de charge

pression d'arrêt d'entrée	310 <sup>4</sup> pascals
température d'arrêt d'entrée	1400 K
diamètre des tubes	16 mm
nombre de Mach à l'entrée	0,5
nombre de Reynolds à mi-échangeur	10 <sup>4</sup>
section de passage du fluide chaud	5,6 m <sup>2</sup>
section totale	6,4 m <sup>2</sup>
longueur de l'échangeur	2,50 m
nombre de tubes	27500
poids/poussée	10,2 %
perte de pression d'arrêt	46 %
coefficient d'échange gaz chauds	118 (M.K.S.A.)
poussée au décollage	210 <sup>5</sup> N.

caractéristiques du circuit d'hydrogène

pression d'arrêt d'entrée	210 <sup>6</sup> pascals
température d'arrêt d'entrée	20 K
diamètre hydraulique	
(cas où l'on choisit des tubes à hydrogène)	1,7 mm
coefficient d'échange pour l'hydrogène	1170 (M.K.S.A.)
nombre de Reynolds	1240

REFERENCES

- [1] P. CONTENSO, P. DUBAN and Y. RIBAUD. "Moteur à cycle inverse" (I.C.E.). Demande de brevet France 8707396,26587
- [2] Y. RIBAUD. Inverse cycle engine for hypersonic air breathing propulsion-9<sup>th</sup> Symp. on Air Breathing Engines Athènes (Grèce), September 4-9, 1989.

## ANNEXE 1 (rappel)

## 1 - COEFFICIENT D'ECHANGE GLOBAL

Si l'on considère une longueur élémentaire  $dx$  de l'échangeur, la puissance calorifique traversant la surface mouillée correspondante  $ds = p dx$ , où  $p$  représente le périmètre mouillé s'écrit :

$dq = hp dx (T_c - T_f)$  où  $T_c - T_f$  représente la différence de température entre le flux chaud et le flux froid et  $h$  le coefficient d'échange global tenant compte des effets de conduction et de convection et qui prend la forme :

$$\frac{1}{hp} = \frac{1}{h_c p_c} + \frac{dy}{p \lambda_m} + \frac{1}{h_f p_f} \quad 1$$

$dy$  représentant l'épaisseur de la paroi métallique séparant les deux flux et  $\lambda_m$  la conductivité thermique du métal.

Les applications numériques montrent que la résistance thermique du métal est négligeable devant celle des deux gaz.

## 2 - LONGUEUR ET SURFACE D'ECHANGE

On distingue deux cas suivant le rapport des capacités calorifiques des deux fluides :

a)  $\dot{m}_f C_{pf} \neq \dot{m}_c C_{pc}$

La longueur  $L$  de l'échangeur est donnée par :

$$L \cdot h p \left[ \frac{1}{\dot{m}_f C_{pf}} - \frac{1}{\dot{m}_c C_{pc}} \right] = \ln \left[ \frac{(T_{cs} - T_{fe})}{(T_{ce} - T_{fs})} \right] \quad 2$$

La surface d'échange est donnée par le produit  $pL$ , l'indice  $S$  correspond aux conditions de sortie et l'indice  $E$  aux conditions à l'entrée de l'échangeur.

b)  $\dot{m}_f C_{pf} = \dot{m}_c C_{pc}$  alors  $T_c - T_f = \text{cste} = (\Delta T)^{ce}$

c'est ce dernier cas qui est étudié au décollage. La longueur de l'échangeur s'écrit alors sous la forme :

$$L = \frac{\dot{m}_c C_{pc} (T_{ce} - T_{cs})}{h p (\Delta T)^{ce}} = \frac{\dot{m}_c C_{pc} E}{p \cdot h (1 - E)} = L_{(E=1/2)} \cdot \frac{E}{1 - E} \quad 3$$

## ANNEXE 2

## FONCTIONNEMENT HORS-ADAPTATION DE L'ECHANGEUR

La géométrie de l'échangeur étant donnée les performances de celui-ci dépendent essentiellement du débit-masse.

Ecoulement turbulent  $Re = \frac{\dot{m}}{\mu} \left( \frac{4}{\pi S n} \right)^{0.5} > 10^4$

Efficacité thermique  $E$  :

$$\frac{1 - E}{E} = 12,82 Pr^{2/3} \cdot \frac{1}{L} \left( \frac{\dot{m}}{\mu} \right)^{0.2} n^{-0.6} S^{0.4}$$

Perte de charge :

$$\rho \Delta p_L = 1,358 \cdot 10^{-1} \cdot \mu^{0.25} \cdot \dot{m}^{1.75} \cdot n^{0.625} \cdot S^{-2.375}$$

Ecoulement laminaire  $Re = \frac{\dot{m}}{\mu} \left( \frac{4}{\pi S n} \right)^{0.5} < 210^3$

Efficacité thermique  $E$  :

$$\frac{1 - E}{E} = 7,310^{-2} \cdot Pr \cdot \left( \frac{\dot{m}}{L \mu} \right) \cdot \frac{1}{n}$$

Perte de charge :

$$\rho \Delta p_L = 25,13 \frac{\dot{m} \cdot \mu \cdot n}{S^2}$$



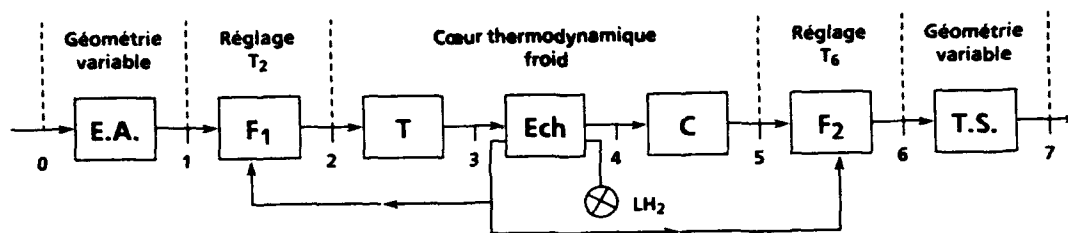


Fig. 1 - Schéma de principe du moteur à composants inversés (Brevet ONERA).

Notations : E.A. : entrée d'air - F<sub>1</sub> : foyer 1 - T : turbine - Ech : échangeur  
C : compresseur - F<sub>2</sub> : foyer 2 - T.S. : tuyère de sortie.

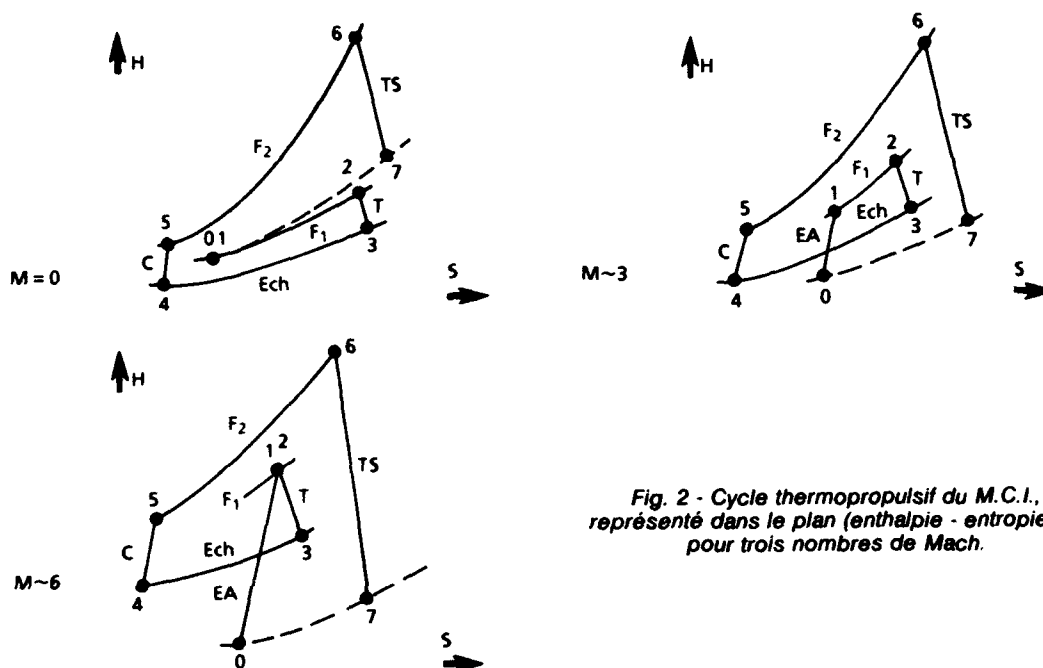


Fig. 2 - Cycle thermopropulsif du M.C.I., représenté dans le plan (enthalpie - entropie) et pour trois nombres de Mach.

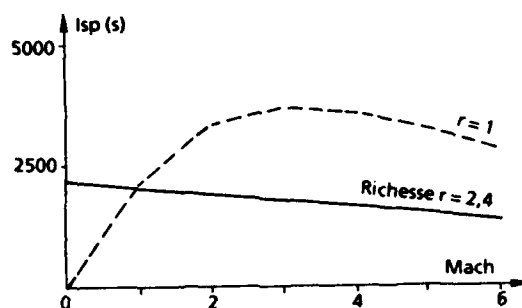


Fig. 3a - Performances maximales : impulsion spécifique.

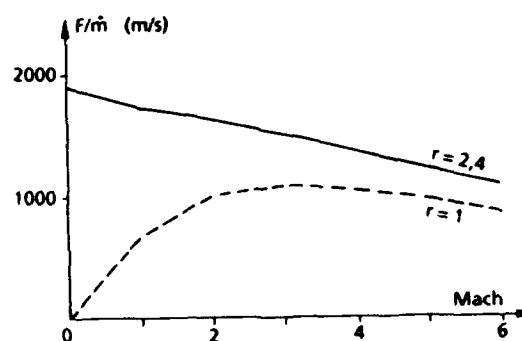


Fig. 3b - Performances maximales : poussée unitaire.

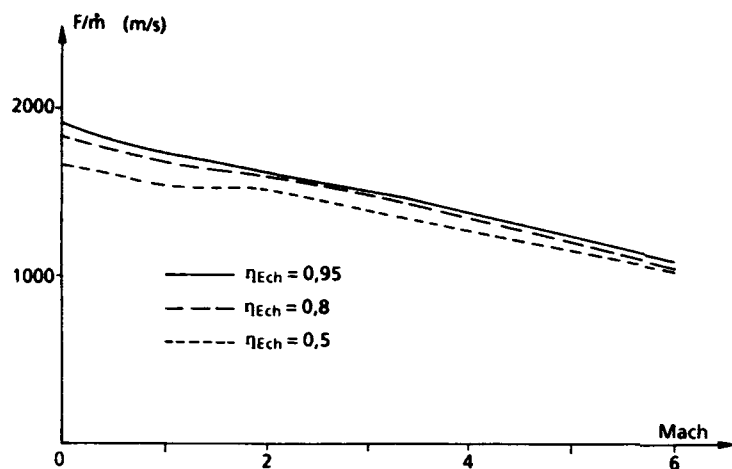


Fig. 4 - Evolution de la poussée unitaire avec le rendement aérodynamique de l'échangeur.

Fig. 5 - Evolution du poids de l'échangeur en fonction du nombre de Mach des gaz principaux à l'entrée. (courbes à  $Nu = cte$ )

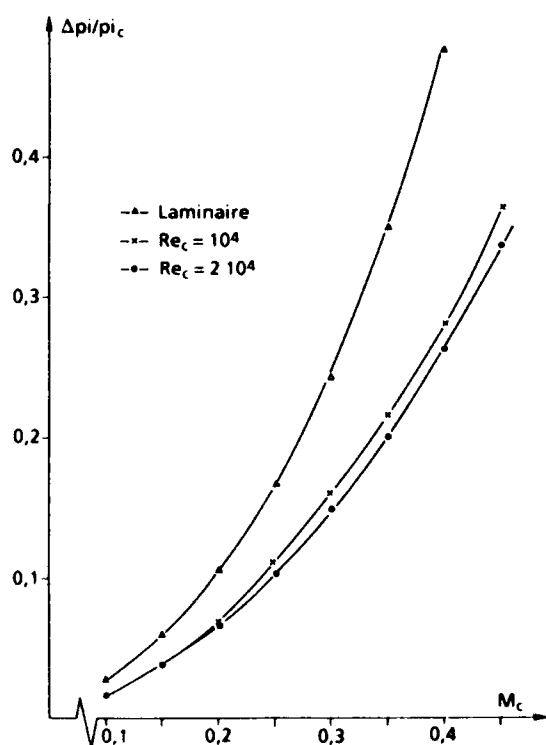
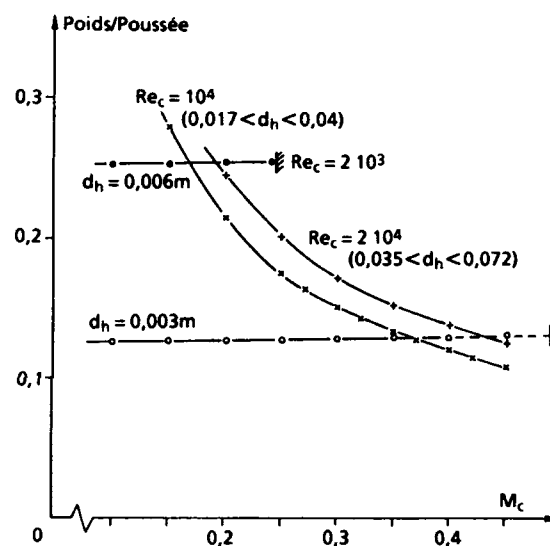


Fig. 6 - Perte de pression d'arrêt dans l'échangeur en fonction du nombre de Mach d'entrée.

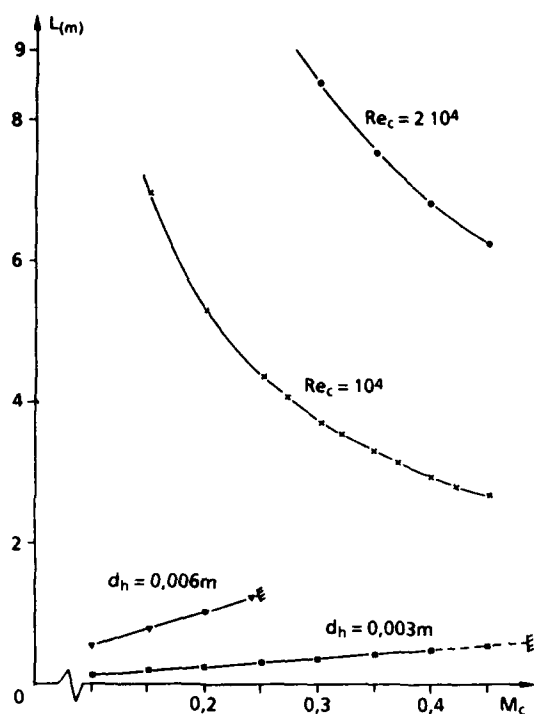


Fig. 7 - Longueur de l'échangeur en fonction du nombre de Mach  $M_c$  (courbes à  $Nu = cte$ ).

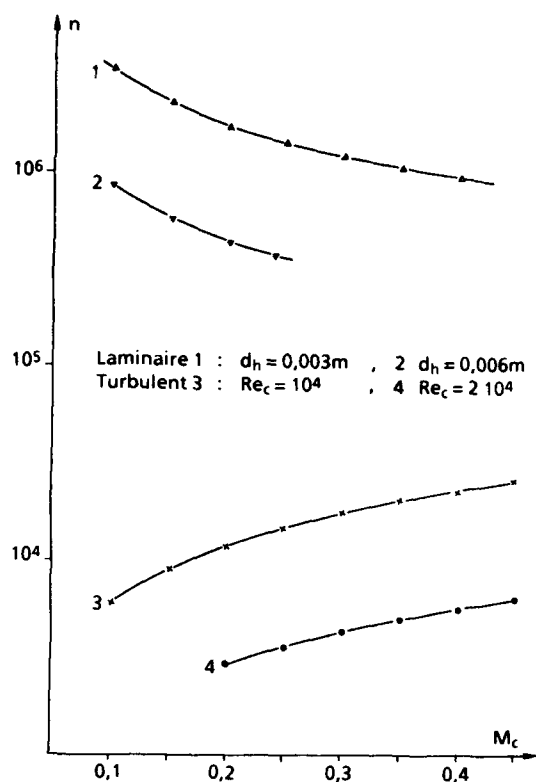


Fig. 8 - Nombre de tubes en fonction du nombre de Mach.

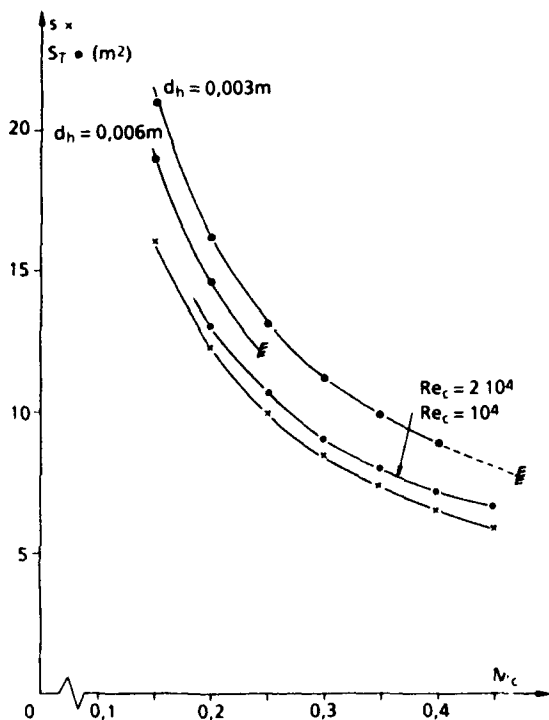


Fig. 9 - Evolution de la section des gaz chauds et du maître-couple de l'échangeur avec le nombre de Mach.

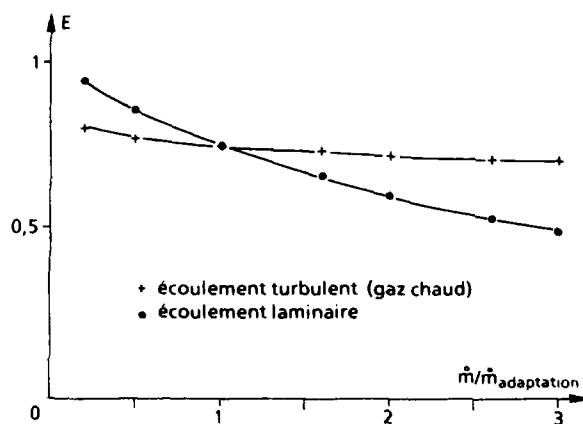


Fig. 10 - Evolution de l'efficacité thermique de l'échangeur avec le débit masse  $\dot{m}$ .

## Discussion

RICAULT

Y-a-t-il des problèmes de givrage ou de condensation des produits de combustion à l'entrée de la turbine?

AUTHOR'S REPLY

Oui, si l'efficacité thermique de l'échangeur est égale à 0.8 et si la température à l'entrée de la turbine est trop faible. Dans les calculs présentés il n'y a ni givrage ni condensation des produits de combustion. Si on peut éviter le givrage alors les performances seront augmentées au décollage.

BRAVAIS

Compte tenu des mauvais coefficients d'échange coté air, ne pensez-vous pas qu'un échangeur à ailettes permettrait de diminuer la masse de l'échangeur?

AUTHOR'S REPLY

Effectivement, les ailettes sont souvent utilisées dans le cas où l'un des gaz a un faible coefficient d'échange par rapport au deuxième gaz - le point délicat, dans le cas qui nous intéresse, est que si nous utilisons des ailettes nous allons augmenter la surface d'échange même si nous pouvons éventuellement gagner sur le poids puisque celles-ci sont très fines, or nous ne pouvons dépasser une perte de pression d'arrêt de 50% et donc la présence d'ailettes va nous conduire à un maître-couple encore plus important.

BRAIG

Your concept makes some sense to me as far as thermodynamics are concerned. But especially at low Mach numbers, I expect a low thrust related to cross section, as by heating up behind the intake, you increase the volume slow, and you continue to increase it by expanding in the turbine.

AUTHOR'S REPLY

Je suis d'accord avec vous mais dans la mesure où la vitesse d'éjection est élevée pour une même poussée on pourra diminuer le poids de l'entrée d'air. D'autre part la pression d'arrêt étant importante à la sortie du compresseur le poids de la tuyère sera plus faible. D'autre part nous n'en sommes qu'au début de l'étude et de nombreuses améliorations sont possibles.

WEYER

At  $Ma=0$  the engine concept you are proposing probably has a very low thrust to weight ratio because of large turbomachines. How can you provide sufficient overall thrust for vehicle take-off?

AUTHOR'S REPLY

Vous mettez l'accent sur le point délicat qui est le poids et le maître-couple important du moteur et c'est bien logique! Seulement il ne faut pas oublier les points positifs : les poids de l'entrée d'air et de la tuyère vont être réduits, la vitesse d'éjection étant importante ainsi que la pression d'arrêt dans la tuyère. D'autre part l'étude ne fait que débiter et de nombreuses améliorations sont possible.

## Design Considerations for Combined Air Breathing-Rocket Propulsion Systems

David L. Kors  
Chief Engineer, Aero propulsion

Aerojet TechSystems  
P.O. Box 13222  
Sacramento, CA 95813-6000

PRA-SA-WPAFB #90-0098 12 FEB 90

**ABSTRACT**

Combined air breathing-rocket propulsion systems have been studied and carried through proof-of-principle demonstrations during the last three decades. Currently, a number of countries are studying and in some cases actually starting development of demonstrator vehicles for hypersonic flight which use combinations of air breathing and rocket propulsion. A summary of this activity including the propulsion options being investigated is discussed in this paper.

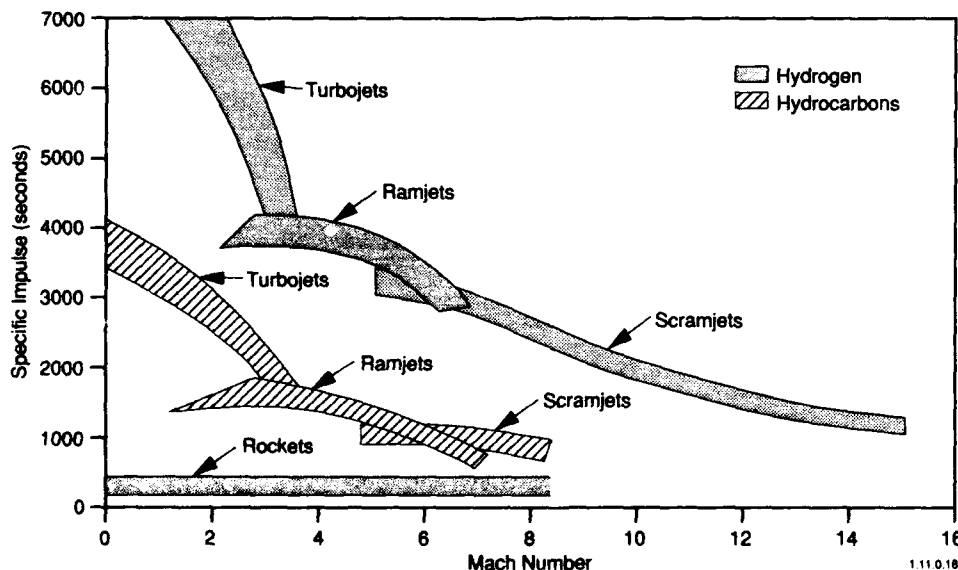
This type of propulsion is much more revolutionary in nature than most previous propulsion developments and thus results in technology challenges that are even more severe than those faced by either conventional air breathing propulsion or rocket designers. These include: 1) propulsion/vehicle integration, 2) engine stability over a wide operating range, 3) high performance over a wide operating range, 4) system level thermal management and 5) advanced materials. A discussion of these technical issues including the impact of underachieved development goals on system level performance is also included in this paper.

**Introduction**

Future military and civilian aerospace objectives of the world's major nations include a strong interest in missions and vehicles that fly at sustained hypersonic speeds within the atmosphere and, in many recent ventures, include space transportation as the ultimate goal. The United States is pursuing their NASP (Ref. 1), the Federal Republic of Germany is progressing on their Sänger vehicle (Ref. 2), and France and Japan are actively studying vehicles that utilize both rocket and air breathing propulsion (Ref. 3 and 4). These advanced hypersonic/space launch vehicles are considered to be justifiable primarily because recent advances in propulsion, materials, electronics, and computational fluid dynamics (CFD) provide substantial technology foundations for a development program by a major nation or a group of nations in the next decade or two.

All of these hypersonic/space launch vehicles utilize combinations of air breathing and rocket propulsion. Air breathing propulsion is used for at least some portion of the flight envelope since flight within the earth's atmosphere can take advantage of air as a source of oxygen for chemical propulsion. Rockets, while required for exoatmospheric flight, have such low specific impulse that the use of air breathing propulsion within the atmosphere may result in a lighter, lower cost vehicle. This advantage is illustrated by the relative levels of specific impulse for various propulsion cycles shown in Figure 1. Air breathing propulsion typically has an order of magnitude higher specific impulse at the low end of the Mach number range and has the potential for a significant increase over rockets at hypersonic flight conditions.

FIGURE 1. SPECIFIC IMPULSE FOR VARIOUS PROPULSION DEVICES.



92-16957

Another conclusion that can be drawn from Figure 1 is that no one propulsion concept is optimum over the entire flight Mach number range. Turbojets and other turboaccelerators have very high specific impulses at low Mach number, but are limited to operation below approximately Mach 5. Ramjets can operate from a Mach number below 2 to approximately Mach 6 and supersonic combustion ramjets (scramjets) cover the upper Mach number flight regime. Chemical rockets, which produce a low, but nearly constant specific impulse for the entire flight, may actually be higher performing at high Mach numbers. These characteristics strongly suggest that some combination of air breathing and rocket propulsion systems might be optimum for space launch/hypersonic flight vehicles which take off from the ground and accelerate to hypersonic conditions within the atmosphere.

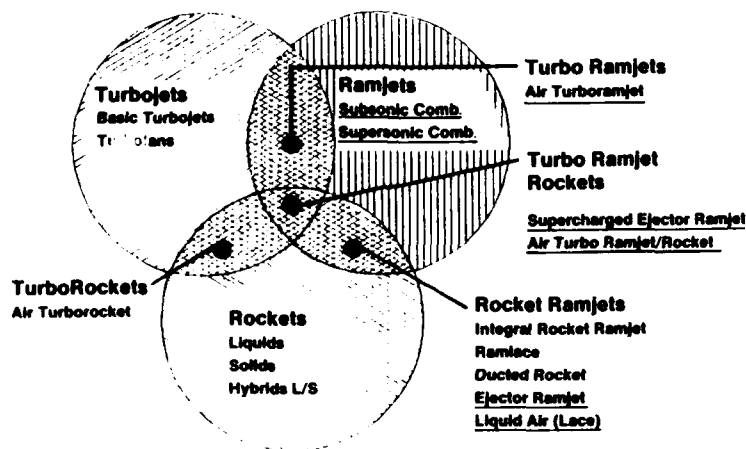
Although a space launch vehicle could carry separate air breathing and rocket propulsion systems, the cumulative weight and volume requirements would impose a large penalty. If both air breathing and rocket propulsion concepts are combined into a single propulsion system, a considerable synergistic benefit accrues due to shared components and functions.

Combined air breathing-rocket propulsion concepts have evolved from the rocket and the two basic air breathing types: 1) the turbojet, 2) and the ramjet. The turbojet is the progenitor of turbomachinery devices which mechanically compress air so that heat can be added prior to expansion through a turbine and an exhaust nozzle. Ramjets are air breathing devices that are accelerated via other propulsion to a speed sufficient to aerodynamically compress the air prior to adding heat and expanding through an exhaust nozzle. Unlike the turbojet and ramjet, which use atmospheric air as an oxidizer, the rocket carries its own oxidizer as well as its own fuel.

Representative combinations of these three basic engine types are listed in Figure 2, where their interrelationships are shown as overlapping areas of the circles representing the three basic engine types. There are combined cycle concepts based on any two and all three of the basic types. Derivatives of the basic types (turbojets, ramjets and rockets) which have potential application for hypersonic flight are listed in Figure 2. There are numerous other concepts beyond those listed, although the bulk of the historical development work cited in the open literature for hypersonic flight are represented by the underlined items in Figure 2.

A previous paper (Ref. 5) describes each of the combined cycle concepts underlined in Figure 2, and reviews the major advances in hypersonic propulsion during the last three decades. In this present paper, the focus is on the unique characteristics and development issues for combined air breathing-rocket propulsion of the future. First, the overall mission/vehicle design considerations are discussed including a review of current world-wide development. This is followed by a discussion of technology challenges for combined air breathing-rocket propulsion systems, including the impact of underachieved scramjet development goals on system level performance.

FIGURE 2. BASIC ENGINES AND COMBINED CYCLES.



#### Overall Mission/Vehicle Design Considerations

Combined air breathing-rocket propulsion systems have potential application on at least three broad categories of missions/vehicles: 1) space launch vehicle, 2) hypersonic cruise airplanes, and 3) hypersonic missiles. Each of these categories will be discussed in terms of design considerations for combined air breathing-rocket propulsion systems. The discussion on space launch vehicles and hypersonic cruise airplanes will be treated as one since development of these two concepts has many similar aspects and is actually being done with common technology demonstrators which are designed to be applicable to both missions. The hypersonic missile application will be discussed separately.

Space Launch/Hypersonic Cruise Vehicles - Using the information in References 1 through 4, Table I was developed, which summarizes the published status of hypersonic/launch vehicle and propulsion development activities for several leading countries of the world. It should be noted that there are reports indicating that the Soviet Union is also active in this emerging technology, but published data is insufficient to catalog in the Table I format.

TABLE 1. HYPERSONIC/SPACE LAUNCH VEHICLE AND PROPULSION DEVELOPMENT ACTIVITIES.							
COUNTRY	MISSIONS	VEHICLE	PROPULSION SYSTEMS	FUELS	CURRENT STATUS	FIRST FLIGHT DATE	REF.
USA	• Space launch • Hypersonic flight	NASP X30 (demonstrator) SSTO	• Ramjet/scramjet • Rockets • Various low speed systems	Cryo H2 • liquid • slush	• Full scale module/ complete engine system tests	1997	1
FRG	• Space launch • Hypersonic flight	Sanger (demonstrator) TSTO	• Turboramjet (1st Stage) • Liquid Rocket (2nd Stage) • Scramjet (future)	Cryo H2	• Ramjet tests • Turboramjet technology tests	1999/2000 (1st stage)	2
FRANCE	• Space launch • Hypersonic flight	STS 2000 (studies) • SSTO  • TSTO	• Turboramjet/ramjet/rocket • Rocket/ramjet/rocket • Scramjet  • Turborocket/ramrocket • Turbofan/ramrocket	Cryo H2	• Concept studies	2010/2020	3
JAPAN	• Space launch • Hypersonic flight	Space Plane (demonstrator) • SSTO • TSTO • A-B Expend. Boosters	• Turboengine concepts • LACE • Ducted Rocket/Ejector Rocket • Scramjets • Rocket	Cryo H2 • liquid • slush	• LACE tests • Turboramjet tests • Turbojet studies • Scramjet design	21st Century	4

The following conclusions can be drawn from examination of the Table I information and more detailed reading of the published data:

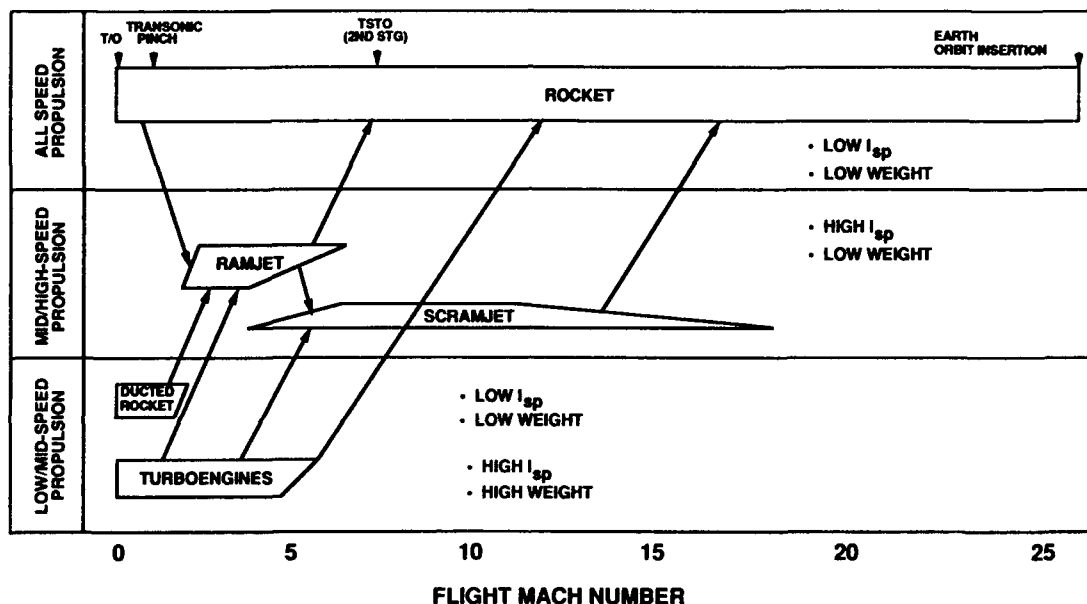
- Both space launch and hypersonic cruise are mission objectives.
- Hypersonic vehicles using combinations of air breathing and rocket engines are planned for first flight within the present decade.
- Both Single Stage to Orbit (SSTO) and Two Stage to Orbit (TSTO) vehicles are being developed.
  - SSTO vehicles will utilize ramjets/scramjets for use in the hypersonic flight corridor because of their inherently high specific impulse and low weight.
  - SSTO vehicles will transition from scramjets to rockets at the upper end of the hypersonic flight corridor.
  - TSTO vehicle first stage propulsion studies include a wide variety of turboengines, rockets, and LACE; actual development to date is limited to combined cycle turboengines and LACE.
- Cryogenic hydrogen is the universal choice for fuel because of its high energy content for performance and its large heat capacity for vehicle and engine cooling.

A combined air breathing-rocket propulsion road map (Figure 3) was constructed based on a synthesis of the propulsion system studies shown on Table I. The interrelationships between propulsion types and the flight spectrum from take-off to orbit insertion are described in the following statements.

- An all rocket propulsion system is capable of performing over the entire speed range from take-off through earth orbit insertion. Its specific impulse is lower than the air breathers except at the higher hypersonic flight conditions; however, its specific weight (engine weight per pound of thrust produced) is also usually lower than air breathers.
- A rocket can also be used as supplemental propulsion for air breathing hypersonic propulsion systems that may require thrust augmentation at 1) take-off, 2) during the transonic high drag pinch-point, 3) high hypersonic flight conditions beyond the range of scramjet effectiveness and 4) exoatmospheric flight into low Earth orbit.
- Low/mid-speed air breathing propulsion is focused on either the various versions of turbomachines that use mechanical compression or the ducted rocket that uses a rocket chamber as an ejector/jet pump to aerodynamically compress the air prior to heat addition.

- Ducted rockets quickly transition to ramjet mode to minimize the impact of their low specific impulse on vehicle performance.
- Turboaccelerators, because of their high specific impulse, can be used until either their specific impulse drops below that of an accompanying ramjet or their rotating machinery can no longer withstand the high energy level in the ram air. In the former case, it will transition to an air breathing ramjet; whereas for the latter case, it will transition either to a scramjet or directly to a rocket for the high speed portion of the flight corridor.
- Mid/high speed air breathing propulsion is the domain of the ramjet. At lower speeds the subsonic combustion ramjet is optimum, but transition to either a rocket or supersonic combustion (scramjet) is required when flight Mach numbers approach and extend beyond Mach 7. At these flight conditions, the flow energy is so high that it must remain as kinetic energy rather than being slowed down to subsonic velocity and converted to available thermal energy in the form of prohibitively high static pressures and temperatures. Thus, the scramjet best fits the wide niche in hypersonic flight between the ramjet and the point where the rocket provides equal or greater performance.

FIGURE 3. AIR BREATHING-ROCKET PROPULSION COMBINATIONS.



Considerations for selecting specific propulsion concepts not only involve the mission objective but also the degree of technical risk willing to be assumed. For example, the space launch/hypersonic flight demonstrator vehicles listed in Table 1 take different paths on the propulsion road map shown in Figure 3 primarily because of the different degree of technical risk assumed by the sponsoring nation. The NASP demonstrator is a maximum risk/maximum payoff concept that derives highest propulsion performance over the entire flight regime by incorporating a low speed system, a combined ramjet/scramjet for much of the regime between take-off and orbit, and a rocket system for orbital insertion. In this way, the higher performance potential of air breathers can be achieved over the entire flight regime. In order to achieve this level of performance, however, the inherent development risk for each of these different modes of propulsion has to be assumed.

The FRG, on the other hand, has elected to assume a lower level of propulsion development risk with their Sanger concept. Referring back to Figure 3, the Sanger takes off with a turboengine and transitions to a ramjet mode at supersonic flight speeds. As the Mach number limit of the ramjet is approached at approximately Mach 7, vehicle stage separation occurs and the rocket-powered second stage takes over for acceleration to orbit. This concept eliminates all development risk associated with the scramjet, but of course sacrifices the superior performance potential of the scramjet for much of the hypersonic portion of the flight path.

The above discussion explains some of the factors going into the selection process for combined air breathing-rocket propulsion systems installed in space launch/hypersonic cruise vehicles. Because of these factors and since the propulsion technology base is not well developed at this time, different designers select different propulsion concepts for basically the same mission definition. However, the selected fuel is the same for each of the major projects listed on Table 1, viz., cryogenic hydrogen in either a liquid or slush (liquid/solid) form.

The reason why hydrogen is the chosen fuel for these applications can be understood by comparing its properties that relate to energy release and cooling capability with corresponding data for representative hydrocarbon fuels (Table 2).



From this comparison, it is apparent that heat of combustion for hydrogen is approximately 2.5 times as much as the hydrocarbons, which is responsible for the very high hydrogen specific impulse in comparison with representative hydrocarbons (Figure 1). Extrapolation of this data indicates that hydrocarbon scramjet specific impulse would be insufficient for vehicles that either cruise at higher hypersonic Mach numbers or, worse yet, must approach orbital velocities.

TABLE 2. COMPARISON OF FUEL PROPERTIES AND CHARACTERISTICS.

FUEL	HEAT OF COMBUSTION	LIQUID DENSITY	MAX HEAT SINK CAPACITY		
	BTU/LB	LB/FT <sup>3</sup>	PHYSICAL	CHEMICAL (ENDOTHERMIC)	TOTAL
HYDROGEN	51 600	4.7	6700	-	6700
METHANE	21 460	28	1350	-	1350
MCH	18 630	48	1016	940	1956
DECALIN	18 240	56	1020	950	1970
JP-7	18 500	48	269	-	269

A comparison of its cooling capability with hydrocarbon fuels results in a similar superior rating for cryogenic hydrogen. As shown in Table 2, its total heat sink capacity is nearly an order of magnitude better than the hydrocarbons, and even the endothermic fuels are not comparable to hydrogen. The additional cooling capability of hydrogen is required for a single stage space launch vehicle such as the NASP where critical heating problem areas require a fuel with a high cooling capacity to provide a practical vehicle design.

The principal negative physical property of hydrogen is also displayed on Table 2, viz., its density. It is approximately an order of magnitude lower than the hydrocarbon fuels. This characteristic must be accepted to achieve the performance and cooling advantages of hydrogen, and results in large vehicles to accommodate the large volume requirements for the low density hydrogen fuel.

Hypersonic Missiles - Both tactical and strategic future hypersonic missiles are possible applications for combined air breathing-rocket propulsion systems. Studies for both types of hypersonic missiles at NASA Langley have concluded that, unlike hypersonic aircraft which use cryogenic hydrogen fuel, missile volumetric and logistic considerations dictate the use of dense, non-cryogenic liquid hydrocarbon fuels (Ref. 6). Although tactical and strategic missiles have vastly different aerodynamic requirements, the propulsion disciplines are similar for both types.

These studies have indicated that hypersonic air breathing missiles have a unique potential for combining speed, range, and maneuverability in a relatively lightweight vehicle. These attributes, which are advantageous to both tactical and strategic missions, are achieved through the careful integration of the propulsion system with the airframe and the synergistical coupling of aerodynamic, propulsion, and structural disciplines.

The NASA Langley hypersonic missile studies assumed booster rocket launch and acceleration to Mach 3.5, followed by dual mode ramjet/scramjet propulsion for acceleration and cruise at Mach 6.0 and 100,000 feet altitude. A rocket booster approach for low speed propulsion is only one of the three options listed in the Figure 3 propulsion road map. The other two low speed options involve air breathing propulsion in the form of either a ducted rocket or various types of turbomachines.

For missile application, the ducted rocket or ejector ramjet (Figure 4), has the advantage of simplicity and low weight similar to the rocket booster, but also incorporates a significant performance improvement over the rocket. This performance improvement becomes more significant with increasing flight Mach number, so that at Mach 2 its specific impulse is nearly twice that of a liquid rocket, as shown in Figure 5 for a typical installation. Another advantage of this combined air breathing-rocket propulsion concept is the inherent thrust margin available from the rocket at ramjet/scramjet cruise conditions. This feature adds a significant control force margin to the missile for greatly improved maneuverability and perhaps survivability.

FIGURE 4. EJECTOR RAMJET CYCLE.

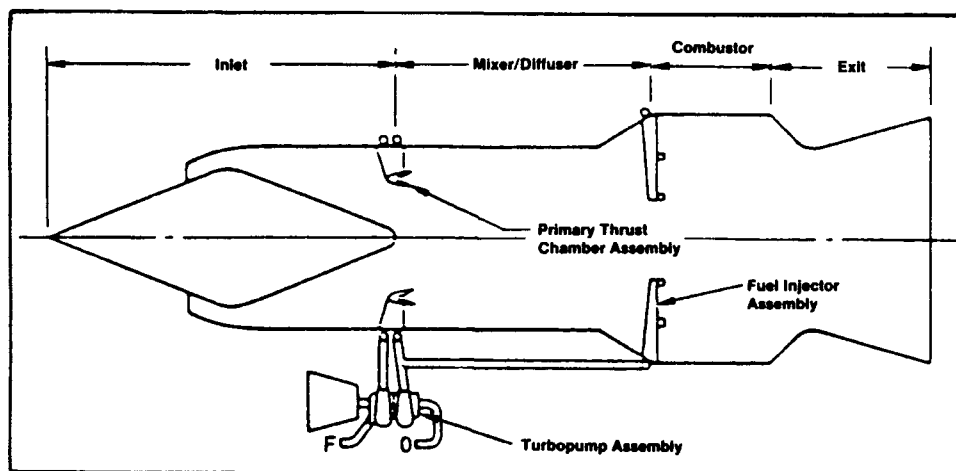
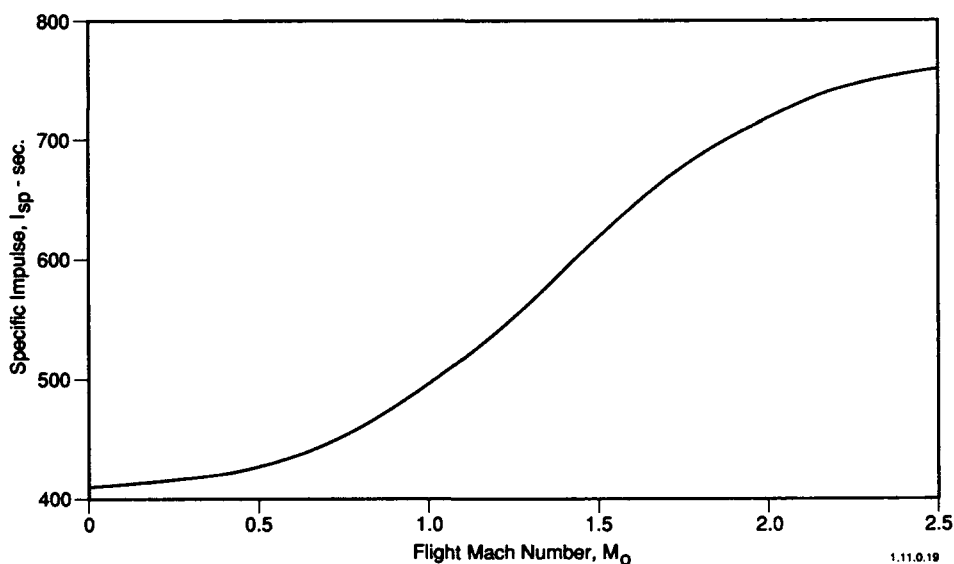


FIGURE 5. DEDUCTED ROCKET SPECIFIC IMPULSE.



#### Combined Air Breathing-Rocket Propulsion Design Considerations

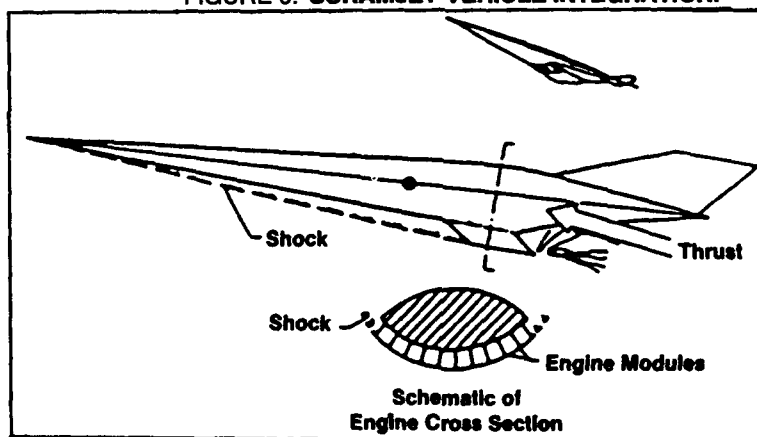
Hypersonic flight using air breathing propulsion introduces a number of development challenges that are listed in Table 3 and were discussed in a previous paper (Ref.5). However, when rocket propulsion is combined with the air breathers, each of these development challenges takes on additional significance. These combined cycle effects are discussed in the following paragraphs.

**Propulsion/Vehicle Integration** - At hypersonic speeds, the propulsion system efficiency must be high, the engine must add minimum drag and weight to the vehicle, and the engine must process as much air as possible. These objectives are best met by considering the entire underside of the vehicle as part of the propulsion system. This concept, referred to as airframe-integration, is illustrated in Figure 6. The concept utilizes the vehicle forebody for part of the inlet compression and the aftbody as part of the nozzle expansion. To obtain the required thrust at the higher Mach numbers, the inlet must capture nearly all of the air processed by the vehicle undersurface bow shock.

TABLE 3. HYPERSONIC PROPULSION REQUIREMENTS.

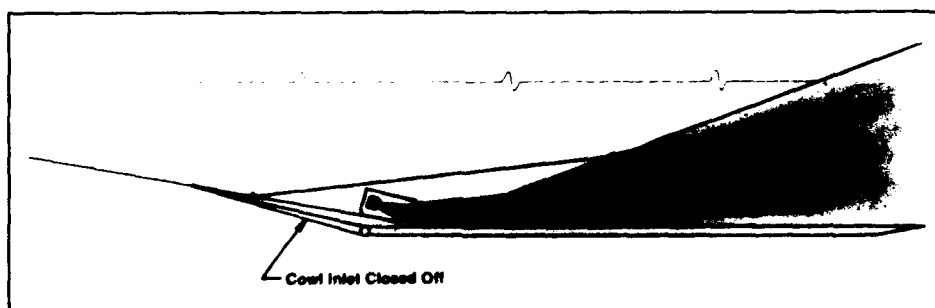
Hypersonic Propulsion Requirements	
• Propulsion/Vehicle Integration	<ul style="list-style-type: none"> <li>— Inlet Capture Area</li> <li>— Thrust/Drag</li> <li>— High Response Controls</li> </ul>
• Engine Stability Over Wide Operating Range	<ul style="list-style-type: none"> <li>— Stable, Started Inlet Flow</li> <li>— Combustion Stability/Inlet Isolation</li> <li>— Multimode Operation</li> <li>— High Response, Vehicle Integrated Controls</li> </ul>
• High Performance Over Wide Operating Range	<ul style="list-style-type: none"> <li>— Large Capture Area Inlets</li> <li>— High Pressure Recovery Inlets</li> <li>— High Component Efficiencies</li> <li>— Large Expansion Ratio Nozzles</li> </ul>
• System Level Thermal Management	<ul style="list-style-type: none"> <li>— High Temperature, Fuel Cooled Structures</li> </ul>
• Advanced Materials	<ul style="list-style-type: none"> <li>— High Strength-to-Weight</li> <li>— High Temperature Capability</li> <li>— Oxidation Resistant</li> </ul>

FIGURE 6. SCRAMJET-VEHICLE INTEGRATION.



In order to integrate a rocket into the closely coupled propulsion/vehicle configuration described above, special care must be taken to assure that the rocket installation minimizes any additional drag and/or weight penalties. One possible integrated installation which meets these criteria is a rocket thrust chamber buried within a ramjet/scramjet duct as shown in Figure 7. This rocket installation does not introduce any additional aerodynamic drag, and minimizes the weight penalty of the rocket by eliminating the need for a separate rocket nozzle extension. The cowl inlet door can be closed off, as shown in Figure 7, during the rocket-only mode of operation or left open if sufficient air is available to produce additional thrust from the air breathing component of the propulsion system.

FIGURE 7. INTEGRAL ROCKET USES ENGINE DUCT FOR EXPANSION.



**Stable Operation Over Wide Operating Range** - To meet this requirement, air breathing hypersonic propulsion systems must provide for 1) stable, started inlet flow; 2) combustion stability/inlet isolation; and 3) integrated engine/vehicle controls to manage the very short time constants. In addition, a combined air breathing-rocket engine has to maintain stable operation over a wide operating range during which it transitions from one cycle to another.

This puts further complication into the engine control system for two reasons. One is that the control parameters for each of the individual operating modes (e.g., turboaccelerator, scramjet, and rocket) are quite different and unique to that cycle. Therefore the number of control parameters are increased and the control system becomes more complex. Second, the transitions from one operating mode to another is a dynamic process that must be controlled so that transient operation does not lead to operating instabilities, and propulsion functions such as geometry variation and engine air and fuel flows are smoothly readjusted.

**High Performance Over Wide Operating Range** - At hypersonic speeds, the propulsion system efficiency must be high. This means that inlet, engine, and nozzle cycle parameters must approach ideal values to produce high net thrust and high specific impulse.

Scramjet performance was calculated using NASA Langley's SCRAM code over a range of hypersonic Mach numbers from 10 to 20. Cryogenic hydrogen was the fuel selected, and was burned in stoichiometric proportions ( $\phi = 1.0$ ). A total engine contraction ratio ( $A_0/A_{min}$ ) of 12.0 and a total engine expansion ratio ( $A_{exit}/A_0$ ) of 2.0 were selected as being representative of engine geometry designed for this flight Mach number range. A freestream dynamic pressure of 1000 lbs. per square foot and a vehicle angle of attack of  $0^\circ$  was assumed for all calculations. In addition, three levels of the major component efficiencies were input to illustrate the effect of achieved component efficiency on engine level delivered performance. The levels of performance and their definitions are explained in Table 4.

TABLE 4. SCRAMJET COMPONENT PERFORMANCE DEFINITIONS AND LEVELS.

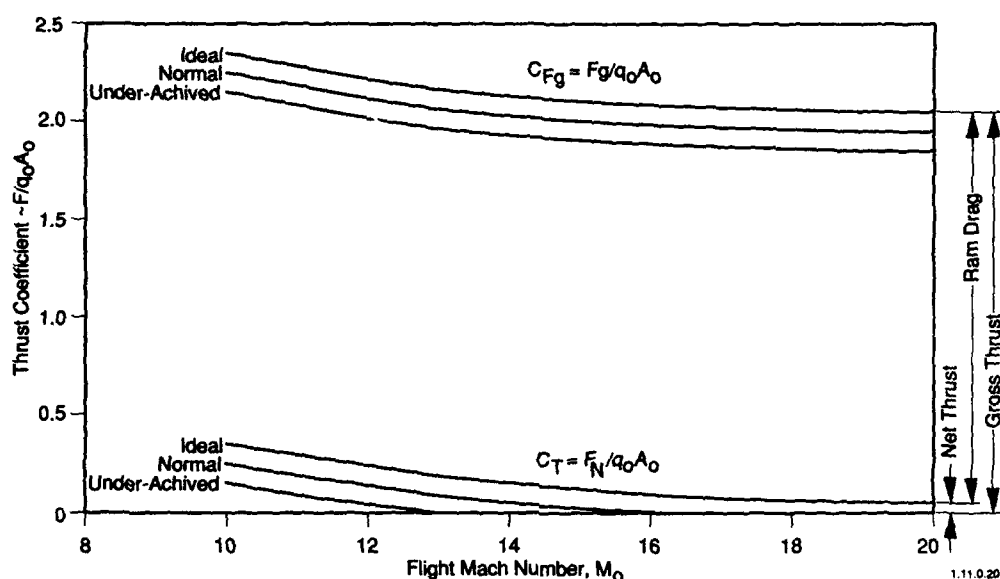
COMPONENT EFFICIENCY	EFFICIENCY DEFINITION	DEVELOPMENT LEVEL		
		IDEAL	NOMINAL	UNDERACHIEVED
INLET, $\eta_{KE}$	KINETIC ENERGY (REF. 7)	100%	97.5%	95%
COMBUSTOR $\eta_C$	ACTUAL ENERGY RELEASE IDEAL ENERGY RELEASE	100%	90%	80%
NOZZLE, $C_N$	ACTUAL STREAM THRUST IDEAL STREAM THRUST	100%	97.5%	95%

The component efficiency levels selected for the "nominal" and "underachieved" definitions were somewhat arbitrarily assumed. It should be noted that scramjet thrust and specific impulse are very sensitive to each of these inputs and assumptions at hypersonic flight conditions. Therefore, the performance levels displayed on the following figures should be taken only as representative values consistent with the inputs selected and not the absolute limit levels of performance for scramjets.

The relative magnitude of gross thrust, ram drag, and net thrust was calculated over a range of hypersonic flight conditions using the above described techniques and assumptions. The results are displayed on Figure 8. The following observations can be derived from an examination of this analysis.

- Ram drag is 90 to over 100% of gross thrust over the range of component performance levels and flight conditions assumed.
- Net thrust is extremely sensitive to levels of component performance assumed, with the degree of sensitivity increasing as Mach number increases.
- Net thrust turns into net drag at the higher hypersonic Mach numbers, with the crossover point depending on the level of component performance achieved.

FIGURE 8. SCRAMJET GROSS THRUST, RAM DRAG AND NET THRUST COMPARISONS.



To determine the impact of underdeveloped component efficiency on scramjet engine developed performance, parametric data was calculated for all combinations of efficiency levels shown on Table 4. This procedure was followed to determine the first-order independent effects of underdeveloped performance for the inlet, the combustor, and the nozzle.

The inlet parametrics are shown in Figure 9, where delivered scramjet specific impulse is plotted vs. flight Mach number. From this data, it is apparent that scramjet performance is very dependent on high inlet kinetic energy efficiency. The specific impulse vs. Mach number slope becomes increasingly steep as  $\eta_{KE}$  decreases, and an  $\eta_{KE} = 98$  to  $99\%$  would appear to be required if scramjet powered flight is to be achieved at higher hypersonic Mach numbers.

The impact of incomplete combustion on scramjet performance is shown in Figure 10. Combustion efficiency is not a strong factor in determining delivered scramjet specific impulse for these conditions. In fact, it is almost insignificant as the flight Mach number approaches 15. Therefore, very high combustion efficiencies are not a design development requirement for Mach 10 or higher scramjet propulsion.

FIGURE 9. EFFECT OF INLET EFFICIENCY ON SCRAMJET PERFORMANCE.

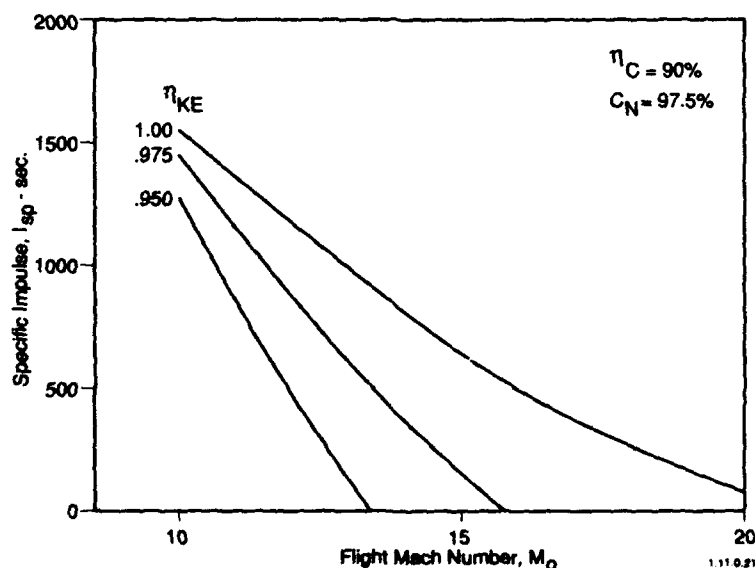
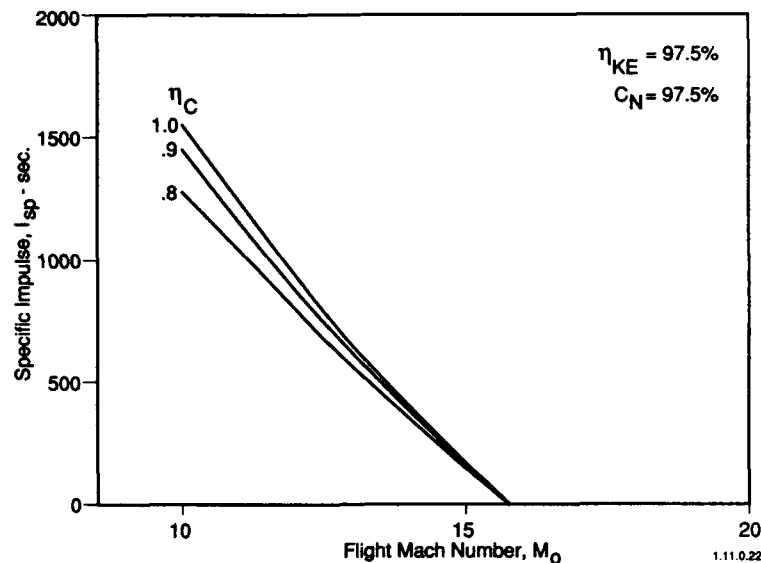
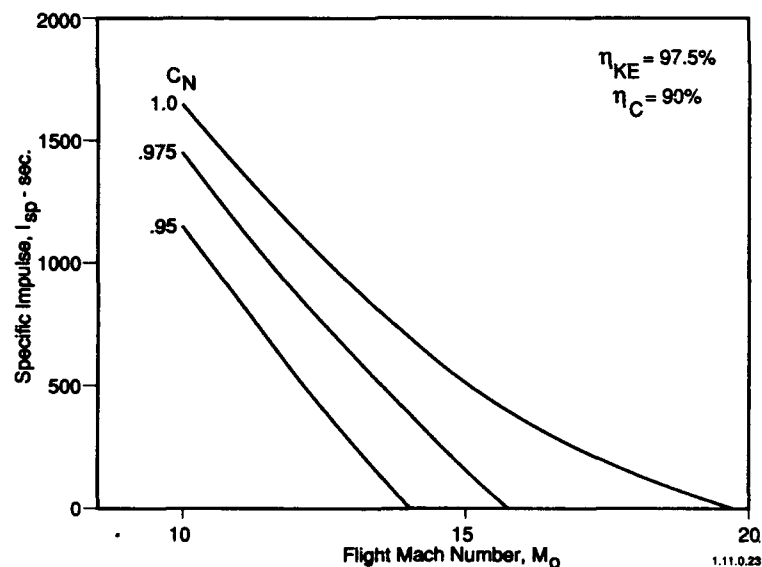


FIGURE 10. EFFECT OF COMBUSTION EFFICIENCY ON SCRAMJET PERFORMANCE.



A high nozzle coefficient is a requirement for achieving acceptable scramjet performance, as displayed in Figure 11. The trend is quite similar to the sensitivity of specific impulse to inlet kinetic energy inlet efficiency. A nozzle coefficient of 98 to 99% is probably a development requirement if a scramjet is to be used at the higher hypersonic Mach numbers.

FIGURE 11. EFFECT OF NOZZLE THRUST ON SCRAMJET PERFORMANCE.



When all of these effects are considered together, scramjet specific impulse vs. flight Mach number is as shown in Figure 12. It can be seen that scramjet specific impulse crosses the rocket level at a flight Mach number that strongly depends on the level of component efficiencies achieved. Consequently, if a hypersonic mission requires flight at hypersonic Mach numbers greater than about 12, either very complete scramjet development must be assured or, more prudently, a high performing rocket system should be incorporated into the total propulsion system. Combined air breathing-rocket propulsion systems provide a capability that can assure that adequate thrust at the highest possible delivered specific impulse is available for further vehicle acceleration even if underdeveloped scramjet performance is not discovered until the flight program determines the actual thrust-drag relationships.

In order to provide maximum rocket specific impulse, installations such as shown in Figure 7 provide an extremely large expansion ratio for a high pressure rocket. This results in an improvement in specific impulse that is estimated to be similar to the trend shown in Figure 13. This analysis indicates that a 5% improvement in specific impulse (500 vs. 475 sec.) results from the increase in expansion area ratio achieved by using the complete scramjet expansion surface vs. the limited expansion of an atypical conventional rocket nozzle.

FIGURE 12. INEFFICIENCY EFFECTS ON SCRAMJET VS. ROCKET COMPARISON.

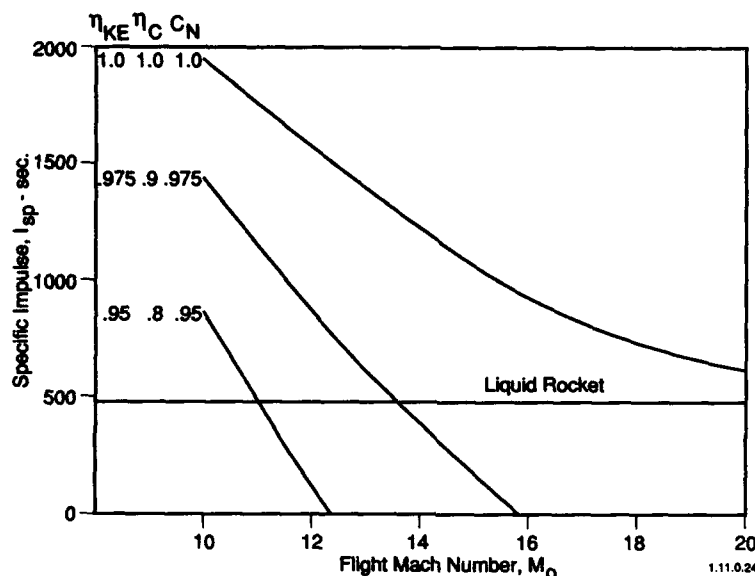
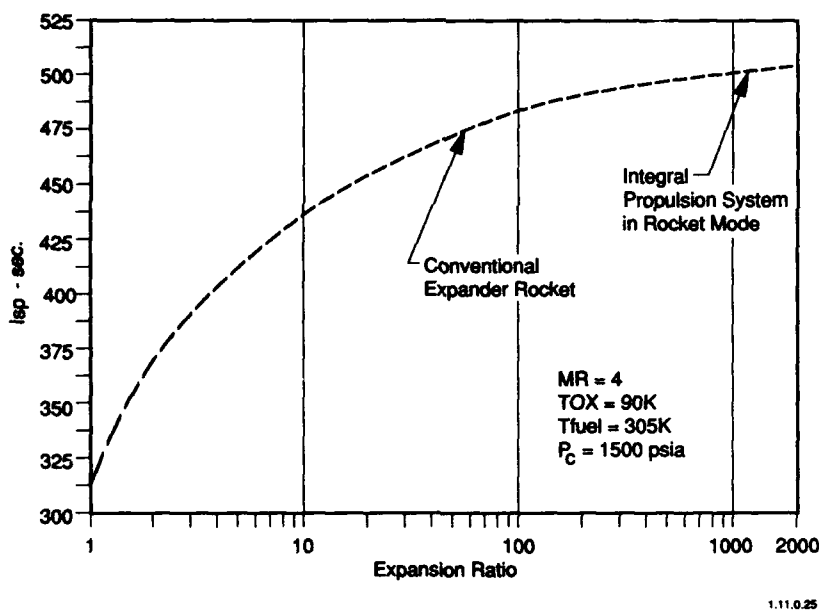


FIGURE 13. INTEGRAL ROCKET EXPANSION PROVIDES HIGHEST PERFORMANCE.

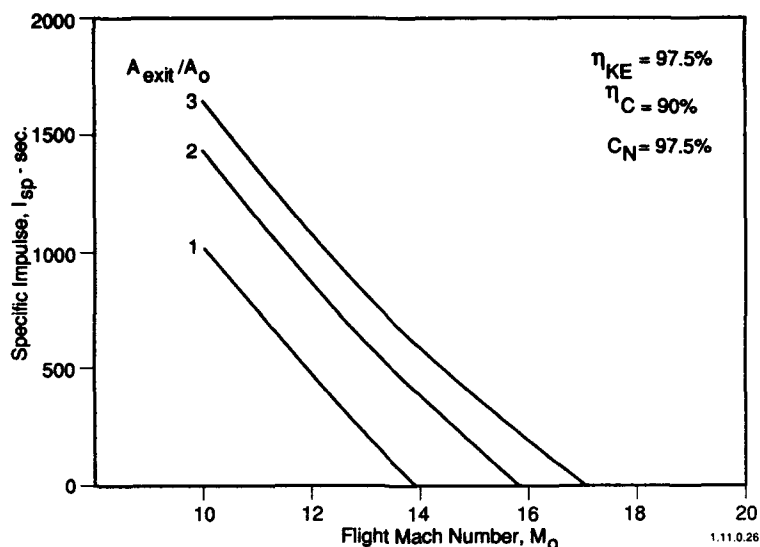


One additional design parameter was examined for its influence on combined air breathing-rocket propulsion at hypersonic flight conditions. This study examined the influence of scramjet total expansion area ratio ( $A_{exit}/A_0$ ) on thrust and specific impulse. The results are displayed in Figure 14 where  $C_T$  and  $I_{sp}$  are plotted vs. flight Mach number for three levels of  $A_{exit}/A_0$ , i.e., 1, 2 and 3. These results indicate that engine expansion area ratio has a strong influence on performance that increases with Mach number.

Typically, there is very little latitude to increase expansion area ratio since hypersonic vehicles usually require the maximum inlet area and expansion area possible to generate enough thrust over the entire flight corridor. For example, with propulsion integrated designs similar to the concept sketched in Figure 6, the inlet can usually capture a quantity of air that is equivalent to a stream tube that is about 50% of the vehicle cross-sectional area. Even using as much of the boat tail area as possible for an expansion surface, the total scramjet expansion ratio,  $A_0/A_{exit}$ , is limited to a factor of somewhere between 1 and 2.

Therefore, if the propulsion thrust is sized at some condition other than hypersonic cruise, it may pay off to shrink the scramjet so as to increase its permissible expansion area ratio and thus increase its specific impulse at the cruise condition and cover the thrust deficient during a portion of the relatively short duration acceleration by using rocket thrust. However, the adverse impact of scramjet downsizing on forebody drag must be included in this trade-off study.

FIGURE 14. EFFECT OF EXPANSION RATIO ON SCRAMJET PERFORMANCE.



**Thermal Management** - Combined air breathing-rocket propulsion systems installed in hypersonic vehicles will pose thermal management problems for the designer. Active cooling of both the airframe nosetip and leading edges may be required in addition to the propulsion system inlet, combustor, and nozzle. These vehicles will use the cryogenic hydrogen fuel to regeneratively cool critical surfaces, which would otherwise quickly lose their strength and melt at the temperatures generated even on a streamlined body at near-orbital speeds in the upper atmosphere. After the hydrogen has been used for cooling, it is imperative that the resultant thermal energy be recouped by using the high temperature propellant in the engine and thus increase the delivered performance.

One additional heat load must be considered when rockets are combined with the air breathers, and that is the requirement to cool the rocket thrust chamber/nozzle. On a performance basis, the most beneficial rocket cooling method is to regeneratively cool these components so that the heat absorbed by the wall is pumped back into the fuel. This increase in fuel enthalpy thus compensates for the energy reduction in the thermal boundary layer of the combustion gases. However, regenerative cooling of the rocket components requires that the temperature of the fuel be kept below a limit determined by the maximum material operating temperature plus the bulk temperature rise of the fuel in the regenerative cooling circuit. This, in turn, limits the amount of heat that can be absorbed by the rocket fuel from the actively cooled airframe surfaces and other components of the propulsion system.

**Lightweight, High Temperature Materials** - To withstand the temperatures for hypersonic flight, materials will have to be lightweight, i.e., high strength to weight ratio, and retain their structural properties even in the very high temperature hypersonic environment. Candidates include ceramic matrix composites, metal matrix composites, and carbon/carbon with oxidation coatings. Besides high temperature strength properties, sufficient ductility will be required to accommodate the thermal strains and provide the cycle life necessary to meet the reusability requirements of future space launch/hypersonic cruise vehicles. Also, the materials used will have to be readily fabricated with integral coolant circuits. Finally, these materials for combined cycle engines will have to meet the demands of variable geometry, necessary for air breathing inlets, combustors, and nozzles over the flight spectrum from sea level static to low earth orbit. Properties associated with sliding friction and sealing such as lubricity and surface finish have to be compatible with the geometry variations required.

#### Concluding Remarks

Air breathing hypersonic propulsion systems are being studied and are currently in the technology validation phase. Demonstrators that will validate the technology for both space launch and hypersonic vehicles are scheduled for initial flight within the present decade.

Because they use the air within the atmosphere for a large fraction of the total amount of required oxygen, they show promise of a large reduction in vehicle take-off weight and total cost, when compared to an all rocket system. For missions requiring exoatmospheric flight and even for flight within the atmosphere, the benefits of rockets are great enough to assure that combined air breathing-rocket propulsion systems will be developed and become operational in the early part of the Twenty-First Century.



The engine development challenges for this type of propulsion are beyond those faced by either air breathing or rocket designers in the past. The following list are considerations for those who are at the cutting-edge of this new frontier for aerospace propulsion.

- Stable operation over wide operating range
- High performance over wide operating range
- Thermal management including active cooling
- Advanced composite materials
- High response control system
- Low density, cryogenic hydrogen fuel
- Propulsion/vehicle integration
- System operation with combined air breathers & rockets
- Verification of design analysis techniques

#### REFERENCES

1. R. Barthelemy, The National Aero-Space Plane Program, July 1989, AIAA Paper No. AIAA-89-5001, .
2. E. Hogenauer and D. Koelle, Sanger The German Aerospace Vehicle Program, July 1989, AIAA Paper No. AIAA-89-5007.
3. P. Cazin, French Space Plane Research, From Hermes to Transatmospheric Vehicles, July 1989, AIAA Paper No. AIAA-89-5006.
4. T. Yamanaka, Space Plane Research Activities in Japan, July 1989, AIAA Paper No. AIAA-89-5008.
5. D.L. Kors, Combined Cycle Propulsion for Hypersonic Flight, October 1987, IAF Paper NO. IAF-87-263.
6. J.L. Hunt, P.J. Johnston, J.M. Cabbage, J.L. Dillion, C.B. Richie, and D.C. Marcum, Jr., Hypersonic Airbreathing Missile Concepts Under Study at Langley, January 1982, AIAA Paper No. AIAA-82-0316.
7. F.S. Billig, D.M. Van Wie, Efficiency Parameters for Inlets Operating at Hypersonic Speeds, June 1987, Proceedings of the VIII International Symposium on Air Breathing Engines, Cincinnati, Ohio, USA.



## CRYOGENIC HYDROGEN-INDUCED AIR-LIQUEFACTION TECHNOLOGIES

by  
William J.D. Escher  
Propulsion, Power and Energy Division  
Office of Aeronautics and Space Technology  
NASA Headquarters  
Washington, DC 20546  
U.S.A.

92-16956



## ABSTRACT

Extensively utilizing a special advanced airbreathing propulsion archives database, as well as direct contacts with individuals who were active in the field in previous years, a technical assessment of cryogenic hydrogen-induced air-liquefaction, as a prospective onboard aerospace-vehicle process, was performed and documented in 1986 (U.S.A. context). This paper summarizes the resulting assessment report prepared under U.S. Air Force sponsorship. It presents technical findings relating the status of air-liquefaction technology, ca. late-1960s, both as a singular technical area, and also as that of a "cluster" of collateral technical areas including: Compact lightweight cryogenic heat-exchangers; Heat-exchanger atmospheric-constituents fouling alleviation; Para/ortho hydrogen shift-conversion catalysts; Hydrogen turbine-expanders, cryogenic air-compressors and liquid air pumps; Hydrogen recycling using slush hydrogen as heat sink; Liquid hydrogen/liquid air rocket-type combustion devices; Air collection and enrichment systems (ACES); and Technically-related engine concepts.

## BACKGROUND

## The Advent of Basic LACE

With the advent of liquid hydrogen as an operational aerospace vehicle propulsion fuel<sup>1</sup>, roughly in the mid-1950s, researchers at The Marquardt Company devised a unique propulsion cycle predicated on the unique cryogenic heat-sink qualities of this fuel. It was referred to as the Liquid Air Cycle Engine (LACE)<sup>2</sup>. A simple schematic of this engine type is presented in Figure 1. Conventionally referred to as "Basic LACE" (to distinguish it from the large number of related concepts since described), this concept utilized the low-temperature, large heat-sink characteristics of its liquid hydrogen fuel in a heat-exchange process with inlet-processed air to be utilized in the combustion process, to cool and ultimately liquefy that air. The rationale for liquefying the air was to permit it to be pumped to high-pressure by means of a lightweight/low-shaftpower liquid pump, of the type used in liquid-propellant rocket engines, rather than a conventional ambient-temperature air compressor of the type used in turbojet engines. These latter, by comparison, are physically large and heavy pieces of rotating machinery, requiring large-shaftpower driving means (e.g., high-output multistage turbines).

As reflected in the schematic diagram, once pumped to high pressure (ranges of 10 to 100 atmospheres were targeted), the liquid air was injected into a rocket-type combustion chamber/nozzle unit, i.e., a rocket-type thrust chamber. In effect, a liquid air/liquid hydrogen rocket engine is achieved in the LACE concept, in which the oxidizer is advantageously supplied from the atmosphere, rather than from a vehicle propellant container. The appealing consequence to performance is that *only the fuel* mass flow is counted in the determination of specific impulse, rather than both fuel and oxidizer as is the case with rocket engines. The oxidizer is considered "free".

However, as clear from the schematic, the weight and concomitant complications of two major pieces of equipment *not* required by rocket engines are now required: an air-induction subsystem ("intake") and a air-liquefaction heat-exchanger subsystem. These represent non-trivial "costs" for this non-tanked source of oxidizer. For one thing, the thrust/weight ratio achievable with LACE is extensively reduced from the ca. 50-100:1 range of liquid rocket engines. For another, since the engine must be operated within the atmosphere, unlike a rocket-powered launch vehicle, which typically exits the atmosphere in the low-supersonic speed regime, a rather different vehicle ascent trajectory is now required. This flight path will be characterized by relatively high aerodynamic structural and aeroheating loads which must now be sustained by the vehicle and its propulsion system.

The specific impulse for Basic LACE is usually stated to be in the range of 1000 seconds, again on a fuel-only mass-flow basis, more than doubling that of hydrogen/oxygen rocket engines. But, very significantly, this is very substantially below the performance of an optimal hydrogen-fueled airbreathing engine, say a turbojet-cycle machine, for which the range of 5000-7000 seconds would be anticipated, depending mainly on stoichiometry. The cause for this variance is mainly a fundamental constraint associated with the basic hydrogen-induced air-liquefaction process: in Basic LACE *much* more than a unity equivalence ratio (stoichiometric) amount of liquid hydrogen fuel is required to liquefy the air, typically a factor-of-eight more.

As will be seen, much of the technology development work to be summarized here, was dedicated to various innovative schemes to get around this intrinsic cycle limitation. A description of these technical approaches, in effect, provides a basic "theme" for the present paper. Also, several propulsion systems which utilize the many technologies brought forward for this purpose (performance improvement) are to be described. One of these, SuperLACE was purported to achieve full obviation of the equivalence-ratio constraint intrinsic to Basic LACE by integrating a number of the de-richening approaches and technologies to be considered in this paper.

## Advanced Airbreathing Propulsion Archival Database (Utilized in the Assessment)

In early 1984, the Plans Office of the AFWAL (Air Force Wright Aeronautical Laboratories) Aero Propulsion Laboratory<sup>\*\*</sup>, Wright-Patterson Air Force Base, took initial steps to reassess the application of advanced airbreathing propulsion for Earth/orbit space transportation missions. Historically, rocket propulsion, solely, has been utilized for launch/space-vehicle propulsion. However, some application studies and a certain amount of technology development effort in support of the airbreathing launch alternative had been conducted in the 1955 - 1965 period. Since then, this R&D effort dropped to less than a "sustaining" level. Consequently, it was judged that not much of substance had been accomplished on the airbreathing option for Earth/orbit space transportation systems in the last two decades, judging from the available technical literature, as well as from personal-contacts with those who had worked in the field earlier.

<sup>\*\*</sup> Now the Aero Propulsion and Power Laboratory,

<sup>\*</sup> Superscripts refer to references listed at the end of the text section of the paper. Wright Research and Development Center (AFSC)

With a renewal of interest in advanced propulsion systems for Earth-to-orbit transportation, and in recognition of this past work, the need to establish an archival data base became apparent. The technical reports of twenty years earlier might have very considerable value in advancing plans for new propulsion systems. This documentation acquisition step was mechanized about mid-1984 by the Aero Propulsion Laboratory through a contracted task by Battelle Memorial Institute's Columbus Division, assisted through a subcontract to the Astronautics Corporation of America's Technology Center. As a consequence, the "Advanced Airbreathing Propulsion Archives Data Base" was established by late 1984 at Battelle, with an initial set of technical documents having been acquired, and suitably indexed and abstracted.

A very evident technical topic in these archival documents is the present subject of cryogenic hydrogen-induced air liquefaction and its directly related set of technologies. Appropriately, the "archives" were extensively consulted in the preparation of the assessment report<sup>3</sup> which this paper attempts to summarize. As covered above, the initial propulsion system application involved was the Basic LACE (Liquid Air Cycle Engine). Subsequently, in support of the Air Force's multifaceted "Aerospaceplane" program of that time-period, substantial funding was applied to support application studies of advanced variants of LACE (e.g., SuperLACE), selected experimental technology development efforts, and a limited hardware system demonstrations of LACE itself, and key aspects of the Air Collection and Enrichment System (ACES). Additional component and subsystem technology development work was accomplished under this aegis, as well, e.g., production and characterization of "slush hydrogen".

This work was conducted mainly in the early and mid-1960s at numerous airframe, engine, and selected aerospace subsystem manufacturers' facilities, as well as at certain Government laboratories. Also, a number of non-aerospace firms were involved. Subjected to a sharply decreased funding level past 1965, this work virtually ceased shortly thereafter. Certain related systems studies continued into the late 1960s, but there were no further experimental hardware developments of note.

\* Now the Aero Propulsion and Power Laboratory, Wright Research and Development Center (AFSC)

#### Background of Special Assessment (Summarized in this Paper)

Consistent with the formation of the advanced airbreathing propulsion archives database, the present assessment was initiated in late-1985, as a subcontracted facet of the Aero Propulsion Laboratory's contracted activity performed by the Dayton, Ohio, office of Science Applications International Corporation (SAIC), under Air Force prime contract F33615-84-C-0100. The presently reported work was conducted under SAIC subcontract by the Astronautics Corporation of America (ACA), at its Madison, Wisconsin, Technology Center. The present author was responsible for this activity as a former employee of ACA.

A significant highlight of the assessment process was the Air Liquefaction Technology Technical Exchange Meeting which was sponsored under ACA's subcontract. By special invitation, some twenty persons having directly applicable experience in one or more air-liquefaction related technology area participated in this two-and-a-half day event. It was held at ACA's Technology Center in Madison on 6-8 May 1986. The numerous expert presentations given during the meeting contributed directly to the final assessment report<sup>3</sup>, which was compiled and given limited, restricted distribution in the Fall of 1986. The present paper is an unrestricted summary of that report.

## INTRODUCTION

### An Interrelated "Cluster" of Diverse Technologies

The cryogenic hydrogen-induced air-liquefaction technical arena, viewed broadly, constitutes not so much a single monolithic technology, but rather a set of interrelated, sometimes disparate technologies, based upon engineering accomplishments of record. Basically, systems-level requirements are seen to dictate which technologies are to be drawn upon, and how. This "cluster of diverse technologies" characterization is reflected graphically in Figure 2.

Along the lines of this portrayal, each of these technologies were, in the basic assessment, briefly characterized and interrelated with other technologies in the context of advanced propulsion system possibilities. This is summarized in this introduction using the following organizational structure:

1. Compact Cryogenic Heat Exchangers and Atmospheric Constituent Fouling Alleviation
2. Increasing the Refrigerative Effect of Cryogenic Hydrogen
3. Air Collection and Enrichment System (ACES)

Specific technological topics (i.e., many of those named in Figure 2) will now be individually introduced under the above named functional headings. For example, para/ortho hydrogen shift-conversion catalysis is to be covered as an important "refrigeration enhancement" measure (Item 2, above).

#### 1. Compact Cryogenic Heat Exchangers and Atmospheric Constituent Fouling Alleviation

Central to this "cluster" of technical areas (Figure 2) is the basic hardware means of conducting the air-liquefaction process: cryogenic-hydrogen/air heat exchangers. Closely associated with air-liquefaction heat exchangers is the problem of atmospheric-constituent fouling and means for its alleviation. The atmospheric constituents in question include water vapor and moisture, the latter in the form of both small and large water droplets (e.g., clouds and precipitation, respectively). Other constituents which can impair heat exchanger operation include carbon dioxide and argon, both found naturally in the Earth's atmosphere. The principal fouling mechanism is the formation of solids (e.g., water ice) on the active heat-exchange surfaces. This significantly reduces the heat-transfer effectiveness (usually represented by a heat transfer coefficient) and can also physically block airflow passages. Both effects degrade heat exchanger performance, reducing the amount of air liquefied by a given amount of hydrogen. In fact, heat exchanger operation can even be terminated by this fouling action.

#### 2. Increasing the Refrigerative Effect of Cryogenic Hydrogen

A number of technologies closely associated with air liquefaction relate to the important performance objective of increasing the "refrigeration effect" of hydrogen as the direct means of liquefying increasing amounts of air (via heat exchange) for a given amount of hydrogen. This need stems from the critical limitation implied in the inherent over-rich operation of elemental air liquefaction cycles (i.e., too much fuel per unit air oxidizer). Functionally, this is a consequence of a basic heat-exchange constraint to be discussed, namely it takes far more hydrogen (as refrigerant) to liquefy a specific quantity of air, than is needed to combust with the resulting liquefied air at stoichiometric conditions, i.e., that "chemically correct" mixture ratio leading to maximum combustion product temperatures. This means that the associated propulsion system must be operated very fuel-rich. Generally speaking, propulsion system performance is maximized at, or near, stoichiometric conditions. Consequently, this "forced" fuel-rich operation detracts from performance, in fact very significantly so as indicated in the case of Basic LACE.

To repeat, the salient propulsion system ramification of this over-rich operation is much lower than maximum-possible specific impulse levels. Thus, there is a strong incentive to "de-richen" the cycle by increasing the refrigeration effect of the available hydrogen. Five examples of quite different refrigeration-enhancement technologies of this kind are listed below and discussed in the main-text section of the paper.

- Para/ortho hydrogen conversion catalysis
- Hydrogen turbine expanders and cryogenic air compressors
- Hydrogen recycle operation, requiring subcooled tanked hydrogen (e.g., "Slush")
- Liquefaction of only part (or none) of the intake air
- Incorporation of a liquid air regenerator boiler unit

### 3. Air Collection and Enrichment System: (ACES)

Mention has been made of the "air collection" approach in which liquefied air is collected in flight, processed onboard, and stored in vehicle containers for subsequent use in effecting powered flight over the remaining mission profile (e.g., ascent to orbit), rather than being immediately consumed in the engine. Such stored liquid air could, in principle, be used to operate a "post-collect" propulsion mode for further acceleration as a liquid air/hydrogen rocket, capable of operating in both the atmosphere and in the space environment. Such a system was initially proposed by the Marquardt Company, ca. 1956, being dubbed the "Air Hoarder" process. However, mainly because of the preponderant inert nitrogen fraction in liquid air, leading to low specific impulse rocket performance, this stored liquid air approach was ultimately judged to be of little interest.

Researchers at General Dynamics' Convair Division later revived this approach, in effect giving it new life, with an innovative concept. This was based on *separating* the liquid air into its two basic constituents, oxygen and nitrogen. The inert nitrogen was disposed of overboard during the collect mode, while the remaining "liquid enriched air" (LEA) was to be stored aboard the vehicle. LEA is essentially liquid oxygen (typically at 90-percent purity, the remainder being nitrogen).

The key to this air collection and enrichment system (ACES) approach was developmental success with the air separation (enrichment) device to be carried onboard the vehicle. Several technical approaches were developed, as will be discussed later. The General Dynamics researchers took steps to patent one separator approach, the rotating cryogenic distillation device, later carried to the full-scale boilerplate hardware stage by Linde Division of Union Carbide Corporation. Their concept will be described later (later Figures 9 and 10).

## LIGHTWEIGHT COMPACT CRYOGENIC HEAT-EXCHANGERS

### Heat Exchanger Technology

Hydrogen-induced air liquefaction technology, to be a practicable advanced aerospace propulsion system approach, assumes that a number of supporting technologies at the component and subsystem level can be developed and suitably integrated. The specific technologies vary with the basic propulsion system design approach. However, there is one fundamental technology which is pivotal in importance for *all* of the leading system approaches: lightweight, compact cryogenic heat exchanger subsystems. This provides the hardware basis for the cooling and liquefaction of air using liquid hydrogen as the coolant or refrigerant.

Figure 3 reflects the key parameters of interest in the basic cryogenic hydrogen/air heat exchange process under consideration. As suggested in Figure 1 (Basic LACE), the heat exchanger is conventionally broken down into two physically separate units, a *precooler*, which removes the sensible heat from the air through heat exchange with the hydrogen, and a *condenser* which removes the latent heat of condensation, liquefying and perhaps subcooling the air somewhat prior to its passage into the sump from which it will be admitted to the liquid air pump (again, see Figure 1). A counterflow heat-exchange process was pursued, that is the air and hydrogen flowed "against each other" in opposite directions. The fundamental thermodynamic constraint which ramifies into the intrinsic highly fuel-rich nature of the Basic LACE system discussed above is that of a "temperature pinch" effect in the condenser. In maintaining a sufficient "driving delta-T" throughout the heat-exchange process, a minimum practical temperature differential of the order of 5 to 15 degrees (Celsius) must be allowed for at the pinch region (upstream and downstream, larger temperature differences then occur). For this condition, in a practical heat exchanger, it works out that only about one-eighth the amount of liquid air is produced as that required for stoichiometric combustion with the hydrogen fuel (and refrigerant).

Typically, bare- or finned-tube tube-and-shell (hydrogen within the tubes) or plate-fin construction was considered for the precooler and condenser assemblies. Airflow was usually directed across the face of the tubes as shown in Figure 4. The tubular units investigated were of both in-line and staggered configurations (with respect to the airflow path). The principal firms performing heat-exchanger work at the time of aerospaceplane were Allied Signal Aerospace (then Garrett AiResearch), who accomplished most of the experimental fabrication and some of the testing, and Marquardt, who carried out major component-level and system-rig testing. Numerous types and patterns were initially screened in hot-water/air characterization tests, prior to fabricating larger units complete with headers and manifolds. Several materials were used in fabricating experimental units, aluminum, stainless steel and nickel. Aluminum alloy construction was generally favored, with tube diameters of about 3 mm (1/8 in) and wall-thicknesses ranging from the order of 0.1 to 0.3 mm.

A representative cross-counterflow tube-and-shell arrangement is shown in Figure 5. "Fluid 1" is cryogenic hydrogen and "Fluid 2" is air. Units of this type, fabricated by Allied Signal, were tested at Marquardt's Research Field Laboratory at Saugus, California in setups of the type shown in Figure 6. Evacuated perlite-insulated casings were used to thermally isolate the heat exchanger in vertical rig testing. Note that the air supply was typically "tanked" air which was dried (of moisture) prior to being admitted into the test hardware, thus conveniently obviating any icing problems in the system-level testing (upper sketch, Figure 6). However, when ambient air was processed, severe icing problems were met (lower sketch).

These small-scale (10 x 10 cm cross-sectional area) heat-exchanger elements were tested both as components and in the context of an overall operating system (lower, and upper sketches of Figure 6, respectively). The liquid air produced was pumped to combustor operating pressure by an electrically driven centrifugal pump. The highlight of this work was the full operation of a small-scale LACE system in which the thrust chamber (8 x 10 cm rectangular cross-section) was successfully operated for several minutes<sup>4</sup>.

### Atmospheric Constituent Fouling of the Heat-Exchanger

As mentioned in the introduction, a salient operational problem of such heat exchangers is atmospheric constituent fouling, e.g., atmospheric moisture freezing out within the heat exchanger, reducing its effectiveness and even blocking further airflow through the system. Other potential contaminants are carbon dioxide and argon, the contaminant of concern being a strong function of the propulsion system type and flight conditions involved. For example, water-icing was the key problem for Basic LACE, whereas CO<sub>2</sub> fouling was of greater concern to air-collect schemes (ACES).

Water icing of heat exchanger heat-transfer surfaces (e.g., tubes, fins, plates) is the primary fouling problem in air-liquefaction systems which operate in the early acceleration flight profile, that is, from launch/takeoff, through relatively low altitudes, where atmospheric water content is concentrated. Excluding rainfall or in-cloud operating conditions for the moment, the most challenging atmospheric conditions for water ice-fouling of heat exchangers would be a sea level pressure, hot, 100-percent relative humidity situation. If "all weather" vehicle operational capability is to be achieved in addition, the icing situation would be further aggravated by an ascent encounter with rain and clouds. Means of physically stripping water droplets from the intake airflow and possibly water-streams from vehicle surfaces upstream of the inlets would be necessary in these instances.

Atmospheric-constituent carbon dioxide and argon fouling phenomena, on the other hand, were considered to be mainly associated with high-altitude, high-speed air liquefaction as employed in the case of onboard air collection type systems, e.g., ACES (Air Collection and Enrichment System; see later discussion). Under typical air-collect flight conditions, say Mach 3 and above 15,000 m, atmospheric water content (in terms of the water-to-air mass ratio) is several orders of magnitude lower than at sea level. Hence, the CO<sub>2</sub>/argon constituents are then of dominant concern, overshadowing the effect of water icing.

Numerous heat exchanger fouling alleviation measures have been considered and several methods have been demonstrated experimentally. Among these are variations on surface finish and coatings (e.g., tube-surfaces which are "slippery" to prevent ice from clinging), element vibration or shocking to disengage solids, pulsed or cyclic flow changes, and various types of additives to the air stream. In addition, numerous new-and-novel ideas have been proposed along the way, and there seems to be much room for development of effective alleviation approaches.

### Potential Problem of Hydrogen Leakage Within the Heat Exchanger

In pursuing practical heat exchanger hardware, with literally hundreds-of-meters of tube lengths, and large multitudes of connections (e.g., tube/header joints), the possibility of higher-pressure hydrogen leaking internally into the airstream being processed looms as a large problem. This could create a fire or explosion hazard. Faulty joints which might "open up" under the stress of operation, cracks and porosities in the materials of construction, and numerous other failure modes (e.g., foreign object intrusion) must be addressed and successfully countered if safe and reliable propulsion flight equipment is to be achieved.

## INCREASING THE REFRIGERATIVE EFFECT OF CRYOGENIC HYDROGEN

It will be recalled from the background discussion that a severe performance penalty is experienced in the Basic LACE system due to its very fuel-rich operation, versus that potentially available, were the cycle to be operated at stoichiometric conditions, namely 1000 vs 5000-7000 seconds of specific impulse. This situation is attributed to that fundamental heat-exchange pinch-temperature condition in the air condensing part of the exchanger discussed earlier. Under the second topic covered in the introduction, a number of methods for ameliorating this problem have been assessed. The leading examples are now discussed topic by topic.

### Para/Ortho Hydrogen Shift Conversion Catalysts

Molecular hydrogen exists in one of two forms with respect to its atomic-nucleus spin orientation. *Para*-hydrogen, the lower energy-state form, has a same-rotation arrangement, while *ortho*-hydrogen has an opposite-rotation orientation. In other words, para-hydrogen nuclei have parallel spin-vectors, whereas ortho-hydrogen nuclei have opposing spin-vectors. As shown in Figure 7, the equilibrium para/ortho composition varies with the temperature of the hydrogen. At ambient temperatures (and higher) "normal" hydrogen is approximately 75-percent ortho-content and 25-percent para-content. At normal boiling-point liquid conditions (20 K, 36 R), the equilibrium material is essentially 100-percent para-form.

Liquid hydrogen as conventionally produced and delivered to the user is essentially 100-percent para-form material. The reason for this is that, were hydrogen to be liquefied at its "normal" 75/25 ortho/para makeup, it would be in a non-equilibrium state. With the passage of time (measured in hours) the higher energy-level ortho state molecules would spontaneously shift to the para form, and in so doing release heat. Thus heated, the liquid hydrogen would fairly quickly boil away into vapor and (normally) be lost. Thus, there would be a gross loss of "storability" of the liquid hydrogen due to the resultant internal heating effect. For this reason, in the production process as hydrogen is being cooled and liquefied, ortho/para shift conversion catalysts are used to accelerate the otherwise much-slower spontaneous shift. Additional refrigeration is provided to remove the ortho-to-para conversion internal heat generation.

Thus, there is a non-sensible/non-latent refrigerative heat-sink "built-into" liquid hydrogen which can be potentially tapped to increase the hydrogen's refrigerative effect in the heat-exchange process with air. If the para-to-ortho shift, allowed for by the rising temperature of the hydrogen, can be implemented, some part of this "built in" shift-conversion heat sink can be capitalized upon for additional cooling capacity. In terms of magnitude, this heat-sink is substantially larger than hydrogen's latent heat of vaporization. That is, roughly speaking, as much low-temperature cooling can be accomplished from the para/ortho shift, as can be gotten from the hydrogen vaporization process.

To accomplish this, para/ortho catalysis of hydrogen can, in principle, be mechanized in the internal hydrogen flow passages of the heat exchanger to significantly enhance the cooling capability of para-form hydrogen in the air liquefaction process. This catalytic effect could strongly promote the endothermic para-form to ortho-form conversion which would naturally, but far too-slowly, take place without catalysis as the hydrogen is warmed up in the heat exchange process. A properly selected catalyst, however, can very positively affect the kinetics of this conversion process. Otherwise, the conversion would not occur at significant levels because of the limited hydrogen residence times in realistic heat-exchanger and engine designs.

Thus, the concept of physically incorporating high-activity para/ortho-conversion catalysts into the heat-exchanger hardware was developed. Significant research was carried out on lightweight, high-efficiency para/ortho shift-conversion catalysts in support of this potential means of augmenting hydrogen's refrigerative effect. This approach is reflected, for example, in the SuperLACE system concept discussed later.

## Hydrogen Turbine Expanders

A second approach for enhancing hydrogen's refrigerative effect is to extract enthalpy (roughly, the "internal energy content" of a material) from the hydrogen by causing it to perform work, thus recooling it for a distinct refrigerative-effect advantage. An exemplary enthalpy-extraction technique is the use of a mechanical work-producing gas-expander device, for flightweight equipment, this is usually in the form of a hydrogen turbine expander. At the cost of a measurable pressure drop, the temperature level of the hydrogen can be significantly reduced, thus allowing it to liquefy more air than otherwise. Since, upstream of the heat exchanger, the liquid hydrogen must be initially pumped to some elevated pressure level in most practical applications, it appears that this pressure drop requirement can usually be accommodated with minimum penalties.

A distinct advantage of the turbine-expander approach is the resulting output of shaftpower. This shaftpower can be productively used to drive pumps, compressors (see next section), and other auxiliary units (e.g., electric generators). Design work accomplished on air-liquefaction based engines to date indicate that, in fact, all or most pump-power requirements can be provided by such hydrogen expanders. The use of a turbine expander is reflected in the SuperLACE system discussed subsequently in the paper; see later Figure 14.

## Cryogenic Air Compressors and Liquid Air Pumps

In some promising propulsion cycles related to air-liquefaction, cryogenic air compression machinery can be productively used. Compressing the very cold gaseous air requires a much smaller, lower-power compressor than required for the same amount of ambient-temperature air. The "cryojel" family of concepts, in fact avoids the final liquefaction step, and compresses all the airflow up to combustor entry conditions, thereby avoiding the condenser pinch-temperature problem (the heat-transfer constraint now, however, moves to the final stages of precooling).

Cryogenic air compression can also assist directly in air-liquefaction dependent concepts. In effect, more air can be liquefied once it is compressed because, both the condensing temperature is raised, and the latent heat of condensation is reduced at increasing air pressure levels. The archives reveal that significant study attention was given to this class of machine, often using turbine-expander drive means, in some aerospaceplane propulsion schemes. The General Electric Company examined one and two-stage centrifugal-compressor concepts as reported in conjunction with the Marquardt work on overall propulsion systems. This represents a third approach for leaning-out the cycle.

Essentially all liquid air using propulsion systems require liquid air pumps. This follows from the fact that the heat-exchanger sump from which the liquid is withdrawn is at low, often subatmospheric pressure. To be effectively utilized in a combustor operating at elevated pressures, a pump must be interposed within the systems. A more-or-less conventional rocket engine type turbopump unit will meet this requirement, with possibly one exception: the low net positive suction pressure (NPSP) requirement just referred to. This may signify special inducer-technology or separate boost-pump needs. Otherwise today's liquid oxygen pump technology should be directly applicable to achieving a high-performance, lightweight liquid air pump.

## Hydrogen Recycling (and Slush Hydrogen)

A fourth, again distinctively different, technical approach for refrigerative-effect enhancement of hydrogen is referred to as hydrogen recycle operation (see later Figure 13 for a simplified engine/vehicle propellant flow schematic). This approach is usefully applied in certain multimode-type combined cycle engines where non-air-liquefaction operation, such as ramjet mode, using hydrogen as fuel, follows the cessation of air-liquefaction operation during flight. Here, additional vehicle-tanked hydrogen, to be later used in such non-liquefaction modes, is "borrowed" for its extra refrigerative effect, thereby augmenting that cooling effect of the hydrogen being immediately consumed. This extra hydrogen, considerably warmed up in the air condensation process, is returned to the vehicle tank, or recycled, as cold gaseous hydrogen.

Within the tank, the recycled hydrogen gas must be reliquefied for basic containment reasons and to restore it for subsequent use as pumpable liquid fuel, e.g., to fuel higher-speed ramjet/scramjet mode operation. This reliquefaction is conventionally accomplished by directly distributing and injecting the recycled warmed-up gaseous hydrogen into the tanked liquid hydrogen. Such hydrogen recycling requires, naturally, an additional heat sink beyond that available in saturated (boiling) liquid hydrogen, as is usually the tanked hydrogen condition. To provide this heat sink, the hydrogen must be initially in a subcooled form. To maximize the amount of heat sink available, and thereby obtain a maximum amount of recycled hydrogen, the hydrogen is usually specified to be a solid/liquid mixture at its triple point temperature (about 13 K, 25 R). In this way both sensible and latent heat-sink is added.

This mixture is descriptively referred to as slush hydrogen which is typically at a 50/50 mixture ratio, solid to liquid, by mass. Figure 8 reflects the normalized (to normal boiling point [NBP] liquid hydrogen) enthalpy and density relationships as a function of subcooling and liquid/solid mass fraction. As can be seen (left-hand scale), slush hydrogen offers an additional advantage of about a 15-percent increase in fuel density over conventionally-tanked saturated liquid hydrogen (leading to reduced tank volume and weight). On the liability side, facility and procedural means for producing and maintaining slush-form hydrogen must ultimately be provided for in a practicable operational setting. This potential drawback has yet to be fully explored or otherwise quantified in terms of cost/benefit aspects. There are, however, new technologies on the horizon which may be advantageously brought to bear on the problem (one of these is magnetic refrigeration<sup>5</sup>).

## Less Than Full-Airflow-Liquefaction Systems

Yet a fifth approach, this time involving overall engine design considerations, increases the refrigerative effect of the hydrogen in terms of reducing the relative amount of air being refrigerated (see later Figure 12 for an illustration of this approach). This is achieved by selecting other than 100-percent of the engine airflow to be liquefied. Observing that it is the air-condensing step, not the preceding air-precooling step, which establishes the amount of hydrogen required to liquefy the air, this generic approach considerably reduces the low-temperature demand on the hydrogen, allowing it to operate on a lesser amount of air than otherwise in the condenser, particularly. This, in turn, acts to lean out the engine cycle -- the critical end-objective.

Numerous design variations exist in the pursuit of this particular approach, including the following examples:

- (1) the cryojel family of engines, such as versions of "SuperLACE" and "PACE" (Precooled Air Cycle Engine), is one in which *none*, or only a small fraction, of the processed air is liquefied. The rest of the air is maximally cooled, and thereby densified, providing for much more compact, lighterweight, and lower-power-demand air-compression devices than conventionally required in, say, turbojet engines (see above discussion of cryogenic air compressors). The net result is increased performance in a lighter-weight engine.
- (2) Split-airflow engines have been conceptualized which fractionally divide the airflow into both a liquefied and a non-cooled airstream, the liquefied air being produced by cryogenic hydrogen heat exchange, pumped to pressure, and burned with hydrogen, under either fuel-rich or stoichiometric conditions, depending on the design (see later Figure 12 for a simplified schematic of the RamLACE engine concept which is based on this approach). This, in turn, provides the means of compressing the non-cooled airstream, following which,

the remainder of the hydrogen is injected and burned. Examples include the Liquid Air Turboaccelerator (LATA) and the RamLACE/ScramLACE concepts. The former uses a conventional mechanical compressor, the latter an air-augmented rocket type "jet compressor". (3) Precooled and/or Intercooled Turboaccelerators are basically conventional turbojet/turbofan-based engines which use their limited available quantities of combustion hydrogen to cool the airstream somewhat, increasing its density to achieve advantages similar to those of cryojets. However, near-saturation conditions are not approached as they are in cryojets. In being compressed, the denser air allows for modest reductions in compressor hardware size and power extraction requirements, at the expense of the weight and airflow pressure-drop in the heat exchanger required.

(4) Hydrogen Expander, Regenerative Hydrogen Air Turborocket, Air Turbo Exchanger, and other such proposed engine types, are technically related to the above turbomachinery based systems, but they differ mainly through heat addition to the hydrogen from combustion processes, sometimes in addition to heating provided by high-speed flight intake air (see, for example, the hydrogen-expander engine discussion in Reference 1). Larger quantities of compressor shaftwork can be extracted through subsequent turbine-expansion with such hydrogen heating, following which, the hydrogen is burned in the engine. These systems are not, however, usually viewed as "air liquefaction related" systems.

#### **Liquid Air Regenerator/Boiler**

Returning to the various methods for enhancing the refrigeration effect of hydrogen, a sixth design approach involves incorporating a second air-precooling heat exchanger in which pumped-up liquid air, not hydrogen, is used as an adjunct upstream (airflow-wise) heat exchanger coolant. This liquid-air-coolant heat exchanger element is usually the first to be encountered by the inducted airflow. Being a regenerative process, the consequential heating and vaporization of the liquid air is advantageous to engine performance, hence, this heat exchanger unit is sometimes referred to as a regenerator/boiler unit. The liquid air regenerator/boiler is especially beneficial to the in-flight air collection system approach to be discussed below. Here, ram-air, taken in at supersonic flight conditions at elevated temperatures (well over ambient temperatures are now experienced, depending on flight speed), adds to the "refrigerant-resource" of the heat-exchange process.

This approach requires special consideration of the heat exchanger materials of construction. Above Mach 3 to 5, other than aluminum alloy construction must be considered because of elevated air temperatures. Such initial air precooling with liquid air obviates another potential problem area of high-temperature hydrogen heat exchangers: increased hydrogen diffusion through elevated temperature thin-walled materials. The increased "leakage" of hydrogen at higher materials temperature into the internal engine airstream could, obviously, constitute a hazard if combustion ensued. Whether this is a "real problem" or not apparently remains unresolved. In any case, liquid air precooling may be usefully employed in future engine designs. (See the SuperLACE system concept presented at the end of the paper.)

### **AIR COLLECTION AND ENRICHMENT SYSTEM (ACES)**

#### **Tanking Up Liquid Oxygen In Flight**

Yet another and different technical approach for performance improvement in certain kinds of air liquefaction systems which have been examined extensively is referred to collectively as the air collection and enrichment system (ACES). Figure 9 is a highly simplified operating schematic of one version of this approach. The vehicle accelerates to its "collect" altitude and speed (typically Mach 3 to 5), and while operating on hydrogen-fueled ramjet mode, air is partially withdrawn from the inlet diffuser at recovery pressure and passed through the heat-exchanger series, beginning with a liquid nitrogen-cooled counterflow-type precooler. This liquid nitrogen has been separated from the liquid enriched air (LEA) which is to be stored for later use in conducting the flight. The warmed up nitrogen is productively dumped into the ramjet as added inert propulsive mass and exhausted through the nozzle overboard.

When the vehicle tank is fully loaded with LEA (typically 90-percent oxygen, 10-percent nitrogen), the collect-mode is terminated and the vehicle reaccelerates on ramjet-mode followed by LEA/hydrogen rocket-mode operation to staging conditions, or flight directly to orbit. In some version of the ACES, a common "multimode thrust chamber" is used for both ramjet and rocket operations, including initial takeoff and climbout to ramjet takeover conditions (Mach 2-3). Marquardt created an inlet-valve controlled rocket/ramjet engine concept, referring to it as the "Hyperjet" for this purpose. This concept was actually static-tested in rocket mode at fairly large-scale (but on storable propellants, not cryogenics).

#### **Air Separation Into Oxygen and Nitrogen - Various Approaches**

The governing technology of the ACES concept is the air-separation device, for which several variants were proposed. The principle one of these is a lightweight and flight-worthy air-separation-process device referred to in General Dynamics' U.S. Patent 3,779,452 <sup>6</sup> as a "rotary cryogenic distillation separator". This patent is reflected in Figure 10. Its operation is akin to that of the standard large distillation-tower air-separation process used industrially all over the world by the industrial gas community. However, the rotation feature provides for much higher than one-gravity acceleration levels on the cryogenic liquid/gas separator trays used in this process, thus greatly compacting and reducing the weight of the apparatus required. The technical problem addressed is the reduction in thickness of the boiling-air "froth" layer. This type of unit was actually built and successfully tested as a non-flightweight, full-scale module by Linde Division of the Union Carbide Corporation under Air Force sponsorship.

An alternative to the cryogenic separator approach, an elevated temperature chemical separation method was conceptualized and explored at the laboratory level in the mid-1970. This device used the principle of reversible "chemical gettering" of oxygen from air. It was not, however, taken to the large-scale experimental level of development enjoyed by the cryogenic separator. More recently (than the 1960s), the use of semipermeable membrane technology, now more highly developed within the industrial gas industry, has been suggested for nitrogen/oxygen separation in flight systems.

In contrast to those techniques reviewed earlier, ACES does not improve the cycle equivalence ratio, but rather increases the effective (not actual) specific impulse of what is basically a rocket engine cycle for the final acceleration phase of flight. As covered above, it does this by collecting and "sorting out" the inert nitrogen component of air (about 80 percent of air by mass), leaving "enriched air", essentially liquid oxygen, with some small amount of remaining nitrogen diluent, to be tanked aboard for subsequent use in the engine.

This provides combustion temperatures and exhaust-gas molecular weights nearly the same as that of a "neat" hydrogen/oxygen rocket, thus improving the overall specific impulse of the system well above that which would be the case with liquid air (LAIR). In ACES vehicle systems, the post-collect vehicle gross weight can be substantially higher than its initial, or takeoff weight (e.g., it can be as much as doubled).

## TECHNOLOGICALLY RELATED PROPULSION SYSTEM CONCEPTS

### RamLACE and ScramLACE (Including Hydrogen Recycle Operation)

One of the techniques for reducing the fuel-richness of the propulsion cycle described earlier, was the option of not liquefying all the air taken aboard through the inlet. An interesting concept of this type derives from the rocket/ramjet type approach explored by numerous organizations over the past several decades. Specifically, the Ejector Ramjet, explored by Marquardt in the mid-1960s was the basis of a series of derivative concepts, some of which utilized an air-liquefaction process. The Ejector Ramjet, a non-air-liquefaction engine concept is a combined-cycle (airbreathing/rocket) system in which an internally mounted primary rocket subsystem provides for an air-augmented rocket mode of operation to accelerate this lightweight, relatively simple engine to ramjet takeover speeds, wherein ramjet-mode was operated for further acceleration and/or cruise. Under Air Force sponsorship, a subscale exploratory research and development program concluding with a 45-cm (18-inch) diameter non-flightweight ground-test series was conducted between 1963 and 1967 by Marquardt.

Simultaneously, under NASA sponsorships a series of Ejector Ramjet derivatives, and other combined-cycle engine types were explored by a team of Marquardt, Rocketdyne and Lockheed-California Company for advanced launch vehicle applications. The database created in this work (Contract NAS7-377) has been recently used in an assessment of combined-cycle propulsion for single-stage-to-orbit applications for the Air Force. The final report for this study provides extensive information on both air-liquefaction and non-liquefaction variants of the basic Ejector Ramjet system<sup>7</sup>.

The initial air-liquefaction variant of the basic Ejector Ramjet is the RamLACE system (Figure 12), in which the primary rocket subsystem utilizes liquid air in lieu of onboard-tanked liquid oxygen. Otherwise, it retains its bimode (air-augmented rocket/ramjet) capability. The association with Basic LACE is readily apparent, however, the basic air-augmented rocket cycle selected (referred to as the diffusion and afterburning cycle) precluded a fuel-rich rocket operation. Excess rocket fuel would combust with the air during the mixing process, penalizing performance and causing other problems potentially. A modification to the Basic LACE approach was necessary, since it is intrinsically a very fuel-rich device. The solution was to operate the primary rocket stoichiometrically, injecting the excess fuel in the afterburner or ramjet combustor. The net effect then, in this split-airflow operations (only a portion of the air is liquefied, namely that required for the primary rockets) was a considerable leaning out of the cycle from an equivalence ratio of 8 to about 4. Specific impulse was increased from about 1000 to 1400 seconds, a measurable improvement.

Subsequent studies of the Ejector Ramjet type engine evolved a version capable of transitioning into supersonic combustion ramjet operation, following ramjet-mode acceleration, the Ejector Scramjet. In analogy, the ScramLACE derivative was conceptualized. ScramLACE is quite equivalent to RamLACE with regard to its air-liquefaction process for initial acceleration. A variant of ScramLACE is Recycled ScramLACE which is portrayed schematically in Figure 13. Through recycling some of the hydrogen during the air-liquefaction mode of operation, as described earlier, the cycle is further leaned out to the order of equivalence ratio of 2, and specific impulse rises to about 2700 seconds. Of course, this requires that slush hydrogen be initially loaded into the hydrogen tank and maintained as such into the flight.

### SuperLACE: Combined Effect of Hydrogen Refrigeration Effect Measures

Thus, there are numerous technical approaches for enhancing the refrigerative effect of the available hydrogen to, in effect, reduce the fuel-richness of the engine operating cycle and thereby increase specific impulse performance. Quite important to note, these techniques are usually not mutually exclusive. That is, they may be utilized simultaneously to compound the additive refrigerative enhancement effect. The Recycled ScramLACE (Figure 13) just described utilized several approaches; two were named: split-airflow and hydrogen recycling, and a third was also used: para/ortho catalysts.

A completely different engine synthesis approach, The Marquardt Company's SuperLACE propulsion system (Figure 14) was conceptualized earlier and applied to aerospaceplane concepts of the early 1960s. It utilized as many as four of the above-discussed technical approaches:

- Para/ortho conversion catalyst
- Turbine expander
- Hydrogen recycle (slush)
- Liquid air regenerator boiler.

By this combination, the engine cycle was specified to operate near-stoichiometrically, achieving a sea-level static specific impulse in the range of 6000 sec. However, this performance level was apparently never demonstrated experimentally, SuperLACE remaining mainly a "paper engine" of those times. It is further described below.

### SuperLACE/ACES - Culmination of Aerospaceplane Propulsion Planning

Figure 15 reflects a compilation of many of the technical approaches and features discussed so far in this paper. This is a generalized specific impulse performance plot over the flight speed range equivalent to that required for attaining low Earth orbit for a single-stage-to-orbit aerospaceplane vehicle concept, ca. the early 1960s. Starting at the low end of the specific impulse scale, a reference hydrogen/oxygen rocket engine case is reflected (horizontal dashed line). The 1000+ second (initial condition) range of Basic LACE (hatched area) is shown over its estimated speed regime of Mach 0 to 8. Its performance decreases with speed, largely a consequence of increasing ram drag in an inlet that completely "stops" the airflow (in order to provide liquid air statically).

The vertically running lines labeled "Hyperjet" refer to that convertible rocket/ramjet concept created by Marquardt, referred to earlier; the lines note several options for shifting from initial rocket mode to ramjet mode, as a function of flight speed and altitude. The hatched area marked "Growth" is an allusion to the supersonic-combustion ramjet (*scramjet*) mode of operation, Mach 8 being judged to be the upper limit of subsonic-combustion ramjet mode. It should be noted that at that time (early 1960s), scramjet operation was only being initially investigated by the propulsion research community.

The descending (with speed) characteristic called out for "ACES" is simply what was expected to be the performance of a hydrogen-fueled ramjet during the acceleration/cruise/acceleration phase where the "air-collect" operation was performed. Operation of ACES at speeds beyond Mach 8, as described above, utilized rocket-mode operation using hydrogen/LEA propellants. The actual specific impulse level achieved is that line just below the reference rocket boundary, a measure of the 10-percent nitrogen diluent in the oxidizer. However, the fact that the LEA was "taken aboard" at intermediate flight-speed conditions, rather than being ground-loaded (as



would be the case with the rocket), provides for an elevation of the performance to an "integrated value" ranging from about 1500 seconds down to just below 1000 seconds at orbital speed.

Finally, returning to the highest performance low-speed, end of the scale, we find "SuperLACE" specific impulse levels of 5500 to 6500 seconds at sea-level, static conditions, then ranging down to about 4500 seconds at ramjet takeover conditions. This is a level of performance which can be estimated for a more-conventional nearly-stoichiometric hydrogen airbreathing turbomachine (e.g., turbojet, variable-cycle engine). To the extent that SuperLACE is a credible concept, this same level of performance is seen to be provided in a lightweight engine (Figure 14) *without* major rotating machinery subsystems.

Although never developed to a prototype stage, SuperLACE is a rather vivid demonstration of the technical *theme* expressed in this paper. That is, starting with the simple Basic LACE concept (Figure 1), combining various technological measures for increasing the refrigerative effect of the liquid hydrogen coolant, combined with steps to minimize the amount of air being liquefied, permits an extensive leaning out of the very fuel-rich LACE operating point, all the way to near-stoichiometric operation in SuperLACE. This yields about a *six-fold* increase in specific impulse, as reflected in Figure 15.

Perhaps the "most advanced" of the aerospaceplane propulsion systems as were contemplated at that time is this combination of SuperLACE and ACES, descriptively, *SuperLACE/ACES* represents the culmination of advanced propulsion thinking of that era. If one were to question this perception by asking "where is scramjet?" he or she would be asked to recall that scramjet operation was only just being *initially contemplated* as a potential "growth" step, at that time (as stated in the figure). Later on, the significance of scramjet-mode operation has been recognized as, perhaps, much more than this.

#### RamLACE/ScramLACE Engine Family: Emphasis on Hypersonic Ramjet Operation

Following on with this thought, the considerable hypersonic ramjet (both subsonic- and supersonic-combustion modes) work accomplished in the mid- to late-1960s, combined with the obvious complexities intrinsic in concepts such as SuperLACE/ACES, led to the creation of alternative kinds of propulsion systems applicable to hypersonic flight. Figure 16 in effect combines previous Figures 1, 12 and 13 (while substituting Recycled RamLACE for its ScramLACE equivalent of Figure 13). As discussed, this Ejector Ramjet based family of engine concepts (discounting Basic LACE for a moment) were evolved at Marquardt, primarily, a number of years after the demise of aerospaceplane. These concepts reflect some of the benefits of the significant advancements made in the interim period, especially those in the hypersonic ramjet field, including ground-tests of a subscale flightweight hydrogen-fueled/cooled subsonic-combustion ramjet at Mach 6 and 8 and testing of dual-mode or convertible engines, capable of both modes of combustion.

Consequently, these newercombined-cycle engine concepts were configured expressly to provide for essentially uncompromised hypersonic ramjet mode operation, in that they provided a clear throughflow passage for air, including all-supersonic flow. The Hyperjet component of SuperLACE/ACES, in general, appears not to be so amenable to the wide speed-range hypersonic ramjet operation. In some views, today, high-performance ramjet/scramjet operation appears vital for achieving high payload fraction single-stage-to-orbit systems, such as those examined in more recent times, e.g.<sup>7</sup>.

The three engine concepts reflected in Figure 16, once again, point up the theme of this paper: progressive cycle leaning-out strategies being applied to raise the specific impulse level of the propulsion system for the hydrogen-induced air liquefaction process in the flight speed regime of Mach 0 to 8 (in the extreme). RamLACE/ScramLACE systems typically convert to ramjet mode at about Mach 3. What this means is that, for this class of propulsion system, the air-liquefaction process is performed only over about one-eighth of the total speed range for a single-stage-to-orbit (SSTO) system. As documented, e.g.<sup>7</sup>, this signifies a lesser contribution of the attendant increased specific impulse gain, than would be the case for the first-stage vehicle of a two-stage-to-orbit system, for instance. For Mach 6 staging, about *half* the speed-range would involve air-liquefaction operation. The added weight of the air-liquefaction equipment now becomes an especially sensitive design-parameter, possibly impacting heavily on payload performance.

#### Current Interest In Air-Liquefaction Based Propulsion Systems

Evidence of reawakening interest in the specific subject of air liquefaction was noted in about 1984, perhaps not so much in U.S. initiatives, but rather by activities of those overseas. The HOTOL concept brought out by UK researchers about that time, based on limited information releases to date, can be inferred to involve some of the technologies covered here. In another corner of the world, Mitsubishi Heavy Industries, Ltd., of Japan, presented a novel air-liquefaction based propulsion system in a 1984 technical paper which mainly described their hydrogen/oxygen rocket engine developments and plans<sup>8</sup>. A second paper, focusing on "Air Condensing Type Air Breathing Propulsion Systems"<sup>9</sup> was presented at the International Astronautical Foundation (IAF) Congress in October of 1986. Yet a third paper, presented in the Fall of 1988<sup>10</sup>, presented a number of variants of the Basic LACE concept naming many of the technologies and concepts addressed in this paper: viz., ACES, recycling of cryogenic propellants and tanked propellants subcooling (slush), cryogenic air compressors, turbine expanders, and the liquid-air regenerator/boiler.

Figure 17 reflects an innovative air liquefaction engine schematic from the initial paper. Note that air precooling and condensing is accomplished using *both* cryogenic hydrogen and oxygen for refrigeration (the latter presumably being used for later rocket-mode operation). In addition, propellants recycling and propellants subcooling to provide needed heat sink are reflected. A novel liquid oxygen direct injection ("lox spray") into the heat exchanger is also included.

Discussed in the most recent paper<sup>10</sup>, and updated occasionally in the technical press, e.g.<sup>11</sup>, is Japan's plan to modify their LE-5 and LE-7 hydrogen/oxygen rocket engine to operate as an advanced LACE system. Complete with individual high-speed inlets, multiples of these units are contemplated as booster engines for launching a "space plane" vehicle. It is stated that payload can be *tripled* by substituting the advanced LACE boosters for solid-propellant rocket boost units. A longer-range target discussed is the "SSTO type space plane", called out as a 350 ton (GTOW) winged horizontal takeoff and landing vehicle powered by 3 advanced LACE units whose engines are stated to be capable of initial specific impulse levels of 1500 to 2500 seconds, increasing to the peak range of 5000 to 6000 seconds at flight speeds of Mach 3 to 6.

## SUMMARY

Consideration of cryogenic hydrogen-induced air-liquefaction, as an onboard aerospace propulsion system process was initiated with the Basic LACE (Liquid Air Cycle Engine) concept very shortly following the selection of liquid hydrogen as an operationally accepted fuel in the mid-1950s. Almost immediately, under the aegis of the U.S. Air Force's *aerospaceplane* program, steps were taken to improve the performance and operational versatility of this LACE starting point. The basic strategy was to lean-out the very fuel rich LACE system. This involved various measures for increasing the refrigerative effect of the liquid hydrogen coolant in the cooling and liquefying of air taken aboard the vehicle, and/or reducing the amount of air required to be liquefied. A rather different air-liquefaction approach was ACES (Air Collection and Enrichment System). This was focused on the in-flight acquisition of tanked liquid oxygen for the final propulsion stage of operation to orbit or to staging conditions (multistage vehicle).

The technologies for accomplishing this strategy, many of which were experimentally developed in the late-1950s/early-1960s, represent a "cluster" of related, but yet often disparate technical approaches. These technologies have been, and continue to be (e.g., cited Japanese work) considered separately, more often together, in the formulation of a set of advanced propulsion system concepts. Among these proposed systems, there may well be one, or several engine concepts which will someday be developed to complement or supplant rockets and conventional turbomachine airbreathing engines for future vehicle systems. Such systems will be targeted to be capable of providing routine and affordable Earth-to-orbit transportation, as well as hypersonic-ramjet sustained high-speed flight within the atmosphere.

## REFERENCES

1. Sloop, J.L., Liquid Hydrogen as an Aerospace Fuel 1945-1949, NASA SP-4404, 1978.
2. Builder, C.H. and Kroil, R.W., Preliminary Model Specification - MA70-XAA Liquid Air Cycle Engine, Marquardt Report No. MR 20,100, June 1960.
3. Escher, W.J.D. and Doughty, D.L., Assessment of Cryogenic Hydrogen-Induced Air Liquefaction Technologies, Astronautics Corporation of America final report under SAIC Subcontract No. 15-860020-82, under U.S. Air Force Prime Contract No. F33615-84-C-0100, September 1986 (limited/restricted distribution).
4. Anon., Liquid Air Cycle Engine, film report by The Marquardt Company, presented at the annual meeting of the Institute of Aeronautical Sciences, 1961.
5. Uherka, K.L., Hull, J.R. and Scheihing, P.E., Recent Advances in Magnetic Heat Pump Technology, ASME Winter Annual Meeting, December 1989, San Francisco, California.
6. Nau, R.A. and Campbell, S.A., Rotary Separator, U.S. Patent 3,779,452, 18 December 1973.
7. Foster, R.W., Escher, W.J.D., and Robinson, J.W., Air Augmented Rocket Propulsion Concepts, Astronautics Corporation of America Report No. AFAL-TR-88-004, 31 January 1988.
8. Hirakoso, H. and Hasegawa, K., LOX/LH<sub>2</sub> Engine Development Status and Future, Mitsubishi Heavy Industries, Ltd. presentation at the American Astronautical Society 1984 annual meeting, San Francisco, California.
9. Hirakoso, H., Ito, T., Hasegawa, K. and Togawa, M., Air Condensing Type Airbreathing Propulsion System, Mitsubishi Heavy Industries Ltd. and National Space Development Agency of Japan, Paper No. IASF-86-180, 36th Congress of the International Astronautical Federation, 7-12 October 1986, Stockholm, Sweden.
10. Hirakoso, H. and Ito, T., A Concept of LACE for Space Plane to the Earth Orbit, Mitsubishi Heavy Industries, Ltd. and National Space Development Agency of Japan presentation at the First International Conference on Hypersonic Flight in the 21st Century, September 1988, Grand Forks, North Dakota.
11. Anon., Mitsubishi Plans to Test Experimental Liquefied Air Cycle Engine Based on LE-5, *Aviation Week & Space Technology*, 31 July 1989 (p. 33)

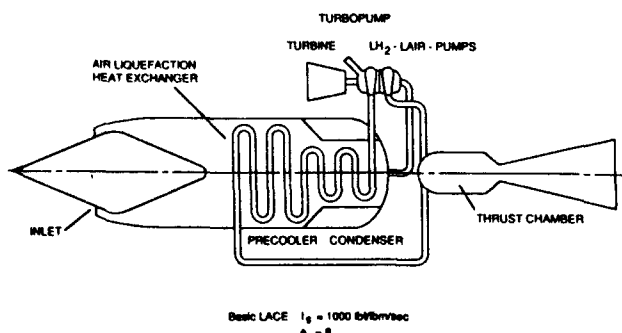


Figure 1 Basic LACE (Liquid Air Cycle Engine) Schematic

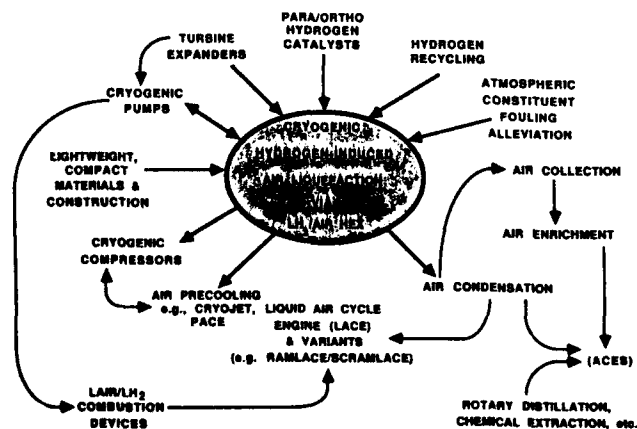


Figure 2 Cryogenic Hydrogen-Induced Air-Liquefaction Related Technologies

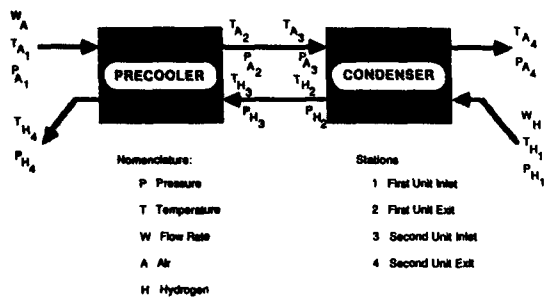


Figure 3 Compact Cryogenic Heat-Exchanger Schematic and Key Parameters

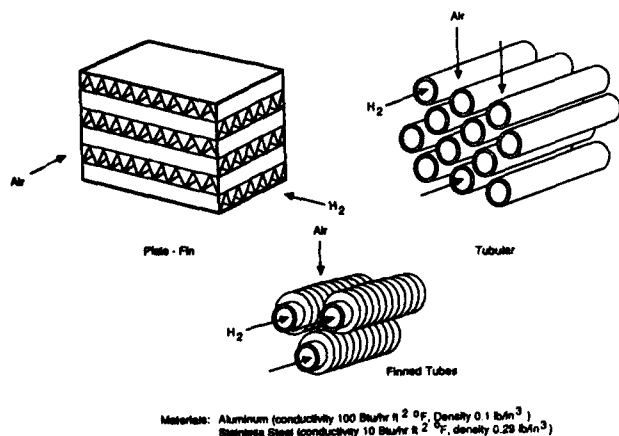


Figure 4 Heat-Exchanger Matrix Designs Typically Selected for Air-Liquefaction Applications

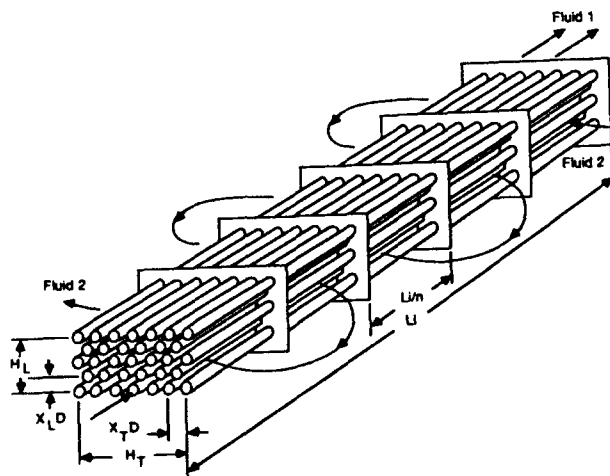


Figure 5 Representative Cross-Counterflow Tube-and-Shell Heat-Exchanger Core with Baffles

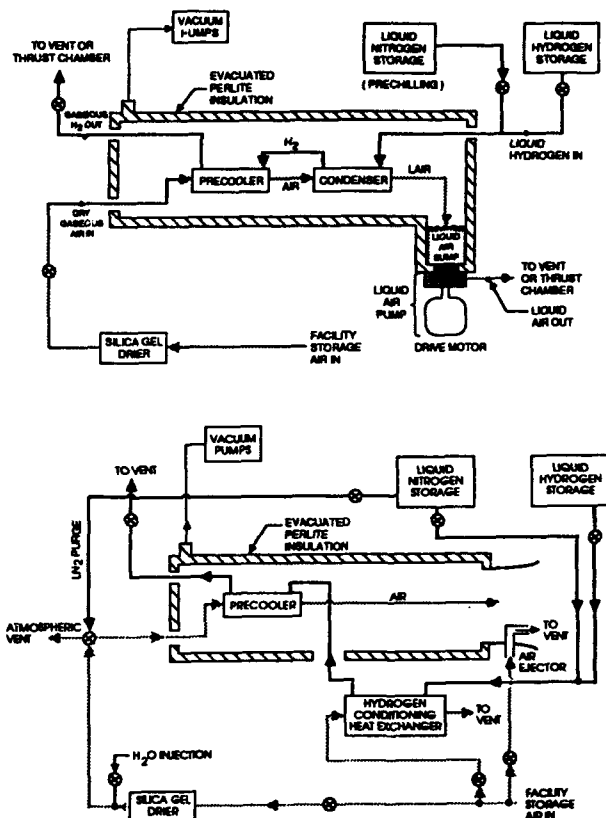


Figure 6 Simplified Schematic Layout of Typical Component (lower sketch) and System (upper sketch) Test Rigs

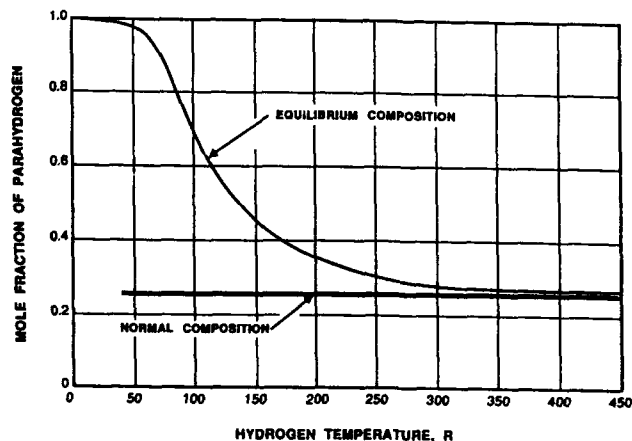


Figure 7 Hydrogen Equilibrium Para-form Content as a Function of Temperature

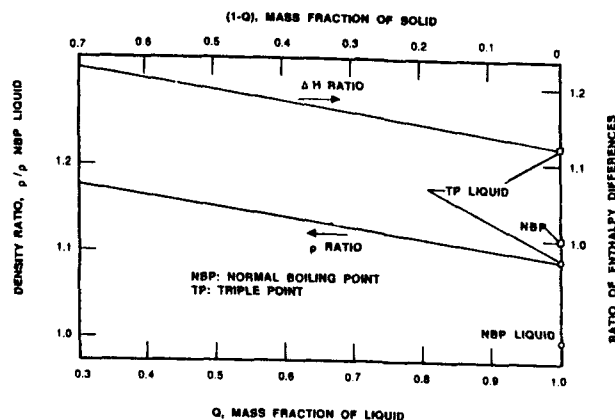


Figure 8 Density and Enthalpy Ratios for Normal Boiling Point (NBP), Triple-Point and Slush Hydrogen

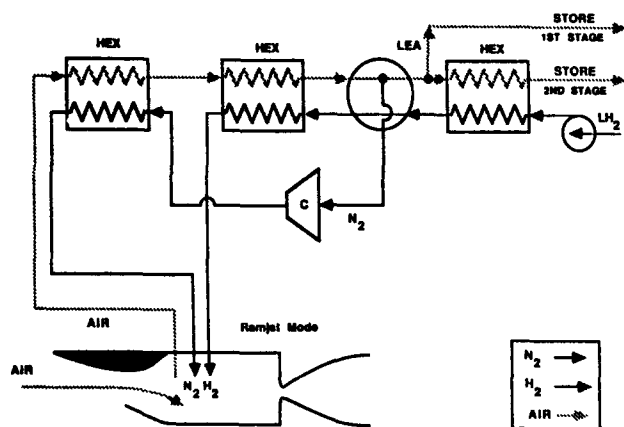


Figure 9 Air Collection and Enrichment System (ACES) Simplified Schematic Diagram

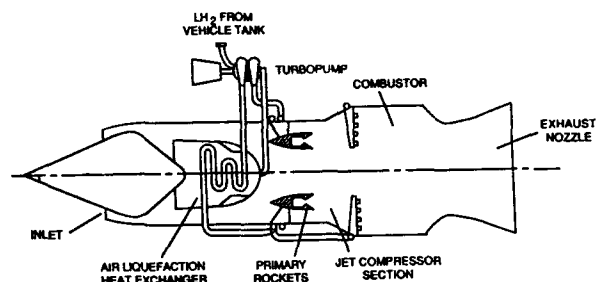


Figure 12 RamLACE Engine Simplified Schematic Diagram

United States Patent [19]  
Nau et al.

[11] 3,779,452  
[45] Dec. 18, 1973

[54] ROTARY SEPARATOR

[75] Inventors: Richard A. Nau, La Jolla; Sterling A. Campbell, San Diego, both of Calif.

[73] Assignee: General Dynamics Corporation, San Diego, Calif.

[22] Filed: Sept. 22, 1968

[21] Appl. No.: 57,742

[52] U.S. CL. 233/32, 233/11, 233/13, 233/18, 233/23, 233/32, 55/206, 55/337, 55/348  
[51] Int. Cl. B01d 45/12  
[58] Field of Search: 233/11, 12, 18, 21-23, 233/27, 183/2, 55/337, 206-207, 345-349

[56] References Cited  
UNITED STATES PATENTS

1,474,245 6/1927 Jones 233/13

1,714,370 5/1929 Humphrey 233/32  
2,170,071 8/1939 Furrer 233/11  
2,351,815 3/1951 Scholz 233/18  
2,974,472 4/1960 Shumron et al. 233/19

Primary Examiner—Reuben Epstein  
Attorney—John R. Duncan

[57] ABSTRACT

The disclosed apparatus is for separation of mixed gases through the combined action of distillation and centrifugal force. A rotor rotates a separator which includes means for condensing from a gas the less volatile of the mixed gases. The separating means comprises a plurality of sieve trays arranged concentrically around the axis.

5 Claims, 6 Drawing Figures

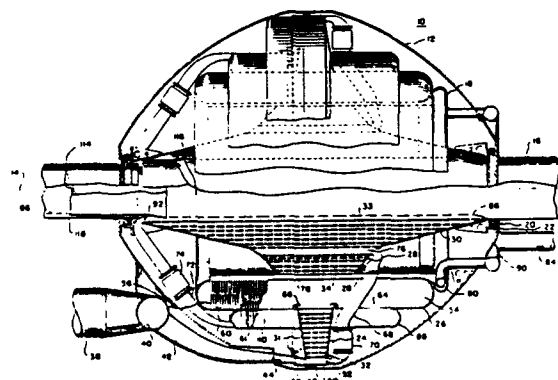


Figure 10 Rotary Cryogenic Air Distillation System Patent (first page illustrated)

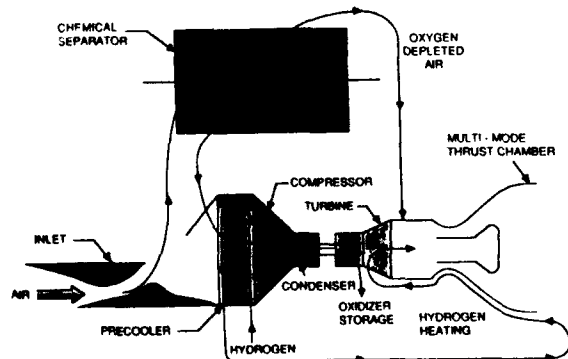


Figure 11 High-Temperature Chemical Air Separation System Schematic Diagram

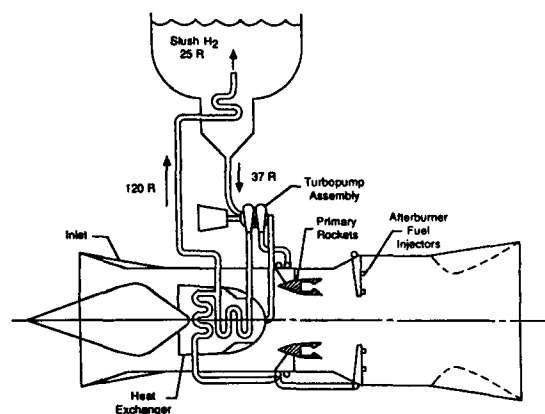


Figure 13 Hydrogen Recycle Operation (ScramLACE example)

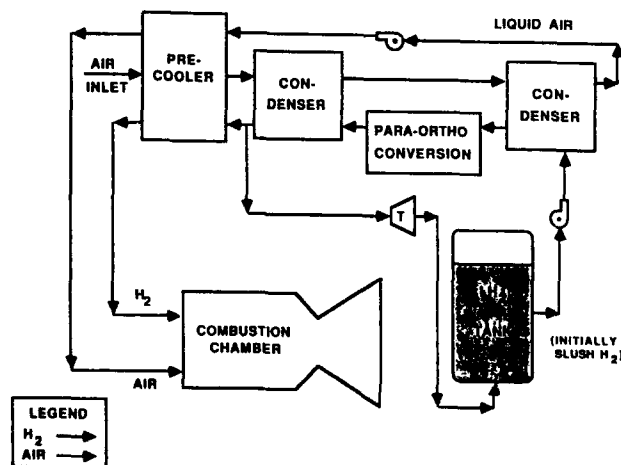


Figure 14 Representative SuperLACE Propulsion System Simplified Schematic Diagram

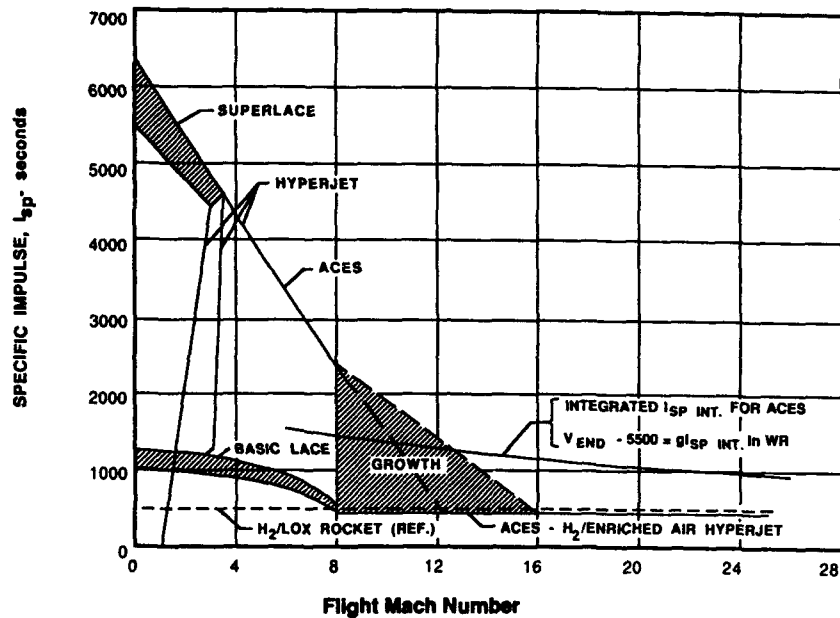


Figure 15 SuperLACE/ACES Characteristic Performance Flight Trends (typical)

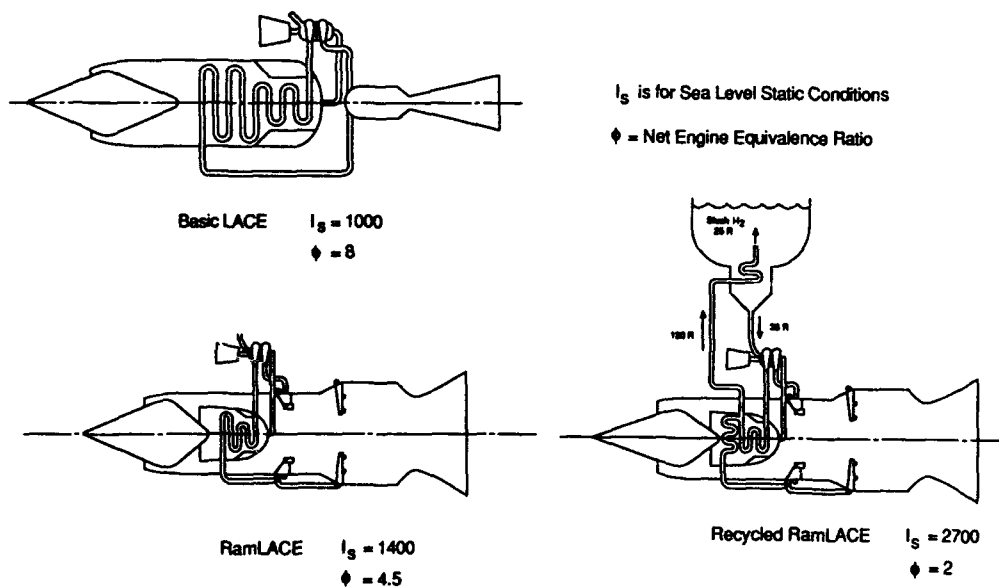


Figure 16 LACE/RamLACE "Cycle Leaning-out" Trends

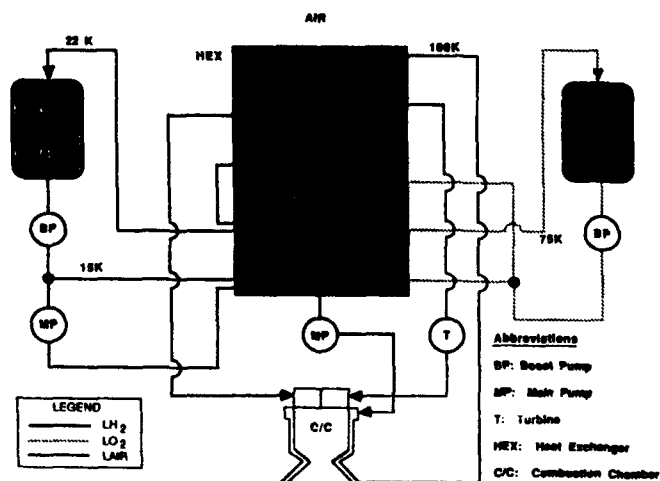


Figure 17 Simplified Flow Schematic for Advanced Air-Liquefaction Engine Assessed by Mitsubishi Researchers (Japan)

## Discussion

### STOLLERY

You mentioned some modern concepts such as HOTOL and the Japanese projects. How would you rate the promise of these modern developments?

### AUTHOR'S REPLY

To the author's understanding, with the notable exception of the cited R&D activities in Japan, not very much has been announced concerning such "modern developments", although inferences that such work is proceeding have been made from time to time (e.g. HOTOL).

For space transport system applications, whereas air liquefaction processes may be a significant benefit to the first-stage vehicle of a two-stage vehicle, such may not be the case in a single stage to orbit (SSTO) system. Here, specific impulse gains in the "low speed" regime, say Mach 0-3, must be put in balance with inert weight gains, operational complexity, possible safety and reliability problems, and added life-cycle costs.

### WEYER

How do you get the water out of the air before liquefaction?

### AUTHOR'S REPLY

There are two distinct forms of water as natural atmospheric constituents : water droplets, as in precipitation or clouds, and water vapour. During the heat-exchanger research and predevelopment activities of the early sixties in the US, numerous technical solutions to this vexing problem were proposed. Without going into any details, two generic approaches were taken in these proposals, both of which focused on water-vapour icing : 1)water/ice removal from the flow stream of air upstream of the critical region in the hydrogen cooled precooler, and 2)water freezing as a fine particulate material, in situ in the airstream which is then allowed to pass on through the heat exchanger. In the latter approach, a fine-particle ice-in-liquid-air slurry was to be formed which would assumedly cause no downstream problems.

### DINI

Did you try to compute the air liquefaction heat exchanger surface? I am thinking it is quite large and voluminous.

### AUTHOR'S REPLY

The author (himself) merely surveyed the applicable technical literature and performed no design calculations leading to estimates of required heat-exchanger active surface requirements. However, the questioner is to be assured that the investigators involved, at the time of this work (1950's and early 1960's), did indeed produce such estimates in quantitative terms of heat-exchanger size and weight, the latter being included as a significant contributing item in engine weight. Integration of the physically large heat-exchanger volumes into the engine and vehicle usually posed a significant design challenge.

AD-P007 948



## AERODYNAMICS OF HIGH SPEED AIR INTAKES

## - STATUS REPORT ON AGARD FDP-WG 13 -

Dr. Wolfgang SCHMIDT  
 MESSERSCHMITT-BÖLKOW-BLOHM GMBH  
 Military Aircraft Division

P.O.Box 801160, 8 Munich 80  
 Federal Republic of Germany

## SUMMARY

Future fighter concepts require air intakes with not only good performance characteristics over an even wider operating range, but also require inlet designs with low signature characteristics. The thrust of the working group's effort is to evaluate existing design tools and experimental capabilities for providing the innovative design concepts that meet the ever demanding challenges for engine inlets of advanced vehicle configurations. The present paper will give a brief survey over the different objectives of the working group.

## 1. SCOPE OF WORK

This study will examine and review semi-empirical inlet design tools, steady and unsteady computational fluid dynamic methods, and existing wind tunnel testing techniques for developing advanced air intake designs. Capabilities, limitations, and fruitful paths for the future will be determined. The effort will probably emphasize supersonic and hypersonic intake designs, where such problems as distortion swirl, buzz and strong shock interactions will receive detailed attention.

The Working Group will cover three main topic areas:

- (1) Computational Methods
- (2) Testing Techniques and
- (3) Design Methodologies.

Membership on the Working Group has been carefully selected to provide a distribution of expertise in these areas.

## 2. MEMBERSHIP OF WG 13

Wolfgang Schmidt	Dornier/MBB	FRG	FDP-Member, Chairman
R.G. Bradley	General Dynamics	US	FDP-Member, Deputy Chairman
J. Leynaert	ONERA	France	FDP-Member
T.J. Benson	NASA Lewis	US	
N.C. Bissinger	MBB	FRG	
E. Farinazzo	AIT	Italy	
E.L. Goldsmith	ARA	GB	
G. Laruelle	ONERA	France	
P.A. Mackrodt	DLR	FRG	
L. Surber	AFWAL/FIMM	US	
D. Welte	Dornier	FRG	
Contact to PEP:			
Ch. Hirsch	University Brussels	Belgium	PEP-Member

## Meetings held:

- September, 1987 Naples Italy
- June, 1988 NASA Langley US
- November, 1988 RAE Bedford GB
- September, 1989 ONERA Modane France

Last Meeting planned for

- October, 1990 DLR Göttingen FRG

AGARD Report will be published as AGARD-AR 270, 1991.

92-16958

### 3. CONTENTS OF THE WORKING GROUP 13 REPORT 270

#### 3.1 Intake Design and Performance (E.L. Goldsmith)

Section	Title	Author	Content
I	Introduction	Goldsmith	Title self explanatory
II	Definition of intake performance parameters & description of intake flows	Goldsmith	Internal flow: ram compression efficiency, engine face flow engine distortion, flow stability, flow quantity. External flow: pre-entry & cowl forces.
III	The initial design process	Surber	The process of 'first guessing' a design & making the initial estimates of performance.
IV	Intake design and performance for long range supersonic a/c	Surber	US post Concorde & STA experience.
V	Intake design and performance for agile strike/fighter a/c	Goldsmith/ Surber	1 Introduction 2 Isolated intakes 3 Intake airframe integration
VI	Intake design and performance for V/STOL Military aircraft	Welte	1 Introduction 2 General concepts & specific examples of flight tested vehicles 3 Performance of representative V/STOL intakes in static & transient conditions 4 Auxiliary intakes Appendix - specific examples of V/STOL intakes
VII	Intake design & performance for airbreathing missiles	Laruelle	VKI Lecture amplified & including input from BAe/RAE

#### 3.2 Numerical Simulation of Intakes (N.C. Bissinger)

Section	Title	Author	Content
I	Introduction	Bradley	
II	Testcases for CFD	Benson/ Bissinger	Detailed Description of Test Cases and Experimental Results
III	Computational Methods	Benson/ Bissinger	Description of CFD Methods used
IV	Analysis of CFD Results	Benson/ Bissinger	Presentation, Comparison and Analysis of CFD Results
V	Conclusions	all	Summary Study Results

##### 3.2.1 Selected Test Cases for CFD Calculations

Test Case	Flow Type	Number of Calculations
1	Transonic Normal Shock/Turbulence Boundary Layer Interactions	4
2	Glancing Shock/Turbulent Boundary Layer Interaction	4
3	Subsonic/Transonic Circular Intake Duct	6
4	Semi-circular Intake	1
5	Circular Pitot Intake	1
6	NASA P8 High Aspect Ratio Mixed Compression Intake	6
7	NASA Lewis 40/60 Axisymmetric Mixed Compression Intake with Bleed	3
8	Tailor Mate A-1 Intake with Fuselage	2



### 3.2.2 CFD Results by Individual Contributors

Data-Formats, scales and plots have been specified and mailed to all participants to ensure ease of comparison.

Besides the CFD results all contributors have been asked to supply information on

- o CFD method used
- o Computer used and CPU Time spend, Memory
- o Grid and Grid Refinements
- o Starting Conditions, Boundary Conditions
- o Convergence History
- o Mass Flow Along Duct - Quality Check of Calculations
- o Turbulence Models, Length Scales
- o Transition Criteria, Conditions used
- o Experience / Difficulties
- o "Tricks".

### 3.3 Air Intake Testing Methods (J. Leynaert)

Section	Title
I	Scope and Purpose
II	Tests of Subsonic Transport Aircraft Intakes
III	Supersonic Air Intake Tests
IV	Transonic and Subsonic Tests of Fighter Plane Air Intakes
V	Special Test Devices
I	Conclusions, Recommendations.

Futhermore, one intake model has been selected and has been tested in different wind tunnels in FRG, France, GB. Comparative results will be discussed.

## 4. CONCLUSIONS

- o Working Group compiled comprehensive information about transport and military aircraft as well as missile intakes
  - design methodology, integration concepts
  - computational tools in advance design as well as for final detailed analysis
  - wind tunnel testing techniques and testing limitations in the speed range subsonic, transonic, supersonic.
- o No information is contained for hypersonic configurations exhibiting real gas effects, however
  - advanced computational tool allow for extensions, if physical model is provided.
- o Validation/calibration of computational tools is extremely difficult due to the limited amount of experimental data.
- o Interference/Interface Air Intake - Engine needs further considerations.

## Discussion

POVINELLI

COMMENT (following the question regarding the use of axisymmetric models for CFD validation)

I would like to mention that although in concept the use of axisymmetric models is sound, any model misalignment or the existence of non-uniformities in the tunnel flow may lead to the development of secondary flows on the model surface. One must, therefore, carefully evaluate these effects.

CAIN

Given the problems associated with the 3D nature of "2D plane flows" in experimental facilities, could you make a comment on whether axisymmetric test cases can truly be regarded as two-dimensional?

AUTHOR'S REPLY

In principal, yes. However, for most test facilities the free stream conditions are not really perfect parallel in disturbed flow. This free stream conditions will also introduce 3-dimensionality into the problem. Furthermore, we have to support interference effects since we have to support the model by either strut or string. Therefore, I do not believe in any real two-dimensional experiment.

STOLLERY

Some comparisons between CFD predictions + Holdens experiments on a compression case have shown that unless the real 3D geometrics is used for the CFD prediction, agreement with experiment is poor.

AUTHOR'S REPLY

I fully agree. Unfortunately, all experiments ment to be 2-D, are 3-D in reality. So, all comparisons should be made on the 3-D basis. But, experimental b.c. are only known at maximum to the 2-D extend.  
Conclusion : new experiments with extensive experimental data for all b.c. are needed badly!

# ETUDES DE PRISES D'AIR POUR LANCEURS AEROBIES HYPERSONIQUES

(Supersonic-Hypersonic inlet Studies  
for Aerospaceplane)

par

C. SANS, P. CHAMPIGNY, P. DUVEAU, et C. GINOVART

Office National d'Etudes et de Recherches Aérospatiales  
Boîte Postale N° 72 - 92322 CHATILLON CEDEX

FRANCE

## RESUME

Les progrès techniques et technologiques ont permis de définir et d'utiliser avec succès des lanceurs de satellites. Pour limiter le coût des lancements, des navettes réutilisables ont ensuite été réalisées. Un nouveau pas sera franchi avec des appareils à décollage et atterrissage horizontal.

Ces appareils, mono ou bi-étage, seront équipés de moteurs nouveaux, capables d'assurer la propulsion dans toutes les phases de vol.

Actuellement, seuls des moteurs combinés paraissent satisfaire à ces exigences. En particulier, le recours à des moteurs aérobies pour des vols atmosphériques semble souhaitable.

D'où la nécessité d'installer des prises d'air ; de leur choix dépendra, en grande partie, la réussite de ces projets. En particulier, le bilan de masse et le coefficient de débit seront des paramètres prépondérants ; la récupération de pression étant de moindre importance car limitée en fait par la tenue mécanique du conduit et donc par son poids.

Dans une première partie, les méthodes de définition envisagées seront présentées. Les principales reposent sur :

- des calculs semi-empiriques qui tiennent compte de l'expérience acquise, des lois d'interaction chocs-couches limites connues, des déversements latéraux et bien sur des pertes par choc ;
- des calculs EULER 2D et surtout 3D dans lequel l'influence du piège à couche limite interne doit être prise en compte ;
- à plus long terme, des calculs basés sur la résolution des équations de NAVIER-STOKES.

Dans la seconde partie, des exemples de dimensionnement de prises d'air seront proposés, en particulier pour des moteurs du type Fusée-stato-fusée.

Pour terminer, les problèmes d'intégration de la nacelle au fuselage seront évoqués. La nature de l'écoulement au droit de la prise d'air étant à prendre en compte dès le début de l'étude afin d'éviter des fonctionnements défectueux ou des traînées externes prohibitives.

## ABSTRACT

Recent improvements in technology have allowed to design rockets to launch satellites. Reusable shuttles were then required to limit launch costs.

A new step will have to be taken towards horizontal take-off and landing aerospaceplanes. These single or two stage vehicles will need new propulsion systems, able to provide enough thrust in the whole flight corridor.

Mixed-propulsion systems seem to be well adapted to this project. During atmospheric flight air-breathing engines will be necessary to improve performances.

Thus inlets will have to be installed. The success of this project will depend upon the choice of the inlets, for which mass estimates and mass flow ratios will be paramount objectives. Pressure recovery seems to be of less importance at high Mach numbers because of structural stresses.

Current design methods will be shown in the first part ; they are based on :

- semi-empirical predictions, using experimental data bases, shock boundary-layer interaction laws, shock and side overflow losses ;
- 2D and 3D EULER codes taking into account the internal bleed effects ;
- and NAVIER STOKES codes for specific problems.

In a second part, some examples of inlet design will be presented for rocket-ramrocket engines.

As a conclusion, problems of inlet integration will be presented. Flow-field in the entry plane of the inlet will have to be taken into account from the very beginning of the studies to avoid limitations and detrimental external drag effects.

## 1 - INTRODUCTION

Depuis plus de 30 ans, des fusées permettent la mise en orbite terrestre de satellites. Leur poids, mais surtout leur nombre est en constante progression et ne semble pas devoir diminuer dans un proche avenir.

Cette évolution et la sophistication toujours plus poussée de ces matériels posent les problèmes des coûts de lancement et de leur récupération éventuelle en cas d'avarie ou en fin d'activités.

C'est pourquoi, nous assistons progressivement à une transformation de moyens de lancement (figure 1), la fusée classique, sans aucune récupération, laissant peu à peu la place à une fusée comportant une navette réutilisable pour laquelle les coûts de lancement sont déjà théoriquement divisés par cinq.

Cette technique, aujourd'hui quasiment maîtrisée, n'est que le premier pas vers un lanceur entièrement autonome et récupérable, susceptible de décoller ou d'atterrir de ou sur les grands aéroports internationaux.

## 2 - GENERALITES

Ce lanceur, cet aéronef, sera-t-il mono ou bi-étage ? Les projets en cours envisagent indifféremment les deux solutions (figure 2). Dans l'immédiat, et dans l'attente d'autres types de propulseurs que ceux envisagés aujourd'hui, ils ont tous recours au mode aérobic pendant une ou plusieurs phases du vol. D'où la nécessité d'installer des prises d'air performantes.

Les moteurs correspondant nécessairement à la combinaison de plusieurs propulseurs élémentaires connus tels que turboréacteur, statoréacteur ou fusée, il est bien évident que selon le concept choisi, la nature et le domaine d'utilisation de la prise d'air seront fondamentalement différents.

En particulier, l'utilisation d'un turboréacteur ou d'une fusée dans la phase de décollage et les nombres de Mach de transition en fin de phase aérobic imposeront des lois de débit et de rendements éminemment variables.

Tout en restant dans des généralités, il est nécessaire à titre d'exemple de citer quelques moteurs types [1] [2] et de préciser, autant que faire se peut, les lois de débits correspondant à la phase aérobic dans chacun des cas (figure 3).

Un des premiers concepts est celui qui associe la fusée et le statoréacteur. Pour ce moteur dit "fusée stato-fusée", le mode aérobic peut démarrer après le passage du transsonique pour fournir une poussée additionnelle au mode fusée et fonctionnera ensuite seul, en combustion subsonique, sur une plage de nombre de Mach pouvant atteindre Mach 6 avant de céder la place au mode fusée pour la mise en orbite. On voit alors que la prise d'air doit capter un tube de courant, dont la section  $A_0$  peut varier dans un rapport de 1 à 5 pour couvrir les besoins du moteur.

Le second moteur combiné envisagé associe le turbofusée, le statoréacteur et la fusée. Depuis le décollage jusqu'à Mach = 2 environ, le turbo assure la poussée, ensuite le turbofusée et le stato fonctionnent conjointement jusqu'aux alentours de Mach 4, puis seul le stato reste allumé jusqu'au mode fusée, cette dernière transition étant au plus tard réalisée à Mach 7.

Dans ce cas, l'optimisation des prises d'air doit être réalisée dans un très large domaine de nombres de Mach. Les performances de celles-ci ayant une influence très prononcée sur celles du turboréacteur.

Le troisième moteur combiné qu'il est nécessaire de citer, car il diffère sensiblement des autres dans le traitement des prises d'air est le fusée-stato-fusée avec un mode de fonctionnement du statoréacteur en combustion supersonique (SCRAMJET).

Après la phase de décollage assurée par la fusée, le stato fonctionne d'abord avec une combustion subsonique, poursuivie aux grands nombres de Mach par une combustion supersonique pour laquelle le ralentissement de l'écoulement par la prise d'air sera limité à des nombres de Mach supersoniques modérés, assurant une bonne combustion. Dans ce cas, la transition terminale vers le mode fusée doit pouvoir être très nettement reportée au-delà de Mach 7, voire Mach 12. Les performances globales seront cependant très sensibles aux efficacités de la prise d'air.

Ces quelques généralités montrent bien que les performances des prises d'air et principalement le coefficient de débit conditionnent en grande partie la faisabilité des projets de lanceurs aérobies et qu'il est nécessaire, au stade de l'avant-projet, de connaître avec suffisamment de précision ces paramètres pour répondre au mieux à la demande des motoristes.

C'est pourquoi, sous l'égide du CNES et en collaboration avec les principaux industriels français SNECMA, SEP, AEROSPATIALE et AMD-BA, l'ONERA cherche à développer des outils qui permettent une meilleure compréhension des écoulements internes et qui puissent fournir les performances escomptées de prises d'air supersoniques.

Ces études se développent autour de trois axes privilégiés qui sont :

- le développement de méthodes semi-empiriques,
- l'adaptation des méthodes numériques,
- les essais en soufflerie.

Les deux premiers points vont être développés avant de montrer leur aboutissement, représenté par le prédimensionnement de quelques concepts de prises d'air associées à un moteur combiné du type fusée-stato-fusée.

Ensuite, quelques problèmes d'intégration du fuseau moteur et donc de la prise d'air seront évoqués.

## **2 - METHODES D'ETUDES DES PRISES D'AIR**

### **2.1 - Méthodes semi-empiriques**

Le but recherché est d'obtenir, le plus rapidement possible et à moindre coût, une estimation suffisamment précise des performances d'une prise d'air géométriquement définie, de manière à permettre l'évaluation de la poussée du propulseur.

Un programme informatique a été développé, sur la base de calculs simples et rapides et l'appui d'une banque de données rassemblant de nombreux essais.

Comme nous allons le voir, ce programme prend en compte :

- les différents chocs issus des rampes de compression,
- le développement des couches limites sur les rampes de compression,
- l'effet de déversement par les flancs, provoqué par la compression de l'écoulement,
- le débit du piège interne en régime supercritique,
- les pertes internes.

#### **2.1.1 - Calcul de l'efficacité maximale**

A partir d'une géométrie donnée, un calcul de couche limite est effectué et permet de définir de nouvelles rampes de compression "engraissées" de l'épaisseur de déplacement  $\delta^*$  de la couche limite.

Ensuite, un calcul classique de chocs obliques (compte tenu éventuellement de leurs intersections et des lignes de glissement associées) est réalisé sur la nouvelle géométrie.

L'efficacité maximale correspond en fait à un régime subcritique pour lequel, le choc interne de recompression se trouve toujours situé dans un plan très voisin de la section droite passant par le bord d'attaque de la carène. Dans ce plan, il est possible de délimiter des zones affectées, ou non selon les cas de calcul, par les ondes de choc issues des rampes de compression (figure 4) et de comptabiliser ainsi l'efficacité théorique due aux chocs obliques et aux différentes portions du choc droit final.

Il reste ensuite à tenir compte des pertes internes. A partir de la base de données disponible à l'ONERA, celles-ci ont été modélisées sous la forme d'un coefficient  $(f)$  fonction uniquement du nombre de Mach infini amont.

Dans ces conditions, l'efficacité maximale de la prise d'air est donnée par une relation de la forme

$$\eta_{02max} = \sum_{j=0}^n \frac{h_j}{H} \left[ \prod_{k=1}^j \left( \frac{p_{ik}}{p_{ik-1}} \right) \right] \left( \frac{p_{1j}}{p_{1j}} \right) \cdot f(M_0)$$

Un exemple de résultat, pour une prise d'air classique à trois rampes de compression externe et une compression interne de  $5^\circ$  dans le plan de la carène est présenté figure 5.

On peut remarquer que l'écart maximal entre les prévisions données par ce calcul et celui qui ne prendrait en compte que les pertes par chocs est divisé par deux.

Il reste toutefois une incertitude liée à la loi de pertes internes qui est un compromis entre différents concepts de prises d'air.

#### **2.1.2 - Calcul du débit moteur maximal**

Les calculs précédents de couche limite, de chocs et de leurs intersections étant effectués, on peut alors calculer un coefficient de débit géométrique en écoulement bidimensionnel ( $\epsilon$  géométrique).

Il faut alors déterminer le débit évacué latéralement (effet tridimensionnel) selon le principe décrit dans [3] et qui a été généralisé à l'ONERA à des prises d'air bidimensionnelles supersoniques avec des rampes de compression à 1, 2 ou 3 dièdres.

La première opération consiste à déterminer les surfaces  $(S_i)$  comprises entre les chocs, le bord d'attaque des flancs, la carène et la ligne théorique qui délimite le tube de courant qui pénètre dans la prise d'air (figure 6).

On suppose alors, que le débit évacué latéralement ( $\epsilon_1$ ) est proportionnel à ces surfaces  $S_i$  et à l'écart de pression  $(p_i - p_o)$  existant sur ces surfaces entre les côtés interne à la prise d'air et externe.

On établit ainsi un coefficient  $G$  :

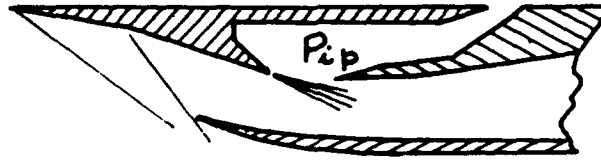
$$G = \frac{1}{A_1} \sum_i S_i \left( \frac{p_i - p_o}{p_o} \right)$$

et alors  $\epsilon_1 = k G$

où  $k$  est déduit d'une corrélation de résultats expérimentaux.

Par ailleurs, le débit du piège interne est calculé en fonction de la pression régnant dans celui-ci ( $p_i$ ) et de sa section de sortie.

La pression  $p_i$  est estimée à partir de la pression derrière les chocs en fin de rampe de compression et de la détente issue du bord de fuite de celle-ci.



Ces débits, retranchés au débit géométrique permettent avec une bonne approximation, l'estimation de celui qui sera disponible pour le moteur.

Un exemple de résultat est présenté figure 7.

## 2.2 - Méthodes numériques

### 2.2.1 - Recherches fondamentales

La prévision des performances des prises d'air nécessite un effort important dans le domaine fondamental, pour développer des modèles théoriques adaptés, conjointement avec les recherches sur le plan purement numérique.

En premier lieu, une compréhension physique approfondie des phénomènes permettra l'établissement des lois à introduire dans les codes numériques. Cette compréhension et la validation des modèles à partir d'expériences est une étape importante nécessaire et préalable à tout développement des méthodes numériques.

Les points les plus délicats de cette modélisation portent sur :

- le développement des couches limites à grands nombres de Reynolds,
- l'influence de la température de paroi,
- les interactions onde de choc/couche limite.

Ce dernier sujet revêt une importance capitale dans la conception des prises d'air, en particulier au travers du comportement de la turbulence au cours de l'interaction.

### 2.2.2 - Codes de calcul

Les codes de calcul existant ou en cours de développement pour d'autres applications nécessitent une adaptation dans le cadre des études de prises d'air.

Actuellement, les définitions de prises d'air peuvent être étayées par les codes de calcul EULER 2D et 3D pour lesquels la prise en compte du piège interne est effective.

Des codes Navier Stokes existent également, mais leur application aux problèmes généraux de la définition des prises d'air au stade de l'avant-projet nécessite encore beaucoup de développement, et ne sera de toute façon envisagée que pour quelques points particuliers.

Les codes de calcul EULER sont donc actuellement les plus utilisés. Parmi les codes disponibles à l'ONERA, celui dénommé FLU3M [8] est le plus adapté à traiter des écoulements supersoniques présentant de fortes discontinuités.

C'est un code multidomaine, qui résout les équations d'EULER 3D instationnaires. Le schéma numérique utilisé est basé sur une discrétisation décentrée de type volumes finis. Pour le calcul des flux numériques, différentes approches sont disponibles : VANLEER, ROE, OSHER, et le second ordre en espace est obtenu au moyen de l'approche MUSCL.

Dans sa version impléte, le code utilise une technique de factorisation de type ADI plan par plan, couplée à une méthode de relaxation GAUSS-SIEDEL dans la troisième direction.

Le traitement des conditions aux limites est réalisé soit par relations de compatibilité soit par calcul des flux.

Dans l'application aux prises d'air supersoniques, le régime de fonctionnement de la prise d'air est fixé par la pression statique en fin de diffuseur et l'écoulement dans le piège est automatiquement calculé en imposant une section de sortie sonique.

Pour des conditions d'utilisation en bidimensionnel (maillage de 25000 points) le temps de calcul est d'environ 1000 secondes sur CRAY 2 pour une convergence atteinte en 5000 itérations.

Un exemple de maillage est présenté sur la figure 8. Il correspond à une prise d'air bidimensionnelle essayée en soufflerie. Cette maquette d'essai comporte de très nombreuses prises de pression qui fournissent les éléments nécessaires à la validation des codes de calcul.

Un tracé des iso-Mach obtenu, pour un fonctionnement en régime supercritique et pour un nombre de Mach infini amont correspondant à l'adaptation ( $M_0 = 2,7$ ) est donné figure 9. Il montre bien la position des chocs dans le conduit interne et le passage du supersonique au subsonique à l'entrée du diffuseur.

Un exemple de comparaison des pressions sur le profil interne de la carène relevées en essai et de celles obtenues par le calcul est présenté sur la figure 10, on peut observer une bonne concordance dans toute la partie amont du profil ou la couche limite n'est pas encore trop développée.

### **3 - DIMENSIONNEMENT DES PRISES D'AIR**

Les méthodes de calcul décrites précédemment rendent de grands services lors de la définition et du dimensionnement des prises d'air ; en particulier elles permettent de connaître avec plus de précision les performances dans tout le domaine, de vol. Cependant, il faut bien reconnaître que ce n'est qu'a posteriori, qu'il est possible de vérifier que la prise d'air déterminée répond bien au problème posé.

Par ailleurs, le choix de sa forme, de sa géométrie, fixe ou variable, du nombre de Mach d'adaptation, etc... ne dépendent pas seulement des performances à réaliser, d'autres critères et non des moindres entrent en jeu, comme par exemple : le poids, les contraintes thermiques et structurales, ou les traînées externes.

Les principes généraux et les différents concepts de prises d'air envisageables pour satisfaire aux besoins des moteurs combinés pour lanceurs aérobie ont été décrits dans la référence [4]. A partir des choix qui ont été proposés, un prédimensionnement de trois types de prises d'air a été réalisé pour un moteur "fusée-stato-fusée".

#### **3.1 - Prise d'air à section de captation fixe**

Une première définition (figure 11) a été établie à partir des résultats d'essais d'une prise d'air adaptée à Mach 2,7, ce qui n'est pas nécessairement le nombre de Mach idéal d'adaptation mais qui a l'avantage de cerner les problèmes relatifs à ce type de prise d'air et de servir de base de comparaison avec une prise d'air du même type adaptée à un nombre de Mach plus élevé.

Pour assurer la mission, et en particulier la poussée nécessaire au moteur, il faut que le débit soit toujours suffisant. Dans le cas d'une adaptation à  $M = 2,7$ , ceci impose un dimensionnement pour le débit le plus élevé (aux environs de Mach 3,5/4,0 pour le moteur choisi en exemple) d'où une section de captation importante. Le débit obtenu à bas nombre de Mach est alors très nettement excédentaire ce qui entraîne une traînée de captation très élevée et la nécessité de mettre en place des trappes de décharge.

Pour limiter ces inconvénients, on peut adapter la prise d'air à un nombre de Mach plus élevé :  $M_a = 4$  par exemple. La loi de débit obtenue ainsi, figure 11, se rapproche de celle nécessaire au moteur, mais en reste toutefois assez éloignée.

Une modification élémentaire, mais pas nécessairement suffisante, consisterait aussi à prolonger vers l'amont les rampes de compression par une plaque plane, à incidence nulle, avec flancs, ceci augmenterait la section de captation à haut Mach en incidence.

En conclusion, ce type de prise d'air, sans aucun artifice, est donc difficilement adaptable à ce genre de mission.

#### **3.2 - Prise d'air à section de captation variable**

Pour mieux répondre aux besoins du moteur, le concept de géométrie variable a alors été envisagé ; la première solution proposée [4] est de faire pivoter l'ensemble rampe de compression-carène autour d'un axe situé dans le piège à couche limite interne (figure 12).

Cette disposition impose la position inversée par rapport au fuselage, c'est-à-dire que la carène serait placée côté fuselage.

Dans ces conditions, en choisissant correctement la section de captation et la longueur de la première rampe (qui présente une déviation nulle sans rotation), la variation du débit et l'augmentation de la compression donc de l'efficacité lorsque le nombre de Mach augmente est assurée par le pivotement de l'ensemble rampes de compression-carène. Pour l'exemple considéré ici, une rotation de  $12^\circ$  est nécessaire pour couvrir la plage des débits demandés.

Cette conception a toutefois un inconvénient qui provient de l'inclinaison de plus en plus forte de la carène et par suite d'une traînée externe importante. De plus, compte tenu de la première rampe, l'ensemble est sensiblement plus long.

#### **3.3 - Prise d'air symétrique à géométrie variable**

Cette dernière conception (figure 13) a l'avantage de supprimer la carène et donc a priori de diminuer la traînée externe. Le fait d'utiliser deux séries de rampes planes, séparées par un premier piège qui absorbe en grande partie les réflexions des chocs, permet de limiter les pertes internes.

Toutefois, des interactions existent avec les flancs comme dans les prises d'air classiques en suradaptation.

La quasi totalité de la compression est interne et des problèmes d'amorçage ou de stabilité de l'écoulement peuvent apparaître (un col à section variable peut pallier cet inconvénient).

Une première série d'essais a déjà été effectuée à l'ONERA (figure 14) dans le domaine  $2 \leq \text{Mach} \leq 5,5$  et les résultats obtenus sont prometteurs.

Ce concept de prise d'air est satisfaisant dans la mesure où celle-ci s'adapte bien aux lois de débit recherchées. Sa longueur est un peu plus importante que dans le cas précédent et son intégration à un ensemble propulsif multi-moteurs plus délicat.

#### 4 - PROBLEMES D'INTEGRATION DU FUSEAU MOTEUR [5]

L'un des aspects et non des moindres, des problèmes rencontrés lors de la définition d'une prise d'air est l'intégration de celle-ci, et donc du fuseau moteur, au fuselage.

Il est bien évident que les définitions précédentes et donc les calculs de performances, ne sont possibles que si l'on a une connaissance suffisamment précise de l'écoulement qui sera capté par la prise d'air.

En particulier, le nombre de Mach, l'incidence, le dérapage éventuel, la hauteur de la couche limite sont des éléments essentiels dont il est nécessaire de tenir compte [6] [7].

De la forme du fuselage, dans sa partie avant, dépendra la hauteur et la nature de la couche limite (figure 15). De nouveau, un compromis sera nécessaire entre les performances intrinsèques de la prise d'air et la traînée externe provoquée par l'étrave qui sépare la prise d'air du fuselage.

La ou les prises d'air occuperont une envergure importante, la figure 16 présente pour  $\text{Mach} = 6$  et  $\alpha = 4^\circ$ , des résultats d'essais pour cinq positions en envergure à partir de la ligne méridienne centrale, les hauteurs de la couche limite varient du simple au double selon que l'on se trouve sur l'axe ou à  $Z/h = 2,4$ ;  $h$  correspondant à la hauteur de la prise d'air ( $h \approx 0,03 L$ ).

#### 5 - CONCLUSION

En conclusion, il est important de rappeler que les performances des moteurs aérobies, dans un domaine de vol très étendu de nombres de Mach (0 à 6 ou 7 et plus dans le cas d'un scramjet) et à des altitudes comprises entre 0 et 30 km, seront pour leur plus grande part, conditionnées par la quantité et la qualité de l'écoulement ingéré par les prises d'air.

De plus, l'étude des prises d'air, avec suffisamment de précision, n'est possible que si l'on connaît l'écoulement au droit du plan de captation et en même temps, les besoins exacts des moteurs.

Ces conditions réalisées, les méthodes de calcul semi-empiriques permettent une approche des performances et de justifier le bien-fondé de la définition géométrique retenue.

Les calculs numériques, s'ils renseignent sur la nature de l'écoulement interne et permettent d'explorer le domaine de vol, ne sont pas encore suffisamment fiables pour juger des performances intrinsèques de chaque concept.

Dans cette optique, des essais en soufflerie restent nécessaire pour recalculer les performances.

#### REFERENCES

- [1] J. CALMON  
L'Aéronautique et l'Astronautique n° 133 - 1988-6
- [2] P. CAZIN  
Activités Françaises sur les avions spatiaux : De Hermès aux véhicules transatmosphériques  
First National Aerospace Plane Conference  
Dayton, July 20-21 St 1989  
ONERA TP n° 1989-91
- [3] I. Mc GREGOR  
Some theoretical parameters relevant to the performance of rectangular air intakes with double-ramp compression surfaces at supersonic speeds  
R.A.E. T.R. 71232 (novembre 1971)
- [4] F. FALEMPIN  
Prises d'air pour lanceurs aérobies  
25eme Colloque d'Aérodynamique Appliquée de l'AAAF  
Talence 12-14 octobre 1988  
ONERA TP n° 1988-153



- [5] M. LECUYER  
Systèmes propulsifs des lanceurs aérobie, aspects généraux de faisabilité et d'intégration au véhicule. Introduction à une étude de caractérisation de l'écoulement à l'intrados d'un lanceur.  
ONERA NT 1/8548 AY (mai 1989).
- [6] C.B. JOHNSON, P.L. LAWING  
Mach 6 Flowfield survey at the engine inlet of a research airplane  
Journal of Aircraft vol 14 n°4, 1977.
- [7] P.L. LAWING, C.B. JOHNSON  
Inlet boundary-layer shapes on four aircraft forebodies at Mach 6  
Journal of Aircraft vol 15 n°1, 1978.
- [8] Ph. GUILLEN, M. BORREL, M. DORMIEUX  
Numerical simulation of perfect fluid flows around complex 3D configurations by a multidomain solver using the MUSCL approach.  
Conference GAMMI/SMIA-IMA sur les méthodes de calcul en mécanique des fluides appliquées à l'Aéronautique - Antibes, mai 1989

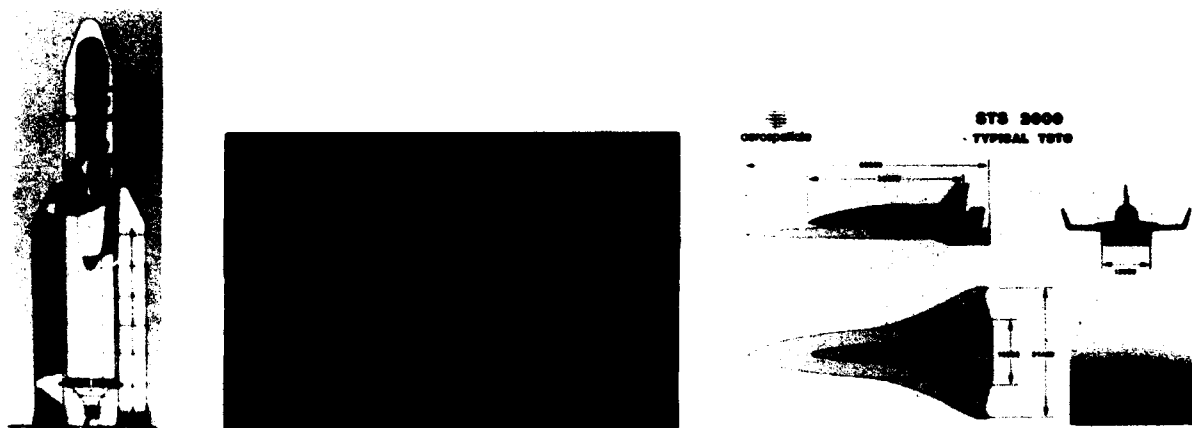


Figure 1 : De la fusée classique ... à la navette .. vers le lanceur

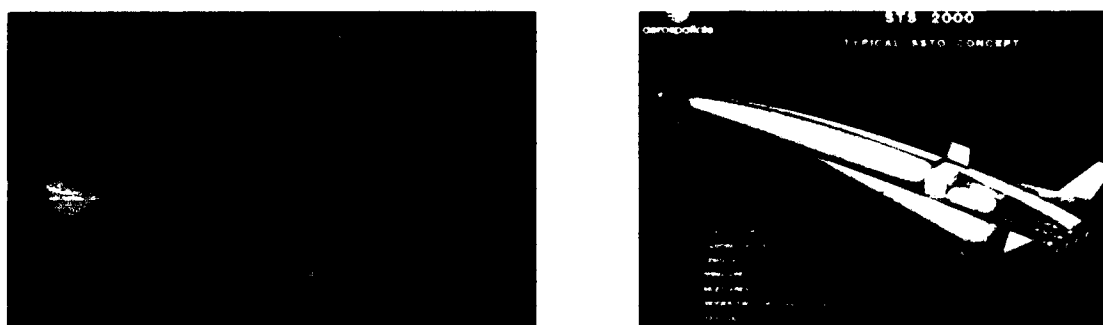
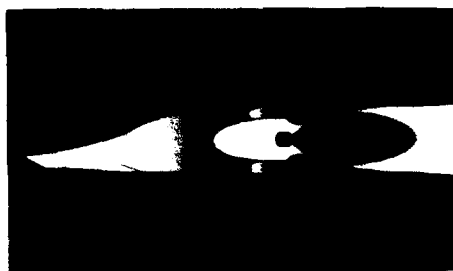
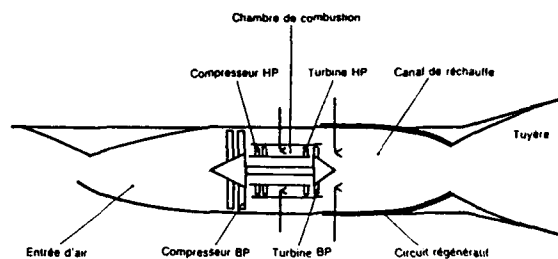


Figure 2 : Lanceurs aérobie : mono ou bi-étage



Fusée - stato-fusée



Turbo soufflante - stato

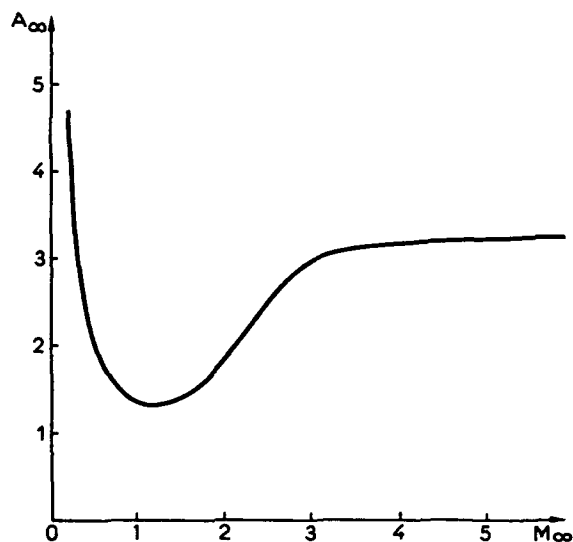
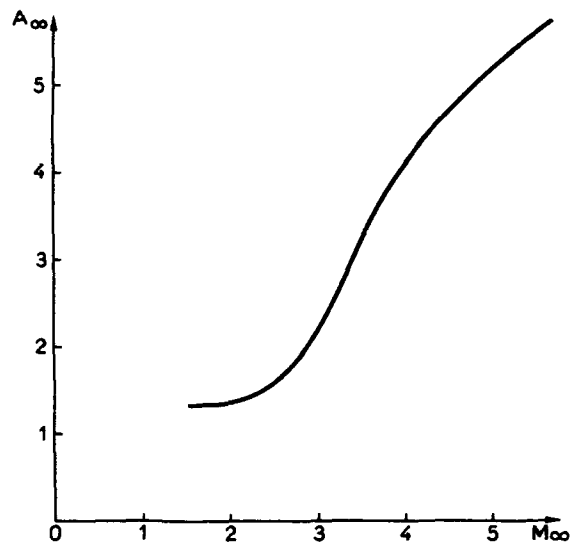
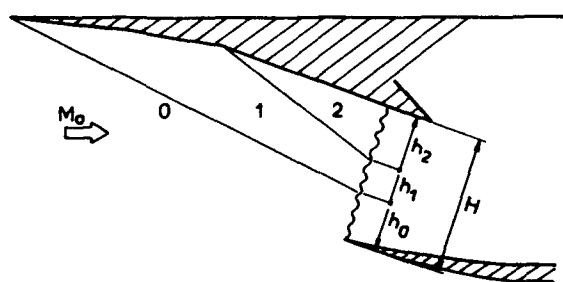


Figure 3 : Moteurs combinés et lois de débit



$$\eta_{02\max} = \sum_{j=0}^n \frac{h_j}{H} \left[ \prod_{k=1}^j \left( \frac{p_{ik}}{p_{i,k-1}} \right) \right] \left( \frac{p'_{lj}}{p_{lj}} \right) \cdot f(M_0)$$

Figure 4 : Calcul de l'efficacité maximale

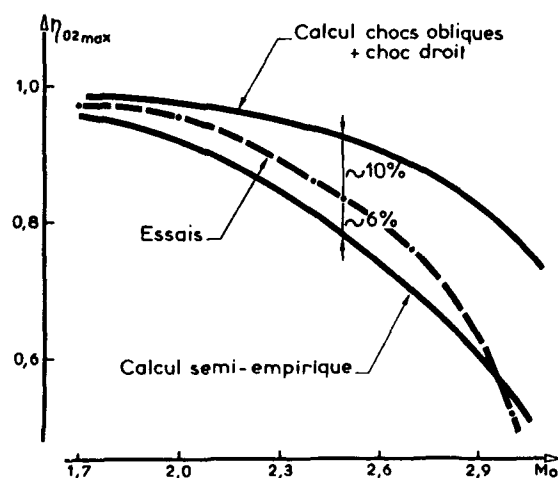
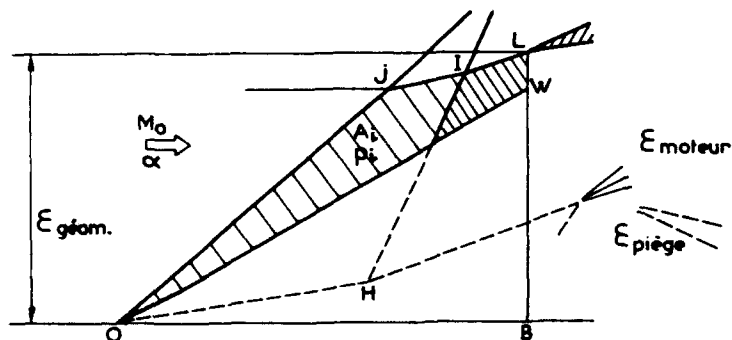


Figure 5 : Exemple de résultat



$$E_m = E_{\text{géom.}} - E_\ell - E_p$$

\*  $E_{\text{géom.}}$  : Chocs obliques

\*  $E_\ell = k \cdot G$

$$\text{où } G = \sum \frac{A_i}{A_1} \frac{p_i - p_0}{p_0}$$

\*  $E_p = \frac{p_{ip} \cdot A_{cp}}{p_{io} \cdot A_{co}} E_{\text{géom.}}$

Figure 6 : Calcul du débit moteur maximal

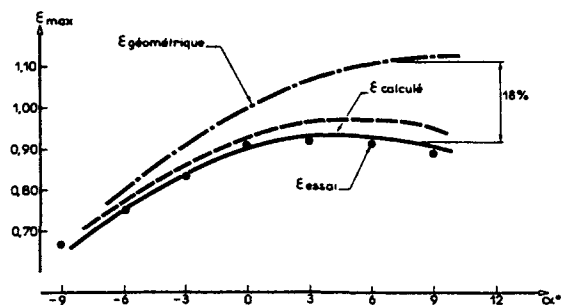


Figure 7 : Exemple de résultat

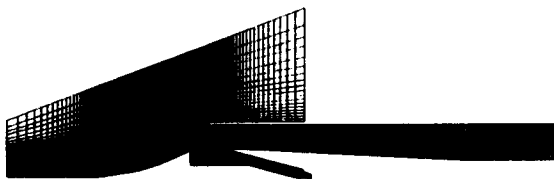


Figure 8 : Code de calcul - Exemple de maillage

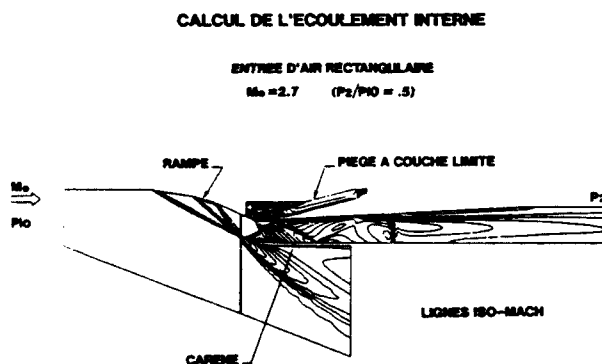


Figure 9 : Code de calcul - Tracé des iso-Mach

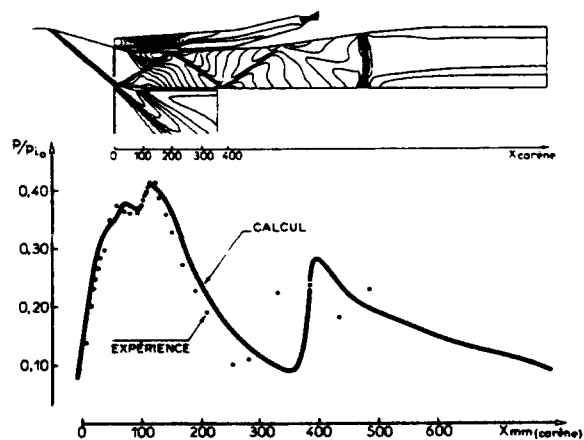


Figure 10 : Comparaisons - Calcul - Expérience

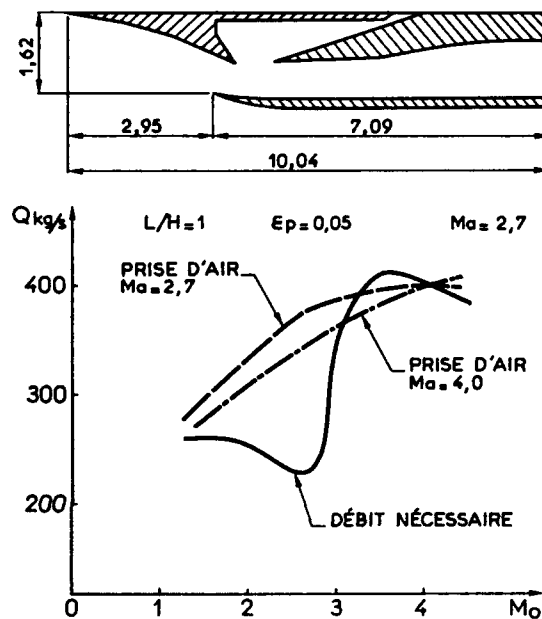


Figure 11 : Définition prise d'air à section de captation fixe

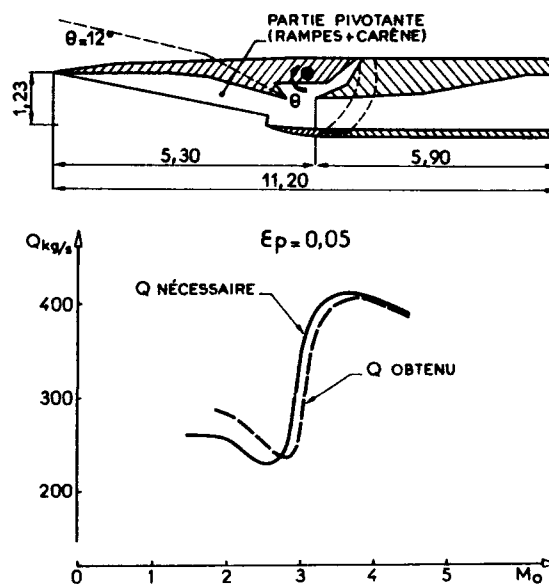


Figure 12 : Définition prise d'air à section de captation variable

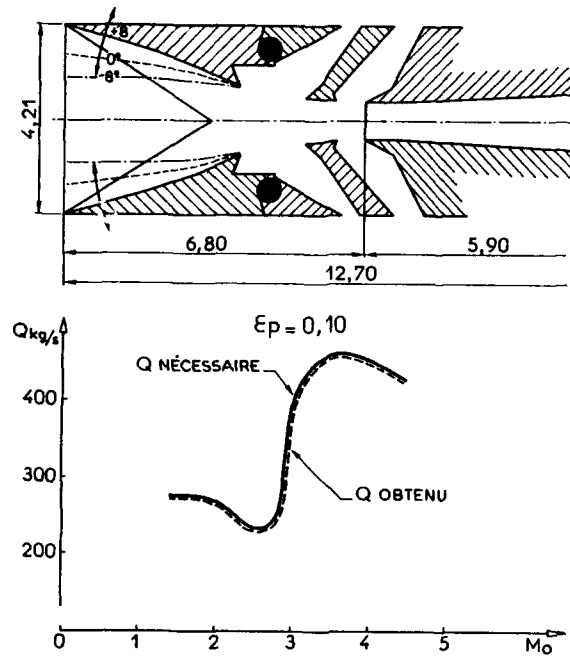


Figure 13 : Définition prise d'air symétrique à géométrie variable

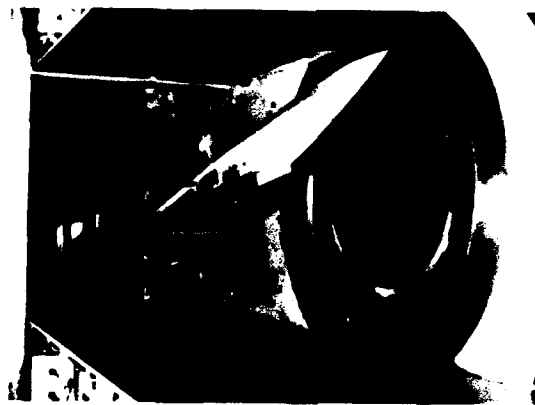


Figure 14 : Montage d'essais de prise d'air symétrique

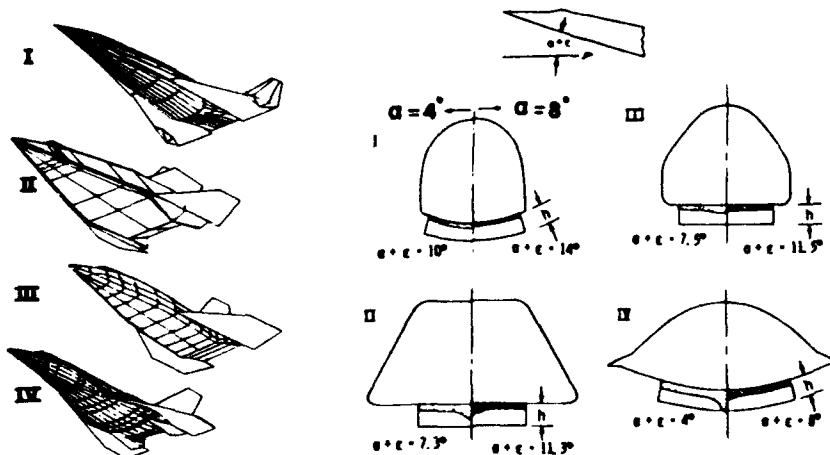


Figure 15 : Hauteur de couches limites en fonction du fuselage

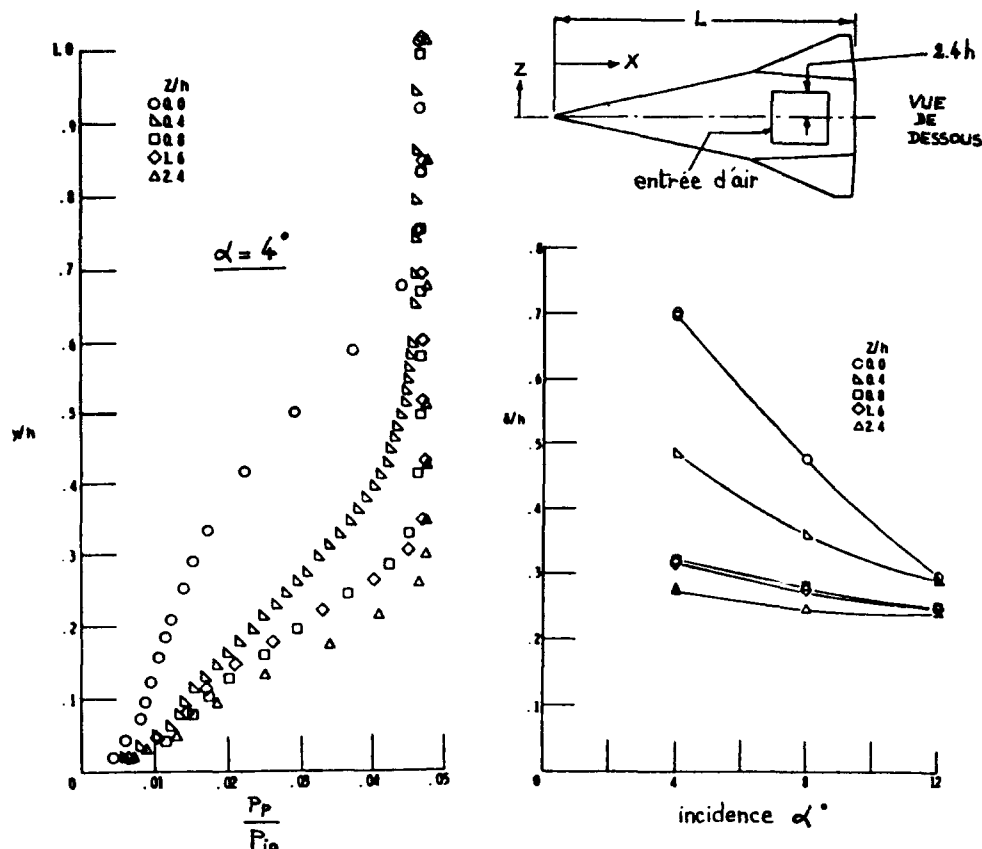


Figure 16 : Couche limite selon l'envergure

## Discussion

SCHMIDT

1) You mentioned that you use Euler Methods. What can be reached with Euler Solutions?

2) What are the real gas effects on internal flows and intake flows?

AUTHOR'S REPLY

1) Dans les cas de calculs avec les codes EULER, les résultats peuvent être considérés comme bons et représentatifs jusqu'au choc de recompression final parce que les interactions sont faibles et parce qu'il n'existe pas de décollement. Dans le cas contraire, il est bien évident que seuls des calculs Navier Stokes sont représentatifs.

2) Les effets de gaz réels n'ont pas une importance fondamentale avant des nombres de Mach voisins de 5 ou 6.

TOWNEND

Your fig. 15 shows the strong connection between cross-section design and boundary layer accumulation along the forebody undersurface centre line. Have you drawn any conclusions with regard to desirable shapes which will avoid complicating the engine designer's problem?

AUTHOR'S REPLY

Avant de procéder au calculs il faut avoir une bonne connaissance de l'écoulement capté par la prise d'air. Il est sûr qu'il faut faire très attention à l'écoulement capté par la prise d'air et la forme du fuselage. Des calculs sont actuellement effectués sur des formes différentes pour essayer de diminuer les épaisseurs de couche limite et d'éviter les problèmes.

# Some ASPECTS OF SHOCK-WAVE BOUNDARY LAYER INTERACTION RELEVANT TO INTAKE FLOWS

By  
J.L. Stollery  
The College of Aeronautics  
Cranfield Institute of Technology  
Cranfield, Bedford MK43 0AL  
England

## SUMMARY

The paper discusses four main topics:

- (i) 'Two dimensional' shock induced separation,
- (ii) Three dimensional glancing interaction,
- (iii) Shock/shock boundary layer interaction, and
- (iv) Hypersonic viscous interaction.

Wherever possible both laminar and turbulent flows are considered and reference is made to experimental data and to the results of mathematical modelling. The paper ends with some thoughts on future research topics and the facilities needed to pursue them.

## LIST OF SYMBOLS

The following symbols are not always defined in the text or in the figures.

C	constant in the viscosity-temperature law $\mu = CT$
$C_f$	skin friction coefficient
D	diameter of leading edge
f	function of, see § 5
h	enthalpy
L	distance to compression corner (see figures)
p	pressure
$\dot{q}$	heat transfer rate
Re ( )	Reynolds number $\equiv \rho_\infty u_\infty ( ) / \mu_\infty$
St	Stanton number $\equiv \dot{q} / \rho_\infty u_\infty (h_r - h_w)$
T	temperature
u	velocity
x )	
y )	Cartesian co-ordinate systems defined in the figures
z )	
$\alpha_i$	wedge angle or compression-corner angle
$\alpha$	value of $\alpha$ for incipient separation
$\delta$	boundary layer thickness ( $y = \delta$ when $u/u_\infty = 0.995$ )
$\delta_L$	value of $\delta$ at $x = L$
$\mu$	viscosity
$\rho$	density

## Suffices

e	value at edge of boundary layer displacement thickness
f.p.	flat plate
o	stagnation point (abbreviation stag. also used)
r	recovery
w	wall
$\infty$	free-stream

## 1. INTRODUCTION

The aerodynamic design of an engine intake for a supersonic or hypersonic vehicle is a very challenging task. Before reaching the combustion zone the airflow has to be slowed down (relative to the aircraft). This can be done very abruptly through a single normal shock wave standing just ahead of a pitot-type intake. Although this has the merit of avoiding shock-wave boundary-layer interaction within the intake, the loss of total pressure makes this simple solution quite unacceptable for flight Mach numbers in excess of  $M_\infty = 1.5$ .

Theoretically shock waves in the intake can also be avoided by the careful design of an isentropic compression surface. In practice the result would be a long, heavy intake, difficult to adjust to varying flight Mach numbers. In reality the intake designers use a number of (mostly oblique) shock waves to compress and decelerate the incoming flow. It is the interactions between these shock waves and the boundary layers growing along the intake walls that can lead to separation and significant modification of the desired flowfield.

Fig.1 shows a mythical hypersonic intake which demonstrates all of the topics discussed here. Quasi two-dimensional interaction occurs at A, B and C and glancing interaction at D and E. In section 2 the conditions for the incipient '2D' separation of both laminar and turbulent boundary layers are reviewed and the effects of separation on the pressure and heat transfer distributions are described.

92-16981

The oblique shock wave BC also interacts with the side-wall boundary layer in the region D, Fig.1. Unfortunately boundary layers are more sensitive to this so-called glancing interaction than to the '2D'-type and the resulting flow is more complex. Section 3 describes such flows and also covers the related types of glancing interaction generated by struts in the intake. These struts may be swept and/or blunt-nosed.

At hypersonic speeds two additional problems may appear. These are shown in Fig.2, namely shock-shock interaction and viscous interaction. The intense heat transfer at sharp leading edges makes some degree of blunting inevitable. If a shock wave from the intake compression surface intersects the bow shock ahead of the blunted intake lip as shown in Fig.2a, a number of complex flows can develop around the lip. These are reviewed in section 4, which draws attention to the high pressures and heat transfer rates that may still occur locally.

The very large shear stresses in hypersonic boundary layers generate high temperatures which reduce the density and so make the layers thick (Fig.2b). The layers can be thick enough to significantly affect the outer flowfield and hence the pressure distribution in which the layer develops. This mutual interference between the external flow field and the boundary layer growth is termed viscous interaction. Unless the way in which the boundary layer modifies the effective shape of the intake is allowed for, the required performance will not be achieved. A simple way of estimating viscous interaction is given in section 5.

## 2. 'TWO-DIMENSIONAL' INTERACTION

No real interaction can be genuinely two-dimensional but the term is used for configurations where there is a substantial spanwise region over which the flow does not change. A configuration relevant to engine intakes is the compression corner (Fig.3) and a considerable amount of data now exists.

### 2.1 Laminar Flow

Typical pressure and heat transfer distributions taken from the work of Needham (Ref.1) at  $M_\infty = 9.7$  are shown in Fig.4. As the turning angle (shock strength) is increased so the pressure rises smoothly until separation occurs. As separation proceeds so the single shock springing from the corner for attached flow is replaced by two shocks from the separation and reattachment regions respectively, with a plateau in the pressure distribution between them. The heat transfer rate distribution differs from the pressure signature in the corner region. One of the characteristics of laminar flow is the local reduction of heat transfer in the corner and separated flow regions.

An important criterion for the intake designer is the angle for incipient separation. A simple dimensional argument at hypersonic speeds (Ref.1) leads to the suggestion that

$$M_\infty^2 \alpha_i^2 = \text{const. } \bar{\chi} = M_\infty^3 (C/Re_L)^{1/2}$$

A correlation of experimental data given in Ref.1 suggests the relation  $M_\infty \alpha_i \approx 1.4 \bar{\chi}^{1/2}$  where  $\alpha_i$  is measured in radians. Although intended for  $M_\infty > 5$  this equation seems to give a rough guide even at supersonic Mach numbers. What is obvious is that supersonic laminar layers are easily separated e.g.  $M_\infty = 3$ ,  $Re_L = 10^6$ ,  $\alpha_i \approx 4^\circ$ . Fortunately in most flight conditions at modest Mach numbers the Reynolds numbers will be high enough for the boundary layer to be turbulent and hence much more resistant to separation.

The mathematical modelling of supersonic laminar flow over a compression corner has been under continual development ever since the 1940's. Simplified analytic methods based on the boundary layer equations gave way to numerical solutions of the integral momentum and energy equations in the 1960's. The explosive growth of computing power, allied to the extensive development of the numerical techniques needed to solve the Navier-Stokes equations for laminar flow, have resulted in powerful and accurate models now being available. The recent paper by Rudy et.al. (Ref.2) shows how attached, incipient and fully separated laminar flows can be calculated. When the real experimental geometry is duplicated the agreement with the measured results is excellent.

### 2.2 Turbulent Flow

The corresponding pressure and heat transfer distributions for turbulent flow over a compression corner are shown in Fig.5. In contrast to laminar flow the heat transfer in the separated region increases and the close similarity in form between the two distributions is obvious. This has led to a number of simple methods of calculating the heat transfer once the pressure distribution is known, (see for example Ref.3 by Coleman and Stollery).

Turbulent flows can turn through much larger angles without separating and a collection of incipient separation data is given in Fig.6a. It is impossible to correlate and explain all the data shown, partly because of the difficulty of defining the incipient separation condition in turbulent flow. Dolling and co-workers (Ref.4) have shown that the flow is unsteady. Hence most measurements of  $\alpha_i$  reflect a mean value and the mean will vary with the technique chosen. Nevertheless a definition of  $\alpha_i$  is useful because at least it gives a value below which the effects of separation are relatively unimportant. Elfstrom (Ref.5) has proposed a separation criterion based on a "slip" Mach number at the wall. Using a particular family of velocity profiles the Mach number profile can be

constructed for any given Reynolds number and wall temperature ratio. Extrapolating the 'linear' part of this profile near the wall down to the surface enables a 'wall Mach number' to be calculated. The incipient separation angle is then defined as the wedge angle needed to detach an inviscid flow at the 'wall Mach number'. This simple method seems to predict the trends with Reynolds number, Mach number and wall temperature as shown in Fig.6. Using his method Elfstrom managed to correlate many of the data shown in Fig.6a. The figure emphasises that even at  $M_\infty = 2$ , turning angles of more than  $10^\circ$  can usually be sustained without separation. At hypersonic speeds  $\alpha_i$  can exceed  $20^\circ$ .

The experimental data measured by Coleman and Stollery (Ref.6) have been used as test cases for the validation of some mathematical models. The Reynolds-averaged compressible Navier-Stokes equations were solved using a variety of turbulence models. Although the results looked promising, at the time of publication (1987) no single model was able to predict all the test cases (Ref.7 and 8).

### 3. GLANCING INTERACTION

In an intake there are likely to be side walls at right angles to the shock generating surfaces. The oblique shocks providing the compression will therefore cut across the side wall boundary layers as shown in Fig.1. Moreover there may be struts or supports in the intake and everywhere there is a strut/wall junction a glancing interaction will result.

#### 3.1 Turbulent Flow

In a glancing interaction the pressure rise across the shock feeds forward through the side-wall boundary layer causing the surface streamlines to deflect well before they reach the shock wave (Fig.7a). For sufficiently strong shocks the side-wall surface-flow lifts off (separates) and rolls up to form a weak vortex as shown in Fig.7b. The separated region interacts with the external flow causing bifurcation of the oblique shock and a complex flow pattern develops in the corner (Fig.7c). Near the reattachment line high pressures and high heat transfer rates are measured.

Experiments have been made with turbulent boundary layers throughout the Mach number range  $1.4 < M_\infty < 11$  though data are sparse for  $M_\infty > 4$ . Most experimenters define the onset of separation using surface oil flow patterns. A comparison between such measurements of incipient separation and the simple criterion due to Korkegi,  $M_\infty \alpha_i = 17^\circ$ , is shown in Fig.8. Note that the measurements at  $M_\infty = 11$  were made in a shock tunnel with insufficient running time for surface oil flow patterns to develop. In this case  $\alpha_i$  was determined from the appearance of a plateau in the streamwise heat transfer distributions and an increase in the fluctuations recorded by the local thin film gauges. It is immediately apparent from a comparison between figures 6 and 8 that the turbulent boundary layer is more susceptible to glancing-interaction than to interaction of a quasi-two-dimensional kind. Thus unless some form of boundary layer control is used it will be difficult to avoid separation from glancing interaction. The only redeeming feature of the flow is that the effects are fairly local and may only affect a small percentage of the mass flow subsequently entering the engine.

There have been a number of mathematical models of the glancing shock interaction generated by a sharp wedge. All simulate steady conditions and confirm the mean features of the flow found experimentally. References can be found in the review by Stollery (Ref.9).

#### 3.2 Laminar Flow

The structure of the flow is very similar for both laminar and turbulent layers but, as expected, laminar layers separate more easily. The amount of laminar data is small but in 1980 the Von Karman Institute in Belgium began a study at  $M_\infty = 2.25$ . Even at a turning angle of  $4^\circ$  the oblique shock wave was strong enough to separate the side wall boundary layer by glancing interaction. In a corresponding numerical experiment Degrez solved the full Navier-Stokes equations. These calculations confirmed the vortical nature of the separated zone and gave good agreement with the measured pressure distributions on the side wall.

#### 3.3 Struts within the Intake

For supersonic inlets there are unlikely to be any struts across the flow but for scramjets the fuel may be added from the base region of wedge-type struts. If these struts have a sharp leading edge then the glancing interaction between the strut-generated oblique-shock and the boundary layer growing along the surface from which the strut is mounted, will be precisely as described above, (sections 3 to 3.2 inclusive). If however the strut is swept, or blunted, or both, then a whole new variety of changes can occur.

Sweeping a sharp edged strut backwards weakens the shock strength at the root so reducing the interaction. But sweep also reduces the Mach number normal to the leading edge so that shock detachment from the leading edge occurs at a lower wedge angle. Usually sweep-back is beneficial and conversely sweep-forward is thought to be detrimental though little experimental data exists.

At high-supersonic speeds and hypersonic speeds some blunting of the leading edge may be essential. A blunt strut generates a curved shock wave standing off from the



leading edge. The interaction of this bow shock wave with the wall boundary layer can generate a rich variety of complex and probably unsteady flows. Figure 9 gives a simplified picture of the mean flow in the strut-wall junction region. Although only two vortices are shown, in practice as many as six have been indicated by surface oil flow patterns. So far as the wall is concerned the maximum pressures and heat transfer rates are recorded near the attachment lines where the flow passing over the vortices returns to the surface, for example the region near the point A in Fig.9.

A more serious problem occurs on the leading edge of the strut. The bow shock causes boundary layer separation which in turn generates an oblique shock springing from the separation line. This oblique shock wave intersects the bow shock and modifies its shape (Fig.9). Immediately below the shock intersection point in the plane of symmetry, the flow is now processed by two (weaker) oblique shock waves instead of by the strong bow shock wave surrounding the rest of the strut. The result is a supersonic stream of high total pressure which impinges on the strut leading edge to give a very localised region of high pressure and very high heat transfer rate (region B, Fig.9). Measurements with turbulent boundary layers at supersonic Mach numbers have indicated local heat transfer rates around three times the stagnation point value. Laminar boundary layers are much more prone to separation so the interaction region for a given strut leading edge diameter is far greater. Laminar flow measurements at  $M_\infty = 14$  along the leading edge of a circular nosed strut reached a peak  $\dot{q}$  of 10 times the stagnation point value, due to the shock/shock interaction described above. This type of flow is also very important near intake lips and will be discussed in greater detail later.

The mathematical modelling of these complex blunt-strut/glancing-interaction flows is improving rapidly. Pictures taken from the work of Hung and Buning (Ref.10) clearly show the vortex formation and match the experimental surface oil flow patterns (Fig.10).

Two ways of reducing the interaction problems are (i) to make the strut leading edge radius as small as possible, (ii) to sweep the leading edge. Figure 11 (from Ref.11) shows the beneficial effect of a small nose radius ( $R_N$ ) but since  $\dot{q}$  is proportional to  $1/\sqrt{R_N}$  there is clearly a limit to the reduction possible. The effects of sweep are very powerful and mostly beneficial. As the blunt edge is swept backwards so the size of the interaction region collapses (Fig.12), the strengths of the vortices are weakened and the pressure and heat transfer rate peaks in the surface distributions are greatly reduced. More importantly the shock/shock interaction pattern is changed and the peak heat transfer rate along the strut leading edge is significantly lowered (Fig.13, taken from Ref.12). The only adverse effect may be due to leading edge contamination. The flow at the leading edge of an unswept strut will be laminar and the maximum heat transfer rate will be the laminar stagnation point value. If the strut is swept and is mounted from a surface over which the boundary layer is turbulent then the turbulent flow in the junction may contaminate the complete leading edge attachment line so significantly increasing the heat transfer rate values. Contamination depends on the radius of the leading edge and the sweep angle, as well as the Mach number and Reynolds number. Poll (Ref.13) has established the conditions under which contamination occurs.

If a straight swept strut spans two surfaces then one junction will have a swept-forward configuration. Intuitively such a junction looks unattractive but there are currently few experimental data on which to base a judgement.

Once again the recent mathematical models of turbulent flow around a swept blunt fin junction show great promise and correctly predict the experimental trends, (Ref.14).

Finally before leaving this section on glancing interaction it is important to emphasise the unsteady nature of many of these flows. Most methods of measurement and flow visualisation record an average or mean property, because they are not fast enough to do anything else. However fast-response pressure transducers and microsecond spark photographs do indicate flow unsteadiness. Turbulent flow is by its very nature unsteady but Dolling (Ref.15) shows that the pressure fluctuations recorded in wind tunnel investigations of the glancing interaction region are greater than those in the oncoming boundary layer. Not surprisingly the unsteadiness effects are larger for blunt struts than for sharp ones. There have not been many studies of laminar glancing interaction but spark photographs suggest that these flows are steady.

#### 4. SHOCK-SHOCK INTERACTION

If the lower lip of an intake has to be rounded to alleviate the heating problem then shock-shock interaction may occur (as shown in Fig.2 and as described in § 3.3). A classic paper by Edney in 1968 (Ref.16) explained this type of interaction and divided the problem into six different classes. He showed that the particular category depended on body geometry, the strength of the impinging shock and its position relative to the body. Figure 14 based on the report by Keyes and Hains (Ref.17) shows the various types of interaction that could arise from an oblique shock wave meeting the bow shock ahead of a cylindrical intake lip. The greatest amplification Factor  $F$  (where  $F = \dot{q}_{\text{peak}}/\dot{q}_{\text{stag}}$ ) occurs for a type IV interaction, where a supersonic jet is created which then impinges on the intake lip. Provided the jet remains laminar it seems that  $F \sim (P_{\text{peak}})^{1/2}$  and so increases with Mach number. If however the supersonic jet becomes transitional or turbulent the peak heat transfer rate is increased still further.

Measurements are difficult because the peak heat transfer rates are very localised and the flow may again be unsteady. The practical importance and the severity of shock/shock interaction was demonstrated as early as 1967 when a strut carrying a ram jet model

below the X-15 burned through during a flight at  $M = 6.7$  and the model tore loose. In Holden's tests (Ref.18), specifically designed to examine the intake lip problem,  $F$  values for a single oblique shock configuration ranged from around 5 for laminar flow and reached more than 20 for turbulent jet conditions.

Of course an intake may have two (or more) wedges to help compress the flow. In Holden's experiments a single wedge of semi-angle  $12.5^\circ$  was replaced by a double wedge system turning the Mach 8 flow through  $7.5$  and then  $5^\circ$  (Fig.15). If the two oblique shocks coalesced just before interacting with the bow shock ahead of the lip, then both the peak pressure and peak heating rate were increased ( $F$  rose from around 20 to nearly 30). However by suitably positioning the lip so that the two oblique shocks were still separated when reaching the lip-bow-shock, the interaction could be spread over a large area. The peak pressure was reduced by a factor of 4 below the single wedge case, whilst  $F$  was reduced from around 20 to 7.

Finally Holden showed that sweeping the cylindrical intake lip  $30^\circ$  reduced the peak heating rate by about 30%, but more tests are really needed. It must be remembered that all the experiments at  $M_\infty = 8$  referred to above, have turbulent impingement conditions onto a laminar stagnation point. If the intake lip is swept there is the danger of turbulent contamination of the attachment line from the lip-root junction. With the jet already turbulent further contamination along the attachment line may be relatively unimportant but if the shock/shock interaction was entirely laminar then contamination by sweeping the lipback, might be very damaging.

As long ago as 1976 Tannehill et.al. (Ref.19) calculated the two-dimensional shock-shock interaction flow field by using a time-dependant, finite difference method to solve the Navier-Stokes equations. Their results at  $M_\infty = 4.6$  looked very promising but no direct comparisons with experiment were possible at that time. Since then numerical results have been sparse.

## 5. VISCOUS INTERACTION

At hypersonic speeds the displacement effect of the boundary layer can be significant, particularly for laminar flow. As an extreme example Fig.16 shows the displacement effect at  $M_\infty = 25$  for a two-wedge intake with each wedge turning the flow through  $10^\circ$ . The difference between the 'real' and inviscid pressure distributions is marked. The boundary layer 'smears out' the pressure rise over much of the second wedge, the only beneficial effect is the reduced heat transfer rate. If the boundary layer is turbulent then the effects of viscous interaction are far less significant but will inevitably modify the pressure distribution (and heat transfer rate) in the neighbourhood of any sudden change of shape.

The analysis used is detailed in Ref.20 but basically the equation set

$$y_e = f_1(\delta^*) \quad (1)$$

$$\delta^* = f_2(p_e) \quad (2)$$

$$p_e = f_3(y_e) \quad (3)$$

has to be solved simultaneously for a given geometric shape,  $y_w(x)$ . The problem can be made accurate (and complex) or approximate (and simple) depending on the choice of  $f_1$ ,  $f_2$  and  $f_3$ . In Ref.20 equation (1) is written as  $y_e = y_w + \delta^*$ , an acceptable approximation at hypersonic speeds. The displacement thickness  $\delta^*$  is expressed as a function of the (as yet unknown) pressure distribution using the momentum integral equation and Eckert's reference enthalpy method. Finally the tangent-wedge rule is used to calculate the pressure distribution assuming that the pressure is constant across the boundary layer ( $p_e = p_w$ ). The heat transfer rate is estimated using Reynolds analogy in its simplest form i.e.  $St = C_f/2$ .

The only difference in the analysis between laminar and turbulent flow lies in the form of equation (2). Expressions for both types of flow and details of the extension from two-dimensional to axi-symmetric flow are given in Ref.20.

Obviously a simple method like this can only give an indication of the main features of viscous interaction. More accurate results can be obtained from programs currently under development which solve the Navier-Stokes equations for supersonic and hypersonic intake flows. For example the application of Navier-Stokes codes to some complex scramjet inlet configurations is described in Ref.21.

## 6. FUTURE RESEARCH AND FACILITIES REQUIRED

This brief outline of just four regions of shock/boundary layer interaction has pinpointed some areas of continued interest to intake designers. The susceptibility of laminar 'two dimensional' flows to separation may limit acceptable wedge angles. Solutions could involve some method of boundary layer control or alternatively transition, since turbulent layers are far more resistant to separation.

Tests already completed show how complex the flows are surrounding glancing interactions. With a sharp-edged-strut the incipient separation angle is far lower than for the corresponding '2D' flow. Once separation has occurred there are doubts concerning the steadiness of the flow. For a blunt-strut, separation is more likely and the degree of flow unsteadiness will increase. The benefits of sweep back are clear but the effects

of sweep forward are unclear. Similarly the utility of fillets does not seem to have attracted much attention.

Few of the experiments on shock/shock interaction have duplicated a '2D' intake geometry so more information is needed, not least to confirm that the flow is steady. Finally the effects of viscous interactions must be considered, if only to ensure that they are small.

Transcending all these detailed questions lie two phenomena which will powerfully influence the whole flow field, namely transition and real gas effects. Facilities have recently become available, and others are being constructed, which more correctly simulate real flight conditions. 'Quiet' tunnels will be able to model atmospheric conditions more closely so that more reliable transition data will be available. Stalker tubes and enhanced shock tunnels will generate flows with significant real gas effects which can be used for direct testing or the validation of CFD codes. Code validation will be crucial because no experimental facility is likely to be able to model completely the real flow in a hypersonic intake.

## 7. REFERENCES

1. Needham, D.A. Laminar separation in hypersonic flow. Ph.D thesis, Imperial College, London University (1965). See also Needham, D.A. and Stollery, J.L. Boundary layer separation in hypersonic flow. AIAA Paper 66-455 (1966).
2. Rudy, D.H., Thomas, J.L., Kumar, A., Gnoffo, F.A. and Chakravarthy, S.R. A validation study of four Navier-Stokes codes for high-speed flows. AIAA Paper 89-1838, (1989).
3. Coleman, G.T. and Stollery, J.L. A correlation between pressure and heat transfer distributions at supersonic and hypersonic speeds. Aeronautical Quarterly, vol.26, November (1975).
4. Dolling, D.S. and Murphy, M.T. Unsteadiness of the separation shock wave in a supersonic compression ramp flowfield. AIAA J. vol.21, no.12, (1983). See also AIAA Papers 90-0377 and 90-0380.
5. Elfstrom, G.M. Turbulent hypersonic flow at a wedge compression corner. J.Fluid Mech. vol.53 part 1, (1972).
6. Coleman, G.T. and Stollery, J.L. Heat transfer in hypersonic turbulent separated flow. I.C. Aero Report 72-05, Imperial College, London (1972). See also J.Fluid Mech. vol.56, part 4, (1972).
7. Horstman, C.C. Prediction of hypersonic shock-wave/turbulent boundary-layer interaction flows. AIAA Paper 87-1367 (1987)
8. Vuong, S.T. and Coakley, T.J. Modelling of turbulence for hypersonic flows with and without separation. AIAA Paper 87-0286 (1987).
9. Stollery, J.L. Glancing shock-boundary layer interactions. Part of a Special Course, "Three-dimensional supersonic and hypersonic flows including separation". AGARD-R-764, (1990).
10. Hung, C.M. and Buning, P.G. Simulation of blunt-fin-induced shock-wave and turbulent boundary-layer interaction. J.Fluid Mech. vol.154, (1985). See also AIAA Paper 84-0457.
11. Fomison, N.R. The effects of bluntness and sweep on glancing shock wave turbulent boundary layer interaction. Ph.D Thesis, Cranfield Institute of Technology, (1986).
12. Hiers, R.S. and Loubsky, W.J. Effects of shock-wave impingement on the heat transfer on a cylindrical leading edge. NASA TN D-3859, (1967).
13. Poll, D.I.A. The development of intermittent turbulence on a swept attachment line including the effects of compressibility. The Aeronautical Quarterly, vol.34, part 1, (1983).
14. McMaster, D.L. and Shang, J.S. A numerical study of three-dimensional separated flows around a sweptback blunt fin. AIAA Paper 88-0125, (1988).
15. Dolling, D.S. Unsteadiness of supersonic and hypersonic shock induced turbulent boundary layer separation. Part of a Special Course, "Three-dimensional supersonic and hypersonic flows including separation". AGARD-R-764, (1990).
16. Edney, B. Anomalous heat transfer and pressure distributions on blunt bodies at hypersonic speeds in the presence of an impinging shock. FFA Report 115, Aeronautical Research Institute of Sweden, (1968).
17. Keyes, J.W. and Hains, F.D. Analytical and experimental studies of shock interference heating in hypersonic flows. NASA TN D-7139, (1973).

18. Holden, M.S. Shock-shock boundary layer interactions. Part of a Special Course, "Three-dimensional supersonic and hypersonic flows including separation". AGARD-R-764, (1990). See also Weiting, A.R. and Holden, M.S. AIAA J. vol.27, no.11, (1989).
19. Tannehill, J.C., Holst, T.L., Rakich, J.F. and Keyes, J.W. Comparison of a two-dimensional shock impingement computation with experiment. AIAA J. vol.14, no.4, (1976).
20. Stollery, J.L. and Bates, L. Turbulent hypersonic viscous interactions. J.Fluid Mech. vol.63, part 1, (1974).
21. Kumar, A. Numerical analysis of flow through scramjet engine inlets. AGARD Conference Proceedings 428 "Aerodynamics of hypersonic lifting vehicles", Bristol, England (1987).
22. Kubota, H. and Stollery, J.L. An experimental study of the interaction between a glancing shock wave and a turbulent boundary layer. J.Fluid Mech. vol.116, (1982).
23. Price, A.E. and Stallings, R.L. Investigation of turbulent separated flows in the vicinity of fin type protuberances at supersonic Mach numbers. NASA TN-D-3804, (1967).
24. Stollery, J.L. and Beyer, U. Hypersonic viscous interaction revisited. Proceedings of the International Conference on Hypersonic Aerodynamics, Manchester, U.K. Published by the Royal Aeronautical Society, London, (1989).

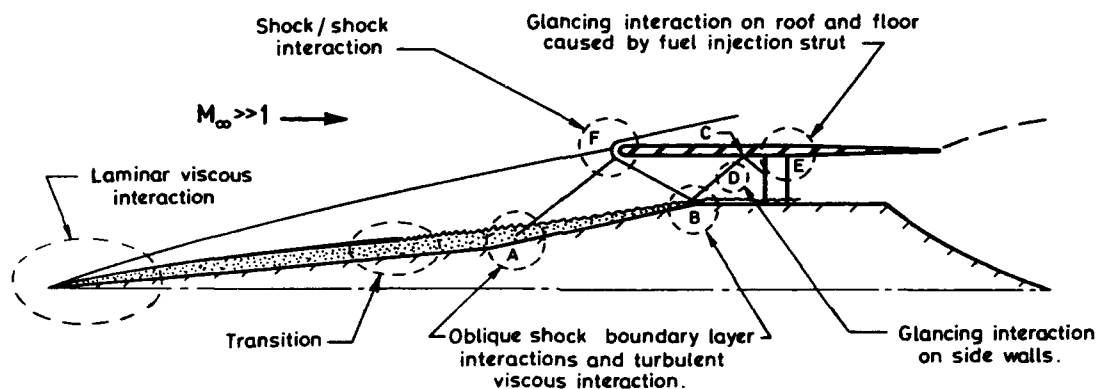


Fig.1. Regions of shock-wave boundary-layer interaction.

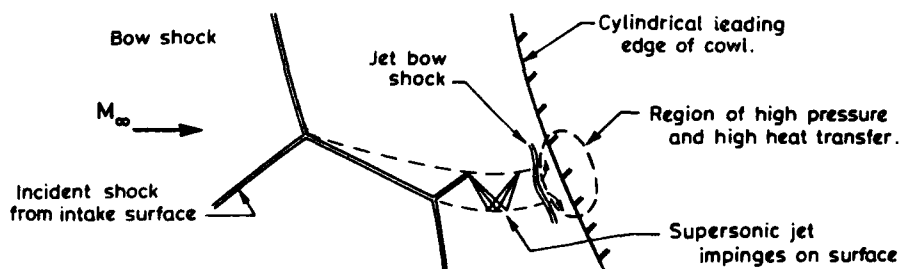


Fig.2a. One type of shock/shock interaction (see also Fig.14).

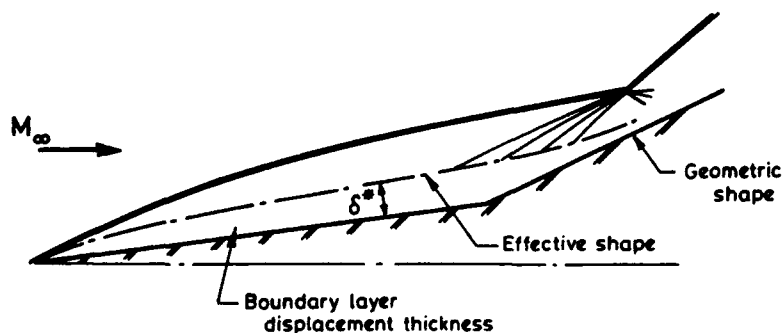


Fig.2b. Viscous interaction.

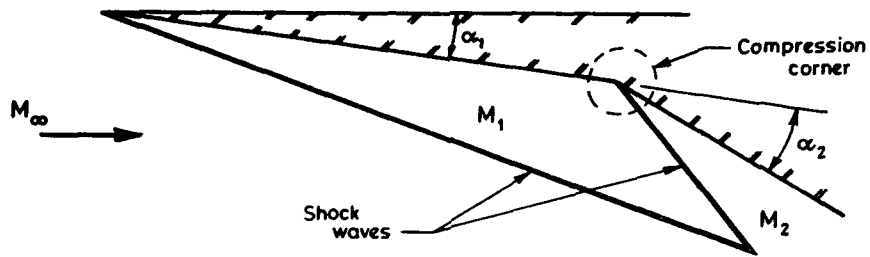
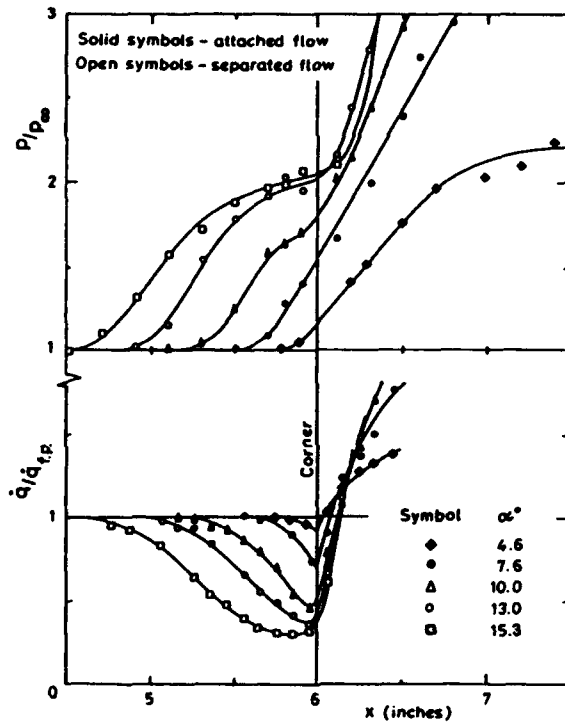
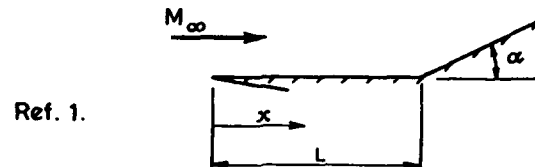


Fig.3. The compression corner region of a double wedge intake.

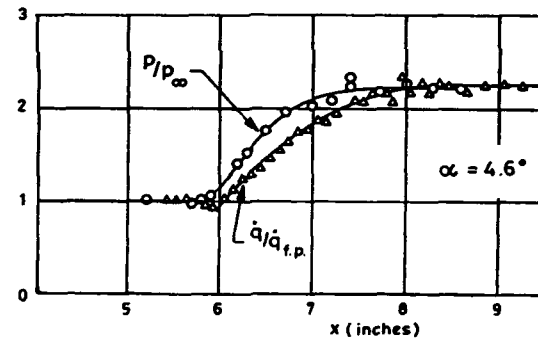


(a) Detailed distributions near the corner.

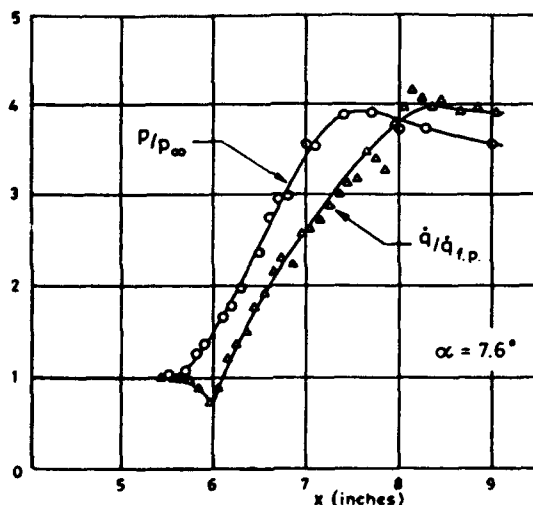
$$M_\infty = 9.7, \quad Re_L = 0.95 \times 10^6, \quad T_w/T_0 = 0.22$$



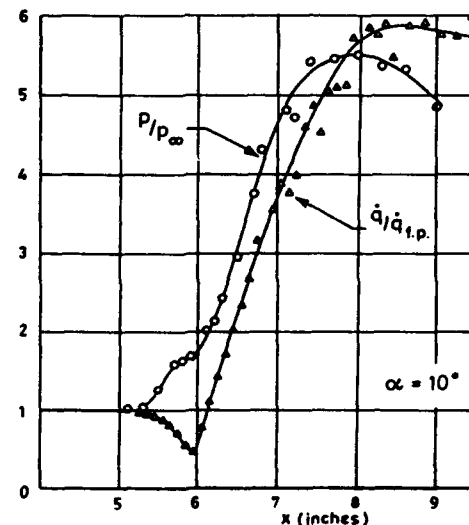
Ref. 1.



(b) Overall distributions, attached flow.

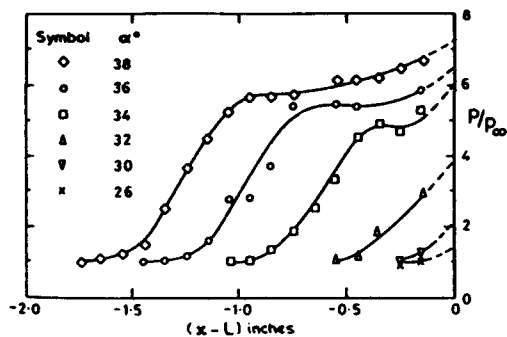


(c) Near incipient separation.

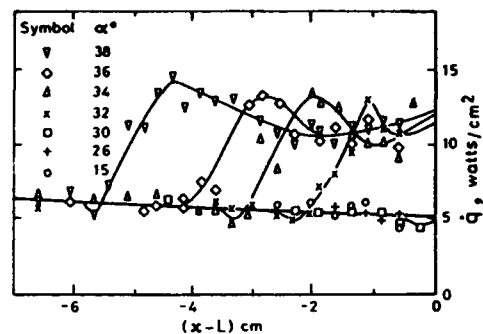


(d) Separated flow.

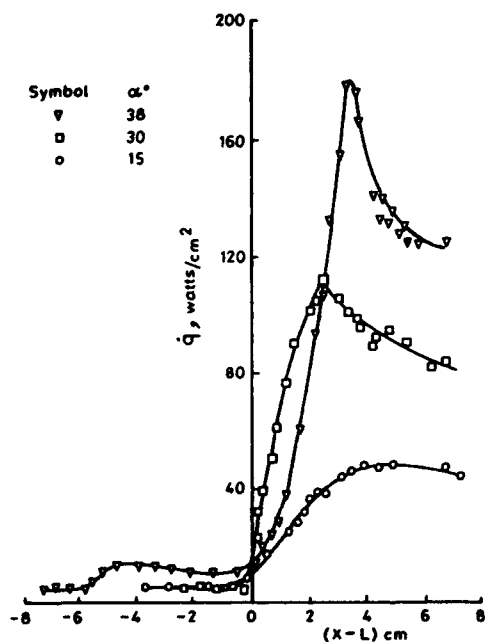
Fig.4. Pressure and heat transfer rate distributions over a compression corner - Laminar flow.



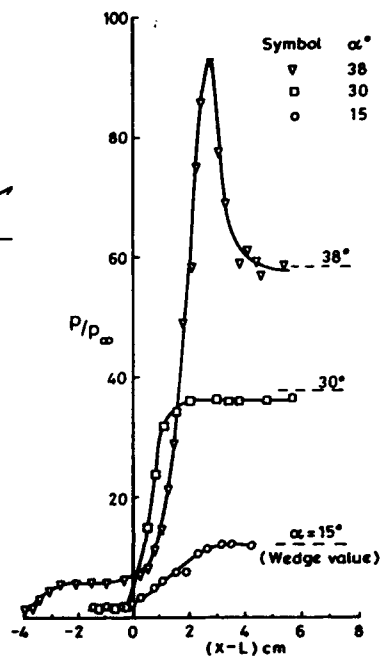
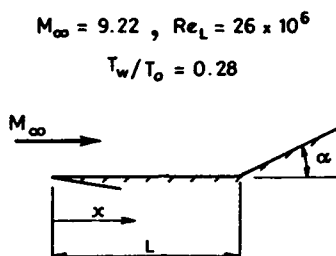
(a) Pressure distribution near the corner.



(b) Heat transfer rates near the corner.

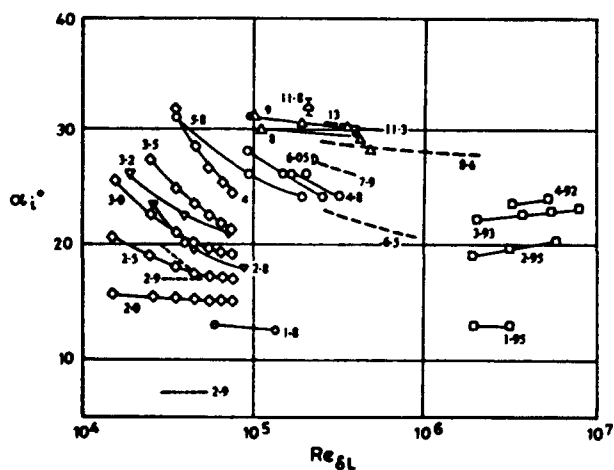


(c) Heat transfer.



(d) Pressure.

Fig.5. Pressure and heat transfer rate distributions over a compression corner - Turbulent flow, (Ref.6).



(a) Data collection, see ref.5.

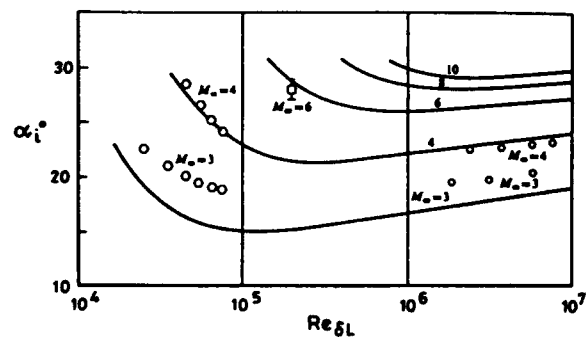
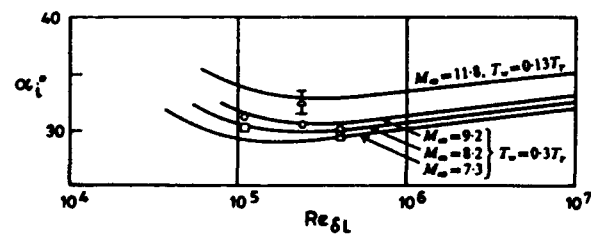
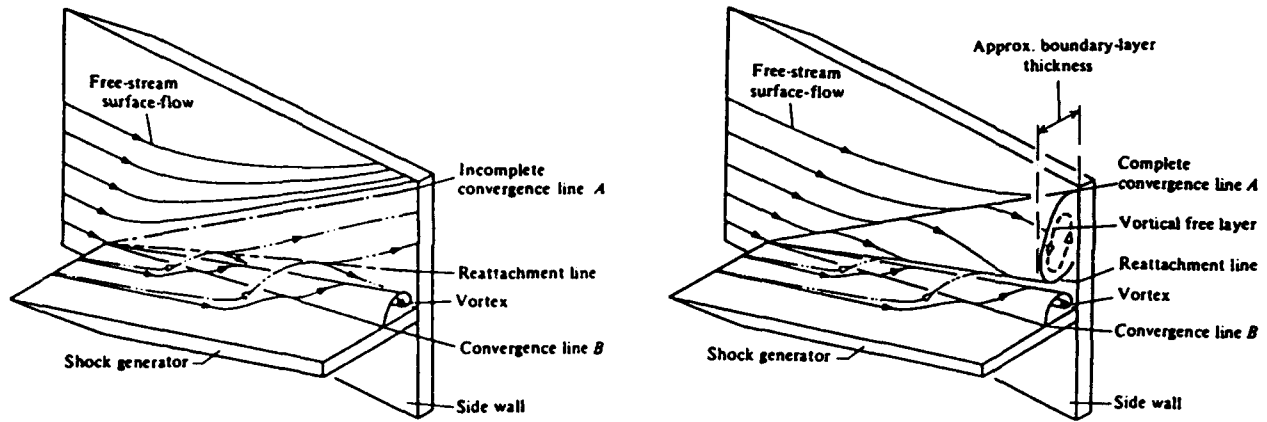
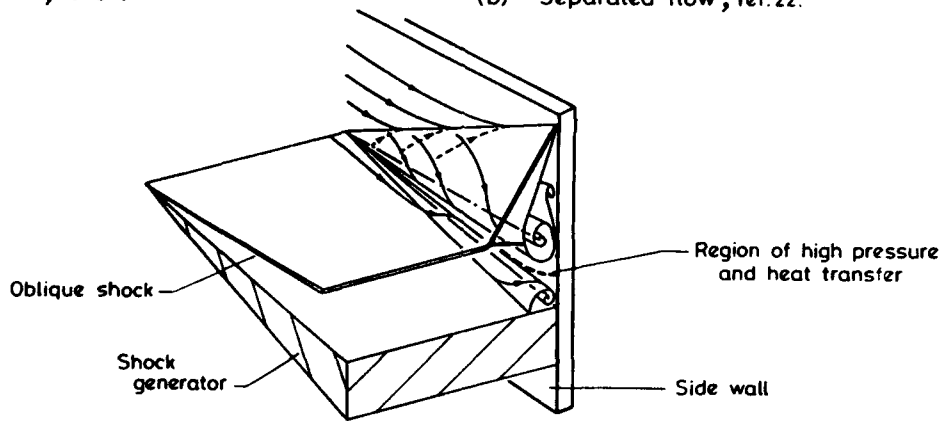
(b) Predicted values of  $\alpha_i$  from ref.5.(c) Predicted values of  $\alpha_i$  from ref.5.

Fig.6. Incipient separation at a compression corner - Turbulent Flow.



(a) Attached flow, ref. 22.

(b) Separated flow, ref. 22.



(c) Sketch of the separated flow field.

Fig. 7. Glancing interaction from a sharp wedge.

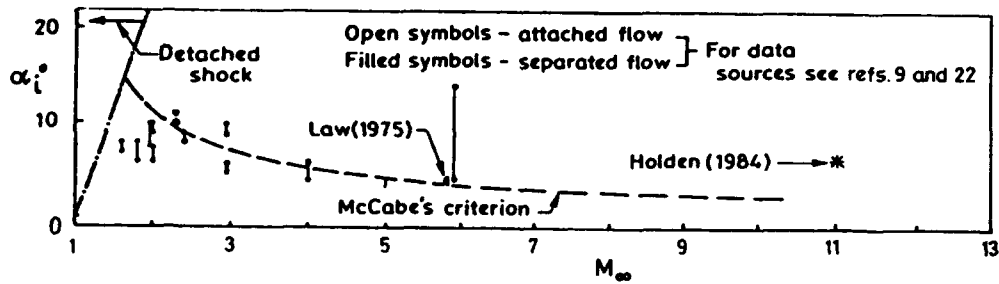


Fig. 8. Incipient separation for glancing interaction - Turbulent Flow.

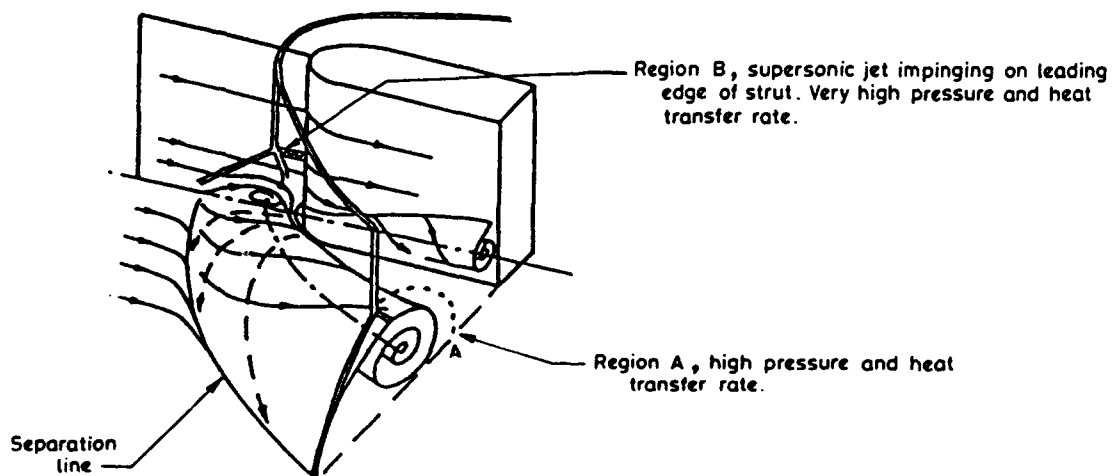
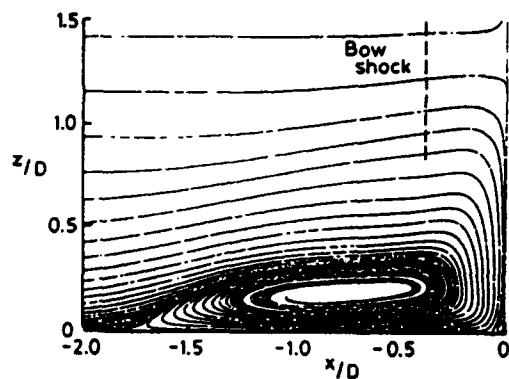
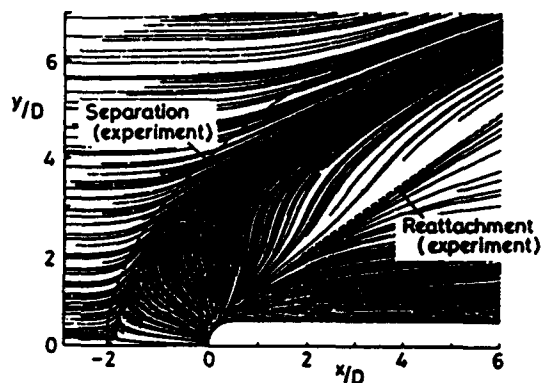


Fig. 9. Glancing interaction from a blunt-nosed strut.



(a) Particle paths in the plane of symmetry



(b) Limiting streamlines on the flat plane.

Fig.10. Calculated flow around a blunt strut, (Ref.10).

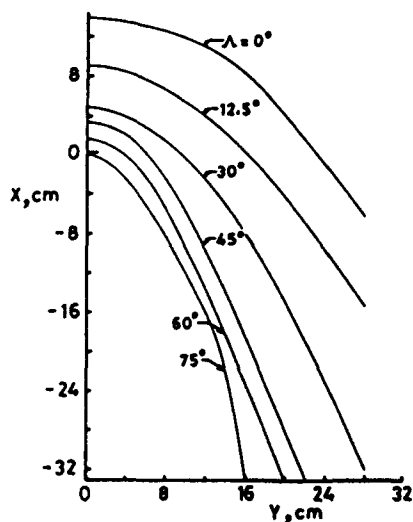


D = 0.375 in = 0.95 cm



D = 1.0 in = 2.54 cm

Fig.11. Effect of leading edge radius on bow-shock/boundary layer interaction, (Ref.11).

Fig.12. Effect of sweep back ( $\Lambda$ ) on the primary separation lines around a blunt strut, ( $D=2\text{in} = 5.1\text{cm}$ , Ref.23).



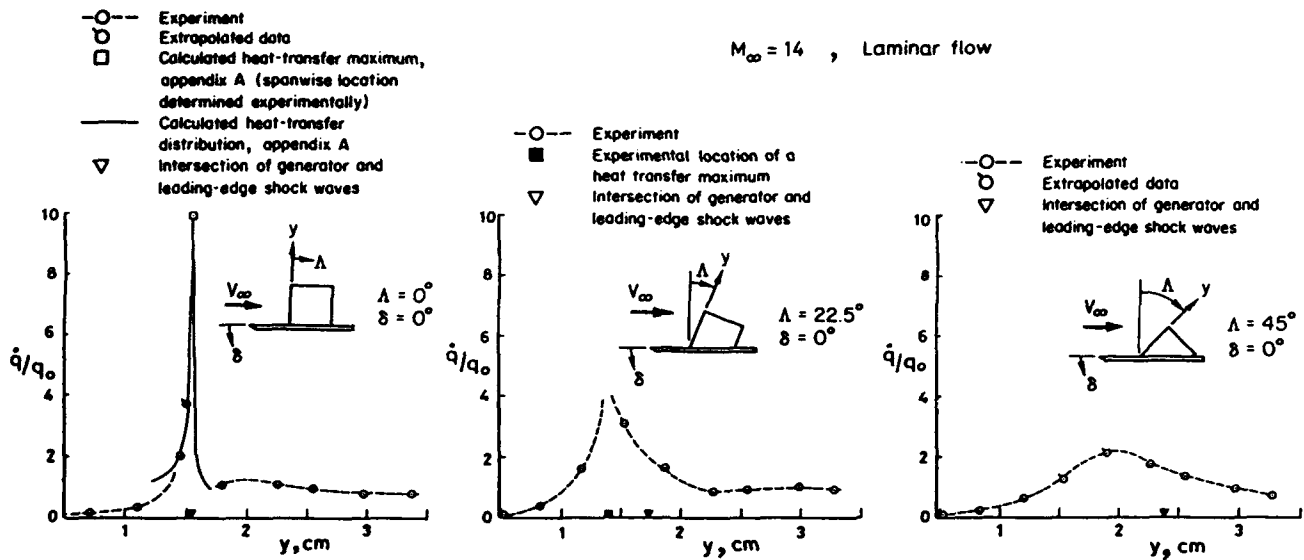


Fig.13. Effect of sweep back on the heat transfer rate distribution along the leading edge of a blunt fin, (Ref.12).

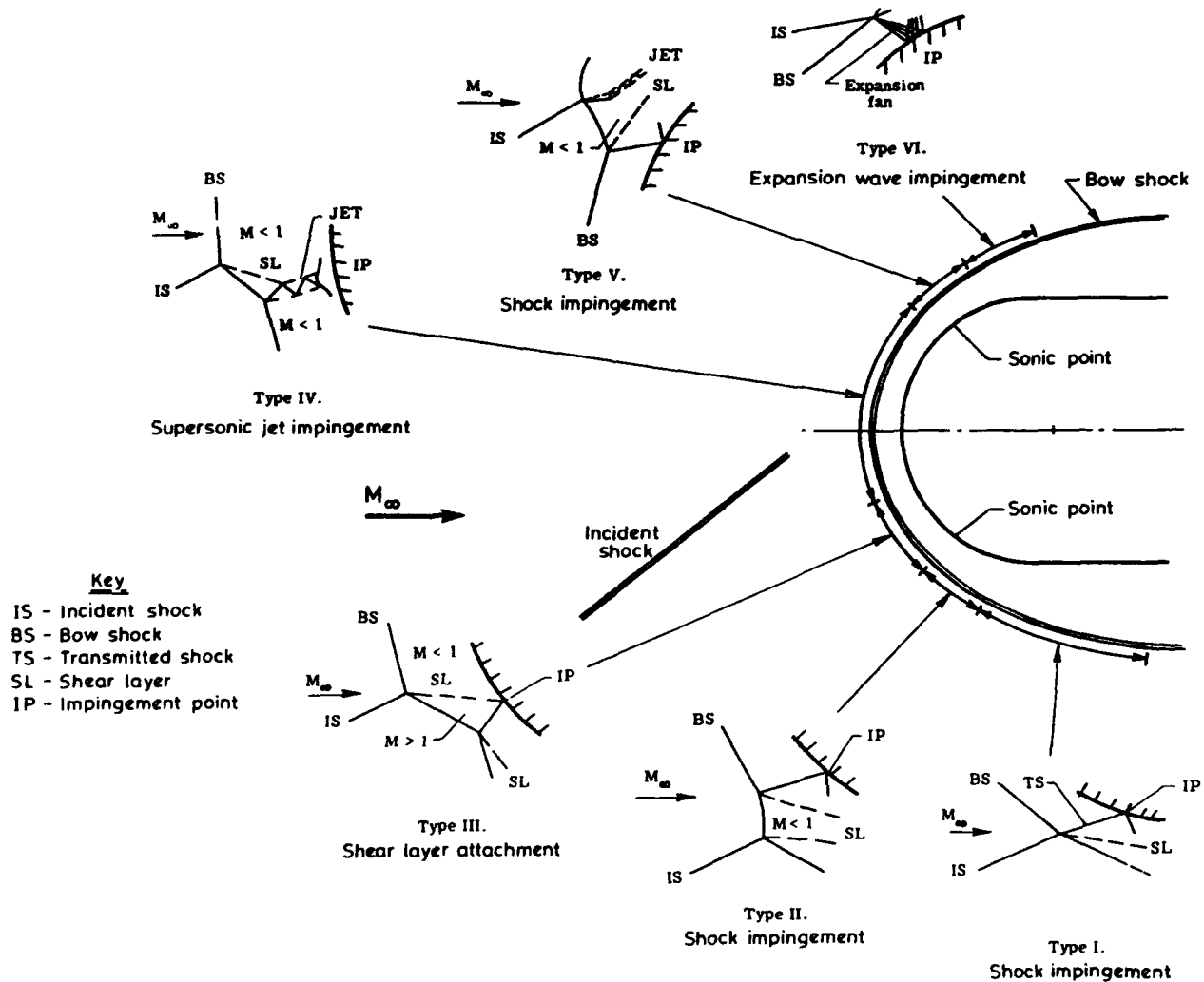


Fig.14. The six classes of shock/shock interaction, (From Ref.17).

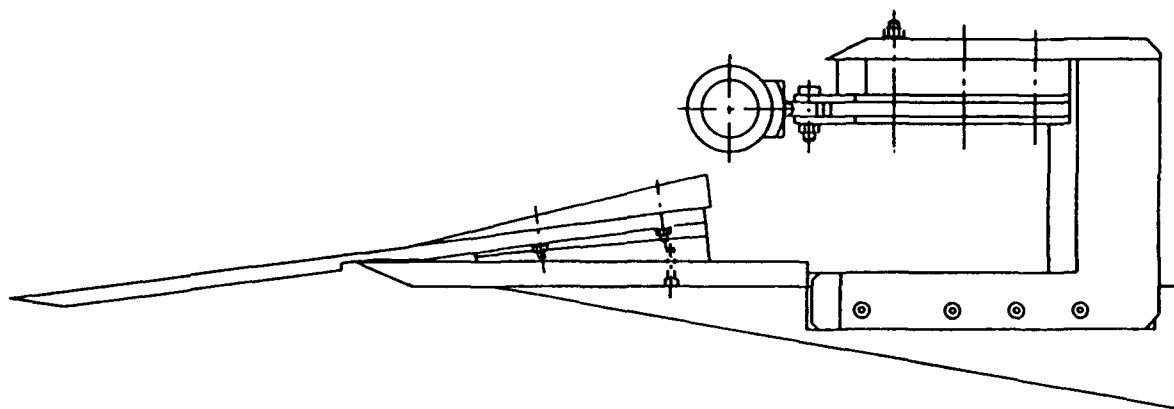


Fig.15. The double-wedge shock interaction model of Holden, (Ref.18).

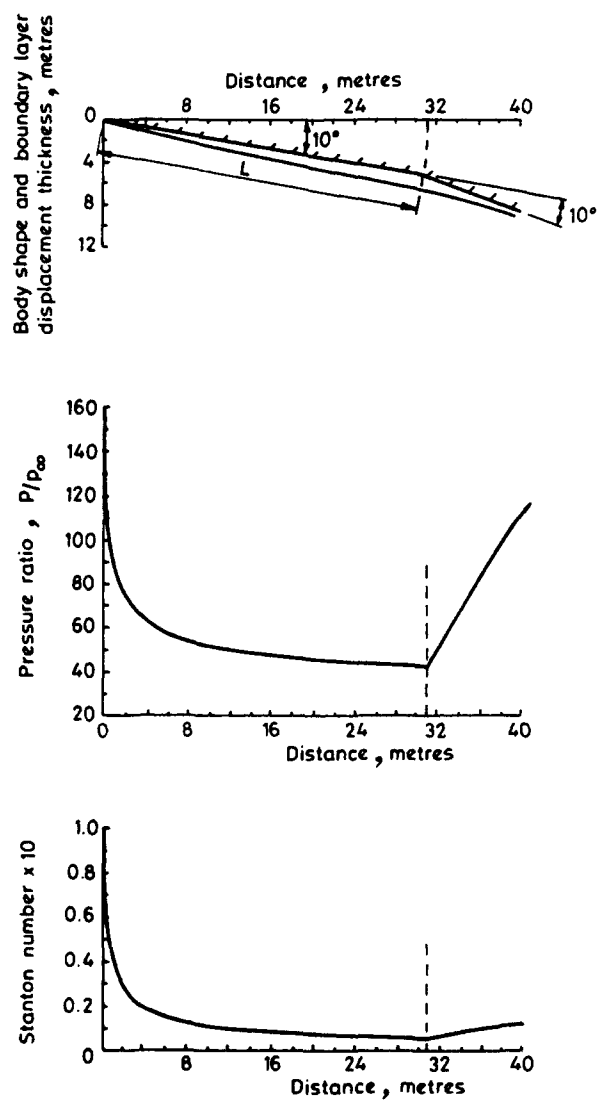


Fig.16. The effects of laminar viscous interaction on a double wedge,  
 $M_\infty = 25$ ,  $Re_L = 10^5$  (Ref.24).

## Discussion

WEYER

You discussed geometric measures to improve the effects of shock - boundary layer or shock - corner flow interaction! What do you think on active boundary layer control to improve the situation and what amount of boundary layer suction e.g. is necessary?

AUTHOR'S REPLY

Active boundary layer control can be effective at a compression corner. Experiments show that slots, suction and blowing can delay separation, but the resulting systems required are complex. My recollection is that when suction is used, a considerable amount of fluid has to be removed.

I do not know of any experiments attempting the active control glancing interaction. Since the area affected by glancing interaction is large, such control might be difficult to achieve.

ONOFRI

What can you say about real gas effects at high flight Mach numbers?

AUTHOR'S REPLY

Up to about Mach 7 real gas effects are small and therefore unlikely to affect the flows described here. Increasingly above mach 7, real gas effects could have to be considered. For example the stand-off distance of bow shock wave ahead of a blunt leading edge will be reduced by real gas effects. Hence the geometry of any shock/shock interaction would be affected.

HOURMOUZIADIS

I was surprised by the trend of the boundary layer thickness in the viscous interaction case. The thickness decreased downstream. This is rather unusual. Was that an attached boundary layer in the forward part of the ramp or was it separated?

AUTHOR'S REPLY

The boundary layer was attached. In the adverse pressure gradient the boundary layer will thin quite fast. You can see that experimentally. It concerns the displacement thickness. The behaviour is different from the low speed behaviour.



## COMPUTATIONAL MODELING AND VALIDATION FOR HYPERSONIC INLETS

Louis A. Povinelli  
National Aeronautics and Space Administration  
Lewis Research Center  
21000 Brookpark Road  
Cleveland, Ohio 44135 U.S.A.

92-16982



## SUMMARY

Hypersonic inlet research activity at NASA is reviewed. The basis for the paper is the experimental tests performed with three inlets: the NASA Lewis Research Center Mach 5, the McDonnell Douglas Mach 12, and the NASA Langley Mach 18. Both three-dimensional PNS and NS codes have been used to compute the flow within the three inlets. Modeling assumptions in the codes involve the turbulence model, the nature of the boundary layer, shock wave-boundary layer interaction, and the flow spilled to the outside of the inlet. Use of the codes in conjunction with the experimental data are helping to develop a clearer understanding of the inlet flow physics and to focus on the modeling improvements required in order to arrive at validated codes.

## INTRODUCTION

This paper presents a review of the hypersonic inlet activities at NASA. Generally, the NASA work has covered the range from Mach 5 to 18. The research has been of a computational and experimental nature with a two-fold objective: (1) to develop an improved understanding of the physics and chemistry of inlet flow fields and (2) to validate the numerical codes used for high-speed inlets. The objectives result from the basic philosophy developed for the National Aerospace Plane project; namely, that numerical codes can be validated using ground test data and extrapolated to higher velocities. Since the ground experimental data base is limited to Mach 8 and lower, extrapolation of the computational methods must be made from Mach 8 to the Mach number, approximately 16, where airbreathing propulsion terminates.

A number of codes have been used to date within NASA for inlet flows. Code development and modifications have taken place over the last several years and the emphasis today is on the application to various inlets that have been tested. Those inlets include the Mach 5 inlet at NASA Lewis Research Center, a General Dynamics Mach 12 configuration and a Mach 18 NASA Langley inlet. Only a limited amount of data is available for each configuration.

The numerical methods used have included a PNS code, the PARC NS code, the SCRAM3D and CFL3D. Generally, the codes employ a Baldwin-Lomax turbulence model. Assumptions are made regarding the state of the boundary layer and spillage has generally not been computed. Thick upstream boundary layers are computed in some cases having a forward extension surface. In this paper a comparison of the experimental and computational results will be reviewed.

## RESULTS

## Mach 12 Generic Inlet

The simple rectangular inlet configuration shown in Fig. 1 was tested at Mach 12.26. A flat plate of 30-in. length preceded the entrance to the inlet in order to simulate the boundary layer growth on the forebody of a hypersonic aircraft. Compression wedges form the top and bottom walls of the inlet and the contraction ratio was equal to 5. Swept sidewalls which connect the upper and lower walls prevent compressed flow from spilling over the inlet sides.

Computations were made with a three-dimensional PNS LBI implicit scheme (Ref. 1) with grids of 80 by 60 by 750 on a Cray X-MP. This solver includes real gas effects (Ref. 2) as well as dissociation and ionization modeling (Ref. 3). For this experiment, however, the inlet air was only heated sufficiently to avoid condensation, and the real gas modeling was not required. The issues that are of importance in this computation are the assumptions regarding the state of the boundary layer, the turbulence model, spillage of flow around the sideplates and shock boundary layer interaction. For the PNS computation it was assumed that the boundary layer was turbulent starting on the leading edge of the flat plate, the cowl leading edge and the sidewall leading edges. The turbulence model used was a Baldwin-Lomax model and spillage was not considered. Modeling of the shock boundary layer interaction involved the use of a flare approximation in order to allow the PNS to march through the region of flow separation. The results of the PNS solution are shown in Fig. 2. Contour plots of constant Mach number within the inlet are shown. The concentration of lines near the walls indicate the boundary layers, while concentrated contours in the freestream indicate shock wave locations. The flow features seen are boundary layer buildup on the flat plate followed by thickening on the sidewalls and ramp surface. Shocks generated by the compression wedges are seen as horizontal lines, and the sidewall shocks are vertical lines.

Basically, the important physics occurring are that the low energy flow in the side-wall boundary layer has been swept up the sidewall by the ramp shock, and then down the sidewall by the cowl shock. Further downstream, the shock waves cross and are distorted by interaction with the sidewall boundary layers and the expansion fan on the ramp surface. Additional complex interactions then occur as the flow moves downstream. The PNS solution fails when the ramp shock wave reflects from the cowl and strikes the ramp surface, resulting in large corner separation of the low energy flow.

An alternate view of the three-dimensional flow is obtained with sidewall particle tracing (Fig. 4). Interaction of the ramp and cowl shocks with the sidewall boundary layer causes the particles to converge near the shock interaction point. The particles are then displaced due to the vortex motion. Flow migration details are evident in this computational simulation. As a sidenote, since the vortex persists downstream, it has been proposed that enhanced fuel mixing could occur with judicious injector locations downstream (Ref. 4).

Navier-Stokes computations have also been carried out for the generic inlet at NASA Langley with CFL3D (Ref. 5). In this case, the boundary layers were assumed turbulent on all surfaces from the leading edges. The turbulence model used was a Baldwin-Lomax model and spillage over the sideplates was not considered. In the vicinity of the shock boundary no special modeling was employed. Figure 5(a) shows the pressure distributions for the ramp and centerline cowl surfaces. Figure 5(b) shows the side plane distributions. Comparison of the CFL3D results and the experimental data show good agreement, particularly along the centerline where shock locations appear to be well resolved by the code. The viscous interactions occurring along the side plane are not accurately resolved. There is a significant underprediction of the pressure on the ramp side (Fig. 5(b)). In addition, CFL3D was used to compute the heat transfer on the ramp and cowl surfaces (Figs. 6(a) and (b)). The experimental peak heat fluxes are underpredicted for the ramp centerline but well predicted for the cowl surface.

For the ramp and cowl side planes (Fig. 6(b)), the peak prediction is lower on the ramp whereas the cowl side prediction is not qualitatively correct. Again, strong viscous effects are predominating along the side walls of the inlet in agreement with the complex behavior shown in Figs. 2 to 4. Further analysis of the Mach 12 inlet is underway at the NASA Centers and industry.

#### Mach 5 Inlet

A rectangular mixed compression inlet designed for Mach 5 operation and tested at NASA Lewis is shown in Figs. 7(a) and (b) (Ref. 6). A series of ramps generate oblique shock waves external to the cowl. An oblique shock from the cowl leading edge reflects from the ramp surface and terminates in a normal shock downstream of the inlet throat. Operation in the wind tunnel was such that a Mach number of 4.1 occurred on the first ramp. The inlet incorporates variable geometry with collapsible ramp and variable bleed exits on the cowl, sidewalls and ramps. Bleed of 0.5 percent was removed on the ramp upstream of the shoulder. Additional bleed from the cowl and sidewalls was approximately 8.8 percent of the capture mass flow. Figure 8 shows the location of pressure rakes and probes in the model. A 0.5-in. strip of grit was applied near the leading edges of the ramp and sidewall to ensure that a fully turbulent boundary layer was ingested by the inlet.

Navier-Stokes computations were carried out using the PARC3D solver (Ref. 7) on the NAS Cray 2. Grid sizes of 151 by 81 by 41 were used with hyperbolic packing so that the first point was at a  $y^+$  of 2. Bleed was simulated by imposing a constant mass flux through the porous bleed surfaces based on the experimental data. The boundary layer was assumed to be turbulent throughout, and the turbulence model was that of Baldwin-Lomax. Flow spillage over the sideplates was also not computed in this case.

The computed ramp pressure results are compared with experimental data in Fig. 9. The agreement of the computations with the data is very good throughout the computed length of the inlet. Figure 10 shows the comparison for the cowl pressure distribution. The disagreement of the results at an  $x/h$  of 4.2 is believed to be due to the fact that one of the translating probe assemblies is located in the same region where the four static pressure taps are located. Because the retracting probe does not completely retract into the wall, additional shocks are generated which biased the data. Pitot pressure profiles were compared with data at various locations along the inlet. Figure 11 shows the pressure profile from rake 3 which was located on the centerline and in the region of the second ramp (Fig. 8). The agreement of data and computation is very good. Along the sidewall, however, the agreement is much poorer, as shown in Fig. 12 for rake 7. The corner effects are not being adequately simulated. An improved turbulence model may improve the comparison in these corner regions. Figure 13 shows the pitot pressure comparison for rake 10 mounted at  $45^\circ$  from the corner of the cowl and sidewall at station 59.6 from the start of the inlet. This region of the flow is dominated by low energy vortical flow as seen in Fig. 14. Large variations in the pitot pressure are seen as one moves from the corner into the stream. Measurements in these regions are also very difficult.

The Mach 5 inlet was also analyzed using the SCRAM3D Navier-Stokes code by Rose (Ref. 8). A Baldwin-Lomax turbulence was used, assuming turbulent boundary layers. These results also reveal strong glancing shock wave-boundary layer interaction leading to large regions of low momentum flow on the sidewalls. Rose carried out a number of numerical experiments to control the vortex phenomena in the corner regions. Figure 16

shows the baseline or no control case, followed by cowl cutback, cowl bleed and removal of a part of the sidewall. These modifications were made near the inlet ramp shoulder. It may be seen that these modifications were ineffective in eliminating the vortex region. Even with the cutback sidewall, the low momentum fluid exists along the entire sidewall. Some attenuation is seen along the cowl surface for that case. It is evident, however, that the shock-boundary layer physics within a rectangular shaped inlet will lead to pressure losses in the corner regions. However, if these regions can be utilized in an "integrated design approach" (Ref. 4), then combustor/nozzle design may benefit substantially. Further computations of the Mach 5 inlet with improved simulation of the bleed zones is underway, as well as further analysis of the test data.

#### Mach 18 Sidewall Compression Inlet

A sidewall compression inlet has been designed and tested at NASA Langley by Trexler. As seen in Fig. 17, the compression occurs on the sideplates. The experiments were run at an entrance Mach number of 18 to 22 with and without a flat plate upstream to simulate fuselage boundary layer buildup. The entering boundary layer was approximately one-third the cowl height. Computations were made by Rose (Ref. 9) using the SCRAM3D code. Laminar boundary layers were assumed on cowl and sidewalls, and a Baldwin-Lomax turbulence model was used.

Figure 18 shows the Mach number contours along the vertical centerplane for an entrance Mach number of 18.1. The contraction ratio was 4 and the cowl leading edge is located at the entrance to the constant area section. All of the convergence occurs along the sidewalls, which generate a pair of shock waves that intersect on the vertical centerplane. A large pressure rise is felt on the ramp surface. Further downstream, the shocks interact with the sidewall boundary layers and reflect and intersect again on the centerplane at the indicated position. A further rise in pressure causes ramp boundary layer separation.

The Mach number contours on the horizontal centerplane are shown in Fig. 19. The intersecting sidewall shocks and the intersecting reflected shocks are visible. Since the sidewall shocks strike the sidewall well upstream of the shoulder, shock cancellation is clearly not achieved. The reflected shock waves, however, are seen to cancel at the shoulder. The strong viscous interaction effects are very evident at these flow conditions.

Calculated Mach number contours are shown in Fig. 20 for both the horizontal and the vertical center planes with an entrance boundary layer. The entrance plate reduces the Mach number from the entrance value to about Mach 12. Separation of the boundary layer on the ramp, caused by the sidewall shock waves, causes a large upstream influence. As the ramp boundary layer thickens, an oblique shock occurs reducing the inlet flow to Mach 8. Sidewall shocks and their intersection are seen in the horizontal centerplane. The sidewall shock wave angle is substantially increased due to the reduced Mach number entering the inlet. The ramp shock falls outside the cowl leading edge. Figure 21 shows a comparison of the experimental and computed surface pressure distributions on the ramp centerline, for the case where the cowl is moved forward. In this particular comparison, the numerical code yields results which are higher than the measured data and also rises faster than measured. Further data analysis and comparisons are underway at the present time, which will lead to a more complete understanding of the flow in this class of inlets.

#### CONCLUSIONS

Through the use of a variety of numerical simulations and experiments, the basic flow features within rectangular hypersonic inlets are becoming better understood. Fast running PNS solvers in combination with much longer running but more sophisticated Navier-Stokes codes are providing a clearer picture of shock structure and boundary layer behavior in inlets. Clearly, the flow fields are highly three-dimensional, viscously dominated and contain significant flow separations. Shock wave-boundary layer interactions persist down to the throat and beyond. As the propulsion community moves towards the validation of these codes, a number of issues still remain which will impede the application of the methods for the design of hypersonic inlets. Perhaps the first concern is that regarding the nature of the boundary layer within the inlet. Although attempts are made to ensure the presence of turbulent layers, for example, questions still remain regarding the existence of transitional layers. Installation of hot film gauges on the walls would provide the numerical analyst with the proper information to use within his computer code; be it laminar, transitional or turbulent. An additional issue is concerned with turbulence modeling and the ability of the Baldwin-Lomax model in regions of glancing shock wave-boundary layer interaction. Current turbulence models appear to yield good qualitative flow characteristics, but may be inadequate for quantitative predictions. Alternate models are needed. A third concern deals with the necessity of including the zone outside of the inlet in order to provide proper boundary conditions for the computation. In spite of these concerns, the understanding and agreement (i.e., on centerline) are very significant. The Mach 5 inlet presents the same concerns but with the complication of bleed flow on all four surfaces. Modeling issues related to turbulence, boundary layer transition and spillage are made more complex with a distributed mass flux boundary condition. Again, it is remarkable that such good agreement, with limited data, was achieved for that inlet. A great deal more effort will be required to analyze the test data and develop the proper modeling for a bulk of the data.

The sidewall compression presents a unique approach to inlet design. Computations of the three-dimensional flow field and associated shock structure provide us with a great deal of physics. The limited data provides a basis for an improvement in current modeling. Use of the experimental data and empirically derived correlations may serve as a basis to produce improved viscous modeling. It is important to point out that in all of these inlet tests, the tunnel flow was sufficiently low to avoid real gas effects. Hence, the comparisons presented in the paper are only aerodynamic in nature. More significant modeling issues will surface as test data is acquired in high-enthalpy flows. Finally, the need to analyze variable geometry with transient disturbances will provide a significant challenge.

#### REFERENCES

1. Reddy, D.R., Smith, G.E., Liou, M.-F., and Benson, T.J., "Three Dimensional Viscous Analysis of a Hypersonic Inlet," AIAA Paper 89-0004, Jan. 1989. (Also, NASA TM-101474, 1989.)
2. Liou, M.-F., "Three Dimensional PNS Solutions of Hypersonic Internal Flows With Equilibrium Chemistry," AIAA Paper 89-0002, Jan. 1989.
3. Yu, S.-T., McBride, B.J., Hsieh, K.-C., and Shuen, J.-S., "Numerical Simulation of Hypersonic Inlet Flows with Equilibrium or Finite Rate Chemistry," AIAA Paper 88-0273, Jan. 1988.
4. Povinelli, L.A., "Advanced Computational Techniques for Hypersonic Propulsion," NASA TM-102005, 1989. Presented at the Ninth International Symposium on Air Breathing Engines, Athens, Greece, Sept. 4-9, 1989.
5. Diley, A., Eppard, W., and Switzer, G., "Zonal Analysis of Two High Speed Inlets," Presented at the CFD Symposium on Aeropropulsion, NASA Lewis Research Center, Cleveland, OH, April 24-26, 1990.
6. Weir, L.J., Reddy, D.R., and Rupp, G.D., "Mach 5 Inlet CFD and Experimental Results," AIAA Paper 89-2355, July 1989.
7. Reddy, D.R., Benson, T.J., and Weir, L.J., "Comparison of 3-D Viscous Flow Computations of Mach 5 Inlet with Experimental Data," AIAA Paper 90-0600, Jan. 1990.
8. Rose, W.C., and Perkins, E.W., "Innovative Boundary Layer Control Methods in High Speed Inlet Systems-Final Report," Contract NAS3-25408, Sept. 9, 1988 (NASA CR in publication).
9. Rose, W.C., Perkins, E.W., and Benze, D.P., NASA Ames Research Review, Dec. 1989.

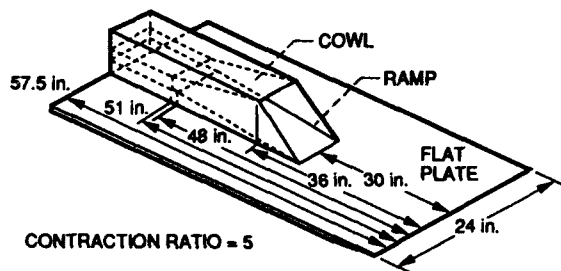


Figure 1. - Generic inlet (ref. 5).

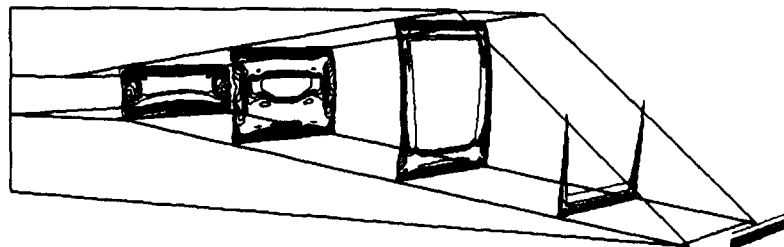


Figure 2. - Mach number contours,  $M = 12.25$  (ref. 1).

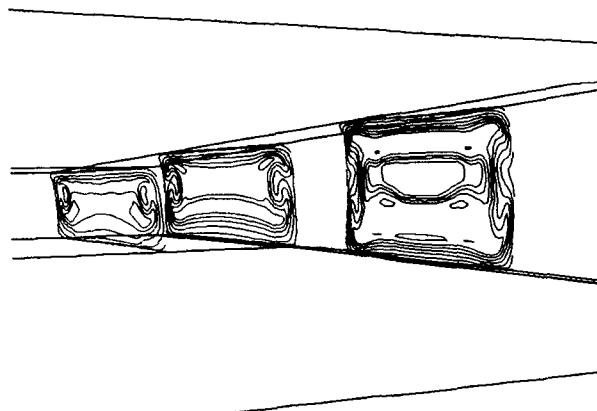


Figure 3. - Mach number contours viewed from aft (ref. 1).

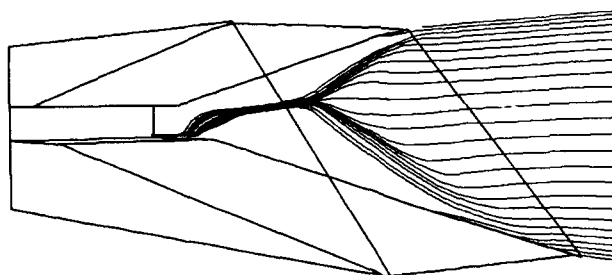
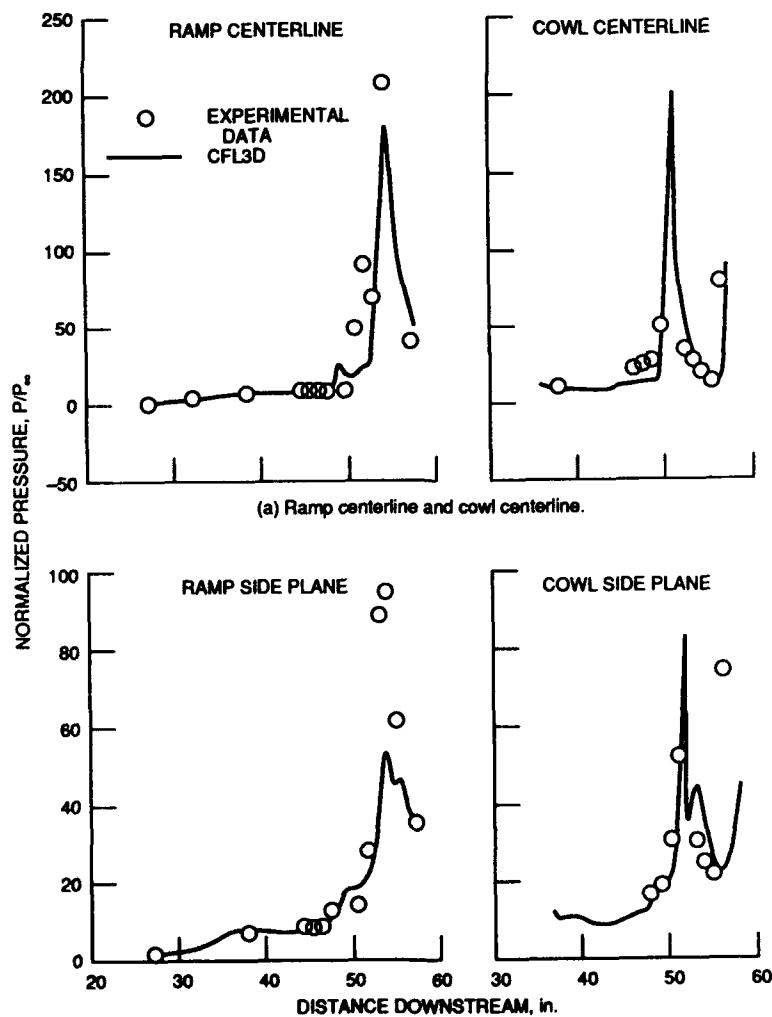


Figure 4. - Sidewall particle tracing,  $M = 12.25$  (ref. 1).

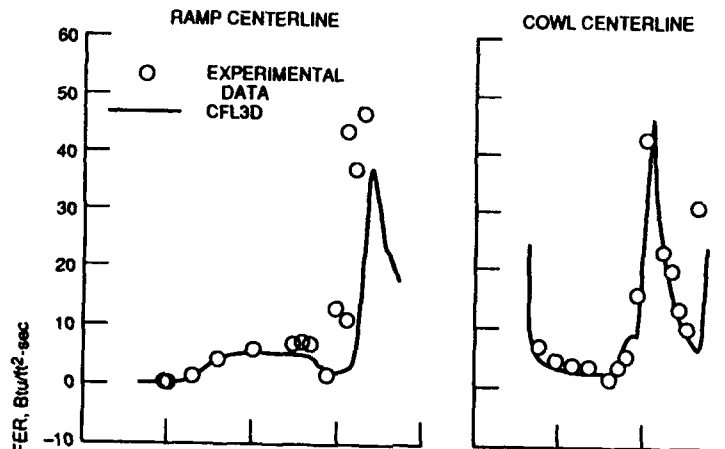


(a) Ramp centerline and cowl centerline.

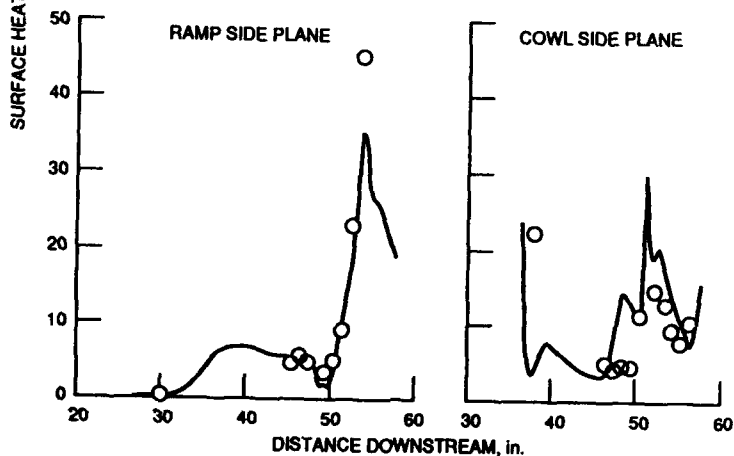
(b) Ramp side plane and cowl side plane.

Figure 5. - Pressure comparisons (ref. 5).



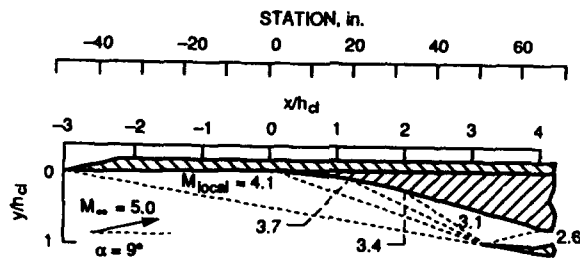


(a) Ramp centerline and cowl centerline.

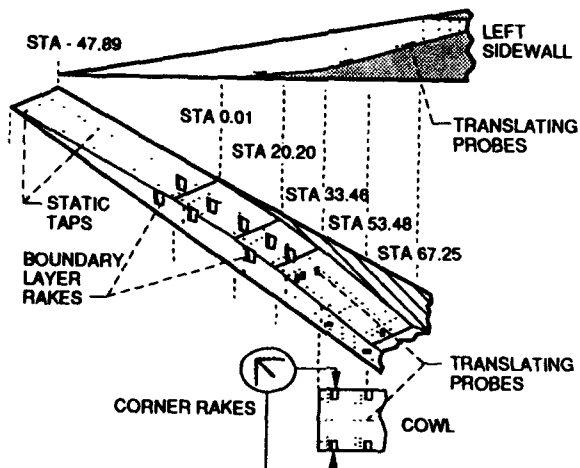


(b) Ramp side plane and cowl side plane.

Figure 6. - Heat transfer comparisons (ref. 5).



(a) Inlet compression system to ramp shoulder.



(b) Instrumentation upstream of inlet shoulder.

Figure 7. - (ref. 6).

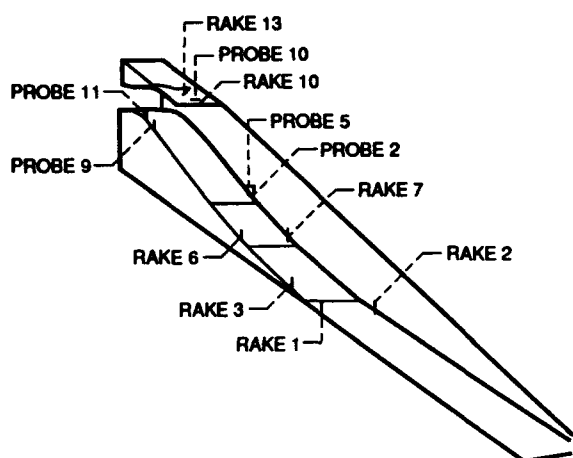


Figure 8. - Location of fixed rakes and translating probes used for pitot pressure measurement (ref. 7).

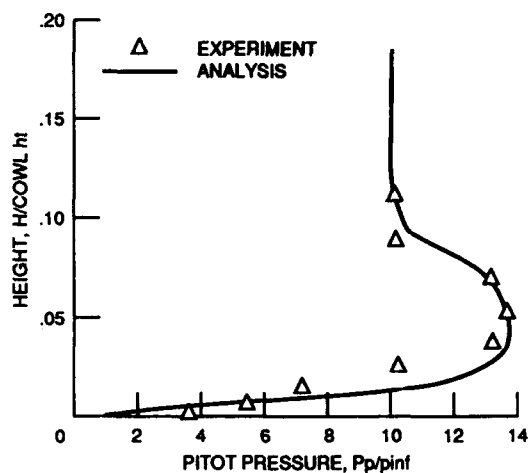


Figure 11. - Rake 3 pitot pressure profile (ref. 7).

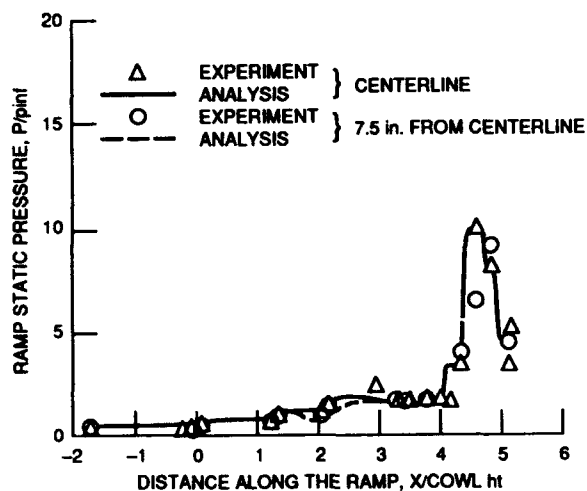


Figure 9. - Ramp static pressure distribution (ref. 7).

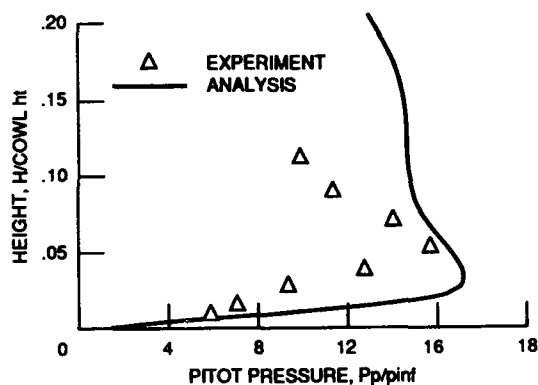


Figure 12. - Rake 7 pitot pressure profile (ref. 7).

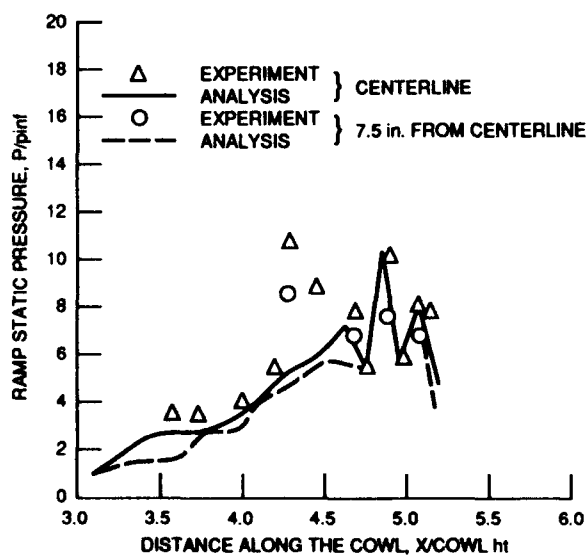


Figure 10. - Cowl static pressure distribution (ref. 7).

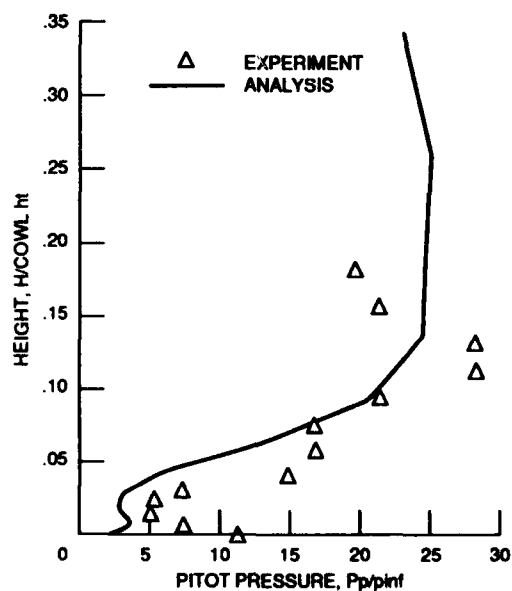


Figure 13. - Rake 10 pitot pressure profile (ref. 7).

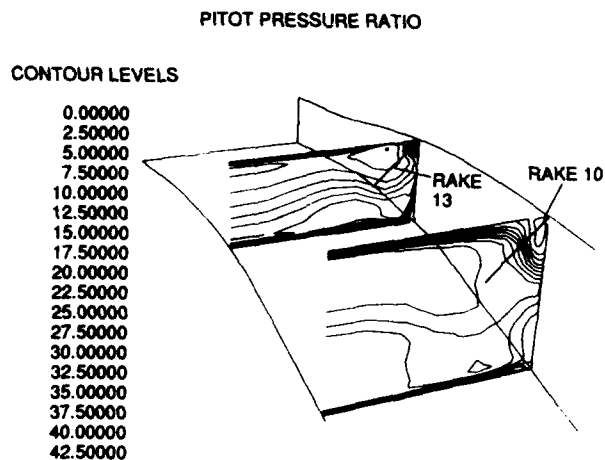


FIGURE 14. - Pitot pressure contour at rake 10 and rake 13 (ref. 7).

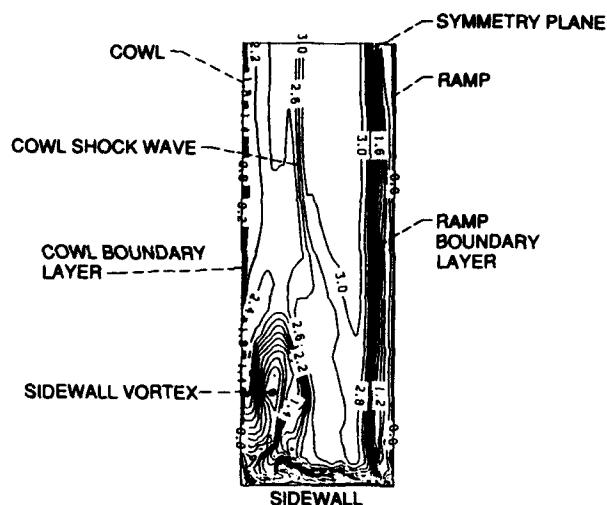


Figure 15. - Orientation of crossflow plane 150 located near the ramp shoulder showing plane of symmetry, sidewall ramp and cowl surfaces (ref. 8).

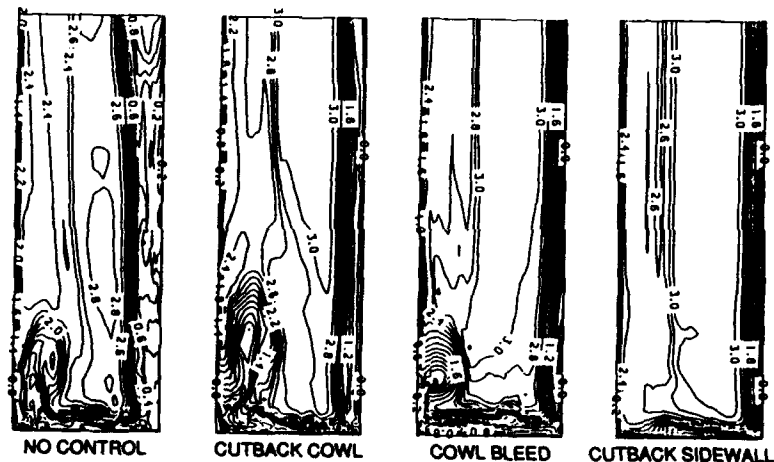


Figure 16. - Comparison of effect of various control methods on mach number contours near ramp shoulder (ref. 8).

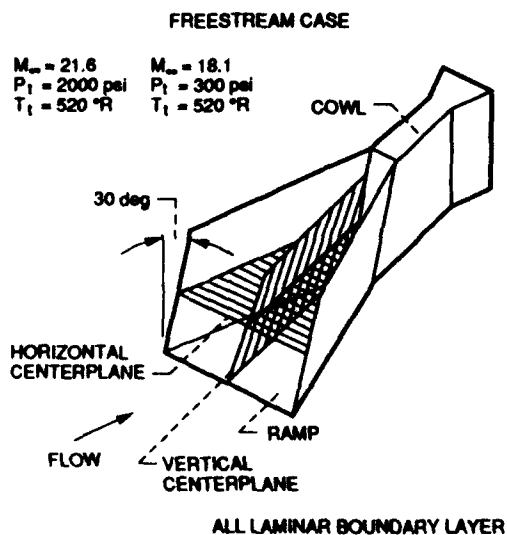


Figure 17. - Sidewall compression inlet schematic (ref. 9).

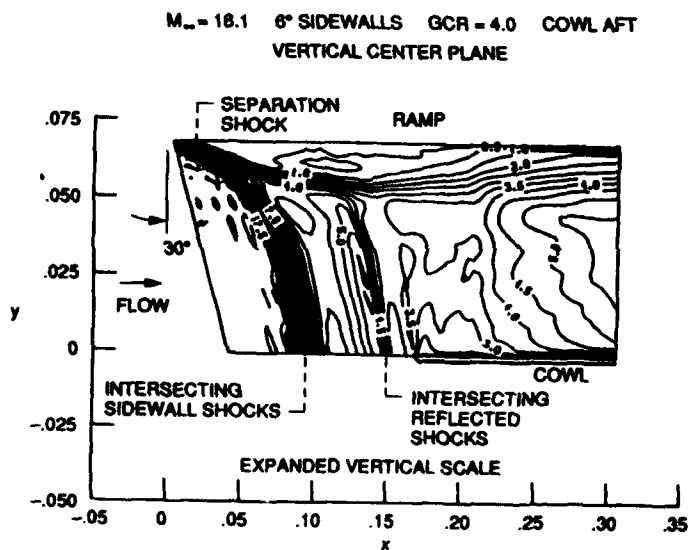


Figure 18. - Mach number contours for freestream case (ref. 9).

$M_\infty = 18.1$  6° SIDEWALLS GCR = 4.0 COWL AFT

HORIZONTAL CENTER PLANE

EXPANDED LATERAL SCALE

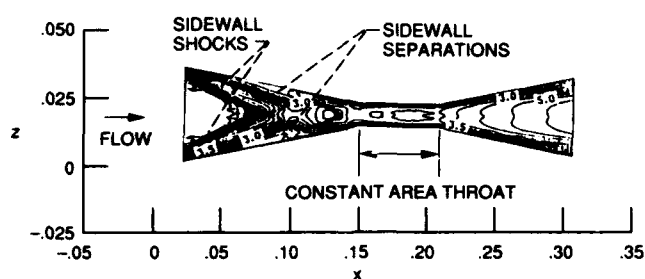


Figure 19. - Mach number contours for a representative freestream case in the horizontal center plane (ref. 9).

$M_\infty = 17.7$  6° SIDEWALLS GCR = 5.0 COWL AFT (100%)

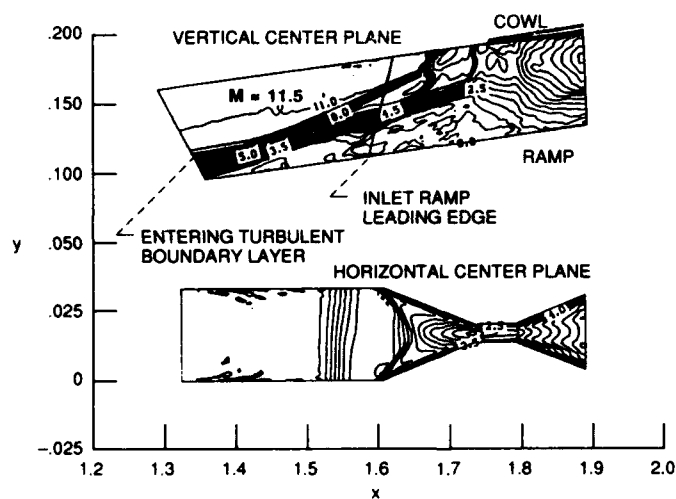


Figure 20. - Mach number contours for entering boundary layer case (ref. 9).

$M_\infty = 17.7$  6° SIDEWALLS GCR = 5.0 WEDGE CASE

RAMP CENTERLINE

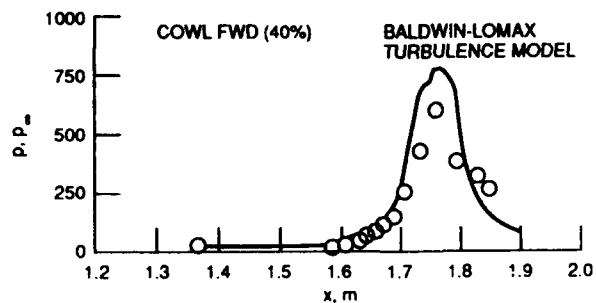


Figure 21. - Comparison of experimental and numerical surface pressure distributions (ref. 9).

## Discussion

### GARNERO

1) Can you give us the CPU time for one calculation, for example for the Mach 12 Generic Inlet, with a three-dimensional PN 5 LBI implicit scheme and CRAY X-MP?

2) Do you think that a Baldwin-Lomax Turbulence Model is sufficient to compute internal aerodynamics in hypersonic inlets or do you plan to use more complex models like K-E model for example?

### AUTHOR'S REPLY

1) 3-D Parabolical Navier-Stokes computations for the Mach 12 Generic Inlet on a Cray X-MP typically take 45 CPU minutes, using a linearized block implicit scheme. Navier-Stokes solutions for the same inlet take much more time, i.e. 10 Hrs of CPU time.

2) The Baldwin-Lomax turbulence has been extensively used for inlet computations. However, it has been found to have significant shortcomings. Higher order turbulence closures have been investigated and are under study. In addition, a program is in place with the objective of developing improved turbulence and transition modeling for hypersonic flows.

### KORZ

The glancing sidewall shocks and the resulting separation and secondary flow would seem to have the potential for a significant input on modular scramjets configurations. Would you comment and indicate if any evaluations of this phenomenon have been carried through the entire scramjet flowfield, including the combustor and nozzle?

### AUTHOR'S REPLY

Scramjet modular configurations would utilize multiple sidewalls over the span of the inlet. At each of the sidewalls, the potential for regimes of secondary flow is present. Hence a considerable fraction of the flow area can be affected by this phenomenon. At the present time, no data has been presented which tracks the secondary flow through the combustor/nozzle in a scramjet. There are measurements in a Mach 3.5 rectangular inlet, however, which does show the persistence of the vortex through inlet, through a normal shock and into a subsonic diffuser. The effect of this secondary flow on inlet performance and inlet unstart must be evaluated. It is noted that the presence of this flow feature may provide some benefit for enhanced mixing of fuel. It has been suggested previously that injection of fuel into the vortical flow region at some point within the aft portion of the inlet may lead to greater fuel spreading and additional time for chemical reaction.

## DESIGN CONSIDERATIONS OF A HIGH EXPANSION RATIO HYDROGEN TURBINE

by  
A.T.Holmes  
Turbine Technology Department  
and  
R.Varvill  
Advanced Projects Department  
Rolls-Royce plc  
P.O.Box 3  
Filton  
Bristol  
BS12 7QE  
England

© Rolls-Royce plc 1990

92-16983

## SUMMARY

The high specific heat of hydrogen compared with air leads to turbine stages which have low pressure ratios for comparable levels of specific work. In high speed propulsion systems designed for reusable space launch vehicles, the choice of scantlings is influenced by the need to minimise weight consistent with the achievement of the required efficiency. The effect of unit increase of mass in a component is, typically, to increase the take-off weight by approximately five units, and efficiencies significantly lower than those of normal aero-gas turbine practice are adopted. A multi-stage turbine design with overall pressure ratio of 7.6 and overall loading  $\Delta H/u^2 = 31.4$  is described in the paper. A parametric study covering a range of mean diameters and number of stages was performed, in which the aim was to establish the trends of efficiency against weight. The final design has ten stages with a common hub diameter.

## INTRODUCTION

This paper describes some of considerations influencing the preliminary design of a hydrogen turbine. The investigation formed part of a wider study performed recently in the U.K. into the technical and economic feasibility of a winged, air-breathing, single stage to orbit (SSTO) launch vehicle.

Some of the broader issues governing the desired mass and performance characteristics of the turbine are discussed; together with a summary of the important differences arising when pure hydrogen is used as a working fluid rather than, for example, air or combustion products. This is followed by a more detailed examination of the aerodynamic and mechanical design philosophy and the manner in which these factors interact.

## GENERAL DESIGN CONSIDERATIONS

The optimisation of a propulsion system and its components cannot be achieved without considering the performance requirements of the vehicle as well. This situation is especially true of air-breathing launch vehicles where the variation of gross take-off weight (GTOW) to weight at main engine cut-off (MECO) is a factor of 5:1; and the payload itself is a mere 15% of the vehicle dry weight.

The overall measures of propulsion system performance are thrust/weight ratio and specific impulse. Vehicle performance (payload fraction) is a complex function of these two parameters, depending on the mission objectives and trajectory profile. An SSTO vehicle launched directly into an equatorial orbit from Kourou favours a high acceleration trajectory employing a relatively high (by air-breathing engine standards) thrust/weight ratio, moderate specific impulse propulsion system. The contribution of the turbine to the overall mass properties of the engine and its specific impulse are obviously dependent on the particular thermodynamic cycle employed.

Early trade-off studies revealed that an optimum isentropic expansion efficiency of around 75% yielded the best compromise between mass and fuel burn.

Some of the turbine cycle parameters are as follows:

Rotational speed $N/\sqrt{T}$	11 rps/ $\sqrt{K}$
Expansion ratio	7.6
Specific work ratio	4789 kJ/kg/K

These factors led to the choice of a multi-stage turbine of 7 - 10 stages with relatively low Mach number blading.

## HYDROGEN AS A WORKING FLUID

Employing hydrogen as a working fluid presents opportunities for improving the specific power output of turbines, but it also results in some unusual mechanical design difficulties.

Figure 1 illustrates a comparison between the thermodynamic and transport properties of

hydrogen and air at room temperature and pressure. The low molecular weight of hydrogen (2.016) results in a specific heat capacity almost fifteen times that of air. However, since both gases are principally composed of diatomic molecules the specific heat ratios ( $\gamma$ ) are almost identical.

The net power output of a turbine is given by:

$$w = mCp_{H_2}T_1[1-(1/R)^{(\gamma-1)/\gamma}]$$

Therefore for the same inlet temperature and overall pressure ratio the hydrogen turbine requires only 1/15th of the mass flow to deliver the same power. However, the volumetric flow rate, given by:

$$V = mRT/P$$

can be shown to be independent of working fluid molecular weight since this reduces to:

$$V = [(\gamma-1)/\gamma]T/P$$

Therefore one would expect turbines using different working fluids but producing the same power output with similar entry conditions to have similar flow areas.

Since the acoustic velocity in hydrogen is almost four times that in air, exceptional levels of specific work output are possible with subsonic blading. The power output per stage is given by:

$$w = \mu u \Delta v_w$$

where  $u$  is the mean blade speed and  $\Delta v_w$  is the change in absolute whirl velocity of the fluid. This may be expressed also as:

$$w = \mu u^2 \Delta H / u^2$$

The aerodynamic loading coefficient  $\Delta H/u^2$  and flow coefficient  $v_w/u$  are largely determined by efficiency considerations. As loading increases above a value of unity the efficiency falls due to increasing secondary and leakage losses. Also, increasing the flow coefficient leads to smaller blade height (reduced aspect ratio) and therefore to further increase in losses. Thus at a fixed target efficiency level, loading and flow coefficients are defined to within a relatively close tolerance band. The mean rotor blade speed  $u$  is normally constrained by either mechanical or aerodynamic considerations. Since the work per stage is given by:

$$w = \mu u^2 \Delta H / u^2$$

it is desirable to increase the blade speed as much as possible in order to maximise the power to weight ratio. However, increasing mechanical stresses ( $\sigma \propto u_{tip}^2$ ) exert an upper limit on the rotor tip speed depending on the strength to weight ratio of the rotor material and the structural efficiency. Also in some instances where relatively small volumetric flow rates are employed and/or low rotor rotational speeds, increasing blade speed (by increasing annulus radius) results in diminishing annulus height to the extent that rising flow losses put an upper limit on blade speed. For this particular application the optimum mean blade speed is close to the structural limit. Therefore at a similar efficiency level and blade speed, the hydrogen turbine produces a stage work only 1/15th that of an air turbine (for the same inlet conditions), due to the reduced mass flow, thus requiring 15 times as many stages. Summarising, if the turbine is structurally limited to the same tip speed as a conventional air turbine, for similar inlet conditions the work per stage of a hydrogen turbine is much lower than that of an air turbine despite the aerodynamic potential for increased blade speed due to low gas Mach numbers.

Hydrogen also introduces mechanical design problems, the most severe being hydrogen embrittlement. This can occur as a result of several physical mechanisms such as:

- (i) Chemical attack - hydrogen reacts with an alloying element, e.g carbon in steel to form high pressure pockets of methane, growing at grain boundaries and internal voids.
- (ii) Internal hydrogen pressure formation - reaction product is molecular hydrogen, relatively immobile in most materials, the hydrogen precipitates at internal interfaces developing high gas pressures.
- (iii) Dislocation interaction - affects the plastic behaviour of material by dislocation pinning etc.
- (iv) Hydride formation - atomic hydrogen can react with some phases within the material to form a less dense hydride phase. This precipitates at regions of high strain and is often a brittle material.
- (v) Lattice bond interaction - hydrogen interacts with the lattice to reduce the crystal bond strength and the intergranular strength.

Within a given material any one or several of these mechanisms can act simultaneously to erode the physical properties.

The embrittlement effect varies noticeably with temperature. At liquid hydrogen temperatures there is insufficient thermal energy to dissociate the molecule and consequently embrittlement seldom occurs. Above 170K effects become noticeable, the degree of embrittlement being affected by surface catalysis effects and relative material solubility levels. At room temperature marked reductions in tensile strength occur, for example the notched tensile strength of nickel superalloys can be reduced to 25% of their normal values. At elevated temperatures, surprisingly the tensile properties can often be more or less restored, though time dependent properties such as creep strength can be severely degraded.

The majority of hydrogen embrittlement studies to date have been aimed at the commonly used aerospace alloys of steel, nickel, titanium, aluminium and cobalt. The behaviour of titanium alloys is largely determined by the relative quantities of the alpha and beta phases present. The alpha phase has a low solubility but reacts to form titanium hydride, conversely the beta phase has a high solubility but does not react. Within complex alloys which are mixtures of the two phases, the beta phase can act as a pathway for attack of the alpha phase; the TiH formed at the phase boundary is brittle and results in an 18% increase in volume. Nickel alloys are severely embrittled by hydrogen especially the higher strength varieties utilised for disc materials. Hydrogen embrittlement has been observed by nearly all the mechanisms mentioned and can occur at temperatures up to 600°C.

The behaviour in hydrogen of the more advanced materials currently under study for spaceplane applications is still poorly understood. Carbon/carbon which is a candidate hydrogen turbine material due to the reducing atmosphere, is not attacked by molecular hydrogen at temperatures up to 1000°C but is rapidly attacked by atomic hydrogen. At typical equilibrium concentrations at turbomachinery temperatures and pressures, sufficient atomic hydrogen exists to liberate significant quantities of methane. Therefore it would appear that development of new coatings is required. Thermodynamic calculations on the reactivity of silicon carbide indicate that significant degradation of materials containing SiC fibre reinforcement could occur.

From a design viewpoint, measures that can be taken to reduce the probability of component failure are:

- (i) Use non-susceptible materials wherever possible.
  - (ii) Avoid designing components with stresses significantly greater than the yield and be careful to avoid local stress-raising features.
  - (iii) Use diffusion resistant coatings (e.g. gold, copper) that inhibit the ingress of hydrogen into the parent material. These coatings, however, only work well at moderate temperatures, due to rising diffusion rates with increasing temperature. Of greatest long-term potential are the catalytic type coatings that inhibit molecular hydrogen dissociation and promote atomic hydrogen re-combination. A considerable advantage of these coatings is that their effectiveness is independent of thickness, therefore they can be applied with an almost negligible mass penalty.
- Another difficulty associated with the use of hydrogen as a working fluid is the possibility of cold welding. In the event of fast rubbing metal to metal contact in an inert atmosphere, the mobile electron clouds within metals can mix causing cold welding, since the oxide film normally present on metal surfaces is not regenerated. This is of particular concern for both rotor and stator tip seal design, and also the internal seals within the turbomachine necessary for cooling systems and bearing load control. The assumption throughout the turbine design is that a non-metallic material must form at least one half of a seal assembly, typically a ceramic liner. The alternative design philosophy of seals which never touch would result in unacceptable performance penalties.

Finally the compatibility of hydrogen with the bearing cooling and lubrication system must be considered. Conventional petroleum based lubricants will hydrogenate when in contact with hydrogen. In this application however, sources of cool (liquid or gaseous) hydrogen were not available, therefore a separate bearing coolant gas, namely helium, was chosen for compatibility with the lubrication system.

#### TURBINE TYPE SELECTION

There are many types of turbine available to the designer, and the selection is based on mass and efficiency considerations. The following discussion briefly describes the reasoning behind the eventual choice of a subsonic, axial flow multi-stage turbine.

##### (i) FLOW DIRECTION

(a) Centrifugal inflow. Centrifugal impellers have a high tip speed capability and are especially well suited to small volumetric flow rates (where axial flow stages would incur severe tip clearance losses). However, they are limited to aerodynamic loadings of about 1.0, thus resulting in many stages to cope with high pressure ratios. Multi-staging of centrifugal turbines is complicated by the ducting, resulting in considerable weight, and this option was rejected.

(b) Radial outflow (Lungstrom). The radial outflow turbine has advantages for a high pressure ratio application in that it can accommodate the expanding flow without a large increase in blade height. However there are formidable stressing problems due to the



offset rotor bending moments, and also the blade speed of the first few stages is inevitably far below the level that can be achieved by well designed axial flow machines. These two disadvantages result in a machine achieving a relatively low power to weight ratio.

(c) Axial flow. The advantages of an axial flow device are that each blade row may be designed at its optimum blade speed for maximum power to weight ratio, and also stage loadings up to 5 or greater may be contemplated. In addition there is a negligible ducting weight penalty when stages are stacked together to form a multi-stage turbine.

#### (ii) SUBSONIC VS SUPERSONIC BLADING

Supersonic flow turbines are extensively employed in rocket engine turbopumps due to their exceptional power to weight ratio and the high expansion ratios. They are especially well suited to hydrogen working fluid where the acoustic velocity is high. The efficiency levels however are rather low for this application, the best designs yet (to the authors' knowledge) being the Space Shuttle main engine turbopumps peaking at 65%. Therefore unless a breakthrough in the design of supersonic turbines is achieved, an alternative subsonic type must be adopted.

#### (iii) PARTIAL VS FULL ADMISSION

Partial admission is an advantage when small volumetric flows are utilised since it permits an increased tip speed whilst maintaining an acceptable blade height to limit tip leakage losses. But there are additional losses due to blade passage filling and emptying at every revolution. No advantage could be shown for partial admission since in any case blade speeds were limited by stress rather than by hub/tip radius ratios.

#### (iv) GEARED VS DIRECT COUPLED DRIVE

Interposing a gearbox between the turbine and the driven component can be an advantage in certain circumstances, for example in liquid rocket systems where a single turbine drives both pumps via a reduction gear. However, a power limit exists above which the weight and complexity of the gearbox become prohibitive. Preliminary trade-off studies showed that a direct coupled drive was lighter.

#### (v) IMPULSE VS REACTION STAGES

The distribution of pressure drop through the blading is of great importance in determining the overall efficiency of the expansion process. In reaction blading the pressure drops are split between the rotor and stator blade rows, depending on the degree of reaction. A 50% reaction turbine for example has equal pressure drops across the rows, more strictly defined as having equal static temperature drops. When operated at a moderate stage loading ( $\Delta H/u^2=1$ ) it attains a high efficiency. To achieve this however, effective tip sealing is essential. As loading is increased, efficiency falls.

Impulse blading has all, or nearly all, of the stage static temperature drop across the stator blades. In practice it is usual to provide a small positive reaction (say 10%) in order to obviate diffusion. Impulse stages can be velocity compounded, an arrangement in which a large pressure ratio is adopted across the first row of stator blades, generating a very high velocity which is then passed through two or more rows of rotor blading with a stator or stators interposed to reverse the flow direction. For hydrogen as a working fluid, it is possible to achieve these high velocities in a subsonic flow. With blading of this type, rotor tip leakages are moderate and only the stator blading, which is easier to seal, need be provided with more effective seals. Conceptually, it is possible to design a series of velocity compounded stages to run in tandem to give the correct overall pressure ratio. At low values of  $u/C_o$  a two-row velocity stage may be more efficient than a single row stage, see figure 2.

In the course of the turbine design it was decided at an early stage to manufacture the rotors as integrally machined blade and disc assemblies (blisks). This was possible since the turbine entry temperature was low enough to permit uncooled blading, therefore the disc head and rotor blades did not need to accommodate cooling passages. The resulting simplification in rotor construction represents a considerable weight saving, although it is not practicable to provide integral shrouding. The aerodynamic design was therefore influenced by the need to balance the unshrouded rotor tip leakage loss against the loss in the more efficient stator hub seals. Together with the efficiency target of 75%, a pressure compounded low reaction design was developed for the required duty.

#### MECHANICAL DESIGN

In order to establish a baseline turbine design, blade and disc materials were limited to the current generation of nickel and titanium alloys. This philosophy led to a high degree of confidence in the proposed rotor construction and resulted in an accurate mass estimate. The turbine inlet temperature is relatively modest by aero engine standards and obviated the need for blade cooling. Uncooled blading allows a simpler rotor construction as the blades can be made integral with the rotor. Udimet 720 was specified for the first and second stages, but for the others the gas temperature is low enough for the creep resistant titanium alloy IMI 834 to be used. Hydrogen embrittlement of the blades and disc rim was prevented by a combination of protective

coatings and judicious design. It was proposed to manufacture the U 720 sections by electro-chemical machining (ECM) and the titanium either by ECM from a forging or a combination of ECM and linear friction welding of separately machined blades to the discs. To ensure an acceptable profile standard, the minimum axial chord was set at 15 mm for manufacturing reasons, a constraint which was adopted in the aerodynamic optimisation procedure.

Following manufacture of the individual stages, the discs are joined near the rims by welding except for a bolted joint between the nickel and titanium faces. The resulting drum is gas-tight, preventing ingress of hydrogen, and is filled with helium under pressure. The disc stresses can be driven to a high level in the inert atmosphere. The stator blading is grouped into segments, assembled from the outside and then keyed into a cylindrical pressure vessel forming the outer shell of the turbine. The dynamic seals within the turbine are designed to run on ceramic liners in order to prevent cold welding. The rotor stages are shroudless, but the stator blades are provided with platforms to allow labyrinth seals to be fitted.

Many types of bearings were considered for this application. Magnetic and aerodynamic types have potential in the long term and do not require lubricants, but these were rejected in favour of simple rolling element bearings. Silicon nitride rollers and balls permit an increased DN value and result in low heat generation rates due to the high stiffness of the material. In order to arrive at an absolute minimum complexity, low mass lubrication system, it was proposed to design a total loss oil system for the thrust bearing. Oil fed from a pressurised tank is atomised by a high pressure helium jet sprayed directly onto the bearing.

The roller bearings may be either grease packed or coated with a solid lubricant; heat removal being effected by external gas cooling. The lubricant initially selected was one of the perfluorinated polyether family, which due to their low vapour pressure are particularly well suited to space applications.

#### AERODYNAMIC DESIGN

A parametric study was performed in which three turbines at different radii were designed to investigate the influence of stage number and diameter on weight. It was evident from the loading chart of Smith (ref. 1) that an exit angle of approximately  $70^\circ$  is optimum at a given stage loading  $\Delta H/u^2$  (see figure 3). Stage mean-line values of reaction, pitch/chord ratio and aspect ratio were assumed, and an efficiency prediction method applied. The stage loading  $\Delta H/u^2$  and  $V_a/u$  required to achieve an overall turbine efficiency of 75% was thus obtained. This procedure was repeated for each of the three values of radius chosen. The higher radius turbine was significantly heavier and was therefore rejected.

The final choice yielded a ten-stage design having a constant hub radius throughout and average stage loading of  $\Delta H/u^2 = 3.1$ . Since only a limited production run was envisaged, design and manufacturing costs had to be minimised, so a "repeating" stage blade design was proposed. Common rotor and stator blade profile geometry on the first nine stages was used, stages 1 - 8 being cropped versions of stage 9. Stage 10 was off-loaded and had different profiles, in order to limit the exit swirl angle.

#### CONCLUSIONS

A high expansion ratio multi-stage hydrogen turbine was designed, having rotors constructed of current generation superalloys.

An optimum mean blade speed was identified which maximised the power/weight ratio, whilst meeting the target efficiency level. The resulting rotor tip speed was close to the structural limit, governed by the disc material; however, due to the high acoustic velocity in hydrogen, the blading was subsonic throughout.

Due to the very high specific heat capacity of hydrogen, ten highly loaded axial flow stages were required to meet the required duty. The degree of reaction was chosen to give the best compromise between leakage losses and diagram efficiency.

The resulting design including rotors, casings and manifolding yielded a specific power output of 0.45 Mw/Kg.

#### REFERENCE

1. Smith, S.F. "A simple correlation of turbine efficiency", Journal of the Royal Aeronautical Society 1965 vol. 65 p. 467

# PHYSICAL PROPERTIES

AT 288K

	<i>Air</i>	<i>Hydrogen</i>
Specific heat      Cp	1150	14300
Ratio of specific heats $\gamma$	1.395	1.4
Gas constant      R	287	4130
Viscosity $\mu$	$1.8 \times 10^{-5}$	$8.8 \times 10^{-6}$
Acoustic velocity	339.6	1290.4

Figure 1

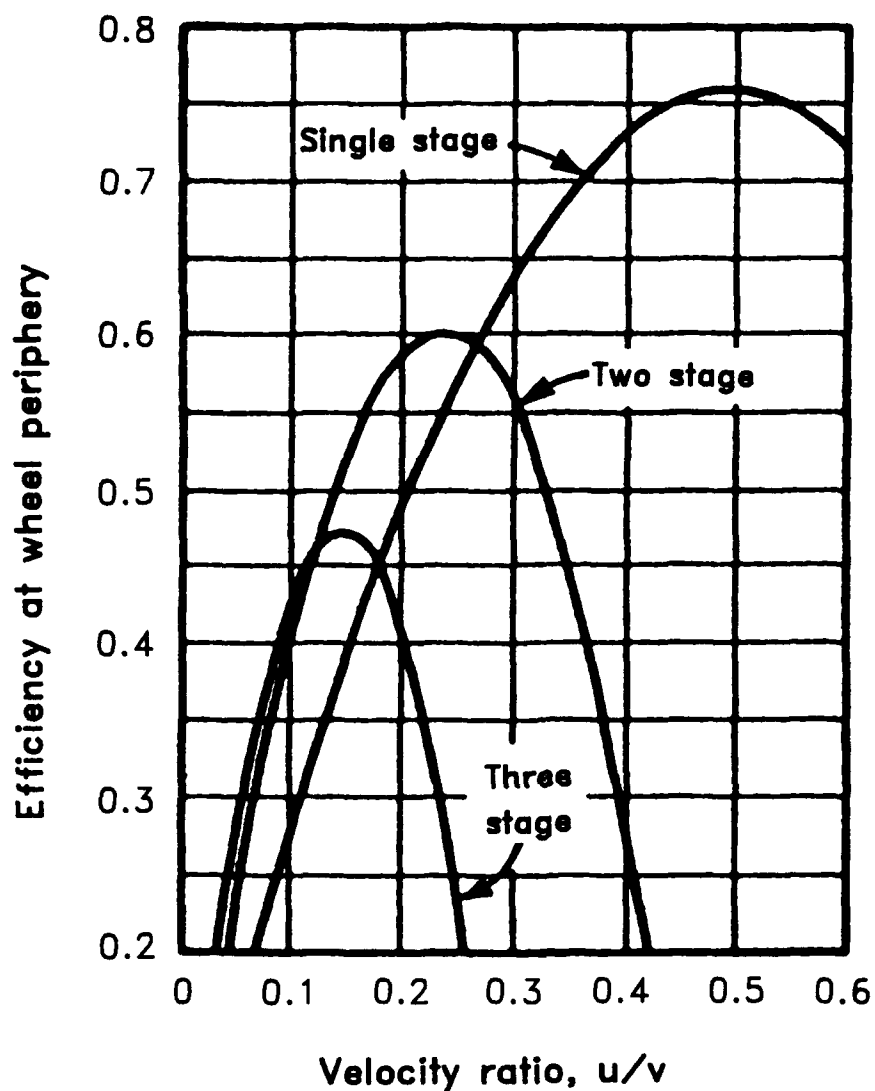
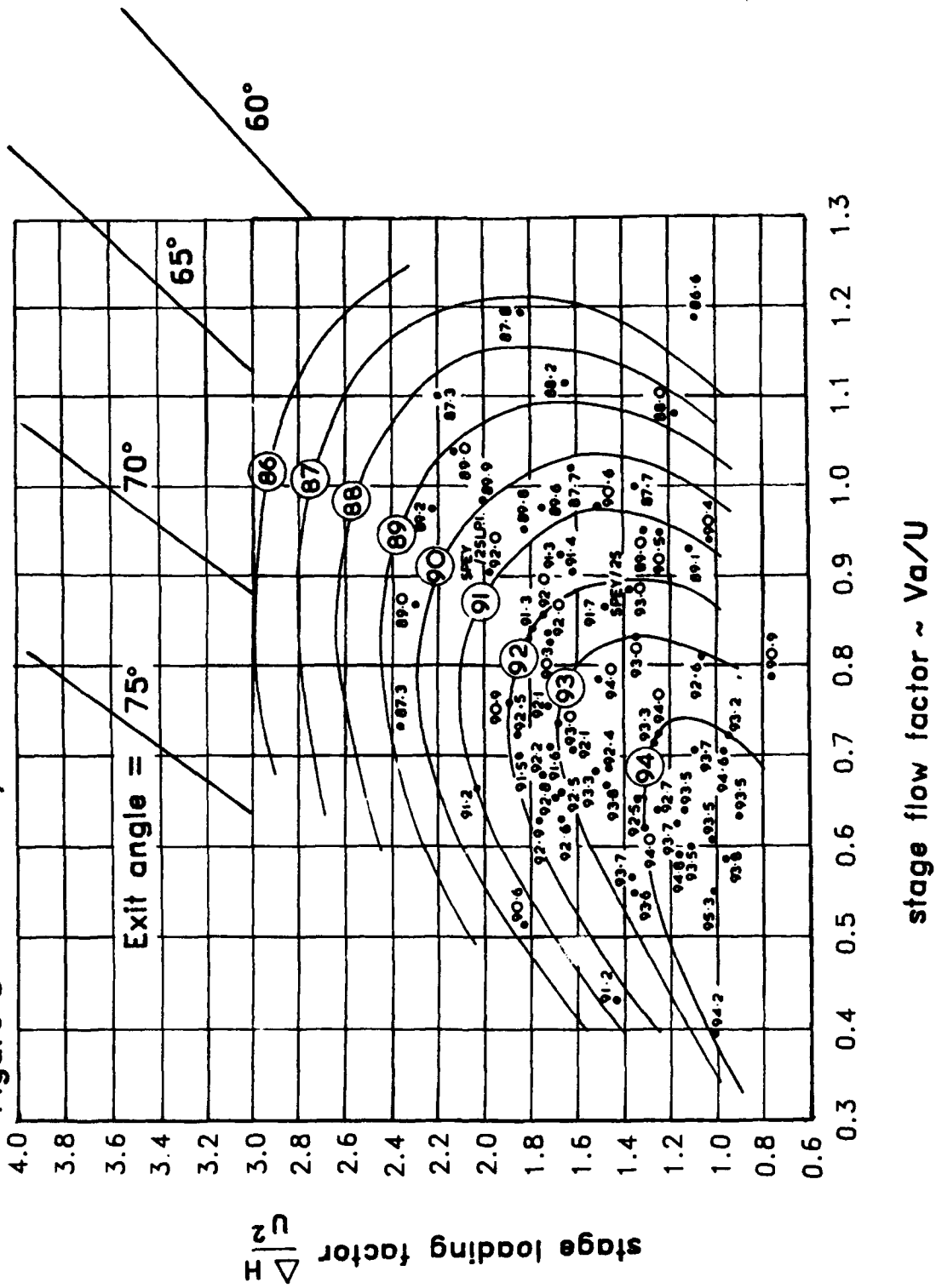


**Figure 2**

Efficiency of impulse turbines having one, two and three stages of velocity compounding  
(from Rocket Propulsion Elements, G P Sutton, D M Ross, John Wiley & Sons)

Figure 3 Efficiency chart from ref. 1



## **ETUDE D'UNE TURBINE MULTI-ETAGES A HYDROGENE POUR DES APPLICATIONS EN PROPULSION COMBINEE**

---

**Yves MARION - Jacques DESCLAUX**  
**Société Européenne de Propulsion**  
**Division Propulsion à Liquides et Espace**  
**BP 802 Forêt de Vernon**  
**27200 VERNON - FRANCE**

Le souci de définir les caractéristiques : performances, encombrement et masse d'un moteur nécessite de connaître avec précision et dès le stade de l'avant-projet la taille de la Turbine et son fonctionnement.

Pour répondre à ce besoin, la Société Européenne de Propulsion a développé des outils simplifiés de prédiction de performances de Turbines multi-étages. Ainsi, à partir des spécifications, de larges études paramétriques sont présentées, conduisant au prédimensionnement optimisé d'une veine aérodynamique corotative. Une version contrarotative est également présentée et comparée. Lors de cette étude, on estime l'influence des principaux paramètres que sont la vitesse périphérique, le nombre d'étages, et le taux de détente, ou le débit, compte tenu d'une contrainte de hauteur d'aubages minimale à respecter.

L'influence de la nature du gaz hydrogène sur le choix des principaux paramètres sera expliquée et comparée avec d'autres gaz plus communément utilisés comme l'air ou le mélange hydrogène - vapeur d'eau.

### **INTRODUCTION**

Le dessin aérodynamique d'une turbine axiale peut en général être divisé en trois phases. La première phase consiste d'abord à déterminer les paramètres globaux de fonctionnement et inclut le fluide utilisé, les niveaux de pression et de température, la puissance requise, le débit, la vitesse de rotation et parfois le rendement. La deuxième phase conduit en général à la détermination du nombre d'étages, de la taille de la turbine et de la hauteur et des déviations des aubes, du taux de détente et du rendement global et pour chaque étages. A la fin de cette phase, on connaît le triangle des vitesses en entrée et sortie de chaque roue. La troisième phase consiste à déterminer les géométries d'aubages respectant les triangles de vitesse et nécessite l'utilisation de codes de calcul sophistiqués, bi ou tridimensionnel, de types fluide parfait ou visqueux.

Ces trois phases sont étroitement liées en ce sens que le niveau de performance requis en phase 1 dépend fortement de la sévérité des triangles de vitesses sélectionnés en phase 2 et de la qualité des profils de la phase 3. En général, lors de la phase 3 des effets additionnels de tenue mécanique comme l'épaisseur des aubes et de leur bord de fuite, les jeux en bout d'aubes sont pris en compte.

Cet article présente une méthode simple pour estimer les performances d'une turbine multi-étages en fonction du nombre d'étages, du rayon moyen de la veine, c'est-à-dire de la vitesse périphérique puisque la vitesse de rotation est imposée, et du taux de détente.

L'optimisation porte sur la recherche du débit minimal entraînant la turbine, sachant que la hauteur d'aubages du premier distributeur ne doit pas être plus petite que 10 mm. Pour chaque étage, des expressions simplifiées du rendement faisant intervenir la géométrie des triangles de vitesse considérée, le facteur de charge de l'étage, l'angle de sortie du distributeur, et les pertes d'aubages seront utilisés.

A partir de spécifications détaillées, deux dimensionnements, l'un corotatif, l'autre contrarotatif seront optimisés et comparés.

### Nomenclature

$C_p$	: Constante du gaz	J/Kg.K
$h$	: Hauteur d'aubes	mm
$H$	: Enthalpie spécifique	J/Kg
$n$	: Nombre d'étages	
$N$	: Vitesse de rotation	tr/mn
$P_u$	: Puissance	en Watt
$P$	: Pression	bar
$Q$	: Débit-masse	kg/s
$R$	: Constante du gaz	J/Kg.K
$R_m$	: Rayon moyen de veine	mm
$S$	: Entropie	J/Kg.K
$T$	: Température	K
$U$	: Vitesse périphérique	m/s
$V$	: Vitesse absolue	m/s
$W$	: Vitesse relative	m/s
$\alpha$	: Angle absolu mesuré par rapport à la direction périphérique	- dégr.
$\beta$	: Angle relatif mesuré par rapport à la direction périphérique	- dégr.
$\gamma$	: Rapport des constantes du gaz	
$\eta_{T-T}$	: Rendement isentropique basé sur un taux de détente total-total	
$\eta_{T-S}$	: Rendement isentropique basé sur un taux de détente total-statique	
$\varphi$	: Coefficient de ralentissement dans un distributeur	
$\psi$	: Coefficient de ralentissement dans une roue mobile	
$\delta_D$	: Pertes d'énergie cinétique dans un distributeur	
$\delta_R$	: Pertes d'énergie cinétique dans une roue mobile.	

### Indices

$e$	=	Entrée de la turbine
$i$	=	Indice de l'étage
$is$	=	Isentropique
$T-S$	=	Basé sur un taux de détente total-statique à travers la turbine ou un étage
$T-T$	=	Basé sur un taux de détente total-total à travers la turbine ou un étage
$u$	=	Composante tangentielle
$t$	=	Quantité totale
$x$	=	Composante axiale
$0$	=	Station de calcul entrée étage
$1$	=	Station de calcul entre stator et rotor
$2$	=	Station de calcul sortie rotor.







Le triangle 2 correspond à un degré de réaction nul et approxime la notion plus usuelle de pression statique constante aux bornes de la roue. On écrit :

$$\begin{aligned}\Delta V_u &= \Delta W_u = W_{u1} - W_{u2} \\ &= 2 W_1 \cos \beta_1 \\ &= 2 [V_1 \cos \alpha_1 - U] = 2 \left[ \frac{V_x}{\sin \alpha_1} - U \right]\end{aligned}$$

$$\text{soit dans ce cas } \frac{\Delta H}{U^2} = 2 \left[ \frac{1}{\sin \alpha_1} \frac{V_x}{U} - 1 \right] \quad (4)$$

#### Expression des pertes dans les aubages

D'après le diagramme enthalpie-entropie, on exprime le travail spécifique isentropique de l'étage en fonction du travail spécifique réel et des pertes d'aubages par la relation :

$$\Delta H_{isT-T} = \Delta H + \delta_D + \delta_R$$

$$\text{où } \delta_D = \frac{V_1^2}{2} - \frac{V_1^2}{2}$$

$$\text{et } \delta_R = \frac{W_2^2}{2} - \frac{W_2^2}{2}$$

représentent les pertes d'énergie cinétique respectivement dans le distributeur et la roue. On introduit en général des coefficients de ralentissement :

$$\varphi = \frac{V_1}{V_{1is}} \text{ et } \psi = \frac{W_2}{W_{2is}}$$

qui dépendent de la géométrie et des paramètres de fonctionnement des aubages. On obtient alors pour  $\delta_D$  et  $\delta_R$  les expressions :

$$\delta_D = \frac{1 - \varphi^2}{\varphi^2} \frac{V_1^2}{2} \text{ et } \delta_R = \frac{1 - \psi^2}{\psi^2} \frac{W_2^2}{2}$$

Ainsi après calculs, on obtient :

- Pour le triangle de vitesses 1

$$\delta_D = \frac{1 - \varphi^2}{2 \varphi^2} V_x^2 \frac{1}{\sin^2 \alpha_1}$$

$$\delta_R = \frac{1 - \psi^2}{2 \psi^2} V_x^2 \frac{1}{\sin^2 \alpha_1}$$

- Pour le triangle de vitesses 2

$$\delta_D = \frac{1 - \varphi^2}{2 \varphi^2} V_x^2 \frac{1}{\sin^2 \alpha_1}$$

$$\delta_R = \frac{1 - \psi^2}{2 \psi^2} \left[ V_x^2 \frac{1}{\sin^2 \alpha_1} + U^2 - 2 U V_x \frac{1}{\sin \alpha_1} \right]$$

### Expression des rendements d'étages

En combinant les relations précédentes, on obtient des expressions simplifiées du rendement d'un étage où interviennent seulement les paramètres suivants :

coefficient de charge  $\frac{\Delta H}{U^2}$ , coefficient de vitesse  $\frac{V_x}{U}$ , angle de sortie du distributeur, coefficient de ralentissement  $\varphi$  et  $\psi$ .

Ainsi, pour le triangle 1,

$$\eta_{T-1} = \frac{\frac{\Delta H}{U^2}}{\frac{\Delta H}{U^2} + \left( \frac{1-\varphi^2}{2\varphi^2} + \frac{1-\psi^2}{2\psi^2} \right) \left( \frac{V_x}{U} \right)^2 \frac{1}{\sin^2 \alpha_1}} \quad \text{avec} \quad \frac{\Delta H}{U^2} = \frac{2}{\tan \alpha_1} \frac{V_x}{U} - 1 \quad (5)$$

qui prend la valeur maximale :

$$\eta_{T-1} = \frac{1}{1 + \left( \frac{1-\varphi^2}{2\varphi^2} + \frac{1-\psi^2}{2\psi^2} \right) \frac{1}{\cos^2 \alpha_1}} \quad \text{pour} \quad \frac{V_x}{U} = \tan \alpha_1$$

Pour le triangle 2,

$$\eta_{T-2} = \frac{\frac{\Delta H}{U^2}}{\frac{\Delta H}{U^2} + \left( \frac{1-\varphi^2}{2\varphi^2} + \frac{1-\psi^2}{2\psi^2} \right) \frac{1}{\sin^2 \alpha_1} \left( \frac{V_x}{U} \right)^2 + \frac{1-\psi^2}{2\psi^2} \left( 1 - 2 \frac{V_x}{U} \frac{1}{\tan \alpha_1} \right)} \quad (6)$$

$$\text{avec} \quad \frac{\Delta H}{U^2} = 2 \left[ \frac{1}{\tan \alpha_1} \frac{V_x}{U} - 1 \right]$$

qui prend sa valeur maximale

$$\text{Pour} \quad \frac{V_x}{U} = \tan \alpha_1 \left( 1 + \sqrt{1 - \frac{b}{A \tan^2 \alpha_1}} \right)$$

$$\text{avec} \quad A = \left( \frac{1-\varphi^2}{2\varphi^2} + \frac{1-\psi^2}{2\psi^2} \right) \frac{1}{\sin^2 \alpha_1}$$

$$\text{et} \quad b = \frac{1-\psi^2}{2\psi^2}$$

## DIMENSIONNEMENT D'UNE TURBINE A HYDROGENE - INFLUENCE DE LA NATURE DU GAZ

Les turbines de moteurs pour propulsion combinée peuvent être alimentées par des gaz de caractéristiques thermodynamiques aussi inhabituelles que de l'hydrogène (noté  $\text{GH}_2$ ).

On étudie la spécificité d'un dimensionnement résultant de l'utilisation de ce gaz avec le dimensionnement d'une turbine à air.

### Rappel des valeurs des constantes de gaz

- Pour l'hydrogène  $R = 4139 \text{ J/Kg.K}$        $\gamma = 1,389$
- Pour l'air       $R = 287 \text{ J/Kg.K}$        $\gamma = 1,4$ .

### Conséquences sur le triangle des vitesses

Pour un même taux de détente, donc à nombre de Mach comparable (les 2 gaz étudiés ont à peu près une même valeur de  $\gamma$ ) la vitesse des gaz est plus grande dans la turbine  $\text{GH}_2$  que dans la turbine à air, soit ici dans le rapport des racines des constantes de gaz, c'est-à-dire :

$$\sqrt{\frac{4139}{287}} = 3,8$$

Inversement pour un même niveau de vitesse, le nombre de Mach dans la turbine à hydrogène est 3,8 fois plus petit que dans la turbine à air.

De même, pour qu'une turbine à hydrogène ait un triangle de vitesse homothétique à celui d'une turbine à air, il lui faudrait une vitesse d'entraînement 3,8 fois plus grande, probablement inacceptable du point de vue mécanique.

### Conséquences sur le rendement

Les charges par étages importantes obtenues pour le dimensionnement de la turbine à hydrogène conduisent à des coefficients de charge  $\frac{\Delta H}{U^2}$  importants et donc à des faibles valeurs de rendement. Cette situation peut être améliorée en utilisant, pour une charge donnée, un grand nombre d'étages et donc des écoulements nettement subsoniques.

### Conséquences sur la hauteur des aubes du distributeur

Pour de mêmes valeurs du débit réduit et du rayon moyen, la hauteur des aubes pour le gaz hydrogène augmente comme le rapport des racines des constantes de gaz. Ce qui est favorable pour le respect de la contrainte sur la hauteur d'aubes du distributeur. Sur la figure 11 on représente pour 3 valeurs de constantes de gaz (hydrogène - gaz de combustion  $\text{H}_2/\text{H}_2\text{O}$  - Air), la hauteur des aubes en fonction du nombre de Mach en sortie du distributeur.

## ETUDE PARAMETRIQUE DU DIMENSIONNEMENT D'UNE TURBINE A HYDROGENE - VERSION COROTATIVE

Les données de base de l'étude correspondent aux spécifications d'une turbine entraînant le compresseur d'un moteur turbofusée expander ayant au point de dimensionnement les performances suivantes :

- Puissance sur arbre       $P_u = 45 \text{ MW}$
- Température d'entrée       $T_{to} = 850 \text{ K}$
- Pression totale d'entrée       $P_{to} \leq 90 \text{ bar}$
- Pression totale de sortie       $P_{ts} = 5,3 \text{ bar}$
- Vitesse de rotation       $N = 6045 \text{ tr/mn}$
- Fluide utilisé  $\text{GH}_2$        $C_p = 14779 \text{ J/Kg.K}$   
     $\gamma = 1,389$ .

On notera la spécificité du gaz utilisé, de l'hydrogène froid, particulièrement énergétique. L'influence de cette spécificité sur le dimensionnement sera analysée plus loin, en effectuant des comparaisons avec d'autres gaz.

### Contraintes prises en compte lors du dimensionnement

Pour des raisons de tenue mécanique, la vitesse périphérique au rayon moyen de la veine ne doit pas dépasser la valeur de 300 m/s.

$$U \leq 300 \text{ m/s}$$

De même, l'utilisation d'une veine de grand diamètre, d'un taux de détente élevé ou d'un grand nombre d'étages conduit à une réduction de la hauteur des aubes du premier distributeur et entraînerait son injection partielle. Pour maintenir un fonctionnement de la turbine en injection totale, on décide que les hauteurs des aubes ne doivent pas être plus petites que 10 mm

$$h_e \geq 10 \text{ mm}$$

### Objectifs de l'étude

Les objectifs de l'étude sont de déterminer le diamètre, le nombre d'étages de la turbine qui respectera les spécifications avec un débit minimal.

### Méthode de prédimensionnement

A partir des conditions du projet correspondant aux spécifications :

- charge globale  $\left( \frac{\Delta H}{\gamma R T_{te}} \right)_0$
- vitesse d'entraînement au rayon moyen  $\frac{U}{\sqrt{\gamma R T_{te}}}$
- débit réduit  $Q \frac{\sqrt{T_{te}}}{P_{te}}$

On choisit les paramètres suivants :

- Nombre d'étages  $n$

Pour notre méthode d'avant-projet, nous avons utilisé une répartition de charge décroissante le long des  $n$  étages. Cette répartition respecte une loi du type  $\frac{\Delta H}{T_t} = \text{cte}$  où  $\Delta H$  représente le travail spécifique réalisé sur un étage et  $T_t$  la température d'arrêt à l'entrée de l'étage. Cette hypothèse conduit à une expression analytique simple de la valeur de la température à l'entrée du  $j$ -ième étage d'une turbine de  $n$  étages.

$$T_j = n+1 \sqrt{T_0^{n+1-j} T_{n+1}^j}$$

Dans cette expression,  $T_0$  et  $T_{n+1}$  correspondent aux températures à l'entrée de la turbine, ce qui est une donnée du prédimensionnement, et à la sortie, quantité qui est connue lorsque la puissance et le débit de la turbine sont connus.

- le débit de la turbine
- le rayon moyen que l'on considère constant entre l'entrée et la sortie de la turbine. Dans cette étude, on n'a pas considéré de turbine à rayon évolutif
- une première estimation des pertes, pour le calcul des coefficients  $\varphi$  et  $\psi$ , que l'on a corrélés de manière simplifiée à la géométrie des aubages (facteur de forme - pas relatif - déviation), ainsi qu'à leur fonctionnement aérodynamique.

### Résultats

En fonction des paramètres étudiés, les principaux résultats obtenus sont les suivants :

- d'après les valeurs des nombres d'étages, débits et vitesses périphériques considérés, les gammes de  $\frac{\Delta H}{U^2}$  obtenus conduisent à l'utilisation d'aubes à action. On a donc calculé les valeurs des coefficients de vitesse d'étages  $\frac{V_x}{U}$  et les rendements d'étages  $\eta_{T-T}$  à l'aide des relations (4) et (6).
- les valeurs des taux de détente de chaque étage et donc la valeur de la pression d'alimentation de la turbine

- les valeurs des hauteurs de sortie de chaque distributeur et en particulier la hauteur du premier distributeur, donc une allure de la veine aérodynamique complète
- une estimation du rendement global de la turbine.

#### Analyse des résultats : pour un taux de détente donné

Sur les figures 1 et 2, on a représenté pour une pression d'alimentation donnée de 41,5 bar, c'est-à-dire pour un taux de détente donné puisque la pression de sortie est fixée, l'évolution de la hauteur d'entrée et du rendement de la turbine en fonction du rayon moyen de la veine (que l'on fait varier de 300 à 500 mm pour respecter la contrainte d'encombrement) et ceci pour différents nombres d'étages. Ces abaques indiquent clairement les sens de variations des différents paramètres.

Ainsi, sur la figure 1, une augmentation du rayon de la turbine entraîne une augmentation de la vitesse périphérique et donc du rendement de la turbine, et ce de manière pratiquement linéaire. Ce qui se traduit, toutes choses égales par ailleurs, par une diminution du débit. Ces deux effets - diminution du débit, augmentation du rayon - se combinent pour expliquer la diminution de hauteur du distributeur. Ce comportement tient au fait que pour la plage de rayon de veine considérée, une diminution du facteur de charge  $\frac{\partial H}{U^2}$  de chaque étage améliore son rendement donc celui de la turbine. Sur la figure 2, la contrainte sur la hauteur d'aubage minimum de 10 mm donne le point de dimensionnement optimal, pour la pression d'alimentation considérée, ici 41,5 bar.

L'influence du nombre d'étages est également indiquée. On a étudié le cas de turbines de 6, 10, 14 étages. Globalement, pour la gamme de paramètres étudiée, une augmentation de son nombre d'étages a conduit à une augmentation du rendement de la turbine. Cette tendance semble d'autant moins marquée que le nombre d'étages est grand. Ainsi, pour un rayon  $R_m = 400$  mm, passer de 6 à 8 étages augmente le rendement de 4 points, de 12 à 14 étages de 1,3 points.

Pour ce qui concerne la hauteur d'entrée du distributeur, l'influence du nombre d'étages est claire. Ainsi, comme on vient de le voir, si l'augmentation du nombre d'étages diminue le débit, elle diminue aussi la charge du premier étage, donc le nombre de Mach en sortie du premier distributeur, ce qui tend à en augmenter les hauteurs, comme indiqué sur la figure 11.

Des deux effets antagonistes, et dans la plage de paramètres considérée, c'est le second qui l'emporte, et globalement, accroître le nombre d'étages augmente les hauteurs d'aubages.

#### Analyse des résultats : pour une hauteur d'entrée donnée

L'abaque de la figure 3 où l'on a représenté l'évolution du débit en fonction du rayon de veine pour différents nombres d'étages et une hauteur de distributeur imposée et égale à 10 mm permet de déterminer le dimensionnement optimal. De cet abaque, on tire les informations suivantes :

- le gain de débit est réel sur toute la plage de nombres d'étages étudiée, mais plus le nombre d'étages est grand, moins le bénéfice est important. Ainsi, pour un rayon moyen de 400 mm, on gagne 0,8 Kg/s de débit en passant de 6 à 8 étages, mais seulement 0,3 Kg/s en passant de 12 à 14 étages
- pour chaque nombre d'étages, il existe un rayon moyen au-delà duquel le gain de débit n'est plus significatif. La valeur de ce rayon correspond au dimensionnement optimal. Cette valeur dépend du nombre d'étages. Ainsi, un dimensionnement optimal correspond à 6 étages et  $R_m = 460$  mm ou 10 étages et  $R_m = 440$  mm, ou 14 étages et  $R_m = 400$  mm.

Cet abaque ne permet pas de définir définitivement et uniquement sur des critères aérodynamiques un dimensionnement optimal. Des coefficients d'échanges corrélant le débit de la turbine (et donc l'ISP du moteur) au rayon moyen, au nombre d'étages et à sa masse (encombrement radial et axial - Disques - Aubes - Carters et arbres) permettent d'optimiser le dimensionnement au niveau du moteur.

A titre d'exemple, on donne en figure 12 la géométrie de la veine aérodynamique d'une turbine de 10 étages vérifiant les spécifications. On donne également en fonction du numéro d'étages, le rendement et le facteur de charge de l'étage.

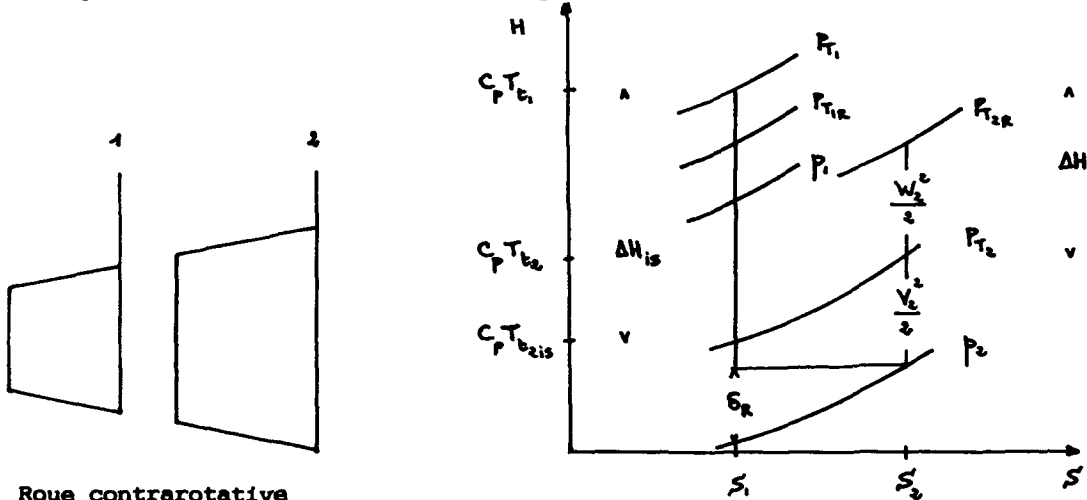
#### ETUDE PARAMETRIQUE DU DIMENSIONNEMENT D'UNE TURBINE A HYDROGENE - VERSION CONTRA-ROTATIVE

A partir de spécifications qui sont les mêmes qu'au paragraphe 2, on a effectué une étude paramétrique du dimensionnement d'une turbine à hydrogène dans le cas contra-rotatif.

On appelle turbine contrarotative une turbine pour laquelle une prérotation est donnée à l'écoulement par un distributeur à l'entrée de la turbine, les roues suivantes, toutes mobiles, fournissent le travail spécifique en tournant alternativement aux vitesses périphériques  $U$  et  $-U$ . Ces deux vitesses, successivement positives puis négatives, peuvent être de valeurs absolues différentes mais ce cas n'a pas été étudié. On a considéré ici des roues axiales, montées sur deux arbres imbriqués et tournant respectivement aux vitesses de rotation  $N$  et  $-N$ , la valeur de  $N$  étant la même que pour la version corotative. On voit donc que pour le dimensionnement contrarotatif, la vitesse de rotation relative des roues mobiles est doublée par rapport au cas corotatif.

#### Notations pour une turbine contrarotative

Pour le 1<sup>er</sup> étage, qui est un cas particulier dans le cas contrarotatif, les notations sont les mêmes qu'en I. Pour le cas des roues suivantes, le diagramme Enthalpie - Entropie ( $H-S$ ) donne les caractéristiques de la détente.



#### Roue contrarotative

Comme pour le paragraphe 1 et avec des notations compatibles avec celles données dans la nomenclature, on définit les deux types de rendements, un rendement total-total :

$$\eta_{T-T} = \frac{\Delta H}{\Delta H_{isT-T}}$$

$$\text{où } \Delta H_{isT-T} = \Delta H + \delta_R = \Delta H + (1 - \psi^2) \frac{W_2^2}{2}$$

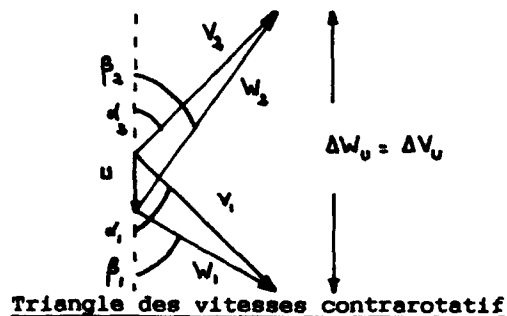
un rendement total-statique

$$\eta_{T-S} = \frac{\Delta H}{\Delta H_{isT-S}}$$

On remarque que dans l'expression des rendements, seules les pertes dans les roues interviennent.

#### Triangle des vitesses

Dans une turbine contrarotative, le rôle d'une roue est double. Une roue doit d'abord assurer un travail spécifique et ensuite redresser l'écoulement comme l'aurait fait un stator, afin d'alimenter correctement la roue suivante. Le triangle choisi a donc l'allure suivante :



vérifiant les relations  $\alpha_1 = \alpha_2$  et  $V_1 = V_2$ .

Comme pour les triangles de vitesses correspondant à des turbines corotatives, on établit des relations simples permettant de répondre à l'avant-projet. Ainsi, la relation entre le coefficient de charge  $\frac{\Delta H}{U^2}$  et le coefficient de vitesse  $\frac{V_x}{U}$  devient :

$$V_{u1} = V_1 \cos \alpha_1 \quad V_{u2} = V_2 \cos \alpha_2 = V_1 \cos \alpha_1$$

$$\begin{aligned} \text{soit} \quad \Delta V_u &= 2 V_1 \cos \alpha_1 \\ &= 2 \frac{V_x}{\tan \alpha_1} \end{aligned}$$

$$\text{et alors} \quad \frac{\Delta H}{U^2} = \frac{2}{\tan \alpha_1} \frac{V_x}{U}$$

De même, pour l'expression du rendement, on obtient après quelques calculs simples dans le triangle des vitesses contrarotatif,

$$\eta_{T-T} = \frac{\Delta H/U^2}{\Delta H/U^2 + \frac{1-\psi^2}{2\psi^2} \left[ \left( \frac{V_x}{U} \right)^2 + \left( \frac{V_x}{U} \frac{1}{\tan \alpha_1} + 1 \right)^2 \right]}$$

qui prend sa valeur maximale pour :

$$\frac{V_x}{U} = \frac{1}{\sqrt{1 + \frac{1}{\tan^2 \alpha_1}}}$$

#### Méthode de prédimensionnement

Les objectifs étant les mêmes que pour le dimensionnement corotatif, l'étude paramétrique a été menée de la même manière. En particulier, on a conservé la même loi de charge sur les étages et la manière de présenter les résultats est la même.

On présente ainsi en figures 4 et 5, pour une pression d'alimentation de 41,5 bar, les évolutions des hauteurs d'aubages du premier distributeur, du rendement de la turbine en fonction du rayon de la veine et pour différents nombres d'étages. Sur la figure 6, on donne l'évolution du débit pour les mêmes plages de paramètres, la hauteur du distributeur valant 10 mm.

#### Comparaison du dimensionnement corotatif et contrarotatif

##### Application numérique simple

On peut comparer de manière simple les deux dimensionnements en calculant, pour un cas de charge d'étage identique, les rendements respectifs du cas corotatif et contrarotatif.

Choisissons par exemple un coefficient de charge  $\frac{\Delta H}{U^2} = 7$ . Pour un angle absolu  $\alpha_1 = 25^\circ$  dans les deux cas, le coefficient de vitesse vaut :

$$\begin{aligned} \text{en corotatif} \quad (\text{Triangle à action}) \quad \frac{V_x}{U} &= 2,098 \\ \text{en contrarotatif} \quad \frac{V_x}{U} &= 1,632 \end{aligned}$$

Avec une hypothèse de pertes dans le stator  $\psi = 0,95$  et dans le rotor  $\psi = 0,9$  pour le cas corotatif, et  $\psi = 0,9$  dans le rotor pour le cas contrarotatif, les expressions des rendements démontrées précédemment donnent :

$$\begin{aligned} \text{en corotatif} \quad (\text{Triangle à action}) \quad \eta_{T-T} &= 0,680 \\ \text{en contrarotatif} \quad \eta_{T-T} &= 0,722 \end{aligned}$$

soit un avantage de 4,2 points en faveur du dimensionnement contrarotatif.

De façon plus complète, on a déterminé les domaines d'intérêts respectifs des dimensionnements corotatif et contrarotatif en représentant sur les figures 9 et 10, les rendements d'étage en fonction du coefficient de charge, une hypothèse étant prise pour les coefficients de pertes.



Sur ces abaques, on voit que pour de faibles valeurs de  $\frac{\partial H}{U^2}$  (turbines peu chargées - turbines à grande vitesse périphérique), l'utilisation d'une turbine corotative est conseillée. Jusqu'à une valeur de  $\frac{\partial H}{U^2} = 6$  pour des valeurs de coefficients de pertes valant  $\psi = 0,95$  et  $\psi = 0,85$ , de  $\frac{\partial H}{U^2} = 2$  pour  $\psi = 0,95$  et  $\psi = 0,90$ . Au-delà de ces valeurs, qui correspondent à des turbines très chargées - turbines tournant à basse vitesse périphérique - on a bénéfice à utiliser une turbine contrarotative.

#### Analyse des résultats

On présente en figures 4 et 5, pour une pression d'alimentation de 41,5 bar, les évolutions des hauteurs d'aubages du premier distributeur, du rendement de la turbine en fonction du rayon de la veine et pour différents nombres d'étages. Pour ces deux abaques, le sens de variation des paramètres est le même que pour le cas corotatif.

Sur la figure 6, on a représenté l'évolution du débit en fonction du rayon de veine pour différents nombre d'étages et une hauteur de distributeur imposée et égale à 10 mm. Cet abaque indique que :

- pour la gamme de rayon de veine étudiée, il existe, pour un nombre d'étages donné, une valeur de rayon optimal pour laquelle le débit est minimal. Cette valeur optimale du rayon est d'autant plus petite que le nombre d'étages est grand. Par exemple, pour une turbine de 8 étages, le débit diminue pour un rayon de veine croissant jusqu'à 460 mm et croît ensuite. Ce rayon optimal vaut 440 mm pour une turbine de 10 étages, 420 mm pour 12 étages et 400 mm pour 14 étages. Une bonne connaissance de ce rayon optimal est primordiale pour effectuer un dimensionnement compétent.

Sur les figures 7 et 8, on a mis en évidence que ce rayon optimal de dimensionnement existe aussi pour les versions de turbines corotatives. Par exemple, pour une turbine corotative de 6 étages, une augmentation de rayon de veine au-delà d'une valeur de 600 mm est défavorable et augmente le débit. Pour une turbine de 20 étages, c'est au-delà de 380 mm que l'on a plus avantage à augmenter le rayon de veine. Toutefois, ces deux turbines, données ici à titre d'exemple, ne vérifient pas les spécifications d'encombrement.

Comme pour le cas corotatif, il est nécessaire de connaître les coefficients d'échanges corrélant le dimensionnement aérodynamique et sa masse pour déterminer les paramètres optimaux de fonctionnement de la turbine.

A titre d'exemple on donne, en figure 13, la géométrie de la veine aérodynamique d'une turbine contrarotative de 10 étages vérifiant les spécifications. On donne également en fonction du numéro d'étage, le rendement et le facteur de charge de l'étage.

#### Comparaison des turbines 10 étages corotative et contrarotative

Sur le tableau suivant, on a résumé les principales caractéristiques des deux turbines sélectionnées.

	Turbine corotative	Turbine contrarotative
Nombre d'étages	10	10
Rendement	0.708	0.744
Débit (Kg/s)	11.9	11.5
Vitesse périphérique (m/s)	278.5	278.5
Pression d'alimentation (bar)	37.5	36.1
Pression de sortie (bar)	5.3	5.3
Température (K)	850	850
Encombrement radial (mm)	940	950
Encombrement axial (mm)		
hauteur d'entrée (mm)	10	10
Masse (Kg)	A déterminer	A déterminer

Du fait des valeurs de coefficient de charge utilisées ( $\frac{\Delta H}{U^2}$  de l'ordre de 6 pour les premiers étages de 4 pour les derniers), on a avantage à utiliser un dimensionnement contrarotatif. Ainsi, le rendement de la turbine contrarotative est supérieur de 3,6 points à celui de la turbine corotative, donnant un gain de débit de 0,4 kg/s. De plus, un dimensionnement contrarotatif, qui diminue l'encombrement axial de la turbine par suppression des distributeurs inter-étages, devrait donner un gain de masse important.

## CONCLUSIONS

Dans ce papier, on a présenté un développement des équations permettant le calcul des rendements de turbines axiales corotatives ou contrarotatives en fonction de leurs triangles des vitesses. On a mis en évidence le domaine d'intérêt respectif des deux variantes, en fonction du coefficient de charge  $\Delta H/U^2$ . Comme application, on a effectué, à partir de larges études paramétriques, le prédimensionnement comparé d'une turbine de forte puissance très chargée en version corotative et contrarotative. Dans notre cas particulier, un avantage a été mis en évidence en faveur de la version contrarotative, bénéfice que l'on a chiffré à 3,6 points de rendement menant à une économie de débit de 0,4 kg/s. On doit noter que les niveaux de rendements annoncés sont calculés à partir des modèles de pertes bibliographiques correspondant à des aubages ayant de bonnes répartitions de vitesses, des pas relatifs, des jeux en bout d'aubes et un effet de blocage de bord de fuite raisonnable. De même, pour déterminer avec précision le domaine d'intérêt respectif des dimensionnements contrarotatifs ou corotatifs, on doit être prudent sur la répartition des pertes entre les roues fixes et les roues mobiles.

## REFERENCES

- [1] - STEWART W.L. : "A study of axial - Flow turbine efficiency characteristics in terms of velocity diagram parameters"  
ASME Publication n°61 - WA - 37
- [2] - BALJE O.E. : "A study on design criteria and matching of turbomachines" - Part A : Similarity relations and design criteria of turbomachines - ASME Journal of engineering for power - Serie A - Vol 84 n° 1 - Jan. 1962"
- [3] - BALJE O.E. : "Axial turbines performances evaluations"  
BINSLEY R.L. : Part A : Loss geometry relation ships  
Part B : Optimization with and without constraints  
ASME journal of engineering for power - october 1968
- [4] - BALJE O.E. : "Turbomachines : A guide to design, selection and theory" - John Wiley & Sons - New-York
- [5] - AINLEY and MATHIEWSON : "A method of performance estimation for axial flow turbines" - British ARC R et M n° 2974 - 1951
- [6] - AINLEY and MATHIEWSON : "An estimation of the flow and pressure losses in blade rows of axial flow turbines". ARC - R et M n° 2891 - 1955
- [7] - KACKER and OKAPUU : "A mean line prediction method for axial flow turbine efficiency" - ASME journal of engineering for power - Paper n° 81 GT 58 - December 1981

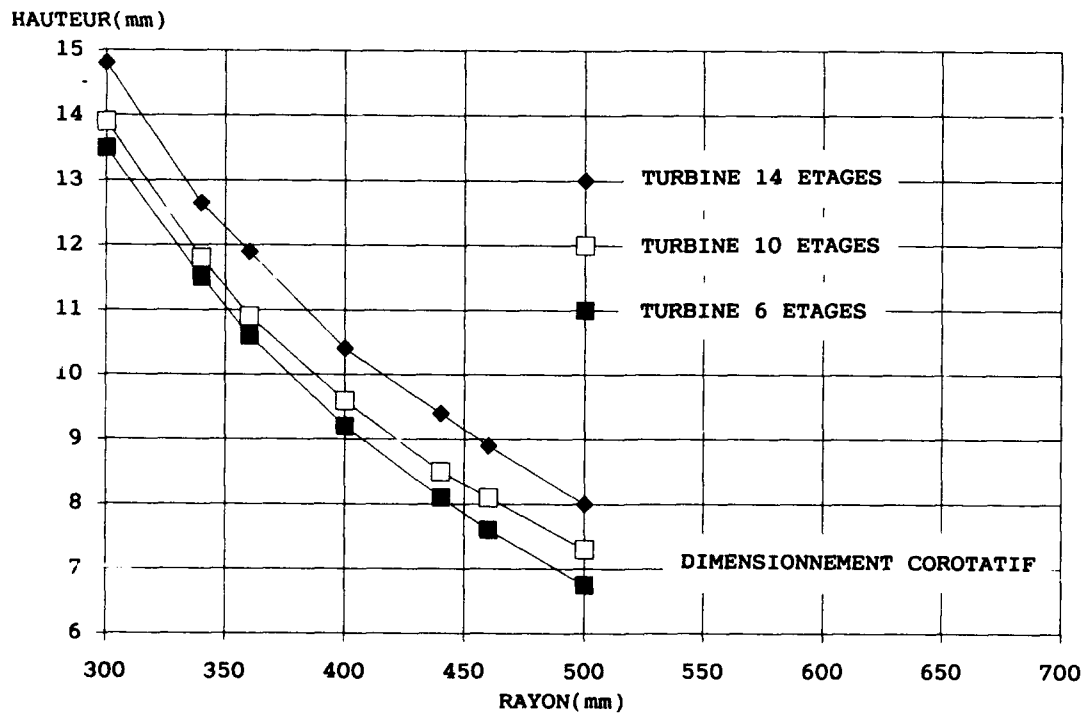
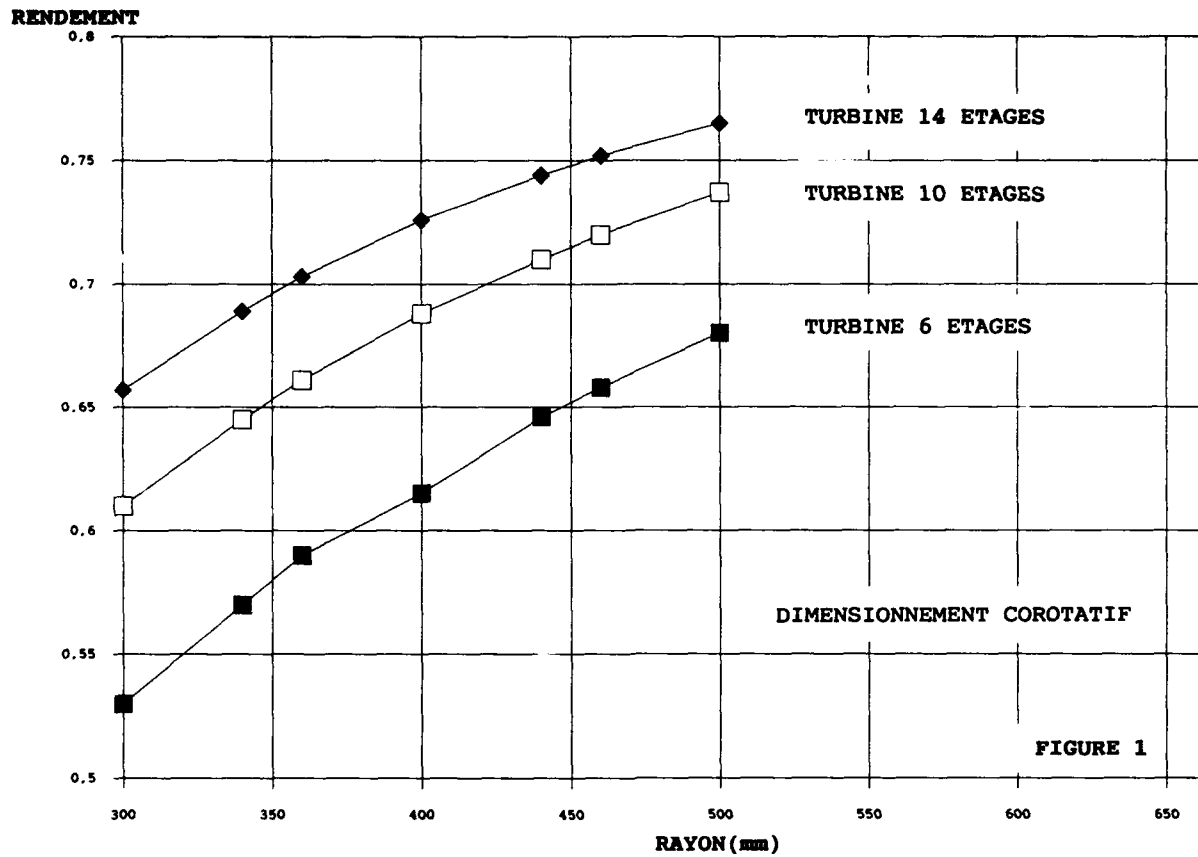


FIGURE 2

FIGURE 3

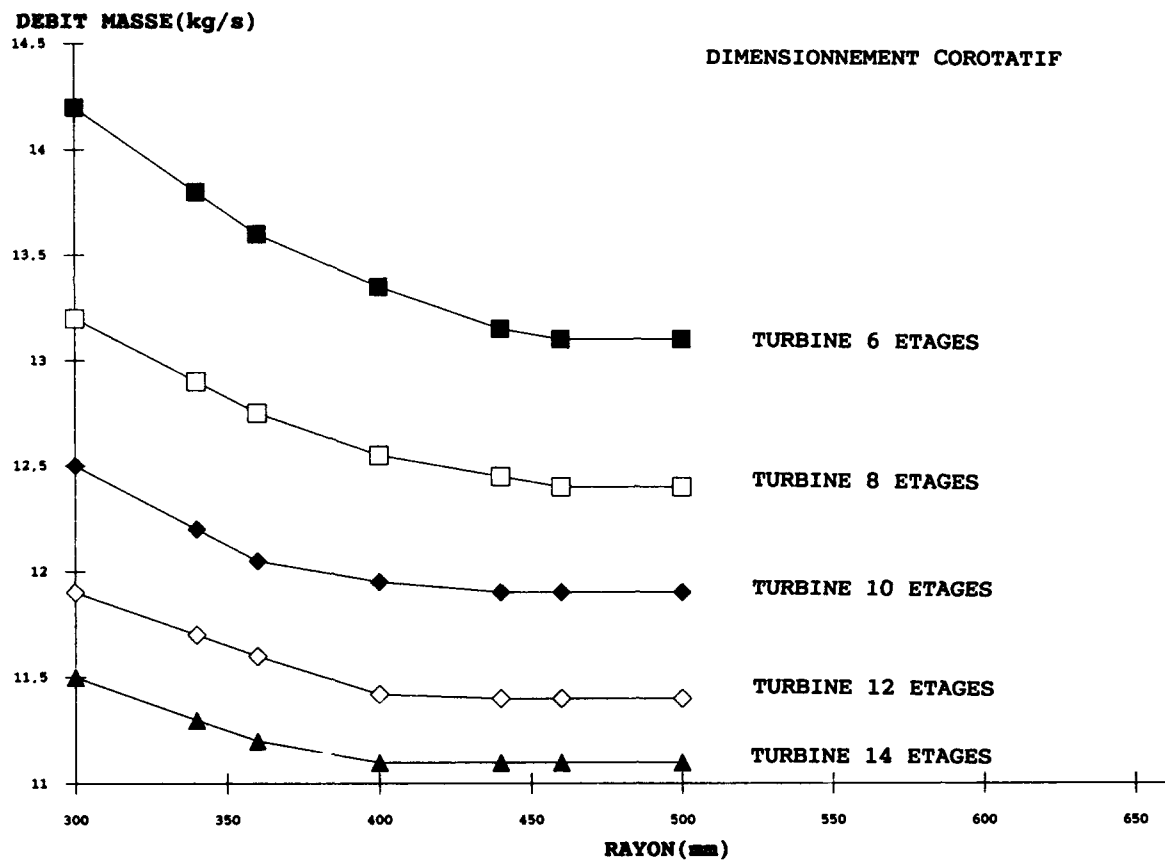
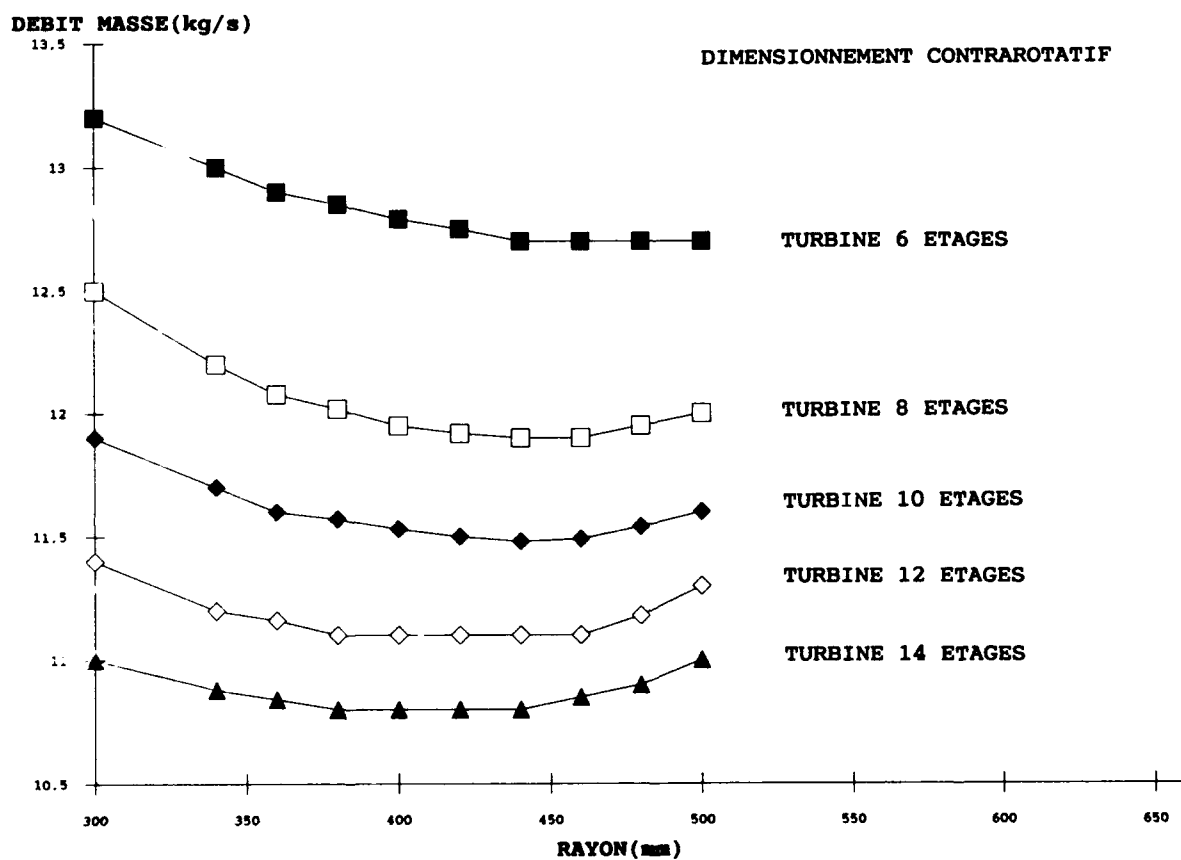
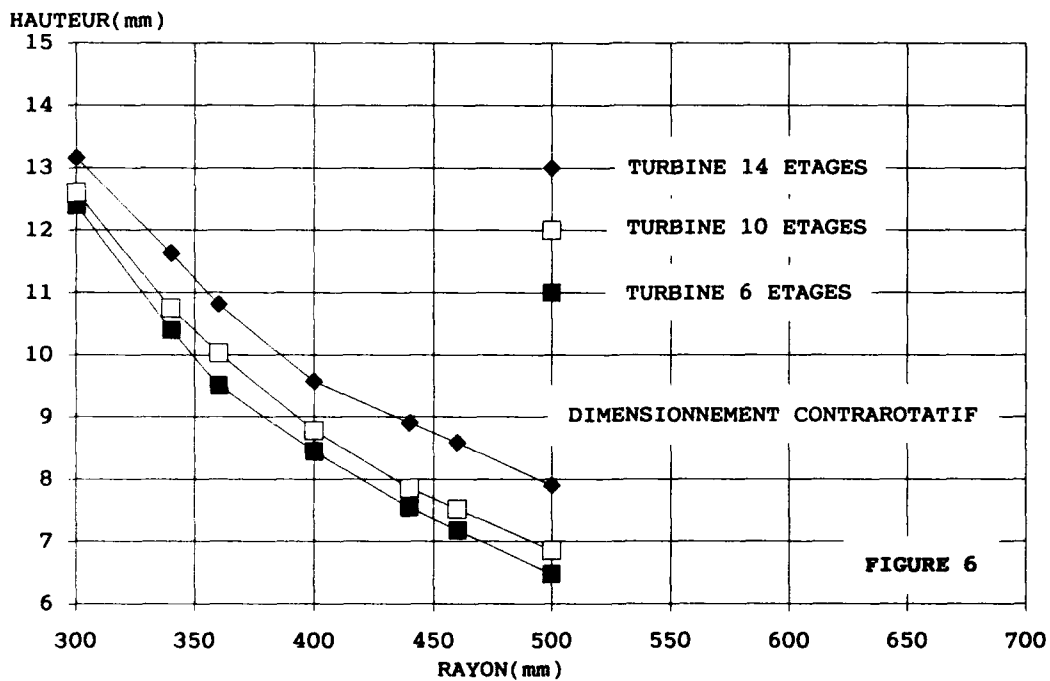
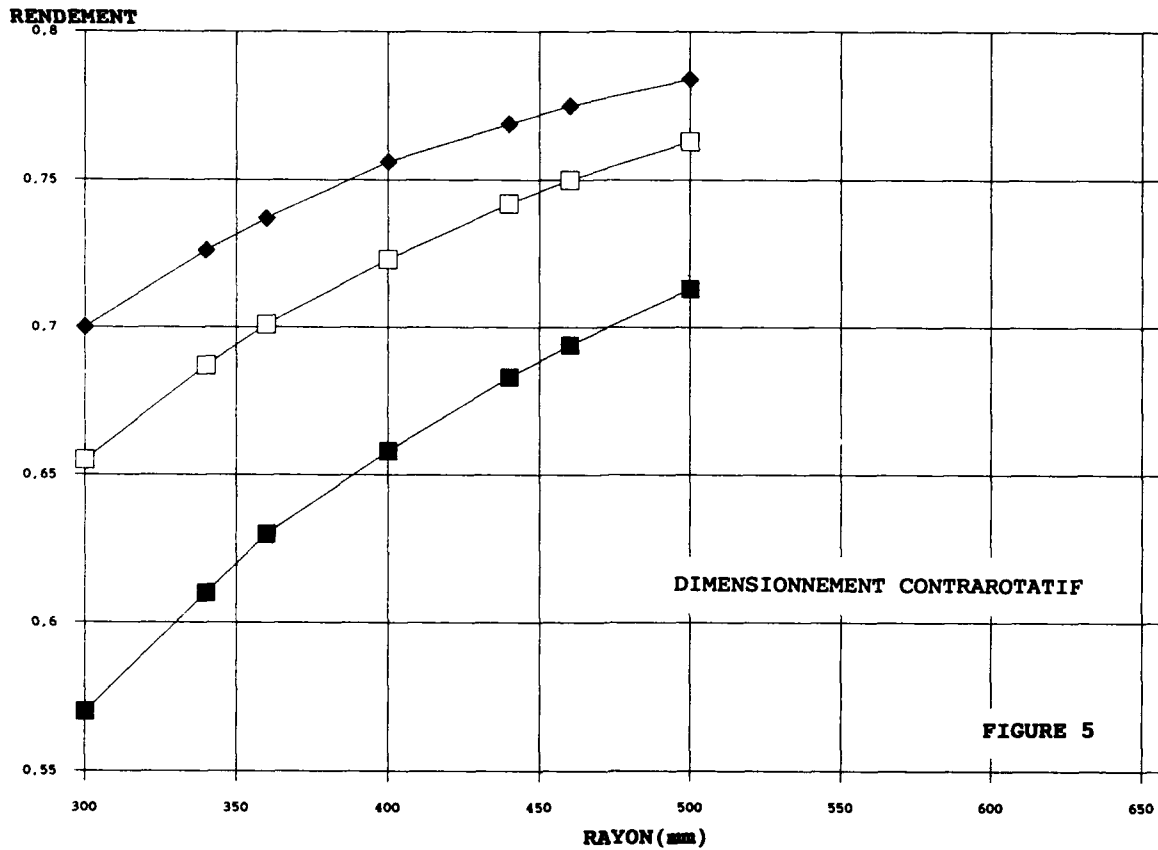
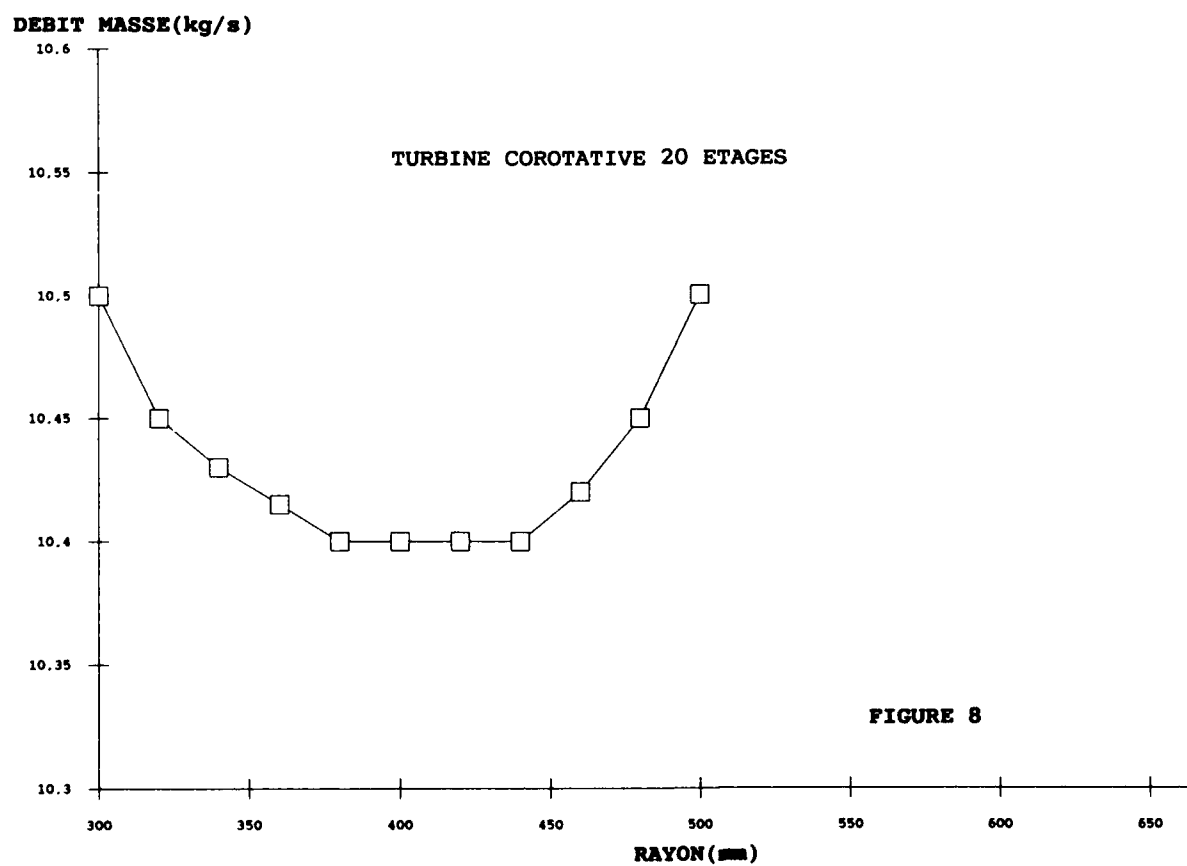
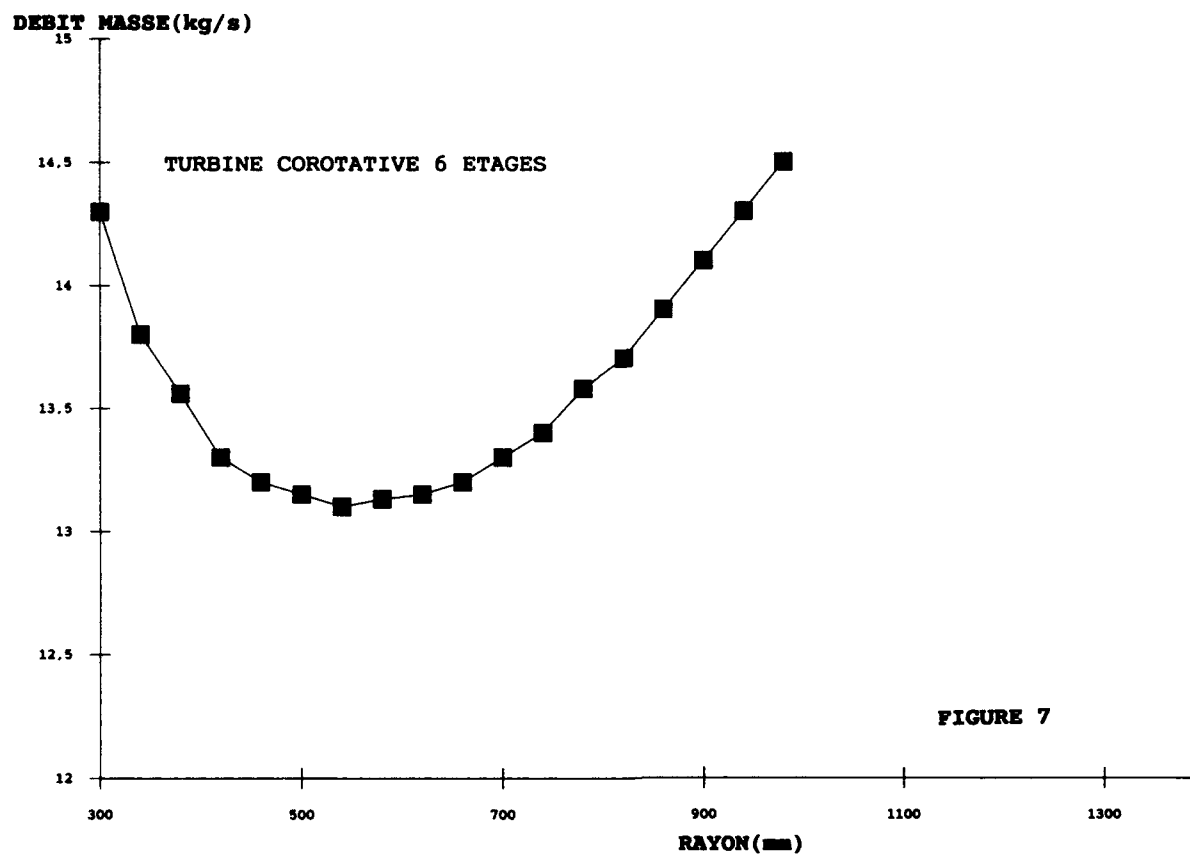


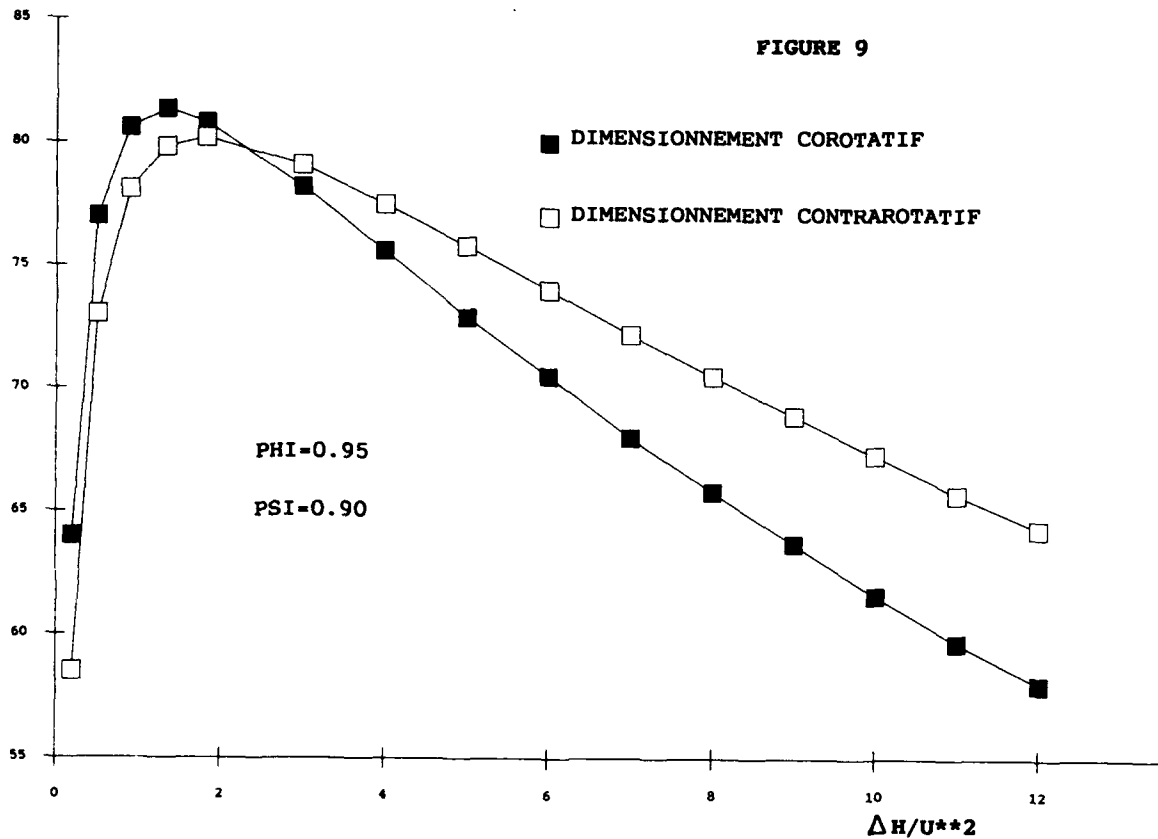
FIGURE 4



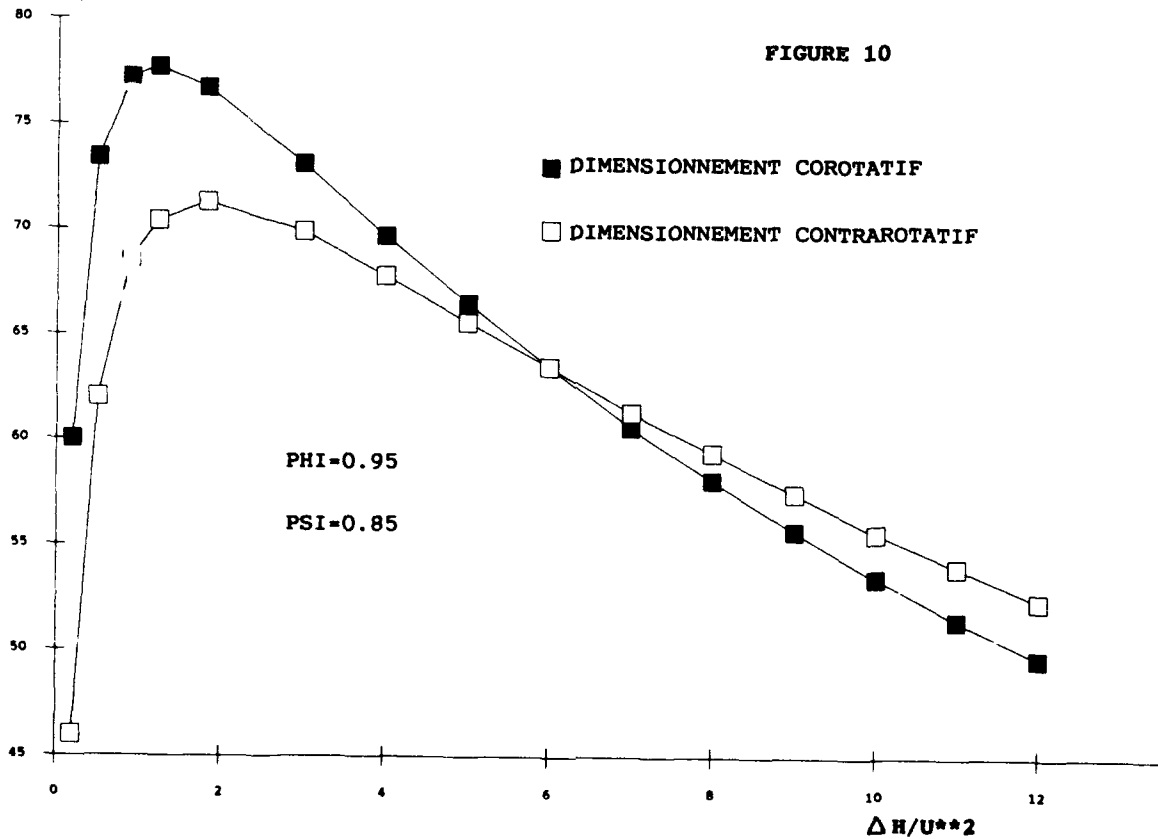




RENDEMENT



RENDEMENT



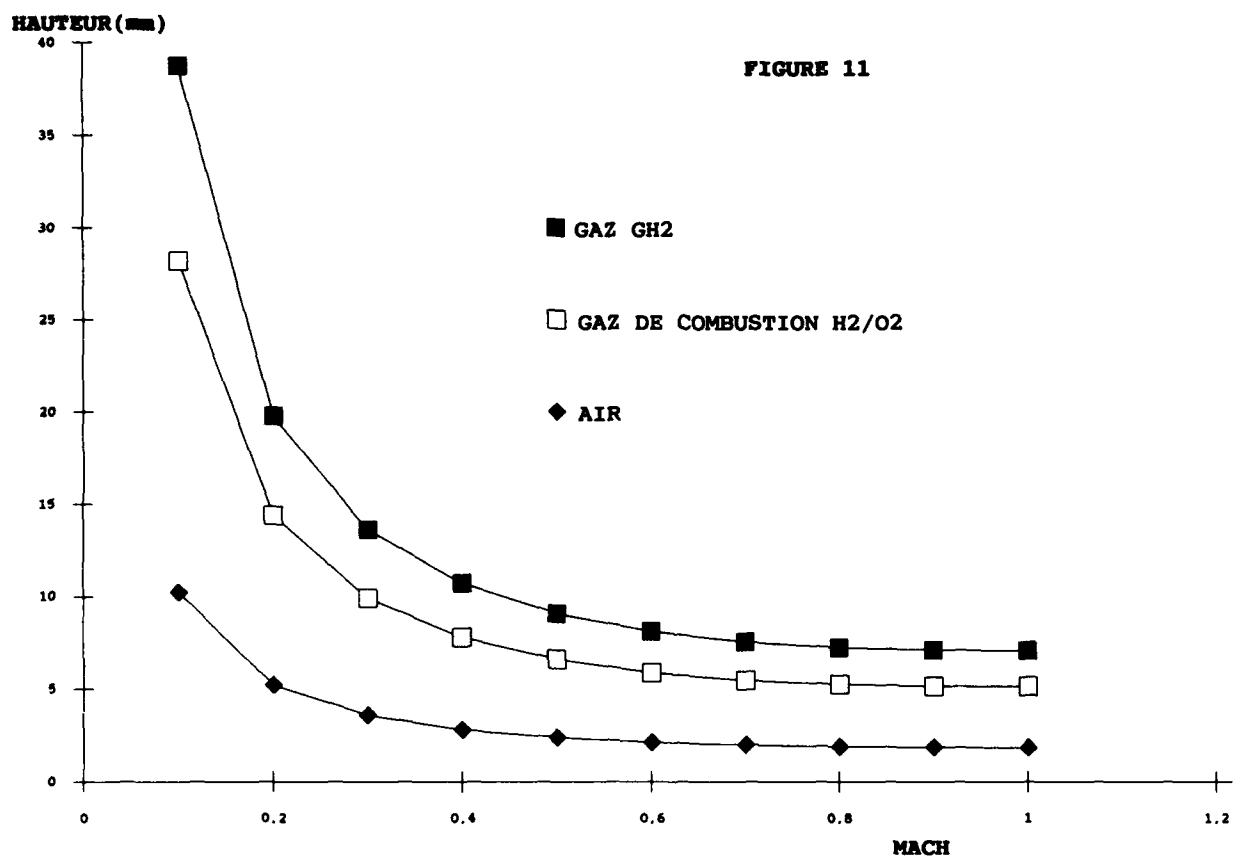
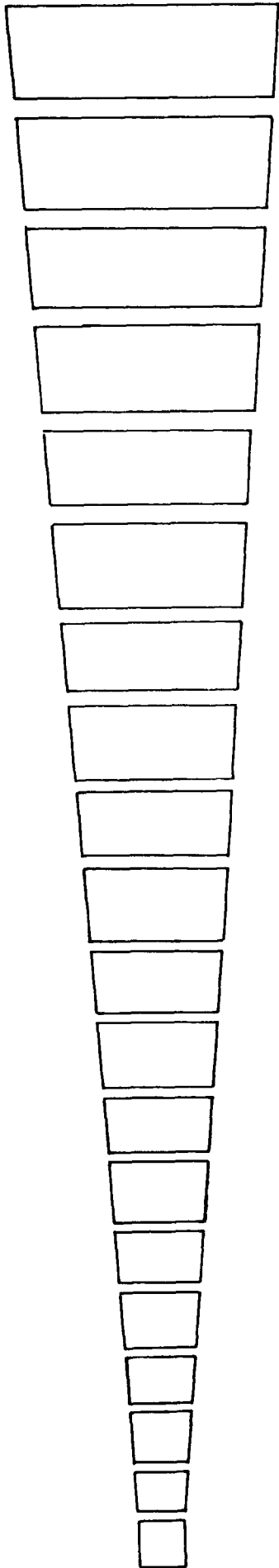




FIGURE 12

TURBINE 10 ETAGES  
COROTATIVE

VEINE AERODYNAMIQUE

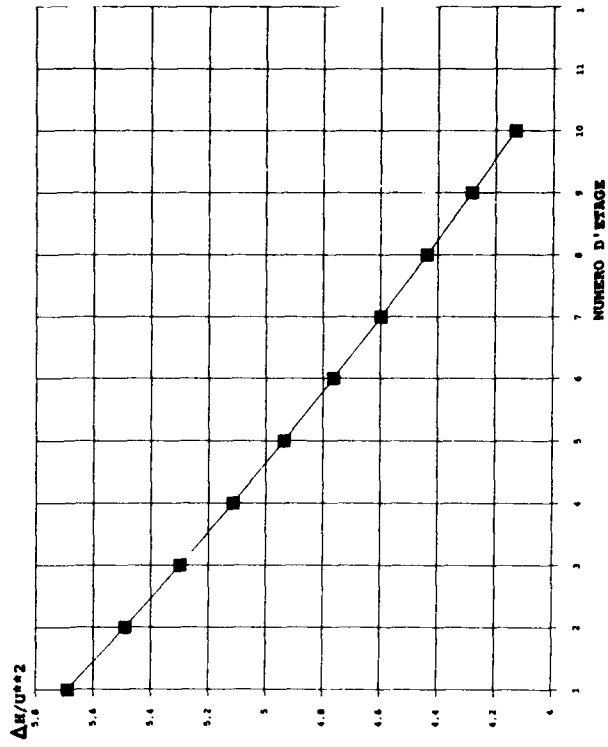
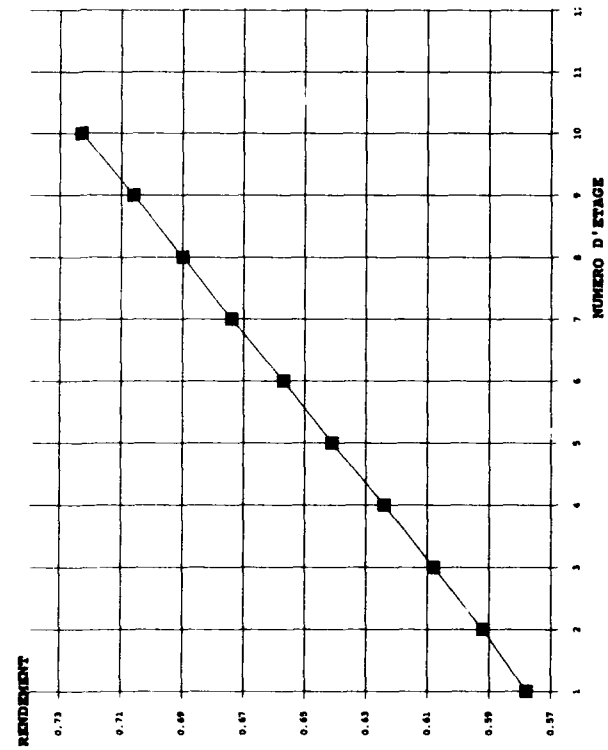
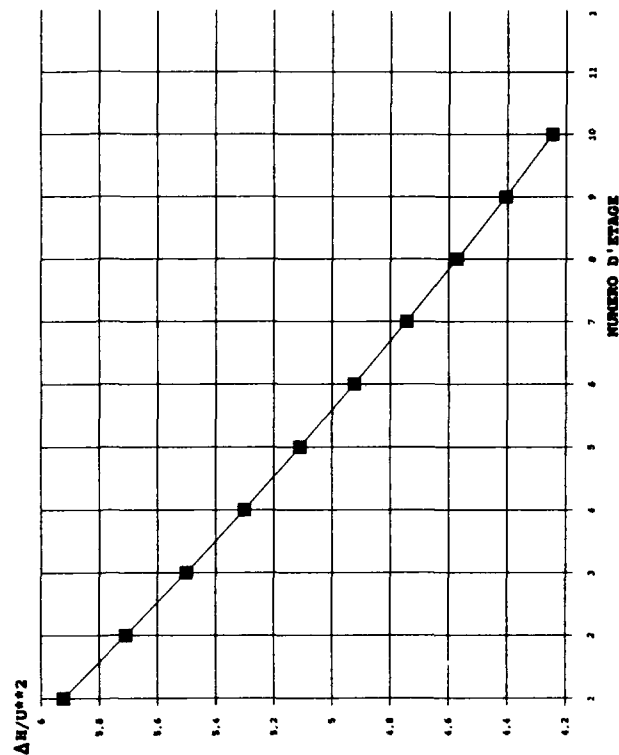
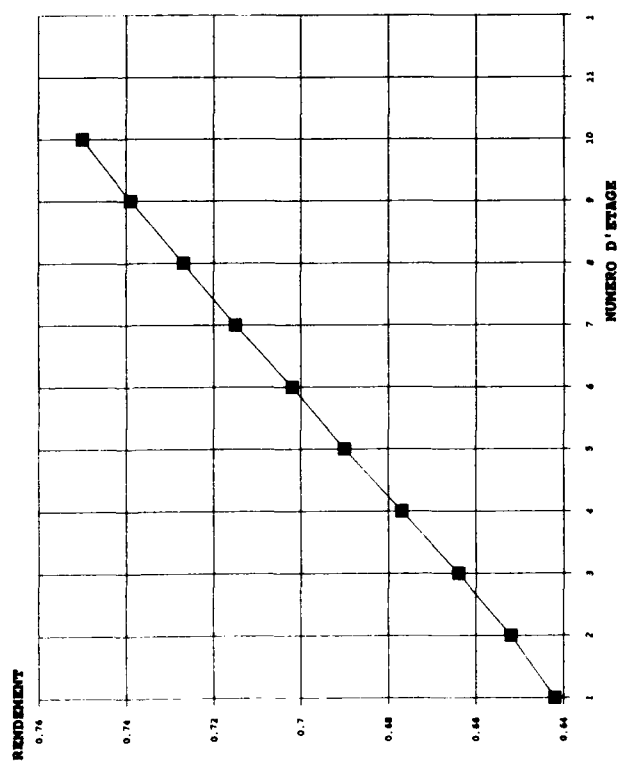
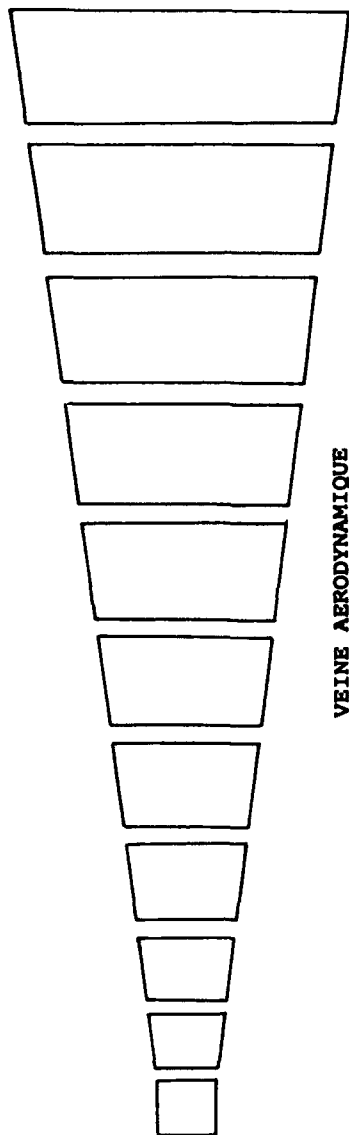


FIGURE 13

TURBINE 10 ETAGES  
CONTRAROTATIVE



## Discussion

HOURMOUZIADIS

You decided to keep  $(\Delta H/T_t)$  constant for all stages and you have a reduction of  $(\Delta H/u^2)$ . Since Mach numbers are very low, why do you decide to keep  $(\Delta H/T_t)$  constant?

AUTHOR'S REPLY

C'est un critère de dimensionnement que nous utilisons fréquemment. On aurait pu faire une étude en utilisant des répartitions de charge constantes sur tous les étages. Cela n'aurait pas modifié les conclusions. Ce critère peut être intéressant pour le fonctionnement hors nominal de la turbine.

# Aerodynamics and Stabilization of Combustion of Hydrogen Jets Injected into Subsonic Airflow

by

J. Koopman, M. Rachner, H. Wiegand, H. Eickhoff

DLR, Institut für Antriebstechnik  
Linder Höhe, 5000 Köln 90, West-Germany

## SUMMARY

The aerodynamics and stabilization of burning hydrogen jets, injected transversally into a subsonic airstream, have been investigated. The structural behaviour of deflecting cold and burning jets were studied by flow visualization. Experiments and numerical analysis on jet penetration have been performed. Flame extinction limits of "wake stabilized" flames were established and correlated.

## NOMENCLATURE

a	-	- constant used in relation (7)
A	$10^5 \text{ kg K/(m}^{1.5} \text{ s)}$	- parameter combination
Ar	$\text{m}^2$	- inlet area
b	m	- width of rectangular H <sub>2</sub> -injection hole
B	m	- channel width
d	m	- diameter of circular H <sub>2</sub> -injection hole
D	m	- combustion chamber diameter
H	m	- channel height
I	-	- momentum density ratio
l	m	- length of rectangular H <sub>2</sub> -injection hole
Kd	-	- constant in equation (2)
Lo	m	- characteristic length of particle path in the wake region
P	$\text{N/m}^2$	- chamber pressure
PH <sub>2</sub>	$\text{N/m}^2$	- total hydrogen pressure
T	K	- combustion temperature
T <sub>air</sub>	K	- air inlet temperature
TH <sub>2</sub>	K	- total hydrogen temperature
TH <sub>2</sub>	K	- hydrogen temperature in expanding jet = $\text{TH}_2 \times (\text{P}/\text{PH}_2)^{(\gamma-1)/\gamma}$
U <sub>air</sub>	m/s	- axial air velocity
U <sub>H<sub>2</sub></sub>	m/s	- axial hydrogen jet velocity
V <sub>air</sub>	m/s	- radial air velocity
V <sub>H<sub>2</sub></sub>	m/s	- radial hydrogen jet velocity
W <sub>air</sub>	m/s	- circumferential air velocity
W <sub>H<sub>2</sub></sub>	m/s	- circumferential hydrogen jet velocity
x	m	- axial coordinate
y	m	- radial coordinate
z	m	- circumferential coordinate
$\alpha$	deg	- jet expansion angle
$\gamma$	-	- ratio of specific heats
$\phi$	-	- equivalence ratio
$\rho$	$\text{kg/m}^3$	- density
$\tau_i$	sec	- induction time
$\tau_R$	sec	- residence time of a particle in the wake region

## 1. INTRODUCTION

In an ongoing national technology program airbreathing propulsion concepts are being investigated for vehicles capable of transporting considerable payloads to heights up to 30 km and flight Mach numbers up to 7. It implies combined turbo- and

ramjet propulsion systems. For ramjet operation the subsonic combustion mode leads to chamber pressures between 1.5 and 10.0 bars, as well as air inlet temperatures between 400 and 2000 K, depending on the flight Mach number  $/1/$ .

One turbo-/ramjet configuration is coaxially arranged. In this case, during the ramjet operation mode, the airflow is bypassing the inactive turbojet through an annular channel and then expands into the can-type combustion chamber. In order to illustrate the overall behaviour of the flow, an example of a 2D-numerical simulation of such a combustion chamber flow is shown in Fig. 1. The incoming flow is deflected towards the symmetry axis by a system of flow guides in order to avoid an inacceptably large wake region in which flow instabilities might occur and which, as numerical studies have shown, would retard mixing. In order to promote hydrogen-air mixing, hydrogen was assumed to be injected transversally from the guide vanes into the deflected air flow. The flow simulation was performed with a Finite Volume-Navier-Stokes-Code for solving turbulent reacting flow fields  $/2/$ . The hydrogen fuel was assumed to be injected through slots resulting in an axisymmetric flow field, and combustion was modelled by assuming chemical equilibrium. The upper part of Fig. 1 shows the flow-field, whereas the lower one shows some radial profiles of unreacted hydrogen. A major feature of the flow is the rather poor mixing of the hydrogen with the air, which is partially due to the assumption of slot injection.

At low flight Mach numbers the need for flame holding arises. One way of flame stabilization is to inject the fuel as discrete jets transversally into the air. In this case the fuel jet with its wake flow serves as a flame holder, whereas at high flight Mach numbers of the ramjet operation regime self-ignition occurs. Homogeneity in the circumferential hydrogen distribution would be promoted by the use of many small diameter hydrogen jets. On the other hand, homogeneity of the radial hydrogen distribution demands hydrogen jets with larger injection hole diameters. Moreover, flame stabilization favours larger diameter hydrogen jets, too. Therefore, in this paper aerodynamic and stabilization characteristics of burning jets injected transversally into a subsonic airstream are addressed in a combined experimental and theoretical study.

## 2. FLOWFIELD MODELLING

A fuel injection system might be formed by transverse jets arranged coaxially. In order to reduce the air flow rate, just one fuel element was studied in a rectangular windtunnel, Figs. 2 and 5. Fig. 2 shows the principal arrangement. This geometry corresponds to a row of jets at the wall of an annular inlet section of a combustion chamber, if the side walls of the channel are substituted by cyclic boundary conditions. This applies if:

- the chamber height  $H$  is small compared to the chamber diameter
- the jet interaction is small due to a high aspect ratio  $b/B$  and  $l/B$ .

The influence of these two different conditions, fixed wall and cyclic boundary conditions, was studied numerically.

The experimental results presented in this paper were obtained for different inlet conditions of air and  $H_2$ , as well as with  $H_2$ -jet diameters of  $d = 0.5$  mm, 1.0 mm and 2.0 mm. Details of chosen parameters will be given later. Also a rectangular  $H_2$ -jet with a  $0.5 \times 1.7$  mm  $H_2$ -injection hole was investigated.

A Finite-Volume-Code was used for solving the stationary 3D-Navier-Stokes-eqns. in primitive variables in a successive manner using the SIMPLE-pressure correction scheme on a nonstaggered grid. A standard  $k-\epsilon$ -model  $/3/$  was used and combustion was taken into account by a one-step-reaction, in which the reaction rate was assumed to be turbulence controlled and modelled by the Eddy-Break-Up-model  $/4/$ . It was not designed to account for combustion stabilization. The numerical flow calculations performed use for convenience rectangular  $H_2$ -jets of  $1 \times b = 0.5 \times 1.7$  mm and  $1.0 \times 3.4$  mm. All calculations were based on a  $43 \times 40 \times 17$  mesh.

The complexe nature of the deflecting  $H_2$ -jet is illustrated in Fig. 3. View A-A reveals a pair of vortices in the wake of the jet, which is crucial for flame stabilization. As the jet is deflected, so do the vortices. Therefore, they can be identified in the downstream crosssection B-B again. At the end of the calculation domain, 120 mm downstream of the jet center, the vortex pair still exists. The jet penetrates deeply into the crossflow, thereby interacting with the upper wall. Replacing the circumferential boundary condition of fixed walls by cyclic boundary conditions proved to have but little effect on all calculations presented. It assures that the results obtained for the channel geometry are indeed transferable to a row of weakly interacting jets.

An impression of the time mean jet spreading is given in Fig. 4. Lines of constant equivalence ratio  $\phi = 0.1$  are shown in crosssections downstream of the  $H_2$ -inlet. A characteristic kidney shape of the jet develops resulting from the deflected vortex pair. The value of  $\phi = 0.1$  was chosen, because it represents the lean burning limit of a well-stirred  $H_2$ -Air mixture.

### 3. EXPERIMENTS

To simulate the airflow conditions with respect to pressure and temperature a continuously operating blow-down windtunnel was used, Fig. 5 /9/. Air is fed from a pressure tank via a throttle valve into an electric air heater. In a nozzle downstream of a smoothing chamber the flow is accelerated before coming into the actual test section. The test chamber, which has a square flow passage of 25 x 40 mm, was manufactured from a forged block. The side walls are 25 mm thick quartz glass screens with a usable area of 190 x 40 mm. By means of inserts with cooling capability, wall temperatures can be adjusted up to 473 K, depending on the type of coolant. Mass flow is controlled by a critical nozzle upstream of the air heater. With another critical nozzle, upstream of the air cooler, the pressure level in the test chamber is maintained.

Gaseous hydrogen is injected through 0.5, 1.0 and 2.0 mm diameter wall bounded orifices. A specially adapted ignition and injection system was used. This system consists of coaxial metal pipes separated by an electrical insulation of teflon, forming the two poles for a high voltage driven spark which ignites the hydrogen flowing through the inner pipe. The air flow deflects the cold hydrogen jet. The electric spark ignites the mixture in the wake of the jet and the resulting flame on its turn ignites the main hydrogen jet, which is located downstream. For igniting the hydrogen jet a static pressure of at least 4.0 bars was necessary.

With air pressures up to 20 bars, temperatures up to 800 K and air velocities up to 120 m/s, it is possible to simulate conditions of the initial operation range of the ramjet mode at moderate flight Mach numbers.

The image of the luminous flame is recorded by a normal TV camera stored on a frame grabber in a PC and visualised at a connected monitor. The monitored grey-level distribution of the light intensity in the shadowgraph allows to define colour ranges.

The structural behaviour of burning and cold jets can be studied by using Schlieren flow visualization techniques. Because of the anticipated small refraction, due to the change in density in and around the hydrogen jet, an optical set-up was selected which allows an optimum utilization of the sensitivity of a Schlieren system. The illumination was done by means of a nanosecond pulsed light source (nanolite) /10/. If the camera, Fig. 6, is substituted by a Hycam high-speed camera and synchronized with the nanolite, each film frame - independent of the image frequency - is only exposed for 50 ns and hence the motion is frozen under the given assumptions. In this way it is possible to photograph extremely fast motions and resolve them in their micro-structure.

Fig. 7 shows two Schlieren images as an example of a cold (7a) and a burning (7b) hydrogen jet. In both cases the parameters were the same as in the calculated flowfield of Fig. 3. A review of all Schlieren images led to the following observations, more or less common to all cases studied :

- There exist sharp jet boundaries separating the jet flow from the flow of the surrounding air as can be seen in Fig. 7.
- These jet boundaries appear more clearly on the Schlieren images of the burning jets, due to the strong density gradients caused by combustion.
- A unique statement on the magnitude of the spreading of the burning jets compared to the cold ones could not be given, because the inner jet boundary could not be identified as clearly as the outer one. This was due to relative wide dark areas at the inner jet boundary on the photographs caused by the less steep, negative density gradients there. Additionally the images show structures outside the focal plane ( $z = 0$ ) of the Schlieren optics, which have, due to the kidney shape of the developing jet, (see Fig. 4) an effect on the image of the inner jet boundary.
- The burning and cold jets exhibit for all chosen flow parameters a micro-turbulence structure consisting of small turbulent eddies of the same order of magnitude  $O(0.5 \text{ mm})$ . In the case of the burning jets the jet boundaries exhibit more regular and roundish structures than for the cold jet flows.

An impression of the dynamic behaviour of the turbulence structure is given in Fig. 8, which shows three successive images taken from a burning hydrogen jet. The motion of large coherent structures can clearly be observed. The tracing of the moving structures on succeeding images allows the determination of the structure convective velocity. Values above the air inlet velocity are to be expected. For  $U_{\text{air}} = 35 \text{ m/s}$  values of 40-70 m/s increasing with axial position were found.

Evaluation of a complete series of high speed images revealed that the local macro-structure of the jet boundary began to form at the inlet of the jet and although being distorted - survived up to the end of the channel, passing the observation section in  $1/300 - 1/1000 \text{ sec}$ .

## 4 RESULTS

### 4.1 JET TRAJECTORIES

Long time Schlieren images represent the axial development of the time averaged jet penetration. A dimensionless form of the penetration curve is :

$$\frac{y}{\sqrt{x}} = f\left(\frac{x}{\sqrt{x}}\right) \quad (1)$$

where  $I$  is the momentum density ratio and  $d/I$  the momentum length scale. This dimensionless form was already used by Brzustowski /11/ in an analytical investigation and by Gollahalli et al. /12/ in an experimental investigation on diffusion flames in crosswind.

Plotting the dimensionless penetration function using a double-logarithmic scaling of the axes exhibits an approximately linear function. In Fig. 9 the correlations for burning hydrogen jets, using different pressure ratios and air inlet conditions given in Tab. 1, were plotted for three different injection diameters  $d = 0.5$  mm,  $1.0$  mm and  $2.0$  mm. An interesting feature of the plot is the approximately same slope found for all three diameters. It corresponds to a power law:

$$\frac{y}{d\sqrt{I}} = Kd \left( \frac{x}{d\sqrt{I}} \right)^{0.21} \quad (2)$$

where  $Kd$  is a constant depending on the diameter  $d$ . Fig. 9 exhibits a decrease of  $Kd$  with increasing jet diameter. Investigating cold jet flow for the same jet diameters the same tendency for  $Kd$  was found. This is in agreement with nonreacting jet penetration correlations given by Holdeman et al. /13/ and - for the plane jet - by Kamotani and Greber /14/. According to Holdeman /13/ the influence of the limited dimensions of the channel crosssection enters the penetration correlation by the  $H/d$  - and  $B/d$  - ratio, resulting in the observed decrease of  $Kd$  with increasing  $d$ . This effect could also be observed in the present numerical calculations of two burning jets with different rectangular injection areas ( $1 \times b = 0.5 \times 1.7$  mm and  $1.0 \times 3.4$  mm).

Table 1 : Parameter values used in Fig. 9

d	0.5	0.5	0.5	0.5	0.5	mm
PH2	11	7	11	31	21	bar
Pair	4	6	6	8.5	8.5	bar
Tair	271	271	271	279	279	K
Uair	34	42	40	61	63	m/s

d	1.0	1.0	1.0	1.0	1.0	mm
PH2	7	11	16	11	16	bar
Pair	6	6	6	8.5	8.5	bar
Tair	279	279	279	279	279	K
Uair	39	57	52	62	56	m/s

d	2.0	2.0	2.0	2.0	2.0	2.0	2.0	mm
PH2	8.6	9.5	10.25	11	12	13	14	bar
Pair	6	6	6	6	6	6	6	bar
Tair	279	283	282	282	282	282	282	K
Uair	56	52	50	48	48	45	39	m/s

Penetration trajectories for cold and burning jets of the same diameter  $d$  were also compared. For the smallest diameter investigated,  $d = 0.5$  mm, no systematic differences between data from cold and burning jets were recognizable within the scattering of the data. For  $d = 1.0$  mm a somewhat larger penetration of the burning jet compared to the cold one was found. This effect could be seen more distinct in case of  $d = 2.0$  mm, where the burning jet shows a much larger penetration than the cold jet, as demonstrated in Fig. 10. This figure is based on parameter variations given in Tab. 2.

In addition to the experiments on jets issuing from three circular hydrogen injection holes, a jet from a rectangular injection hole of  $1 \times b = 0.5 \times 1.7$  mm was investigated. It was found that the penetration was only little influenced by changing the hole orientation. The slope of the dimensionless, double logarithmic plots of the penetration curve turned out to be the same as in case of the three circular holes.

The burning jets from the rectangular holes were observed to penetrate deeper than the cold ones. This also applies to the jets from the circular holes. As an example Fig. 11 shows the penetration of a burning jet and its cold counterpart for the rectangular  $1 \times b = 0.5 \times 1.7$  mm (i.e spanwise orientated, cf. Fig.2) injection hole. As a fictive diameter  $d$  of the rectangular hole, the diameter of a circular hole of same cross-sectional area was used. This resulted in a value of  $d = 1.04$  mm used for non-dimensionalization.

It has been observed that a burning free jet without crosswind shows a somewhat smaller spreading rate compared to the corresponding cold jet /15/. Less spreading should result in a deeper jet penetration as it was observed in the present investigation.

Table 2 : Parameter values for Fig. 10. upper part : cold jet, lower part : burning jet

d	2.0	2.0	2.0	2.0	2.0	2.0	2.0	2.0	2.0	2.0	mm
PH2	6.24	7.05	7.9	8.6	9.5	10.25	11	12	13	14	bar
Pair	6	6	6	6	6	6	6	6	6	6	bar
Tair	279	279	279	279	283	282	282	282	282	282	K
Uair	67	67	67	67	67	67	67	68	68	68	m/s

d	2.0	2.0	2.0	2.0	2.0	2.0	2.0	mm
PH2	8.6	9.5	10.25	11	12	13	14	bar
Pair	6	6	6	6	6	6	6	bar
Tair	279	283	282	282	282	282	282	K
Uair	56	52	50	48	48	45	39	m/s

The experimental investigations were accompanied by numerical flow simulations. Experimentally observed jet boundaries obtained from the Schlieren images correspond to a narrow zone of high density gradients. It appeared reasonable to define the radially outer trajectory of a line of constant equivalence ratio  $\phi$  as the outer calculated jet boundary. The steep gradients of the equivalence ratio at the outer jet edge for the burning as well as for the cold jets cause only a modest sensitivity of the calculated jet boundary on the choice of the  $\phi$ -value traced. In this study a value of  $\phi = 0.1$  was used as it represents the flammability limit of a hydrogen - air mixture /8/. A typical plot of calculated equivalence ratio isolines  $\phi = 0.1$  in all x,y-planes projected on each other can be seen in Fig. 12. The flow case is the same as used in Fig.11. The outermost contour of all projections of  $\phi$  - isolines was taken from Fig. 12, nondimensionalized and sketched in Fig. 11 together with the already discussed penetration trajectories taken from the long time exposure Schlieren images. The same was done for the cold jet with exactly the same parameters chosen. Considering Fig. 11 it can be seen that the calculated cold jet penetration curve exhibits the same slope as found in the experimentally obtained penetration of the cold and burning jet. However, the calculation shows somewhat higher values of penetration. For the burning jet the different slope of the calculated penetration curve compared to the measured data points reveals deficiencies of the numerical flow simulation which might be due to the turbulence as well as the combustion model used. Especially the combustion model is not adequate at the jet base, where it predicts a too fast heat release. Another reason for the observed differences may be a grid dependence of the numerical solution, resulting from the need for a finer grid in the vicinity of the jet base. This asks for a zonal grid scheme.

#### 4.2 FLAME EXTINCTION

Under suitable operating conditions a transverse jet acts as its own flameholder. The wake region depends on the air flow Reynolds number, based on the jet diameter. For the flow around a cylindrical body, combustion promotes the establishment of a well defined steady vortex pair in the wake /16/. Such a counterrotating vortex pair whose rotational axis shows the same orientation as the deflecting mean jet flow, can be identified in the flowfield shown in Fig. 3. The combustion products recirculate and transfer heat into the cold fresh mixture, until ignition occurs. In this way flame stabilization is established by the vortex pair.

The upper part of Fig. 13 represents a digitalized direct photograph of a jet flame, manipulated to distinguish discrete zones of different brightness. It can be



speculated that the high level of brightness visible as the left white spot in this figure corresponds to the region of strong heat release in the wake of the jet. In the lower part of Fig. 13 a separation between non-reacting cold hydrogen and fresh ignited hydrogen is possible.

Before presenting experimental results parameters influencing flame stabilization will be discussed. Following the hypotheses of /17/, /18/ flame blowoff is determined by the ratio of the induction time  $\tau_i$  and a characteristic residence time  $\tau_R$  of a gas particle along its path in the wake of the jet. The burning jet is expected to reach its blowoff limit if the residence time  $\tau_R$  falls below the induction time  $\tau_i$ , that is:

$$\frac{\tau_R}{\tau_i} < 1 \quad (3).$$

The induction time is determined by reaction kinetics and is a characteristic measure of the time needed for the air-fuel mixture to react. Sousonov et. al /17/ give a formulation for  $\tau_i$  for hydrogen air combustion, where  $\tau_i$  exhibits an inversely proportional dependency on the pressure  $P$ , and an Arrhenius type dependency on the resulting combustion temperature. An additional term expresses the influence of mixture equivalence ratio on  $\tau_i$ . For a crude estimation it is sufficient to keep in mind that  $\tau_i$  increases if  $P$  or  $T$  decrease or the mixture composition moves away from stoichiometry :

$$\tau_i = f \left( \frac{1}{P}, \frac{1}{T}, |\phi - 1| \right) \quad (4).$$

Forming  $\tau_R$  by a characteristic length  $L_o$  of the recirculation region and the free stream air velocity  $U_{air}$  we get :

$$\tau_R = \frac{L_o}{U_{air}} \quad (5).$$

As  $L_o$  is a measure for the extent of the wake it is expected to enlarge with jet injection diameter  $d$  and the jet expansion angle. The jet expansion angle has a first order one dimensional dependence on the jet pressure ratio  $PH_2/P$ . We now get for the stability relevant ratio (3) :

$$\frac{\tau_R}{\tau_i} = f \left( P, T, \frac{1}{U_{air}}, d, \frac{1}{|\phi - 1|}, \frac{PH_2}{P} \right) \quad (6).$$

Flow parameter changes which increase  $\tau_R/\tau_i$  are expected to stabilize the flame. From relation (6) we therefore expect the following tendencies: Raising chamber pressure, hydrogen pressure ratio, jet injection diameter or reducing air velocity have stabilizing effects on the flame. The combustion temperature  $T$  in the wake will principally rise if the inlet temperatures of air or hydrogen rise, causing a stabilizing effect according to (6).

In the present investigation the blowoff limits of the hydrogen flame were determined by continuously diminishing the hydrogen pressure for constant hydrogen temperature and constant chamber pressure. A decrease of the jet pressure ratio has a destabilizing effect according to relation (6). This results in a flame blowoff if the jet pressure ratio falls below a limiting value. This pressure ratio was chosen as the dependent variable for the stability measurements. This means stability influencing changes in the independent parameters chosen were compensated by the needed change in the observed limiting  $PH_2/P$ -value to arrive at the blowoff limit.

Fig. 14 shows some results demonstrating the influence of air inlet conditions  $U_{air}$ ,  $T_{air}$  and  $P_{air}$  on stability for a circular hydrogen injection hole with diameter  $d = 0.5$  mm. The results confirm the tendencies expected from relation (6). Fig. 14 already exhibits the problem to find a suited entity reducing the many curves if possible. Using the combination:

$$A := \hat{P} \left( \hat{TH}_2 + a \hat{T}_{air} \right) \sqrt{d} / \hat{U}_{air} \quad (7)$$

where " $\hat{\phantom{x}}$ " denotes values registered immediately before extinction of the flame. Here " $a$ " is a constant obtained from experiment to be  $a = 0.27$ . As abscissa for the plots " $A$ " reduced the many different curves to approximately one functional dependency shown in Fig. 15. It is based on a curve fitting of measurements for parameter combinations using the values of Tab. 3.

Table 3 : Parameter values used for Fig. 15, for constant hydrogen temperature of 290 K

d	1.0	0.5	0.5	0.5	mm
$T_{air}$	290	290	423	573	K
$P_{air}$	2-8	2-12	3-8	3-9	bar
$U_{air}$	30-90	30-80	40-90	55-95	m/s

In addition to the experiments on blowoff limits of transverse jet flames with circular injection holes, experiments on jet flames issuing from a rectangular injection hole ( $1 \times b = 0.5 \times 1.7$  mm of Fig.2), the larger dimension orientated spanwise, were also performed. For the investigated flow parameter range of Tab. 4 the flame could only be extinguished at very low values of the hydrogen pressure ratio :  $P_{H2}/P \approx 1$ . This low pressure ratio was found even for the lowest value of the argument  $A = 0.23$  of relation (7), obtained from the investigated flow parameter combinations of Tab. 4. Consequently this means a considerable improved stabilization of the rectangular jet flames compared to the circular jet flames (cf. Fig. 14). The inserted value of the diameter needed to calculate A was  $d = 1.04$  mm belonging to a fictive circular injection hole with the same crosssectional area as the used rectangular hole.

Table 4 : Operational values for the jet with rectangular injection crosssection

Injection	$1 \times b = .5 \times 1.7$			mm
Tair	293	423	573	K
Pair	2-10	2-10	2-10	bar
Uair	40-90	50-110	65-125	m/s

## 5. CONCLUSIONS

Transverse jet flames are stabilized by recirculating hot combustion products in their wakes at a wide range of conditions. The stabilization range for jet flames issuing from a rectangular jet, with the main dimension orientated spanwise, appeared to be remarkably larger than that for jet flames with circular injection holes. In a first order approach the penetration trajectories of the outer jet boundary, which is controlled by large coherent structures, characterize the mixture behaviour of the observed jets.

Numerical calculations, showing details of the flowfield, are able to predict fairly well jet penetration. Optical methods, like shadow- and Schlieren methods give insight into the interactions of the injected gaseous hydrogen jet with its environment. Short time exposure Schlieren photography illustrates the structure of the jet, high-speed Schlieren cinematography gives an impression of the jet structure dynamics. By long time exposure Schlieren photography the penetration trajectories were determined.

The penetration trajectories show :

- the same functional dependency of the penetration on  $x/d$  and the momentum density ratio  $I$ ,
- a dependence on the diameter of the orifice,
- differences between non-burning and burning jets.

Extinction limits were analyzed experimentally and correlated.

## 6. REFERENCES

- /1/ Kremer, F.J.G. Trajectory optimization considerations for ramjet engines 75th AGARD Symposium of the Propulsion and Energetics Panel on Hypersonic Combined Cycle Propulsion, 28.5.-1.6.90, Madrid, Spain.
- /2/ Chatwani, A.  
Eickhoff, H.  
Koopman, J.  
Neuberger, W. Entwicklung von Rechenverfahren zur Bestimmung der Schadstoffemissionen von Gasturbinen. FVV-Abschlußbericht Vorhaben Nr. 240, FVV-Forschungsberichte Verbrennungskraftmaschinen Heft 319, 1982.
- /3/ Eickhoff, H.  
Koopman, J.  
Neuberger, W.  
Rachner, M. Entwicklung eines Berechnungsverfahrens zur Bestimmung der dreidimensionalen Strömungs- und Verbrennungsvorgänge in Gasturbinenbrennkammern, FVV-Abschlußberichte Verbrennungskraftmaschinen Heft 363, 1985.
- /4/ Spalding, D.B. Mathematical models of continuous combustion, in: Emissions of continuous combustion systems, edited by W. Cornelius and W.G. Agnew, Plenum Press, New York, 1972.
- /5/ Coelho, S.L.V.  
Hunt, J.C.R. The dynamics of the near field of strong jets in cross flows Journal of Fluid Mechanics, vol. 200, pp 95 - 120, 1989.
- /6/ Heister, S.D.  
Karagozian, A.R. Vortex Modelling of Gaseous Jets in a Compressible Crossflow Journal of Propulsion, Vol. 6, no. 1, pp. 85 - 91, 1990.

- /7/ Karagozian, A.R.  
Manda, B.V.S. Flame Structure and Fuel Consumption in the Field of a Vortex Pair, Combustion Science and Technology, vol. 49, pp. 185 - 200, 1986.
- /8/ McCarty, R.D. Hydrogen technological survey - thermophysical properties NASA SP-3089, 1975.
- /9/ Bäumer, K.  
Hartje, J.  
Müller, J.  
Schlundt, D.  
Wanders, K.  
Wiegand, H. Ein Prüfstand zur Simulation dieselmotorischer Gemischbildungsvorgänge, DFVLR-Mitteilung 81-27 (1981).
- /10/ Fischer, H. Ultra-Kurzzeit-Aufnahmen der Grenzschichtstrukturen schneller Strömungsvorgänge, Chemie-Ingenieur-Technik 34, pp. 118 - 119 (1962).
- /11/ Brzustowski, T.A. Hydrocarbon turbulent diffusion flame in subsonic cross-flow in: Turbulent combustion, edited by L.A. Kennedy, AIAA New York, pp. 407 - 430, 1978.
- /12/ Gollahalli, S.R.  
Brzustowski, T.A.  
Sullivan, H. F. Characteristics of a turbulent propane diffusion flame in a cross-wind, Trans. C.S.M.E., 3, 205, 1975.
- /13/ Holdeman, J.D.  
Srinivasan, R.  
White, C.D. An empirical model of the effects of curvature and convergence on dilution jet mixing, AIAA-88-3180, 1988.
- /14/ Kamotani, Y.  
Greber, I. Experiments on confined turbulent jets in cross flow, NASA CR-2392, 1974.
- /15/ Kremer, H. Zur Ausbreitung inhomogener turbulenter Freistrahlen und turbulenter Diffusionsflammen, Dissertation, Technische Hochschule Karlsruhe, 1964.
- /16/ Glassman, I. Combustion, Academic Press, 2nd ed. 1987.
- /17/ Sosounov, V.A.  
Annoushkin, Yu.M.  
Sverdlov, E.D.  
Pajy, D.G. Investigation of hydrogen diffusion flames in direct-flow combustors, Proc. of the 7th World Hydrogen Energy Conf., Hydrogen Energy Progress VII, pp. 2009 - 2024, Pergamon Press 1988.
- /18/ Winterfeld, G. Untersuchungen über die Stabilisierung von Wasserstoff-Diffusionsflammen durch Flammenhalter in Überschallströmungen DFVLR-Forschungsbericht, DFVLR-FB-76-35, 1976.

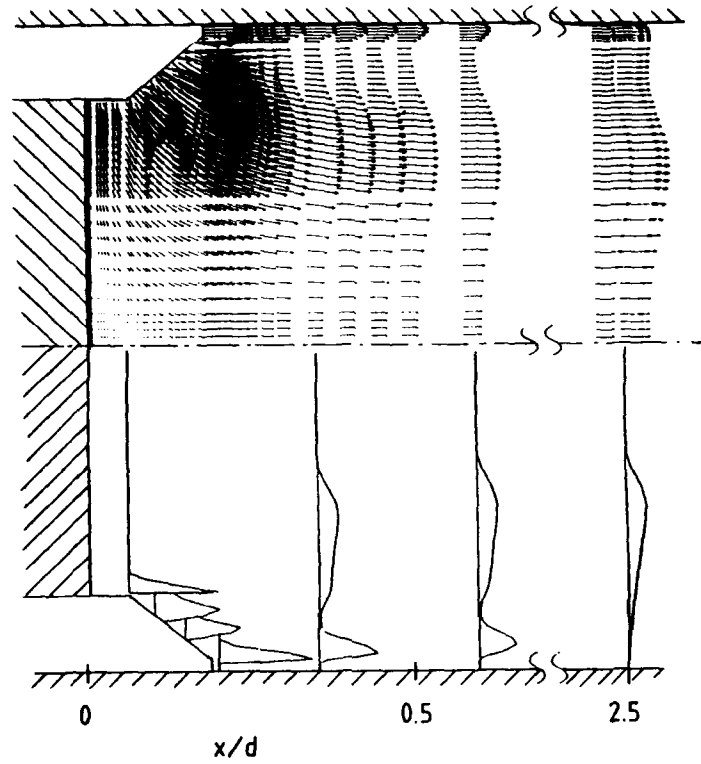


Fig. 1 Ramjet Combustion Chamber.  
 - upper part: Flowfield  
 - lower part: Profiles of Unburned Hydrogen Volume Fraction

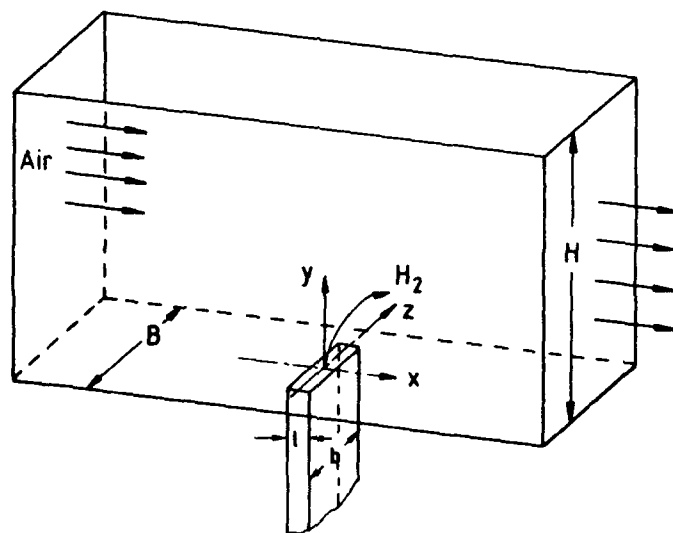


Fig. 2 Basic Channel Geometry.

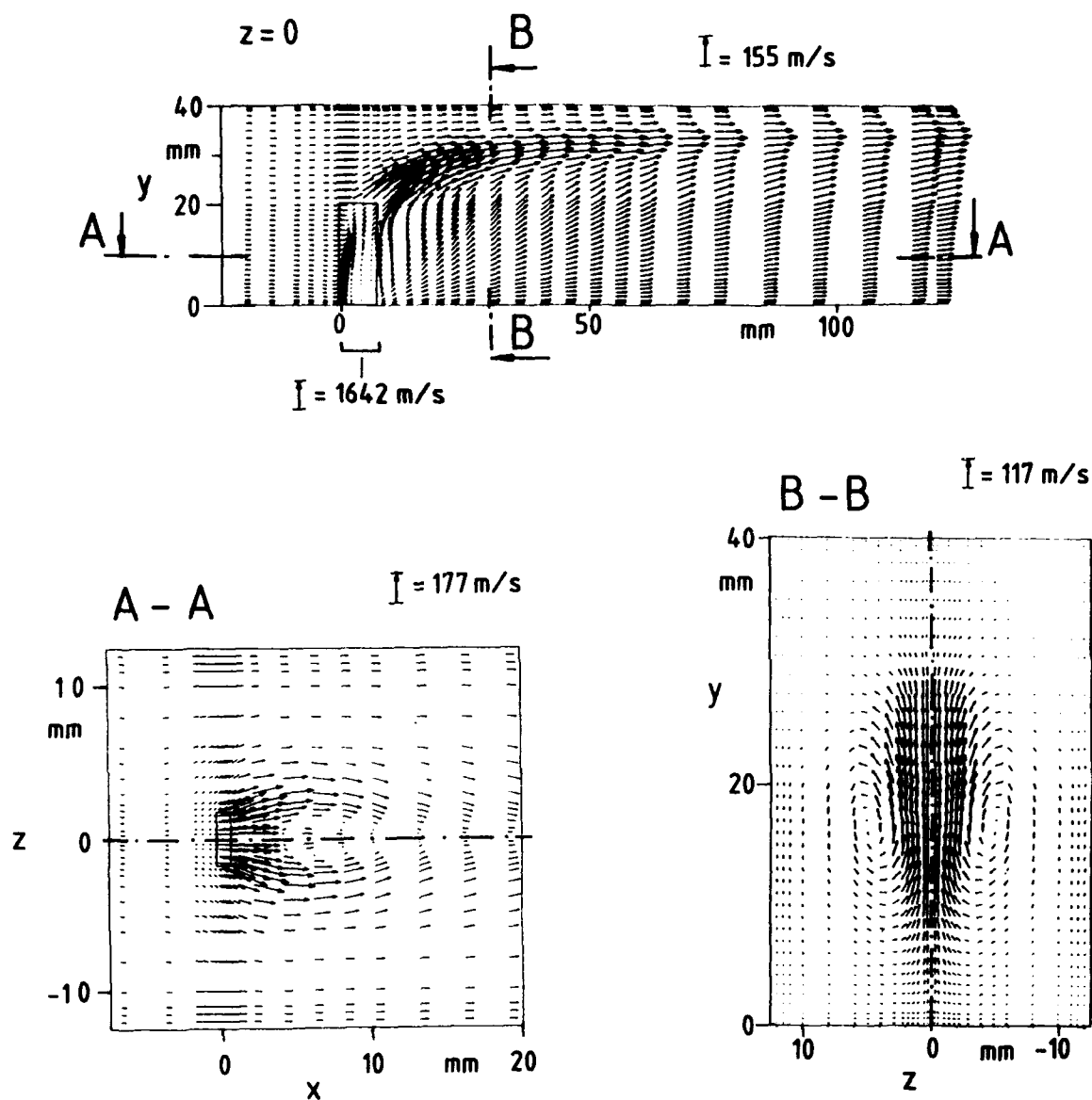


Fig. 3 Flowfield of a Burning H<sub>2</sub>-Jet in Air-Crossflow.  
 (U<sub>air</sub> = 31 m/s, P<sub>air</sub> = 6 bars, V<sub>H<sub>2</sub></sub> = 1150 m/s, I = 95, H<sub>2</sub>-Injection hole  
 1 × b = 1.0 × 3.4 mm)

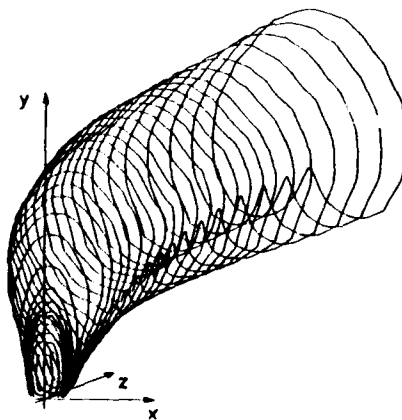


Fig. 4 Perspective View of Calculated Equivalence Ratio Isolines  
 $\phi = 0.1$  of a Burning H<sub>2</sub>-Jet in Air-Crossflow.

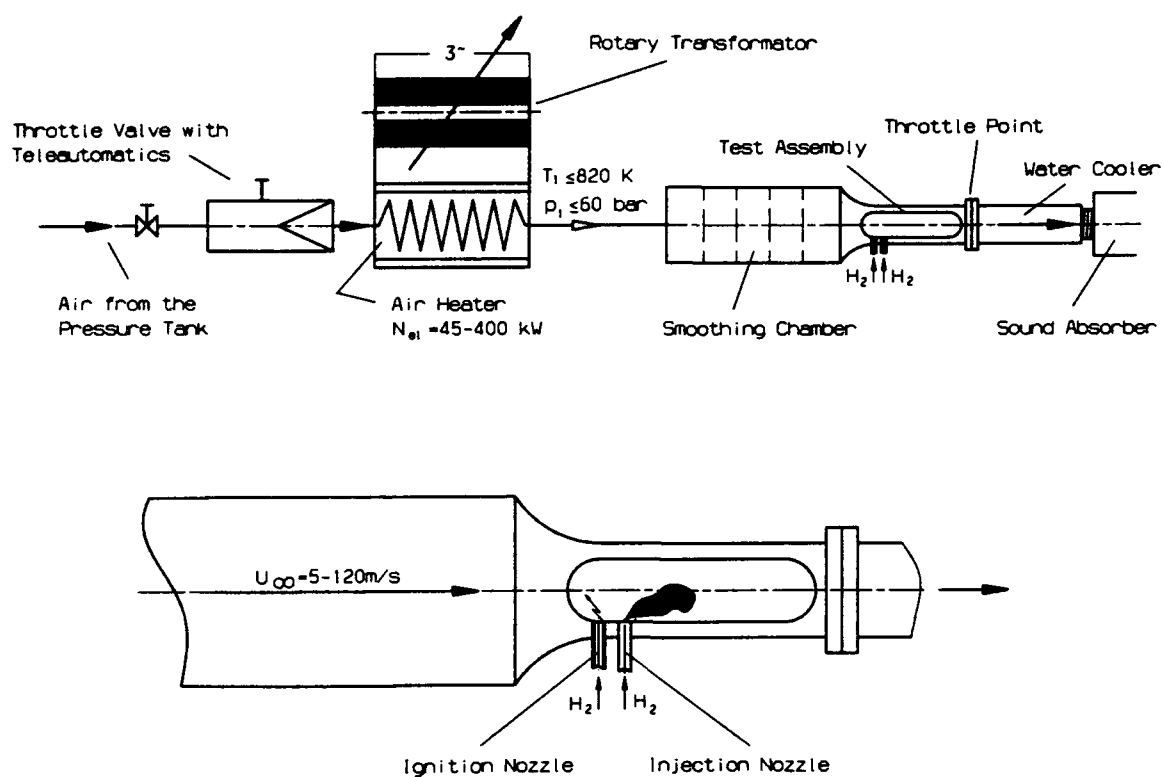


Fig. 5 Schematic Arrangement for the Supply with Compressed Air for Mixture Formation in the Test Chamber incl. the Ignition and Hydrogen Injection System.

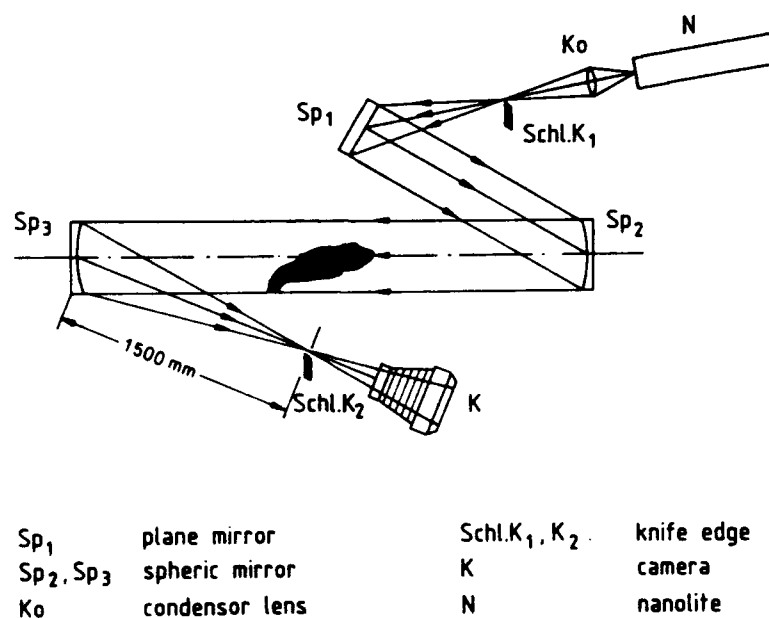


Fig. 6 Schlieren Set-up.

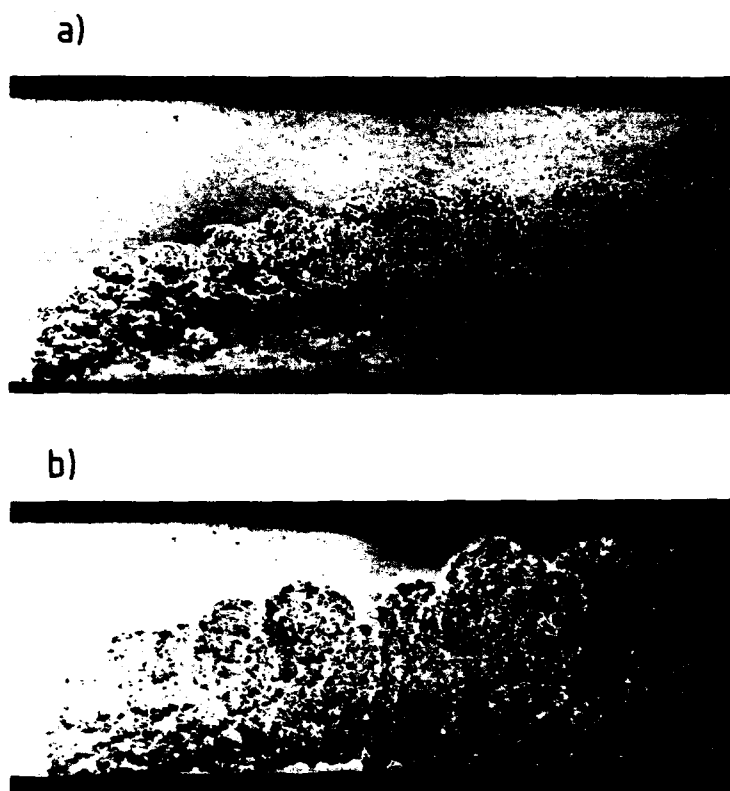


Fig. 7 Schlieren Images of the Deflecting Jet.  
 a) Cold Jet Flow  
 b) Burning Jet Flow

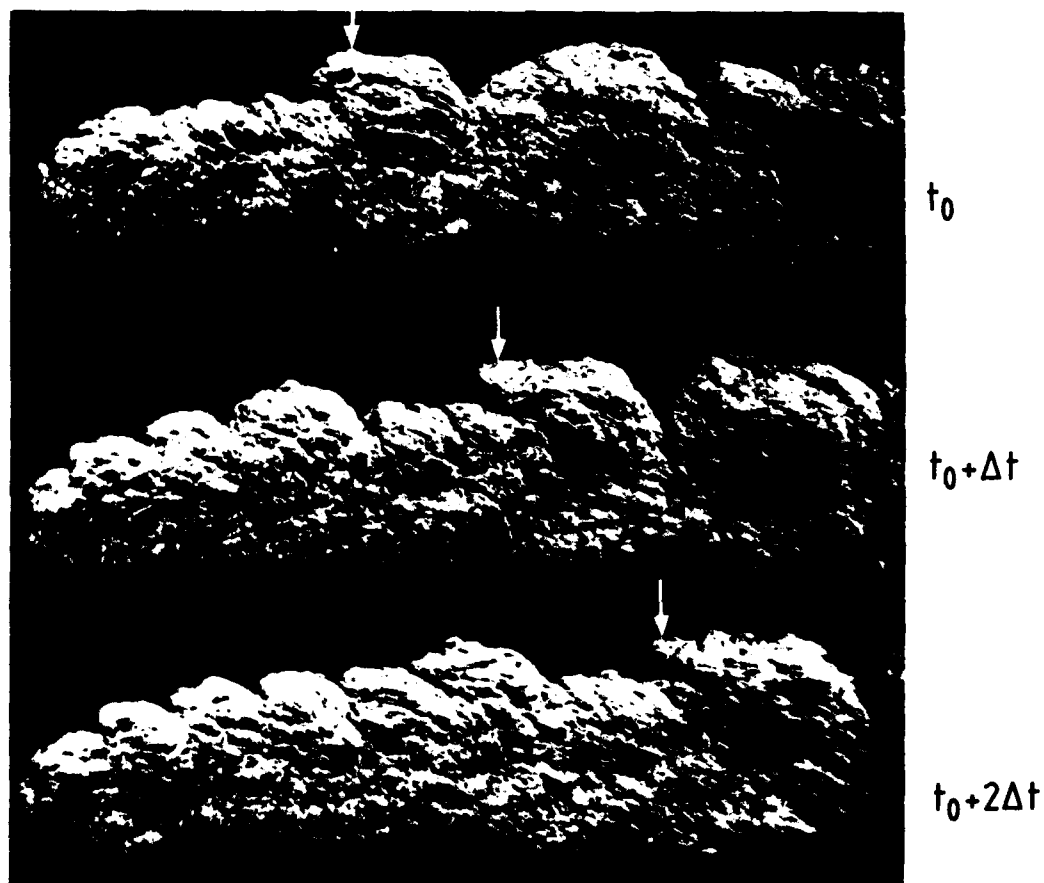


Fig. 8 Time Sequence of Schlieren Images ( $\Delta t = 3/5000$  sec.) of Deflecting Jet.  
 ( $U_{air} = 35$  m/s,  $VH_2 = 1190$  m/s,  $d = 0.5$  mm)

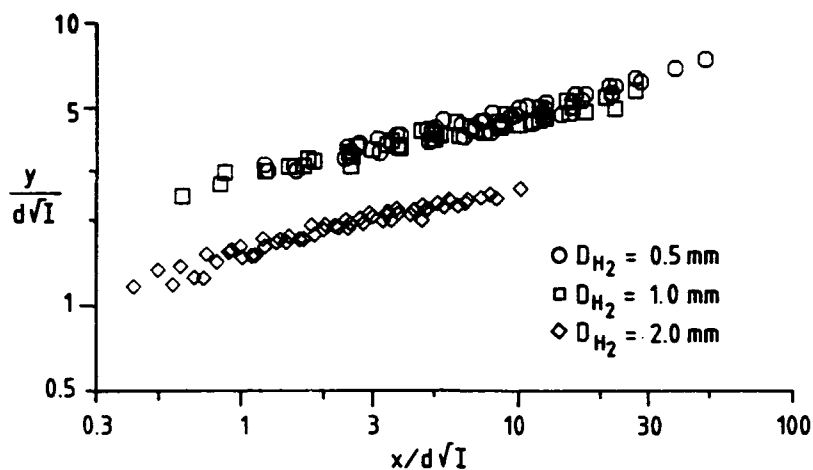


Fig. 9 Penetration Trajectories of Three Burning Jets.  
- Influence of Injection Hole Diameter

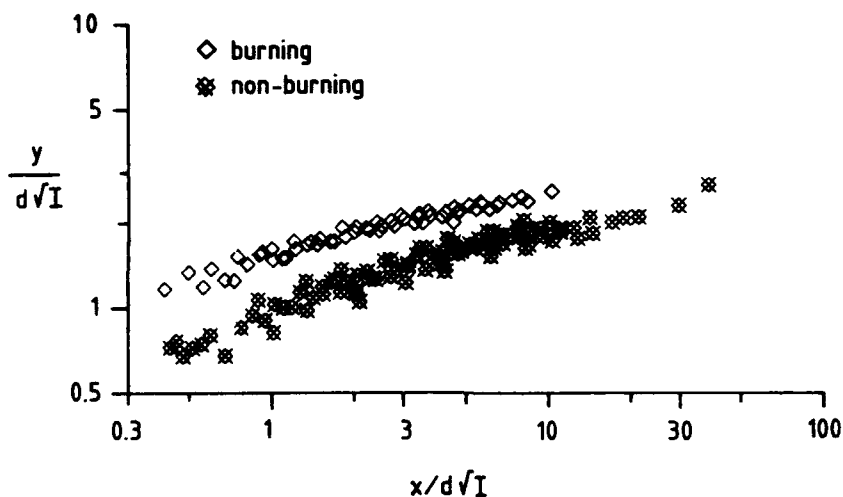


Fig. 10 Penetration Trajectories for the  $d = 2$  mm  
Circular Injection Hole.  
- Influence of Heat-Release

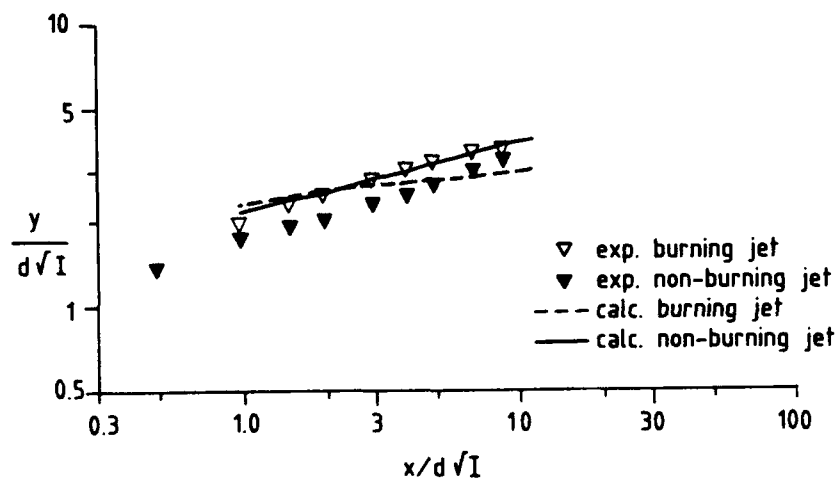


Fig. 11 Penetration Trajectories for the Rectangular  
Injection Hole  $1 \times b = 0.5 \times 1.7$  mm.  
- Experimental Data and Calculated Results



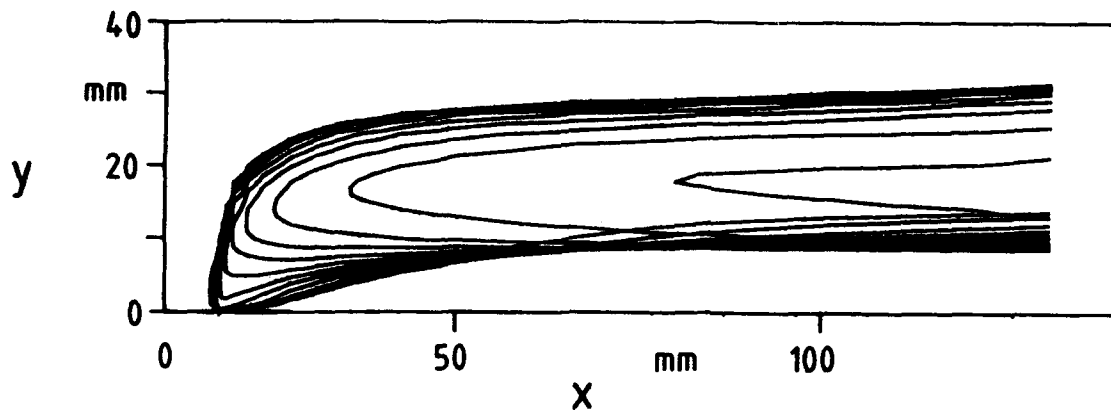


Fig. 12 Calculated Isolines of the Equivalence Ratio  $\phi = 0.1$  of all x,y Planes.

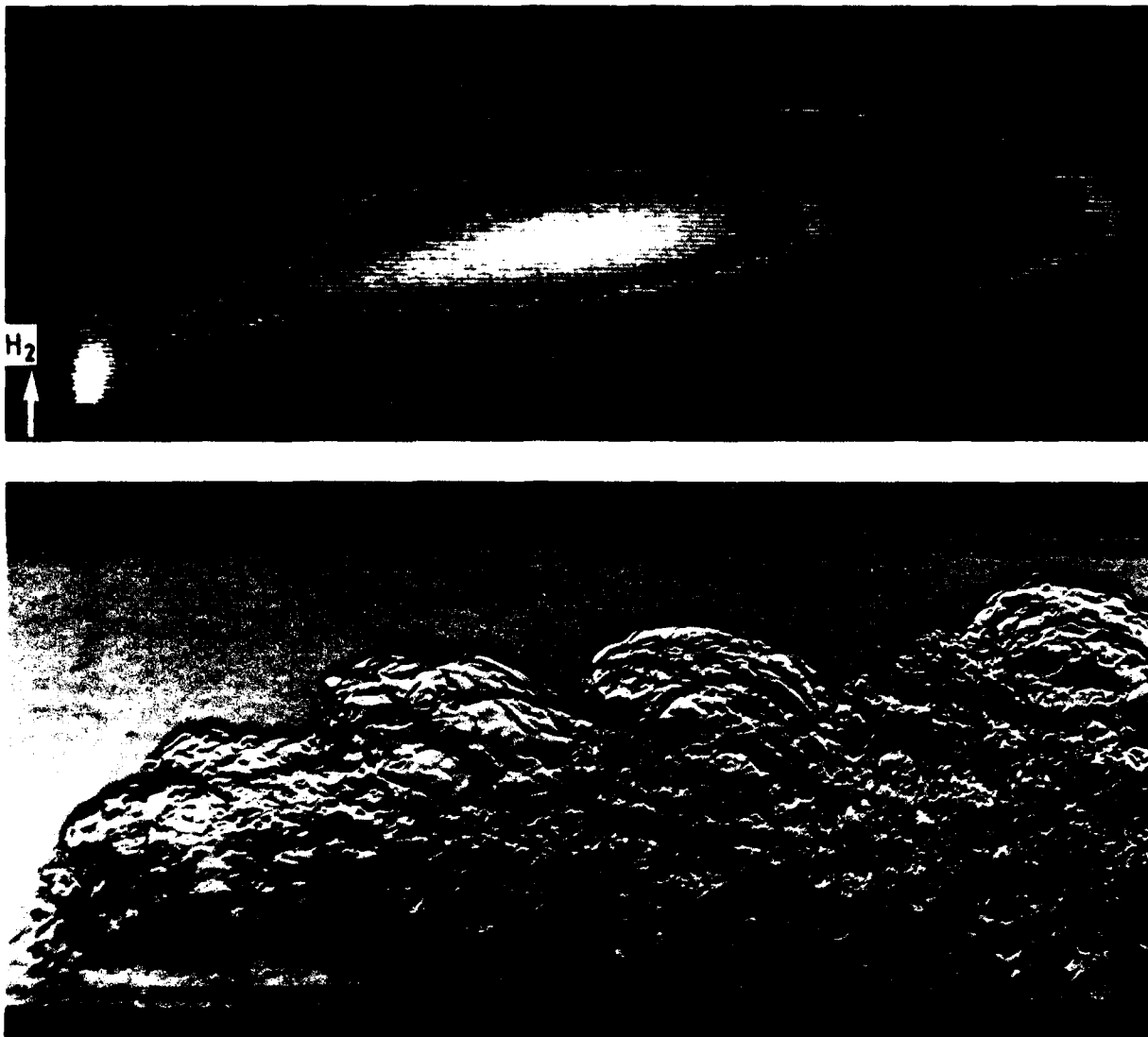


Fig. 13 Burning Jets.  
 - upper part: Digitalized Direct Photography  
 (Uair = 31 m/s, P = 6 bars, VH2 = 1150 m/s, I = 95, l x b = 1.7 x 0.5)  
 - lower part: Schlieren Images  
 (Uair = 52 m/s, P = 8.5 bars, VH2 = 1200 m/s, I = 59, l x b = 0.5 x 1.7)

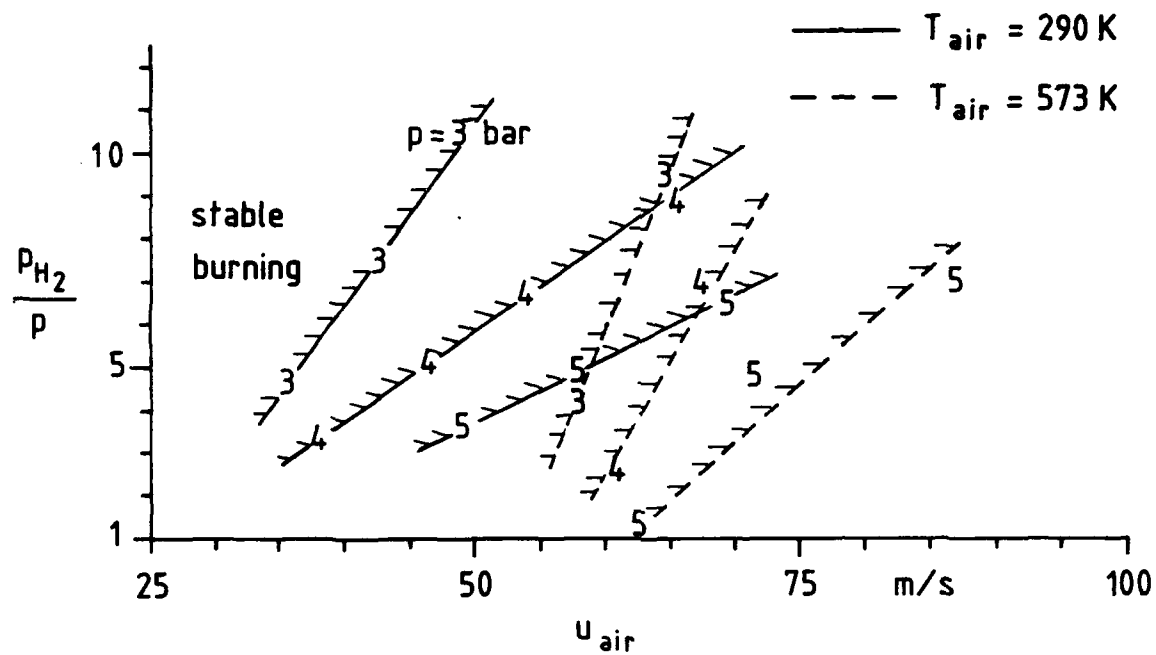


Fig. 14 Extinction Limits.  
- Influence of Air Inlet Conditions for the  $d = 0.5$  mm Injection Hole.

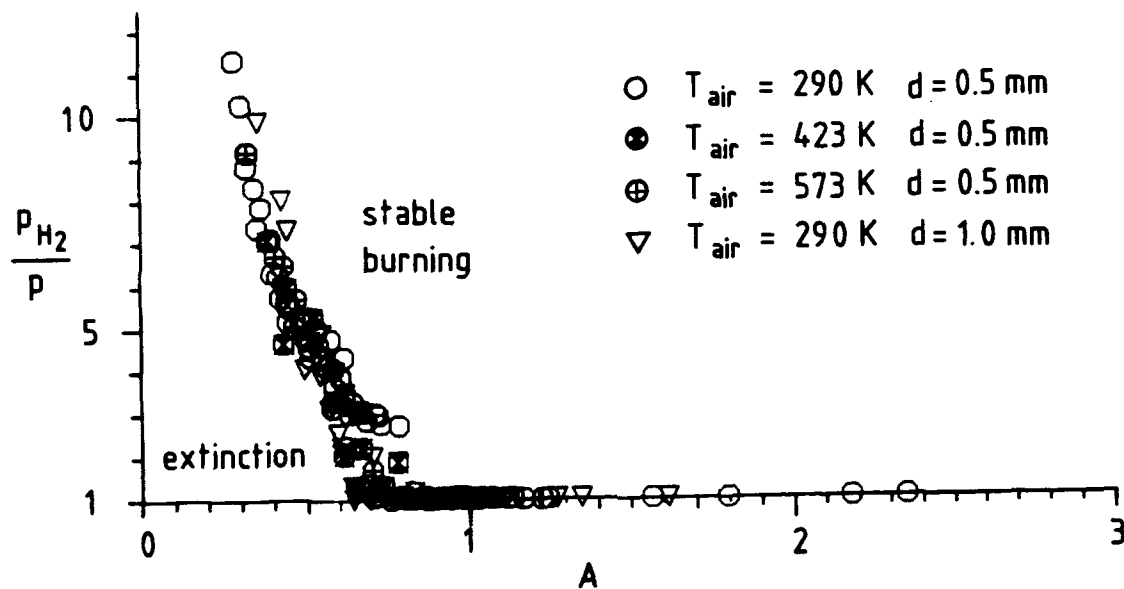


Fig. 15 Extinction Limits.  
- Influence of the Combining Parameter

$$A := \hat{P} (\hat{T}_{H2} + a \hat{T}_{air}) / d / \hat{U}_{air} \quad (a \approx 0.27)$$

## Discussion

HARLOFF

- 1) Have you compared static wall pressure measurements with predictions, especially behind the jet?
- 2) Have you compared computed turbulence quantities with measured quantities?
- 3) Please, comment on your perception of the grid adequacy.

AUTHOR'S REPLY

- 1) Although we measured wall pressures in the inlet flow, as well as downstream of the injection point, we did not compare prediction with measurement.
- 2) The measurement shown are just observations. They give an integral picture. We did not make, until now, any field measurements. So consequently we did not compare computed turbulence quantities with measured quantities. We plan to make LDA field measurements which will enable us to make detailed comparisons between calculated and measured quantities.
- 3) The calculations have been made on one orthogonal grid. Considering the small jet dimensions compared to the channel dimensions, there must be a grid dependence. We are working on a numerical scheme using two different grids. One grid to resolve the jet and its wake, the other grid to resolve the channel flow.

BILLIG

Can you go to higher crossflow velocities in either your experiments or your analysis and if so do you have plans to go to supersonic cross flows?

AUTHOR'S REPLY

We are investigating subsonic airflows. We are planning to go to inlet flow Mach numbers around .65.

WEYER

What is the cross flow Mach number you investigated so far?

AUTHOR'S REPLY

The example I showed was  $M = 0.25$  but we investigated Mach numbers about 0.45. We must achieve higher Mach numbers.

WINTERFELD

COMMENT : It is interesting to note that if you use a cylindrical flow holder for flow stabilisation you find the square root of the diameter of the rod in the correlation for the stabilisation parameter.

Experimental Investigations on the Transition from Stable to Unstable Combustion  
by Means of Active Instability Control

S. Gleis, D. Vortmeyer, W. Rau  
Technische Universität München, Arcisstraße 21, D-8000 München 2

**Summary**

The interaction of numerous parameters affect excitation and development of combustion instabilities, and determine the excited acoustic modes. Therefore, to avoid combustion instabilities, it is essential to make out the sources of disturbances and to interrupt the feed back loop. The newly developed method of "Active Instability Control" (AIC) opens experimental opportunities for this kind of diagnostics, because after having stabilized the oscillating system it starts to oscillate again if the AIC-system is switched off. It takes about 300 msec until the oscillation is again fully developed. During this transition period we are able to register the combustion chamber pressure, the intensity of chemical reaction and the flame contours time resolved by high-speed/-schlieren-cinematography. Experiments with a laboratory combustor showed, that during the onset of instability various mechanisms of excitation can be observed. Further investigations pointed out that although vortex shedding is an important driving force for oscillations, it is not the origin for instability.

92-16985

## 1. Introduction

The appearance of self-excited combustion oscillations in technical combustion chambers is always undesirable as it can extinct the flame and can damage the mechanic structure in extreme situations /1, 2/. In jet-flames, the oscillations frequently occur together with vortex shedding at the nozzle rim. The interaction between pressure oscillations resulting from unstable combustion and vortex shedding has not yet been fully investigated for enclosed jet flames. Literature references on this topic are not entirely consistent. On one side, there are reports that vortex shedding is primarily dependent on flow velocity and nozzle geometry /2, 3, 4/. Other authors show a direct correspondence between combustion chamber acoustics and the frequency of vortex shedding /5/. Using experimental evidence on the transition from stable to unstable combustion this paper shows which mechanism is primarily responsible for these phenomena.

## 2. Active Instability Control of Combustion Oscillations

The experiments described in the present paper make use of the method of "Active Instability Control" (AIC) /6, 7, 8/. AIC is based on the principle of antinoise where an existing sound field is eliminated by

interference with an externally superimposed field. This long known principle has been realized in recent years, generating the control sound field by very fast electronics. Fig. 1 illustrates the experimental setup of the AIC system. A microphone in the combustion chamber registers the pressure oscillations. The signal is filtered and preamplified. The conditioned signal then is phase shifted by a required amount and drives a loudspeaker via a power amplifier.

Provided the correct phase shift and amplification, the interference between the generated sound field and the existing field in the combustor leads to the extinction of the pressure oscillations. The combustion chamber flow becomes stationary and the oscillations of the heat release and pressure decreases to zero as it is observed in fig. 2. A laboratory combustor (propane and air) is operated under oscillatory conditions with a frequency of about 630 Hz and pressure amplitudes of 200 Pa (pp). The oscillation of the heat release rate  $\dot{Q}$  is measured by the intensity of the OH<sup>-</sup>-radical radiation /9/. The time

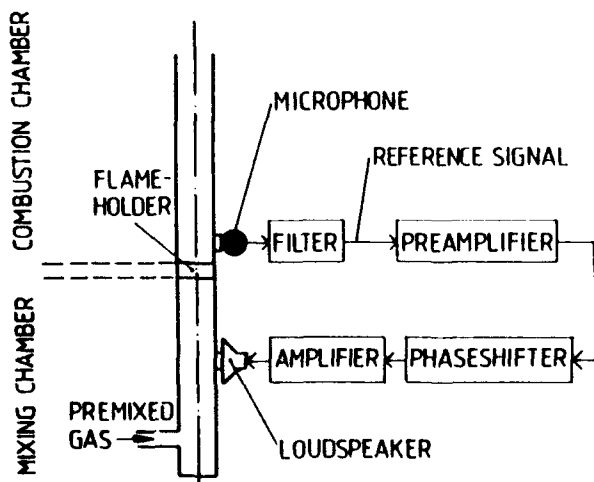


Fig. 1: Flow diagram of the AIC-system  
(Active Instability Control)

zero on the time scale marks the onset of the power input by the loudspeaker. The combustion process is stabilized after 65 msec with only 50 dB of noise left. In contrast to the method of antinoise practi-

cally no loudspeaker power is required to keep the combustion stable once the control has been achieved. Sound pressure and acoustic velocity are diminished by interference, thus reducing the energy fluctuations which are responsible for excitation of the acoustic oscillations. Only the remaining small stochastic perturbations have to be controlled by the AIC. In comparison to this laboratory experiment the technical applications require a scale up by a factor of several orders of magnitude. The largest combustion chamber so far controlled by AIC had a thermal power output of 250 kW /6/. A damping effect of 23 dB was achieved. Besides making technical use of AIC, this method is also suited to investigate what the mechanisms are which cause combustor instability.

## 2.2 AIC as a Method to Investigate the Mechanisms of Combustion Instabilities

If in the case of AIC stabilized combustion the loudspeaker is switched off, naturally the system will be unstable again after a short time. Therefore we are in the position to study the onset of combustion oscillations without disturbancy of the flow field from outside.

The development of combustion oscillations in a laboratory burner (Fig. 1) with a jet flame is shown in Fig. 4. A nozzle with a diameter of 2.7 mm and an annular flame stabilization (Fig. 3) serves as flame holder. The gas (75 % CH<sub>4</sub> + 25 % H<sub>2</sub>) and air to the combustor are supplied premixed with a mixture ratio of  $\lambda=0.95$  (air<sub>stoch</sub>/air). The length of the combustion chamber is 320 mm, the mixing chamber is 145 mm long. The flow velocity near the nozzle exit is approximately 26 m/sec.

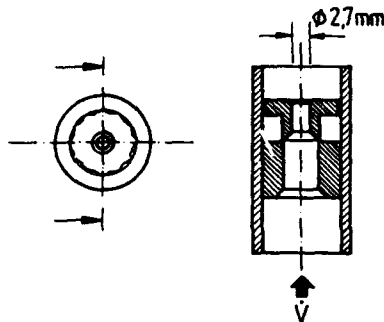


Fig. 3: Nozzle design

The reason for the increase in heat release and pressure oscillations from region one to region two is easily found by measuring the phase shift between both oscillations. While the phase shift is  $\Delta\varphi=20^\circ$  in region one, it becomes zero in region two. Therefor the driving force has become much stronger due to a better fulfillment of the Rayleigh-criterion with an increase of the oscillation amplitudes.

The transition from smaller (region 1) to larger (region 2) amplitudes is reflected by the behaviour of the flame which was recorded by a high speed camera. Schlierenphotos of the flame are presented in fig. 5 with fig. 5a showing the stable flame. Periodic changes in the flame length which correspond to the oscillation in region 1 of fig. 4 are observed in fig. 5b. Fig. 5c reflects the flame changes due to the state of oscillation in region 2 of fig. 4. The changes in flame length is a measure for the heat release fluctuation since the heat release is a function of the flame surface. A closer inspection of fig. 5b and 5c gives evidence that the transition from region 1 to region 2 in fig. 4 goes along with a change in the flame shape. In addition to the pulsating flame in fig. 5b we note an overlapping with vortices in 5c leading to larger amplitudes of energy and pressure oscillations. Now vortex shedding has become the dominant feature in sustaining the oscillations at the same frequency.

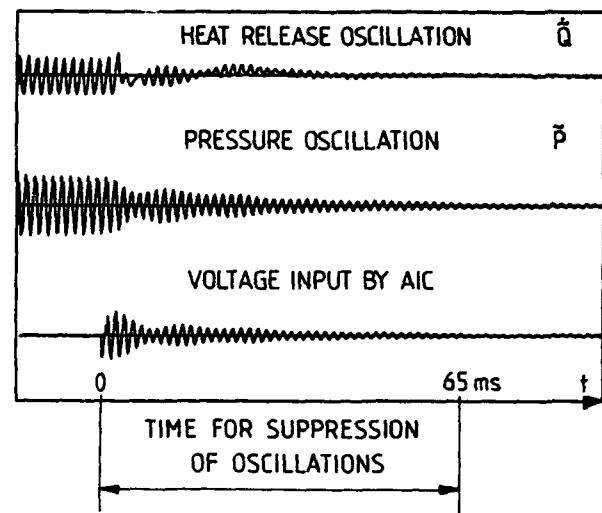


Fig. 2: Suppression of combustion oscillations by AIC  
t>0: AIC-system acting

We note from fig. 4 that after turning off the AIC a steady oscillation with a frequency of 405 Hz is obtained in region one of fig. 4. The pressure amplitude is 130 Pa (pp). The amplitude of the heat release oscillation related to the steady state combustion rate ( $\dot{Q}/\dot{Q}_0$ ) amounts 32 %. After 160 msec a transition takes place to region two which represents the fully developed oscillatory state without any further changes. While the frequency remains unchanged, pressure amplitudes increase to 230 Pa. The heat release amplitude has also become much larger ( $\dot{Q}/\dot{Q}_0=68$  %).

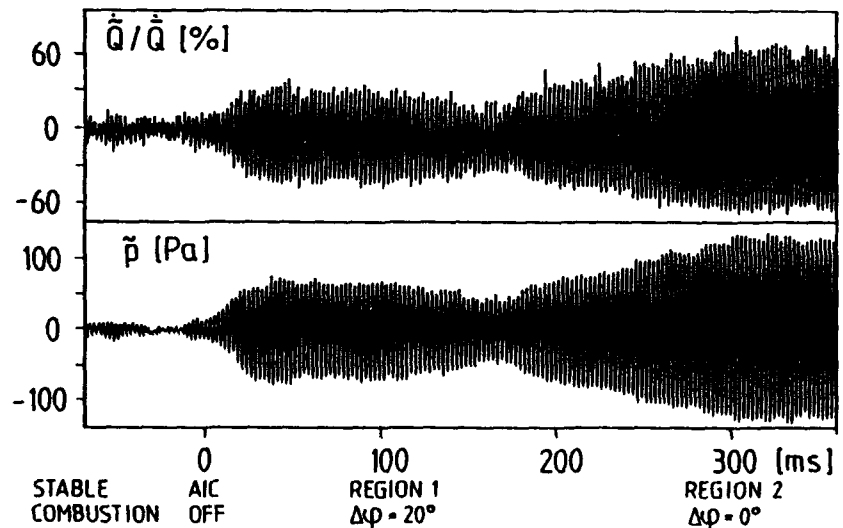
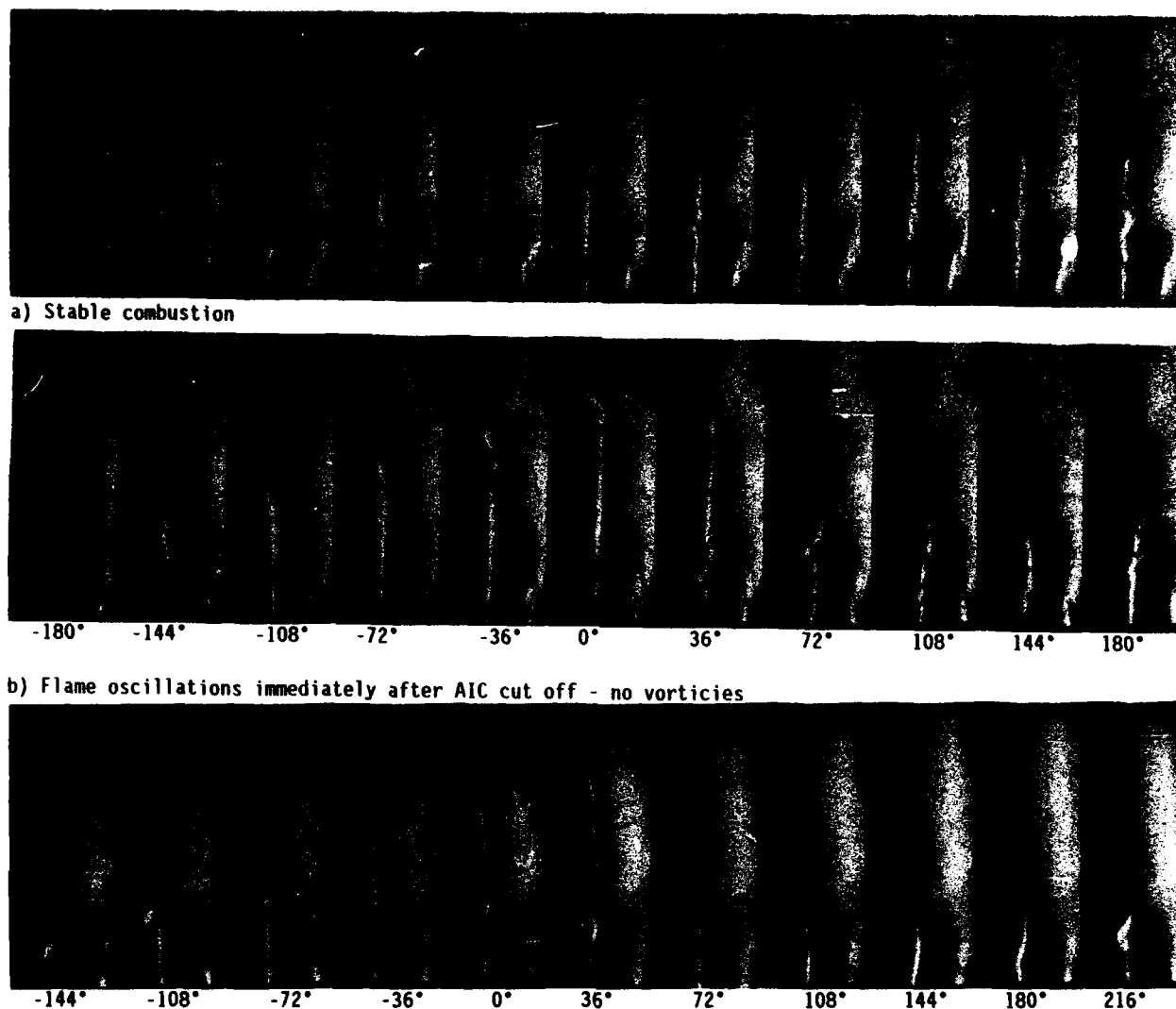


Fig. 4: Transition from stable to unstable combustion



c) Fully developed oscillation with vortices

Fig. 5: Schlieren-photos of flame for one cycle; 0°: Maximum Heat Release

Therefore vortex shedding in jets without and with combustion will be considered somewhat more closely in the next section.

### 3.1 Vortex Shedding in jets without combustion

The previous experiments and also the work of other authors [2, 3, 5, 10] suggest that vortex shedding is an important mechanism to cause heat release fluctuations and thereby to sustain pressure oscillations if Rayleigh's criterion is fulfilled. Whether it is fulfilled or not will certainly depend on the vortex shedding frequency which depends on the flow pattern of the jet. While the situation is quite well known for free jets, there is still a discussion on the interaction between the vortex shedding and the acoustic conditions if the jet is confined by a combustion chamber. We have therefore performed a number of experiments for free and enclosed jets with and without superposed combustion processes.

The vortex shedding of a  $\text{CO}_2$ -jet in air was investigated with the experimental setup of fig. 6a. The jet flow came out of a sharp edged nozzle and was visualized by Schlieren-photography. A Schlierenphoto is displayed in fig. 7 for a nozzle exit velocity of  $6.4 \text{ ms}^{-1}$  and for a

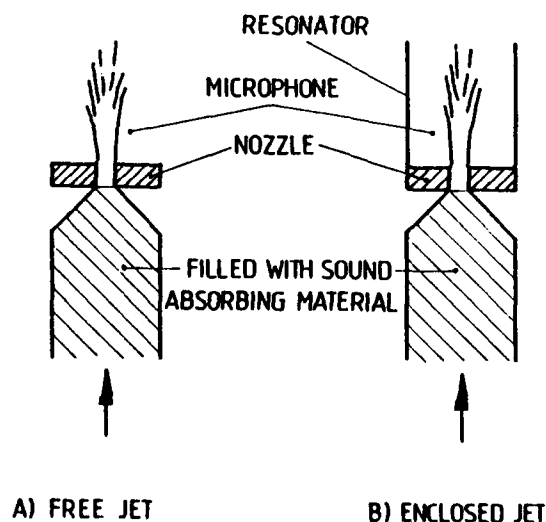


Fig. 6: Vortex shedding in free and enclosed jets experimental setup  
nozzle diameters 2.7, 3.0, 3.5 mm

nozzle diameter of 5 mm. In agreement with other authors /11, 12/ a linear relationship is obtained if the vortex shedding frequency is plotted versus flow rate. The Strouhal number is  $S_r = f \cdot D / u = 1.22$ . The free jet was exposed also to sound waves of a loud-speaker which emitted frequencies of 100, 400 and 700 Hz. It is evident from fig. 8 that the vortex formation adjusts itself to the frequencies imposed from outside. Therefore it is no surprise that vortex shedding from jets in combustion chambers is strongly influenced by the eigenfrequency of the system. Fig. 9 serves as an example. It exhibits Schlierenphotos of an enclosed cold jet with a vortex frequency of 600 Hz corresponding to the eigenfrequency of the combustion tube. A variation of the resonator length changes eigen- and vortex shedding frequencies as plotted in fig. 9. We therefore conclude that the rate of vortex formation is strongly coupled with the eigenfrequency of the tube and provides a mechanism for a still stronger coupling between heat and pressure oscillations.

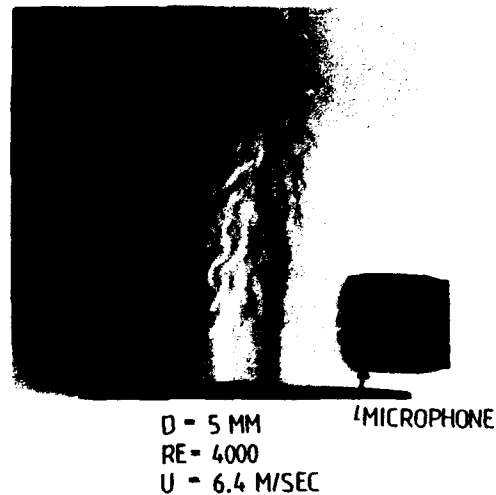


Fig. 7: Schlierenphoto of a  $\text{CO}_2$ -jet in air

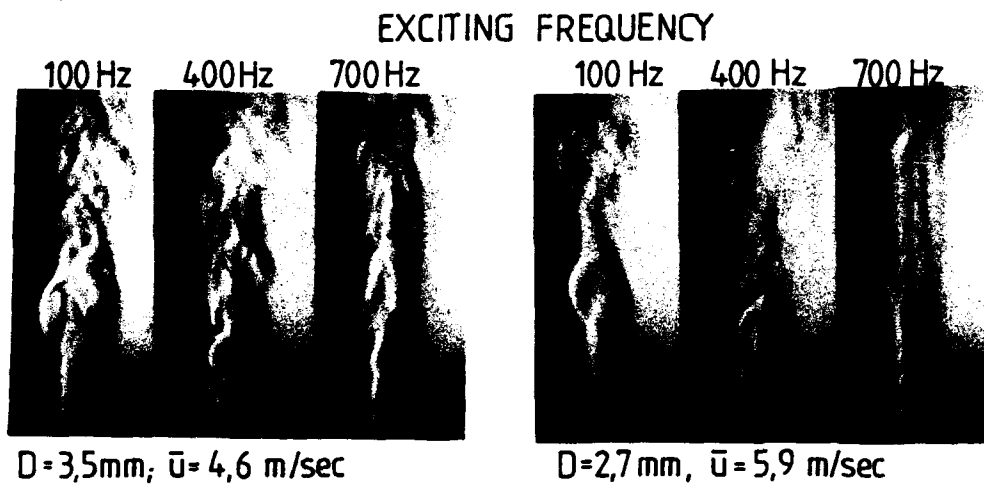
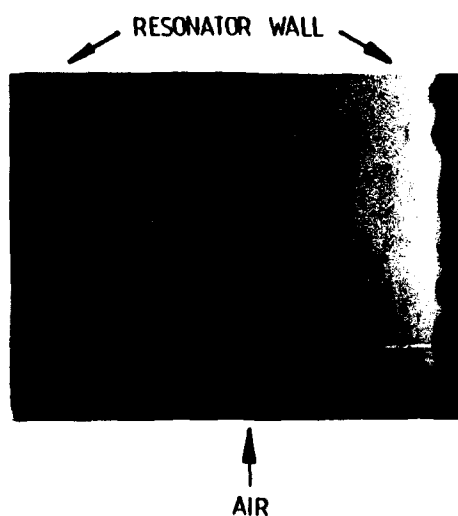


Fig. 8: Vortex shedding in a free jet influenced by acoustic excitation from below



$D = 5 \text{ MM}$   
 $U = 5 \text{ M/SEC}$   
 LENGTH OF RESONATOR 0.15 M

Fig. 9: Schlierenphoto of vortex shedding for an enclosed jet

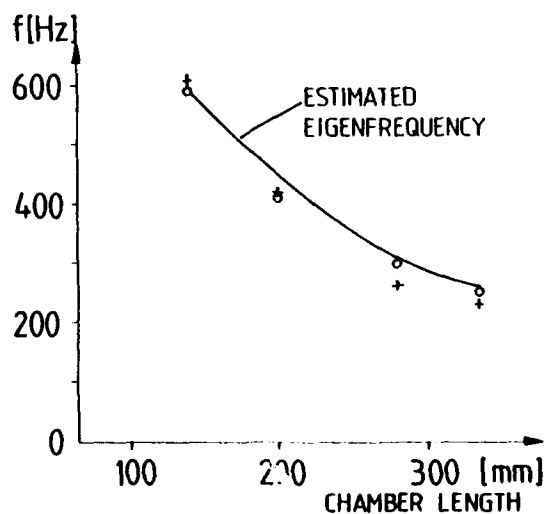


Fig. 10: Comparison of vortex shedding frequency with resonant frequency after  $f = c/4 \cdot (L + L_{corr})$   
 o nozzle diam. 3.0 mm + nozzle diam. 3.5 mm

### 3.2 Vortex Shedding in Jet Flames and Combustion Instabilities

Similar experiments as in section 3.1 were performed with jet flames. While the vortex shedding of free jets was easily influenced by superimposed sound waves, it was found in the presence of flames that the combustion process exerts a strong stabilizing effect on the free jet flow due to the increased viscosity of the hot gas. No vortex shedding was observed even if the amplitudes of the superimposed sound waves were increased by an factor of 100 which was the limit for our apparatus.

Due to the stabilizing effect of the flame on the vortex formation, we were able to observe two different types of combustion oscillation after the AIC-system was switched off. The first type of oscillation is the type as figured out in fig. 4 with two distinct regions. Region 1, which corresponds to the Schlierenphotos of fig. 5b, is initiated by the interaction between sound velocity and the flame. Obviously the pressure amplitudes of the initial oscillations are large enough to initiate vortex shedding, thereby increasing heat and pressure amplitudes leading to the powerful self sustained oscillation in region 2 of fig. 4. The oscillations presented in fig. 11 were measured in the same combustion chamber, which was damped acoustically

by a 10 mm hole in a position 150 mm away from the flame holder. As expected, the amplitudes of heat and pressure oscillations are smaller than in fig. 4 are not sufficiently large to generate vortices. The flame therefore remains in the state of region 1.

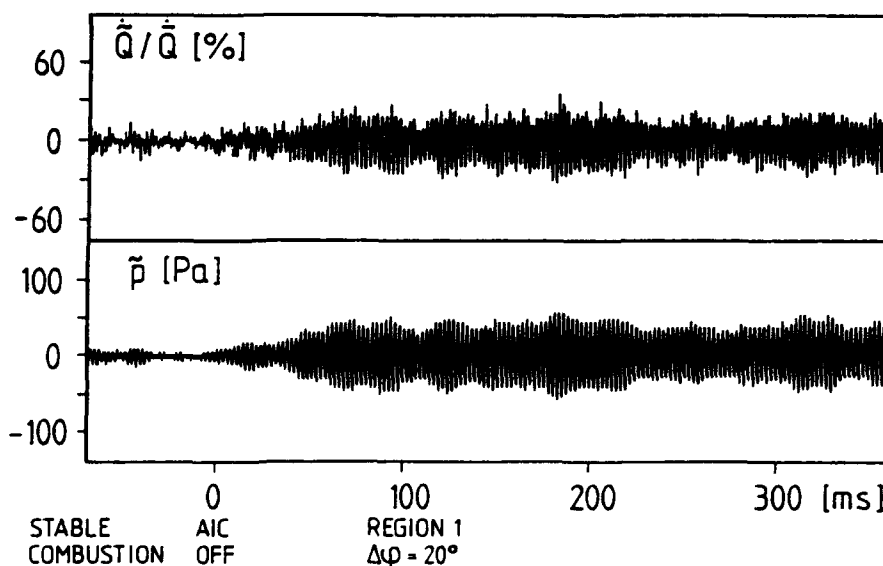


Fig. 11: Transition from stable to unstable combustion with acoustic damping

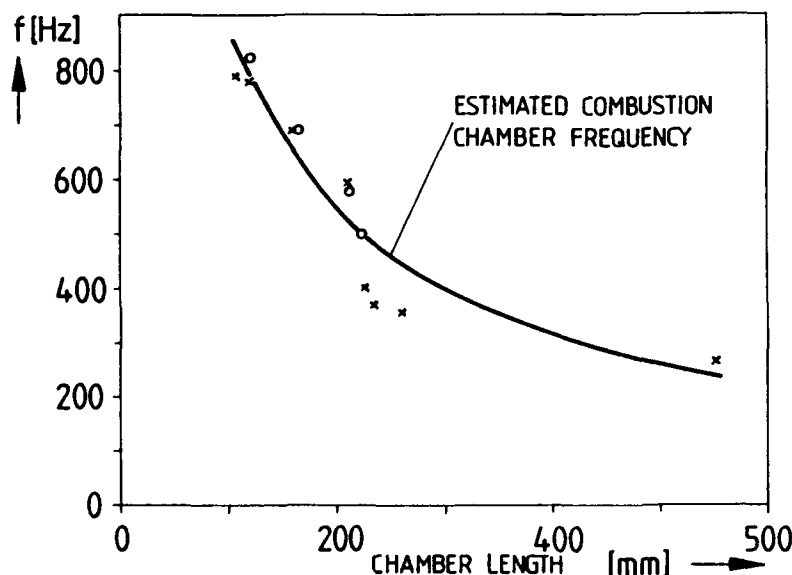


Fig. 12: Comparison of measured combustion oscillation frequencies with resonant frequencies after  $f=c/4 \cdot (L+L_{corr})$   
o nozzle diam. 3.0 mm + nozzle diam. 3.5 mm

Finally the combustion frequencies were compared with the estimated eigenfrequencies of the combustion system for different chamber lengths. Fig. 12 gives evidence that the measured combustion oscillation frequencies follow the calculated eigenfrequencies.

### 4. Conclusions

The application of AIC has shown clearly for the system under consideration that the initial oscillations originated by the interaction between acoustic velocity and flame. Vortex shedding took over as the dominating mechanism after about 150 ms when the pressure amplitudes were large enough to generate vortices. Similar investigations for other systems and geometries are in progress.



References

- /1/ D. Sucker, P. Glas, H. Boenecke: Druckschwingungen in Winderhitzern, 1980, Stahl und Eisen 100, Nr. 22
- /2/ R. Brown, R. Dunlap, S. Young, R. Waugh: Vortex Shedding as a Source of Acoustic Energy in Segmented Solid Rockets, 1980, AIAA 80-1092R, Vol. 18, No. 18.
- /3/ R. Brown, R. Dunlap, S. Young, R. Waugh: Vortex Shedding Studies in a Simulated Coaxial Dump Combustor, 1985, AIAA Journal, Vol. 1, No. 5.
- /4/ R. Dunlap, R. Brown: Exploratory Experiments on Acoustic Oscillations Driven by Periodic Vortex Shedding, 1981, AIAA Paper 81-4068, Vol. 19, No. 3.
- /5/ R. Byrne: A Note on Longitudinal Pressure Oscillations in Ramjet Combustors, 1981, 18th Jannaf Combustion Meeting.
- /6/ W. Lang, T. Poinso, S. Candel: Active Control of Combustion Instabilities, 1987, Combustion and Flame 70, 281-289.
- /7/ T. Poinso, G. Bourienne, E. Esposito, W. Lang: Suppression of Combustion Instabilities by Active Control, 1987, 23rd Joint Prop. Conf., San Diego, AIAA 87-1876.
- /8/ S. Gleis, D. Vortmeyer: Die "aktive Instabilitätskontrolle" als Untersuchungsmethode für selbsterregte Verbrennungsinstabilitäten, 1989, VDI-Berichte Nr. 765.
- /9/ K. H. Becker, D. Kley, R. Norström: OH Chemiluminescence in Hydrocarbon Atom Flames, 1969, Twelfth Symposium on Combustion, 405-413.
- /10/ T. Poinso, A. Trounev, D. Veynante, S. Candel, E. Esposito: Vortex-driven Acoustically coupled Combustion Instabilities, 1987, J. Fluid Mech..
- /11/ V. Kibens: Discrete Noise Spectrum Generated by an Acoustically Excited Jet, 1979, Vol. 18, No. 4.
- /12/ J. Laufer, P. Monkewitz: On Turbulent Jet Flows: A New Perspective, 1980, AIAA Paper No. 80-0962.

## Discussion

LIEBERHERR

1) Has the wave shape of the pressure traces in region 1 and 2 been analyzed? As a rough guess the traces in region 1 might be sinusoidal, indicating a linear coupling, and in region 2 they might be deformed, indicating non linearities as vortex phenomena can be.

2) Has the estimated eigenfrequency of the chamber been calculated by solving the wave equation with varying sound velocity or has an average sound velocity been assumed?

AUTHOR'S REPLY

1) Yes, the waveforms of region 1 and region 2 have been analyzed. The waveshape of region 1 is quite sinusoidal, while the waveshape in region 2 shows a slight deformation to a non linear form. I agree with you that at higher amplitudes non linearities play an important role.

2) The acoustic eigenfrequency of the chamber has only been estimated by the average sound velocity.

HOUMOUZIADIS

The oscillations in the combustion chamber and in the jet are usually coupled with the stability characteristics of the jet flow. Have you observed that with combustion higher amplitudes were necessary to initiate oscillations? Did you investigate cold and hot jets?

AUTHOR'S REPLY

We made, as shown, investigations on cold jet and we found that combustion stabilises the flow pattern, but if there is vortex shedding in the flame you get a large amplification of the pressure oscillations.

WINTERFELD

In a real combustor we have a mixture of longitudinal transverse and radial frequencies. Is this AIC system also applicable to the damping of the different oscillations?

AUTHOR'S REPLY

You should use different loudspeakers or modulate the injection flow of the spray at several points in the combustor. We have not tried this yet.

## DESIGN TECHNIQUES FOR DUAL MODE RAM-SCRAMJET COMBUSTORS

AD-P007 954

W.S. Billig, S. Corda and P.P. Pandolfini  
The Johns Hopkins University  
Applied Physics Laboratory  
Laurel, Maryland 20723, U.S.A.

92-16986

## SUMMARY

This paper will present a disciplined analytical method that describes the different engine operating modes and internal flow structures in dual mode ram-scamjet combustors. Solutions for physical systems are dependent on empirical data bases from unit process experiments which include shock trains, jet penetration and mixing. A synopsis of an experimental data base will be presented and the method by which it is embodied in the analytical models will be discussed. The models will then be applied to develop design procedures for combustor-inlet isolators, discrete hole injectors, controlled shear layer mixing and will establish the efficacy of sudden expansion steps for anchoring shock trains.

## INTRODUCTION

The preferred engine cycles for applications that require efficient propulsion power over the range of flight Mach numbers of 3 to 8 are the dual mode ram-scamjet (DMR) and the dual combustor ramjet (DCR) (Refs. 1-3). The techniques discussed herein are applicable to either of these two types of engines and in many aspects to other engine cycles and/or a broader range of flight speeds. In both the DMR and DCR the structure of the internal flow changes dramatically over the range of operating conditions. At high ER and/or low Mach numbers the flow is dominated by strong internal shocks and a large internal area ratio must be provided to accommodate the heat release. At low ER and/or high Mach number the internal shock structure is weak and optimum cycle performance is obtained in a near constant area-heat addition process. These significantly different operating characteristics introduce difficult design challenges. When strong shock structures are present combustor-inlet interactions must be controlled to prevent inlet unstart. Modulating the effective area ratio of the heat addition process requires tailoring and controlling the injection and mixing processes to avoid or minimize the need for variable geometry.

As contrasted to scramjets operating at very high flight speeds, i.e. above about Mach 12, the axial momentum of the fuel is an insignificant contribution to the engine thrust. Moreover, strong disturbances of the main flow that are created by cross stream injection of the fuel can be tolerated. Thus the benefits of increased fuel penetration and enhanced mixing generally dictate injection from discrete holes transverse to the air stream. The number of grid points needed for a CFD solution capable of resolving the details of underexpanded wall jets interacting with a viscous, shock dominated duct flow is of the order of  $10^6$ . Moreover, when existing turbulence models are applied to this class of flows, the results are suspect. Consequently, alternative methods for design of injector-combustors and the analyses of the flowfields are currently needed.

## APPROACH

The inlet-combustor design methodology is schematically depicted in Figure 1. It begins with parametric sensitivity analysis wherein a broad range of engine geometries, engine cycles, flight trajectories, etc. are examined to determine some insight into which general classes of conceptual engine designs are candidates for meeting specified mission requirements. From the candidates, preliminary conceptual designs of the vehicle and the engine flow path are selected. For these flow paths an engine cycle analysis, RJPA (Ref. 4) is used to provide the sensitivity of engine performance to all of the parameters that can be considered as design variables in the injector, inlet-combustor isolator and the combustor. A corresponding activity, not covered herein, is the design, testing and flowfield analysis of the inlet which provides the inlet variables for RJPA. Fundamental to the utility of this design approach are a number of carefully conducted basic process experiments to provide an empirical data base for four models. These are: jet penetration, mixing, heat transfer/shear and inlet/combustor interaction. Experiments are currently underway that apparently will lead to revisions in the mixing models previously used. A subsequent paper will discuss these revisions and the subject will be treated only superficially herein. The models together with RJPA are used to guide the internal engine flow path. With the internal engine lines established, a simplified finite difference technique is used to analyze the flow. The development of the code is covered in Ref. 5. Techniques for testing the combustor in the free jet (FJ) semi-freejet (SFJ), direct-connect (DC) and semi-direct-connect (SDC) modes are presented in Ref. 6. Finally, the test results and flowfield analysis provide the performance and operating characteristics of the engine, revised design guidelines to repeat the process, if needed, and a calibration and/or validation of the design and assessment codes.

## ANALYSIS OF THE FLOWFIELD

Figure 2 is a schematic representation of the entire flowfield in a dual mode ramjet-scamjet engine. The pressure increases from the free stream,  $P_0$  to  $P_1$  across the forebody shock and to  $P_2$  on the external compression surface. The cowl reflected waves raise the pressure to  $P_3$  at the entrance to the isolator; shocks in the isolator increase the pressure to  $P_4$ . Generally, the pressure at the combustor exit  $P_5$  is lower than  $P_4$  and expansion in the exhaust nozzle further reduces the pressure to  $P_6$ .

The model used to describe the details of the processes taking place in the internal duct is shown in Figure 3. The sketch is typical of the DMR configuration. Gaseous fuel is injected at either sonic or supersonic conditions at angle  $\alpha$  into a supersonic air stream. Design techniques for liquid fueled combustors are similar but are treated elsewhere (see eg. Ref. 7). The blockage due to the combined effects of the injection and heat release generates a "shock train" disturbance that, in general, originates upstream of the fuel injector ports and extends into the combustor. At moderate combustor inlet Mach numbers  $M_i$ , i.e., 1.5 to 4 and typical fuel-air equivalence ratios, i.e., 0.5 to 1.0, the

pressure rise associated with the shock train is of sufficient strength to separate the incoming boundary layer. In the well-designed engine, an isolator is placed between the combustor and the air inlet to prevent the combustion-induced disturbances from disrupting the flow in the inlet. The length of the shock train is defined as the length of the corresponding s-shaped pressure rise and is given as  $S_t$ . The distance that the shock train extends into the combustor is  $S_d$ . Empirical relationships for  $S_t$  and  $S_d$  obtained from correlations of experimental data will be presented later. As flight speed increases,  $M_t$  correspondingly increases and the strength of the pressure rise in the shock train reaches a maximum and then decreases. Thus, the separated zone may not be present at high  $M_t$ .

Downstream of the shock train, mixing and combustion are intensive, with large radial, axial and, perhaps, circumferential gradients in flow properties and chemical composition. This region extends from station s to station e and is labeled "2 or 3D mixing and combustion zone." Further downstream, the mixing and combustion is less intense, and the gradients are considerably weaker. This region extends from station e to station 5 and is labeled "1D approach zone." In the integral models, the flow in this region is approximated by one-dimensional mean flow properties at each axial station. For finite difference solutions either the complete set of the Reynolds' averaged Navier Stokes equations are solved or simplifying assumptions are made. For the simplified model that will be discussed, circumferential symmetry is assumed, and, therefore, regions s to e and e to 5 are indistinguishable. Radial gradients in flow properties and composition are typical but, in general, the gradients decrease as the combustor exit is approached. The control boundary which forms the basis for the integral models comprises the plane at section 4 upstream of the shock train, the throat of the injector, the injector and combustor walls, and the combustor exit plane at station 5. Flow properties on the end planes need not be constant, but to simplify the discussion that follows, representative mean values of  $\rho$ ,  $u$ ,  $p$ ,  $h$  and  $T$  are taken at stations 4 and 5 together with the respective geometric duct areas. For more rigorous analyses when gradients are present, mass averaged values are used in conjunction with a suitably defined area that simultaneously satisfies continuity, energy and mass-averaged total pressure.

To enhance understanding, the initial discussion will be simplified to the case of  $\gamma = 1.4$ , uniform flow at defined flow stations, zero wall shear and heat transfer, and no consideration of fuel mass and momentum. Later these constraints will be relaxed but with the expense of requiring a high speed computer to obtain solutions. Conditions ahead of the precombustion shock are denoted by 4, downstream of the shock by s and at the combustor exit by 5. In this simplified model the wall static pressure distribution is given by

$$P_w A^{\frac{\epsilon}{\epsilon-1}} = \text{constant} = \frac{P_s}{P_4} P_4 A_4^{\frac{\epsilon}{\epsilon-1}} = P_5 A_5^{\frac{\epsilon}{\epsilon-1}} \quad (1)$$

thus the wall force can be obtained from

$$\int_4^5 P dA_x = (1-\epsilon) \left[ P_5 A_5 - \frac{P_s}{P_4} P_4 A_4 \right] \quad (2)$$

In the subsequent discussion, a revised expression for the wall force will be introduced which accounts for the "s" shaped distribution that is schematically shown in Fig. 2.

#### Momentum Equation

$$P_5 A_5 \left( \epsilon + \gamma M_5^2 \right) = P_4 A_4 \left[ \left( 1 + \gamma M_4^2 \right) - (1-\epsilon) \frac{P_s}{P_4} \right] \quad (3)$$

Combining continuity & definition of sound speed

$$P_4 M_4 A_4 / T_4^{1/2} = P_5 M_5 A_5 / T_5^{1/2} \quad (4)$$

Combining (4) and (1)

$$\frac{T_5}{T_4} = \left( \frac{P_5 M_5 A_5}{P_4 M_4 A_4} \right)^2 = \left( \frac{M_5}{M_4} \right)^2 \left\{ \frac{\left[ \left( 1 + \gamma M_4^2 \right) - (1-\epsilon) \frac{P_s}{P_4} \right]}{\left( \epsilon + \gamma M_5^2 \right)} \right\} \quad (5)$$

$$\frac{T_{t5}}{T_{t4}} = \frac{T_5}{T_4} \times \frac{T_5}{T_4} = \left[ \frac{2 + (\gamma-1) M_5^2}{2 + (\gamma-1) M_4^2} \right] \left[ \frac{M_5^2}{M_4^2} \right] \left[ \frac{\left[ \left( 1 + \gamma M_4^2 \right) - (1-\epsilon) \frac{P_s}{P_4} \right]^2}{\left( \epsilon + \gamma M_5^2 \right)} \right] \quad (6)$$

$$\frac{P_5}{P_4} = \left[ \frac{\left[ \left( 1 + \gamma M_4^2 \right) - (1-\epsilon) \frac{P_s}{P_4} \right]^\epsilon}{\epsilon + \gamma M_5^2} \right] \left( \frac{P_s}{P_4} \right)^{1-\epsilon} \quad (7)$$

$$\frac{A_5}{A_4} = \left( \frac{P_s}{P_4} \right)^{\epsilon-1} \left[ \frac{\left[ \left( 1 + \gamma M_4^2 \right) - (1-\epsilon) \frac{P_s}{P_4} \right]^{1-\epsilon}}{\epsilon + \gamma M_5^2} \right] = \left[ \frac{\left[ \left( 1 + \gamma M_4^2 \right) + (\epsilon-1) \frac{P_s}{P_4} \right]^{1-\epsilon}}{\frac{P_s}{P_4} \left( \epsilon + \gamma M_5^2 \right)} \right] \quad (8)$$

$$\frac{P_{t5}}{P_{t4}} = \frac{P_5}{P_4} \frac{P_{t5}/P_5}{P_{t4}/P_4} = \left[ \frac{(1 + \gamma M_4^2) - (1 - \epsilon) \frac{P_5}{P_4}}{\epsilon + \gamma M_5^2} \right]^\epsilon \left( \frac{P_5}{P_4} \right)^{1-\epsilon} \left[ \frac{2 + (\gamma-1)M_5^2}{2 + (\gamma-1)M_4^2} \right]^{\frac{\gamma}{\gamma-1}} \quad (9)$$

Equations (5)-(9) give, respectively  $T_{t5}/T_{t4}$ ,  $T_{t5}/T_{t4}$ ,  $P_5/P_4$ ,  $A_5/A_4$  and  $P_{t5}/P_{t4}$  for specified values of  $\epsilon$  and  $M_5$ . However,  $\epsilon$  and  $M_5$  are not independent and, in general,  $\epsilon = f(M_5)$  is not known a priori. Consequently, the solution is iterative and the computational effort is dependent on the choice of the iteration variable and the particular combination of the basic equations.

A constraint on the range of  $M_5$  values that result in allowable solutions is the "entropy limit." This limit arises when the heat addition is sufficient to thermally "choke" the flow. For heat release in a constant area, frictionless process (i.e. a Rayleigh line) the entropy limit occurs at  $M_5 = 1$ . For other situations, e.g. converging or diverging flows, with or without friction there can be a singularity in the solutions to the conservation equations that, in general, occurs at  $M_5 \neq 1$  (see e.g. Ref. 8). In the completely general case, analytical derivations have been obtained (Ref. 9) but they are so complex that they offer no advantage over direct numerical methods. However, when the process is constrained to  $\epsilon = c$  in the region of station 5, simple explicit relationships (Ref. 10) between  $\epsilon$  and  $M_5$  hold, viz

$$\bar{\epsilon} = \gamma M_5^2 / [1 + (\gamma-1)M_5^2]; \quad \bar{M}_5 = \left[ \bar{\epsilon} / \epsilon + \gamma(1-\bar{\epsilon}) \right]^{1/2} \quad (10)$$

The subsequent discussion will show that the solutions for a shock pressure ratio corresponding to that required to separate the incoming boundary layer will be of special interest. Additional modeling must be introduced to specify this value of  $P_5/P_4$ . For turbulent boundary layers the very simple relationship  $M_{sep}^2 = 0.58 M_4^2$  yields  $P_{sep}/P_4$  values that correlate a wide range of data as shown in Fig. 4. For planar flows the value of  $P_{sep}/P_4$  is obtained from an iterative solution of the oblique shock equation for the shock angle,  $\theta$

$$\left( M_s \right)_{sep} = 0.58 M_4^2 = \frac{(\gamma+1) M_4^2 \sin^2 \theta - [M_4^2 \sin^2 \theta - 1] \left[ \gamma M_4^2 \sin^2 \theta + 1 \right]}{[2\gamma M_4^2 \sin^2 \theta - (\gamma-1)] [(\gamma-1) M_4^2 \sin^2 \theta + 2]} \quad (11)$$

then

$$\left( P_s/P_4 \right)_{sep} = 2\gamma M_4^2 \sin^2 \theta - (\gamma-1)/(\gamma+1) \quad (12)$$

Results for a particular set of initial conditions,  $M_4 = 2.5$  and  $\gamma = 1.4$ , for a combustor having an area ratio of 3 are shown in Figure 5. The pressure-area distributions for several  $T_{t5}/T_{t4}$  values are given for selected values of the pressure ratio across the shock in the combustor inlet. For clarity, only four sets of curves are shown: for no shock, for an oblique shock with  $P_5/P_4 = 2.375 = (P_5/P_4)_{sep}$ , for an oblique shock inlet with  $(P_5/P_4) = 5$ , and for an oblique shock with  $P_5/P_4 = 7.125$ .

Each set of solutions is bounded above by the stagnation temperature ratio that results in a sonic exit limit,  $M_5 = 1$ . The lower bound corresponds to an entropy limit which, in effect, means the solutions from the  $\epsilon = \text{constant}$  family having the same  $P_5/P_4$  but a lower  $T_{t5}/T_{t4}$  would violate the slope constraint from equ. (10). These two constraints result in ranges of possible  $T_{t5}/T_{t4}$  that increase with increasing  $P_5/P_4$ . For any total temperature ratio between approximately 1.0 and the maximum possible value corresponding to a normal shock with  $M_5 = 1$ , there are an infinite number of possible solutions that lie within the prescribed  $P_5/P_4$  bounds. However, it is argued that when sufficient isolator length is provided to confine a shock train having a static pressure rise equal to  $P_5/P_4$ , the preferred solution for the corresponding  $T_{t5}/T_{t4}$  will be the entropy limit solution. Furthermore, when  $T_{t5}/T_{t4}$  exceeds the value corresponding to  $(P_5/P_4)_{N.S.}$ , the downstream slope constraint is relaxed and solutions may exist as long as  $M_5 \geq 1$ . If an isolator is not provided, then the precombustion shock strength cannot exceed  $(P_5/P_4)_{sep}$ , which for  $M_4 = 2.5$ ,  $(P_5/P_4)_{sep} = 2.375$  occurs at  $T_{t5}/T_{t4} = 1.406$  for  $A_5/A_4 = 3$ ,  $M_5 = 2.543$  and  $\bar{\epsilon} = 2.524$ . Higher  $T_{t5}/T_{t4}$  values would require different initial conditions (generally a lower  $M_4$ ) which may or may not be available in a physical apparatus. The solid curve for  $T_{t5}/T_{t4} = 1.016$  with the origin at  $P_5/P_4 = 1$  is the wall pressure distribution meeting the constraint of equ. (10) i.e.  $\bar{\epsilon} = 2.923$  but not constrained to be one-dimensional between stations 4 and 5. The dashed curve is the pressure distribution for a one-dimensional isentropic expansion. The near superposition of the two curves, coupled with the fact that  $T_{t5}/T_{t4} = 0$ , lends additional credibility to the argument that the  $\epsilon = c$  model yields results that closely approximate physically observed flows.

Further discussion of the experimentally observed wall pressure distributions must await the introduction of wall shear and the modeling of a shock train in a flow having gradual rise in pressure as contrasted to the shear-free-step-increase in  $P_5/P_4$  used so far. These refinements will be included in the next section. Other general features of the flow processes, however, can be presented without introducing these complexities.

A rather abrupt increase in shock train pressure rise in low area ratio combustors with small increases in total temperature is depicted in Figure 6. Curves of  $P_5/P_4$  as  $f(T_{t5}/T_{t4})$  for entropy limit solutions are shown for selected values of  $A_5/A_4$ . For a combustor with  $A_5/A_4 = 1.1$  and  $M_4 = 2.5$ , increasing  $T_{t5}/T_{t4}$  from 1.432 to 1.542, a mere 7.7%, doubles  $P_5/P_4$  from 3.56 to 7.125. On the other hand, for large area ratio combustors, e.g.  $A_5/A_4 = 4$ , the shock pressure rise varies about linearly with  $T_{t5}/T_{t4}$ .

Figure 7 shows the effect of combustor area ratio on the total pressure recovery in the heat-addition process. Curves for selected values of  $T_{t5}/T_{t4}$  between 1.1-3.0 are shown. Points above the dashed line correspond to entropy-limit solutions and those below the

dashed line are for shock trains with normal shock pressure ratios. Solutions are shown for  $M_4$  values between 1-2.5. Entropy-limit solutions exist for  $M_4 > 2.5$ , but they are not included. Whereas larger values of  $A_5/A_4$  can accommodate higher heat-release rates, there is an associated loss in total pressure recovery.

It is convenient to introduce an additional reference state to examine some flow structures wherein the flow areas at stations 4 and 5 are not known a priori. Here station 4 is specified as lying on a known isentrope, i.e.  $S_4$  is defined. The reference state  $r$  is the sonic point lying on that isentrope, i.e.  $S_4 = S_r$  and  $M_r = 1$ . Flow station  $r$  may or may not exist in a physical system. Solutions are generated for various values of  $A_5/A_r$  wherein  $M_4$  is treated as an independent variable with conditions corresponding to the isentropic relationship

$$\frac{A_4}{A_r} = \left(\frac{A}{A^*}\right)_4 = \frac{1}{M_4} \left[ \left(\frac{2}{\gamma+1}\right) \left(1 + \frac{\gamma-1}{2} M_4^2\right) \right]^{\frac{\gamma+1}{2(\gamma-1)}} \quad (13)$$

A direct-connect combustor test apparatus is a convenient and pertinent physical system to frame the discussion. Figure 8 is a schematic illustration of plausible flow structures in a direct-connect combustor. The previous discussion covered the flowfield shown in case a, wherein the pre-combustion shock is stabilized in an isolator and conditions at station 4 are known a priori. Case b) is for the case where the heat release occurs downstream and the precombustion shock can be stabilized in the diverging area. Case c) corresponds to high  $T_{t5}/T_{t4}$  and corresponding  $P_5/P_4$  values that cannot be accommodated by the isolator. Case d) is a combustor tailored to heat release schedules such that an isolator is not required. In general, the conditions at 4 for cases b, c and d correspond to  $P_5/P_4 = (P_5/P_4)_{\text{sup}}$  as given by eqs. (11) and (12). However, as shown in Figure 9, the absence of an isolator severely restricts the allowable operating range of ER values.

In Figure 9 the combustor total temperature ratio  $T_{t5}/T_{t4}$  is shown as a function of combustor entrance Mach number  $M_4$  for  $A_5/A_r$  values of 4, 6, 8, 10 and 12. Three families of solutions are shown: 1) shock separated entropy limit solutions which correspond to the limiting  $T_{t5}/T_{t4}$  for cases b, c and d in Fig. 8; 2) normal shock entropy limit solutions which correspond to the limiting  $T_{t5}/T_{t4}$  for case a in Figures 8 and 3) normal shock solutions with  $M_4 = 1$ , which corresponds to the maximum  $T_{t5}/T_{t4}$ . The  $M_4 = 1$  solutions would not occur in direct-connect combustors with these initial conditions, but serve as a useful reference point for engines having an inlet-combustor isolator designed to operate with strong shocks and high back pressures. The curves are general in the sense that limiting  $T_{t5}/T_{t4}$  values can be obtained either for a prescribed  $M_4$  and different  $A_5$  by examining different  $A_5/A_r$  or  $A_5/A_4$  lines, or for a prescribed  $A_5$  by examining different  $M_4$  on a given  $A_5/A_r$  curve.

To fully appreciate the large impact of the isolator on the maximum  $T_{t5}/T_{t4}$ , it is necessary to reintroduce some simple modeling to estimate  $M_4 = f(M_0)$  and  $T_{t5}/T_{t4} = f(ER, T_{t0})$  recognizing the approximate nature of the  $\gamma = 1.4$  and the other simplifying assumptions.

The total temperature ratio is assumed to vary with ER as

$$T_{t5}/T_{t4} = ER \left[ \left( 4500/T_{t4} \right)^{-0.3} \right] \quad (14)$$

and for an inlet with a moderate overall area contraction

$$M_4/M_0 = 0.5 - 0.01 (M_0 - 3) \quad (15)$$

where  $T_{t4} = T_{t0} = T_0 [1 + (\gamma-1) M_0^2/2]$  and  $M_0$  is the corresponding flight Mach number. Table 1 lists values of  $T_{t5}/T_{t4}$  and  $M_4$  over the region where shocks in combustors are of importance in dual mode engine designs.

TABLE 1 - TYPICAL COMBUSTOR INLET CONDITIONS FOR  $\gamma = 1.4$  ANALYSES

$M_0$	$M_4$	$T_{t5}/T_{t4}$		$M_0$	$M_4$	$T_{t5}/T_{t4}$		$M_0$	$M_4$	$T_{t5}/T_{t4}$	
		ER=1	ER=0.5			ER=1	ER=0.5			ER=1	ER=0.5
3	1.50	4.72	2.96	5	2.40	2.58	1.79	7	3.22	1.74	1.37
4	1.96	3.38	2.19	6	2.82	2.07	1.54	8	3.60	1.52	1.26

A cursory look at Figure 9 and Table 1 will show that for  $ER = 1$ ,  $T_{t5}/T_{t4}$  values exceed those for shock separations for all  $M_4 = f(M_0)$ . Even at  $ER = 0.5$ ,  $M_0$  must be greater than 6 to obtain entropy limit solutions that do not exceed shock pressure rises for attached flows.

Since Figures 5 to 7 were for  $M_4 = 2.5$  it is convenient to use this  $M_4$  as the reference point for discussing shock structures in direct-connect apparatus. For  $M_4 = 2.5$ , equ. 15 gives  $M_0 = 5.234$ , equ. 14 gives  $T_{t5}/T_{t4} = 2.436$  at  $ER = 1.0$ ,  $A_5/A_r = 2.443$ ,  $(P_5/P_4)_{\text{N.S.}} = 7.125$  and  $(P_5/P_4)_{\text{sup}} = 2.375$ . Table 2 lists data pertinent to several modes of operation of direct-connect combustors. The  $A_5/A_r$  values are the combustor area ratios for  $M_4 = 2.5$  at the listed  $A_5/A_r$  values that are plotted in Figure 9 plus that for  $A_5/A_r = 6.674$  which corresponds to  $ER = 1$ ,  $\epsilon = \epsilon$  and  $P_5/P_4 = (P_5/P_4)_{\text{N.S.}} = 7.125$ . For  $P_5/P_4 = (P_5/P_4)_{\text{sup}}$  and  $\epsilon = \epsilon$ , ER varies from 0.226 to 0.314, thus for ERs lower than, or equal to, these values oblique shocks could be stabilized at  $M_4$  whether or not there was an isolator provided. Here it is presumed that fuel injection is controlled such that heat is added in such a manner that combustion is completed at the prescribed  $A_5$ . An alternative method for ER values less than  $\epsilon = \epsilon$  would be to stage combustion, moving injection downstream, so as not to exceed the values for  $(P_5/P_4)_{\text{sup}}$  as shown in the lower set of curves in Figure 9. For direct-connect testing without an isolator (Figure 8d) small increases in ER would be obtained by letting the precombustion shock move upstream into the air supply nozzle. The limit would occur with the shock near the throat, which would permit  $ER = 0.334$  at  $T_{t5}/T_{t4} = 1.48$  for  $A_5/A_r = 4$  and  $ER = 0.501$  at  $T_{t5}/T_{t4} = 1.72$  for  $A_5/A_r = 12$ .

**TABLE 2**  
**LIMITING EQUIVALENCE RATIOS IN COMBUSTORS WITH  $M_4 = 2.5$ ,  $\gamma = 1.4$**

$$\frac{P_5}{P_4} = \left( \frac{P_5}{P_4} \right)_{sep} = 2.375; \epsilon = \bar{\epsilon} \quad \epsilon = \bar{\epsilon} \quad \text{NORMAL SHOCK } M_5 < \bar{M}_5$$

$\frac{A_5}{A_1}$	$\frac{A_5}{A_4}$	ER	$\frac{T_{t5}}{T_{t4}}$	$M_5$	ER	$\frac{T_{t5}}{T_{t4}}$	$\frac{P_5}{P_4}$	$M_5$	ER	$\frac{T_{t5}}{T_{t4}}$	$\frac{P_5}{P_4}$	$M_5$
4	1.637	0.226	1.325		0.649	1.932	7.125	1.386	0.724	2.039	7.125	1.0
6	2.456	0.260	1.374	2.320	0.932	2.339	7.125	1.689	1.0	2.436	7.125	1.608
6.674	2.731	0.269	1.387	2.398	1.000	2.436	7.125	1.754				
8	3.275	0.284	1.408	2.551	1.000	2.436	6.470	1.917				
10	4.093	0.301	1.432	2.728	1.000	2.436	5.923	2.109				
12	4.911	0.314	1.451	2.871	1.000	2.436	5.596	2.261				

The large gain in operating range that occurs with the use of an isolator is shown in the listings for  $\epsilon = \bar{\epsilon}$  with  $P_5/P_4 \leq (P_5/P_4)_{N.S.}$ . For  $A_5/A_4 < 6.674$  the maximum ER is still  $< 1$  and for  $A_5/A_4 > 6.674$  ER = 1 and  $P_5/P_4 < (P_5/P_4)_{N.S.}$ . In fact, somewhat larger ER values would be realizable in the direct-connect apparatus with an isolator because the origin of the shock train would recede into the air supply nozzle and most of the shock train pressure rise would still occur in the isolator as shown in Figure 8c. The maximum  $T_{t5}/T_{t4}$  values would be the peaks in the  $A_5/A_4$  curves shown in Figure 9,  $T_{t5}/T_{t4} = 2.372$ , ER = 0.955 in the  $A_5/A_4 = 6$  case and  $T_{t5}/T_{t4} = 2.050$ , ER = 0.731 in the  $A_5/A_4 = 4$  case. The corresponding locations for the shock would be at  $M_4 = 2.273$  and 2.089, respectively. Note that if the example chosen for examination had been for a lower  $M_4$ , e.g.  $< 2$ , the peaks in the  $A_5/A_4$  curves for the normal shock solutions would occur at higher  $M_4$  so the structures shown in Figure 8c would not be observed in direct-connect testing. In an engine having an inlet capable of withstanding higher back pressure, ER = 1 would be attained at the  $A_5/A_4 = 6$  with a normal shock in the isolator with  $M_5 = 1.608$ . For  $A_5/A_4 = 4$ , the maximum ER is 0.724,  $T_{t5}/T_{t4} = 2.039$  with  $M_5 = 1$  as shown in the last column of Table 2.

Whereas, the simplification realized by modeling the precombustion shock as a step rise in pressure was convenient in the introductory discussion, a more realistic pressure distribution is needed to proceed with a description of the flow with finite boundary layers. Since it will be necessary to modify the momentum equ. (3) it is also a convenient place to include shear, wall heat loss and the mass and momentum of the "injectant." The resulting equations are still not too cumbersome if the  $\gamma = \text{constant}$  limitation is retained.

The mass of the injectant and the wall heat loss can be included, simply by adding (1 + f) and  $\Delta Q$  terms to the combined mass, energy and state equation, i.e.

$$\frac{P_5 A_5}{P_4 A_4} = (1+f) \frac{M_4}{M_5} \left[ \frac{T_{t5} - \Delta Q}{T_{t4}} \right]^{1/2} \left[ \frac{2 + (\gamma-1)M_4^2}{2 + (\gamma-1)M_5^2} \right]^{1/2} \quad (16)$$

where  $f$  = mass flow of the injectant/mass flow of the propellant stream. In discussions wherein this method is used to analyze low speed ejector ramjets, the bypass ratio replaces  $f$ , the principal stream becomes the injector with conditions at the discharge plane being station 4, and the captured air stream replaces the fuel;  $\Delta Q$  is usually referenced to  $T_{t4}$ , i.e.  $\Delta Q/T_{t4}$  is modeled to retain simplicity.

Fuel momentum, shear and the pressure distributions in the shock train and in the remainder of the 2 or 3D mixing and combustion zone (see Figure 3) are introduced in a modified form of the momentum equ. (3) i.e.

$$K P_s (A_d - A_4) + K_1 \left[ \frac{P_e + P_s}{2} \right] (A_e - A_d) + (1-\epsilon) (P_5 A_5 - P_s A_e) - \frac{C_f \gamma M_4^2}{2} P_4 A_w \\ - P_5 A_5 \left[ 1 + \gamma M_5^2 \right] - P_4 A_4 \left[ 1 + \gamma M_4^2 \right] - P_f A_f \left[ 1 + \gamma M_f^2 \cos \alpha \right] \quad (17)$$

where

$A_d$  is the duct cross sectional area at the end of the shock train

$A_e$  is the duct cross sectional area at the beginning of the 1D approach zone

$K$  is obtained from empirical relationships which account for the "s" shaped shock train pressure distribution, i.e.  $K = \int_0^d p dA / P_s (A_3 - A_4)$ . Since these modifications to the modeling permit the handling of sudden expansion at station 4, i.e. step geometries, it is also possible to include flow situations wherein  $P_e < P_4$ . This will occur at low ER values with relatively large step area increases. In these cases  $K$  can be obtained by either analytical or empirical methods

$K_1$  accounts for a nonlinear pressure-area distribution in the 2-3D mixing and combustion zone. It, too, can be obtained by analytical or empirical methods. Note that there are combustor geometries that have constant area sections following a step that is sufficiently long to contain the beginning of the 1D approach zone at station e. For these cases  $A_e = A_4$  and equ. 17 is simplified. However,  $P_e$ , in general, is not equal to  $P_4$ .

An interesting special class of solutions are those that have shock trains with pressure rises less than that corresponding to a normal shock, significant heat release in the constant area section and continuing heat release to station 5. Entropy limit solutions

in this region are quite sensitive to minor changes in heat release rates. Thus, considerable latitude exists in the interpretation of existing experimental results. Nonetheless, it is presumed that the simple formulation  $K_2 = P_e/P_i$  will prove to be acceptable from forthcoming analytical and/or experimental data bases. The wall pressure and shear forces are therefore:

$$\int_4^5 p dA = K P_s (A_d - A_4) + \left( \frac{K_2 + 1}{2} \right) K_1 P_s A_e - \left( \frac{K_2 + 1}{2} \right) K_1 P_s A_d + (1 - \epsilon) (P_5 A_5 - K_2 P_s A_e) \quad (18)$$

$$\int_4^5 \tau_w dA_w = C_f q_4 A_w = C_f \left( \frac{q}{P} \right)_4 P_4 A_w = C_f \frac{\gamma M_4^2}{2} P_4 A_w \quad (19)$$

$A_w$  is wall surface area

$C_f$  is mean skin friction coefficient obtained from empirical data or suitable modeling

$P_i$  is the pressure of the injectant

$A_i$  is the cross-sectional area of the injectant

$M_i$  is the Mach number of the injectant

$\alpha$  is the angle of injectant relative to the air stream

Dividing equ. (17) by  $P_4 A_4$  and rearranging with the substitution

$$B = \frac{-\gamma M_4^2}{2} C_f \frac{A_w}{A_4} + \frac{P_i A_i}{P_4 A_4} \left( 1 + \gamma M_i^2 \cos \alpha \right) + \left( 1 + \gamma M_4^2 \right) \quad (20)$$

yields

$$\frac{P_s}{P_4} = \frac{\frac{P_5 A_5}{P_4 A_4} (\gamma M_5^2 + \epsilon) - B}{\frac{A_d}{A_4} \left[ K - \frac{K_1 K_2 + K_1}{2} \right] + \frac{A_e}{A_4} \left[ \epsilon - 1 + \frac{K_1 K_2 + K_1}{2} \right] - K} \quad (21)$$

From the wall pressure distribution

$$A_5/A_4 = \left( P_s/P_4 \right)^\epsilon \left( P_5/P_4 \right)^{1-\epsilon} A_d/A_4 \quad (22)$$

and, with the same method as was used from equs. (7) to (8), gives

$$\frac{P_5}{P_4} = \left\{ \frac{\frac{P_s}{P_4} \left[ \frac{A_d}{A_4} (K + \epsilon - 1) - K \right] + B}{\frac{A_d}{A_4} \left[ K - \frac{K_1 K_2 + K_1}{2} \right] + \frac{A_e}{A_4} \left[ \epsilon - 1 + \frac{K_1 K_2 + K_1}{2} \right] - K} \right\}^\epsilon \left( \frac{P_s}{P_4} \right)^{1-\epsilon} \quad (23)$$

and

$$\frac{A_5}{A_4} = \left\{ \frac{\frac{P_s}{P_4} \left[ \frac{A_d}{A_4} (K + \epsilon - 1) - K \right] + B}{\frac{A_d}{A_4} \left[ K - \frac{K_1 K_2 + K_1}{2} \right] + \frac{A_e}{A_4} \left[ \epsilon - 1 + \frac{K_1 K_2 + K_1}{2} \right] - K} \right\}^{1-\epsilon} \quad (24)$$

The method for obtaining entropy limit solutions, given initial conditions and modeling for  $C_f$ ,  $\Delta Q$ ,  $K$ ,  $K_1$ ,  $K_2$ ;  $A_d$  and  $A_e$ , is to select  $M_5$ , solve (16) for  $P_5 A_5/P_4 A_4$ , solve (10) for  $\epsilon = \tilde{\epsilon}$  then solve (21) for  $P_s/P_4$ , (23) for  $P_5/P_4$  and (24) for  $A_5/A_4$ . For a particular value of  $A_5/A_4$ ,  $M_5$  is then the iteration variable. To obtain the "K" factors it is necessary to examine the character of the shock train structure and the pressure distributions downstream. Results then become dimensional and are dependent on particular geometries. However, one additional simple case which has physical significance is that of a sudden expansion or step combustor geometry wherein the shock train structure does not extend beyond the constant area section  $A_e = A_d$  and  $P_e = P_i$ , as shown in Figure 10a. In this case the prescription  $K = K_2 = 1$ , which is tantamount to assuming that the base pressure is  $P_i$ , and the pressure in any remaining length of the coolant area section is constant. This type of flow has been observed in some experiments.

For this case the effects of each of the additional terms that have been introduced can be examined singly and collectively. To preserve continuity in the discussion, an example previously studied (see e.g. Figure 5) viz,  $M_4 = 2.5$ ,  $A_3/A_4 = 3$ ,  $T_{t5}/T_{t4} = 2.0706$ ,  $C_f = \alpha = \Delta Q/T_{t4} = 0$  can serve as a reference. The entropy limit case from Figure 5 corresponding to these conditions has  $P_5/P_4 = 5$  and  $\tilde{\epsilon} = 2.178$ . Including the  $f$  term in equ. (16) would increase  $P_5/P_4$  to 5.373 ( $\tilde{\epsilon} = 2.148$ ). With  $T_{t5}/T_{t4} = 2.0706$  and the modeling of equ. 14 and 15,  $ER = 0.7458$  and  $f_4 = 0.02175$  for a fuel with a stoichiometric  $f_4 = 0.02917$  (i.e.  $H_2$ ). As in Table 2, the assumed free stream conditions are  $M_0 = 5.234$ ,  $T_0 = 400^\circ R$ . This reference is shown as curve 1 in Figure 10b. Whereas, the length scale remains arbitrary, in this sketch the length and area are linearly related for convenience. Thus  $A_5/A_4 = 1.5$  occurs at  $X/L = 0.25$  and the wall shape in the diverging portion of the combustor would be flat in a planar configuration and very slightly "bell" shaped in an axisymmetric configuration. Curve 1 has a step increase in pressure at the combustor entrance followed by a monotonically decreasing pressure which ignores the presence of the step increase in area. In effect it is the pressure distribution that would correspond to a continuous area distribution (e.g. a cone) and an unrealistically thin incoming boundary layer in a physical system. Curve 2 shows the dramatic decrease



in the shock pressure rise to  $P_s/P_4 = 2.864$  ( $\bar{\epsilon} = 2.057$ ) simply due to the step geometry with  $A_4/A_1 = 1.5$ , since the other additional terms have yet to be introduced. For the remainder of the cases shown in Figure 10b,  $f = 0.02175$  and  $A_4/A_1 = 1.5$ , thus curve 2 can be viewed as a more appropriate reference to examine the effects of shear, wall heat flux and axial fuel momentum.

Curve 3 shows the effects of heat loss to the combustor walls; a value of  $\Delta Q/T_{t4} = 0.02$  was used in this example. This heat loss in the absence of a corresponding increase in fuel temperature causes a trivial decrease in  $P_s/P_4$  to 2.821 ( $\bar{\epsilon} = 2.065$ ). When the fuel is used as a regenerative coolant and the fuel temperature is accordingly increased, the effects balance. Consequently, since the effect is small or negligible,  $\Delta Q/T_{t4}$  was set equal to zero in all other cases. Note, however, when other than normal injection is used, fuel temperature is fundamental to obtaining the contribution of fuel momentum. Curve 4 shows the effect of fuel momentum for a prescribed fuel temperature on the results. To study this effect additional assumptions for  $M_f$ ,  $T_{t,f}$  and  $\alpha$  must be made. The term  $P_{t,f}/P_4 A_4$  from equ. (20) can be expressed as

$$\frac{P_{t,f}}{P_4 A_4} = f \left( \frac{T_{t,f}}{T_{t4}} \right)^{1/2} \left( \frac{\gamma_4 M_4}{\gamma_f M_f} \right)^{1/2} \frac{M_4}{M_f} \left[ \frac{2 + (\gamma_4 - 1) M_4^2}{2 + (\gamma_f - 1) M_f^2} \right]^{1/2} \quad (25)$$

Taking  $\gamma_4 = \gamma_f = 1.4$ ,  $M_4 = 28.965$ ,  $M_f = 2.016$ ,  $T_{t,f} = 2000^\circ R$ ,  $T_{t4} = 2592^\circ R$  and  $f = 0.02175$  yields  $P_{t,f}/P_4 A_4 = 0.0724$ . If coaxial injection is assumed,  $\alpha = 0$  and  $\cos \alpha = 1$ . For these conditions, the effect of fuel momentum is significant, both in reducing  $P_s/P_4$  by about 0.421 to 2.443 ( $\bar{\epsilon} = 2.170$ ) and in increasing the stream thrust in the combustor exit. The latter is an especially important consideration in engine operation at higher flight Mach numbers.

Curves 5 and 6 show the large effects on the pressure distribution due to shear for values of  $C_f$ ,  $A_w/A_4 = 0.1$  and  $0.2$ . Whereas the geometries shown in Figure 10a are arbitrary, they are not unrealistic, in that  $l/d = l/h = 16$ . For this axisymmetric geometry  $A_w/A_4 = 20.303$ , thus the  $C_f$  value for curves 5 and 6 would be 0.0049 and 0.0098. These levels are somewhat more than double the typical range of about 0.002 to 0.0045. On the other hand, for a rectangular combustor having a width  $w = 4h_4$ ,  $A_w/A_4 = 48.546$ , thus  $C_f = 0.00206$  and 0.00412, respectively, for curves 5 and 6.

Note that the  $P_s/P_4$  values for all of the cases exceed  $(P_s/P_4)_{sep} = 2.375$  for  $M_4 = 2.5$ , thus it is implied that an isolator is located upstream of the combustor. The subsequent discussion will show that the required length of the isolator increases rapidly with increasing  $P_s/P_4$ . Longer isolators increase engine weight and internal friction. Moreover, higher  $P_s/P_4$  increases the maximum stress and in turn the structural weight. Consequently, the inclusion of the step can lead to large practical benefits in combustor design and overall vehicle performance.

Engine performance as measured by the thrust coefficient  $C_T$  and specific impulse  $I_{sp}$ , however, is only weakly dependent on the range of effects examined in cases 1-6. This argument is substantiated by the data summarized in Table 3. The shock pressure rise  $P_s/P_4$ , static and total pressure ratios  $P_5/P_4$  and  $P_{t5}/P_{t4}$ , and the combustor exit Mach number  $M_6$  are listed for the various combustion processes. To gain an appreciation of the relative insensitivity of  $C_T$  and  $I_{sp}$  on the details of the flow structure, case 1a has been added. Case 1a is a hypothetical combustion-expansion process that would have the highest possible efficiency. It is comprised of a partial heat addition to Mach 1 in a constant area duct, followed by a constant Mach = 1 heat addition to yield the same overall heat release as cases 1-6. This brings the flow to an area ratio  $A/A_4 = 1.640$  and a pressure ratio  $P/P_4 = 3.068$ . Then to put this case on an "equitable" base with cases 1-6, the flow is isentropically expanded to  $A/A_4 = 3$ . Note that the flow structure in the constant area section would be a constant pressure process initiated by a shock train. The shock pressure rise is obtained from the momentum equ. i.e.

$$P_s/P_4 = \left[ 1 + \gamma M_4^2 \right] / (1 + \gamma) = 4.0625 \quad (26)$$

The heat release is obtained from the energy state and continuity equ. i.e.

TABLE 3

FLOW CONDITIONS AND ENGINE PERFORMANCE  
WITH DIFFERENT COMBUSTION PROCESSES

$$M_0 = 5.234; T_0 = 400^\circ R; q_0 = 1000 \text{ lb}_f/\text{ft}^2; M_4 = 2.5; \gamma = 1.4; T_{t5}/T_{t4} = 2.0706; M_f = 2.5;$$

$$P_{t,f}/P_4 A_4 = 0.0724; f = 0.02175; A_6/A_0 = 1; T_{t,f} = 2000^\circ R$$

CASE	$C_f \frac{A_w}{A_4}$	$\alpha$ DEG	$\frac{\Delta Q}{T_{t4}}$	$\frac{P_s}{P_4}$	$\frac{P_5}{P_4}$	$M_5$	$\frac{P_{t5}}{P_{t4}}$	$A_6/A_0 = 1$				$P_6/P_0 = 1$			
								$M_6$	$\frac{P_6}{P_0}$	$C_T$	$I_{sp}$	$M_6$	$\frac{A_6}{A_0}$	$C_T$	$I_{sp}$
1	0	90	0	5.373	0.6881	1.994	0.3120	3.048	3.800	0.6687	2452	3.991	2.339	0.7288	2672
1a	0	90	0	4.063	0.6402	2.095	0.3399	3.139	3.621	0.6849	2511	4.056	2.332	0.7418	2720
2	0	90	0	2.864	0.7435	1.889	0.2864	2.959	3.991	0.6513	2388	3.923	2.457	0.7025	2576
3	0	90	0.02	2.821	0.7356	1.896	0.2868	2.965	3.951	0.6353	2329	3.930	2.458	0.7144	2619
4	0	0	0	2.443	0.6755	2.019	0.3188	3.071	3.754	0.6729	2467	4.008	2.382	0.7341	2691
5	0.1	90	0	3.450	0.8218	1.758	0.2592	2.854	4.233	0.6309	2313	3.854	2.551	0.7077	2595
6	0.2	90	0	4.160	0.8916	1.656	0.2412	2.778	4.420	0.6149	2254	3.801	2.613	0.6982	2560

$$P_4/P_0 = 28.157; A_0/A_4 = 7.926; T_{t0} = 2592^\circ R; \eta_{KE} = 0.98; \eta_N = 0.98; \left[ \frac{P_s}{P_4} \right]_{N.S.} = 7.125 \quad \left[ \frac{P_s}{P_4} \right]_{SEP} = 2.375$$

$$T_c/T_{t_{5a}} = \left[ 1 + \gamma M_4^2 \right] / \left[ (1+f) M_4 (1+\gamma) \right] = 1.3865 \quad (27)$$

which with equ. (14) gives  $f = 0.007852$ . For the  $M = 1$  heat addition process the area ratio is

$$A_{5b}/A_{5a} = \left[ 1 + f_{ab} \right] \left[ T_{t_{5b}}/T_{t_{5a}} \right]^{\frac{1+\gamma}{2}} = 1.6404 \quad (28)$$

where the temperature ratio,  $T_{t_{5b}}/T_{t_{5a}} = 2.0706/1.3865 = 1.4934$  and the mass ratio for this second phase of combustion,  $(1 + f_{ab}) = 1.02175/1.007852 = 1.01379$ . From the end of the  $M = 1$  heat addition the flow is isentropically expanded to the conditions listed in Table 3. It should be stressed that whereas the flow in the diverging portion of the combustor in case 1a is a sequence of one-dimensional processes, cases 1 to 6 are not so constrained, thus any specification of uniform flow properties at locations other than 4 and 5 is not warranted.

Two nozzle processes are examined, expansion to the free stream capture area, i.e.  $A_6/A_0 = 1$  and expansion to the free stream pressure, i.e.  $P_6/P_0 = 1$ . In both sets of results the listed values of the Mach number  $M_6$ , and either  $P_6/P_0 = 1$  or  $A_6/A_0 = 1$ , correspond to an isentropic expansion from station 5 to station 6. Losses in the expansion process are taken into account by multiplying the exit stream thrust by an efficiency  $\eta_N = 0.98$ , thus

$$C_T = \left[ \eta_N \left( 1 + \gamma M_6^2 \right) \frac{P_6 A_6}{P_0 A_0} - \left( 1 + \gamma M_0^2 \right) - \left( \frac{A_6}{A_0} - 1 \right) \right] (q/P)_0 \quad (29)$$

and

$$I_f = \frac{T_{q_0} A_0}{\dot{w}_f q_0 A_0} = \frac{C_T \left[ T_{t_0} \right]^{1/2} q_0}{f P_0 \dot{m}_0} - \frac{\gamma M_0^2 \left[ T_{t_0} \right]^{1/2} C_T}{2 f \dot{m}_0} \quad (30)$$

To obtain  $P_{t_4}/P_{t_0}$ ,  $P_4/P_0$  and  $A_0/A_4$ , an assumption for inlet efficiency,  $\eta_{KE} = 0.98$  is necessary where

$$\frac{P_{t_4}}{P_{t_0}} = \left[ \left( 1 + \frac{\gamma-1}{2} M_0^2 \right) - \frac{(\gamma-1)}{2} M_0^2 \eta_{KE} \right]^{\frac{\gamma}{\gamma-1}} \quad (31)$$

$$\frac{P_4}{P_0} = \frac{P_{t_4}}{P_{t_0}} \left[ \frac{2 + (\gamma-1) M_0^2}{2 + (\gamma-1) M_4^2} \right]^{\frac{\gamma}{\gamma-1}} \quad (32) \quad \frac{A_0}{A_4} = \frac{P_4 M_4}{P_0 M_0} \left[ \frac{2 + (\gamma-1) M_0^2}{2 + (\gamma-1) M_4^2} \right]^{1/2} \quad (33)$$

which yields  $P_{t_4}/P_{t_0} = 0.6949$ ,  $P_4/P_0 = 28.157$  and  $A_0/A_4 = 7.926$ .

Acknowledging that the absolute values of  $I_f$  and  $C_T$  are only approximate due to the  $\gamma = 1.4$  constraint, some of the more interesting conclusions that can be drawn from the information in Table 3 are:

1) Whereas the total pressure recovery in the "combustor" is quite different in the cases examined, the differences in  $C_T$  and  $I_f$  are quite small, e.g. case 1a has 41% greater  $P_{t_5}/P_{t_4}$  than case 6 but only 11% higher  $C_T$  and  $I_f$  for  $A_6 = A_0$  and 6% higher  $C_T$  and  $I_f$  for  $P_6 = P_0$ .

2) Confining the precombustion shock train to the isolator (case 1) produces 5.6% higher  $C_T$  and  $I_f$  than when the shock train is permitted to extend into the step combustor (case 2). Nonetheless, the corresponding higher pressure and greater length, isolator may lead to using the step as the preferred engine design.

3) Gains in performance of about 8-13% are realized when the nozzle flow is expanded to free stream pressure. This suggests that the nozzle exit/air capture area ratio  $A_6/A_0$  should be in the range of 2.4 to 2.6 for these engine configurations when operating at  $T_{t_5}/T_{t_4} = 2.0706$  and  $M_0 = 5.234$ . However, the increases shown in Table 4 would be somewhat compensated by increased cowl and/or inlet additive drag.

4) Introducing design complexities beyond those required to obtain the flow structures corresponding to cases 1 or 2 with the objective of increasing  $C_T$  and  $I_f$  are not apt to be fruitful. This judgment is based on a comparison of the case 1 and 2 results with those from the optimum process, case 1a. Moreover, the relatively small differences among cases 1, 1a and 2, which hold the other pertinent parameters,  $C_T$ ,  $\Delta Q$  and  $\alpha = 0$ , provides an explanation for the often observed small differences in engine performance reported by various investigators using markedly different models for the combustion process.

5) Increases in shear (cases 5 and 6 vs. case 2) increases the total pressure loss in the combustor and the engine thrust potential. This adds to the previously discussed detrimental effects due to the large increases in  $P_4/P_0$ . At this  $M_0$ , maximum pressure in the combustor and the upstream extent of the shock train are usually of more concern than losses in  $C_T$  and  $I_f$ . This is generally true in the  $M_0$  range of about 5 to 7.5. Above  $M_0 = 7.5$  losses in  $C_T$  and  $I_f$  are relatively more important. Whereas, the net force on the combustor walls decreases as the shear increases, the pressure force increases. This can cause ambiguity in the interpretation of experimental results from direct-connect combustor or complete engine test apparatus. It is difficult to distinguish between the effects due to incomplete heat release and those due to shear. This problem is a principal factor in establishing the need for global measurements of wall force (e.g. with a thrust stand) and the energy release (e.g. by calorimetric means). Table 4 is included

TABLE 4

## THRUST LEVELS IN DIRECT CONNECT AND FREE JET TEST APPARATUS

$$M_0 = 5.234, T_0 = 400^\circ R, P_0 = 0.3622 \text{ psia}, \gamma = 1.4, M_4 = 2.5, T_4 = 1151.8^\circ R, P_4 = 10.196 \text{ psia}$$

$$A_0 = A_6 = 396.3 \text{ in}^2; A_4 = 50 \text{ in}^2; A_5 = 150 \text{ in}^2$$

CASE	$\frac{T_{t5}}{T_{t4}}$	$\frac{C_f A_w}{A_4}$	$\int PdA$ lb <sub>f</sub>	$\int \tau_w dA_w$ lb <sub>f</sub>	TOTAL lb <sub>f</sub>	ENGINE NET THRUST lb <sub>f</sub>
2	2.0706	0	1844.9	0	1844.9	1792.5
5	2.0706	0.1	1947.8	- 223.0	1725.0	1736.4
6	2.0706	0.2	2076.5	- 446.0	1630.5	1692.2
7	1.0000	0	409.8	0	409.8	168.9
	(ISENTROPIC)					
8	2.0492	0	1815.9	0	1815.9	1745.3
	( $\eta_c = 0.98$ )					

to lend insight to this issue. The contribution of wall pressure and shear forces in the combustor and the net force in a direct-connect test apparatus are listed in columns 4-6. The last column lists the net internal force on an engine in a free jet test at the corresponding flight condition. To quantify the results, a particular size direct-connect test apparatus (viz  $A_4 = 50 \text{ in}^2$ ) was arbitrarily selected. The corresponding inlet and nozzle areas in the free jet engine with  $A_6 = A_0$  are  $396.3 \text{ in}^2$ . Cases 7 and 8 have been added to aid in the development of the arguments. Case 7 is for no fuel or heat addition in a shear free combustor and thus corresponds to "engine out" operation of case 2. Case 8 is a minor variant of case 3 which is to show the effects of inefficiency in heat release. In this case, the "combustion efficiency," based on temperature rise, is taken as 0.98, thus  $f = 0.02175$  and  $T_{t5}/T_{t4} = 0.98 (2.0706-1) + 1 = 2.0492$ . Other conditions, not listed in Table 4, for cases 7 and 8, respectively, are:  $P_4/P_1 = 1.0$  and  $2.818$ ,  $P_{t5}/P_{t4} = 1.0$  and  $0.2868$ ,  $P_5/P_4 = 0.1776$  and  $0.7350$ ,  $M_6 = 4.779$  and  $2.966$ ,  $P_6/P_0 = 1.1813$  and  $3.948$ , and  $C_f = -0.0614$  and  $0.6342$ . Ratioing differences of values listed in Table 4 shows that a 1% increase in  $\eta_c$  would produce the same increase in  $\int PdA$  as a 0.014 increase in  $C_f A_w/A_4$ . Thus a discriminator in addition to an integration of wall pressures would be needed to deduce  $\eta_c$  or  $C_f$ . A bulk calorimetric measurement of  $\eta_c$  would provide the discriminator. Likewise, a thrust measurement would suffice, since the same 1% increase in  $\eta_c$  would produce a thrust increase equivalent to reduction in  $C_f A_w/A_4$  of 0.0117. Comparison of the two measurements, or with  $P_4/P_1$ , would provide a test of consistency. The problem of identifying the origin of loss from a measurement of thrust in a free jet engine is even more difficult, due to the addition of losses in the inlet and nozzle losses and the impracticality of making calorimetric measurements. Interestingly, for the selected example, viz an engine operating at  $M_0 = 5$  with  $A_5/A_4 = 3$ , the thrust contribution by the combustor is about equal to the net thrust of the entire engine.

Further refinements in the analysis of flows in combustors requires a more detailed explanation of the flow in shock trains. Before proceeding to this discussion it can be noted that the simplification used so far, viz uniform flow at station 4, f and 5 and a calorically perfect gas (i.e.  $\gamma = \text{constant}$ ) can be removed to handle "real gas" flows. The changes are:

$$\text{MASS FLOW} \quad \frac{\dot{PMA}}{T^h} = \rho u A = \int \rho u dA \quad (34)$$

1D,  $\gamma = c$                       1D                      GENERAL

$$\text{MOMENTUM} \quad PA \left( 1 + \gamma M^2 \right) = PA + \rho u A u_x = \int \left( P + \rho u^2 \right) dA \quad (35)$$

1D,  $\gamma = c$                       1D                      GENERAL

$$\text{ENERGY} \quad C_p T \left( 1 + \frac{\gamma-1}{2} M^2 \right) \left( \frac{\dot{PMA}}{T^h} \right) = \rho u A \left[ h + \frac{u^2}{2} \right] = \int \left( \rho u \right) \left[ h + \frac{u^2}{2} \right] dA \quad (36)$$

1D,  $\gamma = c$                       1D                      GENERAL

$$\text{STATE} \quad P = \rho R T = P = f(\rho, \mathcal{M}, T) \quad (37)$$

1D,  $\gamma = c$                       1D, GENERAL

Current versions of RJPA, in general, handle the equation of state as a mixture of species in local thermodynamic equilibrium. An option is also available to account for "unmixedness" wherein the product species is assumed to comprise equilibrium products and unreacted fuel at the same pressure and temperature. Note that when the general form of the equations is used, it is necessary to define a mean value of  $M$ , in order to define "entropy limit" solutions from Eq. 10.

## INLET-COMBUSTOR INTERACTION MODEL

The model for inlet-combustor interaction is based on a description of a "shock train" or "pseudo shock." The structure is characterized by a series of either oblique or lambda shocks which are spread out over the length,  $s_t$ , as shown in Figures 3 and 11a. For low pressure rises across the "shock train," and/or thin entering boundary layers, local separation is not present. For relatively higher pressure rises and thicker

boundary layers the pressure rise of the first wave of the shock train is sufficient to locally separate the boundary layer. Subsequent waves in the shock train increase the mean pressure, such that pressure rises significantly in excess of that which causes the boundary layer to separate can be maintained. Indeed, normal shock pressure rises are readily observed, as must be the case to permit operation of the dual mode engine cycle in the subsonic combustion mode.

In an engine, if the combustor and inlet are not connected by an isolator that can withstand the pressure rise and separated flow, then the inlet will unstart and combustion gases can be expelled from the engine. In the direct-connect combustor apparatus, shown in Figure 8, if the injector/combustor is close coupled with the air supply nozzle the shock train will recede into the nozzle. To avoid either problem, the inlet-combustor isolator is added to stabilize the shock train. An important design consideration is the isolator length. It must be of sufficient length to prevent inlet unstart, but not overly long, which would result in excessive weight and additional shear losses.

The same type of shock train or "pseudo shock" structure can be generated in an overexpanded or throttled, nonreacting flow. This technique has proved to be quite useful in obtaining data over a broad range of conditions, to provide the basis for design of combustor-inlet isolators. Rather extensive data bases have been obtained for cylindrical (Ref. 11), annular (Ref. 12) and rectangular ducts (Refs. 13-15). The modeling used herein is an extension of that introduced in Ref. 11 to cover all three classes of duct geometry and both the oblique and lambda shock structures. The lambda shock structure shown in the nonreacting case (Figure 14c) is equally cogent in an isolator-combustor. This structure is present at relatively low Mach numbers when the boundary layer is relatively thick. The redundant normal shock waves in the central portion of the flow result in sequential decelerations and accelerations. This process can be quite dissipative. Indeed, the maximum static pressure rise in this flow structure is lower than that corresponding to a single, normal shock.

It appears that it is possible to relate the pressure rises in shock trains in the different duct geometries by a suitable choice of the fundamental length (i.e. length, width, height) scales and the boundary layer parameters. The data and modeling of Ref. 11 from cylindrical ducts with oblique wave structures will serve as the foundation upon which more general modeling will be constructed.

A simplified reconstruction of the structure of the shock train for data from Ref. 11 is shown in Figure 12. In this approximate analysis, expansion fans are represented as single waves and curvature of the waves is neglected, except at points of intersection. Wave angles are constructed to yield local Mach numbers in general accord with the pitot pressure measurements. Calculated local Mach numbers are shown, and comparisons of the corresponding pitot pressure ratios with the measurements at  $r = 0.125$  in. and  $r = 0.375$  in. are given. These comparisons indicate that the general character of the oblique shock structure has been depicted, and that both the compression and expansion processes in reality consist of a multiplicity of oblique waves which produce continuous rather than step changes in  $P_t/P_0$ . Note that the interaction of the probe shock with the duct wave structure also leads to a lack of precise definition of wave locations. The calculated value of static pressure across the initial compression wave is 2.4 and the corresponding local Mach number is 1.98, which is in very close agreement with the separation criteria given in Equ. 11 and 12 and supported by the data in Figure 4. Finally, the flow reconstruction coupled with the wall static pressure data shows that the flow in the duct exit is primarily supersonic for final to initial pressure ratios,  $P_t/P_0$ , less than the corresponding normal shock value.

A striking feature of the pressure distributions from Ref. 11 is the similarity in shape and/or slope of all of the profiles for a given case. Indeed, if all profiles for any one case are shifted by superposing the data points from one with the trace of another, they collapse to a single curve. This suggests that the wave structure for tests with  $P_t/P_0$  lower than the maximum  $P_t/P_0$ , represents just a proportional part of the wave structure present in the maximum case. This argument was substantiated in Ref. 11 from comparisons of pitot pressure measurements similar to those shown in Figure 12. It should be noted, however, if the initial conditions ahead of the shock train would be significantly different, e.g. in a rapidly developing boundary layer, superposition would require introduction of the pertinent boundary layer scale. Granting this argument, it suggests that just the values of  $P_t/P_0$  for the various cases can be used to examine methods for further collapsing of the data. When the end points  $P_t$  from each static pressure rise curve are ratioed to  $P_0$  and these points are plotted vs. the total distance  $s_t$  over which the pressure rise acts, the curves are superposed. For a given  $s_t$ , the larger the  $M_0$ , the higher the required compression. This is the trend that would be expected if one segment of the shock train is examined. If the segment is taken as a fixed length and one simple wave reflection, then the shock angle would be fixed. For a given shock angle, the pressure rise increases with increasing Mach number. From linear theory, it would be expected that  $(M_0^2 - 1)^{-1}$  would tend to collapse the data. This normalization is necessary but not sufficient to obtain the desired "universal" model for shock trains in ducts.

The next step is the consideration of viscous effects, since the shock train is a flow with strong viscous-inviscid interactions. Unfortunately, the data base is limited, thus the remainder of the modeling rests on heuristic arguments. For the same  $P_t/P_0$ ,  $s_t$  was found to vary inversely with  $Re$ , and directly with  $D(\theta/D)^{1/2}$ . Each of these trends is expected. The  $\theta$  values for these tests were obtained from boundary-layer calculations based on the momentum-integral method of Ref. 17. Note, however, that the exponents on  $Re$ , and  $\theta/D$  may be unique to cylindrical geometries and flows with oblique rather than lambda wave structures. As  $Re$  increases, the boundary layer can withstand a larger  $P_{t,\infty}/P_0$  before separating, therefore the initial shock angle is steeper and  $s_t$  is smaller. The inverse scaling with diameter is due to the trend toward geometric scaling, which is not strictly geometric according to the data correlation, unless both  $D$  and  $\theta$  change uniformly. The variation with boundary-layer thickness is, in a qualitative sense, the same as observed by Lustwerk (Ref. 18) and in a quantitative sense, consistent with that described

by McLafferty in Ref. 19. Figures 8-12 of that reference present normalized  $s_t$  vs normalized  $\delta^*$ . Assuming direct proportionality between  $\theta$  and  $\delta^*$ , it is possible to show the  $\theta$  dependence, but considerable scatter is present in the data. In the limit, as  $\theta$  approaches zero,  $s_t$  should also approach zero, since it should be possible to stabilize a single, simple, normal or oblique shock. Just this situation was produced in a combustion experiment described in Ref. 18, in which the boundary layer was removed just upstream of the shock.

Figure 13 shows the degree of success obtained in the correlation procedure, where the results of Ref. 17 are included in the summary. Some scatter is present but a simple quadratic relationship

$$s_t \left[ M_4^2 - 1 \right] \text{Re}^k / [D(\theta/D)^k] = 50 \left( P_s/P_4 - 1 \right) + 170 \left( P_s/P_4 \right)^2 \quad (38)$$

as shown by the correlating curve adequately represents all of the data. The empirical correlation not only defines the end point  $s_t$  of the pressure rise curve, but the entire wall pressure distribution simply by replacing  $s_t$  with  $s$  and  $P_s/P_4$  with  $P/P_4$ .

To apply this model to design of the isolator and combustor, it is also necessary to locate the origin of the shock train relative to the combustor entrance, i.e. the isolator exit. For internal ducts wherein the demarcation between isolator and combustor is crisp, e.g. a step, no ambiguity arises. For other configurations the location of the furthest upstream fuel injector is used to anchor  $s_d$ . The distance that the shock train extends into the combustor  $s_d$  is taken and the value of  $s$  from equ. 38, setting  $P/P_4 = P_{sep}/P_4$  where the separation pressure ratio is from eqs. 11 and 12.

Stockbridge (Ref. 12) has made very extensive measurements of the flow structure of shock trains in coannular supersonic flows. Figure 14 shows static pressure distributions in the annulus for initial Mach numbers of 1.66, 2.35 and 2.89. The corresponding mass flow ratios of annulus to center duct ("gas generator") are 2.51, 0.84 and 2.92, respectively. The axial coordinate has been made dimensionless by dividing by the annular duct wall separation distance. For a nominally constant outer mass flow rate, a decrease in  $w$  denotes an increase in the inner flow, which can then expand further, thereby reducing the annulus exit pressure by ejector action. The character of the pressure rise curves is quite similar to that of the curves from the cylindrical duct. This suggests that the shock train structure may also be similar. Figure 15 summarizes the data for the coannular duct tests using the same ordinate and substituting  $h$  for  $D$  in the parameter on the abscissa. Although the correlation is not quite as good as in Figure 19, it can be argued that it is adequate for using as the basis of design of an isolator.

Data for rectangular ducts is available from Refs. 13-15. Whereas, analysis of the data is still in progress, some preliminary observations can be made. In Ref. 11 the length of duct available for stabilizing the shock train was greater than  $s_t$  for the strongest pressure rise,  $P_s/P_4$ . The boundary layers were relatively thick and the lambda shock structure was clearly observed. Computed flowfields were in general agreement with the observed flow structure. The  $P_s/P_4$  values were significantly greater than  $(P_s/P_4)_{sep}$  but  $(P_s/P_4)_{s.s.}$  could not be obtained. This is rather clear evidence that a highly dissipative shock train structure can be realized. The authors were able to collapse the static pressure traces from the two nominal duct flow Mach numbers  $M_4$  of 1.6 and 2.45. At Mach 1.6 collapsing of the data with superposition required normalization to the upstream boundary layer thickness. At Mach 2.45, collapsing the data in the same manner as that of Ref. 11 sufficed. Effort is now underway to obtain a "universal" correlating equation by adjusting the exponents in  $\text{Re}$ , and  $(\theta/D)$  in equ. 38.

#### INTRODUCTION OF THE SHOCK TRAIN STRUCTURE INTO THE ISOLATOR-COMBUSTOR DESIGN

It is convenient to use examples in discussing the significance of the shock train structure in the isolator-combustor design. The particular conditions are the same as those used to develop Figure 10, viz,  $M_0 = 5.234$ ,  $q_0 = 1000 \text{ lb}_f/\text{ft}^2$ , and  $P_4/P_0 = 28.157$ . The dimensional duct diameter or height is taken as 3 in. Using equ. 38 values of  $s_t$  and  $s_d$  can be found for a range of boundary layer momentum thicknesses. Results are shown in Figure 16. The very strong dependence of the required length of an isolator  $s_0 = (s_t - s_d)$ , on  $\theta$ , is apparent. This suggests that methods to reduce  $\theta$ , such as boundary layer bleed and/or energization could greatly reduce  $s_0$  which may lead to substantial gains in overall vehicle performance. The large increases in required isolator length for higher  $P_s/P_4$  values reinforce the arguments made previously regarding beneficial effect of steps which reduce the  $P_s/P_4$  at a given ER (see Figure 10). Moreover, this also gives additional insight into the strategy of limiting the maximum ER at the flight condition which sets the overall requirement on isolator length. In this procedure,  $s_0$  values are calculated for the entire range of operating conditions and engine geometries. Then for selected values of  $s_0$ , weights are determined to provide the basis for optimizing the overall configuration.

With the shock train pressure distribution and location modeled, it is now possible to obtain the "K factor" introduced in equ. 17 and include this refinement in cycle analyses (e.g. RJPA). Since  $A(x)$  in the combustor is a function of shape, the "K factor" is shape dependent but is not dependent on the scale of the combustor or the momentum thickness of the boundary layer. To obtain  $K$ , equ. 38 is used to define  $P(x)$  and with geometry, i.e.  $A(x)$ ,  $K = \int_0^d p dA / P_4 (A_4 - A_1)$  is calculated using standard numerical integration methods.

#### JET PENETRATION MODEL

The literature is rich with experimental results, data correlations and modeling of jets in cross flow (see e.g. Refs. 21-34). Some controversy exists regarding which of the parameters that have been used, in fact, have a foundation consistent with fundamental aspects of the flow structure. The modeling presented herein in a revision of the method discussed in Ref. 21. The general method for normal injection is extended to include jets at all orientations and revises some features of the correlation parameters so as to be

in closer accord with new insights into the physical structure of the flow. The revised model should also resolve some of the aforementioned controversial issues.

Figure 17 shows schematic representations of typical flowfields that have been observed for angular injection of gaseous jets into a supersonic main stream. They are categorized with regard to the size of the boundary layer relative to the jet diameter  $d_j$  and whether the injection pressure is matched or underexpanded, relative to a representative pressure in the distributed flow. The representative pressure has been named the "effective back pressure"  $P_{eb}$  (see Ref. 21) and is taken as a representative average static pressure around the emerging jet when the boundary layer momentum thickness is small relative to the jet diameter, i.e.  $\theta < d_j$ . When the boundary layer is thick relative to  $d_j$ , i.e.  $\theta \approx d_j$ , the effective back pressure is taken as the pressure required to separate the boundary layer. The matched pressure condition occurs when the pressure in the discharge plane of the jet matches the effective back pressure, i.e.  $P_j = P_{eb}$ . In this case the jet undergoes little if any expansion as it is turned downstream. In many situations  $P_j > P_{eb}$ , consequently the jet is underexpanded. The general barrel-shock structure, terminating in a Mach disk is similar to that observed in injection into a quiescent medium. Downstream of the Mach disk, the jet continues to turn and the pressure in the jet approaches the pressure in the mainstream ahead of the disturbance,  $P_\infty$ .

The structure of an underexpanded jet discharging into a quiescent medium is similar to the structure of a jet into a supersonic cross flow. To relate the two structures it is necessary to equate the height of the Mach disk in a quiescent medium,  $Y_1$  to the arc length along the centerline of the Mach disk  $S_1$  for the jet in cross flow. Modeling is required to obtain  $S_1$  from schlieren photographs, wherein the height of the center of the Mach disk  $Y_1$  is readily discernible. For this the jet centerline is assumed to be a parabola and the angle of the centerline at the Mach disk,  $\delta_1$  is modeled to follow

$$\delta_1 = \delta_j - 180/\pi \sin \delta_j [1 - \exp(-8q_a/q_j)] \quad (39)$$

$$Y_1/S_1 = \left\{ 1 + |\tan \delta_1 / \tan \delta_j| \right\} / \left\{ f(\delta_1) + f(\delta_j) |\tan \delta_1 / \tan \delta_j| \right\} \quad (40)$$

$$\text{where } f(\delta) = 1/2 \csc \delta + 1/2 \tan \delta \ln \cot 1/2 \delta \quad (41)$$

This modeling not only results in maximum vertical displacement of the Mach disk for upstream injection (at  $\delta_j \approx 120^\circ$ ) which is in accord with the experimental results of Ref. 22, but also has the appeal in that  $Y_1 = 0$  for  $\delta_j = 0^\circ$  and  $180^\circ$ . Note that in the general model the correlating dimension was the height of the Mach disk,  $Y_1$  rather than arc length which has the obvious deficiency for injection at angles other than  $90^\circ$ .

The remaining item for relating the two barrel shock structures is the specification of the effective back pressure for injection into supersonic cross flow. The modeling for  $P_{eb}$  in the thin boundary layer is  $P_{eb} = (P_{sj} [0.37(P_{sj} + P_{s1}) + 2 P_\infty] / 4)$  where  $P_{sj}$  and  $P_{s1}$  are the pressures that correspond to oblique (or normal) shocks on an effective solid body at wedge angles of  $\delta_j$  and  $\delta_1$ . This change from the general model yields a more realistic average pressure surrounding the barrel shock at all angles of injection. For  $\delta_j \geq 90^\circ$ ,  $P_{sj}$  is the static pressure downstream of a normal shock in the main flow. These changes lead to nearly perfect correlation between the data sets for barrel shocks in quiescent medium and in cross flow.

Slight changes have also been made in the modeling of the centerline of the jet trajectory from that of Ref. 21. This portion of the jet is treated as an effective body whose local cross-sectional area is given by

$$(A/A_j)^{1/2} = r/r_j - 1 + 1.45 \ln [P_j/P_{eb}] \left[ 1 - \exp(-0.322 S/D_j) \right] \quad (42)$$

The jet penetration model should only be used in the near field of the injector, i.e.  $x/d_j < 50$ . At this point the jet and main flow are nearly coaxial for typical engine operating conditions. The jet penetration model specifies the center of mass of the jet and the cross-sectional area of the effective solid body. The unified theory (Ref. 21) provides a method to obtain the mean flow properties in the main flow, that are consistent with an overall momentum balance of the two fluids. Two of the several methods that can be used to proceed downstream are: 1) global mixing and combustion model, and 2) modular analysis of scramjet flowfields. Method 1 is the subject of a forthcoming paper. Method 2 will be briefly summarized. Both methods have the attribute of minimal computer requirement which is mandatory for use as affordable design tools.

#### SHEAR AND HEAT TRANSFER MODEL

The models for shear and heat transfer are based on a large number of measurements made with liquid and gaseous fuels in direct-connect and freejet engine tests (Ref. 35). By far, the bulk of the measurements were of local and regional heat transfer rates. Consequently, the veracity of the shear parameter depends on the assumption that the modified form of the Reynolds analogy that was used to deduce shear is valid for flows with exothermic reactions. Figure 18 is a graph of the resulting shear and heat flux parameters. The average gas-wall enthalpy difference is defined as

$$\Delta h = h_{t_4} + h_{t_f} + 0.5 f \eta_c \Delta \bar{H}_f - h_w \quad (43)$$

where  $h_{t_4}$  and  $h_{t_f}$  are the total enthalpies of the incoming air and fuel, respectively;  $h_w$  is the enthalpy of air at the average wall temperature;  $f$  is the fuel/air weight ratio,  $\eta_c$  is the combustion efficiency and  $\Delta \bar{H}_f$  is the heating value of the fuel.

#### MODULAR ANALYSIS OF SCRAMJET COMBUSTOR

The general features of the modular analysis of scramjet flowfields presented in Ref. 5 are shown in Figure 19. The first step is to solve the integral equations in accordance with the methods already described for given initial conditions and combustor geometry. This yields the axial pressure distribution  $P(x)$  for modeled values of wall shear  $\tau_w$ , and heat transfer  $Q_w$ , and an assumed value for the combustion efficiency  $\eta_c$ . With  $P(x)$  so

defined, a simplified finite-difference calculation that avoids calculating flow in the separated regions is made to obtain  $r_w$ ,  $Q_w$ , and  $\eta_c$  analytically. Inherent to the finite-difference method are models for kinetic rates and turbulent mixing. The integral solution is then repeated using these values of  $r_w$ ,  $Q_w$ , and  $\eta_c$  to obtain a new  $P(x)$  and so forth. The iteration ends when the flow area  $A(x)$ , obtained from the finite-difference solution, agrees with the geometric area downstream of station  $x$ .

In principle, a finite-difference solution could be obtained using the geometric  $A(x)$ , and thereby avoid depending on  $P(x)$  from the integral method. In practice, the presence of the separated zone would have to be accurately calculated, and the simplifying assumptions that permit the use of the boundary layer or parabolized forms of the Navier-Stokes equations could not be made. The form of the conservation equations would be elliptic and solutions would have to be obtained using time-dependent techniques. References 36 and 37 describe routines for such techniques that require hours of CPU time on the largest computers. Given the uncertainties that still remain in adequately describing kinetic processes, their associated rate constants, the transport properties, and the models for turbulence, the simpler, far less expensive approach has considerable merit.

At present, solutions have been obtained that were based on the assumption that radial and circumferential pressure gradients are negligible, thereby permitting use of the boundary layer form of the conservation equations. Additionally, it is more expeditious to first solve for the inviscid "core" flow in the combustor, iterate for  $P(x)$ , and then solve for the boundary layer using edge conditions from the core flow and a dense grid point spacing in the radial direction. Conversely, if the fuel distribution is unacceptable a new conceptual design may have to be considered.

#### CONCLUSION

These techniques have been used to design several dual mode ram-scamjet engines including SCRAM. Extensive testing of the SCRAM engine at Mach numbers of 5, 6 and 7.2 has firmly established the veracity of these methods.

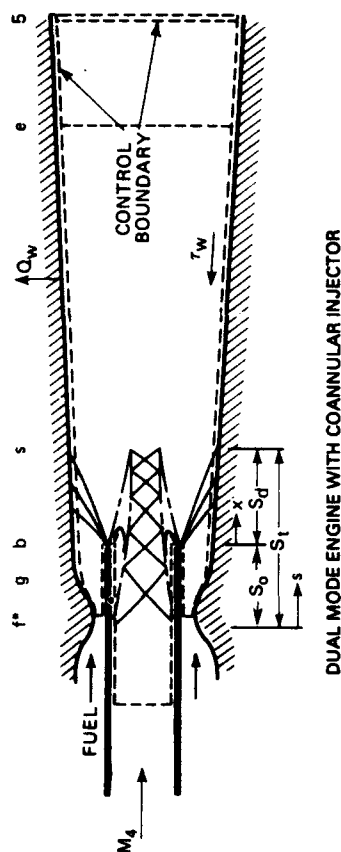
#### REFERENCES

1. Waltrup, P.J., Anderson, G.Y. and Stull, F.D.: Supersonic Combustion Ramjet (Scramjet) Engine Development in the United States. JHU/APL Preprint Series, The 3rd International Symposium on Air Breathing Engines, Munich, Germany, March 1976.
2. Brema, A.: Recent Advances in Mixed Cycle Engine Design and Application. 1st International Symposium on Air Breathing Engines, June 19-23, 1972, Marseille, France.
3. Billig, F.S., Waltrup, P.J. and Stockbridge, R.D.: Integral-Rocket Dual-Combustion Ramjets: A New Propulsion Concept. Journal of Spacecraft and Rockets, Vol. 17, Sept.-Oct. 1980.
4. Pandolfini, P.P.: Instructions for Using Ramjet Performance Analysis (RJPA) IBM-PC Version 1.0. JHU/APL NASP-86-2, Nov. 1986.
5. Schetz, J.A., Billig, F.S. and Favin, S.: Modular Analysis of Scramjet Flowfields. J. Propul. and Power, Vol. 5, No. 2, Mar.-Apr. 1989, pp. 172-180.
6. Billig, F.S., Waltrup, P.J., Gilreath, H.E., White, M.E., Van Wie, D.M. and Pandolfini, P.P.: Proposed Supplement to Propulsion System Management Support Plan Submitted to Robert Williams, Advanced Research Projects Agency. JHU/APL NASP-86-1, July 15, 1986.
7. Waltrup, P.J.: Liquid Fueled Supersonic Combustion Ramjets: Research Perspective. J. of Propul. and Power, Vol. 3, Nov.-Dec. 1987, pp. 515-524.
8. Shapiro, A.H.: The Dynamics and Thermodynamics of Compressible Fluid Flow. The Ronald Press Co., N.Y., 1983.
9. Schetz, J.A., Billig, F.S. and Favin, S.: Approximate Analysis of Base Drag Reduction by Base and/or External Burning for Axisymmetric Supersonic Bodies. AIAA-80-1258. AIAA/SAE/ASME 16th Joint Propul. Conf., June 30-July 2, 1980, Hartford, CT.
10. Billig, F.S. and Dugger, G.L.: The Interaction of Shock Waves and Heat Addition in the Design of Supersonic Combustors. Presented at the XIth Symposium (International) on Combustion, Poitiers, France, July 1968, The Combustion Institute, 1969, pp. 1125-1139.
11. Waltrup, P.J. and Billig, F.S.: Structure of Shock Waves in Cylindrical Ducts. AIAA Jour., Vol. II, Oct 1973, pp. 1404-1408.
12. Stockbridge, R.D.: Experimental Investigation of Shock Wave/Boundary-Layer Interactions in an Annular Duct. J. Propul. and Power, Vol. 5, No. 3, May-June 1989, pp. 346-352.
13. Carroll, B.F. and Dutton, J.C.: A Numerical and Experimental Investigation of Multiple Shock Wave/Turbulent Boundary Layer Interactions in a Rectangular Duct. UIU ENG 88-4015, Gas Dynamics Lab., U. of IL., Aug. 1988.
14. Fejer, A.A., Heath, G.L., Driftmyer, R.T.: An Investigation of Constant Area Supersonic Flow Diffusion. Aerospace Research Lab., U. of Toledo, ARL 64-81, May 1964.
15. Zumpano, F.R., Guile, R.N. and Eckerle, W.A.: High-Aspect-Ratio Supersonic Diffuser Performance Characteristics. United Technologies Corp., East Hartford, CT, Report R89-914767-3, June 1980.
16. Waltrup, P.J. and Billig, F.S.: Precombustion Shock Structure in Scramjet Engines. AIAA Paper 72-1181, New Orleans, LA, 1972.
17. Glowacki, W.J.: Fortran IV (IBM 7090) Program for the Design of Contoured Axisymmetric Nozzles for High Temperature Air. NOLTR 64-219, U.S. Naval Ordnance Lab., White Oak, MD, Feb. 1965.
18. McLafferty, G.H., Krasnoff, E.L., Ranard, E.D., Rose, W.G. and Vergara, R.D.: Investigation of Turbojet Inlet Design Parameters. Report R-0790-13, United Aircraft Corp., East Hartford, CT, Dec. 1955.



19. Lustwerk, F.: The Influence of Boundary Layer on the "Normal" Shock Configuration. Meteor Report 61, MIT, Cambridge, MA, Sept. 1950.
20. Billig, F.S.: Combustion Processes in Supersonic Flow. J. Propul. and Power, Vol. 4, No. 3, May-June 1988.
21. Billig, F.S., Orth, R.C. and Lasky, M.: A Unified Analysis of Gaseous Jet Penetration. AIAA Jour., Vol. 9, No. 6, June 1971, pp. 1048-1058.
22. Cohen, L.S., Coulter, L.J. and Egan, W.J., Jr.: Penetration and Mixing of Multiple Gas Jets Subjected to a Crossflow. AIAA Jour., Vol. 9, No. 4, Apr. 1971, pp. 718-724. (Also see Cohen, L.S., Coulter, L.J. and Chiappetta, L.: Hydrocarbon-fueled Scramjet. Vol. VII, Fuel Distribution Investigation. AFAPL-TR-68-146, Vol. VII, Apr. 1970.)
23. Koch, L.N. and Collins, D.J.: The Effect of Varying Secondary Mach Number and Injection Angle on Secondary Gaseous Injection into a Supersonic Flow. AIAA Paper 70-552. AIAA Atmospheric Flight Mechanics Conf., Tullahoma, TN, May 1970.
24. McClinton, C.R.: The Effect of Injection Angle on the Interaction Between Sonic Secondary Jets and a Supersonic Stream. NASA Technical Note TN D-6669, Feb. 1972.
25. McDaniel, J.C. and Graves, J., Jr.: A Laser-Induced Fluorescence Visualization Study of Transverse, Sonic Fuel Injection in a Nonreacting Combustor. AIAA Paper 86-0507, AIAA 24th Aerospace Sci. Meeting, Reno, NV, Jan. 1986.
26. Orth, R.C., Schetz, J.A. and Billig, F.S.: The Interaction and Penetration of Gaseous Jets in Supersonic Flow. NASA CR-1386, July 1969.
27. Povinelli, F.P., Povinelli, L.A. and Hersch, M.: Supersonic Jet Penetration (up to Mach 4) into a Mach 2 Airstream. AIAA Paper 79-92, AIAA 8th Aerospace Sci. Meeting, N.Y., Jan. 1970 (also NASA TM-X-52721).
28. Rogers, R.C.: Mixing of Hydrogen Injected from Multiple Injectors Normal to a Supersonic Airstream. NASA TN D-6476, Sept. 1971.
29. Schetz, J.A. and Billig, F.S.: Penetration of Gaseous Jets Injected into a Supersonic Stream. J. of Spacecraft, Vol. 3, No. 11, Nov. 1966, pp. 1652-1665.
30. Orth, R.C. and Funk, J.A.: An Experimental and Comparative Study of Jet Penetration in Supersonic Flow. J. Spacecraft and Rockets, Vol. 4, No. 9, Sept. 1967, pp. 1236-1242.
31. Vranos, A. and Nolan, J.J.: Supersonic Mixing of a Light Gas in Air. Pratt & Whitney Aircraft Report, 1964 (also Supersonic Mixing of Helium and Air. Bumblebee Report TG63-53, JHU/APL, June 1964, pp. 131-161).
32. Torrence, M.G.: Concentration Measurements of an Injected Gas in a Supersonic Stream. NASA TN D-3860, 1967.
33. Chrans, L.J. and Collins, D.J.: Stagnation Temperature and Molecular Weight Effects in Jet Interaction. AIAA Jour., Vol. 8, No. 2, Feb. 1970, pp. 287-293.
34. Wagner, J.P., Cameron, J.M. and Billig, F.S.: Penetration and Spreading of Transverse Jets of Hydrogen in a Mach 2.72 Airstream. NASA CR-1794, Mar. 1971.
35. Orth, R.C., Billig, F.S. and Grenleski, S.E.: Measurement Techniques for Supersonic Combustion Testing. MIT press, Progress in Astronautics and Astronautics, Vol. 34, pp. 263-282.
36. Kumar, A.: Numerical Simulation of the Flow Through Scramjet Inlets Using a Three-Dimensional Navier-Stokes Code. AIAA Paper 85-1664, July 1985.
37. Kumar, A.: Numerical Analysis of the Scramjet-Inlet by Using Two-Dimensional Navier-Stokes Equations. NASA TP-1940, Dec. 1981.





DUAL MODE ENGINE WITH COANNULAR INJECTOR

Fig. 3 Model for integral and finite difference solutions for flow processes with diffusive flames.

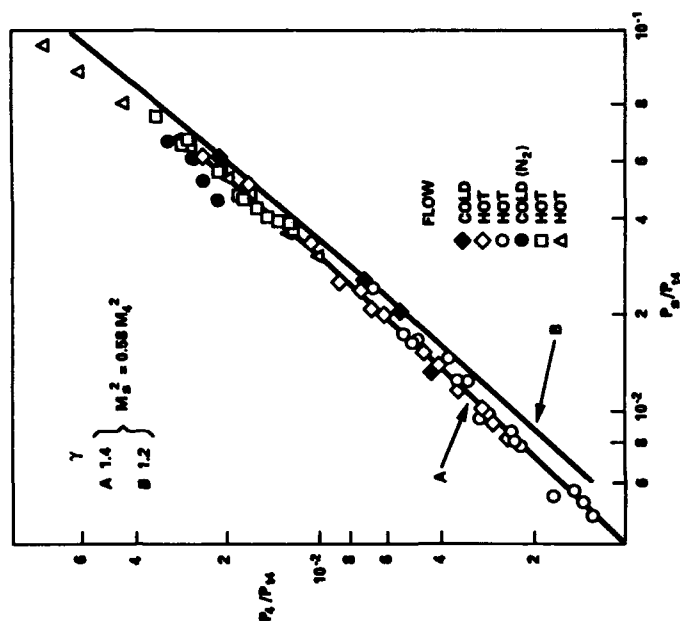


Fig. 4 Separation pressure ratio versus nozzle pressure ratio.

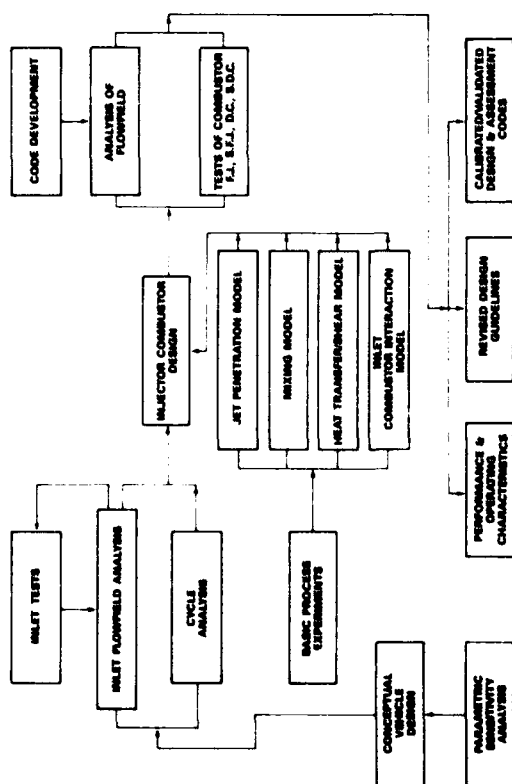


Fig. 1 Injector combustor design methodology.

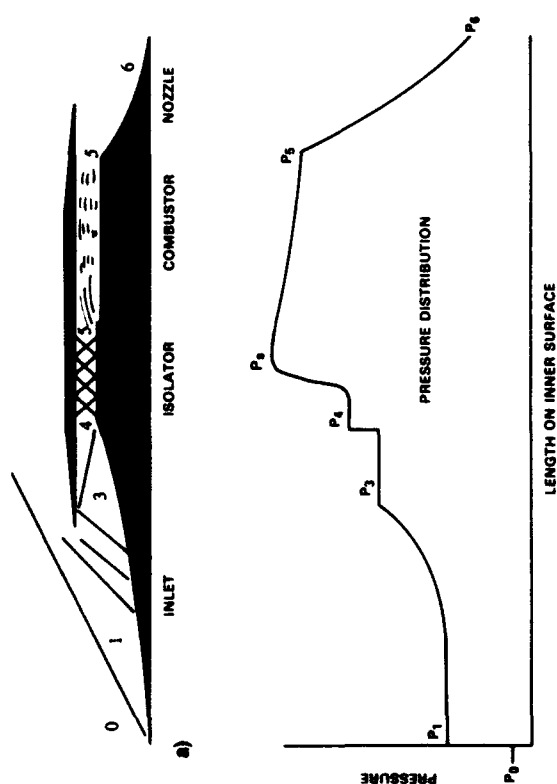


Fig. 2 Flowfield and axial pressure distribution in a dual mode ramjet-scrumjet engine.

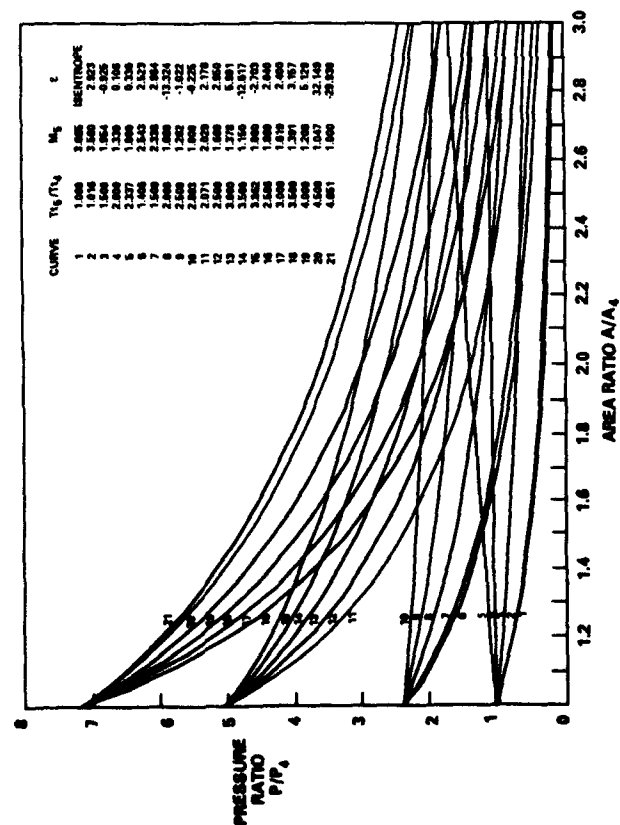


Fig. 5 Combustor pressure distributions for families of  $T_{01}/T_{04}$  at selected  $P_0/P_4$ ;  $\gamma = 1.4$ .

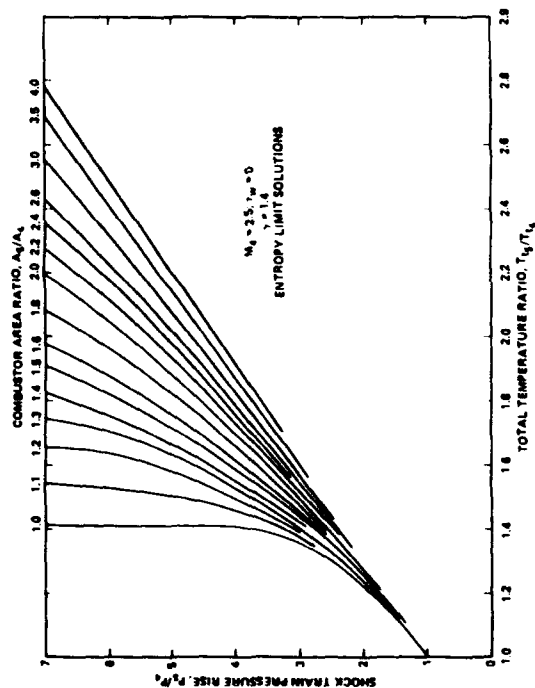


Fig. 6 Shock train pressure rise as function of heat release.

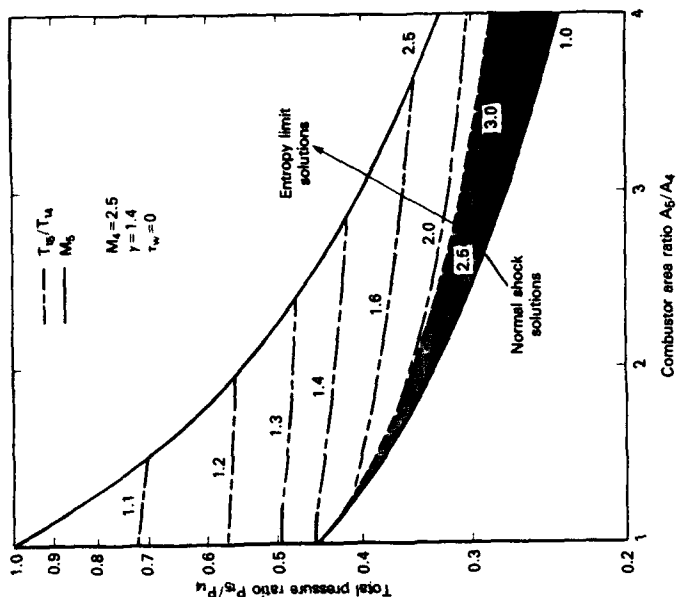


Fig. 7 Total pressure losses for selected heat release rates.

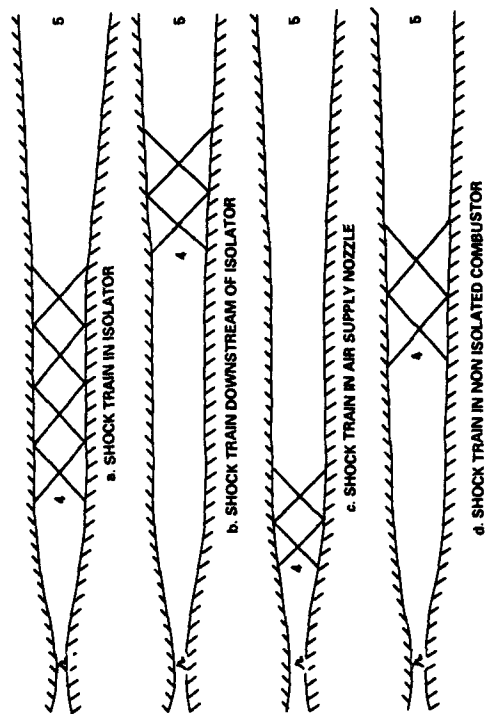


Fig. 8 Shock train structures in direct connect test apparatus.



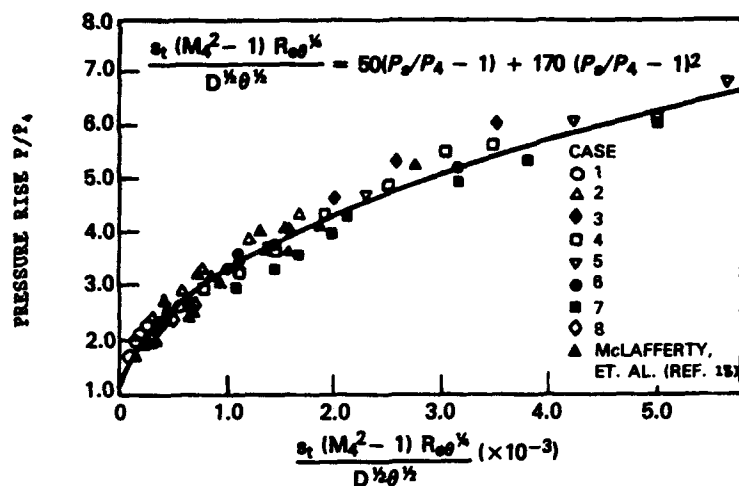


Fig. 13 Shock trains in cylindrical ducts.

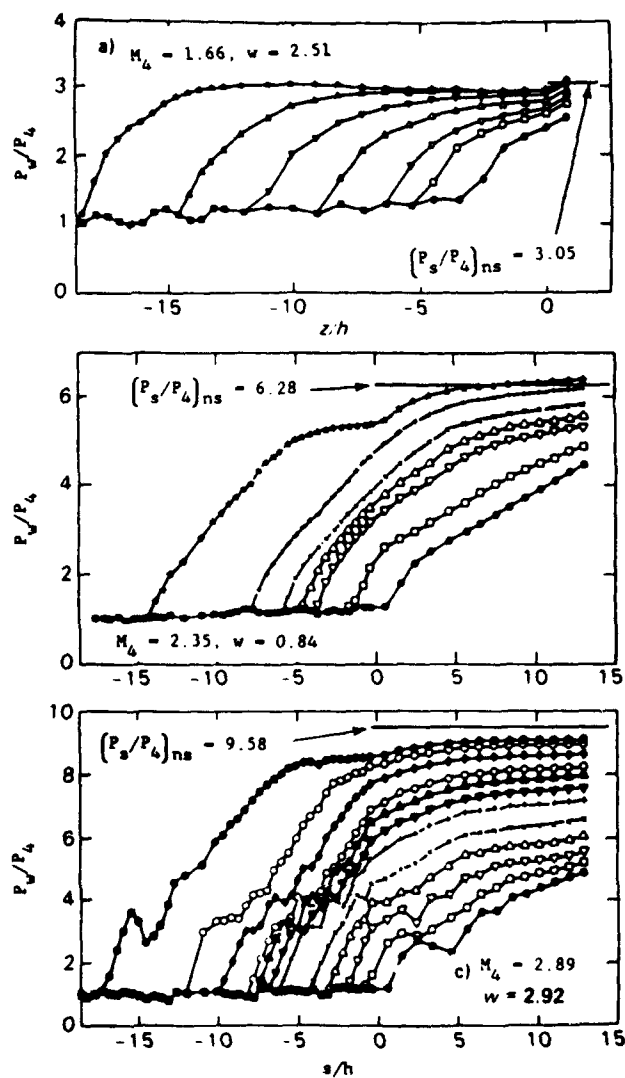


Fig. 14 Shock train pressure distributions in annular ducts.

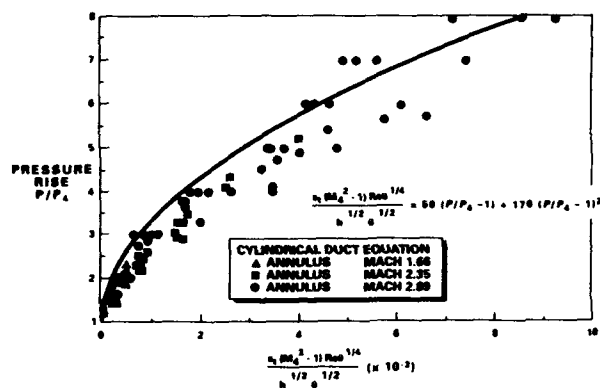


Fig. 15 Shock trains in coannular ducts.

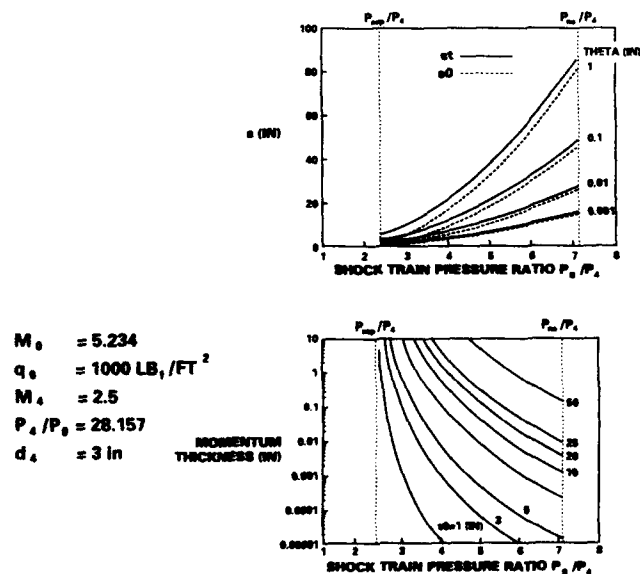


Fig. 16 Isolator design requirements.

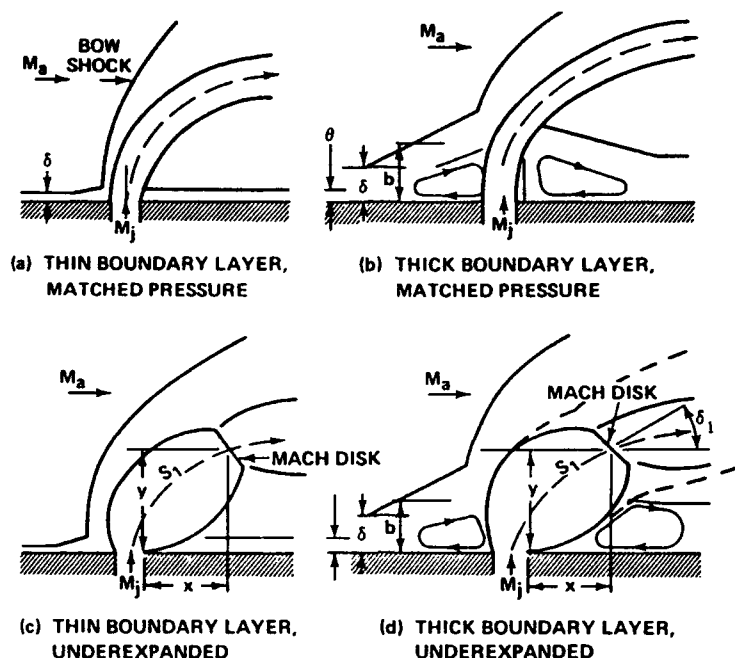


Fig. 17 Structure of jets in supersonic cross flow.

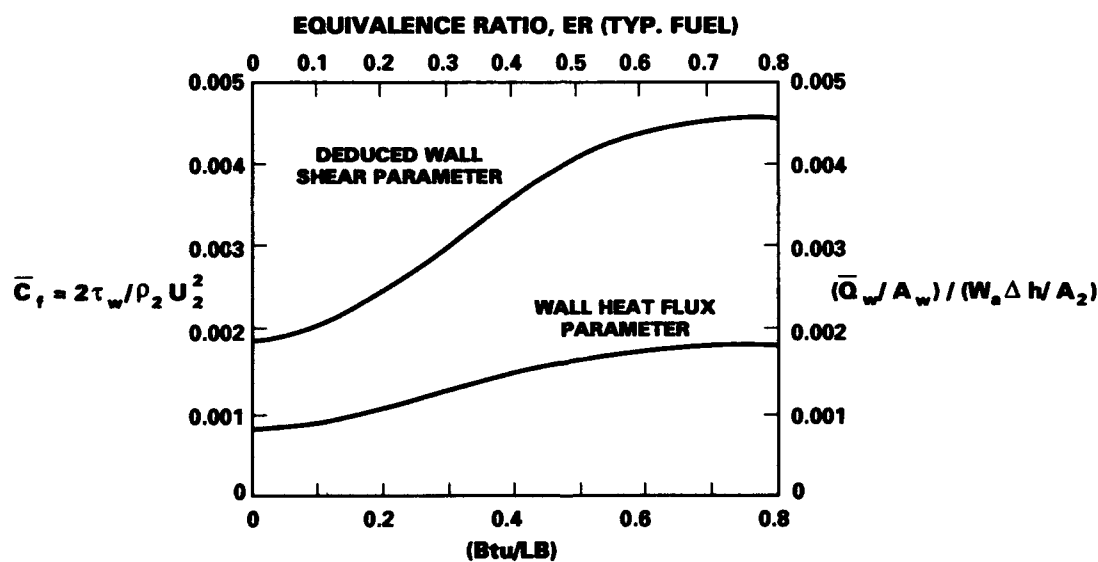


Fig. 18 Combustor wall heat transfer and skin friction coefficient as a function of equivalence ratio.

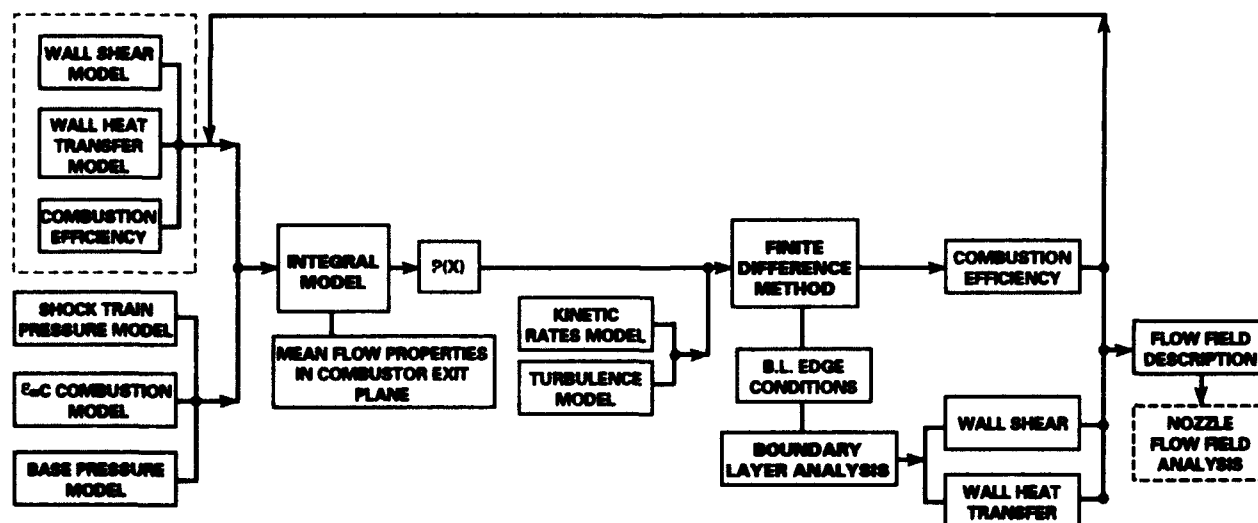


Fig. 19 Method of computation for supersonic combustion analysis.

## Discussion

### WINTERFELD

Is the correlation for the shock train pressure also applicable to the case where the fuel injectors are mounted inside the duct. It seems to me that there is an interaction of the boundary layer and the fuel injection.

### AUTHOR'S REPLY

The principal phenomenon that is causing these shock trains is the overall blockage in the duct caused by the heat release. The interaction of injectors and boundary layer is relatively a second order phenomenon. Most of the shock exist ahead of the injectors. If you go beyond this regime, so that the downstream condition no longer controls the processes, the details of the injector determines the shock structure and it becomes very important.

### RAMETTE

The data you show are for steady flow computation. In the scramjet there are unsteady phenomena as shock-boundary interaction. Do you intend to extend your model to unsteady flow?

### AUTHOR'S REPLY

Professor Adamson at the Michigan's university has just begun that problem. He is using our input and is doing the unsteady flow problem. The data I showed you today are 20 to 25 years old but we run a new finite difference method for a hydrogen combustor. It works fine, the physics have not changed in 25 years.

The unsteady question is an important one because it very much dictates the length. From measurements in the engine we know the magnitudes of the pressure rises for the unsteady part.

### WINTERFELD

You showed us the complicated procedure for the design of a supersonic combustor. What is the value of the first guess using the inviscid flow in this combustor?

### AUTHOR'S REPLY

It is what we do. We start with the inviscid solution, this is a very simple equation. The viscous solution takes two pages. We design on the basis of the inviscid solution. There is a minor adjustment in the shock train, within the empirical modelling of the shock train length.



## USE OF SECONDARY FLOWS FOR RAPID MIXING IN SCRAMJET COMBUSTORS

by

G. V. R. Rao and A. A. Heiba  
Rockwell International Corporation  
Rocketdyne Division  
6633 Canoga Avenue  
Canoga Park, California 91303

92-16987



## SUMMARY

An efficient scramjet combustor requires rapid mixing of parallel supersonic streams of air and injected fuel. The velocity differential between the two streams may not be enough for spreading the mixing layer. To augment the mixing process, secondary flows can be generated by a skewed supersonic nozzle for the fuel. A conical ramp that shields the injector can provide large lateral gradients in the airflow. The Unified Solution Algorithm (USA) code developed by Rockwell International was used to compute inviscid flowfields over typical configurations. The results are presented in this paper. The interaction of the pressure and density gradients in the air and fuel streams at the injector exit appears to be the major source of rapid mixing of the streams.

## INTRODUCTION

Over the past several years, it has been recognized that the use of a supersonic combustion ramjet (scramjet) for hypersonic propulsion is primarily dependent on rapid and efficient fuel-air mixing and reaction. In the very high speed vehicle configurations, both the air and fuel streams enter the combustor at high Mach numbers, essentially in the longitudinal direction. The growth of the mixing layer is reduced considerably as the Mach numbers of the streams are increased as shown by both experimental and theoretical investigations of References (1) and (2).

Several investigators have examined potential techniques for mixing enhancement, noting that rapid mixing of supersonic streams of fuel and air in a short length is essential for hypersonic airplanes. Kumar, Bushnell, and Hussaini (3) suggested techniques for enhancing turbulence and mixing in scramjet combustors. They examined the influence of an oscillating shock numerically for increasing the level of turbulence. Drummond and Mukunda (4) studied the interaction of fuel-air mixing layer with a curved shock. Their computations show that the vorticity generated led to enhanced mixing and reaction.

Some experimental studies also report on mixing enhancement in supersonic shear layers. Menon (5) studied a weak shock interaction with the shear layer, and found that there is a significant spreading of the shear layer downstream of the shock interaction. Experiments carried out by Sullins, et al, (6) show that the spreading rate of the mixing layer can be increased if the pressures in the two streams are different.

Turning to practical applications of mixing enhancement schemes, recent experiments by Northam, Greenberg, and Byington (7) show the use of injector ramp configurations to improve fuel-air mixing. The hydrogen fuel nozzle used in these experiments is a conical nozzle of 1.7 Mach number, and the airflow Mach number is 2.0.

Schadow, et al, (8) experimentally studied the mixing of supersonic coaxial jets. The inner jet was of  $M = 3$  and the outer jet of  $M = 1.8$ . The geometries of the center jet were circular and rectangular of 3:1 aspect ratio. Their results show that rectangular configurations for center jets have better mixing characteristics. Entrainment behavior of elliptic and rectangular jets confined in a circular shroud were compared to a circular jet by Wilson, et al, (9). They found that noncircular jets gave considerably improved entrainment. Swithenbank, et al, (10) found that improved mixing and combustion were obtained by incorporating vortex generating tabs at the trailing edges of the ramp between fuel nozzle and surrounding airflow.

Encouraged by the findings in the above cited investigations, we chose to study the effect of a highly nonuniform fuel jet from an asymmetric nozzle. Unlike a ramp of rectangular configuration, we chose a cone with its axis inclined to the airflow. The interaction between the two nonuniform supersonic flows at the injector exit is expected to generate increased vorticity for mixing enhancement.

## SKEWED NOZZLE IN A CONICAL RAMP

We chose a conical ramp to generate nonuniformities in the oncoming supersonic airstream. This conical ramp surrounds a skewed fuel nozzle whose exit cross section is also circular. The selection of circular cross sections for the ramp and the fuel nozzle reduces the wake area and minimizes base drag. The skewed nozzle contour can be designed to produce a highly nonuniform but shock-free supersonic jet of fuel. A typical configuration for such a nozzle-ramp combination is sketched in Figure 1. The interaction of the nonuniform fuel jet with the surrounding nonuniform airflow is the source of secondary flows to promote rapid mixing. After passing through the shock, the airstream flows around the conical ramp in helical paths. Similarly, the fuel stream flows in helical paths inside the supersonic nozzle. These helical paths upstream of the injector exit are indicated by solid arrows in Figure 1. As the air and fuel streams come together, the airstream squeezes the fuel inwards at the bottom, and the fuel jet plumes upwards at the top. These secondary flows are due to pressure differentials in the two streams and are shown by dashed arrows in Figure 1.

Inviscid flowfield analyses were performed using the USA code developed at Rockwell International. The details of the code and its usage are not discussed here, but can be found in Reference (11). The injector configurations and results of numerical computations are discussed in the following subsections.

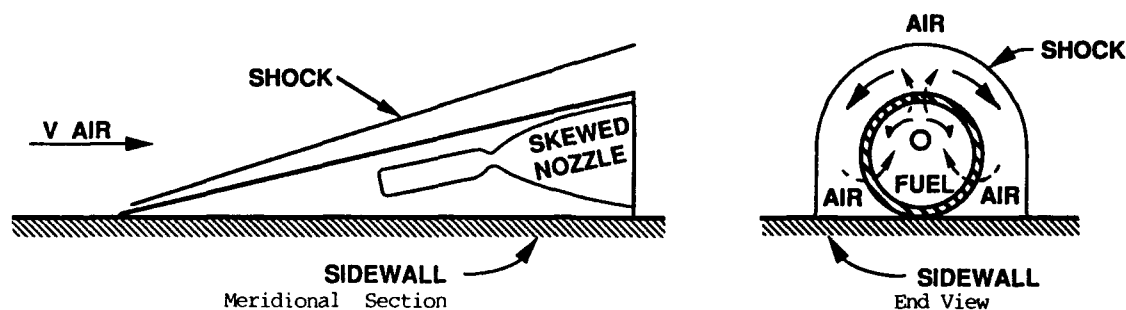


Figure 1. Schematic of Skewed Nozzle in Conical Ramp

### CONICAL RAMP

The fuel flow and airflow have different stagnation conditions, but in the numerical algorithm the reference values for the pressure, density, and velocity must be the same in the two regions occupied by fuel and air. It is easier to choose the nozzle throat conditions as reference values, since the fuel nozzle design needs to be operable over a wide range of combustor conditions.

Since the conical ramp establishes a flowfield into which the fuel jet is injected, the ramp configuration and the flow conditions around it is discussed first. Uniform airflow at the combustor entrance is denoted by its Mach number  $M_i$ , nondimensional pressure  $P_i$ , and nondimensional density  $\rho_i$ . Consider a cone of half-angle  $\beta$  lying on its side along a wall of the combustor so that its centerline is at an angle  $\beta$  to the oncoming flow. Consequently, the windward generatrix of the cone makes an angle  $2\beta$  with the oncoming airflow, whereas the leeward one is aligned with the flow.

In computing the flow around the conical ramp, the airflow is assumed unbounded in the lateral direction except for the plane on which the cone is lying. The Euler solutions of the flow are similar at all cross sections normal to the x-direction of the oncoming airflow. It is sufficient to construct a two-dimensional grid at the nozzle exit with the origin at the center of the cone. The flowfield is exterior to the cone and bounded by the combustor wall. The computational grid is constructed accordingly as shown in Figure 2(a). The lateral boundary of the grid is chosen at a sufficient distance from the cone. The numerical computations are carried out for  $M_i = 3.3$ ,  $P_i = 0.039 P_{ref}$ ,  $\rho_i = 0.47 \rho_{ref}$  and cone half angle  $\beta = 10$  deg. The computed shock configuration and nondimensionalized pressure contours between the cone and the shock are shown in Figure 3. Note that  $P_{ref} = 500$  psi (34.47 kPa) and  $\rho_{ref} = 0.094$  lbm/ft<sup>3</sup> (1.505 kg/m<sup>3</sup>) are chosen corresponding to the fuel nozzle throat conditions as discussed earlier.

### SKEWED NOZZLE

Into the flowfield around the ramp, as established in the preceding subsection, we introduce an appropriate nonuniform fuel jet. Features required by the fuel jet are rapid mixing and entrainment between the two streams. Also, the fuel exiting from the nozzle is to be carried away from the combustor wall. After leaving the conical ramp, the fuel stream must plume outwards in the upper regions and plume inwards in the lower regions as shown in Figure 1. The contour of a supersonic nozzle to meet this objective is not unique, but we chose one typical three-dimensional contour to examine the potential of this concept to enhance mixing. The procedure adopted in arriving at the skewed contour and numerical analyses of the flowfield is described below.

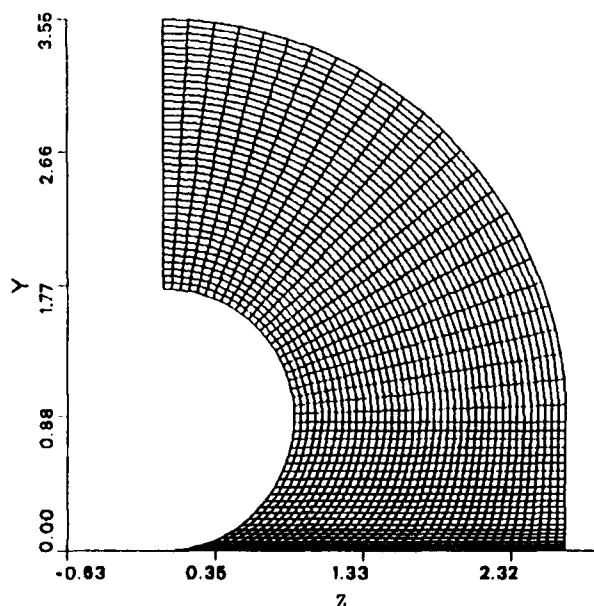
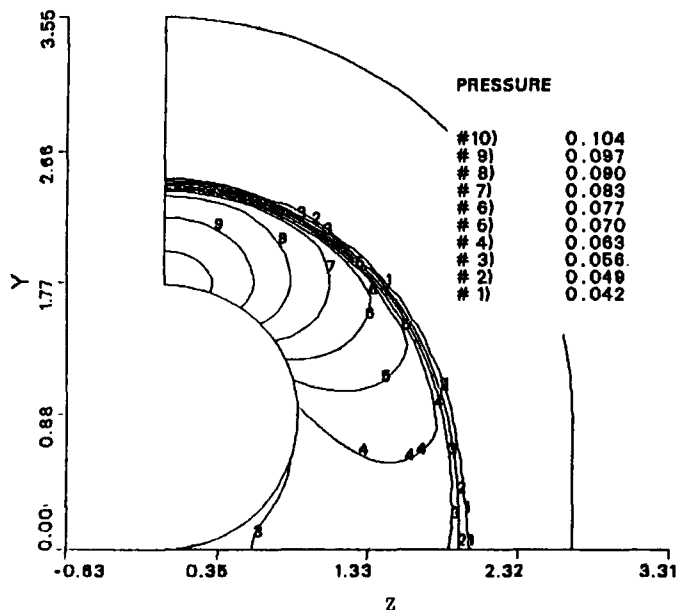


Figure 2. Computational Grid

Figure 3. Nondimensionalized Pressure Contours Around Cone for  $M_i = 3.3$



An axisymmetric nozzle of area ratio 6.2 and length 77% of an equivalent 15 deg cone was designed using the optimum thrust contour program developed at Rocketdyne several years ago based on Reference (12). This contour is shown in Figure 4(a) and in the throat region has a radius of curvature 1.5 times throat radius  $R_t$ .

The maximum wall slope is 25 deg, at  $\xi = 0.644$ , and a wall slope of 16 deg is reached at the nozzle exit at  $\xi = 4.151$ . This optimum thrust contour can also be described in cartesian coordinates  $\xi$ ,  $\eta$ , and  $\zeta$  as

$$\begin{aligned}\xi &= \xi \\ \eta &= R \cos \Phi \\ \zeta &= R \sin \Phi\end{aligned}$$

where  $\Phi$  is the azimuthal angle and  $R$  is defined in terms of  $\xi$  from the optimum thrust nozzle contour program, and depicted in Figure 4(a). Downstream of  $\xi = 0.644 R_t$ , the skewed contour is defined in cartesian coordinates  $x'$ ,  $y'$  and  $z'$  by setting

$$\begin{aligned}x' &= \xi - 0.644 R_t, \\ y' &= \eta - \Delta\eta, \text{ and} \\ z' &= \zeta.\end{aligned}$$

The amount of skewness depends upon  $\Delta\eta$ . For the example, we chose  $\Delta\eta$  such that the curve obtained by setting  $\eta = \zeta = 0$  in the above relations yields a circular arc of radius 19.214  $R_t$ .

The skewed nozzle thus obtained is shown in Figure 4(b) in the  $x'$ - $y'$  plane. The upper wall has an exit slope of 5.15 deg and the lower wall has an exit slope of -25 deg measured from the  $x'$  axis.

Starting with the method-of-characteristics solution for the axisymmetric flowfield at  $x' = 0$ , the three-dimensional flow in the skewed nozzle is solved by using the USA code, referred to earlier in the Euler mode. The computational grid in the  $x'$ - $y'$  plane with 27 points in the  $x'$  direction and 51 points in the azimuthal direction is shown in Figure 5(a). Since the flowfield is symmetric in  $z'$  the computations are limited to the region of positive  $z'$  values. The cross sections are all circular with their centers lying on the grid line passing through the origin. The computational grid in the cross plane at the nozzle exit is shown in Figure 5(b) with 31 points in the radial direction and 51 points in the azimuthal direction.

The numerical results of the flowfield computations showing the nonuniformity at the exit of the skewed nozzle are shown in Figure 6. There are no discontinuities in the Mach number contours nor in the nondimensionalized pressure plots to indicate shocks in the nozzle flow.

#### INTERACTION OF NONUNIFORM AIRSTREAM WITH NONUNIFORM FUELSTREAM

In the preceding sections, the airflow conditions downstream of a conical ramp and the fuel flow conditions at a skewed nozzle exit were described. Now it is necessary to bring the flows together and examine their interaction downstream of the proposed injector configuration. These two flows are computed separately but they are compatible at the mutual boundary because the same values of  $P_{ref}$  and  $\rho_{ref}$  are employed in the computations. The mutual boundary at the injector exit is a circle and no rear-facing step between the nozzle flow and the airflow is considered in our Euler computations. Furthermore, flow separation of the nozzle flow as it meets the combustor wall is to be avoided. Similarly, the fuel jet as it plumes out at the nozzle exit should not cause separation of the external airflow around the cone.

Suitable translation and rotation of the  $x'$ ,  $y'$ ,  $z'$  coordinates shown in Figure 4 can satisfy these requirements and agree with the  $x$ ,  $y$ ,  $z$  coordinate system shown in Figure 2. The nozzle flowfield described in Figure 6 can now be introduced into the interior of airstream described in Figure 2.

Note that across the interface between these two zones occupied by fuel and air there are discontinuities in pressure, density, and tangential velocities. Figure 7 shows these pressures and densities in the two zones as functions of azimuthal

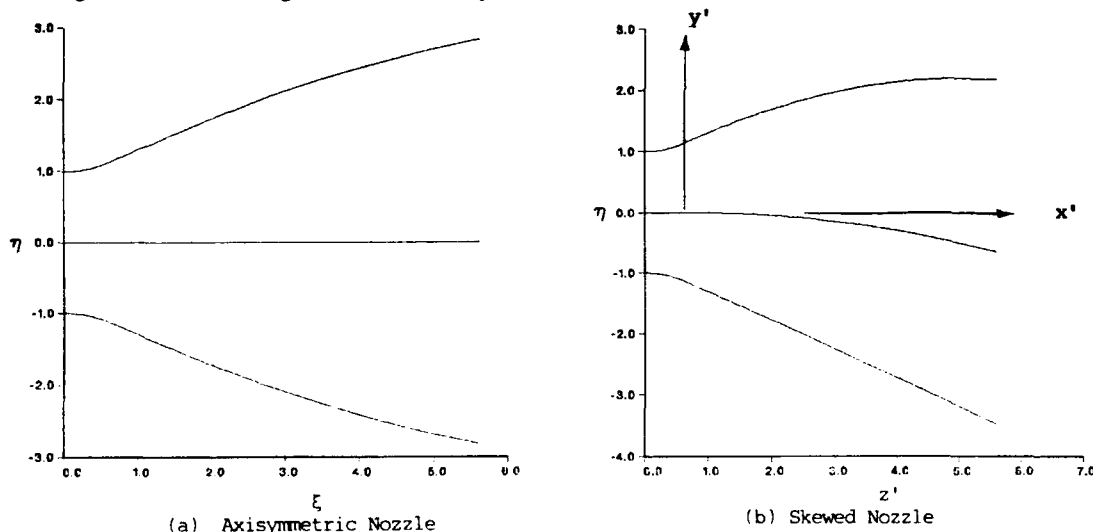


Figure 4. Design of Skewed Nozzle Contour

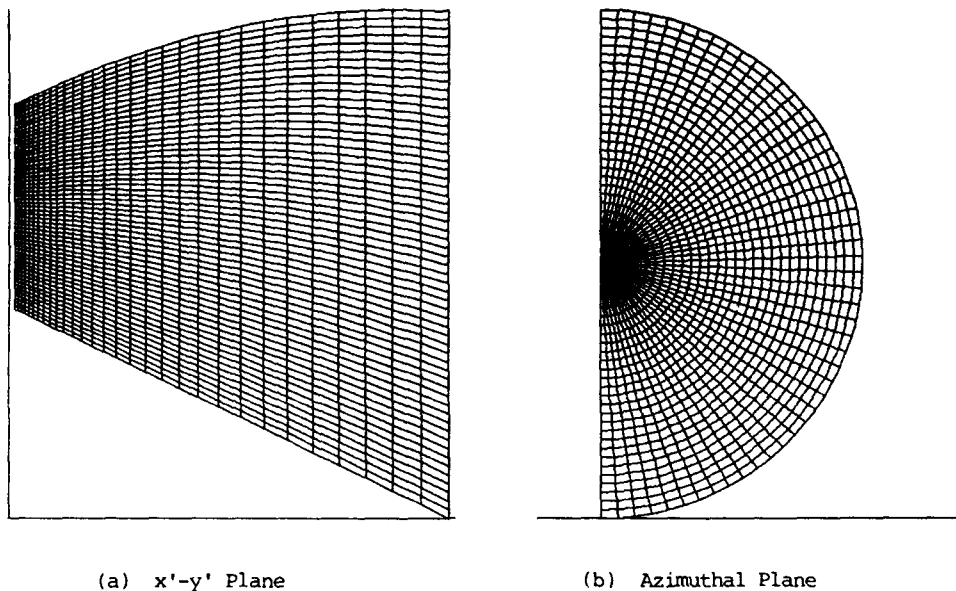


Figure 5. Computational Grid for Skewed Nozzle Flow Analysis

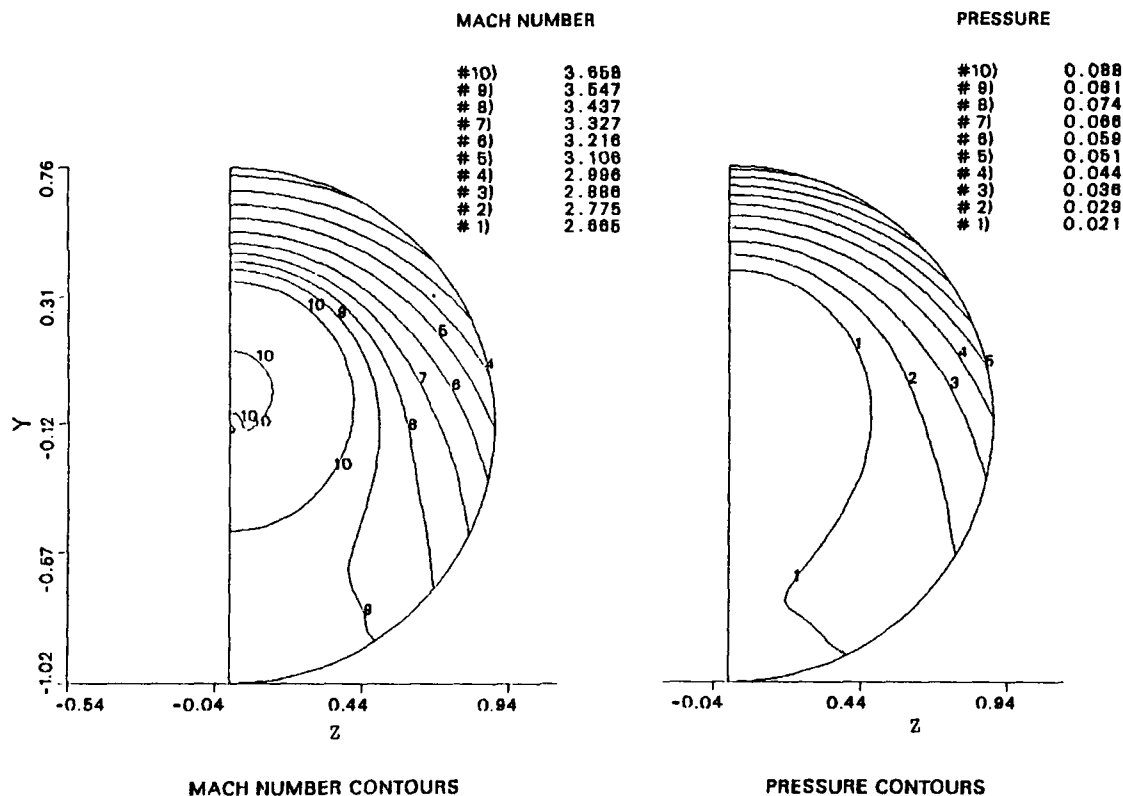


Figure 6. Nonuniform Flow Conditions at Nozzle Exit

angle. Immediately downstream of the nozzle exit, these two flows meet to reach an intermediate value of pressure and a common flow direction. There will remain large differences in density and velocity of air and fuel. It is the strong gradients in pressure, density, and velocity that generate vorticity downstream of the injector.

In the Euler computations considered here employing the USA code, we lack the effects of viscosity, turbulence, and chemical reactions. However, we maintained the identity and continuity of the chemical species of air and hydrogen fuel. The computational grid in the lateral plane is in two zones as mentioned earlier, and the number of grid points are already described in the respective subsection. Forty grid points were chosen in the axial direction, up to a distance of  $L=2D$ . The grid size is increased downstream of this station since we expect reduced gradients in the flow parameters. Between  $L=2D$  and  $L=8D$  we choose 50 grid points.

We examined the numerical solutions at various distances from the injector to evaluate the magnitude of the vorticity vector and also the cross-flow velocities. Figure 8 shows vorticity contours at various distances downstream from the injector. It appears that the vorticity in the flowfield spreads to a lateral distance nearly one diameter from the fuel-air interface at the injector exit. Cross-flow velocity vectors in each of the planes examined are shown in Figure 9. We observe

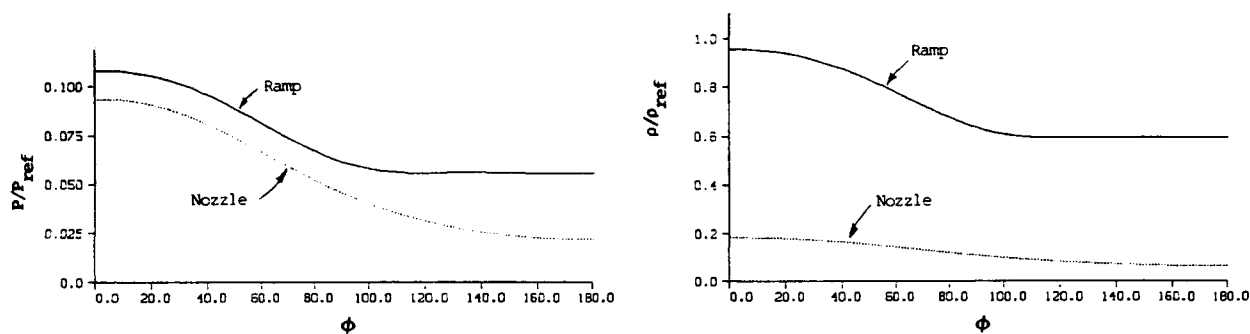


Figure 7. Nozzle Internal and Ramp External Flow Conditions at Injector Exit

that considerable entanglement of the airstream and fuel stream occurs by a downstream distance of 8 times the fuel nozzle diameter. Even with a fine grid, there is considerable smearing and broadening of the gradients of flow parameters inherent in numerical methods. However, one can define the regions of considerable crossflows and increased vorticity downstream of the fuel nozzle.

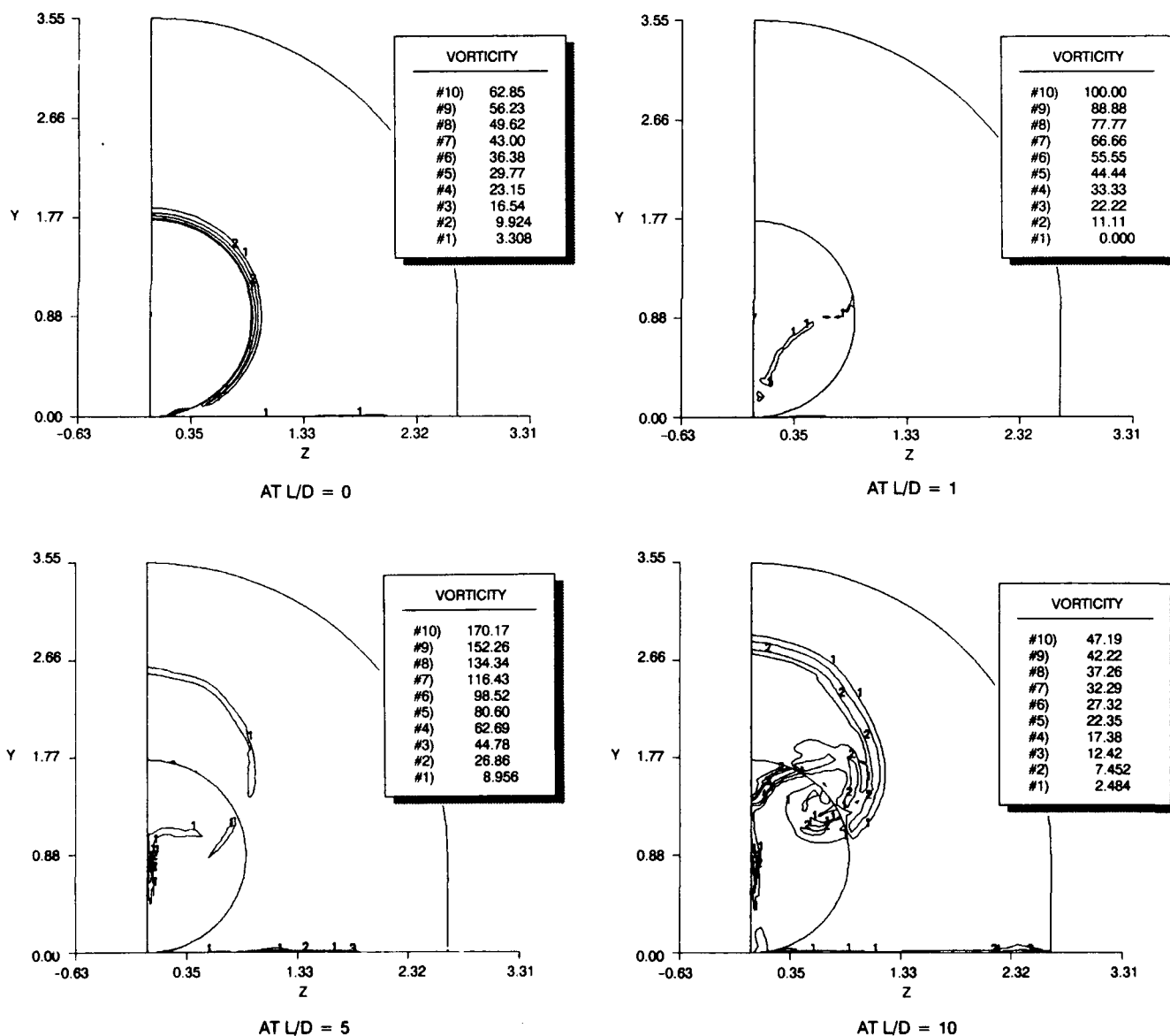


Figure 8. Distribution of Vorticity at Various Downstream Distances

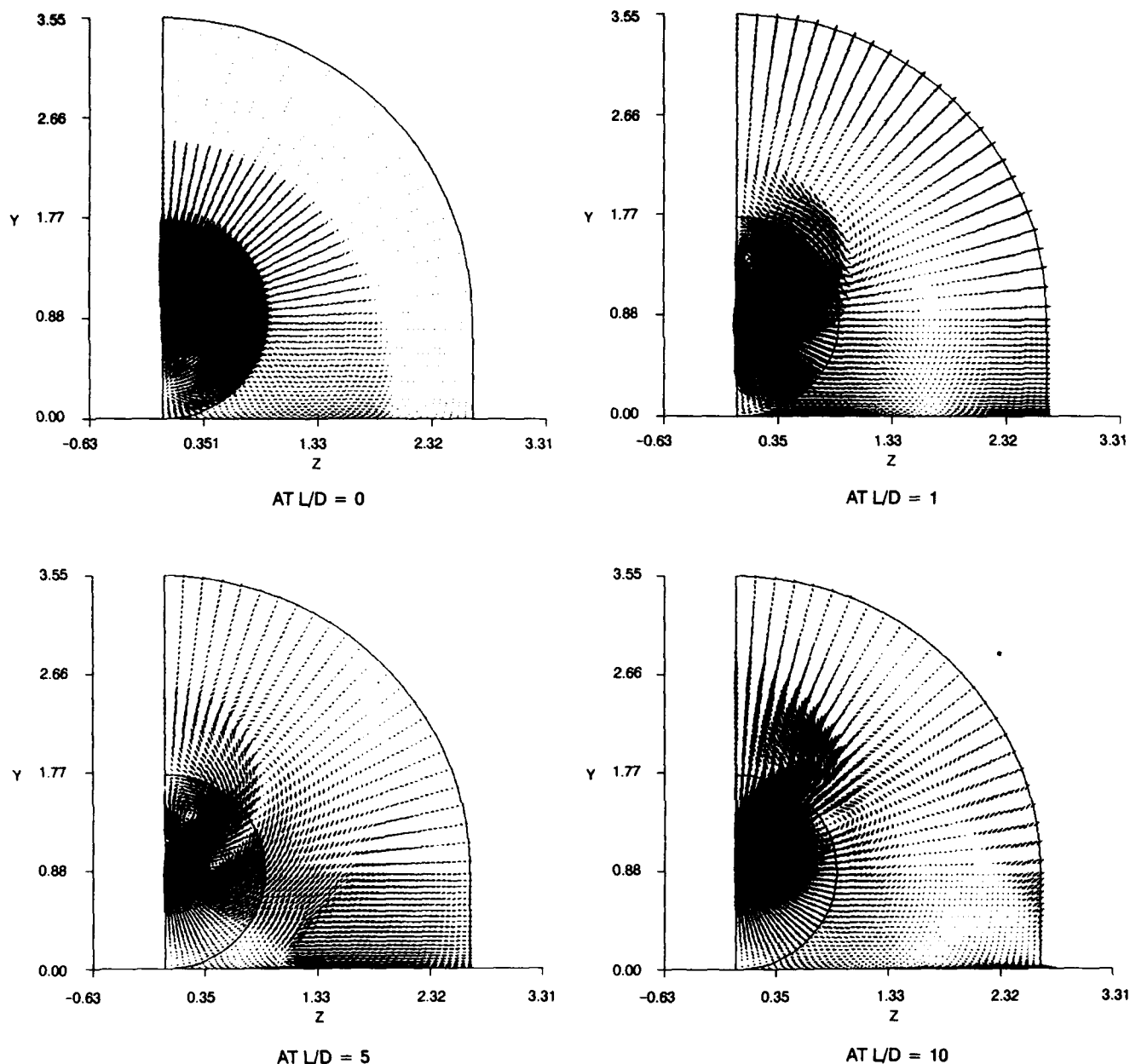


Figure 9. Crossflow Vector Diagrams at Various Downstream Distances

## CONCLUSIONS

It is observed that the nonuniformities in the flows lead to considerable generation of vorticity and entanglement of the two streams from the numerical computations carried out on the interaction of a nonuniform supersonic jet of fuel with a nonuniform supersonic jet of air. Present computations are limited to inviscid, nonreacting, perfect-gas streams since we wanted to explore the potential of the new concept of a skewed fuel nozzle in a conical ramp. The present numerical results indicate that this type of injector contributes to necessary fuel distribution. In the near future, FNS solutions will be computed including chemical reactions to evaluate the mixing and combustion enhancement one can obtain within a limited length of a supersonic combustor.

## REFERENCES

1. Brown, G. L. and Roshko, A., "On Density Effects and Large Structure in Turbulent Mixing Layers," *J. Fluid Mechanics*, V. 64, No. 4, 1974, pp. 775-816.
2. Papamoschou, D. and Roshko, A., "Observations of Supersonic Free Shear Layers," *AIAA Paper 86-0162*, January 1986.
3. Kumar, A., Bushnell, D. M., and Hussaini, M. Y., "A Mixing Augmentation Technique for Hypervelocity Scram-jets," *AIAA Paper 87-1182*, June 1987.
4. Drummond, J. P. and Mukunda, H. S., "A Numerical Study of Mixing Enhancement in Supersonic Reacting Flow-fields," *AIAA Paper 88-3260*, July 1988.

5. Menon, S., "Shock-Wave-Induced Mixing Enhancement in Scramjet Combustors," AIAA Paper 89-0104, January 1989.
6. Sullings, G. A., Lutz, S. A., Carpenter, D. A., and Taylor, M. A., "Experimental Investigation of Shear Layer in Supersonic Flow," 1989 JANNAF Propulsion Meeting, Cleveland, OH, May 1989.
7. Northam, G. B., Greenberg, I., and Byington, C. S., "Evaluation of Parallel Injector Configurations for Supersonic Combustion," AIAA Paper 89-2525, July 1989.
8. Schadow, K. J., Gutmark, E., and Wilson, K. J., "Passive Mixing Control in Supersonic Coaxial Jets at Different Convective Mach Numbers," AIAA Paper No. 89-0995, March 1989.
9. Wilson, K. J., Gutmark, E., Ajdari, E., Schadow, K. C., and Smith, R. A., "Mixing Characteristics of Supersonic Shrouded Jets," AIAA Paper No. 88-0699, January 1988.
10. Swithenbank, J., Eames, I., Chin, S., Ewan, B., Yang, Z., Cao, J., Zhao, X., "Turbulent Mixing in Supersonic Combustion Systems," AIAA-89-0260, 27th Aerospace Sciences Meeting, January 1989, Reno, Nevada.
11. Chakravarthy, S. R., "The Versatility and Reliability of Euler Solvers Based on High-Accuracy TVD Formulations," AIAA Paper No. 86-0243, 1986.
12. Rao, G. V. R., "Exhaust Nozzle Contour for Optimum Thrust," Jet Propulsion, Vol. 28, pp. 377-382, 1958.

#### ACKNOWLEDGEMENTS

The work reported here is supported by the U. S. Department of Defense, NASP Program, under Contract Number F33657-87-C-2214. The authors also wish to acknowledge the help of Armen D. Darian in carrying out some of the numerical computations.

## Discussion

#### STOLLERY

What was the ratio of the nozzle exit diameter of your nozzle to the boundary layer thickness?

#### AUTHOR'S REPLY

The paper we have presented here is based on EULER solution of a non uniform supersonic jet of fuel interacting with a nonuniform air stream bounded by a side wall. Since we are dealing with inviscid flow interactions, the boundary layer on the side wall is ignored. The cross flows discussed in the paper have their origin in the pressure and the density gradients in the inviscid flow. The boundary layer is quit small compared to the exit diameter of the nozzle.

#### WINTERFELD

COMMENT : In the old days of supersonic combustion activities in the sixties we investigated this configuration experimentally and compared it with a ramp of rectangular shape. The aim of that was to show the vortices and how these ramps work and we could not get a lift of the hydrogen jet away from the wall. We wanted to separate the hot combustion from the wall. With a square ramped injector you have clear shock fronts aside and therefore in part of the flow, where you have no shocks, you can get quite clear vortices but with this conical ramp injectors we could not get any succes.

## PERFORMANCE CHARACTERISTICS OF HYPERSONIC DETONATION WAVE RAMJETS

T. M. Atamanchuk, Research Assistant  
 J. P. Sislian, Professor  
 Institute for Aerospace Studies  
 University of Toronto  
 4925 Dufferin Street  
 Downsview, Ontario, Canada  
 M3H 5T6

SUMMARY

One method of heat addition to a supersonic flow is by means of shock-induced combustion or in this particular study a detonation wave. In order to assess the performance potential of a propulsor utilizing such a mode of heat addition a first order inviscid computational scheme based on Godunov's method was developed. This computational method was chosen since it allows one to track flow-field discontinuities such as shocks and slipstreams, thus making it possible to generate a vehicle geometry operating at design conditions for given freestream conditions. This same code was also used to determine the flow-field generated by a given body geometry at off-design conditions. Pressures acting on these planar and axisymmetric bodies were calculated and used to determine various performance parameters over a range of Mach numbers. Two configurations consisting of multiple shock external and internal inlet compression, followed by an oblique Chapman-Jouguet detonation wave, were considered. Aerodynamic performance of planar multiple external shock inlet compression vehicles acting as lifting-propulsive bodies (integrated engine-airframe configurations) was also investigated. Off-design performance of these geometries was evaluated by varying the heat addition to the flow in order to obtain the desired thrust-to-drag ratio. For most body geometries operating at flight Mach numbers less than the design Mach number, it was found that no value of heat addition would maintain the design thrust-to-drag ratio. However, for flight Mach numbers greater than the design Mach number it was found that there usually existed at least two values, and in some cases three, of heat addition which would give the design thrust-to-drag ratio.

LIST OF SYMBOLS

$C_T$	thrust coefficient, $Th/(\dot{m}v_\infty)$
$D$	drag
$H$	total enthalpy
$L$	lift
$M$	Mach number
$\dot{m}_a$	mass flow rate of air
$max$	maximum
$p$	pressure
$q$	heat addition
$Q$	nondimensional heat addition, $q/(C_p T)$
$r$	coordinate; ordinate in planar, radial in axisymmetric case
$T$	temperature
$Th$	thrust
$u$	x coordinate of velocity
$v$	r coordinate of velocity
$V$	total velocity
$x$	coordinate; abscissa in planar, axial in axisymmetric case
$\gamma$	specific heat ratio, $C_p/C_v$
$\eta_p$	propulsive efficiency, $(Th \times V_\infty)/(\dot{m}_a Q)$
$\rho$	density
$\infty$	denotes free-stream condition

92-16988

INTRODUCTION

Hypersonic ramjets have been the subject of many investigations (Refs. 1-8). Cycle analyses of these ramjets show that, in order to avoid very high temperatures and levels of dissociation of the gases and achieve reasonable levels of thrust,

combustion must take place at supersonic speeds. Two main concepts of supersonic combustion have emerged: (1) Injection of gaseous fuel into a supersonic flow where the air and fuel mix gradually and, being at reacting temperature and pressure, simultaneously burn, i.e., the "diffusive" burning supersonic combustion ramjet (Scramjet); (2) shock-induced combustion where a shock is employed to increase the temperature of premixed fuel and air to a point where chemical reaction will start. This is the "shocked-combustion" ramjet (Shcramjet). The rate of chemical reaction (burning) depends on the state of the gas after it has been compressed by the shock and the shape of the confining walls. For extremely fast reactions where the area does not increase rapidly enough, a "detonation wave" is generated. In this case the effects of the heat release are felt in full by the shock, and the wave behaves as a discontinuity across which energy is released. Therefore, the "detonation wave" ramjet is a purely hypothetical particular case of a shcramjet. It should, however, be noted that shock-induced combustion differs from detonations in gases in that the chemical reaction behind the shock does not necessarily affect the shock. A number of ramjet configurations were advanced based on these two concepts of supersonic burning. The scramjet concept has gained more attention and has been quite extensively developed into practical engine configuration.

The full potential of shcramjets has not yet been explored in a systematic manner. Earliest works in this area were those of Dunlap, Brehm and Nicholls (Ref. 2) and Sargent and Gross (Ref. 5), which presented engine performance characteristics (specific thrust, specific fuel consumption) in the flight Mach number range  $3 < M < 10$  based on a simplified one-dimensional analysis. These initial studies were followed by a number of detailed experimental investigations of normal and oblique shock-induced combustion and detonation waves. The phenomenon was found to be stable, reproducible and "friendly" (Ref. 5). It was also concluded that the "shock-induced combustion employed in a hypersonic ramjet offers control of the combustion processes over a wide range of flight and diffusion Mach number" (Ref. 11).

In Ref. 13 Townend studied a more elaborate hypersonic detonation ramjet configuration consisting of multi-shock diffusers optimized by the Oswatitsch criterion and matched (analytically) to strong or Chapman-Jouguet detonation waves (normal or oblique). Thus, in the case of full expansion in the nozzle, one can maximize the thrust for a given heat release, or the propulsive efficiency for the specified cycle temperature. He concluded that Chapman-Jouguet detonation is competitive with heat addition at constant pressure, and that some operating problems of hypersonic detonation wave ramjets - such as premature ignition, dissociation, boundary layer separation induced by detonation - may in some cases be avoided. He emphasized "the need for research on oblique rather than normal detonation and on conical rather than plane waves" (Ref. 13).

More recently, R. B. Morrison published two reports (Refs. 14, 15) on oblique detonation wave ramjets, in which he studied in some detail multishock external and internal compression diffusers, fuel injection losses, combustion chamber configurations, effect of chemistry on oblique detonation wave ramjets, and of real-gas effects on nozzle expansion. Estimates of the propulsion performance of external and internal compression ramjets are also reported based on simplified one-dimensional analysis. He concludes that "the oblique detonation wave ramjet offers a great potential as an airbreathing propulsor to extend the useful range of ramjet flight Mach numbers from 6 to 16 and above. Specific impulses and thrust coefficients that would be obtainable in the above flight range would exceed 70 percent of ideal". Detonation wave ramjets were also investigated by F. S. Billig and co-workers at the Johns Hopkins University, Applied Physics Laboratory (see, for example, Refs. 16 and 17), within the context of a wider study of external burning in supersonic streams.

The concept of heat addition to a supersonic flow by shock-induced combustion has been actively developed in the USSR (see, for example, Refs. 18 and 19). A simple model of a hypersonic ramjet is presented in Ref. 21.

A revival of interest has occurred lately in detonation wave combustion ramjet propulsion for hypersonic flight (Refs. 22-27). In Ref. 22 the oblique detonation wave engine, in combination with a dual-fuel, dual expander rocket engine, has been proposed as a propulsion device for a single stage earth-to-orbit vehicle. In Ref. 23, the analysis performed by Morrison in Ref. 15 has been taken a step further by assuming more realistic working gas properties and considering a more elaborate detonation wave model. The estimated performance parameters (fuel specific impulse, thrust per unit inlet area, etc.) are essentially based on a one-dimensional cycle-type analysis rather than on a specific vehicle geometry. Computational fluid dynamic methods are used in Refs. 24 and 25 to investigate the stability of standing oblique detonation waves. Experimental and numerical simulation of fuel (hydrogen) injection designs as well as the mixing and subsequent formation of an oblique detonation wave are reported in Refs. 26 and 27.

In this paper a first-order Godunov scheme (Ref. 28) was used to determine the geometry of a body and the associated flow-field at design conditions. Propulsive (and in planar cases aerodynamic) performance of these axisymmetric and planar bodies was then determined by integrating the pressure distribution acting on all surfaces. The performance of these geometries operating at Mach numbers greater and less than the design Mach number was also evaluated by use of the above mentioned code. In order to make meaningful comparisons the thrust-to-drag ratio (Th/D) was maintained

constant. This was achieved in the on-design case by assigning a value of heat addition  $Q$  which gave the desired maximum cycle temperature (for results presented here  $T_{\max}/T_{\infty} = 10$ ) and varying the vehicle geometry until a  $Th/D = 1$  (cruise conditions) was achieved. For off-design cases the body geometry obtained from the on-design case was fixed and the heat addition was varied in order to achieve the desired thrust-to-drag ratio. Cruise conditions ( $Th/D = 1$ ) were chosen as a basis of comparison since planar geometries can also act as lifting-propulsive flight vehicles and their performance at these conditions is of greatest interest. Aerodynamic and propulsive performance over a range of maximum cycle temperatures, flight Mach numbers and thrust-to-drag ratios for on-design geometries can be found in Ref. 29.

#### THE COMPUTATIONAL METHOD

The equations for an inviscid, non-heat conducting flow are:

$$\frac{\partial \vec{a}}{\partial x} + \frac{\partial \vec{b}}{\partial r} = \vec{f} \quad (1)$$

where

$$\vec{a} = \begin{pmatrix} \rho u \\ \rho u^2 + p \\ \rho uv \\ \rho uH \end{pmatrix}; \quad \vec{b} = \begin{pmatrix} \rho v \\ \rho uv \\ \rho v^2 + p \\ \rho vH \end{pmatrix}; \quad \vec{f} = -\frac{v}{r} \begin{pmatrix} \rho v \\ \rho uv \\ \rho v^2 \\ \rho vH \end{pmatrix} \quad (2)$$

( $v = 0$  for planar flows) and  $u$ ,  $v$ ,  $p$ ,  $\rho$  and  $H$  are the velocity components in the  $x$  and  $r$  directions, pressure, density and total enthalpy, respectively. These equations were solved using Godunov's first-order scheme (Ref. 28) which requires that the flow everywhere be supersonic. The method was chosen because it allows, if desired, the tracking of discontinuities (shock waves, slipstreams, ...) in the flow with resulting shape (discontinuous) profiles of the flow variables across them (no smearing effect). This capability is essential for the inviscid detonation wave ramjet flow analysis, as it allows the exact determination of the inlet shock intersections with walls, the cowl lip position, the position of the detonation wave, of the slipstream separating the nozzle from the outer flow, and the position of any shocks which are formed or die out in the flow field. It is also essential for off-design cases since it allows one to determine the point where the detonation wave is generated and how the complex shock structure changes as the flight Mach number deviates from design conditions.

If  $S$  is the area of an annulus in the  $x = \text{const}$  plane limited by two circles of radii  $r_+(x)$  and  $r_-(x)$  such that  $r_-(x) < r < r_+(x)$ , then it can be shown that the differential equations of motion, Eq. (1), and the relationships of strong discontinuities are equivalent to the following system of integral conservation laws:

$$\frac{d}{dx} \int_{r_-}^{r_+} \vec{a} dr = (\vec{a} r' - \vec{b}) \Big|_{r_-}^{r_+} + \int_{r_-}^{r_+} \vec{f} dr \quad (3)$$

where  $r' = dr/dx$ , and  $\vec{a}$ ,  $\vec{b}$  and  $\vec{f}$  are given by Eq. (2). In the case of planar flows the integral term on the right-hand side of Eq. (3) vanishes. Integrating the system of equations (3) from  $x_0$  to  $x_0 + h_x$  (see Fig. 1) and applying the mean value theorem to the integrals along the contours of the elemental quadrilateral of the computational grid, the following finite-difference relations are obtained (notations are shown in Fig. 1):

$$(\vec{a} h_r)^{j-1/2} - (\vec{a} h_r)_{j-1/2} = (\vec{A} \Delta - B h_x)_j - (\vec{A} \Delta - B h_x)_{j-1} \\ + h_x \frac{(\vec{f} h_r)^{j+1/2} + (\vec{f} h_r)_{j-1/2}}{2} \quad (4)$$

Here  $\Delta j = r_j - r_{j-1}$ . Vector quantities denoted by capital letters,  $\vec{A}$  and  $\vec{B}$ , represent the value of the vectors  $\vec{a}$  and  $\vec{b}$  along the "longitudinal" sides of the elemental quadrilateral. These values are determined from the solution of the Riemann problem of interaction for two semi-infinite uniform supersonic flows in  $j-1/2$ ,  $j+1/2$  and  $j-1/2$ ,  $j-3/2$  regions. The downstream values of the flow variables (denoted by superscript  $j-1/2$  at  $x_0 + h_x$ ) can be calculated from the system of equations (4). With appropriate boundary conditions given on  $r = R_-(x)$  and  $r = R_+(x)$  (walls, free boundaries, axis of symmetry, ...) and the proper restriction on the step size  $h_x$ , stemming from stability considerations, the whole flow field of interest can thus be determined. It is clear that any strong discontinuity in the flow field (e.g., shocks and slipstreams) generated by the solution of the Riemann problem can be tracked by taking the discontinuity as one of the  $r_+(x)$  "longitudinal" lines in the computational domain.



### ON-DESIGN METHODOLOGY

Based on the above described numerical scheme a computer program was developed to compute the entire flow field and track the strong discontinuities of the two planar or axisymmetric detonation wave powered hypersonic vehicles (Fig. 2, on-design conditions). The main difference between these configurations is the type of compression and the direction the flow is turned in the inlet. It is assumed that the fuel (e.g., hydrogen) is injected either in the inlet or in the channel (Fig. 2) and is thoroughly mixed before the mixture reaches the detonation wave station (for an up-to-date investigation of this problem see Refs. 26 and 27). The temperature of the combustible mixture as it approaches the detonation wave must be less than its ignition temperature. It is raised above the ignition temperature by the shock component of the detonation wave and the rapid energy release couples with this shock to form the detonation wave. The gas (air, air/fuel mixture and the nozzle exhaust) is assumed to be perfect with constant, but different, values of the specific heat ratio on both sides of the detonation wave. The shock tracking capability of the computer program is extensively used to generate the vehicle geometry at design conditions so that any undesirable shock reflections are eliminated.

Two types of multi-shock inlets: external (Fig. 2, configuration I) and internal (configuration II) were considered. To generate the geometries operating at design conditions configuration I employs two equal strength shocks, whereas a three equal strength shock system is assumed for configuration II (see Refs. 14, 15 and 23). By specifying the forebody angle (an input to the computer code) and free-stream conditions at design flight Mach number, the computer will determine the inlet wall angles (at point A in configuration I and at points C and D in configuration II) the shock system and the entire inlet flow field. In the axisymmetric case shock strength equality is satisfied at points A, C and D where the shocks are formed. In configuration I, the leading edge of the cowl is placed at the intersection point B of the inlet shocks, while in configuration II, the leading edge of the cowl is placed on the shock OC. Thus, for given fixed free-stream conditions and inlet configuration, the degree of compression is controlled by the forebody angle which is one of the parameters in the evaluation of the propulsive performance of the detonation wave ramjet. No real-gas effects (caloric imperfections) on the performance of the inlets were considered in the present investigation.

In the first phase of this study the detonation wave is considered as a discontinuity across which a certain amount of heat ( $Q$ ) per unit mass of gas is released (the Chapman-Jouguet model). The specific heat ratio is assumed to be different on both sides of the detonation wave  $\gamma = 1.4$  before and  $\gamma = 1.25$  after the detonation wave. At design conditions the wedge angle which initiates combustion, point B in configuration I and point E in configuration II, was determined from the condition that the detonation wave formed at this point was a Chapman-Jouguet wave. The position at point F where the detonation wave intersects the upper contour of the vehicle is accurately determined by tracking the detonation wave.

The combustion products with the specified value of the specific heat ratio ( $\gamma = 1.25$ ) are expanded from the conditions just behind the detonation wave. Because of the asymmetric location of the nozzle walls and the absence of a sonic throat, the design of a maximum thrust nozzle for given flow conditions of the detonation wave presents a formidable task. Therefore, the asymmetric (half open) nozzle which is formed by the lower surface of the main body of the vehicle and the upper surface of the cowl was designed by assuming that the Chapman-Jouguet detonation wave is immediately followed by a Prandtl-Meyer expansion fan centred at a prescribed radial distance from the point where combustion is initiated along the first characteristic which coincides with the detonation wave (see Fig. 2). The upper contour of the nozzle was formed by the Prandtl-Meyer flow streamline initiated at the intersection point F of the detonation wave and the body, up to point G where its slope is zero, followed by a cosine-type contour which insured a zero slope trailing edge. The length of this portion of the nozzle contour, from point G to the trailing edge I was specified by prescribing the angle between the straight line joining the two points and the horizontal datum. Similarly, the upper surface of the cowl was formed by the Prandtl-Meyer streamline passing through the point where combustion was initiated. For a given flow condition behind the detonation wave it was possible to control the intersection point H of the upper cowl surface and the planar lower surface, and hence the length of the cowl. The same method of cowl design was also adopted for the axisymmetric case. The lower surface of the cowl was aligned with the oncoming flow direction for all configurations except the planar version of configuration I. For this case the lower surface of the cowl was assumed parallel to the forebody wedge lower surface if the slope of the upper surface was greater than zero. If the upper surface slope was negative then the leading edge angle of the cowl was set equal to that of the forebody wedge angle. The thrust (and lift) generated by the two configurations was determined by integrating the pressure along its wetted contour.

### OFF-DESIGN METHODOLOGY

The body geometry used for the off-design cases is simply that obtained in the on-design case, although determining the point to initiate the detonation wave is somewhat different in the off-design case. As a consequence of the mixing assumption

stated above, it was found that the detonation wave could be formed on the surface of the cowl or in midstream between the cowl and the body. Which of these occurs depends on the location of the intake shock wave, which contains the flow between the free-stream and the body, relative to the cowl. For external compression geometries at flight Mach numbers less than the design Mach number the shock wave angle increases so that the entire cowl is located within the inlet flow and by the above assumption within a combustible mixture. Therefore the detonation wave is formed at the leading edge of the cowl as in the design case. For flight Mach numbers greater than the design Mach number the wave angle between the free-stream and body decreases giving rise to two methods by which the detonation wave may be generated, depending on the cowl geometry and orientation. If the upper surface angle of the cowl is greater than zero a shock wave is formed at the leading edge. If this shock wave intercepts the shock wave generated by the body then the intersection point represents the point where the detonation wave starts and continues until it intersects the body. If this leading edge cowl shock dies out before it intercepts the intake shock or if the upper cowl angle is less than zero, in which case the shock wave does not even form, then it is assumed that the intake shock reflects as a detonation wave. For internal compression, the detonation wave was formed at the same location as in the design case. It should be noted that in both configurations the detonation wave generated at off-design conditions will no longer be at the Chapman-Jouguet point.

### PERFORMANCE CHARACTERISTICS

The two configurations (planar and axisymmetric) considered in the present study are shown in Fig. 2. The shocks and sliplines tracked by the computational method are also shown. For given incoming flow conditions and flight Mach number the aerodynamic and propulsive characteristics of these integrated configurations were determined subject to the following conditions.

The total drag of the vehicle is balanced by the generated thrust, i.e., cruise conditions are assumed. For on-design operation:

1. A maximum engine cycle temperature,  $T_{\max}/T_{\infty}$ , is prescribed, where  $T_{\max}$  is the temperature immediately downstream of the point where the detonation wave is initiated.
2. The detonation wave is operating at the Chapman-Jouguet condition at its point of initiation.

The following parameters were evaluated:

- (a) the thrust coefficient,

$$C_T = \frac{Th}{\dot{m}_a V_{\infty}}$$

- (b) the propulsive efficiency,

$$\eta_p = \frac{Th \times V_{\infty}}{\dot{m}_a Q}$$

- and (c) the cruise efficiency,

$$\eta_p L/D$$

where  $Th$  is the total generated thrust,  $\dot{m}_a$  the captured air mass flow rate,  $V_{\infty}$  the free-stream velocity,  $Q$  the heat addition per unit mass, and  $L/D$  the lift-to-drag ratio of the planar configuration. Each point on the performance curves represents a specific computer-generated configuration.

In all cases the inlet or forebody angle was maintained at  $5^\circ$  and the angle between the line joining points F and I (see Fig. 2) and the free-stream was maintained at  $10^\circ$ .

### CONFIGURATION I - PLANAR BODY

This configuration acts as a lifting-propulsive body. Lift is generated by the intake, nozzle section and the lower cowl surface, whereas thrust is generated by the nozzle and the upper cowl surface. As mentioned previously, the cowl lower surface angle relative to free-stream is set equal to the forebody angle in cases where the upper surface leading edge of the cowl is positive. For negative values the angle between the upper and lower leading edge surfaces of the cowl was maintained at  $5^\circ$ . Therefore, one finds that as the Mach number increases beyond a certain value the cowl angle relative to the oncoming flow increases. This results in a noticeable change in flight performance (see Ref. 28 for details) and for the cases studied here ( $(T_{\max}/T_{\infty})_{\text{design}} = 10$ ) occurs at about  $M_{\infty} = 12$ .

Figure 3 is a sketch of a typical  $Th/D$  vs.  $Q$  obtained for this planar configuration, and has a characteristic shape of an inverted V. Several noteworthy conclusions arise from this sketch. For a given body geometry there is one value of  $Q$  which gives a maximum  $Th/D$ . If  $Q$  is decreased then  $Th/D$  decreases. Physically this is due to the fact that the detonation wave angle decreases and is ingested by the nozzle, i.e., it intercepts the nozzle wall downstream of the nozzle inlet, hence the detonation wave is weakened and the nozzle does not feel the full effect of the detonation wave and produces less thrust. If the value of  $Q$  is greater than that corresponding to the maximum  $Th/D$  then the detonation wave intercepts the intake wall before the point where the nozzle begins, thus producing increased drag. This is well illustrated in Fig. 4 which shows a body designed for  $M_\infty = 10$  operating at  $M_\infty = 10.4$  for two different values of  $Q$ , a low and high value, which both give a  $Th/D = 1.0$ . For  $M_\infty = 10.4$  the detonation wave is formed in midstream whereas for  $M_\infty = 11.4$  it is formed on the cowl surface as shown in Fig. 4. The maximum  $Th/D$  occurs when a value of  $Q$  causes the detonation wave to intercept the body at the point where the nozzle inlet starts. Figure 3 shows that this maximum  $Th/D$  decreases as the flight Mach number decreases, with  $Th/D_{max} = 1.0$  at the design point since the design criteria requires that the nozzle begin where the detonation wave intercepts the body. For  $M_\infty < M_{design}$  the  $Th/D_{max} < 1$  and for  $M_\infty > M_{design}$  there are two values of  $Q$  which give  $Th/D = 1.0$ , resulting in low and high temperature conditions since temperature is proportional to heat addition. When the detonation wave is formed by the criteria mentioned previously it is found that up to a flight Mach number of 11.2 the detonation wave is formed within the intake flow, and as the Mach number increases the point where the detonation wave is formed moves away from the cowl and towards the body and farther downstream of the cowl leading edge. However, as this occurs the oblique shock generated by the upper leading edge surface of the cowl is weakened. When the flight Mach number increases beyond 11.2 the cowl shock dies out before it intercepts the intake shock generated by the body. Consequently for Mach numbers greater than this value the detonation wave is now generated on the cowl surface. Figure 4 shows several shock interactions at various conditions. Varying the initiation point of the detonation wave leads to the discontinuity in slope as shown in the plot of  $\eta_p$  vs.  $M_\infty$  (Fig. 5). This figure also shows, as one might expect, that the propulsive efficiency decreases as one deviates from design conditions, particularly for a high value of  $Q$ . The thrust coefficient  $C_T$  curves (Fig. 6) show clearly that the high value of  $Q$  generates a greater thrust than that at design conditions whereas the low value of  $Q$  generates less thrust which is what one anticipates from the discussion above. As one deviates from the design condition the lift-to-drag ratio increases as shown in Fig. 7. This is in agreement with the above explanation since if drag decreases  $L/D$  increases. If thrust increases then drag also increases but the increased drag produced by the intake also contributes to lift as does the increased thrust produced by the nozzle. Cruise efficiency (Fig. 8) is less than that at design conditions, mainly due to the decrease in propulsive efficiency.

In general, as the value of  $Q$  is increased, for a constant value of flight Mach number, the point where the detonation wave intercepts, the body moves forward out of the nozzle and into the intake section. This detonation wave is always reflected by the body as a shock wave for off-design conditions (see Fig. 9). As the  $M_\infty$  approaches the  $M_{design}$  the intersection of the detonation wave and the body which gives a  $Th/D = 1.0$  moves closer to the point where the nozzle is formed (Fig. 10).

For a design Mach number of 12 the leading edge upper surface slope of the cowl is less than zero, resulting in a substantial difference in performance since the cowl now produces only thrust. Consequently the detonation wave is generated on the upper surface of the cowl in all cases and this is reflected in the fact that there are no discontinuous changes in slope for the various performance parameters.

For this design Mach number the  $Th/D$  vs.  $Q$  for various flight Mach numbers is different from that of  $M_{design} = 10$ . As shown in Fig. 11 the  $Th/D$  vs.  $Q$  curve again consists of an inverted V, as was the case for  $M_{design} = 10$ , however this time the maximum is a relative maximum, followed by a relative minimum as  $Q$  increases. If the value of  $Q$  is increased still further the  $Th/D$  increases until at some point the Mach number behind the detonation wave is sonic. It is believed that this result of three values of  $Q$  giving  $Th/D = 1$  is due to the orientation and length of the cowl. Low and mid-values of  $Q$  behave as before however, for high values of  $Q$  the detonation wave reflects from the body as a shock wave and this shock wave reflects from the upper surface of the cowl. Also, as the flight Mach number increases, the point where the reflected shock intercepts the cowl moves back toward the trailing edge. The result is that the relative minimum  $Th/D$  increases with Mach number until at some  $M_\infty$  it is greater than  $Th/D = 1$  (i.e.,  $M_\infty = 13.8$ ). Therefore, at high Mach numbers, there exists only one value of  $Q$ , namely the lower value which gives  $Th/D = 1$ .

Figure 12 shows that at low  $M_\infty$  the mid-value of  $Q$  gives a higher lift over drag than that of the low  $Q$ . This is probably due to the fact that for mid- $Q$  drag increases and so does the thrust and lift. But the negative lift generated by the cowl does not begin to have a significant effect until a higher Mach number is reached. For the high  $Q$ , one sees that the thrust, and hence drag ( $Th/D = 1$ ), increases with decreasing  $M_\infty$  but the lift over drag decreases. This implies that the upper surface of the cowl is rapidly decreasing the lift since it is responsible for any downward force or negative lift produced. This is not surprising considering the fact that there are high pressures acting on the cowl due to the shock wave reflecting off its upper surface.

The propulsive efficiency is shown in Fig. 13 behaving, as one might expect, with higher values of  $Q$  giving lower propulsive efficiency. Cruise efficiency, Fig. 14, is very similar in form to that of propulsive efficiency indicating once again that propulsive efficiency is the dominant parameter.

Examination of Figs. 12 to 14 shows that for low and mid- $Q$ , performance values tend toward the design value as one would anticipate. The high value, on the other hand, does not correspond to the design condition at all, since in this case it so happens that, for this high value of  $Q$ , the thrust produced by the cowl and the nozzle is sufficient enough to counteract the increased drag produced by the detonation wave intersecting the inlet wall. Due to the fact that a high  $Q$  value exists, one finds that for this configuration it is possible to obtain  $Th/D = 1$  for  $M_\infty < M_{\infty, \text{design}}$ . Such values are also shown in Figs. 12 to 14. Temperature plots for the three different values of  $Q$  over a range of  $M_\infty$  (Fig. 15) indicate that they are well within the realm of real-gas effects which are not accounted for in this study. They are presented here for interest since, from a design point of view, such high temperatures and their associated losses are of little practical use.

#### CONFIGURATION I - AXISYMMETRIC

Two axisymmetric bodies, one based on a design Mach number of 10 and the other on 12, were studied. In both of these cases the lower surface of the cowl was aligned with the free-stream. As a result of this common design geometry it was found that for both cases the thrust/drag ratio as a function of heat addition  $Q$  was in the form of an inverted V. As in the planar case, the maximum  $Th/D$  occurs when the detonation wave intercepts the point where the nozzle begins. For values of  $Q$  less than that which gives maximum  $Th/D$ , the detonation wave intercepts the body within the nozzle section. Higher values of  $Q$  cause the detonation wave to intercept the body in the intake section, causing an increase in drag. For low values of  $Q$  the inlet flow expands just prior to the detonation wave, thus weakening the detonation wave. This does not occur for high values of  $Q$ . The effect of heat addition and flight Mach number on the detonation wave for the cases presented here are similar to those for the  $M_{\infty, \text{design}} = 10$  planar case. It should be noted that the cowl length for the Mach 12 design is greater than that for Mach 10. As a result of this longer cowl it is possible that, under certain values of  $Q$  and flight Mach number, the reflected shock wave generated by the body when the detonation wave intercepts it, can also intercept and reflect from the upper surface of the cowl. This occurs when the flight Mach number is large and for high values of heat addition.

Figures 16 and 17 show the thrust coefficient and propulsive efficiency, respectively, for a Mach 10 body design. The thrust coefficient behaves as one might expect; there is a slight rise in propulsive efficiency around Mach 11, but the value of propulsive efficiency never exceeds that obtained at design conditions.

For Mach 12 designs the thrust coefficient is shown in Fig. 18. The discontinuity in slope which occurs for high values of  $Q$  at Mach 13 is due to the shock wave reflecting from the cowl upper surface, as explained above. This behaviour is also apparent in the propulsive efficiency curves shown in Fig. 19. For low values of  $Q$  it is unexpectedly found that the propulsive efficiency decreases to a minimum at about  $M_\infty = 12.4$ , then rises slowly as  $M_\infty$  increases. For this configuration and geometry, as well as all others, the high value of  $Q$  varied more than the low, and that these values of  $Q$  were usually greater than the design values.

It was found that for these axisymmetric geometries no value of heat addition would give a  $Th/D = 1$  or greater for flight Mach numbers less than the design Mach number.

#### CONFIGURATION II - AXISYMMETRIC

The  $Th/D$  curve for this configuration is shown in Fig. 20. It is similar to that obtained for the planar Mach 12 design. However, for the geometry studied here, it was found that the local maximum  $Th/D$  for Mach numbers other than the design Mach number never reach a value of one. However, a very large value of  $Q$  did give a  $Th/D = 1$ , but the Mach number behind this high  $Q$  value detonation wave was only slightly greater than one. As the flight Mach number was increased, the value of  $Q$  also had to be increased until at some point ( $M_\infty = 10.6$ ) the flow was sonic behind the detonation wave.

#### CONCLUSIONS

Based on the results presented here one can conclude that, provided the flight Mach number is greater than the design Mach number (planar or axisymmetric), there exist at least two values of heat addition parameter which would give the design thrust-to-drag ratio for the external compression detonation wave ramjets. There were also cases in which there could be a third high value of heat addition which would give the desired  $Th/D = 1$ ; however, in this case the temperatures obtained were extremely high and well within the realm of real-gas effects. It was found that, for flight Mach numbers less than the design Mach number, the  $Th/D$  was always less than the design  $Th/D$  except in the case where the third value of  $Q$  existed. The existence

of this third high value of heat addition seemed to be completely dependent on the geometry of the body.

For the internal compression geometry studied here it was not possible to obtain  $Th/D > 1$  for flight Mach numbers above or below the design Mach number, except for very large values of  $Q$  which correspond to the high third value discussed above.

In general it can be stated that the off-design performance deteriorates relative to on-design performance, particularly in the case of propulsive efficiency and, where applicable, cruise efficiency. Furthermore, the results obtained seem to suggest that off-design performance is highly geometry-dependent.

#### REFERENCES

1. Partel, G., "General Round-Up in the Ramjet Field and Its Significance to Astronautics", Ninth International Astronautical Congress, Springer-Verlag, Vienna, Vol. 1, 1959, pp. 243-251.
2. Dunlap, R., Brehm, R. L. and Nicholls, J. A., "A Preliminary Study of the Application of Steady-State Detonation Combustion to a Reaction Engine", Jet Propulsion, 28, N6, 1958, pp. 451-456.
3. Roy, M. M., "Supersonic Propulsion by Turbojets and Ramjets", Proc. First Int. Congress of Aeronautical Sciences, Pergamon Press, 1958.
4. Wever, R. J. and McKay, J. S., "An Analysis of Ramjet Engines Using Supersonic Combustion", NACA Tech. Note No. 4386, 1958.
5. Sargeant, W. H. and Gross, R. A., "A Detonation Wave Hypersonic Ramjet", AFOSR Tech. Note No. 59-589, 1959.
6. Avery, W. H. and Dugger, G. L., "Hypersonic Air Breathing Propulsion", Astronaut. and Aeronaut., 2, 1964, pp. 42-47.
7. Arens, M., "The Performance of a Hypersonic Ramjet Using Detonative Combustion", SAE Reprint No. 419A, 1961.
8. Ferri, A., Libby, P. A. and Zakkay, V., "Theoretical and Experimental Investigation of Supersonic Combustion", Polytechnic Inst. of Brooklyn, Aerodynamics Lab., PIBAL 713, 1962.
9. Gross, R. A., "Exploratory Studies of Combustion in Supersonic Flow", AFOSR Tech. Note 59-587, 1959.
10. Gross, R. A. and Chinitz, W., "A Study of Supersonic Combustion", J. Aerospace Sci., No. 7, 1960, pp. 517-524.
11. Rubins, P. M. and Rhodes, R. P. Jr., "Shock-Induced Combustion with Oblique Shocks: Comparison of Experiment and Kinetic Calculations", AIAA J., 1, No. 12, 1963, pp. 2778-2789.
12. Rubins, P. M. and Cunningham, T. M., "Shock-Induced Supersonic Combustion in a Constant-Area Duct", J. Spacecraft, 2, No. 2, 1965, pp. 199-205.
13. Townend, L. H., "Detonation Ramjets for Hypersonic Aircraft", RAE Tech. Rept. No. 70218, 1970.
14. Morrison, R. B., "Evaluation of the Oblique Detonation Wave Ramjet", NASA Contractor Rept. No. 145358 1978.
15. Morrison, R. B., "Oblique Detonation Wave Ramjet", NASA Contractor Rept. No. 159192, 1980.
16. Billig, F. S., "External Burning in Supersonic Streams", 18th Int. Astronaut. Congress, Proc. Vol. 3, 1968, pp. 23-54.
17. Billig, F. S., "Combustion Processes in Supersonic Flow", Proc. 7th Int. Symp. on Airbreathing Engines, 1985, pp. 245-256.
18. Chernyi, G. G., "Supersonic Flow Past Bodies with Detonation and Deflagration Waves", Astronautica Acta 13, No. 5-6, 1968, pp. 467-479.
19. Chushan, P. I., "Combustion in Supersonic Flows Past Various Bodies", J. Comp. Math. and Math. Phys., 1, No. 6, 1969, pp. 1367-1377.
20. Sheng, Y. and Sislian, J. P., "Interaction of Oblique Shock and Detonation Waves", AIAA J. 21, No. 7, 1983, pp. 1008-1014.
21. Sheng, Y. and Sislian, J. P., "A Model of a Hypersonic Two-Dimensional Oblique Detonation Wave Ramjet", University of Toronto Institute for Aerospace Studies UTIAS Tech. Note No. 257, 1985.

22. O'Brian, C. J. and Kobayashi, A. C., "Advanced Earth-to-Orbit Propulsion Concepts", AIAA Paper No. 1386, 1986.
23. Ostrander, M. J., Hyde, J. C., Young, M. F. and Kissinger, R. D., "Standing Oblique Detonation Wave Engine Performance", AIAA Paper No. 2002, 1987.
24. Pratt, D. T., Humphrey, J. W., Glenn, D. E., "Morphology of Standing Oblique Detonation Wave", AIAA Paper No. 1785, 1987.
25. Glenn, D. E. and Pratt, D. T., "Numerical Modeling of Standing Oblique Detonation Waves", AIAA Paper No. 0440, 1988.
26. Adelman, H. G., Cambier, J. L., Menees, G. P. and Balboni, J. A., "Analytical and Experimental Validation of the Oblique Detonation Wave Engine Concept", AIAA Paper No. 0097, 1988.
27. Cambier, J. L., Adelman, H. and Menees, G. P., "Numerical Simulation of an Oblique Detonation Wave Engine", AIAA Paper No. 0063, 1988.
28. Godunov, S. K., Ed., Numerical Solution of Multidimensional Problems of Gasdynamics. Moscow, Nauka, 1976.
29. Sislian, J. P. and Atamanchuk, T. M., "Aerodynamic and Propulsive Performance of Hypersonic Detonation Wave Ramjets", Proc. 9th Int. Symp. on Air Breathing Engines, 1989, pp. 1026-1035.

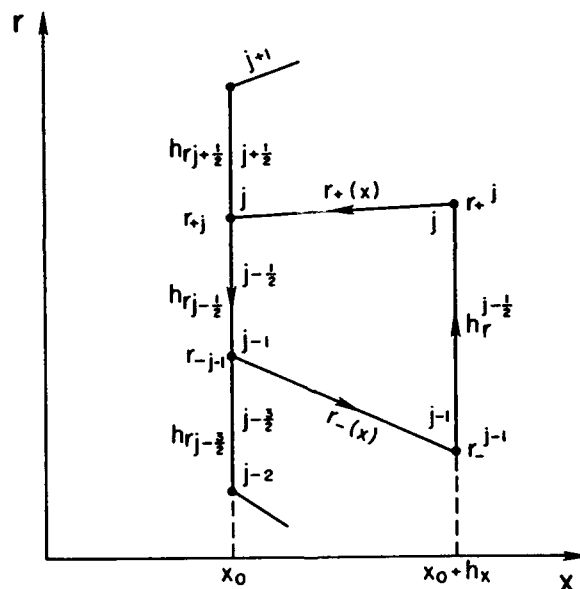


Fig. 1 THE COMPUTATIONAL GRID

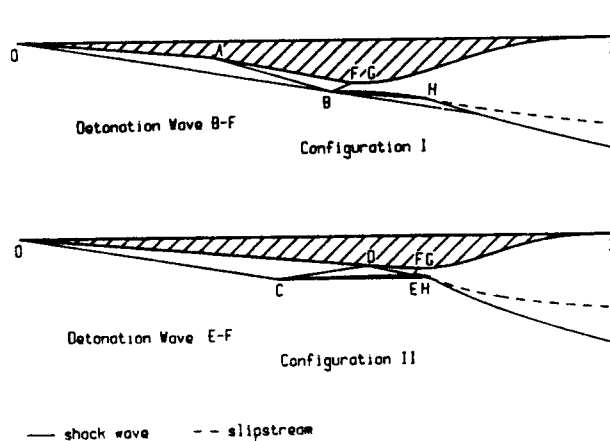


Fig. 2 DETONATION WAVE RAMJET CONFIGURATIONS

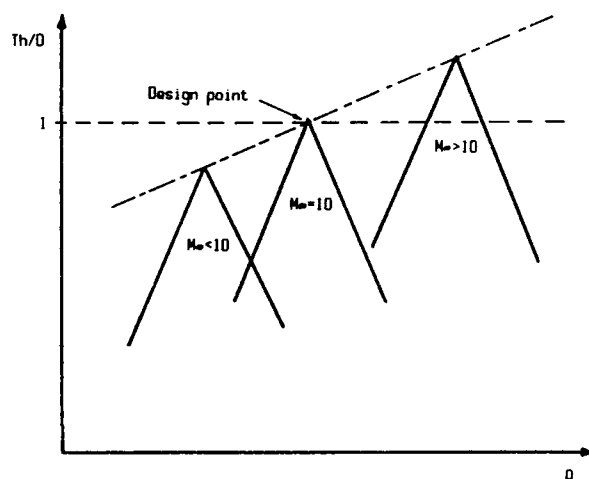


Fig. 3 SKETCH of Th/D vs. Q for Planar Mach 10 Body

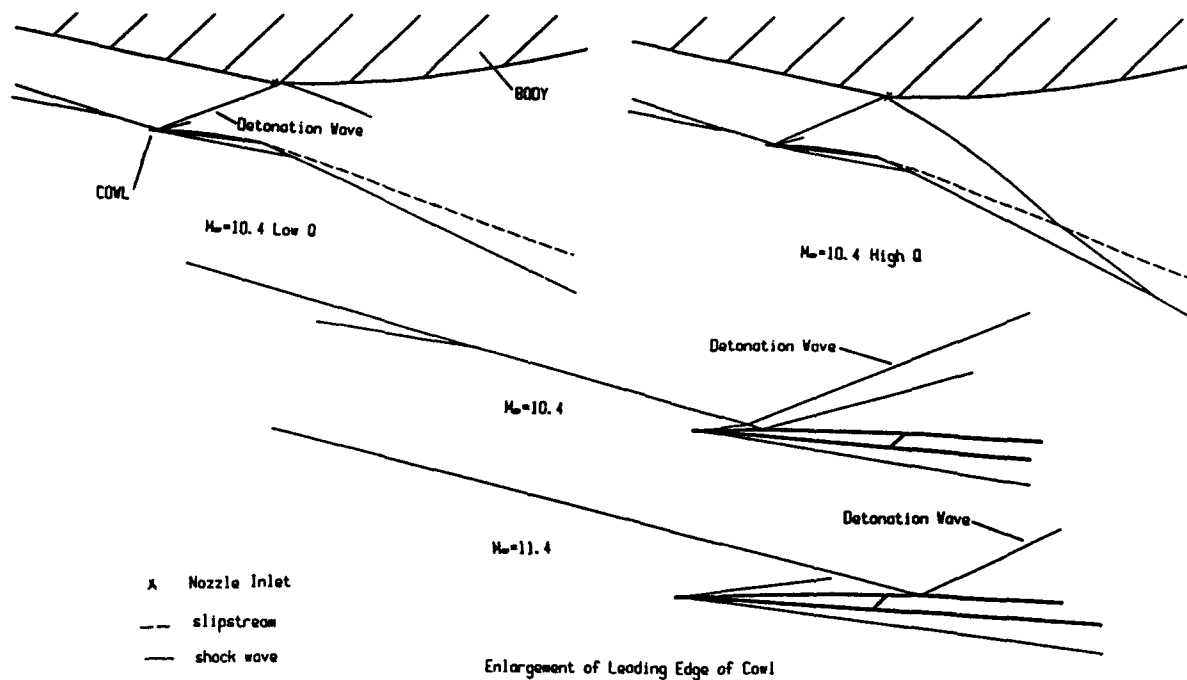
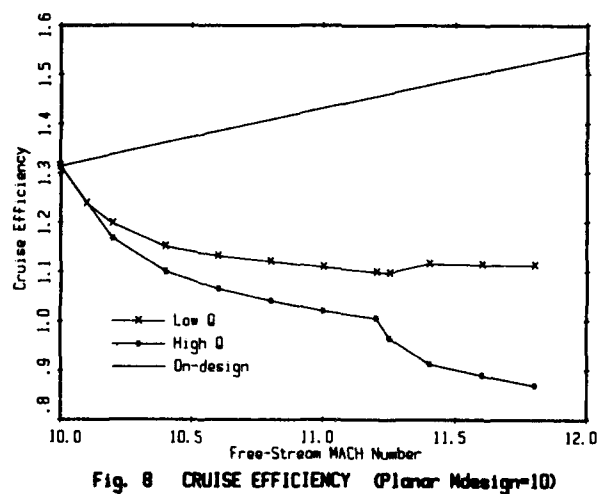
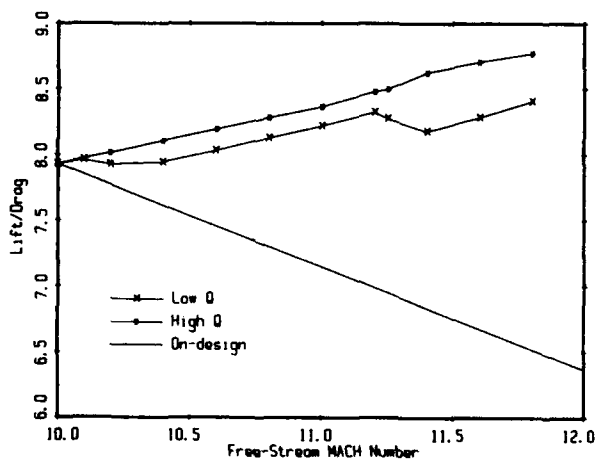
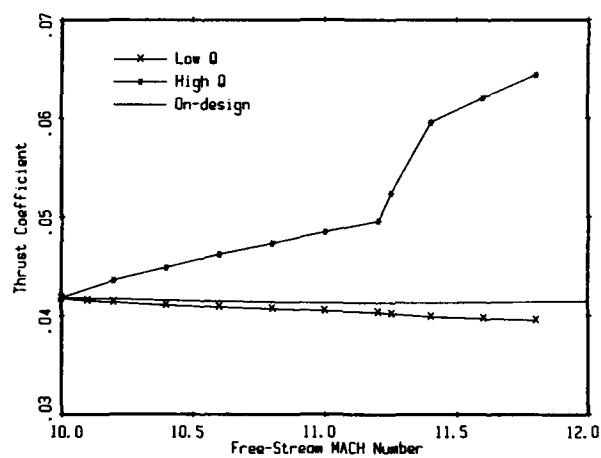
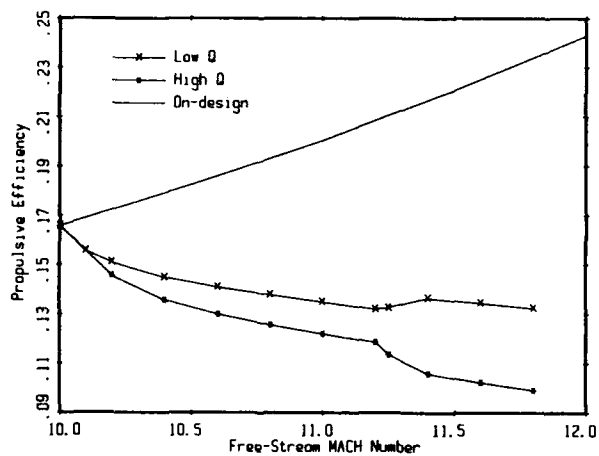


Fig. 4 SHOCK WAVE INTERACTION for Planar Mach 10 Body



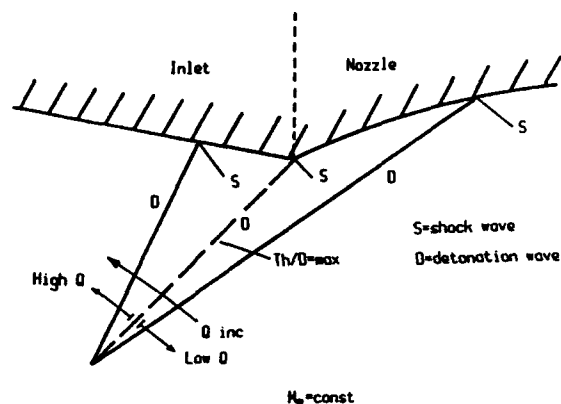


Fig. 9 EFFECT OF HEAT ADDITION ON DETONATION WAVE

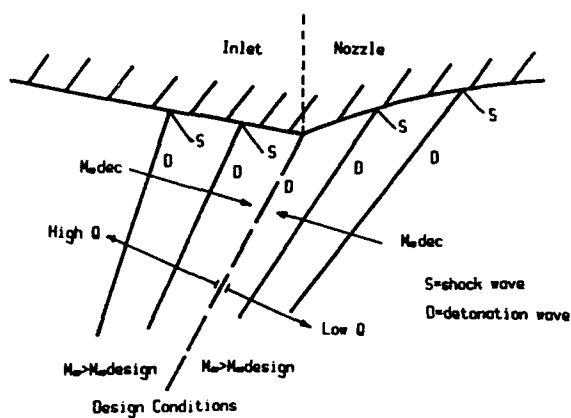
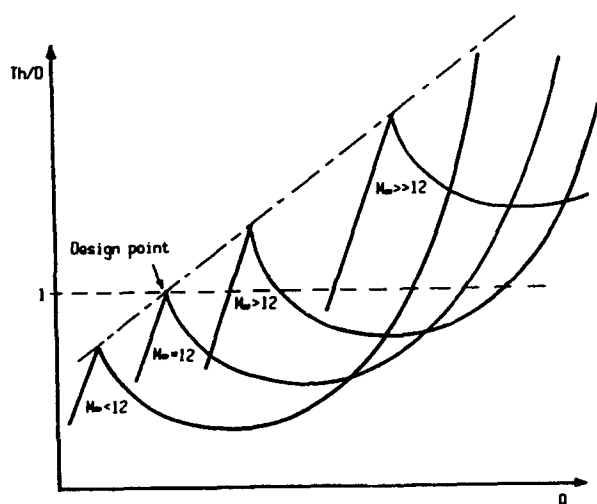
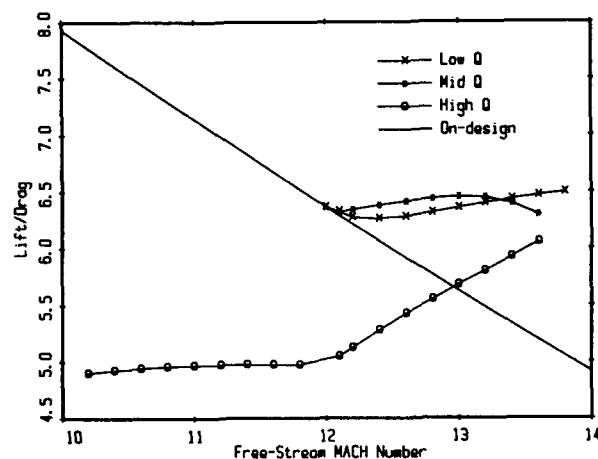
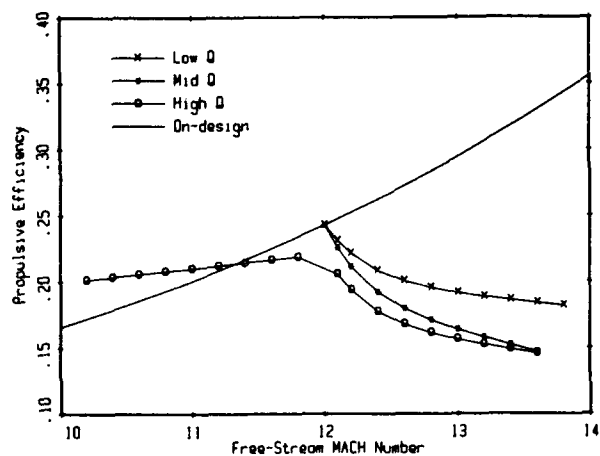
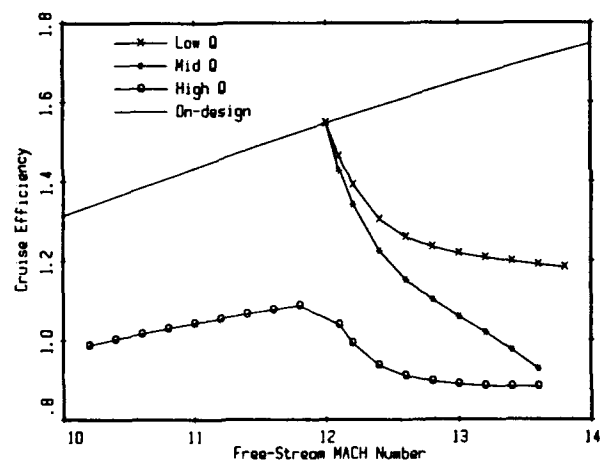


Fig. 10 EFFECT OF FLIGHT MACH NUMBER ON DETONATION WAVE

Fig. 11 SKETCH of  $Th/D$  vs.  $Q$  for Planar Mach 12 BodyFig. 12 LIFT/DRAG (Planar  $M_{design}=12$ )Fig. 13 PROPULSIVE EFFICIENCY (Planar  $M_{design}=12$ )Fig. 14 CRUISE EFFICIENCY (Planar  $M_{design}=12$ )



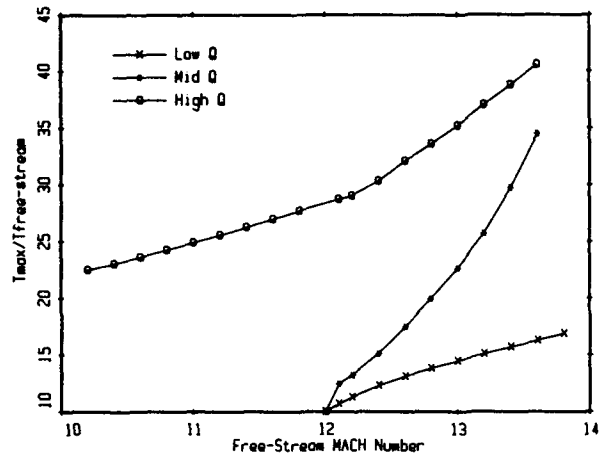


Fig. 15 MAXIMUM TEMPERATURE (Planar Mdesign=12)

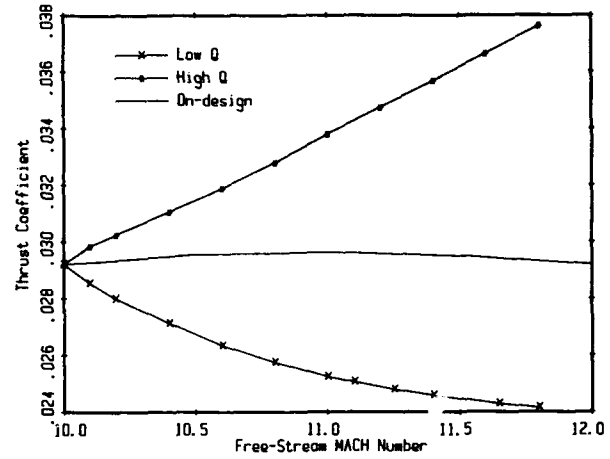


Fig. 16 THRUST COEFFICIENT (Axisymmetric Mdesign=12)

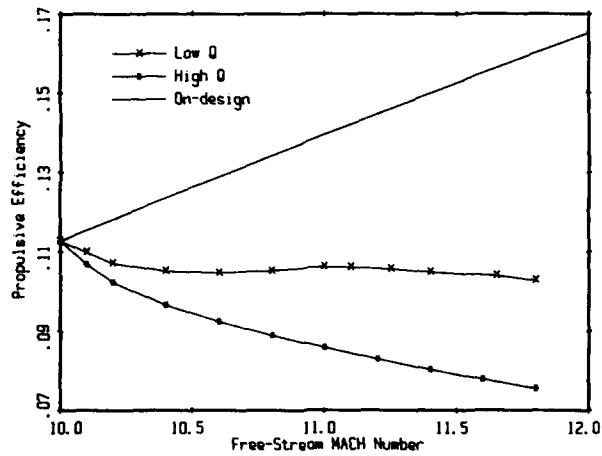


Fig. 17 PROPULSIVE EFFICIENCY (Axisymmetric Mdesign=10)

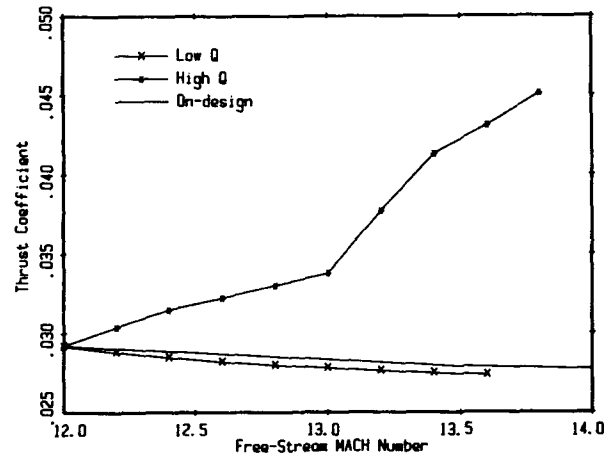


Fig. 18 THRUST COEFFICIENT (Axisymmetric Mdesign=12)

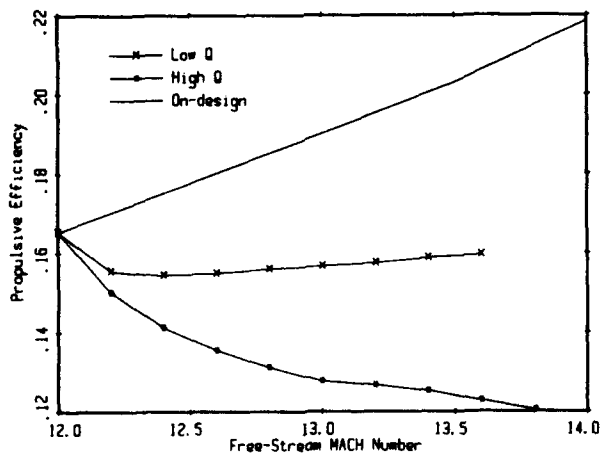
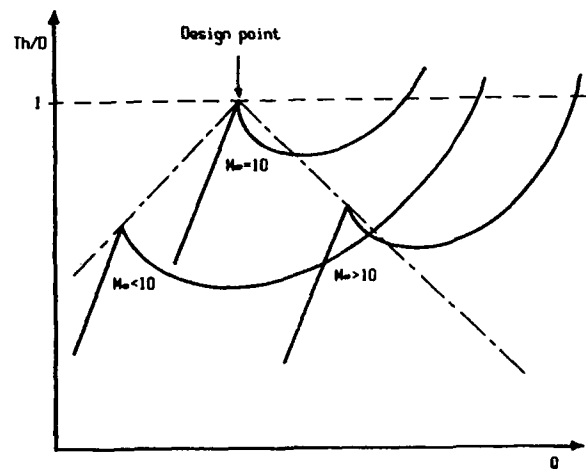


Fig. 19 PROPULSIVE EFFICIENCY (Axisymmetric Mdesign=12)

Fig. 20 SKETCH of  $Th/Q$  vs.  $Q$  for Axisymmetric Internal Compression Body

## Discussion

ESCHER

In this concept, fuel injection and mixing takes place during the inlet or air precompression process yielding a homogeneous fuel/air mixture at the detonation wave.

1) What mixing means have been considered, either conceptual or experimental, for creating such a homogeneous mixture?

2) Can avoidance of "premature" ignition and combustion be assumed (considering the very low ignition energy of hydrogen fuel) by reverse flow components in the boundary layer?

AUTHOR'S REPLY

1) Several methods of mixing are possible. Some concepts involve injecting the hydrogen fuel at various angles relative to the inlet flow in order to induce mixing. Another method, which has been investigated, is the phenomenon of mixing enhancement induced by the oblique inlet compression shocks themselves. Extensive further research is needed to accomplish a sufficient degree of homogeneity of the fuel/air mixture before the detonation wave.

2) This is also another phenomenon which will have to be further investigated. Premature ignition could be avoided by carefully controlling the temperature of the mixture before it reaches the detonation wave. Further research is also necessary in this area.

TOWNEND

The propulsive efficiency values seem low for the Mach numbers and temperatures used. For such flow models, it should be possible to obtain propulsive efficiencies of 50% to 60% as I recall. Please can you comment on this?

AUTHOR'S REPLY

Propulsive efficiency is geometry dependant, so for the design methodology used here one obtains efficiencies which seem low, but, it is not unreasonable to assume higher values are possible since the design methodology here is by no means an optimum one. It should also be noted that as the thrust-to-drag ratio increases so too does the propulsive efficiency. So the results presented here ( $Th/D=1$ ) represent the lowest efficiencies. One also finds that the propulsive efficiency can vary from 0.1 to 0.8 for low to high Mach numbers respectively. More details can be found in reference 29 of this paper.

SCHWAB

You showed examples for Mach numbers between 10 and 12. What are the reasons for the design at these Mach numbers? What happens for design Mach numbers lower than 10?

AUTHOR'S REPLY

The choice of Mach numbers between 10 and 12 was rather an arbitrary choice. The major restriction was computing time and money.

AD-P007 957



# ANALYTICAL AND EXPERIMENTAL INVESTIGATIONS OF THE OBLIQUE DETONATION WAVE ENGINE CONCEPT

by

Gene P. Menees\*

NASA-Ames Research Center, Moffett Field, Mail Stop 230-2  
CA 94035, United States

Henry G. Adelmann† and Jean-Luc Cambier‡

Eloret Institute  
NASA-Ames Research Center  
United States

## ABSTRACT

Wave Combustors, which include the Oblique Detonation Wave Engine (ODWE), are attractive propulsion concepts for hypersonic flight. These engines utilize oblique shock or detonation waves to rapidly mix, ignite and combust the air-fuel mixture in thin zones in the combustion chamber. Benefits of these combustion systems include shorter and lighter engines which will require less cooling and can provide thrust at higher Mach numbers than conventional scramjets. The Wave Combustor's ability to operate at lower combustor inlet pressures may allow the vehicle to operate at lower dynamic pressures which could lessen the heating loads on the airframe.

The research program at NASA-Ames includes analytical studies of the ODWE combustor using Computational Fluid Dynamics (CFD) codes which fully couple finite rate chemistry with fluid dynamics. In addition, experimental proof-of-concept studies are being carried out in an arc heated hypersonic wind tunnel. Several fuel injection designs were studied analytically and experimentally. In-stream strut fuel injectors were chosen to provide good mixing with minimal stagnation pressure losses. Measurements of flow field properties behind the oblique wave are compared to analytical predictions.

## NOMENCLATURE

$C_t$	=	Thrust coefficient
$I_{sp}$	=	Specific impulse
$M$	=	Mach number
ODWE	=	Oblique Detonation Wave Engine
$p$	=	pressure
$q$	=	dynamic pressure
$Re$	=	Reynolds Number
$T$	=	Temperature
TAV	=	Trans-atmospheric Vehicle
$V$	=	velocity
$X$	=	lateral distance from centerline of strut
$Y$	=	vertical distance from nozzle floor
$Z$	=	axial distance from trailing edge of strut
$\phi$	=	equivalence ratio

## Subscripts

$t$	=	total
$\infty$	=	free stream value

## INTRODUCTION

The use of detonation waves to initiate and enhance combustion has been proposed since the 1940's<sup>1</sup>. Some analyses have been made using both normal and oblique waves<sup>2,3</sup>. Normal waves are hard to stabilize and they produce higher stagnation

\*Research Scientist, Associate Fellow AIAA

†Research Scientist, Member AIAA

‡Research Scientist, Member AIAA

92-16989



pressure losses than oblique waves. However, it is not clear that stabilized oblique detonation waves have been established in laboratory conditions<sup>4,5</sup>. While free-running normal detonations have been observed to be classical Chapman-Jouguet waves with sonic gas velocities behind the wave, stationary oblique waves do not necessarily fulfill this condition. We will define an oblique detonation as a wave where the pressure field generated by combustion behind the wave influences the wave itself. This influence is manifested in a rotation of the oblique wave to a more normal orientation. The limiting case is an oblique Chapman-Jouguet detonation where the normal velocity component behind the wave becomes sonic. Further heat addition will cause the wave to detach from the anchoring point and rotate to a more normal orientation.

Several studies have been made recently of the application of oblique detonation waves to hypersonic propulsion<sup>6,7</sup>. These reports have shown that heat addition at an oblique detonation wave can provide combustor performance equal to the conventional scramjet combustor. While the deliberate creation of shock waves may seem to create additional losses, the detonation wave can be considered to be the last wave in a multi-shock diffuser. In addition, there is analytical evidence that heat addition with shocks may not be as inefficient as previously thought<sup>8</sup>. Furthermore, it is highly unlikely that shock waves can be avoided in supersonic combustors with fuel injection and boundary layer regions. Indeed, the design of supersonic combustors should utilize the shock waves to enhance mixing and combustion.

## TRANS-ATMOSPHERIC VEHICLE MISSION STUDIES

In order to determine the performance potential of the ODWE, a simulation of a typical single-stage-to-orbit trans-atmospheric vehicle (TAV) mission was completed. Performance and sizing estimations for the TAV were made using a hypersonic vehicle synthesis code for trans-atmospheric designs<sup>9</sup>. Estimates can be made of aerodynamic characteristics, aero-thermal heating, propulsion system performance and structural/subsystem weights. An automated vehicle closure algorithm iterates the trajectory analysis to close the design on both vehicle weight and volume.

To size the vehicles, a mission was selected which carried a payload of 15,000 pounds into a Low Earth Orbit (LEO) of 120 nautical miles altitude. A horizontal takeoff in the easterly direction from Kennedy Space Center was assumed, with an on-station duration of six hours. Two ascent trajectories were studied, with dynamic pressures of 1000 and 2000 pounds per square foot (psf). The flight path was constrained to give 100 pounds per square inch (psi) duct pressure at lower supersonic Mach numbers and a maximum mean surface equilibrium radiation temperature of 2000 F (1367 K) for high Mach numbers. The speed at which the airbreathing engine thrust was augmented by a rocket was optimized to minimize the gross takeoff weight. A descent trajectory was flown near peak L/D to maximize the descent cross-range capability. Fuel reserves of 2% of mission fuel were assumed for the landing maneuver.

### General Vehicle Design

The general vehicle configuration, shown in Fig. 1, is a lifting body with aft mounted horizontal and vertical tails. The total propulsion system consists of two airbreathing engines, one for Mach numbers below 6, and a scramjet or an ODWE for the remaining part of the flight. In addition, a rocket engine is used in conjunction with the air-breathing engine for the high altitude, high Mach number portion of the trajectory. Liquid hydrogen is the fuel for all engines.

### One-dimensional Engineering Analysis of ODWE

A one-dimensional engineering code was developed to provide the engine data base for an analysis of Trans-atmospheric Vehicles powered by either ODWE or scramjet engines. The engine data was then used in another code for mission analysis studies. The results of these comparisons were presented in Ref.10. The first calculations were made for a scramjet engine. After successful tests of the modifications, a second version of the code was developed to model the ODWE. Both simulations were one dimensional, and involved many simplifying assumptions which are common in this kind of analysis.

A detailed description of this propulsion model was also presented in Ref.10. For the scramjet case, the inlet operates in a four shock mode which gives good performance over all flight conditions. However, for the ODWE case, the oblique detonation wave acts as a diffuser, so fewer inlet shocks are needed. In this mode, two inlet shocks are sufficient. The viscous and pressure drag forces from nose-to-tail on the underbody or engine side of the vehicle are accounted for in the two engine performance parameters, specific impulse and thrust coefficient. The thrust coefficient is defined as the thrust normalized by the product of dynamic pressure and capture area. Engine specific impulse is obtained by dividing thrust by the fuel weight flow rate. The remaining vehicle drag not accounted for in the thrust coefficient, which includes the top, sides, cowl bottom surface and control surfaces is assigned to the vehicle aerodynamic characteristics. The efficiency of the propulsion system depends on various factors including the flight Mach number, dynamic pressure, forebody shape, fuel temperature and equivalence ratio.

### General Engine Performance

The results of the engine performance calculations show that specific impulse and thrust coefficients depend on dynamic pressure, combustion efficiency, fuel temperature and equivalence ratio. Certain trends can be observed. As shown in Fig. 2, it

is evident that higher heat recycling from the engine leads to higher injected fuel temperatures and larger values of specific impulse and thrust coefficient. We assume that the fuel is injected at a constant Mach number of 2.5. As more heat is added to increase the stagnation temperature, significant momentum can be gained from the fuel injection. However, fuel temperature is limited by the amount of heat which can be absorbed from the structure and by the temperature limits of the materials used to store and transport the fuel. In this study, we will assume that 90% of the heat loads have been absorbed by the fuel. The fuel is then heated to a limiting temperature of 1100 K (1520 F), which is representative of the current materials available for fuel storage and transport. If this temperature limit is exceeded, then an amount of fuel in excess of stoichiometric must be used. The resulting equivalence ratio versus Mach number schedule for the scramjet is shown in Fig. 3 for various fuel temperature limits.

Since the ODWE combustor is shorter, a stoichiometric mixture can be maintained to a Mach number of 17.5 compared to 14 for the scramjet, for a fuel temperature of 1100 K. While heat recycle increases engine performance for stoichiometric mixtures, the effect of using excess fuel to maintain a specified temperature limit may increase the thrust coefficients but will lower the specific impulses as shown in Fig. 4. It is clear that the cooling requirements seriously affect the performance of the engine at high Mach numbers.

### Scramjet Engine Performance

The calculated performance of the scramjet engine is shown in Fig. 4 as a function of Mach number for a dynamic pressure of 2000 psf and an equivalence ratio schedule which maintains the fuel temperature below 1100 K. It can be seen that the specific impulse begins to drop at Mach 14 due to the rise in equivalence ratios necessary to maintain the 1100 K fuel temperature limit.

### ODWE Performance

The ODWE performance was also calculated for dynamic pressures of 1000 psf and 2000 psf. In Fig. 4 we compare the performance of both the scramjet and ODWE for the  $q=2000$  psf case. It appears that the ODWE has better performance than the scramjet at high Mach numbers, but has lower specific impulse below Mach 15. The reduced performance at low Mach numbers is due to the steep wave angle of an oblique Chapman-Jouguet (CJ) detonation, and therefore to higher shock losses. The wave angle can be reduced if either the Mach number is increased or the Chapman-Jouguet Mach number is decreased (i.e. the static temperature prior to the detonation wave is increased or  $\phi$  is decreased). Therefore, the ODWE favors operation at high Mach numbers.

The ODWE also takes advantage of a shorter combustor which requires less cooling and less excess fuel at higher Mach numbers than the scramjet. It can be seen in Fig. 4 that the knee in the specific impulse curve, which indicates the start of the excess fueling schedule, begins at a higher Mach number for the ODWE than for the scramjet. Since the problems of mixing and ignition delay impose a long combustor for high Mach numbers, it is clear that increasing the combustor length causes the performance of the scramjet to drop at lower Mach numbers, when fuel must be injected in excess of stoichiometric.

For the ODWE, the benefits of a shorter combustion chamber, which results in a shorter, lighter engine will also be evident in the vehicle size and weight calculations which are discussed later.

### Scramjet Vehicle Performance

A scramjet powered vehicle was modeled using the predicted engine performance data for the trajectory of constant dynamic pressure  $q=2000$  psf. Since the scramjet is very inefficient below Mach 6, a hypothetical engine system with an average effective specific impulse of 1000 seconds was used to propel the vehicle from horizontal takeoff to Mach 6. Aerodynamic heating considerations required that the dynamic pressure of the flightpath begins to drop below the specified value of 2000 psf at Mach 17 to about 250 psf at Mach 22. This low dynamic pressure requirement at high Mach numbers necessitates rocket power augmentation which begins at Mach 18. The amount of thrust provided by the rocket is larger than the thrust produced by the scramjet, and the rocket thrust fraction continues to increase until orbital speeds are reached.

The scramjet powered vehicle which flies a 2000 psf trajectory weighs 460,512 pounds and carries a 15,000 pound payload into orbit. The scramjet engine, low speed engine and rocket motors comprise 8.6% of the takeoff weight. For comparative purposes, a vehicle which flies a 1000 psf trajectory was also studied. This TAV is heavier at 623,000 pounds. The main reason for the increased weight is the lower mass capture per unit area of inlet, which requires a larger, heavier engine and associated structure. Also, the lower thrust-to-weight ratio results in a longer flight time to orbit which consumes a greater amount of fuel.

### ODWE Vehicle Performance

The hypersonic vehicle using the ODWE has somewhat different weight characteristics. Since the ODWE offers superior performance above Mach 15, the point of rocket turn-on is delayed to Mach 19. The ODWE can operate at higher Mach numbers than the scramjet, and continues to provide a higher fraction of airbreathing thrust to orbital speeds. Therefore, less rocket thrust is

needed and a lower mass fraction of liquid oxygen (LOX) is consumed, 12.5% versus 15.9% for the scramjet. This represents a weight savings of 22,000 pounds compared to the scramjet. In addition, the shorter combustor length provided by the ODWE allows a shorter, lighter engine which saves about 5,000 pounds. The ODWE represents 3.7% of the gross weight, compared to 4.4% for the baseline scramjet engine. While the fuel weight fraction is higher for the ODWE, the actual fuel weight is 14,000 pounds lower. As a result of all these factors, the ODWE configuration weighs 409,500 pounds, some 51,000 pounds less than the scramjet vehicle (for  $q=2000$  psf), and carries the same payload of 15,000 pounds to orbit. Note that the payload weight fraction is increased from 3.3% of the takeoff weight for the scramjet to 3.7% for the ODWE.

Since the scramjet has better performance below Mach 15, and the ODWE above Mach 15, a combination of these two engines may be ideal. This hybrid engine would use a two-shock diffuser for the whole Mach range. At low Mach numbers, the mixing length and ignition requirements are less severe, and a relatively short combustor can be used in a scramjet mode. At higher Mach numbers, the diffusing shocks would move aft into the combustor. The engine would operate in the oblique detonation mode in the aft section of the combustor. Therefore, cooling is required only for a fraction of the combustor, and the drop in performance due to cooling requirements would still occur only at very high Mach numbers. The design of such a hybrid engine would require more sophisticated, 2-dimensional analysis. Work in that direction is progressing.

## ANALYTICAL STUDIES OF ODWE

The analysis of the ODWE has been made with levels of sophistication ranging from one dimensional, steady, perfect gas flow<sup>11</sup> to unsteady, 2-dimensional, viscous, shock capturing codes with finite rate chemistry<sup>12,13</sup>. These codes are used to simulate and guide experiments aimed at proving the existence and stability of oblique detonation waves and their use in supersonic combustors.

Proof-of-concept studies of the ODWE are focused on the establishment of stable oblique detonation waves. A NASA-Ames arc heated hypersonic wind tunnel facility has been chosen for the experimental program. This facility can simulate combustor inlet conditions of Mach number and enthalpy. However, it cannot presently reproduce the expected pressures. Therefore it was necessary to determine if the low pressures would prevent the establishment of a detonation wave. This verification was carried out in several ways. The simplest method utilized a 1-dimensional, steady flow, finite rate chemistry program<sup>11</sup> which calculated ignition delays and combustion behavior behind a 30° oblique shock wave. Inputs to this simulation included a hydrogen-air reaction mechanism taken from the literature<sup>12</sup>.

The results of these 1-dimensional calculations demonstrated the strong dependence of ignition delay and combustion rate on pressure and temperature. As temperature and pressure are increased, combustion occurs closer to the wave. However, this program did not simulate any coupling between heat release and wave angle so the question remained whether a detonation had been created. There is very little information in the literature on the spacing between the shock wave and combustion zone for a detonation, except that they appear to be almost coincidental. However, some estimates of coupling can be made by generating characteristics in the combustion zone and determining their intersections with the shock. If these characteristics do not intersect the shock within the bounds of the combustion chamber, then there is not enough coupling to be classified as a detonation. Instead, there is shock induced combustion.

For the nominal experimental conditions, the air in the wind tunnel exits the nozzle at Mach 4.6 with a pressure of 0.016 atm and a temperature of 840 K. Combustion behind a 30° oblique wave takes about 0.5 milliseconds corresponding to a distance normal to the shock of approximately 5 centimeters. Raising the pressure by a factor of 5 shortens the distance to about 0.7 centimeters. This coupling should create a detonation. Indeed, more sophisticated analyses employing a 2-dimensional, fully coupled CFD and finite rate chemistry code have shown the existence of a detonation under these higher pressure conditions<sup>13</sup>.

A solution would be to raise the pressure or temperature to guarantee a detonation in the experiment. While the temperature can easily be increased, this effect could cause the fuel to ignite prematurely. One method of raising the pressure would be to create a preliminary oblique wave in front of the detonation wave. However, this may not be necessary since the introduction of hydrogen fuel will also create oblique shocks which can have the same effect. These effects will depend on the size, shape and number of injectors and their location in the experimental set-up.

It was possible to approximate the static pressure rise due to fuel injection when some simplifying assumptions were made. For example, if the fuel injection was assumed to occur at constant pressure in an inviscid airstream, then the fluid momentum can be related to the stagnation pressure losses. While stagnation pressure and Mach number are reduced by injection, the static pressure and temperature are increased. These increases will be beneficial to the ignition process behind the oblique wave.

If the injection losses are due only to the streamwise component of momentum, then the stagnation pressure losses can be easily estimated<sup>14</sup>. For the case where  $M = 4.6$ , a stoichiometric amount of  $H_2$  injected at room temperature results in a stagnation pressure loss of 12%. This pressure loss is equivalent to an oblique shock oriented at about 21° to the horizontal which turns the flow at about 9.5°. The downstream Mach number is then reduced to approximately 3.7 and the static pressure

and temperatures are raised by factors of 2.4 and 1.3 respectively. These higher pressures and temperatures will shorten the ignition distance behind the oblique wave. The pressure field due to combustion should influence the oblique shock wave and create a detonation. In reality, the hydrogen injection will create shock waves which will cause higher stagnation losses than predicted by this analysis along with higher static pressures and temperatures.

While the increased pressures will shorten ignition delays behind the oblique wave, raising the temperatures may create pre-ignition problems prior to the wave. One consideration for injector design and location is premature ignition of the fuel. A study was made of the effects of introducing fuel at various locations inside the wind tunnel nozzle. The results indicated that fuel must be introduced at a location in the nozzle somewhere downstream of the point where the area ratio is 10. However, extensive modifications would be required to inject fuel in the existing nozzle. This result led to the study of strut type injectors which would be located at the exit of the nozzle.

### Injection Simulations

In order to verify some of the simplified analyses of fuel injection and combustion behavior, a more sophisticated computer simulation was employed. This code is described in detail elsewhere<sup>13,14</sup>. Many different simulations were performed to validate the fluid dynamic and chemical kinetics portions of this code. Once the code was validated, it was used to guide the experimental program. The first simulation consisted of wall injection through an orifice normal to the air stream. This configuration, which could model injection from a flat plate resulted in an oblique shock ahead of the injected fuel. Unfortunately, the penetration of the fuel jet was poor. A similar result has been observed experimentally, where fuel jet penetrations appeared to peak at a value of about five times the orifice diameter<sup>15</sup>.

In an effort to improve the fuel penetration, a projection or finger was added downstream of the fuel orifice. In this case, fuel was forced over the projection further into the air stream. However, a normal shock was also formed upstream of the injector which reduced the flow velocities to subsonic values. Since a detonation can only exist in supersonic flows, this geometry would preclude the establishment of an oblique detonation wave downstream of the injector. A third configuration was examined where the finger was modified to include a ramp on the upstream side. Fuel penetration remained good and the fuel injection shock became oblique. Most of the flow remained supersonic except for a small recirculation zone behind the leeward side of the projection. While this configuration appeared to provide improved penetration and supersonic flow downstream of the injection point, this design would have to be installed on a wall where the high temperatures in the boundary layer region could prematurely ignite the fuel. In addition, the boundary layer might decrease the fuel penetration. For these reasons, it was decided to examine strut type fuel injectors located outside the nozzle. Here fuel could be injected by multiple struts into the core flow region where viscous effects are reduced.

In order to provide a better model of the detonation process, a 2-dimensional combustion code was also developed. This code uses the same Total Variation Diminishing (TVD) algorithm as the injection model to capture strong shocks without smearing or oscillations. Temperature oscillations could incorrectly predict premature ignition and invalidate the detonation conditions. Finite rate chemistry is incorporated in order to model the heat release of the detonation process. The chemistry is fully coupled to the fluid dynamics so that heat release will couple to the shock front and show the correct rotation of the detonation wave. The fluid dynamics and chemical kinetics parts of this code were verified using many existing data sets and conditions<sup>13</sup>.

### Simulation of ODWE Experiment

The focus of this work was the simulation of the flow field in the strut region. This was done first with an Euler (inviscid) computation to obtain the position of the reflected shocks. The computations were done for free stream Mach numbers of 4.5 and 5.4. Two values of the vertical separation between the struts were studied (0.67 inches and 0.75 inches). It was apparent from the results that multiple shock interactions occurred between the struts, as well as shock impingement on the flat surfaces of the struts. It was clear that in the case of high stagnation enthalpy, extreme care should be taken in avoiding locally high temperatures. In order to model the strut injection and mixing, a series of computations were made with greater refinements, which included blunting the leading edge of the struts and providing a high grid density. The full Navier-Stokes equations were solved for an assumed laminar case. The conditions were  $M_\infty = 5.4$ ,  $T_\infty = 42.2K$ ,  $p_\infty = 0.0128$  atm,  $Re_\infty \approx 2 \times 10^5$  per inch. The total length of the strut is approximately 5 inches and transition to turbulence should occur somewhere at the end of the strut. However, because of the leading edge compressive ramp ( $7^\circ$ ) and the porous transpiration plate in the first half of the flat strut section, transition could be expected sooner. There is, however, no definite way to predict the transition with precision and there were no measurements to determine the properties of the boundary layer on the strut. In addition, when fuel injection takes place, the flow obviously becomes turbulent and the algebraic (Baldwin-Lomax) model is then unable to model the correct physics. Ideally a 2-equation model should be used at this point. The development and validation of such a model which uses the turbulent kinetic energy equation is one of the high priority development areas.

An example of the injection patterns for two struts is shown in Fig. 5. This design indicated hot spots on the center strut which caused the fuel to ignite immediately after injection. In fact, it was necessary to inject nitrogen at the tip of the strut to cool the mixture and decrease the oxygen content of the boundary layer<sup>14</sup>. The strut design is discussed in more detail in the next section.

Fig. 5 shows the computed density contours in logarithmic scale for the strut flow field prior to fuel injection. Of special significance is the boundary layer detachment on the top and bottom surfaces, at the start of the trailing ramp section. In addition, weak recompression shocks are seen to originate from the trailing edge itself. This can also be observed in the computed density field, although the pattern is more complex. It appears that weak shocks are thrown off from the pairs of vortices on opposite sides of the strut. The flow between the struts shows a regular diamond pattern from the multiple shock intersections. There is also a recirculation region on the flat plate in front of the first shock impingement. Because of the good resolution of both grid systems and numerical scheme, the pattern of shocks and expansion waves can be observed in detail, especially near the recirculation region.

The corresponding schlieren record is shown in Fig. 6. In this picture, the flow between the two strut surfaces is very complex, and there seems to be larger areas of flow separation and recirculation on the surfaces. It is difficult to obtain clear experimental pictures of the flow. Most of the features of the flow, however, are reproduced by the simulations, especially the strong bow shocks in front of the injectors and the diamond pattern of shock interactions. The mixing predicted by a 2-dimensional simulation is very poor and is below the measured values. This can be explained by the importance of three-dimensional effects with discrete orifice injection, especially longitudinal vortices. In addition, the turbulence levels in the experimental flow are not well known. A more detailed comparison could be obtained only if 3-dimensional computations are performed. These studies are planned for the future.

Once the mixing simulations were completed, efforts were focused on the oblique wave which would be created by the wedge test body. Since the creation of an oblique detonation wave was the goal, the model was extended to include finite rate chemistry and heat release. This code was also validated using existing experimental data. After this code was verified, several detonation cases were simulated. First, an oblique detonation was modeled in premixed hydrogen-air for  $M_\infty=4.2$ ,  $p_\infty=0.1$  atmospheres and  $T_\infty=700$  K which are close to proposed test conditions. The results presented in Fig. 7 show the oblique shock wave without fuel reaction. When reactions are allowed, detonative combustion results and the wave rotates to a more normal position as shown in Fig. 8.

Since the fuel injection simulations indicated rather poor mixing, a case was studied where a relatively unmixed fuel jet encountered the oblique shock. The results given in Fig. 9 show that the oblique wave, which was straight in the premixed case, has been severely distorted by the fuel jet. The low molecular weight and high speed of sound of the fuel contribute to a lower Mach number flow in the fuel rich areas which results in a more normal wave front.

## EXPERIMENTAL STUDIES OF ODWE

### Facilities

The arc-jet facility consists of a 20-MW arc heater supplied continuously with high pressure air. The arc chamber can be pressurized to 10 atmospheres. Air leaving the arc heater passes through a semi-elliptical nozzle with an exit area ratio of 36. A schematic of the test configuration is shown in Fig. 10. Note the injectors and test body which will be discussed later. Enthalpies can range from 5 to 35 MJ/kg (2000- 15,000 BTU/lb<sub>m</sub>) and air flow is variable from 0.05 to 0.68 kg/s (0.1-1.5 lb<sub>m</sub>/s). Nominal test conditions for the ODWE experiment correspond to maximum pressure and minimum current. Upgrading of the facility from 10 atmospheres stagnation pressure to 40 atmospheres is now in progress. This higher pressure will allow a closer simulation of the conditions expected at the inlet of a supersonic combustor. A five stage steam ejector pump maintains test cell pressures down to 13 mm Hg.

### Injector Design

The fuel injection struts are designed to provide good mixing with minimal losses. Analytical evaluations indicated that hot spots and recirculation zones would exist on and around the struts<sup>14,15</sup>. These regions would be undesirable since the goal is to create a well mixed fuel-air stream which would not ignite before the oblique wave. The simulations indicated that the transpiration of cool(300 K) nitrogen would prevent the premature ignition of the hydrogen fuel. The strut design, shown in Fig.11, has a transpiration area ahead of the hydrogen injection orifices. The porous "felt metal" allows nitrogen to transpire at a rate of 0.015 kg/s per strut, which represents about 5% of the main mass flow rate.

Hydrogen is injected through seventeen 1.52 mm(0.060 in) diameter orifices spaced 1.27 cm(0.5 in) apart. The orifices are drilled at an angle of 30° to the flow direction. Two or three struts will be utilized depending on the results of further mixing and combustion studies. The fuel-air ratio can be varied up to two times the stoichiometric value. The fuel rich condition will ensure that most of the test body will be immersed in a stoichiometric or fuel rich flow. An estimate of the air-fuel mixing was made using a semi-empirical mixing model<sup>17,18</sup>. This model, which is for sonic injection into a two-dimensional duct, accounts for strut separation and orifice size and spacing. Based on this correlation, the mixing efficiency for 30° injection of a stoichiometric mixture is 70% after a distance of 12 inches.



## Test Body

The oblique waves will be created by a water cooled wedge located approximately one foot downstream of the struts in the test section. Optical access is provided by 12 inch windows on either side of the test section and a schlieren system will provide photographic records of the wave angle with and without fuel. Pressure and temperature transducers on the wedge will be used to assess the state of combustion behind the oblique wave.

## Mixing Studies

A series of mixing studies were carried out in the hypersonic wind tunnel. The first set of tests were made with two injection struts spaced from 0.5 in to 0.75 inches apart. the extent of fuel mixing was measured by an on-line mass spectrometer. Gas samples were obtained by a probe which was mounted on a traversing table that allowed motion in all three dimensions. Some results of the fuel-air determinations are shown in Fig. 12 for two locations, 0.5 inches and 12 inches behind the strut trailing edge. While mixing is poor at 0.5 inches, it is significantly improved at 12 inches. The further location was representative of the proposed position of the wedge for the detonation tests. Note that the fuel distribution at 0.5 inches resembles the simulated case of Fig. 5 with relatively unmixed jets. The experiment verified the concerns about thermal failure at the areas of shock impingement on the struts. Further mixing tests with multiple struts were carried out only with cold flow to avoid overheating while hot flow tests were run with a single strut.

## Oblique Detonation Wave Studies

After the mixing studies were completed, the wedge test body was installed in the wind tunnel. While the original plan was to locate the wedge 12 inches downstream of the struts, this required the fabrication of new doors for the wind tunnel test section to place the windows in the proper location for viewing. Unfortunately, there was insufficient time to fabricate these doors, so the wedge was located in the field of view with the struts. Only 1.0 inches separated the trailing edge of the strut and the front edge of the strut. While this placed the strut in a relatively unmixed region, it was thought that combustion could occur behind the oblique bow shock of the wedge.

Tests were run with both helium and hydrogen injection to determine the effects on the wedge shock. The effects of fuel injection can be seen by comparing Figs. 13 and 14 for the cases of no injection and injection, respectively. It was observed that the injection of either combustible or inert gases caused a similar displacement of the bow shock. This was due to the low molecular weights and high speeds of sounds of hydrogen and helium. The effect is to lower the Mach number of the flow and cause the oblique wave to be more normal. During one test run, an increase in pressure was observed on the wedge with hydrogen injection, indicating combustion. However, in the limited time remaining for the tests, this phenomenon was not repeated.

## CONCLUDING REMARKS

An experimental and analytical program has been undertaken to study the characteristics of stable oblique detonation waves in a NASA-Ames arc-jet wind tunnel. The analytical models have been used extensively to aid in the experimental design and to ensure a successful experiment.

The existence of stable oblique detonation waves has been predicted previously for premixed hydrogen-air in supersonic flows. However, complete mixing of the fuel and air streams is not possible within reasonable distances in supersonic combustors. Therefore, it is necessary to introduce the fuel in a manner that provides good mixing in short distances with minimal losses. Several injector designs were examined analytically and a strut type was chosen for its ability to introduce the fuel in the nozzle free jet. The mixing characteristics and the effects of incomplete mixing on the detonation wave are still being studied.

The simulation of the strut flow field in the ODWE experiment provided great detail on the shock-shock interactions and shock-boundary layer interactions. Notably, the flow structure near the injector is particularly detailed (shock, Mach disk). The results agree reasonably well with the experimental schlieren records.

A mission analysis study compared the performance of vehicles powered by a scramjet or an ODWE. The results showed that the ODWE had better overall performance than the scramjet. The increased performance allowed the ODWE powered vehicle to weigh less than the scramjet powered vehicle for the same payload weight.

## ACKNOWLEDGEMENT

Support for HGA and JLC by NASA Grant NCC2-388 is gratefully acknowledged.

## REFERENCES

- <sup>1</sup> Roy, M., Comptes rendus a l'Academy des Sciences, February, 1946.
- <sup>2</sup> Townend, L.H., "An analysis of Oblique and Normal Detonation Waves", R.A.E. Reports and Memoranda No. 3638, March, 1966.
- <sup>3</sup> Morrison, R.B., "Evaluation of the Oblique Detonation Wave Ramjet", NASA Contractor Report 145358, January, 1978.
- <sup>4</sup> Rhodes, R.P. et al. "The Effect of Heat Release on the Flow Parameters in Shock Induced Combustion", Technical Report AEDC-TN-TDR-62-78, May, 1962.
- <sup>5</sup> Sargent, W.M. and R.A. Gross, "A Detonation Wave Hypersonic Ramjet", AFOSR TN 59-589, 1959.
- <sup>6</sup> Townend, L.H. "Detonation Ramjets for Hypersonic Aircraft", RAE technical Report 70218, November, 1970.
- <sup>7</sup> Morrison, R.B., "Oblique Detonation Wave Ramjet", NASA Contractor Report 159192, January, 1980.
- <sup>8</sup> Billig, F.S. and G.L. Dugger, "The Interaction of Shock Waves and Heat Addition in the Design of Supersonic Combustors", Twelfth Symposium(international) on Combustion, The Combustion Institute, 1969.
- <sup>9</sup> Gregory, T.J. et. al., "Hypersonic Transport Preliminary Performance Estimates for an All-Body Configuration", AIAA Paper 70-1224, October, 1970.
- <sup>10</sup> Menees, G.P., H.G. Adelman and J.L. Cambier, "Wave Combustors for Transatmospheric Vehicles", ISABE Paper 11-5, presented at the 9th International Symposium on Airbreathing Engines, Athens, Greece, September, 4-8, 1989.
- <sup>11</sup> Bittker, D.A. and Scullin, V.J., "GCKP 84-General Chemical Kinetics Code for Gas-Phase Flow and Batch Processes Including Heat Transfer Effects" NASA TP 2320, September, 1984.
- <sup>12</sup> Oran, E., T. Young and J. Boris, "Application of Time- Dependant Numerical Methods to the Description of Reactive Shocks", Proceedings of the 17th International Symposium on Combustion, The Combustion Institute, 1981, pp 43-54.
- <sup>13</sup> Cambier, J.L., H.G. Adelman and G.P. Menees, "Numerical Simulations of Oblique Detonations in Supersonic Combustion Chambers", AIAA Journal of Propulsion and Power, Vol. 5, No. 4, July-August, 1989, pp.482-491. Also presented at the 8th International Symposium on Airbreathing Engines, Cincinnati, OH, June, 1987.
- <sup>14</sup> Cambier, J.L., H.G. Adelman and G.P. Menees, "Numerical Simulations of the Oblique Detonation Wave Engine", AIAA 26th Aerospace Sciences Meeting, Paper No. 88-0063, Reno, NV, January, 1988.
- <sup>15</sup> Adelman, H.G., J.L. Cambier and G.P. Menees, "Analytical and Experimental Validation of the Oblique Detonation Wave Engine Concept", AIAA 26th Aerospace Sciences Meeting, Paper No. 88-0097, Reno, NV, January, 1988.
- <sup>16</sup> Zuckowski, E.E. and F.W. Spaid, "Secondary Injection of Gases Into a Supersonic Flow", AIAA Preprint 64-110, January, 1964.
- <sup>17</sup> Northam, G.B. and G.Y. Anderson, "Supersonic Combustion Ramjet Research at Langley", AIAA Paper No. 86-0159, Reno, NV, 1987.
- <sup>18</sup> Anderson, G.Y. and R.C. Rogers, "A Comparison of Experimental Supersonic Combustor Performance with an Empirical Correlation of Nonreacting Mixing Results", NASA TM-2429, 1971.

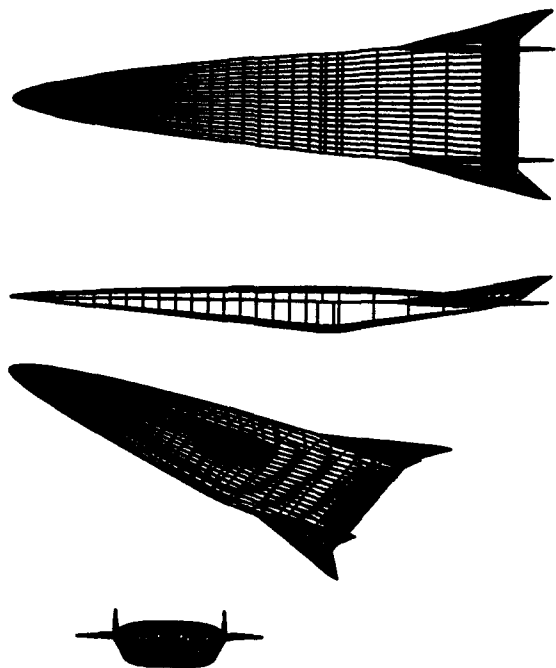


Fig. 1. Schematic of generic hypersonic trans-atmospheric vehicle used in mission analysis study.

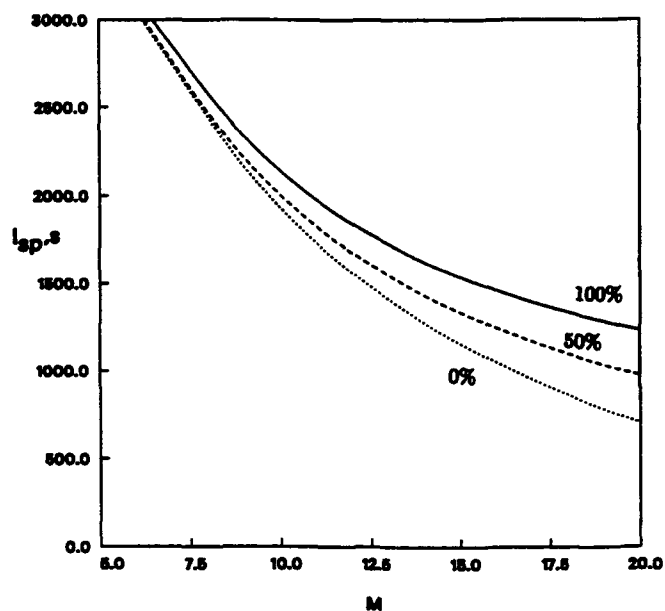


Fig. 2. Specific impulse versus Mach number for scramjet engine ( $q=2000$  psf,  $\phi=1$ ). Cases shown are for 0%, 50% and 100% of the heat load absorbed into the fuel.

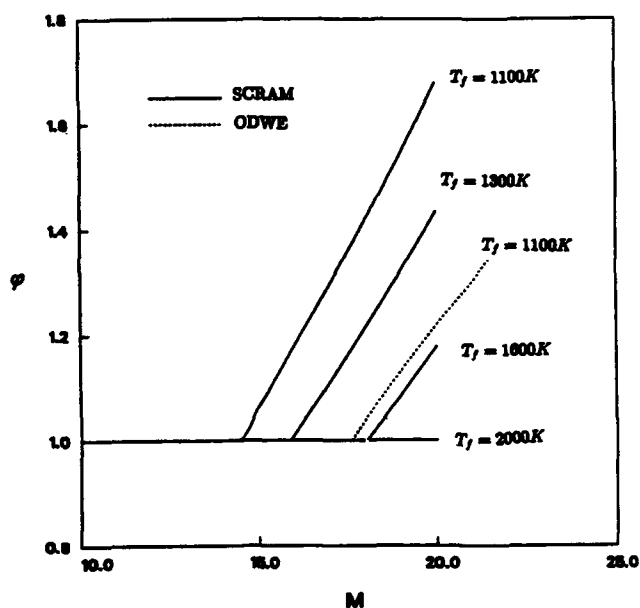


Fig. 3. Equivalence ratio versus Mach number for scramjet and ODWE engines at  $q=2000$  psf. ODWE results are shown for a fuel temperature limit of 1100 K while scramjet results are shown for a range from 1100 to 2000 K (1520 to 3140 F).

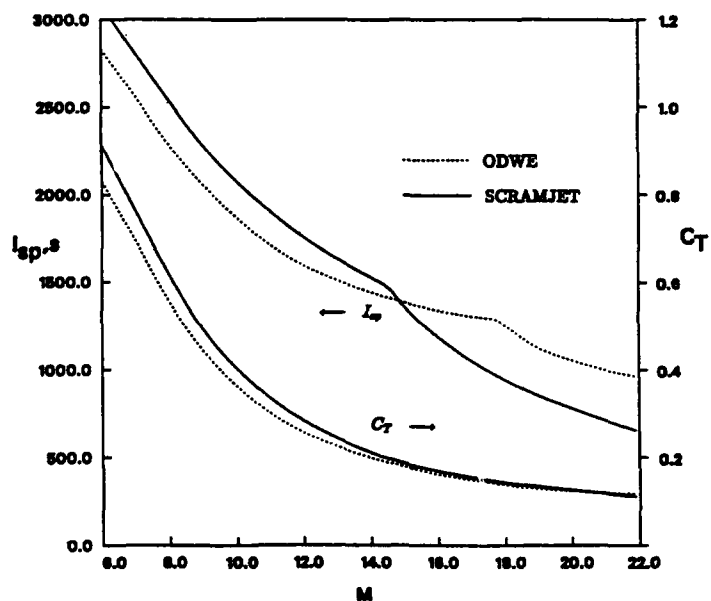
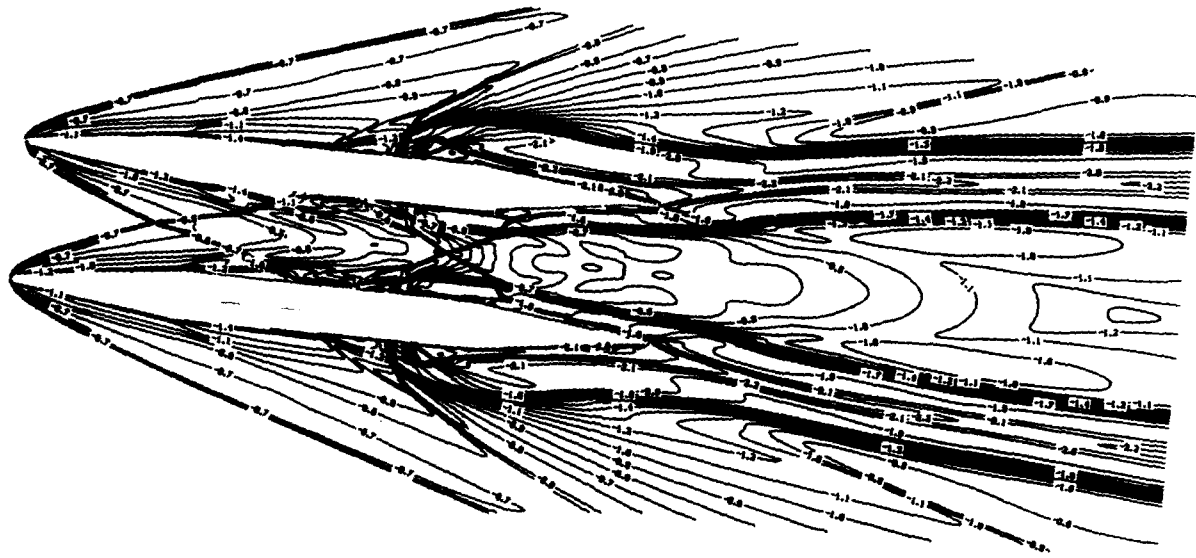


Fig. 4. Comparison of scramjet and ODWE performance characteristics. Shown are  $I_{sp}$  and  $C_T$  profiles for  $q=2000$  psf, 90% of heat loads carried by fuel and 1100 K fuel temperature limit.



**Fig. 5 Predicted logarithmic density contours for fuel injection from two struts in Mach 4.5 flow.**

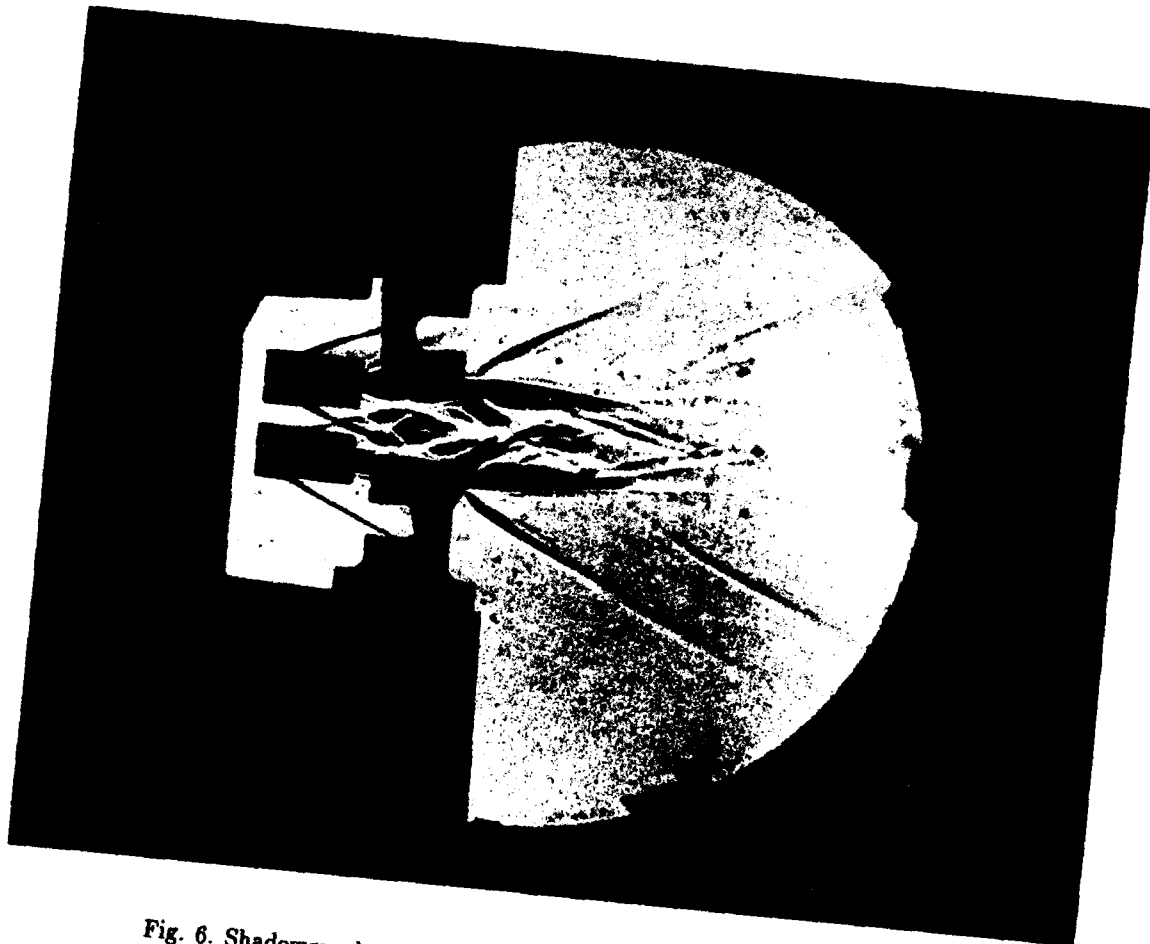


Fig. 6. Shadowgraph of two fuel injection struts in Mach 4.5 flow.

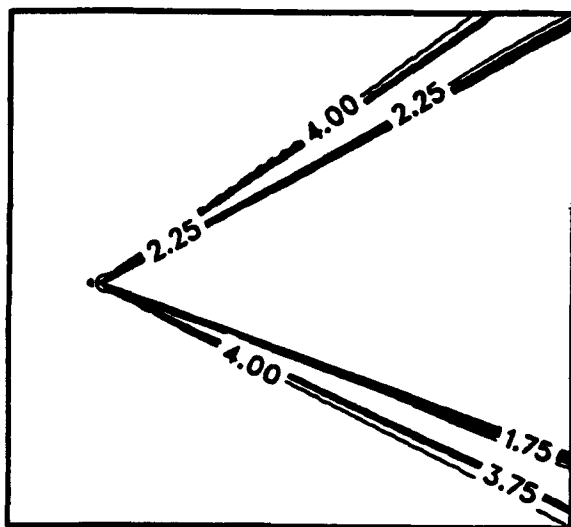


Fig. 7. Mach number contours for non-reacting stoichiometric air-fuel mixture flowing over a wedge at Mach 4.2.

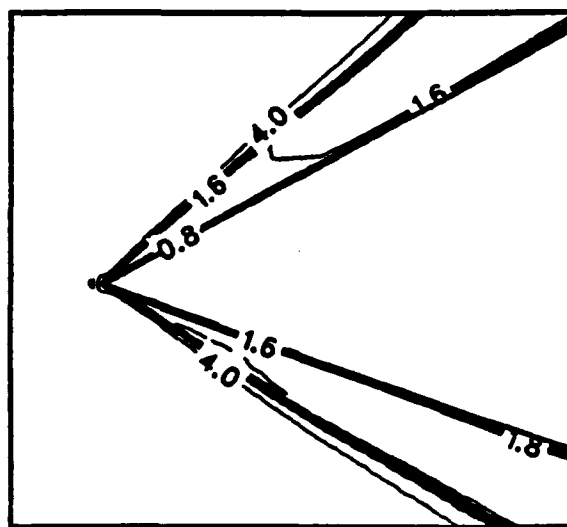


Fig. 8. Mach number contours for reacting stoichiometric air-fuel mixture flowing over wedge at Mach 4.2. The rotation of the wave with combustion indicates a detonation.

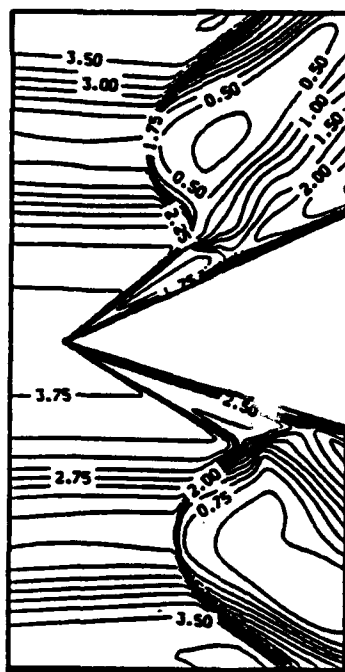


Fig. 9. Mach number contours for relatively unmixed fuel jet flowing over wedge.

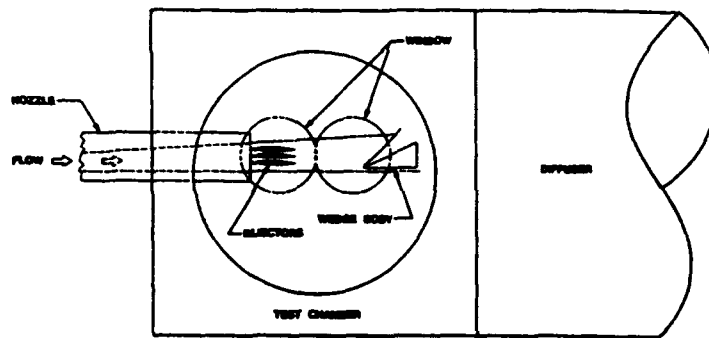


Fig. 10. Schematic of test set-up in 20 MW arc heated wind tunnel. The strut injectors are shown at the exit of the nozzle and the wedge test body is downstream.

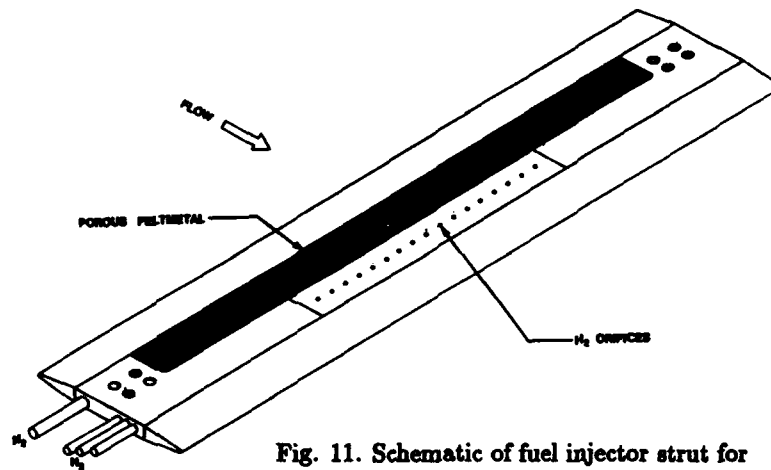


Fig. 11. Schematic of fuel injector strut for ODWE tests.

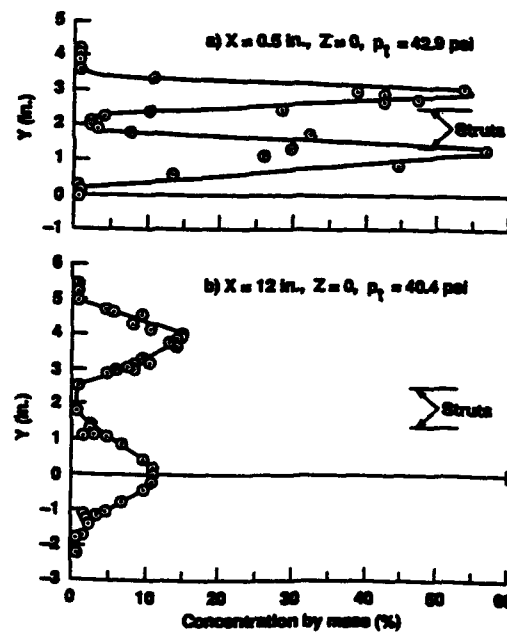


Fig. 12. Measured fuel concentrations at 0.5 inches and 12 inches behind fuel injection struts.



Fig. 13. Schlieren photograph of a shock wave created by a wedge in Mach 4.5 flow. A single strut fuel injector is positioned slightly below the wedge centerline. No fuel is injected in this case.



Fig. 14. Schlieren photograph of an oblique wave created by a wedge in Mach 4.5 flow. Fuel is injected from a single strut. Note the displacement of the lower portion of the wave compared to the previous figure.

## Discussion

WEYER

How do you prevent self-ignition within the area of fuel injection on the struts? In real flight situations the temperature in the boundary layer on the struts will be close to the stagnation temperature, and self-ignition will happen!

AUTHOR'S REPLY

The use of struts for our ODWE experiments was necessary because of the physical constraints of the test facility. They may not be used for a prototype vehicle design/flight situation. However, various transpiration cooling techniques have been proposed for sharp wing leading edges and could be used for injector struts in supersonic combustion. For our test conditions, nitrogen transpiration through "felt metal" was adequate to prevent the pre-ignition predicted by Dr. Cambier's calculations.

SMITH

Did the experimental program include the injection of an inert light gas such as helium to see if the shock wave movement was as expected with chemical reaction?

AUTHOR'S REPLY

Unfortunately, we did not have time to prepare this test because of the time constraints placed on our test schedule. However, it is something to attempt if future opportunities arise.

MARGUET

A quel nombre de Mach de vol minimal pensez-vous que le concept du stato-réacteur à détonation soit intéressant?

AUTHOR'S REPLY

Our initial one-dimensional analysis of the ODWE combustion showed that a performance advantage occurred at Mach numbers greater than 15 relative to the scramjet. A two-dimensional analysis could possibly modify this result somewhat. Nevertheless, we would expect the ODWE to be advantageous in the higher Mach regime approaching orbital speed.

ESCHER

Referring to the theoretical performance comparison between conventional scramjet and the ODWE, two clarifications are requested :

- 1) What is the basis for scramjet having somewhat higher specific impulse for a given flight speed, prior to fuel-rich operation?
- 2) What is the rationale for the ODWE reverting to fuel-rich operation at a significantly higher flight speed than the conventional scramjet engine?

AUTHOR'S REPLY

1) This occurs at Mach numbers smaller than 15 because of greater losses resulting from stronger ODWE diffuser detonation shock system.

2) The ODWE is smaller and lighter than the scramjet and, therefore, has less surface area to cool. Consequently, the necessity for excess fuel is delayed to a higher Mach number.



## WINTERFELD

- 1) What is the stagnation temperature in your last experiments?
- 2) We observed in our early experiments at high stagnation temperature premature combustion around the jets in shock induced combustion.

## AUTHOR'S REPLY

1° I do not have a stagnation temperature. The static temperature was about 800 K. The Mach number was about 4.5.

2) Our calculation did not predict that phenomenon. We were accurate on the prediction of the premature combustion on the surface of the injector struts.

# ETUDE EXPERIMENTALE DE STATOREACTEURS POUR MISSILES ET APPLICATIONS POTENTIELLES POUR LES STATOREACTEURS DANS LA PROPULSION COMBINEE

par

**Alain Chevalier, Pierre-George Sava et Jean-Pierre Minard**

Aérospatiale  
8 rue de Brix, B.P.35  
F-18001 Bourges  
France

## **RESUME :**

**aérospatiale** - Division des Engins Tactiques - a développé pour les besoins de ses programmes opérationnels à ce jour, des moteurs très performants, combinés fusée - statoréacteur à large domaine de vol. Des progrès décisifs ont pu être accomplis dans ce domaine grâce aux méthodes de développement impliquant calculs, modélisation et un important programme d'essais au sol et en vol, ainsi qu'à la précision et à la souplesse des organes embarqués de régulation et de calcul. Le programme d'essais au sol comprend des essais aérodynamiques, des essais analytiques de combustion permettant de connaître le domaine de fonctionnement et d'affiner les performances du moteur (le bilan poussée-trainée est en effet très sensible), des essais d'endurance et de synthèse. Outre l'utilisation des moyens classiques (souffleries en particulier), il a fallu recourir à des installations spécifiques capables de reproduire au sol les conditions de pression, température et débit d'air correspondant avec précision à celles rencontrées lors d'une mission réelle. Ceci est particulièrement important du fait du caractère non permanent des flux dans le moteur pour des trajectoires à fort dénivelé et à Mach variable.

Le développement d'un moteur combiné pour lanceur posera des problèmes expérimentaux analogues, et l'expérience acquise dans le domaine des installations et de la méthodologie d'essais de statoréacteurs de missiles peut être précieuse, bien que les difficultés seront accrues du fait de la grande taille de ces moteurs et de l'étendue du domaine de vol à étudier.

## **1)- LE MOTEUR COMBINE :**

Le GRIFFON ( diapositive n°1 ) était un avion expérimental préfigurant un intercepteur supersonique propulsé par un moteur combiné turboréacteur statoréacteur . Il a été étudié dans les années 1952 à 1961 .

L'association de ces deux moteurs, en un même groupe propulsif permet de profiter au mieux des qualités propres à chaque type de moteur en fonction des conditions de vol :

- bonnes performances de la turbomachine aux vitesses faibles ou modérément supersoniques,
- baisse des performances de la turbomachine lorsque la vitesse s'accroît, compensée par l'augmentation de celles du statoréacteur .

La disposition des deux moteurs était coaxiale, autorisant l'utilisation commune de la prise d'air et de la tuyère . L'adaptation de prise d'air et tuyère fixes, communes au deux propulseurs, est une caractéristique majeure de ce moteur combiné turboréacteur-statoréacteur .

Cette étude a été suivie dans les années 1960-1965 par des projets destinés à réaliser un moteur combiné turboréacteur double flux - statoréacteur à entrée d'air et tuyère variable (diapositive n° 2 ) . Les études et essais réalisés ont permis de valider un domaine de vol étendu ( jusqu'à Mach 4 et 30000mètres d'altitude ) .

Dans le domaine des missiles tactiques, grâce à des projets importants et des progrès réalisés dans de nombreuses techniques ( aérodynamique, systèmes de pilotage et de guidage, matériaux, méthodologie d'essais au sol et en vol, ... ) le début des années 1970 a vu naître des engins d'une nouvelle génération , plus homogènes techniquement et dont la compacité accrue améliore sensiblement les capacités opérationnelles (diapositive n° 3 ) .

Ce sont les statoréacteurs à accélérateur intégré, où le système propulsif est constitué par un accélérateur fusée et un statoréacteur de croisière. Afin de conserver au missile des dimensions et une masse limitées et ainsi permettre son emport sous avion, l'accélérateur fusée a été placé dans la chambre de combustion du statoréacteur. Cette dernière a vu son architecture bouleversée : le nouveau profil de l'alimentation en air a permis de créer des zones tourbillonnaires ( diapositive 3 bis ) dans le flux d'air à l'intérieur de la chambre, assurant ainsi la stabilisation de la combustion sans accroche flamme, ce qui permet d'intégrer l'accélérateur à poudre.

La phase la plus délicate de la mise au point du système propulsif est la transition fusée statoréacteur ( diapositive n° 4 ). En une fraction de seconde l'engin doit assurer :

- l'ouverture des opercules fermant les entrées d'air pendant le stockage, l'emport et le fonctionnement de l'accélérateur,
- l'éjection de la tuyère d'accélération,
- l'alimentation régulée en kérosène et l'allumage du statoréacteur.

Les engins les plus représentatifs de cette nouvelle génération sont :

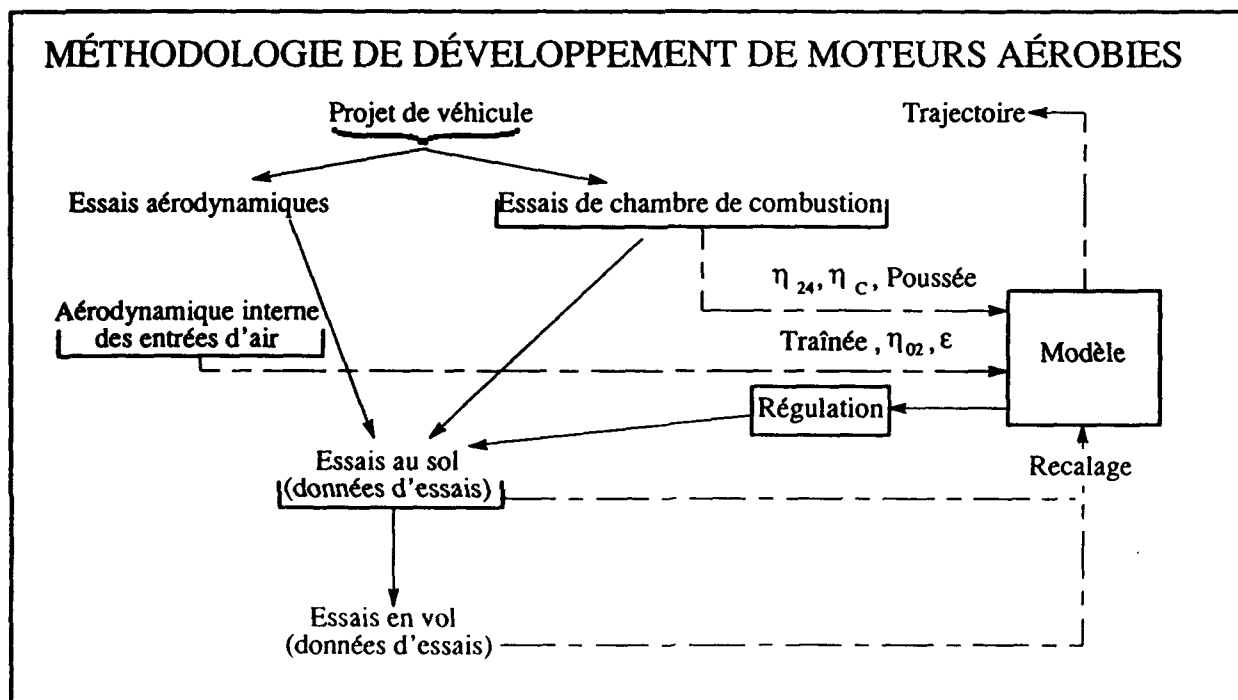
- L'Air-Sol Moyenne Portée ( ASMP ), missile à charge nucléaire dont la mise en service au sein de l'armée française remonte à 1986 ( diapositive n° 5 ),
- L'Anti-Navire Supersonique (ANS) successeur de la famille EXOCET, dont la faisabilité a été démontrée en vol, ( diapositive n° 6 ).

La mise au point de ces propulseurs a pu être accomplie grâce à de nombreux progrès :

- dans les technologies des organes de régulation et de calcul :
  - \* miniaturisation des équipements,
  - \* utilisation de calculateurs numériques offrant une grande souplesse d'utilisation et une grande précision.
- dans les méthodes de développement

## 2)- METHODOLOGIE DE DEVELOPPEMENT DE MOTEURS AEROBIE

La méthodologie de développement peut être résumée sur le schéma suivant



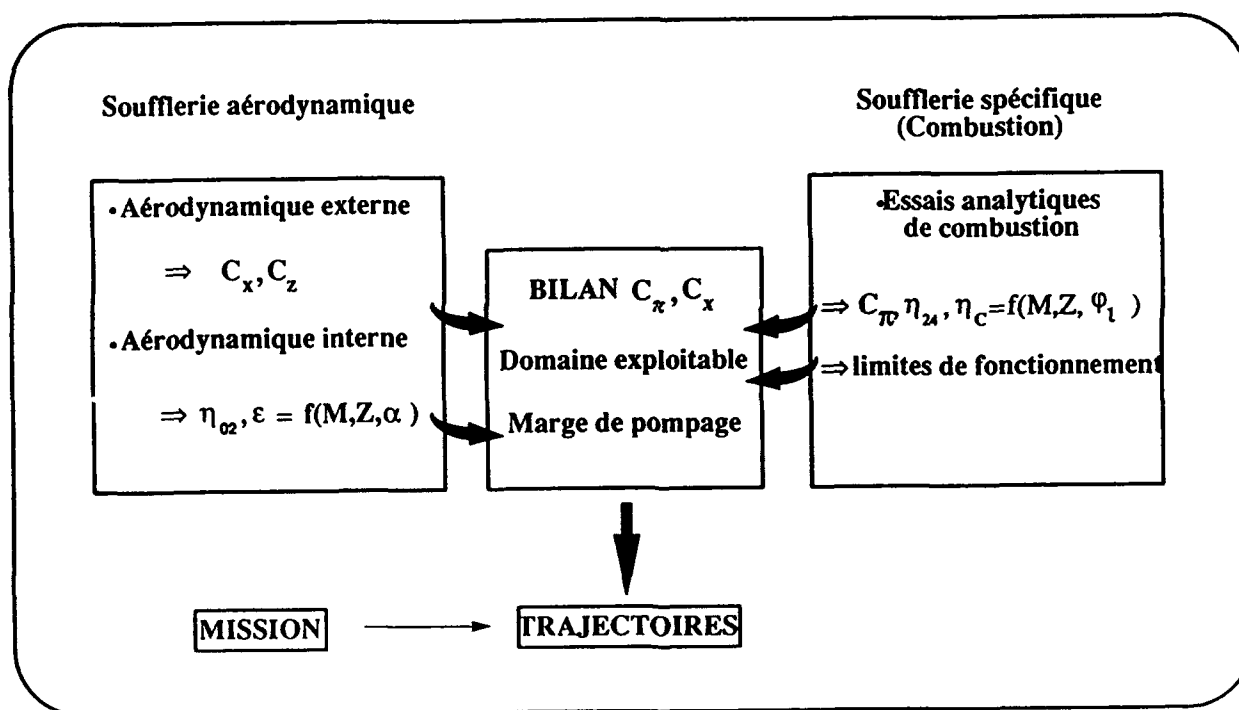
### 3)- METHODOLOGIE D'ESSAIS DE MOTEURS AEROBIE

Le programme des essais au sol comprend :

- des essais aérodynamiques assurant la connaissance des coefficients aérodynamiques globaux de l'engin ( $C_x, C_z$ ) et les caractéristiques de fonctionnement des entrées d'air ( $\eta_{02}, \epsilon$ ).
- des essais analytiques de combustion assurant la connaissance des caractéristiques du statoréacteur (coefficient de poussée  $C_{\pi}$ , rendement de pression  $\eta_{02}$ , rendement de combustion  $\eta_c$ , domaine de fonctionnement (extinction et instabilités)).

*Remarque : les résultats expérimentaux des essais aérodynamiques et de combustion permettent une modélisation de la propulsion du missile (connaissance pour chaque point de vol du bilan  $C_{\pi} - C_x$ , des limites de stabilité du moteur), fournissant ainsi le domaine de fonctionnement opérationnel du missile.*

Cette démarche peut être représentée par le schéma suivant :

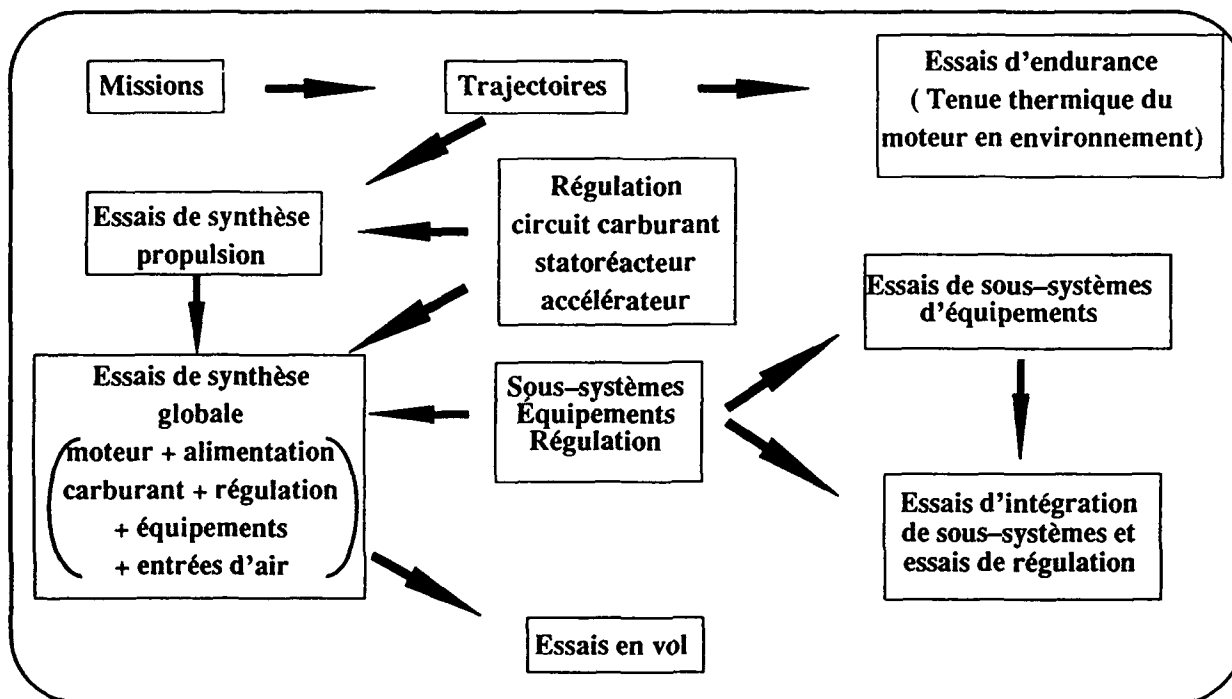


Outre les essais de combustion et les essais aérodynamiques le programme des essais au sol comprend également :

- des essais d'équipements ou sous systèmes
- des essais d'intégration de sous systèmes permettant des validations partielles (alimentation carburant, entrée d'air, régulation, équipements,...)
- des essais d'endurance dont l'objectif est de valider les choix des concepts ou des matériaux de protections thermiques du moteur dans son environnement. Ces essais nécessitent la simulation précise des trajectoires avec reproduction de l'échauffement cinétique externe.

- des essais de synthèse propulsion permettant une validation du fonctionnement du système propulsif complet et plus particulièrement des phases de transition .
- des essais de synthèse globale au sol permettant la validation du système et de son installation de tir avant un essai en vol . Les divers équipements sont embarqués et la définition est celle de l'essai en vol .

Cette démarche peut être représentée par le schéma suivant :



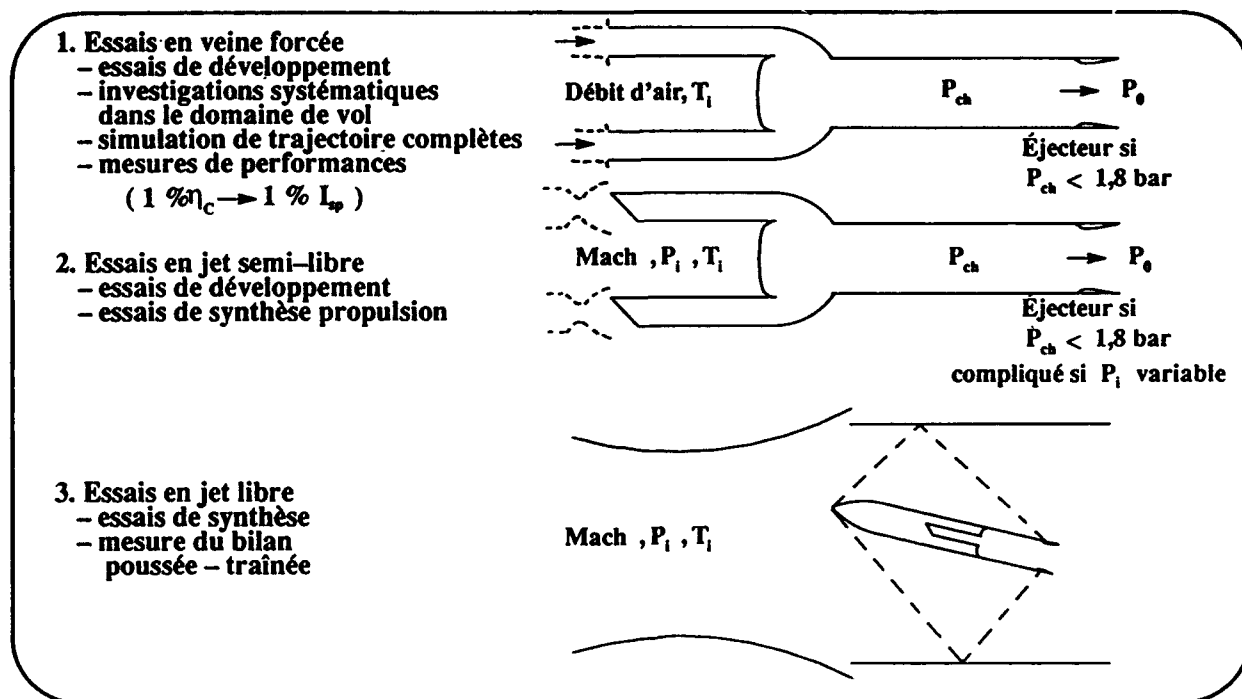
#### 4)- MOYENS D'ESSAIS POUR MOTEUR AEROBIE :

La mise en oeuvre des statoréacteurs pour la propulsion des missiles nécessite donc des moyens d'essais spécifiques très performants, dont les caractéristiques sont liées à celles des engins aérospatiale a développé ces techniques de pointe parce qu'elles étaient indispensables à ses projets de moteurs .

Plusieurs modes d'essais sont possibles :

- la veine forcée VF ( diapositive n° 8 ) permettant des essais analytiques . Ce mode est très souple, il permet, si l'on connaît les caractéristiques de l'entrée d'air, de simuler des trajectoires complètes ,
- le jet semi libre JSL ( diapositive n° 9 ) , par principe à nombre de Mach constant, permet de simuler le fonctionnement du missile complet avec les entrées d'air . On l'utilise pour la mise au point de la transition et pour les essais de synthèse à basse altitude ,
- le jet libre JL, permet d'intégrer le missile complet dans la tuyère

Ces trois modes sont représentés sur le schéma ci-dessous :



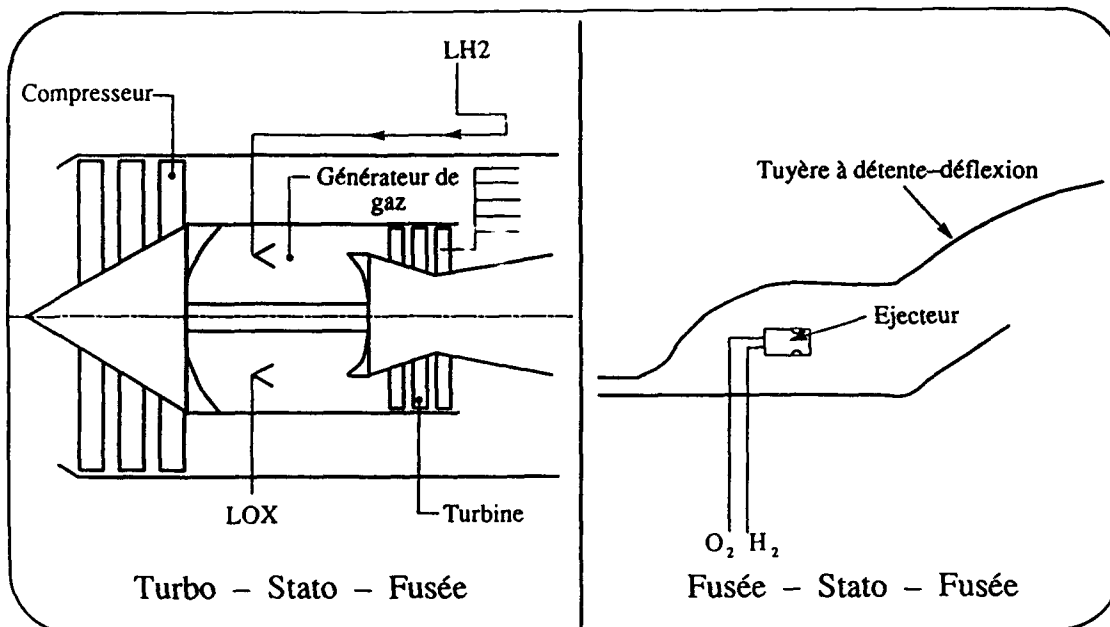
##### 5)- BESOINS EN ESSAIS ET EN MOYENS D'ESSAIS DES MOTEURS COMBINES AEROBIE POUR LANCEURS FUTURS

Le succès d'un programme de lanceur futur aérobique dépend de la très bonne connaissance des performances des moteurs, compte tenu par exemple des coefficients de sensibilité de la masse de charge utile par rapport à leur poussée spécifique et à leur consommation.

aérospatiale mène actuellement une étude dont le but est de fournir des éléments permettant d'apprécier l'intérêt technique et économique des différents moyens qu'il serait envisageable de mettre en place pour l'étude et le développement de tels moteurs.

A titre d'exemple deux concepts de moteurs sont retenus :

- un turbo-statoréacteur-fusée ( diapositive n° 11 )
- un fusée - statoréacteur-fusée ( diapositive n° 12 ).



**Remarque :** *aérospatiale* examine également, dans le cadre de cette étude, un moteur qui associerait la combustion sub et supersonique en statoréacteur :

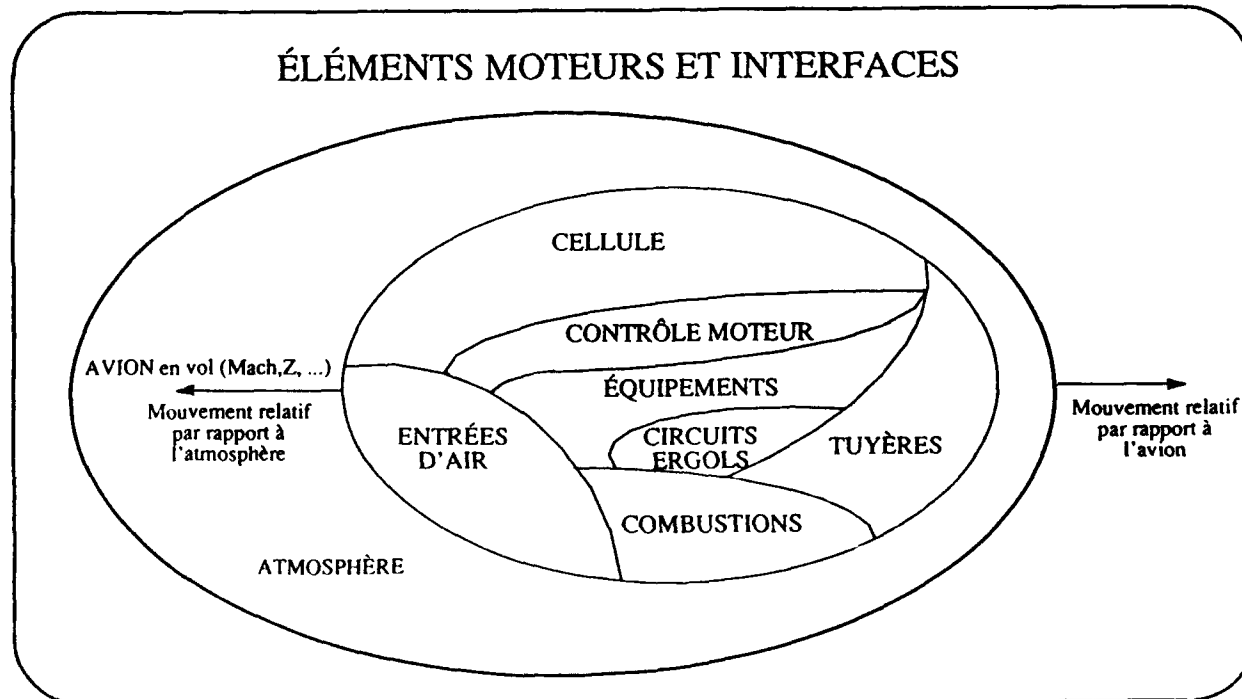
- statoréacteur à combustion subsonique de Mach 2 à 6,
- statoréacteur à combustion supersonique de Mach 6 à 12.

La première différence qui apparaît, si l'on compare un moteur de missile avec celui d'un lanceur futur, est celle de la taille ( diapositive n° 13 ). Ceci ne sera pas sans poser des problèmes au niveau des moyens d'essais ( débits importants pouvant conduire à des échelles réduites, ... ) .

Le corridor de vol d'un tel lanceur, pour des pressions dynamiques comprises entre 0,2 et 0,8 incluant la plupart des lanceurs actuels, dans le domaine de nombre de Mach entre 0 et 6, est par contre, moins sévère ( plus étroit ? ) que celui d'un missile ( diapositive n° 14 )

Chacun des deux concepts de moteur retenu a été, dans un premier temps, décomposé en sous systèmes ( entrées d'air, tuyère et arrière corps, circuit d'ergols, chambre de combustion ) . Une attention particulière a été portée aux interfaces .

## ÉLÉMENTS MOTEURS ET INTERFACES



Les principaux points durs ont été listés

SOUS-SYSTÈMES	DIFFICULTES
ENTREE D'AIR	géométrie variable – intégration – refroidissement – distorsion – dimensions – ....
TUYÈRE ET ARRIÈRE CORPS	géométrie variable – intégration – refroidissement – recombinaisons – interactions de jet – bruit – ....
CIRCUITS D'ERGOLS	gamme de débit – cryotechnie – ....
CHAMBRE DE COMBUSTION	différents modes – transitions – refroidissement – cinétique chimique – mélanges – pollution – ....

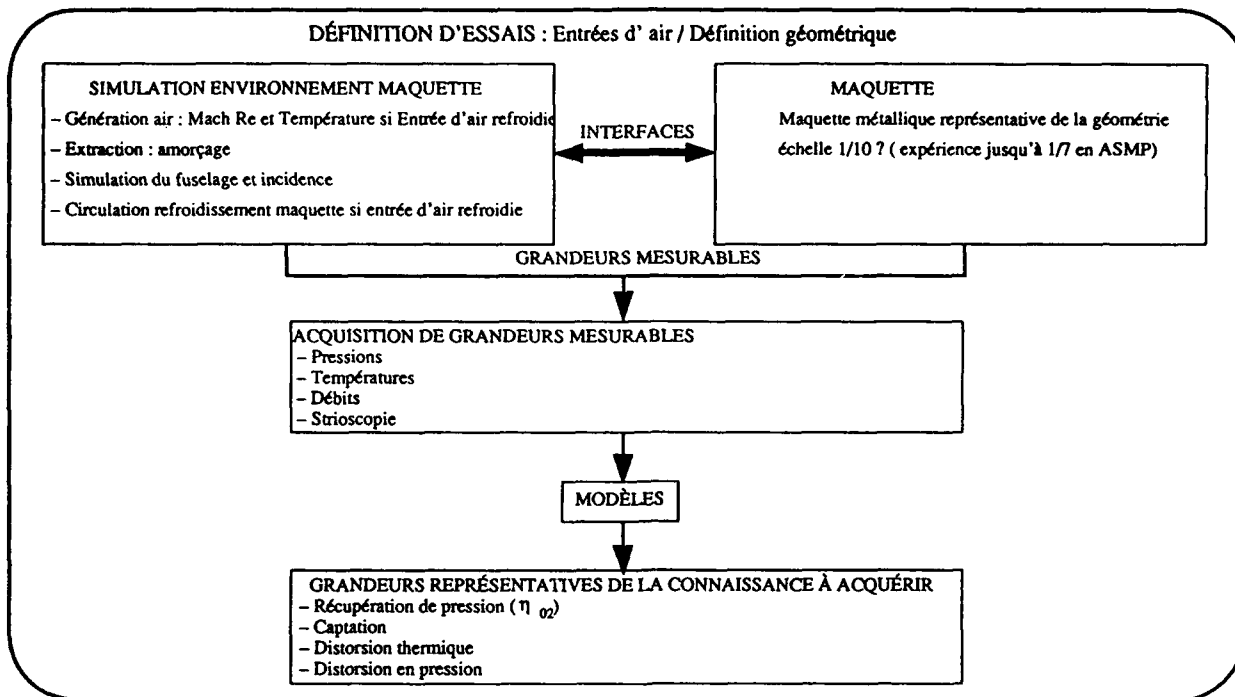
Les besoins en essais ont été obtenus en dressant des listes de données expérimentales nécessaires à la conception et à l'étude des moteurs combinés aérobies, non accessibles ou insuffisantes à l'heure actuelle. De même, les besoins en moyens d'essais liés au caractère aérobique des moteurs ( donc à l'utilisation de souffleries ) ont été recensés en tenant compte :

- des difficultés technologiques en fonction de l'étendue du domaine de vol,
- des possibilités de travailler à échelle réduite, avec ou sans recouplement éventuel avec des essais à échelle 1,
- de la prise en compte de la différence des performances obtenues avec une alimentation en air vicié comparativement à celles rencontrées avec de l'air pur,
- des limites et des coûts des moyens d'essais à mettre en oeuvre.

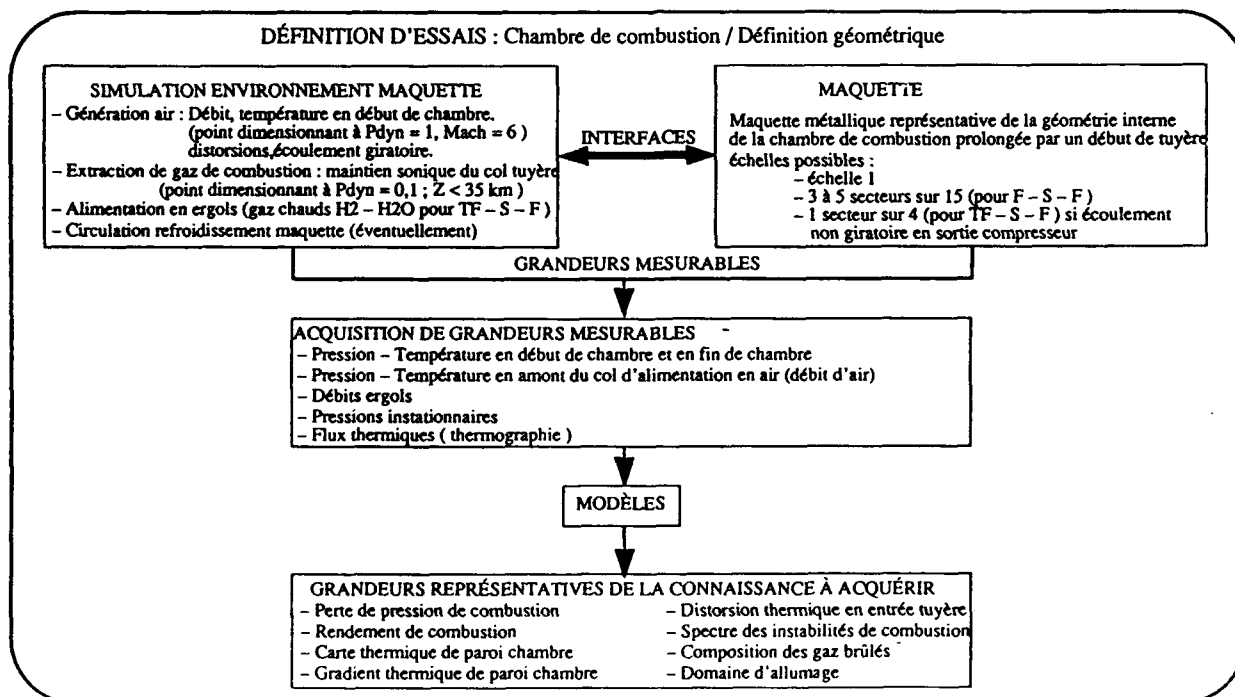
Deux exemples sont fournis ci-après, concernant l'entrée d'air et la chambre de combustion, dans une des premières phases d'étude se rapportant à la définition géométrique.



## EXEMPLE N° 1



## EXEMPLE N°2 :



## 6)- LOGIQUE D'ESSAIS POUR LE DEVELOPPEMENT DE MOTEURS AEROBIE DESTINES AUX LANCEURS FUTURS

L'étude est découpée en plusieurs phases :

- études amont,
- définition des géométries,
- projet,
- synthèse partielle,
- démonstrateur.

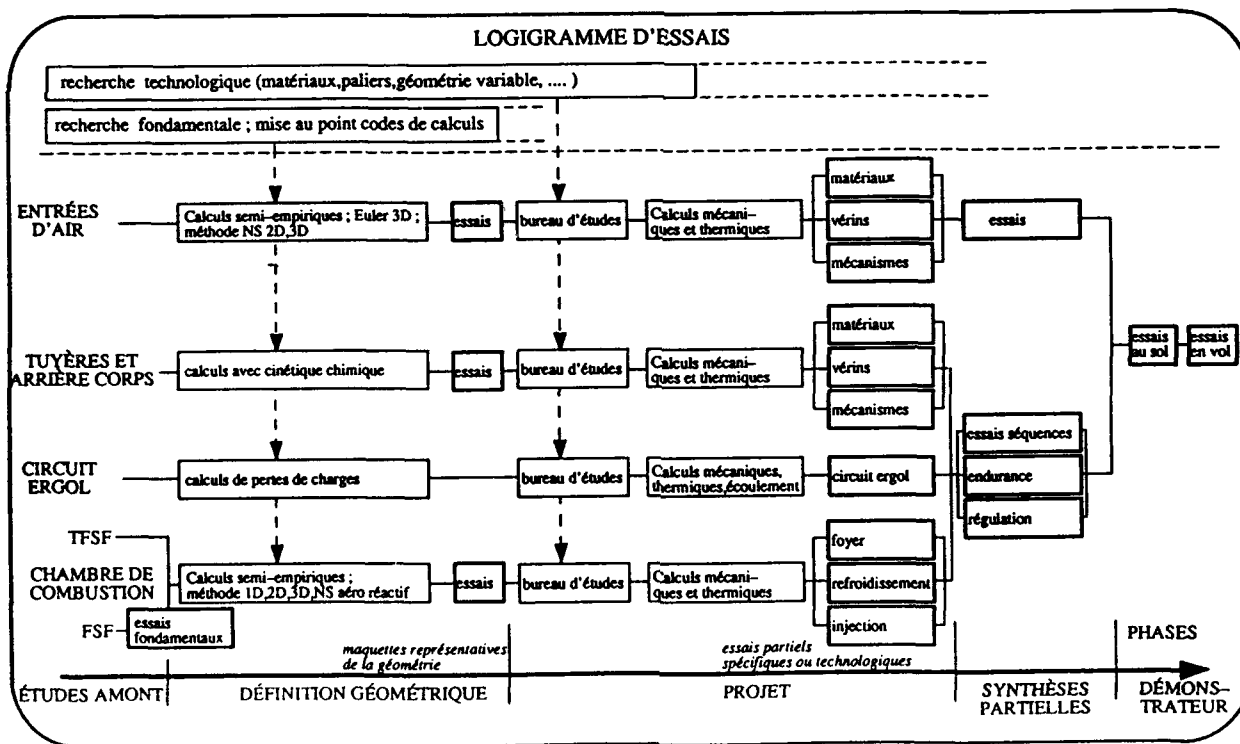
Pour cette dernière phase, l'étude des moyens d'essais aérobies pourra montrer l'impossibilité de valider totalement tous les sous-systèmes ou systèmes au sol. Dans ce cas il sera nécessaire d'étudier la faisabilité d'un moyen d'essais en vol.

En parallèle seront menées :

- des recherches fondamentales ( mises au point de codes de calculs,...
- des recherches technologiques ( matériaux, géométries variables refroidissement,....)

A chaque phase correspond des types d'essais : on retrouve, par exemple, les deux fiches d'essais précédentes correspondant à la définition géométrique des entrées d'air et de la chambre de combustion.

Un schéma complet de la logique d'essais figure ci après.



## 7)- COUVERTURE EN MOYENS D'ESSAIS DU DOMAINE DE VOL D'UNE ETUDE DE LANCEUR FUTUR

### ( STS 2000 ) DE L'aérospatiale

La couverture en moyens d'essais a été principalement réalisée au niveau européen . A titre d'exemple sont présentées la couverture des besoins en génération d'air pour essais aérodynamique d'entrées d'air et celle des besoins en alimentation des moteurs (en veine forcée) .

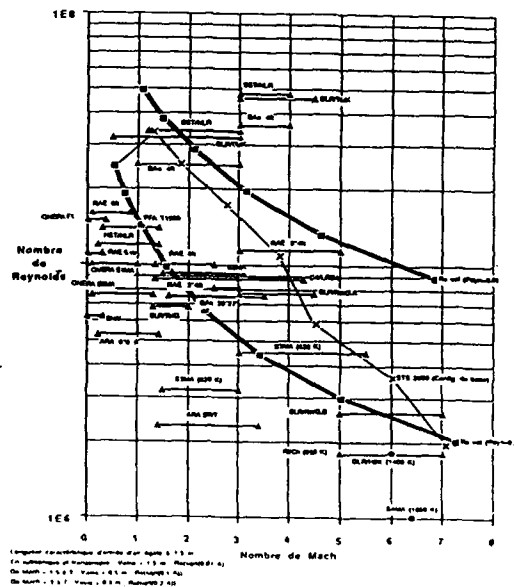
#### SOUFFLERIES AERODYNAMIQUES EUROPEENNES POUR ESSAIS D'ENTREES D'AIR

##### Hypothèses :

- 1 - air sec entrée d'air de 2,34 m<sup>2</sup> ( - 2,8 \* 0,8 / référence STS 2000 )
- 2 - longueur caractéristique de 1,5 m ( - 2,8/2,34 )
- 3 - déviation maximale d'un écoulement de 10°
- 4 - flux d'entrées d'air de 0,27 en subsonique et supersonique
- 5 - flux d'entrées d'air de 0,1 de Mach 1,5 à 2
- 6 - flux d'entrées d'air de 0,2 au dessus de Mach 2

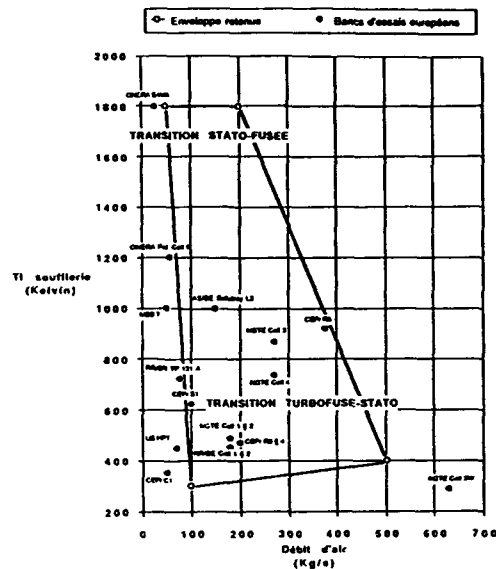
SOUFFLERIE	PAYS	VEINE	MACH		Re	Aérodin. hypothèses	observations
			min	max			
subsonique et transsonique (avec hypothèses 1-5-6)							
RAE 4 m	RU	1,22 * 1,22	0	0,3	1,1E+7	0,30	condition
DM	NL/FFA	0 * 0	0	0,35	5,3E+6	0,45	condition
CHENA FI	F	4,5 * 3,5	0	0,35	1,5E+7	0,25	condition
RAE 80	RU	2,25 * 2,25	0,1	0,65	1,6E+7	0,15	condition
CHENA 81MA	F	0	0,1	1	1,5E+7	0,40	condition
CHENA 82MA	F	1,75 * 1,77	0,1	1,3	7,4E+6	0,11	condition
ENW	E	2,4 * 2	0,2	1,3	0,14		condition / cryogénique
ARA 0,5 * 0,5	RU	3,3 * 3,4	0,2	1,4	5,3E+6	0,16	condition
NETALR	NL	2 * 1,8	0,2	1,4	1,2E+7	0,11	condition
FFA T 1500	S	1,5 * 1,5	0,3	1,4	1,4E+7	0,10	réf. / 15 s à M=1
Mach 1,5 à 2 (avec hypothèses 1-5-6 et 5)							
OLVING	RFA	1 * 1	1,3	2	4,8E+6	0,21	condition
RAE 4 s	RU	2,5 * 2,25	1,35	2,5	1,0E+7	0,40	condition
SMA	F	1,75 * 1,93	1,5	2,1	9,3E+6	0,36	condition
ARA DWT	RU	0,75 * 0,99	1,4	2,4	2,3E+6	0,16	condition
RAE 30 * 27	RU	0,75 * 0,99	1,6	3,5	7,5E+6	0,15	condition
RAE 4 s	RU	1,22 * 1,22	1	4	2,5E+7	0,25	réf. / 7 s
NETALR	NL	1,2 * 1,2	1,2	4	3,4E+7	0,25	réf. / 10 s
OLVING	RFA	0,6 * 0,6	0,5	4,5	2,2E+7	0,12	réf. / 90 s
RAE 3 * 4 s	RU	1,22 * 0,91	2,5	5	6,1E+6	0,22	condition
SMA	F	0,75 * 0,8	1,5	6,5	3,2E+6	0,16	réf. / 10 s à 620 K
Mach 2 à 7 (avec hypothèses 1-5-6 et 5)							
RAE 4 s	RU	1,22 * 1,22	1	4	3,6E+7	0,36	réf. / 7 s
NETALR	NL	1,2 * 1,2	1,2	4	4,0E+7	0,35	réf. / 10 s
CALUBA	F	0,4 * 0,4	1,35	4,5	4,0E+6	0,12	condition
OLVING A	RFA	0,5 * 0,5	3	4,5	7,7E+6	0,14	réf. / 0,4 s
OLVING	RFA	0,6 * 0,6	0,5	4,5	4,0E+7	0,17	réf. / 90 s
RAE 3 * 4 s	RU	1,22 * 0,91	2,5	5	1,1E+7	0,21	condition
SMA	F	0,75 * 0,8	1,5	6,5	1,5E+6	0,23	réf. / 10 s à 620 K
OLVING	RFA	0,6	0	6	1,0E+6	0,15	réf. / 90 s à 1000 K
SMA	F	0,65	0,4	6,4	0,7E+5	0,17	réf. / 30 s à 650 K
ROCK	F	0,3	5	7	1,0E+6	0,08	réf. / 9,4 s
OLVING B	RFA	0,5	5	7	2,0E+6	0,13	réf. / 100 s
FFA Hyp 500	S	0,5	4	7		0,12	

#### COUVERTURE européenne des besoins en génération d'air pour essais aérodynamiques d'entrées d'air



## BANCS D'ESSAIS MOTEURS EUROPEENS

BANC D'ESSAIS	PAYS	Alimentation			Extraction	
		Débit (Kg/s)	Pression (Bar)	Tempér. (K)	Débit (Kg/s)	Pression (Bar)
ONERA SAMA	F	27	100	1600		
ONERA Pal Cell 9	F	55	15	1200	8	0,15
AS Subdray L3	F	150	21	1000	5	0,2
MBB	RFA	50 ?	15 ?	1000 ?		
CEPy RS	F	375	7	925	375	0,05
NGTE Cell 3	RU	270	2	870	270	0,38
NGTE Cell 4	RU	270	3	740	270	0,35
RIVER TP 131 A	RU	77,2	11,38	723	182	0,1
CEPy S1	F	100	2	623	100	0,05
NGTE Cell 1 & 2	RU	180	8,1	480	77	0,5
CEPy RS 4	F	200	2	473	200	0,05
RIVDE Cell 1 & 2	RU	180	5	453	272	0,027
US HPT	RFA	70	1,96	450	70	0,07
CEPy C1	F	50	1,2	352	55	0,05
NGTE Cell 3W	RU	630	1	288	630	0,48

COUVERTURE des besoins en alimentation moteur  
(Veine Forcée)BESOINS EN ALIMENTATION MOTEUR  
(Veine Forcée)

Débit d'air	(Kg/s)	500	200	50	100
PI souffl. (1,3 * PI2)	(Bar)	1,3*4,5	1,3*30	1,3*5	1,3*0,45
T1 souffl. (= T12)	(Kelvin)	400	1800	1800	300
Ac (Veine forcée)	(m <sup>2</sup> )	0,42	0,053	0,08	0,73
PI souffl. (Ac=0,053)	(Bar)	46	39	9,8	8,1

### 8)- CONCLUSIONS:

Il apparaît que dans ces deux cas la couverture existante est globalement satisfaisante ou que les moyens complémentaires ( débits importants à haute température....) pourront être mis rapidement en place, grâce à des financements appropriés

TFSF FSF	BESOINS EN MOYENS D'ESSAIS COUVERTURE EUROPEENNE			
-------------	---	--	--	--

- ENTREES D'AIR :

	Mach	0	2	4	6
Couverture en					
REYNOLDS (Re/Revol)		1	1	0,75	
ECHELLE (L/Lvol)		0,25	0,25	0,20	
TEMPERATURE (T/Tvol)		0,8	0,4	0,8	
SOUFFLERIES		BAe SST/NLR	BAe SST/NLR	ONERA/S4 DLR/H2K	

- MOTEUR Veine Forcée:

	Mach	0	4,4	6
	Ti (K)	300	1000	1700
Couverture en				
PRESSION		100%	100%	
DEBIT		60%	20%	
BANCS MOTEUR		CEPr aerospatiale/Subdrey	ONERA/S4	

Il a également été mis en évidence dans le cadre de cette étude (non achevée à ce jour) que des difficultés apparaissent dans certains secteurs comme :

- la vérification des performances de l'entrée d'air à grande échelle et son intégration,
- la vérification des performances de la tuyère (surtout pour des forts taux de détente) et son intégration vis à vis de l'arrière corps.

Pour ces deux points, des essais en vol avec des composants fortement instrumentés seront certainement indispensables.

THEORETICAL AND EXPERIMENTAL PERFORMANCE OF A SOLID FUEL RAMJET  
COMBUSTION CYCLE FOR HYPERSONIC FLIGHT CONDITIONS

by

P.J.M. Elands, P.A.O.G. Korting and R.G. Veraar  
Prins Maurits Laboratory TNO  
P.O. Box 45, 2280 AA Rijswijk  
the Netherlands

and

F. Dijkstra  
Delft University of Technology  
Faculty of Aerospace Engineering  
P.O. Box 5058, 2600 GB Delft  
the Netherlands

Summary

A research program has been carried out to validate a numerical simulation of the flow and combustion process in the combustion chamber of a solid fuel ramjet with experimental results. Operating conditions were chosen to represent a sustained missile flight at Mach 4 at an altitude of 13 km. Experimental data were obtained by burning cylindrical fuel grains made of polyethylene and hydroxyl terminated polybutadiene in a solid fuel ramjet using a connected pipe facility. For numerical simulation a computer code was developed, describing rotational symmetric steady-state turbulent reacting flows through channels with and without a sudden expansion. Calculations were carried out using polyethylene as a fuel. For the validation emphasis was laid on the regression rate. The results show that the computer code predicts the mean regression rate with reasonable accuracy. The value for the effective heat of gasification is found to be very important. The experiments and the calculations carried out show the feasibility to apply a solid fuel ramjet for sustained hypersonic flight at these conditions.

Nomenclature

A	area
c	characteristic velocity
c <sub>p</sub>	specific heat at constant pressure
C <sub>F</sub>	thrust coefficient
C <sub>D</sub>	drag coefficient
D	diameter
D	drag force
d	diameter
ER	equivalence ratio $(\dot{m}_{air}/\dot{m}_{fuel})/(\dot{m}_{air}/\dot{m}_{fuel})_{st}$
f	mixture fraction
g	variance of mixture fraction
h	step height
h	specific enthalpy
h <sub>v</sub>	effective heat of gasification
k	turbulent kinetic energy
L	length
M	molar mass
m	mass flow rate
p	static pressure
q	heat flux
R <sub>0</sub>	universal gas constant
r	regression rate
S	source term
T	temperature
T	thrust
t	time
u	velocity in x-direction
v	velocity in y-direction
V	flight velocity
x	coordinate
Y	mass fraction
y	coordinate
Γ	diffusion coefficient
c	dissipation rate of turb. kin. energy
η	efficiency
φ	mix ratio (m <sub>air</sub> /m <sub>fuel</sub> )
φ	arbitrary independent variable
ρ	density

92-16990

## Subscripts

a	ambient
air	air
c	combustion
c	chamber
fr	frontal
in	inlet
j	Euler index
N	net
p	port
s	species
st	stoichiometric
th	theoretical
o	initial
o	reference

## Superscripts

-	mean
.	rate
o	reference

## Acronyms

COPPEF	A Computer Program for Parabolic and Elliptic Flows
HTPB	Hydroxyl Terminated Polybutadiene
MMA	Methylmethacrylate
pdf	probability density function
PB	Polybutadiene
PE	Polyethylene or Polyethene
PMMA	Polymethylmethacrylate
PML	Prins Maurits Laboratory
SCMC	Sonic Control and Measuring Choke
SFRJ	Solid Fuel Ramjet
SIMPLER	Semi-Implicit Method for Pressure-Linked Equations Revised

Introduction

For about ten years a joint research program to investigate the flow and combustion process in a solid fuel ramjet (SFRJ) has been carried out by the Prins Maurits Laboratory TNO and the Faculty of Aerospace Engineering of the Delft University of Technology in the Netherlands. It encompasses both theoretical and experimental work and is primarily aimed at getting a better understanding of the flow and combustion process with their mutual interaction in the combustion chamber of an SFRJ.

In an SFRJ air is fed into the bore of a solid fuel grain, see Fig. 1. At the interface between the pyrolyzing fuel and the air combustion takes place. Within the framework of the research program mentioned above, the flow and combustion process have been modeled theoretically [1], while combustion experiments have been performed using a connected pipe facility [2, 3, 4].

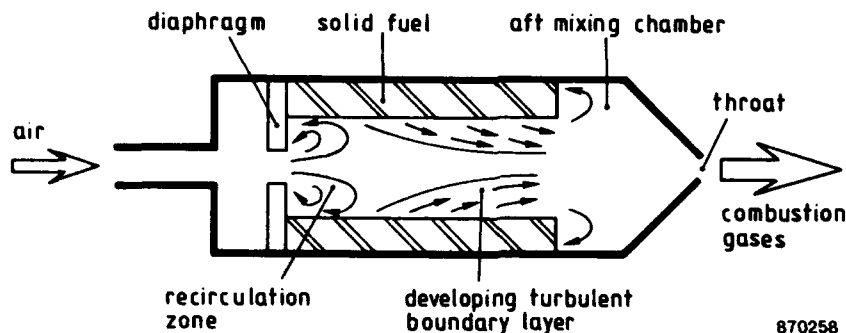


Fig. 1. Schematic view on a solid fuel ramjet combustion chamber.

For this fundamental research, test conditions have been selected that were based on flight conditions at sea level and at Mach numbers up to 3. This normally results in inlet air temperatures between 400 K and 700 K and pressures between 0,4 and 1,0 MPa in the combustion chamber, while the mass fluxes in the bore of the solid fuel grain remain relatively low and may range between 100 and 400 kg/m<sup>2</sup>s. Most of these studies were performed using polymethylmethacrylate (PMMA) and polyethylene (PE) as a fuel, since both of these fuels are readily available and well documented in the literature. In addition PMMA is transparent, which makes it particularly interesting for fundamental combustion research, whereas the heat of combustion of PE is comparable with that of a more

practical non metallized fuel like hydroxyl terminated polybutadiene (HTPB).

Application studies have indicated that SFRJs may also be of interest at higher flight Mach numbers [5]. For instance, the use of SFRJs to propel kinetic energy penetrators in the range between 1 and 2,5 km seems to be extremely advantageous. In that particular case the SFRJ should operate at Mach 4,5 to 5, resulting in inlet air temperatures of about 1500 K and combustion pressures of approximately 4 MPa. The mass fluxes in the bore of the grain may attain values above 1000 kg/m<sup>2</sup>s. Especially at these high flight Mach numbers testing of SFRJs is expensive and requires special dedicated facilities. This is particularly true for a proper simulation of inlet air temperature. The air heater (vitiator type) that is presently available at the test facility of PML can only raise the inlet air temperature up to about 1000 K. A special vitiator that will raise the inlet air temperature up to 2000 K is presently being designed and is expected to become operational by the end of the year. The air however will be polluted by significant amounts of water and carbon dioxide. At these extreme operational conditions, numerical simulation of the flow and combustion process may reduce the costs considerably by eliminating extensive testing. Some testing, however, will always be needed to validate the computational results.

This philosophy was also followed in a study in which the calculated combustion behavior of an air-to-air missile, flying at a speed of Mach 4 at an altitude of 13 km and powered by an SFRJ, is compared with experimental results. For the calculations polyethylene was used as a fuel. The major results of this study are presented in this paper. Since similar experiments were also performed with HTPB, the combustion behavior of PE is also compared with that of HTPB.

#### Theoretical Performance of a Missile

To prepare experiments at realistic hypersonic conditions, an air-to-air missile is considered, flying with a speed of Mach 4 at an altitude of 13 km. This missile, shown in Fig. 2, is performing a horizontal flight in a sustained phase, by generating a thrust which equals the drag of the missile. The sustain engine of the missile is a central dump type solid fuel ramjet engine. The required air is supplied by means of four aft mounted symmetrical inlets. These concern two-dimensional three-shock (two oblique shocks and one normal shock) inlet systems operating at design conditions which results in an inlet total pressure efficiency of 0,48 at Mach 4 [6]. Combined with the atmospheric conditions at an altitude of 13 km [7], a combustion chamber pressure of 1,2 MPa can be obtained.

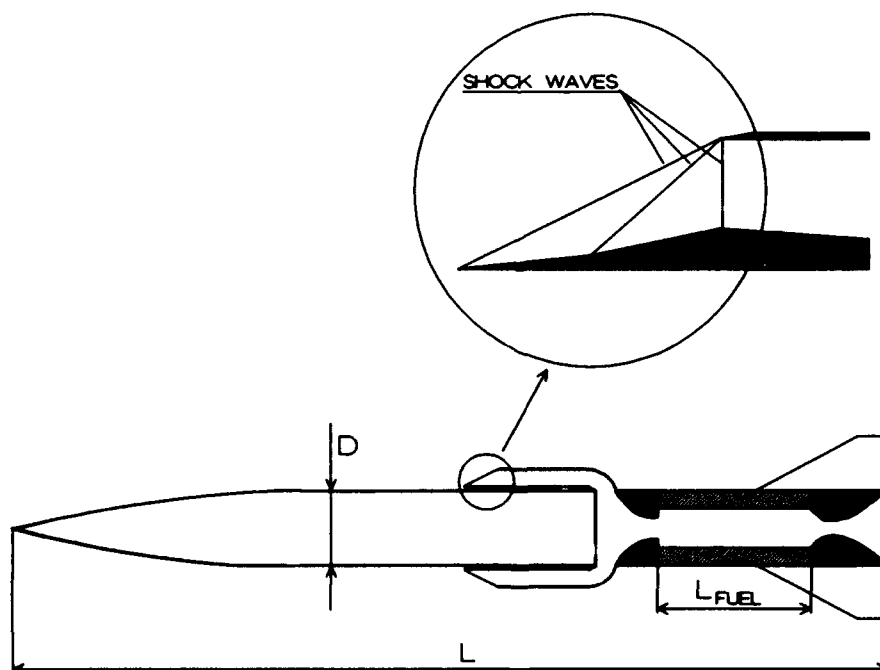


Fig. 2. Schematic view on the SFRJ propelled missile,  $D = 0,1$  m,  $L = 2,0$  m,  $L_{FUEL} = 0,3 - 0,4$  m.

To facilitate comparison of the theoretical performance calculations with experimental data and to avoid scaling effects, the missile is sized to an external diameter related to the geometry of the fuel grains used in the experiments. This results in a missile body diameter of 0,1 m. Assuming an  $L/D = 20$ , the length of the missile becomes 2,0 m. For such a missile a fuel grain with a maximum length of 0,4 m is considered to be acceptable. The fuel block is designed in such a way that stoichiometric combustion is achieved, to obtain maximum thrust per unit of air mass flow.



The net thrust of the propulsion system follows from:

$$T_N = \dot{m}_{air} \left[ C_F \eta_c c_{th}^* (1 + 1/\Phi) - V_0 \right] \quad (1)$$

where  $\eta_c$  is the combustion efficiency and here assumed to be 0,9, while  $V_0$  is the flight speed of 1180 m/s (Mach 4 at 13 km altitude) [7].

The thrust coefficient  $C_F$  follows from the pressure expansion ratio, assuming ideal expansion. The ratio of specific heats of the combustion gases is assumed to be 1,3 during the expansion process, which results in a thrust coefficient of 1,5 [8]. For the combustion of HTPB and PE with air the values of the characteristic velocity are calculated at various equivalence ratios using the NASA SP-273 computer program [9]. The temperature of the air entering the combustion chamber is taken to be 900 K and follows directly from the flight velocity and flight altitude. Both fuels are considered to have a standard initial temperature of 300 K. The results of these calculations are depicted in Fig. 3.

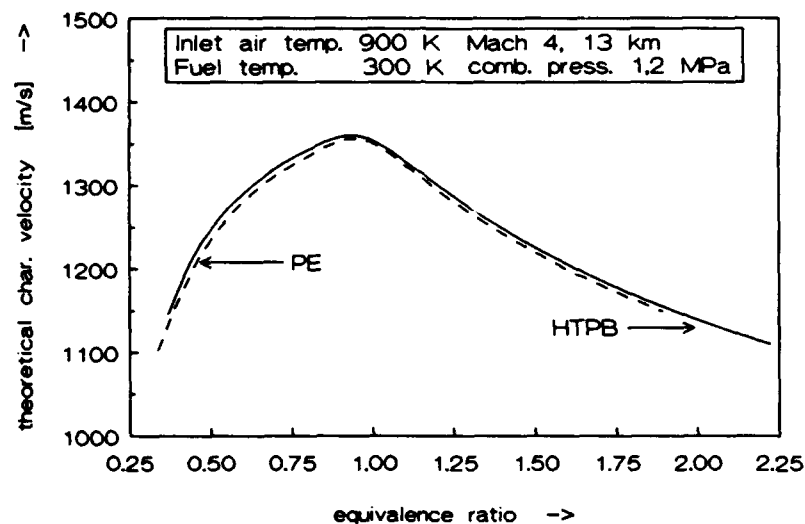


Fig. 3. Theoretical characteristic velocity versus equivalence ratio for PE and HTPB.

The aerodynamic drag of the missile is calculated from:

$$D = C_D 0,5 \rho_a V_0^2 A_{rr} \quad (2)$$

where  $C_D$  is the drag coefficient assumed to be equal to 0,35, and  $\rho_a$  is the ambient density (0,2655 kg/m<sup>3</sup> at 13 km altitude) [7].

$A_{rr}$  follows from the frontal area of the four inlets added to the cross sectional area of the missile body.

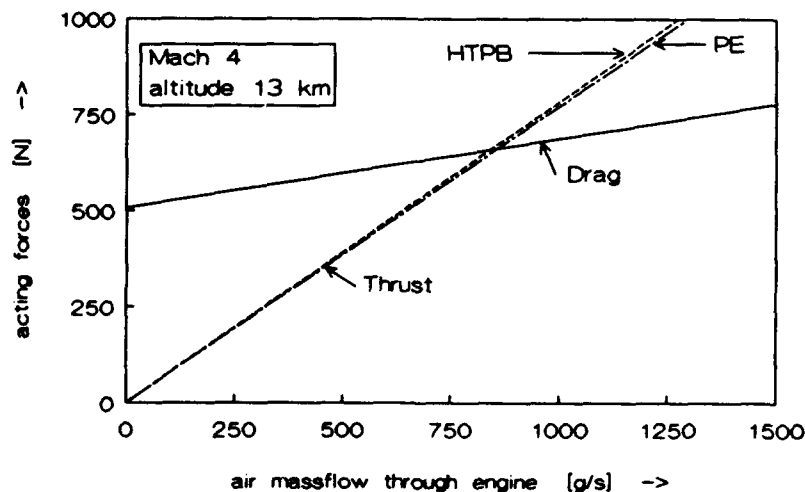


Fig. 4. Acting forces on the missile system assuming stoichiometric combustion.

The results of the theoretical thrust and drag calculations are shown in Fig. 4. From this Figure it can be seen that a theoretical thrust to drag ratio of unity is obtained at an air mass flow rate of about 0,8 kg/s. Air mass flow rates between 0,25 kg/s and 1,0 kg/s were selected for this study.

### Theoretical Flow and Combustion Modeling

To describe the flow and combustion processes in an SFRJ, a computer program, COPPEF, has been developed [1]. This program calculates rotational symmetric (2D) steady-state turbulent flows through pipes with or without a sudden expansion or through a single-sided sudden expansion configuration. Turbulence is accounted for by Favre-averaging of the conservation equations and by modeling terms containing products of fluctuating variables with the high Reynolds number version of the k- $\epsilon$  turbulence closure model. All governing equations can be cast in the following general form :

$$\frac{\partial}{\partial x_j} (\rho u_j \phi) - \frac{\partial}{\partial x_j} \left( \Gamma_\phi \frac{\partial \phi}{\partial x_j} \right) = S_\phi \quad (3)$$

where  $\phi$  can be one of the following variables :  $u, v, p, k, \epsilon, h, f, g$  or  $Y_s$ , where  $\Gamma_\phi$  is a diffusion coefficient, and where  $S_\phi$  is a source term.

The enthalpy  $h$  is defined as :

$$h = \sum_s Y_s h_s \quad (4)$$

where  $Y_s$  is the mass fraction of species  $s$  and

$$h_s = h_s^0(T_0) + \int_{T_0}^T c_{p,s} dT \quad (5)$$

The equation of state is written as :

$$p = \rho R_0 T \sum_s \frac{Y_s}{M_s} \quad (6)$$

The influence of density gradients on the turbulence field is taken into account by a special pressure-velocity correlation term occurring in the equations for  $k$  and  $\epsilon$  [1].

At the inlet of the SFRJ combustion chamber the values of all variables are specified. At the outlet and at the center line a no-gradient condition is specified for all variables, except for the radial velocity which is zero. At the solid wall the temperature, the mass fractions and both velocities are specified. The values of  $k$  and  $\epsilon$  are not specified at the wall but are calculated just near the wall using wall-functions. The two-layer wall-function method of Chieng and Launder [10] is incorporated in the COPPEF computer program. This wall-function method is adapted in the case of a small non-zero normal velocity at the wall. Heat transfer at the boundaries is taken into account by coupling the heat flux to the wall to the near-wall variation of the temperature. Mass transfer at the boundaries is included by the injection of gaseous fuel at the solid wall. The injection velocity is a function of the heat flux.

Four combustion models have been implemented in the COPPEF computer program. Two models, the diffusion flame models, are based on the assumption that the combustion process can be described by one irreversible infinitely fast chemical reaction (mixed is burnt) [11]. In one of these two models, the mass fractions are weighted with the  $\beta$  probability density function (pdf) to take into account the effect of turbulence on the combustion process. Both models require the solution of a transport equation for the mixture fraction  $f$ , while for the  $\beta$  pdf also the variance of  $f$ , called  $g$ , has to be calculated.

The third model is based on finite rate chemical kinetics and involves a large number of species and reactions. Dissociation and formation of intermediates is included. In this model the effect of turbulence on the combustion process is neglected.

The fourth model is the chemical equilibrium combustion model, which calculates the chemical equilibrium of the combustion products. The equilibrium is considered to be reached infinitely fast. This model takes into account dissociation of species and formation of intermediate species. This model is much faster in CPU-time than the finite rate chemical kinetics combustion model. Another advantage is that all kinds of species can be considered, also species for which no kinetic data are available, like MMA or PB. The chemical equilibrium combustion model is based on the STANJAN [12] computer code, which solves for chemical equilibrium by means of calculating element potentials. The equilibrium module is used at every grid node at every iteration cycle.

The choice of the combustion model used in the calculations has a small effect on the regression rate [2]. Therefore it was decided to perform all calculations using the turbulent diffusion flame combustion model, which is expected to yield the most reliable results in flows where mixing is the flame controlling mechanism.

A finite-volume integration method is employed to reduce the system of partial differential equations describing the flow to a system of algebraic difference equations which can be solved numerically. The combined convective-diffusive fluxes at the cell interfaces are approximated with the Power-Law scheme [13]. The solution is done in a segregated approach, in which an iteration procedure takes into account the non-linear coupling between the equations. The strong coupling between the pressure and the velocity field is handled by the SIMPLER-algorithm [13], together with a line continuity and a block correction procedure.

In the COPPEF computer code the regression rate of fuel is modeled as follows [14] :

$$r = \frac{q_{\text{wall}}}{\rho_{\text{wall}} h_v} \quad (7)$$

in which  $q_{\text{wall}}$  is the local heat flux to the wall and  $h_v$  is the effective heat of gasification, which is defined as the amount of heat required to bring 1 kg of polymeric fuel from the initial state, usually solid taken at room temperature, to the pyrolytic (gaseous) state at the pyrolysis temperature. The value of the effective heat of gasification is very important, as was already noticed in Ref. [2]. Normally the value of the effective heat of gasification used for PE is 4,5 MJ/kg [15]. Presently a research study on fuel pyrolysis is being carried out [15,16], where it is believed that the effective heat of gasification of PE is affected by the heating rate of the fuel surface. If the mass flow rate of incoming air is increased, the heat transfer to the wall increases and so does the regression rate, and hence the heating rate. This will affect the surface temperature and therefore it is reasonable to assume that the effective heat of gasification will also increase. Depending on the heating rate the surface temperature will vary from 700 to 1000 K for PE, and the effective heat of gasification will vary from less than 4,0 to more than 5,5 MJ/kg, see Fig. 5. These values depend on the heating rate and on the composition of the pyrolysis products, i.e. whether monomer gas is assumed or several different pyrolysis products (the so-called lump model [16]). Even if the wall temperature is kept constant the effective heat of gasification will still vary with the heating rate, due to the different composition of the pyrolysis gases.

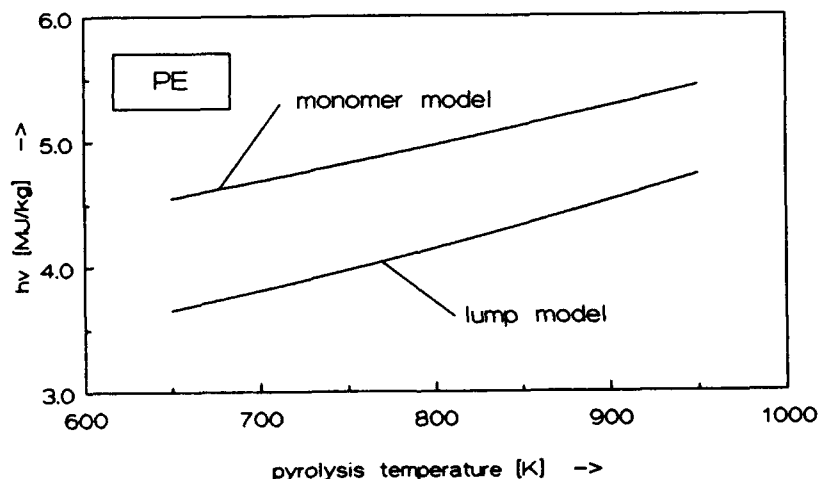


Fig. 5. The effective heat of gasification as a function of the pyrolysis temperature for polyethylene as predicted by two theoretical models.

From this, it was decided to perform also some calculations while varying the effective heat of gasification of PE in accordance to the above described mechanisms. The values chosen for the effective heat of gasification can be found in Table 1.

It was assumed that the convective heat transfer mechanism is dominant and that the radiative heat transfer may be neglected. This assumption is believed to be valid especially at higher mass flow rates.

#### The Experimental Test Facility

At the Prins Maurits Laboratory TNO an experimental facility is available to simulate solid fuel ramjet combustion [17]. A schematic view of the main parts of the facility is given in Fig. 6. Not shown in this Figure is a the computer operated gas supply system, which supplies air, oxygen, hydrogen and methane to the experimental installation. Mass flow rates are controlled by sonic control and measuring chokes (SCMCs), with an accuracy of 3 % [18]. In a vitiator methane is burnt with oxygen, to raise the SFRJ inlet air temperature. During every experiment the oxygen content of the vitiator exhaust gases is kept constant to that of ambient air. A three way valve vents the heated air into the atmosphere before the actual experiment takes place. As soon as steady conditions are reached within the vitiator, the three way valve is opened towards the SFRJ.

Table 1. : Conditions for the experiments and calculations

## • General :

Fuels : HTPB and PE  
 Oxidizer : Air  
 Chamber pressure : 1,2 MPa  
 Air inlet temperature : 900 K  
 Fuel grain length : 0,3 m

## • Experiments :

Initial port diameter : 40 mm  
 Inlet diameter : 25 mm  
 Initial stepheight : 7,5 mm  
 Burning time : 10-15 s for HTPB  
 : 25 s for PE

## • Calculations :

Wall temperature : 800 K (assumed, [15,16])  
 Fuel : PE  
 Turbulent diffusion flame combustion model  
 20 x 20 grid system  
 Uniform inlet velocity profile  
 Inlet turbulence intensity : 0,1

## • Conditions for calculations :

mass flow	port diameter	stepheight	$h/d_p$	$h_v$ (var)	$h_v$ (fixed)
250 g/s	50 mm	12,5 mm	0,25	4,00 MJ/kg	4,5 MJ/kg
500 g/s	60 mm	17,5 mm	0,29	4,25 MJ/kg	4,5 MJ/kg
750 g/s	65 mm	20,0 mm	0,31	4,50 MJ/kg	4,5 MJ/kg
1000 g/s	70 mm	22,5 mm	0,32	4,75 MJ/kg	4,5 MJ/kg

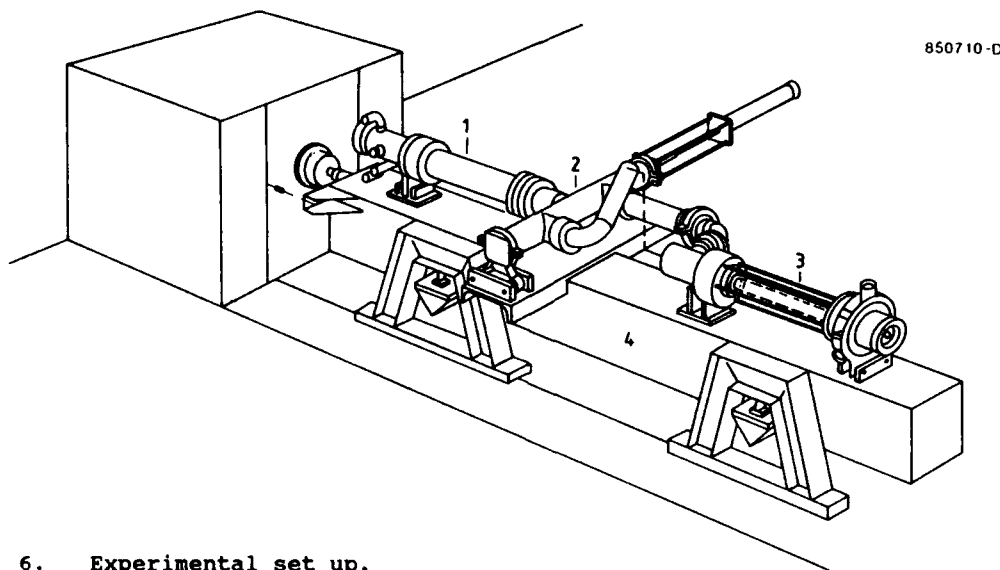


Fig. 6. Experimental set up.

- 1 vitiator.
- 2 three way valve.
- 3 solid fuel ramjet combustion chamber.
- 4 thrust bench.

The SFRJ set up itself consists of an injection chamber, a combustion chamber consisting of a polymeric fuel, and an aft mixing chamber (see also Fig. 1). To ignite the solid fuel grain hydrogen and oxygen are injected in the injection chamber, while this mixture on its turn is ignited by a spark plug. The combustion pressure is controlled by choosing a proper diameter of the nozzle, fitted in the aft mixing chamber. The SFRJ, including vitiator and three way valve, are positioned on a thrust bench, in order to measure the thrust. A data acquisition system is capable of storing 16 digital signals simultaneously.

For the present test series cylindrical fuel grains, made of PE and HTPB were burnt with vitiated air. The fuel grain length was 300 mm, while the initial inner diameter was 40 mm. To simulate Mach 4 test conditions the temperature of the inlet air was kept at approximately 850-900 K, while the combustion pressure was 1,2 MPa. The mass flow rate was varied between 250 and 1000 g/s. All combustion experiments with PE and HTPB had a burning time of 25 s and 10-15 s respectively.

#### Pyrometry

The maximum temperature in the aft mixing chamber was determined, using a two color pyrometer. The pyrometer determines the soot temperature, by measuring the ratio of spectral radiances at respectively 577 nm and 830 nm. It is assumed that the temperature of the soot equals the maximum gas temperature in the aft mixing chamber of the SFRJ.

#### Regression rate measurement

The regression rate in the SFRJ was determined by three different methods. To obtain the overall mean regression rate the weight of the fuel grain was determined before and after a test run. To obtain the local mean regression rate the fuel inner port diameter was measured as a function of the axial coordinate, also before and after the test run.

During several tests the local instantaneous regression rate in the SFRJ was determined using the ultrasonic pulse-echo technique [19]. In this technique ultrasonic transducers are placed on the outer side of the fuel grain. Each transducer emits an acoustic wave into the fuel. This wave is reflected at the burning interface within the combustor, and this reflection (echo) is then received again by the same transducer. The time derivative of the measured pulse-echo time is considered to be proportional to the local instantaneous regression rate, as long as the combustion is quasi-stationary [19].

#### Results and Discussion

To compare theoretical and experimental combustion behavior, emphasis was laid on the regression rate. The regression rate is considered to be one of the most important design parameters since it determines the fuel mass flow rate and hence the mixture ratio and therefore the overall system performance. In addition temperatures were measured and combustion efficiencies were estimated.

Before calculated and experimental results are to be compared, some important comments have to be made.

First of all, the COPPEF computer code assumes a steady state flow and combustion process. However, this assumption is in strong contrast with the actual situation, where, due to regular vortex shedding at the inlet, locally highly fluctuating quantities like velocities, temperatures and species concentrations can be expected. Nevertheless, the regression rates appear to change only relatively slow during the experiment, as will be discussed later on.

Secondly, to simulate an experiment adequately, it is necessary to choose an appropriate fuel grain inner bore diameter. In the experiment this diameter will vary in time, while in the calculation this value is fixed. For the calculations the value of the inner bore diameter was taken to be about 5 mm less than the final averaged inner bore diameter after the experiment. The effect of diameter variation on the calculation results can be significant and will also be discussed in more detail later on.

Thirdly, it is known that the heat transfer is dependent on the axial location, due to different flow conditions. For example one can distinguish the recirculation zone from the developing boundary layer, see Fig. 1. Therefore the effective heat of gasification, the wall temperature and the pyrolysis products will differ with the axial position. In the computer code this has not been taken into account, simply because not enough data are available yet. When carrying out the calculations these quantities have been kept constant and uniform and hence only the regression rate varies with the axial position as a function of the local heat flux.

Finally, the regression rate is dependent on the inlet conditions [11,20]. Variation of inlet conditions was not taken into account in this study. The inlet conditions used for the calculations are specified in Table 1. In this Table the conditions used in the experiments and the calculations are summarized.

#### Observed combustion behavior

Isolated experiments showed that spontaneous ignition and combustion of the fuel grain did not occur within at least 10 s. This is attributed to the fact that the desired level of inlet air temperature was only reached after some time, due to heat losses in the piping between the air heater and the combustion chamber. Therefore it was decided to use the hydrogen oxygen ignition system also in these experiments.

Almost immediately after termination of the ignition the equilibrium pressure in the combustion chamber was reached.

A few experiments were also carried out to investigate the minimum step height to initial diameter ratio to obtain sustained combustion. It was noticed that sustained combustion could be achieved in all cases when using a step height to initial diameter ratio of about 0,19 (7,5 mm / 40 mm). All reported experiments were carried out with this step height to initial diameter ratio.

To investigate the behavior of the regression rate during the combustion process, for some experiments the local instantaneous regression rate was measured continuously at 4 locations along the fuel grain by means of the ultrasonic pulse echo technique. The

results of one experiment with PE at a mass flow rate of 750 g/s are shown in Fig. 7, from which the following can be observed. First of all, the regression rate distribution along the fuel grain changes in time significantly, especially in the region close to the inlet. At the aft end section of the fuel grain the regression rate hardly changes. Secondly, the location of maximum regression rate shifts downstream during the combustion process. Clearly the observed regression rate profile is dependent on time, especially in the first 10 - 15 s of the combustion process. After this time the shape of the regression rate distribution changes only slowly.

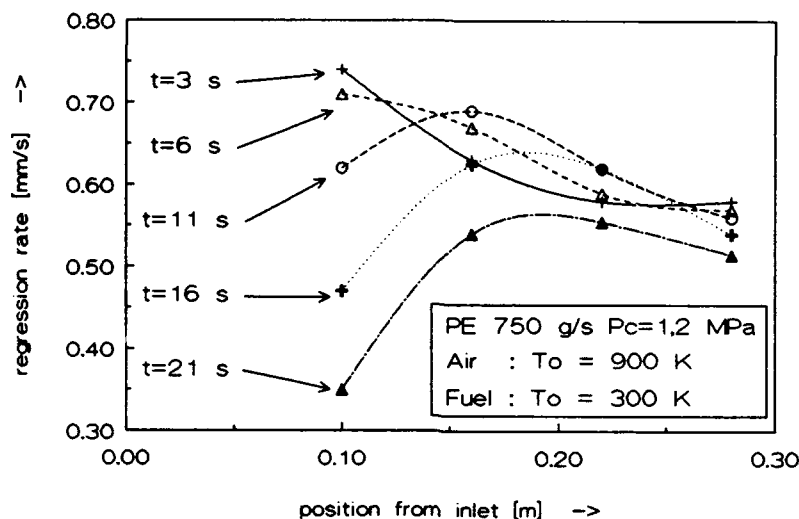


Fig. 7. Experimental regression rate distribution for PE at several axial locations at 5 subsequent instants, obtained by means of the ultrasonic pulse-echo technique.

#### Overall mean regression rate

In Fig. 8 the experimental overall mean regression rate is given as a function of the air mass flow rate, both for PE and for HTPB. From this Figure it can be noticed that the mean regression rate increases at increasing mass flow rate. The observed regression rates are somewhat lower than those reported by Schulte [21,22]. For PE also the overall mean regression rate is calculated both for a constant effective heat of gasification (4,5 MJ/kg) as well as a mass flow rate dependent effective heat of gasification, see Table 1. The agreement between calculated and experimental regression rates is good, especially if variation of the effective heat of gasification with the mass flow rate is applied.

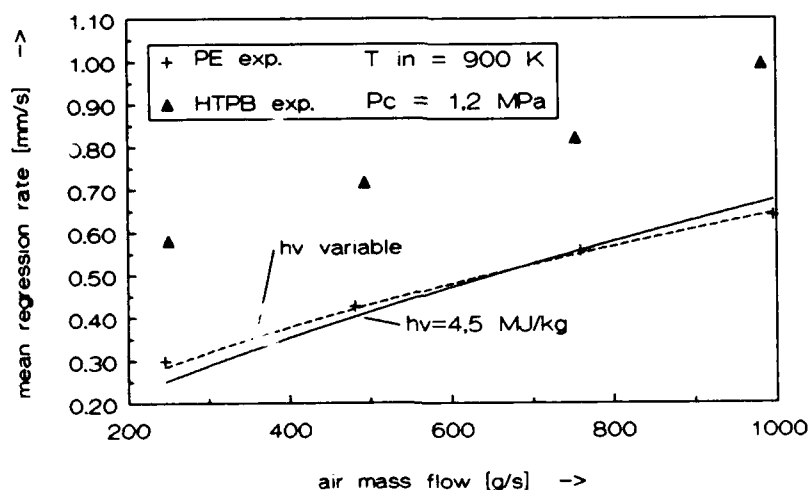


Fig. 8. Calculated and experimental mean regression rates as a function of air mass flow rate, for PE and HTPB.

The experiments with HTPB show regression rates which are one and a half to two times as high as the observed regression rates for PE. A similar behavior was also reported by Schulte [23]. This can be understood by comparing the value of the effective heat of gasification for PE being about 4,5 MJ/kg with the value of the effective heat of gasification for HTPB which is estimated to be 3,2 MJ/kg.

## Local regression rate

For a test condition of an air mass flow rate of 750 g/s calculated regression rate profiles are given in Fig. 9. In these calculations only the fuel grain inner diameter has been varied. The overall mean regression rate is approximately the same for all calculations and is equal to the overall mean regression rate of the experiment. In this Figure also the experimental regression rate profile is shown. This profile was derived from inner bore profile measurements after the test and gives the mean local regression rate. In the beginning of the test the step height to diameter ratio is relatively small (0,19), but this ratio increases rapidly to about 0,32, due the high regression rate. It is a well known fact that the location of the reattachment point, which is considered to be equal to the point of maximum regression rate, depends on the step height to diameter ratio [2]. Hence the regression rate distribution changes during the experiment, see also Fig. 7, and the distribution given in Fig. 9 is the time averaged distribution.

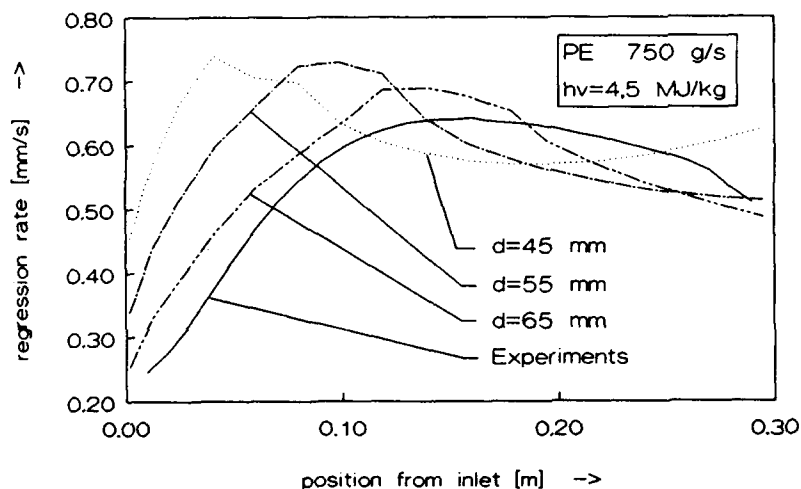


Fig. 9. Local mean regression rate as a function of the axial location. Effect of variation of the inner bore diameter in the calculations.  $h_v = 4,5 \text{ MJ/kg}$ .

In the calculations the regression rate distribution also changes with variation of the step height to diameter ratio (Fig. 9). However, here the diameter and the effective heat of gasification are constant along the fuel grain. Therefore it is not allowed to make a direct comparison between the calculated regression rate profiles and the experimentally determined profile. But it must be concluded that the choice of the diameter in the calculations affects the regression rate distribution, while the choice of the effective heat of gasification affects the value of the regression rate itself, see also Fig. 10. The choice of a diameter that can be considered as a weighted mean of the experiment will yield a fairly good prediction of the local mean regression rate.

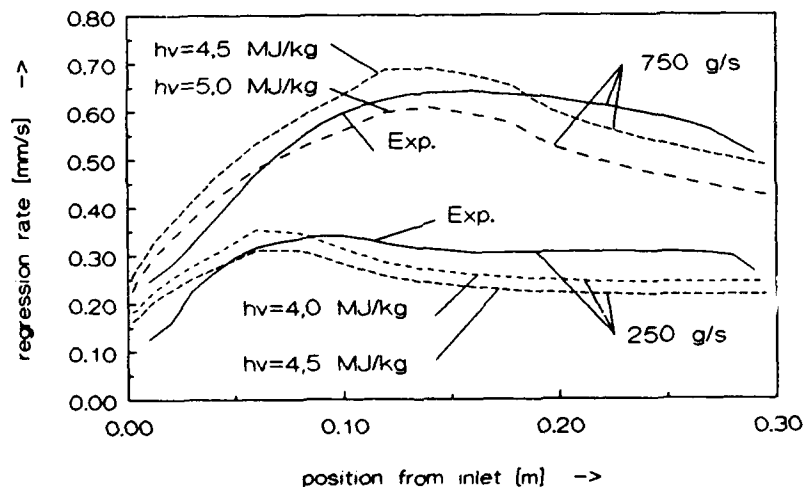


Fig. 10. Comparison of calculated and experimental local mean regression rates for two mass flow rates. Inner bore diameter is 50 mm at 250 g/s and 65 mm at 750 g/s.

## Flame temperature

In Fig. 11 the adiabatic flame temperature at chemical equilibrium is given as a function of the equivalence ratio, both for PE and HTPB. This flame temperature was

determined using a chemical equilibrium code [9]. The temperatures in the aft mixing chamber measured by the pyrometer are also plotted in this Figure. As can be observed, a fairly good agreement between experimental and theoretical temperatures is obtained. Due to the fact that the local equivalence ratio may differ from the overall equivalence ratio, hot spots may occur and will be detected by the pyrometer. However, the maximum temperatures observed by the pyrometer never exceeded the maximum theoretical flame temperature.

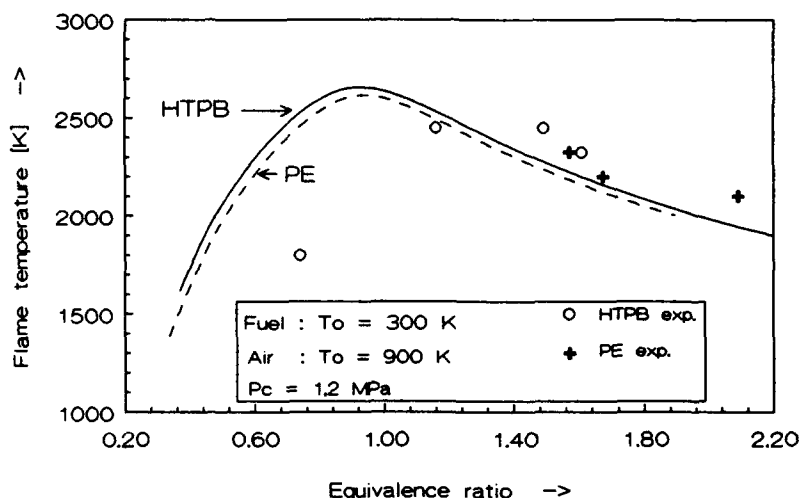


Fig. 11. Adiabatic flame temperature at equilibrium and maximum experimental temperature versus equivalence ratio at specified initial conditions for PE and HTPB.

#### Efficiency and performance

In Fig. 12 the combustion efficiency ( $c_{exp}^*/c_{th}^*$ ) is given as a function of the equivalence ratio. No corrections were made for heat losses. From this Figure it can be seen that the combustion efficiency increases with increasing equivalence ratio, hence with increasing air mass flow rate. Since the residence time of the combustion gases in the engine decreases with increasing mass flow rate, the increase in combustion efficiency may be explained by the increasing ratio between generated heat and heat losses to the wall.

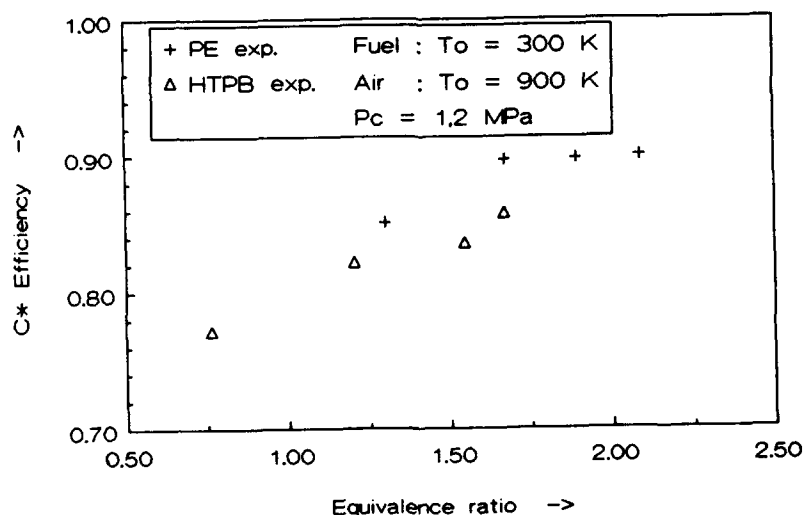


Fig. 12. Efficiency based on the ratio of experimental and theoretical characteristic velocities as a function of the equivalence ratio. Fuels are PE and HTPB.

In contrast to one of the assumptions made earlier in this study for the sustained flight of a missile, a combustion efficiency of 0.9 at stoichiometric conditions was not proved. However, since the observed combustion efficiencies around stoichiometry were rather close to this value, an efficiency even greater than 0.9 may be feasible by increasing the turbulence intensity and by decreasing heat losses. This may be true in particular for PE. The regression rates of PE however are relatively low and require complicated grain designs to provide stoichiometric combustion at grain lengths not exceeding 0.3 - 0.4 m for this missile system. HTPB is a more suitable fuel for this application because of the higher regression rate (Fig. 8.).



### Conclusions

- The value of the effective heat of gasification is very important for the prediction of the mean regression rate in an SFRJ, while the choice of the inner bore diameter affects the distribution of the regression rate along the fuel grain.
- The COPPEF computer code is suitable to predict the mean regression rate and the regression rate distribution of polyethylene in a solid fuel ramjet at operational conditions.
- Using PE or HTPB as a fuel it may be well feasible to propel the specified missile with a solid fuel ramjet engine in the sustained phase of a Mach 4 flight at an altitude of 13 km.
- The ultrasonic pulse-echo technique is very useful to understand the history of the combustion process and the regression rate distribution.

### Acknowledgements

This work has been supported by the Technology Foundation (STW) and the National Fund for Supercomputers (NFS) in the Netherlands.

### References

1. Vos, J.B., 'The Calculation of Turbulent Reacting Flows with a Combustion Model Based on Finite Chemical Kinetics', Ph.D. Thesis, Delft University of Technology, April 1987
2. Elands, P.J.M., Korting, P.A.O.G., Dijkstra, F., Wijchers, T., 'Combustion of Polyethylene in a Solid Fuel Ramjet. A Comparison of Computational and Experimental Results', paper AIAA-88-3043, AIAA/ASME/SAE/ASEE 24th Joint Propulsion Conference, Boston, July 1988, to be published in the Journal of Propulsion and Power.
3. Korting, P.A.O.G., van der Geld, C.W.M., Wijchers, T., Schöyer, H.F.R., 'Combustion of PMMA in a Solid Fuel Ramjet', to be published in the Journal of Propulsion and Power.
4. van der Geld, C.W.M., Korting, P.A.O.G., Wijchers, T., 'Combustion of PMMA, PE and PS in a Ramjet', to be published in Combustion and Flame.
5. Gany, A., 'Solid Fuel Ramjet, Self-Propelled Gun Launched Projectiles', First International Symposium on Special Topics in Chemical Propulsion: Base Bleed, Athens, Nov. 1988.
6. Oswatitsch, K., 'The Efficiency of Shock Diffusers', NACA TM-1140, 1947.
7. U.S. Standard Atmosphere 1962, Superintendent of Documents, U.S. Government Printing Office, Washington D.C., Dec. 1962.
8. Cornelisse, J.W., Schöyer, H.F.R., and Wakker, K.F., 'Rocket Propulsion and Spaceflight Dynamics', Pitman, London, 1978.
9. Gordon, S., and McBride, B.J., 'Computer Program for Calculation of Complex Chemical Equilibrium Compositions, Rocket Performance, Incident and Reflected Shocks and Chapman-Jouguet Detonations', NASA SP-273, NASA Washington, 1971.
10. Chieng, C.C., and Launder, B.E., 'On the Calculation of Turbulent Heat Transport Downstream of an Abrupt Pipe Expansion', Momentum and Heat Transfer Processes in Recirculating Flows, ASME 1980, HTD - Vol.13.
11. Elands, P.J.M., 'The Prediction of the Flow and Combustion in a Solid Fuel Combustion Chamber by Means of Two Combustion Models Based on the Diffusion Flame Concept', AIAA-87-1702, 1987.
12. Reynolds, W.C., 'The Element Potential Method for Chemical Equilibrium Analysis: Implementation in the Interactive Program STANJAN', Version 3, Department of Mechanical Engineering, Stanford University, Jan. 1986.
13. Patankar, S.V., 'Numerical Heat Transfer and Fluid Flow', Hemisphere Publishing Corporation, Washington, 1980.
14. Elands, P.J.M., 'The Modeling of Heat and Mass Transfer Near Solid Boundaries and Comparison with Experimental Results', Faculty of Aerospace Engineering Delft University of Technology, Prins Maurits Laboratory TNO, Report LR-567, PML 1988-C159, Delft/Rijswijk, Nov. 1988.
15. Wilde, J.P. de, 'The Heat of Gasification of Polyethylene and Polymethylmethacrylate', Faculty of Aerospace Engineering Delft University of Technology, Prins Maurits Laboratory TNO, Memorandum LR-M-593, PML 1988-C42, Delft/Rijswijk, Sept. 1988.

16. Wilde, J.P. de, and Elands, P.J.M., 'Fuel Pyrolysis Models for Combustion Calculations', paper to be presented at the 26<sup>th</sup> AIAA/ASME/SAE/ASEE Joint Propulsion Conference, Orlando, July 16-18, 1990.
17. Korting, P.A.O.G., and Schöyer, H.F.R., 'Experimental Connected Pipe Facility for Solid Fuel Ramjet Combustion Studies', Proc. Int. Jahrestagung, ICT 1984, Karlsruhe 1984.
18. Korting, P.A.O.G., and Schöyer, H.F.R., 'A Sonic Control and Measuring Choke for the Precise Control and Measuring of Gas (Oxygen) Mass Flow Rates', Faculty of Aerospace Engineering Delft University of Technology, Prins Maurits Laboratory TNO, Report LR-V-02, PML 1984-C59, Delft/Rijswijk, 1984.
19. Dijkstra, F., Korting, P.A.O.G., and van den Berg, R.P., 'Ultrasonic Regression Rate Measurements in Solid Fuel Ramjets', paper to be presented at the 26<sup>th</sup> AIAA/ASME/SAE/ASEE Joint Propulsion Conference, Orlando, July 16-18, 1990.
20. Wilson, K.J., Schadow, K.C., Gutmark, E., Korting, P.A.O.G., and Dijkstra, F., 'Effect of Inlet Geometry on the Flow and Combustion Processes in a Solid Fuel Ramjet', paper presented at the 31<sup>st</sup> Israel Annual Conference on Aviation and Astronautics, Tel Aviv, February 1990.
21. Schulte, G., 'Fuel Regression and Flame Stabilization Studies of Solid-Fuel Ramjets', Journal of Propulsion and Power, Vol. 2, No. 4, July-August 1986, pp. 301-304.
22. Schulte, G., Pein, R., and Högl, A., 'Temperature and Concentration Measurements in a Solid Fuel Ramjet Combustion Chamber', Journal of Propulsion and Power, Vol. 3, No. 2, March-April 1987, pp. 114-120.
23. Schulte, G., and Pein, R., 'Regression Rate Study for a Solid Fuel Ramjet', ICAS-86-3.9.7.



# HIGHLY INTEGRATED DUCTED ROCKET PROPULSION MODULES FOR FUTURE HYPERSONIC TACTICAL MISSILES

by  
Hermann-L. Weinreich  
Messerschmitt-Bölkow-Blohm GmbH  
and Bayern-Chemie GmbH  
8012 Ottobrunn (München)  
F.R.G.

92-16991



## SUMMARY

Integrated airbreathing propulsion systems for future hypersonic tactical missiles have been studied under funding of the German MOD.

A 30 km range-Mach 5-antiradiation mission was selected for more detailed investigations.

Main aspects for the missile/propulsion design are

- o simple design with no or minimum geometrical variability,
- o no ejecta during boost/sustain transition,
- o high average velocity (transition Mach number well above 3)

To minimize the mass fraction of the required booster propellant

- an optimum, common (non ejectable) boost/sustain nozzle must be adopted;
- the booster pressure should be optimized to use the strength potential of the ramcombustor structure;
- the intake must be closed during boost to reduce drag and to avoid dangerous buzz.

A special two position intake concept permits

- + intake closure during boost,
- + starting of the internal shock system,
- + cruise flight with minimum external drag and high pressure recovery at transition Mach numbers.

Based on promising test results of the DLR/Cologne obtained with a comparable intake model a new family of intakes with different internal compression ratio and lip-bluntness has been designed.

A boron loaded ducted rocket with subsonic self throttling gasgenerator flow has been selected for cruise flight propulsion due to its simple design, excellent combustion stability and the high level of existing experience.

Even at combustor temperatures above the condensation temperature of boron-oxide, the volumetric impulse of boron loaded propellants remains attractive. The ducted rocket gasgenerator can be integrated within the missile forebody which also contains seeker, warhead, electric compartment and missile controls. The missile flight control system is based on jet reaction using minirockets during boost and high pressure intake tap air during cruise.

C/C material has been adopted for the structural design.

The superiority of the ducted rocket powered medium range antiradiation missile has been demonstrated by comparison with a rocket powered missile having the same diameter and payload.

For short range (6 to 12 km) low level missions the solid fuel ramjet with integral boost will be an attractive propulsion concept.

## LIST OF SYMBOLS

A area, cross section  
 $b_{lat}$  lateral acceleration  
 $c_{\infty, c}$  flight velocity, average velocity  
 $c^*$  characteristic velocity  
 $C_{Do}$  zero lift drag coefficient  
 $C_F$  nozzle thrust coefficient  
 $D$  diameter  
 $g$  acceleration of gravity  
 $i_{sp}$  specific impulse  
 $L$  length  
 $m$  mass  
 $M$  Mach number  
 $p$  pressure  
 $S_{ref}$  reference area for aerodynamic coefficients  
 $V$  volume  
 $\Delta x_{EK}$  length of internal contraction zone (Fig. 11)  
 $\Delta x_{ZK}$  centerbody translation for closure of intake entrance

$\alpha$  angle of incidence  
 $\epsilon$  nozzle expansion area ratio  
 $\vartheta_c$  centerbody cone angle (Fig. 11)  
 $\vartheta_{HLi}$  internal cowl angle of intake (Fig. 11)  
 $\varphi_N$  nozzle exit momentum coefficient

## Subscripts

$\infty$  condition at free stream (Fig. 11)  
 $1$  condition at intake exit (Fig. 11)  
 $4$  condition at nozzle throat  
 $5$  condition at nozzle exit  
 $c$  chamber condition  
 $cp$  cruise propellant  
 $E$  condition at intake entrance (Fig. 11)  
 $K$  condition at intake throat (Fig. 11)  
 $L$  nominal intake capture area (Fig. 11)  
 $sol$  shock on lip condition  
 $t$  total condition

## 1. INTRODUCTION

Ducted rockets (also known as solid propellant ramrockets) for military applications are under investigation at MBB and Bayern-Chemie since more than twenty years /1,2,3,5/. The experimental work started with simple fixed flow ducted rockets using medium energy propellants. Since the early 1970's the work concentrated on achieving efficient primary- (gas generator-) and secondary- (ram-) combustion with highly boron loaded propellants. Stable combustion even under severe lateral manoeuvres could be demonstrated during two successful flight tests with the EFA experimental missile in 1981 /5,6/ (Fig. 1).

Meanwhile the effort was focused on variable flow ducted rockets with different amounts of boron content /4,5,6/. Within the predevelopment program for a large antiship missile, a variable flow ducted rocket engine (with integrated booster) was developed to flightweight-prototype status. The performance of the propulsion system was demonstrated successfully in direct connect tests simulating different flight path profiles /7/.

While the engine design and testing was done by MBB, the development of gasgenerator and integral booster propellants was performed by Bayern-Chemie.

All the theoretical and experimental work mentioned above was done for ducted rockets operating in the Mach 2-2.5 regime at sea level and below Mach 4 at high altitudes.

The influence of higher (moderate hypersonic) flight Mach numbers on design and performance of ramjets and ducted rockets were investigated since 1983 under funding of the German MOD.

This paper presents some of the theoretical and experimental results obtained by the ongoing study /8,9,10/.

## 2. DOMINATING ASPECTS FOR MISSILE LAYOUT AND PROPULSION INTEGRATION

The application oriented investigation of potential future hypersonic airbreathing missile propulsion systems was based on anticipated tactical requirements. As illustrated by Fig. 2, a primary requirement for all tactical missiles in Europe will be the capability to fly sea level missions. Therefore the research work concentrated on missile and propulsion designs suitable to low level flight. A typical antiradiation mission (Fig. 3) was selected for a detailed investigation.

### Selection of basic missile configuration:

With increasing flight Mach number

- + the required intake capture area increases with respect to the missile reference area,
- + the interference between intake and fuselage becomes more dominant.

Therefore at hypersonic speeds a separate investigation of rampropulsion and missile fuselage design becomes useless.

- With regard to
- engine integration
  - complexity (cost)
  - structure mass
  - volume
  - aerodynamic characteristics

three families of missile configurations were analysed (Fig. 4):

Waveriders and blended body configurations offer superior lift to drag ratios. At sea level flight conditions, however, the required lift coefficients ( $\sim 50 g$ ) can be attained at low incidence even with conventional bodies with circular cross section. Consequently, the high lift to drag ratios of unconventional configurations are of importance only at high altitude flight.

The governing aerodynamic parameter to determine the cruise propellant mass fraction is the following term of zero lift drag coefficient, missile reference area and missile body volume:

$$\frac{m_{cp}}{m_{transition}} \sim C_{D0} \frac{S_{ref}}{(V_{body})^{2/3}}$$

For a given (required) missile body volume and the corresponding reference area this parameter defines the drag- and thrust-level for cruise flight.

It was demonstrated /8/, that conventional missile configurations exhibit minimum zero lift drag levels especially when they are combined with suitable front intakes.

Their manoeuvrability characteristics are acceptable (and can be improved by adding body-strakes).

Due to the superior properties summarized in Fig. 4, the conventional missile configuration with circular body cross section is best suited for hypersonic sea level missions and was selected for the ducted rocket integration and performance evaluation studies.

## 3. GENERAL ASPECTS FOR DESIGN OF THE BOOST- AND CRUISE PROPULSION SYSTEM

The general requirements for the propulsion system are listed in Fig. 5:

Due to severe kinetic heating (freestream total temperature exceeding 1500 K at  $M_{\infty} = 5$ ) the engine and missile assembly should be kept as simple as possible. The use of adjustable structural components of the engine and missile as

- variable intake geometry
- gas generator throttle valve
- fin controls

should be avoided as far as possible especially during cruise flight.

A high boost end Mach number will help to attain favourable average velocities and to guarantee efficient operation of the ramcombustor even without fuel flow control during cruise phase.

Starting from zero velocity (launch Mach number zero) a booster propellant mass corresponding to 40 % - 45 % of the missile launch mass will be required to attain transition Mach numbers between 3.5 and 4. To minimize the engine mass, the performance of the integral boost motor should be kept as high as possible and not compromised by improper grain and boost nozzle design. On the other side ejectable booster nozzles should be avoided to reduce complexity and risks (endangering) of potential launcher aircraft.

#### Optimization of boost motor mass (Fig. 6):

The required mass of the integral boost motor depends on required velocity increment, non boost propulsion masses and

- o  $isp = c^* C_F$
- o mass ratio propellant/booster-ramcombustor structure
- o boost phase drag losses
- o transition losses

The characteristic velocity  $c^*$  depends on the propellant composition that can be adopted with regard to signature and safety requirements. An excellent nozzle thrust coefficient  $C_F$  requires a nearly optimum nozzle expansion ratio  $\epsilon$  and a proper nozzle contour with high exit momentum coefficient  $g_N$ . The booster burning pressure should be kept as high as possible within the constraints of the ramcombustor structure to obtain a maximum nozzle thrust coefficient and minimum structure masses. The structure mass increases with the required chamber volume, therefore a high volumetric loading with a case bonded grain and a small grain bore area are also required.

Minimum losses of missile velocity during boost-cruise transition can be expected, if a simple transition procedure without nozzle- and port cover ejection can be realized. Minimum boost drag losses will be achieved, when a high thrust level ( $p_c A_4$ ) can be combined with low external drag.

While the combustor entrance must be kept closed (with port covers) during boost in every case, an acceptable external wave drag level requires a closed (or covered) intake entrance area too. As outlined below, the intake closure prior to cruise flight is necessary to avoid buzz during boost and to improve handling properties before launch.

#### Booster design rules:

The structure of the booster chamber (i.e. ramcombustor) should be designed according to maximum strain during cruise flight which depends on

- chamber pressure (determined by transition pressure recovery, flight mission envelope and engine characteristics) and
- manoeuvre loads.

These being the major factors specifying the structural strength, the booster burning pressure should be chosen as high as possible with regard to specific boost impulse, minimum chamber volume and maximum thrust level (acc. to boost phase drag).

The nozzle exit area  $A_5$  will be selected with regard to engine thrust and missile base drag (a possible body flare for missile stabilisation must be taken into account).

The nozzle area ratio

$$\epsilon = A_5/A_4$$

should be kept slightly below the corresponding rocket mode optimum, to make sure that the nozzle thrust coefficient at moderate post transition pressure ratios is not too much mismatched. The resulting nozzle throat area

$$A_4 = A_5/\epsilon$$

should be appropriate with regard to the airbreathing rampropulsion mode, e.g.

- + thrust demand (cruise flight drag level)
- + intake capture area (external drag, payload volume)
- + fuel to air ratio (specific impulse)

and should yield sufficient high boost thrust levels to achieve attractive average velocities combined with moderate boost drag losses.

With regard to the large influence of nozzle exit momentum losses on ramjet thrust at hypersonic speeds, the nozzle divergence angle should be defined well below typical values of solid rocket motors.

## 4. INTAKE INVESTIGATIONS

The most complex component of the airbreathing missile propulsion system is the air intake.

#### General intake system aspects (Fig. 7)

For flight Mach numbers below or around 5 a supersonic combustion engine is not competitive (with regard to performance, booster integration, etc.) to a subsonic combustion ramjet. Therefore, only intakes suitable for subsonic combustion are of interest.

Internal boundary layer bleed could create a large amount of bleed drag and may lead to excessive thermal heating within the bleed area. Consequently, bleed should be avoided.

Closure of the intake entrance area is required

- + to improve handling properties
- + to reduce drag prior to transition
- + and to avoid dangerous buzz during boost.

#### Superiority of the circular front intake (Fig. 8)

The classical disadvantage of the circular front intake is the more difficult payload integration within the intake centerbody. The associated volumetric loss becomes acceptable at hypersonic speeds, where the subsonic duct area of the intake is much smaller than the capture area.

Looking at other evaluation criteria a distinct superiority of the front intake is obvious compared to the side intake arrangement.

### Evaluation of circular front intakes (Fig. 9, 10, 11)

The mixed compression intake has more problems with the starting process than the external compression intake. In basic tests /12, 13/, discussed later on, a practical solution could be demonstrated. In spite of their very high internal friction losses, the performance of the tested mixed compression intakes is by far sufficient to provide a maximum ram-combustor pressure in the order of 100 bar. On the other hand, the mixed compression front intake exhibits a much lower external wave drag, than the external compression intake types shown in Fig. 9. The external compression intake with the low drag cowl has the particular disadvantage that the installation of the required intake entrance closure appears unfeasible.

Therefore, the intake investigations were concentrated on circular mixed compression intakes.

Fig. 10 summarizes the typical features of the intakes under investigation since 1985:

The centerbody contour fits well with the internal contour of the intake cowl, so that the intake entrance is closed, when the centerbody is in the forward position.

If, starting to retract the centerbody, an intermediate geometry of moderate internal contraction is formed, the bow shock can be swallowed and the internal shock system can be established.

With started shock system the internal contraction may be increased far beyond the fixed geometry starting limit. Now the intake operates at high performance with most favourable external drag.

As listed in Fig. 10, the front intake concept with translating centerbody offers two additional advantages:

The lateral discharge of a few percent of high pressure ram air may be sufficient to control the missile.

The opening of the combustor port cover can be combined with the translation of the centerbody, so that a simple propulsion concept without any ejecta may be realized.

Fig. 11 summarizes the principal geometrical data of the mixed compression intakes under investigation.

The amount of internal area contraction depends mainly on the minimum operating Mach number (transition) required by the missile design.

With regard to supersonic friction losses, the length of the internal contraction zone should be kept as short as possible. This is a rather complex task, as

- small internal cowl angles  $\alpha_{HLi}$  and
- the geometrical limitations for the starting of internal supersonic flow (being explained below) tend to create long internal contraction passages.

### First experimental experience with closeable hypersonic front intakes (Fig. 12-16)

Stimulated by the theoretical considerations mentioned before, the DLR Cologne started with the development of an Mach 4.5-intake for initial wind tunnel tests.

The model (Fig. 12) with the designation Hy 1 exhibits a very high degree of internal contraction and has provisions for extensive internal bleed. The intake entrance could be closed by hydraulically activated centerbody translation.

Fig. 12 shows the inviscid flow field and the corresponding Mach number distribution.

Using the centerbody translation, the intake could be started without problems using different bleed configurations.

With regard to

- the massflow losses,
- the associated external drag
- and the internal heating problems

induced by bleed, the intake was modified for operation without boundary layer bleed. This intake with reduced internal contraction was designated as Hy 1A.

The measured pressure recovery at  $Ma = 4.5$  and  $5^\circ$  degrees incidence (cf. Fig. 13)

+ corresponds to a kinetic energy efficiency of 91 %

+ and would result in 107 bar chamber pressure, which is well above the off-design pressure limit of an airbreathing missile accelerating to Mach 5.

The minimum operating Mach number of the Hy 1A-intake is in the 4.2 regime. To proceed with systematic parametric studies and to expand the operational limits to lower Mach numbers (transition Mach numbers  $\approx 3.6$ ) a new family of intake models was designed.

Fig. 14 lists the main design aspects. The modular windtunnel model allows 36 independent geometrical variations.

During the first tests performed at a freestream Mach number of 4.5, we experienced that closeable mixed compression intakes will not start, if

- the initial increase - during centerbody retraction - of internal area contraction is too fast
- or additional intermediate throats are formed during centerbody translation.

These problems can be overcome by adjusting the internal contours of centerbody and intake cowl.

It should be mentioned, that the critical pressure recovery should not be too low just after starting of the internal supersonic compression, when the centerbody is only moderately retracted. Insufficient conditions for the intake start and simultaneous initiation of the ram-combustion may occur, if the critical pressure recovery during the starting process is too poor. The thrust nozzle throat cannot swallow the combustion gases formed from low air- but high propellant-massflow if the combustor pressure is too low. Therefore the intake starting throat area should be significantly smaller than the final design throat area  $A_k$ .

This aspect must be added to the constraints for design of closeable mixed compression intakes, which are summarized in Fig. 15.

The fundamental experimental and theoretical experience gained studying closeable mixed compression intakes is listed in Fig. 16.

Performance, operating and installation characteristics of this type of intake look very promising for low level hypersonic missile applications.

While the currently used centerbody translation gear performs very well with the windtunnel heavy weight models, design studies are under way to explore the feasibility of light weight translation mechanisms.

## 5. PROPULSION SYSTEM SELECTION AND MISSILE PERFORMANCE

For medium range hypersonic low level missions the ducted rocket has been selected (Fig. 17) as the most suitable cruise propulsion system due to

- favourable volumetric heating values of appropriate (boron loaded) propellants,
- excellent functional safety (combustion stability),
- minimum volumetric loss due to grain insulation (with regard to external kinetic heating) using grain arrangements illustrated by Fig. 18.

For short range missions the solid fuel ramjet looks more promising (Fig. 17). A corresponding missile design is presented at the end of this paper.

Main characteristics of the selected ducted rocket propulsion system for the medium range antiradiation mission are summarized in Fig. 18:

Even for ramcombustion temperatures well above the condensation temperature of  $B_2O_3$ , boron is still an attractive propellant ingredient due to its superior density.

A self-throttling gasgenerator with subsonic outflow was selected to avoid a complex thermal protection system or an active cooling system required to protect the actuators of a throttle-valve. The grain configuration depicted in Fig. 18 requires no special insulation against external kinetic heating.

(Case bonded propellants can hardly be used due to external recovery temperatures in the order of 1500 K).

While the missile accelerates after the boost-cruise transition, the propellant burn rate increases slightly due to the simultaneously rising ramcombustor and gasgenerator pressures at increasing flight Mach number. Nevertheless the intake supercritical margin keeps growing with increasing Mach numbers and therefore only a moderate specific impulse can be realized during cruise flight. On the other hand the cruise flight fuel consumption remains very low due to the exceptional low drag of the missile design (with minimum wave- and base drag). The corresponding engine operation at low equivalence ratios offers two additional advantages:

- + the thermal loads are moderate as compared to rocket engine operation,
- + the engine exhibits favourable signature characteristics.

The integration of the payload into the intake centerbody of the antiradiation missile is illustrated by Fig. 19:

An antiradiation seeker with a mass of about 4 kg is housed within the translating cone of the centerbody.

The sliding centerbody tube is supported by the central guide tube, which is fixed to the intake cowl by four or six struts.

The fixed central guide tube contains

- the guidance and control compartment of about 8 kg (including fuze, battery and cooling device),
- a warhead ( $\approx 9$  kg)
- and the ducted rocket gasgenerator.

With regard to kinetic external heating, the conventional arrangement of missile tail controls with actuators housed adjacent to the thrust nozzle cannot be realized.

Canard controls, as depicted in Fig. 20 permit much better provisions for the actuator thermal protection. Taking advantage of the high ram air pressure (well above 50 bars at sea level flight) a simple jet reaction missile control may be realized by lateral discharge of intake tap air. The lateral thrust of the ram air discharge nozzles will be greatly enhanced by interference of the jet with the external hypersonic flow. Thrust enhancement factors in the order of two may be expected.

For lateral thrust control during the boost phase of the missile a minirocket arrangement must be included in the design.

Fig. 21 illustrates the overall arrangement and summarizes key parameters of the hypersonic antiradiation missile under investigation:

- + 53 kg of aluminum loaded composite propellant are required to boost the missile to a Mach 3.6 transition speed at sea level (launch Mach number eq. zero).
- + 23 kg of boron loaded ducted rocket propellant are needed for the 30 km of powered cruise flight at sea level. While the terminal Mach number approaches 5.1, an average velocity of nearly 1500 m/s can be attained (Fig. 22). For target distances of more than 10 km the average velocity of the missile is well above 1200 m/s.
- + Lateral manoeuvres up to 50 g are possible at angles of incidence between 4 and 5 degrees using small strakes along the missile fuselage.
- + With C/C structures of about 30 kg, and a payload corresponding to Fig. 19 (21 kg) the missile launch mass will arrive at 127 kg. The overall fineness ratio of the missile will be about 14.

### Comparison of airbreathing and rocket propulsion:

Fig. 23 shows a comparison of 220 mm  $\varnothing$  antiradiation missiles having the same payload but different cruise propulsion systems:

The integration of the payload within the missile forebody is much easier with the rocket powered missile. The beneficial volumetric loading results in a shorter length of the payload compartment. The wave drag of a (relative slender) 4:1 von Kármán ogive is still below the wave drag of the assumed intake cowl (of only 45 % frontal area) having an intake lip bluntness required for C/C structures. Nevertheless the rocket powered missile exhibits a roughly 30 % higher drag level (at  $M \approx 5$ ) due to increased base and friction drag. Assuming an appropriate boost/cruise grain arrangement providing a 3:1 thrust ratio, 187 kg of aluminium loaded composite propellant are required for the 30 km sea level mission.

The missile is accelerated to Mach 5 within 11.5 km and then cruises with constant speed. Due to the limitation in boost thrust (using a common boost/cruise nozzle) the average velocity is decreased especially for short range missions and reaches only 1200 m/s at maximum range.

With the missile diameter fixed to the value of the ducted rocket system the launch mass of the rocket powered missile will be doubled compared to the airbreather (due to increased drag and much lower specific impulse). The corresponding fineness ratio of 21 is unfavourable with regard to structural loads. The greater missile masses will reduce the manoeuvrability.

Signature and thermal problems are increased, using a rocket propulsion system with a combustion temperature about 1000 K higher than with the ducted rocket.

The insulation of the cruise propellant grain against external kinetic heating would be a major additional design problem for a hypersonic medium range rocket motor.

#### Advantages of rampropulsion for short range missions

While the benefits of air breathing propulsion are evident for medium and long range missions, ram propulsion can be attractive even for short range applications. At Mach 4 + sea level flight conditions, the mass of an integrated ram propulsion system will be favourable (in comparison to a rocket motor) when the flight range exceeds 5 km /5/.

Boost/coast and continuous powered airbreathing missiles have been compared for an hypersonic ground to air mission of 8 km.

For flight durations up to 6 sec. the expensive C/C structure may be substituted by insulated metal or carbon fiber reinforced plastic (CFRP) structures.

Facing roughly 4 sec of extensive kinetic external heating a case bonded cruise propellant grain can be adopted. Under these conditions a solid fuel ramjet as depicted in Fig. 24 may be most attractive. In comparison to a boost/coast rocket powered missile the ramjet offers the following advantages:

- + Superior average velocities at both minimum and maximum target distances due to extreme boost to cruise thrust ratios and continuous cruise propulsion
- + More favourable missile control characteristics due to continuous cruise thrust and reduced Mach number excursions.
- + No excessive kinetic heating associated with extremely high boostend-Mach numbers.
- + Excellent growth potential.

The missile design shown in Fig. 24 has a launch mass of 86 kg, a caliber of 197 mm and an overall length of 2500 mm. A warhead of 10 kg can be delivered over an 8 km target distance within less than 6 sec.

#### 6. CONCLUSIONS

Future hypersonic low level missions can be favourably realized using airbreathing propulsion with

- o conventional missile design with circular body cross section,
- o closeable mixed compression intakes with high pressure recovery at transition but low external drag,
- o solid propellant ducted rocket propulsion with boron loaded propellant and subsonic, self-throttling gasgenerator for medium range missions or solid fuel ramjets for short range missions.

The common boost/cruise thrust nozzle

- + facilitates the transition process
- + avoids dangerous ejecta
- + and gives high boost/cruise thrust ratios which result in superior average velocities even for short range missions.

#### ACKNOWLEDGMENT

Most of the work reported within this paper was initiated and funded by the German MOD, RüFo 4.

#### REFERENCES

- /1/ Crispin, B.  
Betrachtungen zum Gesamtsystem eines Staustrahl- und eines Kombinationstriebwerkes, MBB-Bericht UR-226-74, 1974
- /2/ Weinreich, H.-L.  
Overview of propulsion systems and related fluid-dynamic aspects, AGARD-VKI LS No. 98, Supplement, 1979
- /3/ Besser, H.-L.  
Investigation of Boron Solid Propellant Combustion in Ducted Rockets, AGARD-CP-307, Ramjets and Ramrockets für Military Applications London, Oct. 1981
- /4/ Besser, H.-L.; Strecker, R.; Weinreich, H.-L.  
Advanced Variable Flow Ducted Rocket Propellant Development, Final Report - MBB TN-RT31-7/83, Nov. 1983
- /5/ Crispin, B.  
Ramjet and Ramrocket Propulsion Systems for Missiles, Introduction and Overview, AGARD-LS-136, Monterey, London, Neuberg 1984
- /6/ Besser, H.-L.  
Solid Propellant Ramrockets, AGARD-LS-136, Ramjet and Ramrocket Propulsion Systems for Missiles Monterey, London, Neuberg 1984
- /7/ Thomaier, D.  
Speed Control of a Missile with Throttleable Ducted Rocket Propulsion, AGARD-CP-431, Paper No. 7, Dec. 1987
- /8/ Weinreich, H.-L.  
Antriebskriterien für Hochgeschwindigkeitsflugkörper, Abschlußbericht, BMVg RüFo 4, MBB-Bericht UA-838/84, 30.9.1984
- /9/ Weinreich, H.-L.  
Antriebskriterien für Hochgeschwindigkeitsflugkörper (Hyperschall), Teil 2, Abschlußbericht, BMVg RüFo 4, MBB-Bericht Nr. UA-1018/86, 31.10.1986



- /10/ Weinreich, H.-L.  
Antriebskriterien für Hochgeschwindigkeitsflugkörper (Hyperschall). Teil 3, Zwischenbericht vom 25.3.88 bis 31.1.89, TN-KY25-4/89, 31.1.89
- /11/ Krohn, E.-O.; Triesch, K.  
Hochgeschwindigkeits-Einlauf mit hoher Innenverdichtung, Zwischenbericht 1.7.-31.12.87, DFVLR-IB-39113-87-C-17, Dez. 1987
- /12/ Krohn, E.-O.; Triesch, K.  
Hochgeschwindigkeits-Einlauf mit hoher Innenverdichtung, Abschlußbericht 1.7.-31.8.88, DFVLR-IB-39113-88-C-16, 22.8.1988
- /13/ Krohn, E.-O.  
Persönliche Mitteilung über ergänzende Messungen an dem Hochgeschwindigkeits-Einlauf Hy 1 und Hy 1A, DFVLR-Mitteilungen vom Juni 1988 und 6.1.1989

Fig. 1

#### FIRST DEMONSTRATION OF BORON LOADED DUCTED ROCKET PROPULSION IN FREE FLIGHT

- Two flight tests with MBB EFA missile in 1981
- Tandem boost fixed flow ducted rocket (40% boron)
- Mach 2 to 2.5; max. lateral maneuvers: over 30 g

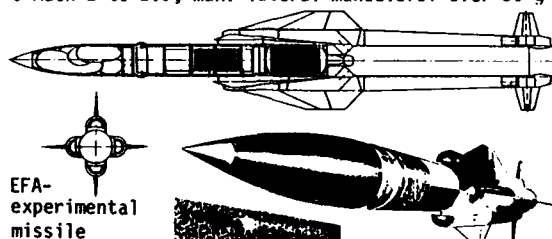


Fig. 2

#### FUTURE TACTICAL MISSILE APPLICATIONS

Flight mission	Flight altitude:		
	Sea level	Medium alt.	High alt.
Anti-Tank	X		
-Radiation	X		
-Ship	X		
-Helicopt.	X		
-Aircraft	X	(X)	(X)
-Missile	X	X	(X)

Fig. 3

#### DATA FOR SELECTED ANTI-RADIATION MISSION

- Launch Mach number  $0 \leq M_{\infty}/\text{Launch} \leq 1$
- Cruise Mach number  $M_{\infty} \approx 5$  (at sea level)
- Range 30 km
- Lateral acceleration  $\approx 50$  g
- Mass of payload  $\approx 21$  kg (seeker  $\approx 4$  kg, warhead  $\approx 9$  kg)

Fig. 4

#### SELECTION OF PRINCIPAL MISSILE CONFIGURATION

Missile configuration	Canard	Delta	Canard-delta
Front intake integration	++	0	--
Side intake integration	0	0	+
Ramcomb./booster integr.	++	0	-
Complexity, costs	++	0	--
Structure mass	++	0	--
Volumetric loading	++	0	--
Zero lift drag	++	+	0
Manoeuvrability	0	+	++
Suitability for M 5 SL	+	0	-

LEGEND: ++ very good, + good, 0 fair, - marginal, -- unacceptable

Fig. 5

## REQUIREMENTS FOR M 5 PROPULSION SYSTEM DESIGN

- Simple assembly (severe thermal heating)
- Fixed geometry sustain motor (complexity)
- Sufficient high  $M_{\text{transition}}$  (favourable  $\bar{c}$ , efficient operation of fixed geometry rampropulsion)
  - ↳ Boostpropellant massfraction  $40 \pm 45\%$
- No ejecta (missile launch from aircraft)

Fig. 6

## OPTIMIZATION OF BOOST MOTOR MASS

- + High  $C_F$ 
  - high  $p_c$ ,
  - opt.  $E$ , opt.  $\varphi_N$
- + Min. structure mass
  - $p_c$  compatible with design of ramcombustor structure
  - opt. volumetric loading
- + Opt. volumetric loading
  - case bonded grain
  - minimum  $A_4 \rightarrow$  high  $p_c$
- + Min. transition loss
  - short transition period
  - no ejecta
- + Min. boost drag losses
  - max. thrust level  $\rightarrow$  high  $p_c \cdot A_4$
  - closed (or covered) intake entrance area during boost (drag, buzz, handling)

Fig. 7

## GENERAL REQUIREMENTS FOR M 5 MISSILE INTAKE

- o Intake suitable for subsonic combustion engine (SCRJ not competitive at  $M \leq 5$ )
- o No internal boundary layer bleed (excessive thermal heating, bleed drag)
- o Requirement for closure of intake entrance area prior to transition (handling, ingestion of debris, boost drag, buzz)

Fig. 8

## COMPARISON OF M 5 MISSILE INTAKE ARRANGEMENTS



Intake arrangement		
External drag (boost & cruise)	++	--
Weight	++	--
Aptitude for closure of intake entrance area	+	-
Payload integration	-	++
Maneuver characteristics	+	-
Complexity, costs	+	-
Ranking	1	2

Fig. 9

COMPARISON OF CIRCULAR FRONT INTAKES ( $M_{so1} \approx 5$ )

Type of intake	Compression: Cowl angle :	mixed small	extern. large	extern. small
Pre entry drag		++	--	--
Cowl drag		++	--	++
Drag of boost configuration		+	--	--
Press. recovery at transit.		0	+	+
" " " cruise		+	++	++
" " " incidence		0	+	+
Mass flow characteristics		0	+	+
Starting problems		-	++	+
Feasib. for clos. of entrance		+	++	--
Ranking		1	2	3

Fig. 10

## FEATURES OF CLOSEABLE FRONTINTAKES

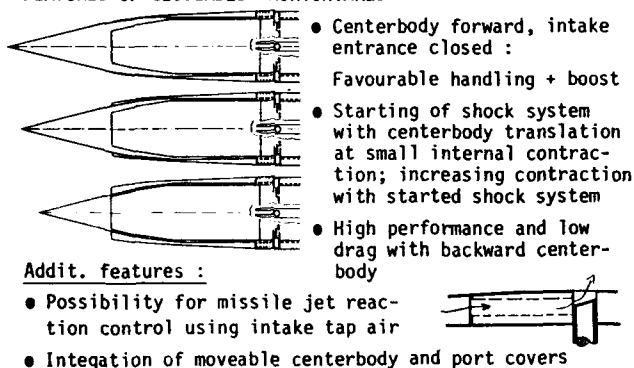
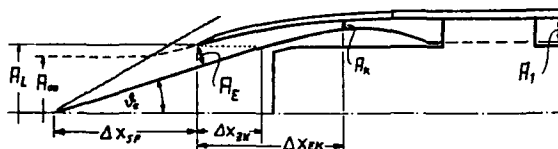


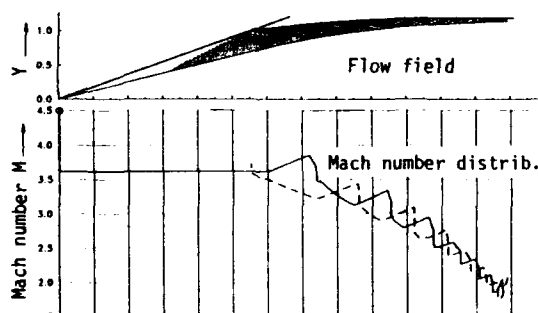
Fig. 11

## GEOMETRICAL CHARACTERISTICS OF CLOSEABLE FRONT INTAKES



Cone angles:	$12^\circ \leq \vartheta_c \leq 15^\circ$
Shock on lip Mach numbers:	$4.5 \leq M_{so1} \leq 5.6$
Internal cowl angles:	$6^\circ \leq \vartheta_{HLi} \leq 9^\circ$
Internal area contraction:	$.25 \leq A_K/A_E \leq 0.4$
Length of intern. contr. zone:	$0.7 \leq \Delta x_{EK}/D_L \leq 2.1$
Centerbody translation:	$0.5 \leq \Delta x_{ZK}/D_L \leq 0.8$

Fig. 12

INVISCID FLOW FIELD AND MACH NUMBER DISTRIBUTION FOR THE DLR HY 1 INTAKE AT  $M_{so1} = 4.5$  [11]

(High internal contraction intake design of the DLR -Cologne with  $A_K/A_E = .26$  and internal bleed)

Fig. 13

## TOTAL PRESSURE RECOVERY OF THE DLR HY 1A INTAKE [12]

HY 1A = modified HY 1 intake without bleed and  
diminished internal area contraction (.30)

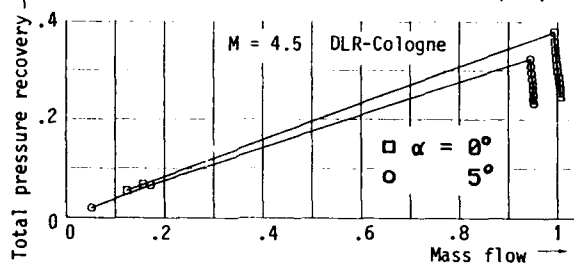


Fig. 14

## DESIGN ASPECTS OF NEW HYPERSONIC INTAKE MODEL FAMILY

- + Lower minimum Mach number → diminished  $A_k/A_E$
- + Reduced supersonic friction → shorter length of intern. contr. zone
- + Systematic parameter studies:
  - ↳ Model-family with
    - o 3 values of internal contraction } 36
    - o 3 " " throat divergence angle } vari-
    - o 4 " " intake lip bluntness } ations

Fig. 15

## CONTOUR DESIGN PRINCIPLES FOR CLOSEABLE INTAKES

- 1 Desired internal contract. with backward centerbody
- 2 Smoothly varying internal cross section
- 3 Short length of internal contraction zone
- 4 Contours giving minimum local expansion and admissible pressure gradients
- 5 Fitting of internal contours for intake closure
- 6 Initially small internal contraction for starting without formation of intermediate throats during centerbody translation
- 7 Starting throat of intake significantly smaller than design throat cross section

Fig. 16

## EXPERIENCE WITH CLOSEABLE MIXED COMPRESSION INTAKES

- Overcontracted intakes can be started if appropriate internal contours are adopted
  - Satisfying performance can be obtained without bleed even at incidence
  - Drag of closeable intakes
    - wave drag of closed configuration
    - pre entry drag below shock on lip Mach number
    - cowl drag
- looks most favourable

Fig. 17

COMPARISON OF RAMJETS AND DUCTED ROCKETS  
FOR MEDIUM RANGE HYPERSONIC SEA LEVEL MISSIONS

Type of ram-jet	$i_{sp}$	$\rho_{cp}$	Off design capability	Reliability	Propellant insulation problems	Completeness, costs
LFRJ	+	0	++	0	-	--
SFRJ	0	+	0	0	-	+
DR	0	+	0	+	+	0

Fig. 18

## CHARACTERISTICS OF SELECTED DUCTED ROCKET

**Propellant:** 40% Boron composite propellant with pressure sensitive burn rate

**Gasgenerator:** Design with selfadjusting subsonic outflow



**Performance:** Low drag → low thrust demand

Operation of combustor with considerable air excess } moderate specific impulse

intake with wide supercritical margin at cruise } at cruise (~6300m/s at M=5)

low fuel consumption  
low signature

Fig. 19

## PAYLOAD INTEGRATION WITHIN CENTERBODY OF ANTI-RADIATION MISSILE INTAKE

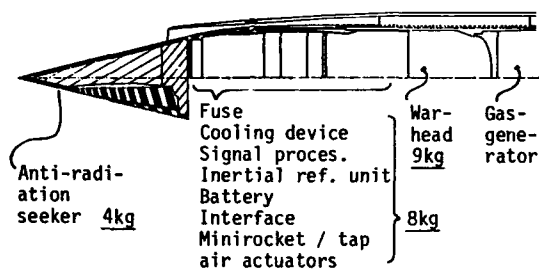


Fig. 20

## PRINCIPAL ARRANGEMENTS FOR ANTI-RADIATION MISSILE CONTROLS

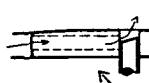
## Conventional canard controls



## Jet reaction controls

## Detail:

High pressure tap air jet reaction control during cruise



Minirocket based jet reaction control during boost

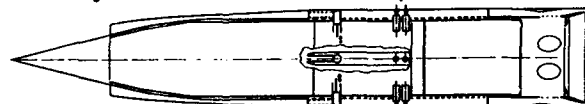
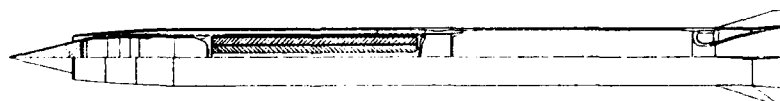


Fig. 21

## 220 MM Ø ANTI-RADIATION MISSILE WITH INTEGRATED DUCTED ROCKET PROPULSION



- C/C structures 30 kg
- Payload 21 "
- Cruise propellant 23 "
- Boost propellant 53 "

LAUNCH MASS 127 kg  
FINENESS RATIO 14 : 1

## Performance:

- + 30 km SL
- +  $c = 1500$  m/s
- +  $b/lat \leq 50$  g
- +  $M_{max} \approx 5.1$

Fig. 22

AVERAGE VELOCITY  $\bar{c}$  AND FLIGHT VELOCITY  $c_{\infty}$  OF  
ANTI-RADIATION MISSILE DEPICTED IN FIG. 21

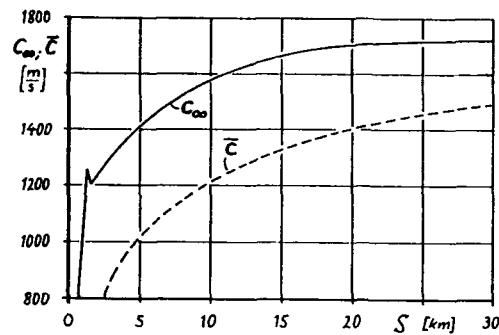
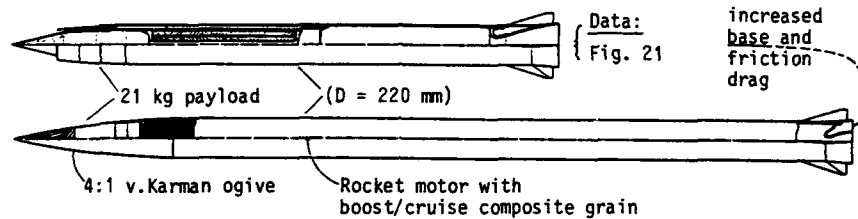


Fig. 23

COMPARISON OF 30 KM SL ANTI-RADIATION MISSILES

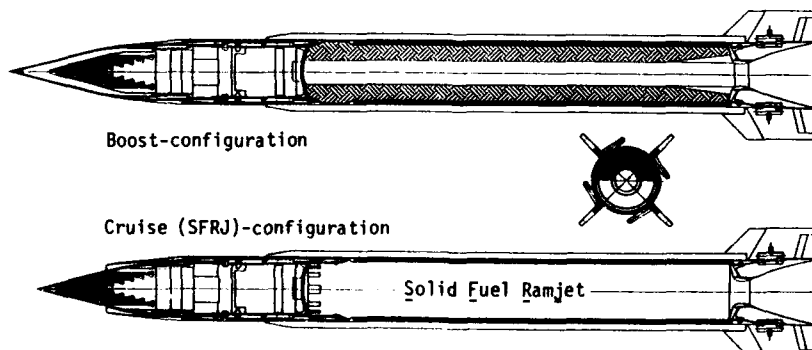


Data of rocket-powered vs. DR-powered missile (Fig. 21):

- Drag at  $M = 5$  : +30% (incr. friction and base drag)
- Propellant : 187 vs 76 kg
- Launch mass : 250 vs 127 kg
- Fineness ratio : 21 vs 14
- Average velocity: 1200 vs 1500 m/s (at 30 km)
- Maneuverability : reduced
- Signature and thermal problems: increased

Fig. 24

HYPERSONIC SHORT RANGE ( $\approx 10$  km) MISSILE WITH INSULATED  
CFRP STRUCTURES AND INTEGRATED SFRJ PROPULSION



## Discussion

WEYER

You described considerable high kinetic efficiencies of the air intakes at high Mach numbers with no bleed. Did you make any detailed flow measurements to study the intake internal flow?

AUTHOR'S REPLY

The kinetic energy efficiency (see Fig 25) which was demonstrated with the Hy 6M-intake model from MBB was obtained using a calibrated plug nozzle measuring technique at the DLR Cologne. This well established measuring technique gives accurate total pressure recovery and mass flow data. For design and function of the ducted rocket these data are quite sufficient. Detailed investigations of the internal flow governed by shock boundary layer interactions would give valuable information for improved intake designs and additional data for CFD-code validation. Due to the available funding however, we could not perform such expensive experimental tests up to now.

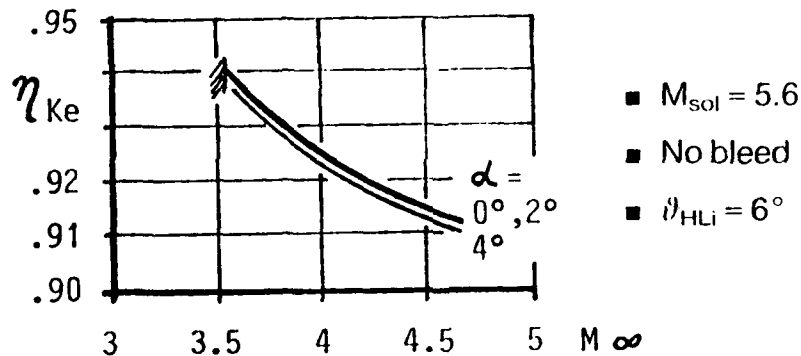


Fig 25 Maximum Critical Kinetic Energy Efficiency Demonstrated with a Hy 6M-Intake Model.

CAZIN

With the choice of the inlet, have you problems with the integration of the seeker?

AUTHOR'S REPLY

Within the overall study discussed in the paper, a preliminary configuration of an antiradiation seeker with conformed antenna was designed. The seeker with no moveable parts and provisions for active cooling is integrated in the conical part of the translating centerbody. For the antiradiation mission, we therefore see no major problem for intake/seeker integration.



# PITOT SURVEYS OF TWO MODERATELY UNDER-EXPANDED JETS

by

T. M. Cain and T. V. Jones  
 Department of Engineering Science  
 University of Oxford  
 Parks Road  
 Oxford  
 England

## SUMMARY

In the free expansion of the exhaust gases of engines flying at altitudes suitable for air-breathing launchers, the turbulent shear layers interact with the jet shock structure, posing a challenge for CFD. A series of experiments in this flow regime is performed to provide data suitable for code validation. Angular and axial Pitot surveys of heated, high pressure, nitrogen jets exhausted from a Mach 3 conical nozzle into a low pressure tank are presented. The results indicate that there is strong turbulent mixing throughout the flowfield downstream of the first Mach disk in addition to a repetitive shock cell structure.

## 1. INTRODUCTION

The Computational Fluid Dynamics (CFD) modelling of low altitude (<70 km) rocket exhaust plume flowfields has direct application to the prediction of infrared signatures and missile aerodynamics [1]. The computer codes developed by Dash *et al.* to meet this need have been extended for application to the problem posed by the operation of scramjet engines [2]. As mentioned by Chuech [3], experimental test data is still required to further verify and 'calibrate' the turbulence prediction methods for these high speed compressible flows.

The underexpanded jets studied in the experiments [3-5] that are currently used for comparison with plume flowfield CFD [3, 6-8] are representative of those produced by supersonic aircraft nozzles. The static pressure at the nozzle exit,  $P_e$ , is only slightly greater than that of the surrounding still air,  $P_b$ , and the ratio of the stagnation pressure,  $P_0$ , to the ambient pressure is less than 20.

Experiments reported in the open literature that are representative of plume formation at an altitude of 30km, where  $P_0/P_b$  is of the order  $10^4$  are mostly limited to flow visualisation studies performed prior to or during the early 1960's [9-12, reviewed in 13]. Attention then was largely focused on the first shock cell in the jet, as is also the case in the more recent base flow studies at FFA [14]. Radiometric work at Calspan [15, 16] has produced spatially resolved infra-red measurements of model reacting rocket plumes that have high-lighted the importance of the viscous/inviscid interactions that occur in the plumes [1]. However, the highest pressure ratio for which detailed measurements of this region have been made appears to be  $P_0/P_b = 4$  with  $P_e/P_b = 60$ . In that experiment by Kalghatgi *et al.* [17], refractive index fluctuations in the exhaust of a liquid bipropellant engine were measured using a crossed beam correlation technique that allowed calculation of rms density fluctuations and convective velocity in the outer mixing layer of the jet but could not detect the shock structure in the plume. The purpose of the present paper is to provide Pitot pressure measurements in the near field of moderately underexpanded jets that correspond more closely to a plume produced by a rocket motor or scramjet engine flying in the stratosphere.

A gun tunnel was adapted for use with small supersonic nozzles. The test gas, is compressed in the tunnel's barrel and is normally expanded in a hypersonic nozzle to generate an intermittent high Mach number stream. In the test described here the gas was only partially expanded in a Mach 3 nozzle to a pressure  $P_e$  and then exhausted into the test section which was at a lower pressure  $P_b$ . Jets with expansion ratios  $P_0/P_b = 18$  and 50 were investigated.

## 2. THE STRUCTURE OF MODERATELY UNDEREXPANDED JETS

When the pressure at the exit plane of a nozzle is much greater than the ambient pressure surrounding the nozzle, the exhaust gas undergoes a rapid expansion in a Prandtl Meyer fan centered at the nozzle lip (Fig. 1). In the inviscid case, the streamline closest to the wall is deflected through an angle sufficient to expand the gas to  $P_b$ . Along all other streamlines, the gas is over-expanded by the fan and its reflections from the axis of symmetry. Part of the recompression to  $P_b$  takes place through compression waves which coalesce into a shock that sits close to the free boundary and is descriptively named the "Barrel Shock". The flow within the barrel shock is not influenced by the external pressure

92-16992



and it assumes the source-like nature that it would in a vacuum. It is well described by the model developed by Albini [18], Boynton [19] and Simons [20] and has been the subject of previous experiments for example Legge *et al* [21] and Anderson *et al* [22].

The flow external to the barrel shock is rotational as the gas has crossed the shock at different locations which results in an entropy gradient across the shock layer. There is also a significant static pressure gradient across it due to the centrifugal acceleration required for it to follow the curvature of the barrel shock. The shock/shear layer is further complicated by the turbulent mixing with the free external stream. Despite these complications, simple models that involve the numerical integration of a single ordinary differential equation that describes the free boundary trajectory, provide adequate profiles of jets up to their maximum diameter [10, 19, 23 reviewed in 24].

In the case of moderately underexpanded jets the barrel shock is too strong to reflect in a regular manner from the axis of symmetry. A Mach stem is formed which in the axisymmetric case is known as a Mach disk. The Mach disk position is controlled by downstream influences which are transmitted upstream through the embedded subsonic region behind the Mach disk. Various models of Mach disk formation have been suggested and they have been reviewed and added to by Peters and Phares [25] and Abbet [26]. The Abbet model used in conjunction with MOC solutions has proved accurate in comparison with some experiments [27] but is restricted in application by the assumption of no mixing along the slipline between the supersonic and subsonic streams downstream of the triple point. Mixing along the slipline, which has been measured [28] and observed [29], reactivates the hot, low momentum subsonic gas, and as stated by Dash *et al*. [30] "must be accounted for in any model of the flow behind the Mach disk".

In the experiments reported here, the turbulent supersonic flow surrounding the Mach disk is found to rapidly mix with the embedded subsonic flow and fluctuations in Pitot pressure are present at all locations downstream of the first shock cell. The magnitude and frequency of the fluctuations is a function of the pitot probe dimensions, but qualitatively they provide a clear indication that the jet is fully turbulent.

### 3. APPARATUS

#### 3.1 Gun tunnel and Nozzles

The gun tunnel is a facility that generates a hypersonic flow for a period of 10 to 100 msec and has been described previously [31]. The Oxford tunnel employs a large high pressure air reservoir to drive a 120g piston down a 10m barrel of 96mm bore. The piston travels supersonically and forms a shock which travels ahead of it at approximately Mach 2.4 in nitrogen. The shock reflects at the end of the barrel and collides with the on-coming piston. This generates a third shock and the process continues until the piston is brought to rest. The nature of the compression is evident in the pressure signal obtained from a Kistler 601 transducer mounted 128mm from the barrel end, Fig. 2.

An estimate of the stagnation temperature is obtained by calculating the entropy increase associated with the consecutive passage of the first four shocks. Each shock is assumed to result in a velocity change of the gas equal to the initial piston velocity (which is derived by iteration from the pressure after the first shock reflection). A polynomial for the specific heat at constant pressure [32] is integrated to calculate the enthalpy and entropy of the nitrogen when solving the conservation equations for each shock. The calculated pressure history is in good agreement with the measured pressure during the passage of the first three shocks but expansion waves emanating from the piston as it decelerates result in weaker subsequent shocks. The actual entropy increase is expected to be bounded by the values calculated for three and four shocks which leads to an estimate of the stagnation temperature of 1203 K to 1233 K when the nitrogen (initially at 16°C) is compressed adiabatically from 1.01 bar to 72 bar. These are the nominal stagnation conditions of the plume gas in these experiments.

Two similar supersonic nozzles "A" and "B" were used in the tests and dimensions are given in Fig. 3. A nozzle was mounted at the end of the barrel and due to the small throat (4.2mm), the flow continued for 1 second. Plume pitot measurements obtained at times other than during a 27 msec period over which the stagnation pressure was steady were subject to disturbances due to wave motion within the barrel, but it is demonstrated that it is possible to remove this influence from the signals by normalisation.

#### 3.2 Test section

The test section is a 0.9 x 0.6 x 0.6 m box that is connected to a 28m<sup>3</sup> dump tank by a 8m long, 0.4m diameter pipe. The nozzle exhausting into the test section creates an ejector action which results in an intense noise field and low frequency (8Hz) oscillations in the test section pressure. The

fluctuations were measured with "Sensortec LX1602A" piezoresistive pressure transducers (50 kHz natural frequency) and found to be uniform within the confines of the test section at frequencies below 500Hz. The ambient conditions do not influence measurements within the first shock cell and by a process of normalisation it is also possible to remove their influence on Pitot measurements downstream of the Mach disk.

### 3.3 Schlieren System

An example of schlieren photographs taken with exposures of 0.1  $\mu$ s (spark source) and 4 msec (shutter) are given in plates 1 to 3. Photographs of both types have been available in the literature for a considerable time, for a variety of under-expanded jets (section 1). Although the photographs are the result of an integration of density gradients across the axisymmetric jet, the system is most sensitive to the area of a shock that has a normal vector which is orthogonal to both the incident light and the Toeppler knife edge. This behavior is evident in plate 1 by the very thin line that the barrel shock produces on the photograph. The location of the shocks in a plane of the jet that cuts through the axis of symmetry can therefore be measured directly for comparison with CFD or analytical predictions. However, it has been found that the location of the barrel shock is rather insensitive to the model of the expansion process and it does not provide a strict test of the prediction methods [19].

### 3.4 Traversing Mechanisms

Two traversing mechanisms were developed to allow axial and angular scans of the jets with a pitot probe during the 27 msec over which the stagnation pressure is constant.

The axial traverse consisted of a round bar held in roller bearings that was free to travel 140mm. (fig. 4) Its position was monitored with a reflective optical switch that detected the passing of thin dark lines inscribed at intervals of 4mm on the bar's surface. A cubic spline was used to interpolate between the marks. A pitot pressure probe was mounted at the upstream end of the bar and a disk was fixed to the rear end. The bar was blown downstream by the action of the jet during the run and the diameter of the disk was chosen to result in a speed of approximately 5 m/s. The motion produced a negligible change in the relative velocity of the probe to the gas which had a speed of 1.6 km/s (the limiting velocity) upstream of the Mach disk. Downstream of this strong shock the velocity would be a factor  $(\gamma+1)/(\gamma-1)$  lower (where  $\gamma$  is the ratio of specific heats) but at that position the stagnation pressure is close to the static pressure, resulting in the probe motion having no measurable influence on the pitot pressure.

An angular traverse was made by mounting a swinging arm on a pivot placed below the jet centerline at the nozzle exit (Fig. 5). The arm was initially set at some angle to the flow and was restrained there by a thin strand of nylon that passed over the nozzle exit. A strong rubber band was attached to the free end of the arm and to a securement point mounted below the centerline of the jet. The strand is given sufficient purchase to counteract the force of the band but it melts when the nozzle starts and releases the arm. The swinging arm and pitot probe that was mounted on it entered into damped simple harmonic motion about the jet centerline, the period of which was adjusted to give an adequate scan during the test time. The probe motion was monitored by a servo potentiometer at the pivot point.

### 3.5 Pitot probes

The pitot probes contained "Kulite XCQ-093" absolute pressure transducers that were fed through hyperdermic tube of lengths that range from 15mm to 35mm and outside diameters of 0.8mm to 2.6mm. The various probe geometries produced no measurable difference in Pitot pressure and it was concluded that the probe shape was not influencing the measurements. A 25mm long, 0.8mm diameter hyperdermic tube was used for the majority of the axial traverses but the length was reduced to 15mm for the angular traverses to attain sufficient rise time to record the peaks in the thin shock layer outside the barrel shock. The frequency response of the Pitot tubes is discussed in section 4.3. Regular calibration of the piezoresistive transducers and associated electronics has demonstrated the system sensitivity has a precision of  $\pm 0.8\%$ .

### 3.6 Data acquisition

Signals from the transducers were multiplexed into a single Hewlett Packard 12 bit analogue to digital convertor and stored in a 64kword memory. The multiplexer switched every 11  $\mu$ s and typically 6 channels are recorded for 0.4 seconds. The data was then transferred to a Hewlett Packard 9836 mini computer where it was processed.

Spectrum analysis of the Pitot and background pressure signals was conducted with a Hewlett Packard 3562A Dynamic Signal Analyzer, sampling a single channel at 256kHz for a period of 80 ms.

## 4. PROCEDURE

### 4.1 Scaling of the jet dimensions

The source nature of the expanding jet, results in density,  $\rho$ , falling with the square of the distance from some point on the centerline near the nozzle exit. Since the velocity of the gas,  $V$ , is essentially the limiting velocity in a steady expansion, the momentum flux ( $\rho V^2$ ) falls with the square of the distance from the source. The barrel shock is formed at a position where the component of the momentum flux normal to it, the Newtonian pressure, is similar to the pressure in the surrounding still air. This results in the plume dimensions scaling with  $L = D^*/(P_O/P_b)$ . The scaling is discussed in more detail by Moran [33] and Draper and Sutton [34].

### 4.2 Scaling of the pitot pressure

**4.2.1 Within the first shock cell.** The pitot pressure,  $P_t$ , within the first shock cell is proportional to the stagnation pressure  $P_O$  and independent of the background pressure  $P_b$ . This follows from the discussion above as the pitot pressure is essentially the modified ( $\gamma$  not equal to 1) Newtonian pressure and the barrel shock marks the limit of influence of the background pressure.

**4.2.2 Downstream of the Mach Disk.** Downstream of the Mach disk the pitot pressure measured on the axis of the jet is observed to rise rapidly and this can only be a consequence of the embedded subsonic region mixing with the surrounding supersonic gas. An inviscid acceleration of the subsonic core would not increase the total pressure of the gas and once it became supersonic the bow shock on the pitot probe would again result in the measured pitot pressure decreasing.

The mixing is sufficiently vigorous that a reasonable estimate of the maximum Pitot pressure downstream of the mach disk can be made by assuming that the jet is one-dimensional with a static pressure equal to the ambient pressure. When entrainment of the background gas is neglected, application of the first law of thermodynamics results in the following expression for the Mach number of the equilibrated jet,  $M$ .

$$M = \left[ \left( \frac{a_O}{U} \right)^2 - \frac{\gamma-1}{2} \right]^{-1/2} \quad (1)$$

where,  $a_O$  is the speed of sound at the stagnation temperature,  $T_O$ , and  $U$  is the velocity of the equilibrated jet.  $U$  can be obtained from the momentum balance for a control volume that extends from the nozzle exit to a station where the pressure is uniform across the jet and equal to  $P_b$ .

$$\frac{U}{U_e} = 1 + \frac{1 - P_b/P_e}{\gamma Me^2} \quad (2)$$

Thus, the Mach number is essentially independent of  $P_b$  at high  $P_e/P_b$  and since the ratio  $P_t/P_b$  is only a function of Mach number (Rayleigh's Pitot formula), the Pitot pressure should be directly proportional to  $P_b$  downstream of the Mach disk.

In section 5 it is demonstrated that normalising the Pitot pressure with the back pressure and plotting it as a function of the non-dimensional plume scale ( $x/L$ ) produces results that are not sensitive to small variations in  $P_b$  or  $P_O$ .

### 4.3 Obtaining Mean Levels from the transient Unsteady Measurements

**4.3.1 Filtering.** The turbulence downstream of the Mach Disk results in unsteady flow even under conditions of constant stagnation and background pressures. The lowest frequency of the turbulent disturbances may be estimated by the ratio of the mean velocity  $U/2$  (Eq. 2) to the jet width and is for the largest jet studied, approximately 6 kHz. This is above the lower estimate for the resonance of the 25mm Pitot tube, which is approximated by the quarter wavelength equation [35]. That is, the resonance,  $f_p$ , is equal to the speed of sound in the tube divided by four times the probe length, which equals 3.4 kHz if the gas in the tube is assumed to have accommodated to the wall temperature. Therefore, filtering the signal with a passband from DC to less than  $f_p/5$  should prevent signal distortion by either the probe or the turbulence.

A third factor to consider is the intense noise field in the test section and its effect on the Pitot pressure in the jet. Spectrum analysis of the signal from a Kulite XCQ-093 25A transducer with a 200 kHz natural frequency, placed in the test section outside of the jet revealed high intensity acoustic noise of a uniform level from 250 Hz to 5 kHz. Beyond this frequency there is a decrease in signal power of 22 dB/decade until 40 kHz.

The scaling procedure of section 4.2 is only applicable for those frequencies for which there was spatially homogeneous variation in the test section. A digital 3 pole Butterworth filter with a cut frequency (-3dB) at 500Hz was found to reduce discrepancies between two pressure transducers placed 0.5m apart in the test section from 20% to less than 2%. The signals were filtered once and then reversed in time and filtered again to remove the frequency dependent time delay inherent in the Butterworth filter. Application of the same filter to a step function constructed with 100 $\mu$ s point spacing resulted in a rise time (10% to 90%) of 900 $\mu$ s. Therefore, a step in Pitot pressure which would occur for instance if the probe was swept downstream of an oblique shock, would typically be smeared over less than 1 D" by the filter.

**4.3.2 A Statistical Approach.** The frequency of the signal was too close to that of the noise for the temporal filter to be completely effective. By taking multiple samples of the mean level over long periods (for example 0.2s) it was possible to discriminate between the signal and the noise on the basis of randomness rather than frequency. This is made possible by the multiple centerline crossings that occur with the angular traverse, or by using slow axial traverse speeds. Measurements taken during periods of varying stagnation and background pressures were quasi-steady as the flow establishment time was short compared to the timescale of the variations in pressure. However, it was necessary to introduce the scaling described in sections 4.2 to correlate the jet over the range of conditions to which it is subjected by the pressure variations. The scaling effectively removes the low frequency disturbance from the measurements, while the averaging removes the noise.

The procedure is implemented by splitting the spatial co-ordinate into typically 300 "bins" and averaging the ordinate ( $P_t/P_b$ ) in each bin. The non-dimensional arc length  $r\theta/L$  was the spatial co-ordinate for the angular traverse.

All the data presented in section 5.3 has been reduced with this method as it was found to be more suitable than the the temporal filter.

#### 4.4 Error Estimation

**4.4.1 Within the First Shock cell.** The error in the ratio  $P_o/P_t$  resulting from uncertainty in the gauge calibrations is less than 2%. Just upstream of the Mach Disk where  $P_t$  is close to the test section pressure a significant component of the error in  $P_t$  is due to the  $\pm 0.3$ mmHg uncertainty in the measurement of the initial tank pressure. Distance from the nozzle exit is measured to within  $\pm 0.5$ mm by the optical detector and angles are measured to within  $\pm 0.15^\circ$  with the servo potentiometer. The jet centerline is established by the symmetry of the radial Pitot profiles. Representative error bars are plotted with the data.

**4.4.2 Downstream of the Mach Disk.** The uncertainty in the Pitot measurements when taken in the turbulent flow behind the Mach disk and during periods of fluctuating stagnation and back pressures, is a stronger function of unsteadiness and the validity of the correlation (scaling procedure) than it is of the accuracy of the pressure and displacement measurements. Confidence limits of 95% are calculated for the mean by using the "Student t-distribution" [36] to analyse the data.

### 5. RESULTS AND DISCUSSION

#### 5.1 Schlieren

The schlieren photograph taken with a spark light source demonstrates the turbulent nature of the jet boundary. In the jet of plate 1 the shear layer between the barrel shock and surrounding air becomes turbulent close to the nozzle exit and the disturbed nature of the shock and its reflection from the triple point would indicate that the turbulence extends across the entire shear layer at the Mach disk position. Streamwise streaks apparent on the schlieren photographs of jets at higher nozzle exit pressure ratios may be due to Gortler vortices [37] forming prior to transition in the concave shear layer and this is currently being investigated. Mach disk position and diameter for a jet from nozzle "A" with  $P_o/P_b=613$  have been measured as 0.91L and .077L respectively. Corresponding figures for a jet with  $P_o/P_b=1885$  are .87L and .054L.

#### 5.2 The First Shock cell

**5.2.1 Plume Model.** In the present study, attention is directed to the plume flowfield downstream of the Mach disk and measurements within the first shock cell are made to define the nozzle exit conditions. A program employing the method of characteristics to calculate the free expansion of the exhaust gas while assuming conical one dimensional isentropic flow to the nozzle exit was written to provide comparison with the experiments. Vibrational equilibrium of the nitrogen within the nozzle was assumed but vibration in the plume and downstream of the bow shock on the Pitot probe was taken as frozen ( $\gamma=7/5$ ).

**5.2.2 The Effect of Stagnation Temperature.** If an isentropic expansion of a gas with  $\gamma = 7/5$  is assumed, the exit Mach number,  $M_e$ , of nozzle "B" is 3.06. The effect of vibrational relaxation when  $T_0 = 1220$  K is to lower  $M_e$  to 2.96 and also to decrease the static pressure at a given Mach number by a factor 0.93 after full recovery of the vibrational energy. Both effects result in a decrease in the predicted Pitot pressure at any particular location in the plume. Agreement between the MOC prediction with relaxation in the nozzle, and the measurements for nozzle "B" obtained at the stagnation condition of  $P_0 = 72$  bar and  $T_0 = 1220$  K is very good (Fig. 6) but data obtained with  $T_0 = 820$  K and  $P_0 = 46$  bar agrees less well with the model and is indistinguishable from the higher temperature experiment. This may indicate that vibration is frozen within the nozzle and that  $M_e$  and total pressure are reduced by some other mechanism. Tests with Nozzle "A" with  $T_0 = 1030$  K and  $P_0 = 53$  bar are also in good agreement with the MOC if vibrational relaxation occurs (fig. 7), in which case the exit Mach number is reduced from 3.07 (for  $\gamma = 7/5$ ) to 3.02, and the static pressure at a given Mach number is reduced by a factor of 0.96.

**5.2.3 The effect of Nozzle Boundary Layer.** Calculations of boundary layer displacement thickness made by integrating the Momentum Integral equation [38] using turbulent, flat plate correlations for skin friction and shape factor [39] indicate that it is 3.1% of the exit radius (with  $P_0 = 53$  bar,  $T_0 = 1030$  K). However, it would require a displacement thickness of 6% to decrease  $M_e$  in the isentropic core sufficiently to reconcile the small difference between the prediction and results. The influence of the boundary layer Mach number profile on the free expansion has not been calculated and may account for the discrepancy.

**5.2.4 The effect of Non-isentropic Core Flow.** An entropy increase due to shocks within the nozzle could also account for low Pitot pressure measurements and the multitude of weak waves emanating from the nozzle that are visible on the schlieren photographs are another possible source of the discrepancy between the MOC solution and the measurements. The sensitivity of the Pitot measurements in the far field to nozzle exit conditions made the measurements of static and Pitot pressure within the strong gradients in the nozzle too inaccurate to adequately define the exit conditions and therefore it may be better to ascertain them from the plume measurements. This approach was taken by Anderson et al [22] to define the orifice discharge coefficient when comparing MOC predictions and experiments on sonic jets. For supersonic nozzles, a comparison of angular pitot profiles in addition to the axial profiles helps to determine the correct combination of entropy increase (drop in total pressure) and Mach number.

**5.2.5 Determining Nozzle Exit Mach Number from Angular Pitot Profiles.** An angular profile at  $x/D^* = 10.8$  for Nozzle "A", is shown to agree well with a MOC solution for  $M_e = 3.0$  in Fig. 8. Solutions for  $M_e = 2.9$  and 3.1 are included on the figure, to indicate the sensitivity of the profile to exit Mach number.

**5.2.6 Nozzle exit Conditions.** The nozzle exit conditions may be able to be calculated from the source conditions and nozzle geometry, to a greater degree of accuracy than given by the one dimensional methods employed in this study. However, for codes that proceed from nozzle exit conditions, the following values for nozzle "A" (which was used for all the following experiments) are suggested: conical with a half angle of 5 degrees,  $M_e = 3.02$  with  $P_0/P_e = 39.4$  (4% above the isentropic value). The absolute values of temperature, and pressure were found to be unimportant over the range studied.

### 5.3 Measurements Downstream of the Mach Disk

**5.3.1 Jets Studied.** Two underexpanded jets were investigated. One with  $P_0/P_b = 1800$  and the other with  $P_0/P_b = 650$ . The nominal stagnation conditions are  $P_0 = 72$  bar and  $T_0 = 1220$  K for both jets, and the background pressure was varied by a factor of 3. The increase in the background pressure results in a corresponding increase in measured Pitot pressures and a  $\sqrt{3}$  decrease in the length scale,  $L$ . However, the scaling procedures described in section 4.2 considerably reduce the difference between the profiles for the two jets (Figs. 9 and 10) which justifies the use of the procedures in the data reduction to decrease the influence of the relatively small variations in the nominal conditions.

**5.3.2 Axial Pitot Profiles.** The rise in Pitot pressure downstream of the Mach disk that is plotted on Figs. 9(a) and 10(a) is due to mixing (section 4.2.2) and is at a rate higher than measured previously for a Mach reflection in an axisymmetric supersonic diffuser [28]. In Back and Cuffel's experiment, the inner edge of the shear layer did not intersect the centerline until approximately 2 Mach disk diameters downstream of the disk. In the present experiments, the Pitot pressure rose within 1 disk diameter, indicating that mixing had reached the centerline. The turbulent nature of the supersonic shock/shear layer surrounding the Mach disk flow is probably the reason for the high mixing rate.

The dynamics of the plume which arise from the shock wave reflections at both the centerline and the free constant pressure boundary (where they are reflected as expansion waves), result in a re-expansion of the plume gas until the low static pressure in the core of the plume again causes the surrounding plume gas to collapse back towards the center. The process is followed for 3 cycles in Fig. 9(b) from which it can be seen that plume gas is beginning to equilibrate with its surroundings in a

non-isentropic manner as expected from the control volume analysis (section 4.2.2).

**5.3.3 Angular Pitot profiles.** Angular profiles at three radial stations are presented for each jet in Figs.9(c) and 10(c). The profiles represent averages of greater than eight scans about the jet axis. The axial co-ordinate of each station is calculated using the average characteristic length  $L$ . Agreement with the axial traverse results for the centerline value of  $P_t/P_0$  is within the 95% confidence intervals.

## 6. CONCLUSION

Results are presented for the pitot pressure distribution in two moderately underexpanded jets issuing from a Mach 3 nozzle. The data has been compared with method of characteristics solutions within the barrel shock as a method of establishing the nozzle exit conditions. Downstream of the Mach disk the data is presented in a form which minimises its sensitivity to boundary conditions and that should make it suitable for testing CFD plume codes.

## 7. REFERENCES

- [1] DASH, S.M., PEARCE, B.E., PERGAMENT, H.S. and FISHBURNE, E.S., "Prediction of Rocket Plume Flowfields for Infrared Signature Studies", *J. Spacecraft and Rockets*, Vol. 17, No. 3, May 1980
- [2] WOLF, D., "Analysis of 2-D and 3-D Rocket and Scramjet Nozzle/Exhaust Flowfields Using the SPAN Family of PNS Solvers", *AIAA paper* 89-1764, Buffalo NY, Jun, 1989.
- [3] CHUECH, S.G., LAI, M.C. and FAETH, G.M., "Structure of Turbulent Sonic Underexpanded Free Jets" *AIAA J.*, Vol.27, No.5, May 1989, pp549-559
- [4] DONALDSON C.D., and SNEDEKER, R.S., "A study of free jet impingement. Part 1. Mean properties of free and impinging jets", *J. Fluid Mech.* Vol. 45, part 2, 1971, pp.281-319.
- [5] SEINER, J.M., and NORUM, T.D., "Aerodynamic Aspects of Shock containing Jet Plumes", *AIAA paper* 80-0965, Jun 1980.
- [6] SMITH, A.G., "Use of Phoenix for prediction of Rocket Exhaust Flows", *3rd Intl Phoenix Users Conference*, Dubrovnik, Sep. 1989.
- [7] HSU, A.T. and LIOU, M.S., "A Computational Analysis of Underexpanded Jets in the Hypersonic Regime", *NASA TM* 101319, 1988
- [8] DASH, S.M. and THORPE, R.D., "Shock Capturing Model for One and Two Phase Supersonic Exhaust Flow", *AIAA J.*, Vol.19, No.7, Jul 1981, pp842-850
- [9] LOVE, E.S., GRIGSBY, C.E., LEE L.P. and WOODLING, M.J. "Experimental and Theoretical Studies of Axisymmetric Free Jets", *NASA TR* R-6, 1958.
- [10] LATVALA, E.K., and ANDERSON, T.P., "Studies of the Spreading of Rocket Exhaust Jets at High Altitudes", *Planetary and Space Sciences*, Jun 1961, pp77-91.
- [11] LEWIS, H. and CARLSON, D.J., "Normal Shock Location in Underexpanded gas and gas-particle Jets", *AIAA J.*, Vol. 2, No. 4, Apr 1964, p776.
- [12] VICK, A.R., ANDREWS, E.H., DENNARD, J.S., and CRAIDON C.B., "Comparisons of Experimental Free-Jet Boundaries with Theoretical Results Obtained with the Method of Characteristics", *NASA TN* D-2327, Jun 1964.
- [13] ADAMSON T.C., "The Structure of the Rocket Exhaust Plume without Reaction at various Altitudes", *Supersonic Flow, Chemical Processes and Radiative Transfer.*, Pergamen Press NY, 1964 pp177-200.
- [14] WHITE, R.A., AGRELL, J., and NYBERG, S.E., "Supersonic Wind Tunnel Simulation of Propulsive Jets", *J. Spacecraft and Rockets*, Vol.22, No.5, Sep 1985, 1985, pp530-535
- [15] DRZEWIECKI R.F., BOYER D.W., PEARCE B.E., and BARAN A.J., "Simulation of Solid Propellant Rocket Exhaust Plumes using a Gaseous Propellant Combustion Technique", *AIAA paper* 89-1763, Buffalo NY, 1989.

- [16] ALBRECHINSKI, T.M., and WURSTER, W.H., "Rapid Scan Instrumentation for Spectrally and Spatially Resolved Radiance Measurement of Short Duration Rocket plumes", *ICIASF Rec-Int Congr. on Instrum. in Aerosp. Simulation Facil.*, Nav. post grad school, Monterey Calif. Sep. 24-26 1979 Publ by IEEE (Cat no. 79 CH1500-8 AES), NY 1979 p 57-71
- [17] KALGHATGI, G.T., COUSINS, J.M., and BRAY, K.N.C., "Crossed beam Correlation Measurements and Model Predictions in a Rocket Exhaust Plume", *Combustion and Flame* 43:51-67, 1981, pp51-67.
- [18] ALBINI, F.A., "Approximate Computation of Underexpanded Jet Structure", *AIAA J.*, Vol. 3, No.8, Aug. 1965, p1538.
- [19] BOYNTON, F.P., "Highly Underexpanded Jet Structure: Exact and Approximate Calculations", *AIAA J.*, Vol 5, No.9, 1967, pp1703-1704.
- [20] SIMONS, G.A., "Effect of Nozzle Boundary Layers on Rocket Exhaust Plumes", *AIAA J.*, Vol10, No11, 1972, pp1534-1535.
- [21] LEGGE, H., DANKERT C. and DETTLEFF, G., "Experimental Analysis of Plume Flow from Small Thrusters", *Rarefied Gas Dynamics, 14th Intl. Symp., Tokyo, 1984*, U. of Tokyo Press, 1984, pp279-286.
- [22] ANDERSON, J.B., ANDRES, R.P., FENN, J.B. and MAISE, G., "Studies of Low Density Supersonic Jets", *Rarefied Gas Dynamics, 4th Intl. Symp., Toronto, 1964*, Academic Press, 1966, pp106-127.
- [23] HUBBARD, E.W., "Approximate Calculation of Highly Underexpanded Jets", *AIAA J.*, Vol.4 No.15, Oct, 1966, p 1877.
- [24] MORAN J.P., "Mixing Layers for Highly Underexpanded Supersonic Jets in Hypersonic Streams", *J. Fluid Mech.*, Vol. 65, part 1, 1974, pp.153-175
- [25] PETERS C.E., and PHARES W.J., "The Structure of Plumes from Moderately Underexpanded Supersonic Nozzles", *AIAA Paper* 70-229, New York NY, Jan 1987
- [26] ABBETT, M.J., "The Mach Disc in Underexpanded Exhaust Plumes", *AIAA Paper* 70-231, New York NY, Jan 1970. Also: *AIAA J.*, Vol. 9, Mar. 1971, p512-514
- [27] FOX, J.H. "On the Structure of Jet Plumes", *AIAA J.* Vol. 12 No. 1, 1974, p105-107.
- [28] BACK, L.H., and CUFFEL, R.F., "Viscous Slipstream Flow Downstream of a Centerline Mach Reflection", *AIAA J.*, Vol.9, No.10, Oct 1971, pp2107-2109.
- [29] YIP, B., LYONS, K., LONG, M., MUNGLE, M.G., BARLOW, R., and DIBBLE, R., "Visualisation of a Supersonic Underexpanded Jet by Planar Rayleigh Scattering", *Physics of Fluids A*, Vol. 1, No. 9, Sep 1989 p1449.
- [30] DASH, S.M., WOLF D.E., BEDDINI R.A. and PERGAMENT H.S. "Analysis of Two-Phase Flow Processes in Rocket Exhaust plumes", *J. Spacecraft and Rockets*, Vol.22, No.3, May 1985, pp367-380
- [31] COX, R.N., and WINTER, D.F., "The light gas Hypersonic Gun Tunnel at A.R.D.E., Fort Halstead, Kent", *AGARD Report* 139, Jul 1957.
- [32] VAN WYLEN, G.J., and SONNTAG, R.E., "Fundamentals of Classical Thermodynamics", 2nd ed., J. Wiley & Sons, 1976, p683.
- [33] MORAN, J.P., "Similarity in High Altitude Jets", *AIAA J.*, Vol.5, No.7, Jul 1967. pp1343-1345
- [34] DRAPER, J.S., and SUTTON, E.A., "A Nomogram for High Altitude Plume Structures" *J. Spacecraft and Rockets*, Vol.10, No.10, Oct 1973, pp682-684.
- [35] NYLAND, T.W., ENGLUND, D.R., and ANDERSON, R.C., "On the Dynamics of Short Pressure Probes: Some Design factors Affecting Frequency Response", *NASA TN D-6151*, Feb. 1971.
- [36] KREYSZIG, E., "Advanced Engineering Mathematics", 5th Ed., J. Wiley and Sons, N.Y., 1983, p950.
- [37] SCHLICHTING H., "Boundary Layer Theory", 6th Ed., McGraw Hill, 1968. p504.
- [38] KAYS, W.M., and CRAWFORD, M.E., "Convective Heat and Mass Transfer", 2nd Ed., McGraw Hill, 1980, Eqn(5.7)

[39] STOLLERY, J.L., "Supersonic Turbulent Boundary Layers: Some Comparisons Between Experiment and a Simple Theory", *Aero. Quart.*, May 1976, pp87-98.

## 8. ACKNOWLEDGEMENTS

This work has been carried out with the support of the Procurement Executive Ministry of Defence. The authors express their thanks to Mr. Trevor Godfrey for manufacturing the traverses and helping with the experiments.

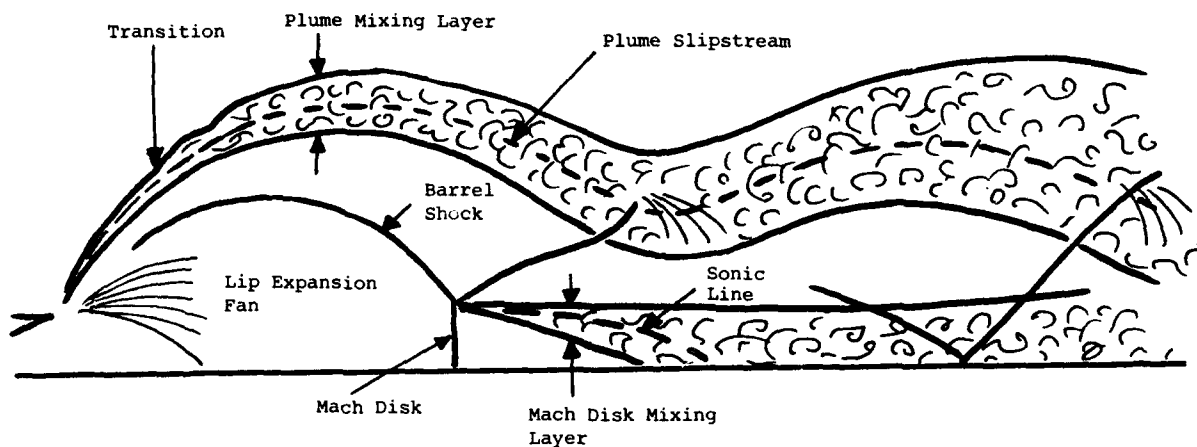


Fig. 1 : Schematic of a moderately underexpanded jet ( after Dash *et al.* [30]).

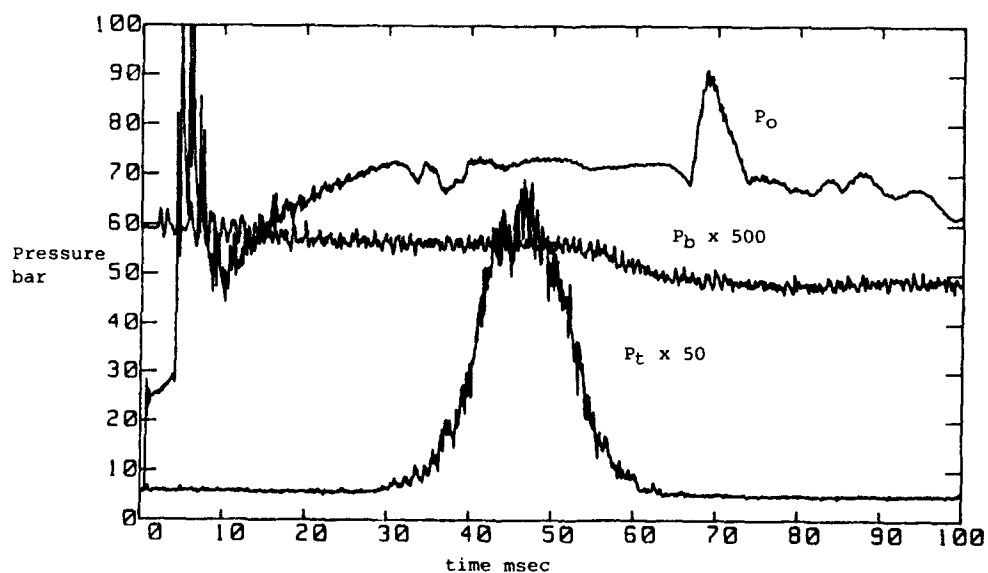


Fig. 2 : Stagnation, background, and Pitot pressure history, during an angular traverse.



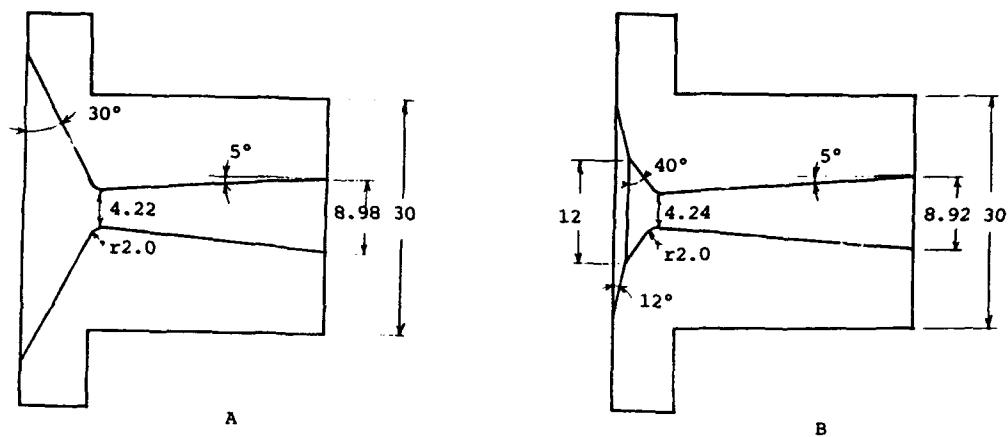


Fig. 3 : Mach 3 nozzles. All dimensions in mm.

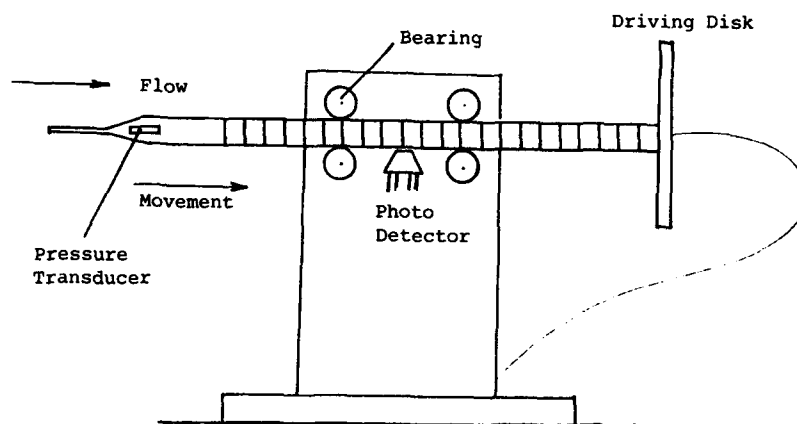


Fig. 4 : Axial traverse mechanism.

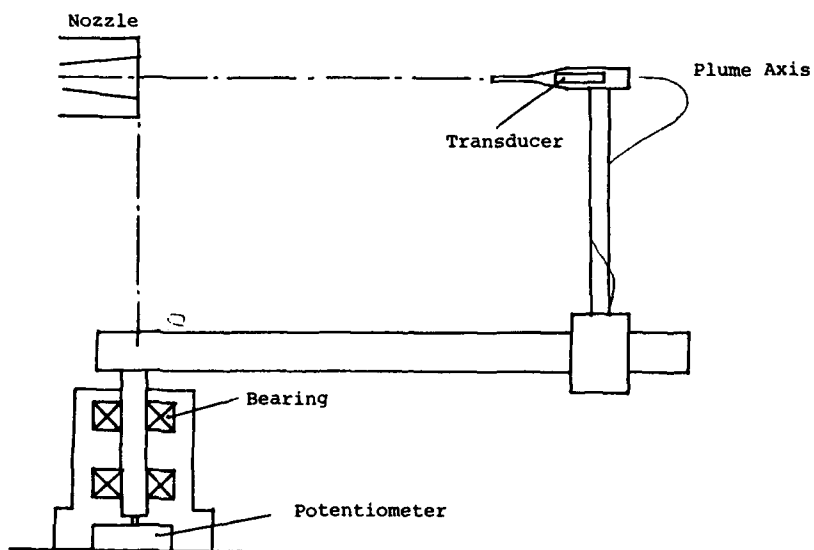
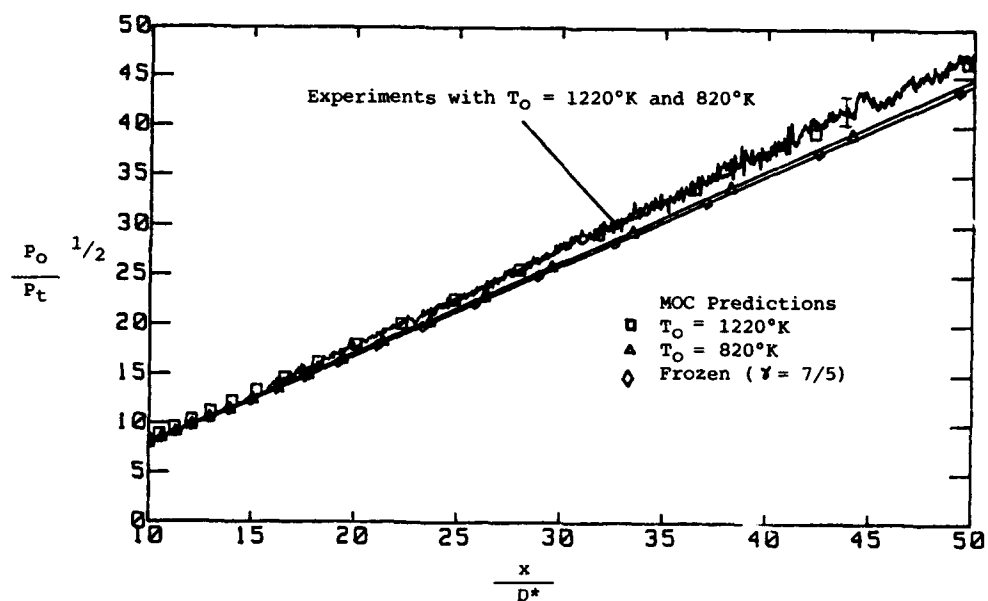
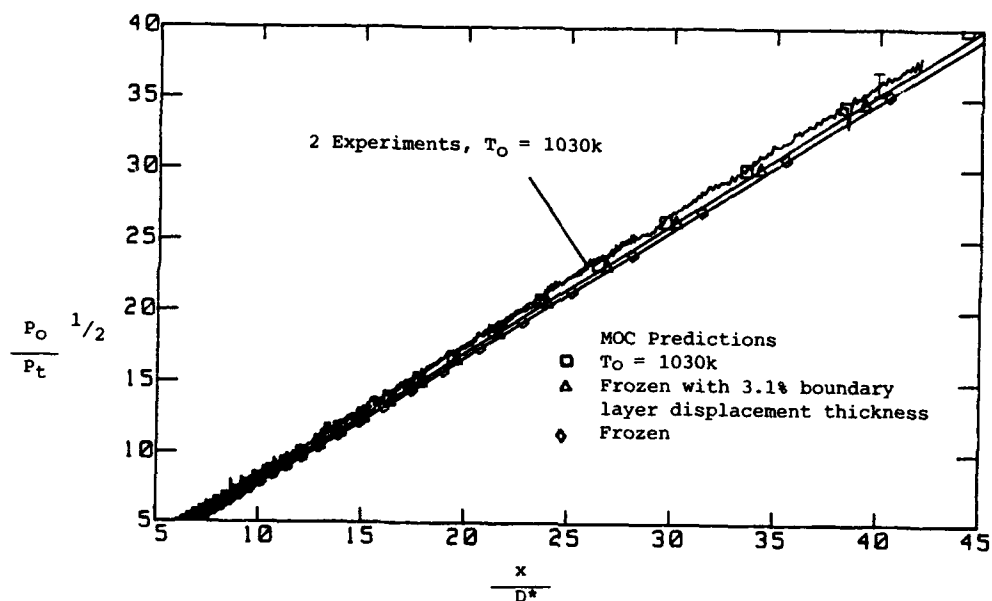


Fig. 5 : Angular traverse mechanism.

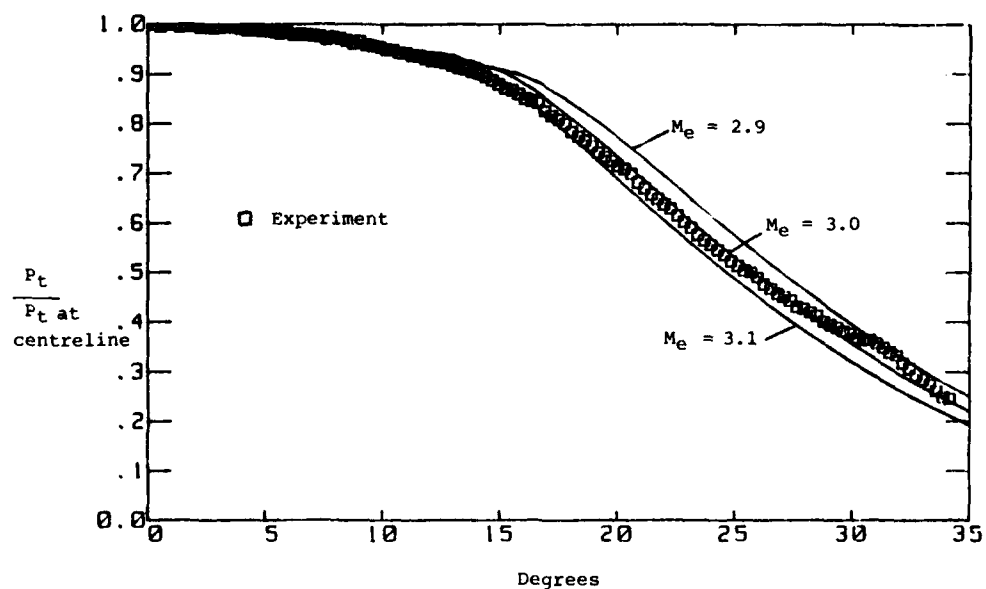
**Fig. 6 :** Measurements and MOC predictions of axial Pitot profiles within the first shock cell. Nozzle B.



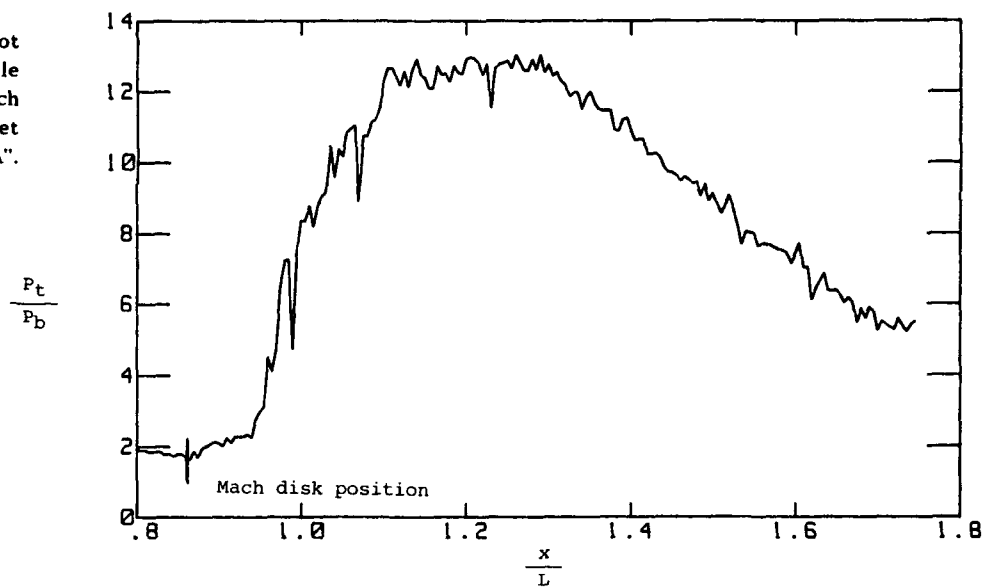
**Fig. 7 :** Measurements and MOC predictions of axial Pitot profiles within the first shock cell. Nozzle A.



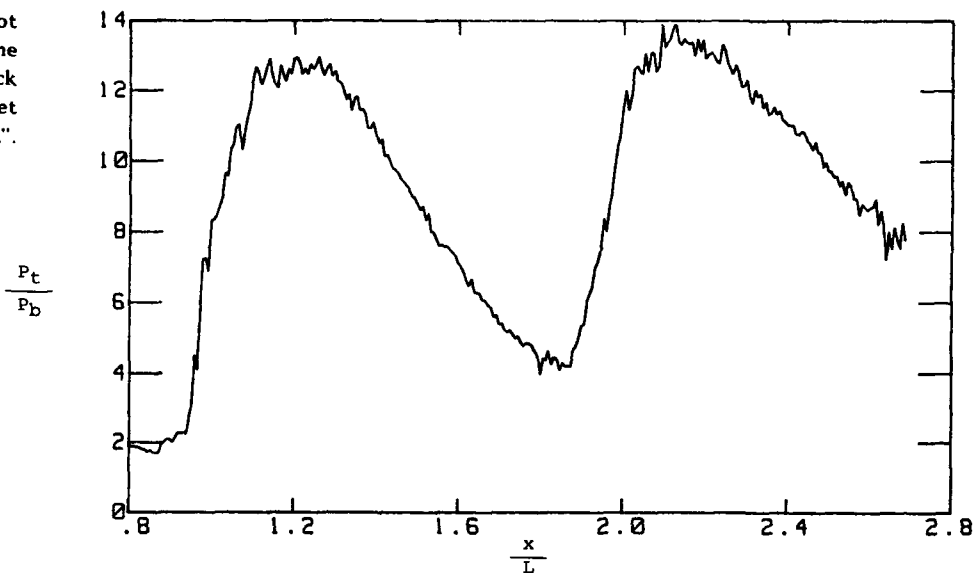
**Fig. 8:** Measurements and MOC predictions of angular Pitot profile at  $r/D^* = 10.8$ , within the first shock cell. Nozzle A.



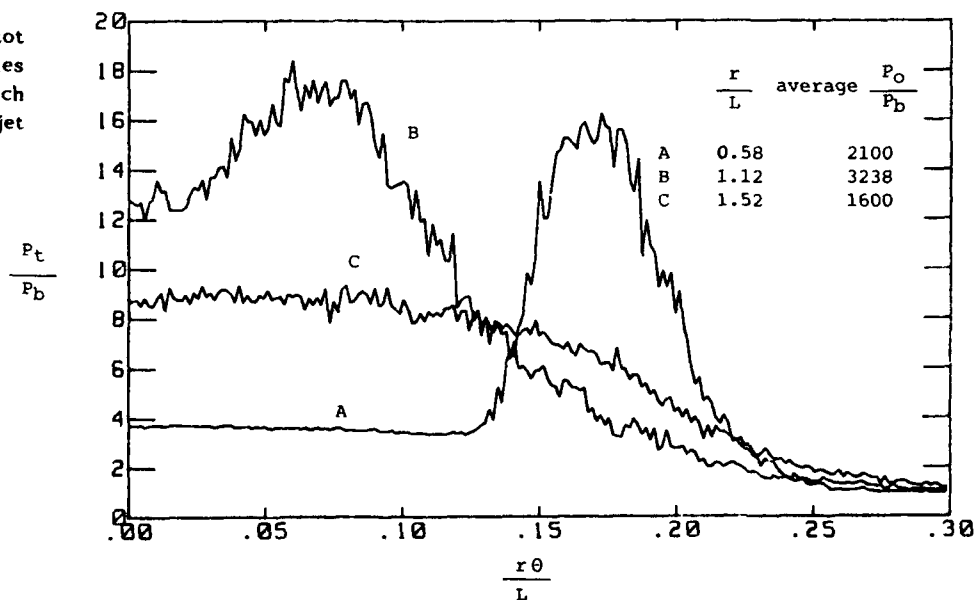
**Fig. 9(a):** Axial Pitot pressure profile downstream of the Mach disk in a nitrogen jet from nozzle "A". Nominal  $P_0/P_b = 1800$ .



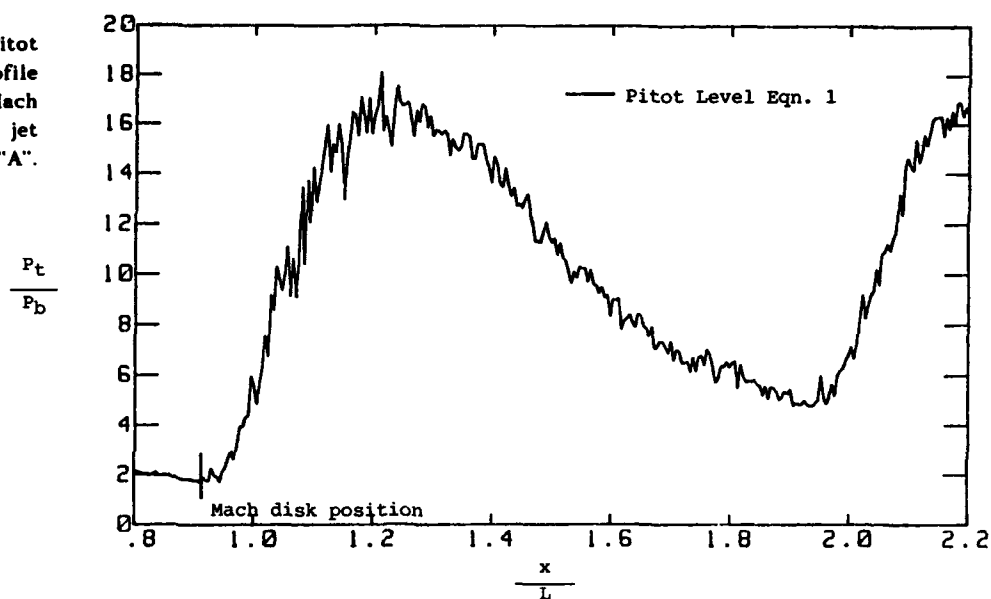
**Fig. 9(b):** Axial Pitot pressure profile in the second and third shock cells in a nitrogen jet from nozzle "A". Nominal  $P_0/P_b = 1800$ .



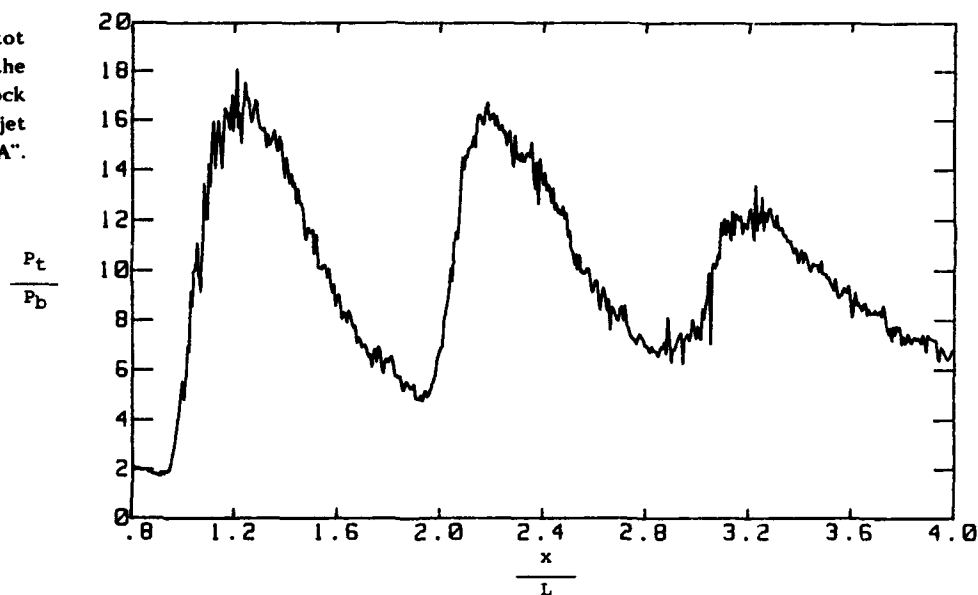
**Fig. 9(c):** Angular Pitot pressure profiles downstream of the Mach disk in a nitrogen jet from nozzle "A".



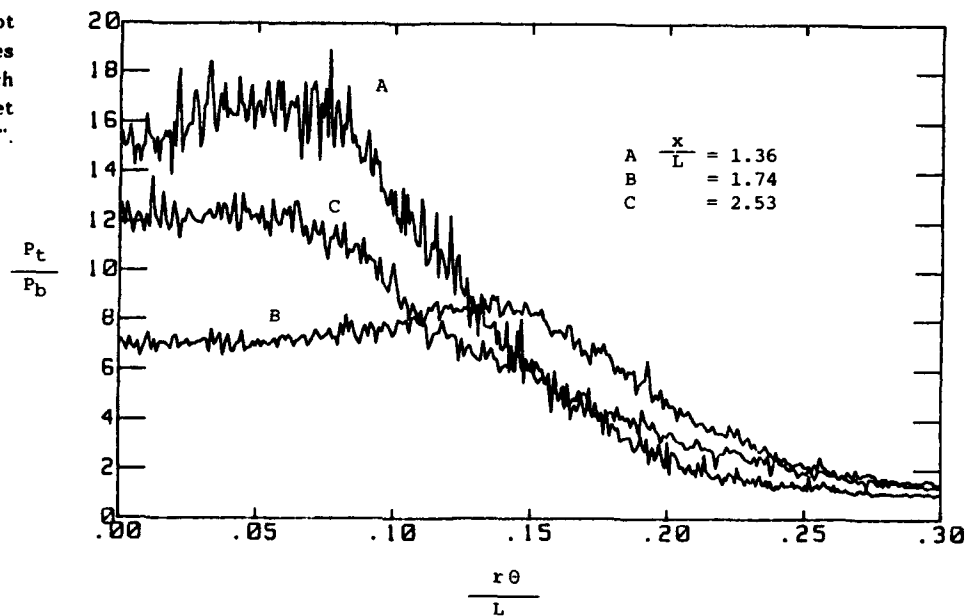
**Fig. 10(a):** Axial Pitot pressure profile downstream of the Mach disk in a nitrogen jet from nozzle "A". Nominal  $P_0/P_b = 650$ .



**Fig. 10(b):** Axial Pitot pressure profile in the second and third shock cells in a nitrogen jet from nozzle "A". Nominal  $P_0/P_b = 650$ .



**Fig. 10(c):** Angular Pitot pressure profiles downstream of the Mach disk in a nitrogen jet from nozzle "A". Nominal  $P_0/P_b = 650$ .



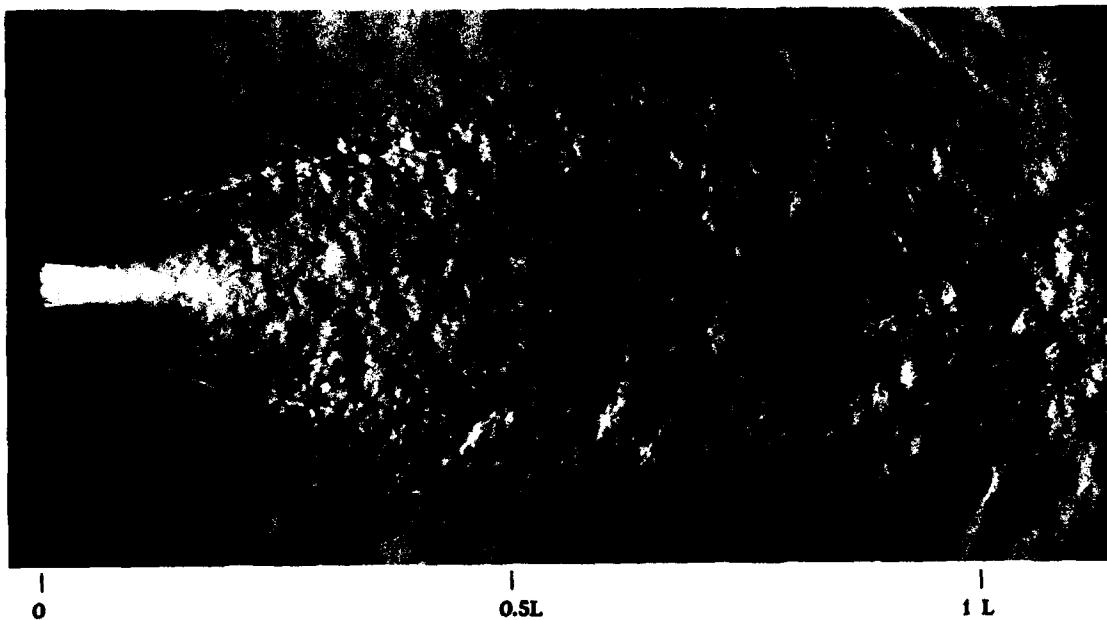


PLATE 1 : Nitrogen jet from nozzle "A",  $P_0/P_b = 1530$ ,  $0.1 \mu s$  exposure.

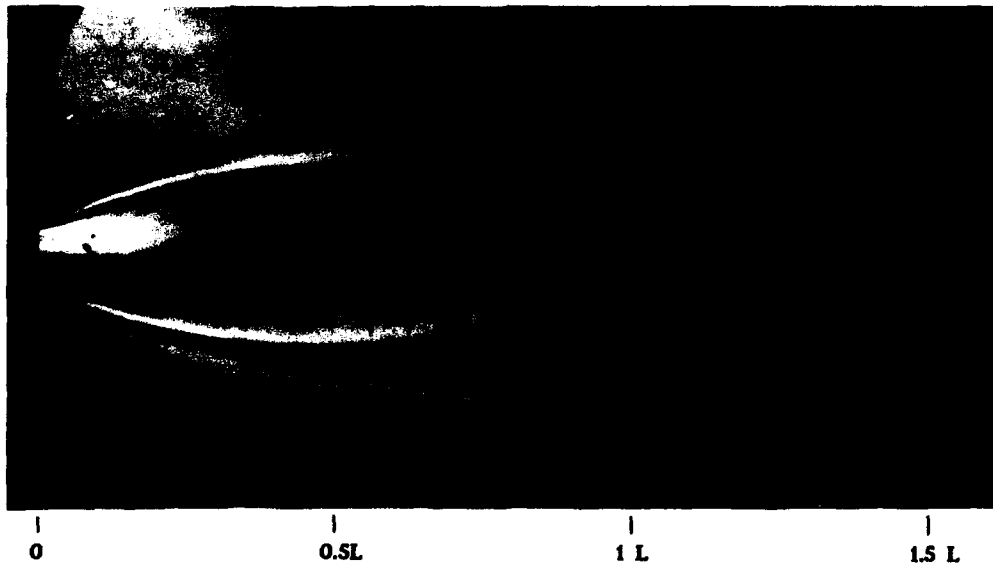


PLATE 2 : Nitrogen jet from nozzle "B",  $P_0/P_b = 624$ ,  $4 \text{ msec}$  exposure.

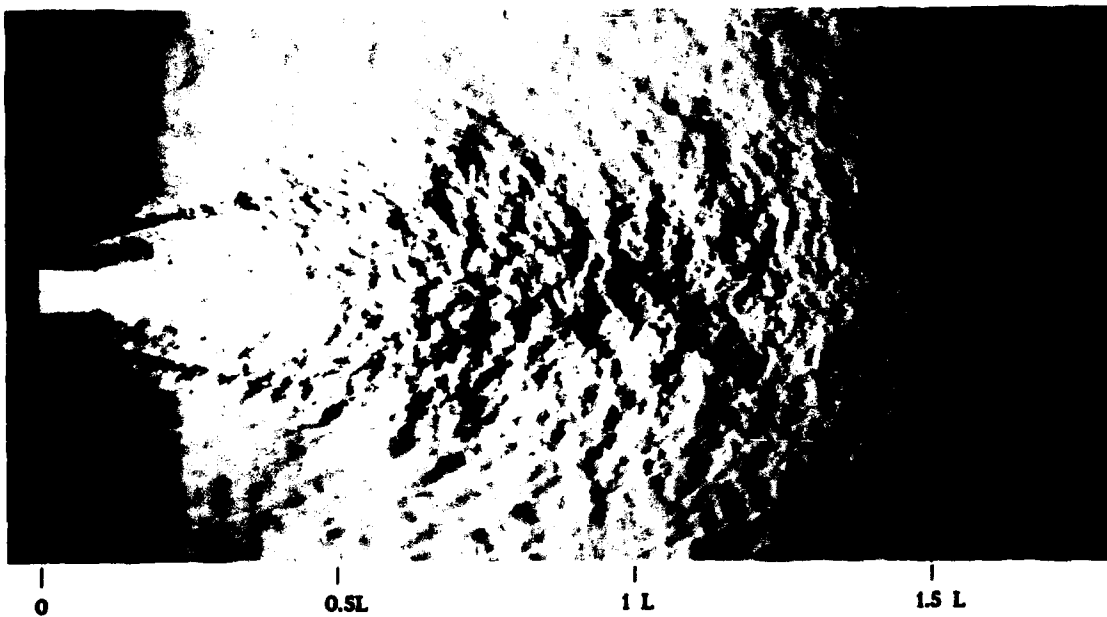


PLATE 3 : Nitrogen jet from nozzle "A",  $P_0/P_b = 629$ ,  $0.1 \mu s$  exposure.

## Discussion

### STOLLERY

How steady were the main features of the flow? For example if you take 6 independant microsecond pictures of the flow is the Mach disc in roughly the same place?

### AUTHOR'S REPLY

The flow external to the barrel shock is unsteady due to the turbulence. Schlieren photographs taken with a spark light source often show kinks in the barrel shock and tilted Mach discs. Long exposure times blur the shocks. The spatial extent of this blurring gives an indication of the RMS variation of the shock position. Measurements of this variation in addition to the scatter in the measurement of Mach disc diameter and position obtained from the short exposures will be presented in the author's D. Phil thesis.

With regard to the unsteadiness associated with the slowly varying stagnation conditions it appears as though it is appropriate to regard the jet as quasi-steady as the scaling procedures discussed in the paper effectively remove this influence.

# THE EFFECT OF COMBUSTOR FLOW NONUNIFORMITY ON THE PERFORMANCE OF HYPERSONIC NOZZLES

by  
P. Goel, S.L. Barson and S.D. Halloran  
Rockwell International Corporation  
Rocketdyne Division  
6633 Canoga Avenue  
Canoga Park, California 91303

AD-P007 961



## SUMMARY

A parametric, 3-D, Euler, CFD study was carried out on a hypersonic vehicle engine nozzle. The configuration analyzed, though generic, is representative of those being considered for current generation vehicles. A series of flow profiles ranging from completely uniform to highly distorted were developed and introduced at the inflow plane of the nozzle in an effort to understand the associated impact on nozzle performance. Nozzle performance is quantified for each case and a qualitative rationale for the performance impact is developed.

## INTRODUCTION

Interest in hypersonic vehicles powered by airbreathing engines has increased dramatically. The engine and airframe on such vehicles are highly integrated, often utilizing the entire underside of the vehicle for compression and expansion of the flow (Figure 1). Nozzle design for these vehicles provides several unique challenges. Hypersonic vehicle nozzles differ dramatically from those of traditional rocket and jet engines in that they are largely nonsymmetric, often exhibiting true three-dimensional flow characteristics. Earlier studies performed by Rao (1) and Foelsch (2) were instrumental in the optimization of the more traditional de Laval type nozzle. However, the nozzle flows typical of hypersonic vehicles can not be modeled accurately as axisymmetric or two-dimensional and, in fact, may be highly nonideal with shocks existing throughout the expanding flowfield. These nozzles are often composed of internal and external portions, the internal part possibly having lateral and vertical geometric expansions. The external portion typically makes up a majority of the expansion surface by utilizing the vehicle aftbody. The internal nozzle (engine) exhaust stream is bounded by the external nozzle above, but is open to the freestream below. A further complication arises from the fact that the flow exiting the engine combustor region and entering the nozzle is nonuniform and difficult to characterize. Proper optimization of the integrated engine-airframe performance must account for all of these flow features by accurately predicting, as a minimum, the complex 3-D flow and shock structures, and ultimately viscous, kinetic, and real gas effects.

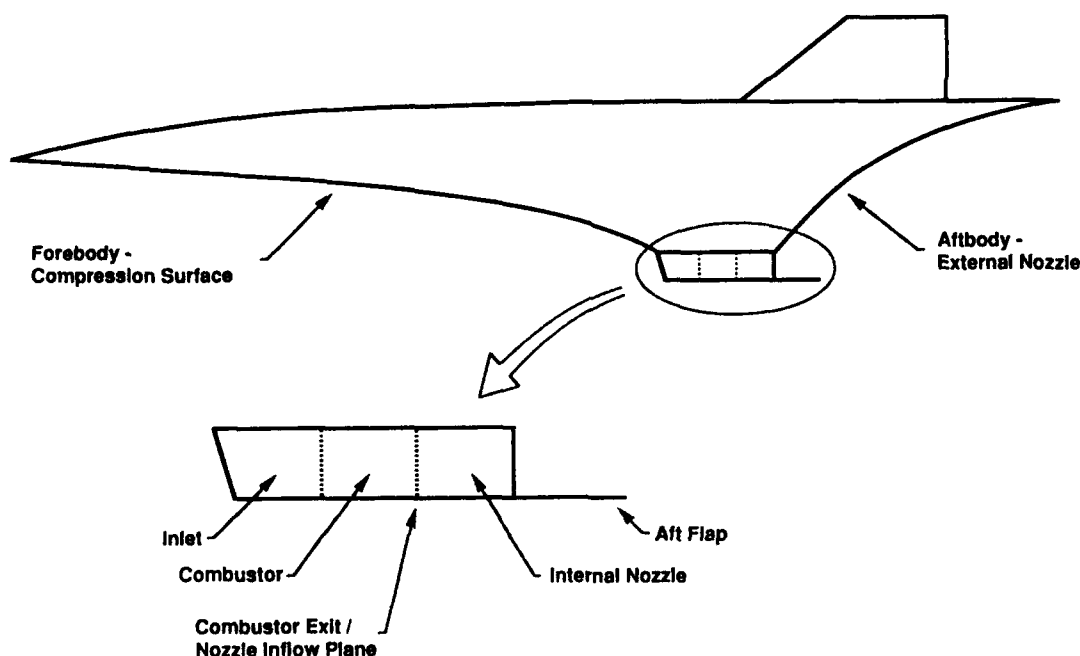


Figure 1. Integrated Airframe and Engine

The Rockwell Unified Solution Algorithm (USA) computational fluid dynamics code (3, 4) has been applied to hypersonic vehicle nozzle analysis. Because the code handles 3-D multistream flows, issues of dimensionality and the two flowstreams (engine and freestream) are largely resolved. However, understanding the effect on nozzle performance due to the nonuniformity of the flow passed to the nozzle remains largely unresolved. As the freestream air is processed it is distorted in several ways before reaching the nozzle. The initial compressions on the vehicle forebody and further contraction within the inlet affect the flow uniformity, often biasing the pressure toward the vehicle side. Boundary layer buildup on the long forebody surface can be significant. Within the combustor, as air and fuel are mixed and burned, additional flow nonuniformity may be introduced or diminished depending on the particular configuration. Thus, a great deal of uncertainty exists as to the detailed nature of the flow being passed to the nozzle.

A detailed description of the combustor exit profile would provide a spatial definition of all basic flow parameters (e.g. Mach number, temperature, pressure, species). Efforts to define this 3-D flow profile have been made both experimentally and analytically. Experimental techniques for detailed descriptions of the combustor exit profile are limited. Nonintrusive techniques such as planar laser-induced fluorescence (PLIF) are promising and showing increased use, but are not yet widespread. Analytical techniques are often limited to one-dimensional thermal cycle calculations and simple two-dimensional flow codes. Additionally, 3-D CFD analysis

92-16993

has been performed in an effort to describe the entire vehicle-engine flowfield including the combustor. While extremely useful as an aid to understanding qualitative effects, computer limitations combined with inadequate physical models for kinetics and turbulence result in profiles of limited quantitative value. Thus, a significant number of 2-D and 3-D nozzle calculations have been based, for lack of better characterization, on 1-D cycle calculations, effectively starting the higher order analysis with a uniform average flow condition.

The study described herein represents a first attempt to understand the sensitivity of hypersonic nozzle performance to inflow nonuniformities. A realistic set of inflow conditions was chosen to make this evaluation. An appropriate set of atmospheric conditions was defined for a generic vehicle flying at Mach 10. The Rocketdyne performance code (PERFO), a 1-D thermal cycle code, was then used to "process" the freestream air accounting for appropriate shock, compression, boundary layer, and combustion effects, thus defining an average combustor exit condition. This was used as an average uniform nozzle inflow condition. The inflow profile was systematically varied, starting with the uniform condition and then introducing an increasing amount of distortion into the pressure profile. Distortion levels introduced were chosen to bracket those that might be encountered in a real engine. Other flow parameters were adjusted according to isentropic relationships while conserving the overall mass and streamthrust of the average profile.

## NOZZLE CONFIGURATION AND FLOW CONDITIONS

The geometry chosen for this study (Figure 2), though generic, is representative of current concepts. It is comprised of two parts, a short internal section and a relatively long external section, simulating a vehicle aftbody. The internal nozzle has parallel top and bottom walls and diverging sidewalls. Thus, the internal nozzle flow expands laterally, but not in the vertical direction. A short flap, set in this case in line with the bottom wall is also included. Such a device might be used for directing the exhaust flow. The external portion, representing the vehicle aftbody, extends from the end of the internal nozzle top wall allowing the flow to expand in the vertical direction. The freestream flow would exist just below the line of the internal nozzle bottom wall and flap.

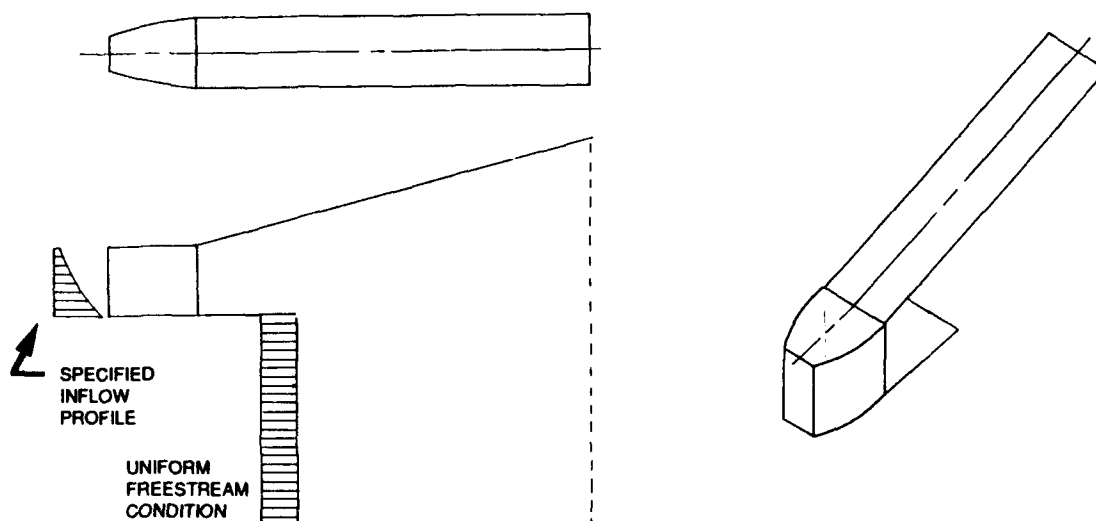


Figure 2. Computational Domain

The average flow conditions applied at the nozzle inflow plane were:

$$\begin{aligned}\text{Pressure (P)} &= 3392.27 \quad \text{lbf/ft}^2 \\ \text{Density } (\rho) &= 1.1067 \times 10^{-2} \quad \text{lbm/ft}^3 \\ \text{Mach (M)} &= 2.45\end{aligned}$$

The ambient freestream flow conditions were:

$$\begin{aligned}\text{Pressure (P)} &= 17.34 \quad \text{lbf/ft}^2 \\ \text{Density } (\rho) &= 7.87 \times 10^{-4} \quad \text{lbm/ft}^3 \\ \text{Mach (M)} &= 10.0\end{aligned}$$

A constant value of  $\gamma=1.25$  (ratio of the specific heats) was used throughout the computational domain.

## COMPUTATIONAL DETAILS

The computational domain includes the internal lateral expansion nozzle, the aftbody (external nozzle) and the freestream below. Because geometry and flow symmetry exist in the lateral direction, only one half of the nozzle was modeled, from the center plane to the sidewall. The portion of the external nozzle analyzed is a projection of the internal nozzle exit plane.

Figure 3 shows the computational grid on the plane of symmetry. The computational domain is comprised of two zones. The first zone contains the internal nozzle and the aft flap and utilizes a total of 6072 grid points. The second zone contains the external nozzle and a portion of the ambient freestream flow, modeled with 16,698 grid points, making a combined total of 22,770 grid points.



The three-dimensional version of the Rockwell USA (Unified Solution Algorithm) code was employed for this computation. The code was run in the time dependent, Euler mode, using approximate factorization, with the third order Total Variation Diminishing (TVD) option. The Rockwell USA code solves the conservation law form of the Euler equation or the full Reynolds averaged Navier Stokes equations using the finite volume approach with the implicit upwind biased solution methodology. Its ability to handle multi-zone domains facilitates the solution of complex geometries.

For this computation, the domain was initialized with values obtained from a one-dimensional isentropic expansion formulation. The calculation was started with an initial CFL of 1 which was ramped up gradually to a maximum value of about 100 over 500 time steps. A typical time step took under three seconds of CPU time on the NASA Ames Cray-XMP. A converged solution for a nonuniform profile case was obtained in about 600 time steps using up a maximum of 30 minutes of CPU time. The solution was considered to be fully converged when the residuals dropped more than four orders of magnitude.

## FLOW NONUNIFORMITY DEVELOPMENT

The nonuniform profiles were developed from the uniform flow values given earlier such that the mass and momentum (stream thrust) of the original uniform flow were the conserved.

To parametrically study the effect of nonuniform pressure profiles at the combustor exit/nozzle entrance plane, three basic variations of the uniform pressure profile were developed. Semi-linear, quadratic, and cubic profiles for the ratio of static pressure to stagnation pressure were first generated. Assuming local one-dimensional isentropic flow at the inlet cross section, the corresponding Mach number profile was then obtained from this pressure profile.

Since

$$U = M \sqrt{\frac{P}{\rho} \gamma}$$

an expression was obtained for the inflow stream thrust from which the stagnation pressure was obtained so as to maintain a constant momentum.

In order to obtain the density profile, the ratio of density to stagnation density was evaluated from the Mach number profile assuming, once again, local one-dimensional isentropic flow at the inlet cross section. The density profile was obtained after the value of stagnation density was calculated from the expression for inlet mass flow. The pressure profiles were designed so that the pressure values would gradually rise from a low to a high value. The profiles can be characterized in terms of a pressure distortion parameter  $\eta_p$ , defined as

$$\eta_p = \frac{P_{avg}}{P_{max}}$$

where

$P_{avg}$  = Area averaged pressure over inflow plane for each profile.

$P_{max}$  = Maximum pressure value in the nozzle inflow plane.

As mentioned previously the distortion levels introduced were chosen to bracket those that might be encountered in a real engine. After developing the three basic distorted profiles, three new inflow pressure profiles were created by inverting the three basic ones. By the previous definition these new profiles would have the same value of  $\eta_p$  as the basic profiles. However, for convenience, they are distinguished by assigning them a negative value. Generating the three inverted profiles was done and to study the effect of high versus low pressures on the cowl surface of the nozzle.

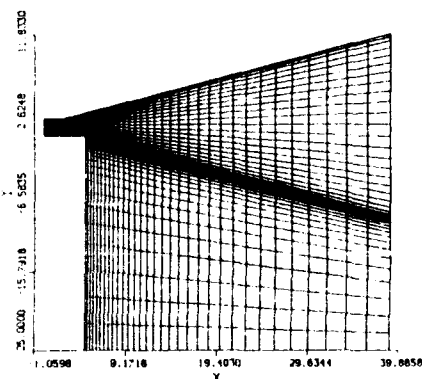


Figure 3. Computational Grid

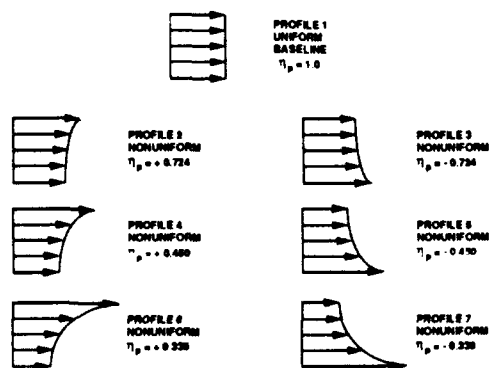


Figure 4. Seven Nozzle Inflow Pressure Profiles

Thus, six profiles with distinct values of  $\eta_p$  ( $\eta_p = \pm 0.338$ ,  $\pm 0.450$ , and  $\pm 0.724$ ) were used. Combined with the uniform profile ( $\eta_p = 1.0$ ) a total of 7 cases were analyzed. Figure 4 shows a schematic of the seven inflow pressure profiles. Figures 5a and 5b show the resulting Mach number and pressure profiles associated with the three positive values of  $\eta_p$ .

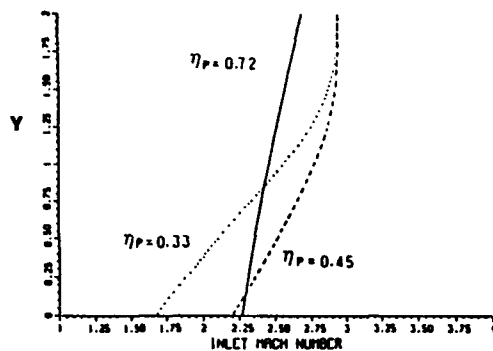


Figure 5a. Inflow Mach Profiles

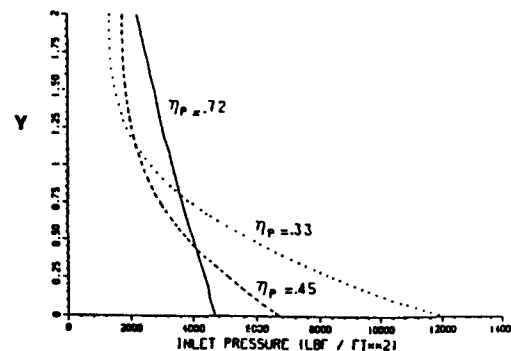


Figure 5b. Inflow Pressure Profiles

### NOZZLE EFFICIENCY, PRESSURE FORCES, AND MOMENTS

In order to quantify and compare the operating and performance characteristics of these nozzles various performance parameters were used. These are:

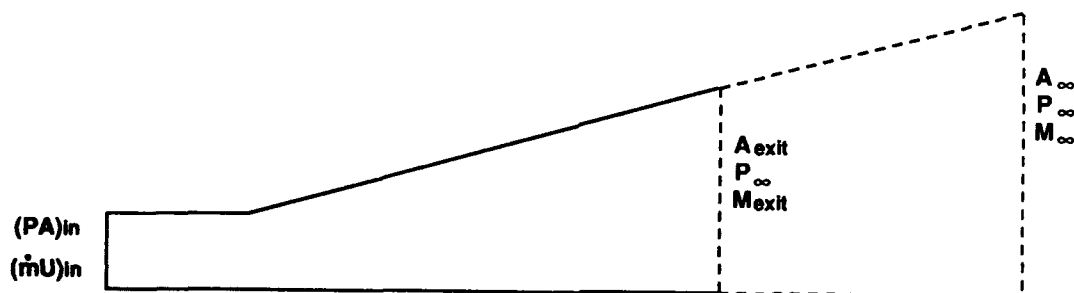
#### i) Nozzle efficiency - $C_{fg}$

This is the ratio of the actual thrust produced by the nozzle to the theoretical thrust that would be produced if the flow through the nozzle were expanded isentropically to the ambient pressure (Figure 6).  $C_{fg}$  is a measure of how well the nozzle performs as related to an ideal isentropic nozzle. It is defined as,

$$C_{fg} = \frac{(\dot{m}U + PA)_{in} + \int PdA - P_{\infty}A_{exit}}{(\dot{m}U + PA)_{in} + \int P_{\infty}dA_{\infty} - P_{\infty}A_{\infty}}$$

where

- $A_{exit}$  = Area of nozzle exit
- $P_{\infty}$  = Theoretical state of nozzle flow isentropically expanded to  $P_{\infty}$
- $P_{\infty}$  = Ambient pressure
- $A_{\infty}$  = Theoretical area for isentropic expansion of flow to  $P_{\infty}$
- $\int PdA$  = Axial pressure force generated by the nozzle
- $\int P_{\infty}dA_{\infty}$  = Theoretical axial pressure force generated if flow in the nozzle was expanded isentropically to  $P_{\infty}$

Figure 6. Calculation of Nozzle Efficiency,  $C_{fg}$ 

The value of the numerator can be obtained directly from the computed results. The denominator, however, can be simplified as follows:

Since

$$\int P_{\infty}dA_{\infty} = (\dot{m}_{\infty}U_{\infty} + P_{\infty}A_{\infty}) - (\dot{m}U + PA)_{in}$$

the denominator thus becomes

$$\begin{aligned} &= \dot{m}_{\infty}U_{\infty} \\ &= \rho_{\infty}U_{\infty}^2A_{\infty} \end{aligned}$$

Furthermore, since

$$U_{\infty}^2 = \left( M_{\infty} \sqrt{\gamma \frac{P_{\infty}}{\rho_{\infty}}} \right)^2$$

the denominator becomes

$$M_{\infty}^2 A_{\infty} \gamma P_{\infty}$$

Thus,

$$C_{fg} = \frac{(\dot{m}U + PA)_{in} + \int PdA - P_{\infty}A_{exit}}{M_{\infty}^2 A_{\infty} \gamma P_{\infty}}$$

In order to evaluate the denominator for the nonuniform profiles, it is assumed that

$$\text{denominator} = \sum_{i=1}^{i=N} M_{i\infty}^2 A_{i\infty} \gamma P_{\infty}$$

whereby each computational cell at the inflow plane is considered as a separate stream tube and is expanded isentropically to  $A_{i\infty}$  where the corresponding Mach number is  $M_{i\infty}$  at the ambient pressure of  $P_{\infty}$ .

## ii) Pressure Forces - $\int PdA$

To evaluate the lift, thrust and lateral forces exerted by the expanding flow on the nozzle, the wall pressures are multiplied with the corresponding normal cell face areas along the axial, vertical, and lateral directions and summed. Thus,

$$\int PdA_x = \text{Axial (thrust) force}$$

$$\int PdA_y = \text{Vertical (lift) force}$$

$$\int PdA_z = \text{Lateral (yawing) force - Reduces to zero for this case due to symmetry}$$

## iii) Moments Due to Pressure Forces

To facilitate proper engine/airframe integration the pitching, rolling, and yawing moments must be evaluated. These moments are generated as a result of the flow expansion and the corresponding pressure forces acting on the walls. The roll, pitch and yaw moments are computed by multiplying the pressure forces calculated above for each cell by the corresponding centroidal distance from a defined origin and summing up the moment in the x, y, and z direction, assigning the appropriate sign convention for the clockwise and anticlockwise moments.

Again, owing to the symmetry of the nozzle along the center plane, the yaw and the roll moments cancel. The pitching moment, however, is important since it directly affects the overall vehicle. Depending on the particular vehicle, additional trim may be required to offset the pitching forces generated by the nozzle, which may result in additional drag.

## RESULTS AND DISCUSSION

For a nozzle to produce maximum thrust, the expanding flow must effectively transfer its pressure energy to solid wall surfaces. Conventional de Laval nozzles generally have solid walls available on both sides for the expanding flow to transfer its static pressure force. Three-dimensional hypersonic nozzles, however, have only a small portion of the outflow area bounded entirely by walls. For the largest surface area, the vehicle aftbody, to be effectively utilized the flow must be "diverted" to allow the high pressure flow to interact with the surface and consequently impart its energy. Flow away from the aftbody has no solid surface with which to interact and therefore makes no contribution to the thrust production. The effect of high pressure as introduced in the assumed profiles is to induce a turning of the internal nozzle flow towards the lower pressure area. When the flow entering the nozzle has a higher pressure on the top, as in profiles 2, 4 and 6 ( $\eta_p = +0.724, +0.450, +0.338$ ), the flow streamlines tend to bend downward toward the lower surface, away from the aftbody. Conversely, when the flow entering the nozzle has a higher pressure on the bottom, (profiles 3, 5, 7) the streamlines tend to turn upward towards the aftbody, thereby allowing higher pressure flow to interact with that solid surface, thus augmenting the thrust. Figures 7a and 7b show this effect through the flow streamlines in the symmetry plane of the internal nozzle and over a short portion of the aftbody. It is seen that for the case of higher pressure acting on the lower side of the internal nozzle ( $\eta_p = -0.45$ ), the stream lines are turned toward the upper wall. Figure 8 shows the pressure profile on the nozzle top wall along the centerline (symmetry plane) for the case of high pressure on the lower side ( $\eta_p = -0.45$ ) and high pressure on the top side ( $\eta_p = +0.45$ ). Higher pressure on the lower side not only turns the flow streamlines upward but also produces a strong shock which impinges on the aftbody just beyond the end of the internal nozzle producing higher pressures on that surface. This shock impingement and the consequent higher pressures which prevail along the top wall augment the thrust over that of the uniform inflow case ( $\eta_p = 1.0$ ) or for that of the inverted inflow profile ( $\eta_p = +0.45$ ). Figures 9a and 9b show pressure contours within different computational planes for profiles 4 and 5, respectively. The formation of a shock and its subsequent impingement on the top wall (profile 5,  $\eta_p = -0.45$ ) can be seen in Figure 9b. This phenomena however is absent in the case of the inverted pressure profile, Figure 9a, ( $\eta_p = +0.45$ ).

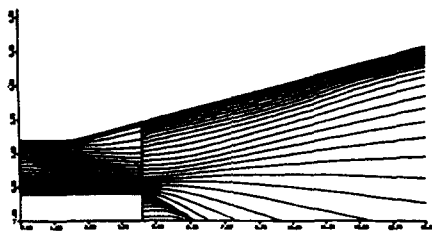


Figure 7a. Streamlines, Profile 4,  $\eta p = +0.45$ ,  
High inflow pressure At Body side

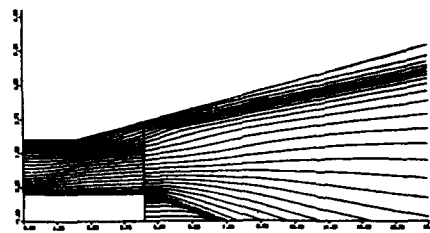


Figure 7b. Streamlines, Profile 5,  $\eta p = -0.45$ ,  
High inflow pressure At Cowl side

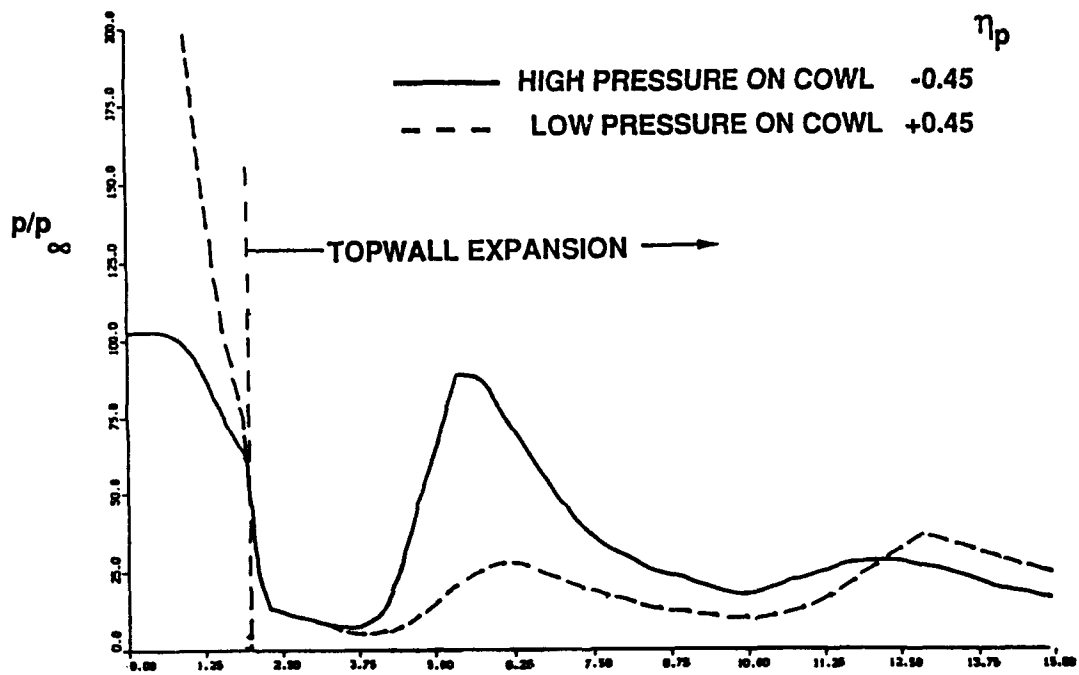
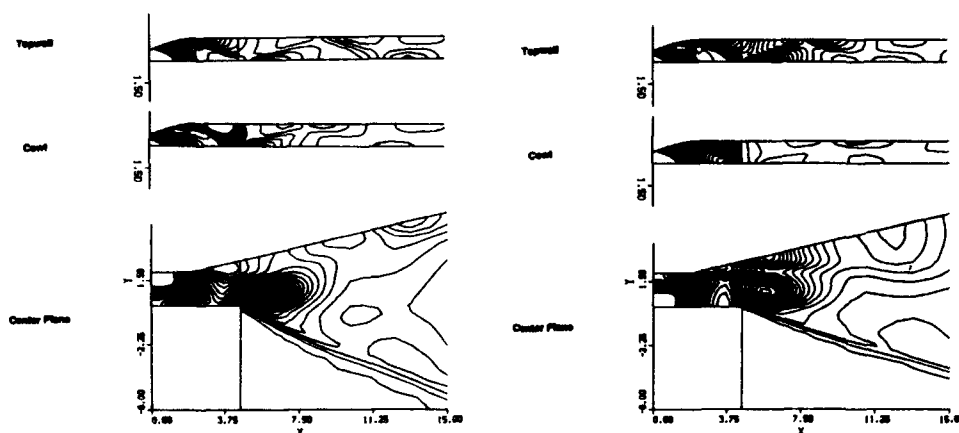


Figure 8. Pressure Profile Along Centerline of Body Surface (Top Wall)



9a. Profile 4,  $\eta p = +0.45$ ,

9b. Profile 5,  $\eta p = -0.45$ ,

Figure 9. Pressure Contours

Figures 10a and 10b compare the pitching moment ratio and the thrust vector angle,  $b$ , for different values of  $\eta_p$ . It is seen that the pitching moment (normalized by that of the uniform case,  $\eta_p=1.0$ ) varies significantly with the level of distortion. The general trend, as depicted by the least squares curve fit in each figure, is toward a decrease in pitching moment for high values of  $\eta_p$  (high pressure at top) and an increase in pitching moment for low values of  $\eta_p$  (high pressure at bottom). This is consistent with the fact that high pressure at the bottom results in higher pressure on the aftbody, the net results being an increased pitching moment.

The plot of thrust vector angle  $b$  shows the opposite trend. As the inflow pressure profile becomes increasingly biased toward the bottom of the internal nozzle the thrust increases. The lift, however, tends to decrease due to the high lower cowl pressures introduced at the internal nozzle inflow plane. The net result is that of a decrease in the thrust vector angle,  $b$ .

Both the pitching moment and the thrust vector angle data are of great significance to the overall vehicle design and performance. However, the total effect can only be evaluated by considering the integrated engine and airframe.

Figures 11a and 11b show the variation of the pressure forces,  $|P_dA|$ , with  $\eta_p$  and the variation of  $C_{fg}$ , nozzle efficiency, with  $\eta_p$ . The nozzle efficiency is directly related to the thrust produced. The nozzle efficiency is directly related to the  $|P_dA|$  (thrust) produced and, as such, it is generally seen that introducing higher pressures on the cowl (bottom of the nozzle) improves the nozzle performance. As one would expect there is a limit to how great the flow distortion can be before the performance is adversely affected.

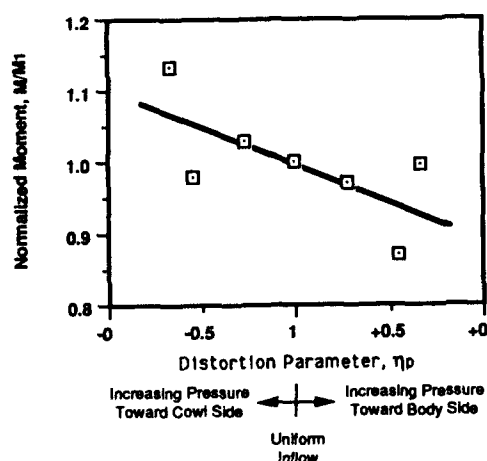


Figure 10a. Moment vs.  $\eta_p$

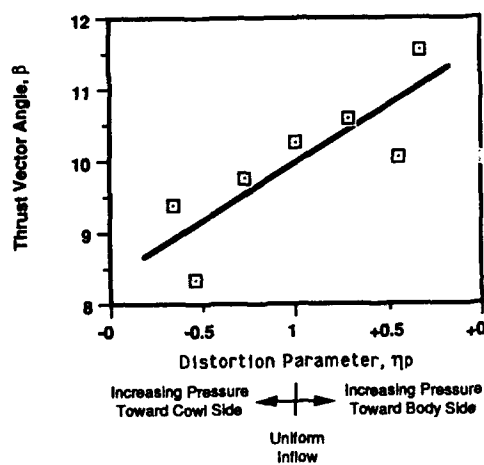


Figure 10b. Thrust Vector Angle vs.  $\eta_p$

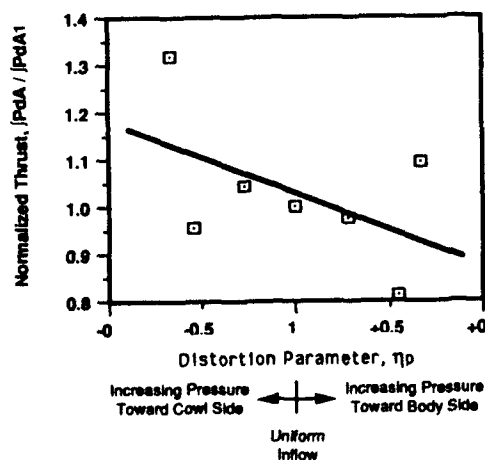


Figure 11a. Thrust vs.  $\eta_p$

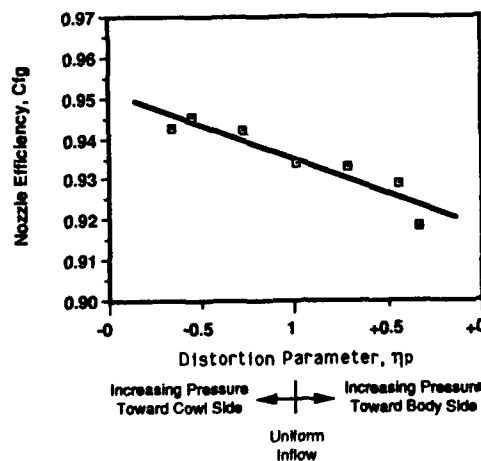


Figure 11b. Nozzle Efficiency vs.  $\eta_p$

## CONCLUSIONS

A parametric three-dimensional Euler CFD study was performed to evaluate the effect of the inflow profile on the performance of an integrated hypersonic nozzle. The incoming flow profile was distorted and seven distinct cases were analyzed. Using  $\eta_p$  as a measure of the distortion, the performance was quantified in terms of thrust ( $J_{pDA}$ ), nozzle efficiency ( $C_{fp}$ ), pitching moment, and the thrust vector angle.

It was found that

1. Nozzle performance is greatly affected by the level of nonuniformity in the inflow profile. Serious effort must be devoted to the accurate characterization of these inflow profiles.
2. Hypersonic vehicle nozzles, as typified by the study configuration, are highly nonideal. Shocks exist throughout the flowfield. Depending on the inflow profile and the particular geometry considered some of the losses associated with the shocks may be recovered if the flow can be made to interact with appropriate solid surfaces.
3. For the particular case analyzed, higher pressures introduced toward the bottom of the internal nozzle resulted in improved axial thrust and nozzle efficiency, but at a cost of increased pitching moment. An integrated engine/airframe analysis would be required to evaluate whether the additional thrust was sufficient to offset the possible increase in trim drag.

## REFERENCES

1. Rao, G.V.R., "Exhaust Nozzle Contour for Optimum Thrust," Jet Propulsion, June, 1958, pp. 377-382.
2. Foelsch, K., "The Analytical Design of a Axially Symmetric Laval Nozzle for Parallel and Uniform Jet," Journal of the Aeronautical Sciences, March, 1949.
3. Chakravarthy, S.R. and Osher, S., "A New Class of High Accuracy TVD Schemes for Hyperbolic Conservation Laws," AIAA-85-0363, January, 1985.
4. Chakravarthy, S.R., "The Versatility and Reliability of Euler Solvers Based on High-Accuracy TVD Formations," AIAA-86-0243, January, 1986.
5. Anderson, J.D., "Hypersonic and High Temperature Gas Dynamics," McGraw-Hill Book Company.
6. Anderson, J.D., "Modern Compressible Flow with Historical Perspective" McGraw-Hill Book Company.
7. McClinton, C.R., Kuehn, M.S., Ray, R.G., and Pinckney, S.Z., "Some Observations on Nozzle Performance Analysis," Fourth National Aero-Space Plane Technology Symposium, February, 1988, Paper No. 28.
8. Shapiro, A.H., "The Dynamics and Thermodynamics of Compressible Fluid Flow," Ronald Press, New York.

## ACKNOWLEDGEMENTS

The work reported here is supported by the U.S. Department of Defense, NASP Program, under Contract Number F33657-87-C-2214. The authors would like to extend their thanks to Mr. W.W. Follett for his suggestions, technical discussions and assistance with the graphics. Appreciation is also extended to NASA Ames for use of the NAS facility Cray X-MP.



# REACTING SHOCK WAVES IN HYPERSONIC PROPULSION APPLICATIONS

M. Onofri\*

Dipartimento di Meccanica e Aeronautica  
Università degli Studi di Roma "La Sapienza"  
Via Eudossiana 18 - Roma 00184  
Italy

92-16994



## SUMMARY

Problems connected to the occurrence of finite rate chemical processes behind shock waves in hypersonic flowfields are analysed and a numerical technique is proposed for their solution. The computational difficulties connected with the presence of large gradients of the species concentrations are considered. A method is proposed, based on a shock-fitting technique for the gasdynamic model and a variable step integration along the streamlines for the energy and species conservation equations. This approach provides the needed resolution where it is actually required, without becoming cumbersome elsewhere, and the relaxation layer behind shocks can be computed efficiently and precisely.

## 1. INTRODUCTION

In this paper a methodology is illustrated to simulate the dissociation phenomena that occur behind shock waves in airbreathing engines operating in hypersonic regime. Typically these phenomena occur both in supersonic inlets operating at high flight Mach numbers and in nozzle exhaust jets, where a strong airframe-engine integration is required or in ramrocket configurations within the mixing duct of ramjet and rocket exhaust flows.

At high Mach numbers the fluid dynamic variables jump through the shock produces a large departure from the equilibrium conditions. A chemical relaxation layer follows the shock, in which dissociation reactions occur in nonequilibrium conditions and the air composition changes with a behaviour characterized by strong gradients of temperature and species mass fractions.

In order to obtain a proper numerical solution, a high spatial resolution is required behind the shock. This can be achieved with adaptive grids, that are quite cumbersome from a computational perspective. A different approach has been recently proposed by the author [1] to compute hypersonic external flows. Here a further possible application of this approach, relevant to the calculation of the internal flows above described, is considered.

Instead of solving the fully coupled equation system, requiring an impractical amount of computational work when implemented on multidimensional flows, the method follows the approach based on an operator splitting for gasdynamics and chemistry firstly proposed by Li [2] and widely adopted [3,4,5]. Accordingly, the set of conservation laws is split in two parts:

- the gasdynamic operator, describing the mass and momentum conservation of the mixture,
- the chemical operator, describing the conservation of the energy of the mixture and of the mass of each individual chemical species.

In flows with dissociation-recombination reactions typical of hypersonic propulsion applications, the variables of the gasdynamic operator have a quasi-linear behaviour and can be solved by standard approaches. The advantage of using integration schemes based on an operator splitting is therefore to bound to the chemical operator the numerical problems relevant to the stiff nature of the equation system and to the nonlinearity of the solution.

The proposed technique takes full advantage of this approach performing the integration over two different grids: a standard one for the gas dynamic equations, and along streamlines for the chemical operator. Due to its one-dimensional nature, the integration along streamlines can be easily performed by using a variable step procedure. In this way high resolution can be provided where it is actually required, without becoming cumbersome elsewhere.

Moreover, the shock is treated by a shock-fitting technique, that provides a consistent and accurate way to describe a reacting shock layer. Indeed, as discussed in the next section, while some problems seem to exist in imposing proper boundary conditions when using a shock capturing procedure, the shock-fitting allows to assign the correct initial conditions for the integration of the chemical variables along the streamlines; thus the relaxation layer behind the shocks can be computed efficiently and accurately.

## 2. SHOCK WAVES IN FLOWS WITH FINITE RATE CHEMISTRY

The solutions of steady inviscid flows with chemical relaxation processes can be strongly affected by the modelling of the shock wave. As a matter of fact, the boundary conditions for the integration of the chemical equations should be enforced at the shock, and a physically consistent modelling of its structure is therefore mandatory. The same

\*Associate Professor

considerations hold in unsteady flows, in order to predict correct shock propagation speeds without generating spurious waves.

The classical description of a "partly dispersed" shock wave [6,7] is based on the following assumptions:

- ahead of the shock and far behind it, the gas is in equilibrium;
- translational and rotational motions across the shock fit the variable conditions so fast that they can be considered in equilibrium;
- vibrational excitation and variations of the chemical composition are much slower processes and can be considered frozen across the fluid dynamic discontinuity of the shock. They relax in a layer following the frozen jump.

It should be pointed out that at the temperatures typical of the hypersonic propulsion applications vibrational phenomena approach equilibrium conditions and thus this assumption may appropriately be used in the modelling. Nevertheless, as shown by Candler in [14], the same assumption yields a large discrepancy with the experimental evidence when the vibrational relaxation layer is of the same order than the fluid dynamic length, for instance due to the small reference length considered. Vibrational nonequilibrium models must be used in these cases.

As a consequence of this modelling the variables describing the chemical composition of the mixture start from the values at the shock and reach the new equilibrium composition with a boundary layer behaviour. In particular, at the shock the mixture composition is still frozen to the values ahead of the shock, and transition from these conditions to the outer solution occurs in a thin layer with strong gradients of the nonequilibrium variables (Fig.1).

Numerical integrations of such a chemical relaxation layer give rise to specific problems that can be summarized by two major items, that will be discussed in the following subsections:

- the singular surface is the position where the boundary conditions for the chemical integration must be imposed and its detection and tracking must be very precise.
- the system of the governing equations is stiff, and demands suitable integration techniques; moreover the variables describing the chemical process have strong nonlinear solutions that need a high space resolution.

## 2.1- Numerical handling of the shocks

In non reacting flows the numerical handling of the shock could be done by using a shock-capturing scheme or a shock-fitting procedure. Nevertheless, as pointed out by Le Veque and Yee [9], in flows with finite rate chemistry the accuracy and reliability of the solutions obtained by shock-capturing approaches could be questionable.

In fact in the solutions of non reacting gas performed by shock-capturing schemes the states ahead and behind the shock are connected through some intermediate states that do not represent the actual physical structure of a shock wave. When the gas is inert this is just a local behaviour that does not affect the flow downstream and the jump relations are then properly obtained as weak solutions of the equations. On the contrary, in a gas with finite rate chemistry, source terms artificially activated by these unphysical intermediate states can wrongly affect the overall computation. To overcome this difficulty Le Veque and Yee [9] suggest either a front-tracking approach or the use of subgridding.

These numerical shortcomings do not occur if a shock-fitting technique is adopted. Actually this approach seems to be the more consistent and accurate way to numerically describe the reacting shock model. The fitting of the frozen shock wave followed by the relaxation layer in nonequilibrium conditions strictly reproduces the internal structure of the "partly dispersed" wave. Moreover, the "frozen-fitted shock" can provide exact initial conditions for integration of the chemical operator.

## 2.2- Numerical integration of the chemical relaxation layer

If two characteristic times are defined, the fluid dynamic time  $\tau_f$  and the chemical relaxation time  $\tau_c$ , the mathematical model for flows with finite rate chemistry is provided by the following set of conservation equations:

- the conservation equations of mass, momentum and energy, that in quasilinear form are

$$\begin{aligned}\frac{D\rho}{Dt} + \rho \nabla \mathbf{q} &= 0 \\ \frac{D\mathbf{q}}{Dt} + \frac{1}{\rho} \nabla p &= 0 \\ \frac{Dh}{Dt} + \frac{1}{\rho} \frac{Dp}{Dt} &= 0\end{aligned}\tag{1}$$

- a state equation, written in the form  $h = h(p, T, \mathbf{C})$ , where  $\mathbf{C}$  is the vector of the  $N$  variables  $c_i$  specifying the state of nonequilibrium of the gas (for example the  $c_i$  mass fractions of the  $i$ -species),
- the rate equation modelling the particular nonequilibrium process, that can always be written in nondimensional form as

$$\frac{1}{Da} \frac{D\bar{c}_i}{D\bar{t}} = \frac{\bar{X}}{\bar{\tau}}\tag{2}$$



where

bars denote non dimensional quantities of  $O(1)$ ,

$Da = \tau_f/\tau_e$  is the Damköhler number that identifies three regimes: equilibrium flow ( $Da \gg 1$ ), frozen flow ( $Da \ll 1$ ), nonequilibrium flow ( $Da \approx 1$ ),

$\tau$  is the local relaxation time for the nonequilibrium process,

$\chi$  is a measure of the departure of the system from the state of equilibrium  $C^*(p, T)$  implicitly defined by

$$\chi(p, T, C^*) = 0 \quad (3)$$

with the state equation that can be written as  $h = h(p, T, C^*)$ .

In principle the integration of the equation system (1-2) should not give rise to any numerical difficulty, provided that locally is always  $Da \approx 1$  or that the equation (3) replaces (2) when the equilibrium limit is approached. However, it is not generally possible to localize in advance when and where the three regimes (equilibrium, nonequilibrium, frozen) will occur and consequently the more general nonequilibrium flow model described by (2) has to be adopted everywhere, even in regions where the solution would be better obtained by solving the equation for the equilibrium state (3). Integration of the equation (2) over the entire computational field can lead to different difficulties for equilibrium flow regions and for nonequilibrium regions, that can be summarized as it follows:

- a) in EQUILIBRIUM or near equilibrium flow regions the integration of (2) gives rise to stiffness problems. In particular, when  $Da \rightarrow \infty$  the higher order derivative is multiplied by a vanishing coefficient and a singular perturbation problem occurs.

The system of differential equations (1-2) becomes then stiffer and stiffer as the equilibrium limit is approached. Stability requirements for explicit techniques force the integration step to be very small, i.e., computationally impractical. Larger integration steps are allowed only if:

- implicit schemes are used to satisfy the stability requirements. Nevertheless the solution, even if stable, can be inexact, since the stiffness of the system of differential equations translates into ill-conditioning of the matrix of the discretized equation system. In these cases appropriate implicit algorithms should be adopted.

- the precision of the solution is ensured by a quasilinear behaviour of the variables (as for example in nozzle flows with regular expansions). On the contrary, if the behaviour is strongly nonlinear, a suitable resolution is mandatory: large steps will not provide reliable results even if stable solutions can be obtained.

- b) in NONEQUILIBRIUM FLOWS behind shocks the chemical variables have a boundary layer behaviour. As above referred, their transition from nonequilibrium conditions towards the new equilibrium state occurs in a thin layer with large gradients. This feature leads to the conclusion that large integration steps for the chemical equations are not allowed, even if implicit techniques are adopted. Reliable results can be achieved only if a suitable resolution is used in order to follow accurately the steep gradients of the solution.

In principle numerical problems can occur not only in integrating the chemical equations, but also in coupling the solutions of chemical and gasdynamic equations obtained independently of each other, when iterative procedures are used. Nevertheless in endothermic reactions like those occurring behind shocks, the gasdynamic variables are not strongly affected by the variations of the chemical variables. In particular, they display a quasi-linear behaviour even if the species mass fraction profiles are highly nonlinear as shown in Fig. 1 reporting solutions for dissociating flows. Consequently the integration of the system (1) can be performed by standard approaches on standard meshes, while linear approximation of the gasdynamic values on the smaller grid used for the integration of (2) can be considered satisfactory and does not yield further numerical difficulties.

From the above considerations it turns out that in chemical relaxation layers the integration techniques for the system (1-2) can be based on separate algorithms for chemical and gasdynamic equations and should satisfy two basic requirements, at least for the solution of the energy and species conservation equations: a) algorithms should be in a suitable implicit form to face stiffness when approaching the equilibrium conditions, b) high resolution should be used where strong nonequilibrium conditions occur. Meeting the latter requirement yields very burdensome calculations. As a consequence, integration techniques including front-tracking and grid refinements are mandatory for multidimensional solutions.

### 3. MATHEMATICAL MODELLING

As discussed in [1,10], extending to reacting flows the quasi-linear lambda formulation [11], the most suitable set of dependent variables has been considered to be  $(A, s, q, C)^T$  where, denoting with  $s$  the entropy,  $a$  the frozen speed of sound defined by assuming a frozen composition of the mixture, and  $\gamma$  the associated frozen specific heat rate, the auxiliary variable  $A$  is expressed as

$$A = \frac{a}{\delta}, \quad \delta = \frac{\gamma - 1}{2}$$

Following the procedure described in [1,10] the system of conservation equations (1) can be written in quasi linear form as

$$A_t + \mathbf{q} \cdot \nabla A + a \nabla \cdot \mathbf{q} = \dot{A} \quad (4a)$$

$$\mathbf{q}_t + \mathbf{q} \cdot \nabla \mathbf{q} + a \nabla A - \theta \nabla s = \dot{\mathbf{q}} \quad (4b)$$

$$s_t + \mathbf{q} \cdot \nabla s = \dot{s} \quad (4c)$$

$$c_{it} + \mathbf{q} \cdot \nabla c_i = \dot{c}_i \quad i = 1, N \quad (4d)$$

where  $\theta$  is the temperature and  $\dot{c}_i$  is the rate of production of each  $i$ -species, which takes into account the effects of all reactions, including forward and backward steps. The other source terms  $\dot{A}$ ,  $\dot{\mathbf{q}}$ ,  $\dot{s}$  are given by

$$\begin{aligned} \dot{A} &= a \sum_i P_i \frac{Dc_i}{Dt} \\ \dot{\mathbf{q}} &= \theta \sum_i Q_i \nabla c_i \\ \dot{s} &= -\frac{1}{\theta} \sum_i \mu_i \dot{c}_i \end{aligned} \quad (5)$$

where with  $\mu_i$  the chemical potentials, and with

$$\begin{aligned} P_i &\equiv \frac{1}{2\delta} \frac{\partial}{\partial c_i} \left[ \ln \left( \frac{\gamma R}{\delta^2} \right) \right] - \frac{e_i}{R\theta} \\ Q_i &\equiv c_p \frac{\partial}{\partial c_i} \left[ \ln \left( \frac{\gamma R}{\delta^2} \right) \right] - s_i \end{aligned}$$

In order to have the mathematical model written in form of compatibility equations, the procedure reported in [11] has been followed and extended to chemical nonequilibrium flows. Thus if eqn. (4b) is dot-multiplied by a unit vector  $\mathbf{w}$  and added to (4a), and defining  $\mathbf{n}, \boldsymbol{\tau}$  two unit vectors lying in the  $x$ - $y$  plane, with  $\mathbf{n}$  forming an angle  $\alpha_0$  with the  $x$ -axis, the following general form for the compatibility equations are obtained:

$$\begin{aligned} (A + \mathbf{w} \cdot \mathbf{q})_t + \mathbf{q} \cdot \nabla (A + \mathbf{w} \cdot \mathbf{q}) + a [\mathbf{w} \cdot \nabla A + \mathbf{n} \cdot \nabla (\mathbf{n} \cdot \mathbf{q}) + \boldsymbol{\tau} \cdot \nabla (\boldsymbol{\tau} \cdot \mathbf{q}) + \mathbf{k} \times \mathbf{q} \cdot \nabla \alpha_0] - \\ - \mathbf{q} \cdot (\mathbf{q} \cdot \nabla) \mathbf{w} - \theta \mathbf{w} \cdot \nabla s + ST = 0 \end{aligned} \quad (6)$$

where

$$ST = \dot{A} + \mathbf{w} \cdot \dot{\mathbf{q}}$$

Assuming  $\mathbf{w} = \mathbf{n}, -\mathbf{n}, \boldsymbol{\tau}, -\boldsymbol{\tau}$  and  $\mathbf{w}' = \boldsymbol{\tau}, -\boldsymbol{\tau}, -\mathbf{n}, \mathbf{n}$ , four compatibility equations are obtained in the Riemann variables  $R_j = A + \mathbf{w}_j \cdot \mathbf{q}$ , namely

$$(R_j)_t + \Lambda_j \cdot \nabla R_j + a \mathbf{w}'_j \cdot \nabla (\mathbf{w}'_j \cdot \mathbf{q}) = \theta \mathbf{w} \cdot \nabla s + \dot{R}_j + \beta + F \quad (7)$$

with  $j = 1, 4$  and where

$$\begin{aligned} \beta &= \mathbf{q} \cdot \nabla \alpha_0 & F &= a \mathbf{k} \times \mathbf{q} \cdot \nabla \alpha_0 \\ \Lambda_1 &= \mathbf{q} + a \mathbf{n} & R_1 &= A + \mathbf{n} \cdot \mathbf{q} \\ \Lambda_2 &= \mathbf{q} - a \mathbf{n} & R_2 &= A - \mathbf{n} \cdot \mathbf{q} \\ \Lambda_3 &= \mathbf{q} + a \boldsymbol{\tau} & R_3 &= A + \boldsymbol{\tau} \cdot \mathbf{q} \\ \Lambda_4 &= \mathbf{q} - a \boldsymbol{\tau} & R_4 &= A - \boldsymbol{\tau} \cdot \mathbf{q} \end{aligned}$$

while the corresponding source terms are:

$$\dot{R}_1 = \dot{A} + \mathbf{n} \cdot \dot{\mathbf{q}}, \quad \dot{R}_2 = \dot{A} - \mathbf{n} \cdot \dot{\mathbf{q}}, \quad \dot{R}_3 = \dot{A} + \boldsymbol{\tau} \cdot \dot{\mathbf{q}}, \quad \dot{R}_4 = \dot{A} - \boldsymbol{\tau} \cdot \dot{\mathbf{q}}$$

The redundancy of the above equation system can be circumvented, still following [11], by a suitable recombination of the equations, thus obtaining for the gasdynamic operator the form:

$$2A_i - 2a S_i + 2a \mathbf{q} \cdot \nabla S + \sum_{i=1}^4 A_i \cdot (\nabla R_i - a \nabla S) - 2\mathbf{q} \cdot \nabla A + 2F = A^* \quad (8a)$$

$$2(\mathbf{q} \cdot \mathbf{n})_i + A_1 \cdot (\nabla R_1 - a \nabla S) - A_2 \cdot (\nabla R_2 - a \nabla S) - 2\beta \mathbf{q} \cdot \boldsymbol{\tau} = U^* \quad (8b)$$

$$2(\mathbf{q} \cdot \boldsymbol{\tau})_i + A_3 \cdot (\nabla R_3 - a \nabla S) - A_4 \cdot (\nabla R_4 - a \nabla S) + 2\beta \mathbf{q} \cdot \mathbf{n} = V^* \quad (8c)$$

where the source terms are defined as

$$A^* = \sum_{i=1}^4 \dot{R}_i - 2\dot{A}, \quad U^* = \dot{R}_1 - \dot{R}_2, \quad V^* = \dot{R}_3 - \dot{R}_4,$$

while the chemical operator still holds its compatibility form (4c,d):

$$\begin{aligned} s_i + \mathbf{q} \cdot \nabla s &= \dot{s} \\ C_i + \mathbf{q} \cdot \nabla C &= \dot{C} \end{aligned} \quad (9)$$

#### 4. INTEGRATION TECHNIQUE

Solution of the system (8,9) can be obtained by integrating the fully coupled system, as indicated in [8,17] for one-dimensional flows. Nevertheless, the extension to multidimensional flows [16] requires a tremendous amount of computational work that is actually not needed, since the high resolution required for integrating the finite rate chemistry is not generally needed for the gasdynamic integration. In fact, in the case of endothermic reactions, the strong variations of the chemical variables have a weak overall effect on gasdynamics, whose variables show a quasi-linear behaviour.

A more efficient strategy, suggested in [2] and currently adopted [3,5,10], consists in decoupling the equation system in two parts, the chemical and the gasdynamic operators, and integrating them separately step by step. In particular, the mixture is considered frozen when integrating the gasdynamics equations, while the flowfield is considered frozen when integrating the chemical operator. Details on the two algorithms are given in the following subsections.

##### 4.1 The gasdynamic operator

The system of equations (8) is integrated by an explicit two levels (predictor-corrector) finite difference scheme, with 2nd order accuracy. The integration is performed on body-fitted non-orthogonal coordinate lines. The formulation of the equations written for non orthogonal H-grids is reported in details in [1,10].

The compatibility equations are discretised in the following way:

- the terms containing derivatives of the Riemann variables are discretized in space by means of upwind derivatives computed with two mesh points at each level. The upwind direction is defined by the sign of the relevant coefficient;
- the terms containing the entropy, as well as the chemical source terms, are treated by an upwind discretisation in space according to the sign of the coefficient of the relevant Riemann variable term;
- the metric source term, which appears when the equations are written in a non orthogonal base, is determined analytically.

The shocks are treated by a shock-fitting procedure, according to the wide tested procedure introduced by Moretti. While details about the technique can be found in [11,12], the main features can be summarised as follows.

At the shock the mixture is considered to have a frozen composition, and the jump-relations are solved starting from the values of the gasdynamic variables ahead of the shock, the direction of the normal to the shock profile, and the value of  $R_i$  behind the shock. As a matter of fact, there is at least one Riemann variable on either side of the shock that has the appealing property to be independent of its value on the other side. That variable can thus be computed correctly without using derivatives approximated by differences taken across the shock discontinuity. Consequently, considering for example one-dimensional flows, and calling the two sides ahead and behind the shock  $A$  and  $B$ , respectively, the following quantity can be defined

$$\Sigma = \frac{R_2^B - R_2^A}{a^A}$$

The relative shock Mach number, defined as  $M = (u^A - w)/a^A$  (where  $w$  is the shock velocity), can then be determined by an iterative procedure based on the calculation of

$$\Sigma = \frac{1}{\delta} \left\{ \frac{[(\gamma M^2 - \delta)(1 + \delta M^2)]^{1/2}}{(1 + \delta)M} + \frac{\delta(M^2 - 1)}{(1 + \delta)M} - 1 \right\} \quad (10)$$

Once the relative shock Mach number has been computed, the shock discontinuity is moved in the new appropriate position connected with the integration step used and the values of the speed of sound, the velocity and the entropy behind the shock are obtained by Rankine-Hugoniot relations.

#### 4.2 The chemical operator

The species conservation equations and the energy conservation equation (9) are integrated along the streamlines. The initial values of  $c_i$  and  $s$  should be prescribed at an initial point of the streamline along with the velocity and pressure along the streamline. The initial point is assumed to be the intersection of the streamline with the side of the cell to which the point belongs, and  $c_i$  and  $s$  are obtained by interpolating between the node values.

Since the integration is performed aiming at the steady state solution, the equations can be written in the form:

$$u C_s = \dot{C}$$

with  $C = (c_i, s)^T$

The integration is performed along the streamline in the direction of the velocity by an implicit scheme based on the following discretized form of the equations:

$$u \frac{(C^{n+1} - C^n)}{\Delta z} = \frac{(\dot{C}^n + \dot{C}^{n+1})}{2}$$

where the source term  $\dot{C}^{n+1}$  is expressed by a first order Taylor expansion with respect to the dependent variables.

A variable integration step is implemented by checking the solution obtained with a tentative step. Once the increment  $\Delta C$  has been computed,  $\Delta z$  is considered inappropriate if the new concentration values are negative or if  $\Delta C/C$  is too large or too small. In this case, the discretization step is changed according to the criterion suggested in [8] and integration performed again.

Nevertheless, since the system of finite difference equations can be strongly ill-conditioned near the equilibrium limit, the use of a direct method of solution can still give problems of accuracy, even if instability is avoided by using implicit algorithms. An iterative procedure of the Newton type is thus adopted for solving the system. This procedure takes few iterations and helps both in solving the stiffness near equilibrium, and to increase the accuracy in regions of strong nonlinearities.

#### 5. RESULTS

Some tests relevant both to internal and external flows have been performed. The preliminary results presented here draw heavily on work done in collaboration with G. Moretti, B. Favini, F. Sabetta and M. Valorani.

The test case for internal flows is that proposed by Montagné in [19]. Its geometry consists of two straight, semi-infinite ducts of different cross sectional area connected by straight walls. This test allows to analyze the basic numerical aspects connected with the solution of supersonic intake flowfields, where endothermic reactions occur. Nevertheless a similar example, but with esothermic reactions, has been used by Bussing and Murmann [16] to test their model including the effects of finite rate chemistry to predict the flowfield behind supersonic flameholders.

The domain of integration is defined by the supersonic entrance section, where the flow is in equilibrium, and an exit section with a flow either subsonic or supersonic. The boundary conditions enforce conservation of total enthalpy at the entrance and impose the normal component of the velocity equal to zero on the axis and on the body.

The results presented here are obtained for nonreacting flows treated by a Moretti's shock-fitting technique [12]. As can be seen from Fig. 2, the scheme provides very accurate solutions. They are actually similar to those obtained by shock-capturing techniques, even if a much coarser mesh has been used. In fact, as can be seen by the comparison with the results in [19,16], the shock-capturing techniques do not yield a similar sharp behaviour for the shock profile. This can (unphysically) activate reactions and wrongly affect the overall calculation.

A different application is reported in Fig. 3 and is relevant to hypersonic nonequilibrium flows about blunt bodies. Details about the technique and the results are in [1,18]. The flowfield considered is the region between the bow shock and the body. In Fig. 3a Mach iso-contours are reported for a freestream Mach = 25 and an angle of attack = 30°.

The mass fraction iso-contours of the atomic oxygen are shown in Fig. 3b; the presence of a large nonequilibrium zone can be recognized from their behaviour.

An assessment of the capability of the proposed technique is presented in Fig. 4, showing the temperature behaviour along the stagnation streamline. As the stagnation point is approached, the flow slows down and the mixture composition tends to its equilibrium value, that should in principle be reached at the stagnation point, where the resident time is infinity and reactions have enough time to be completed. As a consequence of this trend, the temperature drops abruptly by ~ 1000°K.

It is practically impossible to obtain the same results without using a suitably small integration step in this zone. Larger steps cannot indeed describe the nonlinear behaviour of the chemical variables, and yield locally unprecise solutions.

#### References

- [1] Valorani M., Onofri M., Favini B.: "On the Solution of Nonequilibrium Hypersonic Inviscid Steady Flows", *AIAA Paper*, 89-0671, 1989.
- [2] Li, C.P., "Time-Dependent Solutions of Nonequilibrium Dissociating Gases Past a Blunt Body", *Journal of Spacecraft and Rockets*, 9, 571-572, 1972.
- [3] Rakich, J.V., Bailey, H.E., and Park, C., "Computation of Nonequilibrium, Supersonic Three-Dimensional Inviscid Flow over Blunt-Nosed Body", *AIAA Journal*, 21, no. 6, 834-841, 1983.

- [4] Li, C.P., "Implicit Methods for Computing Chemically Reacting Flow", NASA TM 58274, September 1986.
- [5] Gnoffo, P.A., Mc Candless, R.S., and Yee, H.C., "Enhancements to Program LAURA for Computation of Three-Dimensional Hypersonic Flows", AIAA Paper, 87-0280, 1986.
- [6] Vincenti, W., Kruger, C., "Introduction to Physical Gasdynamics", Wiley & Sons, New York, 1967.
- [7] Zel'dovich, Y.B., and Raizer Y.P., "Physics of Shock Waves and High-Temperature Hydrodynamic Phenomena", Vol. 2, Academic Press, 1967.
- [8] Lomax, H., and Bailey, H.E., "A Critical Analysis of Various Integration Methods for Computing the Flow of a Gas in Chemical Nonequilibrium", NASA TN D-4109, 1967.
- [9] Le Veque, R.J., and Yee, H.C., "A Study of Numerical Methods for Hyperbolic Conservation Laws with Stiff Source Terms", NASA TM 100075, 1988.
- [10] Onofri, M., and Lentini, D., "Inviscid Hypersonic Blunt Body Flows with Finite-Rate Chemical Kinetics", 7th GAMM Conf. Num. Meth. in Fluid Mechanics, Louvaine-La-Neuve, 1987, published on Notes on Numerical Fluid Mechanics, 20, ed. by M. Deville, Vieweg, 1988.
- [11] Moretti, G., "A Technique for Integrating Two-dimensional Euler Equations", Computers & Fluids 15, 59-75, 1987.
- [12] Moretti, G., "Efficient Euler Solver with Many Applications", AIAA Journal 26, 655-660, 1988.
- [13] Onofri, M., Lentini, D., "Fast Numerical Solver for Transonic Flows", Computers & Fluids, 17, n.1, 1989.
- [14] Candler, G., "On the Computational of Shock Shapes in Nonequilibrium Hypersonic Flows", AIAA Paper 89-0312, 1989.
- [15] Moretti, G., "A fast Euler Solver for Steady Flows", AIAA Paper 83-1940, 6th AIAA CFD Conference, Danvers, MA, 357-362, 1983.
- [16] Bussing, R.A., and Murmann, E.M., "Numerical Investigation of Two-Dimensional  $H_2$ -Air Flameholding over Ramps and Rearward-Facing Steps", J. Propulsion, 3, No. 5, 448-54, 1987.
- [17] Grossman B., Cinnella P. "The Development of Flux Splitting Algorithms for Flows with Nonequilibrium Thermodynamics and Chemical Reactions", AIAA Paper 88-3596.
- [18] Sabetta, F., Favini, B., Moretti, G., Onofri, M., and Valorani, M., "Euler Flows About Ellipse and Double Ellipse", Workshop on Hypersonic Flows for Reentry Problems", INRIA-GAMNI, Antibes, 1990.
- [19] Montagnè J.L., "Second Order Accurate Flux Splitting Scheme in Two-dimensional Gasdynamics", Lect. Notes in Physics 218, 406-11, 1985.

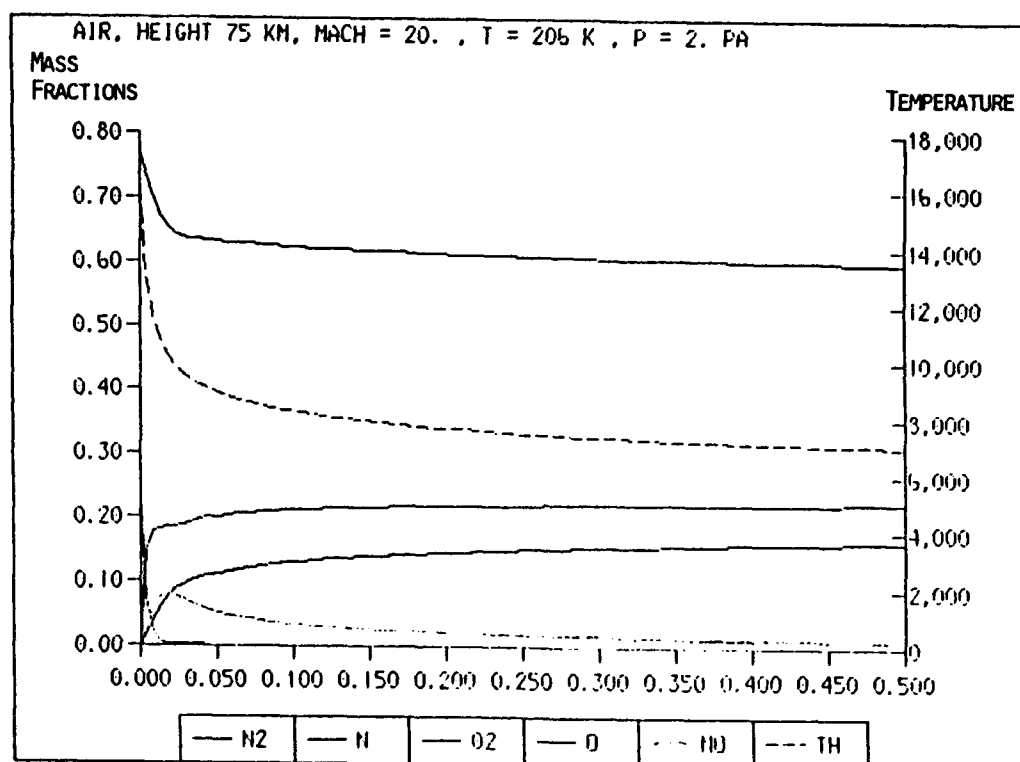
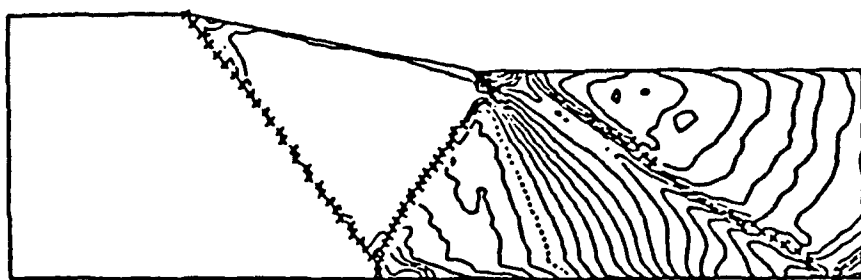
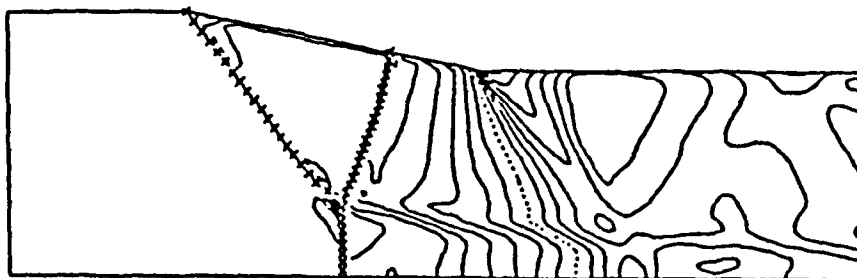


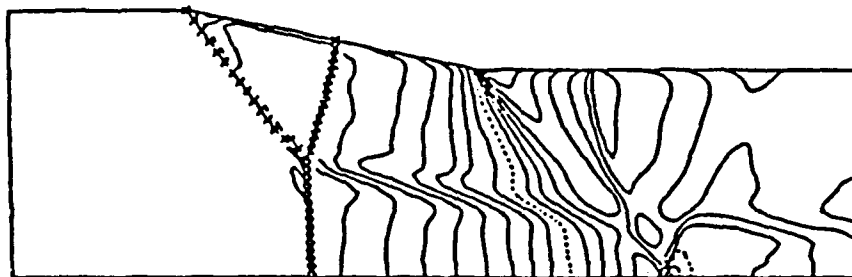
Fig. 1. 1-D solution of temperature and species mass fractions for dissociating air behind a shock wave.



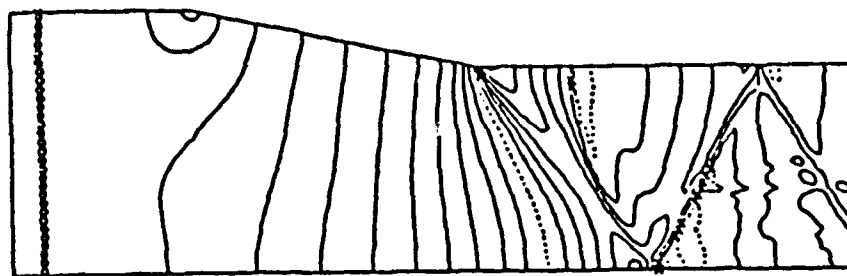
A)



B)



C)



D)

Fig. 2. Transient of a moving shock computed by Moretti's shock-fitting technique.

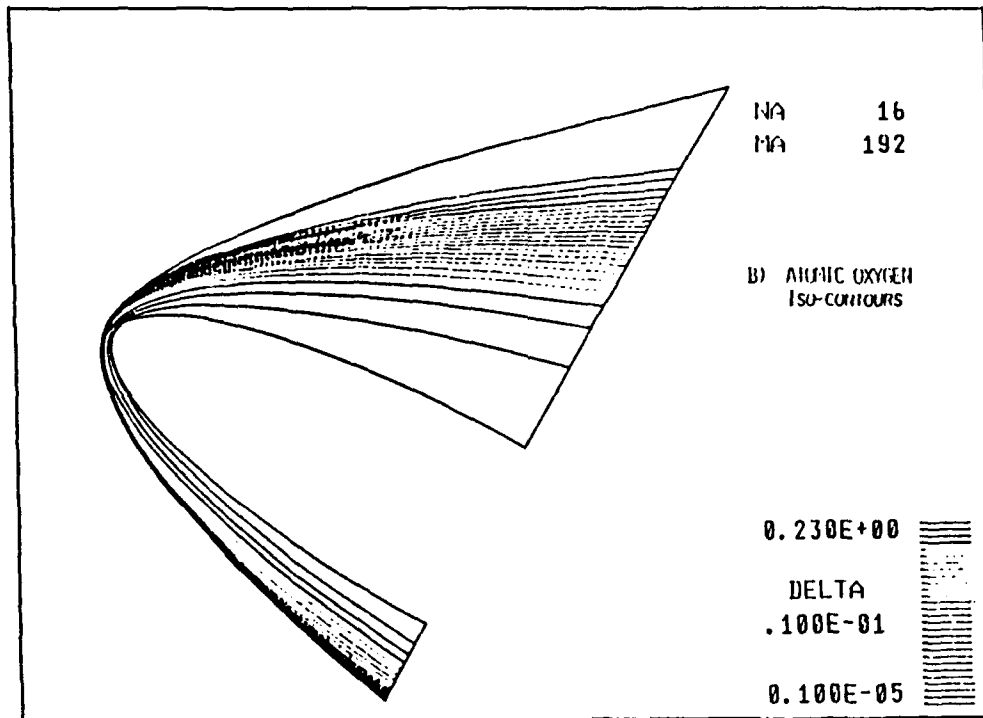
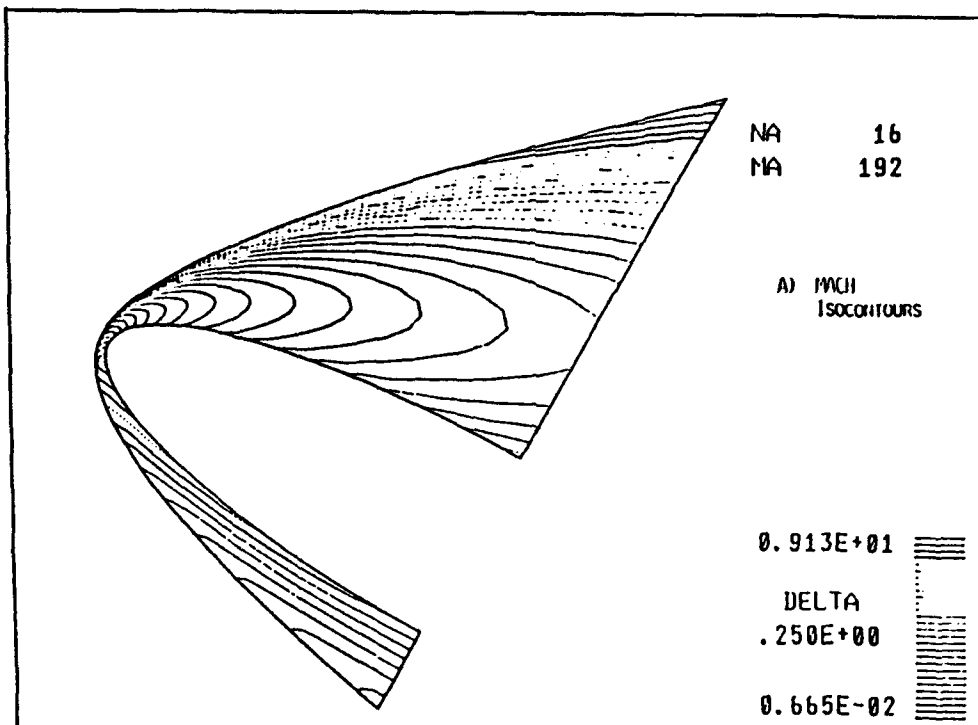
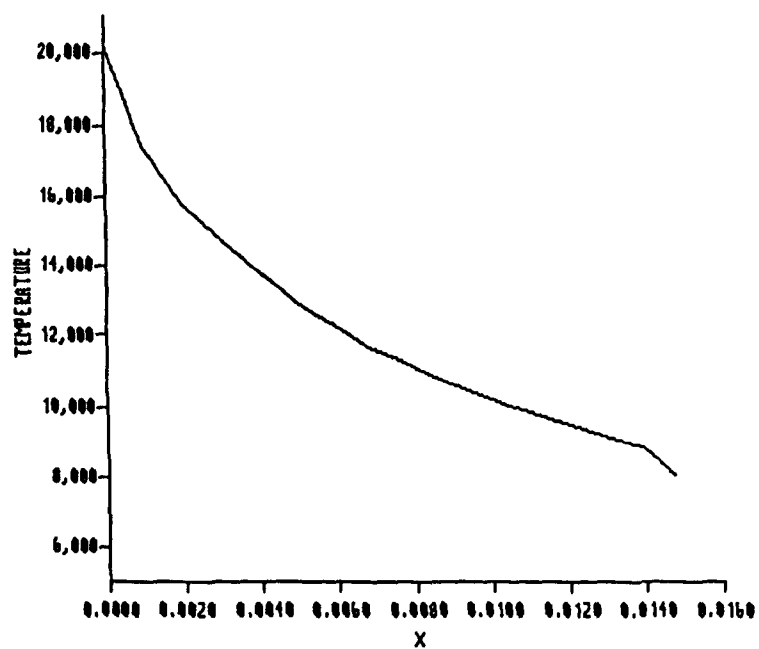
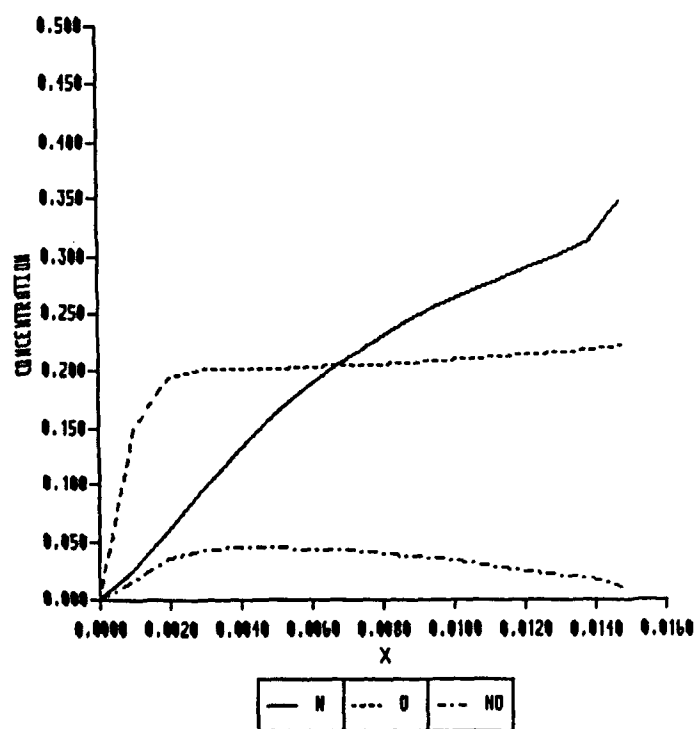


Fig. 3. Hypersonic nonequilibrium flowfield about ellipses:  $M_\infty = 25$ , angle of attack  $\alpha = 30^\circ$ .



a)



b)

Fig. 4. Hypersonic nonequilibrium flowfield about ellipses: temperature and mass fractions behaviours along the stagnation line.





## VISCIOUS THREE-DIMENSIONAL ANALYSES FOR NOZZLES FOR HYPERSONIC PROPULSION

G.J. Harloff, D.R. Reddy, and H.T. Lai  
Sverdrup Technology Inc.  
NASA Lewis Research Center Group  
Cleveland, Ohio 44135

## SUMMARY

E-5267 A Navier-Stokes computer code has been validated using a number of two- and three-dimensional configurations for both laminar and turbulent flows. The validation data covers a range of freestream Mach numbers from 3 to 14, includes wall pressures, velocity profiles, and skin friction. Nozzle flowfields computed for a generic scram-jet nozzle from Mach 3 to 20, wall pressures, wall skin friction values, heat transfer values, and overall performance are presented. In addition, three-dimensional solutions obtained for two asymmetric, single expansion ramp nozzles at a pressure ratio of 10 consist of the internal expansion region in the converging/diverging sections and the external supersonic exhaust in a quiescent ambient environment. The fundamental characteristics that have been captured successfully include expansion fans; Mach wave reflections; mixing layers; and nonsymmetrical, multiple inviscid cell, supersonic exhausts. Comparison with experimental data for wall pressure distributions at the center planes shows good agreement.

## NOMENCLATURE

a sound speed  
 $C_f$  skin friction coefficient  
 $C_h$  heat transfer coefficient  
 $C_p$  specific heat  
 $C_v$  velocity coefficient  
M Mach number  
NPR Nozzle Pressure Ratio  
n nozzle efficiency  
Pr Prandlt number  
 $P_w$  local wall static pressure,  $P_w/P(0)$   
Re Reynolds number  
T temperature  
X streamwise distance  
 $\gamma$  ratio of specific heats

Subscripts:

c combustor exit  
e nozzle exit  
l laminar  
n unit normal  
o freestream condition  
s static condition  
t total condition  
t turbulent  
w wall  
 $\mu$  viscosity  
 $\rho$  density



## INTRODUCTION

Accurate evaluation of nozzle performance is essential to hypersonic propulsion because that performance is highly sensitive to net thrust. Highly integrated fuselage/nozzle configurations may experience complex interaction of shocks, turbulent mixing, differing levels of under/over expansion, and possible boundary layer separation. To simulate these complex interactions, the full Navier-Stokes equations need to be solved and the appropriate computer code carefully calibrated before it can be applied to the hypersonic nozzle flow field. The goal of the current study is to validate the PARC3D code over a range of flowfield conditions and to examine the flow physics and overall nozzle performance over a wide range of flight conditions. The PARC3D code solves the full, three-dimensional Reynolds averaged Navier-Stokes equations in strong conservation form with the Beam and Warming approximate factorization algorithm; the implicit scheme uses central differencing for a curvilinear set of coordinates. The code was originally developed as AIR3D by Pulliam and Steger;<sup>1</sup> Pulliam later added Jamison's artificial dissipation and called it ARC3D.<sup>2</sup> Cooper<sup>3</sup> then adapted the ARC3D code for internal propulsion and renamed the code PARC3D.

### Code Validation

To gain confidence with the PARC3D code simulating the interaction phenomena characteristic of hypersonic nozzle flow, experimental data were selected for code validation as follows: a two-dimensional shock boundary layer interaction at Mach 14 (Holden<sup>4</sup>), and a Haack-Adams body (Allen<sup>5</sup>) with a favorable pressure gradient at Mach 3. Previous configurations examined at NASA Lewis by Reddy and Harloff<sup>6</sup> include: a two- and a three-dimensional hypersonic nozzle at  $M_0 = 5$ , for which comparisons were made with computations of Spradley<sup>7</sup> and others; and a three-dimensional corner flow configuration at  $M_0 = 2.94$  of Oskam et al.<sup>8</sup> The Reddy and Harloff<sup>6</sup> study provided confidence in the PARC codes for a variety of complex shapes and high speeds.

### Two-Dimensional Shock-Boundary Layer Interaction at Mach 14

The two-dimensional experimental data<sup>4</sup> at Mach 14 are used as the first test case. The flat plate length was 1.44 ft, the ramp angle was  $18^\circ$ , and the ramp length was 1.14 ft. The Reynolds number per foot, based on total conditions, was  $32 \times 10^6$  and the computational grid  $399 \times 99$ . The predicted surface pressure coefficient and skin friction are compared to the test data (Figs. 1 and 2): good agreement for both is evident. The predicted negative skin friction for the separated zone is also in good agreement with experiment. As the boundary layer in the experiment was laminar, this study validates the code at hypersonic conditions for laminar flow.

### Haack-Adams Body at Mach 3, Turbulent

The axisymmetric Haack-Adams body,<sup>5</sup> was 3 ft long, had a length to diameter ratio of 10, and a base to maximum diameter ratio of 0.532. The freestream Mach number was 2.96 and the Reynolds number based on static conditions  $0.1 \times 10^6$  cm. Detailed velocity measurements were made at 7 axial stations. Comparison of measured and computed velocity profiles at stations 2 and 7 (Figs. 3 and 4) are in excellent agreement with each other. Axial stations shown in Figs. 3 and 4 were at 0.28 and 0.97 of the body length, respectively. The streamwise pressure gradient is favorable for this configuration, which is similar to the nozzle flow environment. The computed  $C_f$  (Fig. 5) shows excellent agreement with experimental data. This study validates the Baldwin-Lomax turbulence model used in the PARC3D code for attached axisymmetric flow at a single Mach number.

## NOZZLE FLOWFIELD CALCULATIONS

### Two-Dimensional Flowfield Calculations, Mach 5, Laminar

A generic three-dimensional nozzle<sup>7</sup> is shown schematically in Fig. 6. Its length was six entrance nozzle heights, the upper wall has a  $20^\circ$  slope, the lower splitter length was three. The lower wall was horizontal up to one, where the wall expands at a  $6^\circ$  angle. The flow was assumed to be laminar. The grid used was  $199 \times 99$ .

The nozzle entrance flow was assumed to be uniform, and the ratio of specific heats 1.27 for both streams, the nozzle entrance velocity 1610 m/sec., the static pressure  $9206 \text{ N/m}^2$ , the static temperature  $2311^\circ \text{K}$ , and the Mach number 1.657. The corresponding freestream values were: 1765 m/sec,  $506 \text{ N/m}^2$ ,  $261^\circ \text{K}$ , and 5.0, respectively. Upper wall static pressures and values from the GIM code, the Seagull code,<sup>9</sup> and the Method of Characteristics (MOC)<sup>9</sup> are shown in Fig. 7. Pressures near the nozzle entrance are in agreement with the GIM results, but are higher in the aft region. The inviscid results of Seagull and MOC lie between the current viscous solution and the GIM solution in this region. The predicted flowfield is presented in terms of Mach number in Fig. 8. The contact surface between the nozzle flow and the freestream deflects downward, as is evident in the total pressure contour plot and the velocity vectors.<sup>9</sup> Three-dimensional calculations were also performed for this nozzle.<sup>6</sup>

## Two-Dimensional Flowfield, Mach 3 to 20, Turbulent

Figure 9 shows the nozzle geometry used in this study. The initial divergence angle is about  $37^\circ$ .

### Freestream and Combustor Exit Properties

The ratio of specific heats,  $\gamma$ , and the gas constant of the combustor exit are considered constant throughout the entire flowfield (Table I). Because the static nozzle entrance Reynolds numbers, based on nozzle entrance height, are such that turbulent flow is expected for the entire range of Mach numbers studied, turbulent flow is assumed in the whole flowfield.

### GRID

The grid used was  $199 \times 129$ , uniform in the x-direction (Fig. 10). Grids were clustered by being stretched by hyperbolic functions near the upper and lower walls to resolve the boundary layers, as well as downstream of the cowl to resolve the shear layer. The grid was not adapted to the shear layer location, although this has been accomplished by the authors in previous unpublished studies, which indicated that the present grid was sufficient to capture the flowfield.

Boundary conditions are uniform inflow and extrapolated outflow properties for supersonic flow. The supersonic/hypersonic inflow boundary above the exit was assumed to be uniform. For subsonic outflow, the pressure is imposed by the sublayer approximation. These boundary conditions are ideal and more realistic inflow profiles can be accounted for. The wall temperature is assumed to be constant at  $1750^\circ\text{R}$ .

### Mach 3 Flowfield

Velocity vectors for  $M_0 = 3$  (Fig. 11) show that the flow is overexpanded and a shock propagates from the cowl lip to the upper nozzle wall. The exhaust flows along the upper nozzle wall similar to a wall jet. A slight separation occurs on the upper wall ahead of the shock (discussed below in terms of  $C_p$ ). The Mach number contours are shown in Fig. 12. Due to the overexpanded flow at the end of the lower cowl, the shear layer turns upward, which causes a shock to form above it.

Total pressure contours shown in Fig. 13 illustrate the gradient in nozzle and freestream total pressure across the shear layer.

The divergence of velocity provides a scalar measure of density gradients such that compressive and expansive regions of the flow can be visualized as dark and light regions respectively (Fig. 14). The deflection angle of the shock from the cowl end to the upper nozzle wall is about  $39^\circ$  and the Mach number in front of the oblique shock is about 3.5. After the shock reflects off the boundary layer, it propagates in the downstream direction. The boundary layer separates on the upper nozzle wall ahead of the incident shock (further illustrated with the skin friction prediction below). Details of this region show a small region of reverse flow. As the shock interacts with the wall boundary layer, it initially reflects at a sharp angle. As the flow moves over the surface of the separation bubble, it is turned less, as shown by the decrease in magnitude of the compression. At the aft end of the separation bubble, the flow is again turned at a sharp angle and coalesces into the reflected shock downstream of the separation. Below the cowl, a shock emanating from the leading edge of the cowl is observed, and is caused by flow deflection from the boundary layer along the lower cowl wall. The expanding region of the flow downstream of the cowl is also observed.

Wall pressures as a function of  $X$  for the three nozzle wall surfaces (Fig. 15(a)) illustrate that the wall pressure initially decreases with increasing  $X$  for both upper and lower nozzle walls. The interior nozzle shock intersects the upper nozzle wall at about 2.8 ft, as evidenced by the marked pressure rise there. Because the pressure beneath the cowl is greater than the pressure in the nozzle, the shock forms in the nozzle.

Wall skin friction values are shown in Fig. 15(b) for the three surfaces. The skin friction on the upper nozzle wall becomes negative at about 2.8 ft, indicating a small region of reverse flow. The skin friction of the upper cowl wall is slightly higher than that of both the upper and lower walls. The heat transfer for the upper and lower nozzle walls is similar over the cowl's length (Fig. 15(c)) while the rise in the heat transfer coefficient is observed at  $X = 2.8$  ft, where the boundary layer flow separates. In the nozzle the heat transfer is positive, indicating hot gas and a cold wall, but below the cowl the heat transfer coefficient is negative, indicating the reverse.

A large scale separation on the upper nozzle surface is predicted for laminar flow (Fig. 16), whereas the turbulent computations show a small separation.

### Mach 6 Flowfield

Figure 17 shows the velocity vectors for  $M_0 = 6$ . The flow, slightly overexpanded at the cowl exit, expands behind the cowl by means of an expansion fan. The wake is deflected upward, as indicated by the velocity vector angles and the position of the velocity shear layer. No reverse flow at the upper boundary is indicated. Mach number contours for the flowfield (Fig. 18) also indicate the location of the shear layer while Fig. 19 shows its upward deflection as well as total pressure contours.

Wall pressures (Fig. 20(a)) show that the interior wall pressure is overexpanded. The wall skin friction and heat transfer values are shown in Figs. 20(b) and (c) respectively.

### Mach 10 Flowfield

The exhaust flow is underexpanded at Mach 10 as indicated by the downward deflection of the nozzle flow (Fig. 21). There are no indications of shocks inside the nozzle, but a shock propagates from the lower cowl lip downward due to the underexpansion of the flow (Fig. 22). The total pressure contours at  $M_0 = 10$  (Fig. 23) show that the flow is underexpanded and that the shear layer is deflected downward. The shock deflection angle is about  $18^\circ$ . Pressure is constant on the lower wall (Fig. 24(a)),  $C_f$  and  $C_h$  wall values are also shown in Fig. 24.

### Mach 20 Flowfield

The velocity vectors are deflected downward aft of the cowl due to underexpansion (Fig. 25) which causes a shock to propagate from the lower cowl downward. The lower cowl leading edge shock merges with the trailing edge shock about 26 percent of a cowl length downstream of the cowl.

The flow along the curved upper nozzle surface turns and compresses, like flow along a curved ramp, and a curved shock forms inside the nozzle. An upwardly deflected shock behind the end of the upper nozzle wall is evident (Figs. 25 and 26). The Mach number contours are shown in Fig. 26. Total pressure contours (Fig. 27) show the downward deflection of the shear layer. The shock is detached from the lower side of the cowl due to the boundary layer there. The shock from the leading edge of the cowl merges with the shock from the aft end about 18 percent of the length downstream of the cowl. An interior shock along the upper wall turns the flow towards the horizontal axis. This interior shock is typical at overspeed conditions. The nozzle flow is underexpanded (Fig. 28(a)); the upper wall pressure does not follow the lower nozzle wall pressure but instead increases the full length of the nozzle, even inside the cowl. The  $C_f$  and  $C_p$  values are shown in Fig. 28(b) and (c) respectively.

A perfect gas model has been assumed in these calculations, and the constant ratio of specific heats ( $\gamma$ ) has been varied with flight Mach number. This assumption may not be as valid at high Mach numbers as at low Mach numbers and should be further investigated.

### Nozzle Performance

The adiabatic nozzle efficiency,  $N$ , is the ratio of the nonisentropic to isentropic expansion enthalpies between the combustor exit,  $c$ , and the nozzle exit,  $e$ . The velocity coefficient,  $C_v$ , is the ratio of the actual to the isentropic velocity and is the square root of the efficiency. The velocity coefficient increases with Mach number up to  $M_0$  of 10 but decreases at  $M_0$  of 20. For example,  $C_v$  is 0.93 at  $M_0$  of 3, 0.98 at  $M_0$  of 6, 1.0 at  $M_0$  of 10 and 0.94 at  $M_0$  of 20. The reported  $C_v$  values peak at  $M_0$  of 10 because the nozzle design Mach number is close to 10 and the  $M_0$  20 is an overspeed condition for this nozzle. The frozen gas assumption has been successfully used for ramjet, rocket, and hypersonic wind tunnel nozzle flows. Because these values might be different with chemistry accounted for, the above  $C_v$  values should be considered as relative. For example, Ref. 11 has reported that finite-rate chemical recombination of dissociated species affects scramjet nozzle force coefficients, at Mach 20, and that the nozzle flow analyzed was in vibrational equilibrium.

### Three-Dimensional, Single Expansion Ramp Nozzle, NPR = 10, Laminar

Three-dimensional solutions of a single expansion ramp nozzle are performed to simulate the nonaxisymmetric nozzle flowfield in both internal/external expansion regions and the exhaust plume in a quiescent ambient environment. Two different configurations of the nozzle at NPR = 10 are examined. They were selected from the single expansion ramp nozzles experimentally investigated by Re and Leavitt<sup>11</sup> to analyze the effects of various geometrical parameters and pressure ratios on the nozzles' static performance.

The present converging/diverging nozzle has a long upper surface functioning as an external expansion ramp, with a rectangular cross-section in the internal nozzle. The edge of the flat sidewall is highly skewed at the nozzle exit to connect the upper and

lower surface lips. The flow generated by large streamwise pressure differences expands from near reservoir conditions through the nozzle and exhausts supersonically into the quiescent air. The resulting flowfield is characterized by flow expansion inside the nozzle and by exhaust plume interaction with the ambient environment. In particular, a strongly interactive flow structure containing a normal shock, expansion/compression wave reflection, and separation can occur along the external expansion ramp of the upper surface. Around this section, the free shear layer emerging from the lip of the shorter lower surface acts as an artificial nozzle wall, and its trajectory shape can alter the nature of the flow, depending on the ambient conditions below it. The wave structure initiated by the shear layer may include an oblique shock or an expansion fan emanating from the lower nozzle lip. This shear layer can also deflect the flow upwards at a high angle to interact with the upper boundary layer.

A similar pattern exists in the spanwise direction, where the sidewall creates a vertical free shear surface starting at the skewed nozzle exit. At high Reynolds number, the shear layer behind a sharp or blunt trailing edge may not be stable; however high Reynolds number interaction of the free shear layer is even more unstable in a quiescent external environment than in a subsonic or supersonic external stream. Consequently, a steady state solution may not be possible for certain flows with a quiescent external stream. The three-dimensionality of the flowfield, its unsteadiness, and stability considerations are some of the complications of the present problem, although only steady-state solutions are computed.

Converged solutions are compared with the experimental measurements for the pressure distributions on the upper and lower nozzle surfaces. The configuration of the nozzle (Fig. 29) has an upper two-dimensional flap and a shorter, lower two-dimensional flap, both flat in the spanwise direction. Part of the upper flap extending from the throat area functions as an external expansion ramp. The edge of the vertical sidewall is highly inclined. This arrangement gives a rectangular cross section parallel to the exit plane aligned with the tilted edge. Intersections of the tilted edge and the upper and lower nozzle walls normally occur upstream of the ends of the wall surfaces.

Two nozzle configurations are examined (Fig. 30) with identical lower flaps and sidewalls and a nozzle aspect ratio of width to height of 4, with the height measured at the throat. Note that the flow expands to a lower pressure in case 2 because the external expansion ramp is longer. The flat sidewall is assumed to have a very thin thickness (0.0058 cm).

All boundary conditions are treated explicitly. Since a plane of symmetry exists in the spanwise  $z$ -direction, only half of the nozzle flowfield is computed. Symmetry conditions are specified on this centerplane. No-slip velocity and an adiabatic wall temperature are imposed on the nozzle surfaces. In the farfield, still air conditions at 101.3 kPa and 300 °K, are fixed at the upper and lower boundaries in the vertical  $y$ -direction sufficiently far away from the nozzle; similar boundary conditions are imposed at the farfield in the spanwise direction. In the streamwise  $x$ -direction, a stagnation pressure of 1013 kPa and a stagnation temperature of 300 °K are specified at the nozzle entrance. Other variables at this location are computed using the isentropic relationships and a characteristic-like condition extrapolated from the interior. At the outflow boundary, streamwise flux gradients are assumed to be negligible.

For normalization, stagnation quantities at the nozzle entrance are taken as the reference variables. The nozzle throat height and the speed of sound are the reference length and velocity, respectively. The Reynolds number is computed based on these values. The reference temperature, pressure and length are taken to be 300 °K, 1013 kPa, and 2.54 cm, respectively. The corresponding Reynolds number is 5.618 million.

## Grid

The simulated flow includes the nozzle interior and exterior, which contains the downstream exhaust. Since the nozzle has a symmetrical plane at the middle in the spanwise direction, the spanwise regions include the interior half of the nozzle and the flow exterior to the sidewall. The complete domain is then divided correspondingly into subsections to simplify grid generation using an algebraic technique. To resolve the viscous layers, hyperbolic tangent functions are used to cluster grid points in regions near the walls. Patching these separate segments produces a final sheared grid in Cartesian coordinates.

Figure 31(a) illustrates a view of the nonuniform grid in the  $x$ -,  $y$ -plane along the streamwise direction. The grid clusters near the wall surfaces to the exhaust region behind the inclined nozzle exit. Figure 31(b) presents a detailed view of the same grid showing a high degree of grid nonorthogonality, particularly next to the exit. The skewed grid lines result since one of the vertical curvilinear coordinates aligns with the sidewall tilted edge to simplify the application of the boundary conditions. Spanwise views of the grid distribution in the  $y$ - $z$  plane are shown at two different axial locations inside the nozzle (Fig. 32(a)) and downstream in the exhaust plume, (Fig. 32(b)). The vertical coordinates cluster about the interior and exterior surfaces of the sidewall, and are not on a plane with constant  $x$ -coordinate.

The flow starts from the nozzle entrance,  $X = 0$ , where the total pressure is prescribed, expands through the converging/diverging and external ramp sections, and

exhausts into the downstream low pressure region, which is bounded by quiescent boundaries far from the nozzle. The farfield computational boundaries are approximated at distances of 25, 10, and 8 characteristic lengths in the x-, y- and z-directions, respectively. The solutions discussed below have been computed on a 135 by 120 by 50 grid for both cases. Of these, 60 by 40 by 30 grid points are employed in the nozzle interior. The smallest grid is on the order of 0.001 near the wall regions for the y- and z-directions. This grid gives typically two to four subsonic points in the dominant supersonic viscous layers. For the x-direction, the grid is slightly refined near the nozzle exit and is on the order of 0.01. In the figures discussed below,  $i$  and  $j$  indicate the streamwise and spanwise grid indices respectively, while  $x$  and  $z$  represent the corresponding nondimensional coordinates.

#### Case 1:

The converged result of the first case is presented with Mach number, density, and pressure contours at several streamwise and spanwise cross sections; contours are in equally spaced increments over the entire range of values unless otherwise noted. Mach number contours on the center plane (Fig. 33(a)) show a typical exhaust plume containing a steady-state, multiple inviscid cell pattern in the supersonic exhaust core. The flow is sonic at the throat and highly supersonic at the exit. The first inviscid cell appears very irregular and is bounded by an expansion/compression wave system. Because of the inclined trajectory of the exhaust plume, the Mach waves emanate from the ends of the flap surfaces, where the upper and lower free shear layers, which depart from the nozzle walls at different angles, become the expansion and compression ramps. The lower shear layer is very diffusive and largely due to lack of grid resolution along this shear layer. The first cell has an average Mach number of 2.7, while the Mach numbers near the cell centers of the next two cells are about 2.3 and 2.0, respectively, showing a gradual decay of the core center velocities. The core cells reduce in size and numbers towards the sidewall, (Figs. 33(b) to (d)) whose effects become pronounced (Fig. 33(d)) with the appearance of the initial vertical shear layer. The flow inside the nozzle has very thin viscous layers next to the walls, particularly on the lower surface, and thus appears predominantly inviscid.

The spanwise contour views are shown in Figs. 34(a) to (d). Figure 34(a) presents Mach contours at an axial station in the nozzle area, where the clustered regions indicate the upper, lower, and sidewall surfaces. The contours in Fig. 34(b) are located on the external expansion ramp. The structure includes the lower shear, thin vertical shear, and upper boundary layers. In the exhaust region, these free shear layers become thicker with downstream distance (Figs. 34(c) to (d)) in which the plume boundaries are evident. The density contours at the center plane and on the plane next to the sidewall (Figs. 35(a) to (b)) show a pattern very much like Mach contours but out of phase. Density variation is also small across both shear layers.

This same variation occurs for the pressure (Fig. 36) which decays quickly to the ambient value. The contours (Figs. 35(a) and 36) show a weak wave system in the exhaust core, particularly after the first inviscid cell. Figures 37(a) and (b), and 38 depict typical density and pressure contours in the spanwise direction, plotted with smaller increments for clarity. Note that large variations in density and pressure occur inside the nozzle, and the exhaust flow does not deviate much from the perfectly expanded condition. Finally, comparison made with the measured data (Figs. 39(a) to (b)) for the upper and lower surfaces in the center plane show good agreement for wall pressure distributions.

#### Case 2:

Solution of the second case is also presented in terms of the contours of the flow variables. Figures 40(a) to (d) depict the basic flow pattern of the supersonic exhaust into quiescent air. For this geometry, the upper plume boundary is well-defined by the very thin free shear layer which follows the upper nozzle contour, and remains nearly at this height downstream. The other shear layer is also deflected downwards and is diffusive. Although the flow expands to about the same maximum Mach number indicated in case 1, the supersonic inviscid core (Fig. 41(a)) is more extensive. As a result, the fluctuating decrease of the core center velocities becomes smaller. Moreover, the flow is highly asymmetric along the exhaust center line. The sidewall (Fig. 41(d)) causes the initial development of the vertical shear layer, which curves irregularly towards the center plane as it progresses downstream since the spanwise velocity component is large and positive in the initial region of the vertical shear layer, but becomes small and negative downstream. The flow behind the inclined exit consists of two small, separate supersonic regions next to the exit plane.

Spanwise views of Mach contours at various axial locations are given in Figs. 41(a) to (d). The interior cross-sectional view (Fig. 41(a)) shows a thicker expansion layer in the lower half of the nozzle. Figures 41(b) to (d) depict the contours at the axial plane on the external ramp region and the planes in the exhaust region. Density and pressure contours in the streamwise planes are shown in Figs. 42(a) to (b), and 43. A clear indication of the compression/expansion wave reflection can be observed at the first cell boundary Figs. 42(a) and 43 after which the wave structure then becomes very weak with downstream distance. Spanwise variations of density and pressure are illustrated in Figs. 44(a) to (b) and 45. Comparison between the numerical prediction and experiment (Figs. 46(a) to (b)) show very good agreement for the wall pressure distributions in the center plane.

## SUMMARY OF RESULTS

The PARC3D computer code has been validated using a number of two- and three-dimensional configurations with both laminar and turbulent flows. The validation data used included wall pressures, velocity profiles, and skin friction. The validation data cover Mach 3 to 14 with shock-boundary layer interaction and/or boundary layer separation.

Two-dimensional nozzle flowfields were computed and overall performance for a representative scramjet nozzle from Mach 3 to 20. Matching the external pressure at the cowl exit is necessary to avoid waves in the nozzle. At  $M_0$  of 3 and 6 the nozzle flow is overexpanded and shocks are inside the nozzle, while the shear layer is deflected upward. The laminar  $M_0 = 3$  nozzle flowfield showed a massive separation on the upper ramp surface, whereas the turbulent solutions showed only a small separation. At  $M_0$  of 10 and 20 the nozzle flow is underexpanded and shocks are outside the nozzle, while the shear layer is deflected downward. At  $M_0 = 20$ , a shock forms inside the nozzle along the upper wall to deflect the flow from the radial to the horizontal direction.

Three-dimensional solutions were obtained for two asymmetric, single expansion ramp nozzles at a pressure ratio of 10. The computed flow consists of the internal expansion region in the converging/diverging sections and the external supersonic exhaust in a quiescent ambient environment. The fundamental characteristics of the flowfields for the prescribed flow conditions were predicted successfully and include expansion fans; Mach wave reflections; mixing layers; and nonsymmetrical, multiple inviscid cell, supersonic exhausts. Comparison with experimental data for wall pressure distributions at the center planes shows good agreement.

## ACKNOWLEDGEMENTS

This work was supported by the NASA Lewis Research Center under contracts NAS3-24105 and NAS3-25266.

## REFERENCES

1. Pulliam, T.H.; and Steger, J.L.: Implicit Finite-Difference Simulations of Three-Dimensional Compressible Flow. AIAA J., vol. 18, no. 2, Feb. 1980, pp. 159-167.
2. Pulliam, T.H.: Euler and Thin Layer Navier-Stokes Codes: ARC2D, ARC3D. Notes for Computational Fluid Dynamics User's Workshop, The University of Tennessee Space Institute, Tullahoma, TN, UTSI Pub. E02-4005-023-84, 1984, pp. 15.1-15.85.
3. Cooper, G.K.: The Parc Codes: Theory and Usage. AEDC-TR-87-24, Arnold Engineering Development Center, Arnold Air Force Base, TN, Oct. 1987.
4. Holden, M.S.; and Moselle, J.R.: Theoretical and Experimental Studies of the Shock Wave-Boundary Layer Interaction on Compression Surfaces in Hypersonic Flow. CAL Report No. AF-2410-A-1, Calspan Corp., Buffalo, NY, Oct. 1969.
5. Allen, J.M.: Experimental Preston Tube and Law-of-the-Wall Study of Turbulent Skin Friction on Axisymmetric Bodies at Supersonic Speeds. NASA TN D-5660, 1970.
6. Reddy, D.R., and Harloff, G.J.: Three-Dimensional Viscous Flow Computations of High Area Ratio Nozzles for Hypersonic Propulsion. AIAA Paper 88-0474, Jan. 1988.
7. Spradley, L.W.; Anderson, P.G.; and Pearson, M.L.: Computation of Three-Dimensional Nozzle-Exhaust Flow Fields with the GIM Code. NASA CR-3042, 1978.
8. Oskam, B.; Vas, I.E.; and Bogdonoff, S.M.: Oblique Shock Wave/Turbulent Boundary Layer Interactions in Three Dimensions at Mach 3, Part I. AFFDL-TR-76-48-PT-1, June 1976 (Avail NTIS, AD-A033386).
9. Salas, M.D.; and Hunt, J.L. (NASA Langley Research Center): Private Communications regarding the Langley SEAGULL Code, with L.W. Spradley of Lockheed-Huntsville, June 1977.
10. Rizkalla, O.; Chinitz, W.; and Erdos, J.: Calculated Chemical and Vibrational Non-equilibrium Effects in NASP-type Nozzles. AIAA Paper 88-3263, July 1988.
11. Re, R.J.; and Leavitt, L.D.: Static Internal Performance of Single-Expansion-Ramp Nozzles with Various Combinations of Internal Geometric Parameters. NASA TM-86270, 1984.

TABLE I. - FREESTREAM AND COMBUSTOR EXIT PROPERTIES

$M_O$	$T_{O, R}$	$P_{O, psia}$	$M_C$	$T_{C, R}$	$P_{C, psia}$	$\gamma$	$R, \frac{ft-lb_f}{lb_m \cdot ^\circ R}$
3	390	1.7	1.0	4075	11.9	1.25	62.7
6	393	.4	1.5	4220	10.4	1.19	63.4
10	409	.15	1.9	5403	75.0	1.16	66.0
20	468	.03	4.6	5119	25.9	1.18	88.0

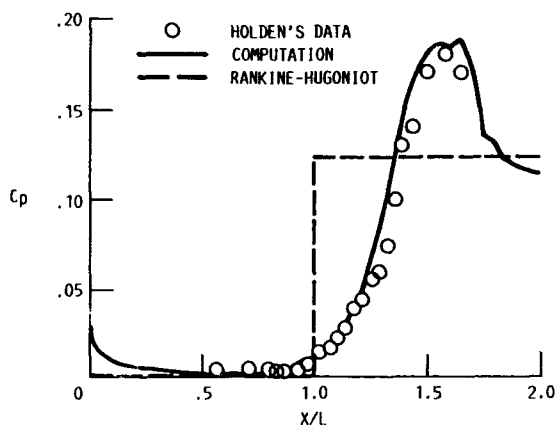
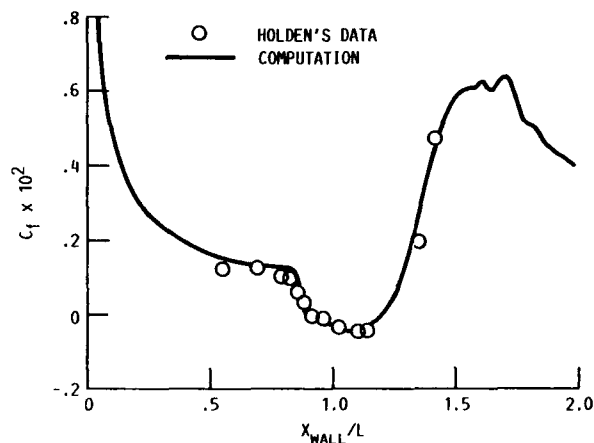
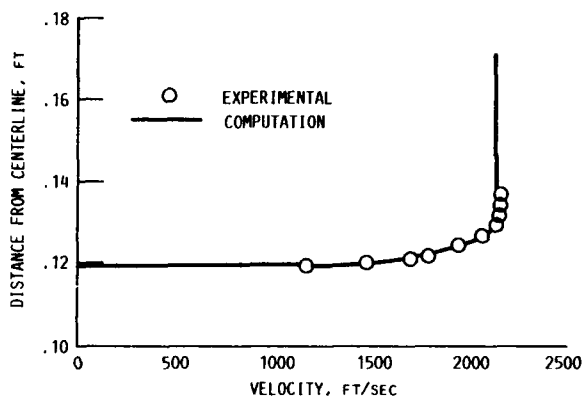
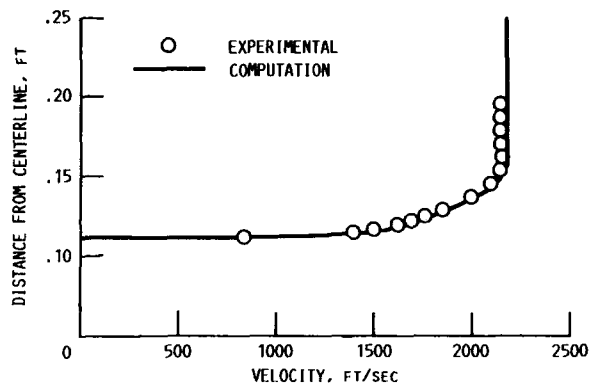
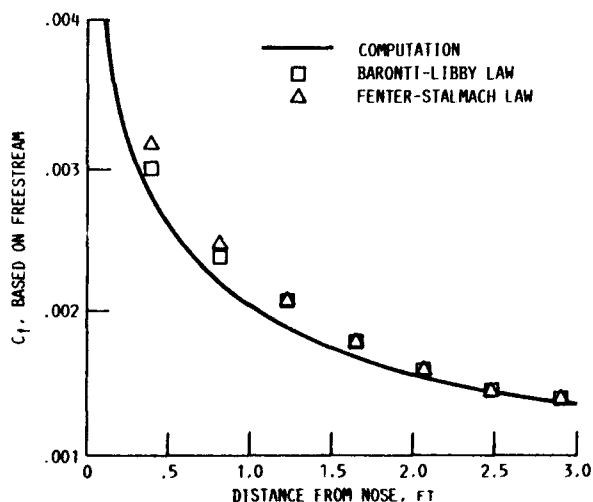
FIGURE 1. -  $C_p$  ON 18 DEGREE RAMP AT  $M = 14.1$ .FIGURE 2. -  $C_f$  ON 18 DEGREE RAMP AT  $M = 14.1$ .FIGURE 3. - HAACK - ADAMS BODY AT MACH 2.96.  
(STATION 2,  $X/L = 0.28$ ).FIGURE 4. - HAACK - ADAMS BODY AT MACH 2.96.  
(STATION 7,  $X/L = 0.97$ ).

FIGURE 5. - HAACK - ADAMS BODY AT MACH = 2.96.

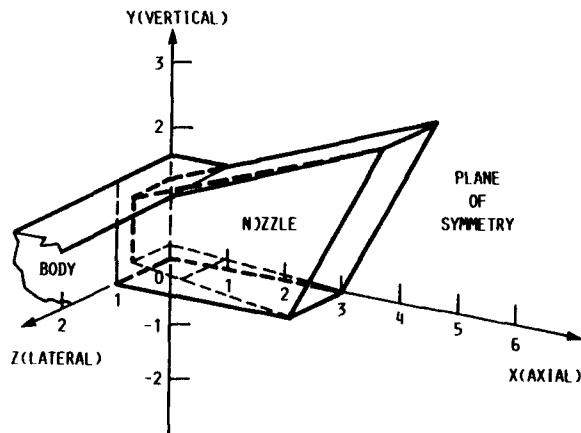


FIGURE 6. - SCHEMATIC OF 3-D NOZZLE.



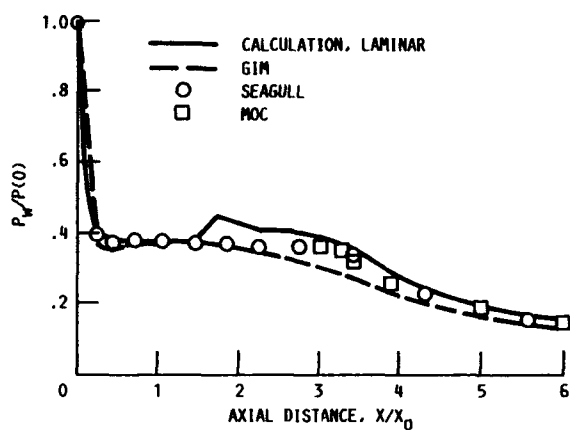


FIGURE 7. - UPPER WALL PRESSURE VERSUS DISTANCE 2-D NOZZLE CALCULATIONS.

$$Y = A_1 + A_2 X + A_3 X^2 + A_4 X^3$$

$$A_1 = .02304$$

$$A_2 = .75459$$

$$A_3 = -.12370$$

$$A_4 = .00600$$

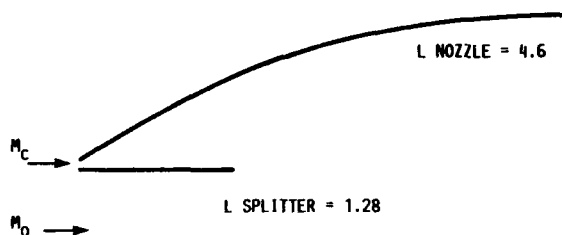


FIGURE 9. - NOZZLE DEFINITION.

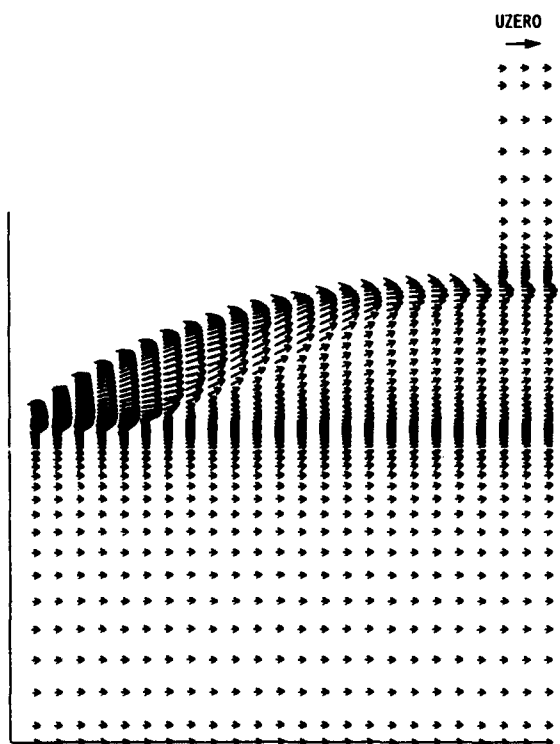


FIGURE 11. - MACH 3, VELOCITY VECTORS.

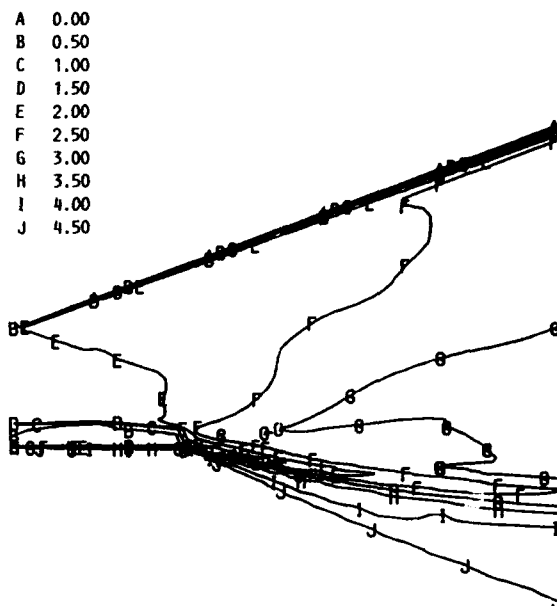


FIGURE 8. - MACH NUMBERS FOR 2-D NOZZLE.

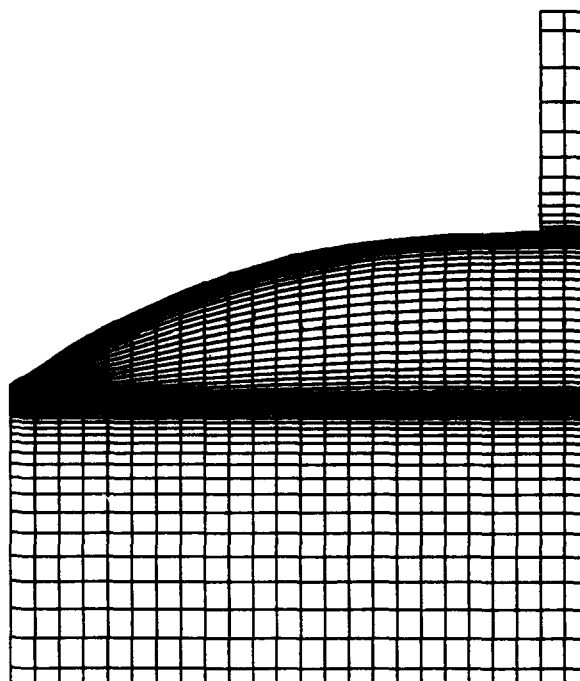


FIGURE 10. - TYPICAL GRID FOR COMPUTATION.

- A 0.00
- B 0.43
- C 0.86
- D 1.29
- E 1.72
- F 2.16
- G 2.59
- H 3.02
- I 3.45
- J 3.88

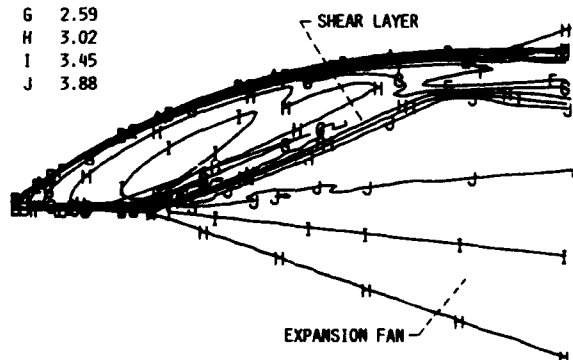


FIGURE 12. - MACH 3, MACH NUMBER CONTOURS.

A	0.00	F	1.75
B	0.35	G	2.11
C	0.70	H	2.46
D	1.05	I	2.81
E	1.40	J	3.16

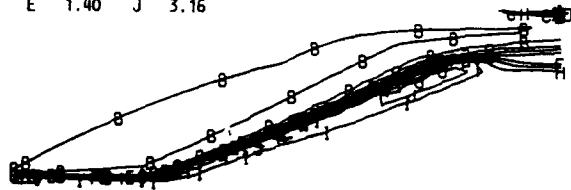


FIGURE 13. - MACH 3, TOTAL PRESSURE CONTOURS.

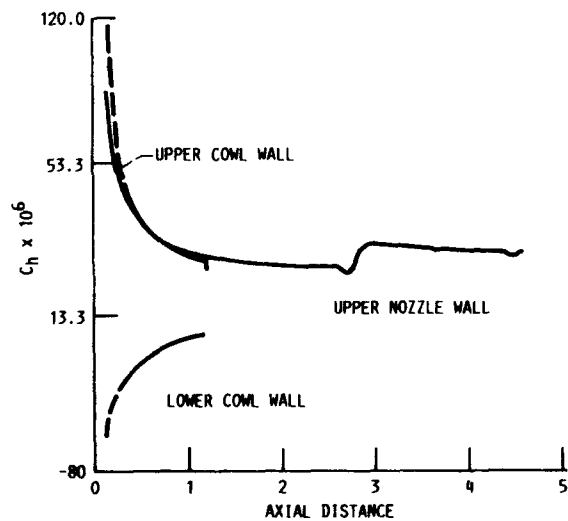
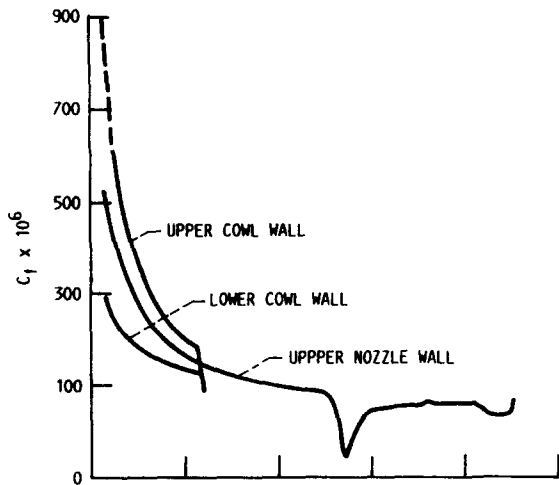
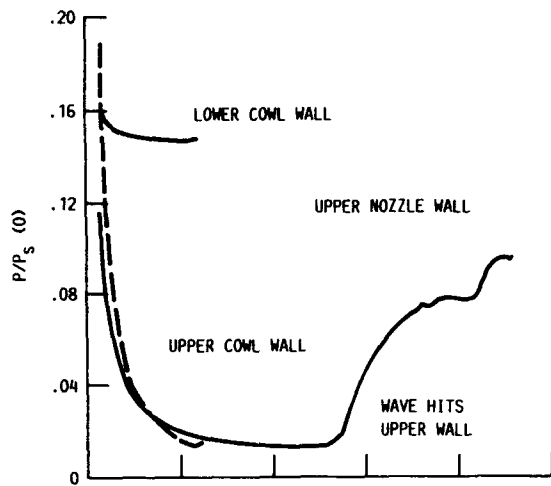
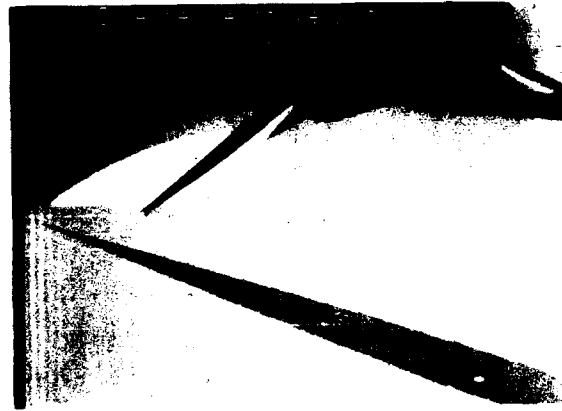
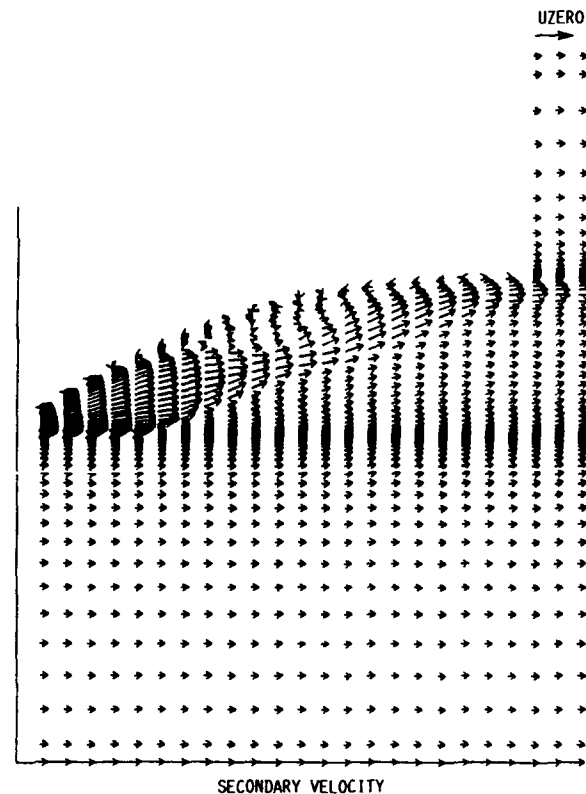
FIGURE 15. - MACH 3,  $P_w$ ,  $C_f$ ,  $C_h$  VERSUS X.

FIGURE 14. - MACH 3, DIVERGENCE OF VELOCITY.

FIGURE 16. -  $M_0 = 3.$ , LAMINAR.

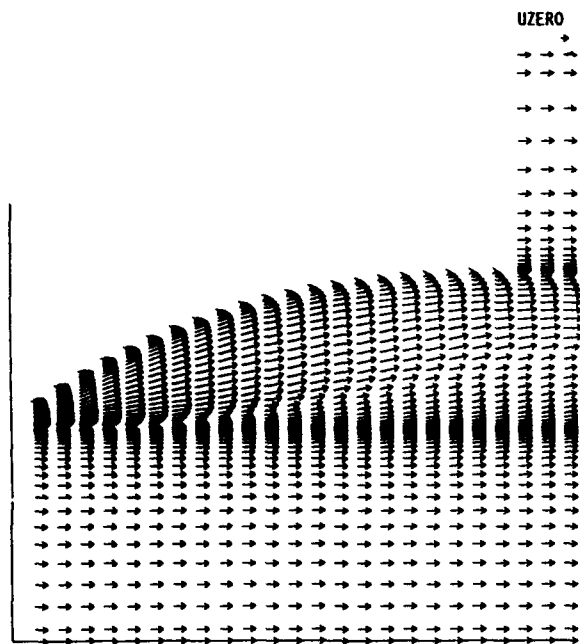


FIGURE 17. - MACH 6, VELOCITY VECTORS.

- A 0.00
- B 0.71
- C 1.42
- D 2.13
- E 2.84
- F 3.55
- G 4.26
- H 4.97
- I 5.68
- J 6.40

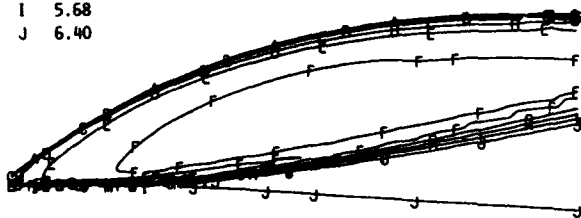
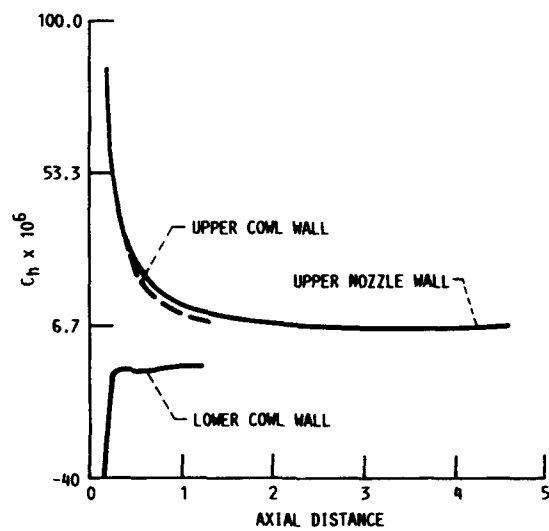
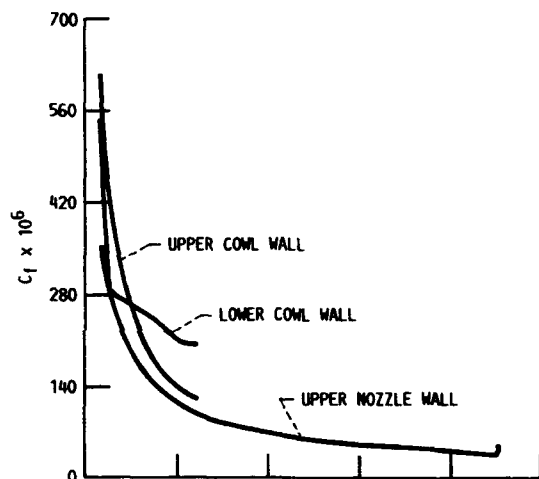
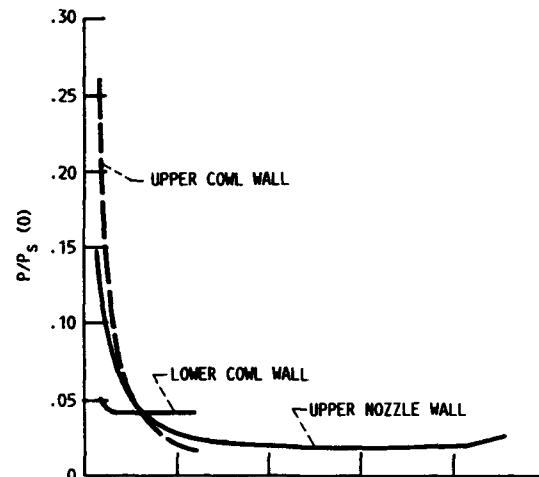


FIGURE 18. - MACH 6, MACH NUMBER CONTOURS.

- A 0.00
- B 15.05
- C 30.11
- D 45.16
- E 60.21
- F 75.26
- G 90.32
- H 105.37
- I 120.42
- J 135.48



FIGURE 19. - MACH 6, TOTAL PRESSURE CONTOURS.

FIGURE 20. - MACH 6,  $P_w$ ,  $C_f$ ,  $C_h$  VERSUS  $x$ .

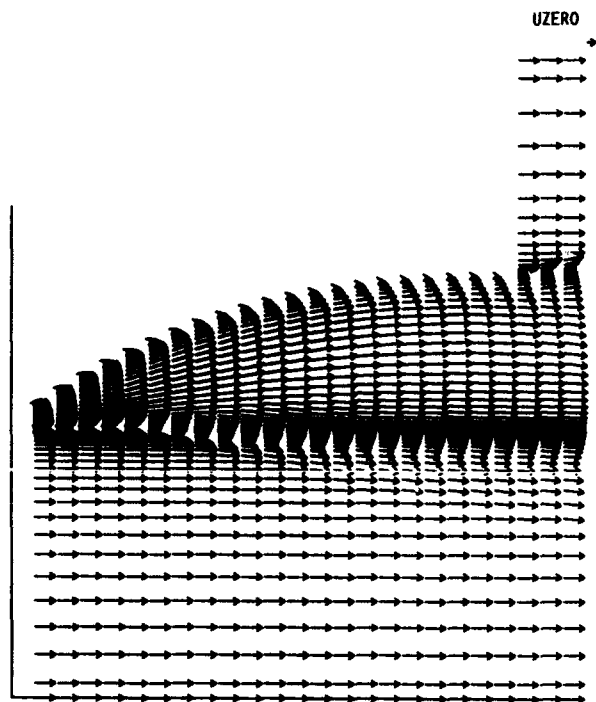


FIGURE 21. - MACH 10, VELOCITY VECTORS.

- A 0.00
- B 1.01
- C 2.03
- D 3.05
- E 4.07
- F 5.08
- G 6.10
- H 7.12
- I 8.14
- J 9.15

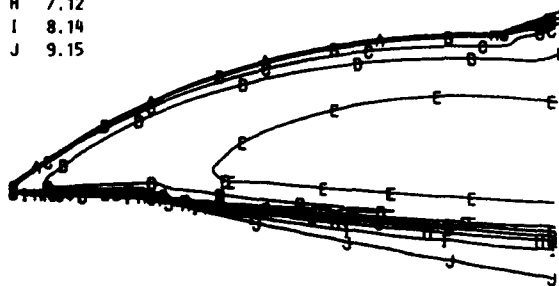


FIGURE 22. - MACH 10, MACH NUMBER CONTOURS.

- A 0.00
- B 240.42
- C 480.85
- D 721.28
- E 961.71
- F 1202.13
- G 1442.56
- H 1682.99
- I 1923.42
- J 2163.84

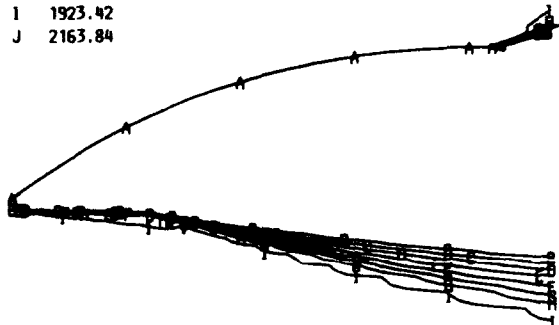
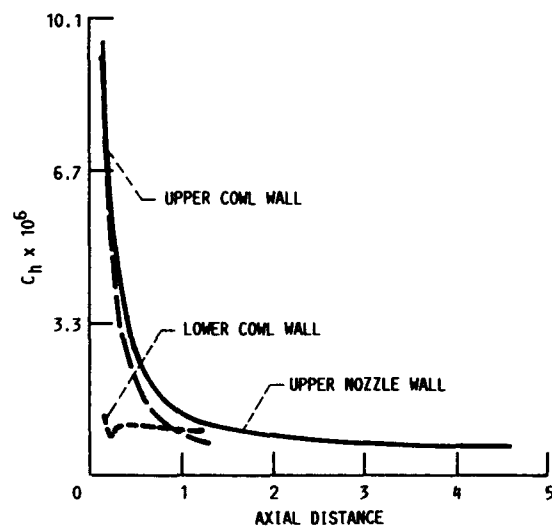
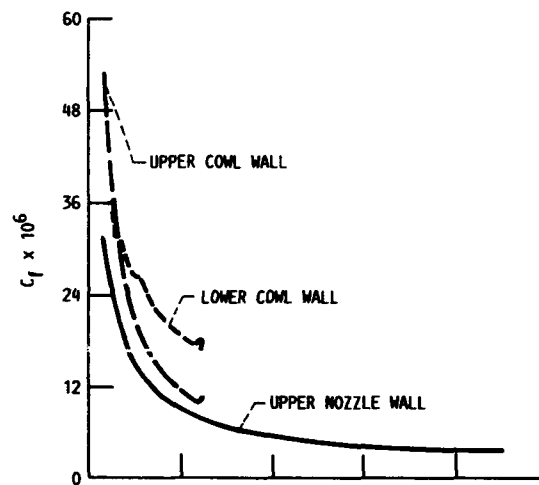
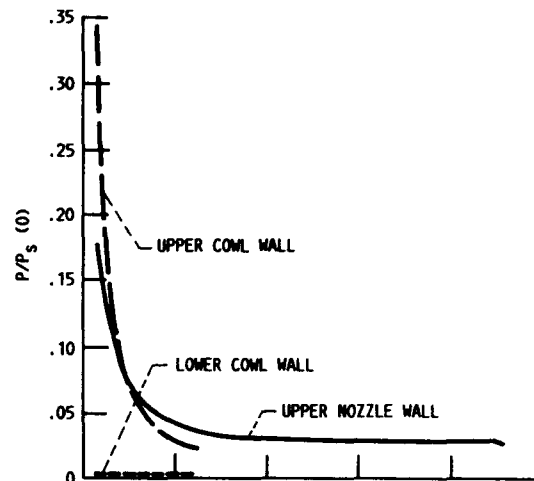


FIGURE 23. - MACH 10, TOTAL PRESSURE CONTOURS.

FIGURE 24. - MACH 10,  $P/P_s$ ,  $C_f$ ,  $C_h$  VERSUS X.

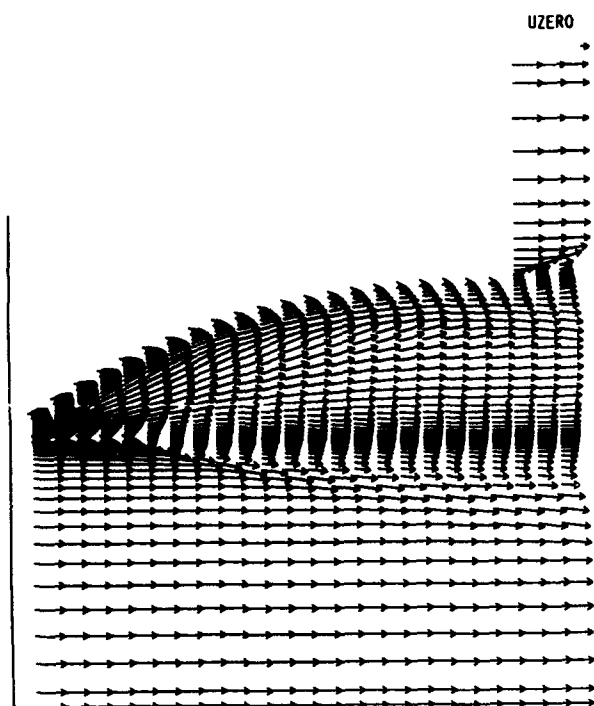


FIGURE 25. - MACH 20, VELOCITY VECTORS.

- A 0.00
- B 2.00
- C 4.00
- D 6.01
- E 8.01
- F 10.02
- G 12.02
- H 14.03
- I 16.03
- J 18.04

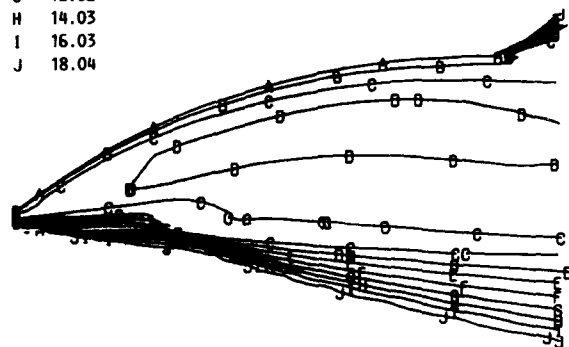


FIGURE 26. - MACH 20, MACH NUMBER CONTOURS.

- A 0.00
- B 1783.24
- C 3566.49
- D 5349.74
- E 7132.99
- F 8916.25
- G 10699.49
- H 12482.74
- I 14265.99
- J 16049.24

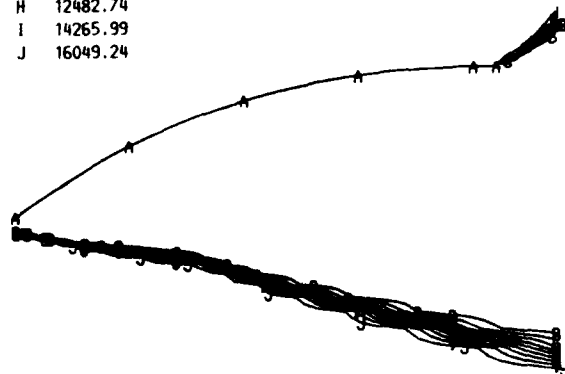
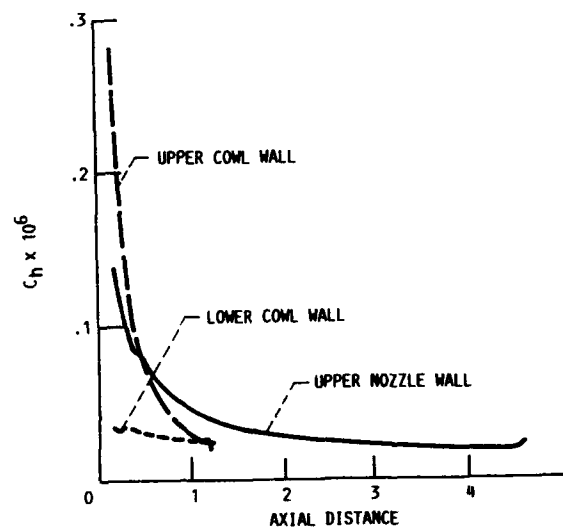
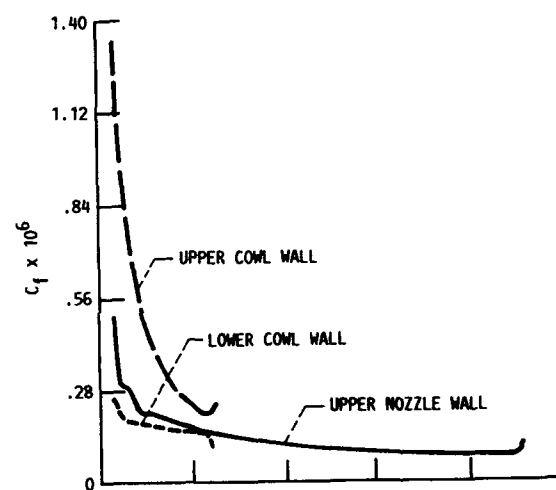
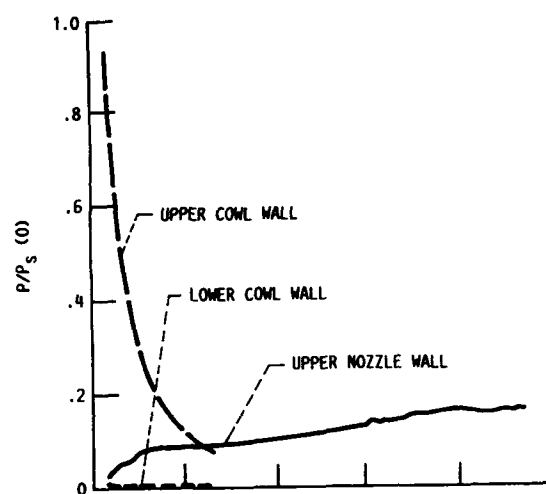


FIGURE 27. - MACH 20, TOTAL PRESSURE CONTOURS.

FIGURE 28. - MACH 20,  $P_w$ ,  $C_f$ ,  $C_h$  VERSUS X.

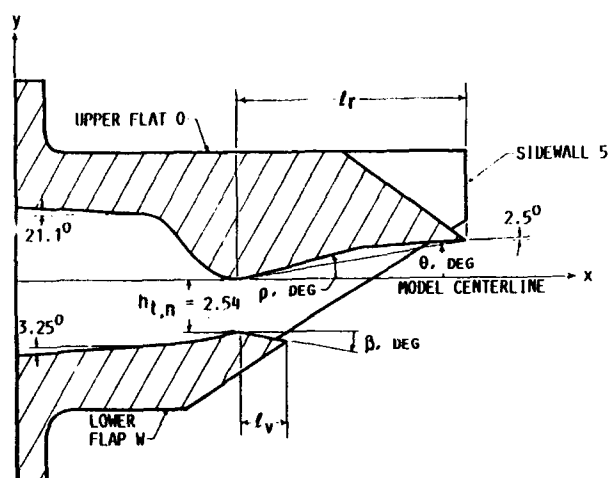


FIGURE 29. - NOZZLE GEOMETRY (FROM REF. [11]).

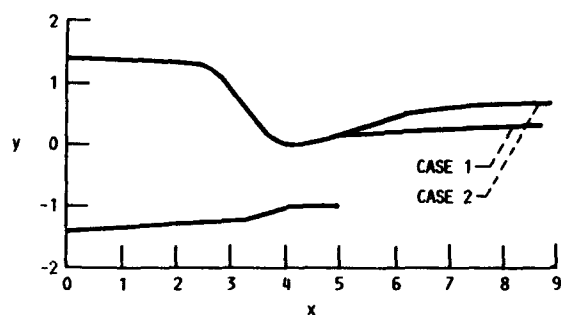
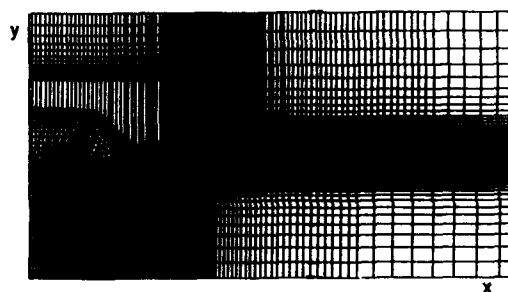
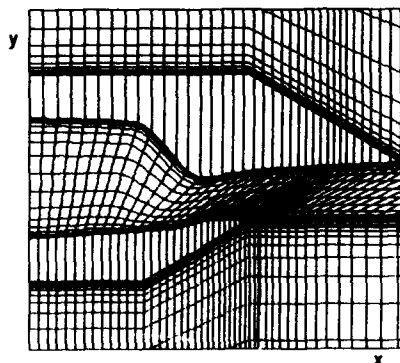


FIGURE 30. - COMPARISON OF TWO NOZZLE CONFIGURATIONS.

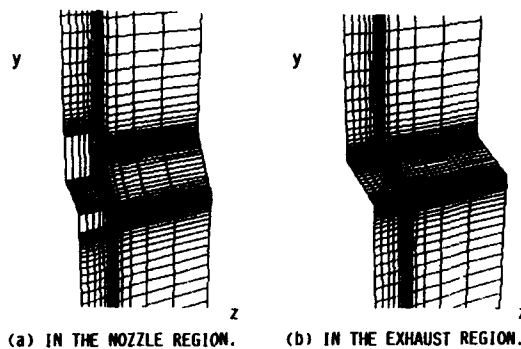


(a) NOZZLE AND EXHAUST GRID.



(b) NOZZLE GRID.

FIGURE 31. - STREAMWISE GRID DISTRIBUTIONS.



(a) IN THE NOZZLE REGION. (b) IN THE EXHAUST REGION.

FIGURE 32. - SPANWISE GRID DISTRIBUTION.

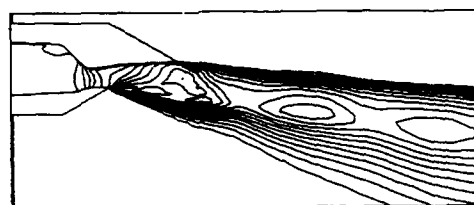
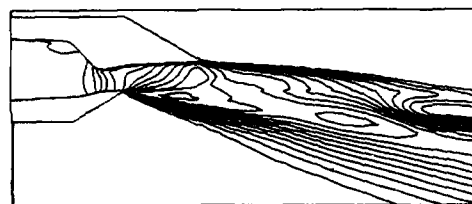
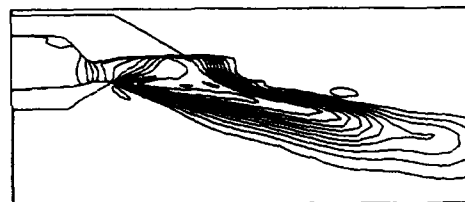
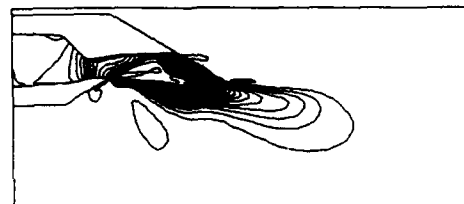
(a)  $l = 1, z = 0.$ (b)  $l = 9, z = 1.365.$ (c)  $l = 13, z = 1.7.$ (d)  $l = 25, z = 1.982.$ 

FIGURE 33. - STREAMWISE MACH NUMBER CONTOURS, CASE 1.

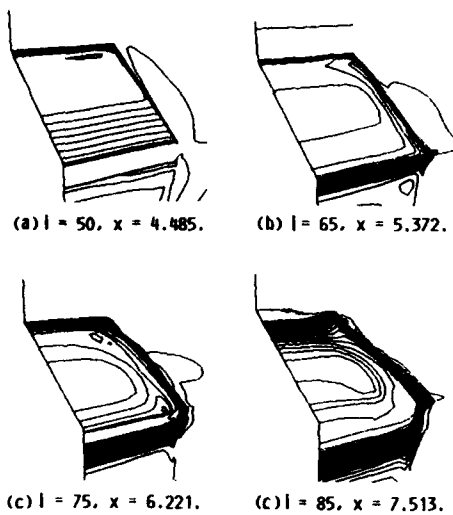


FIGURE 34. - SPANWISE MACH NUMBER CONTOURS, CASE 1

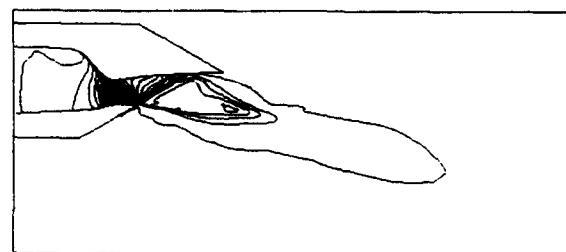
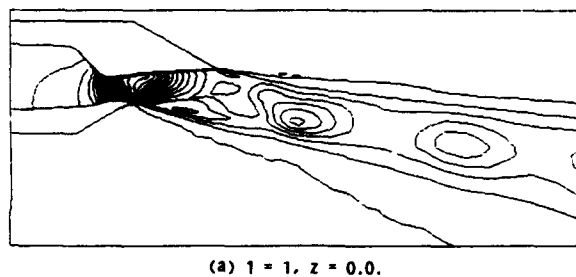


FIGURE 35. - STREAMWISE DENSITY CONTOURS, CASE 1.

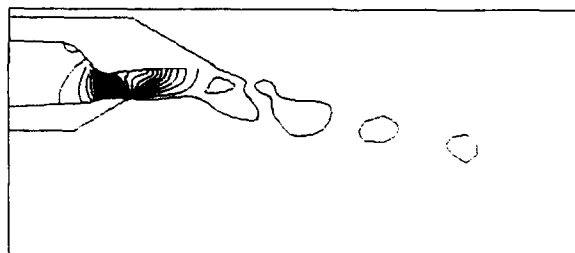
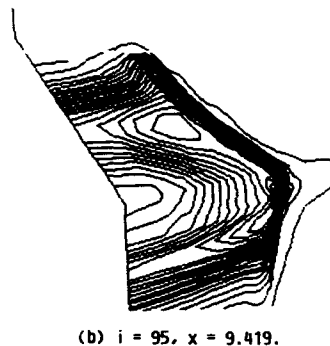
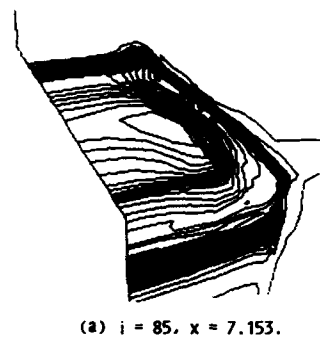
FIGURE 36. - STREAMWISE PRESSURE CONTOURS, CASE 1,  $i = 1, x = 0.0.$ 

FIGURE 37. - SPANWISE DENSITY CONTOURS, CASE 1.

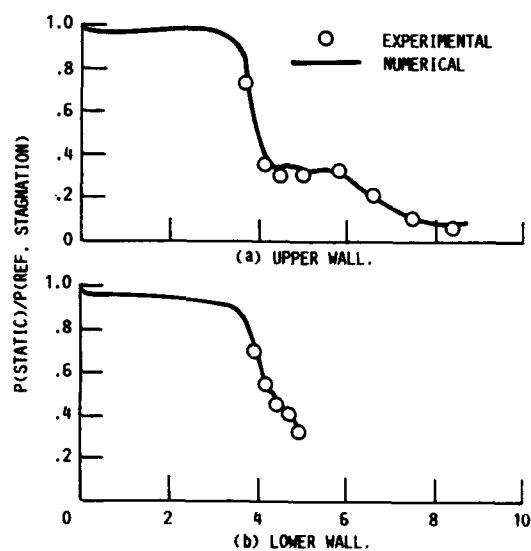
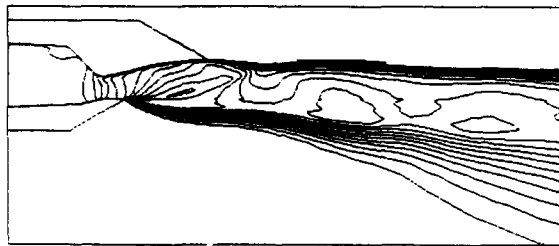
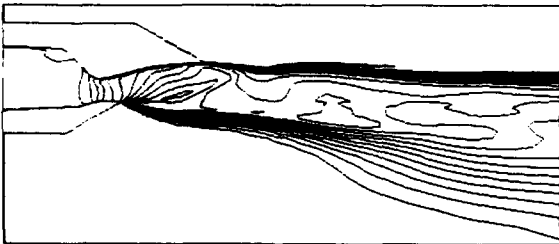
FIGURE 38. - SPANWISE PRESSURE CONTOURS, CASE 1,  $i = 85, x = 7.513.$ 

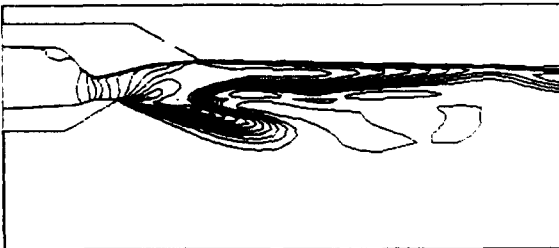
FIGURE 39. - WALL PRESSURE DISTRIBUTIONS, CASE 1.



(a)  $i = 1, z = 0.0.$



(b)  $i = 5, z = 0.767.$

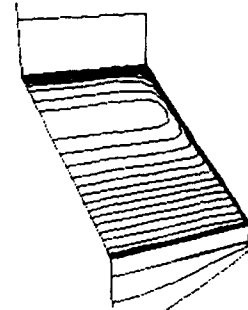


(c)  $i = 13, z = 1.7.$

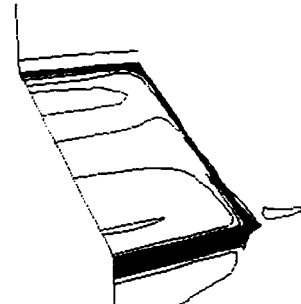


(d)  $i = 25, z = 1.982.$

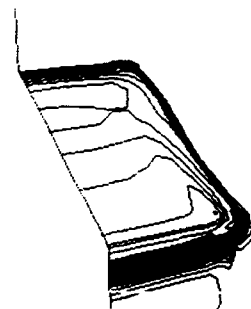
FIGURE 40. - STREAMWISE MACH NUMBER CONTOURS, CASE 2.



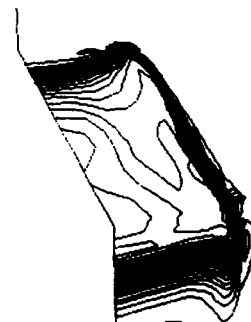
(a)  $i = 53, x = 4.673.$



(b)  $i = 65, x = 5.372.$



(c)  $i = 75, x = 6.221.$



(d)  $i = 90, x = 8.377.$

FIGURE 41. - SPANWISE MACH NUMBER CONTOURS, CASE 2.



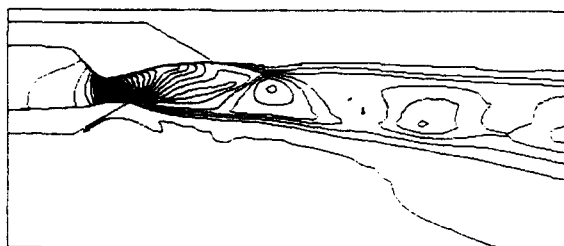
(a)  $i = 1, z = 0.0.$ (b)  $i = 29, z = 1.998.$ 

FIGURE 42. - STREAMWISE DENSITY CONTOURS, CASE 2.

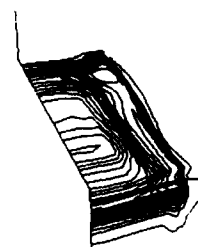
(a)  $i = 85, x = 7.513.$ (b)  $i = 90, x = 8.377.$ 

FIGURE 44. - SPANWISE DENSITY CONTOURS, CASE 2.

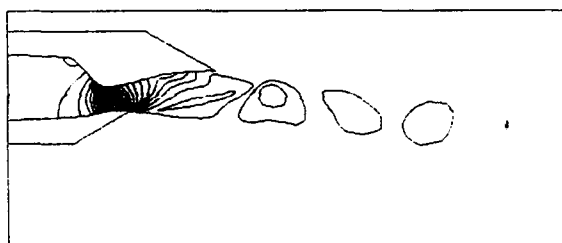
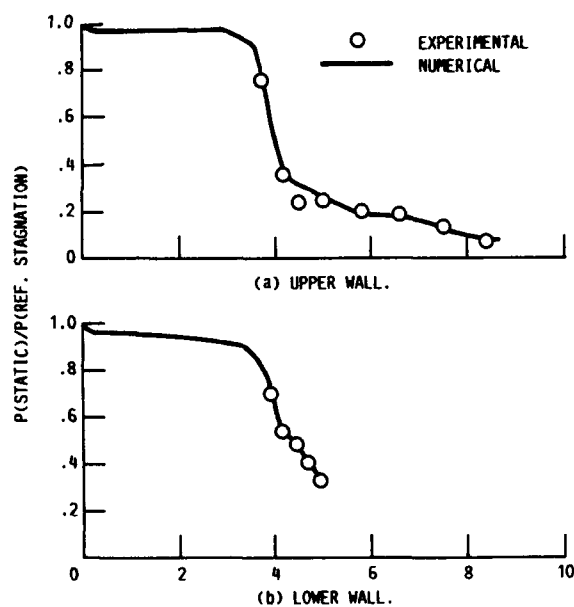
FIGURE 43. - STREAMWISE PRESSURE CONTOURS, CASE 2,  $i = 1, z = 0.0.$ FIGURE 45. - SPANWISE PRESSURE CONTOURS, CASE 2,  $i = 85, x = 7.513.$ 

FIGURE 46. - WALL PRESSURE DISTRIBUTIONS, CASE 2.

## Discussion

WEYER

Did you study the details of the free shear layers - using the computer code - and what type of vorticity exists within supersonic free shear layers?

AUTHOR'S REPLY

The details of the free shear layers have been qualitatively and quantitatively studied. The turbulence model used accounts for the changing length scale associated with the vorticity distribution within the spreading shear layer. However, adequate representation of the shear layer spread rate and vorticity are incompletely understood at hypersonic velocities.

ONOFRI

You showed test cases for high Mach number flows with shocks. Do you think that chemical Kinetics and real gas effects play a substantial role in these cases? What should be their influence on the propulsive parameters?

AUTHOR'S REPLY

The paper presents flowfields using a constant property model. The ratio of specific heats and gas constant were changed with flight conditions. Results for variable real gas properties are outside the scope of the current paper. Including real gas effects will decrease the performance compared to constant property predictions.

HIRSCH

You mentioned the use of a "modified Baldwin-Lomax" model. Could you comment on this and specify the modifications introduced.

AUTHOR'S REPLY

The modifications to the Baldwin-Lomax model are necessary to account for compressibility effects and for shear layers. The compressibility corrections can be found in reference "Hypersonic Turbulent Wall Boundary Layer Computations" by S. Kim and G. Harloff, AIAA 88-2829 AIAA/ASME/SAE/ASEE Int. Propulsion Conference Boston, Mass., July 11-12 1988 or NASA CR-182147 May 1988. The modification for free shear layer is necessary because the Baldwin-Lomax model was developed for wall boundary layers.

SCHWAB

Based on the results obtained for the 2D-SERN nozzle configuration what is the nozzle performance (gross thrust coefficient  $C_{FGI}$ ) for the flight Mach number cases presented? Remark : I could not find the pertinent graph in the paper.

AUTHOR'S REPLY

The computed nozzle velocity coefficients for numbers 3, 6, 10 and 20 are .93, .98, 1.0 and .99 respectively. These are listed in the paper under "Nozzle performance", and should be considered to be qualitative. Real gas effects and grid adaptation would probably change these values.



## 2-D SUPERSONIC NOZZLE DESIGN

Michael Göing and Jörg Heyse  
 MTU Motoren- und Turbinen-Union München GmbH  
 PO Box 50 06 40, D-8000 Munich 50, Federal Republic of Germany

## SUMMARY

In this paper, a method based on the theory of characteristics is presented for two-dimensional, supersonic nozzle design. Individual nozzle configurations for different applications are obtained by combining the geometric attributes of the symmetric, single expansion ramp, and Prandtl-Meyer type expansion nozzles. Corresponding to the design criteria, such as minimum length and optimum thrust efficiency, relations between desired properties of the flow field and nozzle geometry parameters are found, and a family of length-optimized, two-dimensional, supersonic nozzles is defined. The method can be applied for the design of wind tunnel and steam turbine nozzles as well as for thrust nozzle design of high Mach number aircraft.

## NOTATIONS

$c^+, c^-$	left-, right-running characteristics
$f$	factor; defining initial turn angle at lower nozzle wall
$H$	vertical displacement of medium stream line from nozzle throat to exit
$L$	length of nozzle wall
$M$	Mach number
$x$	axial coordinate
$y$	vertical coordinate
$\alpha$	flow angle at nozzle throat
$\beta$	total concave wall turn angle between sharp corner and nozzle exit
$\gamma$	ratio of specific heats
$\delta$	initial turn angle at nozzle wall (sharp corner angle)
$\theta$	flow angle
$\mu$	Mach angle; $= \mu(M)$
$v$	Prandtl-Meyer function; $= v(M, \gamma)$

## SUBSCRIPTS

$E$	design condition at nozzle exit
$l$	lower nozzle wall
$\max$	maximum value
$\min$	minimum value
$u$	upper nozzle wall
$w$	wall

## 1. INTRODUCTION

The exhaust nozzle for high Mach number fighter aircraft is one of the most crucial and challenging components of the propulsion system. The design requirements for the nozzle are high performance, flexibility, and integration with the airframe; this leads to multi-functional nozzle systems with thrust vectoring and thrust reversing. Thrust nozzle systems currently investigated include two-dimensional, rectangular nozzle configurations; references /1/ - /4/.

For hypersonic aircraft, the requirements for exhaust nozzle design are similar. The nozzle pressure ratio varies from 3 at take-off to approximately 800 for Mach 7; the nozzle throat area must be variable by a factor 5. Especially for transonic and high Mach number flight, high nozzle thrust efficiency is necessary to meet the operational requirements of the aircraft. Additionally, integration constraints are very high; in order to reduce weight of the aircraft/propulsion system, the lower aft end of the fuselage must act as a part of the upper nozzle wall. These requirements can be accomplished by two-dimensional, asymmetric nozzle configurations; references /5/ - /8/.

The first step in nozzle design is the determination of ideal, two-dimensional nozzle shapes. Generally, this is accomplished by using an algorithm based on the method-of-characteristics; the isentropic wall contours obtained from this first step form the basis for further design work. In order to meet the performance and integration

92-16996

requirements for the nozzle, the ideal wall contours must be cut back, and an optimum contour adjustment for the variation of ramp angles and throat area must be achieved.

In literature, e.g. references /3/ and /7/, rectangular nozzle design for high Mach number aircraft is based on two ideal configurations, the symmetric (2DCD) nozzle and the single expansion ramp (SERN) nozzle. In order to extend the number of basic configurations in view of integration requirements for different applications, a nozzle design method is presented in this paper resulting in individual, length-optimized nozzle geometries.

## 2. DESIGN CONDITIONS

The discussed method for nozzle design is based on the theory of characteristics; only the supersonic part of the nozzle from throat to exit is investigated. This is possible since the supersonic flow field is independent of conditions upstream of the sonic line. The convergent, subsonic portion should be designed to produce approximately the assumed shape of the sonic line at the nozzle throat; references /9/ and /10/.

In Fig. 2.1, desired properties of the flow field and nozzle geometry parameters are defined. The axial lengths of the lower and upper nozzle walls,  $L_l$  and  $L_u$ , as well as the vertical displacement of the medium stream line from throat to exit,  $H$ , are normalized by the width of the throat.

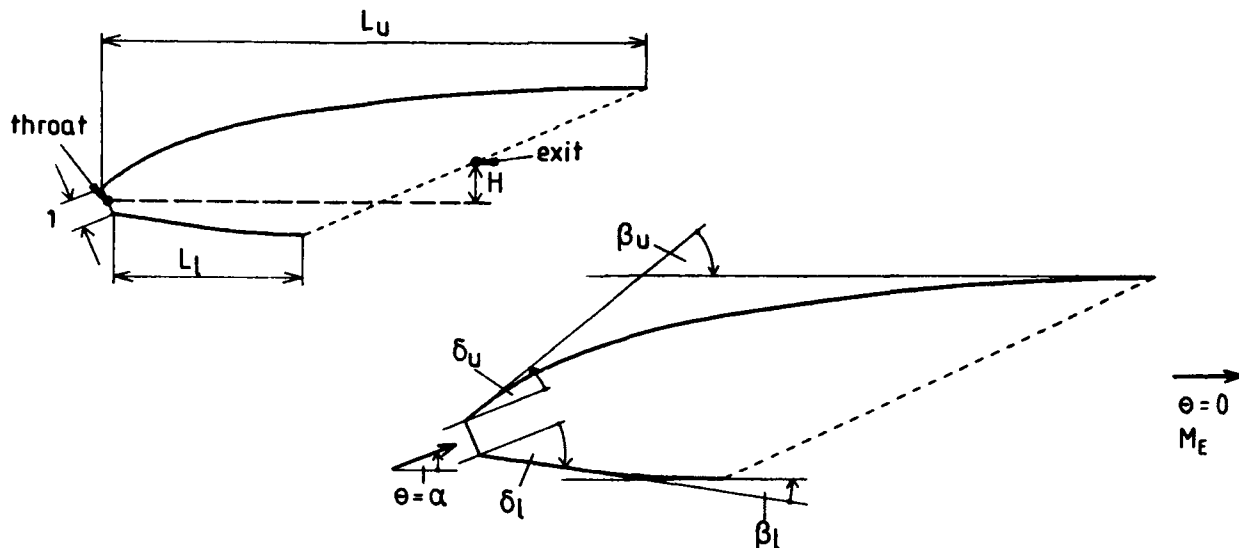


Fig. 2.1: Desired Flow Field Properties and Nozzle Geometry Parameters

The definition of the family of optimized 2-D supersonic nozzles is based on the following assumptions:

- parallel and uniform flow at the nozzle exit, characterized by the desired Mach number  $M_E$  and the flow angle  $\theta = 0$ ;
- parallel, uniform and sonic flow at the nozzle throat, characterized by the flow angle  $\theta = \alpha$ ;
- two-dimensional, irrotational, isentropic flow;
- perfect gas, characterized by the ratio of specific heats  $\gamma$ .

For each combination of the listed design parameters  $M_E$ ,  $\alpha$  and  $\gamma$ , the expansion of flow from throat to exit can be realized by innumerable nozzle configurations. The objective of the described design method is to limit the number of possible configurations to cases with length-optimized wall contours. However, the minimization of nozzle overall length is only part of this investigation. In consideration of applications for various integration aspects, emphasis is put on optimized nozzle geometries with different ratios of lower to upper wall length. Therefore, to define the complete design problem, an additional design parameter is necessary which is introduced in Section 4.

As noted above, a straight sonic line at the throat is assumed for the described design method. According to reference /11/, the assumption of sonic line shape shows only a small influence on the determined wall length for high design Mach numbers at the nozzle exit. For two-dimensional, symmetric nozzles, a comparison between results of design methods with straight and circular arc sonic lines is given in reference /9/; the method based on a curved sonic line results in about 13 % longer wall contours.

In order to provide the required increase in area and the change in flow direction between nozzle throat and exit, the curvature of the wall contours downstream of the throat must be first convex, and then concave. For the presented method, the nozzles are designed as sharp-corner nozzles; the convex part of the contours is contracted to a sharp corner at the throat. This results in nozzle geometries with the smallest ratio of wall length to throat width; reference /10/. The sharp corners at the throat are defined by the initial turn angles of the lower and upper nozzle walls,  $\delta_1$  and  $\delta_u$ .

With regard to boundary layer considerations, a substitution of the sharp corners by circular arcs of small radius is possible without significant consequences for the determined nozzle geometry.

To give further definitions, Mach waves of a general, length-optimized nozzle are shown in Fig. 2.2. At the sharp corners, centered expansion waves are generated. The initial wall turn angles and the strength of the expansion fans, respectively, are related to the design parameters; the determination of these sharp corner properties is one of the key problems of supersonic nozzle design.

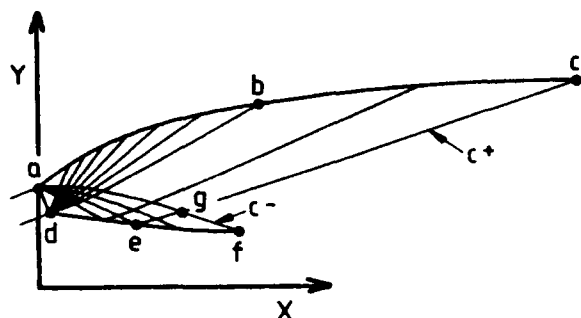


Fig. 2.2:  
Mach Waves of a Length-Optimized Nozzle

The kernel or expansion region of the nozzle, where right- and left-running expansion waves are present, is given by the zone a-g-e-d-a. The simple wave or straightening regions with only one type of expansion waves are defined by the zones a-b-c-g-a and e-f-g-e; at their wall portions a-b-c and e-f, expansion waves which are incident on a contour are extinguished by proper concave wall curvature design. Finally, the desired parallel and uniform exit flow of the nozzle is realized downstream of the straight wave segments c-g and g-f.

The MOC (method-of-characteristics) equations for two-dimensional, irrotational, supersonic flow of a perfect gas can be written as

$$dv + d\theta = 0 \quad ; \quad dy/dx = \tan(\theta - \mu) \quad (2.1a,b)$$

$$dv - d\theta = 0 \quad ; \quad dy/dx = \tan(\theta + \mu) \quad (2.2a,b)$$

Eqs. (2.1) are valid for right-running ( $C^-$ ), and Eqs. (2.2) for left-running ( $C^+$ ) characteristics; the principle procedure for MOC-calculation is given in references /10/, /12/ and /13/.

According to Prandtl-Meyer theory, the flow conditions at the walls immediately downstream of the sharp corners (points a and d) are determined by

$$v_a = \delta_u \quad ; \quad \theta_a = \alpha + \delta_u \quad (2.3a,b)$$

$$v_d = \delta_l \quad ; \quad \theta_d = \alpha - \delta_l \quad (2.4a,b)$$

From the flow direction at the nozzle throat and the initial wall turn angles, the total turn angles of the concave wall contours, between the sharp corners and the nozzle exit, are given by the geometrical relations

$$\beta_u = \delta_u + \alpha \quad (2.5)$$

$$\beta_l = \delta_l - \alpha \quad (2.6)$$

To get more information on requirements for length-optimized nozzle configurations, three well-known nozzle geometries are analysed in the following section.

### 3. ATTRIBUTES OF WELL-KNOWN 2-D NOZZLES

#### Case 1: Symmetric Nozzle ( $\alpha = 0$ )

In Fig. 3.1, Mach waves and stream lines of a two-dimensional, symmetric nozzle are shown. This type of minimum-length nozzle is described in references /9/, /10/, /12/ and /13/.

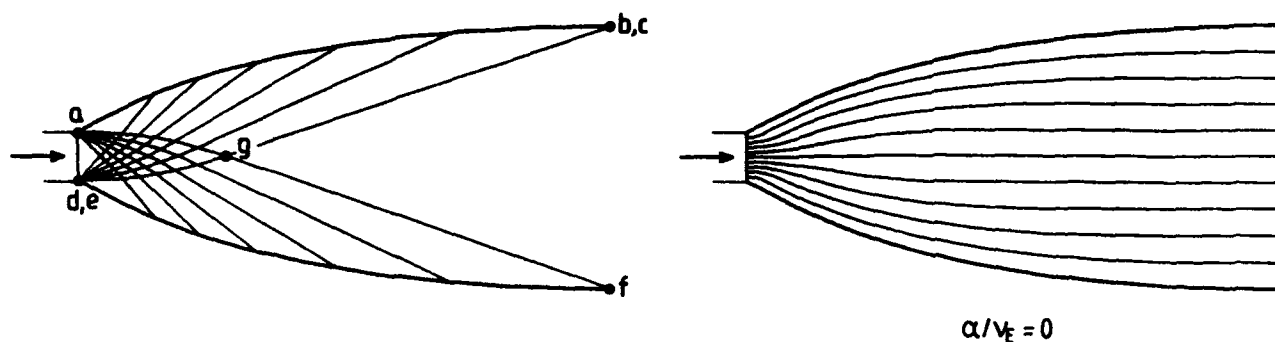


Fig. 3.1: Flow Field of the Symmetric Nozzle - Case 1

To realize minimum length of the nozzle walls, reflections of the expansion waves at the walls are avoided; the waves emerging from the sharp corners are extinguished when they are incident on the opposite wall. The wall points of the nozzle exit (b and f) are defined by the final waves of the expansion fans, a-f and d-b; for that reason, the points b and c as well as d and e are identical.

Since  $\theta = 0$  at the nozzle exit, integration of Eq. 2.1a for the right-running wave a-f gives

$$v_a + \theta_a = v_f = v_E \quad (3.1)$$

where  $v_E = v(M_E, \gamma)$ .

From Eqs. (2.3) and (3.1), and since  $\alpha = 0$  at the throat, the initial turn angle of the upper wall can be determined by

$$\delta_u = v_E/2 \quad (3.2a)$$

Furthermore, from Eq. 2.5, the total turn angle of the upper, concave wall contour is given by

$$\beta_u = v_E/2 \quad (3.2b)$$

Application of Eqs. 2.2a, 2.4 and 2.6 for the left-running expansion wave d-b leads to the following relations for the lower wall

$$v_d - \theta_d = v_b = v_E \quad (3.3)$$

$$\delta_l = v_E/2 \quad (3.4a)$$

$$\beta_l = v_E/2 \quad (3.4b)$$

#### Case 2: Single Expansion Ramp Nozzle ( $\alpha = 0$ )

The centre line of the symmetric nozzle is a stream line, and can be replaced by a straight wall. This leads to the asymmetric nozzle configuration which is shown in Fig. 3.2.

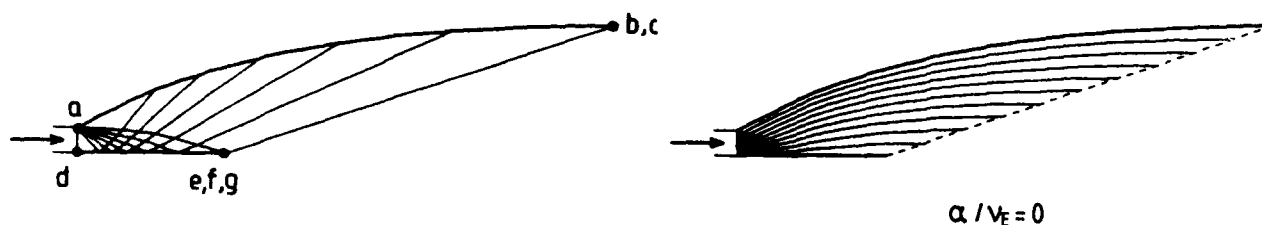


Fig. 3.2: Flow Field of the Single Expansion Ramp Nozzle - Case 2

For this type of nozzle, a sharp corner is only existing at the upper wall; the expansion waves generated at this corner are totally reflected when they are incident on the lower wall. The exit of the nozzle is defined by the wave e-c; the points e, f and g as well as c and b are coincident in location and flow properties.

The geometrical data of the upper wall are the same as for the symmetric nozzle, except for the dimensions which must be doubled due to the assumed reduction of throat width. Therefore, the wall angles are given by

$$\delta_u = v_E/2 \quad ; \quad \beta_u = v_E/2 \quad (3.5a,b)$$

$$\delta_l = 0 \quad ; \quad \beta_l = 0 \quad (3.6a,b)$$

**Case 3: Prandtl-Meyer Type Expansion Nozzle ( $\alpha = v_E$ )**

In Fig. 3.3, Mach waves and stream lines of a nozzle configuration for  $\alpha = v_E$  are shown. The flow is accelerated and turned by an expansion fan which is generated at a sharp corner of the lower wall. Downstream of the last wave d-b, the exit flow conditions of the nozzle are obtained. Expansion waves which are incident on the upper wall are cancelled. The points d, e, f and g as well as b and c are identical.

Since there is no change in slope at point a of the upper wall, the geometry of this wall can be described by

$$\delta_u = 0 \quad ; \quad \beta_u = \alpha \quad (3.7a,b)$$

From Eqs. 2.4 and 2.6, and since  $\alpha = v_E$ , the properties of the lower wall are determined by

$$\delta_l = \alpha \quad ; \quad \beta_l = 0 \quad (3.8a,b)$$

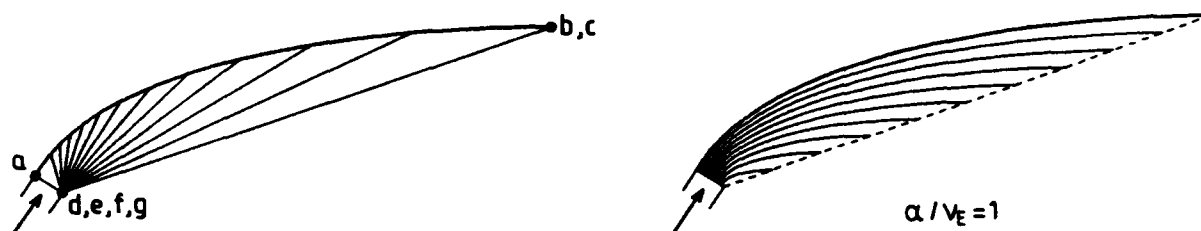


Fig. 3.3: Flow Field of the Prandtl-Meyer Type Expansion Nozzle - Case 3

With regard to boundary layer behaviour and thrust efficiency, one purpose of the design of optimized nozzle geometries is to avoid compression or shock waves within the nozzle area. By means of the described nozzle configurations, further design requirements can be established in order to obtain minimum length of the lower and upper nozzle walls:

- Unnecessary reflections of expansions waves at the walls must be avoided.
- The concave curvature of the longer wall must result in cancellation of all expansion waves which are incident on this wall. For the defined direction of  $\alpha$ , and the condition that compression or shock waves must be avoided, the upper wall is the longer one;  $L_u > L_l$  is also assumed for asymmetric configurations and  $\alpha = 0$ .
- Since all expansion waves, incident on the upper wall, are cancelled, the end of the lower wall must be defined by the final wave emerging from the sharp corner of the upper wall. Therefore, the initial wall turn angle of the upper wall can be determined immediately.
- Reflections of expansion waves at the lower wall must be realized without changing the strength of these waves; therefore, the corresponding portion of the lower wall must be designed as a straight contour.

In consideration of the listed design requirements, the nozzle geometries described in this section form the edge-points of a class of optimized nozzle configurations; these points are defined by limitations for the flow angle at the throat and the initial turn angle at the lower wall.

The flow angle at the nozzle throat is limited to

$$\alpha = 0 \dots v_E \quad (3.9)$$

For  $\alpha < 0$ , nozzle design results in configurations identical to those for  $\alpha > 0$ . For  $\alpha > v_E$ , the desired exit flow of the nozzle could only be realized if compression or shock waves are contained in the nozzle flow field.

For  $\alpha = 0$ , the initial turn angle of the lower wall is limited to

$$\delta_l = 0 \dots \delta_u \quad (3.10)$$

where  $\delta_u = v_E/2$ . By means of the Fig. 3.1 and 3.2, it can be easily checked that, for the assumed nozzle exit flow,  $\delta_l < 0$  or  $\delta_l > \delta_u$  will result in compression or shock waves.

For  $\alpha = v_E$ , the nozzle geometry shown in Fig. 3.3 ( $\delta_l = \alpha$ ) is the only configuration for a flow field without shock waves.

## 4. FAMILY OF OPTIMIZED 2-D NOZZLES

To define a family of length-optimized nozzle configurations, the attributes of the nozzles presented in Section 3 are combined. In Fig. 4.1, expansion waves and stream lines of a combined nozzle are shown.

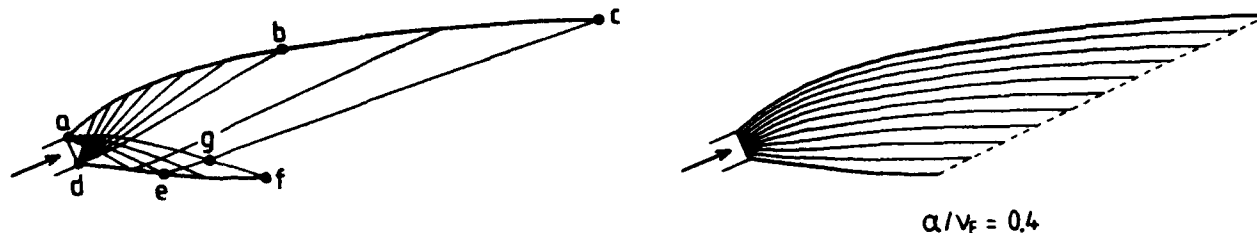


Fig. 4.1: Flow Field of a Combined Nozzle

Since the final wave originating from the sharp corner of the upper wall ends at the lower wall point f, the initial turn angle of the upper wall can be determined. Integration of Eq. 2.1a for the expansion wave a-f, and application of Eqs. 2.3 result in

$$\delta_u = v_E/2 \cdot (1 - \alpha/v_E) \quad (4.1a)$$

From Eq. 2.5, the total concave turn angle of the upper wall can be calculated by

$$\beta_u = \alpha + v_E/2 \cdot (1 - \alpha/v_E) \quad (4.1b)$$

The initial turn angle of the lower wall is not clearly defined; as shown in Section 3 for  $\alpha = 0$ , this angle can be varied within certain limits to realize different ratios of lower to upper wall length. The limits of  $\delta_l$  are determined as follows:

- The minimum value of  $\delta_l$  is given by

$$\delta_{l,min} = \alpha \quad (4.2)$$

This results in a straight and horizontal contour of the lower nozzle wall between sharp corner and exit.

- The maximum value of  $\delta_l$  can be determined for the assumption that the end of the upper wall is defined by the final expansion wave generated at the lower wall (point b in Fig. 4.1). Then, integration of Eq. 2.2a for the left-running wave d-b, and application of Eqs. 2.4 and 4.1a result in

$$\delta_{l,max} = \alpha + v_E/2 \cdot (1 - \alpha/v_E) = \alpha + \delta_u \quad (4.3)$$

Again, for  $\delta_l < \delta_{l,min}$  or  $\delta_l > \delta_{l,max}$ , the nozzle exit flow conditions could only be obtained if compression or shock waves are existing within the nozzle flow field.

As depicted in Fig. 4.1, in general, the strength of the lower wall expansion fan is not sufficient to define the end of the upper wall at point b. To realize the desired exit flow at point c, some waves generated at the upper wall must be reflected at a straight portion d-e of the lower wall. Because of Eqs. 2.5 and 2.6,

$$\delta_u + \delta_l = \beta_u + \beta_l \quad (4.4)$$

and since the strength of any expansion wave within the flow field is not changed except for concave curving of a wall, the rest of the expansion waves are adequate for the required bending of the lower wall contour e-f.

Therefore, the initial turn angle of the lower wall can be defined by

$$\delta_l = \alpha + f \cdot v_E/2 \cdot (1 - \alpha/v_E) = \alpha + f \cdot \delta_u \quad (4.5a)$$

and then, from Eq. 2.6, the total concave turn angle of the lower wall is given by

$$\beta_l = f \cdot v_E/2 \cdot (1 - \alpha/v_E) \quad (4.5b)$$

The parameter f defines the sharp corner angle of the lower wall and the strength of the generated expansion fan, respectively; in order to obtain different ratios of lower to upper wall length of the nozzle, f can be varied within the limits given by Eqs. 4.2 and 4.3

$$f = 0 \dots 1 \quad (4.6)$$

The presented method for individual nozzle design is based on the Eqs. 2.1, 2.2, 3.9, 4.1, 4.5 and 4.6. The design parameters are given by  $M_E$  (or  $v_E$ ),  $\alpha$ ,  $\gamma$  and f; by these parameters, the wall contours of the optimized nozzles are fully determined.



As a result, possible nozzle geometries determined by this method are shown in Fig. 4.2. For constant values of  $v_g$  and  $\gamma$ , the geometry of the nozzle is only dependent on the parameters  $(1 - \alpha/v_g)$  and  $f$ . In the design map of Fig. 4.2, the family of length-optimized nozzle configurations is defined by the lower half-side of the diagram; the edge points of this triangle are given by the special nozzle cases presented in Section 3.

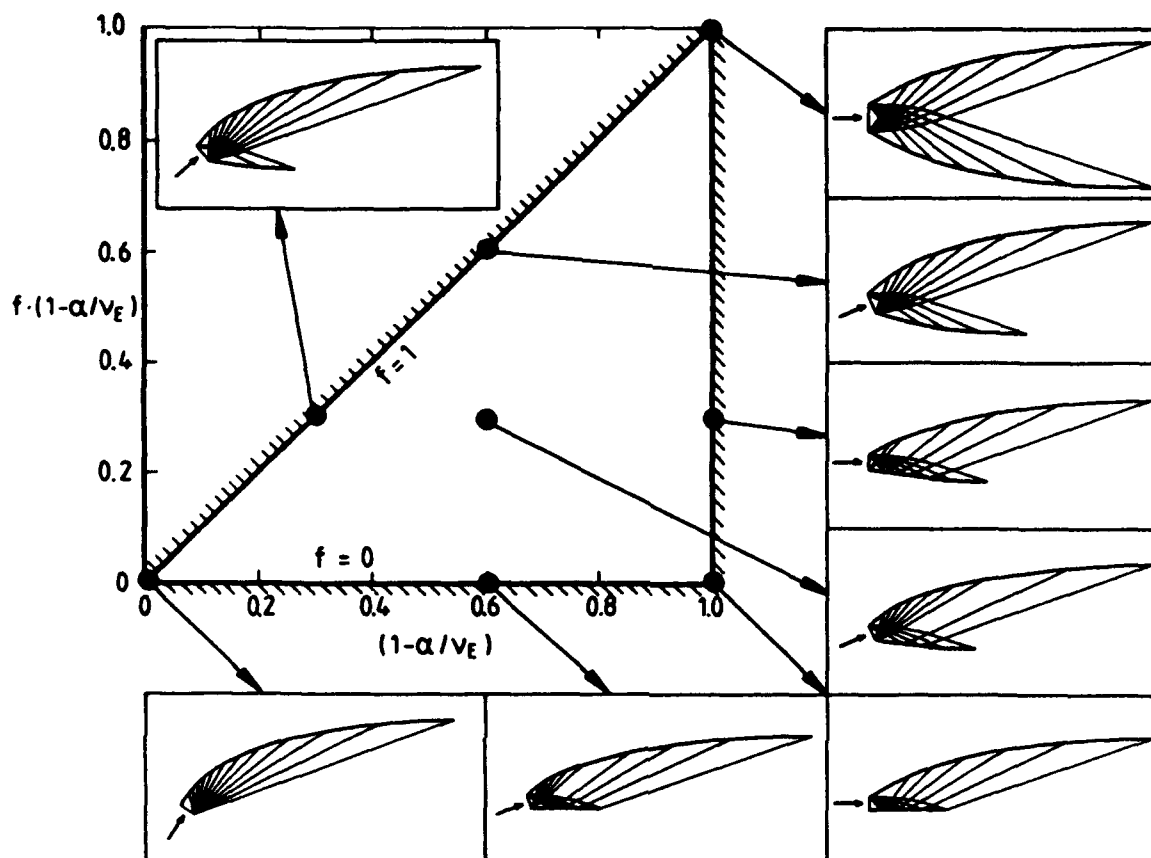


Fig. 4.2: Design Map for the Defined Family of Length-Optimized Nozzle Configurations

For  $f=0$ , the attributes of the cases 2 and 3 are combined. The lower wall is designed as a straight and horizontal contour; the expansion waves which are incident on this wall are totally reflected. For  $\alpha=0$ , a sharp corner is only existing at the upper wall; for increasing values of  $\alpha$ , the initial turn angle of the lower wall is increasing, too, while  $\delta_u$  is reduced. For  $\alpha=v_g$ ; the sharp corner at the upper wall as well as the concave portion of the lower wall will disappear.

For  $f=1$ , the final wave of the expansion fan emerging from the lower wall defines the end of the upper wall; for this case,  $\delta_u$  is decreasing, and  $\delta_l$  is increasing from  $\alpha=0$  to  $v_g$ . For  $f=1$ , the special nozzle cases 1 and 3 are combined.

For  $\alpha=0$ , the initial turn angle of the upper wall is constant;  $\delta_l$  is reduced for decreasing values of the parameter  $f$ ; (combination of the cases 1 and 2).

Finally, for  $\alpha=v_g$ , the nozzle exit flow can only be realized shock-free by the configuration shown in Fig. 3.3 (case 3); therefore, the value of  $f$  is undefined for  $\alpha=v_g$ .

General, length-optimized nozzle configurations are obtained by a variation of the parameters  $\alpha/v_g$  and  $f$ ; by that, the attributes of the three special nozzle cases are combined. As an example, in Fig. 4.1 a nozzle configuration for  $\alpha/v_g = 0.4$  and  $f = 0.5$  is depicted.

## 5. RESULTS AND CONCLUSIONS

In Fig. 5.1, two nozzle configurations with a small ratio of lower to upper wall length are shown for different design Mach numbers. As noted above, the nozzle dimensions are normalized by the width of the throat. Distributions of the Mach number along the walls are presented in Fig. 5.2 for  $M_g = 3$  and  $\gamma = 1.3$ . The differences in Mach number just downstream of the throat are caused by different values of the sharp corner angle. According to the theory of characteristics, the gradient of Mach number along the wall (i. e. acceleration) is not zero at the nozzle exit; reference /9/.

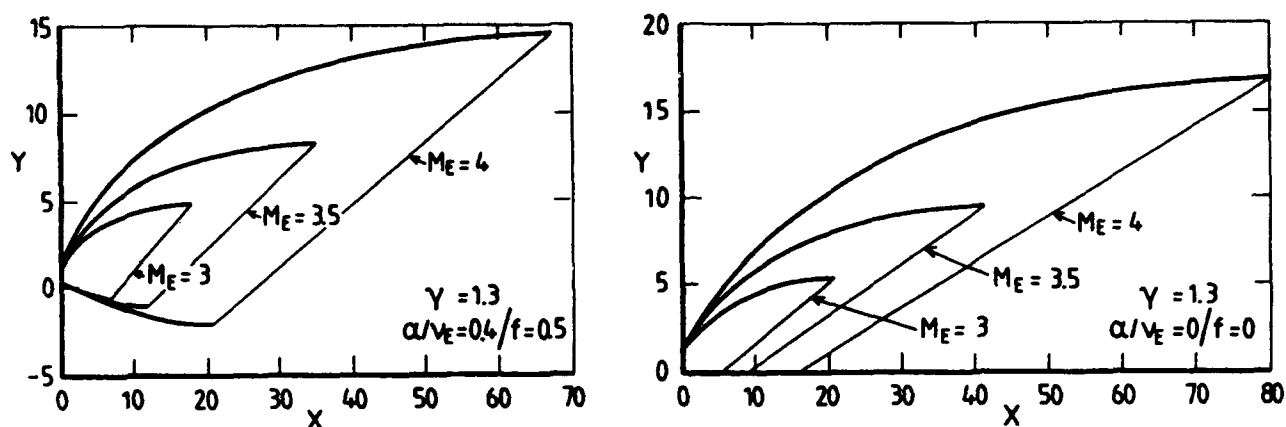


Fig. 5.1: Nozzle Wall Contours for Different Mach Numbers  $M_E$  when  $\gamma = 1.3$

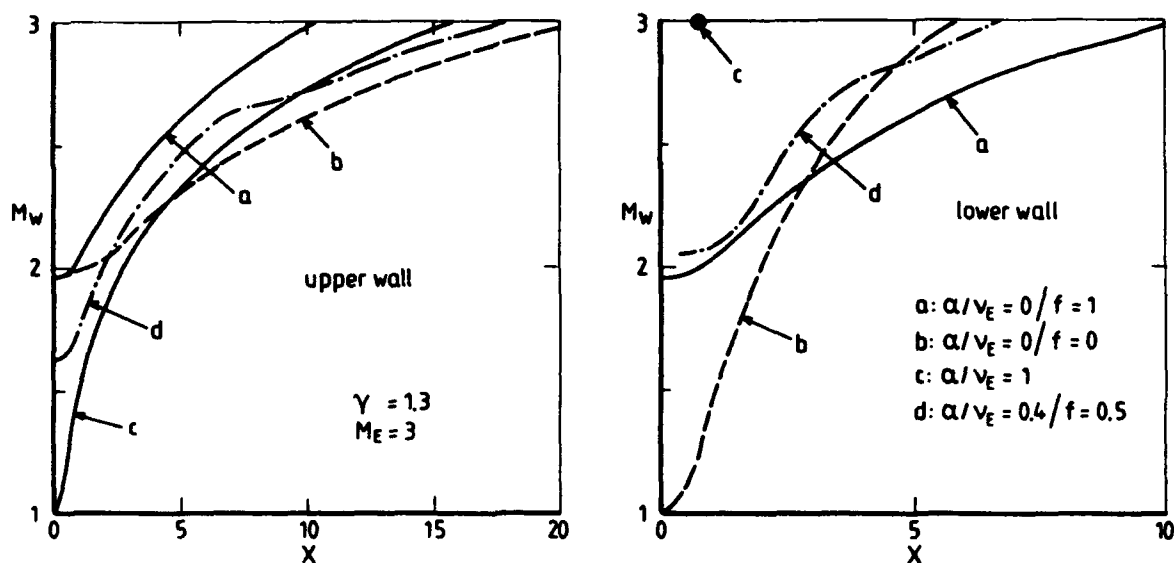


Fig. 5.2: Mach Number Along the Walls for Different Nozzle Configurations when  $M_E = 3$  and  $\gamma = 1.3$

In order to compare the integration capabilities of the nozzle configurations defined in Section 4, the lengths of the nozzle walls and the vertical displacement of the medium stream line from throat to exit are given in Fig. 5.3 - 5.5 for  $M_E = 3$  and 5. As shown in the design map of Fig. 4.2, these dimensions of nozzle geometry are dependent on the parameters  $(1 - \alpha/v_E)$  and  $f$  for constant values of  $M_E$  and  $\gamma$ .

The lower and upper wall lengths are changing in the opposite way for varying values of  $f$ . Minimum overall length of the nozzle can be obtained for  $f = 1$ ; for these nozzle configurations, the upper wall shows the minimum, and the lower wall the maximum length solution. For  $f = 0$ , minimum length of the lower wall is combined with a maximum upper wall length.

For changing design Mach numbers, the tendencies are similar; this is also shown in Fig. 5.6, where the lengths of different nozzle configurations are plotted versus  $M_E$ . Furthermore, the influence of the ratio of specific heats on the wall lengths is given in the figure; since  $v_E$  is reduced for increasing values of  $\gamma$ , the lengths of the nozzle walls are decreasing, too.

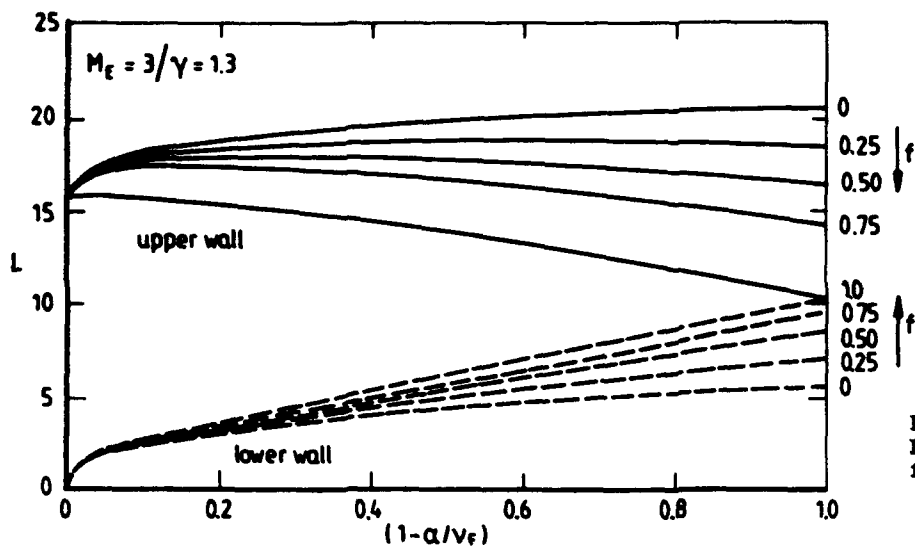


Fig. 5.3:  
Length of the Nozzle Walls  
for  $M_E = 3$  and  $\gamma = 1.3$

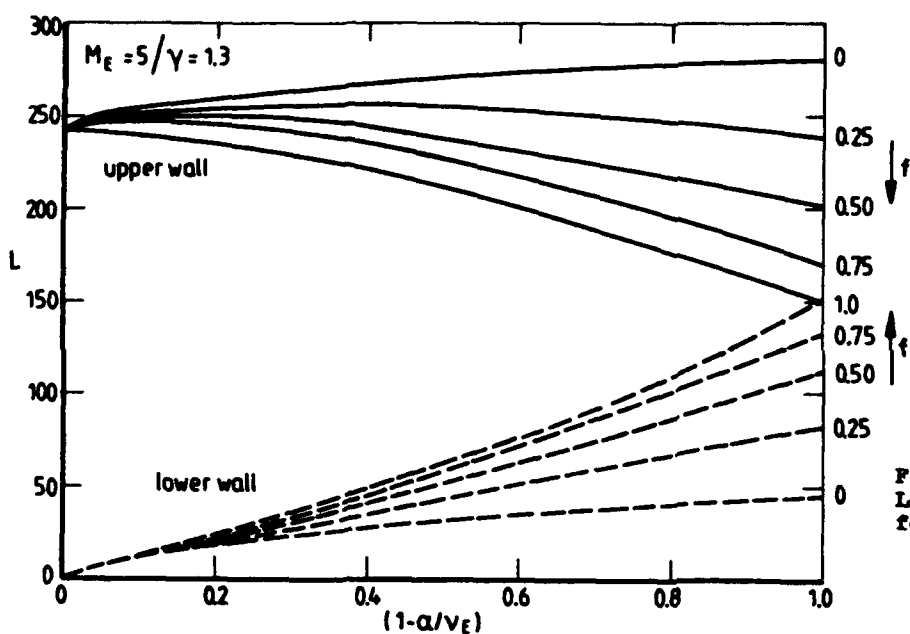


Fig. 5.4:  
Length of the Nozzle Walls  
for  $M_E = 5$  and  $\gamma = 1.3$

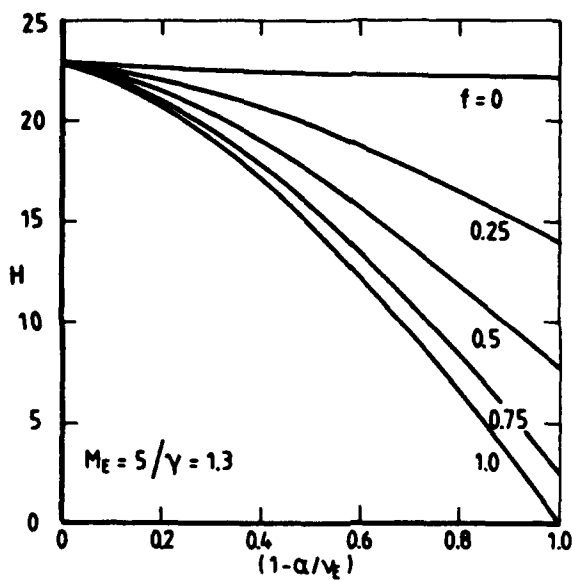
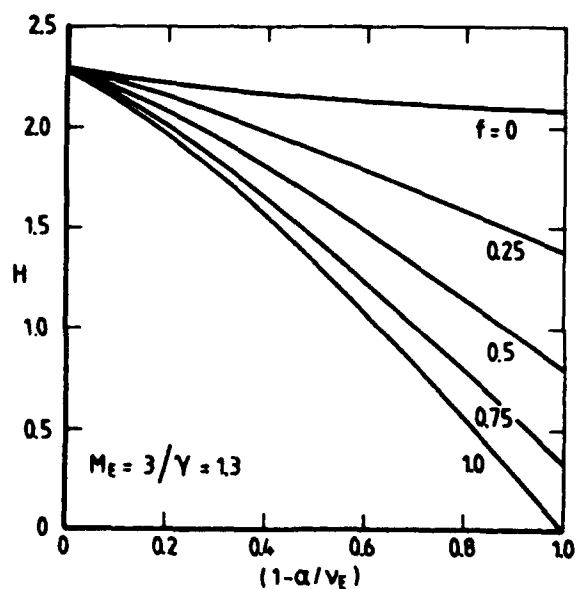


Fig. 5.5: Vertical Displacement of Medium Stream Line from Throat to Exit for  $M_E = 3$  and  $5$  when  $\gamma = 1.3$

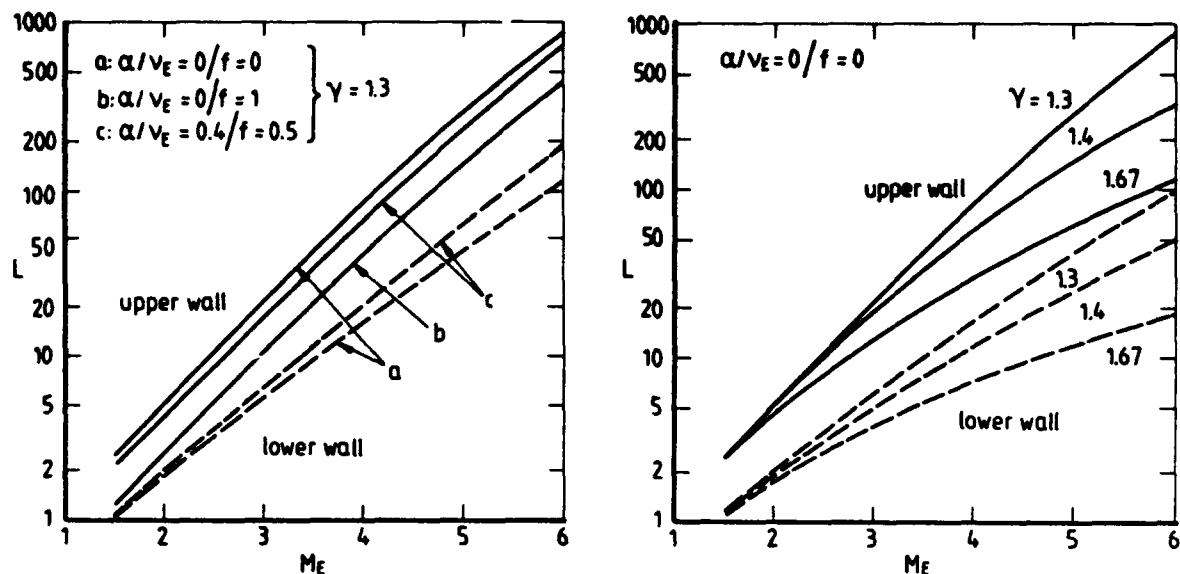


Fig. 5.6: Length of Nozzle Walls versus  $M_E$

The study has shown that length-optimized nozzle configurations still have high overall length to throat width ratios, which is due to the assumptions for the nozzle exit flow. For some applications, e.g. the design of wind tunnel nozzles, the assumed parallel and uniform flow at the nozzle exit is an important design criteria, and therefore, large nozzle dimensions must be accepted.

For other applications, e.g. the design of rectangular thrust nozzles for high Mach number aircraft or hypersonic vehicles, a compromise must be found between performance and integration constraints; for these cases, the determination of isentropic wall contours is only the first step in nozzle design.

#### REFERENCES

- /1/ Dusa, D.J., and Wooten, W.H., "Single Expansion Ramp Nozzle Development Status", AIAA Paper 84-2455, November 1984.
- /2/ Dusa, D.J., "Engine Integration with Aircraft Exhaust Nozzle Systems", Aero-Propulsion, Short Course, University of Tennessee, December 1988.
- /3/ Kuchar, A.P., and Wolf, J.P., "Preliminary Assessment of Exhaust Systems for High Mach (4 to 6) Fighter Aircraft", AIAA Paper 89-2356, July 1989.
- /4/ Berry, F.C., Jr., "The Push for Fighter Engines", AIR FORCE Magazine, pp. 74 - 79, January 1990.
- /5/ Göing, M., and Voss, N.H., "Conceptual and Technological Aspects of Hypersonic Airbreathing Propulsion for SÄNGER", AAF Paper 88-2.3, Space Propulsion Forum, Bordeaux, December 1988.
- /6/ Göing, M., and Voss, N.H., "Airbreathing Propulsion - a Scientific Topic in Hypersonics", EUROAVIA - Symposium on Hypersonics, Munich, July 1989.
- /7/ Schwab, R.R., Göing, M., Aulehla, F., and Weinreich, H.-L., "Einige Gesichtspunkte zur Auslegung eines Hyperschall-Antriebssystems im Hinblick auf die Abstimmung von Einlauf und Heck mit dem Triebwerk", DGLR Paper 88-040, September 1988.
- /8/ Albers, M., Proske, S., Kramer, P.A., Voss, N.H., and Krebs, H., "Evolution of Air - Breathing Propulsion Concepts Related to the SÄNGER Space Plane", IAF Paper 88-247, October 1988.
- /9/ Argrow, B.M., and Emanuel, G., "Comparison of Minimum Length Nozzles", Journal of Fluids Engineering, Vol. 110, 1988, pp. 283 - 288.
- /10/ Shapiro, A.H., Compressible Fluid Flow, Vol. I, The Ronald Press, New York, 1953.
- /11/ Oswatitsch, K., Spezialgebiete der Gasdynamik, Springer, Wien - New York, 1977.
- /12/ Oswatitsch, K., Grundlagen der Gasdynamik, Springer, Wien - New York, 1976.
- /13/ Anderson, J.D., Jr., Modern Compressible Flow, McGraw-Hill, New York, 1982.



## MATERIALS FOR HYPERSONIC ENGINES

Terence M.F. Ronald  
Head, Materials Technology  
NASP JOINT PROGRAM OFFICE  
Wright-Patterson Air Force Base  
Ohio 45433  
U.S.A.

92-16997



## SUMMARY

This paper describes the structural materials development program for the National Aero-Space Plane (NASP). It indicates the materials studied, the approaches followed, and the general properties being developed. The major materials classes include titanium-aluminides, titanium-aluminide metal matrix composites, carbon-carbon composites, ceramic-matrix composites, beryllium alloys and copper-matrix composites.

## PREFACE

The U.S. National Aerospace Plane Program (NASP) is developing the technologies that are considered to be key to the successful operation of hypersonic aerospace vehicles. The general goal of the NASP program is the construction and testing of an experimental, fully reusable vehicle, designated the X-30, that will be used as a manned demonstrator of hypersonic flight. The vehicle will use hydrogen-fueled, air-breathing ramjet/scramjet engines and will be capable of horizontal take-off and landing. It will be designed to expand the envelope of high speed flight in and beyond the atmosphere to the point that access to low earth orbit can be achieved.

To meet weight and performance requirements, the NASP X-30 engines and airframe will make extensive use of uninsulated, load-bearing, lightweight structures. Active cooling with the hydrogen fuel will be used in many cases to keep temperatures within the capabilities of the materials, but to minimize weight it will be vital to have materials that combine low density with the highest possible temperature performance. Because of their potential for satisfying these needs, the materials classes of primary interest include titanium-aluminides, titanium-based metal-matrix composites, carbon-carbon composites, ceramic-matrix composites, copper-matrix composites and beryllium alloys.

The required materials and structures developments have been the subject of an extensive \$150 million program that started in March 1988. Known formally as the NASP Materials and Structures Augmentation Program, it is a cooperative venture of the five prime contractors who are developing concepts for the NASP airframe and engines. In addition to these five companies, the program uses the active participation of more than a hundred specialist subcontractors in addressing the various materials and processes development needs. The scope of the development program extends to the fabrication and testing of full-scale demonstration components of the various materials systems.

Each of the five prime contractors has undertaken the lead role for the development of one of five key classes of materials, with each company participating in the development activities for all five classes. General Dynamics heads the refractory composites area, involving carbon-carbon composites and ceramic-matrix composites. Rockwell has taken the lead for the titanium-aluminide development and scale-up effort, based on the Ti<sub>3</sub>Al and TiAl classes of materials. McDonnell Douglas manages the effort on titanium metal-matrix composites, comprising fiber-reinforced titanium alloys and Ti<sub>3</sub>Al intermetallics. Rocketdyne has the responsibility for high conductivity materials, comprising copper-matrix composites and beryllium alloys. Pratt and Whitney has undertaken the high creep strength materials activity, involving materials and structures intended for hot, actively cooled engine components. This latter area centers on monolithic and reinforced TiAl, using potentially compatible fibers such as titanium diboride.

Almost all of these materials are potentially important for hot, load-bearing structures in both the airframe as well as the engines of the vehicle. On the airframe they would be used as lightweight skin panels of honeycomb-core, truss-core, or integrally stiffened thin sheet configuration. Where necessary they would be cooled with the hydrogen fuel by incorporating appropriate coolant passages into the structures. In the engines they would be used as the sidewall panels in the hot gas path of the ramjet/scramjet. The engine application represents a particularly severe environment in the sense of thermal, acoustic and mechanical loading. In this case the structures will almost certainly have to be actively cooled, meaning that the materials will be in contact with hot hydrogen from the fuel, hot oxygen from the incoming air, and the gaseous products of combustion.

The remainder of the paper describes the various classes of materials that are under development. Because they will find application over all of the vehicle, little distinction is made between the engine and the airframe needs. The general materials classes and associated processes apply equally to all areas, whether they are the small hot gas path panels of the engines or the more extensive regions of the airframe. The specific property requirements will be different—for example, time at temperature—but the materials themselves are not in general engine- or airframe-specific.

## TITANIUM ALUMINIDES

Titanium-aluminide intermetallics are candidates for structures in both the engines and the airframe. They have essentially the same density as titanium but lead to the possibility of much higher use-temperatures. The two intermetallic systems that are of primary interest are based on the Ti<sub>3</sub>Al and TiAl compositions and have potential temperature capabilities of about 815°C and 980°C respectively.

The principal drawback of the aluminides is their limited ductility and toughness properties at temperatures less than a few hundred degrees. Coupled with the requirement for very high fabrication temperatures, this makes their processing difficult. Product forms that require a large amount of metal deformation, such as sheet for honeycomb-core or truss-core panels, must be processed in a carefully controlled manner to avoid cracking of the material during the reduction of the starting material to finished form. In addition, the use of the aluminide components in load-bearing structures must take account of the probability that their ductility and toughness characteristics will be limited in comparison to other materials, such as conventional titanium alloys.

New processing methods are being used to modify aluminide compositions and microstructures to yield structurally useful materials. The goal is to achieve an appropriate balance of strength with toughness or ductility while retaining the low density and high temperature characteristics that make the aluminides so attractive. One useful approach that has been quite successful employs rapid-solidification powder methods to develop improved alloys and much of the NASP-related work in this area uses a rotary atomization process to produce rapidly solidified powder. The powder is consolidated into fully dense billets that are then processed into appropriate product forms. The process is now relatively mature and the equipment has been scaled up to the point that it is capable of making hundreds of kilograms of powder material a day.

Advanced thermal-mechanical processing methods have been developed for both the powder-produced intermetallics and those made using conventional cast and wrought methods. These processes have improved the characteristics of the  $Ti_3Al$ -based alloys significantly and good quality sheet products are being produced. Sheet-processing methods for the harder-to-work  $TiAl$ -based materials have also been developed but have yet to be scaled up to an economical production level. In terms of mechanical properties, significant improvements have been made in the  $Ti_3Al$ -based materials and they can be regarded as good candidates for broad structural use. In the  $TiAl$  materials, a balanced set of mechanical properties--a suitable mix of strength, toughness, ductility, fatigue, and high temperature properties--is still to be achieved.

Because much of the airframe and engine structure will be actively cooled, hydrogen at various temperatures and pressures will be in contact with many of the structural materials. Hydrogen interacts adversely with most titanium alloys, leading to embrittlement in many situations, but the titanium aluminides are more resistant than conventional alloys, with the  $TiAl$  materials being the least affected. Hydrogen-resistant barrier coatings will be needed for all the materials to some extent, and the development of effective coatings is an integral part of the program.

## TITANIUM ALUMINIDE COMPOSITES

Metal-matrix composites based on titanium-aluminides offer significant improvements in stiffness and strength over their monolithic counterparts, making them attractive for the thin-gauge skin structures required for NASP. The basic technical challenge in making these composites is to incorporate reinforcement fibers into the matrix without creating adverse reactions at the fiber/matrix interface.

The conventional method for fabricating metal-matrix composites--involving the hot pressing of sandwiches of matrix material and fibers--is difficult to accomplish with titanium-aluminides. They have poor formability characteristics and they interact with the fiber at the temperatures and times needed for consolidation. There is also a thermal expansion mismatch between the fiber and the matrix that can lead to cracking of the low-ductility matrix on cooling from the consolidation temperature or during subsequent thermal cycling.

In an alternative approach to consolidation, a rapid-solidification plasma-deposition (RSPD) process is used to fabricate titanium-aluminide composites. The matrix material starts as a powder that is fed through a plasma arc to convert it into molten droplets. These are deposited onto reinforcing fibers that are spiral-wrapped on a large diameter drum, where on impact they are rapidly quenched to a solid state. Rotation and translation of the drum allows the build-up of a layer of matrix material on and between the fibers. This solidified deposit of matrix material, containing a single layer of fibers, can be subsequently slit and stripped off the drum and several of these layers can be stacked together and hot pressed to make a multilayer composite.

The RSPD process has been demonstrated successfully with SiC reinforcements in  $Ti_3Al$  matrix materials and useful mechanical properties can be obtained. The equipment itself has been scaled up to a pilot plant size that will allow the production of reinforced sheet material that is about 1x3 m in size. The same process can be used to produce  $TiAl$ -based composites but the inherent brittle nature of this material makes subsequent multi-layer consolidation difficult to achieve. This is principally the result of the thermal expansion mismatch between the fiber and the matrix that produces residual tensile stresses in the matrix on cooling, causing it to crack. Alternative fibers are under development that have a closer expansion match and better chemical compatibility to the  $TiAl$  matrix material than is the case with the SiC fiber. These appear to be promising but this class of composites will require further development to make them reliable structural materials.

## XD COMPOSITES

The XD process can be applied to a variety of materials to form fine, close-spaced distributions of reinforcing second-phase particles. The term XD refers to the proprietary technique that is used to create the reinforcements. In essence, it is a process that results in the fabrication of discontinuously reinforced metal matrix composites where the matrix can be any one of a number of alloys and the reinforcing particles can be varied in terms of composition, size, shape and distribution. A unique feature of the process is that the reinforcements are formed and grown *in situ* within the matrix, as distinct from being mechanically mixed as a separate additive; as a result, the particle/matrix interfaces are clean and well bonded, thereby enhancing the effectiveness of the reinforcements.

The process can be tailored to produce a variety of second phase particle distributions, where the particle shape can vary from spherical to needle-like. Mixtures of different reinforcements also can be formed that include coexisting sizes, shapes and types of particles. In many cases, the dispersoids are very stable and can survive a remelting process; as a result, the material subsequently can be cast into shaped components without destroying the reinforcement.

The XD process has been used to make titanium aluminide composites where the reinforcing phase is titanium diboride. The microstructures resulting from the XD process are attractive principally because they lead to significantly improved strength levels over the useful temperature ranges of the aluminides. The properties are also essentially isotropic, making the materials useful for complex-shaped structures that would be difficult to fabricate from continuous fiber reinforced materials.

## CARBON-CARBON COMPOSITES

Carbon-carbon composites have the potential for use as lightweight structures that could be exposed to temperatures in excess of 1400°C without the need for active cooling. Because of this capability, they are candidates for the airframe, where they could be used as large, integrally stiffened skin panels on the hotter parts of the vehicle. They may be useful also for engine structures.

In general, from the point of view of availability as structural shapes, carbon-carbon composites can be regarded as mature materials. There is a large base of knowledge available regarding their fabrication and practical use and they have been used in a variety of applications. Several companies specialize in the manufacturing of components and there are several basic methods available for making structural shapes.

There are technical problems to solve before they can be used as load-bearing, thin-gauge structural components for NASP. Chief among these is the need for effective oxidation protection in the hypersonic flight environment. Existing protection schemes, usually involving multilayer coatings and sealants, work reasonably well in situations where the material is taken up to a single high temperature and then cooled, but they face significant problems when exposed to complex temperature cycles.

The basic difficulty with existing protection schemes is their use of refractory materials such as silicon carbide as outer protection layers. These work well from a chemical standpoint but they can crack due to the thermal expansion mismatch between the silicon carbide and the carbon-carbon substrate. To alleviate this problem, use is made of additional interlayers that oxidize to form a glass that can flow and seal cracks. Unfortunately, these glasses do not flow readily at intermediate temperatures, reducing their effectiveness over part of the temperature range of interest. Recent advances in coating technology have improved the situation and small coated coupons have withstood the cyclic-temperature loading typical of a NASP environment. These improved protection schemes have yet to be scaled up to the large, complex-shaped components needed for NASP.

## CERAMIC-MATRIX COMPOSITES

Like carbon-carbon composites, ceramic-matrix composites have the potential for use at temperatures in excess of 1300°C, with the added advantage of a much higher degree of inherent oxidation resistance. Unlike the carbon-carbon materials, they are not as mature as a class of structural materials and do not enjoy the same broad base of manufacturing experience. They have not been as widely used and they have limitations when it comes to using them for long times at the higher temperature ranges.

There are two general classes of ceramic-matrix materials that may be important for NASP: glass-ceramic-matrix composites, useful up to temperatures of about 815°C, and advanced ceramic-matrix composites, potentially applicable at much higher temperatures. Glass-ceramic-matrix composites are relatively well characterized and can be fabricated into product forms such as honeycomb-core panels, truss-core panels, and other complex shapes. Advanced ceramic-matrix materials--such as silicon carbide fiber reinforced silicon carbide (SiC/SiC)--are not as mature, principally because of the lack of a fiber that has sufficient stability in the matrix when exposed for long times above 1000°C. Improvements are being made in these materials, and large, complex-shaped demonstration components have been manufactured by specialist companies. A particular interest in the ceramic-matrix materials for NASP stems from their inherent resistance to hot hydrogen and they would be useful for actively cooled engine components.

## BERYLLIUM ALLOYS

Beryllium is a commercially available material that possesses the advantages of low density, high elastic modulus, and very good thermal conductivity. Its disadvantages include poor toughness characteristics, crystallographic-texture-sensitive properties, a limited use-temperature of about 540°C, and environmental concerns associated with the toxic nature of the oxide. In spite of its problems, beryllium is successfully used in a wide variety of applications and there is a considerable body of experience concerning its fabrication and handling.

In addition to the benefits of light weight, its thermal conductivity characteristics make it particularly useful for structural components that are designed to transfer heat efficiently from one location to another. For NASP, the beryllium would be used primarily in heat exchangers or actively cooled engine panels, where it would be in sheet form in honeycomb-core or truss-core panel structures that would contain integral cooling passages within the structure.

## COPPER-MATRIX COMPOSITES

Because the NASP vehicle will make extensive use of actively cooled structure, there is a particular interest in high thermal conductivity materials, including copper-matrix composites. Copper itself has a good thermal conductivity but is heavy and its upper use-temperature is limited by its low mechanical properties. Pitch-based, high modulus graphite fibers have excellent thermal conductivity--better than the copper itself in the direction of the fiber--and the addition of these fibers to copper reduces density, increases stiffness, raises the use-temperature, and significantly improves thermal conductivity in the direction of the fibers.

One approach to the fabrication of these composites starts with a process that places a layer of copper around each fiber in a graphite fiber tow. The coated fibers are subsequently packed together and hot pressed into a fully dense material containing a high volume percent of fibers. In practice, cross-ply lay-ups will be used to tailor the thermal conductivity and compensate for the directional effects of the fiber.

Additional work in this general area addresses discontinuously reinforced copper composites. These are made by adding alloying elements such as niobium to the copper and applying appropriate processing methods to form a very fine dispersion of the alloying addition. In this way it is possible to strengthen the material without lowering the conductivity of the matrix.

## COATINGS

Coatings will play an important role for all materials used in the NASP airframe and engines and are a key part of the development activities for each material system. They can perform several critical functions, including control of temperature and protection against the environment.

For temperature control, they are designed to have high emissivity and to be noncatalytic to the recombination of the dissociated gases present in the hypersonic airflow across the skin. This can lead to a reduction of several hundred degrees in surface temperature. For oxidation resistance, they can provide a suitable barrier that prevents contact of hot oxygen with the underlying material.

The coating issue unique to NASP arises from the need to protect the materials against the effects of the hydrogen used for cooling. Hydrogen diffuses readily through many materials and can form brittle compounds within the material. The development of hydrogen barrier coatings is a critical challenge, especially coatings that are thin, lightweight, resistant to damage, and can be applied to complex shapes, including internal passages. Successful coatings most likely will incorporate multilayer protection schemes involving several thin layers of materials, each performing a contributing function.

## Discussion

BOURY

You have shown a structure of metallic tube in carbon-carbon. Have you noticed some problem of thermal contact between these two materials?

AUTHOR'S REPLY

Yes, there is a problem. There is an expansion mismatch between the materials. We need to have very close contact. We have no solutions with confidence.

STOLLERY

Could you say something about the fatigue life that is expected of modern carbon-carbon material? Engine manufacturers say that in a few years we will have entirely non-metallic engines.

AUTHOR'S REPLY

It is a question of trading off various properties. We can improve fatigue performances in titanium aluminides at the cost of strength. We have to achieve a balanced set of properties. The question of fatigue of carbon-carbon is a different kind of situation. It is not a traditional material. It has to be handled somewhat differently. How do we detect a flaw in these materials?

OBSERVER (BRITISH AEROSPACE)

What are the difficulties to impregnate these materials with optical fibers?

AUTHOR'S REPLY.

The problem is the survival of these fibers during the material autoclave process.



MATERIAUX ET SYSTEMES DE MATERIAUX POURLA PROPULSION COMBINEEAUTEURS :

D. BOURY \* - A. BEURAIN \*\* - A. LASALMONIE \*\*\* - Y. HONNORAT \*\*\*

\* SEP, Saint Médard en Jalles Cedex 33165  
\*\* SEP, Vernon 27207  
\*\*\* SNECMA, BP 81 Evry 91003

France

RESUME

Cet article passe en revue les différentes classes de matériaux qui peuvent être envisagées pour la construction des moteurs hypersoniques à cycle combiné aérobie/anaérobie. On montre que la grande dimension des pièces, des conditions inhabituelles de température et d'ambiance soulèvent des problèmes nouveaux dont la résolution passe par des programmes d'étude de grande ampleur. Les matériaux non métalliques renforcés ont une place aussi importante à prendre que les matériaux métalliques. L'assemblage de pièces aussi dissimilaires nécessite de développer des solutions adéquates d'assemblage mécanique et de résoudre les nombreux problèmes tribologiques qui ne manqueront pas de se poser.

ABSTRACT

This paper reviews the different categories of materials which can be considered for the engineering and production of the future hypersonic combined cycle engines. The large size of the parts associated with the non current conditions of temperature and environment makes arise new problems, the solution of which shall require programs of very large extent. The non metallic reinforced materials have a potential place as large as that of the metallic materials on these developments. The assembly of such dissimilar parts goes through specific solutions of mechanical assembly and the solving of a great deal of tribological problems.

## 1. MISSIONS ET BESOINS GENERAUX

Les véhicules hypersoniques à vocation de lanceurs spatiaux seront très différents des véhicules anaérobies actuels du type ARIANE 5. L'émergence de ce type de véhicule n'est envisageable que s'ils permettent de réduire, de façon sensible, les coûts du kilogramme de charge utile en orbite. Leur intérêt potentiel réside dans la réutilisation du véhicule complet, sur un nombre de missions importantes (200 à 500), et à terme dans une mise en oeuvre et une maintenance réduites.

Deux types de véhicules sont envisageables :

- Mono-étage, propulsé par des moteurs à cycles combinés aérobies-fusées.
- Bi-étage, propulsé par des moteurs aérobies sur le 1er étage, puis fusées sur le 2ème étage, ce dernier étage étant séparé au Mach le plus élevé possible.

Dans les deux cas, on cherchera à prolonger le vol aérobie le plus longtemps possible pour profiter de l'oxygène de l'air disponible comme comburant non embarqué, (de façon à limiter la taille du véhicule). Cela implique des durées de fonctionnement des structures dans des conditions aérothermiques particulièrement sévères (voir Figure 1). Le prolongement du vol aérobie n'est envisageable que si les performances des moteurs à cycles combinés aérobies, dans ces conditions aérothermiques, se révèlent encore supérieures à celles des moteurs fusées cryogéniques actuels ou envisageables (consommation des ergols embarqués par unité de poussée, rapport poussée sur masse ...).

La plupart de ces moteurs utilisent l'hydrogène comme carburant. Cet hydrogène est stocké sous forme liquide et constitue une source de frigories disponible, mais limitée, pour refroidir une partie des structures du véhicule et des pièces de moteur, avant d'être utilisé éventuellement comme source d'enthalpie pour créer un entraînement mécanique, puis injecté dans la chambre propulsive.

Enfin, les lois de trajectoires conduisent à rechercher des indices structuraux très faibles, plus particulièrement sur les monétages où 1 kg de structure est 1 kg de moins de charge utile pour chacune des missions.

## 2. EXAMEN DES BESOINS POUR LES PIECES DU SYSTEME PROPULSIF

Les moteurs à cycles combinés envisagés sont en cours d'évaluation (1) : Turboréacteur -statoréacteur, turbofusée - stato-fusée, fusée-stato, stato à combustion supersonique ...

Un moteur représentatif de la complexité de ces concepts sera retenu pour l'analyse et les développements ci-après ; le turbofusée - statoréacteur -fusée, moteur combiné d'un lanceur monétage. Il est présenté en Figure 2 . Ses cotes principales et les conditions de fonctionnement à un de ses points caractéristiques sont schématisés en Figure 3. Pour chaque type de pièces, il est possible de dresser une liste de conditions générales et spécifiques de fonctionnement et en déduire les besoins en matériaux adaptés - voir Tableaux 1 et 2 pour l'exemple.

A partir de là, il est possible d'envisager deux grandes familles de matériaux disponibles, à améliorer ou à développer pour répondre à ces besoins :

- Les matériaux homogènes essentiellement métalliques,
- Les matériaux composites à matrice métallique ou non.

Une première répartition en est donnée en Figure 4.

### 3. LES MATERIAUX METALLIQUES

La température limite d'utilisation des alliages métalliques est en général nettement inférieure à leur température absolue de fusion  $T$  en raison de deux phénomènes physiques dont l'influence devient significative à partir de  $0.6 T_f$  :

- Les évolutions microstructurales telles que la coalescence des précipités, ou des grains. On peut repousser cette limite en augmentant la fraction volumique de phase durcissante et en rajoutant en solution solide des atomes lourds à diffusion lente ; il existe toutefois une limite liée aux diagrammes de phases.
- Les phénomènes d'oxydation-corrosion qui peuvent conduire à la rupture prématurée des pièces lorsque la surface est suffisamment dégradée, et dont les prémices se font sentir par diffusion du gaz réactif de l'atmosphère dans les zones d'endommagement local (fissures).

#### 3.1. Les alliages métalliques

La Figure 5 illustre les propriétés mécaniques spécifiques des principaux alliages métalliques comparées à celles des composites réfractaires. Le Tableau 3 rassemble les paramètres physiques principaux (autres que mécaniques) des différents types de matériaux. Si l'on excepte les alliages d'aluminium dont l'utilisation est limitée aux températures inférieures à  $300^\circ\text{C}$  on peut distinguer quatre grandes classes d'alliages métalliques pour applications à moyenne et haute température :

a). Les alliages de titane : même pour les alliages les plus réfractaires, de type (Ti834), la température limite d'utilisation sera de l'ordre de  $600^\circ\text{C}$  ; signalons d'autre part que les alliages de titane sont très sensibles à la fragilisation par l'hydrogène et à l'oxygène (feu titane), donc difficilement utilisables dans la turbine.

b). Les alliages de nickel dont on distingue trois types :

- Les alliages forgés conventionnels (INCO718, WASPALOY ...) dans lesquels la résistance optimale est obtenue par un traitement thermomécanique comprenant un forgeage à la presse ou au pilon. Ces alliages peuvent être utilisés sous forte sollicitation mécanique jusqu'à environ  $650^\circ\text{C}$ .
- Au-delà de  $650^\circ\text{C}$  les alliages coulés-forgés ont une teneur en phase durcissante trop faible pour que l'on puisse les utiliser dans les disques très sollicités. On doit alors passer aux alliages élaborés par Métallurgie des Poudres (ASTROLOY, N18 ...) et mis en forme par forgeage isotherme (2). Ces alliages présentent une résistance spécifique exceptionnelle jusqu'à  $750^\circ\text{C}$  environ.
- Au-dessus de  $750^\circ\text{C}$  le taux de phase durcissante nécessaire pour assurer la résistance au fluage impose des alliages coulés non forgeables ; l'effet nocif des joints de grains qui ne constituent plus des obstacles à la déformation est résolu par l'utilisation soit de structures de grains colonnaires soit de pièces monocristallines.

Les superalliages de nickel contiennent des teneurs en chrome et en aluminium leur assurant une résistance intrinsèque à l'oxydation et à la corrosion jusqu'à environ  $900^\circ\text{C}$  pour des durées de l'ordre de la centaine d'heures ; au-delà, des revêtements protecteurs à base de CrAl et NiAl ont été mis au point (3) qui assurent une résistance à l'oxydation efficace jusqu'à  $1200^\circ\text{C}$ .

Les superalliages de nickel qui constituent un matériau bien adapté à la turbine du moteur spatial risquent de poser, au voisinage de la température ambiante un problème de fragilisation par l'hydrogène. Ce point, qui risque d'être important, sera discuté plus loin.

c) Les alliages de beryllium sont en fait intéressants pour leurs propriétés thermiques exceptionnelles et leur coefficient de Poisson anormalement bas (Tableau 3) ; par contre, ils sont pénalisés par leur faible point de fusion, leur très grande fragilité et leur faible résistance et, en ce qui concerne leur mise en oeuvre, par leur toxicité.

d) Les alliages de niobium qui présentent d'excellentes propriétés spécifiques au-dessus de  $1200^\circ\text{C}$  ne peuvent fonctionner en atmosphère oxydante. Leur utilisation nécessitera, à la fois le développement d'alliages plus résistants à l'oxydation et celui de protections.

### 3.2 Les composés intermétalliques :

Ces matériaux dont la composition repose sur la combinaison en proportions définies d'un petit nombre d'atomes organisés cristallographiquement sont très attractifs lorsqu'ils présentent à la fois une faible densité et un module élastique élevé associés à un large domaine de stabilité thermique.

Ces dernières années l'effort a été porté sur les aluminures tels que Ni<sub>3</sub>Al, Ti<sub>3</sub>Al, Tableau 1). Ti<sub>3</sub>Al présente des perspectives intéressantes puisque la ductilité à l'ambiante a pu être améliorée par l'addition de Niobium. Il ne permet toutefois pas des applications au-dessus de 750°C en raison de problèmes d'oxydation et de chute de la résistance au fluage. Des composés plus légers comme TiAl ou présentant des températures de fusion très élevées comme MoSi<sub>2</sub> (4, 5) sont à l'étude.

Les composés intermétalliques sont en général fragiles à l'ambiante et leur résilience est toujours faible. Compte tenu de leur faible ténacité, on envisage essentiellement de les utiliser comme matrice pour des matériaux composites. Sur la Figure 5, figurent par exemple des résultats encourageants pour le système SiC-Ti<sub>3</sub>Al. Ce type de système est toutefois difficile à élaborer et reste à caractériser complètement, en particulier en fatigue thermique et mécanique.

### 3.3 Problème de la fragilisation par l'hydrogène

La turbine du moteur spatial sera alimentée par un mélange riche en hydrogène ; on risque de se heurter alors au problème de la fragilisation par l'hydrogène des matériaux métalliques.

Ce problème, bien connu depuis longtemps dans les aciers présente deux aspects :

- La fragilisation par l'hydrogène interne dissous dans le métal,
- La fragilisation résultant d'une atmosphère d'hydrogène et liée aux phénomènes d'adsorption et d'absorption superficielle.

Les études de laboratoire ont montré que la fragilisation était un phénomène complexe, où interviennent de multiples facteurs, en particulier la microstructure de l'alliage. La Figure 6 montre, dans le cas de l'INC0903, la décroissance très rapide de la ductilité avec la teneur en hydrogène. Cet effet est à relier à la perte importante des caractéristiques de traction entaillée (contrainte, allongement).

La fragilisation par l'hydrogène interne est un phénomène réversible. On peut par exemple retrouver les propriétés initiales grâce à un traitement de désorption à une température de l'ordre de 500°C. Par contre, sous pression d'hydrogène, la tenue en fluage des superalliages de nickel polycristallins est fortement dégradée.

Une caractérisation de cet effet dans les alliages retenus pour la turbine sera nécessaire pour garantir la durée de vie du moteur.

### 3.4 Perspectives

Actuellement, la température d'utilisation maximale des matériaux métalliques est de 1150°C environ. Une extension du domaine d'utilisation est possible, grâce à l'utilisation de barrières thermiques qui consistent en des dépôts de fines couches céramiques (par exemple, Zircône stabilisée). Un dépôt de 0,2 mm d'épaisseur peut conduire à un gain en température de l'ordre de 150°C. Un gain n'est toutefois possible que si la pièce possède un circuit de refroidissement interne.

On peut prévoir deux types d'évolution dans l'utilisation de ces matériaux métalliques :

- Un gain en densité dans le domaine des températures moyennes ( $T \leq 1000^\circ\text{C}$ ) par exemple par l'introduction de composés intermétalliques ou de composites,
- Un accroissement de la capacité en température grâce au développement de nouveaux composés à point de fusion élevé,

Parmi les problèmes auxquels on se heurtera, on peut citer les phénomènes de fatigue mécanique et thermique liés à la rapidité du décolage.

Dans tous les cas se posera, au niveau de la turbine, le problème de fragilisation par l'hydrogène; la protection par dépôt de métaux précieux (or) est efficace, il est toutefois souhaitable de mettre au point des alliages ayant une résistance intrinsèque à l'hydrogène.

## 4. LES MATERIAUX COMPOSITES : GENERALITES

L'utilisation des matériaux composites constitue une voie prometteuse pour étendre le domaine d'utilisation des matériaux massifs, métalliques ou non. Le composite présente l'intérêt d'utiliser la très haute résistance des fibres tout en conservant une certaine ductilité lorsque la matrice est bien adaptée. Toutefois, dans les difficultés liées à ces matériaux il faut citer le comportement anisotrope qui nécessite l'adaptation de la texture au type de sollicitation, et l'utilisation de modèles mécaniques de comportement plus complexes que pour les matériaux monolithiques.

Les applications des composites sont spécifiques à la fois du type de fibres et de matrices ; c'est pourquoi, nous les passerons en revue séparément.

#### 4.1 Composites à base de titane

Ces matériaux se caractérisent pour leur grande rigidité, leur résistance à la rupture élevée combinée à une faible densité (voisine de 4). Dans le sens des fibres, les caractéristiques mécaniques spécifiques jusqu'à environ 700°C sont nettement supérieures à celles d'un superalliage de nickel (Figure 7). Dans le sens travers, ces composites présentent une faible ductilité et une résistance voisine de celle de la matrice ; La tenue à l'impact est bonne en raison de la ductilité de la matrice.

Signalons le rôle essentiel joué par l'interface fibre - matrice : outre le rôle classique du transfert de charge, l'interface conditionne les cinétiques de réaction matrice - fibre.

La très grande réactivité de la matrice de titane impose, si l'on veut utiliser des fibres fines et tissables, la mise au point de traitements d'interface particuliers, tel que le dépôt de graphite pyrolytique (Figure 8). Ces traitements confèrent au composite une bonne stabilité thermique si la température reste modérée (Figure 7).

Industriellement, ces composites sont très difficiles à élaborer, en particulier si l'on cherche à utiliser des matrices intermétalliques telles que Ti3Al, ou TiAl susceptible d'apporter un gain supplémentaire en température.

#### 4.2 Composites à matrice verre

Les composites à matrice verre et à fibres longues peuvent être considérés comme une extrapolation sur les hautes températures des expériences accumulées sur les composites à matrices organiques. Il s'agit en effet d'un renforcement d'une matrice à faible module (60 à 80 GPa) par des fibres à très haut module (200 GPa pour SiC, 300 GPa pour le carbone). L'incorporation de fractions de fibres de 30 à 50% permet d'obtenir un matériau très résistant et à faible densité (2 à 2,5).

On peut distinguer deux classes essentielles de composites :

a) Les composites à renfort de fibres de carbone et à matrice borosilicate qui présentent une résistance à l'ambiante très élevée (600 MPa en traction et 1200 MPa en flexion).

Ces composites sont utilisables jusqu'à 400°C environ (Figure 9). Ils peuvent être obtenus avec des tissages 1D, 2D, 3D ou même 5D.

b) Les composites renforcés par des fibres de SiC (1D, 2D ou tressés).

Ces composites sont moins résistants que les précédents à basse température mais sont utilisables à des températures plus élevées : environ 600°C pour des matrices borosilicates, jusqu'à 1200°C pendant un temps court (1 heure) pour des matrices LAS (Figure 9).

#### 4.3 Composites thermostructuraux

Sous ce vocable la SEP a développé plusieurs familles de matériaux à matrice carbone ou céramique. Elle a ainsi étudié des matériaux composites carbone-carbone (SEPCARB). Ces matériaux conservent des caractéristiques mécaniques élevées à haute température (2500°C environ) mais sont très sensibles à l'oxydation à partir de 400°C. Pour d'autres applications, requérant une durée de vie en atmosphère oxydante (air, gaz de combustion) supérieure à quelques heures, la SEP a développé un procédé de densification chimique en phase vapeur de carbure de silicium (SiC) permettant la fabrication de matériaux composites à matrice céramique et fibres de carbone (SEPCARB-INOX). D'autres matrices céramiques et d'autres procédés ont été étudiés par la suite (Alumine, zircon, mullite ...). Pour des spécifications plus exigeantes de régime à haute température en milieu oxydant elle a développé les CERASEP (SiC-SiC). Il est possible de réaliser avec ces composites des éléments d'assemblage très variés (Figure 10).

#### Propriétés mécaniques et thermiques

Contrairement aux céramiques monolithiques qui présentent un mode de rupture fragile, les composites à matrice céramique possèdent un comportement pseudo-plastique comme le montrent les courbes de traction à différentes températures sous air d'un matériau C/SiC 2D protégé présentées Figure 11. En conséquence, ces matériaux sont peu sensibles au choc ou aux gradients thermiques.

L'évolution de la résistance spécifique en traction des différents composites thermostructuraux en fonction de la température est indiquée Figure 12. De par leur résistance mécanique spécifique élevée associée à une bonne tenue à l'oxydation, les matériaux C/SiC (SEPCARB-INOX) sont de très bons candidats pour la réalisation de composants haute température d'un moteur combiné pour lequel le bilan de masse est primordial.

Des études de la sensibilité à la fatigue de ces matériaux ont été effectuées. L'évolution du comportement en traction après un million de cycles de fatigue en traction-compression a été caractérisée. La résistance mécanique en traction n'est pas dégradée par des sollicitations cycliques. On note en revanche une diminution du module d'élasticité et de l'allongement à rupture.

### Durée de vie des composants

La durée de vie spécifiée des composants d'un moteur combiné sera probablement supérieure à 100 heures. Pour de telles applications, des traitements de finition doivent être utilisés afin de protéger le matériau de l'oxydation par le milieu extérieur (air, gaz de combustion). Des études sur la protection contre l'oxydation ont été menées dans le cadre des travaux sur les protections thermiques d'Hermès.

Des essais de vieillissement de matériaux ont été effectués en cyclage thermique. Des échantillons ont subi 120 cycles thermiques sous air entre la température ambiante et 1500°C avec un palier à haute température de 30 minutes. Cet essai correspond aux spécifications de durée de vie d'Hermès (2 fois la durée de vie de l'avion). 85% des caractéristiques mécaniques initiales ont été conservées après cyclage.

D'autre part, des essais sur pièces réelles ont également été effectués : une pièce correspondant à un bord d'attaque de l'avion spatial Hermès a été testée à la plate-forme solaire d'Almería (Espagne). 15 cycles thermiques de 30 minutes (dont 20 minutes de palier) à une température maximale de 1550°C et deux cycles d'une durée cumulée de palier de 20 minutes à 1750°C, correspondant à une rentrée de sauvegarde ont été appliqués. Des charges mécaniques ont été appliquées à la pièce durant l'essai afin de simuler les charges aérodynamiques présentes lors de la rentrée. Aucune rupture n'est intervenue lors de ces essais.

Un divergent de tuyère du moteur HM7 (Figure 13) en C/SiC a été essayé lors de deux tirs successifs en simulation d'altitude. La durée cumulée de tir est de 1700 secondes et la température maximale de la paroi d'environ 1700°C. Aucune évolution du divergent n'a été observée après ces deux tirs.

### Perspectives d'évolution des composites thermostructuraux

Les principales améliorations envisagées pour les matériaux composites thermostructuraux concernent l'augmentation des caractéristiques mécaniques, l'amélioration de la durée de vie et la connaissance des caractéristiques mécaniques.

Grâce à l'optimisation de la rhéologie de la liaison fibre-matrice et à l'utilisation de fibres plus performantes, une augmentation importante des caractéristiques mécaniques est possible. Une résistance à rupture de 500 MPa pour un matériau 2D C/SiC et de 350 MPa pour un 2D SiC/SiC pourront très probablement être obtenues d'ici 5 à 10 ans. L'utilisation, pour certaines pièces de géométries particulières, de textures adaptées, permettra également de dépasser de façon importante ces valeurs. D'autre part l'utilisation de fibres de SiC présentant une meilleure stabilité thermique permettra dans les mêmes délais d'élever d'au moins 200°C la température limite d'utilisation des matériaux SiC/SiC.

Pendant la même période, des progrès importants continueront d'être réalisés dans le domaine de la protection contre l'oxydation de ces matériaux. Compte-tenu des résultats actuels, l'objectif de la conservation de 80% de la résistance mécanique pour une durée de vie de 100 heures à 1700°C en atmosphère oxydante constitue un objectif tout à fait réaliste à moyen terme.

Une meilleure connaissance du comportement mécanique de ces matériaux permettra d'autre part une plus grande fiabilité du dimensionnement et une meilleure performance des systèmes réalisés à l'aide de ces matériaux. Les principaux domaines d'étude seront lors des prochaines années :

- Le comportement en fatigue,
- La sensibilité au fluage,
- L'établissement de modèles de comportement,
- La détermination de critères de rupture.

La maîtrise des contrôles non destructifs permettra également d'améliorer la fiabilité et la performances des systèmes composites pour la propulsion combinée.

### 5. SYSTEMES MATERIAUX POUR MOTEUR COMBINE

En plus des caractéristiques intrinsèques des matériaux, il est important de considérer les contraintes ou intérêts liés à leur mise en oeuvre dans un système complet.

Ce chapitre expose en fonction du système envisagé (liste non exhaustive correspondant aux sous-systèmes du moteur présentés Figures 2, 3 certains couples "conception/matériaux" envisageables, leurs intérêts et inconvénients respectifs, ainsi que quelques exemples de réalisation se rapprochant des besoins d'un moteur combiné.

#### 5.1 Prise d'air

Les premiers dessins de concepts font apparaître des ensembles de très grandes dimensions soit à section carrée (typiquement 2m x 2m) soit à section semi circulaire (2 à 4m de rayon) pouvant dépasser une dizaine de mètres en longueur. Les pressions internes maximales sont très élevées (5 à 10 Bar) et ce à des températures pouvant atteindre 1350°C.

Une structure métallique éventuellement équipée d'une protection thermique, nécessitant donc un faible refroidissement est envisageable. Une autre conception de type structure chaude faisant intervenir un matériau thermostructural, limitant le refroidissement aux actuateurs, est également possible ; le choix se fera sur un bilan global entre masse du système et besoin en refroidissement.

La conception d'une structure chaude est attrayante mais elle impose une maîtrise des technologies permettant de fabriquer et d'assembler des structures de grandes dimensions, légères, résistantes et rigides. Compte tenu des matériaux envisageables, ces techniques sont assez mal connues, ou au début de leur développement comme dans le cas des matériaux composites à matrice céramique.

En effet, dans le cadre du programme HERMES, une structure de grandes dimensions (1.7 x 0.8 mètre) pour un caisson de gouverne en Sepcarbinox Skinex (texture 3D haute résistance développée par SEP) fonctionnant à 1300°C sous air, est actuellement en cours de développement (voir Figure 14).

## 5.2 Compresseur d'air

L'architecture monoveine du turbofusée-statorfusée présenté Figure 2 devrait conduire à un bilan de masse favorable. Le compresseur d'air devra cependant pouvoir supporter de hautes températures, typiquement 1350°C. Les différentes pièces constituant la veine aérodynamique seront difficiles à réaliser, en particulier les aubes des roues mobiles. Deux technologies sont envisageables :

- La première utilisant les techniques de refroidissement actif mises au point pour les aubes de turbine des turbo réacteurs. Le premier étage du moteur M88 peut ainsi supporter une température de gaz de 1580°C avec une aube en alliage de nickel monocristalline, intégrant des canaux permettant une ventilation par de l'air frais,
- L'autre conception, basée sur une architecture de type aubes en matériau thermostructural rapportées sur un disque métallique, présenterait l'avantage de limiter le refroidissement à une simple ventilation du disque.

Un programme de démonstration de cette technologie pour un matériau composite à matrice céramique "Sepcarbinox" est en cours. Pour cette application le problème particulier du comportement au choc (ingestion d'oiseaux) sera à examiner.

Les disques de rétention de ces aubes seront très fortement sollicités mécaniquement et thermiquement afin de limiter leur ventilation. Les matériaux envisageables sont les matériaux métalliques avancés (intermétalliques à base de titane ...) ou les matériaux composites à matrice métallique (SiC/titane par exemple ...).

## 5.3 Turbine

La turbine de puissance du cycle turbofusée présenté est caractérisée par un grand diamètre et une température de gaz assez modérée. L'objectif sera d'obtenir une pièce légère, performante et sûre. Les solutions et architectures possibles sont relativement nombreuses :

- Disque et aube : métalliques ventilés si besoin,
- Disque en métal ventilé et aube en composite thermostructural,
- Disque en composite à matrice métallique et aube en composite thermostructural,
- Blisk métallique ventilé ou composite.

La Figure 15 présente un exemple de réalisation de type monobloc en matériau composite à matrice céramique de faible dimension.

La réalisation d'une pièce monobloc de grandes dimensions nécessitera un contrôle sévère des défauts sur des pièces critiques pour la sécurité du moteur. Une conception avec aubes en composite à matrice céramique rapportées sur un disque métallique serait alors plus attrayante.

## 5.4 Chambre de combustion aérobique

Les matériaux constitutifs des parois des chambres de combustion aérobiques devront obligatoirement être refroidis activement, compte tenu des très fortes températures atteintes par les gaz de combustion. Les parois se présenteront alors sous la forme d'une enveloppe externe structurale et d'une enveloppe interne refroidie jouant un rôle de protection thermique, éventuellement solidaires. L'enveloppe externe devra supporter une température assez élevée (500 à 800°C), pour utiliser au mieux les capacités de refroidissement du fluide refroidisseur. Un matériau de type composite à matrice verre pourrait alors être intéressant pour réaliser cette virole.

Pour l'enveloppe refroidie, diverses solutions sont possibles :

- Soit une chemise réfractaire ventilée par de l'air (double paroi, film ou multiperforation) refroidi dans un échangeur air/hydrogène,
- Soit un faisceau de tubes assemblés et refroidis par circulation interne d'hydrogène. Des tubes en béryllium seraient intéressants pour obtenir une rigidité importante de cette structure tout en offrant de bonnes propriétés thermiques,
- Soit une coque métallique (alliage de cuivre en propulsion fusée), refroidi par circulation d'hydrogène dans des canaux internes à cette paroi. Pour ces applications, il serait intéressant de diminuer la température de la face chaude de l'enveloppe interne afin de réduire le flux thermique à éliminer, et donc limiter le besoin en refroidissement. De ce point de vue, une coque interne en matériau réfractaire homogène serait plus sûre et plus efficace qu'un dépôt de type barrière thermique.

Les composites à matrice verre présentent une bonne étanchéité mais le gain en température sera faible. Les CMC plus réfractaires présentent par contre une perméabilité trop élevée qu'il faudrait réduire, et des difficultés d'assemblages avec la structure froide.

### 5.5 Divergent de tuyère

Les divergents de tuyère sont généralement des structures refroidies activement par ventilation d'air ou par circulation d'ergol. Pour les moteurs combinés, les surfaces seront importantes et les capacités de refroidissement limitées. Un principe de refroidissement par rayonnement d'une structure réfractaire, bien que conduisant à une perte d'énergie, semble plus intéressant à première vue. L'expérience acquise dans ce domaine avec les matériaux composites thermostructuraux est importante même si des progrès en durée de vie restent à accomplir.

La Figure 13 montre un divergent de type coquetier, en SEPCARBINOX NOVOLTEx texture 3D, développée et brevetée par la SEP, d'un diamètre de sortie de l'ordre du mètre, réalisé pour le moteur du 3ème étage d'ARIANE en 1988/1989. Des divergents en SEPCARBINOX d'un diamètre de sortie de 2,5 mètres sont en cours d'étude.

### 5.6 Couples tribologiques

En raison de la grande diversité des matériaux utilisés dans le moteur hypersonique, existera un nombre important de couples pièce statique - pièce mobile de natures variées.

Dans ce moteur, les conditions sévères de pression, de température et de vibration seront la source de problèmes critiques d'origine tribologique. Plusieurs centaines de types de couples ont été recensés dont les caractéristiques d'usure, de fretting sont différentes. Un certain nombre de solutions sont connues pour résoudre les problèmes de frottement (application de bisulfure de molybdène par exemple), mais l'introduction massive des composites dans le moteur engendrera nécessairement de nouvelles mises au point.

### CONCLUSION

La construction des moteurs combinés, pour la propulsion hypersonique, du type de celui projeté par la SNECMA, fera appel à une grande variété de matériaux qui seront utilisés dans des conditions sensiblement différentes de celles des moteurs aéronautiques actuels. La grande dimension des pièces et les écarts de température très importants qu'elles rencontreront en service posent d'abord le problème de la compatibilité de dilatation de celles-ci ainsi que celui de leur tenue à la fatigue thermique.

Les choix de matériaux se feront en outre en fonction de leur résistance aux agressions des fluides au sein desquels ils travailleront et en particulier de leur comportement vis-à-vis de l'hydrogène, et de leur tenue à l'oxydation et à la corrosion. Compte-tenu des possibilités de détérioration locale des revêtements protecteurs, les matériaux de base devront avoir une résistance intrinsèque suffisante vis-à-vis de ces agressions.

La disponibilité de technologies de production et de mise en oeuvre de ces matériaux sera tout aussi déterminante. Ces technologies devront permettre la réalisation de pièces de grandes dimensions de formes complexes et comprendra la maîtrise des procédés de liaison tels que le soudage, le brasage, le collage, mais aussi des procédés de traitement de surface.

Enfin, la maîtrise des techniques d'assemblage mécanique entre des pièces de matériaux identiques ou disponibles sera indispensable. Elle devra s'accompagner de solutions à tous les cas nouveaux de couples tribologiques dont le recensement aboutit à identifier un nombre considérable.



REFERENCES

1. M. DOUBLIER - P. RAMETTE : 13<sup>ème</sup> Colloque Matériaux pour l'Aéronautique et l'Espace - Paris 1989 - édité par AAAF p. 317
2. C. DUCROCQ - A. LASALMONIE - Y. HONNORAT  
Superalloys 1988, edited by S. REICHMAN, DN DUHL, G. MAURER, S.ANTOLOVICH and C. LUND  
The metallurgical society 1988, p. 63
3. R. MORBIOLI - P. STEINMETZ - C. DURET  
Materials et Science and Engineering 1987, p. 337 - 344
4. G. SAUTHOFF  
Z. Metallkunde vol 77 196, p. 654
5. R.L. FLEISHER  
Journal of metals dec. 1985, p. 16
6. R.J. WALTER - RP. JEWETT and WT; CHANDLER  
Material Science and Engineering  
Vol 5 1970, n°2, p. 99
7. D. ROUX - AM. BRASS and J. CHENE  
Proceedings of 4th Conf. ou hydrogen effects on materials behaviour  
Jackson Lake USA sept. 1989 ASM publication.

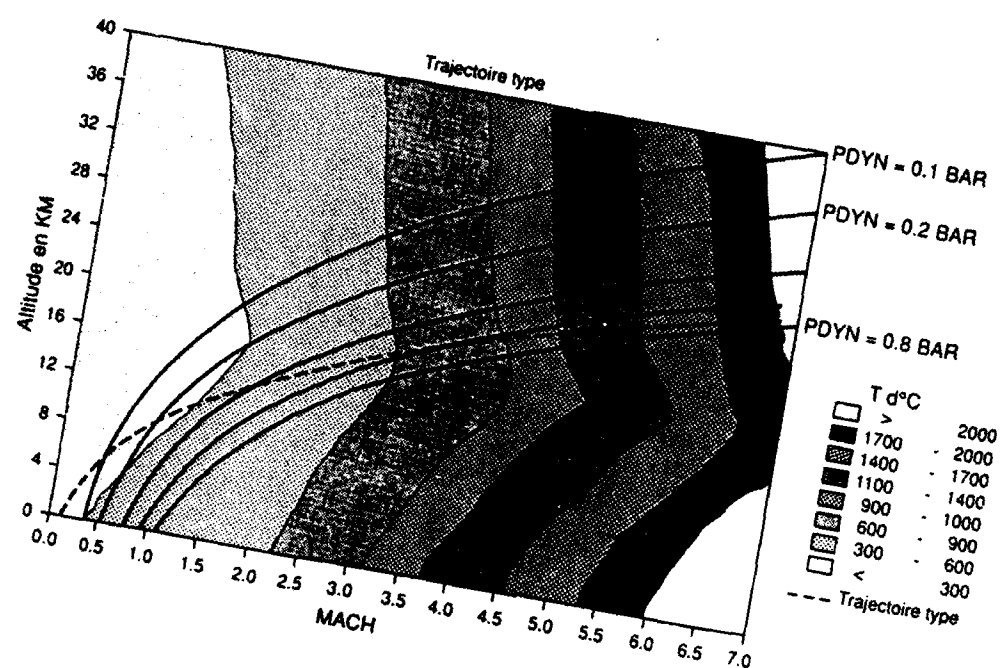


Fig. 1 : Trajectoires types d'un véhicule hypersonique

PROPULSION COMBINEE  
TURBOFUSEE - STATO - FUSEE

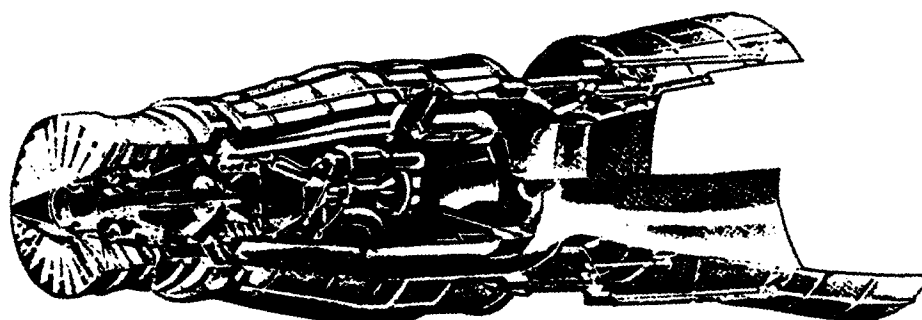


Fig. 2 : Moteur combiné Turbo-stato-fusée

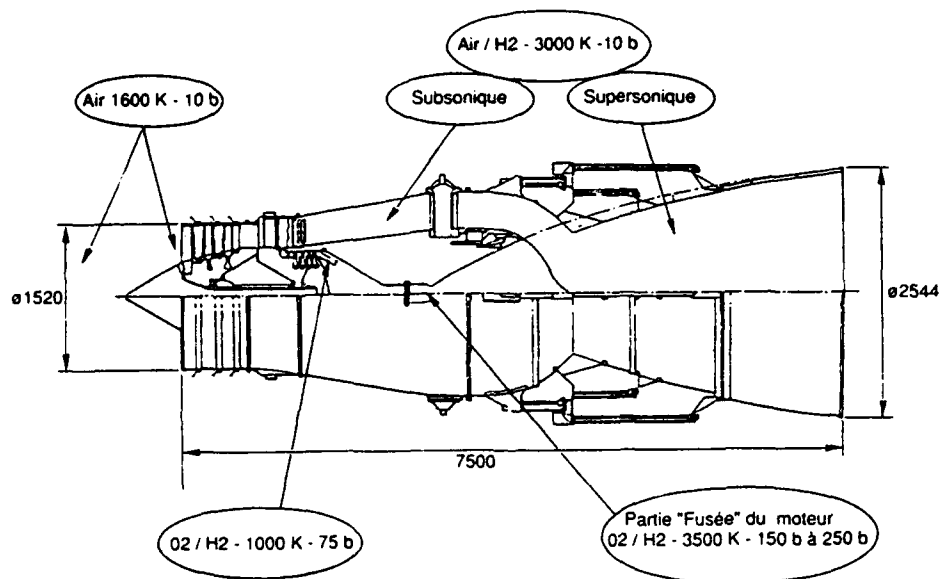


Fig. 3 : Schéma du moteur et conditions de fonctionnement

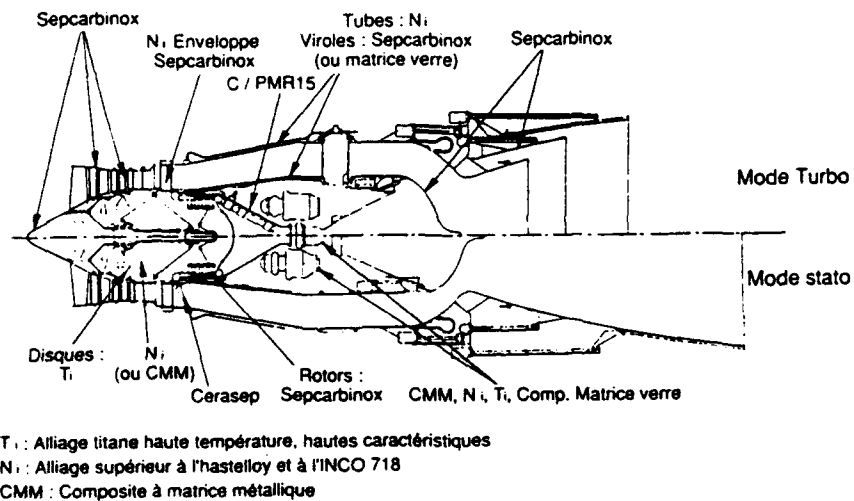


Fig. 4 : Matériaux du moteur Turbo-stato-fusée

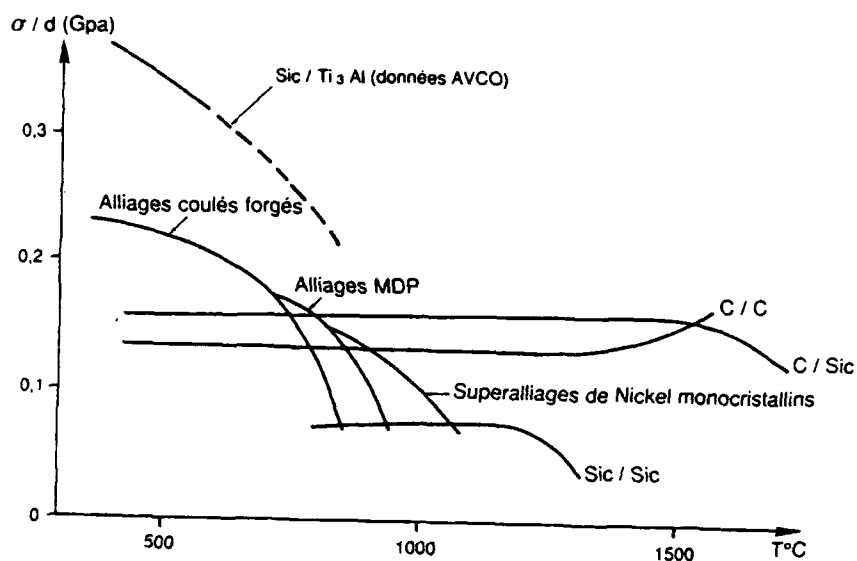


Fig. 5 : Propriétés spécifiques des superalliages de Nickel et des composites réfractaires

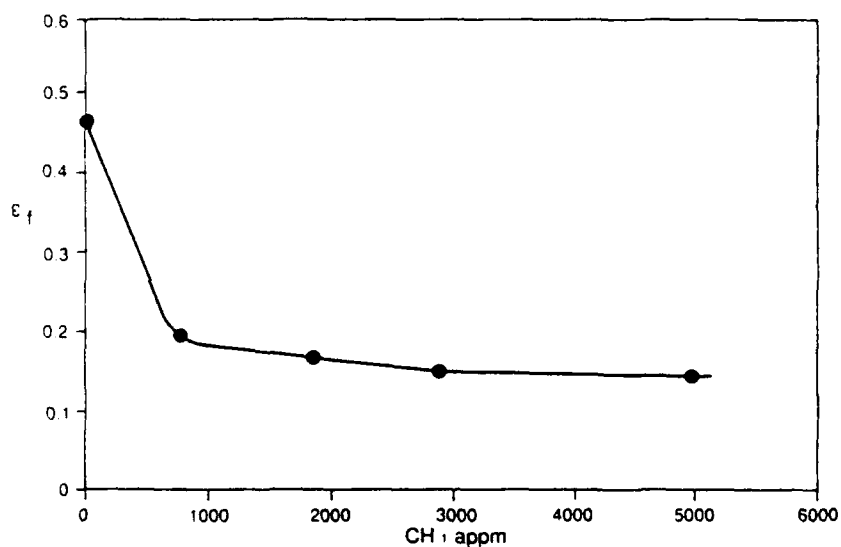
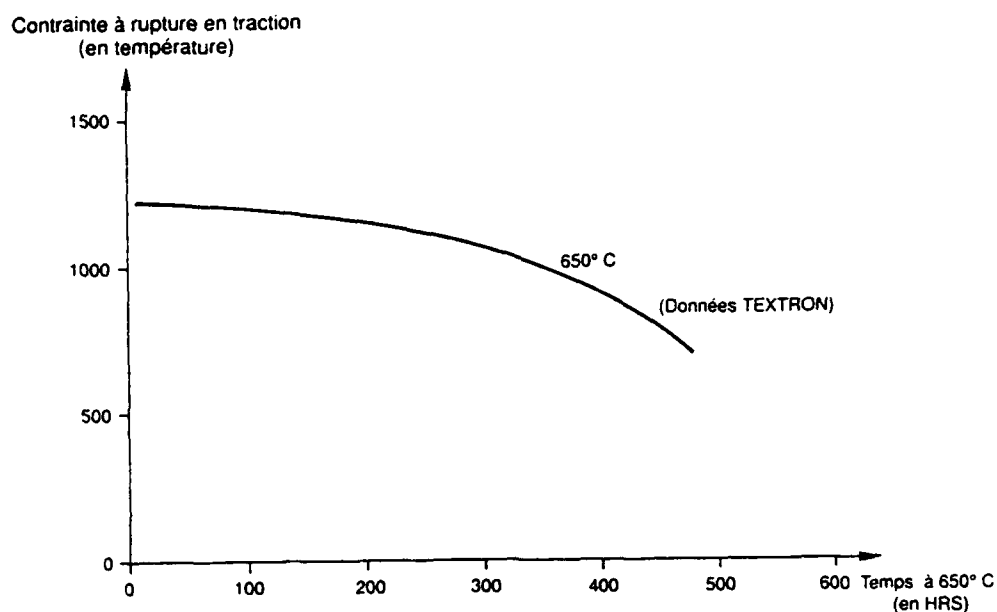
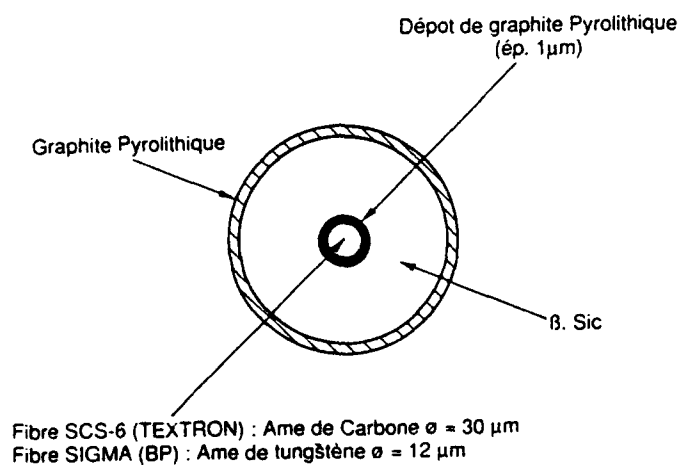


Fig. 6 : Abaissement de l'allongement à rupture due à l'enrichissement en hydrogène (d'après 6)



**Fig. 7 : Contrainte à rupture à 650°C d'un composite à matrice titane - Influence d'un vieillissement à 650°C.**



**Fig. 8 : Constitution des fibres dans un composite à matrice titane**

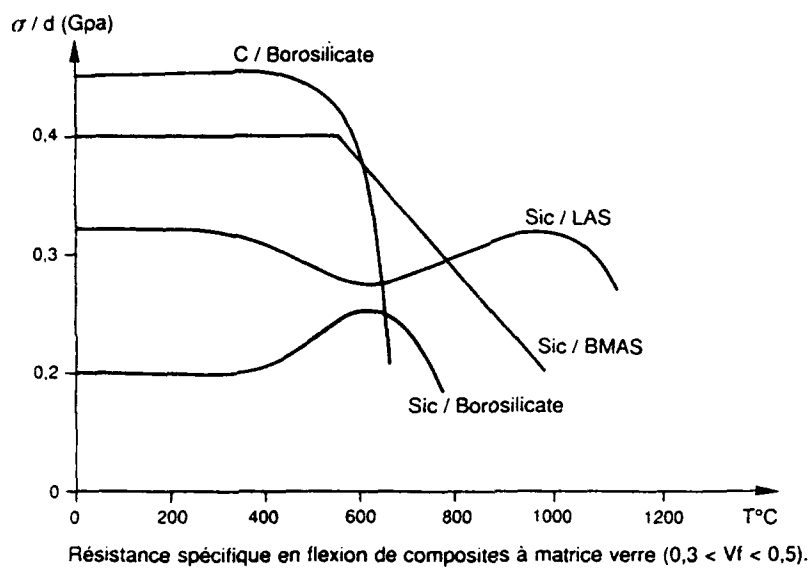


Fig. 9 : Résistance spécifique de divers composites à matrice verre



Fig. 10 : Eléments d'assemblage en composites C/C et C/SiC

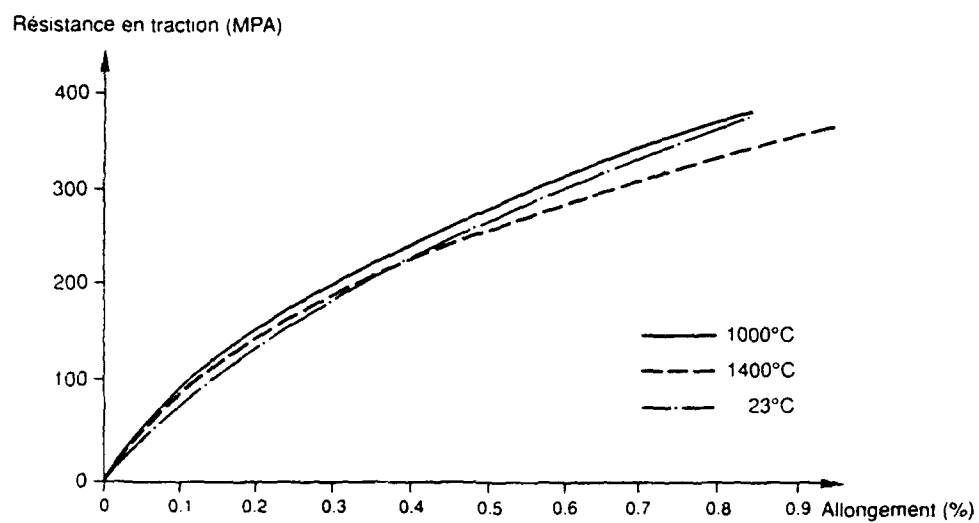


Fig. 11 : Courbes de déformation en traction de composites C/SiC

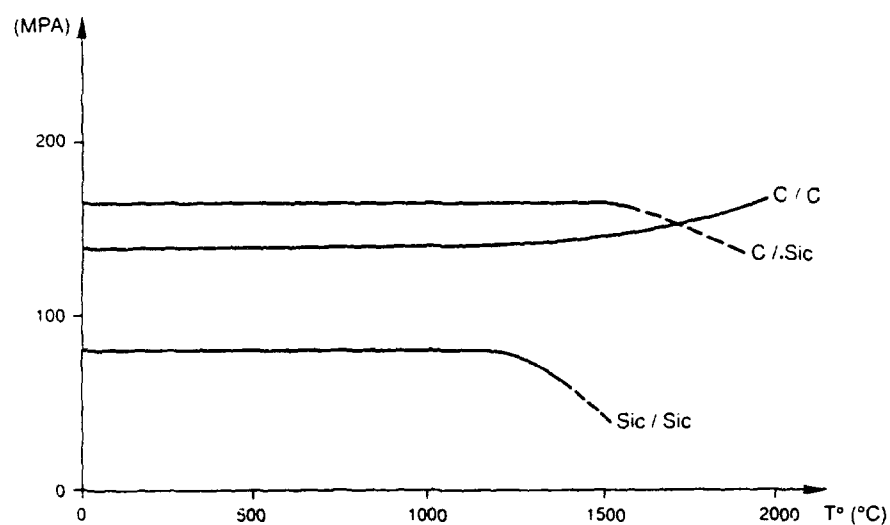


Fig. 12 : Résistance spécifique en traction des composites thermostrostructuraux

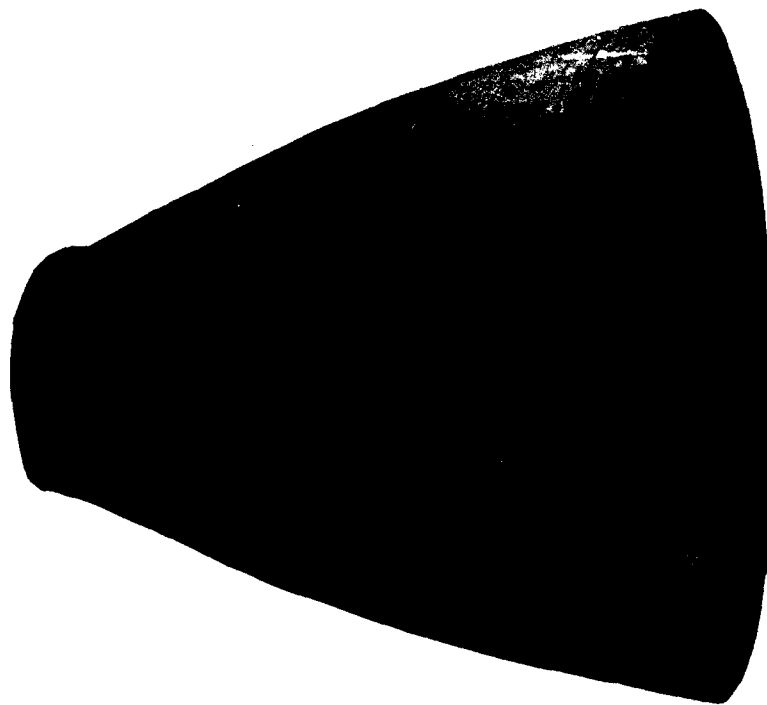


Fig. 13 : Divergent en Sepcarbinox Novoltex

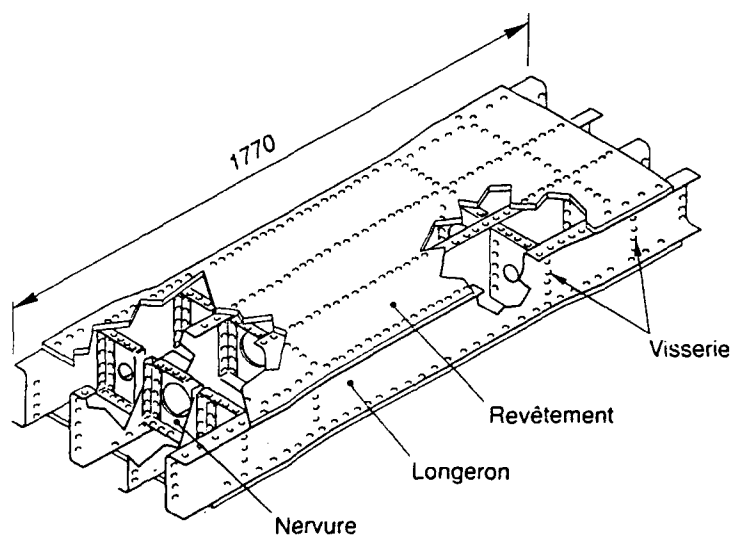


Fig. 14 : Structure pour caisson en Sepcarbinox Skinex



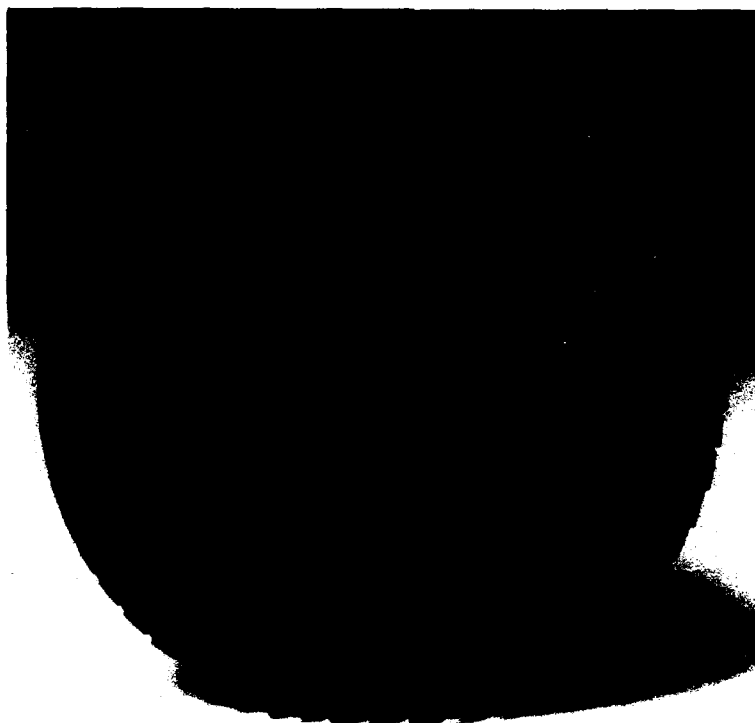


Fig. 15 : Roue de turbine en composite C/SiC

## COMPRESSEUR HAUTE TEMPERATURE

PIECE	FORMES ET DIMENSIONS (mm)	CONDITIONS AMBIANTES	TEMPERATURE DU MATERIAU	CONTRAINTES MAXIMALES	PROPRIETES SPECIFIQUES
CÔNE D'ENTRÉE	$\emptyset = 500$ $H = 300$ $E = 1 \text{ à } 3$	Air 20 B	1600 K	FAIBLE	
AUBE FIXE	$H = 500$ $C = 200$ $E = 10$	"	1600 K	FLEXION TORSION	<ul style="list-style-type: none"> <li>* TENUE EN FATIGUE</li> <li>* RÉSISTANCE À L'IMPACT</li> <li>* RIGIDITÉ</li> <li>* ÉTAT DE SURFACE ET GÉOMÉTRIE BORD DE FUITE</li> </ul>
AUBE MOBILE	$H = 500$ $C = 300$ $E = 20$	"	1600 K	TRACTION CENTRIFUGE FLEXION	<ul style="list-style-type: none"> <li>* TENUE EN FLUAGE ET FATIGUE</li> <li>* RÉSISTANCE MÉCANIQUE ÉLEVÉE DANS UNE DIRECTION</li> <li>* PAO SPÉCIFIQUE POUR MACHINE TOURNANTE</li> <li>* RÉSISTANCE À L'IMPACT</li> <li>* ÉTAT DE SURFACE ET GÉOMÉTRIE BORD DE FUITE</li> </ul>
CARTER	$\emptyset = 1600 \text{ à } 2000$ $H = 600 \text{ à } 2000$ $E = 5 \text{ à } 10$	"	1600 K	PRESSION INTERNE	<ul style="list-style-type: none"> <li>* MATÉRIAU ÉTANCHE</li> <li>* TENUE À L'IMPACT (RÉTENTION D'AUBE)</li> </ul>
CADRE SUPPORT	$\emptyset = 2000$	Air	1600 K	REPRISE D'EFFORT	* PIÈCE COMPLEXE FORTEMENT SOLlicitÉE
DISQUE	$\emptyset_{EXT} = 300 \text{ à } 600$ $\emptyset_{INT} = 200$ $E = 50 \text{ à } 100$	—	1600 K	ÉCLATEMENT TENUE DES AUBES	<ul style="list-style-type: none"> <li>* RÉSISTANCE MÉCANIQUE ÉLEVÉE</li> <li>* TENUE EN FATIGUE ET FLUAGE</li> </ul>
VOILE RACCORD AVEC ARBRE	TRONCONIQUE $\emptyset = 500$ $E = 5 \text{ à } 10$	—	1600 K	CISAILLEMENT	<ul style="list-style-type: none"> <li>* RÉSISTANCE SPÉCIFIQUE ÉLEVÉE</li> <li>* TENUE AU FLUAGE</li> </ul>

TABLEAU 1 : CONDITIONS DE FONCTIONNEMENT DES MATÉRIAUX DU COMPRESSEUR

## TURBINE DE TURBOFUSEE

PIECE	FORMES ET DIMENSIONS (MM)	CONDITIONS AMBIANTES	TEMPERATURE DU MATERIAU	CONTRAINTES MAXIMALES	PROPRIETES SPECIFIQUES
COLLECTEUR (TORE)  DISTRIBUTEUR SUPERSONIQUE	$\varnothing_{EXT} = 1000$ $\varnothing_{TORE} = 100$ $\varnothing_{TORE} = 2 \text{ à } 3$ $H_{AUBE} = 10$	$H_2$ ou $H_2/O_2$  100 BAR	$\leq 1000 \text{ K}$	TENUE A LA PRESSION	<ul style="list-style-type: none"> <li>* ETANCHEITE POUR LE TORE</li> <li>* PIECE COMPLEXE FORTEMENT CHARGEE</li> <li>* ETAT DE SURFACE A AMELIORER (DISTRIBUTEUR)</li> <li>* GEOMETRIE BORD DE FUITE A AFFINER (DISTRIBUTEUR)</li> <li>* FRAGILISATION A L'HYDROGENE</li> </ul>
AUBE RAPPORTÉE (MOBILE OU FIXE)	$H = 10 \text{ à } 50$ $C = 10 \text{ à } 20$ $E = 10$	"	"	EFFORT CENTRIFUGE FLEXION	<ul style="list-style-type: none"> <li>* FRAGILISATION A L'HYDROGENE</li> <li>* PAO ADAPTEE AU CHAMP CENTRIFUGE (AUBE MOBILE)</li> <li>* ETAT DE SURFACE ET GEOMETRIE</li> <li>* FATIGUE ET FLUAGE.</li> </ul>
DISQUE (AUBE RAPPORTÉE) ROUE (AUBE INTEGREE)	$\varnothing_{EXT} = 900$ $\varnothing_{INT} > 300$ $E = 5 \text{ à } 10$	"	"	ECLATEMENT RETENTION DES AUBES	<ul style="list-style-type: none"> <li>* FRAGILISATION <math>H_2</math></li> <li>* FATIGUE</li> <li>* RESISTANCE SPECIFIQUE ELEVEE.</li> </ul>
CARTER	$\varnothing = 1000$ $H = 300$ $E = 5$	"	"	TENUE A LA PRESSION	<ul style="list-style-type: none"> <li>* FRAGILISATION <math>H_2</math></li> <li>* RESISTANCE A L'IMPACT (ARRACHEMENT D'AUBE)</li> <li>* ETANCHEITE A CHAUD</li> </ul>
VOILE DE LIASON AVEC L'ARBRE	TRONCONIQUE $\varnothing = 800$ $E = 5 \text{ à } 10$	"	$\leq 1100 \text{ K}$	CISAILLEMENT EFFORT LOCALISE	<ul style="list-style-type: none"> <li>* HAUTES CARACTERISTIQUES MECANQUES</li> <li>* FLUAGE</li> </ul>

TABLEAU 2 : CONDITIONS ET FONCTIONNEMENT DES MATERIAUX DE LA TURBINE

## CARACTERISTIQUES DES MATERIAUX POUR HAUTES TEMPERATURES

	RE	BASE Ni MC (AMI)	BASE Nb	Ti AL	Ti <sub>3</sub> AL	SiC / Ti BASE 1D	SiC/VERRE 2D	SiC / SiC 2D	C / SiC 2D
DENSITE	1.25	8.6	8.6-9.5	3.8	4.2-4.7	3.3-3.8	2.5	2.5	2.1
DUCTILITE A 20°C (%)	10	16	20	0.5	4	// 0.9 ⊥ 0.4	< 1	0.3	0.9
DUCTILITE A 1000°C (%)		18	40	10	8	// 0.7 ⊥ 1	< 1	0.4	0.9
KIC (MPa - $\sqrt{m}$ )		70		15			~ 15	~ 15	~ 15
TEMPERATURE DE "FUSION"	1290	1350°C	2400°C	1450°C	1600°C				
TENUE A L'OXYDATION (MATERIAU NU)	400	1000°C	900°C	?	600°C	600°C	900°C	600°C	400°C
CONDUCTIVITE THERMIQUE (W/m.K)	150	20	~ 40	22	~ 20	// ⊥	// 1.5 ⊥ 1.5	// 17 ⊥ 7.5	// 12 ⊥ 4
COEFFICIENT DE DILATATION ( $\nu 10^{-6} / K$ )	14	15	8	10		// 6.5 ⊥	// 2.8 ⊥ 1.6	// 3 ⊥ 1.7	// 4.5 ⊥ 4.5
MODULE ELASTIQUE A L'AMBIANTE (GPa)	220	130		178	142			220*	90*

TABLEAU 3 : MATERIAUX POUR PROPULSION HYPERSONIQUE

\* MODULE A L'ORIGINE

REPORT DOCUMENTATION PAGE			
1. Recipient's Reference	2. Originator's Reference	3. Further Reference	4. Security Classification of Document
	AGARD-CP-479	ISBN 92-835-0594-8	UNCLASSIFIED
5. Originator	Advisory Group for Aerospace Research and Development North Atlantic Treaty Organization 7 rue Ancelle, 92200 Neuilly sur Seine, France		
6. Title	HYPERSONIC COMBINED CYCLE PROPULSION		
7. Presented at	the Propulsion and Energetics Panel, 75th Symposium, held in Madrid, Spain, 28th May to 1st June 1990.		
8. Author(s)/Editor(s)	Various		9. Date December 1990
10. Author's/Editor's Address	Various		11. Pages 486
12. Distribution Statement	This document is distributed in accordance with AGARD policies and regulations, which are outlined on the Outside Back Covers of all AGARD publications.		
13. Keywords/Descriptors			
<div style="display: flex; justify-content: space-between;"> <div> <p>Hypersonic vehicles</p> <p>Computational fluid dynamics</p> <p>Hypersonic flow</p> <p>Heat resistant materials</p> </div> <div> <p>Supersonic combustion ramjet engines</p> <p>Missile propulsion</p> <p>Turbojet engines</p> </div> </div>			
14. Abstract			
<p>Contains the 34 papers presented at the Propulsion and Energetics Panel 75th Symposium on "Hypersonic Combined Cycle Propulsion", which was held 28 May—1 June 1990 in Madrid, Spain.</p> <p>The Symposium was arranged in the following sessions: Keynote (1); Technical Review of Hypersonic Propulsion/Mission Requirements (4); Propulsion Concepts (8); Air Intake Flow (4); Turbomachinery (2); Combustion and Ram/Scramjets (9); Nozzle Flow (5); High Temperature Materials (2). The Technical Evaluation Report is included at the beginning of the Proceedings. Reports of the discussions follow each paper.</p> <p>The Symposium offered a large number of experts the opportunity to appreciate and discuss the present status in the broad scope of subjects contributing to hypersonic combined cycle propulsion. Considerable progress in design and analysis, using computational fluid dynamics techniques, was reported. A better fundamental understanding and experimental effort is still required, and in some areas suitable test facilities are not yet available. Subjects for future dedicated meetings are suggested.</p>			

<p>AGARD Conference Proceedings No.479 Advisory Group for Aerospace Research and Development, NATO HYPERSONIC COMBINED CYCLE PROPULSION Published December 1990 486 pages</p> <p>Contains the 34 papers presented at the Propulsion and Energetics Panel 75th Symposium on "Hypersonic Combined Cycle Propulsion", which was held 28 May—1 June 1990 in Madrid, Spain.</p> <p>The Symposium was arranged in the following sessions: Keynote (1); Technical Review of Hypersonic Propulsion/ Mission Requirements (4); Propulsion Concepts (8); Air Intake Flow (4); Turbomachinery (2); Combustion and</p> <p>P.T.O.</p>	<p>AGARD-CP-479</p> <p>Hypersonic vehicles Computational fluid dynamics Hypersonic flow Heat resistant materials Supersonic combustion ramjet engines Missile propulsion Turbojet engines</p>	<p>AGARD Conference Proceedings No.479 Advisory Group for Aerospace Research and Development, NATO HYPERSONIC COMBINED CYCLE PROPULSION Published December 1990 486 pages</p> <p>Contains the 34 papers presented at the Propulsion and Energetics Panel 75th Symposium on "Hypersonic Combined Cycle Propulsion", which was held 28 May—1 June 1990 in Madrid, Spain.</p> <p>The Symposium was arranged in the following sessions: Keynote (1); Technical Review of Hypersonic Propulsion/ Mission Requirements (4); Propulsion Concepts (8); Air Intake Flow (4); Turbomachinery (2); Combustion and</p> <p>P.T.O.</p>	<p>AGARD-CP-479</p> <p>Hypersonic vehicles Computational fluid dynamics Hypersonic flow Heat resistant materials Supersonic combustion ramjet engines Missile propulsion Turbojet engines</p>	<p>AGARD-CP-479</p> <p>Hypersonic vehicles Computational fluid dynamics Hypersonic flow Heat resistant materials Supersonic combustion ramjet engines Missile propulsion Turbojet engines</p>
<p>AGARD Conference Proceedings No.479 Advisory Group for Aerospace Research and Development, NATO HYPERSONIC COMBINED CYCLE PROPULSION Published December 1990 486 pages</p> <p>Contains the 34 papers presented at the Propulsion and Energetics Panel 75th Symposium on "Hypersonic Combined Cycle Propulsion", which was held 28 May—1 June 1990 in Madrid, Spain.</p> <p>The Symposium was arranged in the following sessions: Keynote (1); Technical Review of Hypersonic Propulsion/ Mission Requirements (4); Propulsion Concepts (8); Air Intake Flow (4); Turbomachinery (2); Combustion and</p> <p>P.T.O.</p>	<p>AGARD-CP-479</p> <p>Hypersonic vehicles Computational fluid dynamics Hypersonic flow Heat resistant materials Supersonic combustion ramjet engines Missile propulsion Turbojet engines</p>	<p>AGARD Conference Proceedings No.479 Advisory Group for Aerospace Research and Development, NATO HYPERSONIC COMBINED CYCLE PROPULSION Published December 1990 486 pages</p> <p>Contains the 34 papers presented at the Propulsion and Energetics Panel 75th Symposium on "Hypersonic Combined Cycle Propulsion", which was held 28 May—1 June 1990 in Madrid, Spain.</p> <p>The Symposium was arranged in the following sessions: Keynote (1); Technical Review of Hypersonic Propulsion/ Mission Requirements (4); Propulsion Concepts (8); Air Intake Flow (4); Turbomachinery (2); Combustion and</p> <p>P.T.O.</p>	<p>AGARD-CP-479</p> <p>Hypersonic vehicles Computational fluid dynamics Hypersonic flow Heat resistant materials Supersonic combustion ramjet engines Missile propulsion Turbojet engines</p>	<p>AGARD-CP-479</p> <p>Hypersonic vehicles Computational fluid dynamics Hypersonic flow Heat resistant materials Supersonic combustion ramjet engines Missile propulsion Turbojet engines</p>

<p>Ram/Scramjets (9); Nozzle Flow (5); High Temperature Materials (2). The Technical Evaluation Report is included at the beginning of the Proceedings. Reports of the discussions follow each paper.</p> <p>The Symposium offered a large number of experts the opportunity to appreciate and discuss the present status in the broad scope of subjects contributing to hypersonic combined cycle propulsion. Considerable progress in design and analysis, using computational fluid dynamics techniques, was reported. A better fundamental understanding and experimental effort is still required, and in some areas suitable test facilities are not yet available. Subjects for future dedicated meetings are suggested.</p> <p>ISBN 92-835-0594-8</p>	<p>Ram/Scramjets (9); Nozzle Flow (5); High Temperature Materials (2). The Technical Evaluation Report is included at the beginning of the Proceedings. Reports of the discussions follow each paper.</p> <p>The Symposium offered a large number of experts the opportunity to appreciate and discuss the present status in the broad scope of subjects contributing to hypersonic combined cycle propulsion. Considerable progress in design and analysis, using computational fluid dynamics techniques, was reported. A better fundamental understanding and experimental effort is still required, and in some areas suitable test facilities are not yet available. Subjects for future dedicated meetings are suggested.</p> <p>ISBN 92-835-0594-8</p>
<p>Ram/Scramjets (9); Nozzle Flow (5); High Temperature Materials (2). The Technical Evaluation Report is included at the beginning of the Proceedings. Reports of the discussions follow each paper.</p> <p>The Symposium offered a large number of experts the opportunity to appreciate and discuss the present status in the broad scope of subjects contributing to hypersonic combined cycle propulsion. Considerable progress in design and analysis, using computational fluid dynamics techniques, was reported. A better fundamental understanding and experimental effort is still required, and in some areas suitable test facilities are not yet available. Subjects for future dedicated meetings are suggested.</p> <p>ISBN 92-835-0594-8</p>	<p>Ram/Scramjets (9); Nozzle Flow (5); High Temperature Materials (2). The Technical Evaluation Report is included at the beginning of the Proceedings. Reports of the discussions follow each paper.</p> <p>The Symposium offered a large number of experts the opportunity to appreciate and discuss the present status in the broad scope of subjects contributing to hypersonic combined cycle propulsion. Considerable progress in design and analysis, using computational fluid dynamics techniques, was reported. A better fundamental understanding and experimental effort is still required, and in some areas suitable test facilities are not yet available. Subjects for future dedicated meetings are suggested.</p> <p>ISBN 92-835-0594-8</p>

AGARD

NATO  OTAN

7 RUE ANCELLE · 92200 NEUILLY-SUR-SEINE

FRANCE

Téléphone (1)47.38.57.00 · Telex 610 176

DIFFUSION DES PUBLICATIONS

AGARD NON CLASSIFIEES

L'AGARD ne détient pas de stocks de ses publications, dans un but de distribution générale à l'adresse ci-dessus. La diffusion initiale des publications de l'AGARD est effectuée auprès des pays membres de cette organisation par l'intermédiaire des Centres Nationaux de Distribution suivants. Ces Centres disposent parfois d'exemplaires additionnels; dans les cas contraire, on peut se procurer ces exemplaires sous forme de microfiches ou de microcopies auprès des Agences de Vente dont la liste suit.

CENTRES DE DIFFUSION NATIONAUX

**ALLEMAGNE**

Fachinformationszentrum,  
Karlsruhe  
D-7514 Eggenstein-Leopoldshafen 2

**BELGIQUE**

Coordonnateur AGARD-VSL  
Etat-Major de la Force Aérienne  
Quartier Reine Elisabeth  
Rue d'Evere, 1140 Bruxelles

**CANADA**

Directeur du Service des Renseignements Scientifiques  
Ministère de la Défense Nationale  
Ottawa, Ontario K1A 0K2

**DANEMARK**

Danish Defence Research Board  
Ved Idraetsparken 4  
2100 Copenhagen Ø

**ESPAGNE**

INTA (AGARD Publications)  
Pintor Rosales 34  
28008 Madrid

**ETATS-UNIS**

National Aeronautics and Space Administration  
Langley Research Center  
M/S 180  
Hampton, Virginia 23665

**FRANCE**

O.N.E.R.A. (Direction)  
29, Avenue de la Division Leclerc  
92320, Châtillon sous Bagneux

**GRECE**

Hellenic Air Force  
Air War College  
Scientific and Technical Library  
Dekelia Air Force Base  
Dekelia, Athens TGA 1010

**ISLANDE**

Director of Aviation  
c/o Flugrad  
Reykjavik

**ITALIE**

Aeronautica Militare  
Ufficio del Delegato Nazionale all'AGARD  
3 Piazzale Adenauer  
00144 Roma EUR

**LUXEMBOURG**

Voir Belgique

**NORVEGE**

Norwegian Defence Research Establishment  
Attn: Biblioteket  
P.O. Box 25  
N-2007 Kjeller

**PAYS-BAS**

Netherlands Delegation to AGARD  
National Aerospace Laboratory NLR  
Kluyverweg 1  
2629 HS Delft

**PORTUGAL**

Portuguese National Coordinator to AGARD  
Gabinete de Estudos e Programas  
CLAFIA  
Base de Alfragide  
Alfragide  
2700 Amadora

**ROYAUME UNI**

Defence Research Information Centre  
Kentigern House  
65 Brown Street  
Glasgow G2 8EX

**TURQUIE**

Millî Savunma Bakanlığı (MSB)  
ARGE Daire Başkanlığı (ARGE)  
Ankara

LE CENTRE NATIONAL DE DISTRIBUTION DES ETATS-UNIS (NASA) NE DETIENT PAS DE STOCKS  
DES PUBLICATIONS AGARD ET LES DEMANDES D'EXEMPLAIRES DOIVENT ETRE ADRESSEES DIRECTEMENT  
AU SERVICE NATIONAL TECHNIQUE DE L'INFORMATION (NTIS) DONT L'ADRESSE SUIT.

AGENCES DE VENTE

National Technical Information Service  
(NTIS)  
5285 Port Royal Road  
Springfield, Virginia 22161  
Etats-Unis

ESA/Information Retrieval Service  
European Space Agency  
10, rue Mario Nikis  
75015 Paris  
France

The British Library  
Document Supply Division  
Boston Spa, Wetherby  
West Yorkshire LS23 7BQ  
Royaume Uni

Les demandes de microfiches ou de photocopies de documents AGARD doivent comporter le numéro de série AGARD, le titre, le nom de l'auteur ou du rédacteur-coordonnateur et la date de publication. Les demandes adressées au NTIS doivent comporter le numéro matricule NASA du rapport. Des références bibliographiques complètes ainsi que des résumés des publications AGARD figurent dans les journaux suivants:

Scientific and Technical Aerospace Reports (STAR)  
publié par la NASA Scientific and Technical  
Information Branch  
NASA Headquarters (NIT-40)  
Washington D.C. 20546  
Etats-Unis

Government Reports Announcements (GRA)  
publié par National Technical Information Services.  
Springfield  
Virginia 22161  
Etats-Unis



Imprimé par Specialised Printing Services Limited  
40 Chigwell Lane, Loughton, Essex IG10 3TZ

**AGARD**

**NATO OTAN**

**7 RUE ANCELLE · 92200 NEUILLY-SUR-SEINE**

**FRANCE**

**Telephone (1)47.38.57.00 · Telex 610 176**

**Telefax (1)47.38.57.99**

**DISTRIBUTION OF UNCLASSIFIED**

**AGARD PUBLICATIONS**

AGARD does NOT hold stocks of AGARD publications at the above address for general distribution. Initial distribution of AGARD publications is made to AGARD Member Nations through the following National Distribution Centres. Further copies are sometimes available from these Centres, but if not may be purchased in Microfiche or Photocopy form from the Sales Agencies listed below. N.B. NATO UNCLASSIFIED publications such as this are NOT available from the Sales Agencies.

**NATIONAL DISTRIBUTION CENTRES**

**BELGIUM**

Coordonnateur AGARD — VSL  
Etat-Major de la Force Aérienne  
Quartier Reine Elisabeth  
Rue d'Evere, 1140 Bruxelles

**CANADA**

Director Scientific Information Services  
Dept of National Defence  
Ottawa, Ontario K1A 0K2

**DENMARK**

Danish Defence Research Board  
Ved Idraetsparken 4  
2100 Copenhagen Ø

**FRANCE**

O.N.E.R.A. (Direction)  
29 Avenue de la Division Leclerc  
92320 Châtillon

**GERMANY**

Fachinformationszentrum  
Karlsruhe  
D-7514 Eggenstein-Leopoldshafen 2

**GREECE**

Hellenic Air Force  
Air War College  
Scientific and Technical Library  
Dekelia Air Force Base  
Dekelia, Athens TGA 1010

**ICELAND**

Director of Aviation  
c/o Flugrad  
Reykjavik

**ITALY**

Aeronautica Militare  
Ufficio del Delegato Nazionale all'AGARD  
3 Piazzale Adenauer  
00144 Roma/EUR

**LUXEMBOURG**

See Belgium

**NETHERLANDS**

Netherlands Delegation to AGARD  
National Aerospace Laboratory, NLR  
Kluyverweg 1  
2629 HS Delft

**NORWAY**

Norwegian Defence Research Establishment  
Attn: Biblioteket  
P.O. Box 25  
N-2007 Kjeller

**PORTUGAL**

Portuguese National Coordinator to AGARD  
Gabinete de Estudos e Programas  
CLAF  
Base de Alfragide  
Alfragide  
2700 Amadora

**SPAIN**

INTA (AGARD Publications)  
Pintor Rosales 34  
28008 Madrid

**TURKEY**

Milli Savunma Başkanlığı (MSB)  
ARGE Daire Başkanlığı (ARGE)  
Ankara

**UNITED KINGDOM**

Defence Research Information Centre  
Kentigern House  
65 Brown Street  
Glasgow G2 8EX

**UNITED STATES**

National Aeronautics and Space Administration (NASA)  
Langley Research Center  
M/S 180  
Hampton, Virginia 23665

**THE UNITED STATES NATIONAL DISTRIBUTION CENTRE (NASA) DOES NOT HOLD STOCKS OF AGARD PUBLICATIONS, AND APPLICATIONS FOR COPIES SHOULD BE MADE DIRECT TO THE NATIONAL TECHNICAL INFORMATION SERVICE (NTIS) AT THE ADDRESS BELOW.**

**SALES AGENCIES**

National Technical  
Information Service (NTIS)  
5285 Port Royal Road  
Springfield, Virginia 22161  
United States

ESA/Information Retrieval Service  
European Space Agency  
10, rue Mario Nikis  
75015 Paris  
France

The British Library  
Document Supply Centre  
Boston Spa, Wetherby  
West Yorkshire LS23 7BQ  
United Kingdom

Requests for microfiche or photocopies of AGARD documents should include the AGARD serial number, title, author or editor, and publication date. Requests to NTIS should include the NASA accession report number. Full bibliographical references and abstracts of AGARD publications are given in the following journals:

Scientific and Technical Aerospace Reports (STAR)  
published by NASA Scientific and Technical  
Information Branch  
NASA Headquarters (NIT-40)  
Washington D.C. 20546  
United States

Government Reports Announcements (GRA)  
published by the National Technical  
Information Services, Springfield  
Virginia 22161  
United States



Printed by Specialised Printing Services Limited  
40 Chigwell Lane, Loughton, Essex IG10 3TZ